

THIS FILE IS MADE AVAILABLE THROUGH THE DECLASSIFICATION EFFORTS AND RESEARCH OF:

THE BLACK VAULT

THE BLACK VAULT IS THE LARGEST ONLINE FREEDOM OF INFORMATION ACT / GOVERNMENT RECORD CLEARING HOUSE IN THE WORLD. THE RESEARCH EFFORTS HERE ARE RESPONSIBLE FOR THE DECLASSIFICATION OF THOUSANDS OF DOCUMENTS THROUGHOUT THE U.S. GOVERNMENT, AND ALL CAN BE DOWNLOADED BY VISITING:

[HTTP://WWW.BLACKVAULT.COM](http://www.blackvault.com)

YOU ARE ENCOURAGED TO FORWARD THIS DOCUMENT TO YOUR FRIENDS, BUT PLEASE KEEP THIS IDENTIFYING IMAGE AT THE TOP OF THE .PDF SO OTHERS CAN DOWNLOAD MORE!



REPLY TO
ATTENTION OF:

DEPARTMENT OF THE ARMY
US ARMY RESEARCH, DEVELOPMENT AND ENGINEERING COMMAND
5183 BLACKHAWK ROAD
ABERDEEN PROVING GROUND MD 21010-5424

September 11, 2009

Office of Chief Counsel

Mr. John Greenwald



Dear Mr. Greenwald:

I have enclosed the following record you requested in your Freedom of Information Action requested numbered FP-09-028688/FA-09-0060. The record was previously cleared for public release.

1. Title: Proceedings of the U.S. Army Chemical Research, Development and Engineering Center Scientific Conference on Chemical Defense Research (1991) Held in Aberdeen Proving Ground, Maryland on 19-22 November 1991.

2. Accession Number: ADA269546

3. Date: June 1993

Should you have any questions or concerns regarding your request I can be reached at (410) 436-2289 or brian.may3@us.army.mil

Sincerely,

//SIGNED - BAM//
Brian A. May
FOIA Officer, HQ RDECOM

Enclosure

AD-A269 546



12

EDGEWOOD
RESEARCH,
DEVELOPMENT &
ENGINEERING
CENTER

ERDEC-SP-002

PROCEEDINGS
OF THE 1991 U.S. ARMY CHEMICAL RESEARCH,
DEVELOPMENT AND ENGINEERING CENTER
SCIENTIFIC CONFERENCE ON CHEMICAL DEFENSE RESEARCH
19-22 NOVEMBER 1991

DTIC
ELECTE
SEP 22 1993
S A D

Joseph D. Williams, Jr.
Patricia J. Reeves

RESEARCH AND TECHNOLOGY DIRECTORATE

June 1993

Approved for public release; distribution is unlimited.

U.S. ARMY
CHEMICAL
AND BIOLOGICAL
DEFENSE AGENCY



Aberdeen Proving Ground, Maryland 21010-54

93-21908



93 9 21 02 T

Disclaimer

The findings in this report are not to be construed as an official Department of the Army position unless so designated by other authorizing documents.

REPORT DOCUMENTATION PAGE

Form Approved
OMB No 0704-0188

Public reporting burden for this collection of information is estimated to average 1 hour per response, including the time for reviewing instructions, searching existing data sources, gathering and maintaining the data needed, and completing and reviewing the collection of information. Send comments regarding this burden estimate or any other aspect of this collection of information, including suggestions for reducing this burden, to Washington Headquarters Services, Directorate for Information Operations and Reports, 1215 Jefferson Davis Highway, Suite 1204, Arlington, VA 22202-4302, and to the Office of Management and Budget, Paperwork Reduction Project (0704-0188), Washington, DC 20503.

1. AGENCY USE ONLY (Leave blank) 2. REPORT DATE
1993 June 3. REPORT TYPE AND DATES COVERED
Final, 91 Nov - 91 Nov

4. TITLE AND SUBTITLE
Proceedings of the 1991 U.S. Army Chemical Research, Development and Engineering Center Scientific Conference on Chemical Defense Research, 19-22 November 1991

5. FUNDING NUMBERS
PR-10161102A71A

6. AUTHOR(S)
Joseph D. Williams, Jr. (Compiler); and Patricia J. Reeves (Editor)

7. PERFORMING ORGANIZATION NAME(S) AND ADDRESS(ES)
DIR, ERDEC,* ATTN: SCBRD-RT, APG, MD 21010-5423

8. PERFORMING ORGANIZATION REPORT NUMBER
ERDEC-SP-002

9. SPONSORING / MONITORING AGENCY NAME(S) AND ADDRESS(ES)

10. SPONSORING / MONITORING AGENCY REPORT NUMBER

11. SUPPLEMENTARY NOTES
*When this meeting was held, ERDEC was known as the U.S. Army Chemical Research, Development and Engineering Center, and the authors were assigned to the Research and Research Development and Engineering Support Directorates, respectively.

12a. DISTRIBUTION / AVAILABILITY STATEMENT
Approved for public release; distribution is unlimited.

12b. DISTRIBUTION CODE

13. ABSTRACT (Maximum 200 words)

In this report, 120 papers presented at the 1991 Scientific Conference on Chemical Defense Research are included under the heading of Protection, Synthesis and Properties, Detection, Toxicology, Biotechnology, Environmental Studies, NMR Investigations, Fluid Dynamics, Materials, Decontamination, and Computational Chemistry. In addition, papers are included for posters of each project.

14. SUBJECT TERMS				15. NUMBER OF PAGES
NMR	Synthesis	Materials	Decontamination	1054
Detection	Properties	Biotechnology	Environmental studies	16. PRICE CODE
Toxicology	Protection	Fluid dynamics	Computational chemistry	

17. SECURITY CLASSIFICATION OF REPORT UNCLASSIFIED	18. SECURITY CLASSIFICATION OF THIS PAGE UNCLASSIFIED	19. SECURITY CLASSIFICATION OF ABSTRACT UNCLASSIFIED	20. LIMITATION OF ABSTRACT UL
---	--	---	----------------------------------

Blank

PREFACE

The work described in this report was authorized under Project No. 10161102A71A, Research in CW/CB Defense. This work was started and completed in November 1991.

The 1991 U.S. Army Chemical Research, Development and Engineering Center (CRDEC) Scientific Conference on Chemical Defense Research was held 19-22 November 1991 at the Edgewood Area of Aberdeen Proving Ground, MD. When this Conference was held, the U.S. Army Edgewood Research, Development and Engineering Center was known as CRDEC. The Conference is held annually under the auspices of the Director of Research and is an informal forum for scientific exchange and stimulation among investigators in the wide disciplines related to chemical defense research.

The participants develop some familiarity with U.S. Army basic research in chemical defense and also become personally acquainted with the other investigators and their research interests and capabilities. Each attendee is invited to talk on any aspect of a topic of interest and may make last-minute changes or alterations in his talk as the flow of ideas in the Conference develops.

The papers in these proceedings tend to correspond closely to what was presented at the Conference; however, there is not an exact correspondence.* The reader will find the items related to the Conference itself (the list of attendees, the agenda, and the content of the Conference's sessions) in the appendixes following the papers collected for these proceedings and the indexes pertaining to them.

The use of trade names or manufacturers' names in this report does not constitute an official endorsement of any commercial products. This report may not be cited for purposes of advertisement.

This report has been approved for release to the public. Registered users should request additional copies from the Defense Technical Information Center; unregistered users should direct such requests to the National Technical Information Service.

Acknowledgments

The compiler of the proceedings acknowledges Dorothy Berg (CRDEC): Betty Ward, Nancy Yarrington, Diana McQuestion, Lisa McCormick, Judy Cole, Keith Hicks, and Jeanne Hawtin (Science and Technology Corporation, Hampton, VA) for their assistance in compiling these proceedings.

*In some instances, papers from the Conference are not included. The titles of the missing papers are listed on the first page of the applicable section.

Blank



JOSEPH E. MATTA
1948-1991

Accession For:	
NTIS CRA&I	<input checked="" type="checkbox"/>
ERIC TAB	<input type="checkbox"/>
Unannounced	<input type="checkbox"/>
Justification	<input type="checkbox"/>
By _____	
Distribution/ _____	
Availability Codes	
Dist	Avail and/or Special
A-1	

DTIC QUALITY INSPECTED 1

Dr. Joseph Matta was an exceptional researcher who made significant contributions to the Army. He impacted on everyone he met. He was a warm, sensitive person, a good friend to many of us and an exceptional family man. Joe received his Ph.D degree in physics in 1974 from Lehigh University. He came to CRDEC in 1978 as a research physicist following a brief assignment at the U.S. Bureau of Mines. AT CRDEC, he became an international authority on the relation between the physical properties of non-Newtonian fluids and their break up into liquid aerosols when subjected to various shear forces. His work has led to 40 publications and 7 patents. In 1980 he received the award for the outstanding research paper at this conference. In 1983 he was selected for an Army Research and Development Achievement Award for his work on characterizing the break-up of viscoelastic fluids. Later in FY88, he received the outstanding CRDEC In-house Laboratory Independent Research Award for developing the new elongational rheometer based on his studies with the falling cylinder. In addition to Joe's contributions to the theory and methodology of fluids, Joe's research has had direct impact on a number of programs at CRDEC. He developed a small scale dissemination device to develop data to predict liquid break-up. Munitions Directorate used this method to select the polymer and concentration for the chemical fill for the MLRS Binary Chemical Warhead, a major program which helped convince the Soviet Union to seek a chemical weapons treaty. His recent efforts have been directed toward support of the Strategic Defense Initiative. At the time of his death he was involved with planning experiments and evaluating data to predict the fate of CW liquids in the atmosphere resulting from interception by antimissile missiles.

Because of the nature of Joe's research and expertise, he was frequently at the center of controversy. Joe distinguished himself by focusing the discussions on scientific and engineering issues that could be measured rather than permitting decisions to be made on the basis of politics or program expediency. CRDEC was very fortunate to have Joe Matta as an employee for a dozen years. The outstanding research that Joe produced will continue to contribute to programs for many years. Moreover, his high professional standards, his quiet unpretentious manner, and his approach to solving rather than creating problems serves as a model for all CRDEC employees.

Blank

Keynote Address

by

Captain Christopher J. Cramer

Ladies and gentlemen I suspect that when you first glanced at our programs and saw the subject of this keynote address, you thought "Well of course, this being the first Chemical Defense conference after Desert Storm, it's got to be about the war." I also suspect you continued on to the speaker's name and thought, "Well, I can understand that Schwarzkopf is busy these days, but the best they could get was a lowly CAPTAIN?"

Well, it is certainly true that I will not be able today to shed much more light on Operation DESERT STORM from a geopolitical perspective. But it is also true that the American consciousness and our understanding of our nation's conflicts has tended more to be shaped by the reminiscences of individual soldiers than it has been by the memoirs of those who set the events in motion. Perhaps because the earthy prose of the combatants reaches us more profoundly than does the austere bureaucratized endemic to governmental levels. Or perhaps we find, however misguided, the battlefield to be more romantic than say, the White House situation room.

In any case, I will be speaking today from a purely experiential viewpoint. In some sense I am uniquely qualified to regale this particular gathering with war stories. For on the one hand, I was deployed far enough forward to hear the sounds of the guns (albeit, fortunately, never to be shot at), so perhaps I can give you insight into things CNN was never able to capture. And on the other hand, I worked with a combat support unit which played some role in chemical defense, so where possible, I can highlight those issues.

But I'm getting ahead of myself. I really should start in December of 1990, when a representative of the Chemical Branch came to Edgewood to speak with me, and other chemical officers here at the Center, about our future careers. He assured me that I was at a point in my career where the odds of my being sent to Southwest Asia were virtually nil. Of course, given the quality of Branch's advice in general, I should have gone home and packed my bags that evening. However, things didn't happen quite that quickly.

On January 16th, in the early evening, I was sitting in my car in a nearby hotel parking lot. I was waiting for a friend of mine who was here training for a DESERT STORM related mission. He

was scheduled to depart for Saudi Arabia the next day, and I had invited him to join my wife and I for dinner that night. Shortly after 6 PM, National Public Radio broke into its normal evening news to bring live coverage from reporters in Baghdad, where the first bombs were beginning to fall, and I knew we were at war. Certain events serve as temporal milestones in our memories and, much like the Challenger disaster, or some of the appalling assassinations of the last few decades, I suspect that many of us will continue to have vivid memories of where we were when we first heard the sirens over Baghdad. It has been said that each American generation has had a war to define it --ours was to be no exception. My friend left the next morning and I wished him Godspeed.

For myself, and ten of my colleagues here at the Center, the call was not much longer in coming. On the night of Wednesday, February 6th, we were selected to fill a requirement for chemical officers in the VII Corps, with no further details available. All we knew for sure was that we had to be at Fort Benning on Monday the 11th, and could expect to leave from there by the 14th. I pointed out to my wife that future Valentine's Days could only get better, but she was not particularly comforted.

From working at the Center those of us selected knew only too well how high the threat level was for the Iraqi employment of chemical and biological weapons. At Ft. Benning, it became apparent that the rest of the Army was taking the threat equally as seriously. Considerable time was spent refreshing individuals on the use of protective equipment, nerve agent antidote kits, anti-convulsant injectors and first aid techniques. The final test to ensure that each soldier's protective mask fit him or her was a period in a CS chamber. Taking no chances, the local cadre had made the gas concentration so high that exposed skin felt as though it were being assaulted by fire ants, but no one complained. It is worth noting here that this Center played a key role in ensuring that no soldier left for Saudi Arabia without a perfectly fitted mask. Support teams visited dozens of posts from which deployments were scheduled to provide both assistance and a supply of masks of unusual sizes.

After a whirlwind of preparation, the ten of us became two when the first plane manifest was announced. CPT Dave Flint and I boarded a Tower Air 747 and I began to feel the first hints of surreality as a smiling stewardess explained, in between pointing out the usual emergency exits and flotation cushions, that rifles were to be laid on the floor pointing forward and that pistols should be holstered. Later, the comfortable familiarity of in-flight movies was contrasted by the dozens of heavily armed security personnel surrounding our plane during refueling in Brussels. And finally, we flew in low over the moonscape of the Arabian desert to arrive at King Fahd airport at dusk. Exiting

the plane, the first thing we were told was the location of the nearest ditch in the event of a Scud missile attack. I am sure that many of us felt the urge to suggest to Toto that we were pretty sure we weren't in Kansas anymore.

Replacement centers are always a madhouse, and this first one, for the Army Central Command, was no exception -- especially since the airfield was under blackout. Simply finding one's own baggage was a major challenge. A 747 holds roughly 460 passengers, which translates to 920 duffle bags and 460 field packs. The observation, "Mine is the green one" is not particularly helpful. This situation recurred several times and earned the fond nickname of "The Duffle-Bag Drag". However, after a few iterations of the Drag, orders were taken, orders were cut and Dave and I boarded a C-130 for the flight up to Al Qaysumah and the Replacement Detachment for VII Corps.

We unloaded in a driving rain, which was to begin my experience with the wettest desert one could possibly imagine. I will offer no other observation on this except to note that engineers could contribute greatly to future operations by coming up with canvas extensions for command tracks which can be attached together in a sloping fashion. Many times Lake Persia came crashing through into our Tactical Operations Center after having built up overhead during a heavy rainstorm, leading to much of that earthy prose I mentioned a bit earlier.

We waited at Al Qaysumah for several hours. However, buses repeatedly described as only an hour away somehow never managed to arrive. Eventually, we piled into 5-ton trucks for a ride to the VII Corps replacement center in the vicinity of Hafar al Batin. This gave us the opportunity at about three AM, to learn a new Army acronym -- LID. It stands for "Lost in Desert," which is what we were, mostly wondering how close we were to the border and how far back Air Force free fire zones extended. Finally, around four AM we finally found our way to the repo depot.

I say this whimsically, but frankly this was one of the greatest challenges of Operations DESERT SHIELD and STORM -- figuring out where on Earth one was. The desert is notoriously devoid of landmarks to include any hint of roads. While the dirt and sand are generally packed firmly enough to allow one to travel anywhere, this just means that there are an infinite number of ways to get lost! Fortunately, a number of GPS systems, for geopositioning satellite, were available. They were worth their weight in gold. Any convoy travelling without at least one GPS was asking to get lost.

On the next day, Dave and I parted company. My orders came through for a new home -- the 7th Engineer Brigade, commanded by COL Samuel C. Raines. This brigade was the VII Corps, Corps

Engineers. For those of you not familiar with the various missions undertaken by Corps Engineers, they include everything from breaching minefields and putting in obstacles to building or denying (that is, destroying) roads, helipads, logbases, ammo dumps, POW camps, etc. Engineers make maps, they build bridges, they drill water wells and they fight fires. Engineers are everywhere on the battlefield, and 7th Brigade was no exception. Indeed, it became the largest Engineer Brigade ever formed since World War II. Arriving on February 18th, I was assigned to the S-3, or operations, section of the Brigade staff.

Typically, chemical officers within a tactical staff spend 90% of their time on normal operational matters and 10% on chemical defense related matters. Needless to say, in Saudi Arabia with 7 days to go before G-day, things were anything but typical, and I spent 100% of my time on chemical defense. The Brigade, like many other large units in this operation, was composed of active, reserve, and National Guard components. Between them, they had widely disparate levels of chemical defense equipment. A major effort was required to cross-level stockages of protective garments, decontaminants, chemical agent alarms and Chemical Agent Monitors to ensure that all soldiers had adequate personal protection and to try to provide units facing the highest risk with a reasonable amount of contingency equipment.

By this point, the rapidity of the troop buildup in-theater had made the difficult logistics of ensuring that every single soldier had two sets of chemical protective garments a three-star issue. Lieutenant General Franks, commanding VII Corps, left no doubt in anyone's mind on this matter. Returning again to my scientist's perspective, I can detail at least two challenges with respect to this issue. The first involves decreasing the weight and bulkiness of the protective overgarments without diminishing their effectiveness. The list of absolutely essential equipment which each soldier must carry expands rapidly in a combat situation, and every pound counts. Additionally, decreasing the number of sizes which must be handled by designing the garments to be size-adjustable in some manner would vastly decrease the logistics nightmare. While most soldiers had one set which fit reasonably well, the second was less consistent.

Another focus was the threat of biological warfare, which mandated the vaccination of our forces against not only the local diseases, but also against anthrax bacillus and botulinum toxin. Efforts like this pose not only a logistics problem, with soldier's spread out all over the battlefield, but a doctrinal one as well. Great care is required to ensure continuous, smooth coordination between those portions of the Army which focus on chemical and biological defense from the different perspectives

of operations and of medicine. At the Corps level, this requires constant communication between the Corps Chemical Section and the Corps Surgeon, and this is not necessarily a given.

7th Brigade further had an attached chemical decon company, the 181st from Ft. Hood, Texas. Because they rely on maintenance support from the units to which they are attached, chemical companies are notorious for deadlined, that is, not-working, equipment, and 181 required significant assistance from Brigade to improve its readiness. Moreover, they faced the tremendous challenge of arranging for a continuing supply of the one item essentially required for decon but virtually non-existent in the desert -- water. If DESERT STORM taught the chemical community within the Army only one thing, it was that the ready availability of water can not just be assumed. 181 relied heavily on the Brigade staff for logistics coordination.

Finally, decon sites, both deliberate and hasty, had to be prepared in a variety of locations, and nobody moves earth like the Engineers. In the week before G-day, there was little doubt in anyone's mind that chemical weapons WOULD BE USED. Training was intense. Protective gear was probably kept better track of than were individual weapons in terms of ensuring proximity at all times. And indeed, this may have been the first war in history where male soldiers shaved religiously -- no one was going to risk a weak seal on their protective mask.

On February 21st, I saw the Corps operations order for the ground attack, code named DESERT SABER. Together with the rest of the chemical staff, I made my recommendations for the Brigade's preparation. At a certain time before H-hour, we began taking pyridostigmine bromide, a pre-treatment which enhances the effectiveness of nerve-agent antidotes. We packed our gear, we fitted our flak vests, we drew additional weapons and ammunition, and finally we waited for the storm to break.

I vividly remember the night before G-day, huddling around the shortwave radio with several colleagues, listening to the BBC World Service. The Voice of America and Radio Moscow were universally scorned for dispensing almost entirely propaganda. Correspondents were talking about possible cease-fires, secret Soviet deals, secret European initiatives, and we listened in silence. We knew that the road home now led through Iraq. While apprehensive, many of us were eager to be on that road. Our forward tactical operations center, or TOC, had earlier co-located with several artillery units. Later that evening shells began to roar overhead, prepping the battlefield while the First Infantry Division breached the berm in several locations. The long awaited ground war had become a reality, and its momentum was irresistible.

Roughly 24 hours after the lead divisions had gone through the breach, our TOC moved north as well. As soon as the ground was secure, the Engineers were ordered to begin construction of LOGBASE NELLIGAN 50 kilometers inside Iraq. The objective was to speed supplies to forward units. As matters went, much like Patton's breakout from the Normandy beachhead, our front-line armored columns were outpacing their fuel. Tankers travelled in convoys led by Engineer graders, rolling on the newly cut roads before they were even 10 seconds old.

This, for me, was probably the strangest moment of the entire war. In order to make up for a shortage of non-combat, tactical vehicles, the Saudi government leased a number of commercial 4-wheel drive type trucks to the Army, and our TOC convoy included one such vehicle in which I rode. Thus surrounded by armored command tracks and HMMWV's, wearing a flak jacket and 50 lbs of ammunition, I crossed into Iraq in an air-conditioned Chevy Suburban with U2 playing on the tape deck.

The surrounding spectacle was one which no movie, however panoramic, could do justice to. As far as the eye could see, the desert was laced with military convoys headed north. Skimming only a few feet above the sand, Blackhawks and Apaches swarmed to and fro. Iraqi prisoners could be seen clustered in small groups guarded by MP's; contrary to much press cheerleading, I would not say any of them seemed relieved. Mostly they just seemed exhausted. One group of eight surrendered to our TOC convoy. They accepted food and water and they displayed more dignity than I think I might have managed after being the target of the B-52 strikes which had kept the ground shaking ever since I had reached VII Corps.

And quite frankly, that's roughly the last vivid memory I have before the cease-fire went into effect 100 hours later. As the forward elements in the Corps attack continued to outrun all expectations our TOC jumped on a continuous basis. We jumped in the rain and we jumped in sandstorms, and if anyone can design a pair of sand goggles which will seal against your face while wearing glasses I, for one, will be very appreciative. We jumped during the day and we jumped at night. We jumped until we were exhausted. We had crossed the berm wearing chemical protective overgarments, and we wore them for the entire 100 hours, so we were furthermore filthy, and we stank. In sum, the underlying realities of warfare have changed little over the four odd millennia of recorded civilization, with the possible exception that many of my colleagues were women. Of course, after those 100 hours, it was impossible to ascertain this by appearance. Neither, incidentally, was it possible to distinguish on the basis of performance. I sincerely hope that DESERT STORM will assist in ending the tiresome debate which arises whenever soldiers are assessed by their sex rather than their abilities.

We finally stopped about 30 kilometers southwest of Basra. This location, which we were to occupy for the next several weeks, was in the middle of a former defensive position of the Tawalkana Mech, a Republican Guard division. The one-sided nature of the battle which had occurred there 24 hours earlier was evident. We collected so many abandoned East bloc weapons that our TOC began to look like a Warsaw Pact armory. Numerous untouched Soviet vehicles testified to the speed of the retreat, including tanks which had been dug so deeply into the sand to protect against air attack that their gun tubes were below the surrounding berm, thus preventing them from firing. A few less fortunate vehicles stood testament to the accuracy of allied night-vision equipment and anti-armor weaponry. Allied weapons systems could effectively pick off targets while out of range of Iraqi counterfire -- small wonder the position was so hastily abandoned.

As negotiations began on the cease-fire, many of us finally found time to reflect. To our pleasant surprise, we suddenly realized that chemical weapons had never been used! Probably every chemical officer in Iraq experienced what I did, as countless of my colleagues told me how glad they were that I had been with them during those four blurry days, but how much more grateful still that I had never been called upon to exercise my particular training as a chemical officer.

The failure of Iraq to employ chemical weapons remains one of the greatest mysteries of the war, and probably will for some time to come. It should be pointed out, however, that those who consider this issue from a moral perspective are missing the point. Chemical weapons are not immoral, or, more accurately, they are no less moral than any other lethal means of resolving diplomatic impasse. I saw a number of the dead during my time in Iraq, and the immorality of their deaths did not vary based on the particulars of method. From a purely military standpoint, chemical weapons are simply one item in what General Powell referred to early on as "the big toolbox", and it is the rational preparation of adequate defenses and potential retaliatory actions which renders them ineffective. That preparation is the point of this conference -- indeed, it is the CHARGE of this conference.

Thus, in the past, the combined efforts of a variety of organizations such as this Center, have focused on the three keys of chemical defense -- avoidance, protection and decontamination. The fruits of that labor were evident throughout this most recent operation, perhaps for the first time ever. Our troops had the best detection equipment in the world, including the FOX armored NBC reconnaissance vehicle, which performed admirably, in its first battlefield testing. In terms of personal protection, probably no other Army in history has been so well prepared to

not merely survive a chemical attack, but to virtually ignore it. The realization of these first two goals of avoidance and protection no doubt played a significant role in the Iraqi decision making process, the net result of which is that I do not have to report to you on our efforts in the last area -- decontamination. Frankly, I am certain that many of you in the audience today are owed some small part of the overall debt of gratitude felt by myself, and by all of the soldiers of DESERT STORM, to those whose vigilance and unceasing efforts over the last several decades prepared us for this latest conflict.

But the challenge is not over: if anything it has been increased. For added to the three keys of chemical defense I mentioned earlier is a fourth -- one which is played out more at the strategic level than the tactical but still relies heavily on the same basic science and research as the first three. Thus, after avoidance, protection and decontamination, I would offer the new category of "discorporation." The Bush administration has made the destruction of current stockpiles of chemical weapons throughout the world a major policy goal. Moreover, limitations on the further production of such weapons are sought. Such an ambition relies heavily on developing abilities to monitor and detect illegal production in nations less Happy with what has come to be known, cynically or not, as the "New World Order." Given recent events, the possibility of achieving such a global agreement now seems much more of a reality than it did a mere year ago, when it was the subject of this conference's 1990 keynote address.

What it comes down to, ladies and gentlemen, is this. I have tried to give you some impressions of DESERT STORM which you might have found hard to get from anyone other than a participant, and I have tried to do it in a somewhat whimsical way, but the darker side is that over 250 Americans died during this conflict, and estimates of Iraqi dead range from 10 to 100 thousand. Sitting in this auditorium, it is not possible to truly comprehend these numbers. It is still more difficult to realize that they are not merely statistics -- they represent the failed hopes and dreams of individuals and families. But I think it is important to TRY to understand them, so I offer my own personal experience. Four days after the war ended, three members of my brigade were traveling along Main Supply Route Blue, a road cut out of the sand of the Iraqi desert. In the dust of travel, they never saw the 10-ton truck which hit them head-on, and they were all killed, roughly 500 feet from our TOC. They were returning from the recently installed AT&T satellite uplink, where they had just called their families to tell them the war was over, and they were fine, and they couldn't wait to come home ...

The goal of this conference is to improve chemical defense. Stated more strongly, the goal is, through science and engineering, to render chemical weapons impotent. I choose my words very carefully here. We do not want chemical weapons to be made "less effective", we want them to be "impotent." Accomplishment of this ideal is a small step along the road to a larger one -- that of making warfare obsolete. We owe it to the memories of those three soldiers, who for me at least, serve as a touchstone for the uncounted casualties of all wars, to do this. We owe it still more to the unborn generations who stand ready to receive their heritage. We owe it to all of them to do exactly that, make warfare obsolete, one weapon at a time.

CONTENTS

PREFACE		iii
I. PROTECTION		1
Measurement of Accurate Adsorption Equilibria for Simulant Vapors on 13X Molecular Sieve ..	3	
<i>Amanda B. Brady, David K. Friday, Donna L. Carlile, and Leonard C. Buettner</i>		
Multicomponent Adsorption Equilibria for Vapors of Hydrocarbon and Water on Activated Carbon	9	
<i>M. Douglas LeVan</i>		
Prediction of Binary Vapor Adsorption for a Hexane/Water Mixture on Activated Carbon	17	
<i>Richard A. Matuszko, David K. Friday, and Robert A. Lamontagne</i>		
Characterization of the Armored Vehicle Environment	25	
<i>Jan S. Matuszko, Robert A. Lamontagne, Richard A. Matuszko, and Victoria J. Davis</i>		
Catalytic Oxidation of Hydrogen Cyanide Vapor	33	
<i>Gary B. Howe, J. Jerry Spivey, and George W. Stinagle</i>		
Catalytic Oxidation of GD over a Monolithic Pt/TiO ₂ Oxidation Catalyst	41	
<i>Kathrine J. Clarke, Robert Tom, and G. Lester</i>		
The Role of Water-Soluble Amines in Whetlerite Formulations	49	
<i>V.R. Deitz, C.J. Karwacki, and J.A. Rehmann</i>		
The Relationship of Direct Skin Exposure to Methyl Salicylate (MeS) Vapor to Vapor Carry-Through	65	
<i>Susan H. Bomalaski and John P. Kilian</i>		
II. SYNTHESIS AND PROPERTIES		73
The Cycloaddition Reactions of Sulfonated Dienes with Enamines, Ynamines, Amidines and Thioformamides. New Routes Towards Heterocycles	75	
<i>Albert Padwa, Yves Gareau, Brian Harrison, Bryan H. Norman, and Augusto Rodriguez</i>		
Synthesis, Isolation, Characterization and α_2 -Adrenergic Activities of the Optical Isomers of 4-[1-(1-Naphthyl)Ethyl]-1H-Imidazole	83	
<i>S.S. Hong, D.D. Miller, F.-L. Hsu, C. George, K.L. Romstedt, and D.R. Feller</i>		
α_2 -Adrenergic Activity of New Series of Analogs of 4-[1-(1-Naphthyl)Ethyl]-1H-Imidazole	91	
<i>K. Matsumoto, S.S. Hong, F.-L. Hsu, K.L. Romstedt, D.R. Feller, and D.D. Miller</i>		
Novel Reactions of the S-S and C-S Bonds	97	
<i>S. Munavalli, D.I. Rossmann, D.K. Rohrbaugh, and C.P. Ferguson</i>		
Unusual Reactions of the Di- and Trisulfides with Grignard Reagents	109	
<i>S. Munavalli, D. I. Rossmann, D.K. Rohrbaugh, and C.P. Ferguson</i>		
Phosphorylation of OH Groups on Various Solids by Low-Coordination Phosphorus Species ..	119	
<i>Louis D. Quin, Xiao-Ping Wu, and Stefan Jankowski</i>		
Chemical Properties Update - Theory, Statistics, and Experimental Methods	127	
<i>Elwin C. Penski</i>		
Subambient Applications of Differential Thermal Analysis for the Determination of Vapor Pressure	135	
<i>Ann Brozena and Donald Fielder</i>		
Chemoselective Reactions of Functionalized Piperidines	141	
<i>Harold D. Banks</i>		

	Preassociating α -Nucleophiles	149
	<i>Lewis E. Fikes, David T. Winn, Robert W. Sweger, Morgan P. Johnson, and Anthony W. Czarnik</i>	
III.	DETECTION	157
	Detection Strategies for Treaty Verification: A Fieldable System for Sampling and Analysis of CW Stockpile	159
	<i>S.F. Hallowell, M.J. Heyl, and D.J. Reutter</i>	
	Biodetection of Bacteria by Pyrolysis and Mass Spectrometry	163
	<i>Alvin Fox</i>	
	The Resonance Raman Detection and Identification of Bacteria	169
	<i>S. Chadha, W.H. Nelson, and J.F. Sperry</i>	
IV.	TOXICOLOGY	175
	Sedative, Hemodynamic and Ventilatory Effects of Four Different α_2 -Adrenergic Agonists in Awake Chronically Instrumented Mini-Swine	177
	<i>Byron C. Bloor and Clifford Kim</i>	
	Effects of Sufentanil and Nalmefene on the Auditory Brainstem Response (ABR) in the Ferret	185
	<i>Sharon A. Reutter and Robert J. Mioduszewski</i>	
	Evaluation of Chloropentafluorobenzene as an Intake Simulant	193
	<i>Bruce M. Jamot and Harvey J. Clewell, III</i>	
	Effects of Altitude on Toxic Gas Uptake: CO Inhalation in Healthy Adult Volunteers	201
	<i>James J. McGrath, Richard M. Schreck, and Peter S. Lee</i>	
	Interspecies Differences in Response to Amphetamine, Acetaminophen, Trichloroethylene, and Sodium Thiosulfate	209
	<i>Charles A. Tyson, Carol E. Green, Susan A. Knadle, Shirley J. Gee, Jack E. Dabbs, and Susanna E. LeValley</i>	
V.	BIOTECHNOLOGY	217
	Part I: Molecular Biology	
	Olfaction, Olfactomedin and the Dynamic Range of Smell	219
	<i>Robert R.H. Anholt, David A. Snyder, and Hiroko Yokoe</i>	
	Using a Silicon Microphysiometer to Detect Agents that Alter Cellular Physiology	227
	<i>John C. Owicki, H. Garrett Wada, and J. Wallace Parce</i>	
	Part II: Applications	
	Microbial Degradation of 3-Hydroxypiperidine and 3-Hydroxyquinuclidine	235
	<i>Joseph J. DeFrank and Christine Savage</i>	
	Enzymatic Degradation of GF	241
	<i>Steven P. Harvey</i>	
	The Role of the Pilot Plant in Bioprocess Development	247
	<i>Edward M. Sybert</i>	

VI.	ENVIRONMENTAL STUDIES	255
	Supercritical Fluid Extraction and Organic Solvent Microextraction of Chemical Agent Simulants from Soil	257
	<i>W.H. Griest, R.S. Ramsey, C.-h. Ho, and W.M. Caldwell</i>	
VII.	NMR INVESTIGATIONS	265
	Purity Determination of Chemical Agents by Nuclear Magnetic Resonance Spectroscopy (NMR)	267
	<i>William T. Beaudry and Linda L. Szafraniec</i>	
	Position of Bond Cleavage in the Hydrolysis of Organophosphonate Esters Using ¹⁸ O NMR Analysis	275
	<i>Linda L. Szafraniec, Leonard J. Szafraniec, and J. Richard Ward</i>	
	NMR Spectroscopy Determination of Relative Binding Constants for Arsenical-Antidote Adducts	283
	<i>Richard J. O'Connor, Evelyn L. McGown, Vicky L. Boyd, Kilian Dill, and Susan F. Hallowell</i>	
	Solid-State ³¹ P MAS NMR Study of G-Agent Simulants Adsorbed on Synthetic Resin Catalysts	289
	<i>William T. Beaudry, George W. Wagner, and J. Richard Ward</i>	
VIII.	FLUID DYNAMICS	297

Part I: Liquid Filled Projectiles

Effect of Longitudinal Baffles on the Viscous Liquid-Fill Induced Destabilizing Moment	299
<i>Miles C. Miller</i>	
Including Liquid-Fill Effects in the Tricyclic Theory	309
<i>Daniel J. Weber</i>	
Instrumented Flight Test and Data Reduction of Artillery Projectiles with Selected Fill Ratios	317
<i>David J. Hepner, Daniel J. Weber, and John W. Molnar</i>	

Part II: Rheology and Special Topics

Numerical Simulation of Fluid Dynamics and Payload Dissemination in a Dual-Chamber Grenade	325
<i>Michael J. Nusca</i>	
A Comparison of Elongational Measurements Obtained with the Falling Cylinder and Impinging Jet Rheometer	337
<i>Joseph E. Matta, Raymond P. Tytus, and Douglas R. Sommerville</i>	
Formulation of Preferentially Soluble Polymer Solutions and Comparisons of Their First Normal Stress Difference and Extensional Viscosity	347
<i>Brian S. Ince and Wendel J. Shuey</i>	
Magnet Enhanced Optical Falling Needle/Sphere Rheometer	355
<i>Benjamin Chu, Jian Wang, and Wendel J. Shuey</i>	

IX.	MATERIALS	363
	Equilibrium Solubility and Diffusion Coefficient Measurements and Correlations with Predictive Properties	365
	<i>Brian S. Ince and Wendel J. Shuey</i>	
	Recent Developments in the Fundamentals of Gas Permeation in Rubbery Polymers	377
	<i>C. Richard Desper</i>	
	Emulsion Copolymerization of Methacrylates: A Scale-Up Study	385
	<i>J.M. Park, J.W. Vanderhoff, and S.H. Hong</i>	
	Solvent Effects on the Tensile Properties of Thermoplastic Composites	393
	<i>Vincent M. McHugh, Wendel J. Shuey, Richard W. Brletich, and John M. Henshaw</i>	
	Corrosion Behavior Study of Type II and Type III Anodized Al 5052-0 in Aqueous DS2 Solutions	401
	<i>Chester V. Zabielski and Milton Levy</i>	
X.	DECONTAMINATION	411
	Reaction of VX with Chloramine-B	413
	<i>Yu-Chu Yang, Linda L. Szafraniec, William T. Beaudry, and J. Richard Ward</i>	
	Mechanism of Dehalogenation of Aliphatic Halocarbons such as HD by $W_{10}O_{32}^{6-}$	421
	<i>Craig L. Hill and Daryush Sattari</i>	
	Micellar Charge Effects on Sulfide Oxidation	427
	<i>Andrei Blaskó, Clifford A. Bunton, Houshang Foroudian, Tracey S. Taylor, and Sallyanne Wright</i>	
	Activation of H_2O_2 Using Co-Catalysts in N-Methylpyrrolidinone Solvent	437
	<i>Russell S. Drago and Douglas E. Patton</i>	
	Mechanism of the Hydrolysis of Organophosphinates Catalyzed by Copper (II) N,N,N',N'-Tetramethylethylenediamine (CuTMED)	445
	<i>Masato Nakashima and David M. Alabran</i>	
	Development of the Canadian Reactive Skin Decontaminant Lotion	449
	<i>J. Garfield Purdon</i>	
	Characterization of the Microemulsion Aggregate by Luminescence and Electrochemical Techniques	457
	<i>P.L. Cannon, Jr., S.M. Garlick, S.D. Christesen, N.M. Wong, A.C. Novelli, F.R. Longo, and R.A. Mackay</i>	
	The Hydrolytic Kinetics of Mustard Simulants in Polymer Solutions	489
	<i>Lawrence C. Cerny and Elaine L. Cerny</i>	
XI.	COMPUTATIONAL CHEMISTRY	497
	PBI Hydration Study in the Development of Methodology for the Molecular Modeling of Mechanical Property Trends	499
	<i>Nancy E. Iwamoto</i>	
	Structure Sedative Activity Relationships of Alpha2 Adrenergic Compounds	507
	<i>William P. Ashman, Todd M. Nelson and Brian H. Meehan</i>	
	Some Interrelations of the Heats of Formation of Isosteric and Isoelectronic Oxygen and Fluorine Compounds	515
	<i>Carol A. Deakyne, Andrew D. Fant, Deborah L. Kunkel, and Joel F. Liebman</i>	
	Ab Initio Quantum Chemical Investigations of Solute/Solvent Polarity and Hydrogen-Bonding Parameters	523
	<i>Peter Politzer, Jane S. Murray, and Tore Brinck</i>	

Model of the Active Site Spectroscopy of the Rhodanese Enzyme	529
<i>M. Krauss</i>	
Computer Model for the Spectral Predictions of Nerve Agents	535
<i>Hendrik F. Hamelka and James O. Jensen</i>	
Theoretical Prediction of Vibrational Circular Dichroism Spectra of Hexoses in Linear Form	541
<i>Daniel Zeroka, James O. Jensen, Arthur H. Carrieri, and Janet L. Jensen</i>	

POSTER SESSIONS

XII. PROTECTION POSTERS	553
Barrier Properties of Matrices for Reactive Systems - A Reactivity Probe	555
<i>John W. Halliday and John E. Walker</i>	
Removal of Diethyl Sulfide from Breathing Air by the NRL-1000L Oxidation Catalyst	563
<i>Vasgen A. Shamamian, Kim W. Pierson, and D.S.Y. Hsu</i>	
XIII. SYNTHESIS AND PROPERTIES POSTERS	571
Predicting Liquid Densities of Organic Compounds I: Halogenated and Oxygenated	573
<i>Gerry O. Wood and Travis B. Weaver</i>	
Relations Between Nucleophilicity and Acidity of Oximes	579
<i>Frédéric Guir and François Terrier</i>	
Some Physicochemical and Pharmacological Characteristics of 1-Substituted-4-Phenyl- 4-Piperidinols and their Esters	585
<i>James W. King, William R. Hydro, and W. James Lennox</i>	
Synthesis and Bioactivity of 2-(α -Hydroxy-p-Alkoxybenzyl) and 2-Alkoxyarylamino Analogues of Etonitazene (CS-4640)	597
<i>James W. King, James P. Cleveland, and W. James Lennox</i>	
XIV. DETECTION POSTERS	607
The Identification and Detection of Urinary Metabolites of Sulphur Mustard	609
<i>Robin M. Black, Keith Brewster, Ray J. Clarke, Joy L. Hambrook, John M. Harrison, David J. Howells, and Robert W. Read</i>	
Characterization of Bacteria by Oxidative Pyrolysis-Gas Chromatography-Mass Spectrometry ..	617
<i>Philip B. Smith and A. Peter Snyder</i>	
Tradeoff Analysis of Nonradioactive Source Alternatives for the XM22 Automatic Chemical Agent Alarm	623
<i>Joseph E. Roehl</i>	
Triazine Derivatives as Potential Microsensor Coatings for the Detection of Airborne Contaminants	633
<i>Alan R. Katrizky and Jamshed N. Lam</i>	
Feasibility of Drone-Portable Ion Mobility Spectrometry	641
<i>Neil S. Arnold, Henk L.C. Meuzelaar, Jacek Dworzanski, Paul Cole, and A. Peter Snyder</i>	
Material Test Facility (MTF) Parametric Control and Hazard Containment	649
<i>Gary R. Bodily and Frank D. Anderson</i>	

	Immuno-CAM: The Detection of Bacteria Using an Immunoassay Technique Combined with the Chemical Agent Monitor (CAM)	657
	<i>David A. Blyth, Maryalice Miller, John A. Parsons, and A. Peter Snyder</i>	
	Detection and Identification of O-Ethyl S-[2-Dimethylaminoethyl] Methylphosphonothioate Degradation Products by Chemical Ionization Mass Spectrometry	665
	<i>Dennis K. Rohrbaugh</i>	
	GF Detection Using Ion Mobility Spectrometry	673
	<i>Donald B. Shoff and Lynn D. Hoffland</i>	
XV.	TOXICOLOGY POSTERS	681
	Inhibition of Sulfur Mustard-Increased Protease Activity of Niacinamide, N-Acetyl-L-Cysteine or Dexamethasone	683
	<i>Fred M. Cowan, Clarence A. Broomfield, and William J. Smith</i>	
	Dissociation of Opiate-Induced Sedation and Respiratory Depression in Ferrets by Opiate Antagonist Coadministration: Potential Pharmacological Mechanisms	691
	<i>R. Mioduszewski and S. Reutter</i>	
	The Fate of Sulfur Mustard after Intravenous Intoxication in Rats	699
	<i>A. Maisonneuve, I. Callebat, L. Debordes and L. Coppet</i>	
	Increased Proteolytic Activity in Human Epithelial Cells Following Exposure to Sulfur Mustard	707
	<i>William J. Smith, Fred M. Cowan, and Clarence A. Broomfield</i>	
	Sulfur Mustard-Induced Alterations of DNA Structure and Kinetics in Proliferating Human Cells in Culture	713
	<i>William J. Smith, K. Michael Sanders, James E. Caulfield and Clark L. Gross</i>	
	Enzymatic Cyanide Detoxification	721
	<i>Sidney A. Katz and Harry Salem</i>	
XVI.	BIOTECHNOLOGY POSTERS	729
	Field Emission Scanning Electron Microscopy of the Interaction of <i>Clostridium Difficile</i> with Human Embryonic Intestinal Cells	731
	<i>Sheila Wood and Erica Petersen</i>	
	Detection of Threshold Numbers of <i>Escherichia Coli</i> and <i>Pseudomonas Aeruginosa</i> Using a Hand-Held Detection Device	739
	<i>Sheila J. Wood and Jared M. Veronick</i>	
	Determination of a Unique Epitope Binding Site for a Complement-Lysis-Enhancing Monoclonal Antibody, 3D12, on the Galactose Adherence Lectin of <i>Entamoeba Histolytica</i> Using BIAcore	747
	<i>Sheila J. Wood and William Petri, Jr.</i>	
	The Use of Protease Inhibitors in the Purification of Squid Organophosphorous Anhydrase ...	755
	<i>Karla Kopec-Smyth, Devayani Eswaran, Jeffrey R. Deschamps and Keith B. Ward</i>	
	Immunochemical and Nucleic Acid Screening of Bacteria for Organophosphate-Degrading Enzymes	763
	<i>Tu-Chen Cheng, Joseph J. DeFrank, Maryalice N. Miller, Danielle K. Vervier, and Heather S. Heitz</i>	
	Analysis of Proteins by On-Line HPLC Electrospray Mass Spectrometry	773
	<i>Philip B. Smith and A. Peter Snyder</i>	
	Antibody-Based Fiber Optic Evanescent Wave Sensor	779
	<i>D.E. Menking, K.R. Rogers, J. Heitz, R.G. Thompson, D.G. Menking, and M.E. Eldefrawi</i>	

	Retroviral Vectors: Tools to Express Enzymes Active Against Sulfur Mustard	785
	<i>Marc Boidot-Forget, Vincent Ramisse, and Joëlle Lemaire</i>	
	Use of Surety Exempt-Dilute GD Stock Solution to Determine Initial (Zero Order) Hydrolysis Rates by OPA Anhydrase Preparations	793
	<i>Johnnie M. Albizo and Joseph W. Hovanec</i>	
XVII.	ENVIRONMENTAL STUDIES POSTER	799
	Detection of Thiodiglycol and its Sulfoxide and Sulfone Analogues in Environmental Waters by High Performance Liquid Chromatography	801
	<i>Paul C. Bossle, Michael W. Elzy, and John J. Martin</i>	
XVIII.	NMR INVESTIGATIONS POSTERS	807
	Metal-Ion Promoted Oxidation of DIMP	809
	<i>D. Ralph Leslie and J. Richard Ward</i>	
	DMMP-TC Reaction Study	823
	<i>Leonard J. Szafraniec, Linda L. Szafraniec and V. Bruce May</i>	
	Diffusion of Small Fluorinated Molecules in Polymeric Media Studied Via High-Resolution Solid-State ¹⁹ F NMR Spectroscopy	831
	<i>Paul J. Toscano, E. James Schermerhorn, John Waechter, Peiguang Zhou, and Harry L. Frisch</i>	
	Structure Determination of Compound 34	839
	<i>D. Ralph Leslie, Linda L. Szafraniec, Dennis K. Rohrbaugh, and L.J. Szafraniec</i>	
XIX.	MATERIALS POSTERS	847
	Jet Engine Dissemination of Microencapsulated Aerosols	849
	<i>Mark A. Guelta and Hugh R. Carlon</i>	
	New Test Methods for NBC Survivability	857
	<i>P.S. Grasso and P.L. Cannon, Jr.</i>	
XX.	DECONTAMINATION POSTERS	865
	Adsorption of Mustard from a Chlorofluorocarbon Solvent Using Macroreticular Strong Acid Resin	867
	<i>James H. Buchanan, Dennis K. Rohrbaugh, Philip W. Bartram, and Noel C. DiBona</i>	
	Oxidations of Alkenes Catalyzed by a Mn(III) Porphyrin and Cationic Polymer Latexes	875
	<i>Weiming Zhu and Warren T. Ford</i>	
	Tests of a Reactant-Loaded Decontaminating Polymer Powder Against CW Agents and Thickened Simulants	881
	<i>Nolan Tillman, Mark S. Kaplan, and Gary M. Russo</i>	
	Removal of Thickened Mustard from Painted Test Panels by Liquid Systems	887
	<i>Yu-Chu Yang, J. Richard Ward, Kurt Görgens, and Manfred Zillmer</i>	
	Determination of the Critical Micelle Concentrations of CTAB in Water/1-Alkyl- 2-Pyrrolidinone Mixtures	895
	<i>J.W. Hovanec and J.M. Albizo</i>	

Covalent Attachment of Organic "Handles" to Polyoxometalates with Oxidative Decontamination Activity	901
<i>Gyu-Shik Kim and Craig L. Hill</i>	
Adsorption of VX and TBP by Various Sorbents in 1,2-Dichloroethane	909
<i>J.H. Buchanan and S.H. Hong</i>	
Kinetics of the Hydrolysis of a Model Phosphorus Ester by DS2 Decontaminant Sorbed onto Dow-Corning Polytrap Resin Monitored by NMR	919
<i>S.H. Hong</i>	
Autoxidation of 2-Mercaptoethanol Catalyzed by Cobalt(II) Phthalocyaninetetrasulfonate on Colloidal Particles	925
<i>Sunkara Haribabu and Warren T. Ford</i>	
XXI. COMPUTATIONAL CHEMISTRY POSTER	933
Predicting Oxidation Similarities Between VX and Potential Simulants by Semiempirical Molecular Orbital Calculations	935
<i>George Famini and Philip Barram</i>	
XXII. INDEXES	945
Index A: Authors for Papers in These Proceedings	947
Index B: Organizations of Authors in These Proceedings	951
XXIII. APPENDIXES	953
Appendix A: List of Attendees	955
Appendix B: Agenda	981
Appendix C: Delayed Papers	1001

Blank

I. PROTECTION

NOTE: Papers with the following titles were presented at the Conference but are not included in this document:

Development of Air Purification Systems

Single Component Isotherm Measurement with the Cahn Microbalance

Experimental Studies in Pressure Swing Adsorption

Pressure Swing Adsorption (PSA) Performance Prediction Model

Pressure Drop and Cyanogen Chloride Breakthrough Time for Beds of ASC Carbon with Nonuniform Cross-Sectional Area

Use of X-Ray Photoelectron Spectroscopy to Characterize Reactions on Activated Carbons

Adsorption Properties of Superactivated Carbons

Reaction Kinetics for the Oxidation of Hexafluoropropylene over a 3%Pt/Al₂O₃ Catalyst

Role of Tertiary Amines in Whetlerite Formulations

Aerosol Challenge Tests of Chemical Protective Ensembles

BLANK

MEASUREMENT OF ACCURATE ADSORPTION EQUILIBRIA FOR SIMULANT VAPORS ON 13X MOLECULAR SIEVE

Amanda B. Brady, David K. Friday
GEO-Centers, Inc.
10903 Indian Head Highway
Ft. Washington, MD 20774

Donna L. Carlile, Leonard C. Buettner
U.S. Army CRDEC
Aberdeen Proving Ground, MD 21010-5423

ABSTRACT

The accurate measurement of single component adsorption equilibrium (isotherm) data is critical to the understanding of adsorption-based air purification systems. Measuring adsorption equilibria on hydrophilic adsorbents, such as 13X molecular sieve, is particularly difficult because great care must be taken to insure that all the adsorbed water is removed. The development of an effective drying procedure is important for reproducibility because a chemical must compete with water for adsorption sites. Adsorption equilibria for two simulants, perfluorocyclobutane (PFCBa) and 1,1,2, trichloro, 1,2,2, trifluoroethane (CFC-113), are measured on 13X molecular sieve. Isotherms for the simulants are compared and discussed.

INTRODUCTION

It is necessary to measure isotherms on various adsorbents in order to evaluate their performance in adsorption-based air purification systems. The military is currently seeking to develop advanced collective protection technologies. One potential adsorbent for use in these systems is 13X molecular sieve.

Accurate single component isotherm equilibria data, measured over a wide range of concentrations and temperatures, is fundamental to the understanding of adsorption based processes. However, in order to obtain accurate single component isotherm equilibria data on hydrophilic adsorbents, great care must be taken to remove all adsorbed water.

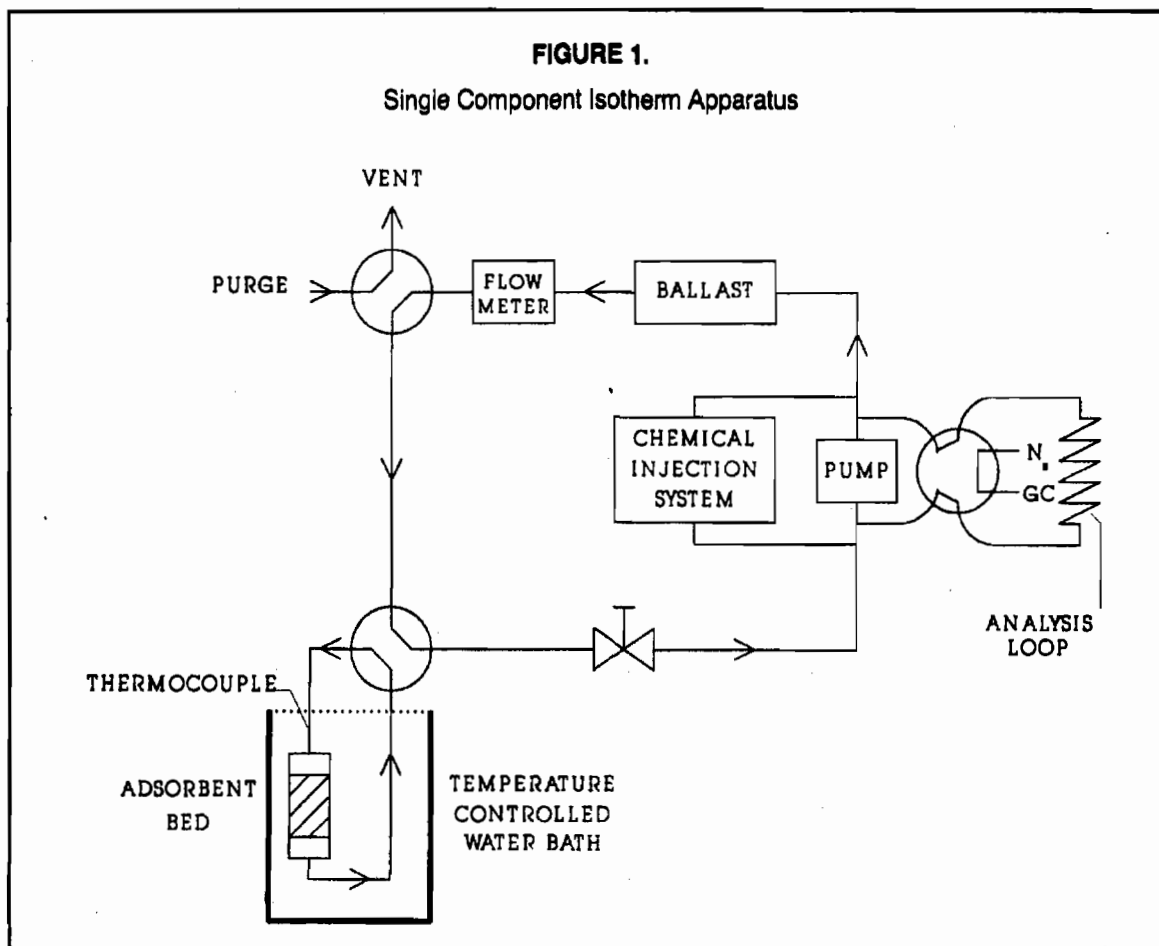
Our objective in this study was to develop a method and procedure to measure adsorption equilibria data for PFCBa and CFC-113 on 13X molecular sieve. The approach used to accomplish this task was to dry the sample thoroughly, obtain an accurate dry mass of the sample, and remove any residual moisture adsorbed during the transfer of the sample from the dryer to the system prior to starting the experiment.

APPARATUS

The apparatus used to measure adsorption equilibria is a closed loop volumetric system, shown schematically in Figure 1. A metal bellows pump circulates the vapor through the system, and a Tylan flow meter measures

FIGURE 1.

Single Component Isotherm Apparatus



the flow in the system. The circulation flow rate can be adjusted using a Whitey needle metering valve. The chemical of interest was introduced in discrete amounts using a pressurized reservoir, three Valco valves with different loop sizes, and two solenoid valves. A Hewlett-Packard 5880 gas chromatograph (GC), with a 5'x1/8" Chromosil 316 in TFE column, equipped with a flame ionization detector (FID), was used to sample the contents of the vapor phase.

There are two four-way valves in the system. The top valve shown in Figure 1 allows the system to be purged with dry air or be in a closed-loop operating mode. The position of the second valve determines whether the adsorbent bed is in the challenge or bypass mode. When the valve is in the bypass position, the adsorbent bed is isolated from the circulating vapor stream. In the challenge position, the contaminated vapor stream is circulated over the adsorbent.

DRYING PROCEDURE

It is well known that small water loadings, as low as 0.05 g/g, can dramatically reduce the adsorption capacity of molecular sieve for other chemical vapors. Previous isotherm data for PFCBa on 13X measured in this laboratory was inconsistent due to this phenomenon. The scatter indicated the need for an effective drying procedure, an accurate dry mass of the sample, and removal of any residual moisture before placing the adsorbent sample into the system.

During the course of this study, two procedures were developed which appear to effectively remove adsorbed water from 13X. The first method used a vacuum oven and the following drying procedure: the 13X sample was dried under vacuum for 24 hours at 503K to 513K, using a helium purge for two hours prior to turning off the oven. The purge continued until the sample reached ambient temperature. When the sample

was placed in the isotherm measurement system, the bed was heated to 493K with a helium purge flowing over the bed for two hours. After the purge was turned off, the system was placed in the closed-loop recirculation mode and a cryogenic trap was filled with liquid nitrogen to remove any residual moisture from the sample and the system. This method effectively removed water from the sample, but was rejected due to damage to the vacuum pump.

A second drying method was developed using a tube furnace. A 2-inch diameter glass tube, filled with 13X molecular sieve, was heated to 573K in the furnace for 36 hours, and then cooled, with a continuous dry nitrogen purge. A small sample was removed from the glass tube and placed in a tared holder. The sample was quickly weighed and placed in the closed-loop system. It was heated to 443K, with a helium bleed of 100 sccm over the sample for two hours. While still at 443K, the system was then placed in the closed-loop circulating mode with a cryogenic trap in line for three hours.

Data obtained using the tube furnace method overlays data using the vacuum oven method. This implies that the two methods are equally effective at removing adsorbed water from the sample.

PROCEDURE

To prepare for each experiment, the system was purged until no trace of chemical was found. After the system was found to be free of any contaminants, the dry 13X sample of known mass was inserted into the loop.

With the sample in the system, a pressure test was performed to insure that there were no leaks which would cause loss of chemical or introduction of impurities into the system. After the pressure test and an external calibration test, the pump was turned on, and the desired system flow was set using a metering valve.

Following the initial setup procedure, the experiment was controlled by computer. The bypass/challenge valve, the temperature bath setpoint, the injection of chemical into the system, and the GC sampling of the

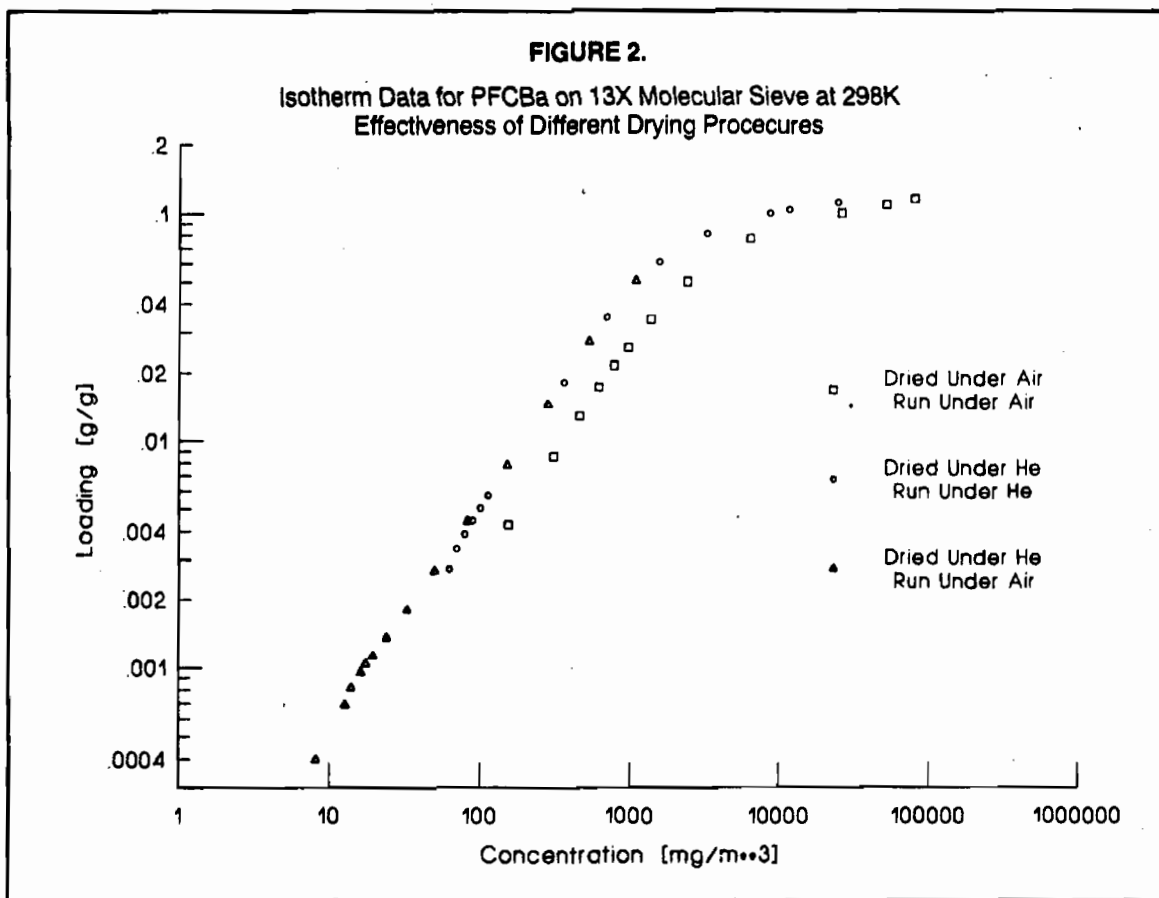


FIGURE 3.

Isotherm Data for PFCBa on 13X Molecular Sieve at 298, 323, and 348K

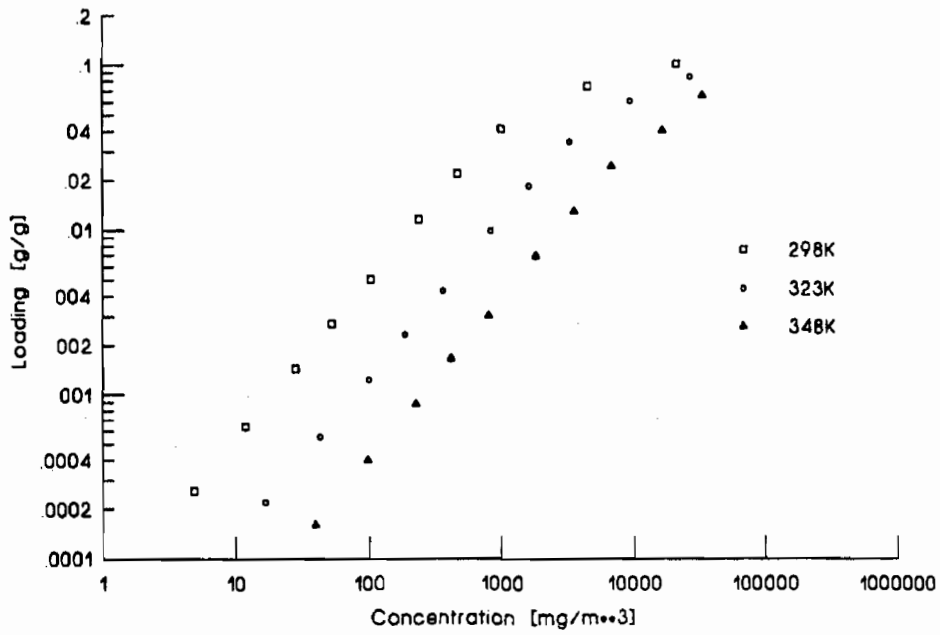
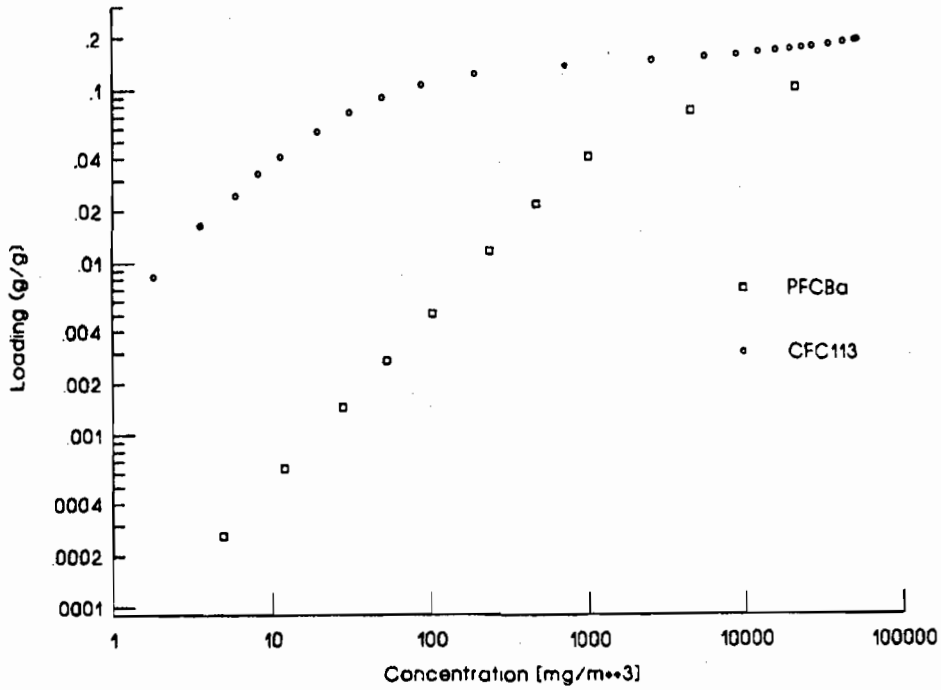


FIGURE 4.

Isotherm Data for PFCBa and CFC-113 on 13X Molecular Sieve at 298K



vapor phase were under computer control. After each chemical injection with the bed in the bypass mode, the vapor phase concentration in the loop was measured using the GC. Based on the difference in the concentration before and after the chemical injection, the amount injected into the system was calculated. The vapor stream was then diverted over the adsorbent sample. The vapor phase concentration was measured at uniform time intervals to determine if equilibrium between the solid and vapor phases had been reached. After each equilibrium point was measured at a given temperature, the computer changed the temperature setpoint to the next desired temperature. The entire cycle of injection, determination of concentration in the vapor phase, passing the vapor over the bed, and determination of equilibrium points at each temperature setpoint was repeated until the desired final concentration was reached.

Immediately following each run, the 13X molecular sieve was allowed to cool to ambient temperature before being weighed to measure an experimental value for the adsorbed phase concentration. This value was used to verify the adsorbed phase concentration computed by the program.

RESULTS AND DISCUSSION

The initial drying process used air only. It was determined that using helium during the drying process in the vacuum oven, and as a gentle purge while the sample was being dried in situ, offered a substantial improvement over the initial drying procedure. This is reflected by the improved loadings measured for PFCBa in Figure 2. However, since the experiments at that time were being conducted under helium, there was the possibility that this improvement could be attributed to the absence of competition between the adsorbate and nitrogen.

To test this hypothesis, a sample was prepared using the same drying procedure described above. But just prior to starting up the experiment, the bed was placed in bypass, and the system was purged with dry air.

It was found that the CFC-113 isotherm measured using the helium drying process which was run under air matched the previous runs which had been conducted under helium alone. The results of this exercise indicate that the higher capacity of the molecular sieve under the

new process using helium was indeed due to the removal of water during the drying process, and not because of an absence of competition between the adsorbate and nitrogen.

Figure 3 shows PFCBa data. The data were collected over five orders of magnitude of concentration and three temperatures, 298K, 323K and 348K. At a concentration of 100 mg/m³, the loading at 298K is 0.0051 g/g, at 323K the loading is 0.0012 g/g, and at 348K the loading is 0.0004 g/g. Therefore, it is important to measure loadings at different temperatures in order to understand how the temperature of the working environment will influence the performance of the adsorbent. For example, if rate processes are the same, the penetration time at 298K will be about 13 times longer than at 348K.

Looking again at the loadings at 100 mg/m³, the ratio of the loadings at 298K and 323K is 4 to 1. The ratio for the loadings at 323K and 348K is 3 to 1. And the ratio for the loadings at 298K and 348K is 12 to 1. This ratio information is important because when trying to regenerate an adsorbent, one may wish to utilize changes in temperature to desorb material from your bed.

Figure 4 is a plot of PFCBa and CFC-113 data plotted at 298K. Both CFC-113 and PFCBa are nonpolar, water insoluble, and have about the same molecular diameter. Since the boiling point of CFC-113 is 320K, while PFCBa boils at 268K, one would expect the capacity for PFCBa to be lower than that of CFC-113.

At concentrations between 1 and 10 mg/m³, the difference in loadings between the two chemicals is approximately two orders of magnitude. At concentrations between 1000 mg/m³ and 10,000 mg/m³ the difference in loadings is much less. The difference in loadings between the two chemicals is only a factor of 4 and 2 at 1000 mg/m³ and 10,000 mg/m³ respectively. These differences in loading capacities of the adsorbent based on the concentration of the adsorbate will have implications on the size and applications of an adsorber bed of that material.

CONCLUSION

The procedure and apparatus developed here successfully measure accurate isotherms on 13X molecular sieve, and may be easily adapted to measure isotherm data for other hydrophilic adsorbents.

BLANK

MULTICOMPONENT ADSORPTION EQUILIBRIA FOR VAPORS OF HYDROCARBON AND WATER ON ACTIVATED CARBON

M. Douglas LeVan
Department of Chemical Engineering
University of Virginia
Charlottesville, Virginia 22903-2442, U.S.A.

A novel volumetric apparatus for measurement of adsorption equilibria has been constructed. Single component adsorption equilibria have been measured for water, hexane, and acetone at temperatures from 25°C to 125°C. Multicomponent adsorption equilibria for water-hexane and water-acetone mixtures have also been measured at 25°C and 100°C. Hysteresis behavior has been measured for water alone and for water-hexane and water-acetone mixtures.

INTRODUCTION

There is a need for a better understanding of the adsorptive behavior of water vapor and mixed hydrocarbon-water vapors on activated carbons. Applications of adsorption processes involving organic compounds and water vapor are numerous and varied and include regenerable military filters. The state of the field is such that few equilibrium data are available. Even measurements of adsorption of pure water vapor on activated carbons have been limited to room temperature. The scientific understanding of how water affects the adsorption of other components is largely lacking. The temperature dependence of hysteresis, the effect of hydrocarbon adsorption on the hysteresis, and effect of water adsorption and its hysteresis on hydrocarbon adsorption are not known.

This paper summarizes some recent research carried out at the University of Virginia on adsorption equilibria for vapors of hydrocarbons and water on activated carbon. The experimental measurements were performed by graduate students under the direction of the author. A more complete description of the investigations including an extensive literature survey may be found elsewhere [1]. Here, a brief overview is given of measurements made with a novel apparatus for hexane, acetone, water, hexane-water, and acetone-water adsorbed on Calgon Type BPL activated carbon. The two hydrocarbons were chosen because of their water solubilities, with n-hexane being essentially immiscible and acetone being completely miscible.

BACKGROUND: WATER ADSORBED ON CARBON

Activated carbons are complicated from both physical and chemical viewpoints. The carbon used in this study is bituminous coal-based. It has both carbonaceous and oxide adsorption sites and contains up to 8% ash.

Adsorption forces are somewhat unusual for water vapor on activated carbon. Unlike most hydrocarbon adsorbates, water does not interact strongly with carbonaceous solids. This results in relatively small amounts adsorbed at low relative pressures, but the isotherm typically rises sharply in some region prior to saturation giving the Type 5 shape [2]. The exact mechanism for adsorption of water vapor on microporous solids is unclear. It is believed that adsorption occurs through a cooperative mechanism involving the hydrogen bonding of water molecules. Theories for the sharp rise in the water isotherm prior to saturation include coalescence of clusters of molecules nucleated around high energy sites such as chemisorbed oxygen atoms and formation of a water monolayer.

A characteristic of water isotherms on microporous carbons is the hysteresis loop. The size and extent of the hysteresis region has been related to the porosity of the carbon. The desorption branch is often attributed to the evaporation of a condensed phase over a narrow pressure range [3]. Other theories suggest the existence of a metastable state. Theoretical studies predict that the hysteresis loop will become smaller with increasing temperature and eventually disappear at a capillary "critical" temperature that is significantly lower than the critical temperature of the bulk fluid [4].

The density of adsorbed water vapor and the energy associated with the adsorption have led to somewhat contradictory viewpoints. Dubinin [3] investigated the energy of adsorption of water molecules in porous solids and concludes that the "nature of interactions in adsorption of water is the same as in the condensation of its vapors in the bulk phase." Gregg and Sing [2] point out that the volume of water adsorbed at saturation, calculated using the Gurvitsch rule, is usually less than that of other adsorbates indicating that adsorbed water may be present in a form less dense than bulk water.

EXPERIMENTS

Apparatus

A diagram of the apparatus is shown in Figure 1. It is contained in an environmental chamber with a programmable temperature controller to allow measurement of isotherms of condensable vapors at elevated temperatures and pressures up to saturation. The experiments are based on recirculating a gas through a closed loop using a magnetic pump. The loop is of small, known volume and additional volume can be added using tanks for measurement of hysteresis. The loop contains a small bed of a known amount of clean activated carbon. Adsorbate is injected into the loop as liquid through an injection port using a gas tight syringe; the amount injected is determined by weighing the syringe before and after injection. Gas concentrations are measured using a gas sampling valve, a gas chromatograph with flame ionization and thermal conductivity detectors, and a digital integrator. Equilibrium has been reached when gas concentrations reach constant values.

Operating procedures are described in detail elsewhere [1]. Data involving hysteresis are measured by slowly cooling the apparatus to the desired adsorption temperature to determine points on the adsorption branch and slowly warming the apparatus to the desired

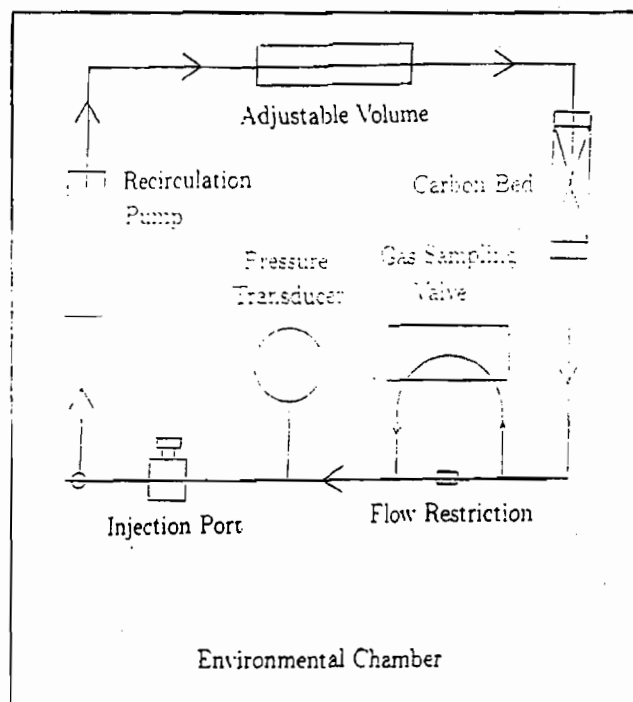


Figure 1: Schematic diagram of apparatus.

temperature for points on the desorption branch.

Materials

The activated carbon used in these experiments is Type BPL (Calgon Carbon Corp., Lot No. 4814-J) in 6×16 mesh form. The adsorbates used were n-hexane (ACS certified 99 mol % pure), acetone (ACS certified 99.5 mol % pure), and water (distilled and deionized).

RESULTS AND DISCUSSION

Because of space limitations, it is possible to show only very limited results. Much more detailed results and discussion are given elsewhere [1].

Isotherms for Pure Hexane and Acetone

Our isotherms for pure hexane and pure acetone at 25°C , 50°C , 75°C , 100°C , and 125°C are shown in Figure 2 over approximately seven decades of pressure. The isotherms are of the Type 1 classification, being strongly concave downward when plotted on rectangular coordinates. Note that the saturation pressures, as indicated by the vertical lines, are reached for all temperatures.

Isotherms for Pure Water

Isotherms for water vapor at 25°C and 100°C are shown in Figure 3. The isotherms at 25°C are similar to those reported by other investigators, including Mahle and Friday [5], for BPL carbon at room temperature. Comparing the hysteresis loops, we see that the

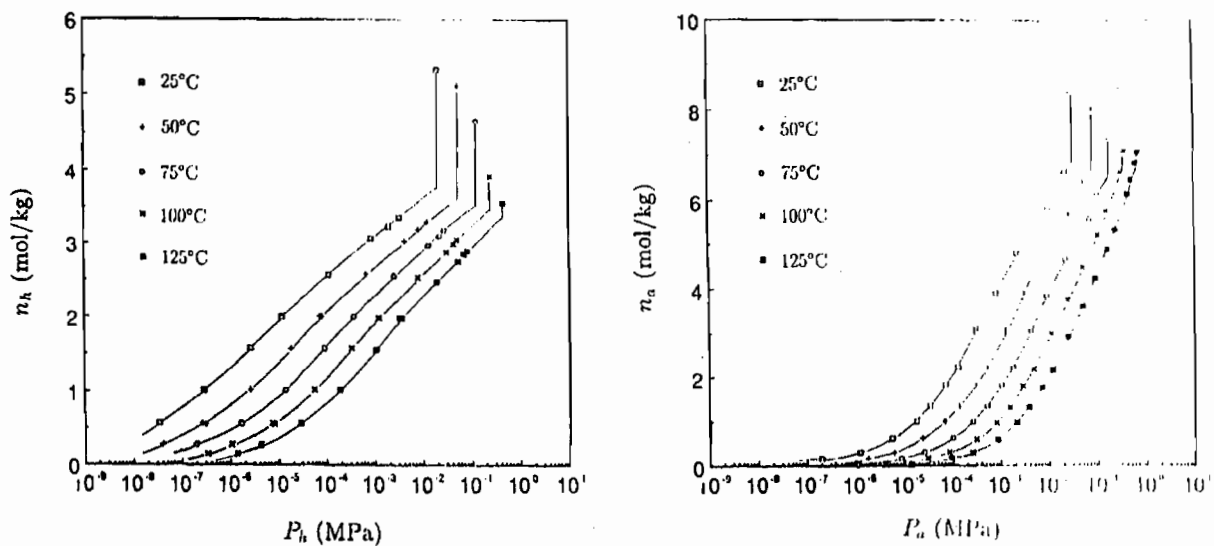


Figure 2: Isotherms for n-hexane (left) and acetone (right) adsorbed on BPL activated carbon.

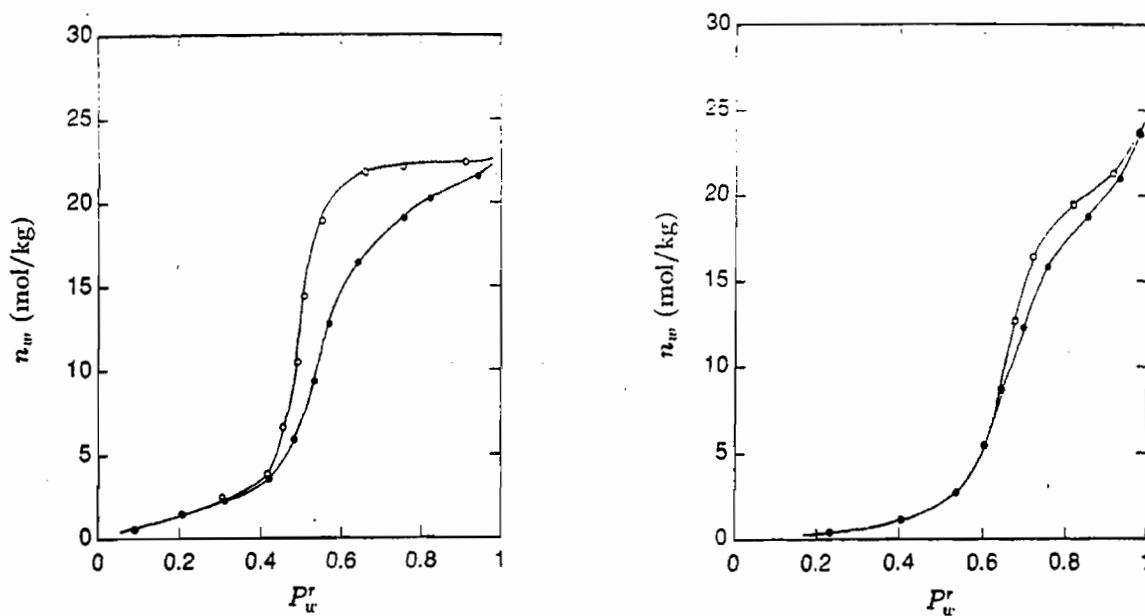


Figure 3: Isotherms for water adsorbed on BPL activated carbon at 25°C (left) and 100°C (right). $P_w^r = P_w/P_w^s$. Filled circles denote adsorption and open circles denote desorption.

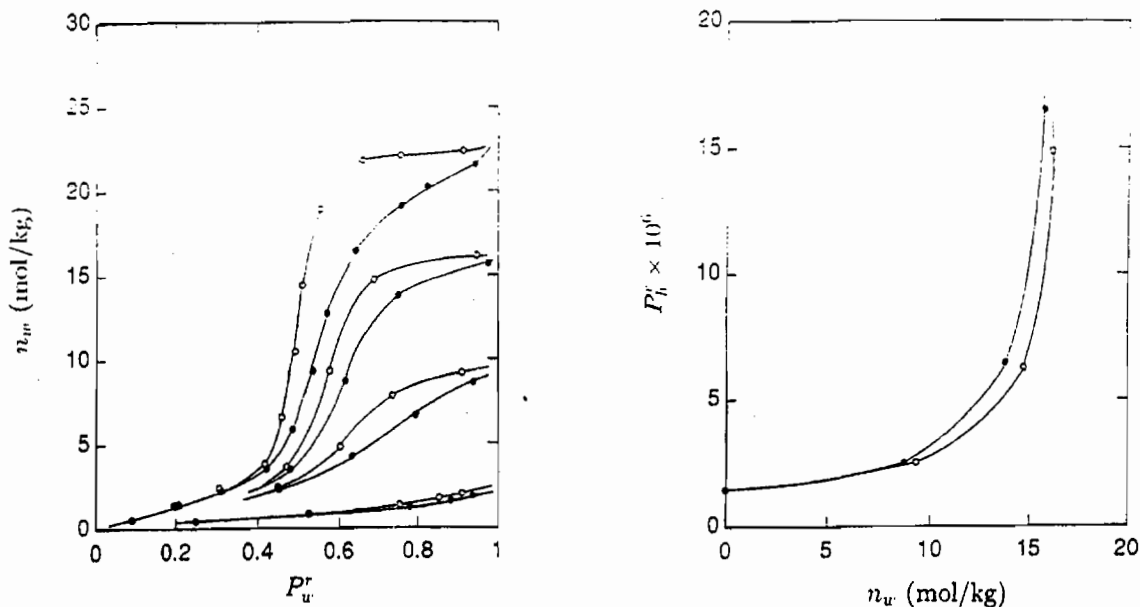


Figure 4: Water-hexane adsorption equilibria. Left: Water isotherms at 25°C for hexane loadings of $n_h = 0$ (top), 0.497, 1.032, and 1.993 (bottom) mol/kg. $P_w^r = P_w/P_w^s$. Right: Effect of water loading on hexane partial pressure at 25°C and $n_h = 0.497$ mol/kg. $P_h^r = P_h/P_h^s$. Filled circles denote adsorption and open circles denote desorption.

hysteresis loop becomes smaller for increasing temperature and shifts to a higher relative pressure. Similar observations have been made by other investigators for the temperature dependence of hysteresis for other systems under cryogenic conditions [4]. Although hysteresis in the water/BPL carbon system did not vanish over the range of temperatures examined, the trends observed in the data suggest that the capillary “critical” temperature does exist for this system.

Coadsorption of Water and Hexane

Experiments were conducted for hexane loadings of 0.497 ± 0.001 , 1.032 ± 0.007 , and 1.993 ± 0.007 mol hexane/kg carbon (nominally 0.5, 1, and 2 mol/kg) at 25°C. Water concentrations were varied from low values to saturation for each of these loadings. Results are shown in Figure 4 (left) along with the pure water isotherm for 25°C. Tests confirmed that the same equilibria were reached independent of the order of introduction of the adsorbed components.

There are two important things to notice in Figure 4 (left). First, the hysteresis loop decreases in size with increasing hexane loading. Second, and most interesting, calculations based on the densities of the pure adsorbates (taken at saturation from Figures 2 and 4) show that the *apparent* total pore volume filled by the hexane and water is significantly less than the total pore volume available for either pure component.

Figure 4 (right) shows the dependence of the hexane partial pressure at constant hexane loading on the amount of water adsorbed for some of the data shown in Figure 4 (left). Here, we see the hexane partial pressure is a strong function of the water loading. The dependence is almost exponential with the partial pressure increasing by over an order of

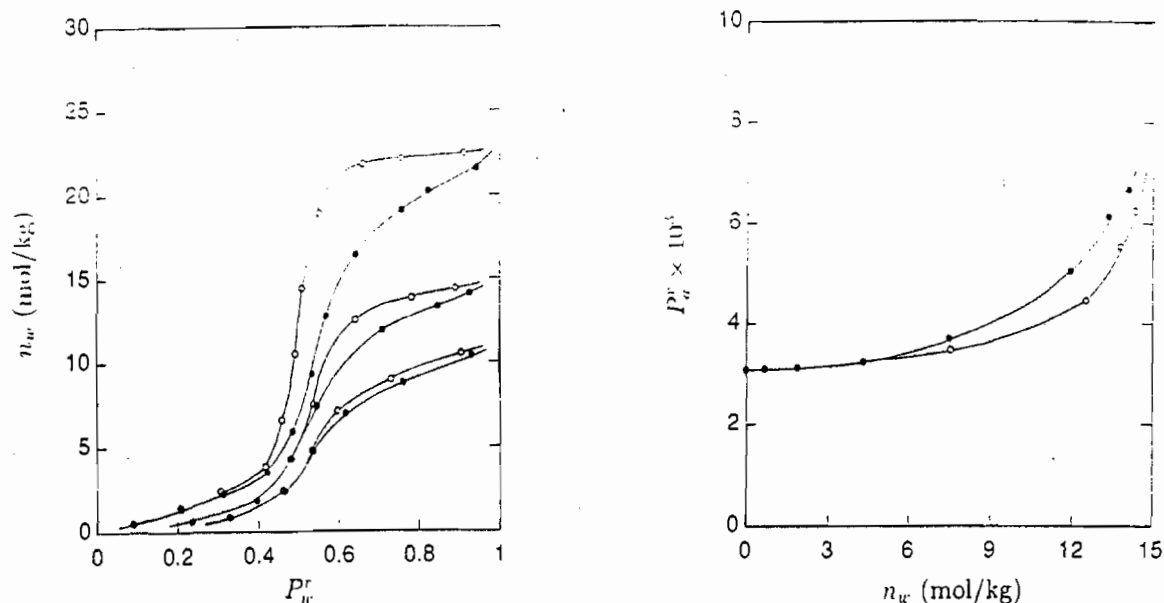


Figure 5: Water-acetone adsorption equilibria. Left: Water isotherms at 25°C for acetone loadings of $n_a = 0$ (top), 1.92, and 3.76 (bottom) mol/kg. $P_w^r = P_w/P_w^s$. Right: Effect of water loading on acetone partial pressure at 25°C and $n_a = 1.92$ mol/kg. $P_a^r = P_a/P_a^s$. Filled circles denote adsorption and open circles denote desorption.

magnitude. An interesting observation is that there are two different equilibrium hexane partial pressures for the same water loading. Thus, the hexane partial pressure depends on the water adsorption path. Experiments performed at 100°C showed similar trends, except that water was able to fill more of the available pore space [1].

Coadsorption of Water and Acetone

As with the hexane-water experiments, the amount of acetone adsorbed was held approximately constant while increasing the loading of water. Because of the miscibility of water and acetone, the vapor phase will reach saturation prior to the point at which the partial pressure of water reaches the pure component vapor pressure.

Water isotherms at 25°C were measured for acetone loadings of 1.92 ± 0.09 and 3.76 ± 0.24 mol/kg (nominally 2 and 4 mol/kg). Figure 5 (left) shows the pure water isotherm at 25°C and the water isotherms for the two acetone loadings. The most striking feature of these data is that the total pore volume is much closer to being filled by the acetone-water mixture than it was by the hexane-water mixture. In addition, there appears to be less water hysteresis than for hexane-water coadsorption.

Figure 5 (right) shows the dependence of the equilibrium acetone partial pressure on the amount of water adsorbed. Although the dependence is seen to be much weaker than that observed for hexane, it is not negligible at higher water loadings. Also, the acetone partial pressure exhibits hysteresis with the higher acetone partial pressure occurring on the adsorption branch of the water isotherm. Results at 100°C showed similar behavior.

CONCLUSIONS

The recirculating constant volume apparatus works well for both pure components and mixtures. Adsorption equilibria can be measured over wide range of temperatures and pressures. Mixture data can be collected in isostere form (i.e., the loading of one component can be held constant).

Isotherms for water on BPL carbon were measured over a range of practical temperatures. The location and size of the hysteresis loop was found to be temperature dependent, with the loop shifting toward higher relative pressures and narrowing as the temperature was increased. The dependence is similar to that for other systems under cryogenic conditions. The data agree with the prediction of a capillary critical temperature.

For the hexane-water system, water isotherms at constant hexane loadings were measured at 25°C and 100°C. Partial pressures of hexane were found to increase significantly at constant hexane loading as the water loading was increased. Hysteresis was observed in the hexane partial pressure depending on whether the system was on the adsorption or desorption branch of the water isotherm. Results at 25°C indicate that water does not completely fill the available pore volume left by adsorbed hexane as the vapor approaches saturation. At high hexane loadings it was found that only a small percentage of the available pore space was filled by the water before saturation. At 100°C the water filled the available pore space much more effectively than at 25°C.

For the acetone-water system, water isotherms at constant acetone loadings were measured at 25°C and 100°C. As with hexane, the partial pressure of the hydrocarbon increased at constant hydrocarbon loading as the water loading was increased, and hysteresis was observed in the hydrocarbon partial pressure depending on whether the system was on the adsorption or desorption branch of the water isotherm. Water was found to fill almost all of the available pore volume as the vapor approached saturation. The most likely explanation for the difference between the observed behavior of water when coadsorbed with hexane or acetone is the solubility of water in the hydrocarbon.

ACKNOWLEDGMENTS

We gratefully acknowledge financial support from the U.S. Army CRDEC, the National Science Foundation, and the Petroleum Research Fund.

REFERENCES

1. Rudisill, E. N., Hacskaylo, J. J., and LeVan, M. D., "Coadsorption of Hydrocarbons and Water on BPL Activated Carbon," *Ind. Eng. Chem. Research*, **31**, in press (1992).
2. Gregg, S. J., and Sing, K. S. W., *Adsorption, Surface Area and Porosity* (2nd ed.), Academic Press, New York, 1982.
3. Dubinin, M. M., "Water Vapor Adsorption and the Microporous Structures of Carbonaceous Adsorbents," *Carbon*, **18**, 355 (1980).
4. Ball, P. C., and Evans, R., "Temperature Dependence of Gas Adsorption on a Mesoporous Solid: Capillary Criticality and Hysteresis," *Langmuir*, **5**, 714 (1989).
5. Mahle, J. J., and Friday, D. K., "Water Adsorption Equilibria on Microporous Carbons Correlated Using a Modification to the Sircar Isotherm," *Carbon*, **27**, 835 (1989).

BLANK

PREDICTION OF BINARY VAPOR ADSORPTION FOR A
HEXANE/WATER MIXTURE ON ACTIVATED CARBON

Richard A. Matuszko¹, David K. Friday¹, and Robert A. Lamontagne²

ABSTRACT

The Adsorbed Solution Theory (AST) is applied to predict binary vapor adsorption of n-hexane and water on activated carbon using only single component adsorption data. The prediction obtained using the Ideal AST (IAST) is compared with predictions obtained from modifications to the AST that allow for non-ideal adsorption. These modifications include use of UNIFAC predicted activity coefficients in a spreading pressure dependent model (SPD), use of pure component saturation adsorption values to predict steric exclusion of water in carbon micropores (MET), and use of a combination of the SPD with the MET. The results indicate that at 25°C the MET produces the best prediction, while at 100°C, the SPD+MET produces the best prediction.

INTRODUCTION

A number of theories for predicting multi-component isotherm behavior from single component data exist today. The most commonly employed theories are the multi-component Langmuir, the Vacancy Solution Model³ (VSM), and the Adsorbed Solution Theory⁴ (AST). The Langmuir and VSM, however, are unnecessarily restrictive in that they require the use of a specific isotherm for correlating the single component data. The AST allows the use of any single component isotherm model. Since the VSM and Langmuir single component models are unable to fit water adsorption on activated carbon (BET type V isotherm), the AST was selected as the candidate for predicting multi-component adsorption behavior.

The AST has been used in various forms incorporating different modifications/simplifications. The most common form of the AST is the Ideal AST⁴ (IAST) where the adsorbed and vapor phases are assumed to be homogeneous, ideal mixtures. The IAST has been used to represent a large matrix of mixtures, but because of the assumptions of ideality, produces serious errors with some systems. Improvements to the IAST have been reported using Spreading Pressure Dependent (SPD)⁵ activity coefficients to correct for adsorbate-adsorbate interactions. Additionally, the concept of Micropore Exclusion⁶ (MET) or adsorption area that is accessible to one component but not to another, has improved the quality of fit for the AST. Unfortunately, past efforts to apply these theories have focused on correlating mixture isotherms and not predicting them.

This paper explores the concept of predicting binary adsorption using the SPD and MET without the use of mixture adsorption data. SPD activity coefficients will be calculated from existing liquid phase excess Gibbs free energy equations. Excluded area for the MET will be predicted from

differences in saturation adsorption values for single component isotherms. These two theories are to be compared with predictions using the IAST.

THEORY

The original SPD as proposed by Talu and Zwiebel⁵ uses a superlattice theory to elucidate molecule-molecule interactions. This approach is unnecessarily restrictive, and cannot adequately represent highly polar and/or hydrogen bonded components. Myers⁶ has proposed a more general form of the SPD where there is a choice of which excess Gibbs free energy (g^E) model to use. This more general form has been selected using the UNIQUAC model for g^E . The UNIQUAC model was chosen because it is the only common g^E model that can adequately represent highly polar and hydrogen bonded species that demonstrate limited miscibility. In addition, the UNIQUAC model can accurately represent activity coefficients for both Vapor-Liquid Equilibria (VLE) as well as Liquid-Liquid Equilibria (LLE). The UNIQUAC model has the form:

$$g^E = g_c^E + g_r^E,$$

The g_c^E is a combinatorial term and the g_r^E is a residual term. Each of these are broken down as follows:

$$g_c^E = RT(x_1 \ln(\phi_1/x_1) + x_2 \ln(\phi_2/x_2) + 5(q_1 x_1 \ln(\theta_1/\phi_1) + q_2 x_2 \ln(\theta_2/\phi_2)))$$

$$g_r^E = RT(-q_1' x_1 \ln(\theta_1' + \theta_2' \tau_{21}) - q_2' x_2 \ln(\theta_2' + \theta_1' \tau_{12}))$$

$$\phi_1 = x_1 r_1 / (x_1 r_1 + x_2 r_2)$$

$$\phi_2 = x_2 r_2 / (x_1 r_1 + x_2 r_2)$$

$$\theta_1 = x_1 q_1 / (x_1 q_1 + x_2 q_2)$$

$$\theta_2 = x_2 q_2 / (x_1 q_1 + x_2 q_2)$$

$$\theta_1' = x_1 q_1' / (x_1 q_1' + x_2 q_2')$$

$$\theta_2' = x_2 q_2' / (x_1 q_1' + x_2 q_2')$$

$$\tau_{12} = \exp(-a_{12}/T)$$

$$\tau_{21} = \exp(-a_{21}/T)$$

r_1 , q_1 , and q_1' are obtained from tables

T is temperature in K

a_{12} and a_{21} are the two fitting parameters

To make the SPD theory truly predictive, the a_{12} and a_{21} values can be obtained from existing LLE or VLE data. In the absence of data, a_{12} and a_{21} can be generated using the UNIFAC group contribution method. For this paper, the n-hexane and water values were obtained using the UNIFAC equation.

Myers' SPD approach incorporates the thermodynamically imperative dependence of g^E on spreading pressure in an adsorption system by the following equation:

$$G^E = (1 - \exp(-C\psi))g^E$$

ψ = spreading pressure

C = constant that depends only on adsorbent

As a result of the linkage between liquid and adsorbed phase excess Gibbs free energies, qualitative behavior of a liquid mixture would be carried over into an adsorbed mixture. Compounds that do not mix well as liquids, are not expected to mix well as adsorbates. Conversely, compounds that attract each other in the liquid phase, will attract each other as adsorbates. These non-idealities manifest themselves in deviations from the vapor pressure expected over the mixture if the system were ideal (Raoult's law). Compounds that do not mix well produce higher vapor phase concentrations than would be found if the liquid/adsorbate interaction were ideal (positive deviations from Raoult's law). Compounds that attract produce lower vapor phase concentrations than would be found if the liquid/adsorbate interaction were ideal (negative deviations for Raoult's law).

The Micropore Exclusion Theory (MET) has been altered to allow for the prediction of excluded areas from single component saturation adsorption values. This modification assumes that differences in saturation adsorption values for a pure component, represent a genuine phenomenon where specific areas of the sorbent surface are excluded to individual compounds. If the saturation values differ, it is assumed that the difference is due to micropore exclusion. The difference in the saturation values is then incorporated into the MET as the amount of excluded adsorption area. A more detailed description of MET predictions and calculations can be found in Matuszko and Lamontagne⁷.

SINGLE COMPONENT ISOTHERMS

An isotherm equation is correlated to single component data for each component. A modified Antoine⁸ equation is used:

$$\ln P = A' - B' / (C + T)$$

Where:	B'	=	$B\theta + b(1 - \theta)$	
	A'	=	$A + (1 + a\theta^{1/2})\ln\theta$	(for hexane)
	A'	=	$A + a\theta$	(for water)
	P	=	Vapor phase partial pressure	
	T	=	Temperature	
	θ	=	Fraction surface coverage (W/W_0)	
	A, B, C	=	Antoine coefficients	
	a, b, W_0	=	Fitting parameters	

Both forms of the equation reduce to the Antoine equation in the limit of saturation. The hexane equation reduces to Henry's law in the limit of zero loading, but the water equation does not. The lack of a Henry's law limit for the water isotherm, however does not pose a problem since the amount of water adsorbed is so low at even moderate vapor phase concentrations.

RESULTS AND DISCUSSION

The adsorption data set of HacsKaylo⁹ for n-hexane and water on activated carbon was used for this analysis. Figures 1 and 2 give single component adsorption isotherms for hexane and water respectively. The data cover a 100°C temperature range in 25°C increments and 6 decades of pressure. Plotted with the data are fits of the respective

LeVan isotherms for each temperature. Coefficient values for these correlations are:

	a	b	WO
n-hexane	0.538	5907	519.42
water	0.33309	3875	474.09

The MET excluded area calculation for hexane and water on BPL carbon produces a result that is inconsistent with molecular size. From the calculations, it appears that the smaller molecule (water) is excluded from portions of the carbon that the larger molecule (hexane) can adsorb. Indeed, a number of organic and water adsorption systems on hydrophobic sorbents produce saturation adsorption values that are higher for the organic than for the water. This anomaly can be ascribed to the hydrophobicity of the adsorbent inhibiting the water from adsorbing as an individual molecule on the surface. However, when water is in sufficient concentration in the vapor phase, the local environment of an individual water molecule is heavily influenced by the other water molecules present. Therefore, if the water adsorbs on the hydrophobic surface in a large enough group, the character of the locality will be dictated by the water and thus become more hydrophilic. As a result, the water will tend to adsorb in clusters. In smaller pores, not enough water can fit to change the local character to hydrophilic, so water does not adsorb there. The net result, an increase of the effective size of water, is shown schematically in Figure 3.

Figures 4-8 give the binary adsorption data points and AST predictions for hexane and water at 25°C and 100°C. The data is given as hexane isosteres, or plots of constant hexane adsorbed phase loading. The hexane loadings investigated are approximately 0.5 moles/Kg carbon (Figure 4), 1.0 moles/Kg carbon (Figures 5 and 7), and 2.0 moles/Kg carbon (Figures 6 and 8). The plots detail how the vapor phase concentration of hexane will change with changes in adsorbed phase concentrations of water.

Figures 4-6 (25°C) show predictions from the IAST and MET, but do not give predictions using the SPD or SPD-MET. The SPD and SPD-MET predictions for these data have been omitted because the adsorbed system is demonstrating negative deviations from Raoult's law while the liquid mixture gives positive deviations from Raoult's law. It is clear that the dominant force in the adsorbed phase is not adsorbate-adsorbate interactions. In each of the three plots, the IAST and MET predictions either lie above or cut through the data. Applying the SPD or SPD-MET to these systems would produce predictions that lie significantly above those of the IAST and MET, thus reducing the quality of the fits.

Figures 7 and 8 (100°C) show predictions for all four forms of the AST. In contrast to the 25°C data, the 100°C data lies above the predictions for the IAST and MET, indicating positive deviations from Raoult's law. Since this is consistent with a liquid mixture of hexane and water, applying SPD activity coefficients should improve the quality of fit for the data. Indeed, for both plots at 100°C, the quality of fit is dramatically improved using the SPD. The best overall fits are obtained using the SPD-MET combination for both 100°C data sets.

CONCLUSIONS

Three possible conclusions can be drawn from the binary data and predictions:

1. The forces that dictate the character of the binary adsorption system are temperature dependent. At 25°C, it appears that the dominant force in the adsorbed phase is one which gives negative deviations from Raoult's law. At 100°C, the dominant force in the adsorbed phase is the adsorbate-adsorbate interaction which can be accounted for with SPD activity coefficients.
2. The quality of the single component correlations is insufficient for accurate AST calculations. The AST requires integration under the single component isotherms, and is thus very sensitive to the quality of the correlation selected. Error in the single component correlations could produce anomalous results in predictions of mixture adsorption.
3. The AST cannot be used for a hexane and water mixture on BPL carbon. The AST assumptions of a homogeneous, two-dimensional phase may not apply for the adsorption of hexane and water on BPL carbon.

REFERENCES

1. Geo-Centers, Inc., Fort Washington, MD 20744.
2. Naval Research Laboratory, Washington DC 20375.
3. Suwanayeeun, S.; Danner, R.P. *AIChE Journal* 1980, 26, 68.
4. Myers, A.L.; Prausnitz, J.M. *AIChE Journal* 1965, 11, 121.
5. Talu, O.; Zwiebel, I. *AIChE Journal* 1986, 32, 1263.
6. Myers, A.L. "Adsorption: Science and Technology"; Kluwer Academic Publishers, Rodrigues, R.E.; LeVan, M.D.; Tondeur, D., Ed. 1989, 15.
7. Matuszko, R.A.; Lamontagne, R.A. "Multi-Component Isotherms for Highly Non-Ideal Mixtures", Proceedings of the 1990 CRDEC Conference on Chemical Defense, 1991.
8. Hacskaylo, J.J.; LeVan, M.D. *Langmuir* 1985, 1, 97.
9. Hacskaylo, J.J. "Thermodynamic Studies of Vapor-Solid Adsorption Equilibria", Ph.D. Dissertation, University of Virginia, August 1987.

**HEXANE ISOTHERMS ON BPL CARBON
WITH A 2 PARAMETER LEVAN FIT**

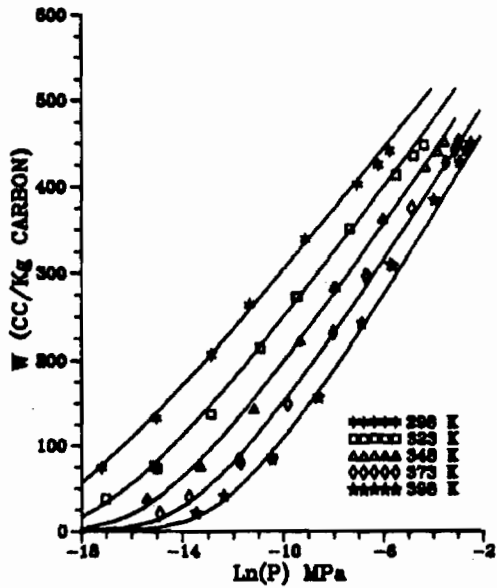


FIGURE 1

**WATER ISOTHERMS ON BPL CARBON
WITH A 2 PARAMETER LEVAN FIT**

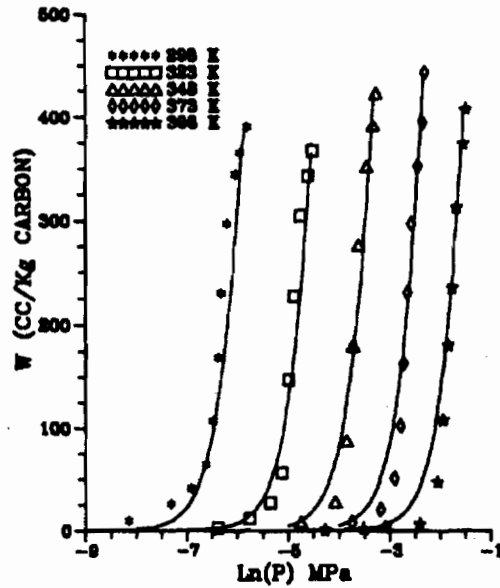


FIGURE 2

WATER ADSORPTION IN CARBON MICROPORES

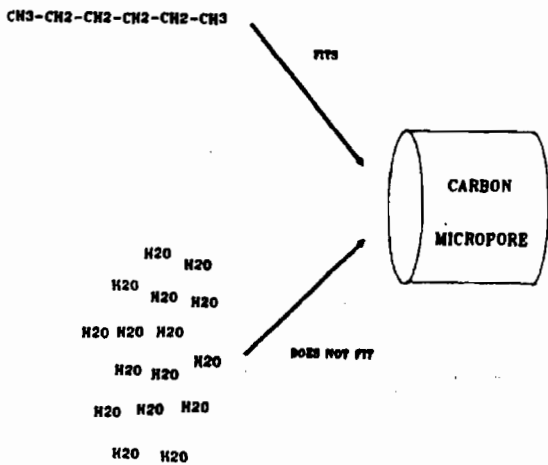


FIGURE 3

**WATER AND HEXANE ON BPL CARBON
DATA AND PREDICTIONS AT 25 °C**

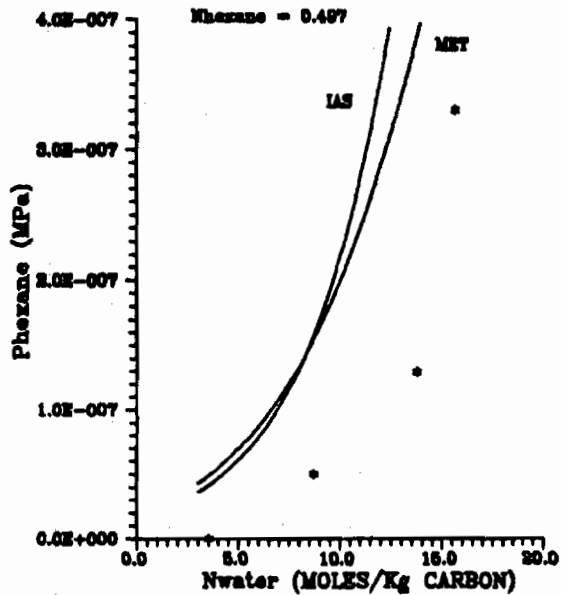


FIGURE 4

**WATER AND HEXANE ON BPL CARBON
DATA AND PREDICTIONS AT 25 °C**

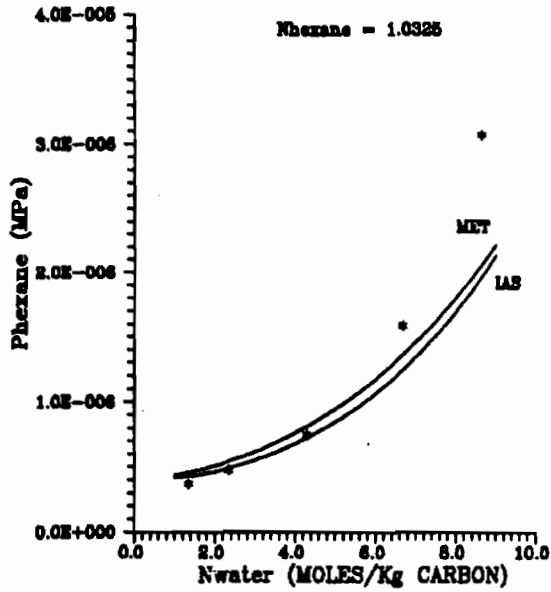


FIGURE 5

**WATER AND HEXANE ON BPL CARBON
DATA AND PREDICTIONS AT 25 °C**

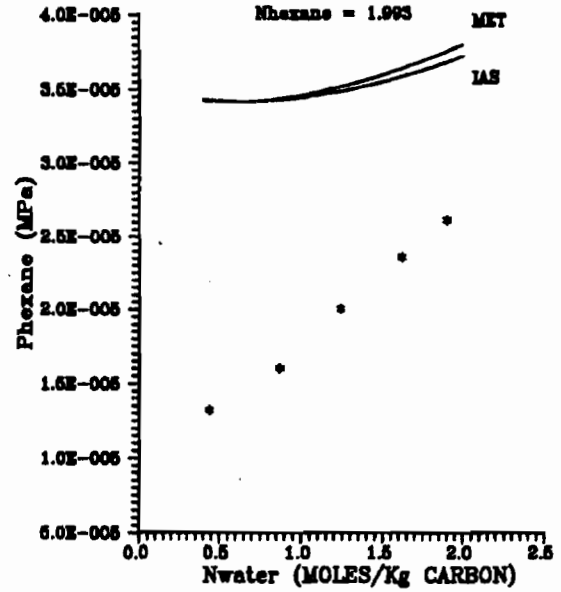


FIGURE 6

**WATER AND HEXANE ON BPL CARBON
DATA AND PREDICTIONS AT 100 °C**

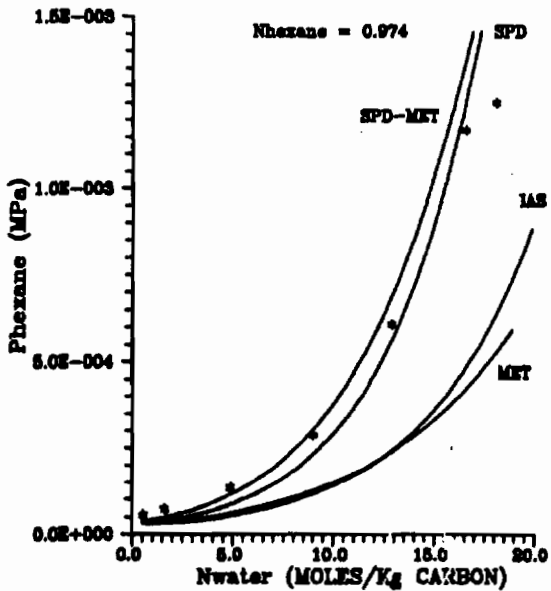


FIGURE 7

**WATER AND HEXANE ON BPL CARBON
DATA AND PREDICTIONS AT 100 °C**

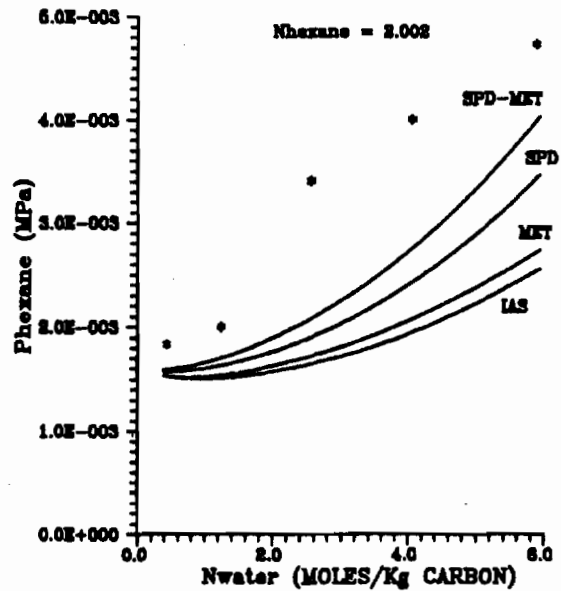


FIGURE 8

BLANK

CHARACTERIZATION OF THE ARMORED VEHICLE ENVIRONMENT

Jan S. Matuszko and Robert A. Lamontagne
Naval Research Laboratory
Washington, DC 20375

Richard A. Matuszko and Victoria J. Davis
Geo-Centers, Inc.
Ft. Washington, MD 20744

The Naval Research Laboratory (NRL) has been tasked to identify atmospheric constituents in an armored vehicle environment in order to aid in the design and optimization of a regenerative air filtration system. Field sampling around diesel engine tanks and turbine engine tanks using carbon tubes is being conducted at representative Army sites in order to determine the contaminants which may adversely affect the proposed filtration system. Methods for analysis include: pH of carbon water extracts, nitrogen BET surface area, and GC/MS of carbon disulfide extracts.

INTRODUCTION:

There has been some concern that vapors generated during armored vehicle operations may adversely affect the proposed Pressure Swing Adsorption (PSA) Collective Protection System (CPS) for armored vehicles. The Naval Research Laboratory (NRL) has had a long history of conducting atmospheric measurements in military environments. Because of this, NRL was asked to determine if the above concern was valid. NRL began a program to identify atmospheric constituents produced during operations conducted with diesel powered tanks and gas turbine powered tanks. Data is being collected using carbon sampling tubes during basic tank operations such as cross country maneuvers, road marches, and motor pools. Additionally, the impact of artillery rounds on the CPS is being determined. Data is being collected on both a short and long term basis.

Once the sample has been collected, some or all of the following tests are then performed on the carbon from the sampling tubes: weight loss measurements, pH tests, surface area measurements and GC/MS hydrocarbon analysis on carbon disulfide extracts. The weight loss measurements indicate the amount of water present on the carbon and therefore the area unavailable for adsorption by low molecular weight hydrocarbons. The pH measurements indicate the amount of use or weathering that has occurred on the carbon filters. The surface area measurements indicate how much of the carbon is available for adsorption. Finally, the GC/MS analysis indicates the degree of weathering as well as the type and amount of contaminants present on the carbon.

EXPERIMENTAL:

EQUIPMENT:

Figure 1 is photograph of a long-term atmospheric sampler that is being used for this project as well as being deployed on Navy ships for a similar project. There are three main components to the sampling system. The first

component, labeled with the numeral one in the figure, consists of five tubes, six cm (D) by fifteen cm (L), filled with BPL carbon (7-Big-V obtained from Chemical Research, Development and Engineering Center (CRDEC) personnel) mounted inside a standard High Efficiency Particulate Air (HEPA) filter. The second component (2) is a volumetric gas flow meter while the third component (3) is a blower motor. The unit is approximately sixty cm (W) by sixty cm (H) by 122 cm (L) and weighs approximately thirty Kg. Atmospheric air is drawn through the carbon sampling tubes by the blower attached to the common plenum and total air volume that has passed through the filters is measured by the flow meter. The carbon tubes can then be removed and replaced with tubes containing unweathered carbon at various intervals.

Figure 2 is a photograph of the short-term atmospheric sampling unit which is installed on tanks and other armored vehicles. The sampling system basically consists of two pumps/meters, tygon tubing, carbon sampling tubes, and a metal bracket. The pumps/meters (Model 224-PCXR7) are manufactured by SKC Inc. and are compact, programmable, and battery operated. The carbon sampling tubes (SKC catalog number 226-16-02) are 10mm x 150mm and contain 1000 mg of coconut charcoal. Each pump/meter can be programmed to run for a period of at least eight hours of continuous service. By using two meters, duplicate samples can be taken concurrently or the same tank environment can be evaluated for a period of up to sixteen hours.

PROCEDURES:

Once the carbon tubes are removed from the long term sampling equipment, they are brought back to the laboratory and analyzed. Carbon from these long-term samplers are divided into four three-quarter-inch sections, measured perpendicular to the air flow, and one remainder section encompassing the rest of the carbon. Weight loss measurements, pH tests, surface area measurements, and GC/MS hydrocarbon analysis are then performed on each section. Carbon from the short term samplers is simply extracted with carbon disulfide and subjected to a GC/MS hydrocarbon analysis.

RESULTS/DISCUSSION:

ARTILLERY TESTING:

The artillery testing data was obtained at the Human Engineering Laboratory (HEL) in Aberdeen, MD when gunnery rounds were being fired for a period of approximately thirty days. A long-term sampler was used and atmospheric data was collected during physiological/psychological artillery testing conducted by HEL in which personnel were dressed in various stages of Modified Overgarment Personnel Protection (MOPP). Data was collected for a range of gunnery rounds fired - from 270 to 819 rounds. The gunnery rounds were blank, but were fired with the standard propellant composed mainly of aluminum perchlorate. The major exhaust components from that type of propellant are listed in the literature as aluminum chloride, carbon monoxide, hydrochloric acid, water, nitrogen, and hydrogen.

The results of the pH tests of these carbons are listed in Table 1. These values can be compared to a reference, unweathered carbon which has a pH of 8.0 plus or minus 0.1. The decrease in the pH of these samples from that of the reference carbon is very significant when compared to the decrease that we have documented for carbon weathered in non-gunnery conditions (a decrease from 8.0 to 7.7). This decrease in pH is most likely related to the HCl vapor produced in relatively high quantities in the propellant exhaust. Additionally, it appears that the number of gunnery rounds fired did not have a significant effect on the pH values measured for each section.

TABLE 1: NORMALIZED pH VALUES OBTAINED FOR GUN SAMPLES (2 HOUR READING)						
SAMPLE #	SECTION					GUNNERY ROUNDS FIRED
	3/4	6/4	9/4	12/4	REMAINDER	
GUN-1	5.1	5.5	6.4	7.3	7.0	270
GUN-2	5.7	6.3	6.7	6.7	6.8	270
GUN-3	5.7	7.2	7.2	7.2	7.5	270
GUN-4	5.5	5.8	6.2	6.2	6.3	540
GUN-5	5.2	5.8	6.0	6.3	6.6	540
GUN-6	4.9	5.6	5.8	5.9	6.7	540
GUN-7	5.7	5.9	6.2	6.2	6.2	810
GUN-8	5.4	5.8	6.0	6.4	6.1	810

Table 2 shows the results of the weight loss measurements. The weight loss measurements obtained in this gunnery environment show a different trend than data obtained in a hydrocarbon environment. In general, the amount of water found on the bed was greatest at the inlet portion and decreased with increasing bed depth. One exception was the remainder section of the Gun-1 sample which may be attributable to experimental error. The increased water present at the inlet portion of the carbon filters could very well be associated with the increased HCl loading that we speculate is present due to the decreased pH values.

TABLE 2. PERCENT WEIGHT LOSS OF CARBON FOLLOWING HEATING (150°F) FOR THREE HOURS						
SAMPLE	SECTION					GUNNERY ROUNDS FIRED
	3/4	6/4	9/4	12/4	REMAINDER	
GUN-1	14.4	8.5	6.3	4.7	11.7	270
GUN-2	10.5	7.7	6.2	5.2	5.8	270
GUN-3	8.8	5.3	4.2	3.3	3.4	270
GUN-4	11.6	9.2	6.6	5.9	5.7	540
GUN-5	11.8	8.1	6.7	5.4	5.6	540
GUN-6	12.7	9.5	6.8	6.3	6.6	540
GUN-7	14.8	10.5	9.0	7.2	7.1	810
GUN-8	14.9	10.9	9.0	8.0	6.8	810

Table 3 shows the surface area values obtained for each sample. In general, the area available for adsorption following weathering in a gunnery environment is not significantly different than the area available in an unweathered sample.

The ion chromatograms of the carbon disulfide extracts of the carbon showed no hydrocarbon peaks. The only peaks present were attributable to the solvent and to compounds which are most likely imparted on the carbon as part of the activation process.

Due to the lack of peaks on the GC trace of these carbons and the weight loss measurements, hydrocarbons were not adsorbed on the carbon samples in this gunnery environment. The pH measurements indicate that a compound (or compounds) are present which caused the pH value of the carbon samples (particularly the inlet samples) to become acidic. The acidic pH is probably due to HCl since it makes up 20% of the composition of the propellant exhaust. Surface area measurements indicate, however, that weathering of this type does not adversely affect the available adsorption area of the carbon.

TABLE 3: SURFACE AREA OF CARBON SAMPLES (M ² /G)*						
SAMPLE #	SECTION					GUNNERY ROUNDS FIRED
	3/4	6/4	9/4	12/4	REMAINDER	
GUN-1	1281	720	1027	1358	1060	270
GUN-2	1063	1158	1017	1131	966	270
GUN-3	1077	1103	998	1038	1037	270
GUN-4	1196	1122	1022	1073	1056	540
GUN-5	1061	1067	1006	1079	1025	540
GUN-6	889	1082	1054	1087	1161	540
GUN-7	1104	1040	1005	1075	966	810
GUN-8	1061	1097	1004	918	1100	810

* Reference Carbon (7-Big-V) = 1114 m₂/g

SHORT-TERM SAMPLES COLLECTED IN A GAS TURBINE-POWERED TANK ENVIRONMENT:

Short-term sampling systems were installed on the bustle rack of M1A1 tanks at Fort Hunter-Liggett in California for a period of approximately two weeks in August 1991. The data was collected during testing sponsored by the Armor Test Directorate in which the new M1A2 tanks were compared with the M1A1 tanks. The tanks participated in a variety of operations including cross country maneuvers, road marches, motor pools and gunnery ranges. Additionally, some samples were obtained while the tanks were being refueled.

Since the amount of the carbon adsorbent in the sampling tubes was small, only the GC/MS analysis was performed on these short term samples. As was the case for the artillery tests, no hydrocarbon peaks were found on the ion chromatograms of these samples.

The environment under which these samples were collected was extremely dusty. The carbon sampling tubes have a wool plug at the entrance to the tube to filter out particulates. Since there were no vapors collected on the carbon and since the environment was so dusty, it was possible that vapors would have been trapped on the wool plug along with the particulate matter. In order to determine if this had occurred, carbon disulfide extracts of the wool plug were also analyzed by GC/MS. The only peak present on each of these wool extracts was the carbon disulfide peak.

It was somewhat surprising that no vapors were collected on the sampling tubes during these tests. This indicates that tank operations do not affect the Collective Protection System of the tanks on a short-term basis. During short-term testing in a naval environment, hydrocarbons are usually collected on the sampling tubes. This may be due to the fact that there are multiple contamination sources in a shipboard environment but only one for a tank environment. Long-term sampling in an M1A1 tank environment should be conducted to ensure that the vapors produced during tank operations will not collectively affect the CPS over longer time periods than those examined in these tests.

SHORT-TERM SAMPLES COLLECTED IN A DIESEL-POWERED TANK ENVIRONMENT:

Short term samplers have been installed on an Army recovery vehicle at the Recovery School in Edgewood, MD. Atmospheric samples have been obtained during recovery operations and during idling time.

Figure 3 is the ion chromatogram of the carbon disulfide extract of an eight hour sample. Figure 4 is the ion chromatogram of a standard containing nC_7 - nC_{17} . The carbon disulfide solvent peak comes off the column at a retention time of approximately 165 seconds. The peak at the approximate retention time 185 is benzene, an impurity in the carbon disulfide solvent. The peak directly preceding the carbon disulfide is inherent to the carbon itself. It is most likely due to the activation process. The peak at the approximate retention time of 210 seconds is chloroform. This is a contamination peak from the GC/MS autosampler and is not a part of the diesel environment. The remainder of the peaks are due to the diesel environment.

It should be noted that the sampling tube was placed in the exit gas plume of the motor. Notice that the lower molecular weight hydrocarbons do not appear on the ion chromatogram. The hydrocarbons appear to be in the range of C_{14} and above. This may not be too surprising in that the materials of interest may be on the soot particles that are not collected in the carbon sampling tubes. Drager tube analysis showed high molecular weight hydrocarbons in the diesel exhaust of approximately 1740 ppm.

CONCLUSIONS

The atmosphere from the following tank operations in both diesel and gas turbine environments have been sampled: artillery tests, cross country maneuvers, road marches and idling time. Both long and short term sampling around artillery firing showed no major effect on the carbon with the exception of lowering the pH of water extracts of the carbon. During short term sampling in the gas turbine powered M1A1 tank environment, no hydrocarbon species were collected on the carbon. It appears that M1A1 tank operations should not have any effect on the Collective Protection System of the tanks on a short-term basis. Long-term samples in the vicinity of M1A1 tanks will be collected at Ft. Hood, Texas to verify this conclusion. Finally, high molecular weight hydrocarbons have been found on carbon from short-term samples collected around diesel tank operations.

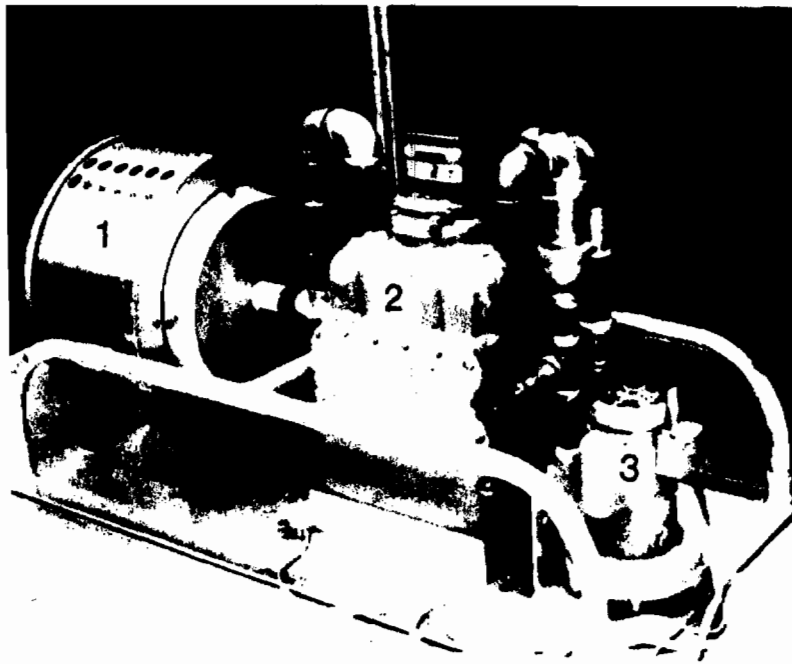


FIGURE 1. LONG TERM AIR SAMPLER

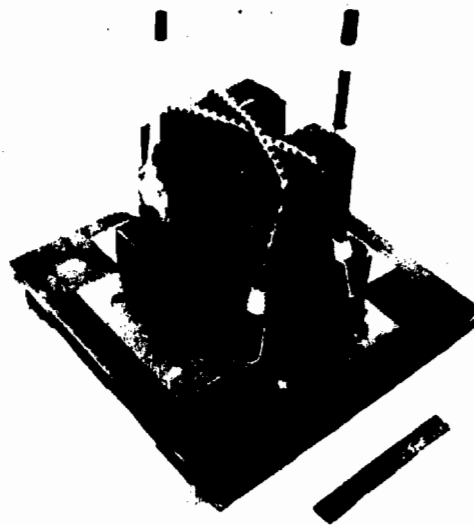


FIGURE 2. SHORT TERM AIR SAMPLER

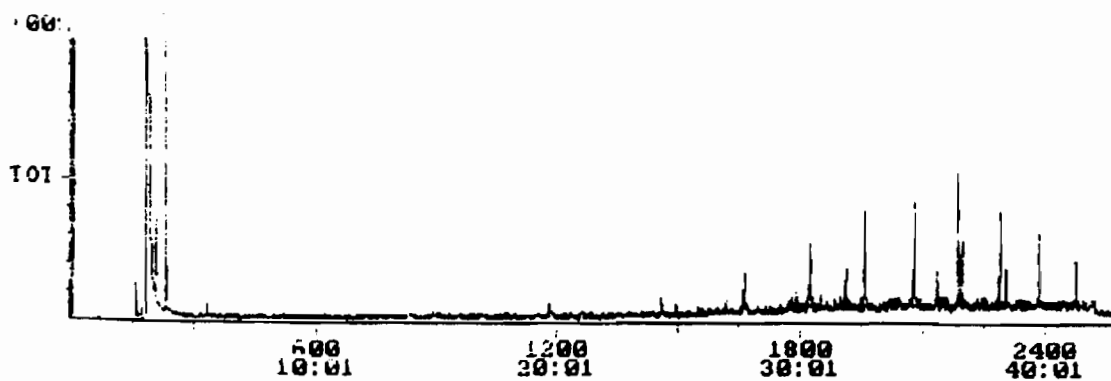


FIG 3. ION CHROMATOGRAM OF 8 HOUR DIESEL ENVIRONMENT

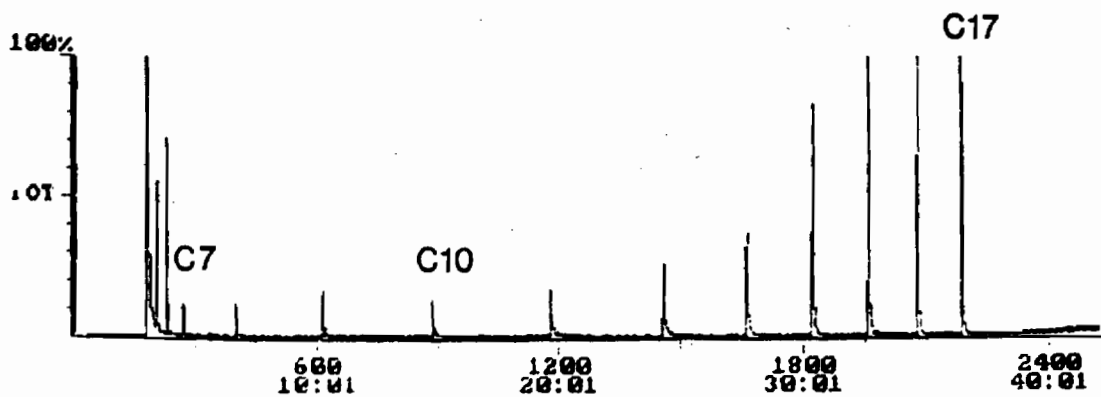


FIG 4. ION CHROMATOGRAM OF nC7 - nC17 STANDARD

BLANK

CATALYTIC OXIDATION OF HYDROGEN CYANIDE VAPOR

Gary B. Howe, J. Jerry Spivey, and George W. Stinagle
Research Triangle Institute

RTI has completed the initial phase of a study to determine the reaction kinetics of the catalytic oxidation of hydrogen cyanide (HCN) vapor over a 2.15% platinum on alpha-alumina catalyst. Reaction rate equations have been derived from experiments involving oxidation of HCN vapor in a packed bed reactor operating under differential conditions. Feed concentrations were varied between 500 and 1200 parts-per-million in both dry and humidified air. Reactor temperature was varied between 180 and 208 degrees Celsius to determine the temperature dependence of the reaction rate. The experimental results have shown an inverse dependence of reaction rate on the HCN feed concentration.

INTRODUCTION

Catalytic oxidation is a proven technology for destruction of volatile organic compounds in automobile exhaust and industrial source emissions. The U.S. Army Chemical Research, Development and Engineering Center is currently engaged in a program to evaluate catalytic oxidation as a technique for the destruction of chemical warfare agents. Such a capability is needed in collective protection systems to produce breathable air for the operators of armored vehicles.

Studies by other investigators have shown that hydrogen cyanide can be oxidized at relatively low temperatures on precious metal catalysts.^{1,2} However, little information has been published concerning the reaction kinetics of HCN oxidation. Intrinsic kinetics are an important aspect of modeling reactor performance and enabling the optimization of reactor design and operating conditions.

EXPERIMENTAL

Shown in Figure 1 is a schematic diagram of the system used to obtain experimental data for determining HCN oxidation rates in this study. The reactor consisted of a 4 mm ID quartz tube housed in a split-tube furnace. A granular catalyst was held in place in the center of the tube with quartz wool plugs at either end. Feed gases were metered with mass flow controllers and blended by passing them through a section of tubing packed with quartz chips. A stream selection valve was used to select either reactor inlet or outlet gas for analysis by gas chromatography (GC). When analyzing the reactor inlet gas, a three-way valve could be switched to provide a dry nitrogen purge flow across the reactor bed. When necessary, part of the nitrogen feed gas could be humidified by passing it through a flask containing deionized/distilled water.

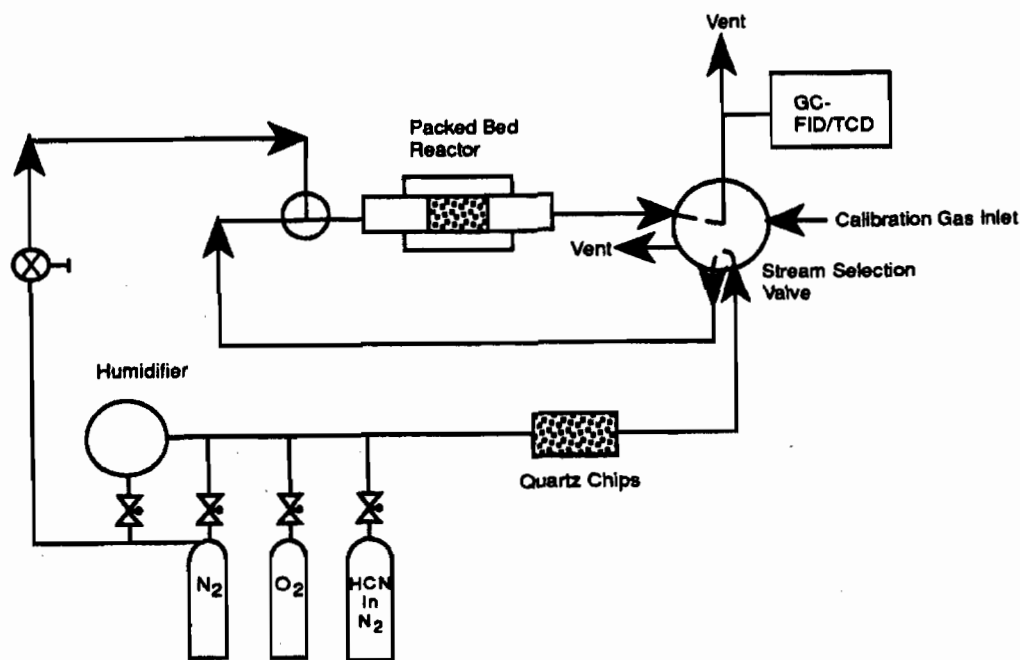


Figure 1. Microreactor System Schematic

The gas chromatograph was configured with packed columns and a thermal conductivity detector (TCD) for the analysis of reaction products and a capillary column with a flame ionization detector (FID) for the analysis of unreacted hydrogen cyanide.

The reactor was packed with a 1 cm long bed of 2.15 percent platinum on alpha-alumina. The catalyst surface area was 1 to 5 m²/g and the particle size was 60/80 mesh. The high platinum loading was selected to provide good resistance to deactivation and high activity at low temperatures. The low surface area alpha-

alumina support was chosen because it has shown superior resistance to degradation from acidic reaction products when compared to high surface area gamma-alumina. The bed was pretreated by heating for 4 hours at 150°C and then overnight at 450°C while purging with dry air.

The reactor was operated under differential conditions (i.e. conversion of less than 10 percent) to minimize concentration and temperature gradients and to simplify data analysis. The use of capillary GC with flame ionization detection made it feasible to measure the small differences between feed concentration and outlet concentration at such low conversions. One limitation of operating under these conditions is that the effect of product inhibition on the reaction rate would not be observed as easily as under integral conditions.

The feed concentration of HCN was varied between 500 and 1200 parts-per-million in both dry and humid (50% relative humidity) air at a reactor temperature of 208°C. At each feed condition, the inlet and outlet concentration of HCN was measured by GC-FID and the outlet concentrations of carbon dioxide and carbon monoxide were measured by GC-TCD. Based on these measurements, the conversion of HCN was determined and reaction rates were calculated.

In addition to determining reaction rates for various HCN concentrations at 208°C, reaction rates were also determined for other temperatures with a feed concentration of 500 parts-per-million HCN in both dry and humid air. This data was needed to determine the temperature dependence of the reaction rate.

A final test performed was to expose the catalyst bed to HCN in humid air for 9 hours to test for deactivation. Test conditions consisted of: 250 °C reactor temperature, 2200 h⁻¹ space velocity, 1000 ppm HCN feed concentration, and 5 percent relative humidity.

RESULTS

Shown in Figure 2 is a plot of the HCN destruction rate versus the average HCN concentration $[(\text{Inlet}-\text{Outlet})/2]$ for feed concentrations ranging from 500 to 1200 parts-per-million in dry air. These rates were measured for a reactor flow rate of 200 sccm which corresponds to a space velocity of approximately $95,000 \text{ h}^{-1}$. As seen in the plot, the reaction rate decreased with increasing HCN feed concentration.

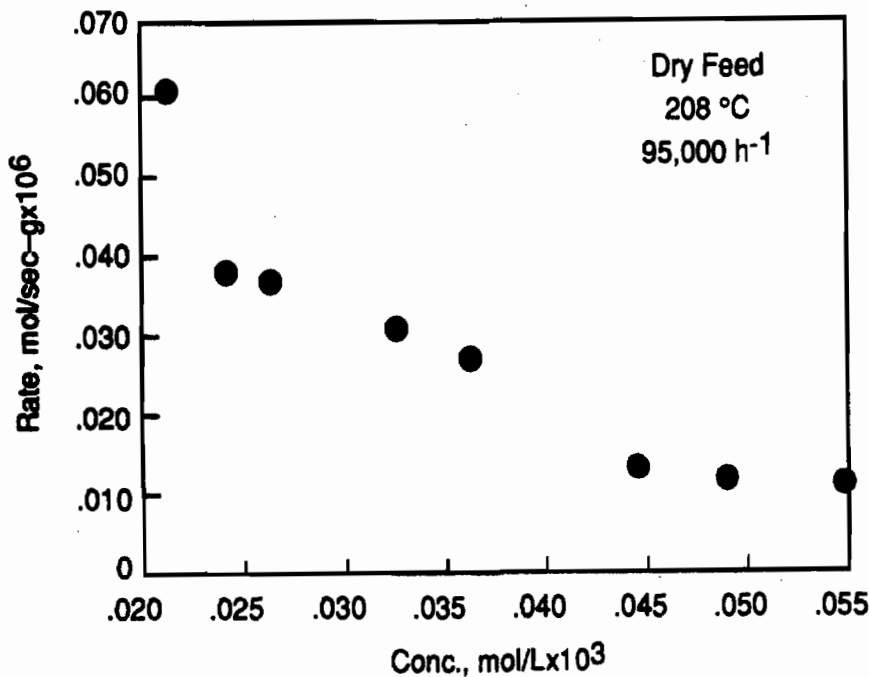


Figure 2. HCN Oxidation on 2.15% Pt/ α Alumina

Two different models were tested for describing the dependence of reaction rate on HCN concentration. The first of these is a simple power-rate law and is shown in equation 1.

$$-r_A = k/C_A^2 \quad (1)$$

The second model is based on Langmuir-Hinshelwood kinetics and is shown in equation 2.

$$-r_A = kC_A/(1+k_1C_A)^3 \quad (2)$$

The model represented by equation 2 is based on the assumption that three sites are involved in each reaction cycle and that the surface reaction controls the rate.

Such a three site model would apply if the reaction mechanism involved dissociation of HCN upon adsorption.

Each model provided about the same goodness-of-fit to the experimental data. Figure 3 shows the curve generated by a non-linear least squares fitting routine using equation 2 as the model. It should be noted that the oxygen concentration was constant for any given HCN feed concentration, and thus is included in the constant k. While the fit of the experimental data to the model does not prove the mechanism suggested above, it does provide some evidence to support it.

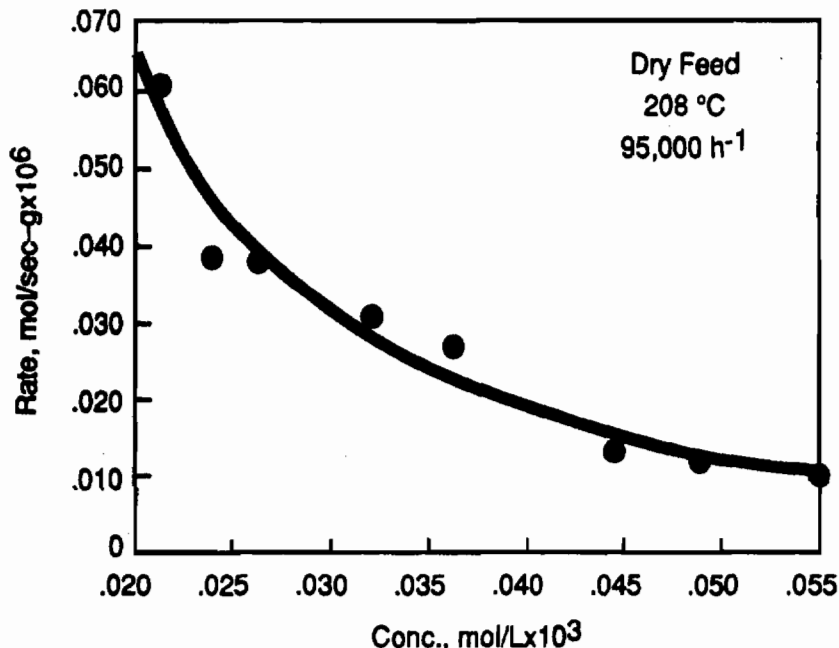


Figure 3. Fit of $r=kC/(1+k_1C)^3$

For sufficiently high HCN feed concentrations, equation 2 reduces to the form of the power-rate law shown in equation 1. This is apparently the concentration region in which reaction rates were measured in this study, since either model provided about the same fit to the experimental data. At sufficiently low HCN concentrations, the second rate expression should become first-order in HCN concentration. Such behavior is typical of catalytic oxidation reactions in which the rate of chemical reaction on the catalyst surface is controlling.³

The same models provided a good fit to the rates obtained at concentrations of HCN from 500 to 1200 parts-per-million in humidified air (50% relative humidity). Figure 4 shows the curve based on the fit of the experimental data with model 2. For a given concentration of HCN, the reaction rate under humid conditions was higher than the rate under dry conditions.

Figure 5 shows an Arrhenius plot of the natural logarithm of reaction rate

versus reciprocal absolute temperature for rates obtained over the temperature range of 190 to 208°C with HCN diluted in dry air at a feed concentration of 500 parts-per-million. As expected, the reaction rate increases with increasing temperature. An activation energy of 28.4 kcal/mol was calculated from the slope of the line.

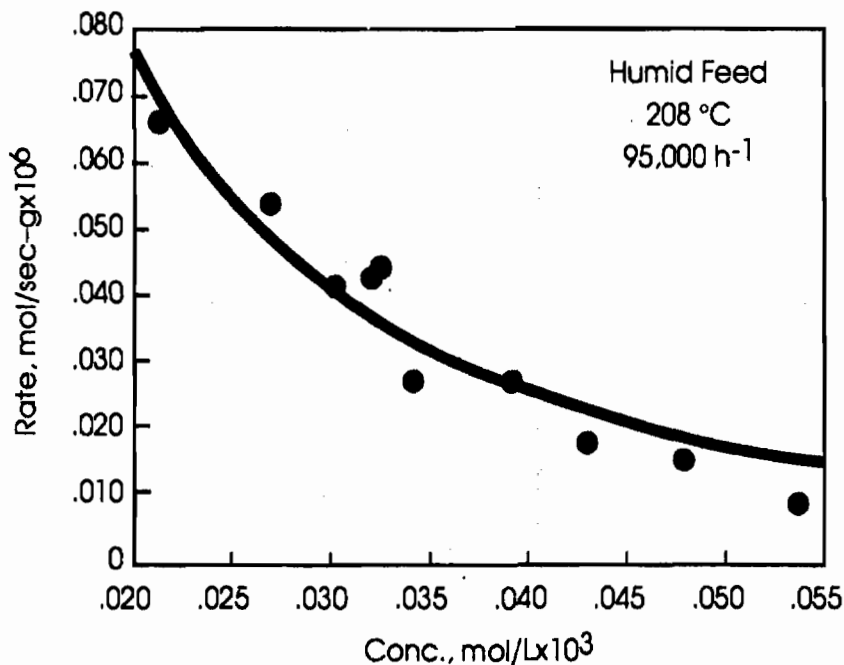


Figure 4. Fit of $r = kC / (1 + k_1C)^3$

Similarly, the natural logarithm of the reaction rate exhibited a linear dependence upon reciprocal absolute temperature for the humidified feed gas. An activation energy of 31 kcal/mol was calculated.

Finally, results of the catalyst deactivation test showed that during a nine hour period of continuous exposure, the HCN conversion remained at greater than 99 percent, and thus there was no apparent deactivation.

CONCLUSIONS

The rate measurements performed under differential reactor conditions show that the intrinsic rate of HCN destruction in both dry and humid air exhibits an inverse dependence on concentration. The form of the rate equation suggests that dissociation of HCN upon adsorption occurs and the surface reaction is rate controlling. Higher rates of reaction were observed when HCN was present in

humid air. There was no evidence of deactivation of the 2.15% platinum on alpha-alumina when exposed to HCN in humid air for 9 hours.

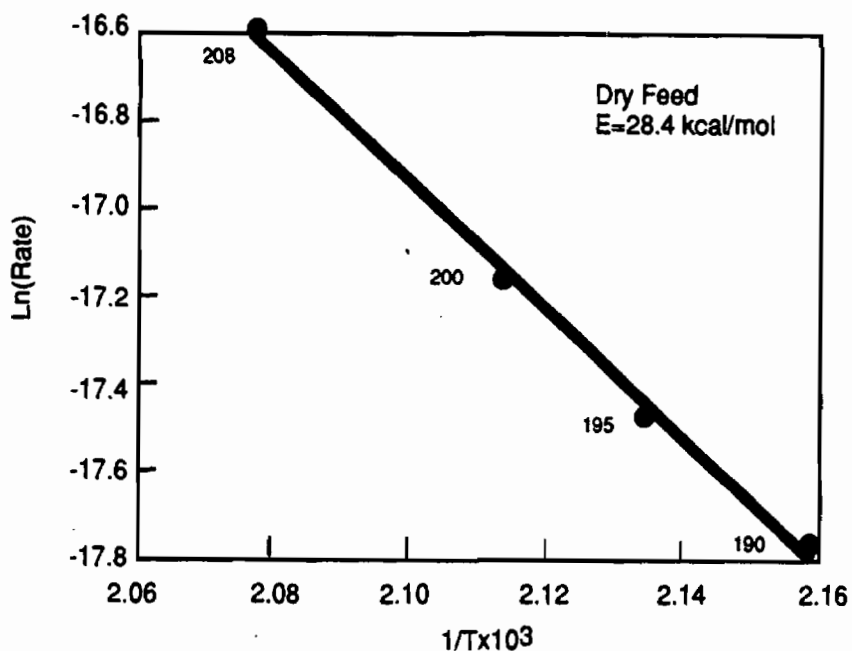


Figure 5. Temperature Dependence of Rate

REFERENCES

1. Lester, G.R., Joy, G.C., "Development and Characterization of Oxidation Catalysts for Air Purification"; Report No. CRDEC-CR-003, October 1988.
2. Lester, G.R., Marinangeli, R.E., "Development and Characterization of Oxidation Catalysts for Air Purification"; Report No. CRDEC-CR-87050, February 1987.
3. Levenspiel, O. *Chemical Reaction Engineering*; John Wiley & Sons: New York, 1972; p 468.

BLANK

CATALYTIC OXIDATION OF GD OVER A MONOLITHIC Pt/TiO₂ OXIDATION CATALYST

Kathrine J. Clarke and Robert Tom
Allied-Signal Aerospace Company
AiResearch Los Angeles Division
2525 W. 190th Street
Torrance, CA 90509

G. Lester
Allied-Signal Research and Technology
50 E. Algonquin Road
Des Plaines, IL 60017

ABSTRACT

Catalytic oxidation of chemical warfare (CW) agents is a promising concept for collective protection in military vehicles. This paper contains a discussion of the performance of a 260-scfm (7400-slpm) monolithic Pt/TiO₂ oxidation catalyst as a function of temperature, pressure, and residence time against nerve agent GD. This study is a continuation of the Air-Force-sponsored chemical and biological agents protection system (CABAPS) program and complements the results reported previously at the 1989 conference.

1. INTRODUCTION

The threat of chemical and biological warfare (CBW) has resulted in the need to develop collective protection systems for personnel in military vehicles. Current systems for CBW protection use particulate filters and Whetlerite charcoal. These adsorption systems have many limitations including finite life, adsorption capacity, and sensitivity to moisture and temperature.

Catalytic destruction of chemical warfare agents is a viable alternative to Whetlerite charcoal because it offers a long life potential and complete destruction, rather than temporary removal, of the chemical agent.

2. BACKGROUND

The relationship between catalytic CW agent destruction and residence time for a given temperature is based on the mass balance of agent in the reactor. For a differential reactor, dV , the mass balance equation is

$$-Q (dCa/dV) = KCa \quad (\text{Equation 1})$$

where: Q = volumetric flow rate
 V = reactor volume
 Ca = concentration of agent in air
 K = generic rate coefficient

Integration of Equation 1 yields

$$\ln (Ca_0/Ca) = KV/Q = k\tau \quad (\text{Equation 2})$$

where: Ca_0 = concentration of agent in air at the inlet of the differential volume
 Ca_0/Ca = concentration reduction ratio
 τ = V/Q = residence time of agent in the differential reactor

Equation 2 shows that the rate coefficient, K , can be determined by finding the reduction ratio for various residence times.

Generally, the rate coefficient is dependent on temperature. The type of dependence is determined by the process controlling the rate. In general, there are four types of rate-controlling processes:

- (a) The intrinsic reaction rate, regime A
- (b) The pore diffusion rate, regime B
- (c) The mass transfer rate, regime C
- (d) The homogeneous reaction rate, regime D

Figure 1 illustrates these as generic processes.

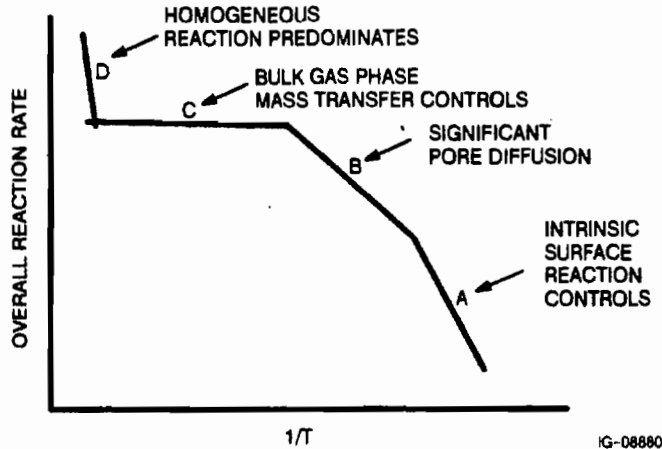


Figure 1. Overall Reaction Rate Temperature Dependence

If the overall reaction is limited by the rate of the intrinsic reaction, its temperature dependence is described by the Arrhenius equation as follows:

$$K = A e^{-E_a/RT} \quad \text{(Equation 3)}$$

where:

- A = preexponential factor
- E_a = the activation energy
- R = the gas law constant
- T = the absolute temperature

In the other extreme, where the homogeneous reaction rate is the controlling process, no catalyst is required. However, the residence time and temperatures required preclude this from occurring on military aircraft.

The ideal operating regime is Regime C, the mass transfer limited regime. In this regime, the limiting factor is mass transfer of the chemical agent from the free stream to the catalyst surface. In this regime, the temperature dependence of K is described by the Hegedus equation modified for square channels:

$$K = S_g (D/2R) (SH)_{lim} \{1 + 0.095 (4R^2G/\rho D L)\}^{0.45} \quad \text{(Equation 4)}$$

where:

- S_g = cell surface area to volume ratio
- D = molecular diffusivity
- R = cell hydraulic radius
- (SH)_{lim} = limiting Sherwood number
- G = feed rate
- ρ = average density
- L = reactor length

The Hegedus equation shows the relatively small effect of density and mass flow rate on the value of K. For a given reactor geometry, K is determined predominantly by the molecular diffusivity of agent, D.

The molecular diffusivity is inversely proportional to pressure and is directly proportional to temperature. Therefore, K is a function primarily of the reaction pressure, and secondarily of the reaction temperature. The relationship between pressure and temperature on molecular diffusivity is as follows:

$$D = \{(0.001858) (T)^{1.5} (1/M_{GD} + 1/M_{air})^{0.5}\} / \{(\sigma)^2 (\omega) P\} \quad \text{(Equation 5)}$$

where: T = reaction temperature
 M_{GD} = molecular weight of agent GD
 M_{air} = molecular weight of air
 σ = collision diameter
 ω = collision integral
P = reaction pressure

This approach was used to correlate the data with live agents.

3. CABAPS TEST UNIT AND FACILITY

The CABAPS test unit is designed for catalytic oxidation of chemical warfare agents. The design point is agent GD at an inlet concentration of 142 mg/cu m and a reduction ratio of 500,000:1. Inlet airflow conditions are 20 lb/min at 450°F and 45 psia.

The test unit is shown schematically and pictorially in Figures 2 and 3, respectively. Contaminated bleed air enters the recuperator, which preheats the air to reduce the electrical power. The air is heated to the catalyst operating temperature by the electric heater. Chemical agent contaminants are catalytically oxidized in the catalytic reactor. Finally, the air passes through the other side of the recuperator, preheating incoming bleed air.

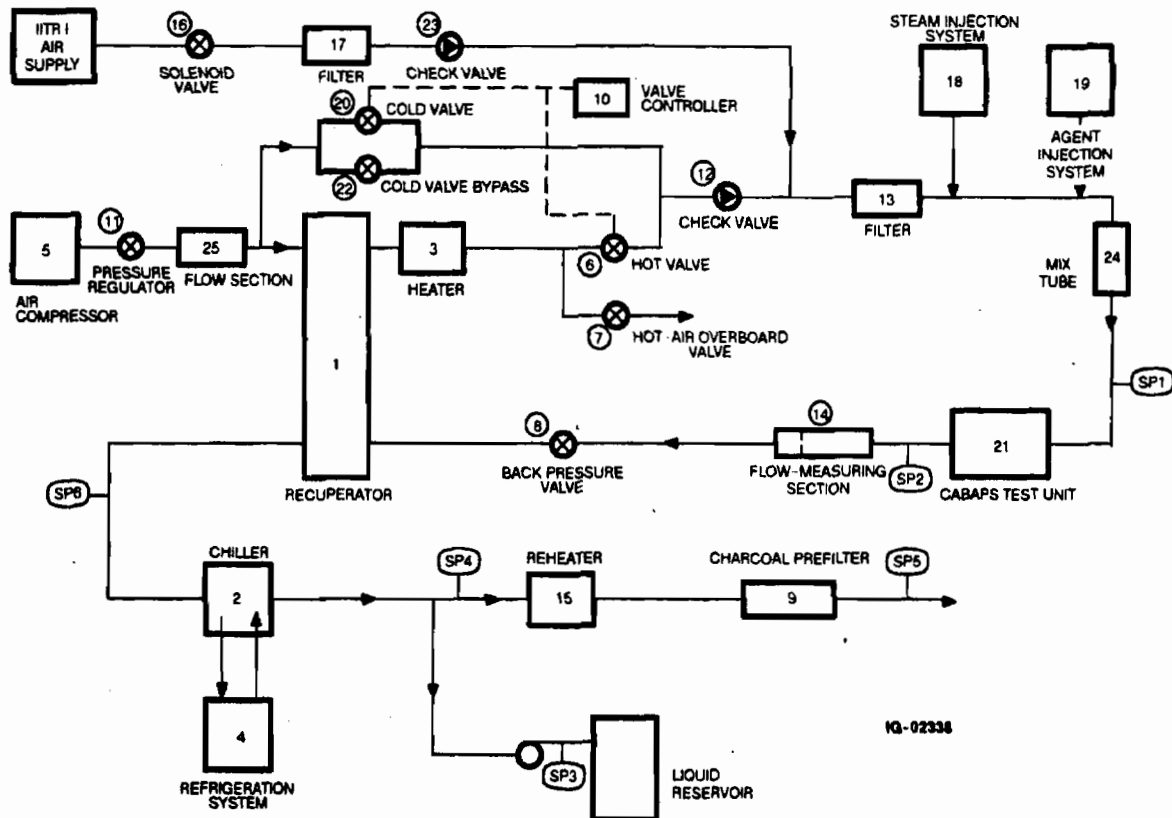


Figure 2. CABAPS Test Facility Schematic

Because the CABAPS is designed for aircraft applications, it is desirable to evaluate its performance under conditions that closely simulate actual aircraft operating conditions. The CABAPS test facility processes air through the compression, pressure regulation, heating, and blending steps required to provide the CABAPS test unit with air at the correct pressure, temperature, and humidity to simulate aircraft engine bleed conditions.

The test facility consists of four major subsystems. They are a pre and post air conditioning subsystem, a steam generator, an agent injection subsystem and a control and data acquisition subsystem. The test facility is shown schematically in Figure 2 and pictorially in Figure 4.

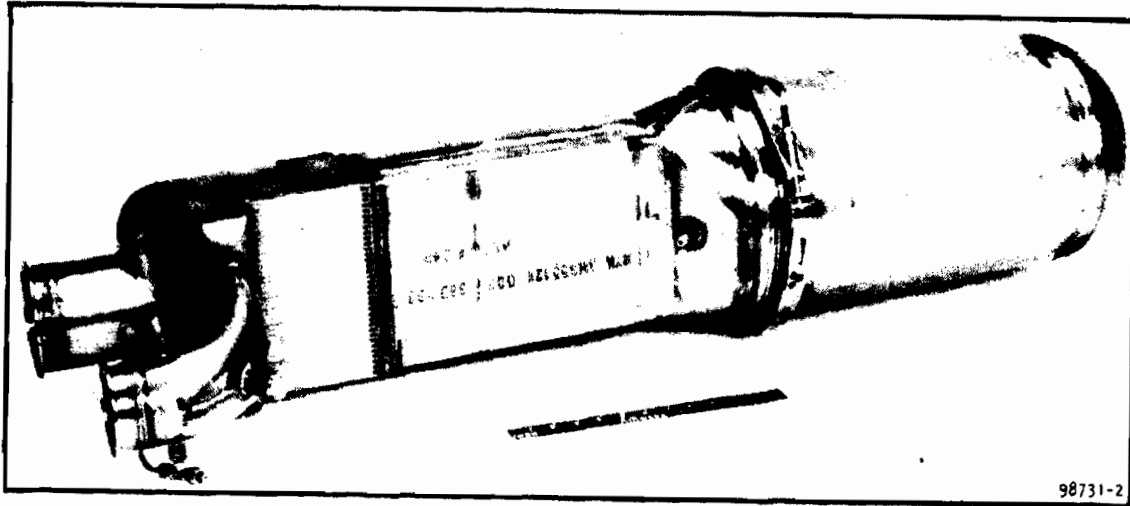


Figure 3. CABAPS Test Unit



Figure 4. CABAPS Test Facility

4. DISCUSSION OF RESULTS
 4.1 LIVE-AGENT TEST RESULTS

The Hegedus equation was used to analytically predict rate constants for the eleven Phase III CABAPS test conditions. The Hegedus equation inputs include the test conditions presented in Table 1 and the following reactor geometric factors:

Factor	Value/Characteristic
Length, in.	12.15
Diameter, sq in.	9.45
Cells per sq in.	600
Cell wall thickness, in.	0.0074
Cell shape	Square

TABLE 1 PHASE III CABAPS TEST CONDITIONS					
Test No.	Pressure, psia	Temperature, °F	Mass Flow Rate, lb/min	Agent GD Inlet Concentration, mg/m ³	Water Flow Rate, gal/min
1	45	650	20	150	0.02
2	45	600	20	150	0.02
3	45	550	20	150	0.02
4	30	650	20	150	0.02
5	60	650	20	150	0.02
6	45	650	25	150	0.03
7	45	650	29	150	0.03
8	45	650	20	50	0.02
9	45	650	20	300	0.02
10	45	475	20	150	0.02
11	45	400	20	150	0.02

To use the Hegedus equation to calculate the reduction ratio for multisegment reactors, the fractional conversion for a single segment, X_{seg} , must first be calculated. The overall reduction ratio in this case for three segments is then calculated from

$$3X_{seg} - 3X_{seg}^2 + X_{seg}^3 = 1 - (C_a/C_{a0})_{overall} \quad (\text{Equation 6})$$

Figures 5 through 7 analytically compare predicted reduction ratios based on the Hegedus predicted rate constant as well as the test measured reduction ratios. Figure 5 shows the natural log of the reduction ratios (normalized for pressure) vs residence time. Figure 6 shows the natural log of the reduction ratios for the 650°F test data vs residence time. The relatively close match between the analytically predicted reduction ratios and the measured reduction ratios indicates that the catalytic reactions are mass transfer rate limited. Values of the rate constant, k_c , for each of the 11 Phase III test conditions are presented in Table 2.

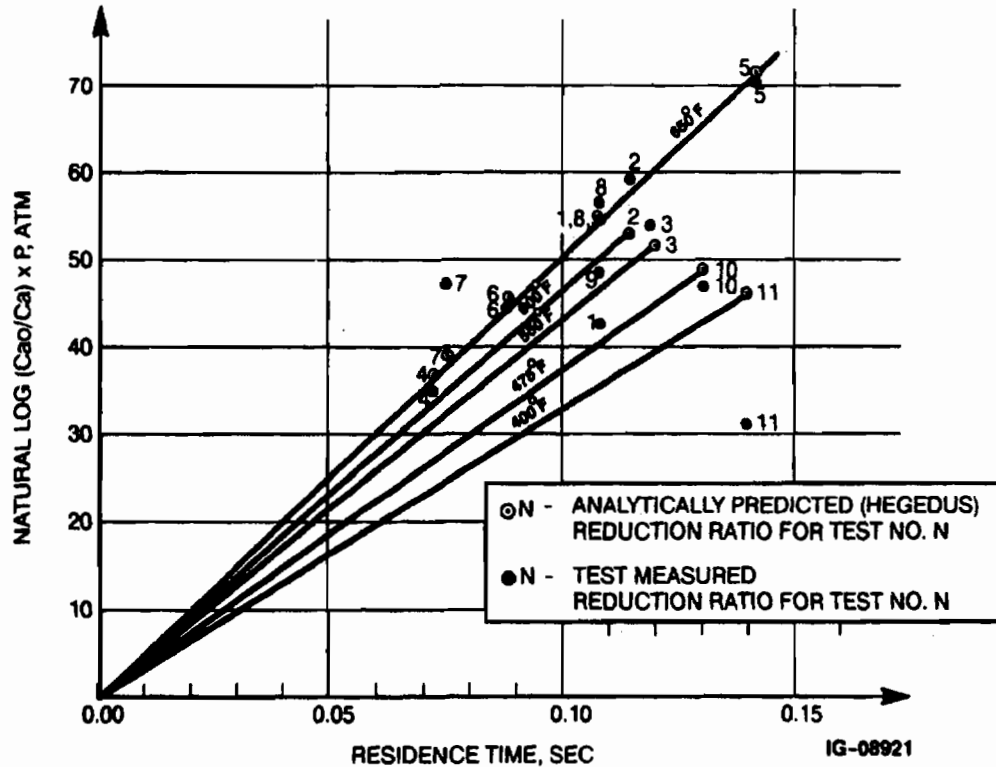


Figure 5. Pressure Normalized Reduction Ratio

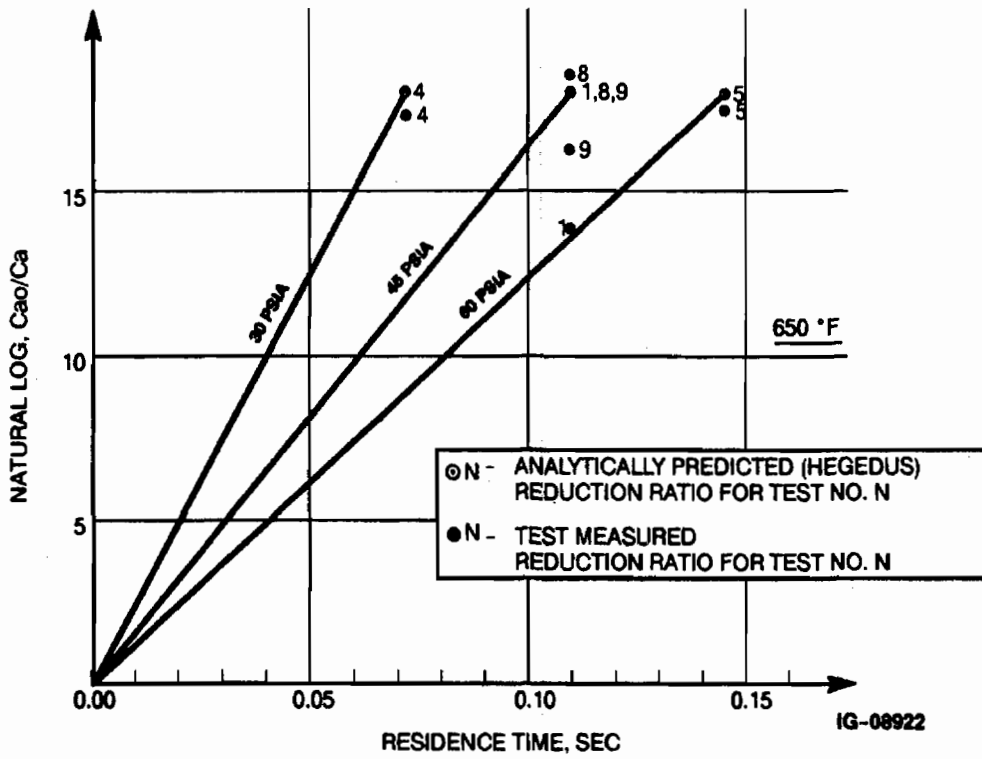


Figure 6. Effect of Pressure

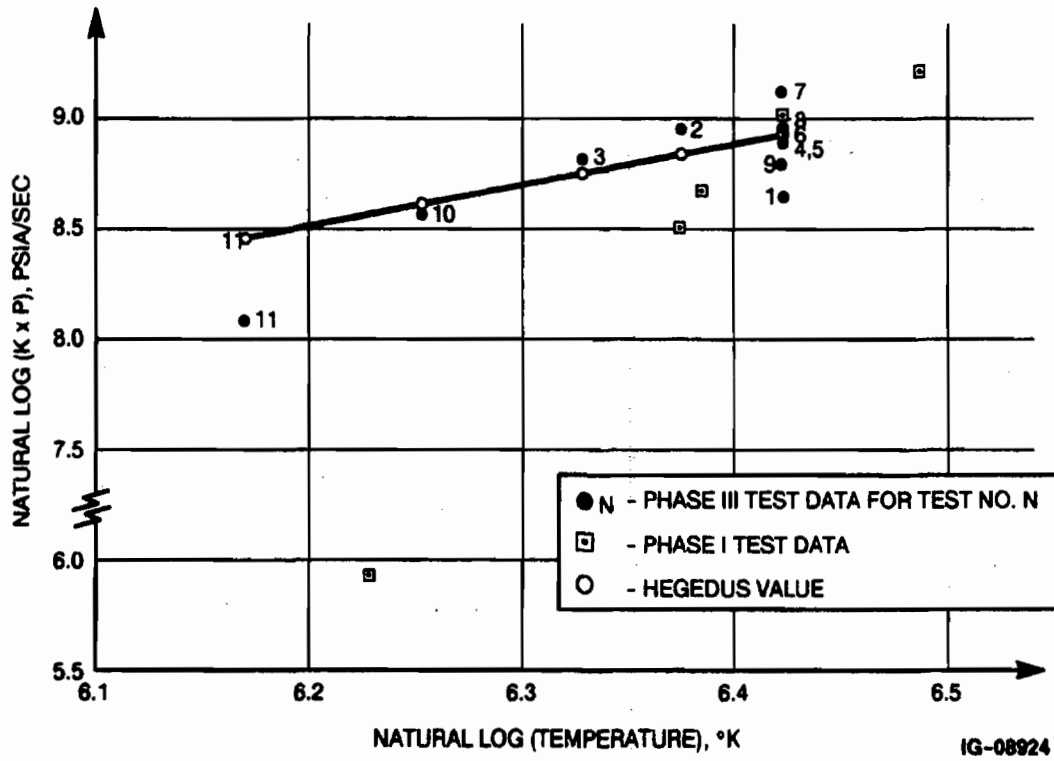


Figure 7. Reaction Constant Correlation

Test No.	Pressure, psia	Temperature, °F	Mass Flow Rate, lb/min	Theoretical Rate Constant, 1/sec	Test Measured Rate Constant, 1/sec
1	45	650	20	165.3	127.4
2	45	600	20	152.6	170.2
3	45	550	20	140.3	147.3
4	30	650	20	248.0	239.2
5	60	650	20	124.0	120.8
6	45	650	25	168.5	166.0
7	45	650	30	170.9	197.4
8	45	650	20	165.3	170.6
9	45	650	20	165.3	149.6
10	45	475	20	122.6	117.9
11	45	400	20	105.8	71.5

Figures 5 and 6 show the relationships between reduction ratio, residence time, rate constant, and the reaction conditions that determine these parameters. The slope of the solid lines from the origin to the plotted reduction ratio points is the rate constant, kH. The slopes of these lines in Figure 5 decrease with decreasing temperature, representing the effect of reaction temperature on kH. Also in Figure 5, points 6 and 7 (the analytically predicted values) are slightly to the left of the 650°F line, illustrating the small influence of mass flow rate on kH. In Figure 6, the slopes of the lines from the origin to data points 4 and 5 differ from the slopes of the other 650°F lines. This indicates the influence of pressure on kH.

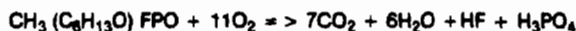
The actual reduction ratio for test 1 was much lower than predicted. This may have been due to DMMP in the sample lines from the previous system checkouts.

In Figure 7, the rate constants (normalized for pressure) determined, during Phase III and Phase I testing, are shown plotted against the natural log of reaction temperature, which is necessary to linearize the data points, and is based on the relationship between temperature and the molecular diffusivity, D.

The rate constants of the Phase III full-scale reactor can be compared with the Phase I microreactor rate constants because reactor geometry has very little effect on the rate constant. Phase I test data show a significant decrease in the rate constant, kc, with decreasing reactor temperature. For the Phase I test run at 450°F, the rate constant was sufficiently low to indicate that the reaction was intrinsically reaction-rate-controlled rather than mass-transfer-rate controlled. This does not appear to be the case for the Phase III tests run at 475° or 400°F.

4.2 REACTOR PRODUCT ANALYSIS

During Phase III testing, the air supply downstream of the reactor was monitored at three separate sampling points for selected products of agent destruction. The reaction product of particular interest is HF. The short-term (15-min) allowable exposure limit for HF is 2.5 mg/m³. Concentrations above this level are potentially harmful. The measured concentration levels of HF at the three sampling points are shown in Table 3. (The samples were actually measuring for fluoride ions). The removal percentages, also presented in Table 3, are based on the expected concentration levels calculated from the following reaction stoichiometry:



The measured HF concentration levels at the condenser outlet are below 2.5 mg/m³ exposure limit for all of the test conditions. However, most of the HF was removed downstream of the reactor. No correlations between HF removal and test conditions could be found.

Table 4 presents the measured concentration levels of H₃PO₄ (the samples measured for phosphorus ions) and the corresponding removal percentages. These results indicate that most of the H₃PO₄ was removed in the reactor, and any remaining H₃PO₄ was removed downstream in the system. These results are in agreement with Phase I microreactor tests results.

5. CONCLUSIONS

This program obtained the necessary data to design, fabricate, and test a full-scale NBC catalytic reactor. Full-scale tests have shown extremely high performance; agent reduction ratios of 200,000,000 (design goal was 500,000) have been achieved in a residence time of less than 0.2 sec. This performance indicates the potential of this approach in providing collective protection for NBC.

TABLE 3
CABAPS HF REMOVAL

Test No.	Inlet Conc. GD, mg/m ³	Stoich Conc. HF, mg/m ³	Reactor Outlet (SP2)		Condenser Inlet (SP6)			Condenser Outlet (SP4)		
			Measured Conc. HF, mg/m ³	Percent of Stoich Removed	Measured Conc. HF, mg/m ³	Percent of Stoich Removed (Recup.)	Percent of Stoich Removed (Total)	Measured Conc. HF, mg/m ³	Percent of Stoich Removed (Cond.)	Percent of Stoich Removed (Total)
1	73.6	8.10	3.28	59.43				0.45		94.41
2	119.6	13.16	4.25	67.68				0.04		99.68
3	110.5	12.16	4.43	63.54				1.94		84.07
4	118.8	13.07	11.41	12.68				1.19		90.90
5	154.5	17.00	12.11	28.77	2.35	53.85	86.19	0.13	12.38	99.26
6	151.0	16.61	12.16	26.80	2.24	56.04	86.50	0.61	9.15	96.32
7	155.3	17.08	14.16	17.12	6.40	41.27	62.54	1.37	27.58	91.99
8	45.8	5.04	3.47	31.05	0.49	55.68	90.18	0.89	-8.43	82.24
9	300.6	33.07	19.42	41.27	12.35	18.46	62.66	1.25	31.69	96.21
10	158.3	17.41	10.76	38.22	1.98	47.33	88.64	0.18	9.77	98.97
11	164.0	18.04	12.89	28.52	3.28	49.70	81.79	0.47	14.67	97.37

TABLE 4
CABAPS H₃PO₄ REMOVAL

Test No.	Inlet Conc. GD, mg/m ³	Stoich Conc. H ₃ PO ₄ , mg/m ³	Reactor Outlet (SP2)		Condenser Inlet (SP6)			Condenser Outlet (SP4)		
			Measured Conc. H ₃ PO ₄ , mg/m ³	Percent of Stoich Removed	Measured Conc. H ₃ PO ₄ , mg/m ³	Percent of Stoich Removed (Recup.)	Percent of Stoich Removed (Total)	Measured Conc. H ₃ PO ₄ , mg/m ³	Percent of Stoich Removed (Cond.)	Percent of Stoich Removed (Total)
1	73.6	39.60	0.21	99.48				0.00		100.00
2	119.6	64.34	0.00	100.00				0.00		100.00
3	110.5	59.45	0.16	99.73				0.00		100.00
4	118.8	63.91	0.00	100.00				0.00		100.00
5	154.5	83.12	0.00	100.00	0.00	0.00	100.00	0.00	0.00	100.00
6	151.0	81.24	2.82	96.53	0.00	3.47	100.00	0.00	0.00	100.00
7	155.3	83.55	3.01	96.40	0.00	3.60	100.00	0.00	0.00	100.00
8	45.8	24.64	1.74	92.94	0.00	7.06	100.00	0.00	0.00	100.00
9	300.6	161.72	0.79	99.51	0.00	0.49	100.00	0.00	0.00	100.00
10	158.3	85.17	0.00	100.00	0.00	0.00	100.00	0.00	0.00	100.00
11	164.0	88.23	0.00	100.00	0.00	0.00	100.00	0.00	0.00	100.00

The Role of Water-Soluble Amines in Whetlerite Formulations

by

V.R. Deitz*, C.J. Karwacki** and J.A. Rehrmann**

*GEO-Centers, Inc. at Naval Research Laboratory

**Chemical Research, Development and Engineering Center

Abstract

The following nine amines in aqueous solutions were sprayed onto two separate ASZM impregnated whetlerites to which no TEDA had previously been added: triethylamine, tripropylamine, tributylamine, triallylamine, tetramethylethylenediamine, triethylenediamine, quinuclidine diethylenetriamine and triethylenetetraamine. These were tested under standard testing conditions with HCN; (CN)₂ was first produced in all cases and in varying amounts. The breakthrough behaviors were significantly different for each amine and other amines than TEDA maybe found useful as a final impregnating agent.

Introduction

Current formulations of whetlerites include TEDA (triethylenediamine) impregnated after the metal compounds had been added to the activated carbon. TEDA was first used in the nuclear-grade carbons to trap radioactive iodine in the nuclear power operations (1) and the carbon when new was very successful. The influence of TEDA on trapping toxic gases, however, has not been completely evaluated and one objective of the present study is to formulate a possible mechanism.

Nine amines have been used in the study and both chemical structures and their acronyms are listed in Table 1; some of the physical properties are given in Table 2. There is a limit to the quantity of amine that can be added since the surface area of the product decreases significantly with excess of 4 to 5 weight percent. The standard test procedure with AC (HCN) as the challenge was conducted in the same manner for each of the amine-treated samples as well as for the original material.

Experimental

Two whetlerites, previously impregnated with ammoniacal solutions of copper, zinc, and molybdenum were used. One of these was a commercial product (Calgon Carbons, Inc.) and the second a laboratory preparation was prepared at CRDEC (J.A. Rehrmann). The amine impregnations were made at NRL by directing a slow spray of the aqueous amine solution into the rotating sample of dry whetlerite. The concentration of amine was adjusted as desired.

The humidified air flow was maintained at 80%RH at the ambient temperature (17-

TABLE 1: The Structures and Acronyms of the Amines Used in this Study

TEDA	TRIETHYLENEDIAMINE	$ \begin{array}{c} \text{CH}_2 - \text{CH}_2 \\ / \quad \quad \backslash \\ \text{N} - \text{CH}_2 - \text{CH}_2 - \text{N} \\ \backslash \quad \quad / \\ \text{CH}_2 - \text{CH}_2 \end{array} $
QUI	QUINUCLIDINE	$ \begin{array}{c} \text{CH}_2 - \text{CH}_2 \\ / \quad \quad \backslash \\ \text{HC} - \text{CH}_2 - \text{CH}_2 - \text{N} \\ \backslash \quad \quad / \\ \text{CH}_2 - \text{CH}_2 \end{array} $
TEA	TRIETHYLAMINE	$\text{N}(\text{C}_2\text{H}_5)_3$
TPA	TRIPROPYLAMINE	$\text{N}(\text{C}_3\text{H}_7)_3$
TBA	TRIBUTYLAMINE	$\text{N}(\text{C}_4\text{H}_9)_3$
TAA	TRIALLYLAMINE	$\text{N}(\text{CH}_2 = \text{CHCH}_2)_3$
TMED	TETRAMETHYLETHYLENEDIAMINE	$(\text{H}_3\text{C})_2\text{NCH}_2\text{CH}_2\text{N}(\text{CH}_3)_2$
DETA	DIETHYLENETRIAMINE	$\text{H}_2\text{NCH}_2\text{CH}_2\text{NHCH}_2\text{CH}_2\text{NH}_2$
TETA	TRIETHYLENETETRAAMINE	$\text{H}_2\text{NC}_2\text{H}_4\text{NHC}_2\text{H}_4\text{NHC}_2\text{H}_4\text{NH}_2$

TABLE 2: Physical Properties of the Amines

	MW	d g/cm ³	σ A ²	m.p. °C	b.p. °C
TEA	101.2	0.726	41.1	-115	88.8
DETA	103.2	0.952	34.91	-39	206.9
QUI	111.2	(1.14)	32.4	+159	-
TEDA	112.2	1.14	32.6	158-160	174
TMED	116	0.770	43.3	-55	120-122
TAA	137.2	0.790	47.6	30	150-151
TPA	143.3	0.753	50.6	-93.5	155-158
TETA	146.2	0.979	43.1	-35	277.4
TBA	185.3	0.778	58.8	-70	216

20°C), and was recorded periodically (optical dew point instruments). The AC was supplied by Matheson Gas Products, Inc. in a calibrated mixture in dry nitrogen. The AC was introduced into the humidified air flow after passing through a mass flow controller.

Samples of the inlet flow and the effluent were delivered to independent chromatographic columns with separate FID detectors. The counts were recorded by HP Integrators (3392A and 3393A). The calibration for mixtures was made after stipulated dilutions of the AC flow with inlet air flow. The target concentrations of the AC challenge was 5 mg/liter (4550 ppm). Other kinetic parameters are given below:

Bed Depth	3.0 cm
Bed Diameter	1.9 cm
Retention Time AC	2.3-2.4 min
Retention Time (CN) ₂	1.85 min
Poropak P Columns	5 feet x 1/8 inch

Results

Typical breakthrough behavior are shown in Figures 1, 2 and 3. The top graph of Figure 1 gives the concentrations of the inlet dose and the two effluent species. The lower graph shows the integrated behavior. Altogether, 34 tests were made with the 9 amines on sub samples of the two whetlerites.

The reproducibility of the results for breakthrough times for AC and (CN)₂ may be seen in Table 3 for the amine-impregnated whetlerites. The alignment for the nine amines (Table 3) is given relative to increasing AC breakthrough times. There is almost a two-fold difference among the amines for both AC and (CN)₂ with the Batch #345 and somewhat less so with the Calgon ASZM. The observed alignments are different for the two starting whetlerites.

For comparison, an alignment is shown (Table 4) relative to increasing molecular diameters of the amines. Little is evident in respect to increasing molecular weights. The molecular diameters were determined from the molecular weight (M), the density (d) of the condensed phase, and N_A Avogadro's Number:

$$\sigma/\text{molecule} = 4(.866) \left[\frac{M}{4\sqrt{2} N_A d} \right]^{2/3}$$

These range from 32.4 for QUI to 58.8 for TBA. The densities in the adsorbed phase are not known. The ranking of σ with the breakthrough times (t_b) is rather poor for both AC and (CN)₂.

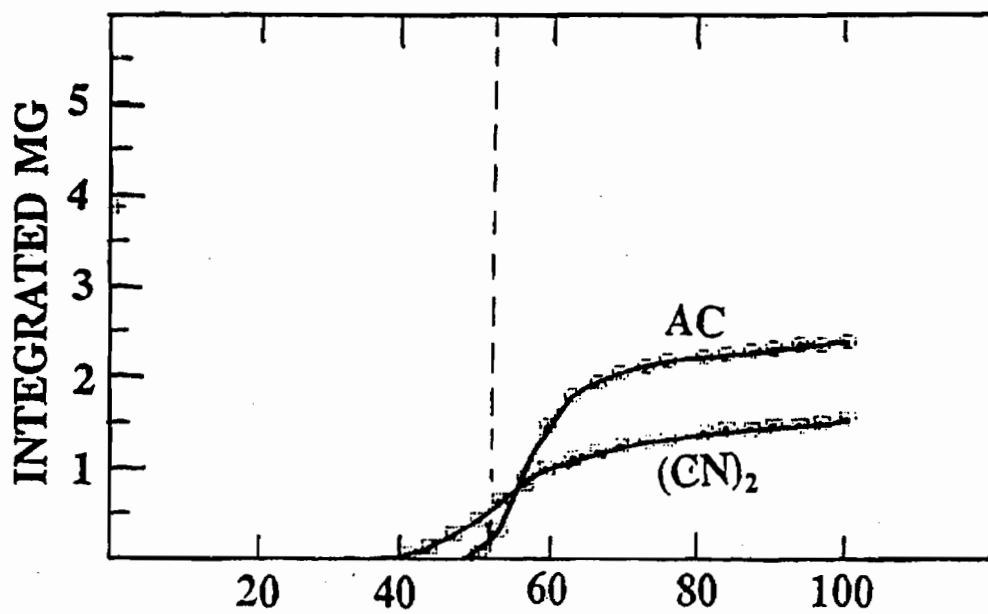
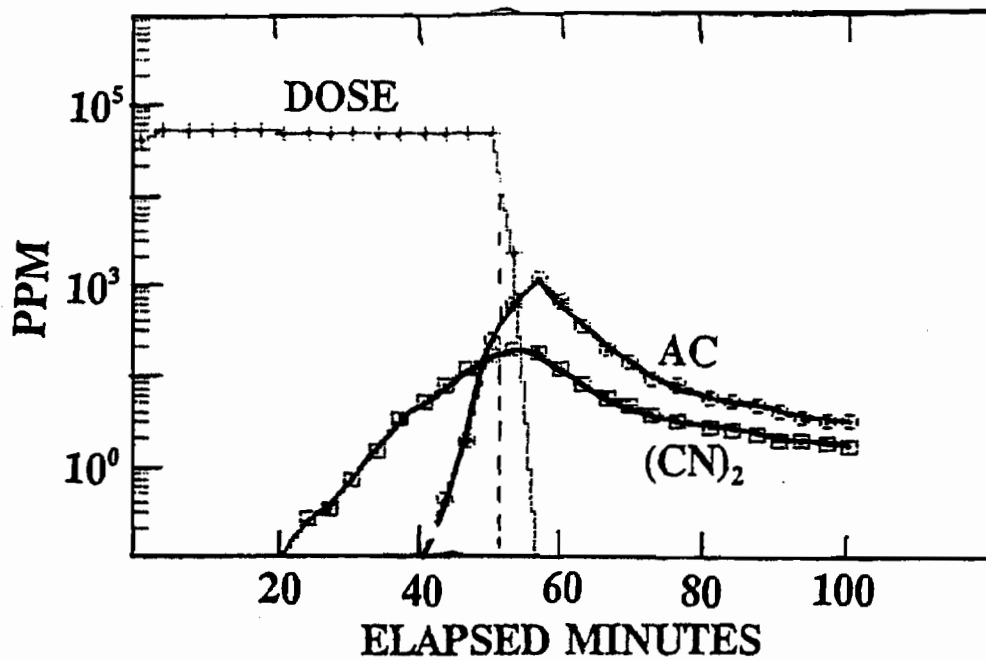


Figure 1. Breakthrough of AC + #345 + TAA Spray
8-26-91

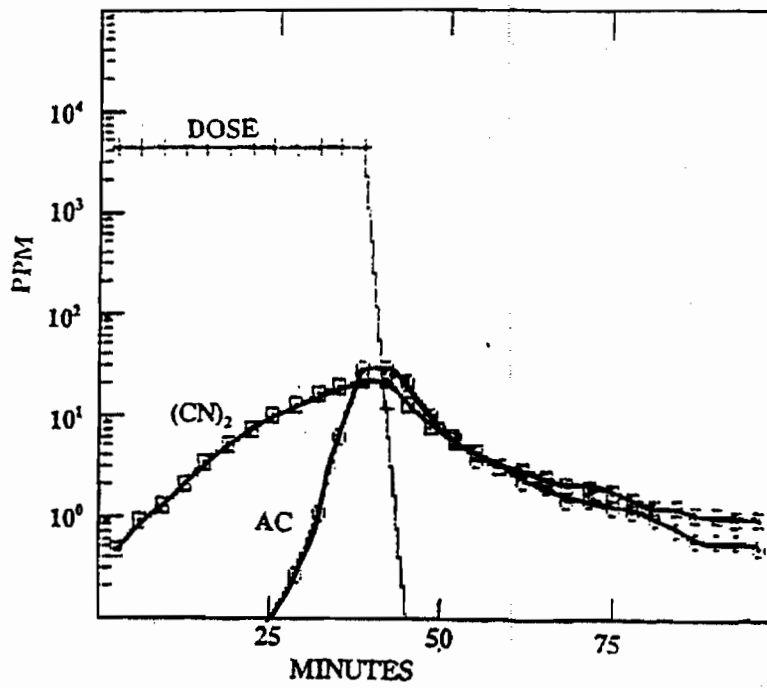


Figure 2. Breakthrough of AC + #345 + TPA Spray
8-20-91

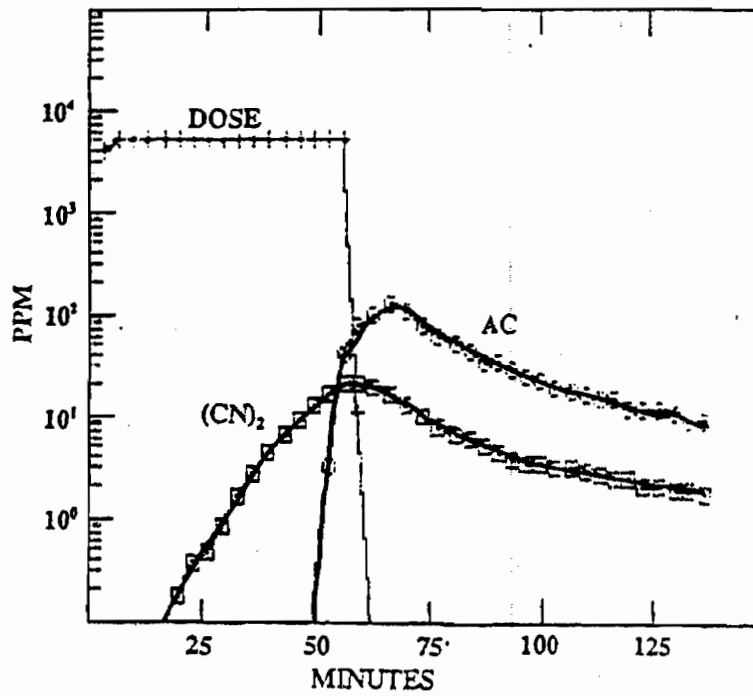


Figure 3. Breakthrough of AC + ASZM + TETA Spray
9-30-91

TABLE 3: Alignment Relative to Increasing AC and (CN)₂ Breakthrough Times (minutes/3cm depth)

	CRDEC Batch #345		CALGON ASZM (no TEDA)		
	AC	(CN) ₂	AC	(CN) ₂	
TPA	31	15	TEA	36	29
QUI	38	27	TAA	37	18
TAA	41	36		41	20
	49	39		38	16
TEDA	42	27	QUI	39	18
TBA	42	28	TEDA	44	40
	37	31	TBA	45	25
TMED	49	18	DETA	46	39
TETA	48	38	TMED	48	41
	42	34		45	39
DETA	55	41	TPA	48	38
TEA	56	35		42	26
	45	41	TETA	57	41
	50	40			
original	51	47	original	48	44
	48	46		41	40
	51	46			

TABLE 4: Alignment Relative to Molecular Cross Sections

Batch #345			\AA^2	CALGON	
AC min	(CN) ₂ min			AC min	(CN) ₂ min
38	27	QUI	32.4	39	18
42	27	TEDA	32.6	44	40
55	41	DETA	34.9	46	39
51	39	TEA	41.1	36	29
45	36	TETA	43.1	52	41
49	18	TMED	43.3	46	40
45	37	TAA	47.6	39	18
31	15	TPA	50.6	45	37
40	30	TBA	58.8	45	25
48	46	NONE		48	44
51	47	NONE		41	40
51	46	NONE			
		HCN	16.2		
		(CN) ₂	21.5		

Discussion

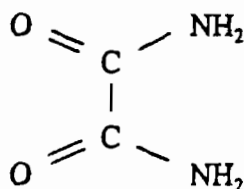
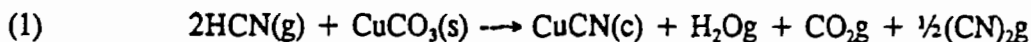
The effluents AC and $(\text{CN})_2$ have been followed for a limited time beyond the effluent toxic breakthrough concentration. Longer dose times were detrimental to a recovery of the base lines of the chromatographic columns and also the reproducibility of the FID detector signals. However, the results (Table 3) do suggest that other amines than TEDA may be helpful in the formulation of new whetlerites.

Several procedures have been undertaken to correlate the results (Table 3) with possible reaction sites on the surface. It is not a simple problem as was shown (Table 4) by the attempt to align the breakthrough times with the molecular cross sections of the amines. The total retention of AC is a considerable larger magnitude than that which penetrates at the breakthrough time, t_b . Table 5 (Batch #324, CRDEC) and Table 6 (ASZM, Calgon) give the sequential integrated doses calculated to t_b for the two series of impregnated carbons, respectively. The results cover the ratio range of 25000 to 45000 for dose to AC effluent. The tabulations, however, do show some correlation with increasing breakthrough times for both the AC and $(\text{CN})_2$ effluents.

A surprising observation is the high efficiency of both whetlerites without the addition of an amine. While this is true for the AC challenge, it needs to be examined for other cyanide test gases, i.e. $(\text{CN})_2$ alone and CNCl .

An examination of the duplicate and triplicate results for some of the amines listed in Table 3 revealed that the larger breakthrough time for a given amine occurred with the higher initial water content. Since the sample weights had been determined before each AC challenge, it was possible to attempt a correlation with the observed breakthrough times. These data are recorded for each test in Table 7 (Batch #345, CRDEC) and in Table 8 (ASZM, Calgon). The tables include the values of t_b for AC and $(\text{CN})_2$.

It is quite reasonable to include the water molecule as a reactant. The reactions below take place with a large free energy formation:



The oxamide formed by eq. (2) and retained by the whetlerite has been reported by other investigators (2,3,4)

The data in Tables 8 and 9 are shown graphically (Figures 4 and 5). The breakthrough times for both AC and $(\text{CN})_2$ increase significantly with moisture content of the

TABLE 5: Integrated AC DOSE and Effluent at t_b
from Batch #345 (CRDEC)

Amine	Integrated AC		Breakthrough Times	
	DOSE mg	Efflu. mg	$t_b(AC)$ min	$t_b(CN)_2$ min
TAA	260	0.01	41	36
TPA	270	0.01	31	15
TEA	312	0.01	45	41
QUI	314	0.01	38	27
TBA	322	0.01	37	31
TETA	322	0.01	42	34
TBA	342	0.01	42	28
TMED	350	0.01	49	18
TEDA	350	0.01	42	27
TETA	415	0.01	48	38
DETA	415	0.01	55	41
TEA	430	0.01	50	40
TAA	431	0.01	49	38
TEA	450	0.01	56	35
NONE	408	0.01	51	46
NONE	388	0.01	51	47
NONE	318	0.01	48	46

TABLE 6: Integrated AC DOSE and Effluent at t_b
from ASZM (Calgon)

Amine	Integrated AC		Breakthrough Times	
	DOSE mg	Efflu. mg	t_b (AC) min	t_b (CN) ₂ min
TEA	245	0.01	36	29
TAA	290	0.01	37	18
TAA	290	0.01	38	16
QUI	315	0.01	39	18
TMED	330	0.01	45	39
TBA	340	0.01	45	25
TEDA	340	0.01	44	40
TPA	347	0.01	42	26
TMED	350	0.01	48	41
DETA	365	0.01	46	39
TPA	370	0.01	48	38
TETA	425	0.01	57	41
NONE	330	0.01	41	40
NONE	355	0.01	48	44

TABLE 7: Initial Water Content versus t_p
Batch #345, CRDEC

initial wt (g)		AC min	(CN) ₂ min
8.690	TEA	50	40
8.667	TMED	49	18
8.667	TEDA	42	27
8.456	QUI	38	27
8.399	TETA	48	38
8.289	TBA	37	31
8.284	TBA	42	28
8.280	TEA	56	35
8.191	DETA	55	41
8.102	TAA	49	38
8.090	TETA	42	34
7.896	TPA	31	15
7.825	TFA	45	41
7.415	TAA	41	36
7.383	TMED	30	15
8.048	NONE	51	47
7.698	NONE	51	46
6.277	NONE	48	46

TABLE 8: Initial Water Content versus t_b ,
ASZM, CALGON

initial wt (g)		AC min	(CN) ₂ min
8.513	QUI	39	18
8.417	TEDA	44	40
8.367	TPA	42	26
8.344	DETA	46	39
8.297	TMED	48	41
8.141	TBA	45	25
8.134	TETA	57	41
8.105	TAA	38	16
8.089	TMED	45	39
7.997	TPA	48	38
7.861	TEA	36	29
7.411	TAA	37	18
6.221	TEA	17	16
6.923	NONE	41	40
8.188	NONE	48	44

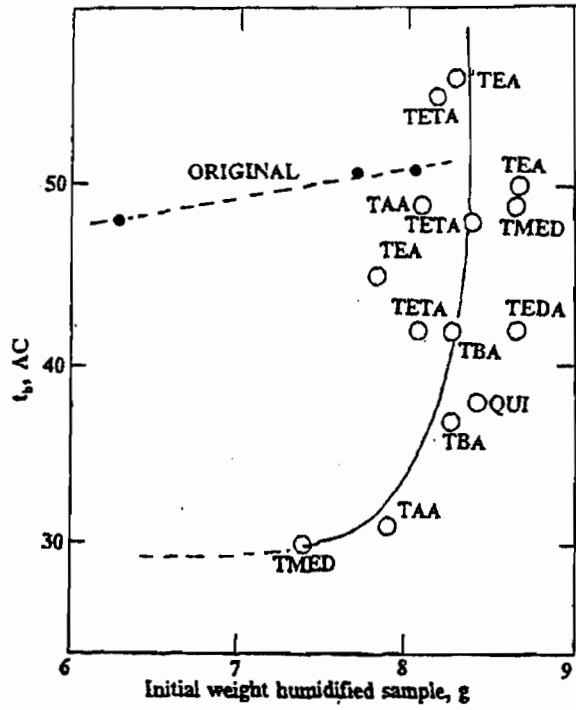


Figure 4: Correlation of t_b for AC with Initial Weight of Humidified Sample (Batch #345, CRDEC)

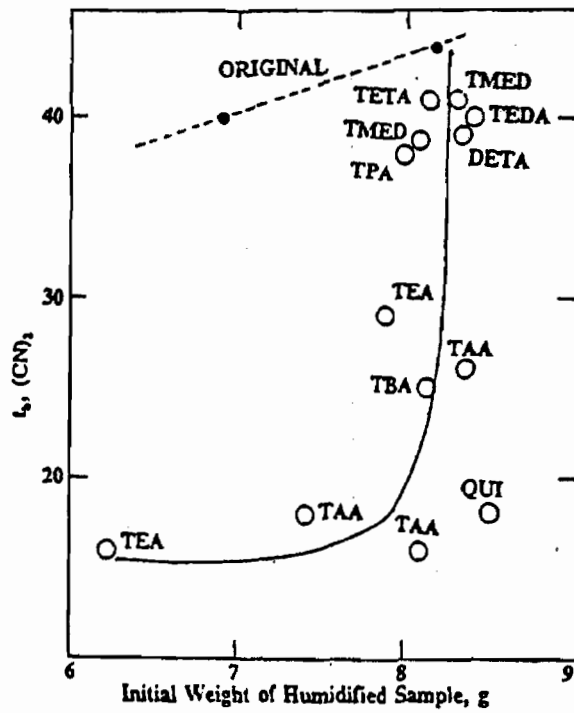


Figure 5: Correlation of t_b for $(CN)_2$ with the Initial Weight of Humidified Sample (ASZM, Calgon)

initial sample. The tests were run with air at 80%RH which supplied considerable excess of water vapor, but it seems essential that the water and amine be together before the AC is introduced.

The preparation of whetlerite by impregnation of dissolved ammoniacal metal salts on a base charcoal in aqueous media can be viewed as a solution adsorption process of the coordination compounds of the metal ions. Metal ions are almost never encountered in solution without shielding which is provided by the solvent molecules and other ligands. In 1941 Bjerrum (5) reported that charcoal could be used as a catalyst to bring about a rapid equilibrium among the various complexes present in the solution. One such case considered was the following:



The equilibrated state lies to the right and is attained very slowly in solution; charcoal proved to be a most effective catalyst in attaining equilibrium even in the absence the OH ion.

The above observations suggest a model that might account for the influence of TEDA and other amines when included in a whetlerite formulation. The amine molecule can substitute or displace some of the normal ligands in the metal ion complexes, namely H_2O , NH_3 , and thus modify the subsequent gas phase adsorption reaction.

Concluding Remarks

1. Other amines than TEDA may be helpful in extending the breakthrough times for the cyanide group of toxic gases.
2. The $(\text{CN})_2$ breakthrough time with an AC challenge is always first followed by that of the AC.
3. The AC challenges to the different amines, integrated to the breakthrough point, are nearly the same in alignment as the breakthrough points themselves.
4. It appears essential that the water and amine be together before the AC is introduced. There is a good correlation in this case between AC life and water content.
5. This study shows that amines differ in the ability to place the water molecule in an optimum orientation around the metal ions in the surface complex and then form the non-volatile product (oxamide) and the volatile $(\text{CN})_2$, not in stoichiometric amounts.

Acknowledgement

We are indebted to William Barger of the Surface Chemistry Branch of NRL for the several computer programs that expedited the calculations in this study.

References

- (1) V.R. Deitz, "Nuclear Grade Activated Carbons and the Radioactive Iodide Problem," *Chemistry & Physics of Carbon* 23, 233-362 (1991).
- (2) B.R. Alves and A.J. Clark, *Carbon* 24, 287 (1984).
- (3) M.M. Ross and V.R. Deitz, *Carbon* 28, 229 (1990).
- (4) P.N. Brown, G.G. Jayson, G. Thompson, and M.C. Wilkenson, *J. Colloid & Interface Sci.* 116, 211 (1987).
- (5) J. Bjerrum, "Metal Amine Formation in Aqueous Solutions," P. Haase, Copenhagen, 235-251 (1941).

The Relationship of Direct Skin Exposure to
Methyl Salicylate (MeS) Vapor to Vapor Carry-Through

Susan H. Bomalaski
Armstrong Laboratories (ALCFTO)
Brooks AFB, Texas 78233

John P. Killian
Rothe Development Corporation
4614 Sinclair Road
San Antonio, Texas 78222

This study considered the use of vapor carry-through as measured by collecting and quantifying off-gassed simulant as an indication of skin exposure. Subjects were exposed to controlled vapor levels of the simulant, methyl salicylate (MeS) wearing or not wearing various combinations of underwear in temperatures approximating those found while wearing a protective ensemble. The use of measured indications of offgassed simulant was not found to be a very sensitive indicator of skin vapor exposure over extended periods of time but seemed to be related to a combination of factors such as total exposure time, exposure concentration and possibly other factors yet to be identified.

INTRODUCTION. Most current protective ensemble materials and configurations provide satisfactory chemical protection during static wear and during mechanical fabric testing. This study was the initial stage of a program to develop and evaluate the experimental techniques needed to help define the chemical protection of candidate ensembles while being used in normal airbase operations. To reach this goal, a technique is needed which will allow estimation of the skin vapor exposure which, when compared to ambient environmental levels will yield a garment protection factor. Considerable shelter processing procedures experimentation (2,3) has been accomplished using vapor carry-through of the mustard simulant MeS, as estimated with closed offgassing booths, to indicate processing effectiveness. A logical extension of this processing testing would be to apply the existing offgassing facilities and sampling techniques to estimate the under ensemble vapor exposures (CTs) that would have been needed to cause the observed levels of vapor carry-through.

FACILITIES AND EQUIPMENT. The exercise and exposure chamber (Exposure Chamber) is a room approximately 12 ft wide by 8 ft high by 24 ft long. It is equipped with a combination heater (8.8 kw) and air conditioner (15.8 kw) and limited humidity control capabilities (1 kg h^{-1}). There are six stations within the room where various exercises are performed. Simulant vapor is generated by using a computer controlled solenoid valve to drip small quantities of methyl salicylate (MeS) into a heated stainless steel cylinder through which approximately 260 l min^{-1} of air is forced by an external blower. The real-time simulant concentration measurements needed to actively control simulant levels in the exercise/exposure chamber are taken using an HNU Systems photolization detector, model PI52-02A

in a direct measurement mode. The calibration, use, and limitations of this device are discussed in reference 3.

The four stainless steel and glass static offgassing booths (OFGBs) were used to estimate subject vapor carry-through. The construction and characteristics of these booths are described in reference 2, Appendix A. These booths are effectively a closed 2.613 cubic meter (m^3) volume with multiple sampling ports for impinger sampling of internal vapor concentrations. The ventilated offgassing booth (VOFGB) is a truncated pyramid similar in construction to the static booths with a volume of 1,710 liters with an adjustable, filtered airflow capability of between 50 and 500 $l\ min^{-1}$. The addition of controlled airflow allows estimates of the actual quantities of simulant carried in to be calculated with a reasonable degree of accuracy.

Methyl salicylate (MeS) was used as the chemical agent simulant for this vapor exposure experiment. MeS has a vapor pressure between that of soman and distilled mustard and has other physical properties similar to chemical agents, such as adsorption on charcoal. The MeS was used to approximate agent vapors. Six impinger samplers were used to monitor average vapor levels during testing. Two impingers were located in the exposure booth. One impinger was used to sample from each offgassing booth. The selection of MeS as a simulant and the techniques used for simulant preparation, detection and sampling, and analysis are described in 1.

EXPERIMENTAL PROCEDURES. The first set of test conditions was exposure to target CTs from 60 to 900 $mg\ min\ m^{-3}$. Four test subjects were used. Vapor exposure time was 60 min with the subjects switching positions every 15 min. Post exposure, three of the test subjects occupied static offgassing booths while the fourth entered the ventilated offgassing booth. The offgassing period was 2 hours in the static booths and 80 min in the ventilated booth. All subjects were exposed wearing underwear, boots, and gas mask with hood. All subjects removed gas mask and hood, changed underwear, and removed boots and socks prior to entering their assigned offgassing booth.

Test procedure two was designed to use a fixed concentration and vary the exposure time to obtain the desired CTs. All four subjects dressed in underwear, socks, boots, and gas mask with hood entered the exposure booth at the same time. On day 1 (low CT) they exited the exposure booth after 20 min. On each of the three remaining test days the exposure time was increased 20 min which resulted in exposure times for the test of 20, 40, 60 and 80 min. All four subjects removed gas mask and hood, boots and socks prior to entering their assigned OFGB. In addition, two of the subjects changed underwear as well resulting in a comparison of OFGB values with and without an underwear change.

Test procedure three was bare skin exposure (no t-shirt) with gas mask and hood, and with and without exercise. For the no exercise condition the target exposure concentration was 6 $mg\ m^{-3}$ for exposure times of 5, 10, 15, and 20 min. All subjects were exposed for 20 min on day 5. All four subjects entered the exposure booth at the same time, after 5 min the first one left, after 10 min the second left, and so on until all have completed their exposure. Each subject was exposed to each time condition. For the exercise condition, all four subjects were exposed to a 20 min exposure (n=4 each day, three days total). To insure the subjects were properly sweaty during the vapor exposure, the exercise period started 40 min before the vapor exposure. The exercises consisted of walking on a treadmill, moving weights, and climbing a ladder. All subjects removed gas mask and hood, changed underwear, and removed boots and socks prior to entering their assigned offgassing booth.

The final test procedure was bare skin exposures (no t-shirt) with gas mask but without hood. The testing included 5 days without exercise and 5 days with exercise. The exposure criteria for the no exercise exposures were for 5, 10, 15 and 20 min. The target concentration was 10 $mg\ m^{-3}$. To insure the subjects were properly sweaty during the vapor exposure, the exercise period started 40 min before the vapor exposure. The exercises consisted of walking on a treadmill, moving weights, and climbing a ladder. At the start of vapor exposure the concentration was increased as quickly as possible to the

target concentration of 10 mg m⁻³. This introduction of simulant vapors required about 1.5 min and generally caused some initial overshoot. After the introduction of vapor the subjects continued to exercise for 5, 10, 15 or 20 additional min. Each subject was exposed to each time condition. All subjects were exposed for 30 min on day 5. The subjects removed gas mask and hood, boots and socks, and changed jockey shorts before entering their assigned OFGB.

RESULTS/DISCUSSION. The results of the first skin vapor exposure experiments are given in Table 1. The offgassing factor (OGF) represents the area under the concentration curve in an offgassing booth. The values presented in the table are the average of three OGFs. The values listed under VOFGB ug are the micrograms of simulant carried into the booth calculated on the basis of the washout of the VOFGB with time. These values represent the carry through of a single individual at the exposure CT. Calibration experiments evaporating known quantities of MeS in the VOFGB have indicated simulant accountability in the 92 to 98% range. The column labeled Exp Bth mg m⁻³ is an average concentration obtained by dividing the CT by the exposure time. These data would indicate there is a moderate to strong correlation between CT and offgassing booth response. The linear regression equation for OGF vs CT is: $OGF = .0173 \cdot CT + .3552$ with an $R^2 = .9204$. Unfortunately, because of the way the exposure was created, a single exposure time with different MeS concentrations, the same correlation also exists between peak concentration and OGF. From this set of data it can't be determined whether the OGF-CT relation would hold for other exposure, time combinations.

TABLE 1

Vapor Exposure in Underwear with Gas Mask and Hood, Underwear Change

Exp Bth CT ^a	Exp Bth mg m ⁻³	OGBths OGF ^b	VOFGB ug	Time
70	1.16	2.60	94.6	60
169	2.82	3.20	113.7	60
199	3.31	2.66	209.4	60
260	4.33	2.46	198.6	60
373	6.22	9.45	358.9	60
738	12.30	13.61	730.2	60
925	15.42	15.68	548.3	60

^a Units of CT are mg min m⁻³

^b Units of OGF are mg min m⁻³

The next experiment, procedure 2, was designed to look at non doffed clothing effects on vapor carry-through. Table 2 lists the results of these tests. The exposure times used were day 1, 20 min; day 2, 40 min; day 3, 60 min; and day 4, 80 min. The column labeled Avg mg m⁻³ is an average concentration over the exposure period obtained by dividing the CT by the exposure time. The two columns labeled OGF are the summation of the area under the offgassing booth concentration curve for each of the identified test conditions. This was the first attempt at maintaining a constant concentration and varying the time. Unfortunately the concentration drifted upwards as the experiment progressed, again creating a situation where the results don't differentiate well with respect to whether CT or concentration is causing the variation in OGF. The linear regression relating OGF to Ct for the with clothing change condition is: $OGF = .00583 \cdot CT + 3.1335$ with an $R^2 = .997$. Again good correlation is shown

between CT and OGF, but, because exposure concentration did vary, a similar correlation exists for concentration ($R^2=.926$). An analysis of variance comparing OGFs from underwear change vs no change this indicates there is a greater than 99% probability the offgassing factors resulting from the two clothing conditions are different with the no change value being significantly larger.

TABLE 2

Skin Exposure with Underwear, Gas Mask and Hood. With and Without Underwear Change

Day	Time	CT ^a	Avg mg m ⁻³	OGF with Change ^b	OGF with No Change ^b
1	20	111.24	5.562	4.515	15.285
				3.15	19.8
2	40	261.66	6.5415	4.005	23.685
				5.04	27.855
3	60	471.5	7.858	6.345	39.63
				5.175	30.48
4	80	648.08	8.101	7.665	20.79
				6	35.055
			Avg:	5.237	26.573
			Std Dev:	1.421	8.232

^a Units of CT are mg min m⁻³

^b Units of OGF are mg min m⁻³

The third set of tests was done to investigate the effects that wet skin, caused by profuse sweating, might have on vapor carry-through as measured by an offgassing booth. This was done because profuse sweating generally occurs inside a chemical protective ensemble unless ambient temperature are low and/or the individual is relatively inactive. Table 3 lists the results of this experiment. The values listed in the column labeled Avg OGF represent the mean value of the OGF of the four subjects exposed to the row CT. The column labeled Std Dev OGF is the standard deviation of four data points representing the offgassing booth response to the row CT. In the Test Cond column, nx indicates no exercise while ex indicates the standard exercise protocol was followed. A review of the Table 3 data indicates that the 5 and 10 min data points would appear to be somewhat less than the remainder of the average OGFs. An analysis of variance of the raw data from which the average OGFs were derived indicated there was a 95% probability that at least one of exposure times (rows) is significantly different from the rest. If the 5 and 10 min data values are left out of the ANOVA, the difference between the mean OGFs was no longer significant. This means there was no significant difference between the 15 and 20 min no exercise and the 20 min with exercise OGFs. Considering that the exercise and no exercise data sets are not different, then if a linear regression is done of OGF vs CT for all of the table 3 values, $R^2=.5833$ which indicates fair correlation between OGF and CT. If the 5 and

10 min exposures are left out of the regression, $R^2=.0016$ which indicates there is virtually no correlation between OGF and CT for the 15 and 20 min exposure times. These results indicate the magnitude of offgassing results data (OGF) is not very sensitive to exposure (CT) for times exceeding 10 or 15 min.

TABLE 3

Skin Exposure in Underwear With or Without Exercise. Underwear Change before Offgas.

Exp Time (min)	Date	Avg CT ^a	Avg OGF ^b	Std Dev OGF	Test Cond
5	7-13 Aug	31.6	2.738	0.429	nx
10	7-13 Aug	63.3	3.746	0.689	nx
15	7-13 Aug	97.1	4.249	0.739	nx
20	7-13 Aug	130.3	3.999	0.904	nx
20	14 Aug	158.4	3.885	0.461	ex
20	15 Aug	165.4	4.403	0.779	ex
20	16 Aug	180.4	4.148	0.123	ex

^a Units of CT are mg min m^{-3}

^b Units of OGF are mg min m^{-3}

The final experiments were done both with and without exercise and without protective hoods. The Table 4 values included in () are the average CTs obtained for each exposure time. Note that the final exposure time for the exercise condition was 30 rather than 20 min thus, this data column has a considerably larger CT. Reviewing the mean OGFs listed in Table 4 again indicates the first two data columns (5 and 10 min exposures) may be lower than the 15, 20, and 30 min exposures. A linear regression analysis of the no exercise data yields: $\text{OGF}=.0339 \cdot \text{CT}+4.438$ with $R^2=.8821$. Even if the 5 and 10 min data columns are not included R^2 remains high at .825 indicating there is a good degree of correlation between OGF and CT for the no exercise condition. The regression analysis of the exercise data yields: $\text{OGF}=.0098 \cdot \text{CT}+8.4439$ with $R^2=.359$. Without the 5 min data condition the R^2 decreases to .113 which indicates there is very little correlation between CT and OGF for exposures longer than 5 min. As a final consideration, a one way ANOVA of the exercise vs no exercise conditions indicated there was no significant difference between the two conditions. Again, exercise made no significant difference in carry-through as indicated by OGF.

Table 4

Offgassing Factors^a Resulting From
Bare Skin Exposure without Hood

A. No Exercise

Sub #	Exposure Time (min)				
	5 (61.9)	10 (126.8)	15 (186.4)	20 (242.3)	20 (279.27)
1	10.11	7.05	11.25	11.04	12.9
2	3.825	11.52	9.315	14.145	15.345
3	9.03	5.88	11.415	9.195	16.365
4	4.305	11.91	8.43	10.62	16.785
Mean OGF:	6.818	9.09	10.103	11.25	15.349
Std Dev:	3.215	3.073	1.467	2.085	1.741

B. With Exercise

Sub #	Exposure Time (Min)				
	5 (92.64)	10 (152.43)	15 (197.11)	20 (259.92)	30 (425.5)
1	8.7	10.245	12.75	12.585	11.265
2	7.65	9.15	12.525	11.415	12.585
3	8.19	7.05	-	14.52	10.755
4	7.815	8.82	11.73	12.33	10.83
Mean OGF:	8.089	8.816	12.335	12.713	11.359
Std Dev:	0.466	1.326	0.536	1.306	0.848

^a Units of Offgassing Factor are mg min m⁻³

CONCLUSIONS

The relation between vapor exposure (CT) and carry-through (OGF) is not very strong for exposures exceeding 10 or 15 min. An attempt to estimate exposure knowing only OGF is probably not practical, however if the time history of the exposure is known such as the relatively short exposure periods normally encountered during don/doff exercises, it provides a good indicator of the relative skin exposure received by processing individuals.

The occasional large variation in offgassing booth results such as the final 20 min data column in Table 4 and the 738 and 921 CT data points in Table 1 indicates there may be factors other than concentration and time that significantly affect the magnitude of OFGB results.

Wearing of any clothing that was directly exposed to vapor into the offgassing booth will have a significant effect on the magnitude of carry-through as indicated by OGFs.

In general, sweaty skin caused by exercise does not seem to have any significant effect on carry-through.

REFERENCES

1. Conkle, J.P., Slate, A.R., Shaffstall, R.M., Kerch, J.N., and Miranda, R.E. Chemical Defense Don/Doff Laboratory Procedures at the USAF School of Aerospace Medicine. USAFSAM-TP-85-5, Dec 1985.
2. Conkle, J.P., Miranda, R.E., Fischer, J.R., Page, R.W., and Bartlett, D.A. Chemical Defense Collective Protection Technology: Volume 1. USAFSAM-TP-86-2 Dec 1986.
3. Kilian, J. P. A Comparison of Casualty Processing Effectiveness in the Survivable Collective Protection System - Medical for Casualties Exposed to Neat or Thickened Simulant. USAFSAM-TR-89-25 Aug 1990

BLANK

II. SYNTHESIS AND PROPERTIES

BLANK

**THE CYCLOADDITION REACTIONS OF SULFONATED DIENES WITH ENAMINES,
YNAMINES, AMIDINES AND THIOFORMAMIDES. NEW ROUTES TOWARDS
HETEROCYCLES.**

Albert Padwa, Yves Gareau, Brian Harrison, Bryan H. Norman

Department of Chemistry, Emory University, Atlanta, Ga. 30322

and

Augusto Rodriguez

Department of Chemistry, Clark Atlanta University, Atlanta, Ga. 30314

Abstract:

Bis (phenylsulfonyl) dienes were found to react smoothly with a variety of enamines and enamine equivalents to give 2+4 cycloadducts in excellent yields. The reactivity of 1,3 bis (phenylsulfonyl) 1,3 butadiene was greater than that observed for 2,3 -bis(phenylsulfonyl) -1,3 -butadiene. The 1,3 isomer can not be isolated and is generated in situ from 1,2,4- tris (phenylsulfonyl)-2-butene. In the absence of a dienophile, the 1,3 isomer dimerizes. The reaction of unactivated enamines with the 2,3 isomer occurs with initial rearrangement to the 1,3 isomer followed by cycloaddition with the enamine. The reaction of several 4-substituted 1,3-bis(phenylsulfonyl)butadienes with amidines and thioformamide gave dihydropyridines and thiopyrans respectively. The 2,3 isomer reacts with an ynamine at subambient conditions to give a 2+2 cycloadduct. The reaction of the 1,2,4- tris (phenylsulfonyl)-2-butene with an ynamine gave 2+4 cycloadducts as did several 4-substituted 1,3-bis(phenylsulfonyl)butadienes.

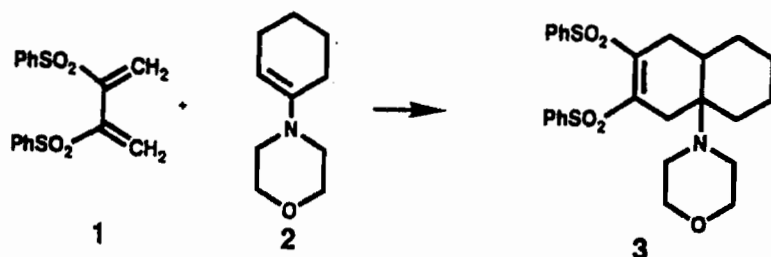
Introduction:

Phenylsulfonyl substituted dienes have been shown to be a versatile substrates for the construction of carbocyclic and heterocyclic rings.¹ These dienes undergo facile Diels-Alder reactions with both electron deficient and electron rich dienophiles. The phenylsulfonyl group enhances chemical reactivity of the diene and adds control to the regioselectivity of the cycloaddition. Once the cycloaddition is completed, the phenylsulfonyl group can be removed by reductive methods thus providing an entry to sulfur free cyclic compounds.

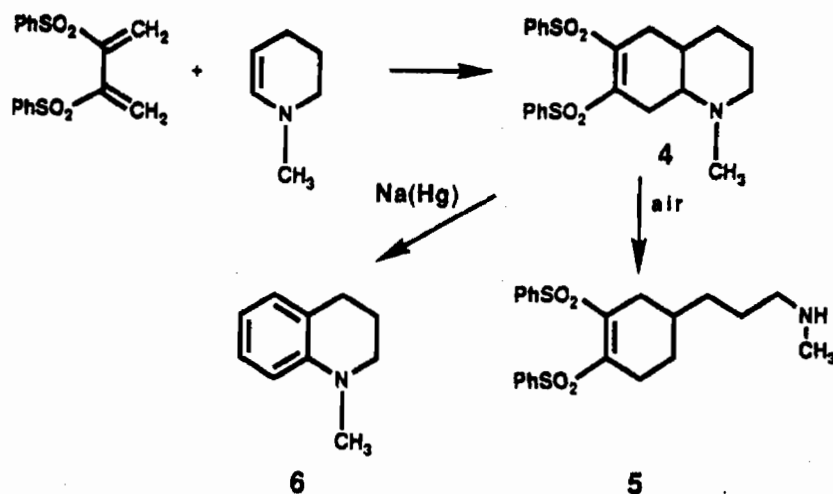
We have exploited the use of 2,3 bis(phenylsulfonyl)butadiene (1) for the synthesis of pyrrolidines², piperidines³ and tetrahydropyridines⁴. As part of our continuing studies in this area we report the cycloaddition reactions of enamines, amidines, indoles, ynamines and thioformamides with sulfur substituted dienes.

Results and Discussion:

The reaction of 1-Morpholino-1-cyclohexene (2) with diene 1 gave, after 24 hours, cycloadduct 3 in 61%. The structure of 3 was assigned on the basis of ¹H-NMR data. The diastereotopic proton at C4 that is cis with respect to the morpholino substituent appears as a multiplet at δ 2.75-2.92 ppm. The trans proton at C4 appears as a multiplet at δ 1.88-2.02 ppm.

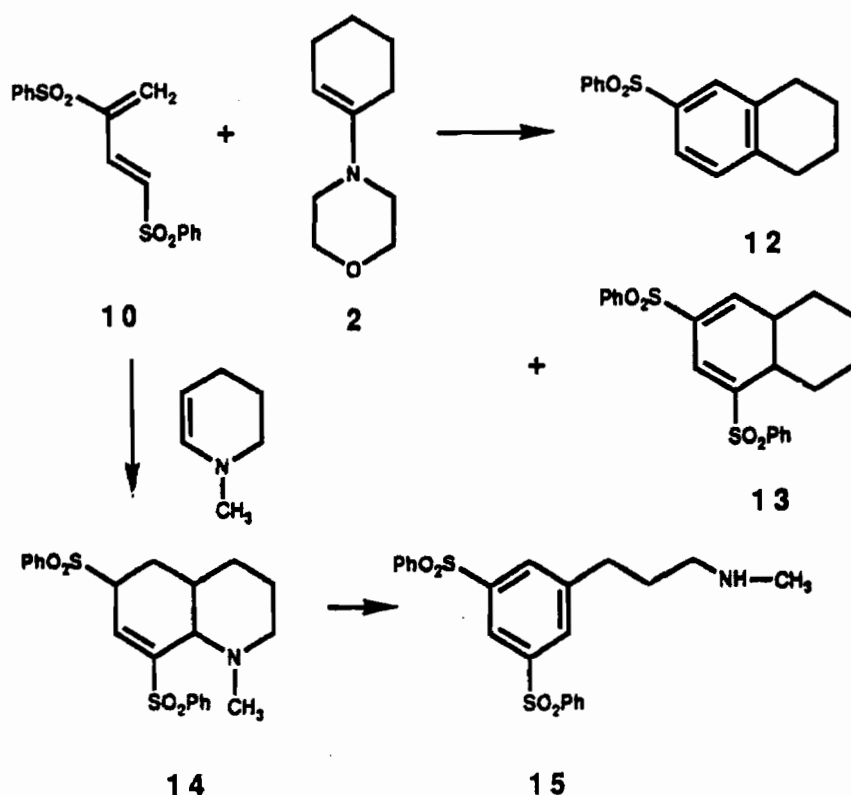


The cycloaddition reaction was next investigated with N-Methyl-1,2,3,4-tetrahydropyridine. Cycloadduct 4 was obtained in 81% after only 8 hours. Cycloadduct 4 was oxidatively unstable and produced amine 5 when exposed to air for prolonged periods or when heated in the presence of air.

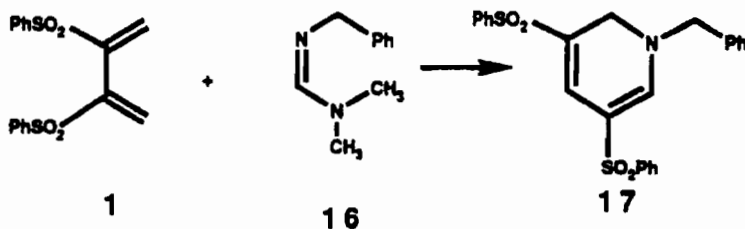


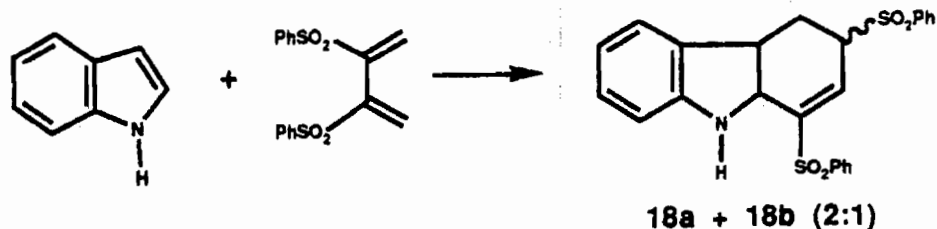
Having established the 2+4 cycloaddition reactions of diene 1 with enamines, we next investigated the cycloaddition reactions of 1,3-bis(phenylsulfonyl)-1,3-butadiene (10). Diene 10 was generated using a sequence described in an earlier communication.⁵ This diene is very reactive and in the absence of a trapping agent, dimerizes under the reaction conditions employed in its generation.

The in-situ generation of 10 and subsequent reaction with enamine 2 gave products in which the morpholine unit had been eliminated. Heating a solution of 9 and 2 in the presence of triethylamine gave 9:1 mixture of tetrahydronaphthalene 12 (89%) and hexahydronaphthalene 13 (7%). Upon further exposure to heat, 13 eliminates phenylsulfonic acid and is converted quantitatively to 12. The formation of 12 is envisioned as occurring via a cycloaddition process followed by elimination of phenylsulfinate and morpholine. Hexahydronaphthalene 13 results from the elimination of morpholine followed by a 1,5 H-shift. The reaction of diene 10 with the N-Methyl-1,2,3,4-tetrahydropyridine gave sulfonylquinoline 14 in 84% yield. Quinoline 14 is air sensitive and oxidizes on standing to secondary amine 15.

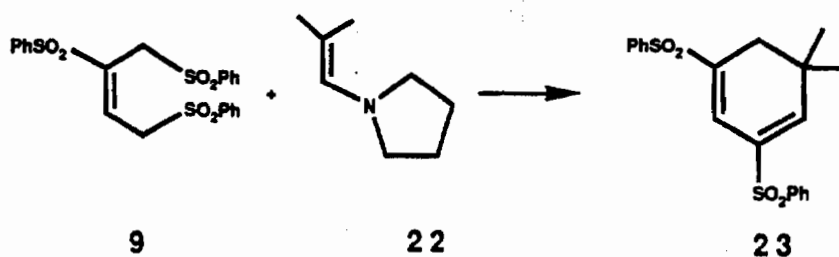


We next probed the reaction of trisubstituted amidines and indoles as enamine reagents. The reaction of diene 1 with N,N-dimethyl-N'-benzyl-methanimidamide required 12 hours of reflux and afforded rearranged dihydropyridine 17 as the sole reaction product (52%). This product is identical to that obtained from the base induced reaction of trisulfonyl 9 with 16. We have found that diene 1 reacts with indole to form a 2:1 equilibrium mixture of epimeric carbazoles 18a and 18b (61%).

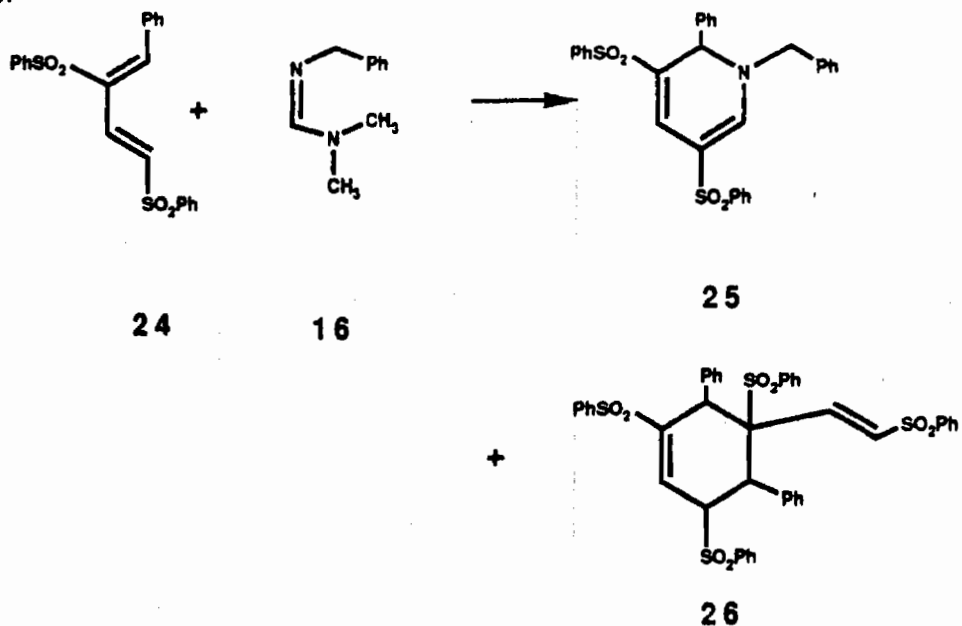




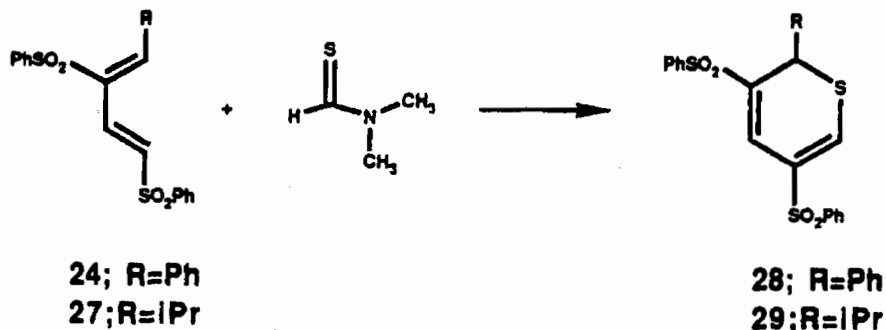
Our observations that the 1,3 bis (phenylsulfonyl)1,3-butadiene -enamine cycloadditions produce carbocyclic rings free of amino functionality, suggested a broad potential for the preparation of bis (phenylsulfonyl) cyclohexadiene carbocycles and heterocycles, provided the initial cycloadducts could be prevented from undergoing aromatization. To prevent the aromatization, the reactions of enamine **22**, amidine **16** and *N,N* dimethylthioforamide with 1,3 bis (phenylsulfonyl)diene were carried out. These three dienophiles contain either a disubstituted carbon or a heteroatom which blocks the initial cycloadduct from aromatization. The reaction of **9** with enamine **22** in the presence of triethylamine gave cyclohexadiene **23** in 74% yield.



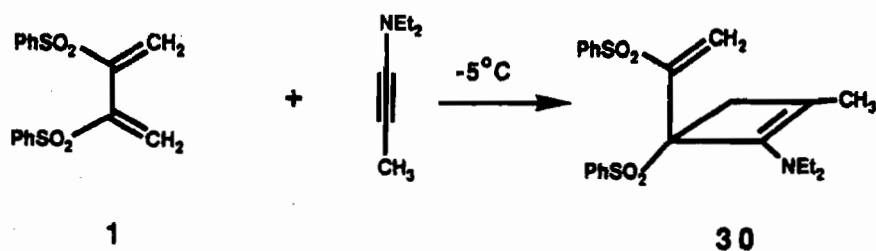
Heating a benzene solution of diene **24** and enamine **16** for seven days gave dihydropyridine **25** (83%) along with a minor amount of the Diels Alder dimer **26** (12%).



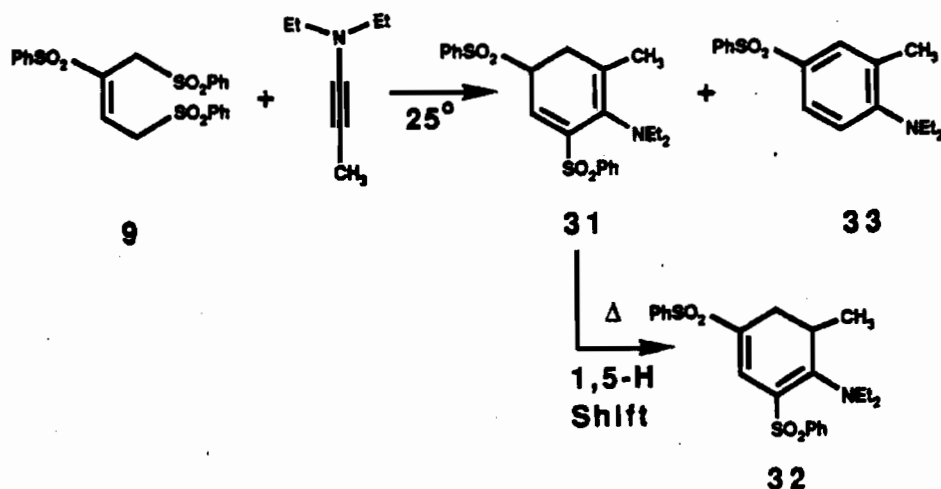
The cycloaddition reaction of N,N-dimethylthioformamide with diene **24** and **27** affords thiopyrans **28** (84%) and **29** (64%) respectively.



The cycloaddition reactions of ynamines with sulfonated dienes have also been examined. Stirring a solution of **1** with 1-N,N-diethylaminopropyne at -5°C gave cyclobutenamine **30** in 81% yield. The structure of **30** was established via proton NMR analysis. The diastereotopic protons on the cyclobutene ring appear as an AB quartet with a coupling constants of $J=13.7$ Hz.

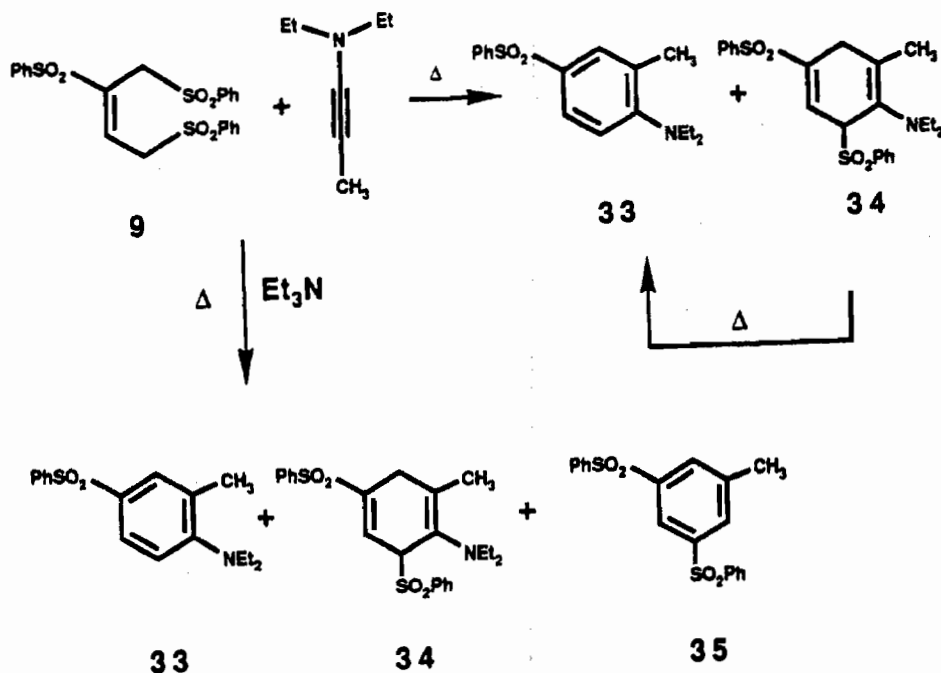


We discovered that trisulfone **9** reacts with the ynamine at room temperature to afford cycloadducts **31** and **33**. This mixture could be easily separated via flash



chromatography obtaining **31** in 67% yield and **33** in 21% yield. Attempted recrystallization of **31** from a warm solution of hexane and methylene chloride induces a 1,5-Hydrogen shift to give amine **32**.

When the reaction of sulfone 9 and 1- N,N-diethylaminopropyne was conducted with refluxing benzene, a 3.5:1 mixture of aromatic amine 33 (65%) and 1,4 cyclohexadiene 34 (19%) was obtained. Adduct 34 could be converted to 33 quantitatively when heating with two equivalents of triethylamine. If triethylamine is added to the above reaction prior to reflux (conditions favoring the generation of diene 10) a 9:1:2 mixture of 33, 34 and a product which has undergone the elimination of diethylamine, i. e. bis (phenylsulfonyl) toluene 35, is obtained.



CONCLUSIONS

In conclusion, we have shown that enamines, indoles, ynamines, amidines and thioformadines react readily with 2,3-bis(phenylsulfonyl)1,3-butadiene and its 1,3 isomer to give cycloadducts in high yield. We have exploited this chemistry to prepare numerous sulfonated carbocyclic and heterocyclic ring systems including: cyclohexadines, tetrahydronaphthalenes, quinolines, dihydropyridines, thiopyrans, tetrahydrocarbazoles and cyclobutenes. We have found that the course of the cycloaddition reaction and the distribution of products depends on the placement of the phenylsulfonyl groups in the diene. For example, the reaction of the 2,3 isomer with indole magnesium salts produces sulfonated allenes while the 1,3 isomer gives carbazoles. With ynamines, the 2,3 isomer produces 2+2 adducts while the 1,3 isomer renders 2+4 adducts. The broad potential of enamine bis(phenylsulfonyl)butadiene cycloaddition process has been demonstrated.

ACKNOWLEDGEMENT

This work was supported by the U. S. Army CRDEC (DAAA15-90-C-1076). Use of the high-field NMR spectrometers was made possible by equipment grants from the National Science Foundation and the National Institute of Health. A. R. thanks the RCMI program of Clark Atlanta University for financial support.

REFERENCES

1. Andell, O. S.; Backvall, J. E. *Tetrahedron Lett.* **1985**, *26*, 4555.
Backvall, J. E.; Juntunen, S. K. *J. Am. Chem. Soc.* **1987**, *109*, 6396.
Cuvigny, T.; du Penhoat, C. H.; Julia, M. *Tetrahedron*, **1986**, *42*, 5329.
2. Padwa, A.; Norman, B. H. *Tetrahedron Lett.* **1988**, 3041; *J. Org. Chem.* **1990**, *55*, 4801; Padwa, A.; Norman, B. H. *Tetrahedron Lett.* **1988**, 2417
3. Norman, B. H.; Gareau, Y.; Padwa, A. *J. Org. Chem.* **1991**, *56*, 2154.
4. Padwa, A.; Harrison, B.; Norman, B. H. *Tetrahedron Lett.* **1989**, 3259.
Padwa, A. Gareau, Y.; Harrison, B.; Norman, B. H. *J. Org. Chem.* in Press.
5. Padwa, A.; Harrison, B.; Murphree, S. S.; Yeske, P. E. *J. Org. Chem.* **1989**, *54*, 4232.

BLANK

SYNTHESIS, ISOLATION, CHARACTERIZATION, AND α_2 -ADRENERGIC ACTIVITIES OF THE OPTICAL ISOMERS OF 4-[1-(1-NAPHTHYL)ETHYL]-1H-IMIDAZOLE

S.S. Hong¹, D.D. Miller¹, F.-L. Hsu², C. George³, K.L. Romstedt⁴, and D.R. Feller⁴

ABSTRACT

Medetomidine (1) is a member of imidazole class of drugs interacting with α_2 -adrenergic receptors. It has been reported that the (+)-isomer of medetomidine is more potent in this system. Recently we have found a naphthalene analog of medetomidine, 4-[1-(1-naphthyl)ethyl]-1H-imidazole hydrochloride (2), to be highly potent in this system. The separation of optical isomers of this naphthalene analog was achieved by using tartaric acid. The optical purity of the isomers was determined by HPLC using a chiral column. The (+)-isomer of 2 was converted to (+)-dibenzoyl-D-tartaric acid salt for X-ray analysis and had the S-configuration. A considerable difference was noted in the biological activities between the two isomers in α_1 - and α_2 -adrenergic system.

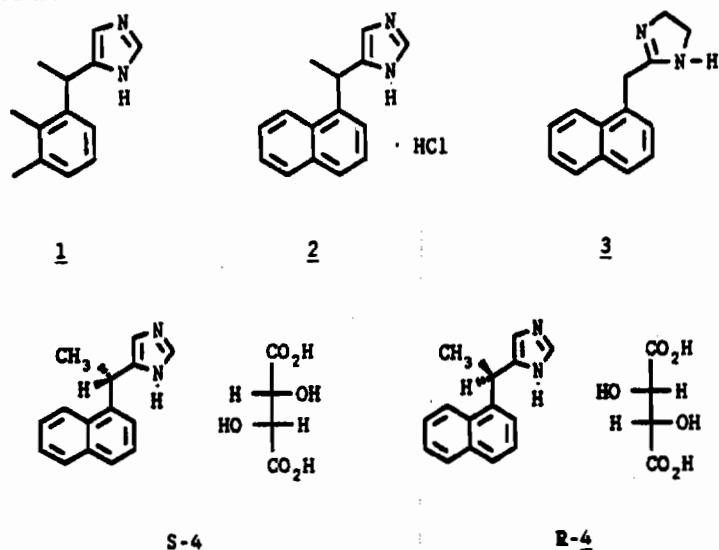
INTRODUCTION

The vast majority of α -adrenergic receptor agonists can be divided into two main classes, the β -phenethylamines and imidazolines. Medetomidine (1) was synthesized by Farnos Group Limited in Finland in 1981. It is one of the most selective and potent α_2 -adrenergic agonists known and is currently used in Scandinavian countries as a veterinary sedative-anaesthetic drug with analgesic properties.⁵⁻⁸ Human phase 1 studies have recently been initiated with medetomidine.⁹⁻¹⁰

The replacement of the 2,3-dimethylphenyl ring system with a naphthyl ring was initially carried out to see if the receptor could tolerate the larger group and if this group might confer increased affinity through enhanced π - π interactions. The naphthyl ring system was also chosen because it was present in naphazoline (3), a potent α -adrenergic agonist.

To determine the stereochemical requirement for binding to the α_2 -adrenergic receptor, the optical isomers of medetomidine were separated.¹¹ Since the d-isomer of medetomidine was more potent than l-isomer, we tried to separate and evaluate the biological

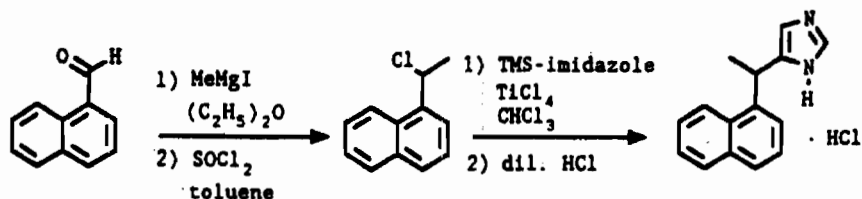
activities of (+)-4-[1-(1-naphthyl)ethyl]imidazole tartaric acid [S(+)-4] and (-)-4-[1-(1-naphthyl)ethyl]imidazole tartaric acid [R(-)-4]. The absolute configurations of S(+)-4 and R(-)-4 were also determined.



RESULTS AND DISCUSSION

The 4-[1-(1-naphthyl)ethyl]imidazole hydrochloride was synthesized as shown in Scheme 1.

SCHEME 1

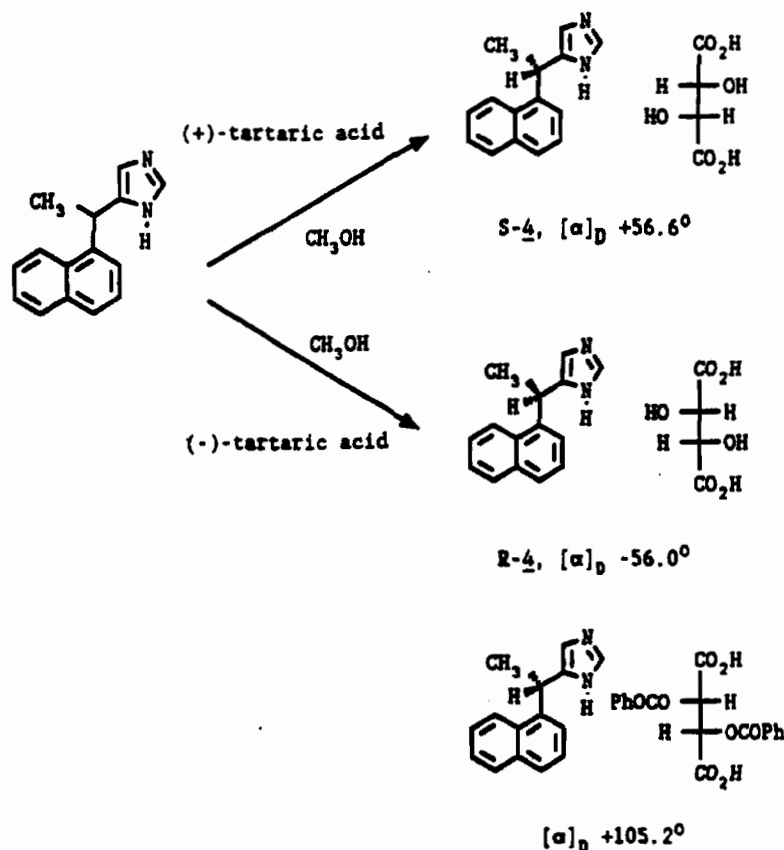


1-Naphthylaldehyde was treated with MeMgI to give an alcohol followed by the treatment of thionyl chloride to give the crude chloro compound. The chloro compound was treated with TMS-imidazole in the presence of $TiCl_4$ to provide the 4-substituted imidazole which was converted to HCl salt.

Racemic 4-[1-(1-naphthyl)ethyl]imidazole was separated into the enantiomers by conversion of the racemate to a mixture of diastereoisomeric salts using the isomers of tartaric acid and separating them by fractional crystallization. The salt formed by addition of (+)-tartaric acid to a solution of the racemic mixture in methanol (Scheme 2) gave (+)-enantiomer after 14 crystallizations from methanol. Once this enantiomer was separated, the remaining salt was converted back to the free base by treatment with sodium hydroxide. This free base was treated with (-)-tartaric acid and (-)-enantiomer was also isolated through 10 crystallizations.

Another approach to the separation of enantiomers of 2 was a chromatographic separation using HPLC. The racemic mixture was separated using an analytical Chiralcel OD^R (Diacel) column.

SCHEME 2



Using a mobile phase of hexane/isopropanol 90:10, the first enantiomer (+ isomer) was eluted at 9.87 min and the other enantiomer (- isomer) was eluted at 16.69 min (Figure 1). The optical purity of each enantiomer was determined using the same conditions described above. Chromatograms of the enantiomers are shown in Figure 2.

To confirm the absolute configuration of the isomeric imidazoles (+)-4 and (-)-4, X-ray analysis of the tartrate salt of (+)-4 was first attempted. This salt did not provide suitable crystals for X-ray analysis; however, suitable crystals for X-ray analysis were obtained with the (+)-dibenzoyl-D-tartrate salt of (+)-4 (Scheme 2). Based on the known absolute configuration of (+)-dibenzoyl-D-tartaric acid, with both asymmetric centers having the S absolute configuration, it was determined that the asymmetric ring junction between naphthalene and imidazole rings of (+)-4 had the S configuration as shown in Figure 3. Thus, the (-)-isomer should have the R configuration.

Medetomidine (1) and anlog 2 have been evaluated for comparative activities on α₁- and α₂-adrenergic receptors in rat aorta and human platelets, respectively (Table 1). The enantiomers of 2 [S(+)-4 and R(-)-4] have been evaluated for their α₂-adrenergic activities in human platelets and compared to that for the enantiomers of medetomidine (Table 2) and also evaluated for α₁- and α₂-adrenergic functional activities in guinea pig ileum preparations (Table 3).

FIGURE 2

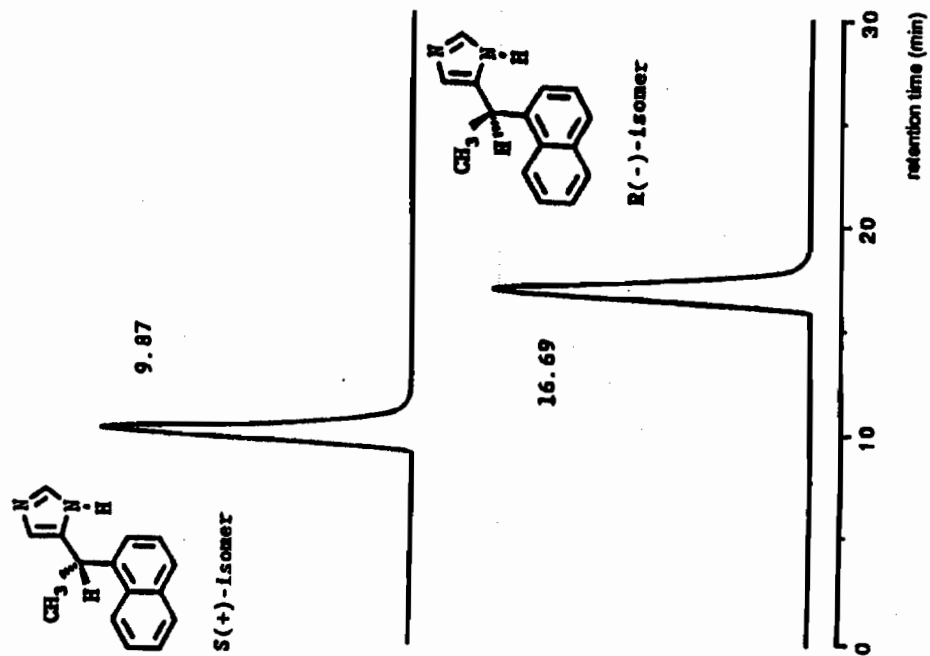


FIGURE 1

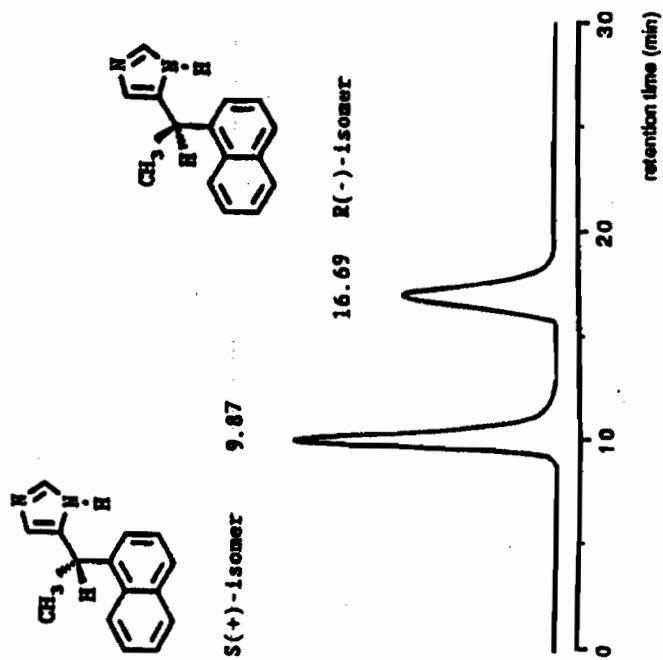


FIGURE 3

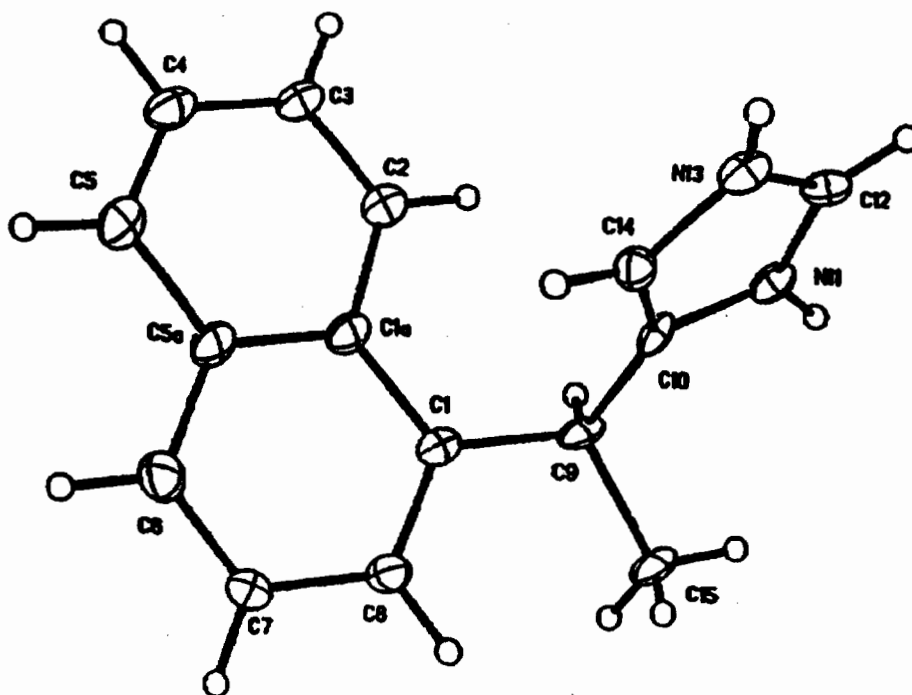


TABLE 1

Compound	Rat Aorta (α_1)			Human Platelets (α_2)	
	$pEC_{50} \pm SEM^a$	Maxima (%) ^b	Potency Ratio ^c	$pIC_{50} \pm SEM^d$	Potency Ratio ^e
Medetomidine (1)	6.51 ± 0.004 (4)	42 ± 7	1.0	5.48 ± 0.20 (4)	1.0
2	6.67 ± 0.141 (4)	27 ± 3	1.4	5.47 ± 0.07 (4)	0.97

^a $pEC_{50} = -\log EC_{50}$ where EC_{50} is equal to the molar concentration of compound which produces 50% of maximum response. ^bData are expressed as the percent maximal analog response relative to phenylephrine (100%). ^cPotency ratio = $EC_{50}(\text{medetomidine})/EC_{50}(\text{analog})$. ^d $pIC_{50} = -\log IC_{50}$ where IC_{50} is equal to the molar concentration of compound which inhibits the response of epinephrine-induced aggregation by 50%. Inhibitor was added 1 min prior to epinephrine (10 μM) in human platelet-rich plasma. Aspirin (1 mM) was included for determination of primary wave aggregation. ^ePotency ratio = $IC_{50}(\text{medetomidine})/IC_{50}(\text{analog})$. ^fValues in parentheses indicate the number of experiments (n).

TABLE 2

Compound	Platelets (α_2)
	$pIC_{50} \pm SEM^a$
<u>2</u>	5.27 \pm 0.22 (6) ^b
S(+)- <u>4</u>	5.21 \pm 0.32 (5)
R(-)- <u>4</u>	6.04 \pm 0.20 (5)
(+)-Medetomidine	5.65 \pm 0.12 (5)
(-)-Medetomidine	5.44 \pm 0.07 (5)

^a $pIC_{50} = -\log IC_{50}$ where IC_{50} is equal to the molar concentration of compound which inhibits the response by 50%. Inhibitors were added 1 min prior to epinephrine (10 μ M) in human platelet-rich plasma. Aspirin (1 mM) was included for determination of primary wave aggregation.

^bValues in parenthesis indicate the number of experiments (n).

TABLE 3

Compound	Ileum (α_1)		Ileum (α_2)	
	EC_{50} (nM) ^a	E_{max} (%) ^b	EC_{50} (nM) ^a	E_{max} (%) ^b
<u>2</u>	15982	24	9	73
R(-)- <u>4</u>	10814	25	c	c
S(+)- <u>4</u>	10635	50	11	84
Oxymetazoline	2028	55	125	87
Phenylephrine	11788	88	62940	62

^a EC_{50} is the concentration which produces 50% of maximum response.

^b α_1 -Receptor efficacy was determined in isolated guinea pig ileum (contractile response) using (-)-epinephrine as a control. α_2 -Receptor efficacy was studied in field-stimulated guinea pig ileum model (supra-maximal voltage, 0.1 Hz, 0.5 msec) using UK-14304 as a control.

^cNo activity up to 100 μ M.

CONCLUSIONS

The replacement of the dimethylphenyl group of medetomidine (1) with a naphthalene ring, as in analog 2, did not diminish α_2 -adrenergic activity while leading to a loss of α_1 -adrenergic activity. The enantiomers of compound 2 were separated using fractional crystallization and enantiomeric purities were determined using an analytical Chiralcel OD^R HPLC column. The absolute configuration of S(+)-4 was determined by X-ray crystallography. From functional assays using guinea pig ileum, R(-)-4 exhibited no intrinsic activity, whereas S(+)-4 showed enhanced α_2 -agonist activity as compared to the racemic 2.

ACKNOWLEDGMENTS

Financial support from U.S. Army CRDEC is gratefully acknowledged.

REFERENCES

1. Division of Medicinal Chemistry and Pharmacognosy, The Ohio State University, 500 west 12th Avenue, Columbus, Ohio 43210.
2. U.S. Army Chemical Research, Development and Engineering Center, Aberdeen Proving Ground, MD 21010-5423.
3. Naval Research Laboratory, 4555 Overlook Ave, SW, Washington, D.C. 20375-5000.
4. Division of Pharmacology, The Ohio State University, 500 West 12th Avenue, Columbus, Ohio 43210.
5. Scheinin, H.; Virtanen, R.; Macdonald, E.; Laintausta, R.; Scheinin, M. Prog. Neuro-Psychopharmacol. Biol. Psychiat. 1989, 13, 635.
6. Kallio, A.; Scheinin, M.; Koulu, M.; Ponkilainen, R.; Ruskoaho, H.; Viinamaki, O.; Scheinin, H. Clin. Pharmacol. Ther. 1989, 46, 33.
7. Pertovaara, A.; Kauppila, T.; Tukeva, T. Eur. J. Pharmacol. 1990, 179, 323.
8. Virtanen, R.; Nyman, L. Eur. J. Pharmacol. 1985, 108, 163.
9. Scheinin, M.; Kallio, A.; Koulu, M.; Viikari, J.; Scheinin, H. Br. J. Clin. Pharmac. 1987, 24, 443.
10. Scheinin, M.; Kallio, A.; Koulu, M.; Arstila, M.; Viikari, J.; Scheinin, H. Current Therapeutic Research 1987, 41, 637.
11. Karjalainen, A. J.; Virtanen, R. E.; Sevolainen, E. J. U.K. Patent Application GB 2 206 880.

BLANK

α_2 -ADRENERGIC ACTIVITY OF NEW SERIES OF ANALOGS
OF 4-[1-(1-NAPHTHYL)ETHYL]-1H-IMIDAZOLE

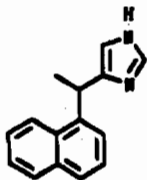
K. Matsumoto¹, S.S. Hong¹, F.-L. Hsu¹, K.L. Romstedt¹, D.R. Feller¹,
and D.D. Miller¹. The Ohio State University, College of Pharmacy,
Columbus, OH 43210 and ²U.S. Army Chemical Research, Development
and Engineering Center, Aberdeen Proving Ground, MD 21010-5423

ABSTRACT

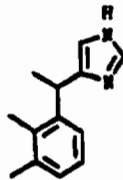
Due to the potent α_2 -adrenergic activity of 4-[1-(1-naphthyl)ethyl]-1H-imidazole (1), an analog of medetomidine (2), we have initiated a structure-activity relationship study of this compound. The study includes replacement of the methyl group with hydrogen, hydroxy, methoxy, carbonyl or trifluoromethyl group and the attempted synthesis of an analog with an indole nucleus instead of the naphthalene ring. In another synthetic effort, some conformationally restrained analogs of medetomidine were prepared. These analogs are tetralin derivatives with a 4-substituted imidazole ring attached at the C-1 position of tetralin. The synthesis of the analogs and their preliminary α_2 -adrenergic activity will be discussed.

INTRODUCTION

There are reported to be two major chemical classes of α -adrenergic agonists, phenethanolamines and imidazolines. Recently, it has been reported that medetomidine (2), a member of a new class of imidazole analogs, is a selective and potent agonist of α_2 -adrenoceptors¹. In the course of our work investigating imidazole analogs, we have found the naphthalene analog (1) has α_2 -adrenergic agonist activity similar to medetomidine².



(1)



Medetomidine (2)

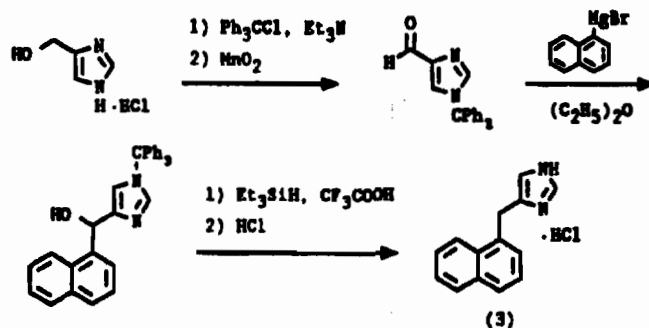
This discovery led us to an extensive structure-activity relationship study of the compound to provide a better understanding of the structural requirements of 4-substituted imidazole analogs for α -adrenergic activity.

RESULTS and DISCUSSIONS

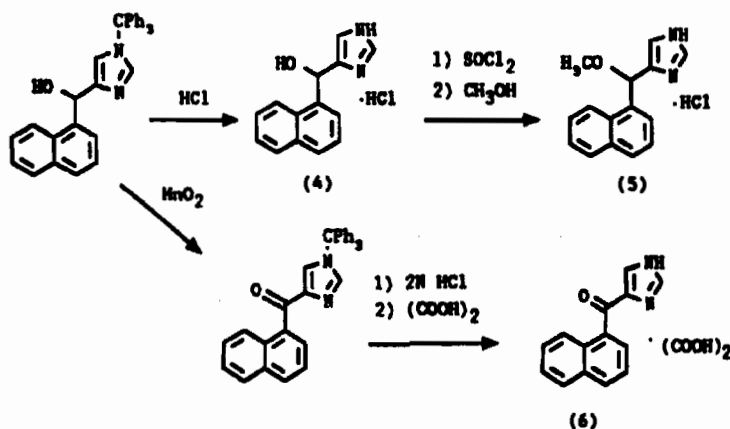
The initial program focused on the replacement of the methyl group of (1) at the benzylic carbon with other functional groups such as hydrogen, hydroxy, methoxy, carbonyl or trifluoromethyl.

Readily available 4-(hydroxymethyl)-1H-imidazole was used as starting material for the synthesis of the hydrogen analog (3). The alcohol was converted to an aldehyde³, which was coupled with naphthylmagnesium bromide to afford the corresponding secondary alcohol. Removal of the hydroxy and triphenylmethyl groups was effected simultaneously by treatment with triethylsilane in the presence of trifluoroacetic acid⁴ to give the analog (3). The hydroxy (4), methoxy (5) and carbonyl (6) analogs were synthesized from the secondary alcohol obtained in the synthesis of (3) as outlined in Scheme 2.

SCHEME 1

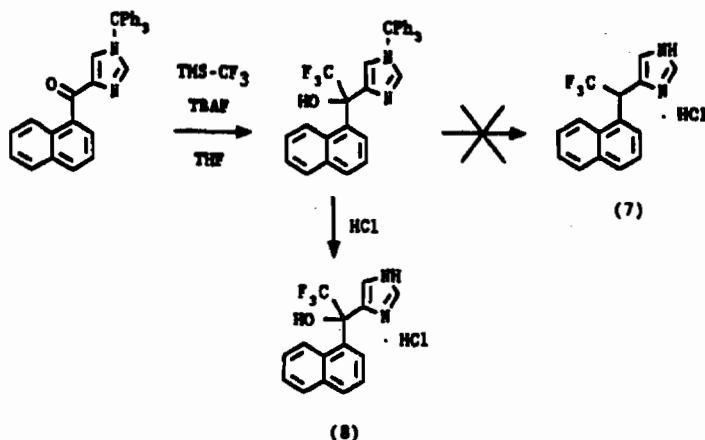


SCHEME 2



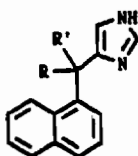
The synthesis of trifluoromethyl analog (7) was initially attempted utilizing a trifluoromethyl anion reagent⁵ as shown in Scheme 3. However, difficulty was encountered in the removal of hydroxy group of the resulting compound. A variety of synthetic reactions are presently being investigated toward the target (7).

SCHEME 3



α -Adrenergic activity of the synthesized analogs were compared with the parent compound (1) as shown in Table 1. The hydrogen analog (3) is 3-fold more potent than the parent compound (1). The other polar analogs did not exhibit potent activity.

TABLE 1
Inhibitory Effect of the Analogs on Epinephrine-induced Human Platelet Aggregation (α_1 -adrenergic activity)

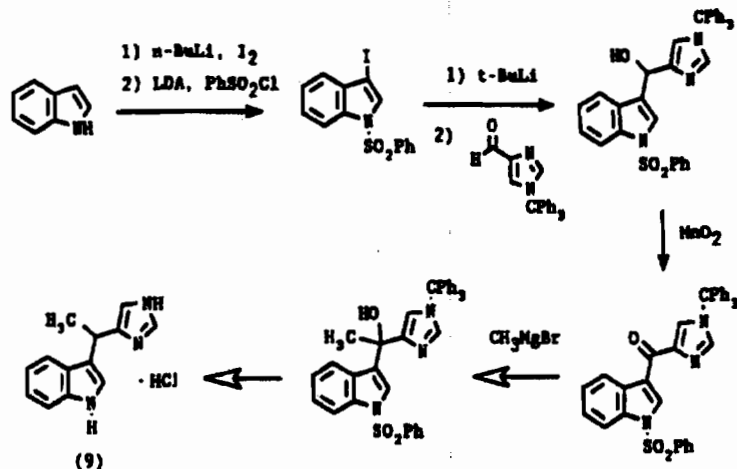


Compound	R	R'	pIC ₅₀ ± SEM
(1)	CH ₃	H	5.27 ± 0.22 [n=6]
(3)	H	H	5.62 ± 0.22 [n=3]
(4)	OH	H	4.31 ± 0.21 [n=3]
(5)	OCH ₃	H	3.55 ± 0.07 [n=3]
(6)	O=		3.98 ± 0.40 [n=3]
(8)	CF ₃	OH	-- ^a

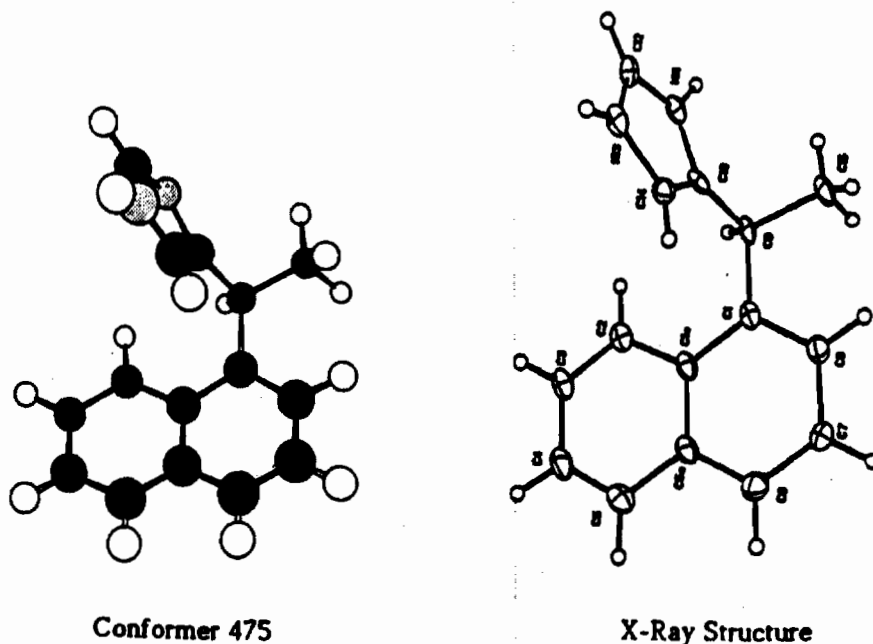
a. No activity at 300 μ M.

In an investigation of the structural requirements of the naphthalene portion of (1), the synthesis of the indole analog (9) was attempted in a similar manner (Scheme 4), and has been partially completed.

Scheme 4



In another program, our efforts were directed toward the design and synthesis of conformationally restrained analogs of (1) such as the tetralin derivative (10). Preliminary conformational analysis of the naphthalene analog (1) using SYBYL (Tripos) suggests that the C-C bonds between the naphthalene and imidazole rings do not possess free rotation. One of the most stable conformers as predicted by the analysis was similar to the crystal structure of (1) as determined by X-ray analysis.



Several rigid compounds, that have analogous 3-dimensional structures to the stable conformers, were designed to examine α_2 -adrenergic activity. The first target, a tetralin derivative (10), was synthesized as shown in Scheme 5. Due to the quaternary carbon, we chose a different synthetic approach that includes cyclization of the imidazole ring⁶. However, its activity was decreased relative to the naphthalene analog (1) on α_2 -adrenoceptor of guinea pig ileum.

SCHEME 5

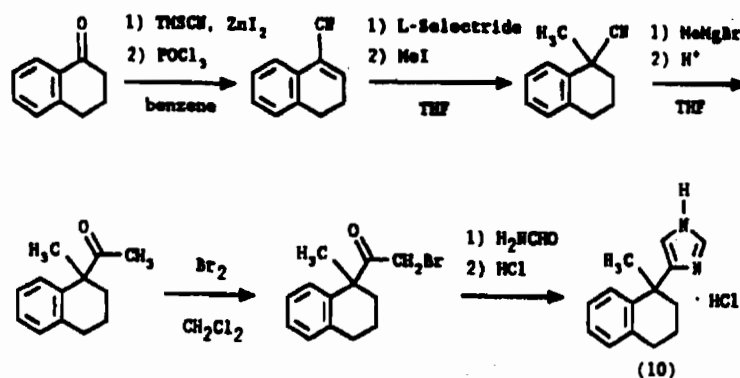


TABLE 2

Comparison of Adrenergic Activities of the Naphthalene and Tetralin Analogs

	α_1			α_2		
	K_i (nM) ^a	EC_{50} (nM) ^b	E_{max} (%) ^c	K_i (nM) ^a	EC_{50} (nM) ^b	E_{max} (%) ^c
	310	15982	24	17	9	73
	10200	>10000	0	8694	1765	70

^a α_1 -Receptor competition studies were performed using 0.2 nM [³H]-prazosin in rat frontal cortical homogenates (prazosin competition as a control)

α_2 -Receptor studies utilized 2.0 nM [³H]-rauwolscine in rat frontal cortical homogenates (yohimbine competition as a control). Phentolamine (10 μ M) was used in each assay to determine the level of non-specific binding. Each assay was validated as to receptor specificity using known adrenergic agents.

^b EC_{50} is the concentration which produces 50% of maximum response.

^c α_1 -Receptor efficacy was determined in isolated guinea pig ileum (contractile response) using (-)-spinephrine as a control. α_2 -Receptor efficacy was studied in field-stimulated guinea pig ileum model (supra-maximal voltage, 0.1 Hz, 0.5 msec) using UK-14304 as a control.

CONCLUSIONS

A variety of functional groups were introduced at the carbon between the naphthalene and imidazole rings of the compound (1) for a study of this structure-activity relationships. The hydrogen analog (3) was 3-fold more potent than the parent compound (1) in human platelets (α_{2A} -adrenoceptor).

Several conformationally restrained compounds were designed based on the results of preliminary conformational analysis of the naphthalene analog (1). The first target, the tetralin analog (10), was synthesized and assayed for adrenergic activities. Although the α -adrenergic activities of the compound are less than those of the naphthalene analog (1), we are planning the other investigation of several members of this class of compounds.

ACKNOWLEDGMENT

We thank the Department of the Army for partial support of this research project.

REFERENCES

1. (a) Savola, J.-M.; Ruskoaho, H.; Puurunen, J.; Salonen, J. S.; Karki, N. T. J. Autonom. Pharmacol. 1986, 5, 275. (b) Savola, J.-M.; Virtanen, R. Eur. J. Pharmacol. 1991, 195, 193.
2. Amemiya, Y.; Hong, S. S.; Venkataraman, B. V.; Patil, P. N.; Shams, G.; Romstedt, K.; Feller, D. R.; Hsu, F.-L.; Miller D. D. J. Med. Chem., in press.
3. Kelly, J. L.; Miller, C. A.; McLean, E. D. J. Med. Chem. 1977, 20, 721.
4. Cordi, A. A.; Snyers, M. P.; Giraud-Mangin, D.; Maesen, V. D.; Van Hoeck, J. P.; Beuze, S.; Ellens, E.; Napora, F.; Gillet, C. L.; Gorissen, H.; Calderon, P.; Remacle, M. D.; Varebeke, P.J.; Dorsser, W.V.; Roba, J. Eur. J. Med. Chem. 1990, 25, 557.
5. (a) Prakash, G. K. S.; Krishnamurti, R.; Olah, G. A. J. Amer. Chem. Soc. 1989, 111, 393. (b) Krishnamurti, R.; Bellew, D.R.; Prakash, G. K. S. J. Org. Chem. 1991, 56, 984.
6. Gregory, G. B.; Johnson, A. L.; Ripka, W. C. J. Org. Chem. 1990, 55, 1479.

NOVEL REACTIONS OF THE S-S AND C-S BONDS

S. Munavalli¹, D. I. Rossman², D. K. Rohrbaugh²
and C. P. Ferguson²

¹Geo-Centers Inc., Ft Washington, MD 20744 and ²US Army, Chemical Research Development and Engineering Center, Aberdeen Proving Ground, MD 21010

Abstract: Evidence presented suggests that the cleavage of organic di- and trisulfides, which occur widely in nature, may proceed via a free radical process. Our recent interest in the chemistry of these sulfur compounds has led us to: (1) the development of a versatile reagent, trifluoromethylthiocopper, for the introduction of the trifluoromethylthio functionality into organic compounds and (2) the examination of the nature and mechanism of the scission of the S-S and C-S bonds by organolithium reagents. This paper describes our recent results.

Introduction: Ubiquitously occurring di- and trisulfides¹ have attracted considerable attention, for they determine the tertiary structure of proteins², take part in energy transfer processes³ and are used in industrial applications, namely polymerization and vulcanization of rubber.⁴ The importance and usefulness of the di- and trisulfides rest primarily on the presence and reactivity of the S-S bond, the heterolytic reactions of which are well recognized.⁵ In contrast, the homolytic scission of the S-S bond is not as readily accepted. The homolysis can be achieved under photolytic⁶ thermal⁷ electrolytic⁸ or radiolytic⁸ conditions. Since the C-S bond of the disulfide is about 5~10 kcal per mole stronger than the S-S bond,⁹ the cleavage generally occurs at the S-S bond.⁹ It should, however, be pointed out that two examples have been cited where the C-S bond fission has been found to occur more readily than the S-S bond.¹⁰ The free radicals formed in the above examples are more stable than those formed in the present case.

In contrast to the disulfides, the S-S bond of the tetrasulfides appears to undergo facile thermolysis.^{11a-b} Flash photolysis of t-butyl tetrasulfide produces perthiyl radicals^{11b}, rather than the thiyl and sulfuranly radicals. This observation has led to the conclusion that the polysulfide radicals $R\cdot(n \geq 2)$ are considerably more stable than the thiyl radicals.^{11c} This inference has been further substantiated by molecular orbital

calculations^{11d}, by the chemical reactivity of the perthiyl radicals^{11c} and the concept of a three-electron bond between the terminal sulfur atoms.^{11e}

Surprisingly, there has been no definitive study of the scission of the S-S bond of the trisulfides.^{12a-c} In principle, the homolysis of the S-S bond of the trisulfides should occur more readily than that of the disulfides and should furnish thiyl and perthiyl radicals. This assumption is indirectly supported by the observation that photolysis of dimethyl trisulfide yielded a mixture of di-, tri-, and tetrasulfides.^{12d} Since the photolysis of a mixture of ethyl trisulfides and n-propyl trisulfide gave only one product, namely ethyl n-propyl trisulfide, a free radical process involving the central S atom has been postulated.^{12e} However, the results of the experiments with labeled S atoms have contradicted the involvement of the central S-atom.^{12f}

An on-going project in our laboratory required the introduction of the trifluoromethylthio moiety (1) into various organic molecules. The first mention of this group was in an obscure French patent.^{13a} However, Haszeldine and co-workers were the first to synthesize bis(trifluoromethylthio) mercury (2).^{13b} Mutteritis et al developed the method for the first large scale preparation of 2.^{13c} The first report of trifluoromethylthiocopper (3) was its *in situ* preparation.^{13c} However, a recent synthesis of 3 has been published.^{13d} Our repeated attempts to prepare 3 according to the published procedure^{13d} failed. In 1988 we developed a procedure for the synthesis of 3 in a pure crystalline form.^{14a} Compound 3 is an excellent precursor of trifluoromethylthiyl radicals.^{14a-b}

Since the reaction of organolithium and Grignard reagents with disulfides has been reported to result in the cleavage of the S-S bond¹⁵, we decided to explore the reaction of organolithium reagents with bis(trifluoromethyl) di- (4) and trisulfides (5) with a view to introduce 1 into organic compounds. Recently we have developed an improved synthesis of 5.¹⁶ This communication describes the results of the reaction of: (1) 3 with mono-, di- and trisulfides (Table 1), (2) 4 and 5 with various organolithium reagents (Tables 2 and 3) and (3) the nature and mechanism of the scission of the S-S and C-S bonds.

Discussion: Table 1 describes the products of the reaction of the trifluoromethylthiocopper with alkyl mono-, di- and trisulfides. The characterization of the mixed di- and trisulfides clearly indicates that the thiyl radical generated *in situ* from the copper reagent causes the cleavage of the S-S and C-S bonds. From the mechanistic point of view, two possible pathways: (a) a stepwise free radical process (Scheme 1a) and (b) a synchronous attack (Scheme 1b) can be envisaged. The stepwise free radical process takes into account the susceptibility of the weak S-S bond to radical attack.^{18a} However, products corresponding to Steps 5 and 6 are not observed. The second pathway incorporates a synchronous attack on sulfur to give an intermediate radical, which then collapses to yield the mixed mono-, di- and trisulfides. Haszeldine and coworkers have proposed a similar synchronous attack to rationalize the formation of methyl trifluoromethyl sulfide.^{18b}

Based on the bond dissociation energies (BDE) of the oxygen-oxygen, carbon-carbon and sulfur-sulfur bonds, it appears that the BDE of the disulfide is almost half-way between the BDE required to cleave the O-O and the C-C bond (Table 4). It is in the neighborhood of 60-70 kcal/mole.^{19f} However, the BDE of the S-S bond of the alkyl trisulfide is 45 kcal/mole^{19f}, about half-way between the alkyl di- and tetrasulfides. The BDE of **4** has been reported to be 53 kcal/mole.^{19d} The corresponding values of **5** and bis (trifluoromethyl) tetrasulfide **6** are not known. Using the above reasoning, the BDE values of **5** and **6** must be considerably lower than that of **4**. If this is true, then the S-S bond of **5** and **6** must be more readily cleaved than that of **4**. In the light of the above inference, it is not surprising that organolithium reagents bring about a scission of the S-S bond of **4** and **5** at -78 °C. The results presented in Tables 2 and 3 can be rationalized on the basis of a single electron transfer (SET) process, which has been advanced as a general mode of reaction of alkyllithiums with organic substrates.²⁰ Also, compelling evidence for the involvement of the free radical intermediates in the reactions of organolithium reagents has been presented.^{20c-d} Recently, Ashby has convincingly demonstrated the wide applicability of the SET pathway to organic reactions.^{20e} With the aid of the SET process, the formation of products listed in Tables 2 and 3 can be conveniently rationalized.

The SET process outlined in Schemes 2 and 3 is initiated by the transfer of an electron from the nucleophile to sulfur atoms of the substrates, which are highly susceptible to radical attack. The radical anion thus formed in

Table 1: Reaction of CF_3SCu with mono-, di- and trisulfides.

	R	CSF_2	CS_2	CF_3SSR	CF_3SSSR	RSC(O)SR
1	C_6H_5			73.8%		
2	C_2H_5		1.2%	9.0%		21.0%
3	n- C_3H_7	0.4%		13.5%		0.3%
4	i- C_3H_7			2.1%		
5	n- C_4H_9	0.9%		29.5%		
6	i- C_4H_9			4.8%		
7	s- C_4H_9			6.8%		
8	t- C_4H_9	1.2%	1.5%	1.6%		
9 ^b	t- C_4H_9				17.2% ^b	
10 ^c	n- C_4H_9	6.9%		0.2%		

^a The yields are calculated from the GC/MS data and are not optimized. Starting materials constituted the rest of the products.

^b Reaction with trisulfide.

^c Reaction with sulfide.

Table 2: $\text{F}_3\text{CSSCF}_3 + \text{R-Li} \longrightarrow \text{Products}$

R	$\text{F}_3\text{CSBu}^{\text{I}}$	$\text{F}_3\text{CSSBu}^{\text{I}}$	$\text{F}_3\text{CSS-C}_5\text{H}_{11}$	$^{\text{t}}\text{BuS-C}_5\text{H}_{11}$			
$^{\text{t}}\text{Bu}$	35%	32.6%	19.39%	13.07%			
$^{\text{n}}\text{Bu}$	$\text{F}_3\text{CSBu}^{\text{II}}$	$\text{F}_3\text{CSSBu}^{\text{II}}$	$\text{F}_3\text{CSS-C}_5\text{H}_9$	C_8H_{18}			
C_6H_5	84.8%	1.00%	0.6%	13.56%			
	$\text{C}_6\text{H}_5\text{S-CF}_3$	$\text{C}_6\text{H}_5\text{SS-CF}_3$	$\text{C}_6\text{H}_5\text{S-C}_6\text{H}_5$	$\text{C}_6\text{H}_5\text{S-C}_2\text{H}_5$	$\text{C}_6\text{H}_5\text{-C}_2\text{H}_5$	$\text{C}_6\text{H}_5\text{-C}_4\text{H}_9$	$\text{C}_6\text{H}_5\text{-C}_6\text{H}_5$
	71.57%	1.31%	2.77%	1.63%	7.35%	1.64%	13.56%

*This definitely arises from the solvent used.

**This may come from disproportionation reactions and/ or the impurities present in the alkyllithium reagent.

***From the dimerization of the butyl radical or phenyl radical.

Table 3: Distribution of Products Formed from the Reaction of Bis-(trifluoromethyl) trisulfide with Organolithium Reagents..*



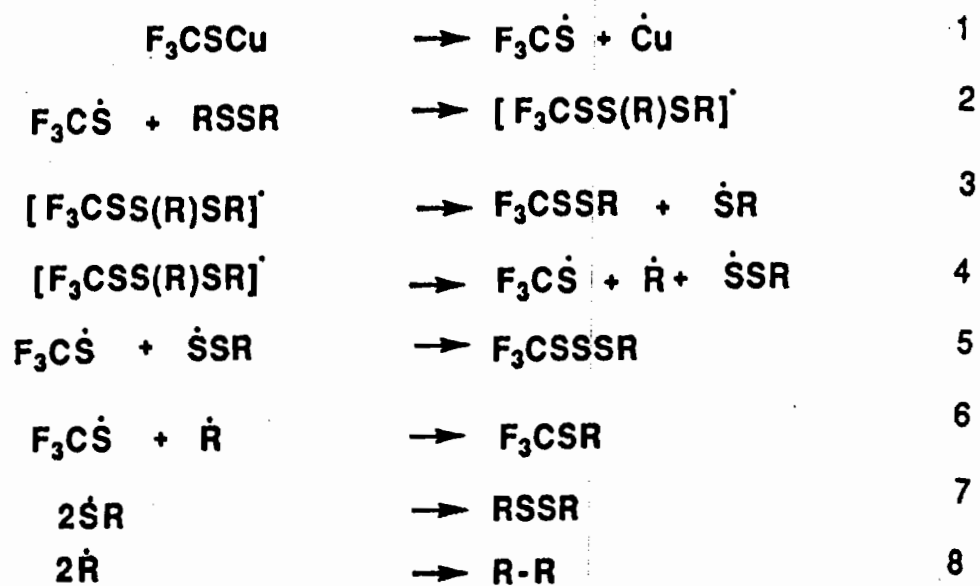
R	CSF ₂	CF ₃ SSSR	CF ₃ SSR	CF ₃ SR	RSSR	RSR	R-R
CH ₃		0.5%	6.3%		0.7%		
n-C ₄ H ₉	0.1%	3.5%	15.5%	7.3%	3.9%	48.4%	8.1%
s-C ₄ H ₉		1.9%	4.2%		0.7%	4.5%	
t-C ₄ H ₉		28.0%	35.0%		17.0%	11.0%	
Me ₃ SiCH ₂		3.4%	21.3%	1.4%			2.1%
C ₆ H ₅			7.1%	10.1%			10.4%

*In view of the high toxicity of the trisulfide, extreme care and caution should be exercised in working with these compounds. The yields are from the GC/MS data and have not been optimized. Starting material and trace amounts of as yet unidentified materials constitute the remaining substances. Similar results have been obtained with LDA.

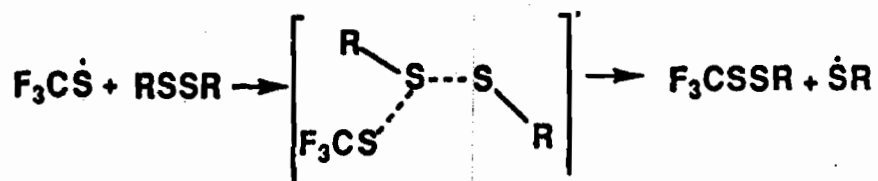
** $(\text{CH}_3)_3\text{SiC}(\text{S})\text{SCF}_3$ has also been identified as a by product of this reaction.

Table 4: Bond Dissociation Energies.

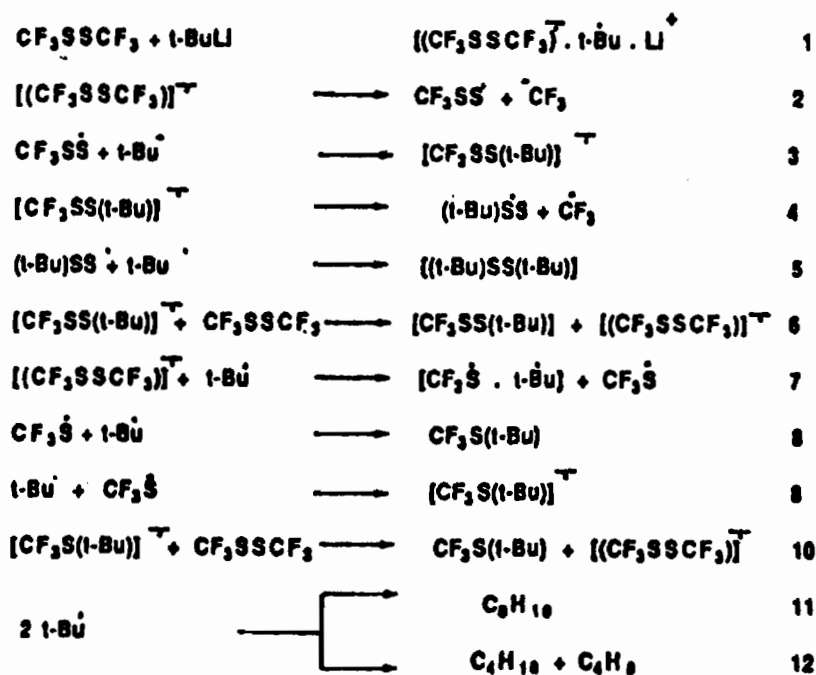
Bond	BDE kcal/mole	Bond length (Å)
OO	3519a	-
C-C	8119a	1.5419a
RS-SR	60-70 ^{19b-c}	2.0419a
CF ₃ S-SCF ₃	5319d	2.0319e
CH ₃ SS-SCH ₃	4519f	-
CF ₃ SS-SCF ₃	-	2.0619g
RSS-SSR	3419h	-
CF ₃ SS-SCF ₃	-	1.8419e
CF ₃ SSS-CF ₃	-	1.8519g



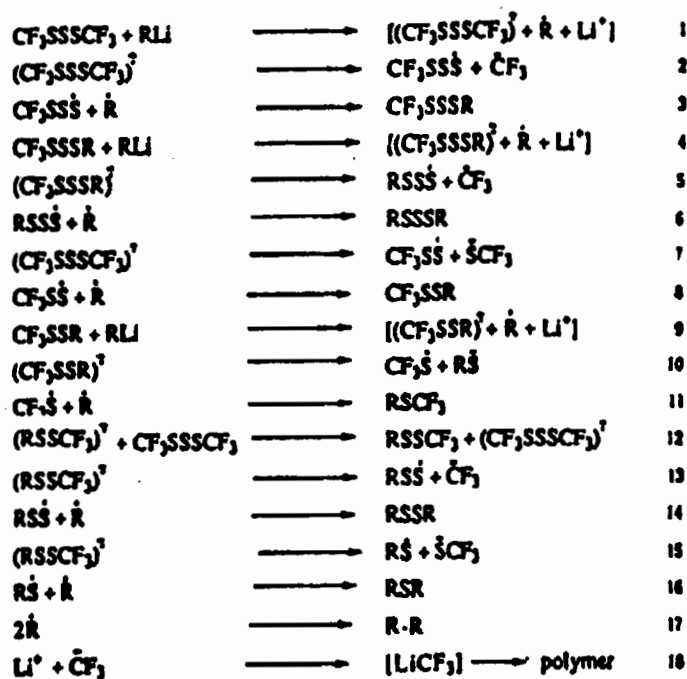
Scheme 1a



Scheme 1b



Scheme 2



Scheme 3

Step 1 fragments and generates a radical and a CF₃ anion. There is precedent for this type of cleavage.^{21a} The formation of mixed radical anions as indicated in Step 3 of Scheme 2 and in Steps 5 and 10 of Scheme 3 has precedents as well.^{21b} The formation of the dimerized products is regarded as a strong confirmation of the presence of free radicals. The fate of LiCF₃ has been described earlier.^{21c} The proposed Schemes 2 and 3 derive their strength and support from the following observations: (1) Many substitution reactions on sulfur have been suggested to occur via a cascade of addition-elimination reactions.^{21d} (2) There are precedents for electron sharing by radicals and nucleophiles with sulfur singly bonded to carbon.^{21e-f} (3) The SET pathway has been suggested as the preferred course even in the case of sterically hindered systems.^{21g-h} (4) The formation of thiyl, perthiyl and sulfuranyl radicals has been invoked to rationalize the products formed from the thermolysis of the trisulfide.²¹ⁱ

EXPERIMENTAL

Warning! Because of the high toxicity associated with bis(trifluoromethyl) disulfide, extreme care should be exercised in working with these compounds. The Mass spectra were recorded on a Finnigen Model 5100 GC/MS equipped with a silica 25m x 0.31 mm (i.d.) SE-54 capillary column (J & W Scientific, Rancho Cordova, CA). Routine GC separations were accomplished with a Hewlett Packard 5890A gas chromatograph equipped with a 30 m x 0.53 mm (i.d.) column (J & W Scientific, Folsom, CA). The solvents were dried and freshly distilled prior to use. The reactions were carried out in a flame-dried, argon purged three-neck flask equipped with a magnetic stirrer, gas inlet tube, and a reflux condenser attached to a dry ice/acetone cooled trap. The temperature of the coolant circulating through the condenser was kept at -20°. The synthesis of 3 and its reaction with phenyl disulfide are described in detail. The remaining reactions were carried out in a similar manner. Table 1 describes the reactions and products that have been identified. The reactions of 4 and 5 with organolithium reagents were carried out by adding the latter in a 1:1 molar ratio to the former cooled to -78 °C. The reactions were terminated by adding moist ether and a saturated solution of ammonium chloride, followed by extraction of the products with ether. After drying over anhydrous sodium sulfate, the solvent was evaporated under reduced pressure and the residue flash

distilled and analyzed by GC/MS. Tables 2 and 3 list the various products that have been characterized by their mass spectral data.

Trifluoromethylthiocopper

Freshly distilled dry acetonitrile (50 mL) and freshly activated copper powder (7.6 g, 0.13 gm-atoms) were placed in a flame-dried, argon gas purged 100 mL three neck flask equipped with gas inlet tube, reflux condenser attached to a dry ice/acetone cooled condenser with an argon gas/vacuum inlet. After cooling the reaction flask to -78° the system was evacuated to 90 mm and bis(trifluoromethyl) disulfide (16 g, 0.08 moles) was sparged into the stirred flask. After stirring at -78° for 1/2 hr the reaction mixture was allowed to warm to ambient temperature and then heated at $55-60^{\circ}$ for 14-16 hr. During the course of the reaction, the copper metal dissolved to give a clear solution. Under an argon atmosphere, the reaction solution was concentrated under reduced pressure and the concentrate cooled overnight (refrigerator) to give 12 g. of a white solid. Overnight drying under vacuum gave a product which was shown to be a 1 : 1 trifluoromethylthiocopper : acetonitrile adduct (GC/MS), m.p. $184-186^{\circ}\text{C}$ (decomp.). Stored over P_2O_5 at ambient temperature, the material is stable for several months without significant decomposition (a year old sample was used in the reactions described in Table 1). MS : 102(F_3CSH); 82(CSF_2); 69(CF_3); 63(FCS); 44(CS); 41(CH_3CN); 42(CH_3CNH); 40(CH_2CN); 39(CHCN); 38(CCN) and 33(SH). The peak $m/e = 42$ is due to the protonization of CH_3CN and is usually observed if the concentration of CH_3CN is relatively high.

Phenyl trifluoromethyl disulfide

A mixture of trifluoromethylthiocopper (1.03 g, 5 mmol.) and phenyl disulfide (1.09 g, 5 mmol.) in 2 mL of dry acetonitrile was stirred at $80-85^{\circ}$ for six hours. The flash distillate of the reaction mixture, consisted of 74% phenyl trifluoromethyl disulfide, and 26% starting disulfide.

References:

1. (a) N. Nishimura, K. Fujiwasa, J. Mizutani and Y. Obata, *J. Agric. Food Chem.* **19**, 992, 1971. (b) J. D. Sandy, R. D. Davies and A. Neuberger, *Biochem. J.* **150**, 245, 1975. (c) L. Schreyen, P. Dirink, and F. van Wassenhove, *J. Agric. Food Chem.* **24**, 336, 1976.
2. A. L. Lehninger, *Biochemistry: The Molecular Basis of Cell Structure and Function*. 2nd Ed. Worth Publishers, New York (1977).
3. (a) Y. A. Vladmirov, D. I. Roshchupkin and E. E. Fesenko, *Photochem. Photobiol.* **11**, 227, 1970. (b) S. Arian, M. Benjamini, J. Feitelson and G. Stein, *Photochem. Photobiol.* **12**, 481, 1970.
4. (a) T. Ferrington and A. V. Tobolsky, *J. Am. Chem. Soc.* **80**, 3215, 1958. (b) M. Morton, *Rubber Technology*. 3rd Ed., Van Nostrand-Reinhold, New York (1987).
5. (a) A. J. Parker and N. Kharasch, *Chem. Rev.* **59**, 583, 1959. (b) R. E. Benesch and R. Benesch, *J. Am. Chem. Soc.* **80**, 1666, 1958. (c) J. L. Kice, *Acc. Chem. Res.* **1**, 58, 1968. (d) A. M. Kiwan and H. M. N. H. Irving, *Chem. Comm.* 928, 1970.
6. (a) P. D. Bartlett and H. Kwart, *J. Am. Chem. Soc.* **74**, 3969, 1952. (b) W. A. Pryor and P. K. Platt, *J. Am. Chem. Soc.* **85**, 1496, 1963. (c) W. A. Pryor and K. Smith, *J. Am. Chem. Soc.* **92**, 2731, 1970. (d) J. A. Franz, B. A. Bushaw and M. S. Alnajjar, *J. Am. Chem. Soc.* **111**, 268, 1989.
7. (a) A. Fava, G. Reichenbach and U. Peron, *J. Am. Chem. Soc.* **89**, 6696, 1967. (b) R. J. Kern, *J. Am. Chem. Soc.* **77**, 1382, 1955.
8. D. M. Graham, R. L. Mieville and C. Sivertz, *Can. J. Chem.* **42**, 2239, 1964.
9. (a) H. Mackle, *Tetrahedron* **19**, 1159, 1963. (b) S. W. Benson, *Chem. Rev.* **78**, 23, 1978. (c) J. L. Franklin and H. E. Lumpkin, *J. Am. Chem. Soc.* **74**, 1023, 1952. (d) W. E. Savage and J. A. Maclaren in *The Chemistry of Organic Sulfur Compounds*, N. Kharasch and C. Y. Meyers (Ed), Vol. 2, Pergamon Press (1966), p.367.
10. (a) E. Block, R. Iyer, S. Grisoni, C. Shah, S. Belman and F. P. Lossing, *J. Am. Chem. Soc.* **110**, 7813, 1988. (b) J. A. Hawari, D. Griller and L. P. Lossing, *J. Am. Chem. Soc.* **108**, 3273, 1986. *J. Chem. Soc., Perkin Trans. 1*, 155, 1972. (b) R. N. Haszeldine and R. B. Rigby, *J. Chem. Soc., Perkin Trans. 1*, 159, 2180, 1972.
11. (a) T. A. Allen, *J. Chem. Phys.* **31**, 1039, 1959. (b) T. J. Burkey, J. A. Hawari, F. P. Lossing, J. Luszyk, R. Sutcliff and D. Griller, *J. Org. Chem.* **50**, 4966, 1985. (c) I. Kende, T. L. Pickering and A. V. Tobolsky, *J. Am. Chem. Soc.* **87**, 5582, 1965. (d) A. Bergson, *Arkiv. Kemi.* **18**, 409, 1961. (e) J. L. Kice, *J. Polym. Sci.* **19**, 123, 1956.
12. (a) J. L. Kice in *Free Radicals*, J. K. Kochi (Ed) Vol. 2, Wiley and Sons, New York (1973), p.711. (b) S. F. Birch, T. V. Collum and R. A. Dean, *J. Inst.*

- Petroleum. **39**, 206, 1953. (c) R. N. Haszeldine and J. M. Kidd, *J. Chem. Soc.* **3871**, 1955. (d) C. D. Trivette and A. Y. Koran, *J. Org. Chem.* **31**, 100, 1966. (e) J. S. Ricci and I. Bernal, *J. Am. Chem. Soc.* **91**, 4078, 1969. (f) B. Millgen, D. E. Rivette and W. E. Savige, *Aust. J. Chem.* **16**, 1020, 1963.
13. (a) French Patent 503,920 (1939). (b) F. W. Bennett, G. R. A. Brandt, H. J. Emeleus and R. N. Haszeldine, *Nature* **116**, 225, 1950. (c) E. Mann, D. D. Coffman and E. L. Mutterties, *J. Am. Chem. Soc.* **81**, 3575, 1959. (d) N. V. Kondratenko, A. A. Kolomeytsev, V. I. Popov and L. M. Yagupolskii, *Synthesis* **667**, 1985.
14. (a) S. Munavalli, D. I. Rossman, D. K. Rohrbaugh, and C. P. Ferguson and F-L. Hsu, *Heteroatom Chem.* (in press). (b) S. Munavalli and D. I. Rossman (unpublished results).
15. (a) G. K. Helmkamp and S. N. Spurlock, *J. Am. Chem. Soc.* **91**, 3606, 1969. (b) M. Morton and R. F. Kammereck, *J. Am. Chem. Soc.* **92**, 3217, 1970. (c) H. Burton and W. A. Davy, *J. Chem. Soc.* **525**, 528, 1948. (d) E. Negishi, *Organometallics in Organic Synthesis* (1980), P.243.
16. S. Munavalli, D. I. Rossman, A. J. Muller, D. K. Rohrbaugh and C. P. Ferguson (submitted to 203rd Annual Meeting, American Chemical Society, San Francisco, Apr. 5-10, 1992).
17. W. A. Pryor, *Mechanism of Sulfur Reactions*, McGraw-Hill Book Co., New York, (1962), p.42.
18. (a) R. N. Haszeldine, B. Higginbottom, R. B. Rigby and A. E. Tipping, *J. Chem. Soc., Perkin Trans. 1*, 155, 1972. (b) R. N. Haszeldine and R. B. Rigby, *J. Chem. Soc., Perkin Trans. 1*, 159, 2180, 1972.
19. (a) S. Sunner, *Acta Chem. Scand.* **9**, 837, 1955. (b) S. W. Benson, *Chem. Rev.* **78**, 23, 1973. (c) A. Hordvick, *Acta Chem. Scand.* **20**, 1885, 1966. (d) C. J. Marden and B. Beagley, *J. Chem. Soc. Faraday Trans. 2*, 2213, 1982. (e) H. J. M. Bowen, *Trans. Faraday Soc.* **50**, 452, 1954. (f) J. L. Franklin and H. E. Lumpkin, *J. Am. Chem. Soc.* **74**, 1023, 1952.
20. (a) H. W. Brown and R. C. Jones, *J. Chem. Phys.* **37**, 1571, 1962. (b) G. Serrettas and J. F. Eastham, *J. Am. Chem. Soc.* **88**, 5168, 1966. (c) H. R. Ward, R. G. Lawler and R. A. Cooper, *J. Am. Chem. Soc.* **91**, 746, 1969. (d) A. R. Lepley and R. L. Landau, *Am. Chem. Soc.* **91**, 748, 1969. (e) E. C. Ashby, *Acc. Chem. Res.* **29**, 414, 1988.
21. (a) K. Alwair and J. Grimshaw, *J. Chem. Soc., Perkin Trans. 2*, 1150, 1973. (b) D. E. Bartak, W. C. Danen and M. D. Hawley, *J. Org. Chem.* **35**, 1206, 1970. (c) R. D. Chambers, J. A. Cunningham and D. A. Pyke, *Tetrahedron* **24**, 2783, 1968. (d) C. Walling, O. H. Basedow and E. S. Savas, *J. Am. Chem. Soc.* **82**, 2181, 1960. (e) E. C. Ashby and J. N. Argyropoulos, *J. Org. Chem.* **50**, 3274, 1985. (f) K. Uneyama, T. Sadakaje and S. Oae, *Tetrahedron Lett.* **5193**, 1969.

BLANK

UNUSUAL REACTIONS OF DI- AND TRISULFIDES WITH GRIGNARD REAGENTS

S. Munavalli^a and D. I. Rossman^b, D. K. Rohrbaugh^b
and C. P. Ferguson^b

(a) Geo-Centers, Inc., Ft. Washington, MD 20744 (b) U.S. Army
Chemical Research Development and Engineering Center,
Aberdeen Proving Ground, MD 21010

Abstract: The S-S bond of naturally occurring di- and polysulfides is of paramount importance to many biological reactions taking place in living systems. Hence, the chemistry of the S-S bond has attracted considerable attention. It is known that Grignard reagents cause the scission of the S-S bond. To further explore the nature and mechanism of the cleavage of the S-S bond by Grignard reagents, we have investigated this reaction. This paper describes the results of the reaction of Grignard reagents with bis(trifluoromethyl) di- and trisulfides and the possible mechanism of the scission of the S-S and C-S bonds.

Introduction: Organic sulfides occur widely in nature and play a prominent part in physiological processes. Hence, the chemistry of the di- and polysulfides has attracted considerable attention and interest. The sulfur-sulfur bond of proteins not only determines their tertiary structure but also controls biochemical reactions catalyzed by enzymes through its reduction and re-oxidation. The scission of the S-S bond and its chemical consequences have been discussed in detail.¹ The reactions attacking the sulfur atom are not one-step reactions but rather are a cascade of reactions with sulfur enlarging its electronic octet.² Disulfides have been shown to undergo facile photolysis in the presence trialkyl boranes to furnish alkyl- and aryl sulfides^{3,4} and in one case the methylthiyl radical thus formed reacted with the solvent used in the reaction.⁵ Grignard reagents couple with vinylic sulfides in the presence of nickel triphenylphosphine to give alkenes/coupled products.^{5,6} Mercapto-de-metallation has been reported to occur when Grignard reagents are reacted with sulfides in the presence of transition metal catalysts.^{7a-d} Disulfides also react with Grignard reagents to give sulfides.^{8a-b} Primary alkylmagnesium halides have been observed to react thermally with di-t-butyl disulfides, while t-butylmagnesium chloride, under similar conditions, did not react.^{8c} Normal addition of

phenylmagnesium bromide to 2,2-thienyl- and di-p-tolyl disulfides yielded phenyl-3-thienyl- and phenyl-p-tolyl sulfides respectively.^{8d} In contrast, the C-S bond has been described as "relatively resistant" and its fission relatively infrequent.^{9a-b} Two exceptions to this general rule have been observed.^{9c-d} However, what these authors failed to mention is the fact that the free radicals thus formed, by their very nature, are expected to exhibit greater stability.

Not many methods are available for the synthesis of unsymmetrical di- and trisulfides. Photolysis of a mixture of two different symmetrical disulfides has been shown to furnish a mixed disulfide.^{8e,10a} The formation of unsymmetrical disulfides via thiyl radical displacement has been observed.^{10b} Barton and coworkers have recently developed and described a versatile reaction using N-hydroxypyridine-2-thione esters to decarboxylate carboxylic acids and deoxygenate tertiary alcohols.^{11a-c} The formation of di- and tetrasulfides on irradiation of dimethyl trisulfide has been reported.^{12a-b} Also, a photochemical exchange between dimethyl- and di-n-propyl trisulfides furnished a single trisulfide, namely methyl n-propyl trisulfide.^{12c} This led to the postulation of the involvement of the central S-atom in the reaction. However, experiments with labeled central S-atom have contradicted the above inference.^{12a} As a consequence, the mechanism of the homolysis of the trisulfide remains as yet undefined.^{1, 9c, 13a-b} Tetrasulfides, on the other hand, undergo facile homolysis as compared to the di- and trisulfides to generate more stable perthiyl radicals.^{9c-d,13c} There are not many examples of the simultaneous scission of both S-S and C-S bonds by Grignard reagents at -78 °C. This paper presents the unusual formation of unsymmetrical di- and trisulfides and the mechanism of the cleavage of the S-S and C-S bonds by Grignard reagents.

Discussion: Recently an improved method of synthesis of bis(trifluoromethyl) trisulfide (1) has been described.^{14a} In continuation of our interest in the chemistry of di- and polysulfides containing the CF₃ functionality^{14b}, the reaction of Grignard Reagents with 1 and bis(trifluoromethyl) disulfide (2) at -78°C has now been investigated. Tables 1 and 2 describe the results. Under similar conditions dialkyl disulfides remained unreacted and were recovered as such.

Polar, free radical and single electron transfer (SET) mechanisms have been advanced to explain and rationalize the products formed during the

reaction of Grignard reagents.¹⁵ Direct ESR evidence of a SH_2 reaction at the site of the magnesium atom of the Grignard reagent has come from the result of irradiation of a mixture of *t*-butylmagnesium chloride and *t*-butyl disulfide.¹⁶ The involvement of alkyl radicals in the reaction of alkyl halides with magnesium has been observed.^{15b-c,16} In a series of elegant papers, Ashby and coworkers have documented evidence for the participation of the SET process in the Grignard reaction.^{15d-e}

Based on the results described in Tables 1 and 2 the reaction of Grignard reagents with **1** and **2** appears to be highly complex, particularly in comparison with the reaction of organolithium reagents with the same substrates¹⁷. This inference is supported by the fact that the mechanism of the Grignard reaction depends on the nature of the Grignard reagents.^{15e-f} In addition, an extensive study of the solvent effects on the course of the reaction has demonstrated the immediate formation of the radical anion (R^-) via the SET pathway.^{15e} Schemes 1 and 2 describe the free radical process taking place during the reaction of **1** and **2** with Grignard reagents. The initial step begins with the cleavage of the S-S bond by the alkyl moiety of the Grignard reagents. The characterization of the mixed sulfides, namely RSCF_3 and RSSCF_3 from **2** and **1**, confirms this contention. The identification of unsymmetrical di- and trisulfides, RSSCF_3 and RSSSCF_3 from the reaction of **2** and **1** with Grignard reagents, clearly suggests the scission of the C-S bond of the substrates and the formation of the thiyl and perthiyl radicals. The fission of the *t*-butyl methyl ether, used as a solvent in the preparation of ethylmagnesium bromide, into *t*-butyl and methyl radicals has been deduced from the products listed in Table 1. There are precedents for the reaction of Grignard reagents with solvents.^{18a-b} Halogen exchange reaction observed in the reaction of **1** with ethylmagnesium bromide and *t*-butylmagnesium bromide and chloride has precedents as well.^{18c-e}

The SET process for the substrates is described in Schemes 3 and 4. The initial step in the SET mechanism is the transfer of an electron from the Grignard reagent to **1** and **2** to form the radical cation/radical anion pair which subsequently collapses to propagate the reaction sequence described in Schemes 3 and 4. The formation of the dimerized products confirms the participation of free radicals in these reactions. The SET pathway is helpful in explaining the formation of many of the products. However, the free radical process appears to be decidedly more useful in rationalizing the origin of the products listed in Tables 1 and 2. Since mono-, di- and trisulfides containing the alkyl moieties derived from the

Table 1 Products of the reaction of Grignard reagents with bis-(trifluoromethyl) disulfide.

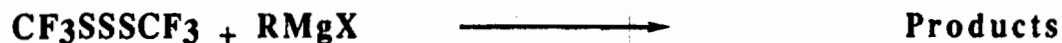


R=C ₂ H ₅ (a)	CSF ₂ 1.02%	F ₃ CSR 15.9%	F ₃ CSC ₄ H ₉ 37.5%	C ₄ H ₉ SC ₄ 10.8% H ₉	C ₈ H ₁₈ 34.6%	
R=CH(CH ₃) ₂ (b)	CSF ₂ 2.2%	40.4%	F ₃ CSSR 10.7%	F ₃ CSC ₃ H _{7-n} 2.3%	i-Prop.SCl 17.4%	12.9%
R=n-C ₄ H ₉ (c)	F ₃ CSR 72.5%	RSR 3.1%	RSC ₅ H ₁₁ 4.6%	F ₃ CSSC ₅ H ₁₁ 4.5%	F ₃ CSSC ₅ H ₉ 7.5%	C ₈ H ₁₈ 7.6%
PhMgBr (d)	CF ₂ 4.8%	CF ₃ SC ₆ H ₅ 88.5%	CF ₃ SSC ₆ H ₅ 5 4.0%	C ₆ H ₅ -C ₆ H ₅ 2.7%		

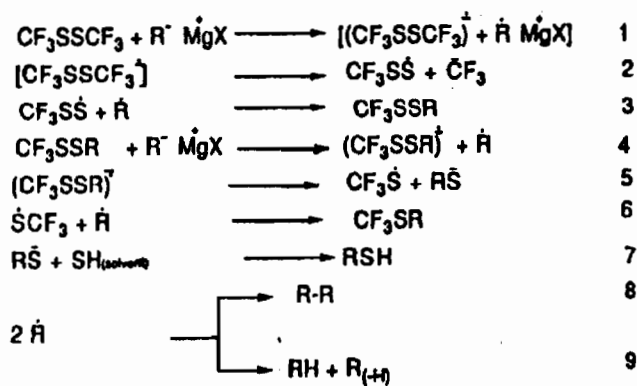
(a) X=Br, solvent= t-BuOMe; (b) X=Cl, Solvent= Et₂O;

(c) X=Cl, Solvent= Et₂O; (d) X=Br, solvent=THF

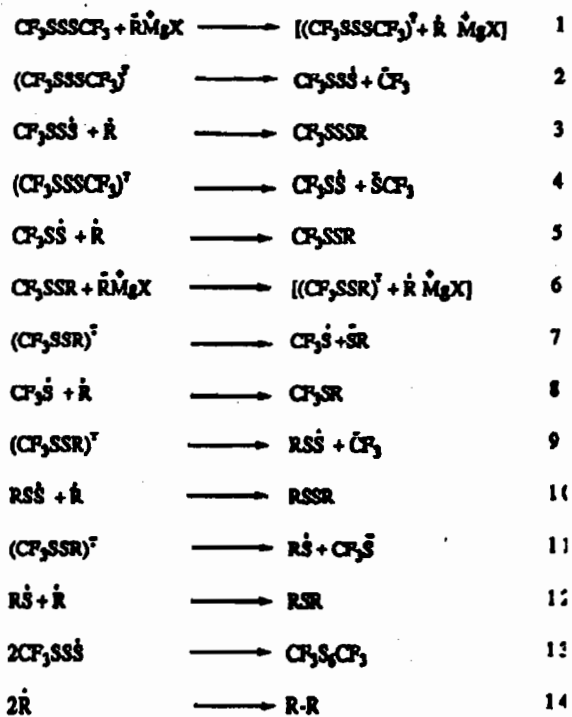
Table 2 Products of the reaction of Grignard reagents with bis-(trifluoromethyl) trisulfide.



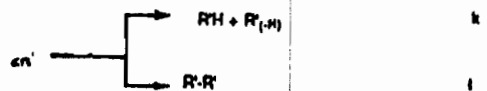
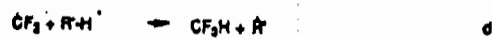
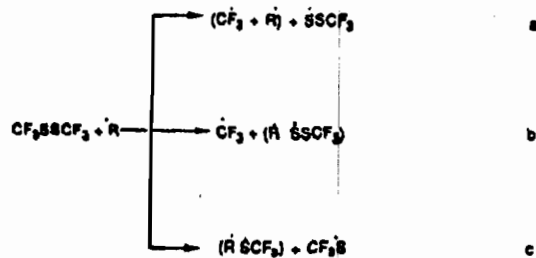
R=C ₂ H ₅	CSF ₂ 3.1%	CF ₃ SSSR 3.5%	CF ₃ SSR 27.5%	CF ₃ SR -	RSCOF 3.0%
	CF ₃ SCOOR 1.3%	RSCSBr 0.7%	CF ₃ S ₃ C ₄ H _{9-t} 3.1%	C ₈ H ₁₈ 7.4%	RSR 3.2%
R=C ₃ H _{7-i}	CSF ₂ 0.9%	CF ₃ SSSR 23.5%	CF ₃ SSR 8.9%	CF ₃ SR -	RSSR 10.3%
	RSR 35.5%	RSC ₄ H ₉ 2.6%	CF ₃ S ₃ C ₄ H _{9-t} 5.8%	(CF ₃ SSS) ₂ 12.9%	
R=C ₄ H _{9-t}	CF ₃ SSR 35.05	CF ₃ SR 6.7%	RSR 28.6%	CF ₃ SCl 12.9%	CF ₃ SSC ₅ H ₉ 0.9%



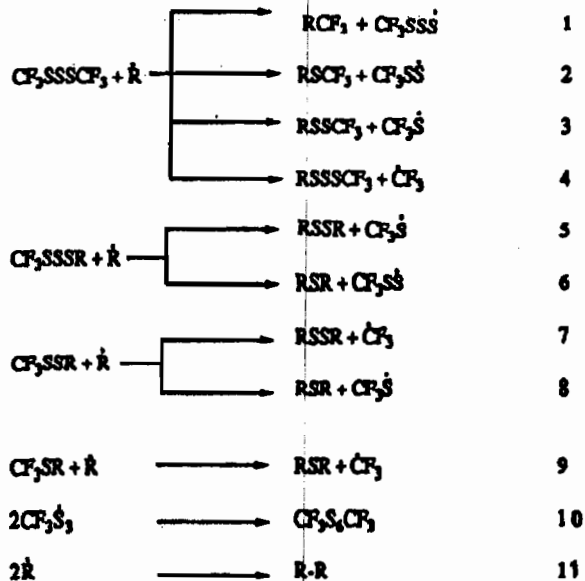
Scheme 1



Scheme 2



Scheme 3



Scheme 4

Grignard reagents themselves are formed, it is apparent that the fission of the C-S bond has definitely occurred. The yields of these products are greater than previously estimated.^{9b}

Conclusions: The present investigation has led us to the following generalizations;

(1) In the reaction we have investigated, two possible processes - the free radical pathway and the SET pathway - are indistinguishable.

(2) For the first time, a simultaneous scission of the S-S and C-S bonds of di- and trisulfides by Grignard reagents at -78 °C has been observed.

(3) This is decidedly due the presence of the highly electron withdrawing trifluoromethyl group.

Experimental Part

General Procedures:

Warning! Because of the high toxicity associated with bis(trifluoromethyl)disulfide via the inhalation route, efficient hoods and extreme care should be used in working with this compound. NMR spectra (¹³C and ¹⁹F) were recorded on a Varian FT-80 or a Varian XL-200 spectrometer. The external reference for ¹⁹F was CCl₃F. Mass spectra were obtained on a Finigan Model 5100 GC/MS equipped with a silica 25 m x 0.31 mm (i.d.) SC-54 capillary column (J and W Scientific, Rancho Cordova, CA). Routine GC separations were accomplished with a Hewlett Packard 5890A gas chromatograph equipped with a J and W Scientific (Folsom, CA) 30 meter DB5 0.53 mm (i.d.) column. The solvents used were dry and freshly distilled. The reactions were carried out in a flame dried, argon gas purged 10 or 25 ml three-necked flask equipped with a magnetic stirrer, a gas inlet, a pressure equalizing dropping funnel and a reflux condenser carrying a dry ice and acetone trap. The temperature of the coolant passing through the condenser was maintained at -20 °C. All reactions were carried out by adding the Grignard reagents to the di- and trisulfide substrates cooled to -78 °C, and terminated by the addition of moist ether and a solution of ammonium chloride. This was followed by extraction with ether, drying the extract and processing it as usual. In calculating the percentages of

the products formed, only sulfur containing products and dimerization and disproportionation products have been taken into account.

References

1. J. L. Kice in "Free Radicals". Vol. II, Chapter 14, J. K. Kochi(Ed), Wiley and Sons, New York, (1973).
2. W. A. Pryor and K. Smith, *J. Am. Chem. Soc.* **92**, 2731, 1970.
3. H. C. Brown and M. M. Midland, *J. Am. Chem. Soc.* **93**, 3291, 1971.
4. H. C. Brown and E. Negishi, *J. Am. Chem. Soc.* **93**, 3777, 1971.
5. H. Okamura, M. Miura and H. Takei, *Tetrahedron Lett.* **43**, 1979.
6. E. Wenkert, E. L. Micheotti and C. S. Swindell, *J. Am. Chem. Soc.* **101**, 2246, 1979.
7. (a) Y. Gendereau, J. F. Normant and J. Villiers, *J. Organometal. Chem.* **142**, 1, 1977. (b) A. Commercant, M. Bourgain, M. Delaumeny, J. F. Normant and J. Villiers, *Tetrahedron Lett.* 3837, 1975. (c) M. Tamura and J. K. Kochi, *J. Am. Chem. Soc.* **93**, 1487, 1971. (d) D. I. Davis, J. N. Done and D. H. Hey, *J. Chem. Soc. (C)* 2021, 1969.
8. (a) E. Negishi, "Organometallics in Organic Synthesis", Wiley and Sons, New York, (1980). pp. 243-247. (b) A. G. Davis and B. P. Roberts in "Free Radicals", Vol. I, J. K. Kochi (Ed), Wiley and Sons, New York, 1973 pp. 57. (c) H. Burton and W. A. Davy, *J. Chem. Soc.* **525**, 1948. (d) H. Burton and W. A. Davy, *J. Chem. Soc.* **528**, 1948. (e) K. Sayamol and A. R. Knight, *Canadian J. Chem.* **46**, 999, 1968.
9. (a). W. E. Savige and J. A. McClaren in *The Chemistry of Organic Sulfur Compounds*, N. Kharasch and C. A. Meyers (Ed), Vol. 2, Pergamon Press, New York (1966). (b) J. A. Francz, B. A. Bushaw and M. S. Alnajjar, *J. Am. Chem. Soc.* **111**, 268, 1989. (c) E. Block, R. Iyer, S. Grisoni, S. Saka, S. Belman and F. P. Lossing, *J. Am. Chem. Soc.* **110**, 7813, 1988. (d) J. A. Hawari, D. Griller and F. P. Lossing, *J. Am. Chem. Soc.* **108**, 3273, 1986.
10. (a) P. M. Rao and A. R. Knight, *Canadian J. Chem.* **46**, 2462, 1968. (b) K. U. Ingold and B. P. Roberts, "Free Radical Substitution Reactions", Wiley and Sons, New York (1981) pp. 209-217.
11. (a) D. H. R. Barton, D. Crich and W. B. Motherwell, *Tetrahedron* **41**, 901, 1985. (b) D. H. R. Barton and D. Crich, *J. Chem. Soc., Chem Comm.* **774**, 1984. (c) D. H. R. Barton, D. Bridon, I. Fernandez-Picot and S. Z. Zard, *Tetrahedron* **43**, 2733, 1987.
12. (a) B. Milligan, D. E. Rivette and W. E. Savige, *Aust. J. Chem.* **16**, 1020, 1963. (b) I. Kende, T. L. Pickering and A. V. Tobolsky, *J. Am. Chem. Soc.*

- 87, 5582, 1965. (c) S. F. Birch, T. V. Collum and R. A. Dean, *J. Inst. Petroleum* **39**, 206, 1953.
13. (a) L. Field in *Organic Chemistry of Sulfur*, S. Oae (Ed), Plenum Press, New York (1977). (b) C. D. Trivette and A. Y. Coran, *J. Org. Chem.* **31**, 100, 1966. (c) T. J. Burkey, J. A. Hawari, F. P. Lossing, J. Luszytk, R. Sutcliffe and D. Griller, *J. Org. Chem.* **50**, 4966, 1985.
14. (a) S. Munavalli, D. I. Rossman, A. J. Muller, D. K. Rohrbaugh and C. P. Ferguson, 203rd Annual Meeting, American Chemical Society, San Francisco, Apr. 5 - 10, 1992. (b) S. Munavalli, D. I. Rossman, A. J. Muller, H. S. Aaron, C. P. Ferguson, J. W. King, D. K. Rohrbaugh and L. C. Buettner, 10th Winter Fluorine Conference, American Chemical Society, St Petersburg, FL., Jan. 28 - Feb. 2, 1991.
15. (a) J. R. Nooi and J. F. Arens, *Rec. trav. Chim (Holland)*, **80**, 244, 1961. (b) J. F. Garst, J. E. Deutsch and G. M. Whitesides, *J. Am. Chem. Soc.* **108**, 2490, 1986. (c) P. Beak and J. W. Worley, *J. Am. Chem. Soc.* **94**, 597, 1972. (d) E. C. Ashby and J. Oswald, *J. Org. Chem.* **53**, 6068, 1988. (e) E. C. Ashby, *Pure and Appl. Chem.* **52**, 545, 1980. (f) T. Holm and I. Crossland, *Acta. Chem. Scand.* **28**, 59, 1971.
16. M. Dagonneau, P. Metzger and J. Vialle, *Tetrahedron Lett.* 3675, 1973.
17. (a) S. Munavalli, D. I. Rossman, D. K. Rohrbaugh and C. P. Ferguson (in press). (b) S. Munavalli, D. I. Rossman, D. K. Rohrbaugh and C. P. Ferguson, 203rd Annual Meeting, American Chemical Society, San Francisco, Apr. 5-10, 1992.
18. (a) K. Okuhara, *J. Am. Chem. Soc.* **102**, 244, 1980. (b) G. Molle, P. Bauer and J. E. Dubois, *J. Org. Chem.* **47**, 4120, 1982. (c) L. G. Screttas and J. F. Eastham, *J. Am. Chem. Soc.* **87**, 3276, 1965. (d) T. Nguyen, A. J. Rubinstein and C. Wakselman, *J. Org. Chem.* **46**, 1938, 1981. (e) A. J. Bridges, V. Fedij and E. C. Turowski, *J. Chem. Soc., Chem. Comm.* 1093, 1983.

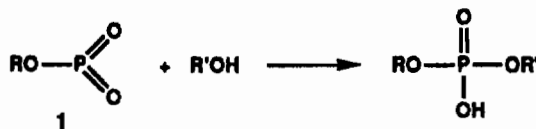
BLANK

PHOSPHORYLATION OF OH GROUPS ON VARIOUS SOLIDS BY LOW-COORDINATION PHOSPHORUS SPECIES

Louis D. Quin, Xiao-Ping Wu, and Stefan Jankowski
Department of Chemistry, University of Massachusetts, Amherst, MA 01003 USA

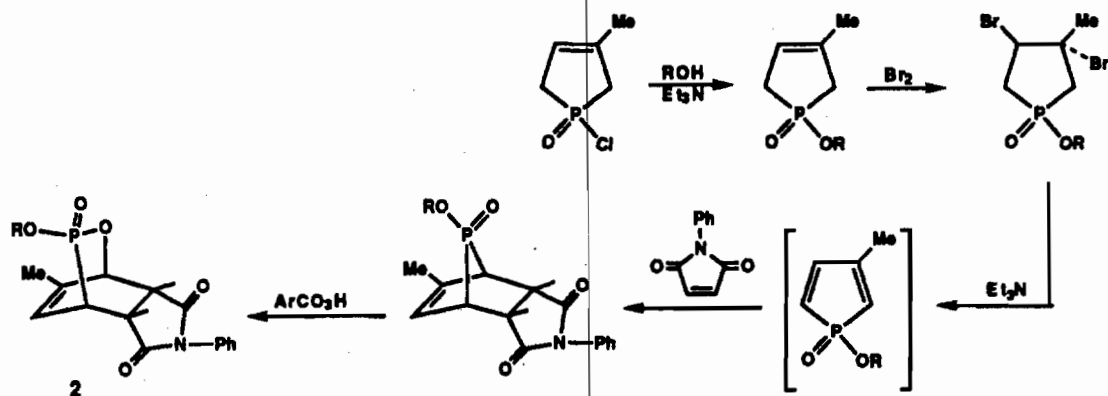
Hydroxy groups on the surface of several different types of solids (silica gel, Zeolites, alumina and cellulose) have been converted to O-ethyl phosphate groups by reaction with ethyl metaphosphate (EtOPO₂) generated in the presence of the solid. Silica gel has also been phosphorylated with two optically active metaphosphates (menthyl and (S)-sec.butyl), as well as by the species PhPO₂ and EtO-P(S)O. The O-ethyl phosphorylated silica gel was used as an HPLC packing, and some valuable characteristics were discovered. Thermal fragmentation of 2,3-oxaphosphabicyclo[2.2.2] octene derivatives provided the various types of 3-coordinate reactive intermediates required. Thermal fragmentation of easily prepared O-alkyl N-substituted phosphoramidates has also been developed for the generation of alkyl metaphosphates.

Alkyl metaphosphates (1) are anhydrides of monoalkyl phosphates that contain phosphorus in the unusual 3-coordinate state. They are highly reactive as electrophiles in solution, and no cases have been reported where the species has been isolated in free form.¹ However, they can function as useful, very potent phosphorylating agents when generated in the presence of OH or NH groups.

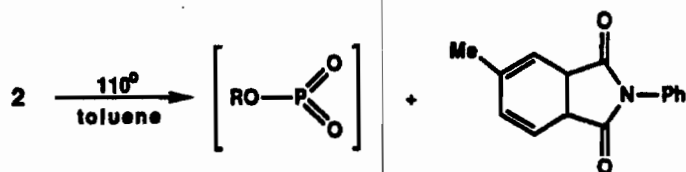


We reported at this Conference in 1990² and in the literature³ that metaphosphates are so active towards OH groups that they effectively attack exposed OH groups on the surface of solid silica gel. This creates a bonded monoalkyl phosphate group directly on the surface; this is a new type of functionalized silica gel with the potential for having useful chromatographic, adsorptive, or catalytic properties. We have continued to develop the method for functionalizing silica gel, and have extended the method to the phosphorylation of other OH-bearing surfaces as well. Our new results are reported in this paper. We have also discovered a new and simple route to metaphosphates that is reported here.

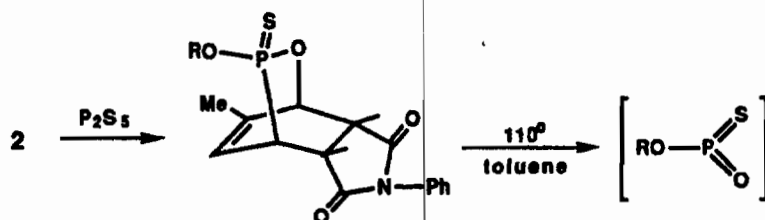
Generation of Metaphosphates by Fragmentation of Bicyclic Compounds. The original method we employed for the generation of alkyl metaphosphates depends upon the ready fragmentation of the 2,3-oxaphosphabicyclo[2.2.2]octene ring system as in structure 2, synthesized as follows.



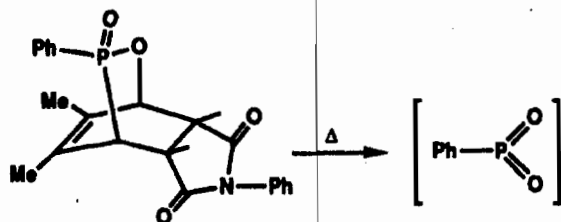
The fragmentation of 2 occurs either thermally or photochemically. In the present work, the thermal method is used.



The phosphoryl oxygen in 2 has been replaced in some cases by sulfur, and the products are then useful as a source of alkyl metathionophosphates.⁴



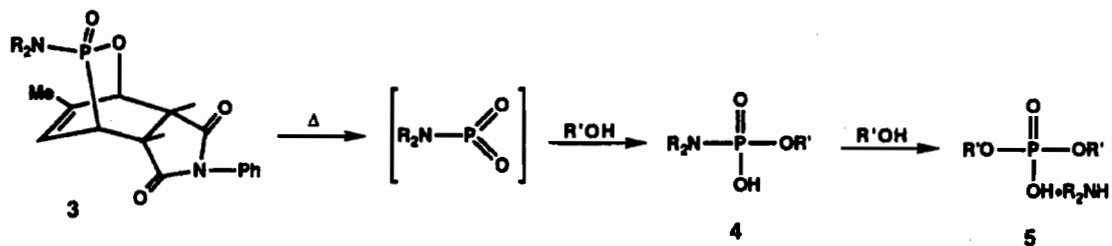
Another variation is the use of alkyl or aryl substituents directly on phosphorus, which leads on fragmentation to metaanhydrides of phosphonic acids.⁵



All of these types of bridged phosphorus heterocycles were used in the present study to phosphorylate various surfaces.

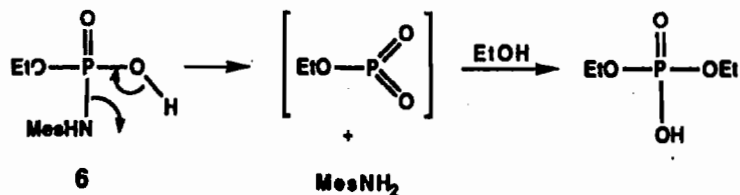
A related structure (3) has also been used in previous work as a precursor of amino derivatives of metaphosphoric acid, which were trapped in the usual way with alcohols. We

noted, however, that the initial O-alkyl N-substituted phosphoramidate trapping products (4) reacted further with the alcohol to give dialkyl phosphate salts (5) as final products.

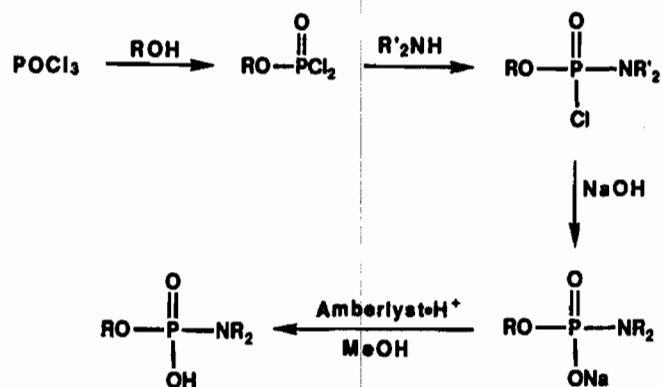


The high reactivity of the initial products (5) called for an explanation, and we came to the conclusion that the reaction involved an alkyl metaphosphate intermediate in a potentially useful process. There are two possible mechanisms to consider for an overall displacement of a group on a phosphoramidate: an addition of the alcohol to give a 5-coordinate intermediate or transition state that then eliminates the amine (AE mechanism), or an elimination of the amine from the phosphoramidate to give the 3-coordinate metaphosphate that then adds the alcohol (EA mechanism).⁶ Normally, one would expect the more common AE mechanism to operate, but we noted that the present reaction was particularly facile when *large* substituents were present on nitrogen. This suggested that relief of crowding as provided by the formation of the planar metaphosphate intermediate in the EA mechanism might be involved, rather than the formation of the more crowded trigonal bipyramid of the 5-coordinate intermediate in the AE mechanism. This has indeed proved to be the case, and has resulted in the discovery of a new and very practical method for the generation of metaphosphates, as described in the next section.

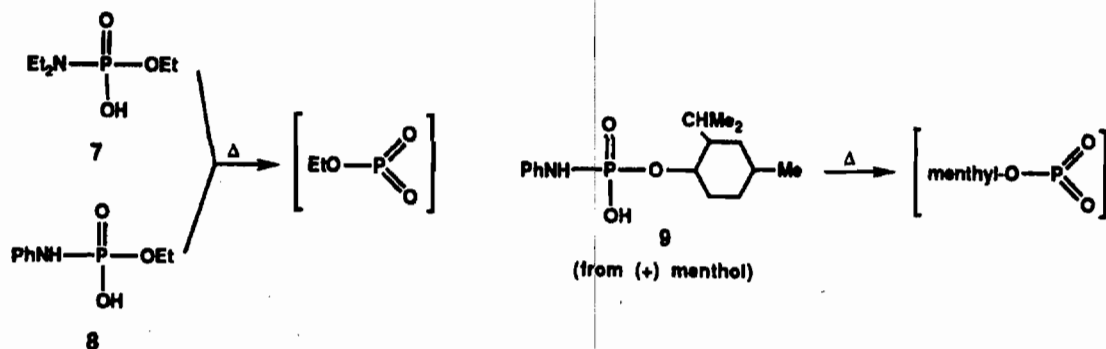
Generation of Metaphosphates by Thermal Fragmentation of O-Alkyl N-Substituted Phosphoramidates. The EA mechanism was conclusively established for the thermal fragmentation of a representative phosphoramidate (6) by kinetic studies. This mechanism would require first-order kinetics, with a rate constant that would be independent of the presence of a trapping alcohol (the AE mechanism would follow second-order kinetics and would be strongly influenced both by type and concentration of the alcohol). Fragmentation of compound 6 in toluene followed first-order kinetics with a rate constant for its disappearance of $1.61 \times 10^{-3} \text{ sec}^{-1}$ at 80°C ; this constant was also obtained when ethanol in varying concentrations was present.



With the fact established that O-alkyl N-substituted phosphoramidates eliminate amines and form metaphosphates, we have proceeded to synthesize some derivatives of this type to explore their utility as phosphorylating agents, particularly to silica gel and other solids. The general method used in the syntheses is shown below.

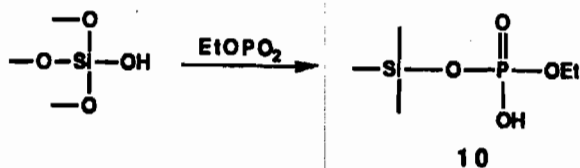


By this method, we have synthesized (in addition to 6) the phosphoramidates 7-9, with yields for each step in the $75 \pm 10\%$ range. Products were characterized by ^1H and ^{31}P NMR. In each case, the phosphoramidates were found to decompose on refluxing in toluene for 10-30 min., and when alcohols were present all phosphorus appeared in the form of the corresponding dialkyl phosphate. Compound 7 gave mixed first order-second order kinetics; the kinetics for 9 have not yet been determined.



Therefore, in continuing our studies of the phosphorylation of OH groups on surfaces, we have included the use of this new method as the source of the metaphosphate reactant.

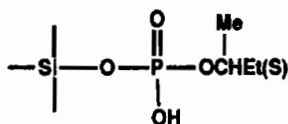
Phosphorylation of Silica Gel. In our previous work,³ we had employed bicyclic ester 2 (R = Et) to phosphorylate the OH groups on the surface of silica gel (Aldrich chromatographic, dried at 196° *in vacuo*). The product was characterized by solid-state ^{31}P NMR spectroscopy using the cross-polarization magic angle spinning (CP-MAS) technique. Silyl groups routinely cause upfield shifts of about 10 ppm when they replace H of an OH group attached to phosphorus, and we would expect



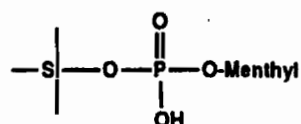
the same effect for a silica-bound phosphate (it is uncommon for solution and solid spectra to differ by more than 1-2 ppm). The silica gel (represented by 10) had a major signal at δ -10.4, suggestive of a bonded phosphate, with a small signal at δ 1.3. It was found that alkyl phosphates simply adsorbed on silica gel give signals in the latter region; they would arise here from some hydrolysis of the metaphosphate. The adsorbed phosphate was easily removed by washing the solid with 2-propanol, leaving the phosphorylated silica gel with only δ -10.4.

The same phosphorylated silica gel (10) has now been produced by heating the solid suspended in toluene containing our new phosphoramidate reagents, 7 and 8. In each case, the ^{31}P NMR spectrum was identical to that for the product from the use of the bicyclic reagent 2 (R = Et). Since the phosphoramidates are much more readily synthesized, they are now considered the reagents of choice for the production of this type of treated silica gel.

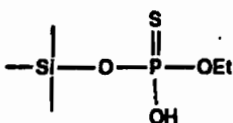
A number of new types of P-functionalized silica gels have been prepared by the two methods we have devised. These materials and their ^{31}P NMR shifts are summarized below.



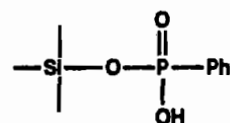
11 (from 2), δ -9.6



12 (from 9), δ -7.1



13, δ 51.9

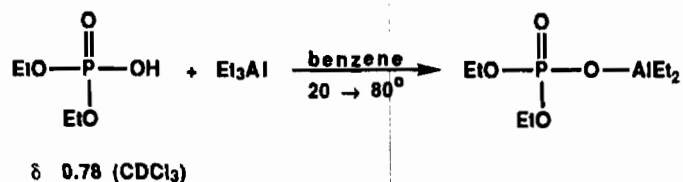


14, δ 10.7

It should be noted that the above list of silica gels includes two (11, 12) that have optically active alkoxy groups on the phosphorus function. These have been prepared specifically for inclusion in studies on the use of phosphorylated silica gels as chromatographic (HPLC) packings; optically active packings have the potential of performing resolutions of racemic mixtures. This possibility is soon to be tested. That the new packings do have applications in HPLC has been established by employing O-ethyl phosphorylated silica (using in this case a special HPLC grade of silica, Exsil 100) for the separation of some mixtures. The most significant result was the accomplishment of the separation of a mixture of aromatic primary amines; untreated silica gel gives broad, tailing peaks for amines, but the new packing gave sharp, nearly symmetrical peaks. The same packing was used for the partial separation of a de-asphalted crude petroleum sample; under conditions where untreated silica gel gave very little eluted material, the phosphorylated silica gel gave rapid, partial separation of the mixture, into fractions much more amenable to further separation, especially by gas chromatography. This is an application of some interest in the analysis of complex petroleum or other liquid fuel mixtures.⁷ Further development of the method is in progress. It is significant that the same HPLC results were obtained when the packing was prepared by phosphorylation with the two very different reagents (the bicyclic 2 and the phosphoramidate 7), attesting further to the formation of the same reactive intermediate from the two quite different precursors.

Phosphorylation of Zeolites. Zeolites are natural or synthetic crystalline aluminosilicates that have tremendous importance as catalysts and adsorbents in the chemical and petroleum industries. Numerous types are known. Since OH groups are present on the surface of Zeolites, we have proceeded to apply our new phosphorylation method to two typical Zeolites (ZSM-5 and Zeolite-Y) to determine if phosphate groups could be attached to them. Indeed, using the bicyclic metaphosphate precursor 2 (R = Et) under the same conditions as used for silica gel, we have produced Zeolites that give characteristic CP-MAS ^{31}P NMR spectra for bonded phosphate groups. The spectrum for Zeolite-Y resembled that from a silica gel in giving a reasonably sharp single product signal, but at higher field (δ -15.8). ZSM-5 gave a more complex, broad signal, over the range δ -5 to -20, but unmistakably indicating surface phosphorylation. In future work, it will be of interest to see if the catalytic properties of these Zeolites have been modified by the presence of surface-bound phosphate groups.

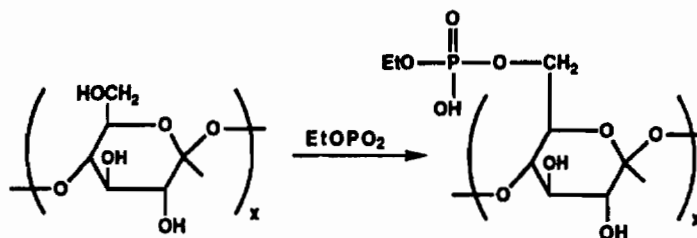
Phosphorylation of Alumina. Hydroxy groups are also known to exist on the surface of various forms of alumina, again materials of enormous industrial importance. We have tested the possibility of modifying alumina by our phosphorylation method. We have generated ethyl metaphosphate from the bicyclic precursor 2 in the presence of dried Brockman acidic alumina, and obtained a product with a reasonably sharp signal at δ -9.6. While this is the same region as found for silica-bound phosphates, we could find no literature that indicated aluminum groups would cause similar upfield shifts. Accordingly, we carried out a synthesis of a model aluminophosphate, involving the known⁸ reaction of diethyl phosphate with triethylaluminum.



The product had a single ^{31}P NMR signal in benzene at δ -14.5. The substantial upfield shift indicates that phosphorylated alumina should also have an upfield signal, as was observed. As for the Zeolites, it will be important to determine if the catalytic properties of aluminas can be usefully modified by this functionalization.

Phosphorylation of Solid Cellulose. Organic polymers containing OH or NH groups represent another class of solids that is potentially sensitive to phosphorylation by metaphosphates. Cellulose is a particularly important material of this type to consider as a substrate because of its involvement in textiles and other fabrics, paper, construction items, etc. Phosphorylation might impart flame resistance to such cellulosic materials; phosphorus compounds of various types constitute the major commercial flame proofing agents on the market today,⁹ but in few cases are these compounds more than just additives. Covalent phosphorylation by metaphosphates would provide a firm bond of the phosphorus group to the solid. We have performed the phosphorylation of cellulose powder (Aldrich, 20 micron) with ethyl metaphosphate as prepared by the phosphoramidate method (toluene, 110°, 15 min). Organic polymers differ in physical structure from the inorganic materials used previously, and may not have the very high surface area and thus the exposed OH groups of the latter. This presents an uncertainty as to the amount of metaphosphate that needs to be generated for a given amount of solid. We assumed that the primary OH groups on the 6-position of the glucose units would be the more reactive; for 1.0 g of cellulose, we calculated 6.2 mmol to be present. To avoid phosphorylation of the secondary OH groups, we employed only 0.5 mmol of ethyl metaphosphate. The CP-MAS ^{31}P NMR spectrum contained two strong signals, one at δ 2.5 as would be expected for attachment of

a phosphate group to the CH₂OH groups.¹⁰ The other signal was at δ -8.7. This is in the region for pyrophosphate groups,¹⁰ and it is possible that phosphorylation of the initially formed O-ethyl phosphate group has occurred. This point will be clarified in future work by reducing the amount of phosphorylating agent. In any case, the results definitely show that the desired phosphorylation of the solid cellulose has occurred. The amount of phosphorus by elemental analysis is 0.64%. Phosphorylation of cellulosic materials and testing for flame resistance is a future goal.



CONCLUSIONS

Reaction of solids bearing OH groups with metaphosphates and related 3-coordinated species is a practical process. It has been established that silica gel, alumina, Zeolites and cellulose can be phosphorylated when metaphosphates are generated in solvents containing the solid in suspension. Useful chromatographic properties have been found in treated silica gel, but it remains to be seen if valuable properties are imparted to the other solids. The range of structural types that can be covalently bonded to these surfaces is considerable, giving the possibility for wide adjustment of the characteristics of the surface. We have shown here that two quite different methods for generation of metaphosphates can be used. They can be generated by thermolysis of derivatives containing the 2,3-oxaphosphabicyclo[2.2.2]octene ring system, or by a newly discovered method that consists of the thermolysis of O-alkyl N-substituted phosphoramidates. The latter method may be subject to some limitations since these are reactive compounds bearing a free OH group which may lead to other reactions with the substrates. This possibility will be explored in future work. Even at this time, however, it is clear that silica gel is easily and efficiently phosphorylated by use of this new metaphosphate precursor. Properties of the new materials that can be produced by our phosphorylation methods may be of interest and are to be studied in future investigations.

ACKNOWLEDGMENT

Support by the Army Research Office through Grant No. DAAL 03-89-K-0101 is gratefully acknowledged.

REFERENCES

1. M. Meisel in *Multiple Bonds and Low Coordination in Phosphorus Chemistry*, M. Regitz and O. J. Scherer, Eds., Georg Thieme, Stuttgart, 1990, pp 415-442.
2. L. D. Quin, X.-P. Wu, J.-S. Tang, and L. C. Dickinson, Scientific Conference on Chemical Defense Research, Edgewood, MD, November, 1990.

3. L. D. Quin, X.-P. Wu, E. Breuer, and M. Mahajna, *Tetrahedron Lett.* **31**, 6281 (1990).
4. L. D. Quin, N. D. Sadanani, and X.-P. Wu, *J. Am. Chem. Soc.* **111**, 6852 (1989).
5. L. D. Quin and X.-P. Wu, *Heteroatom. Chem.* **2**, 359 (1991).
6. A. J. Kirby and S. G. Warren, *The Organic Chemistry of Phosphorus*, Elsevier, Amsterdam, 1967, pp 281-301.
7. J. W. Haas, III, W. F. Joyce, Y.-J. Shyu, and P. C. Uden, *J. Chrom.* **457**, 215 (1988).
8. K. Urata, K. Itoh, and Y. Ishii, *J. Organometallic Chem.* **76**, 203 (1974).
9. A. D. F. Toy and E. N. Walsh, *Phosphorus Chemistry in Everyday Living*, Am. Chem. Soc., Washington, 1987, Chapter 10.
10. J. C. Tebby, *Handbook of Phosphorus-31 Nuclear Magnetic Resonance Data*, CRC Press, Boca Raton, FL, 1991, pp 262-263.

CHEMICAL PROPERTIES UPDATE - THEORY, STATISTICS, AND EXPERIMENTAL METHODS

Elwin C. Penski
Research Directorate
U.S. Army Research, Development and Engineering Center
Aberdeen Proving Ground, MD 21010-5423

ABSTRACT

The physical chemical properties of chemicals are part of a required foundation of data for many applications. This study is part of an effort to establish a solid data groundwork. Methods for calculation of heat capacities, vapor pressures, and enthalpies of formation, vaporization, and fusion are discussed, and some calculated properties of organic liquids are provided. Statistical analysis of vapor pressures and enthalpies of vaporization data for diethyl malonate shows more significant digits than expected. Good agreement of calculated values with the more carefully measured literature values are reported.

LIQUID HEAT CAPACITIES

Heat capacity is defined as the heat, H , absorbed for a degree increase in temperature, T , per unit volume or mass.¹ If the process takes place at constant pressure, then

$$C_p = \text{Heat capacity at constant pressure} = (\delta H / \delta T)_p \quad (1)$$

Over a narrow temperature range, the heat capacity of a liquid is often represented by the following equation:

$$C_p = a + bT + cT^2 \quad (2)$$

where a , b , and c are empirical constants. The equations for broad temperature ranges are much more complex.

Missenard² has developed a functional group method for calculating heat capacities for a few classes of organic liquids in the -25 to 100 °C range. Heat capacities of a group of organic compounds obtained by the Missenard estimation method have been compared with literature values in reference 3 and the calculated values are provided in Table 1. The comparisons are within a few calories per mole per degree; the average deviation is less than 5%. The blanks in the tables are where the Missenard parameters are not available.

The disadvantages of the Missenard estimation method are that it is not applicable to reduced temperatures above 0.75 and that there are no group contribution parameters for organophosphorus compounds. The later problem stems from the fact that practically no experimental measurements of heat capacity for organophosphorus compounds have been made. Insufficient data was available for the chosen compounds to verify the Missenard system at temperatures above 25 °C.

Kopp's rule¹ was also compared to data in reference 3. In most cases this rule produces errors of about 50% or larger for the compounds in Table 1. The Kopp's rule method sums the contributions of elements; whereas the Missenard method sums the contributions of groups of elements.

TABLE 1.
Missenard Calculations of Liquid Heat Capacities

Compound	Heat Capacity cal/(mol K)				
	Temperature, °C				
	-25°	0°	25°	50°	75°
1-Amino-pentane	49.2	50.0	52.0	54.2	-
2-Butanol	36.4	39.4	43.1	46.4	50.2
t-Butyl amine	43.6	44.7	46.9	49.2	-
Chloroethane	22.6	23.2	23.8	24.6	25.5
Cyclohexane	39.0	39.6	40.5	41.7	42.9
Diethyl disulfide	49.2	50.3	51.8	53.5	-
Diethyl malonate	64.9	66.5	68.4	70.95	73.6
Diethyl sulfide	40.3	41.3	42.6	44.1	-
2-Methyl-2-propanol	36.1	38.6	42.3	45.7	49.6
2-Propyl amine	37.4	38.8	40.85	42.95	-

THERMODYNAMIC PROPERTIES

Since World War II, organophosphorus agents have been used in a variety of military situations. The compounds in Table 2 were chosen due to their previous, proposed, or potential use as organophosphorus agent simulants. The compounds are not recommended as simulants for any particular application, but the values are provided to aid in the selection of simulants.

Data obtained from the literature are compared in reference 4 with calculated molar enthalpies of formation, molar enthalpies of vaporization, molar enthalpies of fusion, and the Hildebrand parameter.

Table 2 gives the calculated vapor, liquid, and solid molar enthalpies of formation at 25 °C. Table 3 gives the molar enthalpies of fusion and vaporization, and the Hildebrand parameters at 25 °C. The densities, molecular weights, and molar volumes used in the calculations are given in reference 4. The literature values based on calorimetry data other than static-bomb calorimetry agree well with the calculated heats of formation given in Table 2.

TABLE 2
Calculated Molar Enthalpies of Formation at 25 °C

Chemical (Abbreviation)	Enthalpies of Formation (kcal/mol)		
	Vapor	Liquid	Solid
Tri-n-butyl phosphate (TBPO)	-314.3	-335.1	-343.6
Tri(chloroethyl) phosphate (TCEPO)	-305.4	-327.5	-335.7
Triethyl phosphate (TEPO)	-284.7	-298.2	-301.4
Trimethyl phosphate (TMPO)	-260.8	-272.9	-274.7
Triphenyl phosphate (TPPO)	-170.8	-191.5	-198.2
Tri-i-propyl phosphate (TIPO)	-315.9	-335.0	-337.7
Tri-n-propyl phosphate (TNPPPO)	-299.5	-316.7	-322.5
Tri-n-butyl phosphine oxide (TBPX)	-147.3	-165.1	-172.3
Triethyl phosphine oxide (TEPX)	-117.8	-128.2	-130.1
Trimethyl phosphine oxide (TMPX)	-102.3	-111.7	-113.0
Triphenyl phosphine oxide (TPPX)	0.7	-23.6	-27.8
Triethyl phosphine (TEPN)	-39.6	-48.7	-52.5
Trimethyl phosphine (TMPN)	-22.5	-29.2	-31.2
Triphenyl phosphine (TPPN)	76.5	53.5	49.5
Triethyl phosphite (TEP)	-194.7	-204.1	-207.3
Triisopropyl phosphite (TIP)	-225.9	-240.9	-243.6
Trimethyl phosphite (TMIP)	-170.8	-178.7	-180.6
Triphenyl phosphite (TPP)	-79.1	-98.0	-102.3

TABLE 3
Calculated Molar Enthalpies of Fusion and
Vaporization, and Hildebrand Parameters at 25 °C

Chemical	Heats of Fusion (kcal/mol)	Heats of Vaporization (kcal/mol)	Hildebrand Parameter {(cal/cc) ^{1/2} }
TBPO	8.4	20.8	8.6
TCEPO	8.2	22.1	10.2
TEPO	3.1	13.5	8.7
TMPO	1.8	12.1	10.0
TPPO	6.7	20.7	8.7
TIPO	2.6	19.1	9.0
TNPPPO	5.8	17.2	8.6
TBPX	7.2	17.8	9.3
TEPX	1.9	10.5	9.0
TMPX	1.3	9.4	10.6
TPPX	4.3	24.2	10.1
TEPN	3.8	9.1	7.6
TMPN	2.0	6.7	8.5
TPPN	4.1	23.0	9.8
TEP	3.2	9.4	7.1
TIP	2.7	15.0	8.2
TMIP	1.9	7.9	7.9
TPP	4.2	19.0	8.4

VAPOR PRESSURES

Vapor pressures are one of the most important liquid properties. They strongly influence liquid volatility, reactivity, flammability, solubility, and transfer processes. Vapor pressures are a strong function of temperature - doubling or tripling every ten degrees. They are used to calculate other thermodynamic properties. For such reasons, a very precise knowledge of vapor pressures is required.

Banerjee, Howard, and Lande⁵ describe a structure-vapor pressure relationship for organic compounds that probably is one of the best methods for estimating the vapor pressures of organic compounds. Their relationship is based on the following type of parameters: Kamlet-Taft solvatochromic, structural, molecular volume, and UNIFAC. The size of the errors from the Banerjee, Howard, and Lande method are given in table 4.

TABLE 4
Accuracy of Vapor Pressure Estimation Methods

<u>Compound</u>	<u>% Difference Between Experiment and Calculation</u>
<u>Outliers</u>	
octamethyltetrasiloxane	4,800,000%
hexamethyldisiloxane	110,000
ethylene glycol	15,500
acetic acid	2,137
propionic acid	1,950
diisopropyl ether	1,820
1,1,1-trichloroethylene	1,740
hexane	1,300
formic acid	1,200
<u>Typical Errors</u>	<u>500-1,100%</u>

Table 4 shows that to get data sufficiently accurate for most military purposes, it is necessary to make measurements.

While Brozena and Fielder's⁶ measurement methods are excellent, suspended droplet evaporation methodology has been shown to have some advantages that should be summarized in the literature:

1. At vapor pressures below a few Torr, droplet evaporation measurements can usually be performed much faster (1 day) than with other vapor pressure methods.
2. Compounds with 10% or more impurities may be used if the impurities are substantially more or less volatile than the compound of interest.
3. Only 10 mg of the liquid is required - just enough to form one small droplet.
4. Vapor pressures as low as 0.01 Torr can be measured with no difficulty.

Suspended droplet evaporation methodology has the following drawbacks:

1. The diffusion coefficient of the liquid in the atmosphere used must be known. Very few values are available in the literature. Often the diffusion coefficient must be estimated introducing a small error that is usually less than 15%.

2. While temperature variation is possible, it is not as convenient as some vapor pressure methods.

Many of the vapor pressure equations or values found in the literature or in commercial computerized data bases need to be re-evaluated. Errors run as high as several hundred percent and careful statistical analyses are required. Many CRDEC projects have a strong requirement for such an effort. Due to the high cost of experimental measurements, work has been performed on developing a new computation method that yields interpolated and extrapolated values of vapor pressure of the maximum accuracy. Also it provides 95 % confidence intervals and other types of statistics for measured, interpolated and extrapolated values of vapor pressures, boiling points, volatilities, and heats of vaporization. Commercial statistical software packages will perform some of the statistical operations included in this effort, but such packages will not include all the detailed calculations. Also the details, references, and complete documentation are not provided with most commercial software.

Brozena and Fielder's⁶ diethyl malonate (DEM) data was selected for use in this report due to the fact that it is one of the best series of vapor pressure data found anywhere in the scientific literature. As is apparent from Figure 1, the fit is very good. Figure 1 provides the raw DEM data compared to a fitted Antoine equation plot in a linear form. Error bars are included. They are enlarged by a factor of 20 to make them distinguishable from the fitted line. Figure 2 provides an example of a simple vapor pressure - temperature plot with error bars for a narrow temperature range.

It was found in the statistical analysis that there are more statistically significant digits, three, available than is normally expected for vapor pressure data. In the future, four digits should be reported. Five digits on the heat of vaporization values were found to be significant and should be reported. It has been found in some cases that 14 decimal digits must be carried in the calculation to obtain reliable fits of vapor pressure data.

CONCLUSIONS

- The Missenard method appears to provide satisfactory heat capacities for alcohols, amines, chlorinated hydrocarbons, and esters. The average deviations between the measured values for the compounds selected for this study and calculated values are less than 5% from -25 to 25 °C.
- Examination of the literature indicates that vapor pressures cannot be estimated for military applications with sufficient accuracy. Experimental data must be used.
- A program has been developed that is the first program that does a complete statistical analysis for vapor pressure data and which produces plots with error bars.

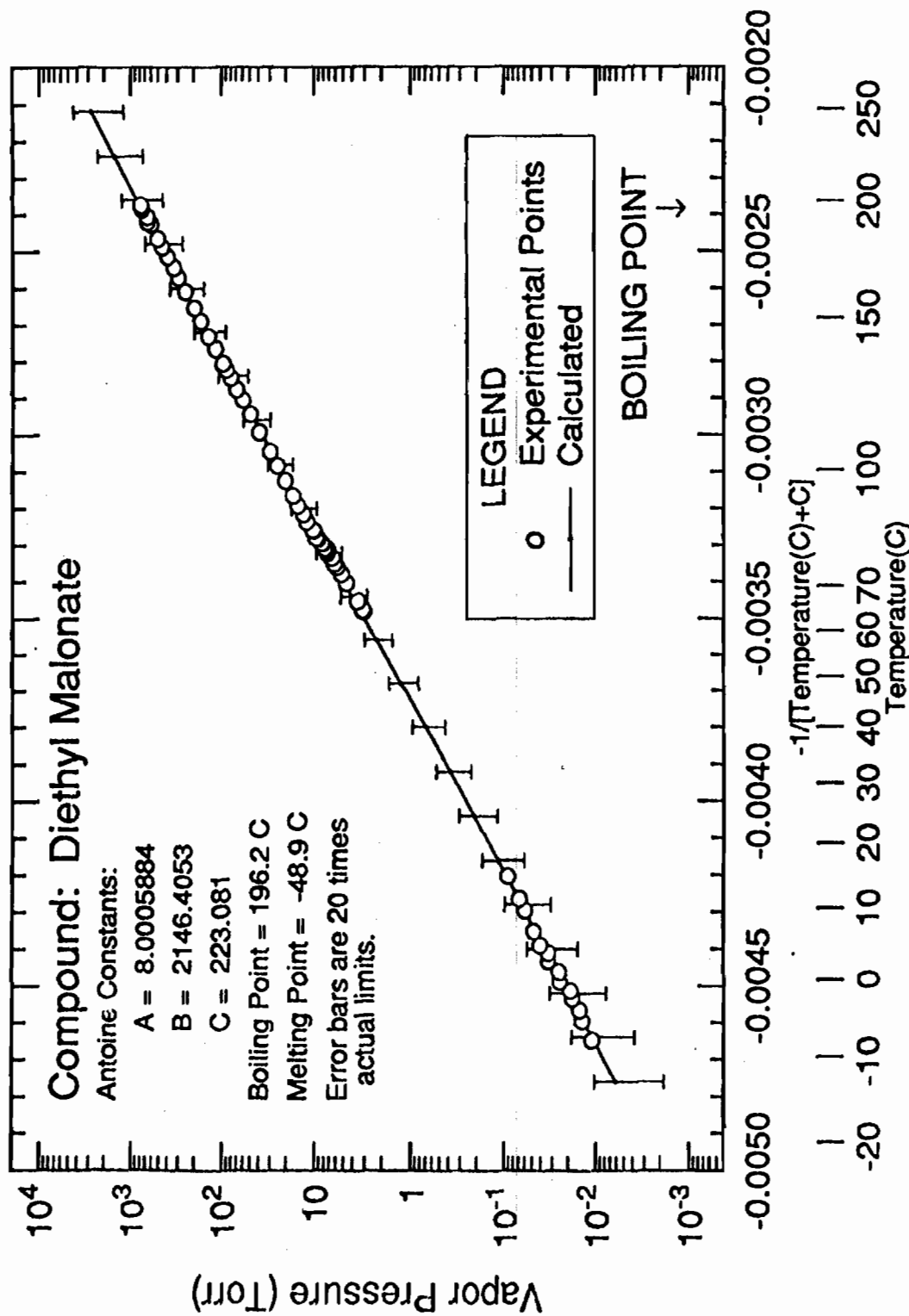


Figure 1. Vapor Pressure Data Compared to Fitted Antoine Equation Calculations with Highly Exaggerated Error Bars.

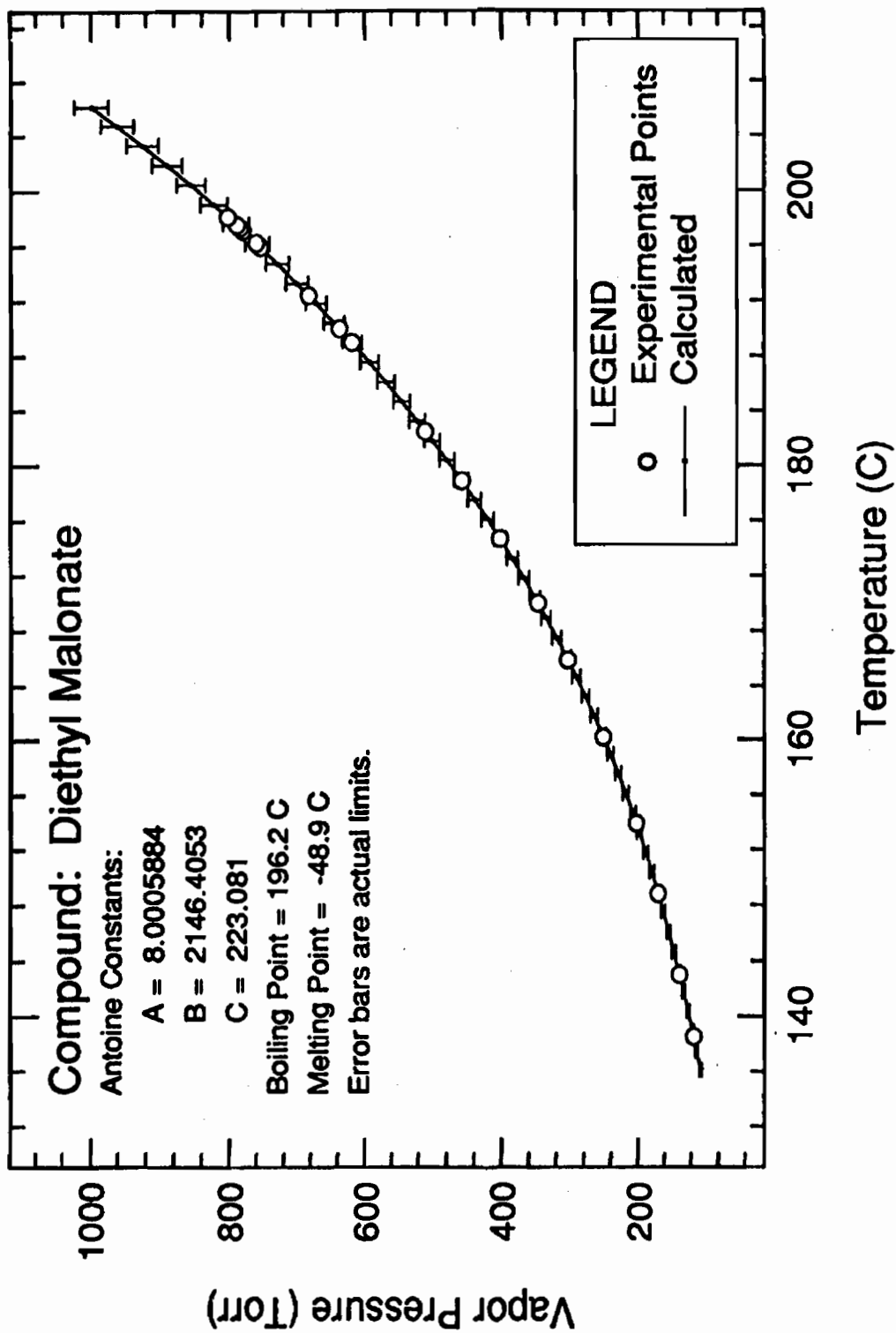


Figure 2. A Portion of the Vapor Pressure Data for DEM Compared to Fitted Antoine Equation Calculations Over a Very Narrow Temperature Range.

- Data for DEM shows that there are more statistically significant digits, three, available than is normally expected for vapor pressure data.
- In some cases suspended droplet evaporation appears to be a useful experimental method for determining vapor pressures.

ACKNOWLEDGEMENTS

Special thanks are due to Donald Bowie and Dr. Kenneth Collins of the Research Directorate, CRDEC, for providing aid in composing and downloading this report and to Donald Fielder, Helen Walker, and Ann Brozena, also of the Research Directorate, CRDEC, for providing technical comments. Thanks are also due Corkey Smith and Patsy D'Eramo, Management Information Systems Directorate, CRDEC, for helping locate information.

REFERENCES

1. Dean, J.A., Lange's Handbook of Chemistry, 13th ed., McGraw-Hill Book Company, New York, NY, 1985.
2. Missenard, F.A., "Additive Method for Determining the Molar Heat Capacities of Liquids," Comptes Rendus de L'Academie des Sciences Vol. 260, No. 21, p 5521 (1965).
3. Penski, E.C., Estimation of Liquid Heat Capacities, I. Review and Evaluation of Missenard Method, CRDEC-TR-199, June 1990, UNCLASSIFIED Report.
4. Penski, E.C., Estimation of Heats of Formation and Other Thermodynamic Properties, IV. Simulants: Phosphates, Phosphine Oxides, Phosphines, and Phosphites, CRDEC-TR-100, September 1990, UNCLASSIFIED Report.
5. Banerjee, S., Howard, P.H., and Lande, S.S., "General Structure-Vapor Pressure Relationships for Organics," Chemosphere Vol. 21, Nos. 10-11, p 1173 (1990).
6. Brozena, A., and Fielder, D., Vapor Pressure of Diethyl Malonate, CRDEC-TR-120, November 1989, UNCLASSIFIED Report.

SUBAMBIENT APPLICATIONS OF DIFFERENTIAL THERMAL
ANALYSIS FOR THE DETERMINATION OF VAPOR PRESSURE

Ann Brozena and Donald Fielder
U.S. Army Chemical Research, Development and Engineering Center
Aberdeen Proving Ground, Maryland 21010-5423

ABSTRACT

In the early 1960's, differential thermal analysis was identified as a useful technique for studying phase transitions of organic materials over a wide temperature range. Several years later, use of DTA for establishing vapor pressure curves for pure liquids over wide temperature and pressure ranges was reported. Since that time, differential scanning calorimetry has replaced DTA as the method of choice for most phase transition studies. Despite the superiority of DSC for investigation of many thermal events, a DTA cell designed with a glass capillary sample holder and thermocouple temperature sensor (such as the DuPont Standard Cell) continues to be a more suitable configuration for measurement of boiling temperatures. Use of this technique with updated commercial instrumentation allows rapid determination (< 2 hrs) of vapor pressure curves of pure liquids over wide pressure (5 to 760 torr) and temperature (-180 to 450°C) ranges using only a small amount (< 1 ml) of sample. Vapor pressure curves of several compounds for which only atmospheric pressure boiling points were available have been established with this technique.

INTRODUCTION

The application of techniques of thermal analysis for the determination of vapor pressure has been described by numerous authors[1-4]. In a 1976 review of parameters affecting the use of these techniques, Seyler[5] concluded that the DTA glass capillary configuration allows attainment of equilibrium boiling conditions which cannot be achieved with the use of other sample holder designs. The lack of widespread familiarity and resulting limited use of this valuable technique for the determination of vapor pressure was noted by Charles[6].

DTA is one of three methods routinely used in our laboratories for the determination of vapor pressure of pure liquids. The small sample size and minimal time required to

establish a vapor pressure curve have resulted in DTA being the technique preferred over the Knudsen effusion method or isoteniscope. Recent incorporation of an accessory which simplifies cooling of the apparatus to liquid nitrogen temperatures (-180°C) has extended the temperature range over which this technique can be used and significantly enhanced the applicability of this method to our work. Vapor pressure curves for perfluoroisobutene (b.p. 7°C) and perfluorocyclobutene (b.p. 0.2°C) have been established using this subambient procedure.

EXPERIMENTAL

Apparatus

A DuPont Model 9900 Thermal Analyzer was used in these experiments. The basic setup has been described previously [1,3]. The major differences between this procedure and those used by Vassallo and Harden[1] and Kemme and Kreps[3] were the use of a computer to control data acquisition and the incorporation of a "Quick Cool" sample holder accessory (TA Instruments). The "Quick Cool" accessory is a Dewar flask designed to hold and rapidly cool the sample cell block for subambient operations through the use of liquid nitrogen. The pressure readout device was a Wallace and Tiernan Type 187 absolute manometer with a precision of 0.1 torr. Instrument calibration was checked using Freon 113 (1,1,2-trichloro-1,2,2-trifluoroethane - b.p. 48°C) and Freon 114 (1,2-dichloro-1,1,2,2-tetrafluoroethane - b.p. 4°C).

Temperature Control

Prior to measuring vapor pressures at very low temperatures, the ability of the DTA to control the rate of temperature increase was investigated. Kemme and Kreps recommended a heating rate of 5 deg/min for accurate determination of vapor pressure. Therefore, it was critical that the cooled cell block did not self-warm at a faster rate.

The cell block was cooled to -180°C and allowed to self-warm. The observed temperature rise was less than $4^{\circ}\text{C}/\text{min}$, indicating temperature control could be maintained using the desired heating rate of 5 deg/min.

Sample Preparation

To load samples that boil below room temperature into the glass capillary tubes, special handling techniques were developed. Compounds that boil below room temperature are usually received in lecture bottles equipped with valves. A small amount of sample (several milliliters) is transferred from the lecture bottle to a Reacti-Vial equipped with a screw-cap and rubber septum. The vial is precooled to a temperature below the boiling point of the compound under study. The sample in the vial will remain a liquid as long as the cap does not leak. Transferring the sample from the vial

to the glass capillary tube is accomplished by cooling the cell block with the capillary in place and discharging the proper amount of liquid using a precooled microsyringe.

RESULTS

Table 1 contains the experimental temperatures and pressures for Freon 113 and Freon 114. The difference between the calculated literature boiling temperature[7] and the experimental temperature is listed at each experimental pressure. These data show good agreement between the experimental data generated with this technique and published values. A plot of the vapor pressure versus temperature curves for these compounds is shown in Figure 1, where the symbols are experimental points and the lines are the vapor pressures calculated from the literature.

TABLE 1

Vapor Pressure Data for Freon 113 and Freon 114

<u>Freon 113</u>				<u>Freon 114</u>			
T (°C)		Δt	P (torr)	T (°C)		Δt	P (torr)
Exp	Lit			Exp	Lit		
46.8	47.6	0.8	761.4	3.1	3.3	0.2	767.3
46.3	47.5	1.2	759.1	-11.2	-11.0	0.2	424.1
46.3	47.5	1.2	759.0	-18.4	-17.8	0.6	300.0
35.7	38.2	2.5	549.3	-25.8	-25.9	-0.1	213.2
28.4	29.6	1.2	400.0	-32.2	-32.2	0.0	149.2
24.2	25.1	0.9	334.8	-39.2	-39.7	-0.5	100.0
18.7	19.8	1.1	270.0	-42.8	-43.7	-0.9	80.0
11.6	12.8	1.2	200.1	-47.6	-48.6	-1.0	60.0
5.3	6.3	1.0	150.0	-53.6	-55.3	-1.7	40.0
-3.4	-2.1	1.3	100.0	-57.7	-59.7	-2.0	30.0
-7.4	-6.5	0.9	80.0	-62.8	-65.8	-3.0	19.9
-12.8	-12.0	0.8	60.0				
-19.7	-19.1	0.6	40.2				
-24.3	-24.1	0.2	30.0				
-29.0	-29.2	-0.2	21.9				
-30.3	-31.3	-1.0	19.1				

Vapor pressure data generated for perfluoroisobutene and perfluorocyclobutene are given in Tables 2 and 3. Each data set was fitted to an Antoine equation. The Antoine constants are listed at the top of the tables and the percent difference between the experimental and calculated pressures is given at each experimental temperature. Plots of these data are shown in Figures 2 and 3, where the symbols are the experimental points and the line is the vapor pressure calculated from the Antoine equation.

FIGURE 1

Literature vs. Experimental Vapor Pressure Data
for Freon 113 and Freon 114

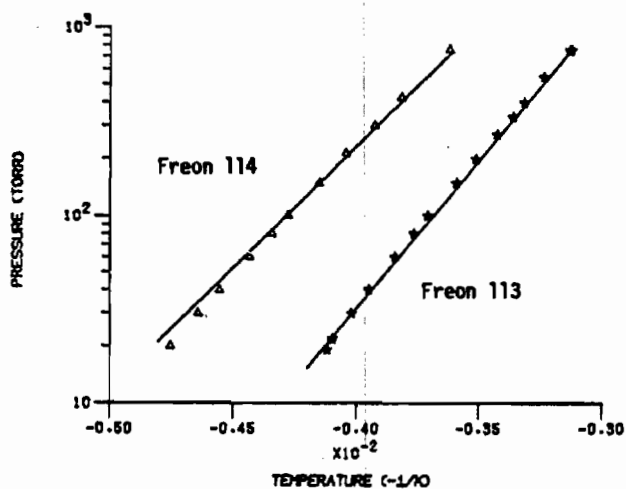


TABLE 2

Vapor Pressure Data for Perfluoroisobutene

Antoine Constants			
A		6.61628	
B		809.878	
C		209.730	
Standard Deviation		0.0021	
Calculated Boiling Point (°C)		7.08	
Temperature (°C)	Pressure (torr)		Percent Difference
	Experimental	Calculated*	
7.2	763.0	763.68	0.09
-8.0	400.0	399.58	-0.10
-17.8	250.3	249.24	-0.42
-27.2	150.3	151.12	0.54
-36.2	89.0	88.96	-0.05
-43.4	55.5	55.87	0.66
-50.1	35.2	34.90	-0.86
-55.4	23.4	23.36	-0.15
-60.9	14.9	14.95	0.33

TABLE 3

Vapor Pressure Data for Perfluorocyclobutene

Antoine Constants			
A			6.71893
B			799.118
C			208.050
Standard Deviation			0.0034
Calculated Boiling Point (°C)			0.16

Temperature (°C)	Pressure (torr)		Percent Difference
	Experimental	Calculated	
0.2	758.0	761.43	0.45
-14.2	400.3	394.98	-1.33
-23.0	250.1	251.50	0.56
-32.0	150.3	151.28	0.65
-38.6	100.4	100.69	0.29
-44.1	70.2	69.95	-0.36
-49.0	50.1	49.50	-1.20
-50.5	44.0	44.34	0.77
-53.6	35.0	35.07	0.21

FIGURE 2

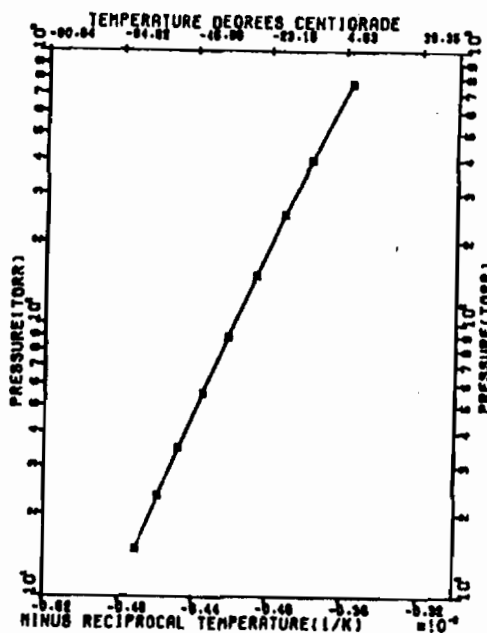
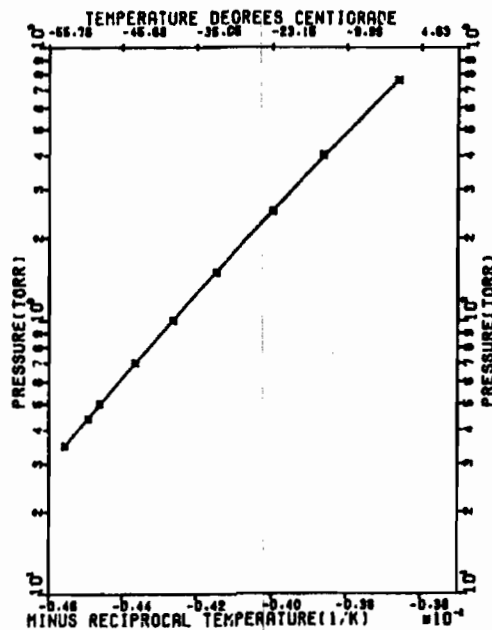
Vapor Pressure of Perfluoroisobutene

FIGURE 3

Vapor Pressure of Perfluorocyclobutene



CONCLUSIONS

A modified DTA technique for measuring vapor pressure has been shown to be a quick, easy method, requiring a very small sample. The use of a "Quick Cool" accessory extends the use of the method to subambient temperatures.

REFERENCES

1. D.A. Vassallo and J.C. Harden, *Anal. Chem.*, **34**, 132, (1962).
2. S. Gordon and C. Campbell, *Anal. Chem.*, **27**, 1102, (1955).
3. H.R. Kemme and S.I. Kreps, *J. Chem. Eng. Data*, **14**, 98, (1969).
4. A.A. Krawetz and T. Tovrog, *Rev. Sci. Instru.*, **35**, 1465, (1962).
5. R.J. Seyler, *Thermochim. Acta.*, **17**, 129, (1976).
6. R.G. Charles, *Thermochim. Acta.*, **38**, 315, (1980).
7. T.E. Jordan, *Vapor Pressure of Organic Compounds*, Interscience Publishers, New York, p. 37, 1954.

Chemoselective Reactions of Functionalized Piperidines

Harold D. Banks
U.S. Army Chemical Research, Development and Engineering Center
APG, MD 21010-5423

ABSTRACT

Many compounds that possess potent pharmacological properties contain functionalized piperidine ring systems. Synthetic transformations that are envisioned for the preparation of these materials are frustrated by the presence of certain functional groups in the precursor molecules that are incompatible with the reagents employed. Recent results have demonstrated that multifunctionality can actually be exploited to increase the yields of the desired substituted piperidines.

We have been interested for some time in the synthesis of piperidines that are functionalized at C₄. If one substituent at this position is an anilido functionality, and a 2'-substituted ethyl group is attached to the heterocyclic nitrogen, the general structure of the fentanyl family of synthetic opioids is obtained. Such compounds are of particular interest because their analgesic activity in animal tests can be more than three orders of magnitude greater than that of the prototypic μ -agonist, morphine.¹ We have also been interested in developing efficient syntheses of the mammalian metabolites of the fentanyls,² with a view toward determining their role in analgesic activity and side effects, as well their use as intermediates in the synthesis of new fentanyl derivatives.

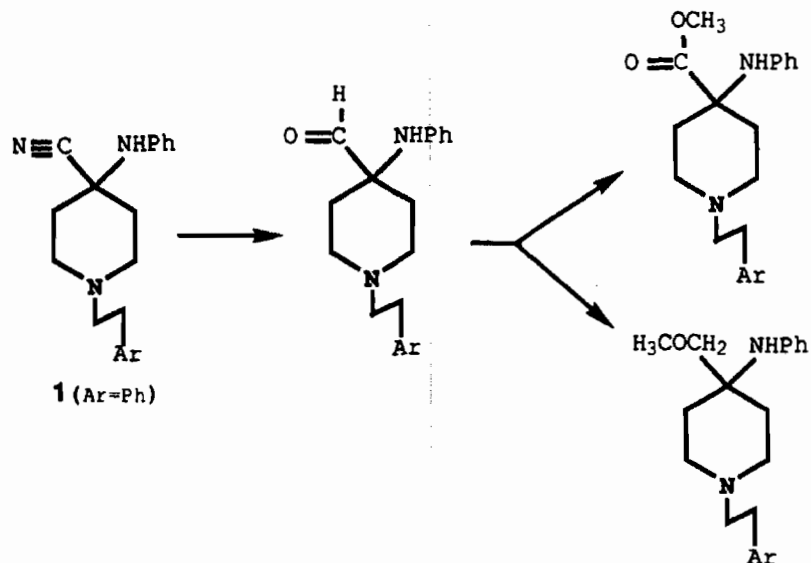
Our synthetic strategies have sought routes to target molecules employing Heathcock's "Golden Rules of Synthesis,":
1) Minimize the use of protecting groups. 2) Use low tech chemistry, i.e., no exotic reagents or conditions. 3) Strive for cascades of reactions, all in one pot.³ This paper will discuss our recent results in the areas of **chemoselection by means of metal catalysis and utilization of 2-piperidinone as a synthon for functionalized piperidones.**

The substrate chosen for the investigation of chemoselective reactions was the potentially versatile intermediate, α -aminonitrile **1**. This compound can be prepared in excellent yield from the corresponding, commercially available ketone. A long standing research goal of a number of research groups has been to develop an efficient syntheses of the 4-methoxycarbonyl and 4-methoxymethyl derivatives. Attempts to hydrolyze **1** to the amino acid under basic conditions consistently lead to reversion to the ketone; acidic conditions, while productive, were far from ideal, since the ring nitrogen required protection as the benzyl derivative, and a two-step process with mandatory isolation and purification of the intermediate 4-amido compound were required, violating the rules given above.⁴

We decided to embark on the oxidation-reduction strategy shown in Scheme I.⁵ in which the key step was reduction of the cyano function to a formyl group. Once the formyl derivative was in hand, numerous methods exist for either oxidation to the

carboxyl function, and for reduction-methylation to the methoxymethyl group.

Scheme 1



Many reducing agents are available to effect the transformation of a cyano function into a formyl group.⁶ Unfortunately, for α -aminonitriles containing a N-H bond, as is the case for **1**, the favored reaction course is proton abstraction, expulsion of the good leaving group, cyanide, followed by reduction of the intermediate imine to a product corresponding to an overall reductive decyanation. Convincing evidence for this reaction course was obtained in studies of the stereochemical consequences of the reduction of *cis*- and *trans*-1-benzyl-3-methyl-4-piperidine.⁷ Reductive decyanation, sometimes accompanied by small quantities of the 4-aminomethyl compound, was the observed reaction course with NaBH₄, Red-Al, Super-Hydride and L-Selectride. No evidence was found for aldehydic product.

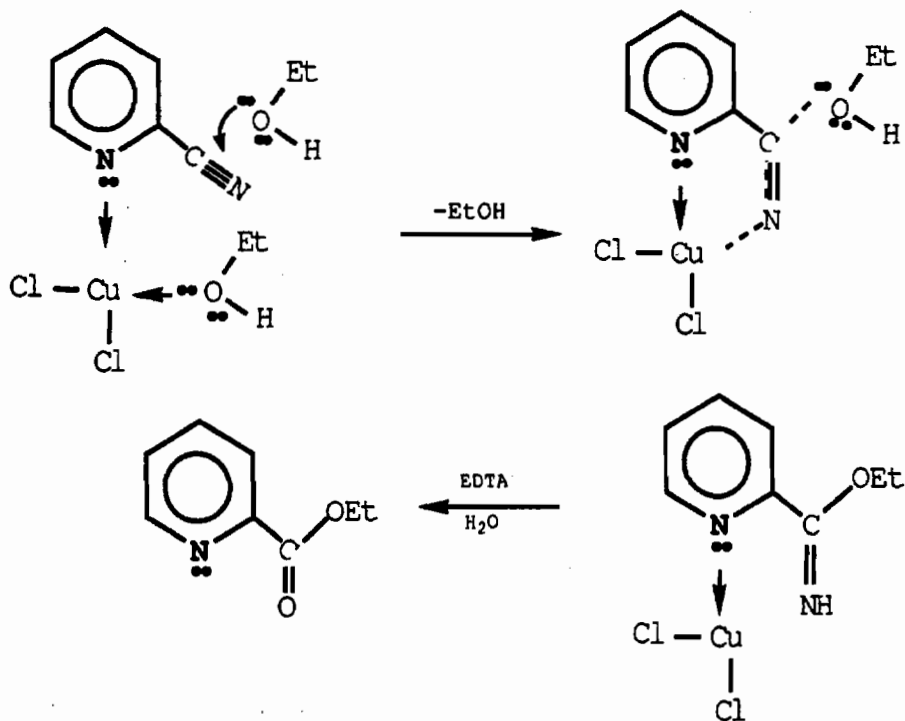
When conditions were changed from basic to acidic as in the Stephen reduction, i.e., dry hydrogen chloride in diethyl ether, followed by anhydrous SnCl₂, a mixture of **1** and the corresponding ketone was produced. It is likely that the insolubility of **1**·2HCl in the reaction mixture thwarted a successful reaction.

Treatment of **1** with DIBAL gave an extremely promising result. The desired **2** was produced in 18% isolated yield (along with the reductive decyanation product which could be readily separated by column chromatography); this represents a minimum yield since conditions for workup have not been optimized. A series of experiments varying the number of equivalents of DIBAL and the mode of addition established that the yield was optimized with five equivalents of the reductant and inverse addition; i.e., addition of the ketone to excess DIBAL.⁸ This result suggests that the softened hard Lewis base-Lewis acid,⁹ DIBAL, is titrating harder piperidine and aniline nitrogens before participating in chemistry at the cyano function. Presumably the failure with other reducing agents was due to the fact that the complexation reactions

envisioned for DIBAL are ineffective or absent. The acidic Al center of DIBAL is presumably effective in complexing with the anilino unshared electron pair vs. its propensity to abstract the anilino hydrogen by means of its pendant hydride.

Some time ago, a fascinating reaction was reported by Barnard (Scheme 2).¹⁰ Yields of greater than 60% of 2-methoxycarbonylpyridine can be obtained by treatment of 2-cyanopyridine with a solution of copper(II) chloride in ethanol. The propensity of pyridine to complex with copper(II) is well-known, and has been exploited for hydrolysis of the ester^{11d} and using other heterocyclic substrates.¹¹ When this chemistry was attempted for **1** using both catalytic and stoichiometric Cu(II), with methanol and ethanol, the only product obtained other than starting material after aqueous EDTA workup was the corresponding ketone. It is reasonable to assume that the Cu(II) complexes with the η^1 electron pair of the cyano function, followed by an S_N1 -type process after departure of the good leaving group, CN^- , or Cu(II) complexation with the unshared electron pair of the anilino group, followed by an S_N2 attack of the alcohol on the C₄ position (Figure 1.)

Scheme 2

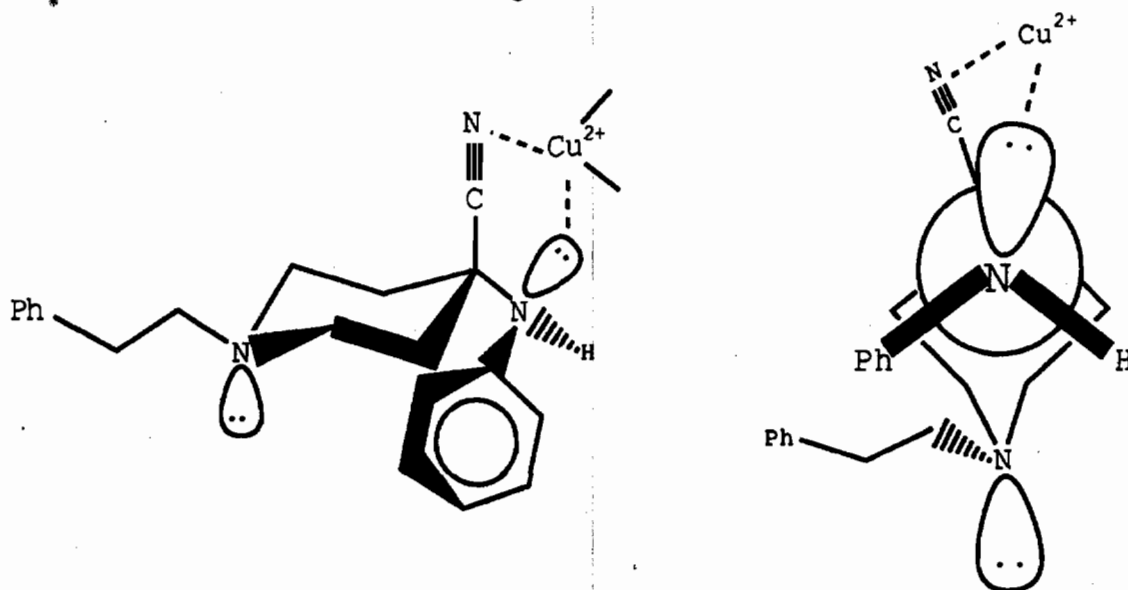


The failure of this reaction could be due to the considerably larger negative entropy requirement (relative to the heteroaromatic systems)^{10,11} to reduce all possible rotational degrees of freedom to the one necessary for attack by the alcohol. In addition, examination of molecular models indicates that the N-C₄ bond of the chair form of the piperidine ring in the transition

state would be in an unfavorable eclipsed conformation, exacerbated by the interaction of the phenyl substituent and the methylene group at C3. Future experiments will be directed toward identification of metal ions that form η^2 complexes with cyano functions.¹²

Synthons are conceptual tools that facilitate the identification of the most promising synthetic routes to target molecules.¹³ Commercially available 2-piperidinone **3** was envisioned as a useful synthon for functionalized piperidines.¹⁴

Figure 1



An intermediate that was targeted in our synthetic approach to these pharmacologically active compounds was 2-piperidin-3-enone. This compound has been prepared in modest yield by the reaction of vinyl acrylic acid with conc. aqueous NH_3 in a high pressure bomb at 180° . In considering the use of **3** as starting material, perusal of the literature unearthed few reactions exploiting the activated α -position of amides.¹⁵ A "simple" method for the synthesis of the 3,3-dibromo derivative **4**, however, was found in the old German literature;¹⁶ this compound was thus chosen as our first intermediate for a series of reactions. It was postulated that dehydrobromination of **4**, followed by regiospecific Michael addition of aniline should provide the interesting 3-bromo derivative. Epoxidation of **4** followed by regiospecific opening with aqueous aniline, and Swern oxidation should lead to the 3-keto derivative, a precursor for the chiral 3-hydroxyfentanyls (mammalian metabolites)² and their derivatives.¹⁷ Unfortunately the Heymon's paper lacks complete experimental details, and our attempts to obtain good yields of product based on reasonable assumptions have been unsuccessful. Under the best conditions to date, a mixture of 1% 3-chloro-, 3% 3-bromo-, 3% 3,3-dichloro-, 27% 3-bromo-3-chloro- and 66% of the desired dibromide **4** was obtained. An intractable oil is also produced. These results indicate that the 3,3-dichlorochlorimide intermediate requires a longer reaction time, more vigorous conditions, or both. Preliminary experiments

using this mixture to find suitable dehydrobromination conditions has shown that excess Et₃N or DBU abstract the amide hydrogen, but not a C₄ hydrogen. Experiments directed toward the use of **3** as a synthon for functionalized piperidines are continuing and will be reported in due course.

CONCLUSIONS

Chemoselective reactions have been discovered for unprotected α -aminonitrile **1**, an important intermediate in the synthesis of highly potent fentanyl derivatives. Most promising is DIBAL reduction using inverse addition. It appears that η^1 chemistry occurs at the cyano group when Cu(II) is employed, and η^2 complexing metal ions should be investigated to effect the desired alcoholysis reaction.

Preliminary experiments have been initiated to explore the viability of 2-piperidinone **3** as a synthon for functionalized piperidines.

EXPERIMENTAL

Reduction of α -Aminonitrile **1 with DIBAL.**⁸ A solution of 1.50 g (4.92 mmol) of **1** in 90 mL of anhydrous THF at 0° contained in a 100 mL round-bottomed flask under Ar was transferred via cannula over a period of 15 min to a solution of 4.38 mL (24.6 mmol) of DIBAL in 60 mL of THF also maintained at 0°. After continuing magnetic stirring at 0° for an additional 75 min. the reaction vessel was cooled to -78°, and the product hydrolyzed by means of the dropwise addition via syringe of 9 mL of MeOH followed by 9 mL of H₂O. The resulting gel was chromatographed on 25 g of neutral alumina with ethyl acetate, followed by chromatography on 20 g of silica gel with n-hexane/ethyl acetate (60/40 v/v) allowed separation of **2** (in 18% yield) and **3**. Interestingly, recrystallization from n-hexane produced two crops of crystals with virtually identical spectroscopic properties: m.p. 80.5 - 81.0° Calc'd for C₂₀H₂₄N₂O·3/2·H₂O: C 77.21; H, 7.78; N, 9.01. Found C, 77.11; H, 7.87; N, 9.01. m.p. 91.0 - 91.5° Calc'd for C₂₀H₂₄N₂O·1/2·H₂O: C, 75.67; H, 7.62. Found: C, 75.30; H, 7.78. ¹H NMR (400 MHz, CDCl₃); δ 9.63 (s, 1H), 7.30-7.13 (m, 7H), 6.76 (t, J = 7.3 Hz, 1H), 6.56 (dd, J = 8.6, 0.9 Hz, 2H), 3.91 (bs, 1H), 2.82-2.77 (m, 2H), 2.75 - 2.70 (m, 2H), 2.63 - 2.59 (m, 2H), 2.44 - 2.40 (m, 2H), 2.13 - 2.06 (m, 2H), 1.93 (m, 2H). ¹³C NMR (400 MHz, CDCl₃); δ 144.7, 140.2, 129.4, 128.7, 128.4, 126.1, 118.8, 114.6 (aromatic carbons), 91.4, 60.3, 48.5, 33.7, 29.6. FT-IR (CHCl₃); 2928, 1730, 1601, 1503, 1260, 1121 cm⁻¹. EI nominal mass spec (70 eV); m/z 309 (M⁺+1, 0.4), 308 (M⁺, 1.7), 209 (M⁺-CHO, 7.0), 217 (M⁺-CH₂Ph, 100.0). R_f value (80/20, EtOAc/n-C₆H₁₄): 0.22.

Reaction of α -Aminonitrile **1 with Ethanolic CuCl₂.** To 0.14 g (1.0 mmol) of CuCl₂ dissolved in 15 ml of absolute ethanol was added 0.30 g (1.0 mmol) of α -aminonitrile **1**. The progress of the reaction was monitored by TLC on silica gel following periodic removal of small samples of the reaction mixture, standard aqueous EDTA workup, and CHCl₃ extraction. When successive TLC analyses were identical, the bulk of the reaction mixture was worked up and subjected to ¹H and ¹³C NMR as well as GC/MS analysis. Only **1** and the corresponding ketone along with aniline could be detected.

Bromination of 2-Piperidinone. To a solution of 10.0 g (101 mmol) of 2-piperidinone dissolved in 75 mL of benzene was added with magnetic stirring 21.0 g (101 mmol) of PCl_5 in portions over a period of 20 min. The two-phase system which was produced became homogeneous upon warming (90°) by means of a water bath. After cooling to room temperature, 32.2 g (10.4 mL, 201 mmol) of bromine was added dropwise to the rapidly stirred mixture. Vigorous evolution of hydrogen halides was observed. The literature procedure¹⁶ stated that crystals separated at this point, but in our hands, two liquid phases were produced. The lower phase was dark and quite dense. The reaction mixture was added to 150 mL of H_2O , and NaHCO_3 was added portionwise until the cessation of CO_2 evolution indicated that it was present in excess. This procedure gave rise to a new heterogeneous mixture of two liquids, with apparent dissolution of the previous dark lower phase. After stirring overnight, the upper layer was separated, and the lower layer was extracted first with 30 mL of benzene, and then with 50 mL of CHCl_3 . The combined extracts were dried over Na_2SO_4 and concentrated on the rotary evaporator to provide 21.5 g of an orange glass containing interspersed crystals. This material was dissolved in acetone, treated with activated C, filtered and the acetone allowed to slowly evaporate. The crystals which formed in this manner were recrystallized to provide 4.08 g of white plates, m.p. = $160 - 162^\circ$. ^1H and ^{13}C NMR as well as GC/MS analysis demonstrated that the crystals were a mixture of 1 3-chloro-, 3% 3-bromo-, 3% 3,3-dichloro-, 27% 3-bromo-3-chloro- and 66% of the desired 3,3-dibromo-2-piperidinone 4.

REFERENCES

1. (a) Van Daele, P.G.H., De Bruyn, M.F.L., Boey, J.M., Sanczuk, S., Agten, J.T.M., and Janssen, P.A.J., "Synthetic Analgesics: N-(1-[2-Arylethyl]-4-Substituted-4-Piperidinyl) N-Arylalkanamides," *Arzneim. Forsch.* 1976, 26 1521- 1531. (b) Bagley, J.R., Kudzma, L.V., Lalinde, N.L., Colapret, J.A., Huang, B-S, Lin, B-S, Jurussi, T.P., Benvenega, M.J., Doorley, B.M., Ossipov, M.H., Spaulding, T.C., and Spencer, H.K., "Evolution of the 4-Anilidopiperidine Class of Opioid Analgesics," *Med. Res. Rev.*, 1991, 11, 403 - 436.
2. (a) Banks, H.D., and Ferguson, C.P., "The Metabolites of Fentanyl and Its Derivatives," CRDEC-TR-88139, U.S. Army Chemical Research, Development and Engineering Center, Aberdeen Proving Ground, MD, September 1988, UNCLASSIFIED Report. (b) Banks, H.D., "The Metabolites of Fentanyl and Its Derivatives. II," U.S. Army Chemical Research, Development and Engineering Center, Aberdeen Proving Ground, MD, in press, UNCLASSIFIED Report.
3. Heathcock, C.H., "Daphniphyllum Alkaloids: Biomimetic Chemical Synthesis of Chemomimetic Biosynthesis," 31st National Organic Chemistry Symposium, Cornell University, Ithaca, New York, 22 June 1989.
4. For an interesting approach involving a hydantoin intermediate, see Feldman, P.L., James, M.K., Brackeen, M.F., Bilotta, J.M., Shuster, S.V., Lahey, A.P., Lutz, M.W., Johnson, M.R., Leighton, H.J., "Design, Synthesis and Pharmacological Evaluation of Ultrashort to Long-Acting Opioid Analgesics," *J. Med. Chem.*, 1991, 34, 2202 - 2208.
5. Banks, H.D. "New Approaches to the Synthesis of Fentanyl Derivatives," Proceedings of the 1989 U.S. Army Chemical Research, Development and Engineering Center Conference on Chemical Defense Research, 14 - 17 Nov. 1989, pp. 333 - 338.
6. Hudlicky, M., "Reductions in Organic Chemistry," Halsted Press/John Wiley & Sons, New York, 1984, p. 200.
7. Von Ostwalden, P.W., Hsu, F-L., Banks, H.D., and Ferguson C.P., "Studies on the Stereoselective Synthesis of *cis*-3-Methylfentanyl," CRDEC-TR-038, U.S. Army Chemical Research, Development and Engineering Center, Aberdeen Proving Ground, MD, January 1989, UNCLASSIFIED Report.

8. Posner, G.H. and Cho, C.G., CRDEC Contract 90-P-7468, completed 7 Dec. 1990, H.D. Banks, COR.
9. Ho, T-L., "Chemoselectivity of Organometallic Reactions, A HSAB Appraisal," *Tetrahedron*, **1985**, *41*, 1 - 86.
10. Barnard P.F., "Metal-promoted Reactions of 2-Cyanoacrydine: Iron(II), Cobalt(II), Nickel(II) and Copper(II) Complexes of O-Methypyridine-2-carboximidate," *J. Chem. Soc. (A)*, **1969**, 2140 - 2144.
11. (a) Chin, J., "Developing Artificial Hydrolytic Metalloenzymes by a Mechanistic Approach," *Acc. Chem. Res.*, **1991**, *24*, 145 - 152.
(b) Breslow, R., Fairweather, R. and Keana, J., "Metal-Catalyzed Hydration of Phenanthroline Nitrile," *J. Am. Chem. Soc.*, **1967**, *89*, 2135 - 2138. (c) Belokon, Y.N., Tararov., Savel'eva, T.F., Vitt, S.V., Pasknova, E.A., Dotdayev, S.C., Borisov, Y.A., Struchkov, Y.T., Batasanov, A.S. and Belikov, V.M., "Copper(II) Ion Promoted Direct Hydrolysis of 2-Cyanopyridine to Picolinic Acid. Intramolecular Catalysis by the Coordinated N-b-Hydroxyethyl Group," *Inorg. Chem.*, **1988**, *27*, 4046 - 4052. (d) Fife, T.H. and Przystas, T.J., "Divalent Metal Ion Catalysis in the Hydrolysis of Ester of Picolinic Acid. Metal Ion Promoted Hydroxide Ion and Water Catalyzed Reaction," *J. Am. Chem. Soc.*, **1985**, *107*, 1041 - 1047. (e) Houghton, R.P., "Metal Complexes in Organic Chemistry," Cambridge University Press, New York, 1979, pp. 185 - 186 and references cited therein.
12. Cotton, F.A. and Wilkinson, G., "Advanced Inorganic Chemistry," 5th Ed., John Wiley & Sons, New York, 1988, pp. 360 - 361.
13. Corey, E.J. and Cheng, X-M., "The Logic of Chemical Synthesis," John Wiley & Sons, New York, 1989.
14. The use of functionalized piperidinones as synthons for piperidines (the amide function is reduced by a suitable reagent) has been employed by others. See for example, Petit, S., Nallet, J.P., Guillard, M., Dreux, J., Chermat, R., Poncelet, M., Bulach, C., Simon, P., Fontaine, C., Barthelmebs, M. and Imbs, J.L., "Syntheses et activites psychotropes de 3,4-diarylpiperidines. Correlation structure-activite et recherche d'une activite antihypertensive," *Eur. J. Med. Chem.*, **1991**, *26*, 19 - 32. *Our concept is unique in that rather than introduce functionality into an acyclic molecule which is then cyclized (these reactions can be troublesome!), functionality is introduced into the already cyclized, inexpensive starting material, 3. It should also be noted that 3 has the unshared pair of electrons on the ring nitrogen protected in the form of conjugation in the amide linkage.*
15. For example, a-sulfenylation has been accomplished:
(a) Zoretic, P.A. and Soja, P., *J. Org. Chem.*, **1976**, *42*, 3587.
(b) Gassman, P.G. and Balchunis, R.J., *J. Org. Chem.*, **1977**, *42*, 3236.
16. Heymons, A., "Eine einfache Methode zur Darstellung von d,l -Prolin," *Chem. Ber.*, **1933**, *66*, 846 - 848.
17. Lalinde, N.L., Moliterni, J., and Spencer, K.H., "N-Aryl-N-(1-substituted-3-alkoxy-4-piperidinyl)amides and Pharmaceutical Compositions and Methods Employing Such Compounds," U.S. Patent 4,994,471, 1991.

ACKNOWLEDGEMENTS

The author is indebted to Linda L. Szafraniec and William T. Beaudry for their superb ¹H and ¹³C NMR determinations, and to Dennis Rohrbaugh for his thorough GC/MS analyses. Skillful literature searches by Patsy D'Ermo and Corky Smith of the Technical Library were indispensable.

BLANK

PREASSOCIATING α -NUCLEOPHILES¹

Lewis E. Fikes,² David T. Winn, Robert W. Sweger,
Morgan P. Johnson,³ and Anthony W. Czarnik
Department of Chemistry
The Ohio State University
Columbus, Ohio 43210

Abstract

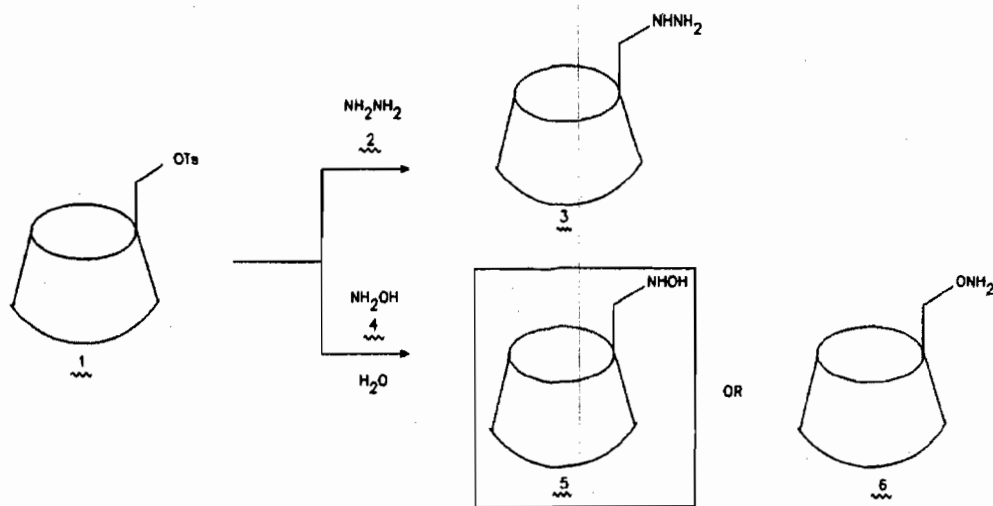
The reaction of β -cyclodextrinyl-1⁰-tosylate with hydrazine affords β -CDNHNH₂; reaction with hydroxylamine yields β -CDNHOH. Each compound reacts with esters as preassociating α -nucleophiles. The hydroxylamine derivative, which we have examined most extensively to date, demonstrates saturation kinetics and is as reactive at pH 7 as at pH 9.5.

Research on cyclodextrin (CD) transacylase mimics has been amongst the most fruitful in the artificial enzyme field. While most proteases function efficiently at pH 7.4, β CD itself is well-known to be inert at this pH; rather, it reacts rapidly with esters only when its 2⁰-hydroxyl groups (pK_a 12.1) have begun to deprotonate.⁴ Thus, the synthesis of synthetic transacylases with reactivity at neutral pH presents itself as an important goal of practical significance. Towards this end, CD's have been prepared bearing imidazole as a group with reactivity at pH 7;⁵ pendant coordination complexes have likewise been employed.⁶ However, as potential pendant groups, α -nucleophiles such as hydrazine or hydroxylamine offer unique properties. (1) In solution, α -nucleophiles

show enhanced reactivity towards acyl transfer as compared to isosteric alcohols or amines.⁷ (2) Despite their greater reactivity towards acyl compounds, hydroxylamine (pK_a 5.97) and hydrazine (pK_a 8.0) are less basic than isosteric amines (pK_a 9-10), and thus exist in a reactive ionic form near neutral pH. (3) Both hydroxylamine and hydrazine transacylate alkyl esters and amides. (4) Because they are physically small, pendant α -nucleophiles would necessarily reside close to the CD binding pocket. We now report on the syntheses, characterizations, and reactivities of β CDNHNH₂ and β CDNHOH.

Reaction of β CD-1⁰-tosylate (1 in Scheme I) in anhydrous hydrazine (2) at room temperature showed the complete loss of starting material after 4 h. Precipitation from EtOH gave the crude product (3),

Scheme I



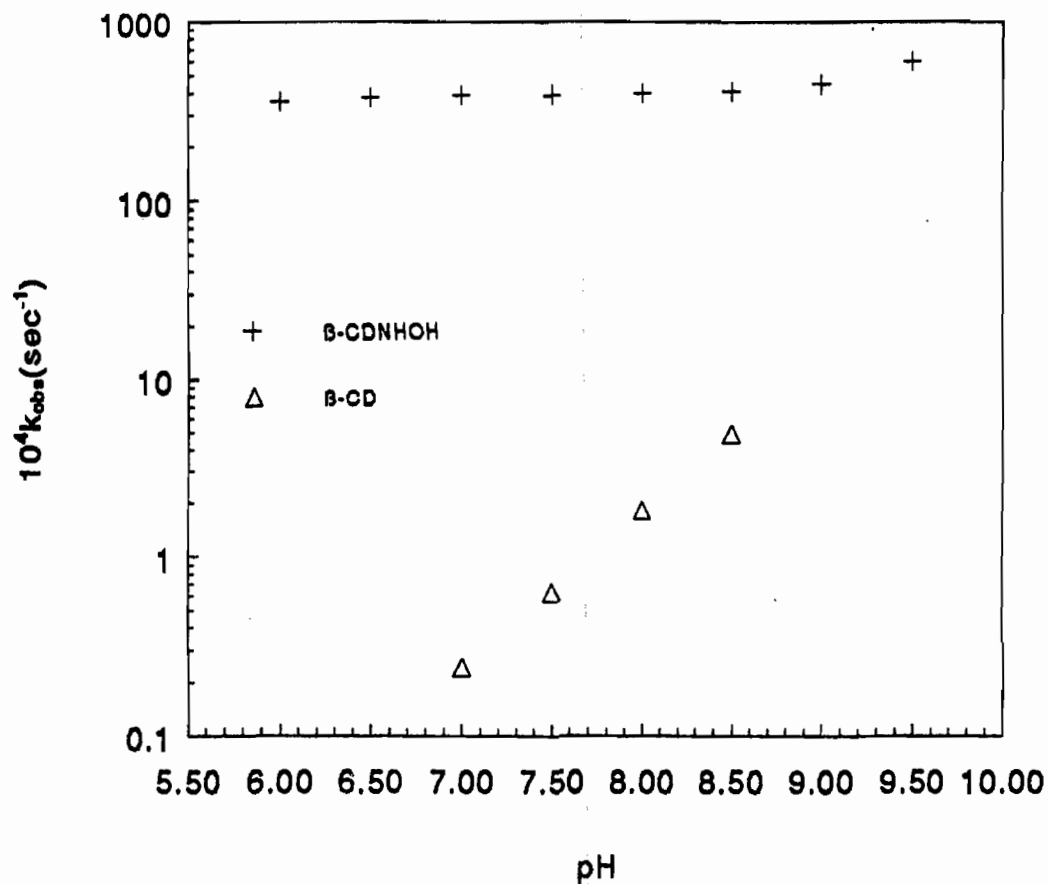
which contained some physically entrained NH_2NH_2 as determined by ^1H NMR in D_2O /acetone.⁸ Dissolution in minimal H_2O , followed by reprecipitation from EtOH, was repeated 5 times, which gave 3 as a water-soluble, colorless solid in 60% yield. In a precisely analogous manner, reaction of 1 with a 6% aqueous solution of hydroxylamine (4) at 90 °C for 3 h, followed by multiple reprecipitation from EtOH, gave 5 in 86%. While either the N- or the Q-alkylation product might have been formed, catalytic hydrogenation, which yielded βCDNH_2 and not βCD itself, confirmed the former. ^1H and ^{13}C NMR, FAB mass spectrometry, and elemental analyses were fully supportive of the structure assignments for 3 and 5. Notably for an unsymmetrically substituted CD derivative, 5 yields colorless plates (dec 207-210°C) from water.

Both βCDNHNH_2 and βCDNHOH are acylated rapidly by *p*-nitrophenylacetate (pNPA) with saturation behavior. The reaction of pNPA (0.05 mM) fully complexed to 5 at pH 7.0 and 25°C is faster than that with equimolar CH_3NHOH , demonstrating an effective RNHOH concentration of 37 mM. βCDNHOH is acylated as efficiently at pH 7.0 as at pH 9.5; furthermore, the rate of acyl transfer is 1500-times faster than that afforded using equimolar βCD , which is not reactive under neutral conditions (Figure 1).

Figure 1

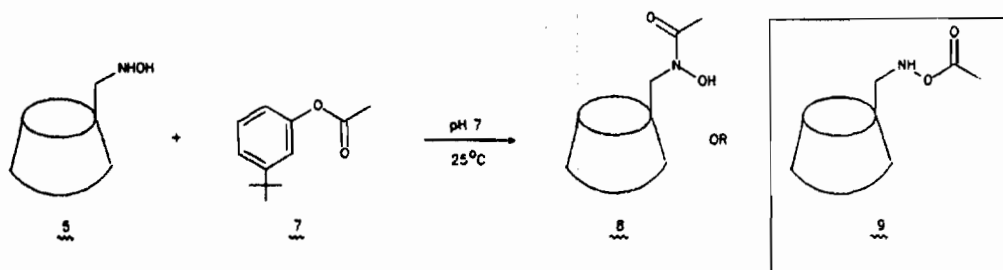
Reaction of p-NPA with β -CD's

Effect of pH on k_{obs} (0.1 M buffer)



As shown in Scheme II, β CDNHOH binds and is acylated by a less activated ester (7) at pH 7.0 and 25°C. The intracomplex reaction

Scheme II



([5]=20 mM; [7]=0.82 mM) occurs with a half-life of 7.5 minutes; a reference reaction (minimal DMSO added for solubility) with CH₃NHOH and βCD shows $t_{1/2}$ =4.8 h, while the hydrolysis of 7 without added βCDNHOH occurs to less than 5% after 7 days. Once again, either N- or Q-acylation, leading to 8 or 9, is possible. The ¹H NMR spectrum of the acylation product in DMSO-d₆ reveals a one proton, D₂O-exchangeable triplet at δ 7.65. Decoupling experiments demonstrate one-bond coupling to a single, diastereotopic H-6 proton (δ 3.07) on the modified CD residue, which permits assignment as an NH proton, and thus an unambiguous assignment of the acyl enzyme mimic as 9. Because Q-acylhydroxylamines hydrolyze more rapidly than structurally related esters, the deacylation kinetics of 9 are currently under investigation.

Experimental Section

6-Deoxy-6-hydrazinyl-β-cyclodextrin (3). Anhydrous hydrazine (4.0 mL, 128 mmol) was added to β-cyclodextrin-6-Q-tosylate (1 g) with stirring. In approximately 15 min a clear brown solution was obtained, which was stirred for 4 h. The solution was concentrated in vacuo (vacuum pump) with low heat (50°C) to give a clear, light brown, viscous oil, to which double distilled (dd) water (2 mL) added. The colorless solution was added dropwise to stirred ethanol (60 mL) producing a white precipitate, which was filtered to give a white powder. The white powder was reprecipitated from ethanol repeatedly until no signs of free hydrazine remained as evidenced by ¹H NMR in D₂O upon the addition of acetone.

After removal of free hydrazine by reprecipitation 3 was obtained as a white powder (580 mg, 60%): mp 180-210°C dec.; R_f 0.68 (silica gel; ethyl acetate/ isopropyl alcohol/ ammonium hydroxide/ water, 7:7:4:4); 1H NMR (D_2O) δ 2.86 (dd, 1, CH_2NHNH_2), 3.08 (dd, 1, CH_2NHNH_2), 3.40 (t, 2, H-4 of substituted glucose unit), 3.47-3.83 (m, 32, H-2, H-3, H-4, H-5, H-6), 4.95 (m, 7, H-1); ^{13}C NMR (D_2O) δ 54.69 (C-6'), 58.31 (C-6), 70.58 (C-5'), 72.70 (C-5), 72.90 (C-3'), 72.95 (C-3), 73.85 (C-2'), 73.93 (C-2), 81.71 (C-2'), 81.94 (C-4), 84.10 (C-4'), 102.43 (C-1), 102.73 (C-1); FAB mass spectrum, m/e 1150 (M^++1).

Anal. Calcd for $C_{42}H_{72}N_2O_{34} \cdot 7 H_2O$: C, 39.56; H, 6.80; N, 2.20. Found: C, 39.88; H, 6.78; N, 2.24.

Addition of a slight excess of acetone (3 equiv) to a D_2O solution of 3 that contained free hydrazine afforded the following results: 1H NMR (D_2O) δ 1.68 (s, 3.5, hydrazine bishydrazone), 1.73 (s, 1.5, hydrazine monohydrazone), 1.74 (s, 1.5, β -CD-NHNC(CH₃)₂), 1.80 (s, 1.5, hydrazine monohydrazone), 1.83 (s, 1.5, β -CD-NHC(CH₃)₂), 1.92 (s, 3.5, hydrazine bishydrazone), 2.10 (s, 1.3, (CH₃)₂CO), 3.05-3.79 (m, 42, H-2, H-3, H-4, H-5, H-6), 4.94 (m, 7, H-1).

Addition of a slight excess of acetone to a sample of 3 that did not contain free hydrazine afforded the following spectral results: 1H NMR (D_2O) δ 1.75 (s, 2.4, β -CD-NHNC(CH₃)₂), 1.82 (s, 2.4, β -CD-NHNC(CH₃)₂), 2.14 (s, 8.3, (CH₃)₂CO), 3.03-3.84 (m, 42, H-2, H-3, H-4, H-5, H-6), 4.98 (m, 7, H-1); FAB mass spectrum (DMSO), m/e 1190 (M^++1) for β -CD-NHNC(CH₃)₂.

6-deoxy-6-N-hydroxylamino- β -cyclodextrin (5). A stirred solution of $NH_2OH \cdot HCl$ (15.3 g, 220 mmol) in 1.3 M aqueous NaOH (300 mL) was reacted with β CD-OTs (11.4 g, 8.8 mmol) at 90 C for 3 h. The solution

was cooled, filtered and concentrated to 75 mL. The resulting concentrate was slowly diluted with a 1:1 solution of EtOH/2-propanol (1500 mL) to give a white ppt which was filtered and twice dissolved in H₂O (50 mL) and concentrated to 20 mL. The now alcohol free solution was lyophilized to give the desired product as a fluffy white solid. (8.7 g, 86% yield): ¹H NMR (DMSO-d₆) δ 2.83 (dd, 1, CH₂NHOH), 3.17-3.43 (m, H-3, H-4, CH₂NHOH), 3.55-3.79 (m, H-2, H-3, H-6, H-5'), 4.05 (s, 6, C₆-OH), 4.82 (d, 7, H-1), 5.86 (m, 14, C₃-OH, C₂-OH), 7.14 (s, 1); ¹³C NMR (DMSO-d₆) δ 54.67 (C-6'), 59.98 (C-6), 68.28 (C-5'), 71.77 (substituted glucose unit), 72.59 (C-5), 72.32 (C-3), 73.00 (C-2), 81.06 (substituted glucose unit), 81.56 (C-4), 84.36 (substituted glucose unit), 101.97 (C-1); FAB mass spectrum, m/e 1173 (100%, M⁺+Na), 1151 (95%, M⁺+1).

The above sample contains a small amount of NaCl, as determined by microanalysis. A salt-free preparation for elemental analysis was obtained using the free base form of NH₂OH (50% aqueous solution obtained from SACHEM, Austin, TX), which was identical to the sample obtained using NH₂OH·HCl by TLC and NMR.

Anal. Calcd. for C₄₂H₇₁N₁O₃₅·9H₂O: C, 38.44; H, 6.84; N, 1.07. Found: C, 38.79; H, 6.31; N, 0.81. (Note: although the observed H analysis varies from the theoretical by 0.53%, all other characterizations are consistent with the proposed structure.)

Conclusions

The mounting of α -nucleophiles onto the primary side rim of β -cyclodextrin affords new α -nucleophiles that can bind potential substrates. Because hydroxylamine is much less basic than isosteric amines, it shows high reactivity at physiological pH.

References and Notes

- 1) Accepted for presentation at the 6th International Symposium on Cyclodextrins, Chicago, IL.
- 2) On faculty leave from Ohio Wesleyan University, Delaware, OH.
- 3) NSF/OSU Young Science Scholars Program participant, Summer, 1989.
- 4) VanEtten, R. L.; Clowes, G. A.; Sebastian, J. F.; Bender, M. L. *J. Am. Chem. Soc.* 1967, 89, 3253.
- 5) (a) Cramer, F.; Mackensen, G. *Angew. Chem.* 1966, 78, 641; (b) Iwakura, Y.; Uno, K.; Toda, F.; Onozuka, S.; Hattori, K.; Bender, M. L. *J. Am. Chem. Soc.* 1975, 97, 4432; (c) Breslow, R.; Doherty, J. B.; Guillot, G.; Lipsey, C. *J. Am. Chem. Soc.* 1978, 100, 3227; (d) Ikeda, T.; Kojin, R.; Yoon, C.-J.; Ikeda, H.; Iijima, M.; Hattori, K.; Toda, F. *J. Inclusion Phenom.* 1984, 2, 669.
- 6) (a) Breslow, R.; Overman, L. E. *J. Am. Chem. Soc.* 1970, 92, 1075; (b) Akkaya, E. U.; Czarnik, A. W. *J. Am. Chem. Soc.* 1988, 110, 8553; (c) Breslow, R.; Singh, S. *Bioorg. Chem.* 1988, 16, 408; (d) Rosenthal, M. I.; Czarnik, A. W. *J. Incl. Phenomena.* 1991, 10, 119.
- 7) Jencks, W. P.; Carriuolo, J. *J. Am. Chem. Soc.* 1960, 82, 1778.
- 8) The 1:1 hydrazone between acetone and hydrazine yields methyl singlets at 1.72 and 1.81 ppm (D_2O); the 2:1 bishydrazone yields methyl singlets at 1.68 and 1.91 ppm. The 1:1 hydrazone between acetone and β CDNHNH₂ yields somewhat broadened methyl singlets at 1.74 and 1.83 ppm. Likewise, the 1:1 hydrazone between acetone and hydroxylamine yields methyl singlets at 1.75 and 1.79 ppm; β CDNHOH does not form a hydrazone with acetone.

ACKNOWLEDGMENT

This work was supported by a grant from The Office of Naval Research. FT-NMR spectra were obtained with equipment funded in part by NIH grant 1 S10 RR01458-01A1. L.E.F. acknowledges a faculty summer fellowship from the ACS Petroleum Research Fund. A.W.C. thanks the A.P. Sloan and Dreyfus Foundations for support in the form of fellowships and Eli Lilly and Co. for support in the form of a granteeship.

III. DETECTION

NOTE: Papers with the following titles were presented at the Conference but are not included in this document:

The Use of Ammonia as a Reagent in an Ion Mobility Spectrometer

Detection of Agents Using the Sulfur Chemiluminescence Detector

Current Status of a Fraunhofer Line Discriminator (FLD) for the Characterization of Chemical Simulant Clouds

Detection of Nonvolatiles Via Liquid Injection into Atmospheric Pressure DC and RF Glow Discharge Sources and Pulsed Time-of-Flight Mass Spectrometry

Color-Change-Based Detection of Bacterial Toxins

Characterization of an Unknown Polypeptide from *Naja Naja atra* (Chinese)

Recognition of Chemical Markers for Biodetection in GC/MS Data: Feature Selection, Fingerprinting, and Discriminant Analysis

UV Resonance Raman Rapid Detection and Identification of Single Bacterial Cells

BLANK



**DETECTION STRATEGIES FOR TREATY VERIFICATION: A FIELDABLE SYSTEM FOR
SAMPLING AND ANALYSIS OF CW STOCKPILE**

S.F. Hallowell, M. J. Heyl, D. J. Reutter

**Research Directorate, U.S. Army Chemical Research, Development and
Engineering Center, Aberdeen Proving Ground, MD 21010-5423**

Research Funded by: Defense Nuclear Agency (DNA)

ABSTRACT

The evolving multinational treaty to end CW production and stockpile makes provisions for sampling and analysis of stockpile content in the least intrusive fashion possible, with analysis preferably done on-site during the inspection. The purpose of analysis of some select items from the chemical stockpile is to verify compliance with the treaty. Chemical analysis of selective items must be done quickly, in order guide inspectors during the inspection. However, the quality of the data must be quite good, with the risk of false results minimal: the data must withstand legal scrutiny by the international community. Here, we discuss our technical approach to sampling and analyzing contents of CW items to determine compliance with a CW treaty.

The overall treaty verification program objectives are to examine the evolving treaty, to identify different scenarios that will require verification, and to present a range of options to the policy community on what activities are necessary to assure compliance with the treaty. The program focuses on evaluating existing technologies against verification requirements: a basic guidance is to avoid major development programs to develop new items. Therefore, existing sensors, detection systems, and sampling and analysis protocols are evaluated for suitability in this program. Once potential equipment/procedures are identified, subsystems are developed in order to produce scenario specific protocols for verification.

Ten distinct verification scenarios have been identified that will probably require inspection activities. The first five scenarios address scenarios that are involved in the initial declaration of a CW stockpile, and the subsequent elimination of the stocks and production facilities. Inspections for these situations examine whether the host country is in compliance with treaty agreements. Three more scenarios are related to allowed industrial activities that are pertinent to the CW treaty including production of small quantities of CW compounds, production of precursor substance, and production of CW related substances. The last two scenarios are challenge

situations in which it is believed that a host country has either illegally used or produced stockpiles. A key issue is the role of sampling and analysis in verification activities. The questions that must be answered include "Is sample acquisition and subsequent chemical analysis a necessity for verification? If so, where and how will the sample be analyzed? What level of quality must be achieved in reporting a result that must be defended as being correct to the international community?" There are also a number of other ancillary concerns with sampling and analysis, including waste management, transport of surety material across international borders and safety of inspectors that must be addressed.

Examination of each verification scenario against these questions suggests that sampling and analysis are probably not appropriate for all scenarios, but may be essential to establish verification for some scenarios. We have identified that sampling and analysis could be a useful part of compliance inspection regimes addressing CW stockpile declaration, destruction of CW stocks, production of CW materials at small scale facilities and production of precursor or CW related material materials. Sampling and analysis would be an essential part of inspection regimes for noncompliance scenarios including investigation of use of CW compounds or clandestine production/stockpile. However, the kinds of samples acquired, the kinds of chemical analyses done and the level of quality of the results may vary quite a bit. For instance samples acquired for compliance inspections will mostly be of neat material. Qualitative identification is more important than quantitation, and quality control measures need not address absolute quantitation. In contrast, for a challenge inspection, results must be legally defensible to the international community, since the finding of noncompliance to a treaty could lead to international sanctions against the offending country. The evolving treaty identifies a number of rights and obligations of both inspectors and the host country that are pertinent to sampling and analysis concerns. Additionally, the treaty mandates that analysis be performed on-site, if possible. It also calls for verification activities to be conducted in the least intrusive manner possible, along with a number of other guidances.

After these kinds of initial assessments, both equipment and potential laboratory configurations must be identified that will fulfill requirements for sampling and analysis within the constraints of the treaty. The CRDEC treaty field test program has been designed to develop and validate operational concepts for each scenario. The three basic stages include the development of a baseline survey, an equipment field trial that identifies potential equipment and procedures that can be used, and finally a system field demonstration of operational concepts. This paper focuses on the program for stockpile declaration (scenario 1). The basic verification aims for this situation are to confirm the accuracy of the host countries declaration, and to ensure that no undetected removal of chemical munitions occurs. Sampling and analysis play a small, orchestrated part in the overall activities that occur which include bunker inventory, physical measurements and secure and monitoring activities. It is arguably the most technically demanding and expensive activity, requiring both instrumentation and skilled operators.

In order to sample munition contents, a sample plan was developed that called for a limited number of chemical items to be drilled and tapped, with

filler material tested for chemical identity. We adopted a criteria of 90% confidence that the stockpile was at least 90% as the host state declared it to be. This plan identifies that 22 munitions must be sampled, with results in agreement with host declared contents. Our initial equipment trial evaluated a number of pieces of equipment (developed for other applications) for suitability in this program. This included specialized glove boxes developed for depot use to handle leaking munitions (the so called Ammunition Peculiar Equipment (APE models 1981 and 1982), a number of reagent based detector systems including both military and commercially available items, (M8 paper, M272 water test kit, M256A1 detector kit, M-18 kit and Draeger tubes), Army developed detector systems designed for field use (Chemical Agent Monitor, MMI) Army depot monitoring systems (Minicams, DAAMS tubes), industrial fieldable detector systems (Viking Spectratrak 600 GC-MS, Miran portable IR), liquid handling systems, and other detector systems. The basic technical issue was the suitability of applying equipment that was developed for other purposes for this program. The APE's had to be modified to accommodate sample lines. Most of the reagent based systems suffer from various degrees of false positive response to other chemicals, but are quite appropriate as safety measures where false positives are highly acceptable but not false negatives. Some systems, like the Minicams, are much more sensitive than they need be for this application. The MMI was designed for battlefield use, but lacks certain hardware and software features that allow its use as an analytical device. At the equipment field trial, all equipment was evaluated with respect to intrusiveness to host, effectiveness (defeatibility, difficulty, and performance) and cost. The field trial identified that the most suitable items would be the APE's, M-8 paper with Draeger tubes, and a combination of two out of three, Miran portable IR, Minicams, and Viking GC-MS. Additionally, a mobile lab equipped with a GC/FPD and GC/MS could analyze dilute liquid samples. Another finding from the field trial was that if verification of contents was done at the site of the APE 1982, environmental controls would be necessary for the Minicams, since the APE 1982 is located outside. This led to the development of a highly mobile detector lab. This was, in essence, a van designed to house two functional Minicams, a GC-MS, a sorbent tube collection system, and ancillary equipment. The van was modified to accommodate heat traced teflon sample lines from the APE's to the instrumentation, in a closed loop fashion, with effluent flushed back into the APE's. The van was designed to be accompanied with a portable power generator that could support 6 kilowatts in order to run the instrumentation, if power was not available.

Having completed the equipment field trial, three basic systems of sample acquisition and analysis were evaluated. Firstly, the utility of using reagent based colorimetric indicators (such as Draeger tubes or M-8 paper) was evaluated. The tests were performed within the APE glove box by operators wearing Army level B protection. Secondly, the analysis of head space vapor from the munition fill was evaluated. This was accomplished by connecting the Viking GC-MS and Minicams detectors located within the sample van to the interior of the APE with 50 foot heat traced sample lines. The third sampling and analysis system that was evaluated was simply the acquisition of a neat sample of munition fill, the dilution of it, and transport to the location of a satellite laboratory with the appropriate chain of custody. The system evaluation criteria included assessments of the compatibility of equipment, set up time, complexity of operation, turn around

time for analysis, quality of data, field ruggedness, operational requirements, waste management, operator skill, and transportation requirements. Findings of this exercise suggested that the performance of reagent chemistry at the site of sample acquisition is useful for preliminary confirmation of agent identity. The acquisition of dilute liquid samples from munitions or bulk containers for analysis at a modular lab is probably the best primary method for verification. This modular lab could also be used to analyze sorbent tube samples taken with small battery operated pumps from either the chemical item, or as a sample taken for first entry monitoring into and igloo. The modular lab should contain two out of the following three detector systems: Minicams, Miran 1A, Viking GC-MS. The sample van was a little cramped, but demonstrated that it could serve as a modular lab. Because of the amount of time required to start up Minicams (approximately 1-2 hours during full systems demonstration) it seems be less time and labor intensive to locate the modular lab in the vicinity of sample collecting activities, with transport of samples to lab site, rather than locating the van several times during the day. The relocation of the sample van to multiple sites during one day requires the complete shut down of all instrumentation contained within it, and set up and calibration time after relocation takes too long. Analysis of vapor (head space) samples during the sample process yielded immediate, dramatic confirmation of chemical identity with typically about 12 minutes turn around time. It does not produce chemical waste. However, this operation is fairly complex and requires careful engineering control, since small quantities of agent vapor are introduced in a closed loop fashion into the sample van, and this is not the system of choice.

CONCLUSIONS

On site sampling and analysis of chemical items as a part of a treaty verification inspection of chemical stockpiles is technically feasible. The best procedure seems to be the use of reagent based detector kits as preliminary agent verification screens during the sampling procedure, followed by the preparation of dilute samples that are transported with chain of custody procedures to the site of a highly mobile lab. The sample identity should be confirmed using two different physical methods of detection in order to minimize the possibility of false positive results. In this exercise, we used a a gas chromatograph equipped with a MS detector and a gas chromatography equipped with a flame photometric detector for verification of sample identity. However, we recommend that instruments with three different kinds of detectors be bought along on inspections, with two out of three instruments used on any given inspection.

BIODETECTION OF BACTERIA BY PYROLYSIS AND MASS SPECTROMETRY

Alvin Fox
Department of Microbiology and Immunology
University of South Carolina
Columbia, S.C.

ABSTRACT

Biodetection, involving mass spectrometry, requires identification of chemical markers present in target organisms (e.g. *Bacillus anthracis*) and absent in others. After release from whole cell polymers and derivatization complex mixtures of bacterial sugar and fatty acid isomers are readily distinguished by gas chromatography-mass spectrometry (GC-MS), but this is difficult to achieve routinely by MS-MS. Some of these compounds can be recognized after pyrolysis (e.g. anhydrogalactose derived from galactose of *B. anthracis*). Polar substances (e.g. dipicolinic acid found in spores of bacilli) may be amenable to analysis by MS-MS, but will not pass readily through a GC-MS system; instead the pyrolysis product pyridine is often studied. Some compounds (e.g. butenoic acid pyrolytically generated from the bacterial storage compound, hydroxybutyrate) are amenable to analysis by both GC-MS and MS-MS. Thus MS-MS and GC-MS have their distinct advantages and disadvantages in analysis of specific chemical markers, (DeLuca, Sarver, Harrington, and Vorhees, 1991; Gilbert, Fox, Morgan, 1990). Our current strategy involves defining primary markers for key biological agents using chemotaxonomic principles; this usually employs derivatization and GC-MS. The significance of the marker in discrimination among bacterial species is assessed by analyzing multiple strains of relevant bacterial species. Subsequent analysis by pyrolysis followed by GC-MS (py GC-MS) and py MS-MS is vital in assessing the utility of "secondary" chemical markers derived from these compounds. Studies in progress to determine the carbohydrate profiles of the vegetative and spore forms of strains of *Bacillus anthracis* and *Bacillus cereus* are presented as an example of some of the steps involved in identification of "primary" chemical markers.

INTRODUCTION

Biodetection using mass spectrometry must ultimately be based on the presence of chemical markers present in specific organisms (e.g. *Bacillus anthracis* and absent in other bacterial species (e.g. *B. cereus*). In the case of sporulating organisms differences between vegetative cells and spores must be documented. Pyrolysis MS-MS or GC-MS can identify compounds generated from chemical markers ("secondary chemical markers"). Primary chemical markers must first be defined that have validity based on taxonomic principles. This can be achieved by examining multiple strains of relevant bacterial species. Figure 1 outlines a modular approach to solving the problems of biodetection which involves integrating the expertise of mass spectrometrists, microbial chemotaxonomists and computer experts in solving some of the basic research problems in applying pyrolysis and mass spectrometry to rapid biodetection. The remainder of this article will be concerned with current progress in defining some of the chemical markers

present in vegetative and sporulating *B. anthracis* which may of use in their differentiation from other bacilli (an example of Module 1).

Figure 1. Modules in developing a biodetection scheme based on chemical markers

MODULE 1: Identification of primary chemical markers by derivatization and GC-MS (or liquid chromatography-mass spectrometry without derivatization).

MODULE 2: Identification of secondary chemical markers by pyrolysis and GC-MS

MODULE 3: Identification of secondary chemical markers by pyrolysis and MS-MS

MODULE 4: Computer assisted searching of bacterial chromatograms for primary and secondary chemical markers

MODULE 5: Computer assisted automated use of chemical markers in biodetection

Many aspects of the taxonomy of bacilli remain unresolved and additional studies are clearly needed, especially comparisons of their ribosomal RNA (Claus and Fritze, 1989). *B. anthracis* and *B. cereus* are closely related species that differ in few characteristics (Ezell, Abshire, Little, Lidgerding and Brown, 1990). Indeed *B. anthracis*, has a high degree of genetic homology with *B. cereus* as well as *B. thuringiensis* as demonstrated by DNA-DNA hybridization (Kaneko, Nozaki and Aizawa 1978). Fatty acid profiles of these three species are also similar (Lawrence, Heitefuss and Seifert, 1991). 16S rRNA cataloging places *B. megaterium*, *B. cereus* and *B. subtilis* in a cohesive group with *B. subtilis* as the most distantly related; this study did not include strains of *B. anthracis* or *B. thuringiensis* (Stackebrandt, Ludwig, Weizenegger, Dorn, McGill, Fox, Woese, Schubert, and Schleifer, 1987).

Demonstration of production of lethal toxin by *B. anthracis* is a reliable way of identifying anthrax strains. Alternatively, *B. anthracis* can be differentiated from *B. cereus* and *B. thuringiensis* by the presence of the cell wall galactose-N-acetylglucosamine polysaccharide using monoclonal antibodies. These monoclonal antibody do not recognize galactose in *B. anthracis* spores (Ezell, Abshire, Little, Lidgerding and Brown, 1990). From this work it is unclear whether galactose is absent in the polysaccharide of these spores or alternatively simply inaccessible due to presence of the spore coat. A study has been undertaken to define sugars present in both the vegetative and spore forms of *B. anthracis* in comparison to other species of bacilli. These chemical markers may then be exploited in biodetection, once unique pyrolysis products have been identified as previously (Morgan, Watt, Ueda and Fox, 1990; Watt, Morgan and Fox 1991).

METHODS

B. anthracis is only highly pathogenic if it contains two virulence plasmids. PX01 encodes the lethal toxin, whilst PX02 codes for genes involved in synthesis of the polyglutamic acid capsule necessary for survival in the host (Ivins, Ezell, Jemski, Hedlund, Ristroph, Leppla 1987). Non-pathogenic strains of *B. anthracis* lacking one or both of the two virulence plasmids were kindly donated by Dr Stephen Leppla, Fort Detrick, Maryland. Two "avirulent" strains (one containing PX01 and one PX02) could potentially generate a daughter "virulent" strain possessing both plasmids. Thus safe microbiological practices are essential. Strains of *B. cereus* were obtained from the American Type Culture Collection.

Bacilli were grown in nutrient broth with shaking at 37°C, since the organisms are strict aerobes. Under these conditions *B. anthracis* were present during their first several days almost exclusively in the vegetative form, but almost totally in the spore form after several weeks. *B. cereus* did not readily form spores under these culture conditions. Although subsequent work has shown plates of *B. cereus* and *B. anthracis* readily convert to spores in a few days at room temperature. Flasks were tightly sealed to avoid aerosolization, particularly in the case of *B. anthracis*. The organisms were harvested by centrifugation, washed three times in distilled water and sterilized by autoclaving. In this fashion both vegetative and sporulating cells were harvested from the same media. Sporulation was assessed by staining with malachite green or phase contrast microscopy.

Carbohydrate profiles of bacilli were determined as alditol acetates. Five mg of each sample were hydrolyzed in 2 N sulfuric acid. The mixtures were then neutralized with N,N-dioctylmethylamine. The aqueous phase was passed first through a C18 column to remove hydrophobic contaminants and then aldoses reduced with sodium borodeuteride. Acetic acid-methanol (1:200; vol/vol) was added several times, and the samples dried to remove borate, which otherwise inhibits the acylation reaction. The alditols were then acylated with acetic anhydride at 100°C overnight and then extracted with acid and alkaline solutions to remove polar contaminants. GC-MS analyses were carried out with a mass-selective detector (model 5970; Hewlett-Packard Co., Palo Alto, CA) interfaced to a GC (model 5890; Hewlett-Packard) equipped with an automated sample injector and an SP-2330 fused-silica capillary column (Fox, Morgan, Gilbert, 1989).

RESULTS

Both vegetative *B. anthracis* and *B. cereus* were found to contain ribose, glucose, muramic acid, glucosamine and mannosamine. Additionally *B. anthracis* contain galactose and *B. cereus* contain galactosamine (see Figure 2 and Table 1). All sugars present were proven to be aldoses (as opposed to alditols) by observation of mass spectra. For example, the mass spectra of non-deuterated alditol acetates of aminohexoses are dominated by m/z 144 and 360 produced by cleavage between C2 and adjacent carbons (C1 and C3) in the alditol chain (see Figure 3); m/z 84 is generated from 144 by loss of acetic acid. When using sodium borodeuteride as reducing agent aldoses (on conversion to alditols) gain two deuteriums, one of which remains after acetylation. Thus aldoses and alditols (after conversion to alditol acetates) can be distinguished by m/z differences of 1. Mannosamine present in bacilli contained m/z 85 and 145 as predominant ions confirming its identity as an aldose.

Figure 2. Carbohydrate profiles of vegetative (A) *B. anthracis* and (B) *B. cereus*

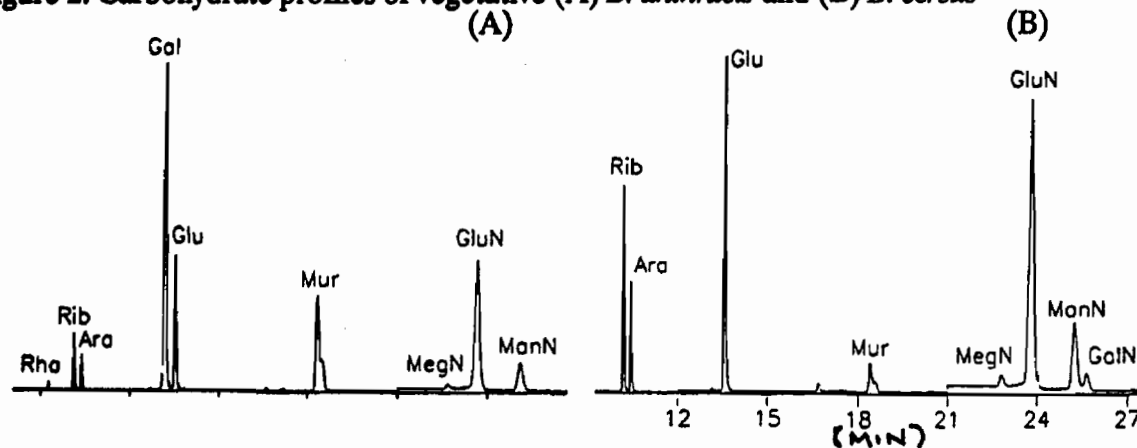


Figure 3. Mass spectra of (A) mannosamine from *B. anthracis* as deuterated alditol acetate. (B) mannosamine standard as alditol acetate

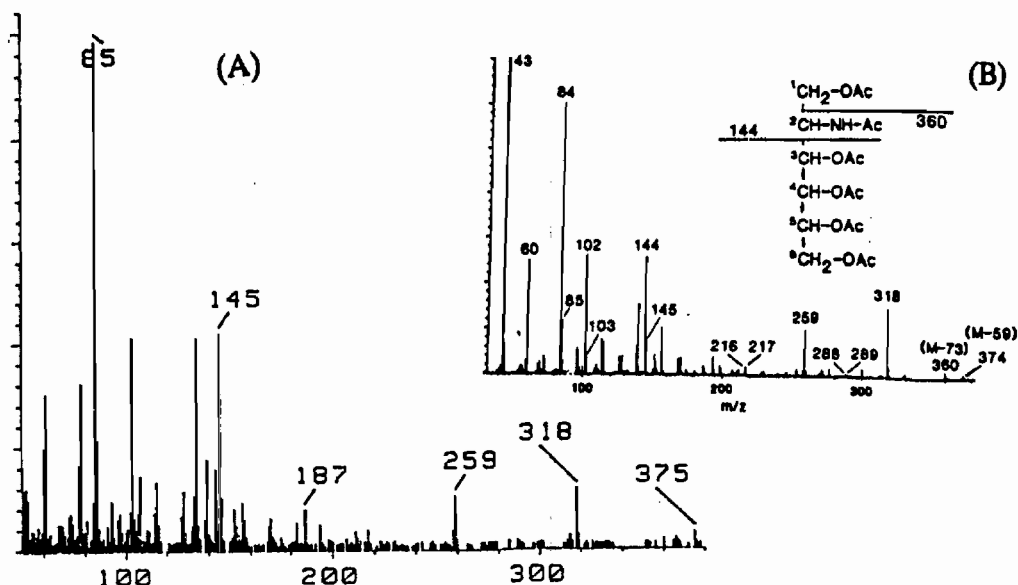


Table 1. Carbohydrate profiles of vegetative *B. cereus* and *B. anthracis*

Organism	Rha	Rib	Gal	Glu	Mur	GluN	ManN	GalN
<i>B. cereus</i>								
14579	--	0.12	0.04	0.96	0.14	2.79	0.81	0.96
12826	--	0.27	0.00	1.72	0.30	2.70	1.09	1.20
6464	--	0.36	0.008	1.33	0.19	6.71	1.41	1.94
<i>B. anthracis</i>								
NNR-1Δ-1	0.013	0.52	2.03	0.59	0.48	2.83	0.76	--
ΔNH-1	--	0.25	2.0	1.10	0.83	3.23	0.73	--
VNR-1Δ-1	--	0.52	2.36	0.12	0.51	3.23	1.00	--
NNR-1	0.01	0.24	3.01	1.22	1.73	4.27	0.88	--

Rha = rhamnose, Rib = ribose, Gal = Galactose, Glu = glucose, Mur = muramic acid, GluN = Glucosamine, ManN = mannosamine, GalN = galactosamine.

B. anthracis spores, unlike vegetative cells, additionally contained large amounts of rhamnose, a 3-O-methyl deoxyhexose (possibly 3-O-methylrhamnose) and low amounts of galactosamine. Interestingly, both the vegetative and spore forms of *B. anthracis* contain galactose. Figure 4 compares selected ion chromatograms of carbohydrates of the spore and vegetative forms of *B. anthracis* (see Table 2). In these chromatograms the 3-O-methyl deoxyhexose peak is not seen, since the characteristic ion was not monitored. This sugar peak was obvious in total ion chromatograms, eluting just before rhamnose. This suggests the existence of a distinct spore polysaccharide in *B. anthracis*. O-methylated sugars are relatively uncommon in nature and thus standards were not available. The mass spectra of O-methylated sugars are dominated by breakage of bonds between C-O-methyl and adjacent C-O-acetyl groups (Carpita and Shea, 1989). For a deuterated 3-O-methyl deoxyhexose alditol acetate this would produce m/z 203 and 190 as primary fragments. Other ions, as for other alditol acetates, include loss of acetic acid (m/z 60) e.g. m/z 143 from 203 and m/z 190 from 130 or ketene (m/z 42) e.g. m/z 101 from 143 and 88 from 130 (see Figure 5).

Figure 4. Carbohydrate profiles of (A) vegetative and (B) spores forms of *B. anthracis*.
(A) (B)

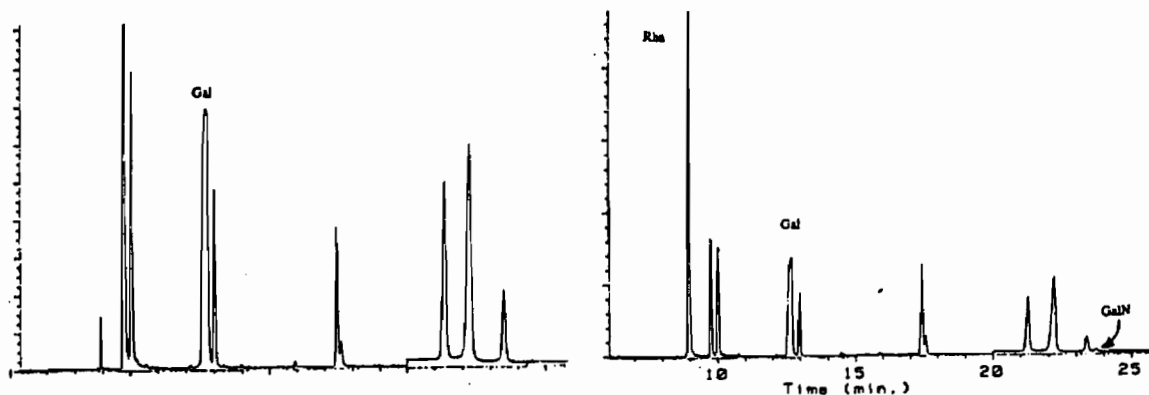


Figure 5. Mass spectra of 3-O-methyl deoxyhexose as deuterated alditol acetate.

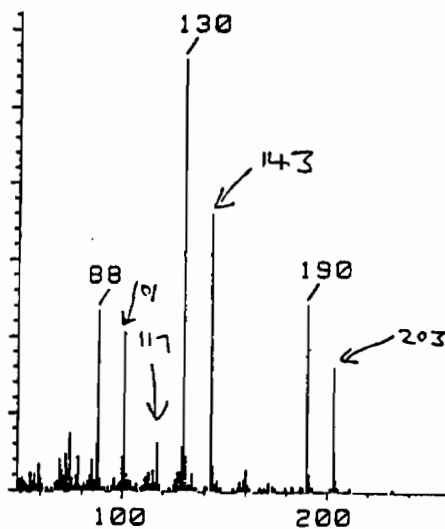


Table 2. Carbohydrate profiles of vegetative and sporulating *B. anthracis*

Organism	O-Me Dhex	Rha	Rib	Gal	Glu	Mur	GluN	ManN	GalN
Δ NH-1									
Vegetative	--	0.006	0.58	3.06	1.59	1.26	3.38	0.52	--
Spore	0.04	0.24	0.23	2.77	0.78	1.84	4.47	0.75	Tr
NNR-1 Δ -1									
Vegetative	--	0.024	1.04	2.61	0.76	0.74	2.51	0.44	--
Spore	0.19	0.98	0.71	2.03	0.62	1.74	2.91	0.34	0.29

O-Me Dhex = 3-O-methyl deoxyhexose, Rha = rhamnose, Rib = ribose, Gal = Galactose, Glu = glucose, Mur = muramic acid, GluN = Glucosamine, ManN = mannosamine, GalN = galactosamine.

CONCLUSION

B. anthracis and *B. cereus*, closely related species of bacilli have distinct carbohydrate profiles. Both the spore and vegetative forms of *B. anthracis* contain galactose as a major sugar. Previous work has suggested that the pyrolysis product anhydrogalactose may be a useful marker for use in biodetection. The potential utility of galactose as a marker for *B. anthracis* is improved by now demonstrating that it is present in both spore and vegetative forms of the cell. There are major differences between the carbohydrate composition of vegetative and spore forms of *B. anthracis*. Interestingly the spore contains large amounts of rhamnose and a 3-O-methyl deoxyhexose. The identification of anhydrosugars derived from these compounds on pyrolysis could prove highly important in deployment of a rapid biodetection protocol. In a general sense the work emphasizes the importance of defining in chemical and microbiological terms bacterial samples before performing pyrolysis GC-MS or MS-MS studies to identify secondary chemical markers.

REFERENCES

Carpita N. and Shea E. Linkage structure of carbohydrates by gas chromatography-mass spectrometry (GC-MS) of partially methylated alditol acetates. In: Analysis of carbohydrates by GC and MS. Bierman C. and McGinnis G. (Eds.). CRC Press, Fl. 1989.

Claus D., and Fritze D. Taxonomy of *Bacilli*. In: *Bacillus*. Harwood C. (Ed.). Plenum Press, NY. 1989.

DeLuca S., Vorhees K. and Noguera A. A pyrolysis-tandem mass spectrometry study of the biological components in bacteria. Oral presentation, Pyrolysis Mass Spectrometry and Biosensors, Setubal, Portugal, 1991.

Ezell J., Abshire A., Little S., Lidgerding B. and Brown B. Identification of *Bacillus anthracis* by using monoclonal antibodies to cell wall galactose-N- acetylglucosamine polysaccharide. J. Clin Microbiol. 1928: 223-231. 1990.

Fox A., Gilbert J., and Morgan S. Analytical microbiology: a perspective. In: Analytical microbiology methods: chromatography and mass spectrometry. Fox A., Larsson L., Morgan S., and Odham G. (Eds.). Plenum, NY, NY. p.p. 1-17. 1990.

Fox A., Morgan, S.L., and Gilbert J. Preparation and analysis of alditol acetates by gas chromatography and mass spectrometry. In: Analysis of carbohydrates by GC and MS. Bierman C. and McGinnis G. (Eds.). CRC Press, Fl. 1989.

Ivins R., Ezell B., Jemski J., Hedlund K., Ristorph J., and Leppla S. Immunization studies with attenuated strains of *Bacillus anthracis*. Infect. Immun. 52: 454-458. 1986.

Kaneko T., Nozaki R., and Aizawa K. Deoxyribonucleic acid relatedness between *Bacillus anthracis*, *Bacillus cereus* and *Bacillus thuringiensis*. Microbiol. Immunol. 22:639-641. 1978.

Lawrence D., Heitefuss S., and Seifert H. Differentiation of *Bacillus anthracis* and *Bacillus cereus* by gas chromatographic whole cell fatty acid analysis. J. Clin. Microbiol. 1508-1512. 1991.

Morgan S. L., Watt B., Ueda K. and A. Fox. Pyrolysis GC/MS profiling of chemical markers for microorganisms. In: Analytical microbiology methods: chromatography and mass spectrometry. Fox A., Larsson L., Morgan S., and Odham G. (Eds.). Plenum Press, NY, NY. 1990.

Stackebrandt E., Ludwig W., Weizenegger M., Dorn S., McGill T., Fox G., Woese C., Schubert W., and Schleifer K. Comparative 16S rRNA oligonucleotide analyses and murein types of round-spore-forming bacilli and non-spore forming relatives. J. Gen Microbiol. 133:2523-2529. 1987

Watt B., Morgan S., and Fox A. 2-butenoic acid, a chemical marker for poly- β hydroxybutyrate identified by pyrolysis gas chromatography-mass spectrometry in analyses of whole cells. J. Analyt. and Appl. Pyrol. 20:237-250. 1991.

THE RESONANCE RAMAN DETECTION AND IDENTIFICATION OF BACTERIA

S. Chadha and W. H. Nelson, Department of Chemistry
and J.F. Sperry, Department of Microbiology
University of Rhode Island, Kingston, RI 02881

Resonance Raman methods allow the direct detection of chemical taxonomic markers in bacteria at low concentration in the presence of other cell constituents and other species which interfere with conventional IR or Raman spectra. For example, with 488 nm excitation (1) chromobacteria exhibit simple, intense, species-specific resonance Raman carotenoid spectra which can be obtained from a single cell in pure culture or from mixed cultures. Conventional Raman and IR spectroscopy do give rise to characteristic spectra for markers but they suffer from severe sensitivity and interference problems and lack specificity need in detection. From most bacteria excited in the visible region conventional Raman spectra are very feeble, show little spectral detail, and suffer serious fluorescence interference.

Excitation of bacterial resonance Raman spectra in the visible and near UV regions generally is not advantageous either. In the best of examples resonance Raman spectra of bacterial carotenoids can be susceptible to fluorescence interference. However, an even more important reason for not using visible or near UV excitation is that no bacterial chemical markers of taxonomic significance other than carotenoids are strongly excited in these regions. Fortunately, if spectra are excited at wavelengths shorter than 254 nm bacterial fluorescence and other background fluorescence is negligible. Also, a number of compounds of taxonomic significance absorb strongly in the 190-260 nm region, and give rise to specific, intense resonance Raman spectra. The most intense spectra are derived from nucleic acids protein aromatic amino acids and proline(2,3), calcium dipicolinate(4,5), and quinones(6,7).

Each of the bacterial taxonomic markers shows a simple distinctive resonance Raman spectrum. However, of even greater significance to identification is the observation that each set of resonance Raman spectra shows intensity values which strongly and characteristically vary as a function of excitation wavelength. For example, at 242, 251 and 257 nm, various nucleosides, nucleic acids, quinones and calcium dipicolinate are selectively excited. At 231 and 222 nm all spectra reflect, nearly exclusively, protein aromatic amino acid

and proline peaks. At 218 nm excitation the nucleic acid peak intensities begin to increase again along with those of protein tyrosine and tryptophan. At 200 nm excitation(8) nucleic acid peaks again become prominent.

Bacterial spectra substantially reflect the tendencies of markers to exhibit peak intensities which are strongly affected by excitation wavelengths. With 257, 251 and 242 nm excitation bacteria having different DNA nucleic acid molar base pair ratios show substantial spectral differences. These are most apparent in the ratio of intensities of the 1530 cm^{-1} peak due to cytosine and the 1458 cm^{-1} peak due to combined contributions of adenine and guanine. With 242 nm excitation the ratio of the 1530 cm^{-1} and 1485 cm^{-1} peak intensities has been shown to be proportional to the DNA molar percent G+C(Figure 1). This ratio in bacteria can be measured accurately and related to the DNA molar base-pair ratios even if cultural conditions are varied substantially(9,10) and the amounts of rRNA vary dramatically.

Excitation with 242 nm light appears ideal for assessing relative amounts of rRNA and protein as well. The peak excited near 1620 cm^{-1} is due to tryptophan and tyrosine and its intensity appears to be a rough measure of total protein. Spectra excited from cultures of different ages (Figure 2) show much more intense nucleic acid peaks early in the cultural cycle. Correspondingly, the protein peak is much stronger later. What is clear is that early in the cycle during the rapid growth stages, the relative amounts of nucleic acid are substantially greater as reflected by the reduced ratio of the 1620 cm^{-1} peak intensity to that of either the 1485 cm^{-1} or the 1575 cm^{-1} A+G pronounced nucleic acid peak intensities.

Spectra excited at 231 nm are totally different from bacterial spectra excited at 242, 251 or 257 nm. The 231 nm spectra suggest that they reflect protein content and structure almost entirely. Spectral differences between organisms are modest, but measureable, and, independent of cultural conditions.

Spectra excited at 222 nm resemble those exhibited at 231 nm. However, differences in spectra due to Gram-type are more pronounced(Figure 3). Also spectra appear to have small contributions due to DNA but not RNA. This is inferred from the observation that nucleic acid peak intensities do not appear to be a function of cultural growth rate. Because 222 nm-excited spectra may reflect differences in structural proteins as well as the nature of cell walls and DNA composition, these spectra seem most suited to fingerprinting bacteria. Spectra excited at 231 nm also potentially appear useful as "fingerprints".

If the exciting line is changed to 218 nm, larger RNA contributions appear. Since these are dependent upon cultural conditions, 218 nm-excited spectra appear less useful for fingerprinting. Spectra excited at 200 nm to date suffer from low signal-to-noise ratios. Still, it is possible to detect substantial RNA contributions which differ with cultural conditions.

Spectra obtained with 251, 242, 231, 222, 218 and 200 nm excitation have involved 10 Hz Nd-Yag excitation of rapidly-flowing cells at 1-5 mw average power. In the bulk sample experiments it has not been possible to determine sensitivity limits since sample volumes have been relatively large and poorly defined. To precisely determine the sensitivity limits of the UV resonance

Raman experiment for bacterial detection we have built a specially-designed micro-Raman spectrometer capable of exciting single cells and small groups of cells selectively.

Figure 4 schematically represents the UV Raman micro system. UV laser light is produced as a continuous wave by frequency doubling the 514.5 nm output of a Spectra Physics Model 2000 Argon ion laser equipped with a Model 395B cavity extender. A KDP crystal was used within this cavity to produce the stable 257 nm output. A relatively small fraction of the laser beam (typically less than 3 mw) was directed by a beam splitter down the microscope optical axis and focussed onto a 5 micron-diameter spot on the sample by means of the optical system shown in Figure 5.

The optical system collected the Raman scattered light originating from the sample and focussed it on the slit of a Spex Triplemate spectrograph equipped with gratings optimized at 250 nm. The dispersed spectra were detected with a blue-sensitive EG&G OMA II optical multichannel analyzer which was able to obtain a complete spectrum in 16 microseconds. Usually, for the best sensitivity, scan times of up to one minute have been used.

The optical system shown in Figure 5 required the use of a 90/10 quartz beam splitter which passed only 10% of the laser beam to the Ealing Optics 36X Cassagrain objective. The Cassagrain objective focussed the beam on the sample and collected the Raman scattered light. This feeble Raman scattered light spectrum was then 90% transmitted through the beam splitter and focussed by means of a quartz lens on the slits of the spectrograph. By inserting a mirror into the optical axis an image of the sample was directed to a video camera which directed the image of the sample onto a video monitor. The spot size of the beam at the sample was determined visually for the purpose of counting the organisms by noting the bright blue fluorescence produced by the bacteria when illuminated by the UV light. The spot size has been confirmed by burning a spot onto a calibrated plate.

Live bacteria were immobilized on glass slides by means of 0.1 M polylysine solution which was allowed to dry on the slide surface before bacteria were introduced. Recently-cultured bacteria suspended in buffer were applied directly to treated plates and pressed gently with a cover slip to enhance adhesion. The wet slide was placed on a cold microscope stage adjusted to maintain the temperature near 0 degrees Centigrade. Bacteria maintained in this fashion could be illuminated for up to one minute without showing changes in spectra. Spectra were identical to those obtained from flow samples.

Typical spectra of Bacillus subtilis taken from a monolayer of attached cells, which completely filled the laser beam spot, are shown in Figure 6. Such spectra are the result of illuminating about 50 cells. By choosing a section of the plate having a low bacterial density it was possible to excite bacteria in precisely known numbers. Figure 7 shows spectra obtained from one cell of Micrococcus luteus.

Spectra of single cells to date have been of low quality and suggest that for better results several cells need to be excited. However, considering the 3% throughput of the spectrograph used, conservatively, in practice it will be possible to increase the signal level by at least a factor of 10 without changing the optical system or the laser power. Thus, it should be possible

to obtain single cell resonance Raman spectra of good quality.

The excitation wavelength, 257 nm, is not ideal either. It was chosen simply because it was the only one available in a CW source. CW light had to be used if the light was to be focussed nondestructively on the sample to the extent needed. Fluorescence interference at this wavelength is substantial. Excitation at shorter wavelengths will avoid fluorescence interference completely and further enhance the signal to noise ratio of the bacterial spectra.

It is apparent on the basis of these results that it is possible to detect single bacterial cells using UV resonance Raman spectroscopy. Furthermore, with additional instrument refinements it appears certain that such spectra will be of high enough quality to allow the use of all resonance Raman information currently extracted from bulk samples. Hence, it should be possible to use such spectra for bacterial identification as well.

REFERENCES

1. Dalterio, R.A., Baek, M., Nelson, W.H., Britt, D., Sperry, J.F. and Purcell, F.J. (1987) The resonance Raman microprobe detection of single bacterial cells from a chromobacterial mixture. *Appl. Spectros.* 41, 241-244.
2. Dalterio, R.A., Nelson, W.H., Britt, D. and Sperry, J.F. (1987). An ultraviolet(242 nm excitation) resonance Raman study of live bacterial components. *Appl. Spectrosc.* 41, 417-422.
3. Britton, K.A., Dalterio, R.A., Nelson, W.H., Britt, D. and Sperry, J.F. (1988). Ultraviolet resonance Raman spectra of *E. coli* with 22.5-251.0 nm pulsed laser excitation. *Appl. Spectrosc.* 42, 782-788.
4. Manoharan, R., Ghiamati, E., Dalterio, R.A., Britton, K.A., Nelson, W.H. and Sperry, J.F. (1990). UV resonance Raman spectra of bacteria, bacterial spores, protoplasts and calcium dipicolinate. *J. Microbiol. Meth.* 11, 1-15.
5. Ghiamati, E., Manoharan, R., Nelson, W.H. and Sperry, J.F. (1991). UV resonance Raman spectra of *Bacillus* spores. *Appl. Spectrosc.* (accepted for publication).
6. Baek, M., Nelson, W.H. and Hargraves, P.E. (1989). Ultra-violet resonance Raman spectra of live cyanobacteria with 222.5-251.0 nm pulsed laser excitation. *Appl. Spectrosc.* 43, 159-162,
7. Manoharan, R., Ghiamati, E., Britton, K.A., Nelson, W.H. and Sperry, J.F. (1991). Resonance Raman spectra of aqueous pollen suspensions with 222.5-242.4 nm pulsed laser excitation. *Appl. Spectrosc.* 45, 307-311.
8. Peticolas, W.L., Moenne-Loccoz, P., Nelson, W.H. and Sperry, J.F. (1991). Unpublished data. To be submitted to *Applied Spectroscopy*.

9. Manoharan, R., Ghiamati, E., Nelson, W.H. and Sperry, J.F. (1991). The effect of cultural conditions on far UV resonance Raman spectra of bacteria. *J. Microbiol. Meth.* (submitted for publication).

10. Nelson, W.H. and Sperry, J.F. (1991). UV resonance Raman spectroscopic detection and identification of bacteria and other microorganisms. Ch:4, pp. 97-143 in "Modern Techniques for Rapid Microbiological Analysis" W. H. Nelson, ed., VCH Publishers, New York, N.Y.

FIGURES

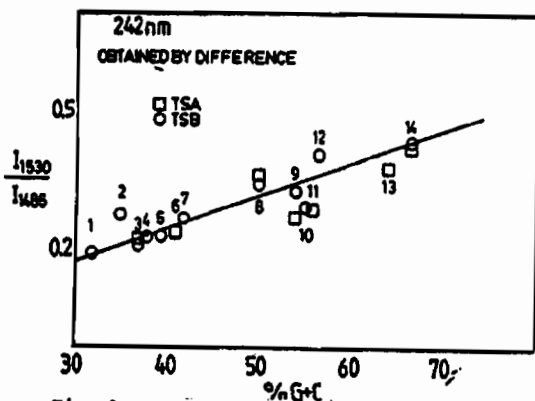


Fig. 1. A plot of I_{1530}/I_{1485} vs. known percent molar G+C for 14 bacterial species (10) grown on trypticase soy agar (TSA) or in trypticase soy broth (TSB).

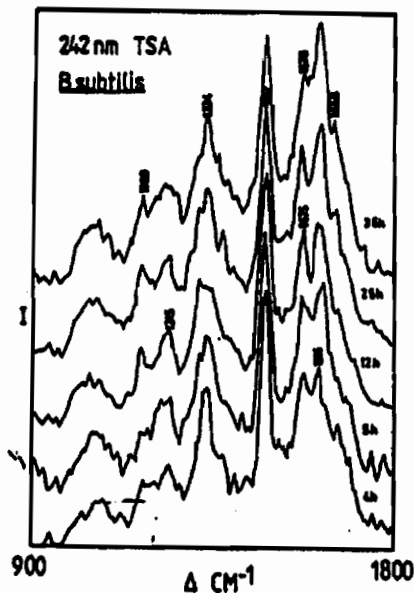


Fig. 2. Spectra excited at 242 nm showing effects of cultural age for *B. subtilis*.

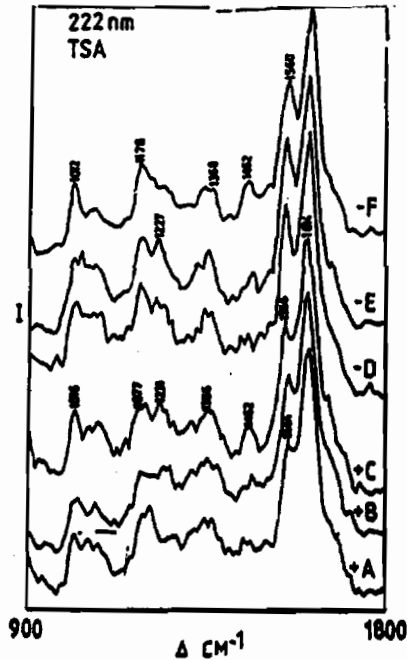


Fig. 3. Resonance Raman spectra excited at 222 nm of Gram-positive *B. megaterium*(A), *E. simulans*(B) and *B. subtilis*(C) compared with those of Gram-negative *A. hydrophila*(D), *E. aerogenes*(E) and *E. coli*(F).

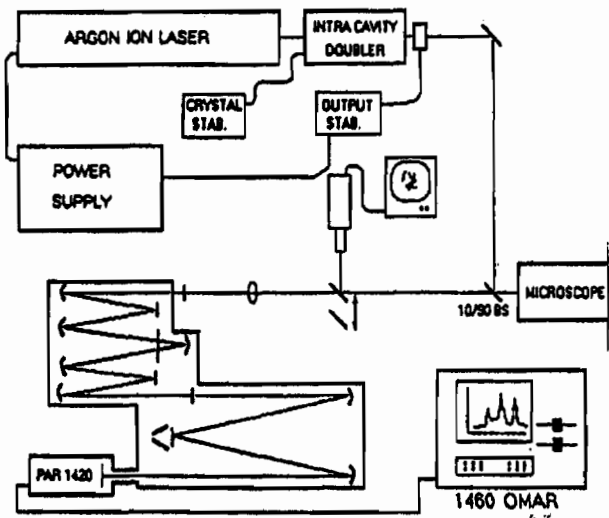


Fig. 4. Schematic representation of the UV micro-Raman system.

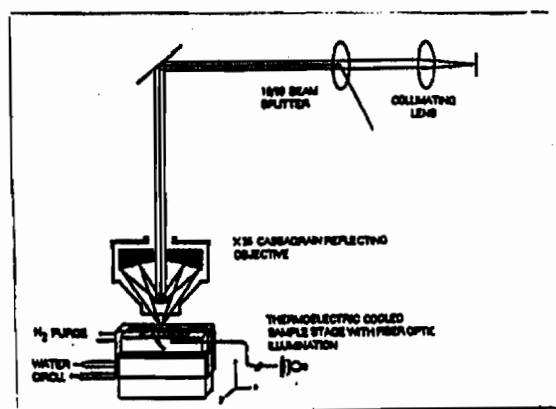


Fig. 5. Schematic representation of the micro-Raman optical system.

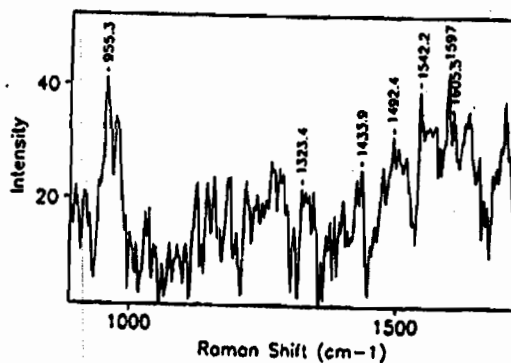


Fig. 7. Spectra of Micrococcus luteus (1 cell).

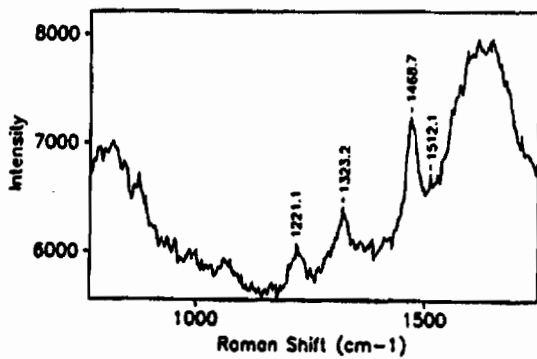


Fig. 6. Spectra of Bacillus subtilis (150 cells).

IV. TOXICOLOGY

NOTE: A paper with the following titles was presented at the Conference but is not included in this document:

The Toxicology of Chromium

BLANK

SEDATIVE, HEMODYNAMIC AND VENTILATORY EFFECTS OF FOUR DIFFERENT α_2 -
ADRENERGIC AGONISTS IN AWAKE CHRONICALLY INSTRUMENTED MINI-SWINE

Byron C. Bloor, Ph.D.
Clifford Kim, M.D.

Department of Anesthesiology
UCLA School of Medicine
Los Angeles, CA

ABSTRACT:

α_2 -Adrenergic agonists are now recognized to have sedative qualities without respiratory depression or addiction liability. Sedative, hemodynamic, and ventilatory properties of the α_2 -adrenergic agonists A-62033 (A-6) (0.01, 0.1, 1.0, & 3.5 $\mu\text{g}/\text{kg}$), YA-II-085 (YA-5), YA-II-058 (YA-8), and UK-14304 (UK) (each @ 1, 10, 100 $\mu\text{g}/\text{kg}$) were studied in chronically-instrumented Yucatan Swine. Maximum (transient) increase in blood pressure (370%) and the least anesthetic effect (13%) occurred with A-62033 while UK caused the greatest anesthetic effect (83%) with 1/3 less effect on blood pressure than A-62033. HR was decreased least by UK and most by A-62033. End tidal CO_2 was not increased by any compound: indicating that there was no respiratory depression even in the presence of marked sedation.

INTRODUCTION:

The first α_2 -adrenergic agonist was *accidentally* introduced into clinical therapeutics in 1962 as an antihypertensive, prior to knowledge of its mechanism of action or the complex profile of its qualities. As our understanding of this class of compounds has increased, it is being realized that α_2 -adrenergic agonists have many characteristics similar to the narcotic class. These effects include reduced vigilance (i.e. sedation) and analgesia.

Most of the α -adrenergic agonists are not entirely selective for either the α_1 or α_2 -adrenoceptor. An agonist that activates both receptor types can have a complex activity profile. Designing agonists that activate both α_1 and α_2 (i.e. nonselective) has been and remains beneficial when designing compounds for clinical antihypertensive use. For example, α_1 -adrenergic agonists result in arousal (i.e., amphetamine effect). The α_1 -induced arousal effect can offset the sedative effects caused by α_2 -adrenergic effects. This allows the antihypertensive effects to predominate with minimal sedation. Thus far, the majority of the interest in α_2 -adrenergic agonists has been centered on antihypertensive use, resulting in the development of compounds optimal for this specific purpose.

The realization that the highly selective α_2 -adrenergic agonists have qualities similar to the opioids and the understanding that the opioid Mu receptor and the α_2 -adrenoceptor activate similar signal transduction systems has resulted in a new explosion of activity. This has been heightened by the fact that there are benefits to be gained by exploiting the differences between these systems. In contrast to the narcotics α_2 -adrenergic agonists are anxiolytic and provide muscle flaccidity (the opioids cause muscle rigidity). More importantly, the α_2 -adrenergic agonists are without clinically-significant respiratory depression or addiction liability. This realization has now stimulated considerable research into the *non-antihypertensive* uses of α_2 -adrenergic agonists.

When focusing on the anesthetic qualities of α_2 -adrenergic agonists, there are at least 2 distinct groups of side-effects that can limit their usefulness: 1) hemodynamic changes resulting from peripheral vasoconstriction; i.e., increased blood pressure and 2) centrally-mediated hemodynamic effects

culminating in reduced blood pressure and heart rate.

At least 4 α_2 -adrenoceptor subtypes have been recognized, albeit the functional significance of these receptor subtypes is not known. It is anticipated that some, if not all, of the different effects elicited by α_2 -adrenoceptors agonists will eventually be attributable to a given α_2 -adrenoceptor subtype. In this way, side-effects may be minimized.

In an attempt to identify α_2 -agonists with different profiles of sedative and hemodynamic qualities, 4 different α_2 -adrenergic agonists were studied in chronically-instrumented Yucatan Swine.

METHODS:

All procedures were approved by both the UCLA Animal Care Committee and the CRDEC Laboratory Animal Use Review Committee. Prior to experimentation, each pig was acclimated to handling and to the laboratory environment. Each pig was surgically implanted with instrumentation to allow the measurement of cardiac and hemodynamic function.

Surgical preparation: All surgeries were performed aseptically. The animals were premedicated with atropine and ketamine (10 mg/kg) following which they were induced by mask with isoflurane (ISO) (up to 4.5%) in oxygen. Once deeply anesthetized, the trachea was intubated with a cuffed endotracheal tube, after which the animal was brought to the surgery room connected to a mechanical ventilator adjusted manually to maintain normal end-tidal pCO₂ (35 ± 5)mmHg. A catheter was inserted into an ear vein and maintenance fluids started. Blood pressure was intrasurgically monitored from an arterial catheter. End-tidal ISO level was maintained at about 2.4% to keep the animal anesthetized throughout the surgery. A left thoracotomy was performed in the fourth and fifth intercostal space to expose the heart. The aorta, pulmonary artery, azygos vein, circumflex and the left anterior descending artery were identified and isolated.

Placement of Doppler Probes: All Doppler measurements were made with a 6-channel VF-1 Pulsed Doppler Flow/Dimension System (Crystal Biotech). Pulsed Doppler blood velocity crystals were placed around the circumflex and left anterior descending coronary arteries. The cables from these probes were tunneled subcutaneously to the back just caudal to the scapula. Each cable (or catheter) was brought out through a separate exit site.

Hemodynamic Measurements: Silastic catheters were placed in the descending aorta, left atrium and azygous vein (used as a conduit to the coronary sinus). Each catheter was exteriorized. An implantable electromagnetic flow probe was placed around the pulmonary artery for continuous measurement of cardiac output.

After all instrumentation was sutured in place and tested, the animal was closed. The animal was then allowed to recover from the anesthesia under close supervision. Butorphanol (0.5 - 0.75 mg/kg i.m.), an analgesic, was given as needed for the first 3 days. The wound dressing was changed daily and the catheters aseptically flushed. Each animal was maintained on ceftriaxone antibiotic therapy for 10 days postoperatively.

Sedative and hemodynamic determinations: After the swine had recovered from the preparative surgery (at least 2 weeks), the effects of 4 synthetic alpha₂-adrenergic compounds (UK, YA-8¹, YA-5, and A-62033) were tested. The implanted probes and catheters were connected to the recording equipment with the animal positioned awake in a sling. Initially, awake baseline measurements were recorded. The swine was then anesthetized by mask using ISO (up to 4.5%) in oxygen. Once deeply anesthetized, intubated, and connected to a semi-closed anesthesia circuit the animal was allowed to breathe ISO spontaneously at approximately 1.8% in oxygen.

MAC determinations: Minimum Anesthetic Concentration (MAC) is a measure of the minimum amount of an anesthetic agent necessary to prevent a purposeful movement in 50% of the animals in response to a painful stimulus (in these studies an atraumatic tail clamp). Many agents (including potent narcotics and alpha₂-adrenergic agonists) are not capable of achieving 1 full MAC by themselves. Testing compounds in conjunction with a known anesthetic is required. To be able to quantify the sedative/anesthetic nature of an unknown compound, it is added to the known anesthetic, following which

¹ YA-II-058 is also known as medetomidine.

the known anesthetic is reduced until the same anesthetic level is achieved (1 MAC). If the known anesthetic can be removed entirely, then the unknown is considered "fully" anesthetic at 1 MAC. If only a portion, such as 50%, of the known anesthetic can be removed after being given a test agent then the unknown is only capable of producing that proportion of the anesthesia (i.e. 0.5 MAC). In this way, compounds can be measured and assigned a quantitative number as to their efficacy for sedative/anesthetic action. The known anesthetic in these experiments was ISO. The 1 MAC level was determined in each animal by standard published techniques for this laboratory.¹ This was the anesthetized (Anesth) baseline value. A dose of one of the alpha₂-adrenergic agents was then given and MAC redetermined. All hemodynamic values were recorded at all times. The reduction in the ISO requirement to maintain 1 MAC caused by an alpha₂-adrenergic agent was considered to be the anesthetic sparing effect of that agent and is reported herein as a fraction of MAC.

Example: If control MAC is 1.8% end-tidal ISO, and if after compound "A" (the alpha₂-adrenergic agent) is given, MAC is reduced to 1.1% end-tidal ISO, then the MAC fraction is $100 \times (1.8 - 1.1)/1.8 = 38.9\%$. Compound A can provide 39% of a 1 MAC anesthetic or is 39% anesthetic sparing (of ISO).

Measurements: Aortic, coronary sinus, and left atrial pressures were obtained from the implanted catheters. Cardiac output and coronary blood flow were measured by electromagnetic and pulsed Doppler methodologies respectively. End-tidal pCO₂ and ISO levels were measured by mass spectrometry (Perkin-Elmer #1100). Minute ventilation and respiratory rate were measured using a pneumotachograph (Validyne #871).

Drug delivery: All drugs were mixed in normal saline and given over 2 minutes by syringe infusion pump. UK, YA-8, and YA-5 were given at the same 3 doses: 1.0, 10 and 100 µg/kg. The three A-62033 doses given were 0.01, 0.1, and 1.0 µg/kg. These doses were selected to provide a broad dose range (3 orders of magnitude) with the lowest dose having minimal effects.

Data gathering and reporting: Continuous measurements were recorded on both a strip chart and magnetic tape recorders. Selected intervals were analyzed by computer. MAC determination require that 2 time points be used, one when the animal responds to a tail clamp stimulus, the other when the animal did not respond. All values are averaged for these 2 time points. For approximately 15 minutes surrounding the drug infusion, data was analyzed for maximum and minimum values. This allows us to report the transient hemodynamic effects. These values are reported as the "peak" values obtained during the 15 minutes after drug infusion.

Statistical analysis was performed using analysis of variance for repeated measures for intra-group differences and general linear models analysis of variance for inter-group differences. Where significance was found within or between treatment groups, Fisher's LSD was used to isolate the differences. Differences were considered to be significant if probability (p) was less than 0.05.

Results:

Anesthetic effects (see Table 1): The combined ISO baseline MAC was found to be $1.74 \pm 0.05\%$. A-6 had minimal anesthetic effects, while UK had significant effects at all dose levels. The highest dose of UK provided 82% of a 1 MAC anesthetic level.

Hemodynamic effects: The combined awake mean arterial blood pressure (MABP) was 111 ± 5 mmHg. This was significantly decreased to 72 ± 4 mmHg by 1 MAC ISO at the anesthetized baseline. MABP data is shown in Table 2. The transient (i.e. peak) increase in systemic arterial blood pressure caused by the rapid i.v. administration of the compounds studied was large, particularly for the highest dose of A-6. In a pilot study a dose of 3.5 µg/kg resulted in a MABP of 320 mmHg (estimated-transducer outside of calibrated range). This dangerously high blood pressure precluded doses over 1 µg/kg being used in this study. For all compounds by the time of the MAC determination, approximately 30 minutes following compound administration, MABP returned to a level between the awake control and the anesthetized baseline.

Heart rate (see Table 3) was increased by the ISO anesthesia when compared to the awake baseline. The largest reduction in HR occurred concomitantly with the transient increase in blood pressure. This reduction in heart rate was not associated with any cardiac dysrhythmias. Except for the 1 µg/kg dose of A-6 and the 100 µg/kg dose of YA-5 heart rate returned to a level not significantly different than the

awake control by the time of the MAC determination.

TABLE 1

	0.01 µg/kg	0.1 µg/kg	1 µg/kg	10 µg/kg	100 µg/kg
Compound	Dose 1	Dose 2	Dose 3		
A62033	11% ± 7%	11% ± 3%*	13% ± 8%*		
			Dose 1	Dose 2	Dose 3
YA-II-085			9% ± 4%	15% ± 2%*	37% ± 9%*
YA-II-058			4% ± 4%	20% ± 5%*	57% ± 2%*
UK-14304			20% ± 5%*	52% ± 4%*	82% ± 5%*

TABLE 1. The anesthetic sparing action expressed in % of a 1 MAC anesthetic (mean ± SEM) for the 3 doses of each of the 4 compounds tested. ★ = p<0.05. 100% would indicate a full 1 MAC anesthetic.

TABLE 2

Compound	Awake BL	Anes BL	Dose 1 @ Peak	Dose 1 @ MAC	Dose 2 @ Peak	Dose 2 @ MAC	Dose 3 @ Peak	Dose 3 @ MAC
A62033	118±11	68±6*	75±2*	82±6*	117±5	73±6*	176±21*	91±9*
YA-II-085	117±5	75±2*	89±2*	86±6*	115±13	74±7*	128±8	78±4*
YA-II-058	106±2	73±5*	93±8	82±5*	122±10*	76±6*	154±6*	107±5
UK-14304	101±2	71±4*	89±3*	77±5*	119±3*	84±3*	156±3*	96±4

TABLE 2. The mean arterial blood pressure (mmHg; mean ± SEM) is shown during the Awake Baseline (BL), the anesthetized (Anes) BL, and the 3 dose levels for the 4 compounds studied. The values shown at "peak" are taken during the maximal MABP change after the compound was given. Values shown at "MAC" are the values during the MAC determination (approximately 30 minutes after dose delivery). ★ = significantly different that awake baseline, p<0.05.

TABLE 3

Compound	Awake BL	Anes BL	Dose 1 @ Peak	Dose 1 @ MAC	Dose 2 @ Peak	Dose 2 @ MAC	Dose 3 @ Peak	Dose 3 @ MAC
A62033	108±7	128±11*	98±7	112±10	91±8	100±8	49±5	85±6*
YA-II-085	114±10	125±10	111±12	124±11	86±7*	110±6	78±7*	99±12*
YA-II-058	94±3	112±3	93±12	105±4	81±14	99±6	59±10*	72±6
UK-14304	83±8	108±3	96±2	100±2	60±4	87±9	44±10*	84±21

TABLE 3. The heart rate (beats/min; mean ± SEM) is shown during the Awake Baseline (BL), the anesthetized (Anes) BL, and the 3 dose levels for the 4 compounds studied. The values shown at "peak" are taken during the maximal MABP change after the compound was given. Values shown at "MAC" are the values during the MAC determination (approximately 30 minutes after dose delivery). ★ = significantly different that awake baseline, p<0.05.

Cardiac output (see Table 4) was also increased by 1 MAC ISO anesthesia. Simultaneously with the peak increase in MABP caused by these compounds, cardiac output decreased markedly in the highest dose groups. The compounds with the largest effects were A-6 and UK the compounds with the largest increase in MABP. Similar to other hemodynamic parameters measured, following the transient rise in blood pressure CO also moved toward normal by the time of MAC determination.

TABLE 4

Compound	Awake BL	Anesth BL	Dose 1 @ Peak	Dose 1 @ MAC	Dose 2 @ Peak	Dose 2 @ MAC	Dose 3 @ Peak	Dose 3 @ MAC
A62033	1.6±0.2	2.0±0.3	1.5±0.1	2.0±0.2	1.0±0.2*	1.6±0.1	0.4±0.1*	1.4±0.2
YA-II-085	1.4±0.1	1.8±0.3	1.6±0.3	1.9±0.2	1.0±0.2*	1.9±0.3	0.9±0.3*	1.6±0.1
YA-II-058	2.3±0.2	2.0±0.3	1.6±0.3	2.1±0.2	1.6±0.3*	2.1±0.3	0.9±0.2*	1.7±0.2*
UK-14304	2.0±0.3	1.6±0.3	1.0±0.4*	1.4±0.3	0.8±0.3*	1.4±0.3*	0.6±0.3*	1.0±0.2*

TABLE 4. The cardiac output (liters/min; mean ± SEM) is shown during the Awake Baseline (BL), the anesthetized (Anes) BL, and the 3 dose levels for the 4 compounds studied. The values shown at "peak" are taken during the maximal MABP change after the compound was given. Values shown at "MAC" are the values during the MAC determination (approximately 30 minutes after dose delivery). ★ = significantly different that awake baseline, $p < 0.05$.

Coronary blood flow was generally unchanged except for a transient decrease during the peak effect of the 10 and 100 µg/kg doses of YA-5 and YA-8.

Ventilatory effects: Minute ventilation was not changed by any compound except for the highest dose of A-6 where ventilation was significantly elevated. End-tidal CO₂ (see Table 5) was significantly elevated by ISO anesthesia alone. End-tidal CO₂ was not elevated by any compound above the anesthetized baseline. End-tidal CO₂ did return to a level not significantly different from control (except for A-6) by the highest dose.

TABLE 5

Compound	Awake BL	Anesth BL	Dose 1 @ MAC	Dose 2 @ MAC	Dose 3 @ MAC
A62033	3.7±0.3	4.8±0.3	4.0±0.1	4.2±0.3	4.9±0.2
YA-II-085	4.0±0.3	5.1±0.2	4.8±0.2	4.5±0.3	4.6±0.3
YA-II-058	3.6±0.3	5.9±0.6	5.9±0.6	5.9±0.8	5.3±0.8
UK-14304	3.5±0.2	5.7±0.7	5.0±0.6	4.3±0.6	4.1±0.6

TABLE 5. The end-tidal CO₂ (%; mean ± SEM) is shown during the Awake Baseline (BL), the anesthetized (Anes) BL, and the 3 dose levels for the 4 compounds studied. The values shown at "peak" are taken during the maximal MABP change after the compound was given. Values shown at "MAC" are the values during the MAC determination (approximately 30 minutes after dose delivery). ★ = significantly different that awake baseline, $p < 0.05$.

DISCUSSION: The four α_2 -adrenergic agonists studied demonstrated different profiles with regard to sedative and hemodynamic effects (see Table 6). The anesthetic effects were studied by determining the required dose of a known anesthetic, ISO, to produce 1 MAC anesthesia^{1,2} and then redetermining the ISO dose requirement to maintain a 1 MAC anesthetic level after administering the test compound. With these test compounds the reduction in the ISO requirements ranged from virtually nothing for A-6 to 82% for the 100 $\mu\text{g}/\text{kg}$ dose of UK (see Tables 1 and 6 for a comparison). Due to the time necessary for ISO washout, a maximum of a 90% reduction in anesthetic requirement can be measured by this technique. The effects of the UK approached this limitation.

ISO in anesthetic concentration is a known vasodilator, thus the decrease in MABP from 111 (awake baseline) to 72 mmHg (anesthetized baseline). The ISO-induced vasodilation also resulted in an increase in cardiac output and a reflex-induced increase in heart rate. α_2 -Adrenergic agonists are known vasoconstrictors. The 4 compounds studied resulted in a wide range of pressor effects. YA-5 had peak MABP elevations which brought the animals blood pressure back to the awake level; i.e., had little effect. A-6 was the most potent vasoconstrictor. In doses 1/100th of the other compounds, it resulted in largest systemic blood pressure increases. At slightly higher doses, 3.5 $\mu\text{g}/\text{kg}$, MABP was increased to almost lethal levels. Increases in blood pressure result in a baroreceptor-mediated reduction in heart rate. The transient increases in blood pressure (i.e. at peak blood pressure change) were associated with a concomitant reduction in heart rate and a reduction of cardiac output. These transient peripherally-mediated effects on blood pressure were the most concerning effects found and most likely could have been eliminated by a slower dose administration.

α_2 -adrenergic agonists result in a centrally mediated reduction in blood pressure, which is limited to the extent that blood pressure is dependant on sympathetic tone. In these ISO anesthetized pigs no further reduction in blood pressure was found to result from administration of the α_2 -adrenergic agonists studied, suggesting a low sympathetic tone, consistent with the known effects of ISO-anesthesia. α_2 -adrenergic agonists are also known to decrease heart rate through a vagally-mediated mechanism. This effect was present; however, heart rates remained above 70 beats/min, presenting no physiologic problems (i.e. at the time of MAC determinations). The observed reduction in cardiac output is likely due to reduced metabolic demand.

ISO is known to cause mild ventilatory depression. This was evidenced by the increase in end-tidal CO_2 measured at the time of the anesthetized baseline. The addition of the α_2 -adrenergic agonists resulted in less ISO being needed to maintain 1 MAC anesthesia. The reduction in the elevated end-tidal CO_2 by the α_2 -adrenergic agonists in this study is consistent with the evidence that these compounds by themselves are not respiratory depressants^{3,4}. When the ISO requirement was reduced by the α_2 -adrenergic agonists, less ISO-induced ventilatory depression was present, resulting in the end-tidal CO_2 returning toward normal.

Although this study demonstrated differing profiles of effects for the 4 α_2 -adrenergic agonists studied, it does not suggest the mechanism(s) producing these differences. Futures studies will have to be carried out to explain why these differences exist. These studies should include examining the extent these compounds activate α_1 -adrenoceptors and their ability to penetrate the CNS. For example, A-6 may have it's marked vasopressor action partially through an α_1 -adrenoceptor and not have much sedative action because it does not penetrate the CNS as well as other compounds. Conclusions regarding selectivity toward α_2 -adrenoceptor subtypes and functions will have to wait until these and other possible explanations are addressed.

TABLE 6

Compound	Maximum Anesthetic Effect	Maximal Sustained Blood Pressure Change	Maximal Sustained Cardiac Output Change	Maximal Sustained Heart Rate Change
A-62033	13%	-23%	-13%	-21%
YA-II-085	37%	-33%	+14%	-13%
YA-II-058	55%	0%	-26%	-23%
UK-14304	82%	-5%	-50%	-0%

TABLE 6. Summarizes the maximum changes seen for sedation, MABP, cardiac output, and heart rate for the 4 compounds studied. Values are expressed as the mean % change from the awake baseline.

CONCLUSIONS

The 4 α_2 -adrenergic agonists studied demonstrated a widely differing profile of sedative and hemodynamic effects. Rapid injection of these compounds produced transient increases in blood pressure and decrease in heart rate lasting less than 30 minutes. Slower administration would minimize these effects. Only slight sustained changes in blood pressure were found. A-6, the compound with the largest effect on blood pressure was remarkably (100 times) more potent in hemodynamics effects than the other compounds studied. A dose (outside this study) of 3.5 $\mu\text{g}/\text{kg}$ resulted in potentially lethal blood pressures. Doses of 100 $\mu\text{g}/\text{kg}$ of the other 3 compounds resulted in sustained increases in mean blood pressure of 4 to 44% by comparison to the anesthetized baseline. A-6, the compound with largest blood pressure effects, had the least anesthetic effect (maximally 13%). UK had a marked anesthetic effect yielding 82% of a full 1 MAC anesthesia. This compound had the least sustained changes in blood pressure or heart indicating that if the drug had been given more slowly the initial changes could have been avoided. The reduction in CO is consistent with reduced metabolic requirements produced by the UK-induced anesthesia. No ventilatory depressant effects of these compounds were found.

REFERENCES

1. Bloor BC, Flacke WE. Reduction in halothane anesthetic requirement by clonidine, an alpha-adrenergic agonist. *Anesth Analg* 1982; 61:741-745.
2. Eger EI, Saidman LJ, Brandstater B. Minimum Alveolar Anesthetic Concentration: A Standard of Anesthetic Potency. *Anesthesiology* 1965; 26:756-763.
3. Bloor BC, Abdul Rasool I, Temp J, Jenkins JS, Valcke C, Ward DS. The effects of medetomidine, an alpha₂-adrenergic agonist, on ventilatory drive in the dog. *Acta Veterinaria Scandinavica* 1989; 4:65-70.
4. Belleville JP, Ward DS, Bloor BC, Maze M. Ventilatory effects of dexmedetomidine in humans. *Anesthesiology* 1990; 73:A1167.(abstract)

BLANK

EFFECTS OF SUFENTANIL AND NALMEFENE ON THE AUDITORY BRAINSTEM RESPONSE (ABR) IN THE FERRET

Sharon A. Reutter and Robert J. Mioduszewski

Toxicology Division, US Army CRDEC, APG, MD

ABSTRACT

ABRs were used to monitor effects of the anesthetic, sufentanil, and the opiate antagonist, nalmeferene, on brainstem activity, in order to prove the hypothesis that ABRs reflect respiratory depressant effects of sufentanil. Adverse effects on transmission, amplitude, and morphology were reversed by nalmeferene. Reversal of effects paralleled reversal of respiratory depression. Dynamic changes in amplitude and morphology were interpreted as reflections of central nervous system drug levels; however, they did not mirror peripheral plasma levels. Electrophysiological confirmation is provided of nalmeferene antagonism of respiratory depressant effects of sufentanil. Peripheral plasma levels are not a good indicator of adverse brainstem effects.

BACKGROUND

Synthetic opiates, such as sufentanil, are potent, rapidly acting anesthetics. Sufentanil is widely used as an anesthetic agent for humans, but its usefulness is somewhat limited because it produces apnea (cessation of respiration) as an undesirable side effect. Nalmeferene is a long-acting opiate antagonist.

Although it is generally accepted that ABRs are relatively refractory to drug effects¹, it was hypothesized that ABRs would reflect the respiratory-depressant effects of sufentanil and that they would provide electrophysiological confirmation of nalmeferene antagonism of those adverse effects. The hypothesis was predicated by: 1) studies of premature human infants^{2,3} in which it was demonstrated that ABRs are abnormal in children who are subject to apnea and 2) recent studies of the effects in ferrets of carfentanil, another synthetic opiate, in which it was shown that carfentanil produces ABR abnormalities similar to those reported for human infants subject to apnea^{4,5}.

MATERIALS AND METHODS

Neutered, descended male ferrets (Marshall Farms) were surgically implanted with vascular access ports for intravenous (IV) injection and permitted to recover for at least one week. Sodium pentobarbital was obtained from Sigma. Sufentanil (N-(4-(methoxymethyl)-1-[2-(2-

thienyl) ethyl]-4-piperidiny]-N-phenylpropanolamide-2-hydroxy-1,2,3-propane-tricarboxylate) and nalmefene (17-(cyclopropylmethyl)-4,5-epoxy-3,1,4-dihydroxymorphinan-6-methylene) were provided by the Organic Chemistry Branch, Chemical Division, Research Directorate, U.S. Army Chemical, Research, Development, and Engineering Center, APG, MD. Baseline ABRs were recorded under pentobarbital anesthesia (30 mg/kg, intraperitoneal injection), and the animals were permitted to recover for at least one week. One group received sufentanil alone (10, 31, 100, 318, 1000, or 3180 ug/kg, IV). The other group received a cocktail of sufentanil and nalmefene (15:1 molar ratio; doses of sufentanil as above). Blood samples were drawn at 2, 10, 30, and 60 minutes post-injection for analysis of plasma sufentanil and nalmefene concentrations by sensitive and specific radioimmunoassay procedures at Harris Laboratories, Inc., Lincoln, NB. Four animals were tested at each dose. ABR testing was not complete on all animals because of limited sleep time at some doses. Body temperature was monitored via a rectal temperature probe with an analog display (Yellow Springs Instrument Co.) and recorded at five minute intervals. Ventilatory function was monitored with an "Oxymax" system⁶, beginning at 20 min post-injection. Respiratory pauses were considered to be "apnea" when breathing stopped for at least 10 sec on at least two occasions during a one minute measurement period.

ABRs were recorded non-invasively with standard clinical scalp electrodes, affixed with "EC-2" cream (Grass), using a Bio-logic "Navigator" system. Impedances averaged 3 kOhms. A notch filter and artifact rejection were employed; linear filters were set at 100 and 3000 Hz; amplification was about 100,000. The electrode montage was "vertex" (defined as the intersection between the posterior corners of the eyes and the medial attachments of the ears) referenced to the right ear. The stimulus was a 19/sec rarefying click delivered to the right ear by a tubal insert ear phone. The stimulus intensity was varied between 95 and 0 dB; the auditory threshold was determined for each animal. Animals with abnormal Baseline ABRs were excluded from the study. All responses were replicated.

The major components of the response (Fig. 1) were manually identified and labelled using cursors within the system. Calculations of peak latencies were automatically performed. Data were plotted off-line. Quantitative data analysis for statistical treatment focused upon the first set of 95 dB, 85 dB, and 75 dB responses recorded post-injection. (Salient findings were not intensity-dependent.) Subsequent response pairs were qualitatively analyzed for changes over time. The parameters which were measured were brainstem transmission time (BST), peak amplitudes, and peak latencies (Fig. 1). Morphology of responses was observed, but not quantitated. Statistical analysis was performed using the t-test and linear regression functions of the "Minitab" program on the VAX mainframe.

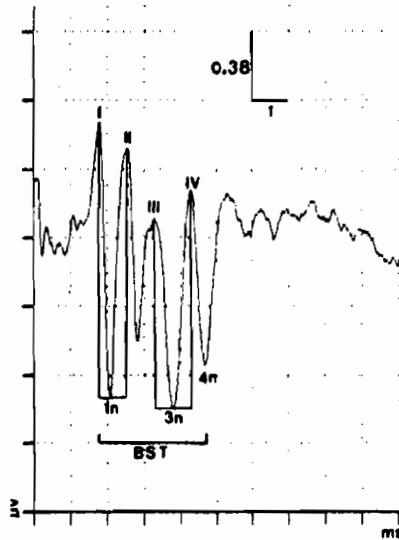
FINDINGS

Clinical. With co-administration of sufentanil and nalmefene no apnea was observed and no deaths occurred—even at the highest dose, 3180 ug/kg, which is approximately 10 times the LD₅₀. Although anesthesia was achieved, sleep time was markedly reduced by nalmefene.

Brainstem transmission time. Effects on BST at 20 min post-injection were reported earlier⁷. Dose-response effects were minimal when analyzed as a whole; however, analysis of high (3180 ug/kg) and low (31 ug/kg) doses in the same animals (n = 3) did reveal significant differences between those doses (data not shown) for the later time points (t ≥ 40 minutes). Since there were no significant dose effects for the first sets of responses (t ~ 20 minutes) the data were averaged across doses. Sufentanil significantly prolonged the BST. This was reversed by co-administration of nalmefene. BSTs were even shorter with sufentanil plus nalmefene than for Baseline responses (Table 1)! Although the data were somewhat confounded by temperature differences between the groups, Baseline BSTs for the two groups were virtually identical, even though the temperatures were significantly different (100.4 vs 99.7; p < < 0.0001).

Moreover, analysis of changes in the BST over time with temperature decrement (Fig. 2) revealed a fairly consistent shift to the right--increased BST with sufentanil.

Figure 1



NORMAL AUDITORY BRAINSTEM

RESPONSE. Ferret 64, pentobarbital anesthesia, 95 dB stimulus. The horizontal axis is measured in milliseconds, as represented by the grid. The vertical axis is measured in fractions of microvolts, as represented by the grid. Brainstem transmission time (BST) was measured as the time interval between waves I and 4n. Amplitudes were measured as follows: wave I--from I to 1n; wave II--from II to 1n; wave III--from III to 3n; wave IV--from IV to 4n. The "amplitude index" is the sum of the individual amplitudes of the four peaks.

Table 1

95 dB BRAINSTEM TRANSMISSION TIME

Baseline	(n)	Sufentanil	(n)	Baseline	(n)	Sufentanil plus Nalmefene	(n)
3.05±0.03	(22)	*3.28±0.04	(17)	3.04±0.03	(18)	#@2.94±0.04	(18)

* significantly longer than Baseline; p = 0.000

@ significantly shorter than Sufentanil; p = 0.000

significantly shorter than Baseline+; p = 0.043

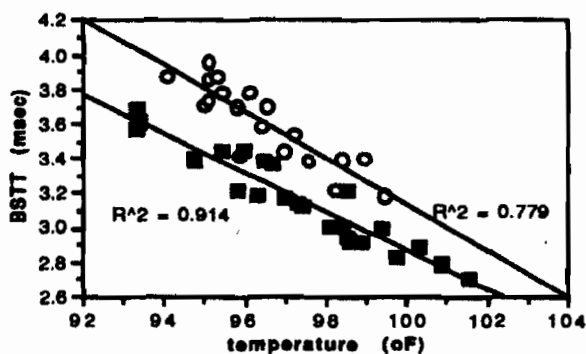
Key: mean±standard error
BST in msec

Amplitude and morphology. An "Amplitude Index" for each response was derived by adding together the individual amplitudes of the four peaks (Fig. 1). To compensate for the (expected and) observed inter-individual variation, response amplitudes were normalized by dividing by the Baseline amplitude index for the appropriate stimulus intensity. The drug-induced effects were very complex. There was no clear-cut dose or drug effect--either for sufentanil alone or for the sufentanil-nalmefene cocktail (Fig. 3). However, similar to the findings observed for the BST, animals that received two different doses of sufentanil exhibited more pronounced or opposite effects at the higher dose (Fig. 4). Similar observations were made with the cocktail and (data not shown). The most marked changes in amplitude were observed at the two higher doses of the cocktail (Fig. 3). Under both conditions dynamic changes in amplitude and morphology were observed throughout the recording period; this was

not seen under Baseline (control) conditions. Some animals exhibited amplitude enhancement, ranging from slight to profound (Figs. 3-5). In such cases, response morphology was usually better than observed on Baseline recordings (Figs. 4,5), and auditory thresholds were often lower. Other animals had amplitude depression, ranging from mild to severe (Figs. 3-5). This was usually accompanied by deteriorating response morphology and increasing auditory thresholds. Still other animals had initial amplitude depression, followed by amplitude enhancement and improved response morphology (Fig. 5). Subjectively there was good correlation between the clinical condition of the animals and the morphology and amplitude of the responses; animals that were in poor condition had poor responses.

Plasma drug levels. Plasma levels did not correlate with real time changes in amplitude and morphology observed during the recording session (Figs. 6,7; data not shown for all doses). No correlation was noted between BST and plasma levels of drug.

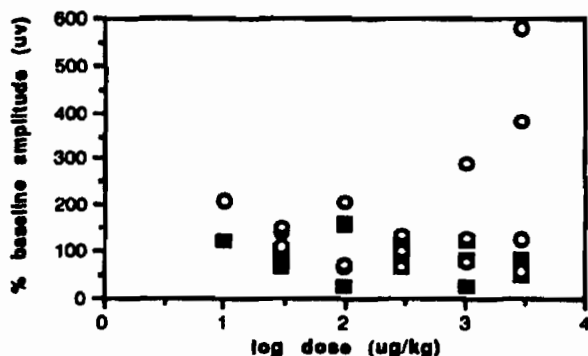
Figure 2



EFFECTS OF BODY TEMPERATURE ON BRAINSTEM TRANSMISSION TIME.

Filled symbols = data points recorded under pentobarbital anesthesia. Open symbols = data points recorded following administration of 3180 ug/kg sufentanil. A consistent shift to the right was observed at all doses (data not shown). However, at the lower doses of sufentanil, the correlation between body temperature and BST diminished markedly. The reasons for this were unclear.

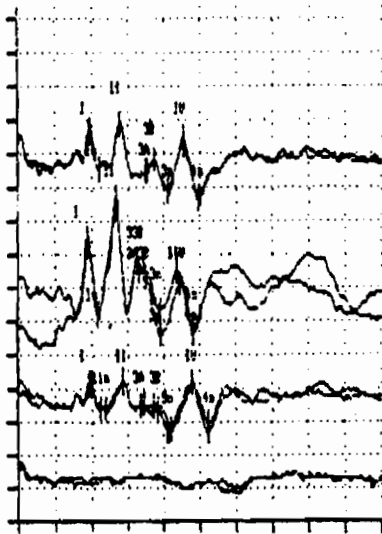
Figure 3



EFFECTS OF DOSE ON AMPLITUDE, 20 minutes post-injection.

Closed symbols =sufentanil. Open symbols = sufentanil plus nalmeferene. Marked inter-individual variability is demonstrated by amplitude enhancement for some animals and amplitude depression for others. Individual amplitude enhancement with sufentanil alone tended to be more marked at the lower doses (especially at later time points). Individual amplitude enhancement with the cocktail was most pronounced at the higher doses.

Figure 4

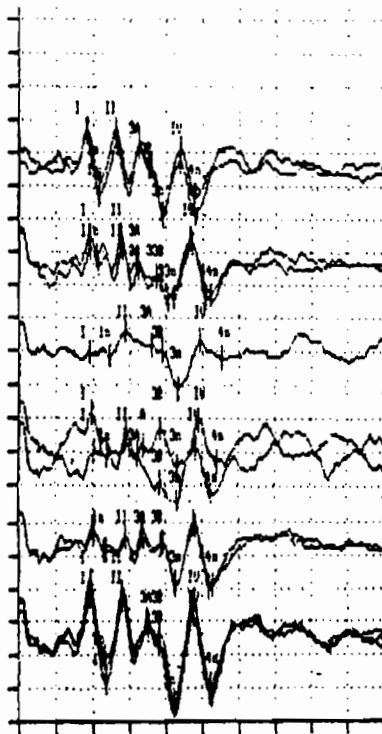


DOSE EFFECTS ON ABR AMPLITUDE AND MORPHOLOGY.

Ferret 67, 75 dB stimulus.

The first tracing is the Baseline; the next is the response following 10 µg/kg sufentanil (~ 20 minutes post-injection); the last two tracings are the responses following 1000 µg/kg sufentanil (20 and 40 minutes post-injection, respectively). Note the marked amplitude enhancement at the lower dose. At the higher dose the amplitude was initially depressed and then deteriorated further until the response was lost. The animal was dead the next morning (the time of death is unknown).

Figure 5



DYNAMIC CHANGES IN AMPLITUDE AND MORPHOLOGY.

Ferret 836, 75 dB stimulus.

The first tracing is the Baseline, followed by recordings (in order) from 20-60 minutes post-injection with 100 µg/kg sufentanil. Note the initial deterioration of amplitude and morphology, followed by further deterioration and lack of reproducibility, then progressive recovery with ultimate enhancement of amplitude and morphology.

SUMMARY AND CONCLUSIONS

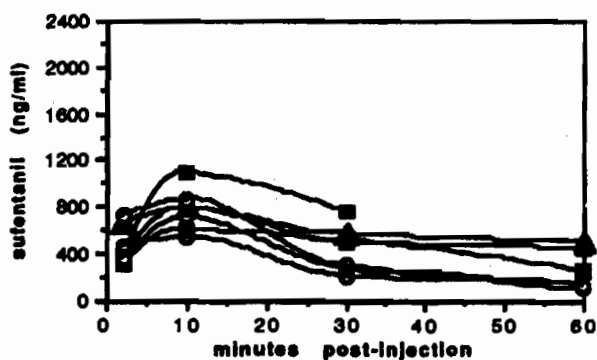
Sufentanil adversely affects ABRs in the ferret, as evidenced by prolongation of the BST. The effect is interpreted as a reflection of general brainstem depression. This interpretation is supported by the finding that no apnea was observed with co-administration of nalmeferne, and there was no prolongation of BST.

Sufentanil has a secondary effect on ABRs--amplitude enhancement and/or depression. Although a dose effect cannot be directly demonstrated, amplitude enhancement appeared to occur at lower concentrations--either lower administered sufentanil doses, effective sufentanil doses reduced by nalmeferne, or reduced levels within the central nervous system (CNS) as the drug was apparently metabolized. Amplitude enhancement appeared to be somewhat exacerbated by nalmeferne.

Peripheral plasma concentrations did not correlate in a real time manner with apparent drug levels within the CNS, as evidenced by ABRs. This interpretation is supported by the fact that dynamic changes in amplitude and morphology were observed when peripheral plasma levels were at a relatively steady state and by the correlation between morphology and clinical condition of the animal.

In summary: 1) ABRs have been demonstrated to be a potentially useful clinical tool when respiratory centers may be compromised. 2) Electrophysiological confirmation is provided of antagonism by nalmeferne of adverse effects of sufentanil on the brainstem. 3) Peripheral plasma levels may not reflect effective drug levels within the CNS. 4) ABRs may be a useful intra-operative tool for evaluating effective CNS levels of sufentanil and similar agents.

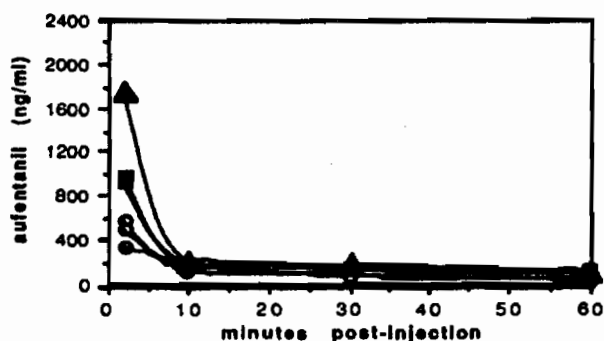
Figure 6



PLASMA LEVELS OF SUFENTANIL FOLLOWING ADMINISTRATION OF 1000 UG/KG SUFENTANIL OR SUFENTANIL PLUS NALMEFENE.

Closed symbols = sufentanil; open symbols = sufentanil cocktail; triangles = Ferret 67 (Fig. 4). Contrast this figure (6) with the time course in Figure 4. Note that Ferret 67's amplitude and morphology for the 1000 ug/kg dose are better when the peripheral plasma levels were higher, rather than lower.

Figure 7



PLASMA LEVELS OF SUFENTANIL FOLLOWING ADMINISTRATION OF 100 UG/KG SUFENTANIL OR SUFENTANIL PLUS NALMEFENE. Closed symbols = sufentanil; open symbols = sufentanil cocktail; triangles = Ferret 836 (Fig. 5). Contrast this figure (7) with the time course in Figure 5. Note that the peripheral plasma levels were relatively constant while the ABRS underwent marked depression and then enhancement.

REFERENCES

1. Stockard, J.J., Stockard, J.E., and Sharbrough, H.W.: Non-pathologic factors influencing brainstem auditory evoked potentials, Am. J. EEG Technol., 18:177-209, 1978.
2. Henderson-Smart, D.J., Pettigrew, A.G., and Campbell, D.J.: Clinical apnea and brain stem neural function in preterm infants. N. Engl. J. Med., 308:353-357, 1983.
3. Reutter, S.A.: Brainstem Evoked Responses and Apnea in Preterm Infants, Ph.D. Dissertation, George Washington, Univ., Washington, D.C., 1985.
4. Reutter, S.A., Legaspi, N.Q., Armstrong, R.D., and Mioduszewski, R.J.: Effects of carfentanil on auditory brainstem responses (ABRs) in ferrets, Proceedings of the 1989 U.S. Army Chemical Research, Development and Engineering Center Scientific Conference on Chemical Defense Research 14-17 November, 1989, pp 911-916, CRDEC-SP-024, August 1990.
5. Reutter, S.A. and Mioduszewski, R.J.: Effects of carfentanil on auditory brainstem responses (ABRs) in ferrets. The Toxicologist, 10:306, 1990.
6. Mioduszewski, R.J. and Reutter, S.A.: Dissociation of opiate-induced sedation and respiratory depression in ferrets by opiate antagonist coadministration: potential pharmacological mechanisms, Proceedings of the 1991 U.S. Army Chemical Research, Development and Engineering Center Scientific Conference on Chemical Defense Research 19-22 November, 1991.
7. Reutter, S.A., Mioduszewski, R.J., Legaspi, N.Q., Armstrong, R.A., and Pullen, R.: Effects of sufentanil and nalmefene on brainstem transmission in the ferret, Proceedings of the 1990 U.S. Army Chemical Research, Development and Engineering Center Scientific Conference on Chemical Defense Research 13-16 November, 1990.
8. Rossi, G.T. and Britt, R.H.: Effects of hypothermia on the cat brain-stem auditory evoked response. Electroenceph. Clin. Neurophysiol., 57:143-155, 1984.

BLANK

EVALUATION OF CHLOROPENTAFLUOROBENZENE AS AN INTAKE SIMULANT
Bruce M. Jarnot and Harvey J. Clewell III, Toxicology Division,
Armstrong Laboratory (AL/OET), Wright Patterson AFB OH

ABSTRACT

The U.S. Air Force has been actively developing safe intake simulants for chemical warfare agents, to provide accurate and quantitative real-time assessment of troop proficiency and gear efficacy during CW field exercises. Chloropentafluorobenzene (CPF₅B) was identified and evaluated as a candidate inhalation simulant, and was determined to possess desirable physicochemical and toxicological properties. These include rapid uptake, low metabolism and toxicity, rapid and predictable clearance, detectability by existing portable "breathalyzer" technology and by fielded CWA detectors, realistic canister breakthrough, and commercial availability.

INTRODUCTION

The US Air Force and other NATO agencies have programs for the development of intake simulants to live agents for use in chemical warfare training exercises. These intake simulants will allow quantitative assessment of troop proficiency and chemical defense gear efficacy. Inhalation simulants provide information on inhalation exposure, primarily assessing proficiency of mask use. Current intake simulants, such as methyl salicylate rely on troop feedback by sense of smell, and do not allow for quantitative and objective determination of exposure. For the past several years the Air Force has been developing candidate uptake simulants that would allow objective quantitation of inhalation exposure, allowing real-time prediction of decrement in performance had the exposure been to a live agent.

BACKGROUND

In a 1982 study funded by the Air Force, A. D. Little developed a list of candidate chemical simulants for the agents sarin, soman, and tabun¹. Vapor pressure was used as the initial screening criteria, with acceptable candidates designated as volatile (0.27-2.1 mmHg), intermediate (0.03-0.27), low (0.0001-0.03), or non-volatile (less than 0.0001). From available sources, a list of 120 compounds falling into one of the four vapor pressure categories was compiled. These candidates were further screened through a literature search based on chemical properties, available toxicological data, and detection in body fluids. The list was narrowed to seven candidates: Four volatile (dimethyl sulfoxide, dipentene, butanethiol, and hexanethiol) and three intermediate (methyl benzoate, benzyl alcohol, and octanoic acid). While none of the compounds fully met all Air Force specified criteria, all had documented approved human exposure. A more exhaustive search for compounds having low or intermediate vapor pressure yielded six chemicals which met a majority of physical criteria and had low toxicity: diethyl sebacate, dibenzyl ether, isoamyl benzoate, amyl phenylacetate, n-octyldecanethiol, and phenylethyl phenylacetate². During this period, the Air Force Toxic Hazards Division also evaluated the toxicological risk associated with dimethylmethylphosphonite (DMMP), which had been proposed as a general Air Force training simulant. Possessing similar physical characteristics to organophosphate nerve agents, detectability with agent field detectors, and having low acute toxicity, DMMP appeared to be an ideal agent simulant. However, toxic effects seen after longer-term exposure, including testicular atrophy in rodents³, precluded its use on troops. The compounds identified by A. D. Little as candidate simulants all failed to satisfy the minimal criteria for an acceptable uptake simulant when

re-evaluated by the Air Force. The primary deficits involved detectability and biological inertness; due to extensive and often complex metabolism, it would not be possible to quantify exposure by measuring the compound or a single metabolite in a bodily fluid. Rather than continue to screen the literature for acceptable compounds, an alternate approach was developed: the requirements for a simulant would be defined, and a compound developed to meet these criteria⁴. In particular, selection was to be based on:

- resistance to biological metabolism;
- partitioning properties between air, blood, and tissues;
- physical characteristics (to generate realistic exposures);
- detectability in low concentration.

INTAKE SIMULANT DEVELOPMENT

Perfluorocarbons were initially chosen as the class of compounds to be investigated based on their relative detectability and biological inertness. It was determined, however, that perfluorocarbons were not sufficiently taken up by biological tissues to serve as an intake simulant, so compounds in which one or more of the fluorines was replaced by another halogen were also investigated. Replacement of a fluorine by bromine significantly increased tissue solubility, but also led to rapid metabolism. Substitution with chlorine instead of bromine gave compounds with intermediate properties. Of the seven commercially available fluorohalocarbons evaluated in the study⁴, chloropentafluorobenzene (CPF_B) was identified as the most promising candidate, providing good detectability, desirable partitioning characteristics, relative biological inertness, and acceptable physical properties.

Figure 1 shows the results of gas uptake analysis of CPF_B. In the gas uptake analysis, several animals are maintained in a closed chamber, and the air is continuously recirculated. Oxygen is replenished and carbon dioxide is scrubbed as necessary to maintain stasis. A known amount of a volatile chemical is then added to the chamber, and the concentration of the chemical in the chamber is monitored over time. The rapid initial decline in the chamber concentration of CPF_B seen in Figure 1 is due to uptake by the animals' tissues and demonstrates that CPF_B is readily absorbed. Following the tissue uptake phase, any further decline in chamber concentration would indicate loss of chemical due to metabolism. The fact that the concentration curve for CPF_B almost levels out after the first few hours reflects the fact that CPF_B is not extensively metabolized. By way of comparison, the chamber concentration of bromopentafluorobenzene decreased by more than 20% between hours 3 and 6 under the same conditions. A physiologically based pharmacokinetic (PB-Pk) model for CPF_B was developed, and the closed chamber data was analyzed to quantify the rate of metabolism. It was determined that metabolism was first-order, with a rate constant of 2/hr⁴.

SIMULANT EVALUATION: PHYSICAL PROPERTIES

As shown in Table 1, CPF_B is a volatile, non-flammable liquid with a very high vapor density (which helps to prevent excessive vertical dispersion when released). It is unreactive and is compatible with essentially all materials; therefore it does not present any unusual storage or handling difficulties.

Table 1: Physical Properties of CPF_B

Chemical State (20°C)	colorless liquid
CAS Registry Number	344-07-0
Chemical Formula	C ₆ ClF ₅
Molecular Weight	202.51
Boiling Point (°C)	102.0
Flash Point (°C)	not flammable
Liquid Density (g/ml)	1.66
Vapor Density (x air)	7.0
Vapor Pressure (mmhg, 20°C)	14.1
Volatility (mg/m ³)	1.53 x 10 ⁵

FIGURES

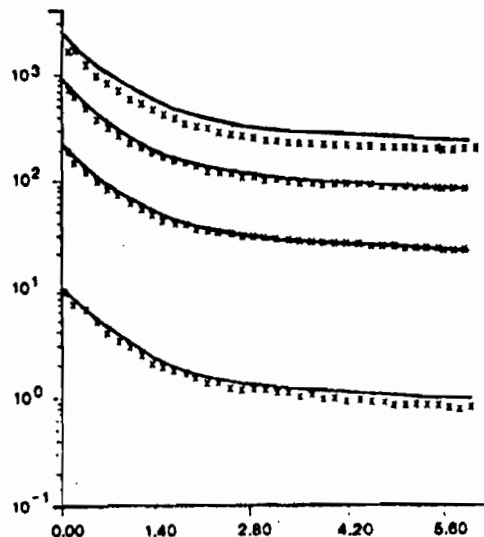


Figure 1 Computer simulation (solid line) vs. observed data (+) for rats exposed to 10, 250, 1000, and 1800 ppm CPFB in a closed chamber system.
-- CPFB conc. (ppm) vs. Time (hours)

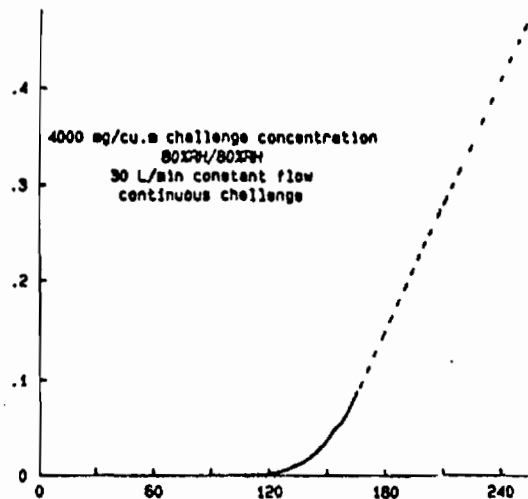


Figure 2 CPFB penetration curve for an ASC/T carbon filter canister; 4000 mg/m³ challenge, 30 L/min constant air flow (80% RH).
-- CPFB conc. (g/m³) vs. Time (min)

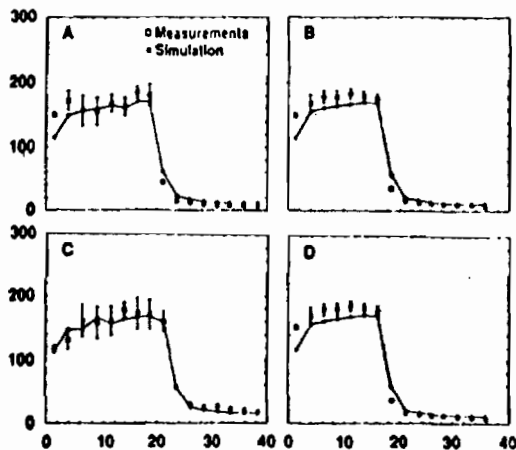


Figure 3 Computer simulation (solid line) vs. observed data (+) for four rhesus monkeys during and after 20 minute, 300 ppm CPFB exposures.
-- CPFB conc. (ppm) vs. Time (min)

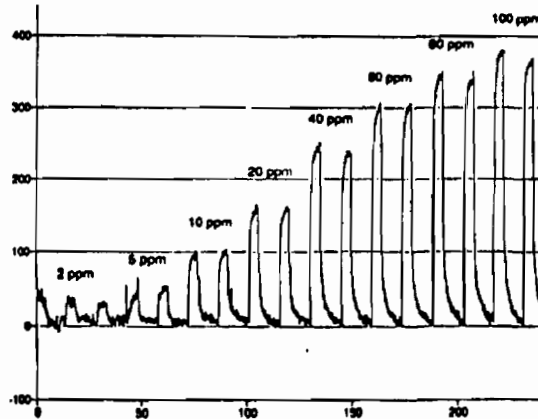


Figure 4 Direct-reading chlorohydrocarbon sensor response curve to 2-100 ppm CPFB challenge in air.
-- Signal (mV) vs. Time (min)

Agent Mimicry CPFB possesses physical properties appropriate for the generation and maintenance of a reasonable field exposure environment, and the simulation of a non-persistent CW agent (see Table 1). Canister penetration studies (Figure 2) indicate CPFB is readily adsorbed by a dynamically conditioned (80% RH) carbon filter with a capacity (Ct) of approximately 480,000 mg min/m³. Using a 4000 mg/m³ challenge and a 30 L/min 80% RH airstream, CPFB had a breakthrough time of 120 minutes. The penetration profile after breakthrough is fairly steep, and is consistent with the behavior of many other organics with boiling points near 100°C.

Exhaled Air Analysis To assure that measurement of CPFB in exhaled air could be used to determine total exposure, a study was conducted in which rats were exposed by inhalation for 1 hr. to CPFB at 300, 600, and 1200 ppm, and expired CPFB concentrations were monitored for 1 hr post-exposure⁵. Exhaled breath concentrations an hour after the end of the exposure were still greater than 1% of the exposure concentration. The PB-Pk model for CPFB was modified to utilize actual measured ventilation rate data, and was then used to demonstrate the ability to accurately estimate exposure concentration on the basis of post-exposure exhaled breath analysis. As a further evaluation of the breath analysis concept, inhalation exposures to CPFB were conducted on 8 anesthetized rhesus monkeys⁶. CPFB concentrations in expired breath were measured during and after 15 min. exposures at 300 ppm. The PB-Pk model was again used to relate exposure concentration and exhaled-air concentrations. The results are shown in Figure 3. The continued presence of significant concentrations of CPFB (greater than 1% of exposure concentration) in exhaled air more than 20 minutes following the exposure, and the ability of the model to relate exposure and exhaled air concentrations demonstrate the feasibility of using breath analysis for exposure determination in field exercises.

Field Analysis Since CPFB is perhalogenated, it is well suited to real time detection at low concentrations in the environment or in exhaled breath using a direct reading sensor or an electron capture detector (ECD). Figure 4 illustrates the linear response of a direct reading chlorohydrocarbon sensor (Transducer Research Inc, Naperville, IL) to 2-100 ppm CPFB. This sensor would be well suited for field detection, providing suitable sensitivity and excellent selectivity without O₂ or H₂O interference. With only minor modification, an off-the-shelf portable explosives vapor analyzer (Scintrex, Concord, Ontario, Canada) utilizing an electron capture detector could serve as a portable CPFB breathalyzer, providing detection to 1 ppt by volume. This would provide a method for non-invasive, real time assessment of troop exposure using exhaled breath without the need for sample preconcentration.

Practicality CPFB is commercially available (Aldrich Chemicals, Milwaukee, WI) at reasonable cost in liter quantities. Larger volumes could be produced at significantly lower cost (Bristol Chemicals, U.K.). As CPFB is a neutral, non-reactive and non-flammable halocarbon, it presents no problems in routine handling or transport.

SIMULANT EVALUATION: TOXICOLOGICAL STUDIES

In order to assure that CPFB could be safely used as an intake simulant, a number of studies were performed to evaluate its potential toxicity. These studies were designed to elucidate any short-term or chronic effects, and to assess the likelihood that CPFB could be carcinogenic or teratogenic.

Acute Toxicity The primary irritation hazard, sensitization potential, and acute inhalation toxicity of CPFB were evaluated by Kinkead et al⁷. CPFB demonstrated no potential for skin sensitization in tests on guinea pigs, and was only a mild skin and eye irritant in rabbits. Short-term exposure to CPFB vapor poses no serious hazard by the inhalation route as all rats survived a 4-hour exposure to an upper limit concentration of 4.84 mg/L (581 ppm), a concentration much higher than that which is likely to be encountered in the field. Similarly, oral dosing⁸ indicates an LD₅₀ of greater than 5 g/kg, which would classify CPFB as "practically non-toxic".

Mutagenicity/Genotoxicity CPFEB was tested for potential genotoxic activity by three different laboratories^{9,10,11} using a battery of in vitro assays. The first attempt to perform these assays⁹ was compromised by experimental difficulties associated with the tendency of CPFEB to precipitate out of solution and to dissolve the dishes. In the second study¹⁰, it was again noted that CPFEB dissolved the standard plastic dishes, so the study was performed in specially designed glass dishes. A third study¹¹ was performed by a reference laboratory since the results of the first two studies seemed to be somewhat equivocal. CPFEB does not appear to be mutagenic. The Ames Salmonella reverse mutation assay was uniformly negative in all studies, both with and without the addition of a rat liver S9 metabolic activation system. Similarly, all of the laboratories obtained negative results when CPFEB was tested in mammalian cell culture for mutagenic activity at the HGPRT locus in Chinese hamster ovary cells. The results of tests for genotoxicity were less consistent. There was some evidence of CPFEB-induced sister chromatid exchange and/or chromosomal aberration in the earlier studies, but the final study detected no increases in chromosomal aberrations and only observed sister chromatid exchange with the addition of liver S9 metabolic activation. In the case of the assay for unscheduled DNA repair synthesis in primary rat hepatocytes, the first study suggested that CPFEB produced increased repair of DNA damage; however, both the second and third studies failed to confirm this finding. Cell transformation results were also variable, with only the second study showing any indication of an ability of CPFEB to induce morphological transformation in vitro in BALB/c-3T3 cells. To resolve the question of whether CPFEB could act as a genotoxic or cytotoxic agent under in vivo conditions, a 21-day exposure of mice to CPFEB at 30, 100, and 300 ppm was performed¹³. Under these conditions CPFEB did not induce an increase in sister chromatid exchange in the bone marrow of the exposed mice, and the rate of cellular proliferation in the bone marrow was not altered. Similarly, assessment of the micronucleated polychromatic and normochromatic erythrocyte populations during the exposures indicated a general absence of genotoxic activity. The PB-Pk model for CPFEB described earlier was used to assess the tissue exposure to CPFEB during this study¹³. Based on the modeling, bone marrow tissue exposure to CPFEB during the in vivo study was similar to the concentrations used in the in vitro assays. The lack of in vivo response appears to reflect differences between the in vivo and in vitro situation rather than failure to achieve sufficient tissue exposure levels. Full evaluation of the potential for CPFEB to be carcinogenic would require a lifetime animal bioassay. However, a reasonable assessment of the likelihood that CPFEB could act as a carcinogen can be made on the basis of the above results, taken together with the rather unremarkable results of the chronic exposures. CPFEB does not appear to be mutagenic, either in the presence or absence of metabolic activation, and the questionable in vitro suggestions of genotoxicity were not born out by the in vivo studies. In addition, chronic exposure⁸ did not produce any of the tissue changes, such as peroxisomal proliferation, which typically accompany promotional carcinogenesis. Therefore, it is not likely that CPFEB would be carcinogenic, even under the conditions of a lifetime bioassay.

Chronic Toxicity Ten Fischer-344 rats and six B6C3F1 mice of each sex were exposed to 30, 100, and 300 ppm CPFEB for 3 weeks¹². Exposure to the highest concentration caused a reduction in the growth rate of rats, but did not affect the growth rate of mice. Both rats and mice showed a dose related increase in liver weights. Mice showed clear evidence of liver toxicity (hepatocytomegaly and hypertrophy) at the highest exposure concentration. Another treatment-related change in the livers of male and female mice and female rats was an increase in the incidence of single-cell necrosis in all CPFEB-exposed groups. The formation of hyaline droplets in the kidneys of male rats was also noted, but the severity of the lesion was minimal, and no other kidney effects were seen. In order to better evaluate the impact of prolonged or repeated exposure to CPFEB, as well as to determine a no-observable-effect level, a 13-week exposure of rats and mice was carried out at concentrations of 1.2, 6, and 30 ppm⁸. No treatment-related effects were observed at any concentration in either species. In particular, the single cell necrosis seen in the 3-week study at 30 ppm was not observed in the 13-week study at the same concentration. A review of the tissues from the earlier study confirmed the finding of an increase over

control, but both the number and severity of the lesions were so slight that it was felt the finding was biologically unimportant. Thus the only adverse effects seen were those noted for the 300 ppm exposure concentration in the 3-week study. A concentration of 30 ppm was therefore recommended as a no-effect level in humans to protect individuals subjected to repeated inhalation of CPFB for extended periods.

Teratogenicity To evaluate the teratogenic potential of CPFB, time-mated Sprague Dawley rats were dosed orally at 0.3, 1.05, and 3.0 g/kg/day on days 6 through 15 of pregnancy¹⁴. There was a significant reduction in maternal body weight and a significant increase in maternal liver weight at the highest dose. The percentage of post-implantation fetal loss was also greater only at the highest dose. Fetal weight and length differed significantly from the controls at both the high and intermediate doses, indicating a slightly increased fetotoxicity compared to the dam. The number of malformations and variations observed at any of the doses did not differ from controls, suggesting that CPFB is not teratogenic.

SUMMARY

CPFB possesses a remarkable combination of properties, making it an attractive candidate for use as an intake simulant in chemical defense field training exercises. It is volatile and unreactive, simplifying dissemination, and mimics the performance of typical vapor threats in terms of persistence and canister penetration. It does not appear that CPFB would present any significant health hazards to personnel under the envisioned use. A thorough toxicological evaluation indicates that CPFB is not acutely toxic, teratogenic, or carcinogenic. Chronic liver toxicity was observed only after prolonged exposure to high concentrations. To assure personnel safety, it is recommended that field exercises be designed to avoid repeated, prolonged exposure to concentrations greater than 30 ppm. Since field analytical methods can measure CPFB at part per billion levels, this should not be an impediment to use.

REFERENCES

1. Arthur D. Little, Inc. (1982) "Development of candidate chemical simulant list: the evaluation of candidate chemical simulants which may be used in chemically hazardous operations" AFAMRL-TR-82-28, A.F. Aerospace Medical Research Laboratory, WPAFB, OH.
2. Arthur D. Little, Inc. (1982) "Development of candidate chemical simulant list: the evaluation of candidate chemical simulants which may be used in chemically hazardous operations" AFAMRL-TR-82-87, A.F. Aerospace Medical Research Laboratory, WPAFB, OH.
3. MacEwen, J.D., and E.H. Vernot (1985) "Subchronic 90-day continuous inhalation exposure to dimethylmethylphosphonate" In 1985 Toxic Hazards Research Unit Annual Report AAMRL-TR-85-058, H.G. Armstrong Aerospace Medical Research Laboratory, WPAFB, OH, pp. 117-123.
4. Jepson, G.W., H.J. Clewell, III, and M.E. Andersen (1985) "A rapid, physiologically based method for evaluating candidate chemical warfare agent uptake simulants" AAMRL-TR-85-045, H.G. Armstrong Aerospace Medical Research Laboratory, WPAFB, OH.
5. Vinegar, A., D.W. Winsett, M.E. Andersen, and R.B. Conolly (1990) "Use of a physiologically based pharmacokinetic model and computer simulation for retrospective assessment of exposure to volatile toxicants" Inhal. Toxicol. 2, pp. 119-128.
6. Crank, W.D., and A. Vinegar (1991) "A physiologically based pharmacokinetic model for chloropentafluorobenzene in primates to be used in the evaluation of protective equipment against toxic gases" Toxicol. Indust. Health (in press).

7. Kinkead, E.R., W.J. Bashe, D.M. Brown, and S.S. Henry (1986) "Evaluation of the inhalation toxicity and sensitization potential of chloropentafluorobenzene" In 1986 Toxic Hazards Research Unit Annual Report AAMRL-TR-87-020, NMRI-87-2. H.G. Armstrong Aerospace Medical Research Laboratory, WPAFB, OH, pp. 131-135.
8. Kinkead, E.R., S.K. Bunger, E.C. Kimmel, C.D. Flemming, H.G. Wall, and J.H. Grabau (1991) "Effects of a 13-week chloropentafluorobenzene inhalation exposure of Fischer 344 rats and B6C3F1 mice" Toxicol. Indust. Health 7:4, pp. 309-318.
9. Tu, A., M.G. Broome, and A. Sivak (1986) "Evaluation of chloropentafluorobenzene in a battery of in vitro short term assays" AAMRL-TR-86-003, H.G. Armstrong Aerospace Medical Research Laboratory, WPAFB, OH.
10. Steele, V. (1987) "Biological activity of chloropentafluorobenzene" AAMRL-TR-87-039, H.G. Armstrong Aerospace Medical Research Laboratory, WPAFB, OH.
11. Kutzman, R.S., B.C. Myhr, T.E. Lawlor, D.C. Valentine, R.R. Young, H. Murli, M.A. Cifone, and B.M. Jarnot (1990) "Genetic toxicity assessment of chloropentafluorobenzene" AAMRL-TR-90-048, H.G. Armstrong Aerospace Medical Research Laboratory, WPAFB, OH.
12. Kinkead, E.R., B.T. Culpepper, H.G. Wall, R.S. Kutzman, C.D. Flemming, C.J. Hixon, and R.R. Tice (1989) "Evaluation of the potential of inhaled chloropentafluorobenzene to induce toxicity in F-344 rats and B6C3F1 mice and sister chromatid exchanges and micronuclei formation in B6C3F1 mice" AAMRL-TR-89-037, H.G. Armstrong Aerospace Medical Research Laboratory, WPAFB, OH.
13. Kinkead, E.R., H.G. Wall, C.J. Hixson, R.R. Tice, R.S. Kutzman, and A. Vinegar (1990) "Chloropentafluorobenzene: short-term inhalation toxicity, genotoxicity and physiologically-based pharmacokinetic model development." Toxicol. Indust. Health 6:6, pp. 533-550.
14. Cooper, J.R., and B.M. Jarnot (1992) "An evaluation of the teratogenicity of chloropentafluorobenzene (CPF)B" The Toxicologist 12 (in press).

BLANK

EFFECTS OF ALTITUDE ON TOXIC GAS UPTAKE: CO INHALATION IN HEALTHY ADULT VOLUNTEERS

James J. McGrath
Department of Physiology
Texas Tech University Health Sciences Center
Lubbock, TX 79430

Richard M. Schreck
Peter S. Lee
Biomedical Science Department
General Motors Research Laboratories
Warren, MI 48090-9055

We tested the hypothesis that toxic gas uptake is enhanced at altitude in volunteers using carbon monoxide (CO) as a model gas and a sensitive, fast-response laser spectrometer to measure CO in expired air. Breath samples were collected at sea level (330 ft) and at altitude (11,540 ft) from five volunteers breathing 9 ppm CO for one hr. Breath CO increased 15% with altitude (from 3.01 to 3.46 ppm) in subjects breathing air and 22% (from 4.07 to 4.97) in subjects breathing CO. Changes in breath CO correlated with similar changes in blood carboxyhemoglobin levels. These results indicate that CO may be useful to model toxic gas uptake at altitude.

When humans ascend to altitude the most obvious and immediate systemic response is increased pulmonary ventilation caused by the decreased partial pressure of oxygen (PO₂) in the air. The consequent decrease in arterial blood PO₂ stimulates chemoreceptors, impulses from which increase the rate and depth of breathing (1). Thus, blood oxygenation in the lung is improved by the increase in the average concentration of oxygen in the alveolar gas and the decrease in atelectasis. Although increased pulmonary ventilation increases alveolar PO₂, it may also increase the dose of toxic gases and particles in the air which is delivered to the respiratory system. This study was conducted to compare toxic gas uptake by the body at sea level and at high altitude using carbon monoxide (CO) as a test gas and a newly-developed, extremely sensitive, fast-response laser spectrometer to measure CO in the breath.

Protocols for the experiment were reviewed by the Institutional Review Boards of Texas Tech University Health Sciences Center, General Motors Research Laboratories and Texas A & M University. Five non-smoking human volunteer subjects were recruited for the study and breathed CO for one hour at sea level and high altitude. A control group of twenty non-smoking subjects (10 male and 10 females) was also recruited to control for the effects of altitude on endogenous CO levels.

CO (9 ppm in breathable air) for the exposure studies was obtained premixed from Scott Medical Product (Plumsteadville, PA). Gas from the cylinders was delivered via a pressure regulator to a polyethylene distribution bag and to the five volunteers through five 3-cm diameter low pressure air lines. Each volunteer was fitted with a conventional MSA respiratory protective mask (Mine Safety Appliances, Pittsburgh, PA) which had been modified to allow comfortable delivery of the CO mixture. To verify that CO was flowing through the bag and into the respirators throughout the exposures, two battery powered Ecolyzer Model 211 carbon monoxide monitors (National Draeger, Inc., Pittsburgh, PA), calibrated against a 45 ppm CO standard, were placed inside the transparent distribution bag.

Air samples were collected in aluminized Mylar bags (Quintron Instruments, Milwaukee, WI). Each bag had two orifices, a larger one with a one-way valve which permitted air to enter the bag and a smaller one equipped with a Luerlock fitting to facilitate removing gas samples for analysis. The mouthpiece, T-fitting and closed plastic sleeve attached to the larger orifice, coupled the system to the volunteer's respiratory system.

All volunteers provided an alveolar air sample during quiet respiration by exhaling about half the lung air volume and blowing the second half into the sleeve/bag arrangement which captured the last air exiting the lung. When a predetermined amount of exhaled upper lung air accumulated in the sleeve (approximately 500 mL) a small back pressure developed which permitted the last air exiting the lung to fill the bag below. In practice, subjects were asked to sit in the upright position and breathe normally. At the end of a normal inspiration they held their breath for 10 seconds, exhaled approximately half their breath, then put the mouthpiece to their lips and blew until the Quintron bag was at least half full. This provided a 250 to 500 mL sample of the last air to leave the lungs for analysis. Expulsion of approximately half the exhaled breath plus trapping the next 500 mL in the sleeve minimizes the dilution of the alveolar air trapped in the sample bag with air from the anatomical dead space. After the sample was taken, the T-fitting was removed and a tapered plastic plug was inserted into the larger orifice to prevent the sample from leaking during storage. Bags were shipped for analysis from the test site to Warren, MI by surface freight carrier to prevent possible sample loss due to pressure changes.

Alveolar air samples were analyzed for CO using a newly developed tunable diode laser spectrometer (2). The samples required no preparation for introduction into the spectrometer and the anticipated concentrations of several parts per million CO were well within the measurement capability of the instrument. Since the system requires a small sample volume for analysis, the 250 to 500 mL samples drawn in the Quintron bags were adequate for analysis and yet easily transported from test site to laboratory.

Mixed venous blood, drawn at the site of each experiment by lancing the finger and collected in a miniature plastic container, was immediately frozen in dry ice. Later the samples were analyzed for carboxyhemoglobin (COHb) by gas chromatography at the Physiology Labs at Texas Tech University in Lubbock, TX using a technique described by Dahms and Horvath (3) and Lee et al (4).

Alveolar air samples were collected from all subjects at College Station, Texas (altitude 330 ft; 100 m). All were nonsmokers and had experienced no recent CO exposure. The background air concentrations of CO at College Station were low (< 1 ppm CO), consistent with its location. The five subjects then breathed 9 ppm CO for one hour while at rest and alveolar air samples were taken again. Blood samples were taken

after each alveolar air sample. Over a period of several days, the volunteers traveled by bus to Hoosier Pass, Colorado (altitude 11,540 ft; 3518 m), with most of this elevation being gained the day before arrival. After approximately 20 hours at high elevation, alveolar air and blood samples were drawn. The five volunteers then underwent a second one hour exposure to 9 ppm CO by modified respirator while seated in a van. After breathing CO, each of the five volunteers provided a second air and blood sample.

At sea level, breathing 9 ppm CO increased alveolar air CO levels from 3.01 to 4.07 ppm, an increase of 1.06 ppm or 35% above baseline (Table 1). At altitude, CO exposure increased alveolar air CO levels from 3.46 to 4.97 ppm, an increase of 1.51 ppm or 44%. Ascending to altitude in the absence of inhaling CO increased alveolar air CO levels by 0.45 ppm or about 15% in the five subjects.

TABLE I.
ALVEOLAR AIR CO LEVELS IN SUBJECTS EXPOSED TO
9 PPM CO FOR ONE HOUR

Subject	330 feet (100)		11,500 feet (3,518 meters)	
	Carbon Monoxide (ppm)		Carbon Monoxide (ppm)	
	Pre	Post	Pre	Post
JWF	2.03	3.16	4.71	2.83
VPT	2.27	4.52	3.56	5.65
JRG	3.90	4.69	2.58	2.62
LQP	5.88	3.83	3.16	8.78
JJM	0.99	4.17	3.30	-
Mean	3.01 ^a	4.07	3.46	4.97
	±1.91	±0.61	±0.78	±2.89

^aValues are means ± SEM

Analysis of the alveolar air samples from the unexposed subjects showed similar CO levels of 1.83 and 1.94, respectively, for the males and females with an overall value at low altitude of $1.89 \pm .66$ ppm, (Table 2). A brief time at altitude caused the alveolar air CO levels to rise in each group to 2.31 and 2.54 ppm, respectively, in the males and females with an average increase of 28% for the two groups combined.

TABLE 2.
ALVEOLAR AIR CO IN SUBJECTS BREATHING AIR

Subjects	330 feet (100 meters) Carbon Monoxide ^a (ppm)	11,500 feet (3,518 meters) Carbon Monoxide ^a (ppm)
Males (10) ^b	1.83 ± 0.54	2.31 ± 0.66
Females (10)	1.94 ± 0.78	2.54 ± 1.39
Both (20)	1.89 ± 0.66	2.43 ± 1.07

^aValues are means ± SEM

^bNumbers in parentheses indicate numbers of subjects per group

Figure 1 is a plot of expired breath CO concentration versus blood COHb levels measured on the volunteers before and after CO exposure at both altitudes. The correlation coefficient for the linear regression fit of the line was .48 with all points considered and if the two low values at "POST-HIGH" are excluded because they appear to be diluted with fresh air from the upper airways, the coefficient improves to .50.

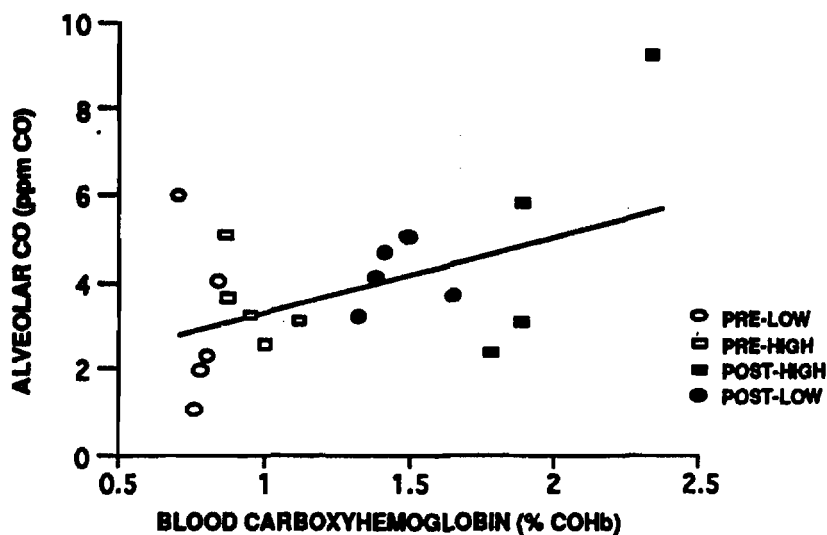


FIGURE 1. Correlation between blood COHb and alveolar air CO before (pre) and after (post) breathing 9 ppm CO for one hour at sea level and altitude.

CONCLUSIONS

These results indicate that breath CO levels and blood COHb levels increase in subjects breathing CO to a greater extent at altitude than at sea level and are in accord with the predictions of Collier and Goldsmith (5). These workers transformed and rearranged the Coburn-Foster-Kane equation (6), and derived an equation expressing COHb in terms of endogenous and exogenous sources of CO. Thus,

$$\text{COHb} = \frac{F_{\text{ICO}} (P_{\text{B}}-47)}{10^6 K} + \frac{V_{\text{CO}} Z}{K}$$

where: $Z = \frac{1}{D_{\text{LCO}} + \frac{P_{\text{B}}-47}{V_{\text{A}}}}$

$$K = \frac{F_{\text{CO}_2}}{M \times \text{SO}_2}$$

COHb is the percent COHb; F_{ICO} is the fraction of inspired CO in parts per million; P_{B} is the barometric pressure in torr; V_{CO} is the rate of CO production in milliliters per minute at standard temperature and pressure, dry (STPD); D_{LCO} is the CO diffusing capacity in milliliters per minute-torr; V_{A} is the alveolar ventilation in milliliters per minute at STPD; \bar{P}_{CO_2} is the mean partial pressure of pulmonary capillary O_2 in torr; M is the Haldane coefficient; and SO_2 is the percent oxyhemoglobin (O_2Hb).

According to this relationship, a given F_{ICO} will result in a higher percent COHb at high altitudes (where PO_2 is reduced). Moreover, these workers predict an increase in COHb at altitude even in the absence of inhaled CO (due to endogenous production of CO).

Increased pulmonary ventilation, a well-described phenomena associated with ascent to altitude (7), is but part of a series of changes tending to restore oxygen tension in the tissues toward normal sea level values despite the lower ambient PO_2 . Although we did not measure ventilation, previous studies of low-altitude sojourners experiencing comparable changes in elevation have reported a resting pulmonary ventilation of 9.94 L/min at 518 m increasing to 12.44 and 14.29 L/min on the first and second day, respectively, at 3940 m (1). Therefore while our subjects were indeed resting during the one-hour exposure, their increased rates of ventilation at altitude produced a more rapid uptake and loading of the blood with CO than occurred at sea level in one hour. It may be postulated that longer CO exposure periods at sea level would produce a greater rise in COHb and less of a difference with altitude.

At altitude, moreover, in subjects breathing ambient air, CO excretion as measured in the expired breath is likewise higher than at sea level. Under both conditions the breath CO levels are directly correlated with blood COHb levels. CO in the exhaled air of man, derives from CO produced by catabolism of hemoglobin and other hemoproteins. The normal catabolism of hemoglobin and the breakdown of non-hemoglobin heme produce approximately 0.4 mL/hr of CO endogenously (8). Transport of this endogenously produced CO by the blood results in an average background COHb level of 0.4-0.7 percent. Certain drugs, chemical exposures and disease states (e.g. hemolytic anemia) can

increase CO production within the body and may cause COHb levels of 4-6 percent (6, 9). Body CO stores are influenced by both endogenous as well as exogenous sources of CO, and the level of CO in the breath is directly related to the concentration of COHb in the blood (10).

Beginning with the work of Jones et al (11), the relationship between COHb in blood and CO in exhaled breath has received a great deal of study. Most of this work has involved a much wider range of COHb levels, past 20% in some cases, and shows a generally linear relationship between the two parameters with varying degrees of goodness to the fit of the regression line. The results of Lambert et al (12), which used a CO-Oximeter verified by a gas chromatograph are similar to ours in showing scatter in the data in the region below 3% COHb for the nonsmoking population. Whether this phenomena is caused by unanticipated variable or uncertainties in the sampling procedure is not known. Lambert and colleagues used the 20 sec breath-holding procedure after full expiration and inspiration as recommended by Jones et al (11). Our preliminary studies showed apparent dilution of CO₂ in the alveolar air by this procedure using a fast response CO₂ monitor and so our sampling protocol was modified to exclude the wash-in of fresh ambient air by a deep breath. Our subjects breath-held for 10 sec after a tidal inhalation, then to further exclude fresh air from the sample, they exhaled roughly one third of the air in their lungs, finally delivered the remaining lung air to the sample sleeve and collection bag. In our tests, this gave the most consistent results with the highest values for exhaled CO₂. Since the laser spectrometer is extremely accurate for orders of magnitude lower levels of CO than measured, we presume that the variability did not arise from this source. The transport of the sample bags from Colorado to Michigan and subsequent handling, or other anomalies in the sample collection procedure may be partially responsible for the scatter in our results. In both groups the measured blood hemoglobin levels increased slightly due to a small reduction in plasma volume or hemoconcentration during the trip, rather than an actual altitude-related increase in hemoglobin over this brief period.

Thus we conclude that CO is a good model for toxic gas uptake studies because its absorption is well understood, it can be easily monitored with available instruments, and, based on the work of Collier and Goldsmith the effects of altitude can be explained and compensated for. We may also conclude that, in general, the uptake of any non-reactive toxic gas would be expected to follow this pattern of increased absorption during the several days following ascent to altitude.

ACKNOWLEDGEMENTS

The authors would like to acknowledge LaQuetta Purkiss and Robert Wooley for their excellent technical contributions. This study was supported in part by General Motors Research Laboratories.

REFERENCES

1. N.K. Burki, "Effects of acute exposure to high altitude on ventilatory drive and respiratory pattern," J. Appl. Physiol: Respir. Environ. Exercise Physiol. 56(4):1027-1031 (1984).
2. P.S. Lee and R.F. Majkowski, "High resolution infrared laser spectroscopy for isotope analysis - measurement of isotopic carbon monoxide," Appl. Phys. Lett. 48(10):619-621 (1986).
3. T.E. Dahms and S.M. Horvath, "Rapid accurate technique for determination of carbon monoxide in blood," Clin Chem. 20:533-537 (1974).
4. P.S. Lee, K. Chen and J.J. McGrath, "Gas chromatographic determination of carbon monoxide in blood," General Motors Research Report, BI-132 (1979).
5. C.R. Collier and J.R. Goldsmith, "Interactions of carbon monoxide at altitude," Atmos. Environ. 17:723-728 (1983).
6. R.F. Coburn, R.E. Forster, and P.B. Kane. Consideration of the physiological variables that determine the blood carboxyhemoglobin concentration in man. J. Clin. Invest. 44: 1899-1910 (1965)
7. C.S. Houston and R.L. Riley. Respiratory and circulatory changes during acclimitization to high altitude. Am. J. Physiol. 149: 515-580 (1947)
8. R.F. Coburn, W.S. Blakemore and R.E. Forster, "Endogenous carbon monoxide production in man," J. Clin. Invest. 42(7):1172-1178 (1963)
9. R.D. Stewart, "The effect of carbon monoxide on humans," J. Occup. Med. 18(5):304-309 (1976).
10. R.D. Stewart, R.S. Stewart, W. Stamm and R.P. Seelan, "Rapid estimation of carboxyhemoglobin level in fire fighters," JAMA 235(4):390 (1976).
11. R.H. Jones, M.F. Ellicott, J.B. Cadigan and E.A. Gaensler, "The relationship between alveolar and blood carbon monoxide concentrations during breathholding," J. Lab. Clin. Med. 51(4):553-564 (1958).
12. W.E. Lambert, S.D. Colome, and S.L. Wojciechowski, "Application of end-expired breath sampling to estimate carboxyhemoglobin levels in community air pollution exposure assessments", Atmos. Environ. 22(10):2171-2181 (1988).

BLANK

INTERSPECIES DIFFERENCES IN RESPONSE TO AMPHETAMINE, ACETAMINOPHEN, TRICHLOROETHYLENE, AND SODIUM THIOSULFATE

Charles A. Tyson, Carol E. Green, Susan A. Knadle,
Shirley J. Gee, Jack E. Dabbs, and Susanna E. LeValley

SRI International, 333 Ravenswood Avenue, Menlo Park, CA 94025

ABSTRACT

The potential of *in vitro* systems for providing data on interspecies differences in response to drug and chemical exposures is being evaluated to aid in human risk assessment. Here we report on studies with isolated hepatocytes (HEP) and renal proximal tubule (RPT) cultures exposed to four compounds of commercial interest. In metabolite analysis and covalent binding studies, amphetamine and acetaminophen produced different results in HEP or RPT from different species. Trichloroethylene produced the same toxic metabolite in human as in rat HEP but at lower levels. Sodium thiosulfate reversed cyanide-induced adenosine triphosphate depression in rat but not in human HEP.

INTRODUCTION

Interest in the use of *in vitro* systems for toxicological applications has grown dramatically over the last decade.^{1,2} The impetus for this surge has been the need to acquire more detailed information on toxicity mechanisms for improving estimates of human risk from exposure to drugs and environmental chemicals. Data from well-validated *in vitro* models have *prospective* value for estimating the relative toxic potentials of drugs and chemicals early in their development process. Those compounds likely to have adverse effects in humans can be identified, and money and resources for animal testing can be reduced by focusing only on the most probable candidates. These systems can also generate *retrospective* data to help clarify the significance for humans of findings in laboratory animals.

Two key issues need to be addressed before *in vitro* systems are used for these applications: (1) How accurately do they model *in vivo* response, and (2) what information can they provide to aid in risk assessment? Techniques have been developed for isolating and culturing most cell types from animal and human organs, making possible comparative studies in these tissues that are directly relevant to humans. Thus, *in vitro* approaches offer a means of monitoring for interspecies differences in response and of obtaining data for dosimetry response profiles of human exposure.

Research in our laboratory over the last decade has centered on validating hepatocyte (HEP) systems from liver and proximal tubule fragments (PTF) from kidney as models for *in vivo* response and applying these models to acquire valuable toxicologic and pharmacologic information not otherwise available. Liver and kidney are two principal organs that handle foreign compounds in the body, and they are common targets for the adverse effects produced by those compounds. The studies described here are examples of our validation results, including questions that may be raised or answered by these approaches.

METHODS

Isolation Procedures

Detailed methods for isolating hepatocytes from either whole liver or biopsy specimens by collagenase perfusion are described elsewhere.^{3,4} Cell viability of the freshly isolated cells was assessed by trypan blue exclusion; preparations with <80% viable cells were not used.

PTF were isolated *in situ* by a modified collagenase perfusion method in which deferoxamine was added to the perfusate to reduce oxidative damage to cells during isolation.⁵ When primate kidneys (whole organ or sections) were received at the laboratory, the perfusion was conducted by direct cannulation of the renal artery or insertion of a cannula into a vessel on the outer surface and the procedures thereafter were the same.⁶ PTF viability was determined primarily by measuring nystatin-stimulated oxygen consumption.^{5,6} Only preparations with >35% stimulation retained enough viability throughout the experiment (4 hr or longer) to be used.

Culture Conditions

Both HEP suspension (1×10^6 viable cells/ml of culture medium) and monolayer ($\sim 0.25 \times 10^6$ viable cells/ml) cultures were used, depending on the experimental objectives. A coculture system—HEP attached to culture dishes with erythrocytes suspended in the medium—was also used, and the experimental conditions are described in earlier publications.⁷ The culture medium was

hormone-supplemented Waymouth's 752/1 containing either 0.2 or 2.0% bovine serum albumin (BSA).^{4,6-8} All incubations were conducted at 37°C under an atmosphere containing 20% or higher O₂, 5% CO₂, and the balance N₂. HEP suspensions were shaken at 70 osc/min in airtight Erlenmeyer flasks with sidearms for serial sampling.

PTF were incubated in suspension in the same medium containing 2% BSA at a protein level of 0.5 mg/ml with shaking under essentially the same experimental conditions.⁶ Cell content was based on protein determination, because individual cells in the PTF cannot be conveniently counted under a light microscope.

Assays

Amphetamine (AMP) metabolism was monitored by using D-[7-¹⁴C]AMP sulfate (Research Products Intl., Mt. Prospect, IL), and high-pressure liquid chromatography was used for metabolite separation.⁴ Acetaminophen (APAP)-protein adducts were determined immunochemically after electrophoretic separation of the proteins by using an affinity-purified anti-APAP antibody developed in Dr. E. A. Khairallah's laboratory at the University of Connecticut (Storrs).^{9,10} Trichloroethylene (TCY; [U-¹⁴C] radiolabel from Amersham, Arlington Heights, IL) and its metabolites were assayed by gas chromatography.⁸ In cyanide (CN) antidote experiments, cytotoxicity was monitored by determining cell adenosine triphosphate (ATP) levels by using the luciferin-luciferase assay after aspiration of the erythrocyte-containing culture medium and solubilization of HEP.⁷ All chemicals and other reagents were purchased from established commercial suppliers and used without further purification.

RESULTS AND DISCUSSION

AMP Metabolism: Interspecies Differences

AMP metabolism in animals proceeds by either of two principal pathways: ring hydroxylation to form *p*-hydroxy-AMP; or oxidative deamination on the side chain, which forms phenylacetone, benzoic acid, and hippuric acid as the principal metabolites. Incubation of AMP with HEP from different species *in vitro* for 4 hr yielded the metabolite distributions shown in Figure 1.⁴ Rat HEP produced mainly *p*-hydroxy-AMP; metabolism of AMP by HEP from the other species, including humans, produced mainly metabolites of oxidative deamination. The *in vitro* data accurately corresponded to the predominant pathway for each species *in vivo*.⁴ Although a precise comparison between *in vivo* and *in vitro* rates of AMP disposition is difficult, in general the rate of hepatic AMP metabolism correlated inversely with the amount of AMP excreted unchanged in animal and clinical

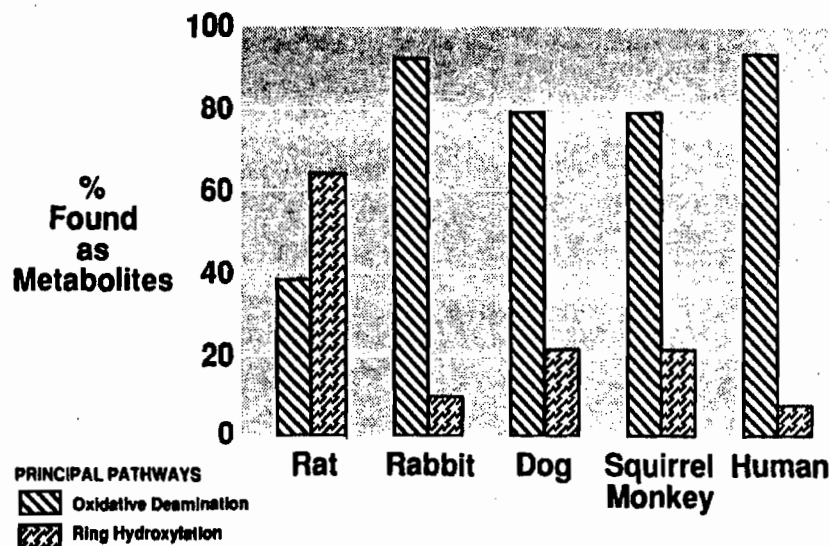


Figure 1. AMP metabolism. *In vitro* 4-hour incubation with HEP.

studies. The metabolism of APAP by HEP was unique for each species examined, but the rat, the most commonly used species in toxicity and metabolic disposition studies, clearly was not representative of human response and therefore would not be the most appropriate species for testing APAP.

APAP Metabolism and Organ Injury: Interspecies Differences

Excessive doses of APAP induce target organ effects (cytotoxicity and necrosis to liver and kidney) and death in animals through formation of an active metabolite mediated by cytochrome P-450 in cells. Covalent binding of APAP to cell proteins is implicated in its toxicity, and immunochemical techniques have recently become available to help identify the proteins affected.⁹

Incubation of APAP for 4 hr in mouse (a species susceptible to its action) and human HEP produced the binding pattern shown in Table 1.^{6,10} The bands labeled *in vitro* for each species corresponded precisely to those found in the livers *in vivo* at high APAP doses and fairly closely to each other. (The human liver came from an overdose fatality.) In contrast, incubation of APAP with PTF from mice, rats, and a baboon kidney (human kidney was unavailable at the time) showed a marked difference in response.⁶ No APAP-protein adducts were found with the rat or baboon, raising a question about which species is more like humans in its susceptibility and response. Experiments with human PTF may help to resolve this question and determine the most suitable animal model for studying APAP's effects on kidney.

TABLE 1
Protein Arylation Patterns in Liver and Kidney
Cells Determined by Immunochemical Analysis

Liver Cells		Kidney Cells		
Mouse ^a	Human ^a	Mouse ^a	Rat ^b	Baboon ^b
<u>130</u> kD	<u>130</u> kD	<u>130</u> kD	None	None
<u>58</u>	62	<u>58</u>	detected	detected
<u>44</u> (M)	58	<u>44</u> (M)		
33	52	33		
30	38			

kD = kilodaltons. M = microsomal protein. All other proteins were cytosolic. Underline indicates major or predominant proteins. ^aIncubations were for 4 hr. ^bIncubations were for 8 hr (lifetime in culture).

TCY Metabolism in Relation to Carcinogenic Potential

In vivo studies in several laboratories have demonstrated that the mouse, in which TCY induces hepatocarcinogenicity, metabolizes TCY much more actively than does the rat, a resistant species. Other studies have implicated a metabolite, trichloroacetic acid (TCA), as the procarcinogen. The potential for TCY-induced hepatocarcinogenicity in exposed humans has caused considerable concern to regulatory agencies, and comparative metabolism studies in rat and human HEP could provide relevant data on this potential.

Incubation of TCY with rat and human HEP for 4 hr produced the principal metabolites shown in Figure 2, which are the same as formed *in vivo* by these species.⁸ Compared with rat HEP, much lower levels of TCA were present in the human cell incubations. These data were produced under identical experimental conditions; on the basis of metabolism alone, they suggest that humans are even more likely than rats to be resistant to TCY-induced hepatocarcinogenicity.

Sodium Thiosulfate as a Cyanide Antidote

The currently recommended treatment for CN poisoning in this country is a combination of NaNO₂ and sodium thiosulfate. To evaluate other candidate antidotes of interest to USAMRDC, we developed a hepatocyte-erythrocyte coincubation system as a prescreen for effectiveness.⁷ The response to NaNO₂ and Na₂S₂O₃ separately in this system was qualitatively similar to that *in vivo*, and the combination was likewise more effective than either alone.

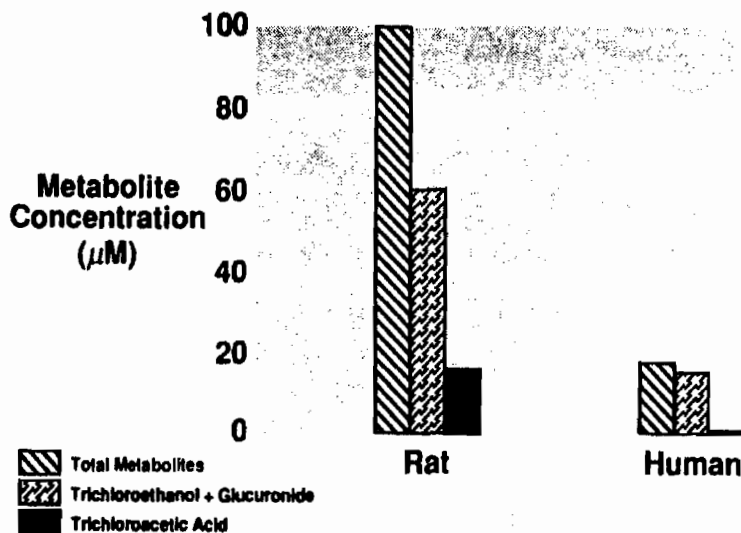


Figure 2. Trichloroethylene metabolism. *In vitro* 4-hour incubation with HEP.

A comparison of the results from the prescreen using rat and human cells is shown in Figure 3. NaNO_2 and $\text{Na}_2\text{S}_2\text{O}_3$ were each partially effective in reversing CN-induced ATP depression in rat HEP; their combination was most effective.⁷ In contrast, NaNO_2 but not $\text{Na}_2\text{S}_2\text{O}_3$ reversed ATP depression in the human cell culture and the combination appeared totally dependent on the NaNO_2

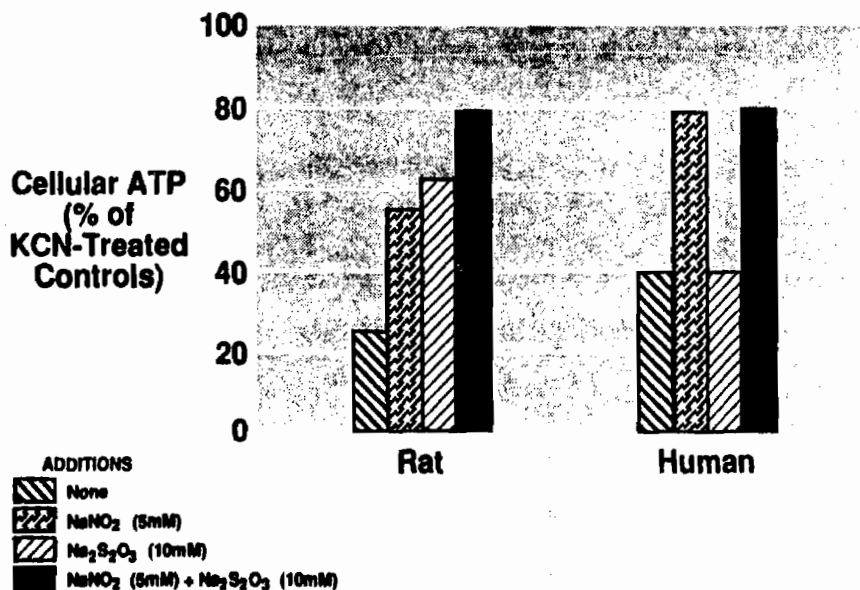


Figure 3. Antidote reversal of cyanide-induced cytotoxicity.

component.¹¹ The apparent lower effectiveness of $\text{Na}_2\text{S}_2\text{O}_3$ as a CN antidote in human HEP corresponds to the known lower rhodanese enzyme activity in human compared with rat liver. The benefits offered by $\text{Na}_2\text{S}_2\text{O}_3$ for human therapy may therefore need closer examination; these results justify continued research to find more effective antidote treatments.

CONCLUSIONS

Studies to determine the pharmacological value and the potential adverse effects of chemicals for humans are routinely conducted in laboratory animals. However, the extrapolation of results to humans carries considerable uncertainty because of interspecies variations in dose response. Qualitative and quantitative differences in metabolite formation are a major reason for these variations.

In vitro systems offer an alternative to whole animal testing for acquiring such information. The examples given here and others in the literature support the validity of these cell systems as models for predicting the metabolic disposition of chemicals *in vivo*. The availability of human tissue for response comparison opens up opportunities for answering important questions in the safety assessment process. *In vitro* studies coupled with *in vivo* testing for dosimetry and improved risk assessments are an imminent reality.

ACKNOWLEDGMENTS

The authors gratefully acknowledge receipt of human donor livers from the California Donor Transplant Network, San Francisco; the Stanford University Medical Center, Palo Alto; and the National Disease Research Interchange, Philadelphia, which made this research possible. This work was supported by the National Institutes of Health (GM28157 and ES55109) and the Department of Defense (DAMD 17-82-C-2211).

REFERENCES

1. Goldberg, A. M. *In Vitro Toxicology New Directions*. Alternative Methods in Toxicology Vol. 7, Mary Ann Liebert, New York, 1989.
2. McQueen, C. A. *In Vitro Toxicology Model Systems and Methods*. Telford Press, Caldwell, New Jersey, 1989.

3. Green, C. E., J. E. Dabbs, and C. A. Tyson. (1983). Functional integrity of isolated rat hepatocytes prepared by whole liver vs. biopsy perfusion. *Anal. Biochem.* **129**, 269-276.
4. Green, C. E., S. E. LeValley, and C. A. Tyson. (1986). Comparison of amphetamine metabolism using isolated hepatocytes from 5 species including humans. *J. Pharmacol. Exp. Ther.* **237**, 931-936.
5. Green, C. E., J. E. Dabbs, C. A. Tyson, and E. J. Rauckman. (1990). The effect of oxygen tension and antioxidants on isolated rat renal proximal tubules. *Ren. Fail.* **12**, 147-156.
6. Tyson, C. A., S. D. Cohen, and E. A. Khairallah. (1991). Comparative toxicity: Mechanistic studies on acetaminophen action *in vitro* and *in vivo* in various species including man. *In Vitro Toxicology Mechanisms and New Technology*. Alternative Methods in Toxicology, Vol. 8, Goldberg, A. M. (ed.) Mary Ann Liebert, New York, pp. 163-170.
7. Gee, S. J., S. E. LeValley, and C. A. Tyson. (1987). Application of a hepatocyte-erythrocyte coincubation system to studies of cyanide antidotal mechanisms. *Toxicol. Appl. Pharmacol.* **88**, 24-34.
8. Knadle, S. A., C. E. Green, M. Baugh, M. Vidensek, S. M. Short, X. Partos, and C. A. Tyson. (1990). Trichloroethylene biotransformation in human and rat hepatocytes. *Toxicol. In Vitro* **4**, 537-541.
9. Bartolone, J. B., K. Sparks, S. D. Cohen, and E. A. Khairallah. (1987). Immunochemical detection of acetaminophen-bound liver proteins. *Biochem. Pharmacol.* **36**, 1193-1196.
10. Birge, R. B., J. B. Bartolone, S. G. Emeigh Hart, E. V. Nishanian, C. A. Tyson, E. A. Khairallah, and S. D. Cohen. (1990). Acetaminophen hepatotoxicity: Correspondence of selective protein arylation in human and mouse liver *in vitro*, in culture, and *in vivo*. *Toxicol. Appl. Pharmacol.* **105**, 472-482.
11. C. A. Tyson. *Mechanism of Chemical Action and Treatment of Cyanide Poisoning*. Annual Progress Report, AD #A192091 on Contract DAMD17-82-C-2211, SRI International, Menlo Park, CA, June 1, 1986.

V. BIOTECHNOLOGY

NOTE: Papers with the following titles were presented at the Conference but are not included in this document:

Part I: Molecular Biology

Olfactory Receptor Binding Protein

Suppression Cloning of a Novel Calcium Channel Subunit cDNA

Advances in the Isolation, Reconstitution and Cloning of a Neuronal Receptor-Ion Channel Complex, the NMDA Receptor

Comparison of Receptor-Based LAPS and Fiber-Optic Biosensors

Chemical Agent Biosensor Method with Electrochemical Transduction by Ion Channel Synthesis

Part II: Applications

Genetic Manipulation of Organophosphate Hydrolase Processing

Catalytic Monoclonal Antibodies: Novel Biotechnology Poised for Application

Enzymes in Supercritical Fluids

Plant Cell Cultures for the Production of Bioactive Compounds

BLANK

OLFACTION, OLFACTOMEDIN AND THE DYNAMIC RANGE OF SMELL

Robert R. H. Anholt, David A. Snyder and Hiroko Yokoe
Department of Neurobiology, Duke University Medical Center, Durham, NC 27710.

Initial interactions between odorants and olfactory neurons occur at their ciliated dendritic tips, where odorants bind to odorant receptors and initiate a transduction cascade, which leads to excitation of the cell. We have identified the major protein of the lower mucus layer that covers the chemosensory surface in frog olfactory tissue. This 57 kD protein, which we have named "olfactomedin," is heavily glycosylated and produced by sustentacular cells of the neuroepithelium and by submucosal glands. We hypothesize that carbohydrate residues on olfactomedin may sequester water from the lower mucus layer to provide a more favorable environment for odorants to interact with receptors at the chemosensory membrane. Thus, by facilitating stimulus access olfactomedin may lower the threshold for odorant detection and, hence, expand the dynamic range of smell.

Introduction: Odor recognition and olfactory transduction.

Odorants are recognized and discriminated by olfactory receptor neurons located in the olfactory neuroepithelium. These cells are bipolar neurons. The chemoreceptive region of the cell consists of a dendrite that projects toward the nasal lumen and ends in a dilatation, the "dendritic knob." This knob carries a group of cilia that are embedded in an extracellular mucous matrix which lines the nasal cavity. There is now solid evidence that initial chemosensory events occur at these dendritic cilia.¹⁻³ Odor recognition is followed by a cascade of signal transduction events that ultimately evoke a generator potential, which leads to excitation of the cell. The resulting action potentials travel along the cell's axon to the olfactory bulb of the brain, where the first synaptic relay takes place and decoding of the olfactory message is initiated. Olfactory receptor neurons differ in their responsiveness to odorants and different odorants stimulate distinct subpopulations of olfactory neurons.^{4,5} Thus, the molecular structure of an odorant is converted into a spatial and temporal pattern of neuronal activity, which is processed by the brain and ultimately perceived as a characteristic odor quality.

Upon arriving at the ciliary membrane, odorants are thought to interact with receptors. Recently, cDNAs have been described, which encode a multigene family of putative odorant receptors expressed uniquely in olfactory tissue.⁶ These proteins

are members of the superfamily of G-protein-coupled receptors and contain the seven transmembrane domain structure characteristic of this superfamily. They are closely related forming a distinct subfamily of receptors and exhibit extensive sequence variations within the third, fourth and fifth transmembrane domains, thought to reflect differences in odorant binding specificities. Although binding of odorants to these proteins or interactions between these proteins and second messenger systems have not yet been demonstrated, it is reasonable to expect that this diverse, olfactory tissue-specific array of novel G-protein-linked receptors indeed represents the long-sought-after odorant receptors.

The arrival of odorants at the chemosensory membrane initiates a chain of signal transduction events. Olfactory cilia are highly enriched in adenylate cyclase⁷⁻¹¹ and its associated regulatory G-protein.¹²⁻¹⁴ Both the adenylate cyclase and the G-protein have been cloned and are olfactory-tissue specific isoforms, named adenylate cyclase type III¹⁵ and G_{olf},¹⁴ respectively. When the integrated accumulation of cyclic AMP is measured in the presence of odorants and GTP, stimulation of the enzyme by micromolar to millimolar concentrations of some, but not all, odorants is observed.^{8,9} Furthermore, rapid quench-flow measurements revealed transient increases in cyclic AMP in response to submicromolar concentrations of odorants, such as isomenthone and citralva.^{10,11}

Soon after it became clear that cyclic AMP plays a central role in olfaction, several laboratories investigated its effect on protein phosphorylation¹⁶ and ion channel function.¹⁷ In 1987, Nakamura and Gold discovered a cyclic AMP-gated conductance on the dendritic cilia, olfactory knob and soma of olfactory receptor cells.¹⁷ Since their studies used excised patches they concluded that cyclic AMP opened channels directly. Cyclic GMP also opens the olfactory channel and is even more potent than cyclic AMP. Whether this activation by cyclic GMP has physiological significance or is merely coincidental is not clear. Cloning of the cyclic nucleotide-activated channel from rat olfactory tissue showed it to be homologous to its cyclic GMP-activated counterpart of photoreceptor cells.¹⁸ Electrophysiological studies have shown that application of forskolin or analogues of cyclic AMP leads to depolarization of olfactory receptor cells.¹⁹⁻²¹ These studies consolidated the notion that one pathway for olfactory transduction consists of odorant-stimulated generation of cyclic AMP via G_{olf} and subsequent opening of cyclic nucleotide-activated channels to evoke the generator potential.

Based on the observation that some odorants fail to activate adenylate cyclase,⁸ the notion that additional transduction pathways may participate in olfaction was pursued. Odorants that fail to stimulate adenylate cyclase, such as pyrazine, may activate phospholipase C and cause the generation of inositol triphosphate, which in turn may lead to calcium mobilization.^{11,22} In catfish olfactory receptor cells odorant-activated influx of calcium has been documented with fura-2, a calcium-dependent fluorescent dye.²³ In this system generation of inositol triphosphate opens calcium channels in the ciliary plasma membrane.²³

The involvement of multiple transduction pathways in olfaction suggests that mechanisms through which these pathways can communicate with each other must exist. Further studies demonstrated that calmodulin mediates crosstalk between the calcium signalling pathway and the cyclic AMP pathway.²⁴ Calcium bound to

calmodulin activates the olfactory adenylate cyclase type III via a mechanism independent of activation by odorants. Furthermore, isolated olfactory receptor cells from newt fail to undergo inactivation when exposed to high concentrations of odorants in the absence of external calcium or in the presence of internal EGTA suggesting that desensitization to odorants may be calcium-dependent.^{25,26} It is possible that following the initial, rapid, transient increase in cyclic AMP concentration, calcium influx resulting from the response to odorants may cause a secondary sustained rise in cyclic AMP concentration and that cyclic AMP-dependent and calcium-dependent protein phosphorylation may contribute to desensitization.

Discovery and characterization of olfactomedin

We have generated a library of monoclonal antibodies (mAbs) against frog olfactory cilia to identify proteins that are uniquely expressed in olfactory tissue and associated with the chemosensory membrane. By virtue of their tissue-specific expression and ciliary localization such proteins are expected to play important roles in olfaction. We characterized 84 antibody producing hybridomas. Among these antibodies, we identified seven that recognize proteins only in preparations of olfactory cilia, but not in membranes from olfactory nerve, brain, respiratory cilia, heart, liver, lung or kidney.²⁷ These mAbs revealed different immunoreactive patterns on western blots. Some antibodies react with a band at 57 kD. Others reveal immunoreactivity at the same position, but in addition stain a 120 kD polypeptide. One antibody stains only the 120 kD band. Several of the antibodies also stain high molecular weight material, which is retained in the stacking gel and does not enter the resolving gel. During the course of our studies it became clear that all of these mAbs recognize different molecular forms of the same protein, which we have named "olfactomedin."²⁸

We have shown that olfactomedin occurs in its native form as a 120 kD homodimer, composed of two disulfide-linked 57 kD monomers. Reduction with 2-mercaptoethanol converts the dimer into the monomer. The molecule possesses at least three distinct types of antigenic determinants. Some antigenic regions are less accessible in the dimer than in the monomer, whereas the determinant for at least one antibody depends on the integrity of the dimer. Finally several antibodies recognize both molecular forms.

Olfactomedin is heavily glycosylated and carbohydrate moieties dominate its immunogenicity. We took advantage of olfactomedin's strong binding to the lectin *Ricinus communis* agglutinin I (RCA) to purify the protein to homogeneity by affinity chromatography on RCA-agarose.²⁸ We then raised a rabbit polyclonal antiserum against olfactomedin. Evaluation of the reactivity of our mAbs with purified olfactomedin and competition studies between the polyclonal antiserum and our mAbs showed conclusively that our mAbs indeed all recognize the same molecular entity.

Immunohistochemical studies at the light microscopic level using horseradish peroxidase-labeled secondary antibodies and at the electron microscopic level using gold-labeled secondary antibodies localized olfactomedin to the secretory granules of sustentacular cells and the acinar cells of submucosal glands. Immunogold labeling studies at the electron microscopic level on unfixed freeze-substituted samples

showed that olfactomedin is localized in the mucus, surrounding the proximal regions of olfactory cilia, the dendritic knobs and microvilli of sustentacular cells. Two distinct mucous layers could be resolved. Most of the gold particles, reflecting olfactomedin, were restricted to the lower smooth mucus layer. Horseradish peroxidase-labeled sections at the light microscopic level reveal frequent punctate deposits of reaction product along olfactory cilia. Thus, the combined data obtained from light microscopic and electron microscopic studies indicate that olfactomedin is produced by olfactory glands and sustentacular cells and deposited at the mucociliary surface of the olfactory neuroepithelium.²⁸ Moreover, olfactomedin is produced in massive quantities and may represent up to 5% of the total protein content of olfactory membranes. Partial amino acid sequence analysis of olfactomedin's N-terminus shows no homology to any known protein, indicating that olfactomedin's sequence may be unique.

Olfactomedin and the dynamic range of smell.

The fact that olfactomedin is produced only in olfactory tissue and that it is deposited in massive quantities in the lower mucus layer adjacent to the chemosensory membrane suggests that it plays an important role in olfaction. Although its precise function remains to be established, we speculate that olfactomedin together with previously identified odorant binding proteins may facilitate access of hydrophobic odorants to the chemosensory membrane.

After entering the nasal cavity with the inspired air, odorants partition into the mucus which they must traverse to gain access to odorant receptors. The air/water partition coefficients for many odorants favor accumulation of odorants in the aqueous phase.²⁹⁻³¹ Unfortunately, empirical measurements of odorant concentrations in the olfactory mucus *in vivo* are unavailable. In addition, for some classes of especially hydrophobic odorants (e.g. musks) the solubility limit places constraints on the concentration of odorant that can be accommodated in the water phase. It is, therefore, not surprising that glands and sustentacular cells of the olfactory epithelium secrete proteins that bind hydrophobic odorants to facilitate their transport in the mucus.³² The best characterized of these odorant binding proteins is a pyrazine binding protein,^{33,34} which is a member of a family of hydrophobic ligand carrier proteins³⁵ and which in the rat is secreted by the lateral nasal gland.³⁶ We view these previously identified odorant binding proteins as shuttle proteins that facilitate the transfer of odorants from the inspired air into the superficial mucus layer and mediate their transport to the chemosensory membrane. We postulate that olfactomedin, which is restricted primarily to the lower mucus layer, may provide a favorable milieu for interactions between odorants and their receptors after odorants have been released from these odorant binding proteins.

Some evidence which emphasizes the importance of components of the mucus comes from electrophysiological studies. When responses of mucus-depleted isolated olfactory receptor neurons to odorants are measured a narrow dose-response curve between concentrations of 10 and 100 mM is observed, a concentration range that approaches the aqueous solubility limits of the odorants tested.^{37,38} However, in preparations that retain olfactory mucus, robust responses of single neurons to concentrations as low as 1 pM of odorant can be obtained.³⁹ These data are more in line with behavioral and psychophysical observations which show that many

odorants can be detected at submicromolar concentrations and that the dose-response behavior for odorant detection typically spans several log units which indicates that the olfactory system operates over a wide dynamic range. Since olfactomedin is the most prominent component of the lower mucus layer, it is likely to be involved in lowering the threshold for neuronal activation by odorants. We hypothesize that carbohydrate moieties on olfactomedin may provide arrays of hydroxyl groups that can interact with water in the lower mucus layer. This sequestration of water would account for the viscosity of this layer and create a hospitable environment into which hydrophobic compounds could be released from odorant binding proteins. Thus, by facilitating stimulus access, olfactomedin may lower the threshold for odorant detection and, hence, expand the dynamic range of smell.

CONCLUSIONS

We have discovered a novel olfactory glycoprotein, named "olfactomedin," which is expressed exclusively in olfactory tissue. Olfactomedin is produced by sustentacular cells and submucosal glands and deposited in the lower mucus layer which surrounds the proximal regions of chemosensory cilia of olfactory receptor neurons. The tissue specific expression of olfactomedin and its accumulation at the mucociliary surface suggest that this protein plays an important role in olfaction. We hypothesize that olfactomedin through sequestration of surface water provides an environment which facilitates access of hydrophobic odorants to odorant receptors at the chemosensory membrane. Thus, olfactomedin may enhance the ability of the olfactory system to detect odorants at low concentrations and may, at least in part, be responsible for the characteristic wide dynamic range of smell.

ACKNOWLEDGEMENTS

This work was supported by grants from the U.S. Army Research Office (DAAL03-89-K-0178) and the National Institutes of Health (DC00394).

REFERENCES

1. Anholt, R.R.H. (1991) Odorant recognition and olfactory transduction: The new frontier. Chemical Senses 16: in press.
2. Anholt, R.R.H. (1989) Molecular physiology of olfaction. Am. J. Physiol. 257 (Cell Physiol. 26): C1043-1054.
3. Reed, R.R. (1990) How does the nose know? Cell 60: 1-2.
4. Duchamp, A., Revial, M.F., Holley, A. and MacLeod, P. (1974) Odor discrimination by frog olfactory receptors. Chem. Sens. Flavour 1: 213-233.
5. Sicard, G. and Holley, A. (1984) Receptor cell responses to odorants: Similarities and differences among odorants. Brain Res. 292: 283-296.
6. Buck, L. and Axel, R. (1991) A novel multigene family may encode odorant receptors: A molecular basis for odor recognition. Cell 65: 175-187.

7. Pace, U., Hanski, E., Salomon, Y. and Lancet, D. (1985) Odorant-sensitive adenylate cyclase may mediate olfactory reception. Nature **316**: 255-258.
8. Sklar, P.B., Anholt, R.R.H. and Snyder, S.H. (1986) The odorant-sensitive adenylate cyclase of olfactory receptor cells: Differential stimulation by distinct classes of odorants. J. Biol. Chem. **261**: 15538-15543.
9. Shirley, S.G., Robinson, C.J., Dickinson, K., Aujla, R. and Dodd, G.H. (1986) Olfactory adenylate cyclase of the rat: Stimulation by odorants and inhibition by Ca^{2+} . Biochem. J. **240**: 605-607.
10. Breer, H., Boekhoff, I. and Tareilus, E. (1990) Rapid kinetics of second messenger formation in olfactory transduction. Nature **345**: 65-68.
11. Boekhoff, I., Tareilus, E., Strottman, J. and Breer, H. (1990) Rapid activation of alternative second messenger pathways in olfactory cilia from rats by different odorants. EMBO J. **9**: 2453-2458.
12. Pace, U. and Lancet, D. (1986) Olfactory GTP-binding protein: Signal-transducing polypeptide of vertebrate chemosensory neurons. Proc. Natl. Acad. Sci. U.S.A. **83**: 4947-4951.
13. Anholt, R.R.H., Mumby, S.M., Stoffers, D.A., Girard, P.R., Kuo, J.F. and Snyder, S.H. (1987) Transduction proteins of olfactory receptor cells: Identification of guanine nucleotide binding proteins and protein kinase C. Biochemistry **26**: 788-795.
14. Jones, D.T. and Reed, R.R. (1989) Golf: An olfactory neuron specific-G protein involved in odorant signal transduction. Science **244**: 790-795.
15. Bakalyar, H.A. and Reed, R.R. (1990) Identification of a specialized adenylyl cyclase that may mediate odorant detection. Science **250**: 1403-1406.
16. Heldman, J. and Lancet, D. (1986) Cyclic AMP-dependent protein phosphorylation in chemosensory neurons: Identification of cyclic nucleotide regulated phosphoproteins in olfactory cilia. J. Neurochem **47**: 1527-1533.
17. Nakamura, T. and Gold, G.H. (1987) A cyclic nucleotide-gated conductance in olfactory receptor cilia. Nature **325**: 442-444.
18. Dhallan, R.S., Yau, K.W., Schrader, K.A. and Reed, R.R. (1990) Primary structure and functional expression of a cyclic nucleotide-activated channel from olfactory neurons. Nature **347**: 184-187.
19. Kurahashi, T. (1990) The response induced by intracellular cyclic AMP in isolated olfactory receptor cells of the newt. J. Physiol. **430**: 355-371.
20. Frings, S. and Lindemann, B. (1991) Current recording from sensory cilia of olfactory receptor cells in situ. J. Gen. Physiol. **97**: 1-16.
21. Firestein, S., Darrow, B. and Shepherd, G.M. (1991) Activation of the sensory current in salamander olfactory receptor neurons depends on a G protein-mediated cAMP second messenger system. Neuron **6**: 825-835.
22. Breer, H., and Boekhoff, I. (1991) Odorants of the same odor class activate different second messenger pathways. Chemical Senses **16**: 19-29.
23. Restrepo, D., Miyamoto, T., Bryant, B.P. and Teeter, J.H. (1990) Odor stimuli trigger influx of calcium into olfactory neurons of the channel catfish. Science **249**: 1166-1168.
24. Anholt, R.R.H. and Rivers, A.M. (1990) Olfactory transduction: Crosstalk between second messenger systems. Biochemistry **29**: 4049-4054.
25. Kurahashi, T. (1989) Activation by odorants of cation-selective conductance in the olfactory receptor cell isolated from the newt. J. Physiol **419**: 177-192.

26. Kurahashi, T. and Shibuya, T. (1990) Ca²⁺-dependent adaptive properties in the solitary olfactory receptor cell of the newt. Brain Res. **515**: 261-268.
27. Anholt, R.R.H., Petro, A.E. and Rivers, A.M. (1990) Identification of a group of novel membrane proteins unique to chemosensory cilia of olfactory receptor cells. Biochemistry **29**: 3366-3373.
28. Snyder, D.A., Rivers, A.M., Yokoe, H., Menco, B.Ph.M. and Anholt, R.R.H. (1991) Olfactomedin: Purification, characterization and localization of a novel olfactory glycoprotein. Biochemistry **30**: 9143-9153.
29. Getchell, T.V., and Getchell, M.L. (1990) Regulatory factors in the vertebrate olfactory mucosa. Chemical senses **15**: 223-231.
30. Senf, W., Menco, B.Ph.M., Punter, P.H., Duyvensteyn, P. (1980) Determination of odor affinities on the dose-response relationships of the frog's electro-olfactogram. Experientia **36**: 213-215.
31. Hornung, D.E. and Mozell, M.M. (1981) Accessibility of odorant molecules to the receptors. In: Biochemistry of Taste and Olfaction (ed. R.H. Cagan and M.R. Kare), pp.33-45, Academic Press, New York, N.Y.
32. Carr, W.E.S., Gleeson, R.A. and Trapido-Rosenthal, H.G. (1990) The role of perireceptor events in chemosensory processes. Trends Neurosci.**13**: 212-215.
33. Pelosi, P., Baldaccini, N.E. and Pisanelli, A.M. (1982) Identification of a specific olfactory receptor for 2-isobutyl-3-methoxypyrazine. Biochem. J. **210**: 245-248.
34. Pevsner, J., Trifiletti, R.R., Strittmatter, S.M. and Snyder, S.H. (1985) Isolation and characterization of an olfactory receptor protein for odorant pyrazines. Proc. Natl. Acad. Sci. U.S.A. **82**: 3050-3054.
35. Pevsner, J., Reed, R.R., Feinstein, P.G. and Snyder, S.H. (1988) Molecular cloning of odorant-binding protein: member of a ligand carrier family. Science **241**: 336-339.
36. Pevsner, J., Hwang, P.M., Sklar, P.B., Venable, J.C., and Snyder, S.H. (1988) Odorant-binding protein and its mRNA are localized to lateral nasal gland implying a carrier function Proc. Natl. Acad. Sci. U.S.A. **85**: 2383-2387.
37. Firestein, S. and Werblin, F. (1989) Odor-induced membrane currents in vertebrate-olfactory receptor neurons. Science **244**: 79-82.
38. Firestein, S., Shepherd, G.M. and Werblin, F.S. (1990) Time course of the membrane current underlying sensory transduction in salamander olfactory receptor neurons. J. Physiol. **430**: 135-158.
39. Frings, S. and Lindemann, B. (1990) Single unit recording from olfactory cilia. Biophys. J. **57**: 1091-1094.

BLANK

USING A SILICON MICROPHYSIOMETER TO DETECT AGENTS THAT ALTER CELLULAR PHYSIOLOGY

John C. Owicki, H. Garrett Wada, and J. Wallace Parce

Molecular Devices Corporation, 4700 Bohannon Drive, Menlo Park, CA 94025

The silicon microphysiometer is an instrument that uses the silicon-based light addressable potentiometric sensor to detect many physiological events in cultured cells noninvasively and in real time. It does so by measuring changes in the rates at which cells acidify their environments, reflecting subtle changes in energy demand and pH regulation that generally attend physiological alterations. To date (11/91) the activation of 15 different cellular receptors by agonists (and inactivation by antagonists) has been detected in this way under pharmacologically relevant conditions. The instrument is also the basis of an *in-vitro* toxicological assay for ocular irritancy. The ability to detect a broad range of agents on the basis of their effects on cell function, usually within minutes of initial contact, may make the microphysiometer useful for chemical defence. This possibility is strengthened by the ability of the system to evolve to meet new threats and its ready integration with enzyme-assay and immunoassay methodologies based on the same sensor.

INTRODUCTION

There are two broad strategies to detect the presence of a substance that can affect a living system: structural and functional. Structural approaches include mass spectroscopy, NMR, immunoassays, and HPLC; they give information about the presence of molecules with particular structural characteristics without direct reference to how these molecules might affect an organism. Functional approaches include bioassays and enzyme assays, and they report physiological effects without giving much direct structural information about the molecules causing these effects.

These strategies are complementary. Structural methods are particularly useful to test for a particular agent, or when all possible agents are known and it is practical to test for each one. Functional methods, on the other hand, are better when the fundamental concern is whether a sample is biologically active, or when it is not possible to assay for all possible agents.

In this paper we describe the silicon microphysiometer, a system for detecting agents that perturb the physiology of living cells. It is a rather general implementation of the functional strategy. We briefly summarize the principles and design of the instrument, and the results obtained to date. For more details, the reader should consult our previous publications on the subject¹⁻⁶. We close by discussing the likely evolution of the silicon microphysiometer.

PRINCIPLES AND INSTRUMENTAL DESIGN

The fundamental principle of the silicon microphysiometer is that the metabolic activity of cells—particularly the rate of energy metabolism—is closely tied to the physiological state of the cells. Hence, changes in physiological state are reflected in changes in metabolic activity. These changes in metabolic activity are detected by a non-invasive chemical sensor that provides real-time information about the interaction of the cells with their chemical environment.

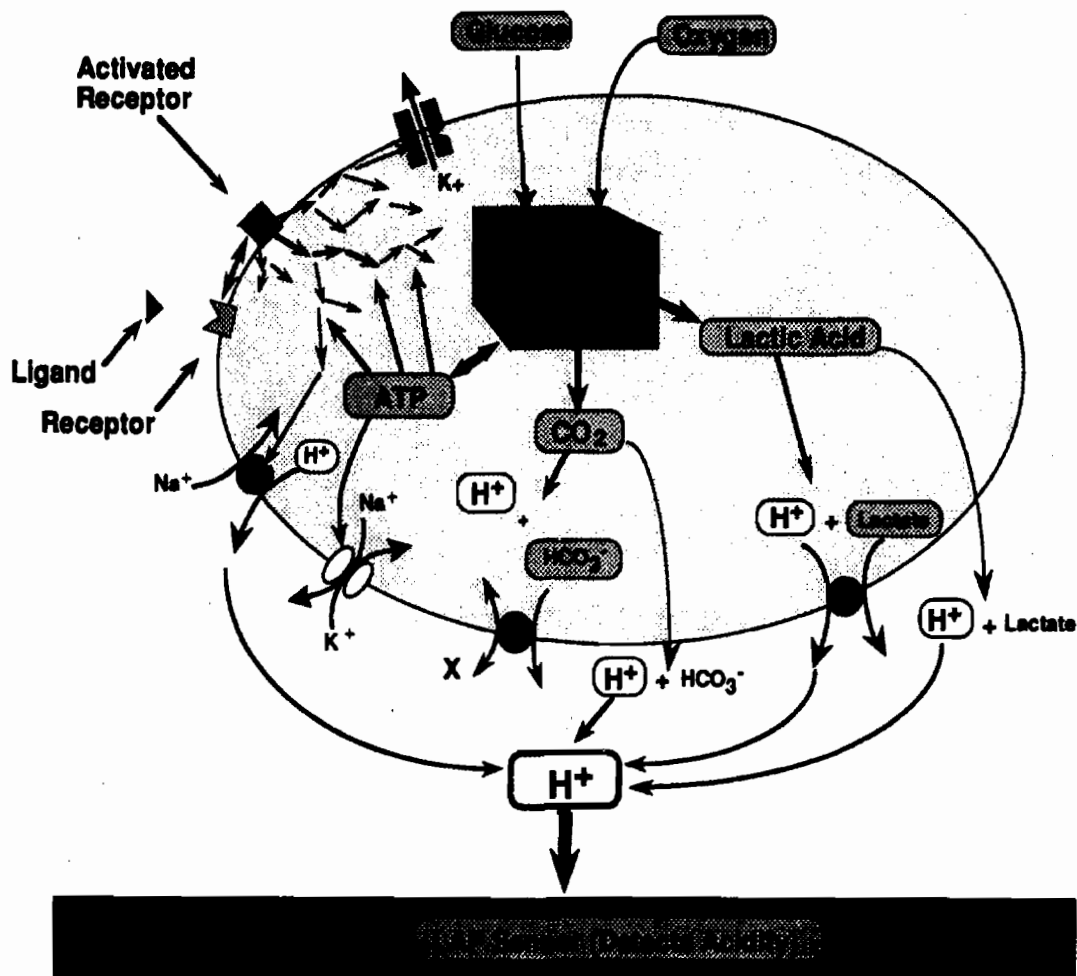


FIGURE 1. Schematic depiction of the biological processes involved in extracellular acidification, as detected by the silicon microphysiometer. Shown are the production of metabolic acids by energy metabolism, the transport of the acids out of the cell, and coupling of physiological processes such as receptor activation to energy metabolism and, hence, to extracellular acidification.

Metabolic activity can be defined in several ways. As Figure 1 indicates, one could in principle monitor the rate of oxygen or glucose consumption, or the rate of production of heat, lactic acid, or carbon dioxide. The optimal choice depends largely on the available means of detection.

We have chosen to measure the rate at which cells excrete acid (principally lactic acid and carbon dioxide), largely because of the availability of the light addressable potentiometric sensor (LAPS) for making pH measurements⁷. Like a glass pH electrode, the LAPS draws no direct current and is therefore essentially non-perturbing. Unlike a glass pH electrode, it has low electrical impedance and a planar geometry that render it particularly suitable for making measurements in small (nL to μ L) volumes. The LAPS is based on silicon technology and can be micromachined to give structures for retaining or manipulating cells and culture medium⁸. Finally, the LAPS performs well out of the research laboratory under real-life conditions: it is the basis of the commercial ThresholdTM immunoassay system^{9,10}.

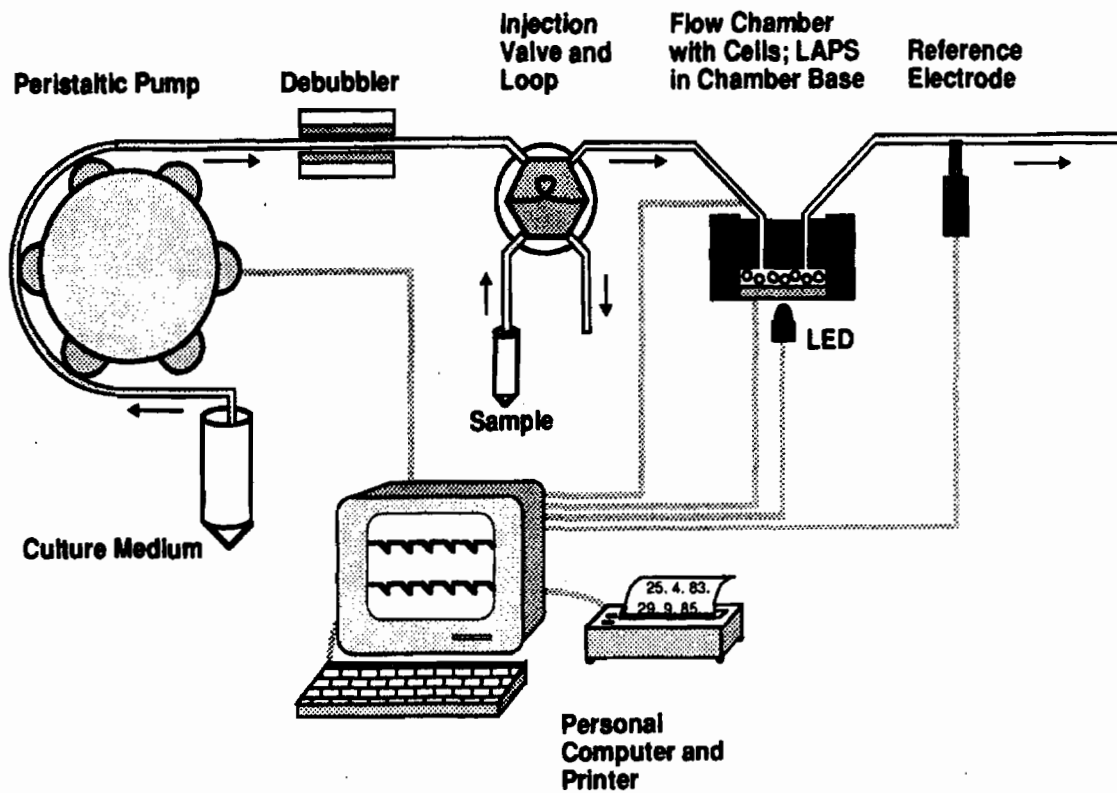


FIGURE 2. Schematic system diagram of the silicon microphysiometer. See the text for details.

Figure 2 is a schematic diagram of the silicon microphysiometer. Living cells are placed in a flow chamber in diffusive contact with the LAPS and are supplied with nutrient culture medium via a peristaltic pump. A valve of the type used in liquid chromatography determines which of two streams of medium bathes the cells; alternatively, it can be configured as a sample-injection loop. In either configuration, the cells can be exposed to a sample for a pre-determined time. An instrument typically contains eight flow chambers operated in parallel.

A personal computer controls the flow of medium. While the flow is on ($\sim 1 \mu\text{L/s}$), the LAPS reports a steady pH close to that of the fresh medium. When the flow is halted, acidic metabolic products build up in the cell chamber and the pH steadily decreases. *This acidification rate, which is monitored by the computer, is the measure of metabolic rate that is reported by the silicon microphysiometer.* After about 30-60 s, when the pH has decreased by about 0.05-0.10, the flow is restarted. Fresh medium enters the chamber, and the original steady pH is restored until the next measurement of acidification rate. Standard cell-culture medium is used, except that pH excursions are increased by eliminating bicarbonate buffer.

Adherent cells such as fibroblasts and neurons are cultured directly on a disposable porous membrane, covered with a second membrane, and inserted into the cell chamber. Nonadherent cells such as lymphocytes or yeast are immobilized between the two membranes in a thin fibrin clot or collagen matrix. Typically 10^5 to 10^6 cells are loaded into a flow chamber; data are obtained only from the central $\sim 3 \mu\text{L}$ of the chamber, containing 10^3 to 10^4 cells. The acidification measurement generally does not injure the cells; some have survived and grown as long as six days in the device¹¹.

PHYSIOLOGICAL CHANGES OBSERVED WITH THE SILICON MICROPHYSIOMETER

Two subjects, receptor activation and cytotoxicity, have comprised the bulk of studies performed with the silicon microphysiometer to date. Receptor activation is typically observed as an increase in extracellular acidification rate, while cytotoxicity is observed as a decrease. We next summarize the results from both areas.

As is suggested in Figure 1, the activation of a cellular receptor by a ligand (neurotransmitter, cytokine, or hormone) sets in motion a complicated series of events leading to some physiological response. Some of these events change the demand for energy, thus changing the rate of energy metabolism. Others may alter intracellular pH, causing protons to be transferred between the cytoplasm and extracellular medium. As a point of logic, both must cause changes in the rate of excretion of protons, but are the changes large or long lived enough to detect?

In most cases they can be detected with the silicon microphysiometer. For a wide variety of receptors operating by different mechanisms, a saturating dose of agonist increases the acidification rate by 10-100%. The increase may be immediate (<1 min) or may develop over ~15 min; it may decay quickly (~1 min) or may persist essentially as long as the agonist is present. Antagonists can be detected by inhibition of agonist-induced activation. Dose-response relationships depend on the system under study and are similar to those obtained with assays for the appropriate second-messenger, such as cyclic adenosine monophosphate.

The receptors whose activation has been observed in the silicon microphysiometer include the m_1 and m_3 muscarinic acetylcholine^{2,12}, β_2 adrenergic², prostaglandin E¹³, D₁ and D₂ dopamine^{14,15}, insulin/ILGF¹⁶, epidermal growth factor^{1,2}, glutamate (kainate)⁶, γ -interferon¹⁷, interleukin-2¹¹, interleukin-4¹⁷, T-cell¹⁸, and granulocyte-macrophage colony stimulating factor¹⁹. Figure 3 shows data from one representative example, the activation of glutamate receptors in hippocampal neurons and glia by kainate, an analog of the excitatory neurotransmitter glutamate⁶. Also shown is the inhibition of this response by kynurenate, a competitive antagonist of kainate. This study bridges the subjects of receptor activation and cytotoxicity. The overstimulation of glutamate receptors in the central nervous system has been linked to neuronal death, a process termed excitotoxicity. Using the silicon microphysiometer, it was found that brief (10 min) exposure of hippocampal neurons and glia to a toxic dose of kainate caused an initial stimulation of acidification rate, followed by an apparently irreversible decline over a period of hours that reflected an inhibition of cell metabolism⁶.

The most thorough application of the silicon microphysiometer to toxicology has been as an *in-vitro* assay for ocular irritancy. A pilot experiment found good correlation between the ocular irritancy *in vivo* of eight common solvents and detergents and the concentrations of these compounds sufficient to depress acidification rates of human skin cells (keratinocytes) by 50% after approximately five minutes of exposure¹. A subsequent study of 17 preparations representative of consumer products found a correlation coefficient of 0.87 for the rank order of irritancies determined *in vitro* and *in vivo*^{3,20}. Similar results have been obtained recently on another panel of 19 surfactants using murine L fibroblastic cells instead of human keratinocytes²¹.

The severity of a response to a toxic insult is a matter of duration as well as intensity. Since the measurements in the silicon microphysiometer are non-destructive, it is convenient to monitor the aftermath of exposure to a toxic compound to determine whether, and on what time scale, the cells recover. Experiments of this type are as yet sparse^{1,3}, but it is apparent that data on recovery provide information somewhat different from data on intensity (concentrations giving 50% inhibition for a fixed time of exposure).

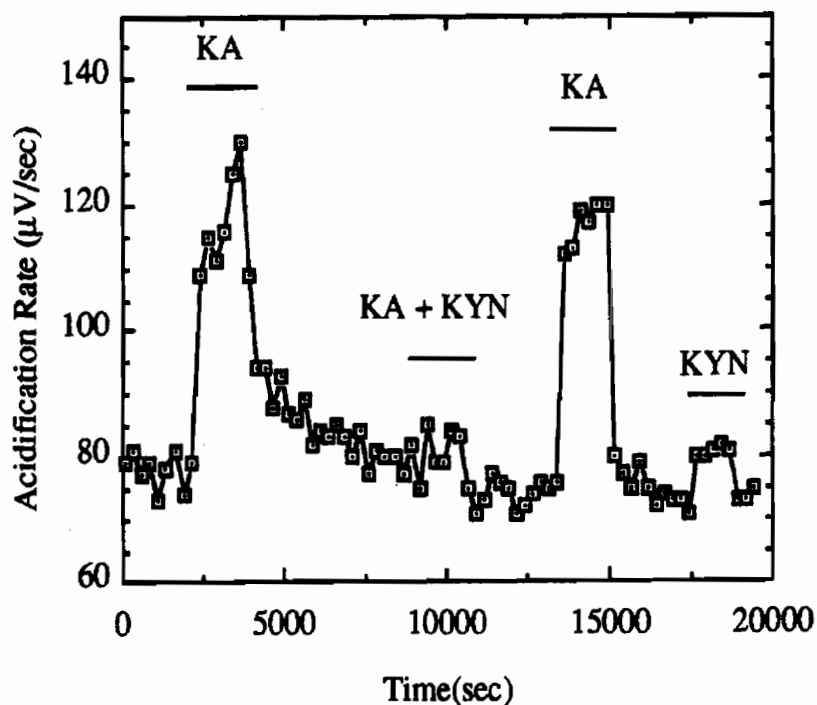


FIGURE 3 Detection of the activation of glutamate receptors using the silicon microphysiometer. The figure shows that 500 μ M kainate (KA), a glutamate agonist, promptly and reversibly stimulates the extracellular acidification rate of co-cultures of neurons and glia from the hippocampus of the fetal rat. The stimulation is abolished by 1 mM kynureate (KYN), a competitive glutamate antagonist. After Raley-Susman *et al.*⁶

None of these studies of ocular irritancy used cells from the eye, yet they were successful. One reason is that the irritants tested probably act by mechanisms that operate in most cell types. For example, detergents interfere with the barrier properties of cell membranes. Good correlation between *in-vivo* and *in-vitro* toxicity might also be expected when model cell systems are exposed to other classes of toxic compounds that also act on widely distributed biological activities, for example as metabolic poisons do.

CONCLUSIONS AND FUTURE DIRECTIONS

Since its debut two years ago¹, the silicon microphysiometer has been shown to detect the presence of cell-affecting agents ranging from neurotransmitters and their antagonists through ocular irritants. It does so according to their ability to alter cellular physiology, not their activity in some structure-based assay. This is very useful for applications in which physiological information is the goal and in which it is not feasible to screen with a structural method for all the relevant compounds that might be present.

It is notable that one instrument spans this range of applications. The specificity necessary for each case is provided not by the silicon microphysiometer itself, but by the choice of cells and chemicals that are employed with it. It should be possible to generalize the capabilities of the instrument further, to include also immunoassays, receptor-binding assays, and enzyme assays on a single platform. Immunoassays already exist in the LAPS-based Threshold system. LAPS-based assays for the binding of ligands to the nicotinic acetylcholine receptor have been developed²². The feasibility of enzyme assays has been demonstrated in a LAPS-based assay

for anticholinesterase agents: acetylcholinesterase acidifies as it produces acetic acid from acetylcholine, and anticholinesterase agents inhibit this acidification²³. The flexibility and open architecture of the silicon microphysiometer should allow it to be adapted to changing performance requirements without extensive re-engineering.

Other improvements will involve the cells used in the system. Using recombinant genetic techniques, it should be possible to improve the sensitivity of acidification rate to agents of interest. This might be done by increasing the number of receptors on a cell, or by manipulating signal-transduction pathways. If a single instrument is to detect a wide variety of agents, it would be convenient to transfect many different kinds of receptors into one optimized host cell line, thereby keeping the number of different types of cells to a manageable level.

A further improvement in the cells is logistical. Work with mammalian cells usually requires fairly sophisticated cell-culture equipment in a laboratory setting. The ability to preserve cells by freezing in some central facility, and then distribute and thaw immediately before use, would relax requirements for facilities at the point of use. These requirements could be relaxed even further if the required biological activities were engineered into cells that are more robust than typical mammalian cells.

The final improvement discussed here is the use of more sophisticated silicon fabrication technology. Miniaturization has benefits beyond the convenience of working with a smaller instrument and smaller volumes of reagents; it will also allow better time resolution as fluid paths shorten, plus increased multiplicity of assays. Existing micromachining methods permit the construction not only of fluidics channels on the LAPS chips, but also such active devices as valves and pumps.

In conclusion, the characteristics of the existing versions of the silicon microphysiometer, coupled with the improvements that seem feasible, suggest that the system will be useful for chemical-defense applications.

ACKNOWLEDGEMENTS

The work described here was supported in part by CRDEC and DARPA (ARO DAAL03-86-C-0009) and by DARPA (MDA972-92-C-0005).

REFERENCES

- ¹Parce, J.W., Owicki, J.C., Kercso, K.M., Sigal, G.B., Wada, H.G., Muir, V.C., Bousse, L.J., Ross, K.L., Sikic, B.I., and McConnell, H.M.: *Detection of Cell Affecting Agents with a Silicon Biosensor*. *Science* 246:243-247 (1989).
- ²Owicki, J.C., Parce, J.W., Kercso, K.M., Sigal, G.B., Muir, V.C., Venter, J.C., Fraser, C.M., and McConnell, H.M.: *Continuous Monitoring of Receptor-Mediated Changes in the Metabolic Rates of Living Cells*. *Proc. Natl. Acad. Sci. U.S.A.* 87:4007-4011 (1990).
- ³Bruner, L.H., Kercso, K.M., Owicki, J.C., Parce, J.W., and Muir, V.C.: *Testing Ocular Irritancy in Vitro with the Silicon Microphysiometer*. *Toxicology in Vitro* 5:277-284 (1991).
- ⁴McConnell, H.M., Rice, P., Wada, H.G., Owicki, J.C., and Parce, J.W.: *The Microphysiometer Biosensor*. *Current Opinion in Structural Biology* 1: 647-652 (1991).
- ⁵Owicki, J.C. and Parce, J.W.: *Biosensors Based on the Energy Metabolism of Living Cells: The Physical Chemistry and Cell Biology of Extracellular Acidification*. *Biosensors and Bioelectronics* (in press).
- ⁶Raley-Susman, K.M., Kercso, K.M., Owicki, J.C., and Sapolsky, R.M.: *Effects of Excitotoxin Exposure on Metabolic Rate of Primary Hippocampal Cultures: Application of Silicon Microphysiometry to Neurobiology*. *J. Neurosciences* (1991 in press).

- ⁷Hafeman, D.G., Parce, J.W., and McConnell, H.M.: *Light-Addressable Potentiometric Sensor for Biochemical Systems*. **Science** 240:1182-1185 (1988).
- ⁸Bousse, L.J., Parce, J.W., Owicki, J.C., and Kercso, K.M.: *Silicon Micromachining in the Fabrication of Biosensors Using Living Cells*. **Technical Digest IEEE Solid State Sensor and Actuator Workshop** 173-176 (1990).
- ⁹Kung, V.T., Panfili, P.R., Sheldon, E.L., King, R.S., Nagainis, P.A., Gomez, B., Ross, D.A., Briggs, J., and Zuk, R.F.: *Picogram Quantitation of Total DNA Using DNA-Binding Proteins in a Silicon Sensor-Based System*. **Anal. Biochem.** 187: 220-227 (1990).
- ¹⁰Briggs, J., Kung, V.T., Gomez, B., Kasper, K.C., Nagainis, P., Masino, R.S., Rice, L.S., Zuk, R., and Ghazarossian, V.E.: *Sub-Femtomole Quantitation of Proteins with Threshold, for the Biopharmaceutical Industry*. **BioTechniques**. 9: 598-606 (1990).
- ¹¹Wada, H.G., Owicki, J.C., and Parce, J.W.: *Cells on Silicon: Bioassays with a Microphysiometer*. **Clinical Chemistry** 37: 600-601 (1991).
- ¹²Miller, D.L., Owicki, J.C., and Parce, J.W.: *Real-time Detection of Agonist-Induced Acetylcholine Receptor Activation*. **FASEB J.** 5:A1600 (1991) (abstract).
- ¹³Parce, J.W., Owicki, J.C., and Kercso, K.M.: *Biosensors for Directly Measuring Cell-Affecting Agents*. **Annales de Biologie Clinique** 48: 639-641 (1990).
- ¹⁴Salon, J.A., Johnson, R.A., and Civelli, O.: *Real-Time Measurements of Human D₁ and D₂ Receptor Activity with a Silicon-Based Biosensor*. **Soc. Neurosci. Abstr.** 17(1): 76 (1991) (abstract).
- ¹⁵Rosser, M.P., Kozlowski, M.R., and Neve, K.A.: *Effects of Dopamine D₂ Receptor Activation Measured by a Novel Technique: Microphysiometry*. **Soc. Neurosci. Abstr.** 17(1):818 (1991) (abstract).
- ¹⁶Rice, P.A., Owicki, J.C., Parce, J.W., and McConnell, H.A.: *Transient Responses Detected in a Microphysiometer*. **FASEB J.** 5:A1014 (1991) (abstract).
- ¹⁷Indelicato, S.R., Zeilinski, P., Meyer, L., and Kercso, K.M.: *Real-Time Assessment of Cellular Metabolism from Cytokine Mediated Stimulation of Colon Carcinoma Cells (COLO-205) as Measured by a Microphysiometer*. Abstracts of the 5th International Conference on Immunopharmacology, Tampa, Florida, 27-30 May 1991.
- ¹⁸Wada, H.G., Nag, B., Fok, K.S., Sharma, S.D., McConnell, H.M., and Clark, B.R.: *Antigen Specific Stimulation of T-Cell Metabolism by MHC II-Peptide Complex as Measured by the Silicon Microphysiometer*. **FASEB J.** 5:A1457 (1991) (abstract).
- ¹⁹DeVries, J.K., Indelicato, S.R., Meyer, L., and Wada, H.G.: *Real-Time Assessment of Cellular Metabolism from GM-CSF Mediated Stimulation of TF-1 Cells as Measured by a Microphysiometer*. Abstracts of the 3rd International Workshop on Cytokines, Stresa, Italy, 10-14 November 1991.
- ²⁰Bruner, L.H., Kain, D.J., Roberts, D.A., and Parker, R.D.: *Evaluation of Seven in Vitro Alternatives for Ocular Safety Testing*. **Fundament. Applied Tox.** 17:136-149 (1991).
- ²¹Cartroux, P., Cottin, M., Dossou, K.G., and Rougier, A.: *The Silicon Microphysiometer: A New Tool for Testing Ocular Irritancy in Vitro*. Abstracts of the 3rd. **Colloquium of Société de Pharmaco-Toxicologie Cellulaire**, Paris, 18 October 1991.
- ²²Eldefrawi, M., and Rogers, K.: *Comparison of Receptor-Based LAPS and Fiber-Optic Biosensors*. Paper in this volume.
- ²³Fernando, J.C., Rogers, K.R., Valdes, J.J., and Eldefrawi, M.E.: *An Anticholinesterase Biosensor System Based on Silicon Detector Potentiometry*. Paper in this volume.

BLANK

MICROBIAL DEGRADATION OF 3-HYDROXYPIPERIDINE AND 3-HYDROXYQUINUCLIDINE

Joseph J. DeFrank and Christine Savage
U.S. Army Chemical Research, Development and Engineering Center
Aberdeen Proving Ground, MD 21010-5423

ABSTRACT

The benzilate ester of 3-hydroxyquinuclidine (BZ or QNB) is a potent antagonist of the muscarinic acetylcholine receptor. In addition to its use in neuropharmacological research, BZ was once considered for use as a temporary, incapacitating agent in chemical warfare. As part of a program to use biotechnological methods for the detoxification and destruction of hazardous chemicals of military origin, the search for microorganisms that could totally degrade BZ was initiated. For the initial enrichment studies BZ was not utilized in order to avoid possible health hazards. Instead, the primary constituents of BZ, 3-hydroxyquinuclidine (3-quinuclidinol, QO) and benzoic acid were used as sole sources of carbon. In addition to QO, the simpler but related compound 3-hydroxypiperidine (3-piperidinol, 3PO) was utilized as a carbon source in enrichments. Soil samples were obtained from a variety of locations on the Edgewood Area of APG as well as off-post sites. A number of isolates were obtained that could utilize QO and/or 3PO as sole carbon and energy source. This report provides some preliminary characterization information about these isolates.

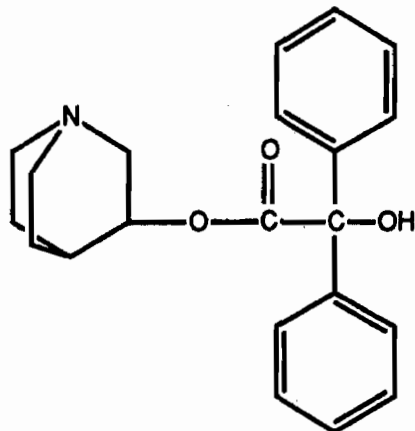
INTRODUCTION

The destruction of the incapacitating agent BZ [1] (Figure 1) by microorganisms can be envisioned to take place through a number of different routes. The microorganism(s) could attack the intact BZ molecule at either the quinuclidinyl or benzilate moiety. That portion of the molecule would be degraded until attack on the remaining portion could occur. Alternatively, the ester linkage between the two portions of the molecule can be chemically (spontaneous hydrolysis) or biologically cleaved to yield the two products 3-quinuclidinol (QO) and benzoic acid. Due to the difficulties involved in the use of BZ itself as a carbon source for enrichment studies, the relatively non-toxic component QO was targeted for initial study. Because of the similarity to 3-piperidinol (3PO), this simpler compound was also used as a carbon source in enrichment studies. It was hoped that microorganisms capable of using 3PO for growth could potentially co-metabolize the QO. The structures of the parent compounds of QO and 3PO, quinuclidine (Q) and piperidine (P) are also shown in Figure 1.

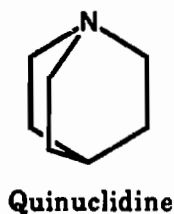
Although there have been reports in the literature [2,3] concerning the metabolism of piperidine and a related compound morpholine (Figure 2), a search revealed no studies on the metabolism or degradation of either 3-quinuclidinol or 3-piperidinol by microorganisms. The

lack of previous research in the degradation of these or related compounds means that possible pathways will require *de novo* determination.

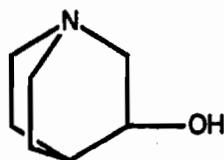
FIGURE 1: Structure of BZ and related compounds



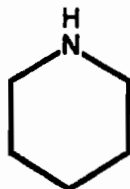
BZ (QNB, quinuclidinylbenzilate)



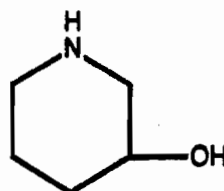
Quinuclidine



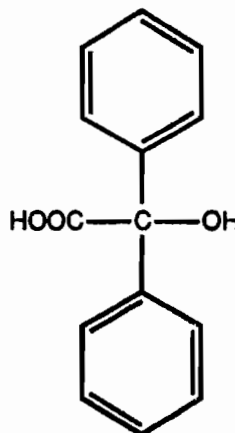
3-Quinuclidinol



Piperidine



3-Piperidinol



Benzilic Acid

This paper describes preliminary efforts at the isolation and characterization of microorganisms capable of growth and metabolism of QO and/or 3PO.

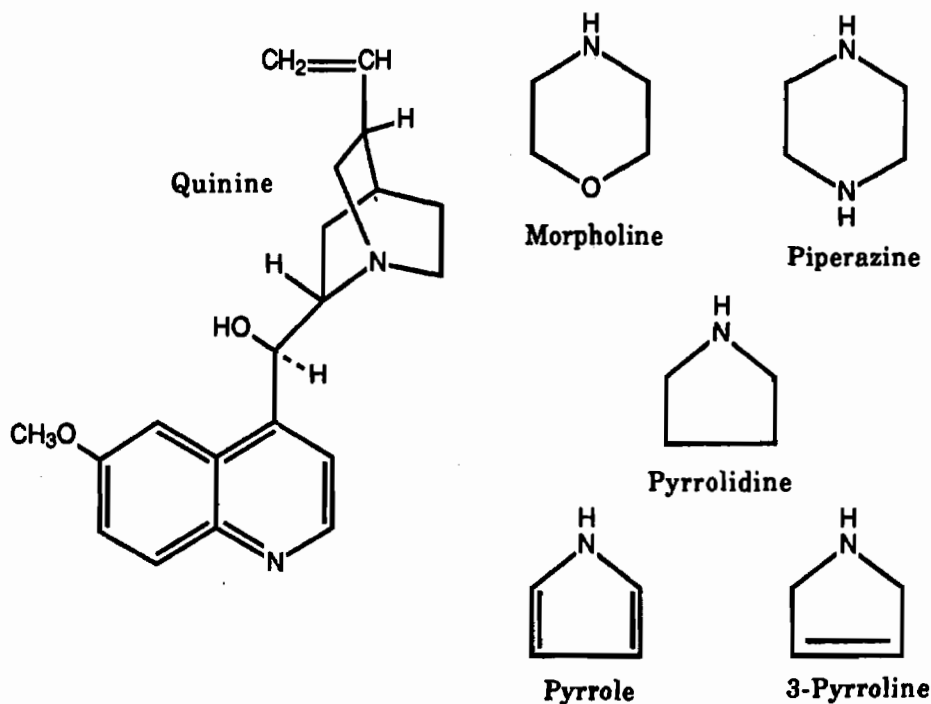
MATERIALS AND METHODS

Materials: Components of the Minimal Media described below were of standard research grade. The carbon sources utilized in these studies were all obtained from Fluka Chemical Company.

Organisms: Soil samples were taken at random from sites in the Edgewood Area of Aberdeen Proving Ground, Maryland and elsewhere in Harford County, MD. None of the sampling locations were known to be or likely to have been exposed to BZ in the past. The occurrence of QO

and/or 3PO in the environment is unknown although the quinuclidinyl base structure is found in the naturally occurring alkaloid quinine and related compounds.

Figure 2: Natural and synthetic compounds structurally related to BZ, QO, etc.



Growth Conditions: Initial enrichment studies were conducted in Minimal Medium #1, consisting of (g/l): KH_2PO_4 , 2.0; $(\text{NH}_4)_2\text{SO}_4$, 1.0; Wolin Salts Solution [4], 10.0 ml; and carbon source (QO or 3PO), 2.0. The pH of the media was adjusted to 7.0 with either NaOH or HCl. Soil samples were resuspended in 5 ml of Phosphate-Buffered Saline (PBS) and shaken at room temperature for 1-2 hours. The soil suspension was allowed to settle for ~10 minutes and an aliquot of the supernatant used to inoculate culture tubes containing 5 ml of media plus carbon source. The enrichments were incubated at room temperature or 30°C until evidence of growth was observed.

In later enrichments and growth studies Minimal Medium #2 was utilized. This consisted of (g/l): Na_2HPO_4 , 2.5; KH_2PO_4 , 1.5; $(\text{NH}_4)_2\text{SO}_4$, 2.0; NaCl, 1.0; Wolin Salts Solution, 10.0 ml; and carbon source, 20 mM; pH 7.0. For volatile carbon sources, the neat liquids were added to the tubes of sterile media just prior to inoculation. For growth on solid media, agar (18 g/l) was added to either of the Minimal Media above.

Although the initial enrichments utilized QO and 3PO as sole carbon sources, in some of the later studies two additional substrates were examined. These were the two parent compounds: quinuclidine (Q) and piperidine (P). The HCl salts of these compounds were utilized at a concentration of 20 mM.

Growth was determined by monitoring the increase in absorbance at 650 nm with a Spectronic 21 spectrophotometer (Bausch & Lomb). The absorbance due to uninoculated media was used to standardize the instrument and was subtracted from the experimental values.

RESULTS

Although preliminary results indicated that a number of isolates had been obtained that were capable of growth on QO and Q, in subsequent subculturing studies the growth potential of the isolates decreased or disappeared. After plating of the liquid enrichment cultures on solid media containing either QO or Q as the sole carbon source, single colonies were selected and purified by replating several times. However, after return of these isolates to liquid media they failed to grow on either QO or Q.

FIGURE 3: Growth of isolate CS13

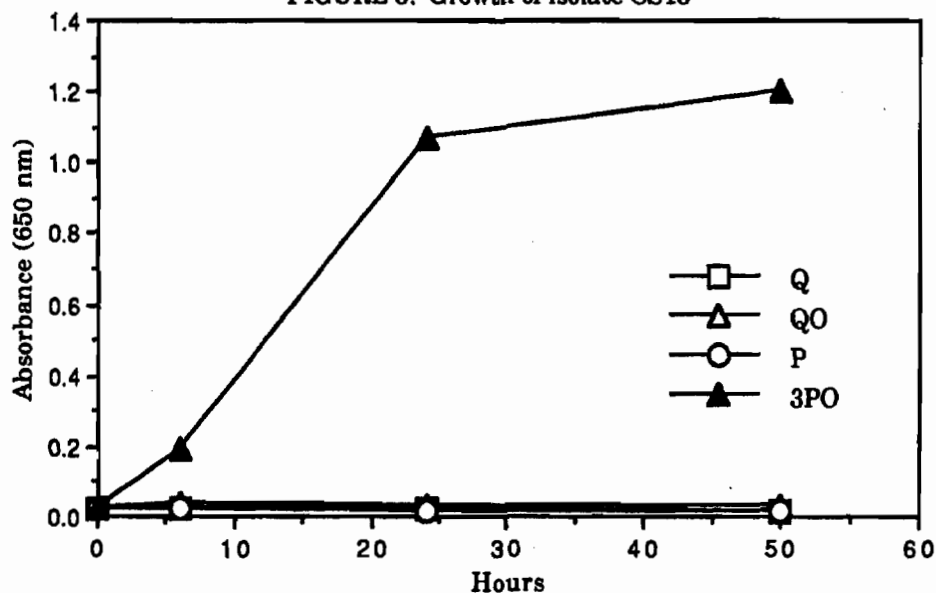
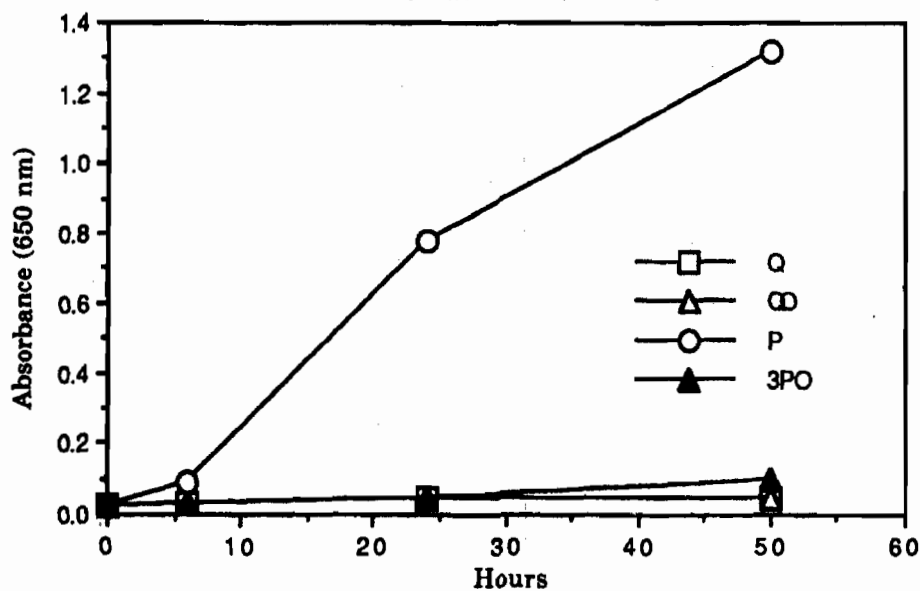


FIGURE 4: Growth of isolate CS20



In contrast to QO and Q, enrichment cultures with P or 3PO as sole source of carbon led to the isolation and purification of a variety of microorganisms capable of utilizing these com-

pounds as shown in Figures 3 and 4. A summary of the ability of the purified isolates to grow on these four carbon sources is given in Table 1.

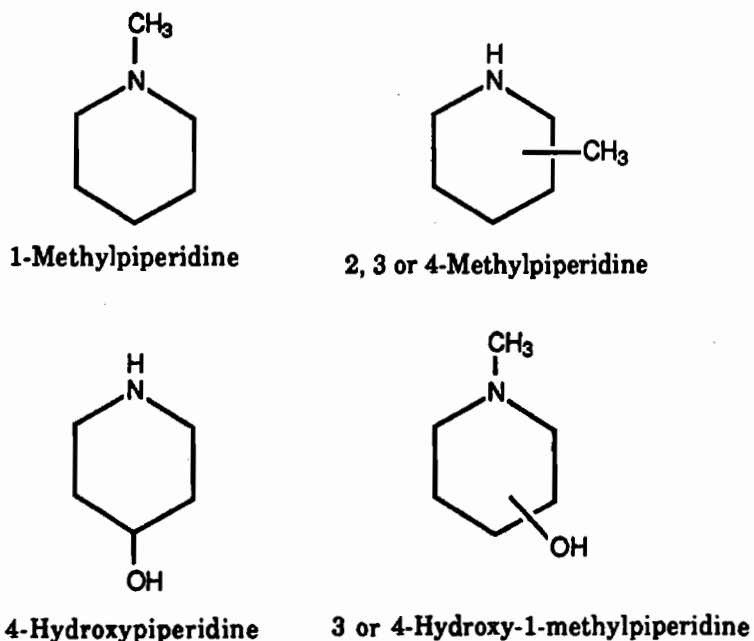
It now appears that the cultures growing on QO and/or Q in liquid culture were mixed cultures composed of a number of microorganisms that are required for growth. The reason why some of the isolated bacterial strains could grow quite well on solid media but not in liquid remains to be determined. A possible explanation would be that there are trace contaminants in the agar that fulfill nutritional requirements of the microorganisms. In liquid cultures these materials are not present, so only the mixed cultures will grow.

TABLE 1: Substrate profile of purified bacterial isolates.

Isolate	Relative Growth on:			
	Q	QO	P	3PO
CS12	○	○	●●●	●
CS13	○	○	○	●●●
CS15	○	○	●●●	○
CS16	●	○	●●●	●
CS17	○	○	●●●	○
CS19	○	○	●●●	●
CS20	○	○	●●●	●

○ = no growth
 ● = slight growth
 ●● = moderate growth
 ●●● = good growth

FIGURE 5: Compounds not supporting growth of CS isolates.



The analogs of P and 3PO shown in Figure 5 were tested as possible growth substrates for the mixed cultures and purified isolates obtained on Q, QO, P, and 3PO. None of these isolates showed any significant growth after up to 1 week of incubation. This indicates that some or all

of the enzyme systems involved in the metabolism of P and 3PO have a high degree of substrate specificity.

In addition, the lack of significant growth of CS13 on P and of the other isolates on 3PO would suggest that these related compounds are metabolized by different pathways.

CONCLUSIONS

Initial attempts at obtaining purified bacterial cultures capable of growing on and mineralizing the BZ component 3-quinuclidinol (QO) have as yet been unsuccessful. However, the ability of mixed cultures to grow on this compound demonstrates that it can be biodegraded. These results suggest that the use of mixed cultures of QO degrading bacteria, in conjunction with strains capable of degrading benzoic acid, will provide an alternative technology for the destruction of BZ. Future efforts will focus on the use of selective pressure techniques to obtain purified cultures that will utilize QO as both the sole carbon and nitrogen source. Studies to determine the metabolic pathway for QO in these cultures will also be undertaken. In addition, enrichment studies with benzoic acid will be initiated. When purified or mixed cultures are available for the degradation of both compounds they will be examined separately and together to determine their activity on BZ.

REFERENCES

1. World Health Organization, Geneva. 1970. Health Aspects of Chemical and Biological Weapons. 49-51.
2. Agarwal, M., U. Roy, and O.P. Shukla. 1988. Piperidine catabolism and DOPA decarboxylase synthesis in a *Pseudomonas*. Biol. Mem. 14:187-98.
3. Knapp, J.S., A.G. Calley, and J. Mainprize. 1982. The microbial degradation of morpholine. J. Appl. Bacteriol. 52:5-13.
4. Wolin, E.Z., M.J. Wolin, and R.S. Wolfe. 1963. Formation of methane by bacterial extracts. J. Biol. Chem. 238:2882-2886.

ENZYMATIC DEGRADATION OF GF

Steven P. Harvey

ABSTRACT

The purified enzyme OPAA-2 and crude lysates from several halophilic bacteria which had previously been shown to have activity against other G agents were tested to determine the extent of their activity against GF. Fluoride electrode assays were conducted in triplicate at pH 7.2 with and without Mn^{2+} and at pH 8.5 with Mn^{2+} . The isolates chosen for testing with GF were those which had previously shown the most promising activity against GA, GB and GD. All of the isolates tested had activity against GF.

INTRODUCTION

During the recent United Nations inspection of Iraq (UNSCOM 9), it was found that one of the chemical agents being produced by Iraq was GF (O-cyclohexyl methylphosphonofluoridate) (personal communication from William Dee¹). Although many enzymes have been demonstrated to catalyze the hydrolysis GA (N,N-dimethylphosphoramidocyanidate), GB (O-isopropyl methylphosphonofluoridate) and GD (O-pinacolyl methylphosphonofluoridate), none have previously been shown to have activity against GF. In order to develop a practical enzyme-based chemical agent decontaminant, it is necessary to be able to enzymatically decontaminate as many different agents as possible.

MATERIALS AND METHODS

Bacterial Strains Used

Halophile JD species were provided by Joseph J. DeFrank of U.S. Army CRDEC and *Alteromonas* species were provided by Darrel Sldedjeski and Joseph Leahy, Department of Microbiology, University of Maryland. JD 26.1, JD 28.3, *A. espejiana*, *A. haloplanktis DS*, *A. haloplanktis JL*, *A. nigrifaciens* and *A. undina* were grown on HM medium (50 g NaCl, 10 g $MgSO_4$, 10 g proteose peptone, 6 g yeast extract, 5 g casamino acids, 2.5 g HEPES per liter, pH 6.5). *A. rubra* was grown on Instant Ocean Medium (38 g Instant Ocean, 5 g proteose peptone and 1 g yeast extract per liter, pH 7.0).

Fluoride Electrode Enzyme Assays

OPA anhydrase activity was assayed by monitoring fluoride

release with an ion-specific electrode as described (Hoskin, 1986.) The reaction medium contained 500 mM NaCl, 50 mM Bis-Tris Propane, pH 7.2 or 8.5, 3 mM GF (in isopropanol), 1 mM MnCl₂, and 1-25 ul of enzyme solution (1 ul was used for purified OPAA-2 assays, 5 ul was used for *A. undina* assays and 25 ul was used for all other assays) in a total volume of 2.5 ml with constant stirring. The enzyme sample was preincubated in the reaction medium for 1 minute before reaction was initiated by the addition of GF. The reaction was monitored for 4 minutes and the rate of fluoride release corrected for spontaneous GF hydrolysis. One unit of OPA anhydrase activity is defined as that which catalyzes the release of 1.0 umole of fluoride per minute at 25 degrees C. Specific activity is expressed as units per milligram of protein.

Determination of Protein Concentration

The Coomassie Protein Assay Reagent (Pierce) was used for determination of protein concentration with bovine serum albumin as the standard.

Preparation of Crude Enzyme Extracts

Frozen, harvested cells were resuspended in 10 BM buffer (10 mM Bis-Tris Propane, 0.1 mM MnCl₂, pH 7.2) at a ratio of 1 g of cells for each 3 ml of buffer. The cells were disrupted by sonication for 1 min at high power with a Heat Systems XL Sonicator. Cellular debris was removed by centrifugation at 46,000 X g for 30 min at 4 degrees C. The crude cell supernatant which contained OPA anhydrase activity is referred to as the crude extract.

RESULTS

Activity of Purified OPAA-2 Enzyme against GF

Figure 1 shows the results of enzymatic hydrolysis of GF with the purified OPAA-2 enzyme. This enzyme provided by Tu-cheng Cheng of U.S. Army CRDEC was purified from the *Alteromonas* strain JD 6.5 and has previously been shown to have activity against GB, GD and several related substrates (personal communication from Tu-cheng Cheng). As was the case with the other substrates, activity was enhanced approximately twofold by the addition of Mn²⁺ to the assay buffer and approximately threefold by the increase in pH from 7.2 to 8.5.

Purified OPAA-2 Activity Against GF

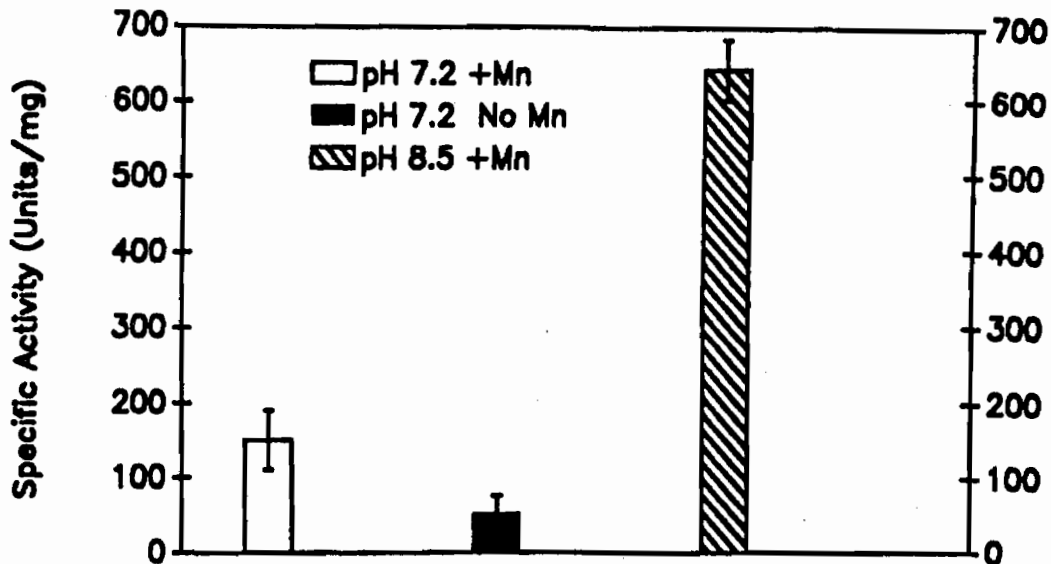


Figure 1. Purified OPAA-2 activity against GF. All assays were in triplicate.

Activity of Crude Lysates of Various Halophiles Against GF

Figure 2 shows the results of enzymatic hydrolysis of GF with crude lysates of various *Alteromonas* and JD-series halophiles. Strains tested were those which had already been shown to have various degrees of activity against other G agents. Basic patterns seen are: 1) Those strains activated by the addition of Mn^{2+} (*A. espejiana*, *A. haloplanktis DS*, *A. haloplanktis JL*, *A. nigra* and *A. rubra*), 2) Those strains activated by increase in pH from 7.2 to 8.5 (*A. espejiana* and JD26.1), and 3) Those strains which show a de-activation by increase in pH from 7.2 to 8.5 (*A. haloplanktis DS*, *A. haloplanktis JL*, and *A. undina*). In the case of strains which do not show any activation with the addition of Mn^{2+} (*A. undina*, JD28.3 and JD26.1, it cannot necessarily be said that the enzyme does not require Mn^{2+} since it is possible that the enzymes could have become loaded with Mn^{2+} during growth.

When compared to the results obtained with other

organophosphate substrates such as GA, GB, GD and diisopropyl fluorophosphate (personal communications from Joseph DeFrank and Tu-chen Cheng), the results obtained with GF, in terms of pH and Mn²⁺ effects, are consistent with the hypothesis that it is the same enzyme which catalyzes the hydrolysis of all these substrates.

GF Activity: Halophile Crude Lysates

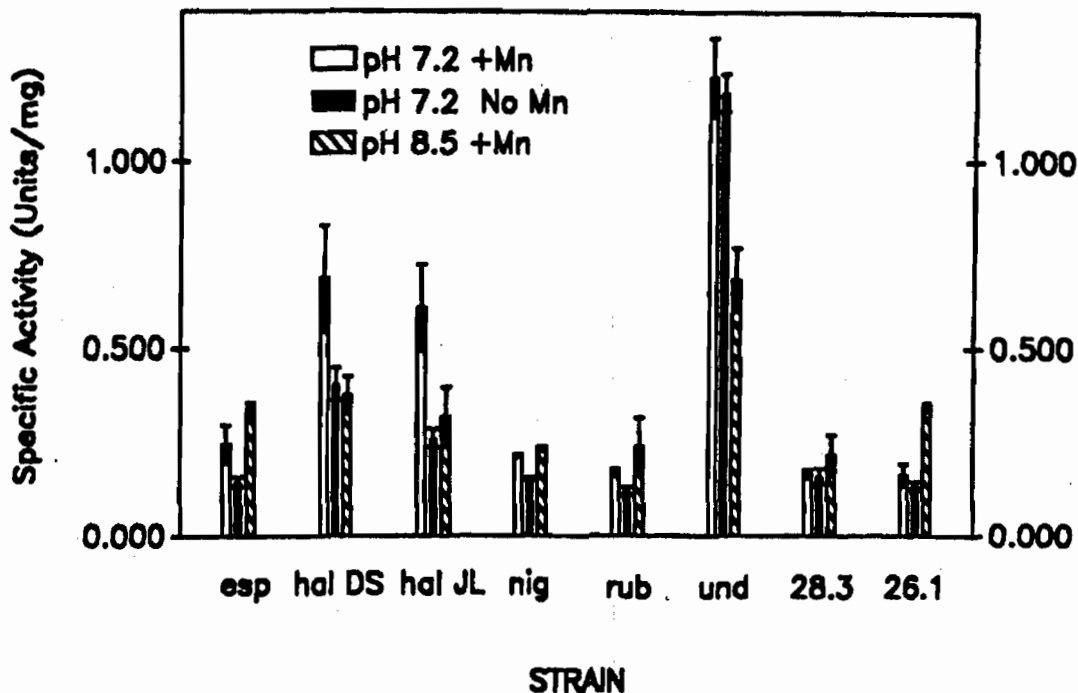


Figure 2. Activity of *Alteromonas* and JD-series halophiles crude lysates against GF. Abbreviations are as follows: esp = *A. espejiana*, hal DS = *A. haloplanktis* DS, hal JL = *A. haloplanktis* JL, nig = *A. nigra*, rub = *A. rubra*, und = *A. undina*, 28.3 = JD28.3, 26.1 = JD26.1.

CONCLUSIONS

Enzymatic hydrolysis of GF has been demonstrated with both purified OPAA-2 enzyme and with several JD-series and halophilic bacteria. Activity profiles were similar to those seen with other organophosphate substrates, particularly the other G agents. Enzymatic hydrolysis has now been demonstrated for GA, GB, GD and GF. The crude lysates of *A. haloplanktis*-DS, *A. haloplanktis*-JL, JD28.3, JD26.1, *A. undina*, and *A. rubra* each show activity on all four G agents.

REFERENCES

1. Personal communication from William Dee, Deputy Director UNSCOM 9 inspection team.
2. Hoskin, F.C.G. 1986. Inhibition of a soman and diisopropyl phosphonofluoridate (DFP)-hydrolyzing enzyme by mipafox. *Biochem. Pharmacol.* 34:2069.

BLANK

THE ROLE OF THE PILOT PLANT IN BIOPROCESS DEVELOPMENT

Edward M. Sybert
Bioprocess Scale-up Facility
Engineering Research Center
University of Maryland
College Park, MD 20742

ABSTRACT:

Implementing an efficient bioprocess at the commercial scale requires well planned and coordinated development at the pilot plant scale. Chemical processes based on the use of microorganisms, cells, or enzymes acting as "biocatalysts" require complex feedstocks or nutrients, close control of process conditions, and often, multi-step purification processes to recover an active product from the reaction mixture. Information available from the laboratory, while extensive, usually does not include data on alternative feedstocks, control set points, and other engineering parameters. The product may be destined to go into production in a new custom-built facility or it may be scheduled into an existing plant. If a new facility is to be constructed, equipment must be specified, and a product flow scheme must be developed. If an existing facility is to be used, with minimal alteration, then the process variables will be constrained by the operating envelope of the installed equipment. It is therefore the role of the pilot plant, working between the laboratory and the production facility, to develop a reproducible and efficient process tailored to the prevailing conditions.

INTRODUCTION:

Implementing an efficient bioprocess at the commercial scale requires well planned and coordinated development at the pilot plant scale. Chemical processes based on the use of microorganisms, cells, or enzymes acting as "biocatalysts" require complex feedstocks or nutrients, close control of process conditions, and often, multi-step purification

processes to recover an active product from the reaction mixture. Information available from the laboratory, while extensive, usually does not include data on alternative feedstocks, control set points, and other engineering parameters. In order to make the transition from a labor-intensive, discontinuous laboratory procedure to an efficient, integrated production process; a great deal of additional work must be done. The pilot plant, by definition, is the setting in which science and engineering come together to develop and optimize a new production process.

In order to simplify this discussion, the example of a bacterial fermentation will be used. Processes developed around yeast, fungal, insect or mammalian cells will have many points in common. Many of the same principles will also apply to enzyme based processes.

SCALE-UP vs SCALE-DOWN:

Before process development can begin, it must first be known whether an existing production facility will be used; or a new plant will be constructed and equipped specifically for the process. If a new, dedicated facility is to be designed; then a scale-up approach, free of constraints of existing plant design and equipment may be taken. In this mode, the pilot plant stage will be one of selecting or designing the most efficient equipment for each step of the process. The results of these studies will be the basis for the design of the full scale production facility. Thus, the process is designed with free rein at the pilot scale and then scaled-up to the full production plant. From the beginning, it must be kept in mind that the overall project cost must be related to the product value. Thus, the process development cost, the proposed plant construction and start-up cost, and the cost of labor, utilities, and raw materials must be judged as they will relate to the revenue stream to be generated. Along these lines, the design and equipment of the pilot plant are intended to mimic the envisioned production plant on a smaller scale, keeping financial commitment to the process or product at a minimum while maximizing the opportunity to uncover potential full scale problems and seek optimum solutions. Past experience with similar processes will provide guidance in the initial selections. The equipment selected will allow real-time data acquisition and process control for the first time in the project, as emphasis shifts from the unconstrained quest for knowledge in the laboratory to the optimization of yield in the pilot plant.

As each piece of equipment necessary to the process is identified, a small scale version will be installed for running tests. It is fundamental that the operating characteristics of the pilot system be predictable as process scale changes. The cause and effect relationship between the operating features of the pilot equipment and the process results must be known and incorporated in the design and selection process. The basic

principles of engineering play a central role. Heat transfer, mixing times, power consumption, shear effects, and oxygen transfer are key elements in designing any bioreactor or product purification system.

If an existing facility is to be used with minimal alteration, the process variables will be constrained by the operating envelope of the already installed equipment. The pilot plant will then work with a scale-down approach to fitting the new process to the plant and refitting the plant to the process. In many cases, a pilot plant will already be associated with an existing production facility; and its equipment will have been selected with the foregoing in mind. If a pilot plant is not already available, equipment should be selected or designed to model the production equipment on a workable scale. As in the case of the greenfield plant, the engineering knowledge of how to predict the effects of changing equipment scale is central to this step; and the development team should be working under the constraints of the existing or proposed production equipment that the process will eventually run on. The mission then must focus on maximizing the productivity within these constraints. It is therefore the role of the pilot plant, working between the laboratory and the production facility, to develop a reproducible and efficient process tailored to the prevailing conditions.

In reality, since many bioprocesses share common processing needs, a well designed and equipped production facility can be made to serve a new process quite well. As in the case of the greenfield plant, a clear idea of the budget allocated for process development, retrofitting the production plant, and start up costs must be obtained prior to initiating the project.

LABORATORY DATA:

The laboratory's principal investigator (PI) will be a storehouse of knowledge but will not have specific information on the engineering aspects of scale-up and other production issues. The PI must be part of the project team. Ideally, there will be microbiologists, enzymologists, biochemists, and chemical engineers involved at various stages of a successful scale-up project.

The laboratory, as the starting point of any new process, provides its most productive strain along with data on the substrate needs and expected product yield. Hopefully, simple, reliable, and rapid assays will be available for both critical substrate components, byproducts, and desired products.

STRAIN DEVELOPMENT:

It is crucial that the master cell line will have already been optimized prior to scale-up work being seriously undertaken. This may be a joint responsibility of the laboratory and the pilot plant. At the same time, the stability of the culture must be tested, and master and working cell banks established. Historically, far greater improvements in yield have resulted from manipulation of the strain than have come about through process changes.

MEDIUM FORMULATION:

The basic nutritional requirements of the cells will be available from the PI. In many cases a defined medium formulation will be available from which critical elements may be determined. The pilot plant staff will use this information to select more cost effective alternatives. The carbon source may be starch, molasses, sulfite waste liquor, or even hydrocarbons in place of glucose. The nitrogen may come from corn, cottonseed, or soybean meal; corn steep liquor, urea, or even gaseous ammonia rather than the more familiar inorganic salts. Vitamin and mineral requirements are usually met by blending, where necessary, the above mentioned complex carbon and nitrogen sources which are usually rich in both. Oxygen and water, although often forgotten as medium components, nevertheless, make up the largest portions; and must be given due consideration. The pilot plant will test the production plant water supply for suitability early in the development process. Minimal treatment for the fermentor fill water, where required, may consist of settling, filtration, or in the extreme case, ion exchange. In some processes, and more often in later purification steps, distilled water or "water for injection" (WFI) quality standards may be imposed. Oxygen, supplied by air injection or sparging, is a major cost factor in that compressors and sterilizing filters or incinerators, used to remove contaminants, must be employed. In making media component selections, such factors as cost per active constituent, supply volume, lot-to-lot variability, shipping and storage forms, and any pre-treatment requirements are considered. Equally important in the system approach, is the impact of raw materials on the final purification process. All materials entering the process should be selected with this in mind. Often, minor ingredients can have a major impact on efficiency of product separation and purification. The quest for a well characterized, reproducible process may necessitate the pre-treatment or blending of raw materials as outlined earlier. These steps must be included in the evaluation of a candidate component to ensure overall process efficiency.

MEDIUM STERILIZATION:

Among its many advantages over the simple test tube or shake flask, the bioreactor offers many options for achieving and maintaining a contaminant-free environment for the desired cell line. In the pilot plant, most fermentors are in-place steam sterilizable using built-in coils or jackets. The significance of this feature, coupled with the fermentor's agitation system, is that the heating and cooling rates may now be controlled. The medium may be sterilized with the bioreactor or separately, depending on the volumes involved and the heat stability of the components. Samples may be withdrawn, and the sampling valves re-sterilized, before and during the processing.

INITIAL BIOREACTOR STUDIES:

In the early stages of a pilot plant process development effort, off-the-shelf equipment may be used to begin familiarizing the pilot plant staff with the growth and production characteristics of the biosystem under controlled growth conditions. A variety of bioreactor types including stirred tanks, airlift, and fluidized bed designs may be explored to determine if any advantage of design exists. All systems under evaluation must be well instrumented and capable of both monitoring and controlling the reaction conditions in a reproducible fashion. The PI will supply starting points from the months or years of research conducted in the laboratory prior to bringing the process to scale-up. Optimum conditions for the growth of microorganisms or cell lines in simple laboratory glassware will be compared with results in bioreactors. Temperature studies will confirm whether optimal cell growth and product formation occurs at the same or different values. The effect of pH on growth and yield may be investigated using on-line titration equipment to maintain preselected values. Dissolved oxygen sensors, coupled with automated agitation speed and airflow controllers allow the effects of high or low oxygen levels to be evaluated. The presence or absence of substrate or product inhibition will be established. The relationship, if any, between growth and product formation will be investigated. From these and other data, the operating mode, whether batch, fed batch, or continuous operation, will be selected.

It is then the task of the pilot plant team to manipulate the conditions within the bioreactor in such a way as to investigate the effects of the environment on growth and productivity; and then select for control purposes, a set of parameters which are directly related to the results desired. The pilot plant reactor control systems provide the opportunity to test the effects of various individual or multiple changes in a controlled environment. A series of tests may be run, manipulating one variable at a time, as outlined above, and results may be plotted in

units of cell or product yield. Interrelated variables are then tested in combinations to provide additional data.

SCALE-UP PARAMETERS:

Once the preliminary studies in standard bioreactors have been completed, sufficient data should be available to determine the critical parameters for scaling-up the process. The temperature studies, along with the coil or jacket specifications of the reactor will define the heat removal (or addition) characteristics required of the production system. Likewise, the culture's oxygen requirements, in combination with the mixing and air sparging capabilities of the pilot plant vessel will allow the staff to calculate the needed power, impellor size, and mass transfer characteristics of the full scale fermentor using proven formula. The results of the pH studies will determine the design and sizing of the acid or base addition systems. The operating mode studies, coupled with the growth characteristics of the culture in the small bioreactors will influence the selection of a single or multiple stage process with appropriate medium addition systems.

UNIT OPERATIONS AND THE SYSTEM APPROACH:

While the ultimate goal of the systems approach to process development requires that each step be designed to work with all other steps; at the pilot plant, the proposed process is broken down into discreet unit operations so that each may be evaluated and optimized. Such unit operations may include: fermentation, cell separation, extraction, concentration, crystallization, and drying. A mass and energy balance may then be computed for each operation; and the effects of altering conditions may be studied for each independently. While each unit operation is being optimized, consideration must be given to the effects on other steps that choices may have. Once all steps have been optimized, dynamic studies must be run to determine if the full process can be run in balance. Appropriate holding or accumulation points may be built into the process to allow for run-to-run variability. Data will be collected on reproducibility and normal upper and lower bounds will be established.

TRANSFER TO PRODUCTION:

The objectives of the pilot plant in developing a new process will have been met when a fully documented process plan is ready to be turned over to the production staff. Since the pilot plant, operating either under scale-up or scale-down philosophy, runs out all its trials with the full scale production equipment in mind; the process plan will include all pertinent information needed to start-up and run each step at full scale. A process transfer team, with members from both pilot and production

plants, will oversee the translation of the standard operating procedure (SOP) documents from pilot to full scale parameters. They will also coordinate any training of production staff that may be required. While the final installation or refitting of the production plant is underway; the transfer team will provide guidance from their experience in running the development trials. During the start-up of the full scale equipment, the process transfer team will supervise the plant operations and observe that all monitored variables are within expected limits. If any unforeseen problems occur, data will be taken back to the pilot plant for evaluation; and additional testing may be undertaken. When all details of the process have been tested and found to be satisfactory; the pilot plant may then be freed-up to begin work on the next project.

TECHNOLOGY BRIDGE:

As it has been described, the pilot plant serves as the technology bridge from the scientific laboratory to the production plant.

BLANK

VI. ENVIRONMENTAL STUDIES

NOTE: Papers with the following titles were presented at the Conference but are not included in this document:

Integrating Liquid-Solid Extraction with Ion Mobility Spectrometry (IMS) for Monitoring Semi-Volatile Organic Compounds in Water

Novel Methods for Investigating Chemical Migration and Transformation in Soil

Dose/Response Relationships of HC (Hexachloroethane) Smoke: Foliar Injury of Trees

Low Pressure Burner Apparatus for Incineration Studies

BLANK

SUPERCritical FLUID EXTRACTION AND ORGANIC SOLVENT MICROEXTRACTION OF CHEMICAL AGENT SIMULANTS FROM SOIL*

W. H. Griest, R. S. Ramsey, C. -h. Ho, and W. M. Caldwell
Analytical Chemistry Division
Oak Ridge National Laboratory
Oak Ridge, Tennessee 37831-6120

ABSTRACT

Experiments with chemical warfare agent simulants suggest that supercritical fluid extraction can achieve good extraction recoveries of agents in soil and produce less laboratory waste than current organic solvent extraction methods. Two-ppm spikes in 1 g of Rocky Mountain Arsenal Standard Soil were extracted using 5% methanol in carbon dioxide at 300 atm for 2 min at 60°C. Recoveries (n=3) were $79 \pm 23\%$ for dimethylmethylphosphonate, $93 \pm 14\%$ for 2-chloroethylethylsulfide, $92 \pm 13\%$ for diisopropylfluorophosphate, and $95 \pm 17\%$ for diisopropylmethylphosphonate. A 5 min ultrasonic micro-scale extraction using methanol is more reproducible but less efficient.

INTRODUCTION

Army protocols (1) for determining chemical warfare agents in soils involve manual solvent extraction by shaking and injection of a few μL of the solvent extracts into gas chromatographs equipped with P- or S-selective detectors. Agents HD (bis[2-chloroethyl]sulfide), GB (O-isopropylmethylphosphonofluoridate) and VX (O-ethyl-S-2-[diisopropylaminoethyl]methylphosphonothioate) are extracted from 33 g of soil with 100 mL of chloroform. The mass of toxic waste left from the extraction is considerable, and the sensitivity of the gas chromatography (GC) analysis is limited primarily by the solid:liquid ratio because the solvent extract is not concentrated.

Supercritical fluid extraction (SFE) (2-8) has been used to achieve more rapid and complete extractions of pollutants from soil and with essentially no toxic waste than traditional Soxhlet and ultrasonic solvent methods. Richards and Campbell (2) found that 25 ppm of EPA base/neutral/acid target compounds in soil were recovered better (80.2% average recovery for 18 compounds) by 30 to 40 min of SFE of 2 g of soil using 2% methanol in carbon dioxide at 390 atm and 80°C than by Soxhlet or ultrasonic extractions. The SFE extract was collected in 2-mL of hexane. The 16 hrs of

*Research sponsored by the Office of the Program Manager, Rocky Mountain Arsenal, under IAG 1989-C110-A1 with the U. S. Department of Energy under contract DE-AC05-84OR21400.

Soxhlet extraction with 10 g of soil achieved an average recovery of 66.4% using 1:1 hexane:acetone (EPA SW-846 method 3540), and ultrasonic solvent extractions of 10 g of soil using 1:1 methylene chloride:acetone (EPA SW-846 method 3550) recovered an average of 58.6%. Similarly, Onuska and Terry reported (7) better than 93% recovery of 200 ppb 2,3,7,8-tetrachlorodibenzo-p-dioxin from 50 mg of soil using 2% methanol in carbon dioxide at 310 atm and 40°C for 30 min. Soxhlet extraction of 1 g of soil by SW-846 method 3540 yielded only ca. 65% recovery. If the SFE is interfaced on-line with the gas chromatograph (4,5), detection limits can be considerably improved over off-line collection and analysis of the extract because the entire extract is transferred to the instrument.

These findings suggest that SFE could improve the determination of chemical warfare agents in soil by decreasing toxic waste, achieving equal or better recoveries with less soil, and allowing increased sensitivity. This paper reports an evaluation of SFE using agent simulants, and a comparison with a micro-scale ultrasonic solvent extraction method.

GAS CHROMATOGRAPHIC ANALYSIS OF CHEMICAL WARFARE AGENT SIMULANTS

This study used simulants which have structural features similar to the actual agents but which lack the very high toxicity of the latter. DMMP (dimethylmethyl phosphonate) was the simulant for agent VX, DIFP (diisopropylfluorophosphate, also referred to as diisopropylphosphonofluoridate) and DIMP (diisopropylmethyl phosphonate) modelled agent GB, and CES (chloroethylethyl sulfide) was used in place of HD. In addition, DEAT•HCl (diethylaminoethanethiol hydrochloride), a byproduct from VX manufacture, also was tested. The DMMP and DIMP were from Alfa (Danvers, MA), and the CES, DIFP, and TEP (triethylphosphate internal standard for GC) were purchased from the Aldrich Chemical Company (Milwaukee, WI). The free base of DEAT was prepared by dissolving DEAT•HCl in water at pH 11, extracting with diethyl ether, and evaporating the solvent. Solvents were Burdick and Jackson distilled in glass grade from American Scientific Labs, Inc. (Atlanta, GA).

Off-line gas chromatographic analysis of the simulants was conducted on two instruments. The initial work was done on a Perkin Elmer model 3920 using a 30 m x 0.53 mm ID x 1.5 μ m DB-5 film thickness fused silica capillary column with a 7 mL/min. flow rate of helium. The column oven was temperature programmed from 70°C (after a 4 min. isothermal hold) to 150°C at 8°C/min. with the injector and flame ionization detector held at ca. 120°C and 200°C, respectively. Three μ L were injected slowly using the solvent flush technique, and quantitation was performed by the method of internal standards using a Maxima chromatography data system on an IBM XT personal computer. Later work used a Varian model 3400 gas chromatograph equipped with the same column and a 1:1 split of the column effluent to flame photometric (P mode) and electron capture detectors. The column oven temperature program was 70°C (2 min. isothermal hold) to 130°C at 4°C/min. The injector was held at 200°C and the detectors were maintained at 220°C. A 1 μ L injection was made using the solvent flush technique, and quantitation was conducted by the method of internal standards using either a Maxima chromatography data system or a model 4400 Varian integrator.

As suggested by previous work (9,10), all of the simulants were separated and determined in a single GC run of about 20 min, as shown by the chromatogram (A) at the bottom of Figure 1. Low ppm solution concentrations were determined using the flame ionization detector, and sub-ppm concentrations with the combination of flame photometric (P-mode) and electron capture detectors.

SFE OF SIMULANTS FROM SOIL

SFE was performed using two commercially available devices. A Suprex SFC/200A supercritical fluid chromatograph was used for most of the work. The column was replaced with a Brownlee HPLC guard column or a Keystone Scientific SFE vessel holding ca. 1 g of soil. The UV detector was replaced with a high pressure shut-off valve and a ca. 30 cm length of 25 μm ID fused silica tubing from SGE, Inc. was attached to the valve outlet for a restrictor. The experiments with 10 g of soil were performed using an ISCO System 1200, a ca. 30 cm length of 50 μm ID fused silica tubing, and a 5 mL extraction cell. The SFC grade carbon dioxide and 5% methanol in carbon dioxide were obtained from Scott Specialty Gases (Plumsteadville, PA).

The SFE procedure consisted of weighing ca. 1 g of Rocky Mountain Arsenal Standard Soil into an extraction cell, and injecting a known volume of simulant spiking solution into the soil a cm or two from the inlet end, assembling the cell and letting the sample set for 15 min. at room temperature. The cell was installed in the apparatus and allowed to warm up to operating temperature. The inlet valve was opened to admit supercritical fluid to the cell, and the outlet valve was then opened to begin the collection of the extract. In early work, the fused silica restrictor tubing was dipped into a vial containing 3 mL of methanol and TEP internal standard, while later, the volume of methanol was 2 mL and the TEP was added after the SFE was completed. The extractions were conducted at 60°C and 300 atm (unless otherwise listed). The vial containing the collecting solution was placed in a beaker of water at room temperature to prevent ice formation when extractions were carried out longer than 5 min.

It was found that pressures around 300 atm are needed to extract low ppm concentrations of agent simulants from 1 g samples of soil. As shown in Table 1, straight supercritical carbon dioxide at 60°C and 300 atm can easily extract the CES from soil in 5 min, but it was not able to efficiently extract the phosphonates and fluorophosphate even at higher extraction pressures or longer extraction times. Experiments in which supercritical carbon dioxide was bubbled through methanol spiked with the simulants showed that the latter were not volatilized from the collection solution by the decompressing supercritical fluid. DIMP has been recovered from water (8) in unknown yield using supercritical carbon dioxide. For soil, a 5% methanol modifier is necessary in the carbon dioxide to recover all the simulants, and at 300 atm and 60°C, good recoveries are achieved in a 5 min. SFE. Even low-polarity compounds such as five-ring polycyclic aromatic hydrocarbons and tetrachlorodibenzodioxin require methanol modifiers in their SFE from sorptive matrices (3,4,7).

As shown in Figure 1, a single SFE is sufficient for the simulants. In contrast, the agent manufacturing byproduct DEAT•HCl was recovered in low and irreproducible yield, typically 10% per extract fraction. This may be due to a low solubility of the compound in the supercritical fluid and/or strong sorption of the compound by the soil. Reaction of the amine with carbon dioxide to form a urea derivative also is possible (8), but is not consistent with the observed extraction behavior. Figure 1 (B) - (D) show that while the simulants are extracted in the first 10 min. SFE fraction, DEAT•HCl continues to slowly extract in subsequent fractions. The free amine did not extract at all, suggesting that sorptive interactions with acidic sites on the soil may be the limiting factor. Nitrous oxide has been used successfully (8) to extract basic amines from soil, and may be useful here. The DEAT•HCl also was not recovered (3%) from ultrasonic extraction using methanol (see below).

In early SFE development work two peaks were recovered for the CES. This peak eluted immediately before CES (see Figure 1 [B]) in GC. Published retention data (9) and CES decomposition studies (11) of concentrated CES suggested that the new product could be 1,4-dithiolane. However, our gas chromatography-mass spectrometry of the peak showed major ions at

m/z of 120 (apparent M), 75, 58, and 45, suggesting that the new product is a methyl ether derivative, possibly methoxyethylethylsulfide (MEES), rather than 1,4-dithiolane, which has ions at m/z of 120 (M), 92, 61, and 46. Rohrbaugh et al. (11) postulate that the first step in the decomposition of CES is the formation of a reactive ethylene sulfonium ion via an S_N1 mechanism. Reaction of this product with methanol (solvent) could product MEES. The new product was observed in methylene chloride solvent extractions of the soil, but not when carbon dioxide/methanol was bubbled through a spiked solution of simulants in methanol (see Table 2). It was not observed in the work reported in Table 1 where fresh spiking solutions were used. The controlling factors in its production have not yet been identified, but could include the catalyzing influence of soil.

In earlier work with 25 μ m ID fused silica restrictor tubing, problems were encountered with tubing breakage at the point where the tubing dipped into the methanol collection solution. This was thought to result from ice crystal formation in the tubing. A small, ca. 10 mg layer of calcium chloride or sodium sulfate was placed in the downstream end of the extraction cell to trap water extracted from the soil. Tubing breakage was not solved, and, as listed in Table 2, the recoveries of the phosphonates were reduced. However, the CES recovery was improved, possibly from removal of water, which could act as a nucleophile to react with the CES sulfonium ion intermediate. With sodium sulfate, the production of the methoxyethylethylsulfide (MEES) also was increased such that the sum of the MEES and CES recoveries accounted for the CES spike. Sheathing the last 10 cm of the 25 μ m ID tubing with 325 μ m ID fused silica tubing minimized breakage. However, breakage has not been as much of a problem with the larger bore 60 μ m ID fused silica tubing, and extraction recoveries appear to be equivalent.

Extraction of soil masses larger than 1 g is feasible. Experiments with 10 g masses of soil spiked at 2 ppm each simulant and extracted for 20 min. yielded good recoveries: DMMP - 70%, CES - 81%, DIFP - 103%, and DIMP - 110%. None of the simulants were detected in second and third 20 min. SFE fractions, suggesting that the lower recoveries of DMMP and CES could have been from purging out of the collecting solution. It is quite likely that detection limits may be lowered by an order of magnitude using the larger mass of soil.

COMPARISON OF SFE WITH MICRO-SCALE ULTRASONIC SOLVENT EXTRACTION

A micro-scale ultrasonic extraction was developed for a direct comparison with the SFE. For this extraction method, 1 g samples of RMA soil were weighed into 2 dram vials, and were spiked in the same manner as for the SFE experiments, except that the sample was shaken for a few sec. before standing. Two or 3 mL of methanol were added, the vial was recapped, and set in an ultrasonic bath (Branson 52, Branson Cleaning Equipment Co., Shelton, CT) for 5 min. An aliquot of the extract was analyzed by GC in the same manner as were the SFE extracts. Analysis of the extracts after 0, 5, 10, and 15 min. of ultrasonication in the bath showed that the optimum extraction time was 5 min. DIFP recoveries were not improved by longer extraction times.

As shown in Table 1, the SFE recoveries were slightly higher but less reproducible than those achieved using a single ultrasonic solvent extraction (5 min.) with methanol. These SFE recoveries of simulants also are much higher but less precise than those reported by D'Agostino and Provost (12) for sequential ultrasonic extractions with hexane and methylene chloride of triethylphosphate and agents GB, HD, and GD (soman) spiked at 5 to 50 ppm in soil. The conditions for the solvent extraction probably are better controlled at this stage of SFE technology development. Richards and Campbell (2) suggest that non-uniformity of supercritical fluid flow may contribute to the lesser reproducibility of recoveries. More careful packing of the SFE cell and better restrictor design should improve reproducibility.

CONCLUSIONS

The results of experiments with simulants suggest that SFE holds considerable promise for providing a rapid and efficient means of recovering chemical warfare agents from soil with a minimum of waste left for disposal.

REFERENCES

1. USATHAMA Method 29Y, "Mustard in Soil," SOP No. TOE-85, Rev. 1, 10 Sept., 1985, and USATHAMA Method 29U, "GB & VX in Soil," SOP No. 104, 1 Apl., 1987, U. S. Army Toxic and Hazardous Materials Agency, Edgewood, MD.
2. M. Richards and R. M. Campbell, "Comparison of Supercritical Fluid Extraction, Soxhlet, and Sonication Methods for the Determination of Priority Pollutants in Soil," LC-GC, 9, 358-364 (1991).
3. S. B. Hawthorne and D. J. Miller, "Supercritical Fluid Extraction and Recovery of PAH from Air-Borne Particulates," in Proceedings of the 1987 EPA/APCA Symposium on Measurement of Toxic and Related Air Pollutants, APCA, Pittsburgh, PA (1987) pp. 63-68.
4. S. B. Hawthorne and D. J. Miller, "Extraction and Recovery of Organic Pollutants from Environmental Solids and Tenax-GC Using Supercritical CO₂," J. Chrom. Sci., 24, 258-264 (1986).
5. B. W. Wright, S. R. Frye, D. G. McMinn, and R. D. Smith, "On-line Supercritical Fluid Extraction-Capillary Gas Chromatography," Anal. Chem., 59, 640-644 (1987).
6. M. Ashraf-Khorassani and L. T. Taylor, "Nitrogen Oxide versus Carbon Dioxide for Supercritical Fluid Extraction and Chromatography of Amines," Anal. Chem., 62, 1177-1180 (1990).
7. F. I. Onuska and K. A. Terry, "Supercritical Fluid Extraction of 2,3,7,8-Tetrachlorodibenzo-p-dioxin from Sediment Samples," J. High Resol. Chrom., 12, 357-361 (1989).
8. J. Hedrick and L. T. Taylor, "Quantitative Supercritical Fluid Extraction/Supercritical Fluid Chromatography of a Phosphonate from Aqueous Media," Anal. Chem., 61, 1986-1988 (1989).
9. P. A. D'Agostino and L. R. Provost, "Gas Chromatographic Retention Indices of Chemical Warfare Agents and Simulants," J. Chrom., 331, 47-54 (1985).
10. Z. Witkiewicz, M. Mazurek, and J. Szulc, "Chromatographic Analysis of Chemical Warfare Agents," Ibid., 503, 293-357 (1990).
11. D. K. Rohrbaugh, T.-C. Yang, and J. R. Ward "Identification of Degradation Products of 2-Chloroethylethyl Sulfide by Gas Chromatography-Mass Spectrometry," Ibid., 447, 165-169 (1988).
12. P. A. D'Agostino and L. R. Provost, "Identification of Chemical Warfare Agents, their Hydrolysis Products and Related Products in Soil," CRDEC Conference on Chemical Defense, Aberdeen Proving Grounds, MD, April, 1990.

Table 1. SFE Recoveries of Chemical Warfare Agent Simulants from Rocky Mountain Arsenal Soil

Extraction ^a			Recovery (%), Avg. ± Std. Dev.					
Fluid	Pressure, Atm.	Time, Min.	Spike, ppm	Replicates	DMMP	CES	DIFP	DIMP
CO ₂	300	5	2	2	12	95	17	43
CO ₂	300	12	2	1	9	90	ND	15
CO ₂	350	12	2	1	4	93	59	7
CO ₂ /MeOH	300	5	2	3	79±23	93±14	92±13	98±25
CO ₂ /MeOH	300	5	12	3	73±9	ND	86±10	95±17
MeOH ^b	-	5	2	3	80±3.5	85±15	63±4.2	87±6.1

^a SFE at 60°C using 25 μm ID restrictor and conditions shown. 1 g of soil extracted, and supercritical fluid decompressed in 2 mL of methanol. Analysis by GC-FPD/ECD.

^b Ultrasonic extraction of 1 g spiked soil with 2 mL of methanol for 5 min.

Table 2. Effects of Restrictor and Drying Agents on SFE of Simulants

Variable ^b	Replicates	Recovery ^a (%), Avg. ± Std. Dev.				
		DMMP	MEES ^c	CES	DIFP	DIMP
25 μm ID Restrictor	3	96±3.2	24±11	28±11	71±19	97±11
60 μm ID Restrictor	1	103	29	27	75	93
CaCl ₂ ^d	2	5	27	40	94	14
Na ₂ SO ₄ ^d	1	51	40	60	101	57
Spiked MeOH ^e	1	98	0	96	92	103

^a Recoveries from spiked Rocky Mountain Arsenal Standard Soil: DMMP: 32 ppm, CES = 10.6 ppm, DIFP = 10.7, DIMP = 16.2 ppm. Analysis by GC-FID

^b SFE conditions: 5% methanol in CO₂ at 300 atm, 60°C, 10 min. extraction of 1 g soil spiked as noted in (a), and supercritical fluid decompressed in 3 mL of methanol.

^c Methoxyethylethylsulfide recovery from spiked CES.

^d 25 μm ID restrictor used, ca. 10 mg of drying agent packed in bottom of SFE cell.

^e Supercritical CO₂/methanol bubbled through 3 mL of methanol spiked with simulants at concentrations equivalent to 100% recovery from soil.

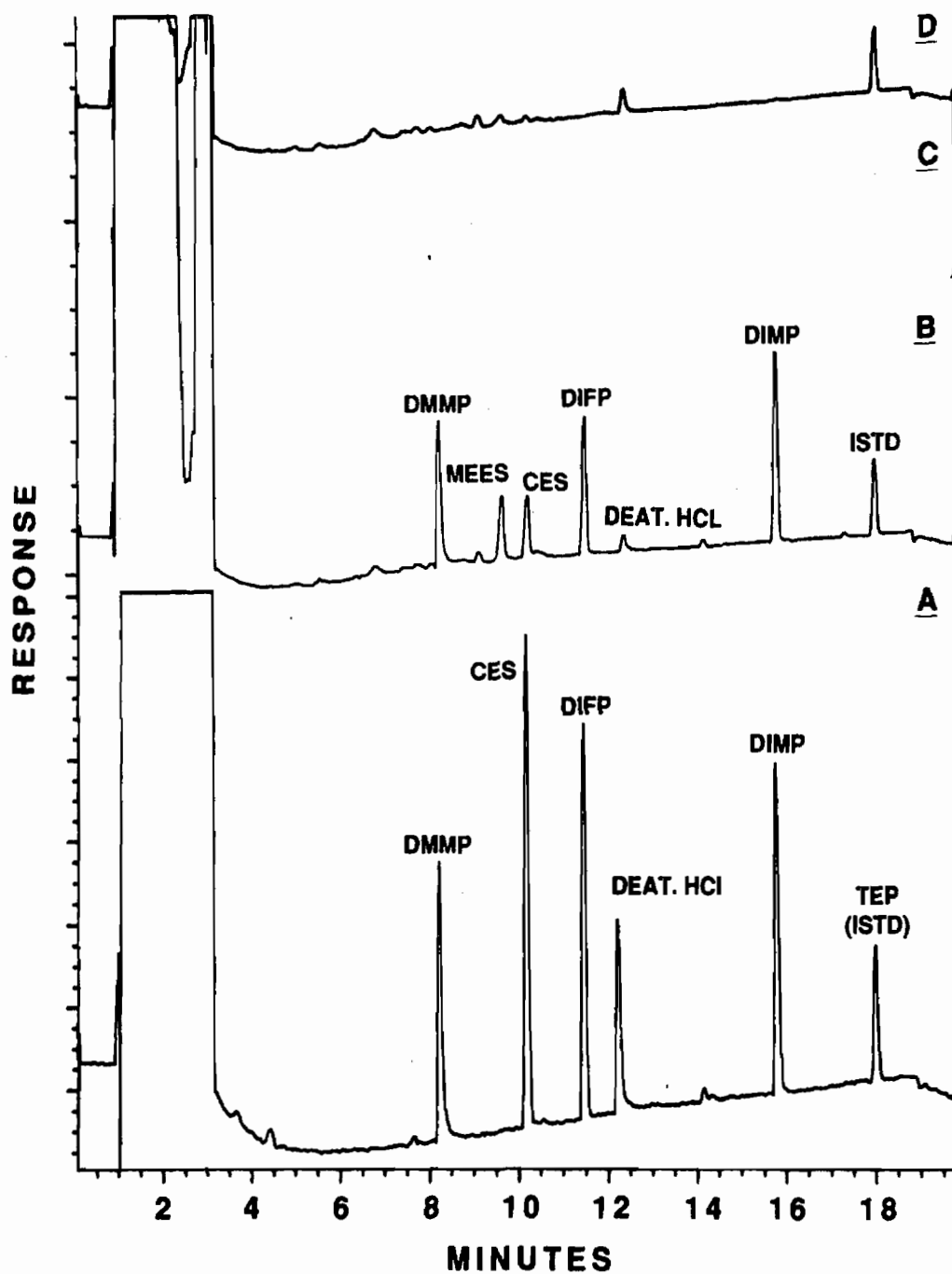


Figure 1. Gas Chromatographic Analysis (Flame Ionization Detector) of (A) Simulant Standard and (B) First 10 min. SFE of Spiked Soil, (C) Second 10 min. SFE of Soil, and (D) Third 10 min. SFE of Soil. (Acronyms are defined in Experimental Section, and SFE conditions are listed in footnote (b) of Table 2.)

BLANK

VII. NMR INVESTIGATIONS

NOTE: A paper with the following titles was presented at the Conference but is not included in this document:

Use of ^{31}P Nuclear Magnetic Resonance (NMR) to Assess Blistering Agent Damage to Skin

BLANK

PURITY DETERMINATION OF CHEMICAL AGENTS BY NUCLEAR MAGNETIC
RESONANCE SPECTROSCOPY (NMR)

William T. Beaudry and Linda L. Szafraniec
U.S. Army Chemical Research Development and Engineering Center
Aberdeen Proving Ground, Maryland 21010-5423

ABSTRACT

Nuclear magnetic resonance (NMR) spectroscopy techniques have been developed to identify and quantitate the impurities present in samples of isopropyl methylphosphonofluoridate (GB), pinacolyl methylphosphonofluoridate (GD), O-ethyl N,N-dimethylphosphoramidocyanidate (GA), S-(2-diisopropylaminoethyl) O-ethyl methylphosphonothiolate (VX), bis(2-chloroethyl) sulfide (HD) and dichloro-(2-chlorovinyl) arsine (L). The data obtained from multinuclear NMR spectra are combined to calculate a weight percent purity for each agent. The detection limit for impurities depends on the field strength of the NMR instrument used, the experimental conditions, the NMR active nucleus observed and the size of the NMR tube. The techniques developed are not restricted to chemical agents but can be used to obtain the weight percent purity of any compound provided the impurities present can be identified.

INTRODUCTION

For many years nuclear magnetic resonance (NMR) spectroscopy has been available to the chemist as an analytical method for the structural identification of compounds. Unfortunately, NMR has been a largely insensitive technique when compared with other analytical methods. This relative insensitivity greatly reduced the utility of NMR and restricted its use to compounds rich in abundant and sensitive nuclei (i.e. ^1H and ^{31}P). Fortunately NMR has recently undergone a tremendous technological revolution with the incorporation of high field superconducting magnets and Fourier Transform pulse signal averaging. The number of observable nuclei has rapidly expanded (now virtually unlimited), and instrument sensitivity has increased by several orders of magnitude. With these greatly expanded capabilities, NMR can now be successfully applied to analytical and chemical problems in more sensitive and versatile ways.

The methods outlined below were developed to determine the purity of chemical agents but are in no way restricted to these materials since the method is material independent. In principle, any compound may be analyzed by these methods provided all the NMR active nuclei that are in, or suspected

to be in the sample are observed and the sample is homogeneous (all components are miscible).

EXPERIMENTAL PROCEDURES

Materials. The GB sample used as an example in this study was from stocks maintained under the CASARM program and was used as received.

Procedure. The neat sample was placed into a clean, dry 5 mm O.D. Pyrex NMR tube. The tube was capped with a pressure cap, and the top of the tube was wrapped with Parafilm. Multinuclear NMR spectra were taken to observe all nuclei suspected to be in the sample. ^{31}P , ^1H , ^{19}F , and ^{13}C spectra were collected for GB. The entire chemical shift range for each nucleus was scanned at high amplitude so that all impurities at the 0.5 mole % level were detected. The overall mole % purity for the sample was calculated using the information from all spectra recorded. Identification of impurities was made and a weight percent purity calculated from the mole % data.

Instrumentation. The NMR spectra were recorded using a Varian XL-200 or a Varian VXR-400S superconducting multinuclear NMR system. All spectra were recorded using tetramethylsilane in chloroform as an external reference for ^1H and ^{13}C spectra, trifluoroacetic acid for ^{19}F spectra, and 85 % phosphoric acid for ^{31}P spectra. Spectra were recorded at probe temperature (ca. 21 °C), and quantitative data were obtained by digital integration of peak areas.

RESULTS AND DISCUSSION

The NMR spectrum taken (^{31}P , ^1H , ^{19}F , or ^{13}C) shows of all the nuclei of the observe type in the sample. For example, the ^{31}P NMR spectrum shows at least one resonance from every different ^{31}P nucleus in the sample. The area of each resonance is directly related to the amount of that ^{31}P nucleus in the sample. The position of the resonance from a standard reference (its chemical shift) is characteristic of the molecular environment of the ^{31}P nucleus and allows the assignment of each resonance to a specific chemical compound. The ^{31}P chemical shift values for the "standard chemical" agents have been tabulated and reported previously.¹

In a like manner, resonances in the ^{13}C , ^1H and ^{19}F spectra are assigned to the chemical agents, decomposition products or common additives. (Table 1).

TABLE 1

Common Impurities Found in Samples of Neat GB	
Impurity	Structure
Ethyl methylphosphonofluoridate (Ethyl GB)	$\text{CH}_3\text{P}(\text{O})(\text{OCH}_2\text{CH}_3)(\text{F})$
Isopropyl methylphosphonic acid (GB Acid)	$\text{CH}_3\text{P}(\text{O})[\text{OCH}(\text{CH}_3)_2](\text{OH})$
Methylphosphonofluoridic acid (Fluor Acid, FA)	$\text{CH}_3\text{P}(\text{O})(\text{F})(\text{OH})$
Diisopropyl methylphosphonate (DIMP)	$\text{CH}_3\text{P}(\text{O})[(\text{OCH}(\text{CH}_3)_2)_2]$
O-Ethyl O-isopropyl methylphosphonate (Diester)	$\text{CH}_3\text{P}(\text{O})(\text{OCH}_2\text{CH}_3)[\text{OCH}(\text{CH}_3)_2]$
Tri-n-butylamine (TBA)	$(\text{CH}_3\text{CH}_2\text{CH}_2\text{CH}_2)_3\text{N}$
Tri-n-butylamine (protonated) (TBA-H ⁺)	$(\text{CH}_3\text{CH}_2\text{CH}_2\text{CH}_2)_3\text{N}^+\text{H}$
H ⁺	Exchangeable protons
2-Propanol	$(\text{CH}_3)_2\text{CH}(\text{OH})$

Unknown resonances are evaluated based on characteristic chemical shifts to determine likely chemical structures. For a general discussion of the assignment techniques employed, a number of texts are available.² The chemical shifts for a number of chemical agents and related compounds have been collected in several reports.³⁻⁷

A set of spectra for a sample of GB is shown in Figures 1-4. Common impurities found in samples of GB are listed in table 1. The resonance lines for GB and the identified impurities are assigned and noted on each of the sub-spectra. The resonance areas are separately expanded, integrated and tabulated. The resonance areas then are used to calculate a mole percentage for each compound in every sub-spectrum. The calculations will be illustrated using the data obtained from Figures 1-4.

Analysis of Sub-spectra. Components identified in the ³¹P spectrum (Figure 1) are listed in Table 2. A normalized area (Col 4) representing the

TABLE 2

Sub-Spectra Data From Figure 1.

³¹P DATA

Identified Compound	Integrated Area	Number of ³¹ P atoms	Normalized Area	Mole % by ³¹ P
GB	3184.5	1	3184.5	95.8
Ethyl GB	37.5	1	37.5	1.1
Fluor Acid	46.2	1	46.2	1.4
GB Acid	12.0	1	12.0	0.4
DIMP	43.9	1	43.9	1.3
Diester	1.0	1	1.0	(0.03)

moles of each component is obtained by dividing the total area for each component (Col 2) by the total number of ³¹P nuclei in that component (Col 3). The mole percentage of each component (Col 5) is then calculated from the ratio of its normalized area to the area for all components (Eqn 1).

$$\text{Mole \% Y} = \frac{\text{Normalized } ^{31}\text{P Area Y}}{\sum \text{Normalized } ^{31}\text{P Area Y}} \times 100\% \quad (1)$$

The resulting percentage for GB is the mole % purity of the sample by ³¹P NMR.

The same procedure is followed for each of the remaining sub-spectra (Figures 2-4) and the data are collected in table 3. Note that the "amount" of GB in the sample is very different in each sub-spectrum and would not be accurately represented by any one sub-spectrum alone. The large differences result from the specificity of the individual sub-spectra to components containing the observe nucleus. Thus, while the ³¹P spectrum shows all the species which contain a ³¹P nucleus, any component without ³¹P is completely absent and would be overlooked (e.g. 2-propanol or tri-n-butylamine). The actual purity of the sample can only be represented by the combination of the data from all of the sub-spectra.

TABLE 3

¹H, ¹⁹F and ¹³C Sub-Spectra Data From Figures 2-4.¹H DATA

Identified Compound	Integrated Area	Number of ¹ H Atoms	Normalized Area	Mole % by ¹ H
GB	1320.0	1	1320.0	94.5
Ethyl GB	29.0	2	14.5	1.0
TBA-H ⁺	82.0	6	13.7	1.0
2-Propanol	10.0	1	10.0	0.7
H ⁺	46.6 ^a	1	23.3 ^b	1.7
DIMP	31.0	2	15.5	1.1

¹⁹F DATA

Identified Compound	Integrated Area	Number of ¹⁹ F Atoms	Normalized Area	Mole % by ¹⁹ F
GB	3329.0	1	3329.0	97.8
Fluor Acid	31.1	1	31.1	0.9
Ethyl GB	44.5	1	44.5	1.3

¹³C DATA

The spectrum confirms the presence of the following compounds:

GB	Ethyl GB	TBA	GB Acid
	Fluor Acid	DIMP	2-Propanol

- a. Includes all exchangeable protons.
 b. Contributions from the H⁺ in 2-Propanol (10) and TBA-H⁺ (13.7) have been subtracted from the total H⁺ area from Column 2.

TABLE 4

Calculated Weight % Purity of GB From the Combination of
³¹P, ¹H, ¹⁹F and ¹³C NMR Data

Compound	MW	Normalized Area	Mole Fraction	MW Avg Area	Calculated Weight %
GB	140	3184.5	0.941	131.731	94.2
Ethyl GB	126	37.5	0.011	1.396	1.0
FA	98	46.2	0.014	1.338	1.0
GB Acid	138	12.0	0.004	0.489	0.3
DIMP	180	43.9	0.013	2.333	1.7
Diester	166	1.0	(0.0003)	0.049	(0.04)
TBA-H ⁺	205	34.2 ^a	0.010	2.072	1.5
2-Propanol	60	25.0 ^a	0.007	0.443	0.3
Excess H ⁺ (HF)	20	0.1 ^{a,b}	(0.0002)	0.001	<0.001

- a. "Computed" normalized ³¹P integral area.
 b. Contributions to the exchangeable H⁺ from FA (46.2) and GB Acid (12.0) have been subtracted from the "computed" normalized ³¹P integral area

Combination of Sub-Spectra. The ^{31}P sub-spectrum contains the largest number of identified compounds and will be used as the basis for the combined purity calculation. In principal, any one of the sub-spectra may be used for the calculation; however, fewer calculations are required when using the sub-spectrum with the largest number of identified components.

The calculation begins with the tabulation of all the identified components from the ^{31}P sub-spectrum with their measured areas (Table 4, Col 1+3). All of the components not in the ^{31}P sub-spectrum but in any one of the other sub-spectra are then added to the list without measured areas. Because the 2-propanol, tri-n-butylamine and excess acid (e.g. HF) are not observed in the ^{31}P sub-spectrum, it is necessary to compute an area to represent them (in terms of ^{31}P area) from one or more of the other sub-spectra. This is done by constructing a conversion factor from the measured area of any component which is common to the sub-spectrum where the impurity is observed and the ^{31}P spectrum. Ethyl GB and GB are identified in all of the sub-spectra and either of their areas may be used as the basis for the conversion factor (Eqn 2).

$$^{31}\text{P Area Y} = ^1\text{H(or } ^{19}\text{F, } ^{13}\text{C) Area} \quad \times \quad \frac{^{31}\text{P Area Z}}{^1\text{H(or } ^{19}\text{F, } ^{13}\text{C) Area Z}} \quad (2)$$

where Y is the compound whose area is to be determined and Z is the compound found in both of the sub-spectra. Substituting the Ethyl GP for Z in eqn. 2, the areas for 2-propanol and TBA are calculated and listed in Table 4, Col 3. The total exchangeable proton area from the ^1H spectrum is converted to a "total" ^{31}P exchangeable proton area in the same manner. This area is adjusted by subtracting contributions from each of the already identified compounds which have an exchangeable proton(s). The area remaining is excess acid as HF. In this case, only FA and GB acid areas were subtracted since 2-propanol and TBA- H^+ were accounted for in the ^1H sub-spectrum before conversion to a ^{31}P area. At this point, an area representing each identified component has been measured or calculated. The mole fraction of each component is then calculated from the ratio of its normalized area to the total normalized area for all components and tabulated (Table 4, Col 4).

$$\text{Mole Fraction Y} = \frac{\text{Area Y}}{\Sigma \text{Area Y}} \quad (3)$$

Calculation of Weight % Purity. The mole fraction data from table 4 is converted to weight % data by multiplying the mole fraction of each component by its molecular weight (MW) to obtain a MW averaged area (Table 4, Col 5). The weight percentage of each component is then calculated (Eqn 4) from the ratio of each area to the total area for all components (Table 4, Col 6).

$$\text{Weight \% Y} = \frac{\text{MW Avg Area Y}}{\Sigma \text{MW Avg Area Y}} \quad \times \quad 100 \% \quad (4)$$

The resulting percentage in Table 4 for GB (94.2 %) is the weight % purity of the sample by multinuclear NMR.

The procedures outlined above for a GB sample are general and can be applied to any sample provided that:

- a. NMR spectra are collected for all nuclei known or suspected to be in the sample.
- b. Identification of the impurities is made from the NMR data collected or from alternate techniques (e.g. GC-MS, FT-IR).
- c. The sample is homogeneous and all components are miscible.

CONCLUSIONS

Nuclear magnetic resonance (NMR) spectroscopy techniques have been developed to determine the purity of chemical warfare agent samples and to identify and quantitate the impurities that are present. The data obtained from multinuclear NMR spectra can be combined to calculate a weight percent purity for each agent when all observed impurities are identified. The techniques developed are not restricted to chemical agents but can be used to obtain the weight percent purity of any compound provided the impurities present can be identified and the sample is homogeneous.

REFERENCES

1. Szafraniec, L. L. and Klapper, H., ARCSL-TR-81040. ³¹P Nuclear Magnetic Resonance(NMR) Data on Organophosphorus Compounds: Compilation 1970-1979. CONFIDENTIAL REPORT, Jan 1982.
2. Modern NMR Spectroscopy (A Guide for Chemists), eds. Sanders, J. K. and Hunter, B. K., Oxford University Press, New York, NY, 1987; or Interpretation of Carbon-13 NMR Spectra, eds. Wehrli, F. W. and Wirthlin, T., Heydon & Son Ltd., Philadelphia, PA, 1978.
3. Szafraniec, L. L., Klapper, H., Bradford, H. R., Alford, K. N., and Botto, R. E., EC-TR-74061. The ¹H NMR Spectral Parameters of Some Phosphoramido Type Agents and Their Intermediates. CONFIDENTIAL REPORT, Nov 1974.
4. Szafraniec, L. L., Klapper, H., and Alford, K. N., EC-TR-73047. The ¹H and ³¹P NMR Spectral Parameters of Some Trivalent Phosphorus Compounds Containing a C-P Bond. CONFIDENTIAL REPORT, Feb 1974.
5. Szafraniec, L. L., Klapper, H., and Alford, K. N., EC-TR-74046. The ¹H NMR Spectral Parameters of Some Pentavalent Phosphorus Compounds Containing a C-P Bond. CONFIDENTIAL REPORT, Sep 1974.
6. Beaudry, W. T. and Szafraniec, L. L., CRDEC-TR. ¹³C NMR Data on Organophosphorus Compounds: Compilation 1978-1988. In Preparation.
7. Crutchfield, M. M., Dungan, C. J., Litcher, J. H., Mark, V., and Van Wazer, J.R, ³¹P Nuclear Magnetic Resonance." Topics in Phosphorus Chemistry. Vol. 5. Interscience Publishers, New York, NY. 1967.

FIGURE 1

³¹P NMR Spectrum of GB

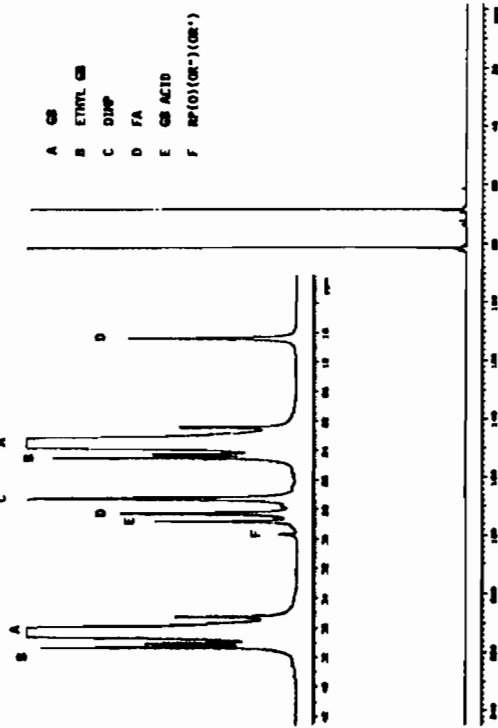


FIGURE 2

¹H NMR Spectrum of GB

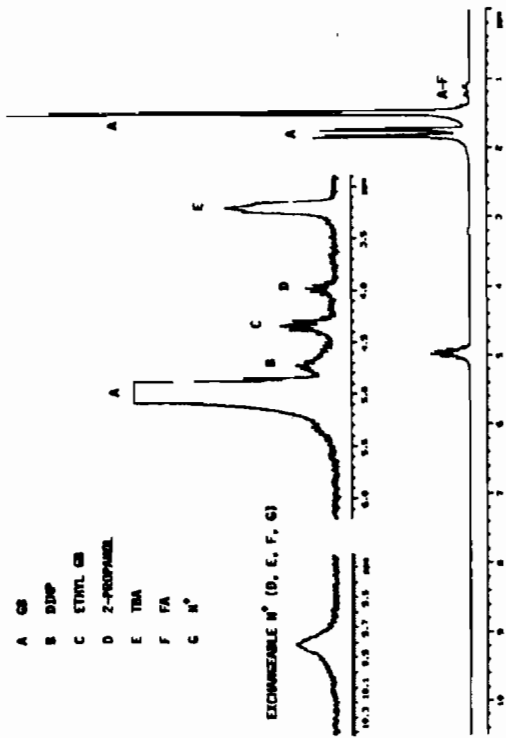


FIGURE 3

¹⁹F NMR Spectrum of GB

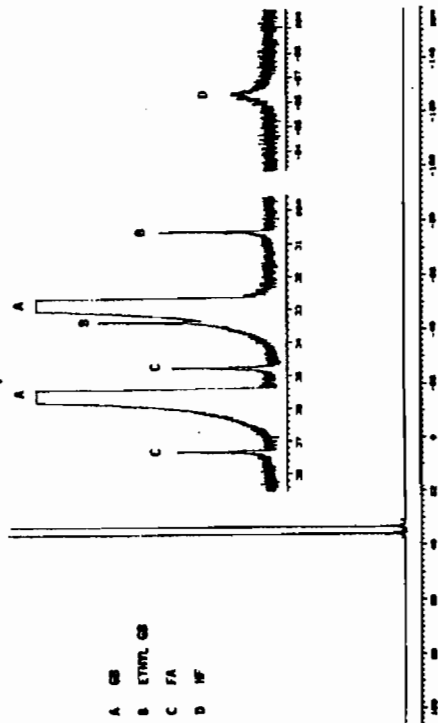
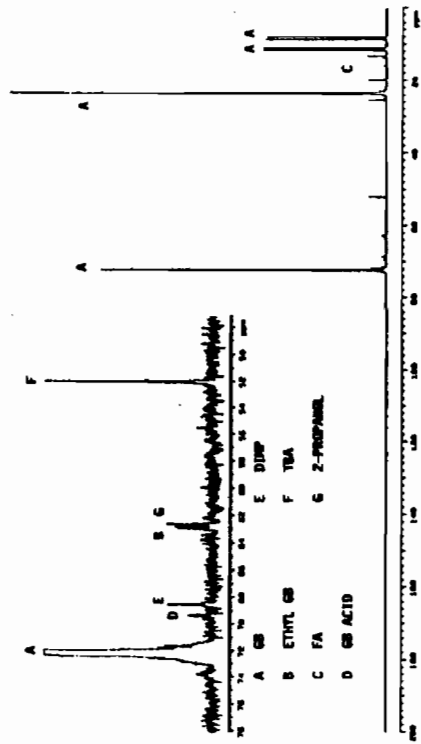


FIGURE 4

¹³C NMR Spectrum of GB



·BLANK

POSITION OF BOND CLEAVAGE IN THE HYDROLYSIS OF
ORGANOPHOSPHONATE ESTERS USING ^{18}O NMR ANALYSIS

Linda L. Szafraniec, Leonard J. Szafraniec, and
J. Richard Ward

U. S. Army Chemical Research, Development & Engineering Center
Aberdeen Proving Ground, MD 21010-5423

ABSTRACT

Recently, we reported that EA5928 (O-isopropyl t-butylphosphonofluoridate) hydrolyzed by parallel reaction paths producing isopropanol as well as fluoride ion. At neutral pH, the production of isopropanol predominated. In order to refine our understanding of the mechanism of hydrolysis of EA5928, the hydrolysis was repeated in ^{18}O enriched water with pH ranging from 1-14. The products were analyzed by NMR to determine the site of cleavage during hydrolysis. The results showed that isopropanol was produced exclusively by C-O bond cleavage. The rate coefficient for C-O cleavage was pH independent, while the rate of P-F cleavage was proportional to hydroxide ion concentration. The hydrolyses of DMMP and DIMP were also monitored in ^{18}O enriched water over the same pH range. It was shown that hydrolysis proceeded with both P-O and O-C cleavage with the P-O path proportional to hydroxide ion concentration and the C-O cleavage independent of pH.

INTRODUCTION

Phosphonofluoridates such as sarin and soman are potent neurotoxins. These organophosphorus esters inhibit the acetylcholinesterase enzyme by formation of a covalent bond with the enzyme. A review of the literature as well as a crystal structure for the enzyme were recently published.¹ The hydrolysis of these compounds is of interest both from the standpoint of decontamination as well as understanding the pharmacokinetics of intoxication.² Recently, we examined the hydrolysis of the phosphonofluoridate, EA5928, where we found that hydrolysis occurs by parallel paths to produce isopropanol as well as the expected fluoride ion.³ On the other hand, the toxic phosphonofluoridates such as sarin and soman hydrolyze in neutral solution exclusively to form fluoride ion and the corresponding O-alkyl methylphosphonic acid.⁴ In this article we extend our studies on the hydrolysis of organophosphorus esters by the use of ^{18}O water in order to discern the position of bond scission in EA5928. In addition, the hydrolysis of diisopropyl methylphosphonate (DIMP) and dimethyl methylphosphonate (DMMP) were monitored in ^{18}O water.

EXPERIMENTAL

MATERIALS: The O-isopropyl t-butylphosphonofluoridate (EA5928) and the diisopropyl methylphosphonate (DIMP) were prepared in-house. The dimethyl methylphosphonate (DMMP, Aldrich) was dried over molecular sieve before use. All substrates were greater than 97% pure by multinuclear NMR analysis.

The following buffer solutions were prepared using 50% D₂O (Stohler Isotope Chemicals), 25% H₂¹⁸O (MSD Isotopes) and 25% triply distilled H₂O. All materials used to prepare the buffer solutions were used as received.

- pH 1: 0.10M HCl (prepared from 1N HCl, Fisher Sci)
- pH 4: 0.05M Potassium Hydrogen Phthalate, KHC₈H₄O₄ (Fisher Sci, C.P.)
- pH 10: 0.025M Sodium Bicarbonate, NaHCO₃ (Allied Chem Co. Baker & Adamson powder)
- 0.025M Sodium Carbonate, Na₂CO₃ (Allied Chem Co., Baker & Adamson, ACS grade, anhydrous)
- pH 12: 0.05M Potassium Chloride, KCl (Allied Chem, B&A Quality)
- 0.012M Sodium Hydroxide, NaOH (Chemical Commodities Agency, Inc.)
- pH 14: 1 M Sodium Hydroxide, NaOH (Chemical Commodities Agency, Inc.)

GENERAL PROCEDURE: A weighed amount of substrate was placed into a 5-mm o.d. Pyrex NMR tube, and the appropriate amount of buffer was added to make a 0.01M solution. The top of the NMR tube was flame-sealed for samples stored in the oven (Precision Sci., GCA Corp.) at elevated temperature (65 ± 1°C) or closed with a pressure cap and wrapped with Parafilm for samples run at ambient temperature. Spectra were recorded periodically using a Varian VXR-400s FTNMR spectrometer system operating at 100 MHz for ¹³C and 162 MHz for ³¹P. All spectra were recorded at probe temperature (22 °C), and quantitative data were obtained by digital integration of the peak areas of interest.

The psuedo-first order rate coefficients reported were determined from the first 20% of each reaction. (i.e., initial rate).

RESULTS

The first observation from our experiments is that the formation of isopropanol from the hydrolysis of EA5928 occurs exclusively by cleavage at the carbon-oxygen bond. Table 1 summarizes the observed first-order rate coefficients measured at 65 °C from pH 1-14. Cleavage at the P-F bond is both acid and base catalyzed in accord with other phosphonofluoridates,⁵ while the reaction at the C-O bond is pH independent. At pH 14 the rate of hydrolysis of EA5928 is too fast to measure by NMR at 65 °C, therefore the hydrolysis was measured at ambient temperature to yield a value of 140 hr⁻¹ at 22 °C. At high pH the hydrolysis is exclusively P-F cleavage, while at neutral pH values, the proportion of reaction via C-O cleavage increases as the contribution from the pH dependent P-F path drops. At pH 4, in fact, the hydrolysis is almost exclusively by means of C-O cleavage.

TABLE 1

Hydrolysis of EA5928 at 65 °C As a Function of pH
k, obs, hr⁻¹, X 10²

<u>pH</u>	<u>P-F</u>	<u>C-O</u>
1	5.2	2.1
4	0.02	2.0
10	1.8	2.2
12	11.7	1.6
14	140 ^a	--- ^b

^a Rate coefficient at 22 °C.

^b Not observed.

The pH dependence of P-F cleavage and the pH independence of C-O cleavage are both consistent with previous experiments on phosphorus esters.⁶⁻¹⁰ These studies showed that hydrolysis in caustic favored attack at phosphorus by the "hard" nucleophilic hydroxide ion, whereas the hydrolysis at carbon was due to nucleophilic attack either by the "soft" nucleophile water, or by an S_N1 reaction at the carbon center. Either S_N1 or S_N2 substitution at carbon would be pH independent, since the concentration of water is invariant.

The apparent lack of P-O cleavage in EA5928 apparently reflects the greater ease of fluoride ion to act as a leaving group relative to the more basic isopropoxide moiety. The real question is why C-O cleavage is still observed at relatively high pH values (pH 10-12) in EA5928 relative to other phosphonofluoridates.

An answer to this question can be inferred from Hudson and Keay's work⁸ in which the effect of varying the alkyl group on a series of phosphonate esters was studied. They contrasted the effect on alkaline and acid hydrolysis of changing the alkyl group on the phosphorus. Their data are summarized in Table 2, where the relative rates of hydrolysis of diisopropyl alkylphosphonates are reported. The key point is that substitution of the t-butyl group for a methyl group causes a pronounced change on the relative rate of hydrolysis (0.002 vs 1) in alkaline solution, whereas the change in relative rate in acid solution is less dramatic (0.33 vs 1). Hudson and Keay used these results to infer that alkaline hydrolysis occurred at the phosphorus center while acid hydrolysis involved reaction at the carbon center on the alkoxy group. Thus, substitution of t-butyl for methyl in EA5928 would slow the attack at phosphorus to the point that the C-O cleavage can compete with P-F cleavage, if their hypothesis is correct.

TABLE 2

The Effect of Substitution of the Alkyl Group on the Relative Hydrolysis Rates of Diisopropyl Alkylphosphonates^a

<u>Substituent</u>	<u>Relative Hydrolysis Rate</u>	
	<u>Alkaline</u>	<u>Acid</u>
Methyl	1	1
Ethyl	0.16	0.5
n-Propyl	.062	.5
n-Butyl	.039	.33
t-Butyl	.002	.33

^a Data from reference 8

In order to test Hudson & Keay's prediction, we then examined the hydrolysis of diisopropyl methylphosphonate (DIMP) and dimethyl methylphosphonate (DMMP) in the presence of ¹⁸O labelled water. Tables 3 and 4 summarize the data for the hydrolysis of DIMP and DMMP. One sees that in caustic solution, only P-O cleavage is observed, while C-O cleavage becomes apparent near neutral pH. In acid solution, only C-O cleavage is observed as predicted by Hudson and Keay. Again, attack at the phosphorus center is proportional to the concentration of hydroxide while the path for C-O cleavage is invariant except at pH 1. Note that for DIMP, the second-order rate coefficient for the hydroxide-catalyzed path would be underestimated because of the intrusion of the pH independent path for C-O cleavage.

Table 5 reproduces data from our earlier³ study in which the second-order rate coefficients for hydroxide ion catalysis are tabulated for a series of O-isopropyl alkylphosphono-

fluoridates including EA5928. One sees that the presence of the t-butyl group on EA5928 slows the relative rate of hydrolysis relative to the other phosphonofluoridates in accord with Hudson and Keay's work with diisopropyl alkylphosphonates.⁸ The result that hydrolysis of EA5928 at neutral pH is primarily C-O cleavage may explain why EA5928 is relatively non-toxic, since the lack of reactivity at the P-F center would preclude phosphorylation of acetylcholinesterase.

One final point in discussing the mechanism of EA5928 hydrolysis rests with distinguishing whether C-O cleavage is S_N1 or S_N2. Keay¹⁰ measured the hydrolysis of an O,O'-dialkyl methylphosphonate containing an optically active alkoxide ligand and found that the alcohol produced was racemic, implying an S_N1 path. By analogy, one would predict that the C-O cleavage seen for EA5928, DIMP, and DMMP would be unimolecular as well. Chloride ion is present in the pH 1 solutions which could act as a nucleophile if attack at the carbon center were S_N2. The pH 1 solutions were examined for the presence of methyl chloride or isopropyl chloride using ¹³C NMR. No alkyl chlorides were detected which is consistent with an S_N1 process. A more definitive experiment, however, would be to monitor the hydrolysis of a methylphosphonofluoridate containing an optically-active O-alkyl group such as the pinacolyl group on soman.

Another interesting result regarding hydrolysis is evident from the pH 1 solutions of DIMP and DMMP. At pH 1, measurable amounts of methylphosphonic acid (MPA) are formed from the hydrolysis of the O-alkyl methylphosphonic acid. The data below summarize the percent of MPA formed by P-O and C-O cleavage at pH 1:

Compound, CH ₃ - $\begin{array}{c} \text{O} \\ \\ \text{P} \begin{array}{l} / \text{OR} \\ \backslash \text{OH} \end{array} \end{array}$	%C-O	%P-O
R = methyl	9.2	90.8
R = isopropyl	42.5	57.5

One notes first that there is a significant contribution from P-O cleavage in contrast to the parent diesters which hydrolyzed solely by C-O cleavage at pH 1. The second point is that the methyl derivative relies almost exclusively (91% vs 9%) on P-O cleavage to form MPA. The facility for the methoxide ligand to be displaced from phosphorus more readily than isopropoxide is consistent with S_N2 attack at phosphorus. Recall that DMMP hydrolysis at pH 14 was too fast to measure at 65 °C. These results can be compared to the hydrolysis of the fully substituted phosphate ester, trimethyl phosphate (TMP), and the disubstituted hydrolysis product dimethyl phosphate.⁶

The hydrolysis of TMP at pH 1 is exclusively C-O cleavage, while the disubstituted ester hydrolyzes by both P-O and C-O paths.⁶

TABLE 3

Rate Coefficients for P-O and C-O Cleavage During Hydrolysis of DIMP at 65 °C

pH	<u>k, obs, hr⁻¹, x 10²</u>	
	<u>P-O</u>	<u>C-O</u>
1	-- ^a	0.14
4	-- ^a	0.022
10	0.007	0.027
12	0.11	0.04
14	18.5	-- ^a

^a Not observed

TABLE 4

Rate Coefficients for P-O and C-O Cleavage During Hydrolysis of DMMP at 65 °C

pH	<u>k, obs, hr⁻¹, x 10²</u>	
	<u>P-O</u>	<u>C-O</u>
1	-- ^a	0.084
4	-- ^a	0.047
10	6.3	-- ^a
12	120	-- ^a
14	930 ^b	-- ^a

^a Not observed

^b 21.8 °C Reaction too rapid to follow at 65 °C.

TABLE 5

Second-Order Rate Coefficients for Hydroxide-Ion
Catalysis for O-Isopropyl Alkylphosphonofluoridate Hydrolysis
at 25 °C

Alkyl	k, M ⁻¹ s ⁻¹	Ref
Methyl	26.0	a
Ethyl	9.0	b
Isopropyl	2.0	b
t-Butyl	0.0002 ^c	3

^a R.L. Gustafson and A.E. Martell, J. Am. Chem. Soc., **84**, 2300 (1962)

^b L. Larsson, Acta Chem Scand, **11**, 1131 (1957)

^c Monitored at 20 °C in buffered solution

CONCLUSIONS

1. The hydrolysis of EA5928 proceeds by parallel reaction paths producing both fluoride ion and isopropanol as products of the reaction. The reaction to produce isopropanol is exclusively C-O cleavage.
2. Reaction at the phosphorus center exhibits both acid and base catalysis. Reaction at the carbon center is pH independent. Hence, the greatest contribution from C-O cleavage occurs at a pH of 4, where reaction at the phosphorus center is at a minimum.
3. The ability to see parallel reactions in EA5928 as contrasted to other phosphonofluoridates seems to result from the t-butyl group suppressing reaction at the phosphorus center while having less effect on the reaction at the carbon center.
4. Hydrolysis of DIMP in ¹⁸O water also showed contribution from C-O cleavage at neutral pH values. As in EA5928, reaction at the P-O center was base catalyzed, while hydrolysis from C-O cleavage was pH independent from pH 4 to pH 14.
5. Search for evidence of parallel reaction paths in methylphosphonofluoridates should center on the region near pH 4 where the P-F hydrolysis path will be at a minimum.

REFERENCES

1. J.L. Susman, M. Harel, F. Frolow, C. Oefner, A. Goldman, L. Tolker, and I. Silman, "Atomic Structure of Acetylcholinesterase from Torpedo California: A Prototypic Acetylcholine-Binding Protein," Science, **253**, 872-879 (1991).
2. H.P. Benschop and L.P.A. DeJong, "Toxicokinetics of Soman: Species Variation and Stereospecificity in Elimination Pathways," Neuroscience and Biobehavior Reviews, **15**, 73-77 (1991).
3. L.L. Szafraniec, W.T. Beaudry, L.J. Szafraniec, and J.R. Ward, "Parallel Hydrolysis Paths for Nucleophilic Displacement on a Phosphonofluoridate," Bioorg Chem, **18**, 160-164 (1990).
4. J.R. Ward, Y. Yang, R.B. Wilson, W.D. Burrows, and L.L. Ackerman, "Base-Catalyzed Hydrolysis of 1,2,2-Trimethylpropyl Methylphosphonofluoridate - An Examination of the Saturation Effect," ibid, **16** 12-16 (1988).
5. J. Epstein, "Rate of Decomposition of GB in Seawater," Science, **170**, 1396-1398 (1970).
6. C.A. Bunton, "Hydrolysis of Orthophosphate Esters," Acc Chem Res, **3**, 257-265 (1970).
7. W. Mabey and T. Mill, "Critical Review of Hydrolysis of Organic Compounds in Water Under Environmental Conditions," J. Phys Chem Ref Data, **7**, 383-415 (1978).
8. R.F. Hudson and L. Keay, "The Hydrolysis of Phosphonate Esters," J. Chem Soc, **1956**, 2463-2469.
9. P.W.C. Barnard, C.A. Bunton, D.R. Llewellyn, C.A. Vernon, and V.A. Welch, "The Reactions of Organic Phosphates. Part V. The Hydrolysis of Triphenyl and Trimethyl Phosphate," J. Chem Soc, **1961**, 2670-2676.
10. L. Keay, "The Acid-Catalyzed Hydrolysis of 2-Octyl Ethyl Methylphosphonate," J. Org Chem, **28**, 1426-1427 (1963).

NMR SPECTROSCOPY DETERMINATION OF RELATIVE BINDING CONSTANTS FOR ARSENICAL-ANTIDOTE ADDUCTS

Richard J. O'Connor, Evelyn L. McGown, Vicky L. Boyd, Letterman Army Institute of Research, Presidio of San Francisco, CA 94129-6800, Kilian Dill, Department of Chemistry, Clemson University, Clemson, SC 29634-1905, Susan F. Hallowell, U.S. Army Chemical Research, Development and Engineering Center, Aberdeen Proving Ground, Maryland 21010-5423

ABSTRACT

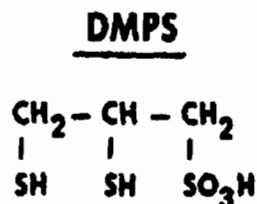
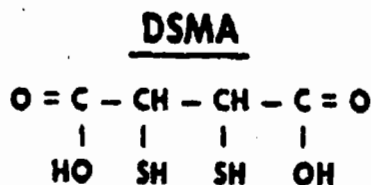
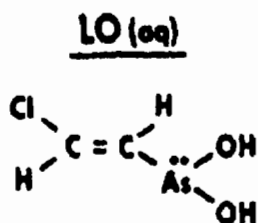
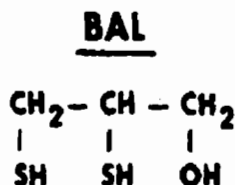
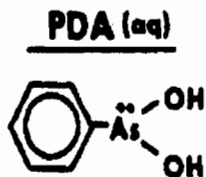
NMR has been used to study the interaction of Lewisite type arsenicals and their antidotes. The adducts formed have been characterized by carbon and proton NMR. Having accomplished this, we were then able to determine relative binding constants of several arsenical-antidote adducts by using proton nuclear magnetic resonance spectroscopy. The principle antidotes used were BAL (2,3-dimercaptopropanol), DMPS (2,3-dimercaptopropanesulfonic acid) and DMSA (2,3-dimercaptosuccinic acid). Both BAL and DMPS had a higher affinity than DMSA for the two arsenicals studied.

INTRODUCTION

In order for an antidote to be effective for arsenic poisoning, it must be able to chelate and extract the tissue-bound arsenic. The association constants for the arsenic-chelate complexes would be a useful tool to compare antidotes. Dithiols form particularly stable heterocyclic adducts with organic-arsenicals and are the most effective antidotes to date. The classical antidote, British anti-lewisite (BAL), was developed in the 1940's as a topical antidote to lewisite, however it suffers from various drawbacks, such as stability, solubility, and cytotoxicity [1,2]. In spite of its drawbacks, it is still the recommended arsenic antidote in the United States [3]. A replacement for BAL should be less toxic, less lipophilic, and more water soluble. Two analogs to BAL, DMSA and DMPS, have polar moieties (carboxylic and sulfonic acids) which make them more water soluble and less lipophilic, and they are less toxic. We have conducted research dealing with the cytotoxicity and efficacy of various antidotes [3-5] and have observed that neither DMSA nor DMPS competes as effectively for arsenic in cultured cells as BAL [5]. Earlier we had investigated and characterized the structure of various As-antidote adducts in the hope that the information concerning various electrostatic and steric factors may lead to the development of better

antidotes [6-9].

In this report we present 'relative' association constants for various arsenical-antidote complexes and these values were obtained via NMR spectroscopy. The arsenicals were phenyldichloroarsine (PDA) and trans-2-chlorovinylarsine oxide (LO) and the antidotes investigated were BAL, DMPS, and meso-DMSA.



EXPERIMENTAL SECTION

The organic-arsenicals, antidotes (disulphydryl compounds) and adducts were purchased or synthesized as previously described [6-11]. Deuterated NMR solvents were purchased from Merck, Sharpe, and Dohme (West Point, PA, USA) or Aldrich Chemical Co. (St. Louis, MO, USA).

All ^1H -NMR spectra were recorded on a Varian XL-300 FT NMR spectrometer operating at 300 MHz with a spectral window of 4,000 Hz. Typically the experiments consisted of several consecutively accumulated data blocks, each containing 640 transients. Each block could be monitored and accessed separately, thus assuring attainment of equilibrium before analysis.

Each equilibrium studied consisted of several NMR experiments; for each, equal amounts of the arsenical-disulphydryl adduct had been placed into individual 5 mm NMR tubes and stored in the freezer until needed. The concentrations ranged from 10 to 100 mM depending on solubility constraints. The binding experiments were performed by placing a known amount of the competing disulphydryl into one of these NMR tubes and measuring the

components of the mixture after attainment of equilibrium. Free arsenical was below detectable limits, thus individual binding constants were not determined. The concentrations of the free antidote and the adducts could be ascertained, provided appropriate specific resonances were identified and integrated. The procedure would yield only one point in the binding curve per NMR tube, but the method ensured sample stability and integrity.

The experiments were designed to span a wide enough concentration range of the competing antidote such that the above measurements allowed us to calculate relative binding constants. An example is given below for the system containing PDA, BAL and DMSA. The ratio of the two individual binding constants ($K_{relative}$) can be defined as:

$$K_{relative} = K_{BAL} / K_{DMSA} = [PDA \cdot DMSA][BAL] / [PDA \cdot BAL][DMSA]$$

The concentrations of the four components were measured or calculated from the spectral data. The product $[PDA \cdot DMSA][BAL]$ was plotted versus $[PDA \cdot BAL][DMSA]$ and $K_{relative}$ was determined from the slope.

No single solvent system was found compatible with all combinations of arsenicals and antidotes under study. Several solvent mixtures were tried. The most practical solvent systems were a mixture of D_2O and methanol- d_4 , D_2O and acetone- d_6 , D_2O , and in one case methanol- d_4 was the only suitable solvent.

Some assumptions were necessary due to the complexity of some spectra, presence of isomers, overlap of resonances and/or solubilities. For example, DMSA and PDA·BAL are produced in the reaction between PDA·DMSA + BAL. The amount of free DMSA was assumed to equal the concentration of PDA·BAL observed. This was considered a valid assumption because no free PDA was detected. In the reaction between PDA·DMSA + DMPS, the amount of free DMPS was assumed to equal the initial concentration of DMPS minus the concentration of bound DMPS (overlap of resonances prevented the unequivocal integration of free DMPS).

RESULTS AND DISCUSSION

A representative 1H -NMR spectrum for one experiment in the equilibrium study of the PDA·DMSA adduct with DMPS is shown in Fig. 1. The resonance assignments associated for each molecule were made previously [7,8]. The resonances for free DMSA and bound DMSA are clearly discernible and do not overlap with other resonances, therefore their integral values were used to determine their concentrations in this experiment. Fig. 2 shows the plot of the data for the PDA·BAL plus DMSA equilibrium in which the slope of the plot yielded $K_{relative}$.

The results obtained with PDA and lewisite oxide are summarized in Table 1. When DMPS or BAL competed with DMSA for PDA, their binding constants appeared to be ten times greater than that of DMSA. When BAL and DMPS competed, their binding constants were comparable (0.93). The binding constant of LO with DMPS was 12.5 times greater than that of DMSA, a result similar to that observed with PDA. When BAL and DMSA were the competing antidotes, the binding constant for BAL was approximately twice that for DMSA. Thus the BAL/DMSA result obtained with LO was consistent with that obtained with PDA, though the difference was not as striking.

The above results indicate that the relative binding constants of the three disulphydryl compounds toward organic arsenic are rated as follows:

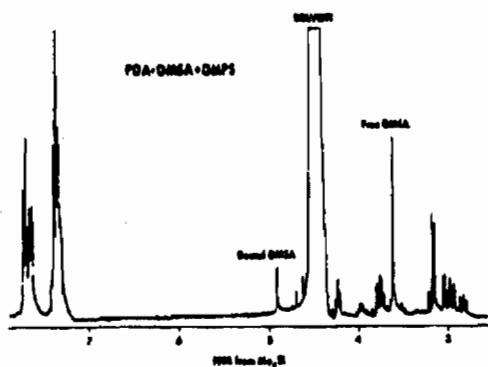


Fig. 1. $^1\text{H-NMR}$ spectrum of the equilibrium between the PDA·DMSA adduct and DMPS. Sample and spectral conditions are provided in the experimental section and Table 1. The initial ratio of PDA·DMSA to DMPS in this sample was 5:2.

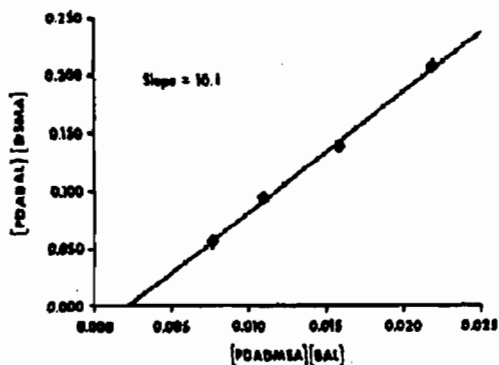


Fig. 2. Plot of the NMR equilibrium data for the PDA·DMSA/BAL system. K_{relative} is derived from the slope.

$\text{BAL} \approx \text{DMPS} > \text{DMSA}$. The binding constants of BAL and DMPS were an order of magnitude higher than that of DMSA in all but one case. The exception was the LO/BAL/DMSA experiment, where the relative constants differed by only two-fold. The main difference was that this disulphydryl study did not contain any D_2O . The deuterated water could allow the various arsenicals to ionize more appreciably and hence greatly influence the binding. This indeed may be the case because our related studies using HPLC [12], indicate that a strong protic solvent will influence the association constants. This means that our one study which contained no D_2O should not be directly compared to the others, and that under physiological conditions, these 'relative' constants may be slightly altered than what we determined.

TABLE 1

$$\text{"Relative" Rate} = \frac{[C][D]}{[A][B]}$$

STUDY	A	B	C	D	"Relative" Rate	Solvent System
1	PDA·BAL	DMPS	PDA·DMPS	BAL	0.93	$\text{CD}_3\text{OD}:\text{D}_2\text{O}(1:1)$
2	PDA·DMSA	BAL	PDA·BAL	DMSA	10.1	D-6 Acetone: D_2O (3:2)
3	PDA·DMSA	DMPS	PDA·DMPS	DMSA	10.4	D_2O
4	LO·BAL	DMPS	LO·DMPS	BAL	1	_____
5	LO·DMSA	BAL	LO·BAL	DMSA	1.67	CD_3OD
6	LO·DMSA	DMPS	LO·DMPS	DMSA	12.5	D_2O

¹ No solvent was found that was compatible with all four compounds.

The three antidotes studied above form identical 5-membered heterocyclic rings upon reaction with organic-arsenic. Therefore, differences in equilibrium constants must be due to substituents on the carbon backbone. The weaker binding of DMSA may be explained by steric hindrance due to its bulky carboxyl groups. Charge could also be a factor in the case of ionizable molecules, although it is not a straightforward explanation. BAL, a neutral molecule, and DMPS (with its ionizable sulfonic acid moiety) have essentially identical binding constants, whereas DMSA, with two ionizable groups, has a considerably lower binding constant. Other factors, such as the environment around the arsenic atom (solvation, possible interactions of the arsenic atom with the adduct functional groups) and pH may also influence the relative binding constants.

Finally, we synthesized a new potential antidote, 2,3-dithioerythritol (DTE), in the hopes that its slightly increased polarity, due to its additional hydroxymethyl group, would make it more soluble and less toxic than BAL. Its structure is identical to DMSA, where the carboxyl groups have been replaced with hydroxymethyls. In fact, we synthesized it by the reduction of DMSA with borohydride. The preliminary experiments proved very encouraging [9]. Enough DTE was synthesized and purified to carry out two animal studies: the first involved testing BAL versus DTE in the eyes of rabbits to compare damage in the eye, and the second involved checking the efficacy of DTE and the other antidotes in mice when challenged with an organic-arsenical. Unfortunately, the final results showed DTE to be a no gain situation. DTE proved to cause just as much damage in the eyes of rabbits as BAL, and the mice survived no better than with BAL or DMPS.

CONCLUSIONS

NMR was used to determine "relative" binding constants of several arsenical-antidotes adducts. Within our experimental conditions, the strength of the binding can be rated as BAL \approx DMPS > DMSA towards the organic-arsenicals used (solubilized Lewisite oxide and Phenyldichloroarsine). A new potential antidote, DTE, was compared to BAL and DMPS in animal studies, but no biological advantage was proven.

REFERENCES

1. Waters, L.L. and Stock, C. (1945). *Science* 102, 601-606.
2. Peters, R.A., Stocken, L.A., and Thompson, R.H.S. (1945). *Nature* 156, 616-619.
3. Klaassen, C.D. in Gilman, A.G., Goodman, L.S. and Gilman, A. (eds.), 'Heavy Metals and Heavy Metal Antagonists.' In: *The Pharmacological Basis of Therapeutics*, Macmillan, New York, 1985, 1605-1627.
4. Aposhian, H.V. (1983). *Ann. Rev. Pharmacol. Toxicol.* 23, 193-215.
5. McGown, E.L., Harbell, J.W., Dumlao, C.R. and O'Connor, R.J. in Lindstrom, R.E. (ed.), 'Proceedings of USAMRDC Fifth Annual Chemical Defense Bioscience Review', U.S. Army Medical Research and Development Command, 1985, pp 291-301.
6. O'Connor, R.J., McGown, E.L., and Dill, K. (1986). USAMRDC-Letterman Army Institute of Research Publication No. 222.
7. Dill, K., Adams, E.R., O'Connor, R.J. and McGown, E.L. (1987). *Magn. Reson. Chem.* 25, 1074-1077.
8. O'Connor, R.J., McGown, E.L., Dill, K. and Hallowell, S.F. (1989). *Magn. Reson. Chem.* 27, 669-675.
9. Boyd, V.L., Harbell, J.W., O'Connor, R.J. and McGown, E.L. (1989). *Chem. Res. Toxicol.* 2, 301-306.
10. Dill, K., Adams, E.R., O'Connor, R.J., Chong, S. and McGown, E.L. (1987). *Arch. Biochem. Biophys.* 257, 293-301.
11. Dill, K., Davis, S.D., Adams, E.R., O'Connor, R.J., McGown, E.L. and Hallowell, S.F. (1989). *Drug Chem. Toxicol.* 12, 337-343.
12. McGown, E.L., Boyd, V.L., Youn, S.H., Gong, S., Dill, K. and O'Connor, R.J., (unpublished results).

SOLID-STATE ^{31}P MAS NMR STUDY OF G-AGENT SIMULANTS ADSORBED ON SYNTHETIC RESIN CATALYSTS

William T. Beaudry, George W. Wagner* and J. Richard Ward

**Research Directorate, U.S. Army Chemical Research,
Development and Engineering Center
Aberdeen Proving Ground, MD 21010 (U.S.A.)**

***National Research Council-CRDEC Research Associate**

A powder containing sorptive and reactive resins that was developed for the removal and subsequent catalytic degradation of toxic organophosphorous esters is characterized using dimethyl methylphosphonate (DMMP), p-nitrophenyl diphenyl phosphate (PNDP) and ^{31}P MAS NMR. The results for DMMP confirm, spectroscopically, that the adsorbed ester partitions between the sorptive and reactive resin components. Variable temperature ^{31}P MAS NMR results further demonstrate that any molecular exchange between these sites is occurring at a rate less than 300 s^{-1} , even at $50\text{ }^{\circ}\text{C}$. PNDP hydrolyzes on the resin powder to yield diphenyl phosphate (DPP) and p-nitrophenoxide. The anionic DPP product appears to be tightly bound to the resin suggesting the formation of a stable intermediate with the reactive quaternary amine groups.

INTRODUCTION

Characterizing chemical reactions on synthetic resins are of current interest in our laboratory, since such resins may be tailored to adsorb and react with toxic organophosphorous esters which inhibit cholinesterase activity.¹ In particular, macroreticular resins possess a porous network which should enhance adsorption and provide sites to attach reactive functional groups.^{2,3} The United States Army recently adopted a kit for skin decontamination using macroreticular resins⁴ in lieu of natural clays such as "Fuller's earth." The resin employed is actually a mixture of three components: a high surface area, carbonaceous macroreticular styrene/divinylbenzene resin and two macroreticular styrene/divinylbenzene ion-exchange resins. The strong acid resin contains sulfonic acid groups while the strong base resin has quaternary amine groups. In solution the toxic, cholinesterase-inhibitors, such as sarin or soman, are rapidly hydrolyzed in strong base and also exhibit acid-catalyzed hydrolysis.⁵

In order for the resin mixture to function catalytically, molecular exchange must exist between the sorptive and reactive sites and the reactive sites must be able to effect a heterogeneous reaction with the adsorbed liquid. Previous studies in our laboratory with O,O'-diisopropyl phosphorofluoridate (DFP) have suggested partitioning in the resin mixture.⁶ Evidence of this partitioning is the apparent low reactivity observed for DFP adsorbed on the resin, despite the apparent high reactivity with the individual reactive resin components. The nature of this partitioning must be understood in order to design effective systems which both adsorb and react with liquid contaminant.

This study employs ^{31}P Magic Angle Spinning (MAS) NMR to probe the adsorption and reaction of organophosphorous esters at the molecular level. ^{31}P MAS NMR is perhaps uniquely suited for this purpose, since NMR cannot only distinguish various molecular adsorption sites,⁷⁻¹⁰ but also determine the occurrence and rate of molecular exchange between adsorption sites.¹¹⁻¹⁵

EXPERIMENTAL

Dimethyl methylphosphonate, purchased from Aldrich, was used without further purification. Para-nitrophenyl diphenyl phosphate, provided by Dr. F. R. Longo, CRDEC, was found to be greater than 99% pure by ^{31}P NMR. Ambergard[®] XE-555 Resin, Amberlite[®] IRA-900 Strong Base Resin, Amberlyst[®] XN-1010 Strong Acid Resin and Ambersorb[®] XE-348F Carbonaceous Synthetic Adsorbent were obtained from Rohm & Haas Company. The latter three materials are similar to the components in the XE-555 resin powder. The IRA-900, XN-1010 and XE-348F resins, manufactured in the form of small beads, were crushed with a ball mill to yield fine powders. The strong base IRA-900 resin, initially in the chloride form, was exchanged with an aqueous 5% NaOH solution to yield the hydroxide form. The resin was subsequently washed with deionized water to remove NaCl and excess NaOH and then filtered and dried in air at room temperature.

Solution ^{31}P NMR spectra were obtained at 81 MHz on a Varian XL-200 NMR spectrometer. ^{31}P MAS NMR spectra were obtained at 101 MHz using high-power proton decoupling on a home-built 6T FT-NMR spectrometer equipped with a Doty Scientific variable temperature 5mm double-tuned MAS probe. ^{31}P spin-lattice relaxation times (T_1) of less than 2 s are observed for adsorbed DMMP and PNDP which are greatly reduced from their solution values. The short T_1 values alleviate the need for the cross-polarization (CP) technique and, therefore, the more quantitative conventional FT experiment was used. All chemical shifts were referenced to an external sample of 85% H_3PO_4 . Positive chemical shifts are at higher frequency (lower field) than the reference.

RESULTS FOR DIMETHYL METHYLPHOSPHONATE (DMMP)

The first phase of the study involves identifying the various adsorption sites on the resin powder. DMMP is an ideal candidate for this purpose since it is a small, simple molecule which is stable except at very high or low pH. Therefore, the molecule is not expected to react with the acid or base groups on the resin. This surface probe permits NMR spectra to be obtained which are not complicated by interfering reaction products and allows for the straightforward observation of chemically different adsorption sites.

^{31}P NMR spectra of DMMP vapor adsorbed on the resin powder are shown in Figure 1. The top spectrum was obtained under normal solution NMR conditions and reveals two overlapping peaks at 38 and 29 ppm. The relative narrowness of these resonances immediately indicates that DMMP is undergoing fast isotropic "liquid-like" motions on the resin which averages the broad chemical shift anisotropy (CSA) powder pattern expected for static organophosphorous esters.¹⁶⁻¹⁹

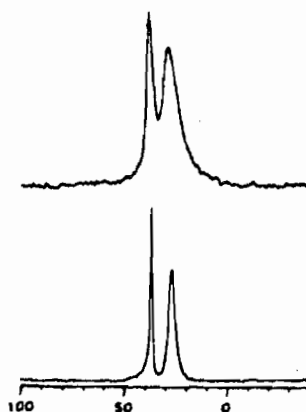


FIGURE 1

^{31}P NMR spectra of DMMP vapor loaded on the resin powder obtained using normal solution NMR conditions (top spectrum) and MAS with high-power proton decoupling (bottom spectrum).

The bottom spectrum was obtained using MAS with high-power proton decoupling. This technique greatly enhances the resolution of the twin peaks as compared to the spectrum obtained without MAS. The narrow downfield resonance occurs at 36.2 ppm which is the same value observed for DMMP in methanol solution. Methanol extraction of the DMMP from the resin results in only the presence of DMMP in the filtrate; thus DMMP does not react with the resin but, in fact, resides in two different adsorption sites. The spectra further show that any molecular exchange occurring between the two sites is slow on the NMR timescale ($1 - 10^6$ s) by virtue of the presence of both individual resonances.²⁰ The width of the peaks in the lower MAS spectrum (ca. 100 Hz) places an upper limit on the exchange rate of 300 s^{-1} at room temperature.

In order to identify the nature of the two adsorption sites, ³¹P MAS NMR spectra were obtained for DMMP vapor adsorbed on the three individual resins similar to the components in the resin powder (spectra not shown). In the case of the carbonaceous macroreticular adsorbent, a rather broad resonance is detected at 33 ppm (slightly shifted from the solution value of 36 ppm) along with CSA spinning sidebands indicating that the molecules are rather rigidly held. Conversely, DMMP remains highly mobile on the macroreticular strong base and strong acid ion-exchange resins yielding sharp resonances at 36.9 and 36.3 ppm, respectively. Only in the case of the strong base resin does a second signal occur at 25.5 ppm. Therefore, the second site is associated with DMMP adsorbed at quaternary ammonium hydroxide base sites. A second signal not detected for DMMP adsorbed on the strong acid resin, but this does not rule out the possibility of DMMP adsorption at sulfonic acid sites. This resonance could be coincident with the sorptive signal. A complete listing of ³¹P MAS NMR assignments for DMMP adsorbed on the various resins is given in Table 1.

TABLE 1

³¹P MAS NMR Assignments for Organophosphorous Esters Adsorbed on Various Resins

Ester	XE-555	XE-348F	IRA-900(OH)	XN-1010
DMMP	36.2 ^a 26.3 ^b	33 ^a	36.9 ^a 25.5 ^b	36.3 ^a
PNDP	-17.9	-17.8	-17.1	-17.9
DPP	-10.1	not observed	-9.6	not observed
DPPA	not observed	not observed	not observed	-10.7
PNPPA	not observed	not observed	not observed	-11.7

^aMacroreticular region. ^bQuaternary ammonium hydroxide ion-exchange sites.

³¹P MAS NMR spectra obtained from samples of various DMMP weight-percent loadings (spectra not shown) indicate that adsorption at the base sites is favored during small weight-percent vapor loadings. Conversely, the macroreticular region is allowed to fill at large weight-percent liquid loadings. The relative ratio of the two resonances in these spectra did not change over a several month period indicating that the DMMP partition achieved during the loading process is stable at room temperature. The relative capacities of the two sites is in keeping with the expected greater capacity of the macroreticular adsorption sites, yet DMMP in the small weight-percent vapor loaded samples does not redistribute to maintain the same constant ratio between the sites.

A reasonable explanation for the adsorption behavior of the resin powder is that the reactive sites facilitate the adsorption of DMMP vapor into the macroreticular region. This can be rationalized by the fact that DMMP is very soluble in water which is expected to be predominately adsorbed at the ion-exchange sites. The reported water content of the strong base and acid resins are ca. 70% and 50%, respectively. It is interesting to note that in contrast to the macroreticular acid and base ion-exchange resins, DMMP vapor adsorbed on the carbonaceous macroreticular resin (which only contains about 2% water) is rather rigidly held. All three resins rapidly assimilate DMMP liquid to yield adsorbed DMMP which is highly mobile and liquid-like.

The possibility of chemical exchange between the macroreticular sorptive region and the reactive base sites was further investigated by variable temperature ^{31}P MAS NMR. Variable temperature spectra recorded up to 50°C for DMMP adsorbed on both the resin powder and the strong base ion-exchange resin (not shown) yield no features attributable to molecular exchange. On the contrary, at the higher temperatures the lines actually sharpen due to the increased rate of motion of the molecules within their respective adsorption environments. If molecular exchange were occurring between the sites at a rate approaching the width of the resonances (ca. 100 Hz), then a significant line broadening contribution would be evident as the temperature is raised. Therefore, molecular exchange is very slow (less than 300 s^{-1}) even at 50°C . Site exchange might be observable by NMR above this temperature, however the quaternary ammonium hydroxide groups begin to decompose at ca. 60°C . The variable temperature spectra were reversible within the temperature range studied. Magnetization-transfer experiments^{11,13,14} would enable the calculation of more precise migration rates for organophosphorous esters adsorbed on these synthetic resin catalysts. We are currently modifying our spectrometer to perform these experiments in-house.

It should be noted that molecular exchange between the sites must occur at an appreciable rate in order for the resin to function as an effective catalyst. The lack of a fast exchange, as seen for DMMP, could account for the slow reaction rate found for DFP in our previous study.⁹

RESULTS FOR P-NITROPHENYL DIPHENYL PHOSPHATE (PNDP)

Unlike the DMMP surface probe, PNDP is expected to be more unstable with respect to hydrolysis²¹⁻³¹ and, thereby, to react with the acid and base groups in the resin powder. In basic solution, the major hydrolysis products are diphenyl phosphate (DPP) and p-nitrophenoxide (a yellow chromophore), although significant amounts of p-nitrophenyl phenyl phosphate (PNPP) and phenoxide also form.^{21,24} For acid-catalysis, diphenyl phosphoric acid (DPPA) and p-nitrophenol are the sole reported products.³¹ PNDP is a white solid at room temperature which necessitates the use of a solvent in order to load the compound onto the resin.

^{31}P MAS NMR spectra of PNDP adsorbed on the resin powder from 95% (v/v) ethanol/water solution are shown in Figure 2. Two peaks are present at -10.1 and -17.9 ppm in the spectrum of a 1 day old sample (top). The large upfield peak at -17.9 ppm, which has the same chemical shift observed for PNDP in solution,²¹ is assigned to PNDP adsorbed on the macroreticular region of the resin. The spectrum observed for adsorbed PNDP is different than the spectrum of neat PNDP solid³² indicating that the ester does not merely precipitate as the ethanol evaporates, but is rather highly dispersed on the resin. The lack of spinning sidebands for the two peaks indicates that both adsorbed PNDP and the other adsorbed species are highly mobile and "liquid-like." The small downfield peak at -10.1 ppm is due to the hydrolysis product, DPP, as confirmed

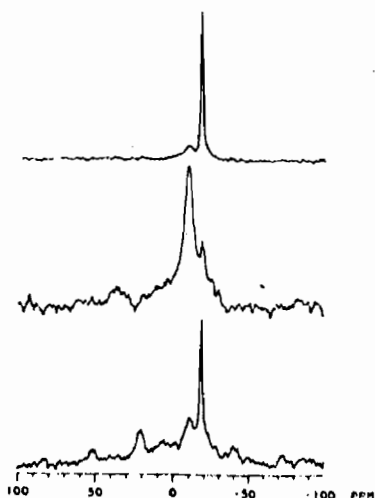


FIGURE 2

^{31}P MAS NMR spectra of PNDP adsorbed on the resin powder from ethanol solution. Top: 1 day old sample, stored in a capped 5mm NMR tube. Middle: 23 day old sample, stored in a capped 5mm NMR tube. Bottom: sample remained exposed to air.

by extraction and analysis by solution NMR;²¹ however, no PNPP product is detected. Thus, the observed DPP hydrolysis product demonstrates that the reactive sites are accessible to PNPP, although no distinct signal is observed for PNPP adsorbed at the acid/base sites.

Solvents play a major role in polymer-supported solution-phase catalysis,^{2,34} and ordinarily the resin powder would only contain adsorbed water. Therefore, the effect of coadsorbed solvent on the reaction was investigated in the following experiment. A PNPP/ethanol loaded sample was allowed to dry in air just to the point where no visible solvent remained, at which time a portion of the sample was removed and placed in a capped 5mm NMR tube. The rest of the sample remained exposed to air in order to allow further unrestricted loss of ethanol and equilibration with ambient moisture. The portions were allowed to stand for 23 days before their ³¹P MAS NMR spectra were recorded. These spectra are also shown in Figure 2. For the capped sample (middle), the conversion of PNPP to DPP is nearly complete with only a small signal remaining for unreacted PNPP. Also, note that the signal for DPP lacks CSA spinning sidebands indicating that the product is still very liquid-like. However, the spectrum of the air-exposed portion (bottom) reveals a reduced conversion along with a DPP product which is being very rigidly held by the resin.

¹H MAS NMR indicates that no significant amount of highly-mobile ethanol remains at the end of the drying period; however, less mobile ethanol would not be detected as a result of severe linebroadening due to ¹H-¹H dipolar interactions. The capped sample does contain considerably more mobile water than the air-exposed sample, but water is ruled out as capable of enhancing hydrolysis since partially-dried samples wet with water only do not yield increased PNPP conversions. Therefore, these results suggest that coadsorbed ethanol, although of limited mobility, is responsible for promoting PNPP hydrolysis, most likely by promoting PNPP migration rather than allowing release of DPP to regenerate "used" sites. This interpretation is supported by the fact that no turnover is observed when excess PNPP is allowed to react with the resin in ethanol solution even though smaller amounts react completely within 4 days. Also, DPP product is not extracted by ethanol or water (acidification is necessary in order to dislodge the product from the resin).

To determine the reactivity of PNPP with the various components of the resin powder, ³¹P MAS spectra were also recorded for PNPP adsorbed on the carbonaceous macroporous adsorbent and the strong acid and strong base macroporous ion-exchange resins (spectra not shown). PNPP adsorbed on the carbonaceous macroporous adsorbent yields a single peak at -17.8 ppm, which confirms the previous assignment of this resonance to PNPP adsorbed in the macroporous region. As expected, no reaction products are observed on this purely sorptive component. PNPP adsorbed on the strong base resin hydrolyzes in the same manner as on the resin powder as indicated by a peak at -9.6 ppm, which is similarly assigned to the hydrolysis product DPP. In support of this assignment, the initially tan strong base resin rapidly becomes

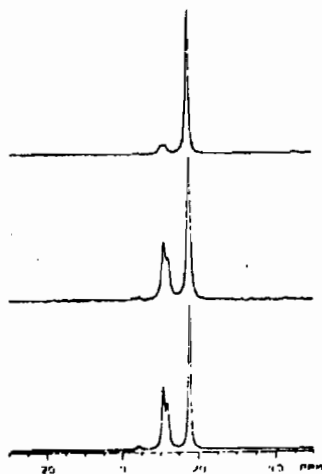


FIGURE 3

³¹P MAS NMR spectra of PNPP adsorbed on the macroporous strong acid resin. Top: 1 day old, stored in a capped 5mm NMR tube. Middle: 40 days old, stored in a capped 5mm NMR tube. Bottom: sample exposed to air for 6 additional days.

yellow after being slurried with the PNDP/ethanol solution, consistent with the release of the p-nitrophenoxide chromophore. The strong base resin further parallels the resin powder behavior in that the spectrum of an air-exposed, 15 day old sample shows a poor conversion along with a large CSA for the immobilized DPP product, whereas the capped control sample yielded a much better conversion along with a highly mobile, liquid-like DPP product. Again, these findings are consistent with the DPP anion remaining bound to the quaternary amine ion-exchange sites, and enhanced PNDP hydrolysis due to its greater mobility in the presence of elevated amounts of coadsorbed ethanol.

Spectra obtained for PNDP adsorbed on the strong acid resin, Figure 3, are quite different than the spectra obtained for both the resin powder and strong base resin. Again, the peak at -17.9 ppm in the spectrum of a 1 day old sample (top), is due to PNDP adsorbed in the macroreticular region. The peaks at -10.7 ppm and -11.7 ppm are assigned to the acid-catalyzed hydrolysis products, diphenyl phosphoric acid (DPPA) and p-nitrophenyl phenyl phosphoric acid (PNPPA), based on the chemical shifts of these species in solution. The spectrum taken after the sample had been kept for 40 days in a capped 5mm NMR tube (middle) shows further hydrolysis of PNDP with DPPA apparently being the favored product. Solvent extraction of the strong acid resin yields the same relative amounts of PNDP, DPPA and PNPPA in the filtrate indicating that the products are easily removed and not tightly bound to the sulfonic acid ion-exchange sites. The bottom spectrum was obtained from the same sample after it had been exposed to air for 6 days and shows further DPPA and PNPPA formation along with the appearance of a third peak at -4.4 ppm (product not identified). Even after long-term air exposure, the neutral acid products on the strong acid resin remain highly mobile and liquid-like in the absence of coadsorbed ethanol, indicating an increased mobility of the neutral species as compared with the anionic base-catalyzed products.

CONCLUSIONS

³¹P MAS NMR spectra of DMMP adsorbed on the resin powder provide direct evidence for the partitioning of adsorbed organophosphorous ester occurring between two different adsorption sites. Comparison of spectra obtained for DMMP adsorbed on strong acid and strong base ion-exchange resins and a carbonaceous macroreticular adsorbent (the three components of the resin powder) allow the assignment of the two adsorption sites to the macroreticular region and the quaternary ammonium hydroxide ion-exchange sites. No resonance is detected for DMMP adsorbed at sulfonic acid ion-exchange sites. Variable temperature spectra obtained for DMMP adsorbed on both the resin powder and the strong base ion-exchange resin indicate that DMMP exchange between the macroreticular region and the quaternary amine sites cannot be occurring at a rate greater than 300 s⁻¹.

The results obtained for the hydrolysis of PNDP adsorbed on the resin powder (from ethanol solution) reveal that the anionic DPP product appears to be tightly bound to the quaternary amine ion-exchange sites rendering the reaction stoichiometric. PNDP hydrolysis is enhanced by the presence of coadsorbed ethanol consistent with an increased rate of diffusion to available reactive sites. Product immobilization does not occur for acid-catalyzed hydrolysis on the strong acid resin where the neutral DPPA and PNPPA products remain highly mobile, even in the absence of coadsorbed ethanol. However, the analogous acid-catalyzed process does not occur on the resin powder. The reason for the apparent lack of reactivity of the resin powder sulfonic acid groups remains unclear.

ACKNOWLEDGEMENTS

The ³¹P MAS NMR experiments were conducted at the National Institutes of Health, Bethesda, MD, and we are grateful to D. Torchia for the use of the 6T NMR spectrometer and H. Cole for her helpful assistance with the operation of the instrument. This work was done while one of the authors (G.W.W.) held a National Research Council-CRDEC Research Associateship.

REFERENCES

1. T. C. Bruce and S. J. Benkovic, Bioorganic Mechanisms, Volume II, W. A. Benjamin, New York, 1966, Chapter 6, pp. 100-159.
2. A. Guyot, Pure & Appl. Chem., **60** (1988) 365.
3. D. C. Sherrington, Pure & Appl. Chem., **60** (1988) 401.
4. Ambergard[®] XE-555 Resin Material Data Safety Sheet, Rohm and Haas Company, 1989.
5. J. R. Cox, Jr. and O. B. Ramsay, Chem. Rev., **64** (1964) 317.
6. D. R. Leslie, W. T. Beaudry and L. L. Szafranec, Sorption and Reaction of Chemical Agents by a Mixed Sorptive/Reactive Resin, CRDEC Technical Report, Aberdeen Proving Ground, MD, in press.
7. L. Baltusis, J. S. Frye and G. E. Maciel, J. Am. Chem. Soc., **109** (1987) 40.
8. L. Baltusis, J. S. Frye and G. E. Maciel, J. Am. Chem. Soc., **108** (1986) 7119.
9. J. H. Lunsford, W. P. Rothwell and W. Shen, J. Am. Chem. Soc., **107** (1985) 1540.
10. W. P. Rothwell, W. X. Shen and J. H. Lunsford, J. Am. Chem. Soc., **106** (1984) 2452.
11. H.-H. Limbach, B. Wehrle, M. Schlabach, R. Kendrick and C. S. Yannoni, J. Magn. Reson., **77** (1988) 84.
12. A. Schmidt and S. Vega, J. Chem. Phys., **87** (1987) 6895.
13. W. T. Ford, M. Periyasamy, H. O. Spivey and J. P. Chandler, J. Magn. Reson., **63** (1985) 298.
14. W. T. Ford, M. Periyasamy and H. O. Spivey, Macromolecules, **17** (1984) 2881.
15. D. Suwelack, W. P. Rothwell and J. S. Waugh, J. Chem. Phys., **73** (1980) 2559.
16. N. E. Burlinson, B. A. Dunell and J. A. Ripmeester, J. Magn. Reson., **67** (1986) 217.
17. T. M. Duncan and D. C. Douglass, Chem. Phys., **87** (1984) 339.
18. A.-R. Grimmer and U. Haubenreisser, Chem. Phys. Lett., **99** (1983) 487.
19. J. Herzfeld, R. G. Griffin and R. A. Haberkorn, Biochem., **17** (1978) 2711.
20. R. K. Harris, Nuclear Magnetic Resonance Spectroscopy, Pittman, London, 1983, Chapter 5.
21. B. A. Burnside, L. L. Szafranec, B. L. Knier, H. D. Durst, R. A. Mackay and F. R. Longo, J. Org. Chem., **53** (1988) 2009.
22. B. L. Knier, H. D. Durst, B. A. Burnside, R. A. Mackay and F. R. Longo, J. Solution Chem., **17** (1988) 77.
23. R. A. Mackay, F. R. Longo, B. L. Knier and H. D. Durst, J. Phys. Chem., **91** (1987) 861.
24. S. H. Gellman, R. Petter and R. Breslow, J. Am. Chem. Soc., **108** (1986) 2388.
25. R. A. Moss, K. Y. Kim and S. Swarup, J. Am. Chem. Soc., **108** (1986) 788.
26. D. A. Jaeger and D. Bolkal, J. Org. Chem., **50** (1985) 4635.
27. D. R. Jones, L. F. Lindoy and A. M. Sargeson, J. Am. Chem. Soc., **106** (1984) 7807.
28. R. A. Moss, K. W. Alwis and J.-S. Shin, J. Am. Chem. Soc., **106** (1984) 2651.
29. C. A. Bunton, F. de Buzzaccarini and F. H. Hamed, J. Org. Chem., **48** (1983) 2457.
30. C. A. Bunton and L. Robinson, J. Org. Chem., **34** (1969) 733.
31. C. A. Bunton, S. J. Farber and E. J. Fendler, J. Org. Chem., **33** (1968) 29.
32. The room temperature ³¹P MAS NMR spectrum of neat PNDP solid yields two resonances at -17.9 and -12.6 ppm which also display completely isotropic CSA's indicative of rapid isotropic molecular tumbling within the crystal lattice of the solid. The relative intensity of two signals vary smoothly as the temperature is raised with the downfield resonance nearly disappearing just prior to the melting point at ca. 50 °C. As the temperature is lowered, a rather abrupt onset of an observable CSA occurs at ca. -45 °C where the two resonances are of equal intensity. This infers the presence of two equally populated crystal lattice sites in the rigid phase formed at this temperature. Similar behavior has recently been observed for crystalline phosphoric acid, although only a single resonance is detected in the low temperature rigid phase of this solid.³³
33. A. J. Vila, C. M. Lagler, G. W. Wagner and A. C. Olivieri, J. Chem. Soc., Chem. Commun., (1991) 683.
34. F. Svec, Pure & Appl. Chem., **60** (1988) 377.

BLANK

VIII. FLUID DYNAMICS

NOTE: Papers with the following titles were presented at the Conference but are not included in this document:

Part I: Liquid Filled Projectiles

Progress in the Moment Calculation for a Spinning and Nutating Cylinder with Silicone Fluid

Effect of Low Viscosity Additives on the Moments Caused by Viscous Fluids in a Spinning and Coning Cylinder

Part II: Rheology and Special Topics

Nonlinear Dynamics of Fluidized Suspensions and Interactive Aerodynamics

BLANK

EFFECT OF LONGITUDINAL BAFFLES ON THE VISCOUS LIQUID-FILL INDUCED DESTABILIZING MOMENT

Miles C. Miller

U.S. Army, Chemical Research, Development and Engineering Center
Aberdeen Proving Ground, Maryland 21010-5423

ABSTRACT

Experiments were conducted on the CRDEC Laboratory Test Fixture for Non-Rigid Payloads to investigate the effects of various longitudinal baffle arrangements on the destabilizing moment created by a viscous liquid in a cylindrical container undergoing the simultaneous spinning and coning motion of a projectile in flight. The baffles consisted of radial walls running the entire longitudinal length of the cylinder which effectively divided the cylinder into different pie-shaped cavities. One, two, three and four cavity baffle configurations were evaluated in a nominal cylindrical container filled with liquids having a viscosity range from 1K to 100K cSt. The resulting liquid-induced rolling moments and non-dimensional liquid-induced yawing moments are presented as a function of Reynolds number.

ACKNOWLEDGEMENT

The author would like to thank Daniel R. Van Reenen and John W. Molnar, Research Directorate for their assistance in the experimental and data analysis aspects of this study.

LIST OF SYMBOLS

AR	aspect ratio (c/a)
a	canister inside radius
C'	baffle configuration (number of lateral cavities)
c	canister inside half length
C'_{LSM}	generalized liquid side moment coefficient ($M_{LSM} / \omega^2 a^2 m_L \tan\theta$)
C'_{LRM}	generalized liquid rolling moment coefficient ($M_{LRM} / \omega^2 a^2 m_L \tan^2\theta$)
M_{LRM}	liquid fill induced rolling moment
M_{LSM}	liquid fill induced side moment
m_L	total liquid mass
R_a'	Reynolds number - $\omega' a^2 / \nu$
t	time
θ	canister coning angle
ν	liquid fill kinematic viscosity
ν_a	kinematic viscosity of additive
σ_N	yawing motion of projectile in flight (via yaw sonde)
τ	non-dimensional coning rate (Ω / ω')
ϕ	spin rate of projectile in flight (via yaw sonde)
Ω	canister coning rate
ω	canister spin rate (relative to coning reference frame)
ω'	canister absolute spin rate ($\omega + \Omega \cos \theta$)

INTRODUCTION

Significant progress has been made over the past ten years in developing mathematical methods to predict the occurrence of flight instabilities in spinning projectiles created by their liquid-fills.^[1] The results of this effort allow the entire liquid-fill projectile flight instability problem to be presented in a single three-dimensional plot as shown in Figure 1. The liquid-fill induced destabilizing moment is depicted as a function of the liquid-fill characteristics (Reynolds number) and the projectile motion (non-dimensional coning frequency).

This plot graphically illustrates the entire range of conditions including both low and high viscosity regions corresponding to high and low Reynolds numbers, respectively. Of particular note, is the presence of a large peak moment acting over a narrow frequency ratio range at the higher Reynolds number region where the inertial effects dominate and the large moment occurring over a broad frequency range in the viscosity dominated, low Reynolds number region. Recent research emphasis has been on establishing means of preventing these instabilities from occurring.

For low viscosity (i.e., high Reynolds numbers) liquid-fills, a resonance condition is created with the liquid-fill producing large destabilizing yawing moments in response to the projectile nutation motion. The frequencies of the inertial waves which cause the destabilizing moment are a strong function of the payload geometry. A small change in the length to diameter ratio of the payload compartment can shift these liquid frequencies away from the nutation frequencies seen in flight, thereby avoiding a resonance condition. In this manner, payload geometries can be selected to prevent this type of instability.

While flight instabilities associated with low viscosity fluids can be easily and effectively prevented, the situation with reducing or eliminating instabilities for high viscosity fluids is not as simple because these are relatively insensitive to changes in the payload container aspect ratio.

One technique involves the addition of a small amount of an immiscible, low viscosity liquid additive to the highly viscous liquid-fill.^[2] The slightly higher density additive is centrifuged out to the inside surface of the payload container during flight subsequently reducing the destabilizing moment. Only a small amount of additive is required to achieve this effect as shown in Figure 2. Recent instrumented flight tests^[3] demonstrated that this approach can dramatically improve the flight instability of liquid-filled artillery projectiles.

Figure 3 shows the yaw sonde data (indicating the yawing motion and spin rate as a function of time during flight) of a 155mm artillery projectile with two different liquid-fills. On the left, the fill was composed of 10K cSt Silicone Fluid and produced a severe flight instability with an increase in yaw angle and decrease in spin rate characteristic of a viscous liquid-fill instability. The right side of the figure presents the flight data for the same projectile and liquid-fill, but having 5% by volume of water (which is immiscible in silicone fluid, and has a slightly higher density) added to the payload container. As can be seen, a stable flight is achieved with the additive.

While the additive was successful for the lower viscosity fluids tested, it was not as effective for the very high viscosities. As illustrated in Figure 4, the additive was not capable of preventing the instability. This might be due to the inability of the additive to be distributed quickly enough to the outside of the container during the rapid spin-up transient the projectile undergoes during gun firing. The destabilizing effect occurs before the additive has time to be effective.

The XM761, White Phosphorus (WP), Smoke Screening, 155mm artillery projectile, illustrated in Figure 5, contained WP saturated, cotton wicks in a cylindrical canister. A cruciform, longitudinal baffle was located in the canister, solely for structural purposes. The liquid WP resulted in unstable flights.^[4] Experiments were conducted on the Laboratory Test Fixture for Non-Rigid Payloads with this canister configuration (both with and without the baffle) filled with liquids having a wide range of viscosities. The no-baffle data shown in Figure 6 revealed the ability of a homogenous, viscous liquid-fill to create a destabilizing moment. Similar tests with the baffle in place indicated that the moment was greatly reduced for the high viscosities, but became larger at the lower viscosities. Since the baffle did not provide an across-the-board solution for all viscosities and because of the emphasis on understanding and predicting the general phenomena of viscous liquid-fills, the baffle approach was not pursued at the time. The purpose of the current study is to investigate the influence of longitudinal baffles in more detail.

LONGITUDINAL BAFFLE CONFIGURATIONS

The baffles consisted of radial walls running the entire longitudinal length of the cylinder which effectively divided the cylinder into different pie shaped cavities as illustrated in Figure 7. One, two, three and four cavity baffle configurations were evaluated, where the one cavity configuration represented the "no-baffle" case. The

baffle wall thickness was selected to provide a dividing wall which was sufficiently thick to survive structurally under firing conditions. Thus, the same items tested on the fixture could be eventually flight tested. In all of the baffles, the baffle walls extend to the inside surface of the canister, effectively isolating each cavity from one another. One of the four cavity arrangements, however, includes a small gap. This was done to match, somewhat, the earlier XM761 baffle situation and to determine if a gap is critical to the baffle performance.

EXPERIMENTAL APPROACH

A series of experiments were completed at the U.S. Army Chemical Research, Development and Engineering Center (CRDEC) on the Laboratory Test Fixture for Non-Rigid Payloads⁵¹ shown in Figure 8. This apparatus forces a spinning, liquid-filled cylindrical container to undergo fixed-angle coning motion. Thus, the liquid-fill experiences the same basic dynamic environment it would have in a spinning and nutating projectile. A silicone fluid was used to represent a homogenous, highly viscous, liquid-fill. The procedure was to mount the filled container to the fixture frame at a coning angle (θ) of 20 degrees. The container was spun about its longitudinal axis to a spin rate of about 9,000 RPM. The fixture frame was then rotated about a vertical axis until the spinning container assumed a coning motion at the fixed value desired for that particular test run. At that point, the container spin turbine air was cut-off allowing the container and liquid-fill to despin at a constant coning angle and constant coning rate. The resulting container spin rate versus time data were used to compute the net despin moment acting on the canister at the various spin rates. Subtracting out the contribution to this moment due to the bearing friction (which had been previously determined with similar tests using an empty container), results in the despin moment induced by the liquid-fill. This is sometimes called the "liquid rolling moment" (M_{LRM}) and is directly related to an associated "liquid side moment" (M_{LSM}) which is described by the following simple expression:

$$M_{LSM} = M_{LRM} / \tan \theta$$

These terms are illustrated in Figure 9. Thus, the measured liquid induced despin moment is a measure of the destabilizing liquid yawing moment.

DESTABILIZING MOMENT

Figures 10 through 12 contain the liquid-induced rolling moment (i.e., despin moment) as a function of spin rate for the various baffle configurations for liquid fill viscosities of 100K, 10K and 1K, respectively. For the 500 RPM coning rate shown, the moment at a spin rate of 6,000 RPM is of primary concern in that this represents the projectile flight motion for the critical Zone 4 firing condition. At this transonic flight condition, the projectile has its lowest aeroballistic stability and is most susceptible to a liquid-fill instability.

From Figure 10 (100K cSt), it can be seen that all of the baffle configurations act to reduce the destabilizing liquid-induced moment compared to the no-baffle case, with the baffles being more effective (in reducing the liquid moment) with an increasing number of cavities. In Figure 11 (10K cSt) however, the baffles both decrease and increase the moment. Further, in Figure 12 (1K cSt), the baffles always increase the moment. In general, the presence of the gap in the baffle lowered its effectiveness.

DESTABILIZING MOMENT COEFFICIENT

The moment data from all of the tests were reduced to generalized liquid moment form (C'_{LSM}) which is only a function of Reynolds number. Figures 13 through 17 includes data for the different baffle configurations. The data seem fairly consistent for the lower Reynolds numbers (i.e., high viscosities), but seem erratic for some cases at the higher Reynolds numbers (i.e., low viscosities). This is probably attributed to the existence of a resonance instability for some of the baffle configurations which is exacerbated at the higher Reynolds numbers. The cavities represent an effective aspect ratio which could create this resonance condition.

Figure 18 represents the non-resonance data, and indicates the effect of the longitudinal baffles and the immiscible, low viscosity additive on reducing the viscous liquid destabilizing moment. The figure contains a stability boundary line for the nominal 155mm artillery projectile which has been established from previous flight and laboratory tests. If the liquid-induced moment coefficient is below this line, a stable flight will be obtained. Conversely, if the curve is above this boundary, an unstable flight will occur. The data show that for the no-baffle case, an unstable flight will result for Reynolds numbers between 3 and 1000. As can be seen, the baffles are effective in providing a stable flight below a Reynolds number of around 70. Whereas, the additive is effective in providing stable flight above this Reynolds number.

CONCLUSIONS

1. Longitudinal baffles can both increase and decrease the destabilizing moment produced by a viscous liquid in a spinning and coning cylinder depending on the Reynolds number and baffle configuration.
2. For Reynolds numbers on the order of 10, all baffle configurations reduced the destabilizing moment relative to the no-baffle case, with the amount of reduction increasing with the number of transverse cavities created by the baffles. Both a three and four cavity, longitudinal baffle would reduce the destabilizing moment sufficiently to provide flight stability for a 155mm projectile having a 100K cSt fluid fill.
3. For Reynolds numbers on the order of 100, the baffles are not as effective as at the lower Reynolds number and, in fact, for certain configurations, significantly increase the destabilizing moment over the no-baffle case. A four cavity baffle would reduce the destabilizing moment sufficiently to produce a stable flight for a 155mm projectile having a 10K cSt fluid fill.
4. For Reynolds numbers on the order of 1000, all baffles significantly increase the destabilizing moment over the no-baffle case. The use of any of the baffle configurations would result in an unstable flight for a 155mm projectile having a 1K cSt fluid fill whereas this liquid-fill would produce a stable flight without a baffle.
5. The presence of a gap between the outer edge of the baffle and the inner surface of the cylinder (of about 6% of the cylinder diameter) significantly degrades the effectiveness of the baffle in reducing the destabilizing moment.
6. While not providing an "across-the-board" solution to the viscous liquid fill flight stability problem, baffle configurations can be selected to meet specific payload and projectile situations. Longitudinal baffles offer a means of stabilizing liquid-filled projectiles without a severe payload penalty (10-15%) and are not affected by flight motion transients. In this regard, the baffles are most effective for liquid-fills for which there are no other means of obtaining stable flights.

REFERENCES

1. Miller, Miles C.; "Liquid-Filled Projectiles, New Problems - New Solutions", Proceedings of the ADPA Ninth International Ballistics Symposium, Shrivenham, England, 9 April - 1 May 1986.
2. Miller, Miles C.; "Elimination of Viscous Liquid-Fill Flight Instability by Means of Lower Viscosity, Immiscible Additive", AIAA 29th Aerospace Sciences Meeting, Paper No. AIAA-91-0679, 7-10 January 1991.
3. Miller, Miles C. and Joseph, Daniel D.; "Proceedings: Workshop on Problems of Rotating Fluids", CRDEC-SP-038, July 1991.
4. Miller, Miles C.; "Flight Instabilities of Spinning Projectiles Having Non-Rigid Payloads", AIAA Journal of Spacecraft and Rockets, Vol 16, No. 1, Pp 62-64, January/February 1981.
5. Miller, Miles C.; "Laboratory Test Fixture for Non-Rigid Payloads", Proceedings of the International Congress on Instrumentation in Aerospace Simulation Facilities, ICIASF 89 Record, September 1989, Pp 350-364.

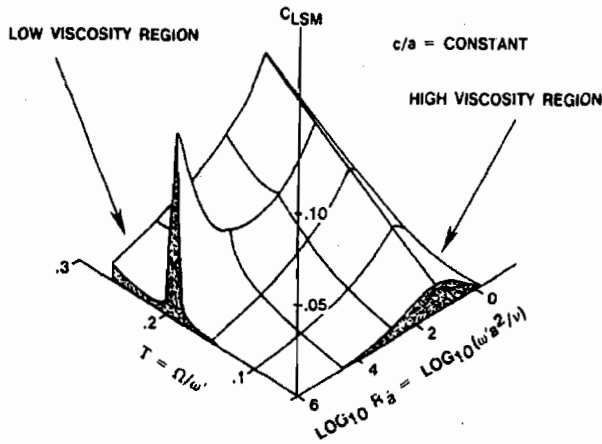


Fig. 1 Destabilizing Liquid-Moment Effect

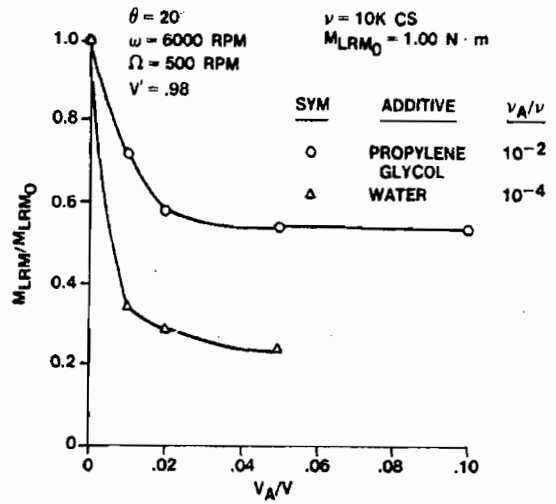


Fig. 2 Effect of Immiscible, Low Viscosity Additive

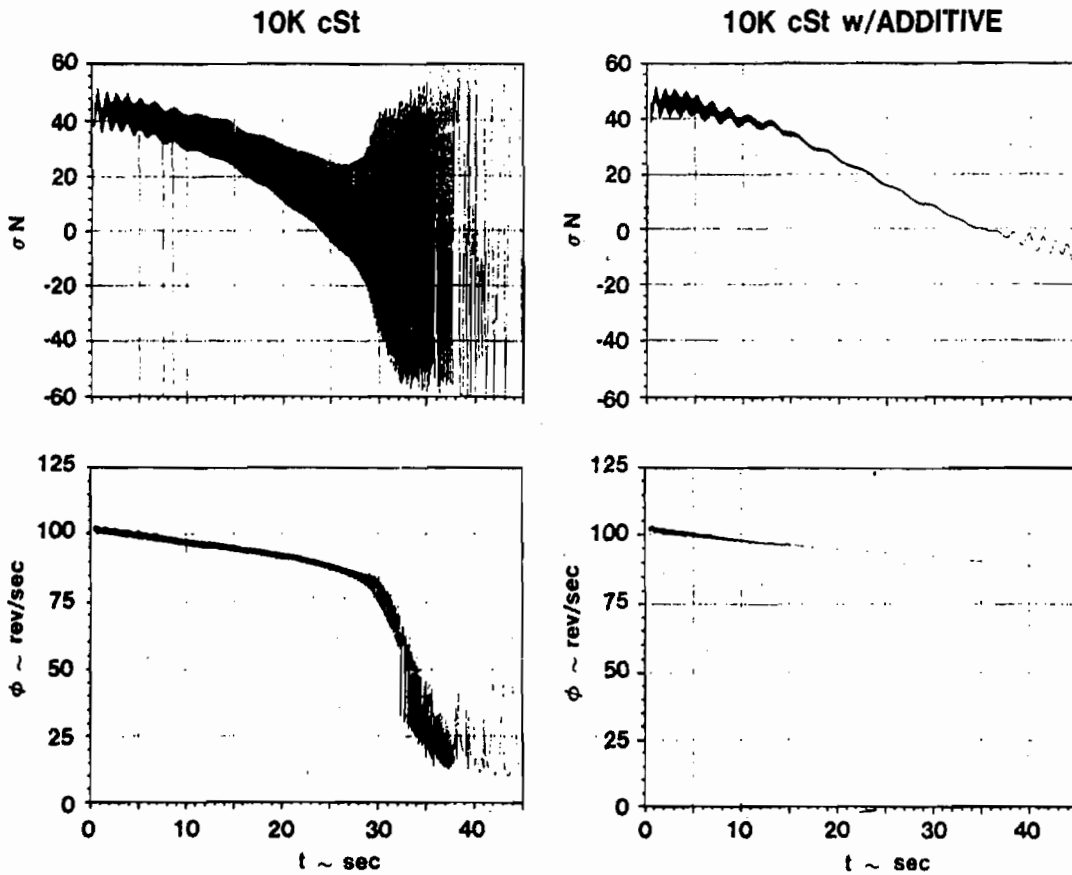


Fig. 3 Influence of Additive on Flight Performance (10K cSt liquid-fill)

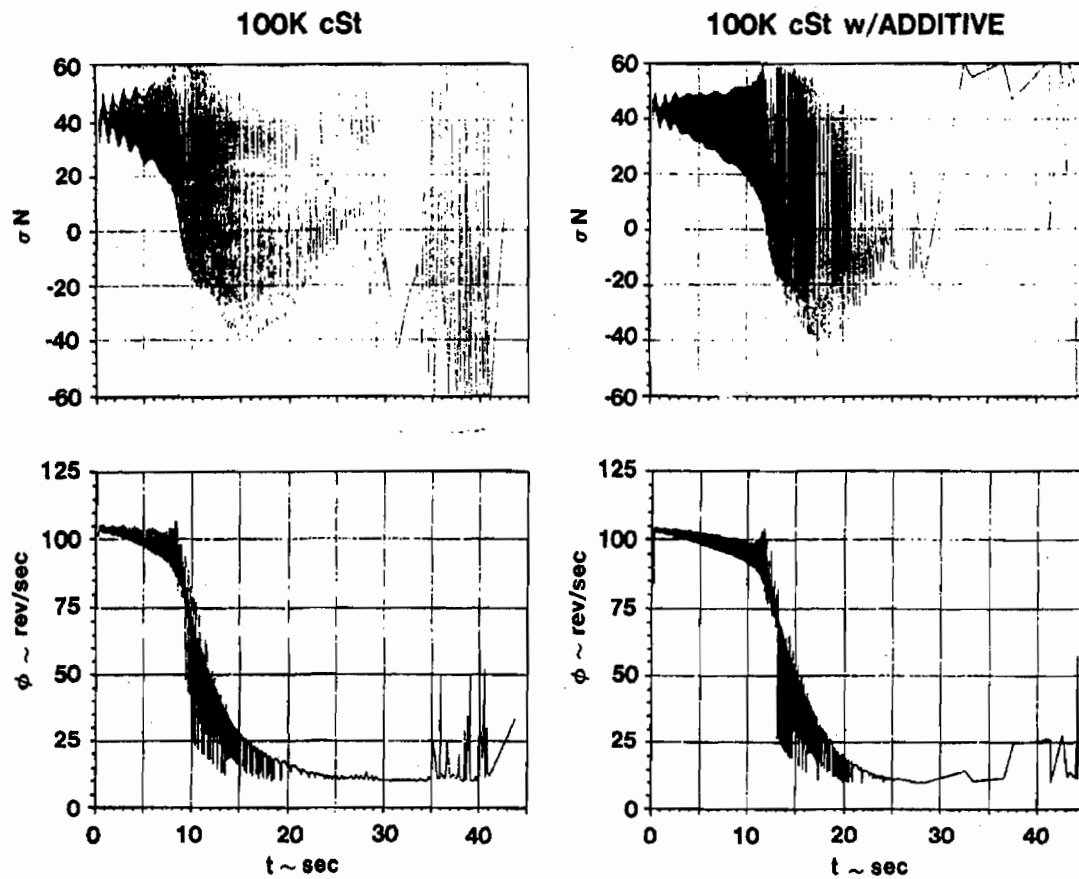


Fig. 4 Influence of Additive on Flight Performance
(100K cSt liquid-fill)

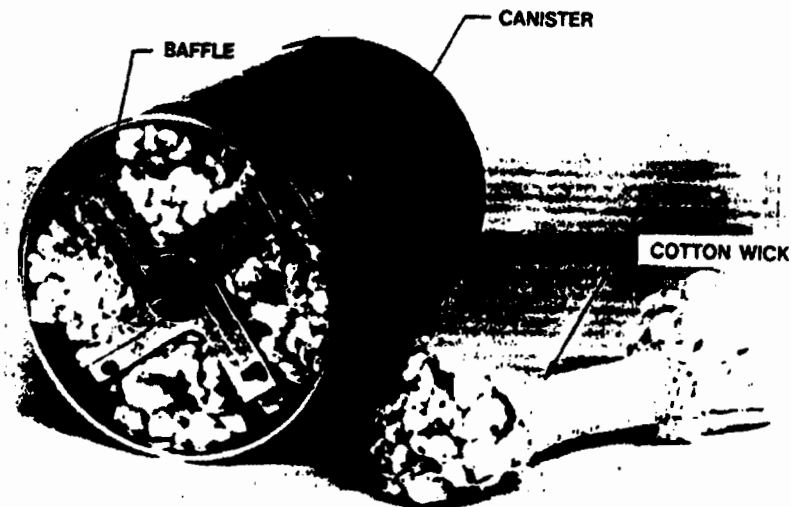


Fig. 5 XM761 Payload Arrangement

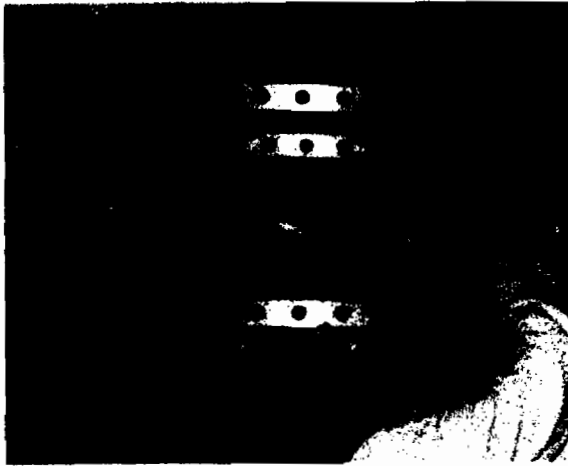


Fig. 8 CRDEC Laboratory Test Fixture For Non-Rigid Payloads

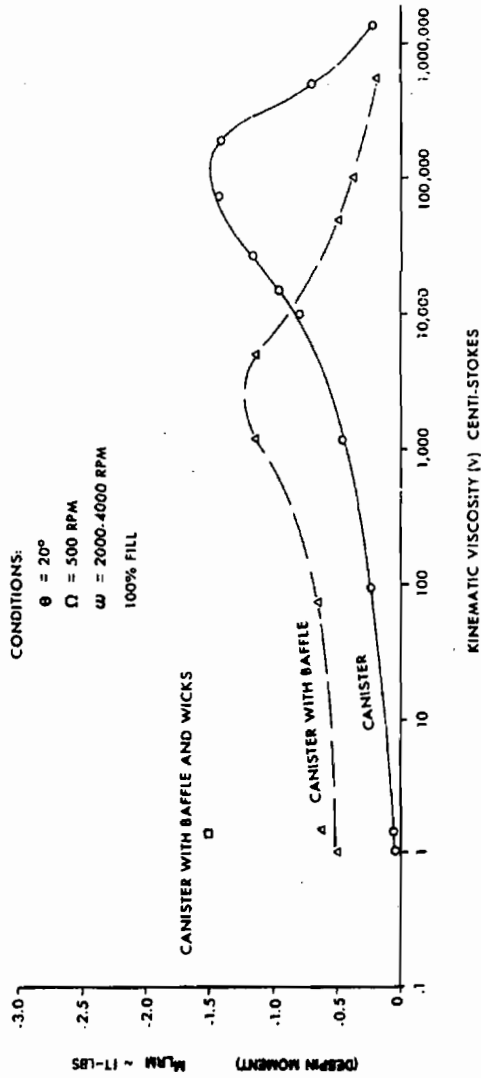


Fig. 6 Effect of XM761 Baffle

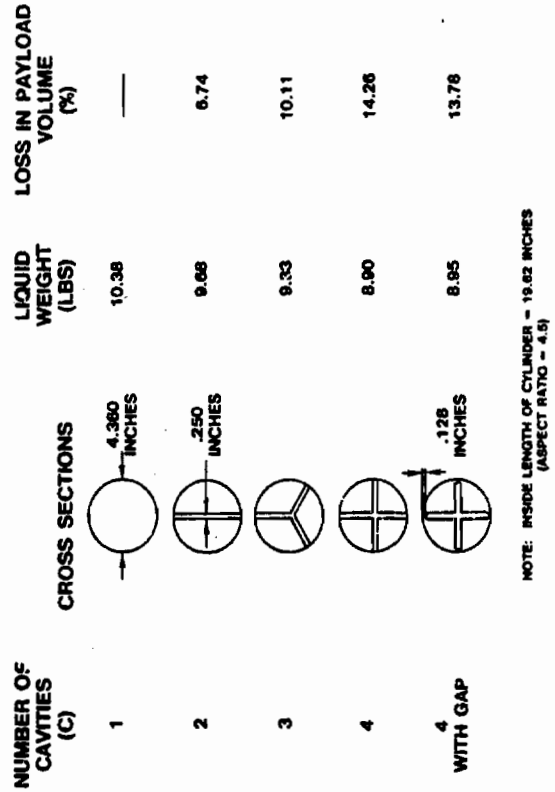


Fig. 7 Baffle Configurations

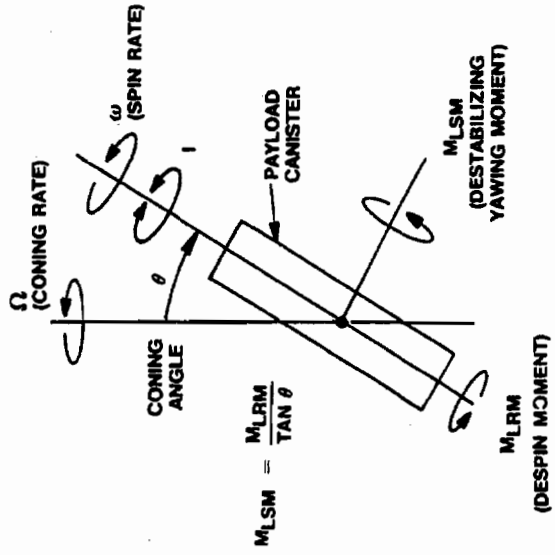


Fig. 9 Fixture Terminology

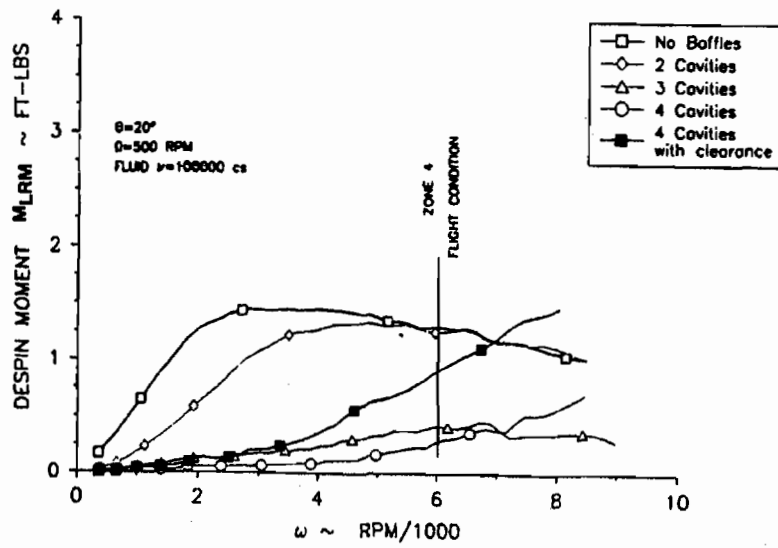


Fig. 10 Liquid Rolling Moment for Baffle Configurations (100K cSt)

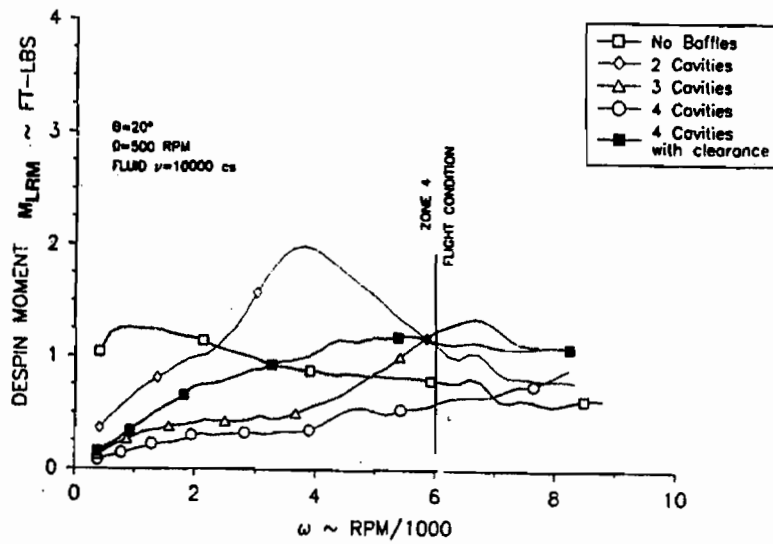


Fig. 11 Liquid Rolling Moment for Baffle Configurations (10K cSt)

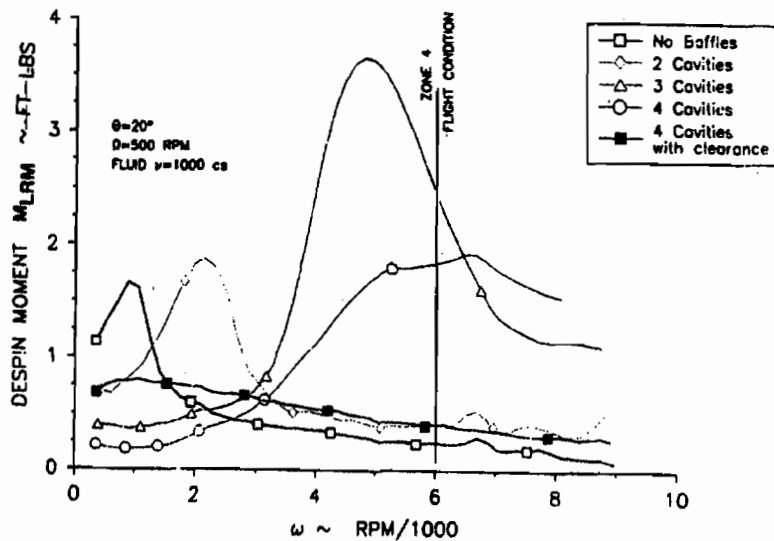


Fig. 12 Liquid Rolling Moment for Baffle Configurations (1K cSt)

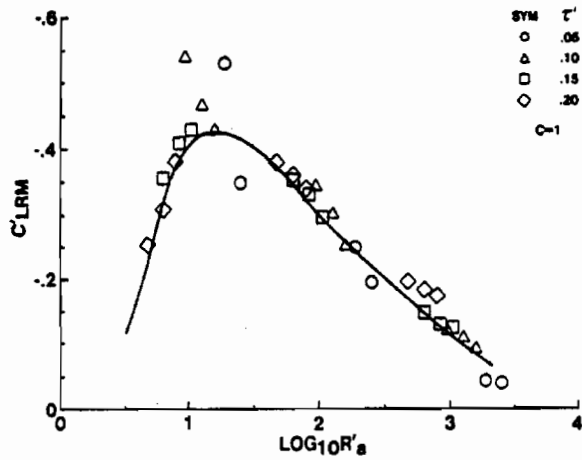


Fig. 13 Liquid Side Moment Coefficient for $C' = 1$ Baffle Configuration

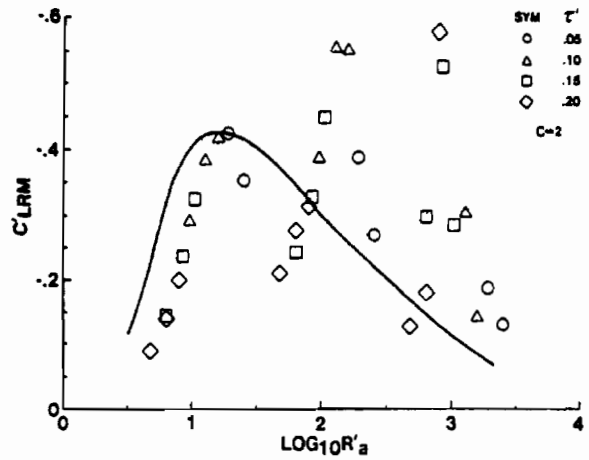


Fig. 14 Liquid Side Moment Coefficient for $C' = 2$ Baffle Configuration

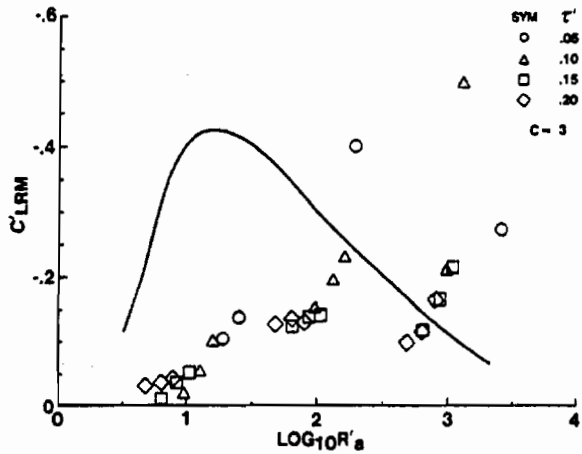


Fig. 15 Liquid Side Moment Coefficient for $C' = 3$ Baffle Configuration

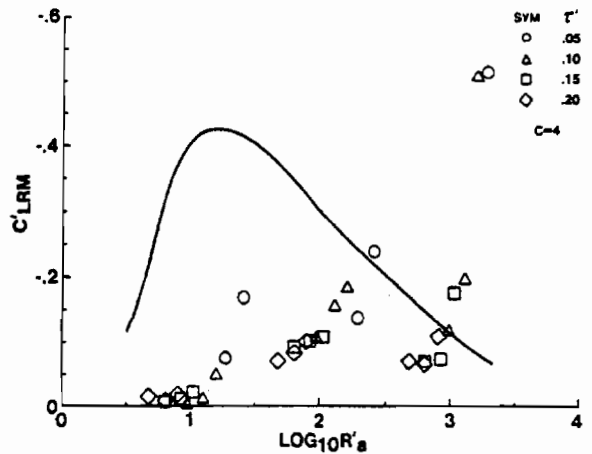


Fig. 16 Liquid Side Moment Coefficient for $C' = 4$ Baffle Configuration

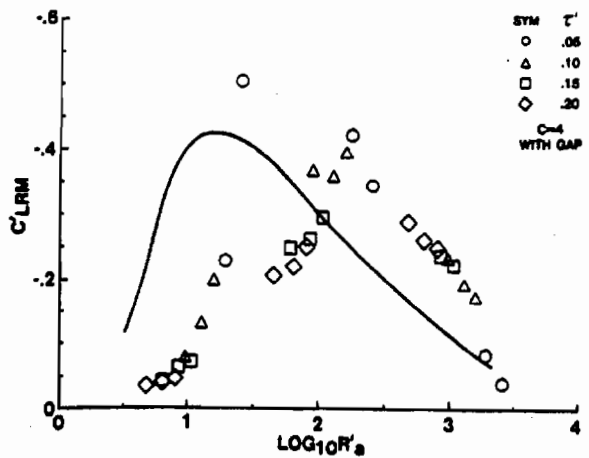


Fig. 17 Liquid Side Moment Coefficient for $C' = 4$ (With Gap) Baffle Configuration

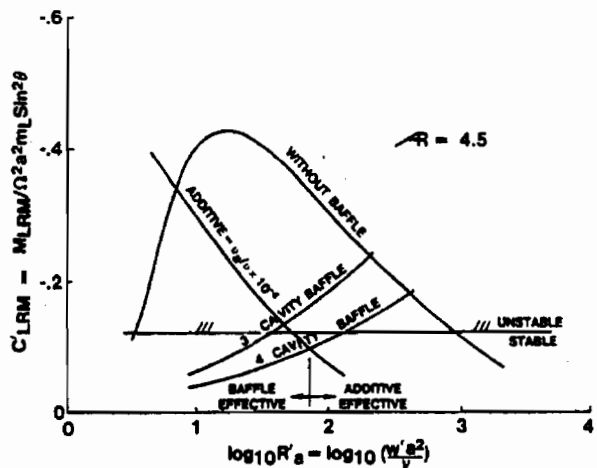


Fig. 18 Destabilizing Liquid Moment Coefficient as a Function of Reynolds Number

BLANK

INCLUDING LIQUID-FILL EFFECTS IN THE TRICYCLIC THEORY

Daniel J. Weber

U. S. Army, Chemical Research, Development and Engineering Center
Aberdeen Proving Ground, Maryland 21010-5423

ABSTRACT

The Tricyclic Theory is a simplified mathematical description of the flight motion and stability of a spinning projectile. The conventional theory provides a detailed insight into the relative contributions to the flight motion of a projectile due to various aerodynamic and inertial parameters. This theory has been modified to include the effects of a liquid-fill. A computer program has been prepared which computes and graphically displays the complex projectile motion and can use either theoretical estimates of liquid-fill characteristics or experimental data from the CRDEC Laboratory Test Fixture for Non-Rigid Payloads. This approach allows a preliminary assessment of a liquid-filled projectile's stability to be made much faster than using the current six degree-of-freedom programs. Flight stability predictions from the Modified Tricyclic Theory are compared with flight test results.

LIST OF SYMBOLS

C_{NRP}	liquid induced side moment coefficient	V	velocity
$C_{m\dot{\alpha}}$	dynamic stability derivative coefficient	α	angle-of-attack
$C_{m\alpha}$	static stability derivative coefficient	α_0	initial angle-of-attack
$C_{m\dot{\beta}}$	aerodynamic trim derivative coefficient	$\dot{\alpha}_0$	initial time rate of change of α
$C_{m\beta}$	Magnus moment derivative coefficient	β	angle-of-sideslip
d	reference diameter	β_0	initial angle-of-sideslip
I_x	roll moment of inertia	$\dot{\beta}_0$	initial time rate of change of β
I	transverse moment of inertia	δ	control deflection angle
K_1	length of nutation arm	θ	test fixture nutation angle, analogous to ϵ
K_2	length of precession arm	ν	kinematic viscosity
K_3	length of aerodynamic trim arm	ϵ	complex angle of attack, $\beta + i\alpha$
M_{LSM}	liquid induced side moment	$\lambda_{1,2}$	nutation and precession damping exponent (real part of m)
$M_{LSM\theta}$	liquid induced side moment due to θ	ρ	atmospheric density
$M_{LSM\beta}$	liquid induced side moment due to θ and β	σ_N	total angle of attack in sun fixed axes (yawsonde data)
$M_{p\beta}$	Magnus moment due to β	τ	defined by equation 7
M_q	pitch moment due to pitch rate, q	ϕ	roll rate measured in sun fixed axes (yawsonde data)
M_α	pitch moment due to α	$\omega_{1,2}$	nutation and precession frequency, (imaginary part of m)
$M_{\dot{\alpha}}$	pitch moment due to $\dot{\alpha}$		
M_δ	moment due to control deflection, δ		
$m_{1,2}$	complex roots to differential equation		
$N_{1,2,3}$	constants in linearized aeroballistic equation		
p	spin rate		
q	pitch rate		
q'	dynamic pressure, $\frac{1}{2}\rho V^2$		
S	reference area		
s_g	gyroscopic stability factor		
t	time		
Δt	Tricyclic Theory time step		

INTRODUCTION

The Tricyclic Theory provides a relatively complete solution to the aeroballistic equation which describes the free flight motion of a rolling vehicle. Until now, the Tricyclic Theory only considered the influence of the projectile's physical properties (moments of inertia, diameter) and aerodynamic characteristics (static and dynamic stability, Magnus, trim moment or trim angle) in determining the flight motion.^[1] A flight dynamicist using this theory can parametrically analyze the flight characteristics of a projectile to determine factors which have the greatest influence on its stability. The problem with this approach is that the influence of the payload on the projectile flight motion is ignored. This assumption is fine for solid payloads but not for liquid payloads. It has been shown experimentally, theoretically and through firing tests that liquid-fills can cause flight instabilities.^[2] Presently there are several analytical and computational methods available to determine the effects of a liquid payload on the flight stability of a projectile.^{[3] [4] [5]} The drawback to these methods are that they are complicated to use, require large computers, a substantial amount of computer time is required and the results are sometime difficult to interpret. By including the liquid payload effects in the Tricyclic Theory, many of these drawbacks are eliminated. The Tricyclic Theory is easy to use, employs conventional aeroballistic and aerodynamic definitions and nomenclature, can run on many different types of computers, executes quickly and produces results in a graphical format for easy interpretation.

CONVENTIONAL TRICYCLIC THEORY

In the Tricyclic Theory, the complex total angle-of-attack, $\xi = \beta + i\alpha$, is determined from the linearized aeroballistic equations of projectile motion. The assumptions required to linearize the aeroballistic equations are based on the following: small angles, constant aerodynamic coefficients, non-thrusting vehicle, rotation and mass symmetry and a rigid body. The mathematical representation of this motion is described by a linear, second order, differential equation.

$$\xi + N_1 \dot{\xi} + N_2 \ddot{\xi} = N_3 e^{ip\alpha} \quad (1)$$

where N_1 , N_2 and N_3 are constants defined as:

$$N_1 = \left[-ip \frac{I_x}{I} - \frac{M_q + M_{\dot{\alpha}}}{I} \right] \quad (2)$$

$$N_2 = \left[-ip \frac{M_{p\beta}}{I} - \frac{M_{\alpha}}{I} \right] \quad (3)$$

$$N_3 = i \left[\frac{M_{\delta}}{I} \delta \right] \quad (4)$$

solving equation (1) yields the following solution:

$$\xi = K_1 e^{m_1 t} + K_2 e^{m_2 t} + K_3 e^{ip\alpha} \quad (5)$$

where K_1 , K_2 , and K_3 are the nutation, precession and trim arms, respectively. The Magnus moment along with the other aerodynamic terms appear in the relations for m_1 and m_2 which are defined as:

$$\begin{aligned} m_{1,2} &= \lambda_{1,2} + i\omega_{1,2} \\ &= \left[\left(\frac{M_q + M_{\dot{\alpha}}}{2I} \right) \left[1 \pm \tau \right] \pm M_{p\beta} \frac{\tau}{I_x} \right] + i \left[\frac{pI_x}{2I} \left[1 \pm \frac{1}{\tau} \right] \right] \end{aligned} \quad (6)$$

the subscript 1 and 2 denote the nutation and precession motion, respectively. τ is expressed as follows:

$$\tau = \frac{\frac{pI_x}{2I}}{\left[\left(\frac{pI_x}{2I} \right)^2 - \frac{M_{\alpha}}{I} \right]^{1/2}} = \frac{1}{\left[1 - \frac{1}{s_g} \right]^{1/2}} \quad (7)$$

and s_g is the gyroscopic stability factor which must be greater than 1 for stability. s_g is defined as:

$$s_g = \frac{\left[\frac{p I_x}{2I} \right]^2}{M_{\alpha}} \quad (8)$$

Figure 1 illustrates the different components of the Tricyclic Theory. The magnitudes of the nutation, precession, and trim arms are K_1 , K_2 , and K_3 , respectively. Each arm rotates at the following rates: ω_1 for nutation, ω_2 for precession, and p for trim. Also, the magnitude of the nutation and precession arms can increase or decrease depending on the sign of λ_1 and λ_2 , respectively. ξ is the distance between the tail of K_1 (i.e., flight path) and the head of K_3 (i.e., projectile's nose). A typical conventional Tricyclic Theory simulation of a spin stabilized projectile is shown in Figure 2. The simulation is started at the position labeled "1" and follows the plotted curve. The small loops represent the projectile's nutation and the large loop is the precession. The simulation depicted in Figure 2 does not include liquid-fill effects. The next step is to eliminate the rigid body assumption and to include the liquid fill effects.

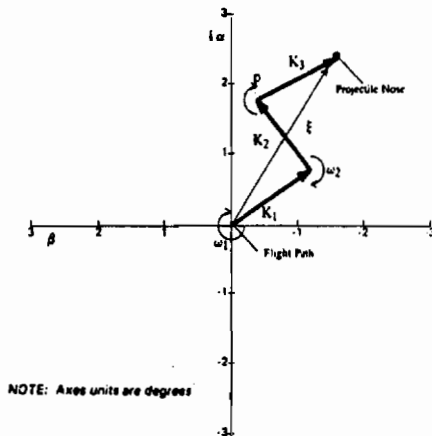


Figure 1: Tricyclic Theory Terminology

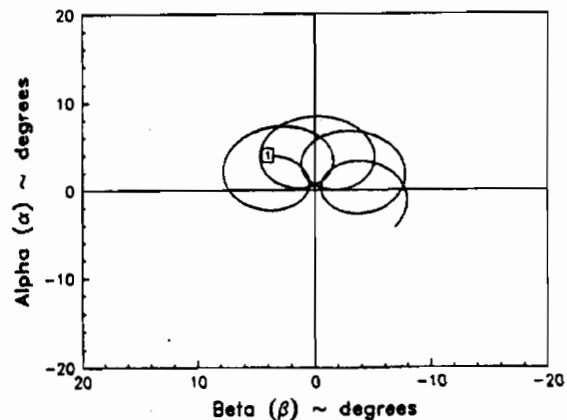


Figure 2: Typical Conventional Tricyclic Theory Simulation

MODIFIED TRICYCLIC THEORY TO INCLUDE LIQUID-FILL EFFECTS

To incorporate the liquid-fill effects into the Tricyclic Theory, the liquid payload moment had to be included in the mathematical expressions of the theory. It is known that the liquid-fill moment behaves in a similar manner to that of the Magnus moment for a spinning projectile.^[6] The Magnus moment is a function of projectile spin rate and total angle-of-attack. The liquid-fill moment can also be expressed as a function of spin rate, angle-of-attack and nutation rate. Since the nutation and spin rate are constants in the Tricyclic Theory, the two moments behave the same. To include the liquid-fill moment, the Magnus moment term in equation (6) was modified. The liquid-fill effect, expressed as a side moment was added to the Magnus term and thus equation (6) becomes:

$$m_{1,2} = \lambda_{1,2} + i\omega_{1,2} \\ = \left[\left[\frac{M_q + M_{\alpha}}{2I} \right] \left[1 \pm \tau \right] \pm \left[M_{ps} + M_{LSM_{ps}} \right] \frac{\tau}{I_x} \right] + i \left[\frac{p I_x}{2I} \left[1 \pm \frac{1}{\tau} \right] \right] \quad (9)$$

Since, both the Magnus and liquid side moments are part of the real term of equation (9), only the precessional and nutational damping of the projectile are affected.

INDUCED LIQUID SIDE MOMENT COEFFICIENT

All aerodynamic terms used in the theory are entered as coefficients and thus, the liquid-fill moment must also be converted to a coefficient. The liquid-fill moment can be estimated using any of the available computer programs developed for liquid-filled projectiles or by a direct measurement of the liquid-fill moment using the laboratory test fixture for non-rigid payloads.^[7] The latter method was used to determine the liquid-fill coefficients in the following examples.

The conversion of the test fixture results to coefficients is accomplished by first determining the nutation rate of the solid projectile. Since, the liquid-fill only influences the projectile's damping and not its angular frequencies, the conventional Tricyclic Theory (i.e., solid body) provides the same nutation rate whether the shell is solid or not. Knowing the nutation rate of the projectile and the liquid-fill viscosity, the appropriate test fixture data can be determined. For a given liquid payload viscosity, test results encompassing the range of values experienced in flight are available for: nutation rates of 200-500 rpm in 100 rpm increments, nutation angles of 5-20° in 5° increments and spin rates of 200-8000 rpm. Figure 3 shows typical test fixture results, M_{LSM} versus nutation angle (θ) for various constant spin rates (p), for $\nu = 100,000$ cSt and an $\omega_1 = 500$ rpm. It should be noted that the test fixture coning or nutation angle (θ) is analogous to the total complex angle-of-attack (ξ) used in the Tricyclic Theory. The results from Figure 3 are fitted with straight lines and the slopes ($M_{LSM,p}$) are determined. $M_{LSM,p}$ versus p are shown in Figure 4 for different fluid viscosities.

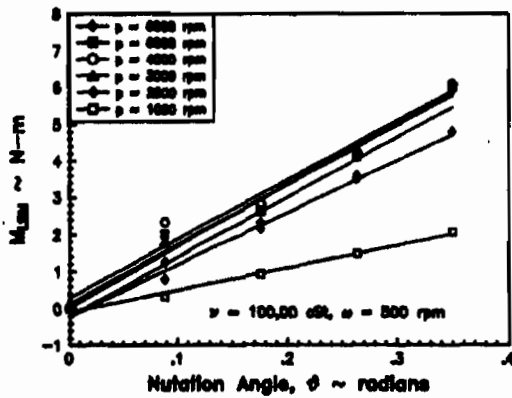


Figure 3: M_{LSM} Versus θ for Constant Spin Rates

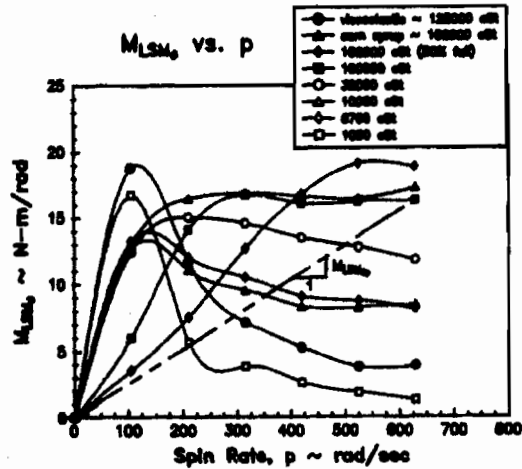


Figure 4: $M_{LSM,p}$ Versus p for Viscosities

To be consistent with the definition of the Magnus coefficient, the derivative $M_{LSM,p}$ is determined from Figure 4. A problem occurs at this point in the calculation of $M_{LSM,p}$ for a given fluid, since the derivative is not constant with spin rate. This problem is avoided because of a basic assumption of the Tricyclic Theory that, the spin rate is constant. In order to obtain the correct liquid-fill moment for a given set of flight conditions, $M_{LSM,p}$ is assumed to be the slope of the straight line through the origin and the intersection of the M_{LSM} versus p curve at the desired projectile spin rate. As an example, the slope of the dash line in Figure 4, for a 100,000 cSt fluid and a spin rate of 6000 rpm, represents the value of $M_{LSM,p}$ for this fluid and spin rate. This approach is reasonable because of the assumed constant spin rate and since M_{LSM} is a linear function of θ . With $M_{LSM,p}$ calculated, the liquid side moment coefficient is determined by the following equation which is analogous to the Magnus coefficient:

$$C_{NRP,p} = \frac{2 V M_{LSM,p}}{q' S d^2} \quad (10)$$

For each of the fluids shown in Figure 4 values of $C_{NRP,p}$ were determined, and these results are listed in Table 1.

COMPARISON OF TRICYCLIC THEORY TO FLIGHT TEST RESULTS

As an example, to show that the Modified Tricyclic Theory can accurately predict the stability of a projectile, a comparison will be made with flight test results.¹⁸ The tabulated test results are provided in Table 2.

Comparison of E1-9394 With the Modified Tricyclic Theory

The yawsonde flight record from D'Amico and Miller, of projectile E1-9394 is shown in Figure 5. Sigma N (σ_N) is a measure of the angular displacement with respect to the position of the sun and the velocity vector of the projectile. σ_N is analogous to the complex angle-of-attack plane used in the Tricyclic Theory. Also shown in Figure 5 for this round, is the associated spin rate ($\dot{\phi}$) versus time. $\dot{\phi}$ is the projectile's spin rate measured in

TABLE 1. C_{NRP_p} Determined Experimentally for Various Fluid Viscosities

Fluid Description	C_{LSM_p}
1,000 cSt Silicone	0.054
6,700 cSt Silicone	0.350
10,000 cSt Silicone	0.336
32,000 cSt Silicone	0.490
100,000 cSt Silicone	0.676
100,000 cSt Silicone (50% full)	0.781
100,000 cSt corn syrup	0.780
100,000 cSt viscoelastic	0.160

Note: $p = 6000 \text{ rpm}$, $\omega_1 = 500 \text{ rpm}$

TABLE 2. Flight Test Results (1978) for 155 mm Liquid-Filled Projectiles

Round No.	Type of Fluid	Viscosity ν (cSt)	Comments
E1-9391	corn syrup	1.92×10^5	unstable
E1-9392	glycerol	1.03×10^3	stable
E1-9393	corn syrup	1.92×10^5	unstable
E1-9394	corn syrup	1.92×10^5	unstable
E1-9395	corn syrup	2.14×10^6	stable
E1-9396	glycerol	6.34×10^3	constant yaw

Note: transonic launch $\approx 320 \text{ m/s}$, initial yaw $10^\circ\text{-}12^\circ$, all rounds were conditioned to 22° C except for E1-9395 and E1-9396 which were conditioned to 4° C .

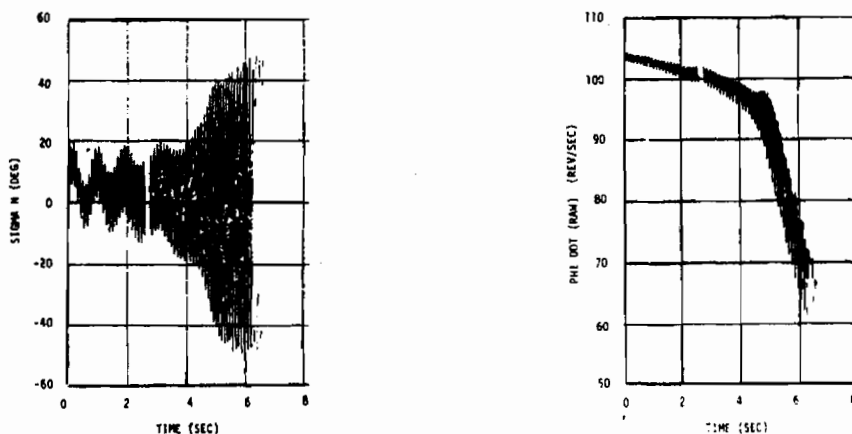


Figure 5: Yawsonde Flight Test Data for Round E1-9394

the sun reference frame. Using test fixture liquid-fill results a coefficient for corn syrup was found to be $C_{NRP_p} = 0.78$. A typical Modified Tricyclic Theory simulation for a 155mm projectile using flight test firing conditions and laboratory test fixture results for corn syrup, is shown in Table 4. Note that the damping constants indicate that the round is stable in precession (λ_2) and unstable in nutation (λ_1). A graphical representation of the results in the angle-of-attack plane is shown in Figure 6. The major differences between the actual and predicted angular growth is due to the spin decay of the real projectile. As the spin decreases, the yaw growth will increase. A high spin rate is required to stabilize the projectile. The Tricyclic Theory holds the spin rate constant at the launch condition of 6000 rpm, whereas the spin rate of the flight test round begins to fall off rapidly after 5 seconds. The constant spin rate in the Tricyclic Theory provides more stability than the projectile experiences in flight. However, the Modified Tricyclic Theory predicts the unstable flight motion due to the liquid-fill.

TABLE 3. Typical Tricyclic Simulation, Initial Conditions and Results

Initial Conditions	
$I_x = 0.176 \text{ kg-m}^2$	$\alpha_o = 0.^\circ$
$I = 1.786 \text{ kg-m}^2$	$\dot{\alpha}_o = 0.^\circ/\text{sec}$
$S = 0.019 \text{ m}^2$	$\beta_o = 0.^\circ$
$d = 0.155 \text{ m}$	$\beta_{\dot{o}} = -220.^\circ/\text{sec}$
$\rho = 1.055 \text{ kg/m}^3$	$V = 320 \text{ m/sec}$
$C_{m\alpha} = 4.450$	$p = 6000 \text{ rpm}$
$C_{m\dot{\alpha}} = -10.00$	$\Delta t = 0.0035 \text{ sec}$
$C_{n\dot{\beta}} = 0.500$	$t_{\text{max}} = 30.00 \text{ sec}$
$C_{m\delta} = 0.0$	$\delta = 0.^\circ$
$C_{LSM\beta} = 0.78$	
Results	
$q = 54056. \text{ N/m}^2$	$\tau = 1.302$
$s_g = 2.44$	$K_1 = 4.618^\circ$
$\omega_1 = 523.6 \text{ rpm}$	$K_2 = 4.618^\circ$
$\omega_2 = 68.7 \text{ rpm}$	$K_3 = 0.0^\circ$
$\lambda_1 = 0.115 \text{ sec}^{-1}$	$\lambda_2 = -0.330 \text{ sec}^{-1}$

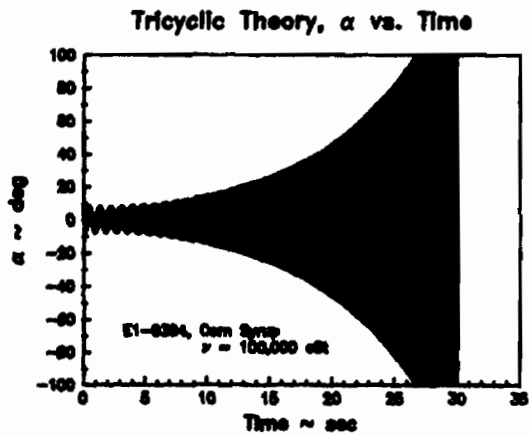


Figure 6: Tricyclic Flight Simulation for Round E1-9394, α Versus Time

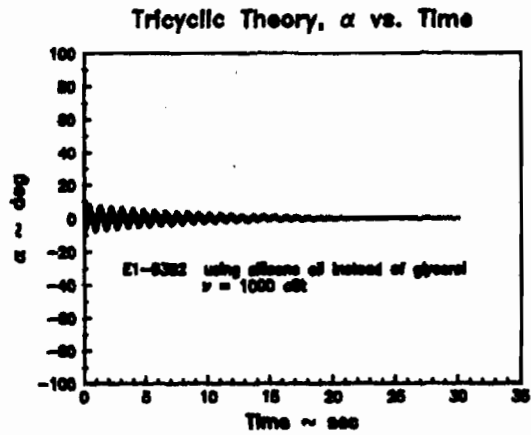


Figure 7: Tricyclic Flight Simulation for Round E1-9392, α Versus Time

Comparison of E1-9392 With the Modified Tricyclic Theory

The flight test of E1-9392 with a glycerol fill indicated a stable flight. For the Tricyclic analysis, test fixture results for a 1000 cSt Silicone fluid which is similar to glycerol, was used to calculate a $C_{NRP\beta} = 0.0535$. The Tricyclic Theory predicted a stable flight for round E1-9392 as shown in Figure 7 which matches the corresponding flight results.

Comparison of E1-9396 With the Modified Tricyclic Theory

One final comparison was made between round E1-9396 and the Modified Tricyclic Theory. From the yawsonde data, round E1-9396 was neutrally stable with a constant nutation angle. For the Tricyclic analysis, instead of glycerine at 4 °C and a viscosity of 6340 cSt, Silicone oil was used with a viscosity of 6700 cSt. The cold temperature for the flight projectile caused the glycerin to have a higher viscosity. Silicon oil at a viscosity of 6700 cSt has a $C_{NRP\beta}$ of 0.3500. The α versus time plot from the Modified Tricyclic Theory is shown in Figure 8 which is in good agreement with the flight test results.

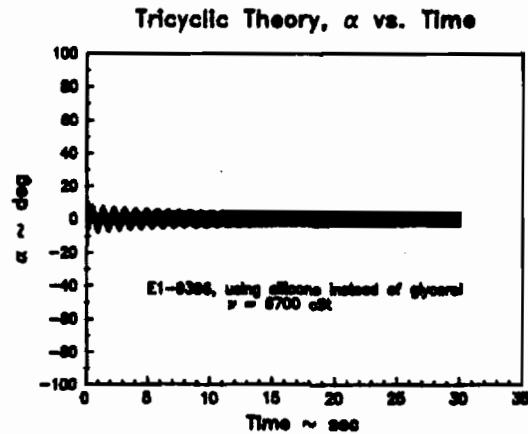


Figure 8: Tricyclic Theory Simulation for Round E1-9396, α Versus Time

CONCLUSIONS

1. The conventional Tricyclic Theory has been modified to include non-rigid payload (i.e., liquid-fill) effects.
2. Liquid-fill effects can be determined from theory or laboratory experiments.
3. Advantages of the Modified Tricyclic Theory are: ease of use, quick execution, and results presented graphically for ease of interpretation.
4. Predictions from the Modified Tricyclic Theory show good agreement with flight test results.
5. The Modified Tricyclic Theory is extremely useful as an initial screening tool for liquid-filled projectiles designers. Thus, allowing bad designs to be eliminated early which permits the designer to concentrate on the more stable configurations.

REFERENCES

1. Vaughn, Harold R.; "A Detailed Development of the Tricyclic Theory", Sandia Laboratories, SC-M-67-2933, Feb 1968.
2. Miller, M. C.; "Flight Instabilities of Spinning Projectiles Having Non-Rigid Payloads", *Journal of Guidance, Control and Dynamics*, Vol 5, No. 2, Mar-Apr 1982.
3. Murphy, C. H.; "Angular Motion of a Spinning Projectile with a Viscous Liquid Payload"; *Journal of Guidance, Control and Dynamics*, Vol 6, Pp 280-286, Jul-Aug 1983.
4. Hal, P.; Sedney, R. and Gerber, N.; "Fluid Motion in a Spinning Coning Cylinder via Spatial Eigenfunction Expansion", U. S. Army, Ballistic Research Laboratory, BRL-TR-02813, Aug 1987.
5. Li, R. and Herbert, T.; "Computational Study of the Flow in Spinning and Nutating Cylinders", *AIAA Journal*, Vol 28, No 9, Sep 1990.
6. Vaughn, H. R.; Wolfe, W. P. and Oberkampf, W. L.; "Numerical Solution for a Spinning, Nutation, Fluid-Filled Cylinder", Sandia Laboratories, SAND83-1789, Dec 1983. Unlimited Distribution
7. Weber, D. J. and Miller, M. C.; "Liquid Induced Rolling and Yawing Moment Coefficients for Viscous Newtonian Fluids in a Spinning and Coning Cylinder", Proceedings of the 1988 CRDEC Scientific Conference on Chemical Defense Research, CRDEC-SP-013, Vol. I, Pp 505-511, August 1989.
8. D'Amico, W. P. and Miller, M. C.; "Flight Instabilities Produced by a Rapidly Spinning, Highly Viscous Liquid", *Journal of Spacecraft and Rockets*, Vol 16, No. 1 Jan-Feb 1979 Pages 62-64.

BLANK

INSTRUMENTED FLIGHT TEST AND DATA REDUCTION OF ARTILLERY PROJECTILES WITH SELECTED FILL RATIOS

David J. Hepner

Launch and Flight Division
U.S. Army Ballistic Research Laboratory
Aberdeen Proving Ground, MD 21005

Daniel J. Weber

John W. Molnar

U.S. Army Chemical Research,
Development, and Engineering Center

ABSTRACT

Projectiles containing various fills of silicon oil and water were fired in an effort to quantify the stability improvement when a low viscosity, immiscible fluid is added to a highly viscous payload. Yawsondes were used to measure the projectile yaw and roll histories. An unstable liquid-fill flight was typified by a large growth in fast-mode yaw followed by a rapid despin. The reduction of the fast-mode yaw damping indirectly produced a measure of the magnitude of the liquid side moment coefficient. The reduction to the liquid side moment coefficient was predicated on the ability to measure aerodynamic fast-mode damping for projectiles at various yaw levels near transonic speeds. The roll history provided an indirect measurement of the liquid roll moment coefficient. A reduction in the destabilizing liquid side moment was evident when low viscosity additives were used to lubricate the interior cavity surface.

LIST OF SYMBOLS

a	cavity radius	α	fast-mode yaw amplitude
C_{lsm}	liquid side moment coefficient	α_0	initial fast-mode yaw amplitude
C_{lrm}	liquid roll moment coefficient	ϵ	projectile fast-mode damping rate - $\ln(k/k_0)/\gamma$
I_x	projectile axial moment-of-inertia	ϵ_{aero}	aerodynamic fast-mode damping rate
I_y	projectile transverse moment-of-inertia	ϵ_{liquid}	damping rate due to liquid fill
M	liquid roll moment	γ	inertial coning rate
m	mass of liquid in a fully filled cavity	ϕ	roll rate measured by yawsonde
k	$\sin(\alpha)$	ρ	local atmospheric density
k_0	$\sin(\alpha_0)$	ρ_0	atmospheric density at spark shadowgraph range
p	inertial spin rate	σ	ratio of inertial moments - I_x/I_y
\dot{p}	time rate-of-change of p	σ_n	compliment of sun-angle
\dot{p}_{aero}	time rate-of-change of spin simulation	τ	non-dimensional coning rate - γ/p

INTRODUCTION

The instability of high viscosity fluids in a spin-stabilized carrier has been extensively documented by theoretical studies coupled with laboratory and flight tests. Recent experimental spin-fixture tests show that the addition of an immiscible, low viscosity, higher density fluid can reduce the liquid roll moment produced by the high viscosity bulk material¹. From this data, it can be inferred that a reduction in the destabilizing liquid side moment is also a result². The magnitude of the liquid side moment is the predominant parameter deciding the yaw stability of a properly designed spin-stabilized liquid-filled shell.

The stability of a liquid-filled shell can be simplified to the balance between the undamping effect of a destabilizing liquid payload to the designed stability of the shell as a payload carrier. The underlying premise is that the carrier maintain enough fast-mode damping to overcome the internally generated liquid destabilizing side moment.

$$\epsilon = \epsilon_{\text{liquid}} + \epsilon_{\text{aero}} \frac{\rho}{\rho_0} \quad (1)$$

The total damping rate, ϵ , can be measured by the examining the fast-mode component of the yaw history. The liquid damping, ϵ_{liquid} , results after subtracting known aerodynamic damping data, ϵ_{aero} , measured at a spark shadowgraph range facility. The density ratio in (1) is used to scale experimentally determined aerodynamic damping to local flight atmospheric conditions. The projectile shape, mass properties, and flight characteristics such as Mach number, angle-of-attack, and spin and yaw rates are also required to define the aerodynamic damping of the payload carrier.

The fluid physicals, cavity geometry, fast-mode yaw magnitude and damping rate, frequency, and the spin rate are required to theoretically define the liquid side moment using existing liquid-fill fluid dynamics². A liquid side moment coefficient can be defined by appropriate scaling of the liquid damping rate².

$$C_{\text{ism}} = \frac{I_x \epsilon_{\text{liquid}} \left(\frac{2\ell}{\sigma} - 1 \right)}{ma^2 \rho \gamma k} \quad (2)$$

Flight testing provides the indirect experimental moment coefficient measurements for evaluation of laboratory results and improvements to codes that are currently unable to predict the liquid side moment for small amounts of additives with a dramatically different viscosity.

The roll history of a liquid filled projectile is directed by the despinning moments caused by aerodynamic roll damping and internal liquid roll moment. The liquid roll moment can be defined to express the difference between the measured roll despin rate and the rate predicted due to aerodynamic roll damping.

$$M = I_x (\dot{p} - \dot{p}_{\text{aero}}) \quad (3)$$

Similar to the side moment coefficient, a liquid roll moment coefficient can be defined².

$$C_{\text{irm}} = \frac{M}{ma^2 \rho \gamma k^2} \quad (4)$$

The magnitude of the liquid roll moment coefficient is the negative of the liquid side moment coefficient for steady-state spin and yaw conditions².

FLIGHT TEST CONFIGURATION

The projectile configuration in Figure 1 was chosen based on prior tests and the availability of spark shadowgraph data to define the magnitude of the aerodynamic damping for transonic launches. The cavity was designed as a right circular cylinder with an aspect ratio of 4.48. Table 1 lists the various configurations of the payloads. Three configurations used a 98% fill of silicon oil with viscosities 100kcs, 35 kcs, and 10 kcs.

Three configurations were similarly prepared with 5% water substituted for 5% of the oil. One configuration was 50% filled with oil. One additional configuration was 98% filled with a viscoelastic fluid (nominal viscosity of 100kcs). The viscoelastic fluid was chosen to verify spin-fixture findings that displayed a marked reduction in liquid roll moment due to the inherent shear thinning property of the fluid.

The rounds were fired from an M109 track vehicle. Eight were fired with yaw induction using a one-half muzzle brake. The remaining rounds were fired without yaw induction using a standard muzzle brake.

LIQUID MOMENT COEFFICIENT DATA REDUCTION

Yawsondes are used to measure the free-flight motion of a variety of cannon launched projectiles. Typical yawsondes utilize two optical sensors to determine the motion of the projectile with respect to the sun³. An FM/FM telemetry system transmits sensor data to a ground telemetry receiver. The raw data consist of a succession of pulses whose phase relationship is a function of solar aspect angle and whose period is a function of roll rate. The reduction method uses interpolative threshold detection on the pulses to determine pulse occurrence times. The rolling motion of the projectile is easily determined by measuring the repetition rate of pulses from one sun sensor. The phase relationship between two sensors contain the peak-to-peak angular motion of the projectile about the trajectory. These data are processed into the Eulerian roll rate of the projectile, $\dot{\phi}$, and a solar aspect angle, σ_n . Transformation from Eulerian roll and yaw rates to inertial spin and yaw rates is discussed by Pope⁴.

The Sigma-N and Phi-Dot data for CRDEC1 are shown in Figures 2 and 3 respectively. The data clearly show a large growth in fast-mode yawing motion followed by a rapid despin. Extracting the fast-mode motion with digital filtering and demodulation techniques yields the amplitude of the fast-mode motion (Figure 4) and the transformed inertial yaw frequency (Figure 5).

Radar velocimetry data was collected for each round. Iterative comparison of simulated velocity data to measured radar velocimetry data was accomplished using a modified point-mass trajectory program. Inputs include measured velocity data, yaw history, projectile physicals, launch conditions, meteorological data, impact data, and drag as a function of yaw and Mach number. Outputs include a cartesian position versus time history, density ratio, Mach number and simulated spin history. The simulated spin history only includes aerodynamic roll damping effects. Figure 6 displays the simulated inertial spin history with the inertial spin history for round CRDEC1. The time rate-of-change of the two spin rates can be used to produce the liquid roll moment of equation (3) (Figure 7).

Non-linear damping rates for transonic launches at various angles of attack and Mach numbers were measured using a Ballistic Research Laboratory spark shadowgraph facility⁵. Data generated from the testing of similar projectiles provided several measurements of the fast mode damping for $0.5 < M < 1.0$ and fast-mode amplitudes less than 5° . Figure 9 displays this measured data and an approximate fit for $0.5 < M < 0.92$. The number of range measurements is not sufficient enough to produce aerodynamic fast-mode damping as a function of angle and Mach number. For simplification, the aerodynamic fast-mode damping rate is used as a function of Mach number. The in-flight damping rate and the aerodynamic damping rate scaled by the simulated density ratio are shown as a function of Mach number in Figure 9 for CRDEC1. The reduction to ϵ_{liquid} is simply a subtraction of these two damping rates based on Mach number.

After obtaining the damping and the liquid roll moment, equations (2) and (4) are used to produce the side and roll moment coefficients for CRDEC1 shown in Figure 10. The sign of the roll moment coefficient is changed to aid in the comparison of roll and side moment coefficients. The liquid side moment coefficient is measured at Mach numbers below 0.8 ($t=3$ seconds) and prior to the onset of large amplitude motion ($\alpha < 15^\circ$, $t < 7$ seconds). Limiting to this time frame yields a constant liquid side moment coefficient of 0.05. The liquid roll moment coefficient measurement is made at large yaw amplitudes after the rapid despin occurs. Figure 10 shows a liquid roll moment coefficient of -0.045. Projectiles that did not reach an amplitude of yaw greater than 15° did not exhibit significant variation from the simulated spin history. Hence, these flights did

not yield a measurable liquid roll moment.

The fast-mode damping of a violently unstable round contrasts greatly to the results of a stable round. The Sigma-N history of CRDEC7 in Figure 11 clearly shows a damping fast-mode motion ($\epsilon < 0$). Figure 12 displays the measured damping rate with the scaled range data. Oscillations in the damping data shown at lower Mach numbers is a result of the uncertainty in measurement of small yaw amplitudes. There is little difference between the aerodynamic and total damping rates. This infers that the total damping for CRDEC7 is not discernible from the fitting used in the determination of the aerodynamic damping. For this case, the reduced liquid moment coefficient is near zero.

FLIGHT TEST RESULTS

Yawsonde data was obtained for all sixteen rounds fired. Sigma-N histories were reduced in the field to measure the initial yaw induction levels and to ensure the proper operation of the yawsonde. A binary answer to the stability of a round was obtained by examination of the fast-mode damping in each Sigma-N history. In addition to initial launch conditions, meteorological data consisting of temperature, humidity, air density, and wind direction and speed was collected at one-half hour increments.

A tabular listing of the damping, roll moment and the liquid moment coefficients is included in Table 1. Measurements of the damping rate, yaw amplitude, yaw frequency, spin rate, and simulation data involving mach number and density ratio are simultaneously required to produce the the side and roll moment coefficients. Estimates of these parameters were used when measured data was lacking or insufficiently resolved. Rounds exhibiting rapid growth were evaluated using the method previously described. Rounds exhibiting rapid damping were dominated by aerodynamic damping making evaluation of the liquid side moment coefficient restricted to zero. Rounds exhibiting extremely slow growth or damping in yawing motion were evaluated to have a liquid damping rate roughly equal to aerodynamic damping rate. Determination of the damping rate could not be made for a viscoelastic payload fired without yaw induction (CRDEC14) due to extremely small fast-mode motions ($\alpha < 0.2^\circ$).

The reductions of the yawsonde data to liquid moment coefficients was encumbered by the difficulty in the acquisition and fitting of radar data to establish the Mach number and density ratio. Density ratio and Mach number estimates, when required, were based on the examination of the time and magnitude of the yaw growth rate. Clearly, similar flights encounter nearly the same trajectory (density ratio) and velocity (Mach number). Where no comparison could be made, an estimate of the average aerodynamic damping scaled by density ratio was used for Mach number less than 0.8.

Table 1. Summary of projectile physicals, flight stability, and liquid moment coefficients.

CDREC #	Transverse moment-of-inertia I _y (kgm ²)	Axial moment-of-inertia I _x (kgm ²)	Nominal fluid viscosity (kcs)	Fluid fill oil/water (%)	Actual fluid mass (kg)	100% fill mass m (kg)	Yaw induced	Fast-mode stability	Fast-mode damping ϵ	Clsm	Liquid roll moment (Nm)	Clrm
1	1.7869	0.17268	100 kcs	98/0	4.99	5.12	yes	no	0.003	0.05	-15	-0.045
2	1.7861	0.17552	100 kcs	98/0	4.99	5.12	no	no	0.0025	0.045	-17	-0.15
3	1.7872	0.17275	100 kcs	93/5	4.99	5.13	yes	no	0.002	0.045	-15	-0.04
4	1.7907	0.17559	100 kcs	93/5	4.99	5.13	no	no	0.001	0.030	*****	*****
5	1.7849	0.17508	10 kcs	98/0	4.98	5.11	yes	no	0.001	0.025	-12	-0.03
6	1.7893	0.17549	10 kcs	98/0	4.99	5.11	no	yes	0.0	0.02	*****	*****
7	1.7866	0.17526	10 kcs	93/5	4.99	5.12	yes	yes	-0.002	0.0	*****	*****
8	1.7888	0.17570	10 kcs	93/5	4.99	5.12	no	yes	0.0	0.02	*****	*****
9	1.7837	0.17523	35 kcs	98/0	4.88	5.12	yes	no	0.002	0.04	-15	-0.03
10	1.7868	0.17538	35 kcs	98/0	4.99	5.12	no	no	0.002	0.035	*****	*****
11	1.7899	0.17583	35 kcs	93/5	4.99	5.13	yes	no	0.001	0.025	-15	-0.04
12	1.7858	0.17512	35 kcs	93/5	5.01	5.13	no	yes	0.0	0.025	*****	*****
13	1.7610	0.17578	viscoelastic	98/0	5.47	5.55	yes	yes	-0.002	0.01	*****	*****
14	1.7911	0.17601	viscoelastic	98/0	5.47	5.55	no	yes	*****	*****	*****	*****
15	1.7886	0.17557	100 kcs	50/0	2.49	5.12	yes	no	0.0035	0.055	-17	-0.045
16	1.7882	0.17555	100 kcs	50/0	2.47	5.12	no	no	0.0035	0.050	-25	-0.03

For rounds containing 100kcs oil, the substitution of 5% water for oil results in a lower liquid moment coefficients, yet all the rounds remained unstable. For the 10kcs payload configuration, fast-mode stability can be achieved by reducing the initial launch disturbance (CRDEC5 vs CRDEC6). The substitution of water stabilizes the yaw-induced condition (CRDEC5 vs CRDEC7). For an intermediate payload viscosity of 35 kcs, the substitution of water only stabilizes the launch condition of no yaw induction (CRDEC 10 vs CRDEC12).

Examination of the fast-mode damping in Figure 9 supports the range data taken for higher Mach numbers ($0.9 < M < 1.2$). The flight region of Mach number of 0.6 to 0.7 is dominated by large amplitude yaw, rapid despin, and higher yaw frequency. Since the aerodynamic properties at this flight condition are not known, no comparison of the range data to measured flight data is possible. If, however, the theoretical linear dependence of side moment coefficient with yaw angle displayed by equation (2) can be experimentally shown, then the flight data in Figure 9 data displays aerodynamic damping for this flight condition. Simply stated, either the aerodynamics, the nonlinearity of side moment with yaw angle, or the highly transient nature of the flight condition on total side moment causes the undamping at large angle of attack. Confidence in the measurement method is shown by the apparent agreement with aerodynamic data for small amplitude, steady motions as shown in Figure 12 for a stable round.

The reduction of spin data to liquid roll moment provides no greater confidence in determining the relative stability than that found by observing the roll history itself. Further scaling to liquid roll moment coefficient provides some indication of the magnitude of the liquid side moment for projectiles experiencing large angles of attack. At the onset of rapid despin, the liquid roll moment coefficient is determined under rapidly changing conditions of yaw amplitude, (Figure 4), yaw frequency (Figure 5), and spin (Figure 6). Thus, while roll data for large amplitude motion can be used as an indication of a significant liquid side moment, the magnitude of this measurement is subject to the transient nature of each parameter used in the calculation. After a large limiting yaw behavior is achieved (typically 45° - 50°), the roll moment coefficient approximates the negative of the side moment coefficient as supported by Reference 2. Roll moment coefficients are contained in Table 1 for projectiles reaching fast-mode yaw levels greater than 15° .

CONCLUSION

The addition of an immiscible low viscosity fluid to an unstable high viscosity payload produces a decrease in the destabilizing liquid side moment coefficient as measured by yawsonde data. The improvement in stability is dependent upon the launch and flight conditions, carrier aerodynamics, payload geometry, and fluid properties. The reduction of the fast-mode component of the yaw history provides an indirect measure of the magnitude of the liquid side moment. A reduction of roll data to liquid roll moment coefficient can be used to indicate the presence of a significant liquid side moment for a projectile growing to a large angle-of-attack.

REFERENCES

1. Miller, Miles, C., "Laboratory Test Fixture for Non-Rigid Payloads," Proceedings of The International Congress on Instrumentation in Aerospace Simulation Facilities, (ICIASF), 89 Record, Sept. 1989, pgs 350, 364.
2. Murphy, C.H., Bradley, J.W., and Mermagen, W.H., "Side Moment Exerted by a Spinning, Coning, Highly Viscous Payload," ARBRL-TR-3074, Ballistic Research Laboratory, Aberdeen Proving Ground, Maryland, December, 1989. (ADA218746)
3. Mermagen, W. and Clay, W., "The Design of a Second Generation Yawsonde," BRL-MR-2368, Ballistic Research Laboratory, Aberdeen Proving Ground, Maryland, April 1974. (AD780064)
4. Pope, Russel, L., "Further Analysis of Yawsonde Data From Some Liquid Payload Projectiles," BRL-MR-3329, Ballistic Research Laboratory, Aberdeen Proving Ground, Maryland, December, 1983.
5. D'Amico, William P., Jr., Wall, J.M., and Kochenderfer, J.W., "Aerodynamic Testing of an All-Steel Generic Base for ICM-Type Projectiles," Proceedings of the 10th International Symposium on Ballistics, San Diego, California, 27-29 October, 1987.

155mm Spin-Stabilized Liquid-Filled Shell
 cavity length = 51.25 cm
 cavity radius = 11.43 cm

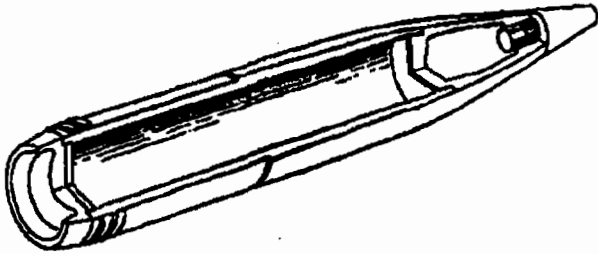


Figure 1. The projectile configuration and cavity dimensions.

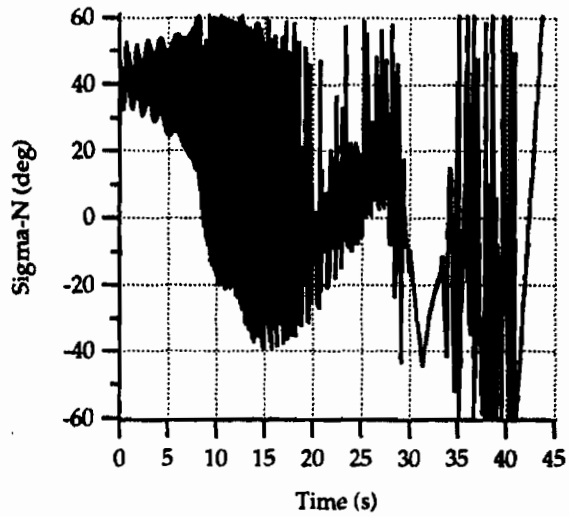


Figure 2. Sigma-N history for CRDEC1.

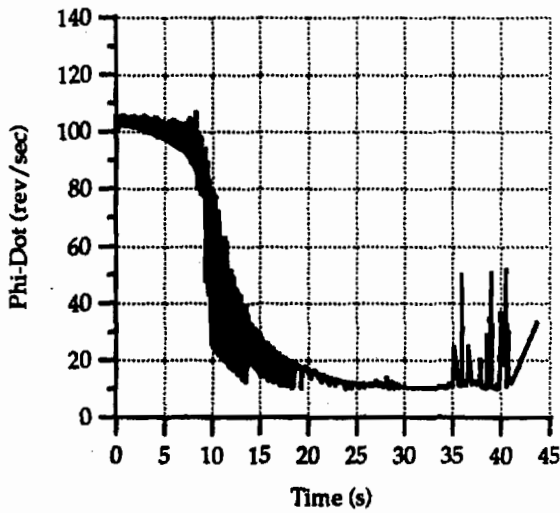


Figure 3. Phi-Dot history for CRDEC1 .

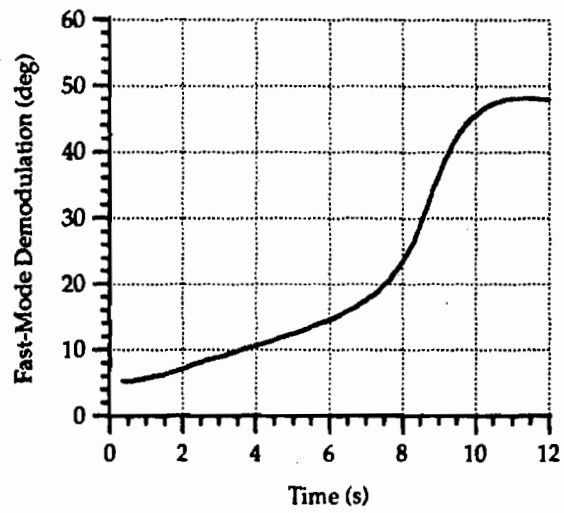


Figure 4. Fast-mode amplitude demodulation.

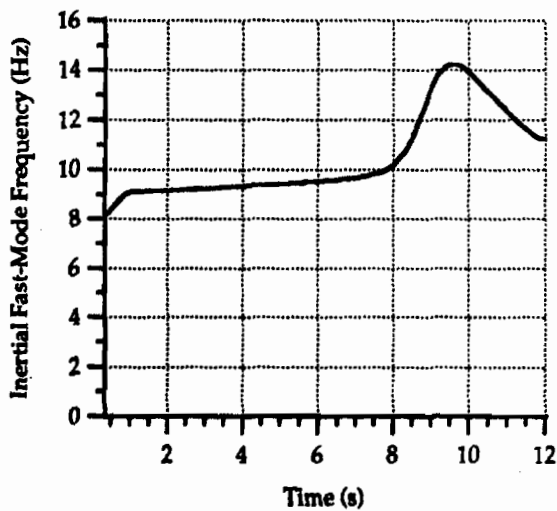


Figure 5. Inertial fast-mode frequency history.

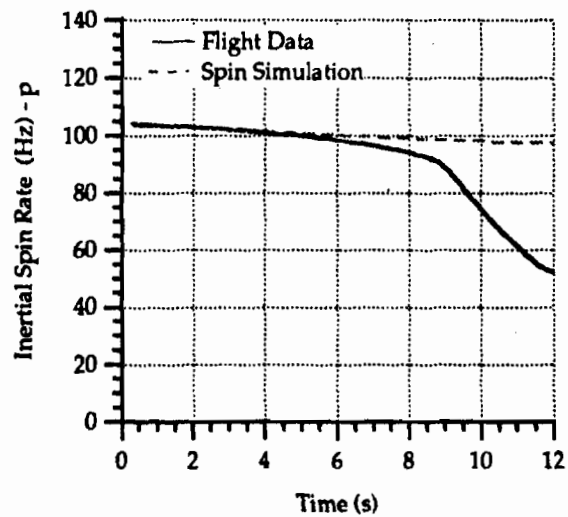


Figure 6. Inertial spin and simulation.

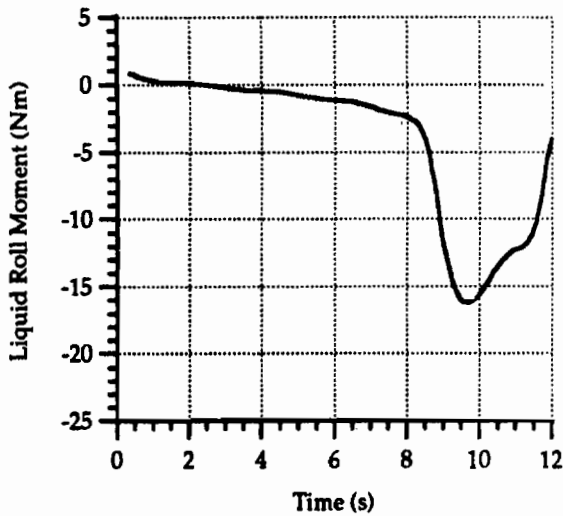


Figure 7. Liquid roll moment magnitude.

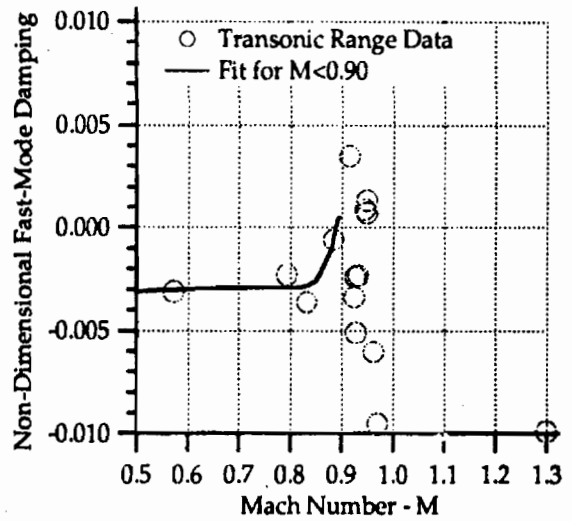


Figure 8. Spark shadowgraph range data.

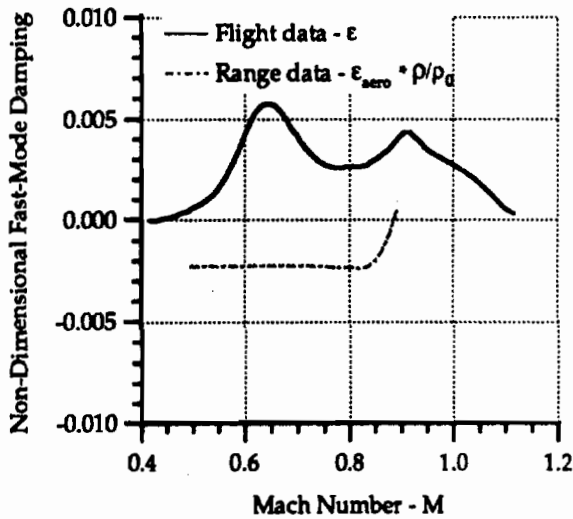


Figure 9. Fast-mode damping data for CRDEC1.

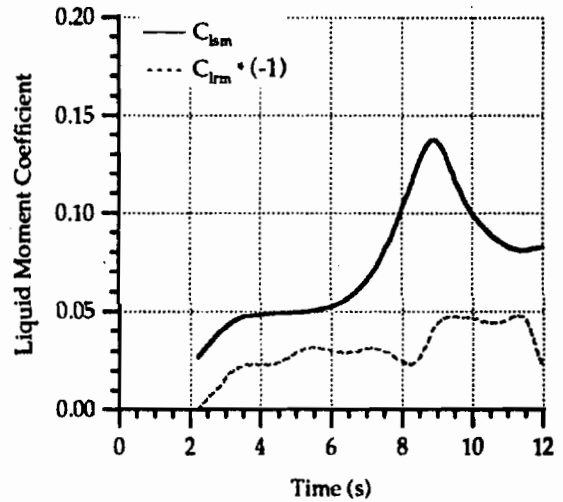


Figure 10. Moment coefficients data.

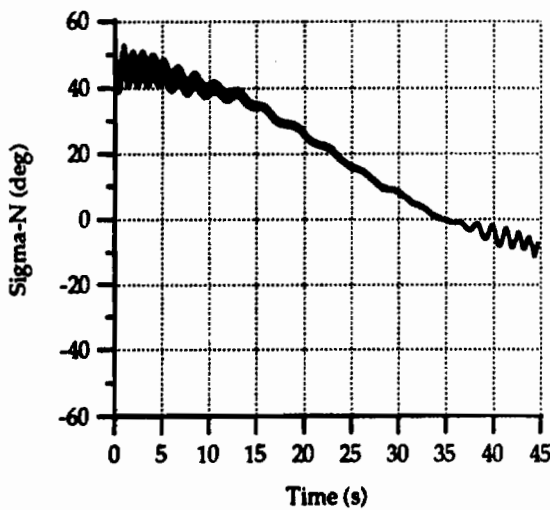


Figure 11. Sigma-N history for CRDEC7.

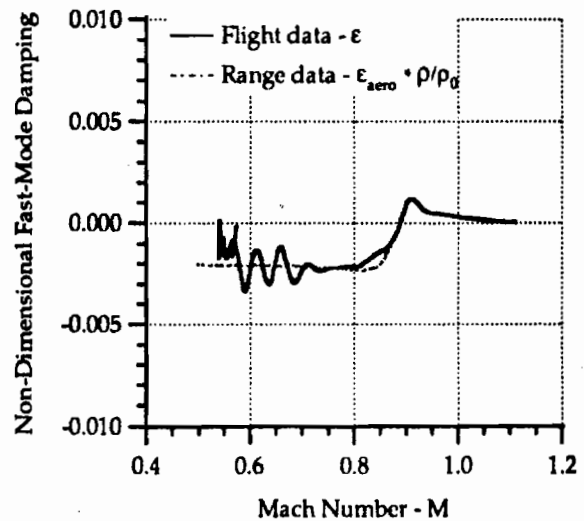


Figure 12. Fast-mode damping data for CRDEC7.

BLANK

NUMERICAL SIMULATION OF FLUID DYNAMICS AND PAYLOAD DISSEMINATION IN A DUAL-CHAMBER GRENADE

Michael J. Nusca

Launch and Flight Division
U.S. Army Ballistic Research Laboratory
Aberdeen Proving Ground, MD 21005

Abstract

The internal design of a grenade used for the thermal dissemination of solid payload into the atmosphere can consist of two concentric cylinders; a pyrotechnic device in the outer annulus and payload material bonded to the wall of the inner cylinder. The two chambers are connected. Combustion of the pyrotechnic produces a high pressure within the grenade. A pressure difference between the atmosphere and inside the grenade induces a thru-flow that thermally erodes and vaporizes the material in the inner chamber. This material in gaseous form is entrained in this flow and expelled from the grenade. Payload dissemination can be simulated using computational fluid dynamics (CFD) to solve the Navier-Stokes equations along with chemical species conservation equations. The pyrotechnic combustion is not modelled. Using chamber dimensions and payload chemical properties this simulation yields velocity, pressure, temperature, density and chemical composition of the gas in the inner chamber and exiting the grenade. Numerical simulations can be compared to experimental data, aid in understanding the physics of dissemination, and used to conduct parametric design studies.

Introduction

The dissemination of solid payload material as a gaseous cloud from a container can be accomplished using a pressurized system (e.g. compressed CO₂ cartridge), a mechanical system (e.g. plunger) or a pyrotechnic system (i.e. central burster or hot/cold gas flow). In the latter technique, dissemination of the payload is realized after ablation and vaporization of the material from exposure to the thermal effects of pyrotechnic combustion. Experimental programs at the U.S. Army CRDEC (Chemical Research Development and Engineering Center) are being used to test the efficiency (i.e. high rate of dissemination and low temperature/high concentration of payload material in the dissemination cloud) of the thermal/ablation method. These tests can involve highly instrumented full-scale and small-scale grenade models ignited within large test chambers. Numerical simulation in support of such tests (being conducted at the U.S. Army Ballistic Research Laboratory, BRL) are required to aid in data reduction, contribute to the physical understanding of thermal dissemination, and conduct parametric studies that may guide future tests.

The internal design of a grenade used for the thermal dissemination of solid payload into the atmosphere can consist of two concentric cylinders; a pyrotechnic device in the outer annulus and payload material bonded to the wall of the inner cylinder. The two chambers are connected. Combustion of the pyrotechnic products

a high pressure within the grenade. A pressure difference between the atmosphere and inside the grenade induces a thru-flow that thermally erodes and vaporizes the material in the inner chamber. The material in gaseous form is entrained in this flow and expelled from the grenade. Figure 1 shows the internal schematic of a generic grenade configuration.

Numerical simulation of the fluid dynamics associated with payload dissemination from a grenade is accomplished in the present study using the Navier-Stokes equations along with equations that govern chemical species ablation and diffusion. Chemical reactions may be but are not necessarily involved. An implicit finite-difference scheme based on successive-over-relaxation is used to solve these equations for the physical domain of interest. This domain resides within the inner chamber of the grenade; thus, the flow within the grenade is modeled excluding combustion of the pyrotechnic. Using chamber dimensions and payload chemical properties this simulation yields velocity, pressure, temperature, density and chemical composition of the gas in the inner chamber and exiting the grenade.

Numerical Simulation

The BRL RAMCOMB (RAMjet COMBustion) computer code was originally developed for the numerical simulation of combustion in a tubular solid-fuel ramjet (SFRJ) projectile.^{1,2} Solid fuel regression rate and projectile thrust predictions compared favorably with in-flight and ground test data. For the SFRJ application the RAMCOMB code simulated a mass-controlled (stoichiometric) reaction of non-premixed solid fuel and oxygen using classical diffusion flame assumptions. The code has also been used to simulate finite-rate premixed gaseous fuel combustion in the ram accelerator projectile launch system³ with reaction rates formulated in terms of temperature and chemical species mass fraction. Application of the code to payload dissemination simulation for grenades involves chemical species ablation and diffusion without chemical reactions. The governing equations, boundary and initial conditions as well as the solution method are outlined below.

Governing Equations

Since the grenade payload chamber geometry is axisymmetric (Fig. 1) the governing equations can be written in cylindrical coordinates. The velocity components in this system are u, v , and w for the radial (r), azimuthal (θ), and axial (z) directions, respectively. Axisymmetric flow is assumed thus, all θ -derivatives are ignored; however, the azimuthal velocity component and the azimuthal momentum equation are retained (for future consideration of chamber rotation). Since steady flows are considered, time derivatives ($\partial/\partial t$) are ignored. The conservation equations for global mass, momentum (radial, axial, azimuthal) and species mass conservation are given by,^{3,4}

$$\nabla \cdot \rho \vec{V} = \frac{1}{r} \frac{\partial(r\rho u)}{\partial r} + \frac{\partial(\rho w)}{\partial z} = 0 \quad (1)$$

$$\nabla \cdot [\rho u \vec{V} - \vec{\tau}_r] - \frac{1}{r} [\rho v^2 - \tau_{\theta\theta}] + \frac{\partial p}{\partial r} = 0 \quad (2)$$

$$\nabla \cdot [\rho w \vec{V} - \vec{\tau}_z] + \frac{\partial p}{\partial z} = 0 \quad (3)$$

$$\frac{1}{r} \nabla \cdot [r(\rho v \vec{V} - \vec{\tau}_\theta)] = 0 \quad (4)$$

$$\frac{1}{r} \left[\frac{\partial}{\partial r} (r\rho u m_j + r J_{j,r}) + \frac{\partial}{\partial z} (r\rho w m_j + r J_{j,z}) \right] = 0 \quad (5)$$

Energy conservation for a compressible flow is expressed by the First Law of Thermodynamics. The steady form of the First Law states that the net rate of stagnation enthalpy ($\dot{h} = h + V^2/2$) inflow for a control

volume is equal to the sum of the shear work done by the contents of the control volume on the surroundings ($\bar{\tau}$) and the heat transfer to the surroundings.⁴

$$\nabla \cdot \left[\rho \bar{V} \bar{h} + \bar{J}_h + \sum_j h_j \bar{J}_j + \bar{J}_k - (u \bar{\tau}_r + v \bar{\tau}_\theta + w \bar{\tau}_z) \right] = 0 \quad (6)$$

where \bar{J} is a flux term for mass ($\bar{J}_j = (\mu_{\text{eff}}/Re) \nabla m_j = \Gamma_j \nabla m_j$), heat ($\bar{J}_h = (\mu_{\text{eff}}/Pr) c_{p,j} \nabla T = \Gamma_h c_{p,j} \nabla T$), and turbulence kinetic energy, k , ($\bar{J}_k = (\mu_{\text{eff}}/Pr) \nabla k = \Gamma_k \nabla k$). Where Γ represents the diffusion coefficient. The mass fraction and molar specific enthalpy for species j are m_j and h_j , respectively. The density, pressure, velocity vector and velocity magnitude are given by $\rho, p, \bar{V}, V = \sqrt{u^2 + v^2 + w^2}$, respectively.

In Equations 2-4,6 the shear stress ($\bar{\tau}$) includes the Reynolds stress with an effective fluid viscosity expressed as the sum of the molecular and turbulent viscosities, $\mu_{\text{eff}} = \mu + \mu_t$. The flow Reynolds number, Re , represents the ratio of mass flux ($\rho V L$) to fluid viscosity, μ_{eff} . Molecular viscosity (μ) is defined using Sutherland's expression⁵

$$\mu = 2.270 \times 10^{-6} \frac{T^{1.5}}{T + 198.6} \quad (7)$$

Turbulent viscosity (μ_t) is described in the next section of this paper.

The calorically perfect gas assumption can be used to determine the specific heat of the mixture, $c_{p,j}$, when the temperature dependence of the species is not well determined. The specific heat can also be formulated using an explicit temperature dependence obtained from tabulated data (\bar{R} is the universal gas constant).⁶

$$c_{p,j}/\bar{R} = A_1 + A_2 T + A_3 T^2 + A_4 T^3 + A_5 T^4 \quad (8)$$

Mixture temperature (T) is obtained from the conservation of energy (Eq. 6) expressed in terms of the stagnation enthalpy,

$$\bar{h} = T \sum_j c_{p,j} m_j + \left[1 - \frac{1}{Pr} \right] \frac{V^2}{2} + \left[\frac{1}{Sc} - \frac{1}{Pr} \right] \frac{\bar{V}^2}{2} + \left[\frac{1}{Sc} - \frac{1}{Pr} \right] \sum_j h_j m_j \quad (9)$$

where \bar{V} is the magnitude of the turbulent (fluctuating) velocity, \sqrt{k} . The Schmidt number, $Sc = \mu_{\text{eff}}/(\rho \Gamma)$, (ratio of momentum transport to mass transport) is assumed to be unity. The Prandtl number, $Pr = c_p \mu_{\text{eff}}/\kappa$, (ratio of momentum transport to heat transport) is assumed to be nearly unity (9) which is considered adequate for gaseous flows. The thermal conductivity of the gas mixture is denoted κ .

The mixture equation of state for a thermally perfect gas follows from Dalton's Law,

$$p = \rho \bar{R} T \sum_j \frac{m_j}{\mathcal{M}_j} \quad (10)$$

where $\bar{R} = \bar{R} \sum_j \mathcal{M}_j$, \mathcal{M}_j is the molecular weight of species j , and \bar{R} is the specific gas constant. Equation 10 is used to recover the density from the numerical solution of the governing equations.

The stream function-vorticity form of the governing equations has been widely utilized and facilitates the use of numerically efficient Gauss-Seidel relaxation algorithms. Stream function, ψ , and vorticity, ω are defined using,⁴

$$\frac{\partial \psi}{\partial r} = r \rho \omega, \quad \frac{\partial \psi}{\partial z} = -r \rho u, \quad \omega = \nabla \times \bar{V} = - \left[\frac{\partial}{\partial z} \left(\frac{1}{r \rho} \frac{\partial \psi}{\partial z} \right) + \frac{\partial}{\partial r} \left(\frac{1}{r \rho} \frac{\partial \psi}{\partial r} \right) \right] \quad (11)$$

The governing equations are derived in Reference 2 and can be expressed in the form of a general variable, ϕ . This variable can represent stream-function, vorticity, azimuthal velocity, stagnation enthalpy, species mass fraction, turbulence kinetic energy, or turbulence dissipation rate.

$$a_\phi \left[\frac{\partial}{\partial z} \left(\phi \frac{\partial \psi}{\partial r} \right) - \frac{\partial}{\partial r} \left(\phi \frac{\partial \psi}{\partial z} \right) \right] - \frac{\partial}{\partial z} \left[b_\phi r \frac{\partial}{\partial z} (c_\phi \phi) \right] - \frac{\partial}{\partial r} \left[b_\phi r \frac{\partial}{\partial r} (c_\phi \phi) \right] + r d_\phi = 0 \quad (12)$$

For example, $\phi = \psi$, $a_\phi = 0$, $b_\phi = 1/(\rho r^2)$, $c_\phi = 1$, $d_\phi = -\omega/r$ (which yields Eq. 11). For N species only $N - 1$ specie equations ($\phi = m_j$) must be solved, since the sum of the mass fractions must equal unity. In effect the global continuity equation (Eq. 1) is the N th specie equation since the summation of all specie equations yields the continuity equation.

The pressure can be recovered from the $\psi - \omega$ form of the equations after a converged solution of Equation 12 is achieved or after each iteration, if pressure variations are expected to have a significant effect on density. The radial and axial momentum equations (Eq. 2 and 3) can be rearranged to yield:

$$\frac{\partial p}{\partial z} = P_1(r, z) \quad \text{and} \quad \frac{\partial p}{\partial r} = P_2(r, z) \quad (13)$$

where P_1 and P_2 are functions of ρ , V and \bar{r} . Then along any path from point A to point B in the flowfield, the pressure is given by:

$$p_B - p_A = \int_A^B (P_1 dz + P_2 dr) \quad (14)$$

Since p is a scalar, $p_B - p_A$ should be path independent and therefore, can serve as a consistency check on the converged solution. In most cases a pressure difference is desired to form the pressure coefficient at a point. However, if the pressure at point B is required the pressure at point A is assigned to a known inlet value and integration proceeds from the inlet to point B .

Turbulence Model

A two-equation turbulence model has been suggested by Kim and Chung⁷ for multiple species flows. This model describes the turbulence viscosity (μ_t) as a function of turbulence kinetic energy (k) and dissipation rate (ϵ) as $\mu_t = \rho C_3 k^2 / \epsilon$. A set of partial differential equations is written for k and ϵ .

$$\rho w \frac{\partial k}{\partial z} + \rho u \frac{\partial k}{\partial r} - \frac{1}{r} \left[\frac{\partial}{\partial z} \left(r \mu_k \frac{\partial k}{\partial z} \right) + \frac{\partial}{\partial r} \left(r \mu_k \frac{\partial k}{\partial r} \right) \right] = G - \rho \epsilon \quad (15)$$

$$\rho w \frac{\partial \epsilon}{\partial z} + \rho u \frac{\partial \epsilon}{\partial r} - \frac{1}{r} \left[\frac{\partial}{\partial z} \left(r \mu_\epsilon \frac{\partial \epsilon}{\partial z} \right) + \frac{\partial}{\partial r} \left(r \mu_\epsilon \frac{\partial \epsilon}{\partial r} \right) \right] = \frac{C_1 G \epsilon}{k} - \frac{C_2 \rho \epsilon^2}{k} \quad (16)$$

$$\frac{G}{\mu_t} = 2 \left(\left(\frac{\partial w}{\partial z} \right)^2 + \left(\frac{\partial u}{\partial r} \right)^2 + \left(\frac{u}{r} \right)^2 \right) + \left(\frac{\partial w}{\partial r} + \frac{\partial u}{\partial z} \right)^2 \quad (17)$$

where, $\mu_k = \mu + \mu_t / \lambda_k$, $\mu_\epsilon = \mu + \mu_t / \lambda_\epsilon$, $\lambda_k = 1$, $\lambda_\epsilon = 1.3$, $C_1 = 1.44$, $C_2 = 1.92$, $C_3 = .09$. These equations are solved along with the Navier-Stokes equations (Eq. 12) using,

$$\begin{aligned} \phi = k, a_\phi = 1, b_\phi = r \mu_k, c_\phi = 1, d_\phi = r(G - \rho \epsilon) \\ \phi = \epsilon, a_\phi = 1, b_\phi = r \mu_\epsilon, c_\phi = 1, d_\phi = r(C_1 G \epsilon / k - C_2 \rho \epsilon^2 / k) \end{aligned}$$

Boundary and Initial Conditions

The boundaries of the inner grenade chamber (see Figure 1) are the inlet (connected to the pyrotechnic chamber), the exit (nozzle throat), the symmetry axis, the chamber wall lined with payload material, and a section of solid wall along the nozzle. Since the governing equations (Eq. 12) are elliptic the conditions along these boundaries must prescribe values of the dependent variables, the gradient of the dependent variables in the normal direction, or an algebraic relation which connects the values of the dependent variables to the normal component of velocity.

At the inlet plane, radial profiles of all dependent variables, ψ , ω , m_j , \bar{h} , v , k , and ϵ as well as values for V , T , p , ρ , and μ_{eff} are specified. It is assumed that the flow at the inlet plane consists of air and that the

diffusion of payload into the airstream from the chamber wall does not effect the inlet flow. During actual grenade operation the inlet flow consists of pyrotechnic combustion gases (e.g. H₂O, CO₂). A subsonic inlet flow velocity assumption is used in accordance with the elliptic nature of the governing equations. Initial conditions for all dependent variables are supplied by the inlet boundary conditions. The turbulence model is initialized using $k = k_\infty = \alpha V^2$, $\epsilon = k^{1.5} C_3^{-0.5} / (.37 x^{0.8} Re^{-0.4})$. The initial turbulence kinetic energy is specified as $(1 - \alpha)\%$ of the inlet kinetic energy.

The exit plane is located at the nozzle throat where the flow is assumed to be subsonic. The streamlines at the exit plane are assumed to be parallel to the symmetry axis; thus, the gradients of all dependent variables along streamlines are zero. These assumptions are reasonable since experience for large Reynolds numbers has shown that the exact nature of the exit plane boundary conditions has little effect on the flowfield solution when convection is significant (i.e. large inlet mass flow).^{8,9}

For mass continuity, the symmetry axis is considered to be a streamline of the flow, thus $\psi = \text{constant}$. Along the symmetry axis $r = 0$, thus $\partial\psi/\partial z = \partial\psi/\partial r = 0$ via Equation 11. The value of ψ along this boundary can be determined from values of ψ adjacent to the boundary using a one-sided finite-difference for $\partial\psi/\partial r$ at the axis. From Equation 11, the boundary value for ω is zero. The axis boundary values for the remaining dependent variables, ϕ , are determined from $\partial\phi/\partial r = 0$.

The no-slip condition ($u = w = 0$, and $v/r = \Omega$, where Ω is the wall spinrate) is applied to the solid walls. Therefore $\psi = \text{constant}$, via Equation 11. For convenience $\psi = 0$ is chosen. One-sided finite-differences for $\partial\psi/\partial r$ and $\partial\psi/\partial z$ are used in Equation 11 to determine the wall value for ω . For an inert wall, the normal gradient of all mass fractions, $\partial m_i / \partial n$, are set to zero. For a wall with payload material, the boundary condition is based on the assumption that the payload material is continually vaporizing ($m_{\text{payload}} = 1, m_{\text{air}} = 0, m_{\text{mixture}} = 0$). The wall temperature is set to the vaporization temperature of the payload, $T_{\text{wall}} = T_{\text{vap}}$. Figure 2 shows the results of a thermogravimetric analysis of yellow dye (i.e. payload material).¹⁰ The percent weight loss of the sample is plotted as a function of temperature. Note that vaporization of the material (i.e. significant weight loss) occurs over a narrow temperature range, supporting the use of such a boundary condition. The rate of burning (regression rate) on the payload surface varies as a function of position along the surface and is computed from the temperature gradient normal to the wall,

$$\dot{r} = \frac{-\kappa_p}{\rho_p h_{\text{vap}}} \frac{\partial T}{\partial r} \quad (18)$$

where κ_p and ρ_p are the thermal conductivity and density of the solid payload, and h_{vap} is the heat of vaporization of a unit mass of payload. Values of the thermal conductivity, density, and heat of vaporization can be determined for most grenade payload materials.

The boundary conditions for the payload surface are based on the assumption of single diffusion, i.e. diffusion of gaseous payload molecules into the airstream without diffusion of air molecules into the payload material. Single diffusion has been studied by R.D. Present.¹¹ The general equation of mutual/thermal diffusion is given by,

$$G_i = n_i u_i - n \Gamma \frac{d}{dz} \left(\frac{n_i}{n} \right) + \frac{n_i \Gamma_T}{T} \frac{dT}{dz} \quad (i = 1, 2) \quad (19)$$

where n_i = molecular density, $n = \sum_i n_i$, u_i = convection velocity, z = diffusion direction, Γ = mass diffusion coefficient ($V\lambda/3$, λ = the molecular mean free path), and Γ_T = thermal diffusion coefficient ($\kappa/(\rho h_{\text{vap}})$). The equation of "single diffusion" can be obtained by assuming that air molecules ($i=1$) are moving in a boundary layer so that $u_1 \approx 0$ and payload molecules ($i=2$) are at rest, $u_2 \equiv 0$. In addition, the payload molecules are closely packed so that $n_1 \ll n_2$. As a result,

$$G_1 = 0, \quad G_2 = -(n_1 + n_2) \Gamma \frac{d}{dz} \left(\frac{n_2}{n_1 + n_2} \right) + \frac{n_2 \Gamma_T}{T} \frac{dT}{dz} \quad (20)$$

The mass diffusion terms of Equation 20 are incorporated in the J_j terms of Equation 5.

The payload surface boundary condition may also be prescribed using a surface ablation model such as described in Reference 12. In this model the payload vaporization temperature and heat of vaporization are

prescribed as functions of the pressure applied to the material surface. An equation similar to Equation 18 is used along with these functions in a iterative/coupling procedure with the governing equations in order to prescribe the payload surface boundary condition. The use of an ablation model, as opposed to assuming that the payload surface is continually vaporizing ($T_{\text{wall}} = T_{\text{vap}}$), is more critical for cases where the vaporization characteristics of the material are a strong function of pressure and temperature (i.e. unlike that shown in Fig. 2). The major drawback to using an ablation model is the increased computational cost of the iterative procedure and the requirement of experimental data in the form $T_{\text{vap}} = T_{\text{vap}}(p)$, $h_{\text{vap}} = h_{\text{vap}}(p)$. Inclusion of an ablation model into the numerical simulation of payload dissemination will be addressed in future papers.

Boundary conditions for turbulence variables, k and ϵ , are $k = 0$, $\epsilon = .056\mu(\partial u/\partial r)^2/\rho$ for solid walls and $k = 10^{-6}V_{\infty}^2$, $\epsilon = k^{1.5}/L$ for the inlet flow. Along the chamber axis and exit plane $\partial k/\partial r = \partial \epsilon/\partial r = 0$, $\partial k/\partial z = \partial \epsilon/\partial z = 0$, respectively.

Computational Algorithm

Equation 12 can be reduced to a successive-substitution formula for flow variable ϕ at each node on the computational grid. Central finite-differences are used for the diffusive and source terms and upwind differences for the convective terms. Using upwind differencing in the specie conservation equations (Eq. 5) reduces the occurrence of negative specie mass fractions in mixing layers. The resulting system of equations for the entire grid is solved using a Gauss-Seidel relaxation scheme.² Each iteration cycle is made up of M sub-cycles, where M is the number of equations being considered (M must be at least 2 since the equations for $\phi = \omega/r$ and $\phi = \psi$ are the minimum required to define the flow). In each sub-cycle, grid points are scanned row by row and a single variable is updated. The variables ω/r and ψ are updated in order followed by all other variables. When all sub-cycles are completed a new iteration cycle is started in which the values of the variables from the latest iteration are immediately used. This is consistent with the Gauss-Seidel methodology.¹³ Convergence is satisfied when the greatest relative change in any flow variable, ϕ , over all grid points is smaller than a prescribed tolerance.

Results

In order to demonstrate the numerical method, simulations were performed for an experimental grenade model loaded with yellow dye payload material that has been the subject of testing at CRDEC. In these tests the grenade's inner chamber was instrumented with pressure transducers and thermocouples (for temperature measurements). The chamber was lined with yellow dye payload material about .25 inches in thickness. A typical test run yields measured values for the chamber inlet pressure and temperature (due mainly to pyrotechnic ignition) of about 3.5 psig (1.24 atm) and 425 C. The nozzle or exit plane values were measured as 1.5 psig (1.1 atm) and 375 C. These values were used as boundary conditions for the numerical simulation. The chemical properties of the yellow dye payload material were measured as $T_{\text{vap}} = 241$ C, $H_{\text{vap}} = 102.9$ J/g, $\mathcal{M} = 273$ g/mole. The density and thermal conductivity of the dye have not been measured but were taken as $\rho_p = 1.8$ g/mole and $\kappa_p = .00143$ cal/s-cm-C, respectively. Sensitivity studies using the present numerical model show that the predicted payload regression rate depends significantly on the value of κ_p and less on the value of ρ_p . The inlet gas was assumed to be air with $\mathcal{M} = 28.8$ g/mole and the \mathcal{M} of the air/payload gas mixture taken as 150 g/mole.

Figure 3 shows the computational grid (or mesh) used for flowfield simulation within the grenade's inner chamber, bounded axially by the inlet and nozzle and radially by the symmetry axis and chamber wall. The chamber is cylindrical with an overall length of 4.0 inches and .375 inches in diameter. These dimensions represent the chamber shape before payload surface regression. Note that the vertical axis in Figure 3 has been magnified by a factor of 10 over the horizontal axis for clarity. About 131 grid points were used in the axial direction with 35 points in the radial direction; the grid points were unevenly distributed in order to cluster points along the boundaries (except at the symmetry axis). Figure 4 shows the computed

velocity vectors (i.e. arrows whose length is representative of the magnitude of local gas velocity and direction indicates the orientation of the local velocity) displayed at every 6th axial grid point and every other radial point (for clarity). A thick boundary layer that develops along the chamber wall (i.e. payload surface) can be observed. The computed chamber exit velocity is approximately 121 ft/s. The surface of the payload material was allowed to ablate (i.e. regress) for .25 seconds resulting in the shape shown in Figure 5 (computational grid). Note that the material surface has been blunted at the chamber inlet but more evenly eroded over most of the surface with the exception of a discontinuity at the payload/nozzle wall junction ($x = 3.5$ inches). Figure 6 shows the computed velocity vectors for this chamber shape. Due to the contour of the chamber entrance, the flow is significantly accelerated (indicated by longer arrows in the figure) forming a thin boundary layer along the payload surface. The computed chamber exit velocity is approximately 276 ft/s. Figure 7 shows the distribution of payload regression rate (Eq. 18) along the payload surface for both the initial time and .25 seconds elapsed time. Payload regression rate is largest near the chamber inlet and nearly uniform over most of the payload surface. The regression rate increases with elapsed time.

Figure 8 shows radial profiles of axial velocity component at both the initial and elapsed time as well as two axial positions along the chamber - midlength, $x = 2$ in, and the exit plane, $x = 4$ in. Consistent with the imposed boundary conditions the velocity is zero at the chamber wall ($r = .1875$ in) and the velocity gradient is zero at the chamber axis ($r = 0$). The retarding effect of the wall boundary layer on the velocity profile can also be observed. Note that the profiles at chamber midlength show the payload surface regressing from $r = .1875$ in to about .195 in from the centerline while the profiles at chamber exit show no wall regression since the chamber wall is solid at this location. Comparing the chamber midlength profiles with those at the exit plane show that the boundary layer (or mixing layer) thickens with axial location downstream of the inlet. Comparing the initial time profiles with those at the elapsed time show that the gas flow is significantly accelerated as the payload surface regresses.

Figure 9 shows radial profiles of gas temperature at both the initial and elapsed time as well as two axial positions along the chamber - midlength, $x = 2$ in, and the exit plane, $x = 4$ in. Consistent with the imposed boundary conditions the temperature is T_{vap} at the payload surface while the temperature gradient is zero at both the chamber axis and the solid chamber wall at the nozzle (adiabatic wall condition). Note that the profiles at chamber midlength show the payload surface regressing from $r = .1875$ in to about .195in from the centerline while the profiles at chamber exit show no wall regression since the chamber wall is solid at this location. Within the boundary layer established on the payload surface the temperature of the air/payload mixture is gradually increased until it reaches the centerline (i.e. inlet) value. Comparing the chamber midlength profiles with those at the exit plane show that the thermal boundary layer thickens with axial location downstream of the inlet. Comparing the initial time profiles with those at the elapsed time show that the gas flow is slightly hotter at any chosen radial position within the mixing layer.

Figures 10 and 11 show radial profiles of mixture (payload/air) mass fraction at both the initial and elapsed time as well as two axial positions along the chamber - midlength, $x = 2$ in, and the exit plane, $x = 4$ in. Consistent with the imposed boundary conditions the mixture mass fraction, m_{mix} , is zero at the payload surface (i.e. $m_{payload} = 1$, $m_{air} = 0$) and along the chamber centerline (i.e. $m_{payload} = 0$, $m_{air} = 1$). Along solid walls (i.e. chamber exit) and at the chamber centerline the gradient of m_{mix} is zero. The mixture mass fraction is exactly or nearly unity at some point in the flowfield where $m_{payload}$ and m_{air} are equivalent. Note that the profiles at chamber midlength show the payload surface regressing from $r = .1875$ in to about .195in from the centerline while the profiles at chamber exit show no wall regression since the chamber wall is solid at this location. Comparing the chamber midlength profiles with those at the exit plane show that the chamber core flow, consisting of air ($m_{mix} = 0$), thins from a radial position of about .12in to .10in at the initial time and .15in to .13in at the elapsed time. The diffusion of payload material into the core flow is advanced with axial position as the boundary layer imposed on the payload surface grows. Comparing the initial time profiles with those at the elapsed time show that the mixing layer, of highest mixture concentration (i.e. 1), follows the payload surface as regression progresses.

Conclusions

Material dissemination from the payload chamber inside a dual-chamber grenade has been simulated using computational fluid dynamics. A thermal dissemination technique that uses the hot, moving gases generated from combustion of a pyrotechnic within the grenade has been investigated. The dissemination process is initiated by ablation and vaporization of the payload material from exposure to the thermal effects of pyrotechnic combustion. This material in gaseous form is entrained in this flow and expelled from the grenade. The Navier-Stokes equations along with chemical species conservation equations were used to simulate the diffusion and convection processes of the flowfield within the grenade's payload chamber. Numerical simulations reveal that diffusion of the payload material is accomplished within a boundary layer that is established along the payload surface (chamber wall) and that a core flow, basically unaffected by the payload ablation, resides over about one-half of the chamber diameter. Thermal exposure of the payload mixture to the hot combustion gases from the pyrotechnic is concentrated in this layer where the temperature is below that of the core flow gases. As the payload surface regresses, the flow thru the chamber is accelerated and the diffusion/mixing layer follows the regressing surface which results in an expansion of the core flow. The regression rate increases with elapsed time (since pyrotechnic ignition) as the shape of the payload surface (chamber wall) is contoured by material ablation.

Acknowledgement

This work was supported by Mr. Miles C. Miller of the Aerodynamics Research and Concepts Assistance (ARCA) Branch, Physics Division, Research Directorate, U.S. Army Chemical Research, Development, and Engineering Center (CRDEC), Aberdeen Proving Ground, MD.

References

1. Nusca, M.J., Chakravarthy, S.R., Goldberg, U.C., "Computational Fluid Dynamics Capability for the Solid-Fuel Ramjet Projectile," AIAA Journal of Propulsion and Power, Vol. 6, No. 3, May-June 1990, pp. 256-262. See also, BRL-TR-2958, U.S. Army Ballistic Research Laboratory, Aberdeen Proving Ground, MD, December, 1988.
2. Nusca, M.J., "Steady Flow Combustion Model for Solid-Fuel Ramjet Projectiles," AIAA Journal of Propulsion and Power, Vol. 6, No. 3, May-June 1990, pp. 348-352. See also, BRL-TR-2987, U.S. Army Ballistic Research Laboratory, Aberdeen Proving Ground, MD, April, 1989.
3. Nusca, M.J., "Numerical Simulation of Reacting Flow in a Thermally Choked Ram Accelerator - Model Development and Validation," BRL-TR-3222, U.S. Army Ballistic Research Laboratory, Aberdeen Proving Ground, MD, April, 1991. See also, AIAA-91-2490, Proceedings of the 27th AIAA Joint Propulsion Conference, June 24-27, 1991, Sacramento, CA, and Proceedings of the 28th JANNAF Combustion Subcommittee Meeting, Brooks AFB, San Antonio, TX, Oct. 28 - Nov. 1, 1991.
4. Schlichting, H., Boundary Layer Theory, 7th ed., translated by J. Kestin, McGraw-Hill, NY, 1979.
5. Ames Research Staff, "Equations, Tables, and Charts for Compressible Flow," NACA Report 1135, 1958.
6. Stull, D.R., and Prophet, H., "JANNAF Thermochemical Tables," 2nd ed., National Bureau of Standards, NSRDS-Rept. 37, June 1971.
7. Kim, Y.M., and Chung, T.J., "Finite-Element Analysis of Turbulent Diffusion Flames," AIAA Journal, Vol. 27, No. 3, March 1989, pp. 330-339.

8. Bradshaw, P., Cebeci, T., and Whitelaw, J.H., Engineering Calculation Methods for Turbulent Flows, Academic Press, New York, 1981.
9. Khalil, E.E., Spalding, D.B., and Whitelaw, J.H., "The Calculation of Local Flow Properties in Two-Dimensional Furnaces," International Journal of Heat and Mass Transfer, 1975; Vol. 18, pp. 775.
10. Personal communication with A. Turetsky, U.S. Army Chemical Research Development and Engineering Center (CRDEC), Aberdeen Proving Ground, MD, December 1991.
11. Present, R.D., Kinetic Theory of Gases, McGraw-Hill Book Co., New York, 1958.
12. Moss, J.N., "Radiative Viscous-Shock-Layer Solutions with Coupled Ablation Injection," AIAA Journal, Vol. 14, No. 9, Sept. 1976, pp. 1311-1317.
13. Carnahan, B., Luther, H.A., and Wilkes, J.O., Applied Numerical Methods, John Wiley and Sons, New York, 1969.

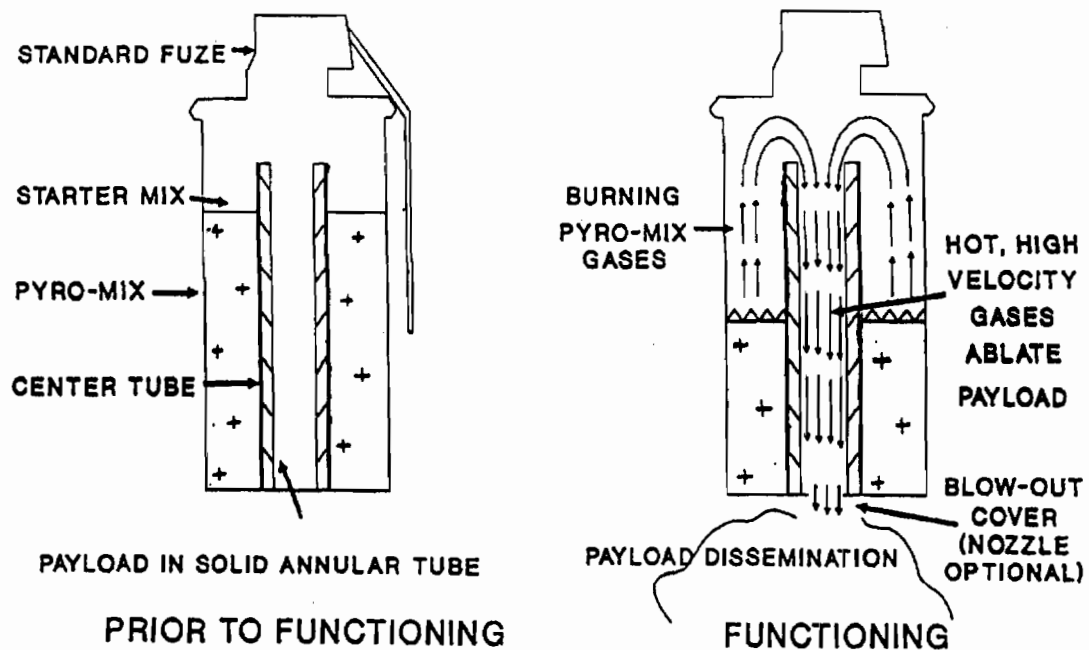


Fig. 1. Schematic showing operation of the dual-chamber grenade thermal dissemination method (from M. Miller, U.S. Army CRDEC, used with permission).

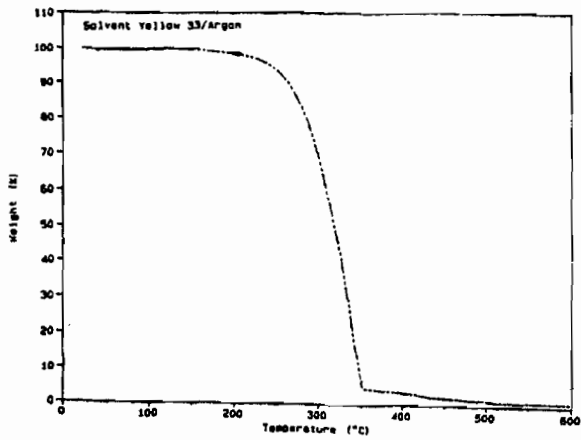


Fig. 2. Measured weight change (%) of solvent yellow dye sample during heating from 0 to 600 C in an argon atmosphere. Measurements done using thermogravimetric analyzer at CRDEC (Ref. 10).

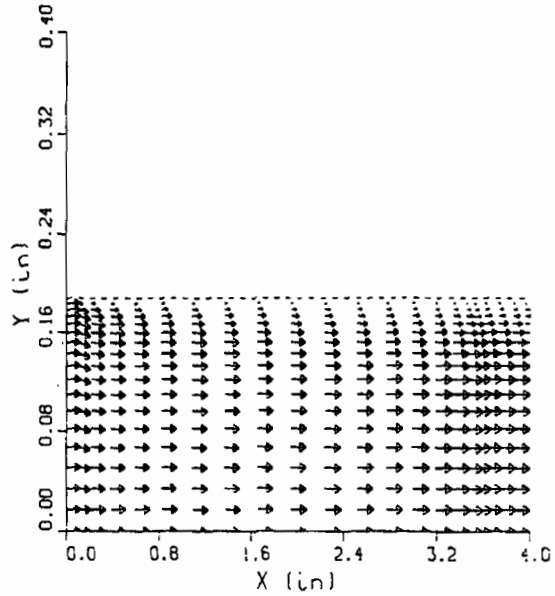


Fig. 4. Computed velocity vector field for initial chamber shape.

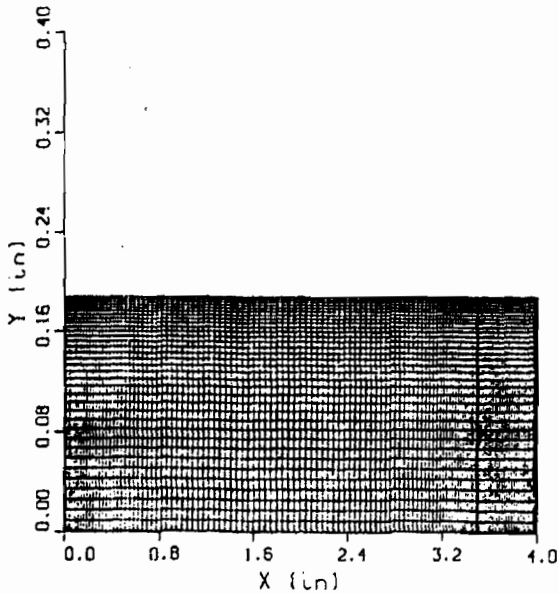


Fig. 3. Computational grid for initial chamber shape.

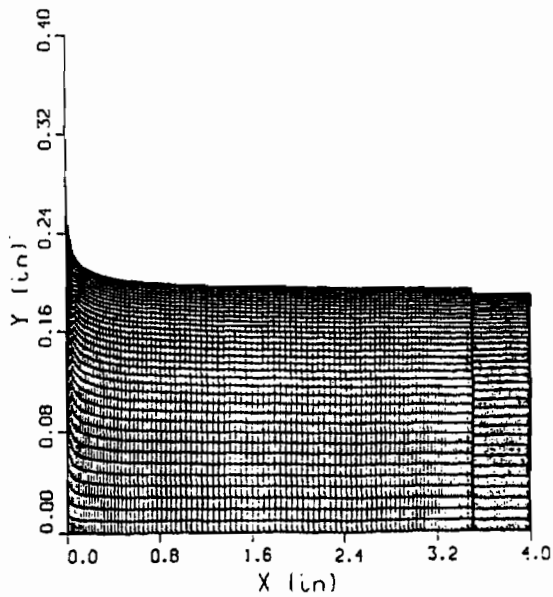


Fig. 5. Computational grid for chamber shape after .25 seconds of payload surface ablation.

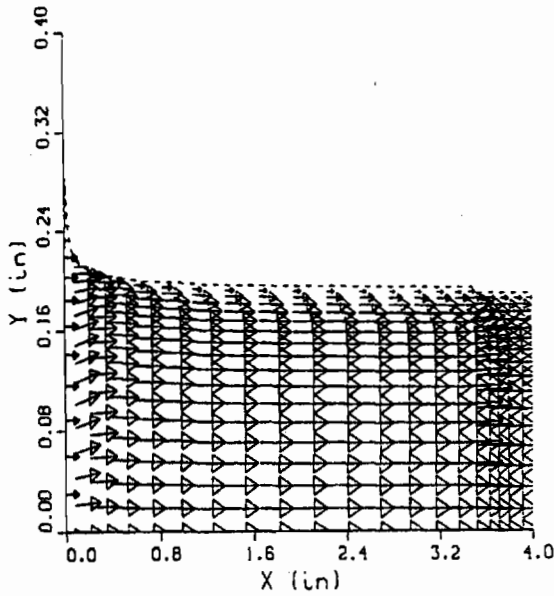


Fig. 6. Computed velocity vector field for chamber shape after .25 seconds of payload surface ablation.

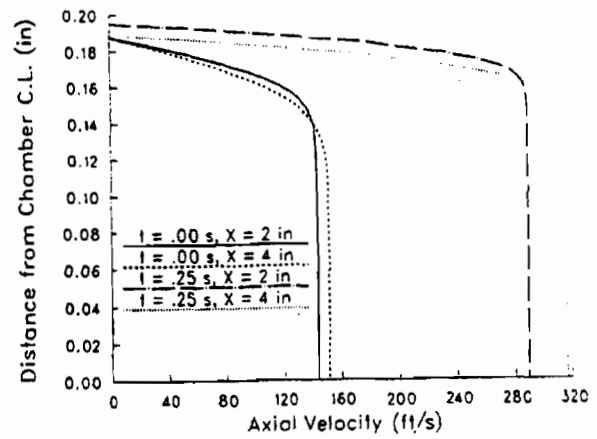


Fig. 8. Computed radial profiles of axial component of gas flow velocity; results for initial and elapsed time shown at the chamber midlength and nozzle exit.

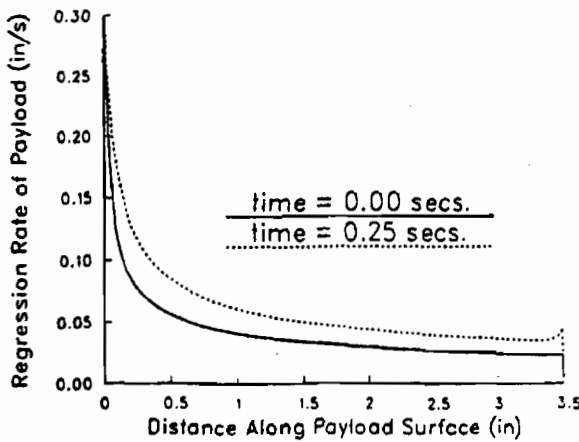


Fig. 7. Computed payload material regression rate as a function of distance along payload surface; results for initial and elapsed time shown.

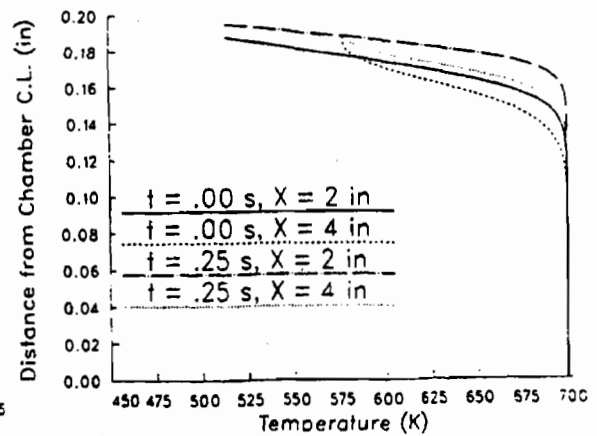


Fig. 9. Computed radial profiles of gas temperature; results for initial and elapsed time shown at the chamber midlength and nozzle exit.

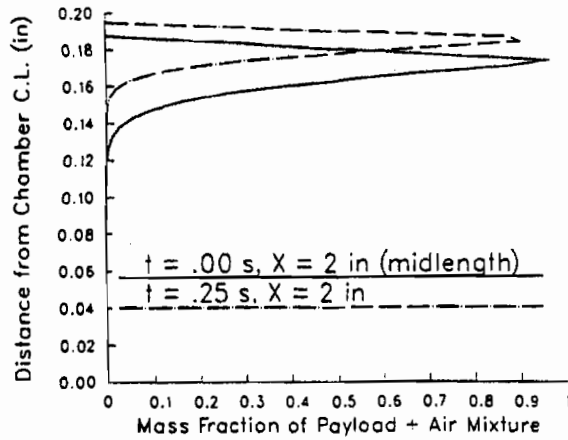


Fig. 10. Computed radial profiles of gas composition (mixture mass fraction); results for initial and elapsed time shown at the chamber midlength.

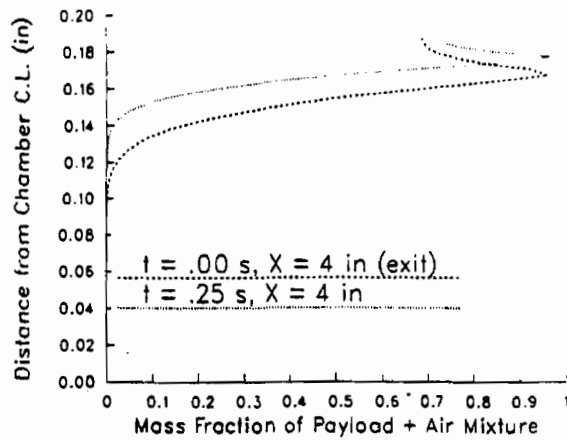


Fig. 11. Computed radial profiles of gas composition (mixture mass fraction); results for initial and elapsed time shown at the chamber nozzle exit.

**A COMPARISON OF ELONGATIONAL MEASUREMENTS OBTAINED
WITH THE FALLING CYLINDER AND IMPINGING JET RHEOMETER**

Joseph E. Matta, Raymond P. Tytus, Douglas R. Sommerville, ¹

ABSTRACT

A comparison is presented of elongational measurements made using two different methods: the impinging jet and the falling cylinder apparatus, developed at CRDEC. Measurements were made on three thickened solvents having various concentrations of co-polymer K-125 (80% polymethyl methacrylate and 20% ethyl/butyl acrylate).

INTRODUCTION

Previous falling cylinder tests (1) have measured the elongational viscosity for select Newtonian and viscoelastic liquids. Results indicated Trouton viscosities for the Newtonian liquids tested, while results for the viscoelastic liquids indicated a viscosity increase with time, with the initial viscosities approximately equal to the Trouton viscosity.

This paper presents additional measurements for 3 viscoelastic liquids using the falling cylinder technique which is described in great detail. Test results are compared to elongational flow measurements obtained using an impinging jet rheometer. Liquid flow in an impinging jet rheometer is not purely extensional, however, it has a strong extensional component. Because of this, it has found application as an extensional viscosity indexer i.e. comparing the elongational viscosity of different liquids. A very good reference for the impinging jet rheometer can be found in a short course publication in Rheological Measurements published by the University of Minnesota Center for Interfacial Engineering. (2)

FALLING CYLINDER TECHNIQUE

Liquid is inserted between 2 cylinders, the upper fixed and the lower momentarily held stationary. The lower cylinder is quickly released. Three forces then act on the lower cylinder (figure 1); the ligament force, the drag force and the lower cylinder weight. The sum of these forces results in a downward acceleration which stretches the liquid.

For simple extensional flow the following relationships are applicable

$$T_{11} = \eta_e \dot{\epsilon} + \frac{\sigma}{r}$$

$$\dot{\epsilon} = -2 \frac{V_r}{r}$$

where T_{11} is the ligament stress, η_e is the extensional viscosity, $\dot{\epsilon}$ is the extension rate, σ is the liquid surface tension, V_r is radial velocity and r is the ligament radius.

Thus, in order to calculate the elongational viscosity the ligament stress and extension rate must be determined. The ligament force can be calculated using Newton's Second Law if the lower cylinder acceleration is known. Radius versus time measurements would permit calculations of both a ligament stress and extension rate.

EXPERIMENTAL SET-UP

Figure 2 shows a schematic of the falling cylinder system. The diameter of both the upper and lower cylinder is 6.35 mm. Lower cylinder weights of .563 and 1.652 grams were used to stretch the liquid sample. The set-up procedure required positioning the lower cylinder on a retractable air piston, placing approximately 30 mg of liquid sample on top of the lower cylinder and then positioning the upper cylinder to contact the liquid and then lock it in that position. A recording video system with 2 cameras simultaneously records the lower cylinder displacement and ligament radius after the piston is activated.

LIQUIDS TESTED

The liquids tested are shown below. Samples 1065 and 1140 were mixed using co-polymer K-125 from lot # 3-6326. The Battelle sample lot number was not known.

1065 Sample- Methyl salicylate - 5.2 g/dl
 1140 Sample- Triethyl phosphate- 4.9 g/dl
 Battelle Sample- Triethyl phosphate- 4.2 g/dl

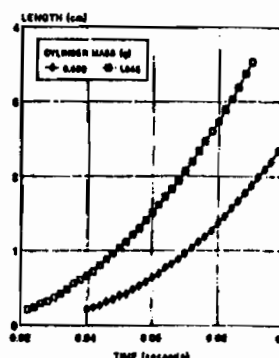
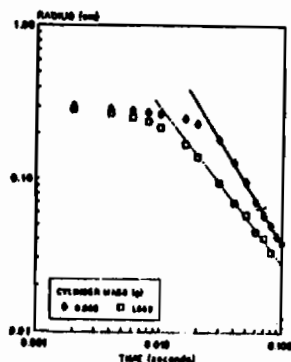
Weissenberg Rheogoniometer measurements of zero shear viscosity and normal stress, measured at 428.9 1/sec, are shown below. The Trouton viscosities are equal to 3 times the zero shear viscosity values. The magnitude of the normal stress indicates the relative elasticity of the liquids, the higher the stress the more elastic the liquid. Measurements were made at 73 F.

	poise	dynes/cm ²
	-----	-----
1065 Sample-	10	3,991
1140 Sample-	10	24,945.5
Battelle Sample-	8.7	15,466.2

EXPERIMENTAL RESULTS

Measurements of ligament radius and lower cylinder displacement were made from a split screen video display of the recorded event. The display on the left side was used to measure the ligament diameter with a resolution of .00833 cm/pixel. The right display was used to measure the lower cylinder displacement with a resolution of .0265 cm/pixel. A video recording rate of 500 FPS resulted in a .002 second exposure rate. A measuring reticle contained in the video readout system was used to determine the pixel position of the surface edge being measured.

Typical measurements of ligament radius and lower cylinder displacement is shown below for the 1065 sample.



It can be seen that the radius slope is constant on a log/log plot after a time which relates closely to a 2 mm displacement of the falling cylinder. This 2 mm distance was also found to be a significant distance in the original study. A radius versus time relationship was easily obtained from this plot. Appropriate extension rates were calculated using this relationship and were found to be an inverse function of time for all the liquids.

The lower cylinder displacement data was used to determine the cylinder acceleration. A nonlinear regression was used to establish a displacement versus time relationship. The original study indicated a constant acceleration for viscoelastic liquids after the 2mm cylinder displacement. Regressions were calculated from the 2mm displacement time to approximately .1 seconds. Accelerations determined from these relationships permitted calculations to be made of ligament force and Ligament stress using the ligament radius data.

CALCULATED ELONGATIONAL PARAMETERS

Tables of the calculated extensional viscosity and extension rate for each liquid and lower cylinder weight are shown in figure 3.

In general, the results for the 3 test liquids agree with the results obtained in the original study for the viscoelastic liquids tested ; the Trouton viscosity was approached at the early times; and ,as a function of lower cylinder weight, the initial extension rate increased as the weight was increased and the extensional viscosity increased at a higher rate and to higher values as the weight was increased. The most significant deviation from these trends was found for the 1065 sample which indicated a much lower viscosity than the Trouton value and also exhibited a lower rate of increase in extensional viscosity at the larger lower cylinder weight. Possible reasons for this will be discussed later.

IMPINGING JET MEAUREMENTS

Impinging jet elongational viscosity versus extension rate data is shown in figure 4. The measurements were made on a Rheometric's Fluid Extensiometer (RFX) by Mr. Clarence Hermanski of the Dupont Agricultural Products Group in Wilmington, Delaware. His assistance in obtaining the impinging jet data is greatly appreciated. It is evident from the figure that the elongational viscosity increases with extension rate; the Trouton viscosity is approached at the low extension rates; and a significant difference in liquid response is noted for the two triethyl phosphate liquids.

COMPARISON COMMENTS

Comparison of the elongational viscosity data for the two techniques is shown in figure 5. The falling cylinder extensional viscosity data at the 2mm displacement time was used to compare with the impinging jet data. The RFX data was extrapolated at extension rates equal to those obtained for the two lower cylinder weights at the 2 mm displacement time.

In general, the falling cylinder results are comparable to that of the impinging jet and are somewhat lower in magnitude. The two exceptions are the previously mentioned 1065 sample which had a much lower viscosity than the Trouton value and the Battelle sample at the larger lower cylinder weight which indicated a higher viscosity than that measured by the impinging jet. The best agreement was found for the 1140 sample. The falling cylinder data indicated higher than Trouton viscosity for this sample which agrees with the impinging jet results.

The 2mm displacement distance impacts directly on the elongational viscosity measurement obtained using the falling cylinder technique. An analysis was made to determine the reason for this dependence.

Previous tests using Newtonian liquids indicated that extension rates were approximately constant during the early test times and calculated extensional viscosities were also found to be constant. A radius versus time plot was made on log-normal graph paper for each of the test liquids used in this study. Results for each sample indicated a linear decrease in radius over a significant interval of time. This corresponds to an exponential decrease in radius with time over this interval which results, using the equation for extension rate, in a constant rate of ligament extension. Figure 6 shows the calculated extension rates and corresponding time intervals for the 3 test liquids. Included are the extension rates obtained at the 2 mm displacement times. Good agreement is noted for both calculated extension rates. Based on this analysis, a constant extension rate exists prior to the 2mm displacement time, and if the ligament stress build-up is complete, a constant viscosity as well. This agrees with the elongational viscosity calculations at the 2 mm displacement time which are comparable to impinging jet results obtained at constant extension rates.

The extensional viscosities were recalculated using the constant extension rate calculated above. The results are shown in the figure 7. Drastic changes are not indicated, however, the 1140 sample now indicates an increase in elongational viscosity with cylinder weight i.e. extension rate. This agrees with the RFX data. More tests, however, are required to confirm such agreement on a consistent basis.

Poor results for sample 1065 using the larger lower cylinder weight may have been caused by a combination of small sample elasticity and high cylinder weight which results in an acceleration rate very close to that of gravity. Present methods for calculating the acceleration from test data are not precise and significant errors can result for small acceleration differences. A better method of determining cylinder acceleration is required. This need would be eliminated if a direct measure of ligament force was available.

Test results for the Battelle sample using the smaller lower cylinder weight cannot be explained. There is a possibility that the 1140 sample was inadvertently used instead of the Battelle sample. This sample will be retested.

CONCLUSIONS

1. Reasonable agreement between falling cylinder and impinging jet elongational viscosity measurements was indicated.
2. It was shown that falling cylinder measurements at early times approximate a constant rate of extension experiment.
3. A better technique to determine cylinder acceleration is required for calculating elongational viscosity. A direct ligament force measurement would eliminate this need.
4. More testing is required to determine the range of elongational viscosities that can be measured using the falling cylinder technique.

REFERENCES

1. J.E. Matta and R.P. Tytus, "LIQUID STRETCHING USING A FALLING CYLINDER", 1989 Proceedings of CRDEC Scientific Conference on Chemical Defense Research.
2. C.W. Macosko, "RHEOLOGICAL MEASUREMENTS", Notes for an extensive short course given by the University of Minnesota Center for Interfacial Engineering, August 19-23, 1991.

¹ Commander, U.S. Army Chemical Research, Development and Engineering Center, ATTN: Operational Sciences Branch, Aberdeen Proving Ground, MD 21010-5423

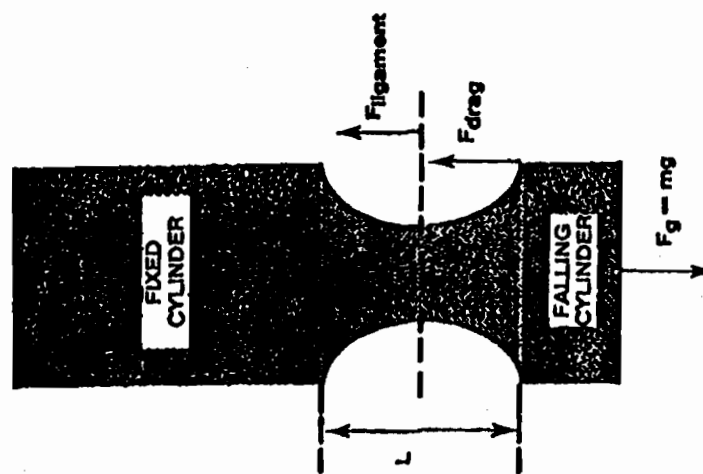


Figure 1

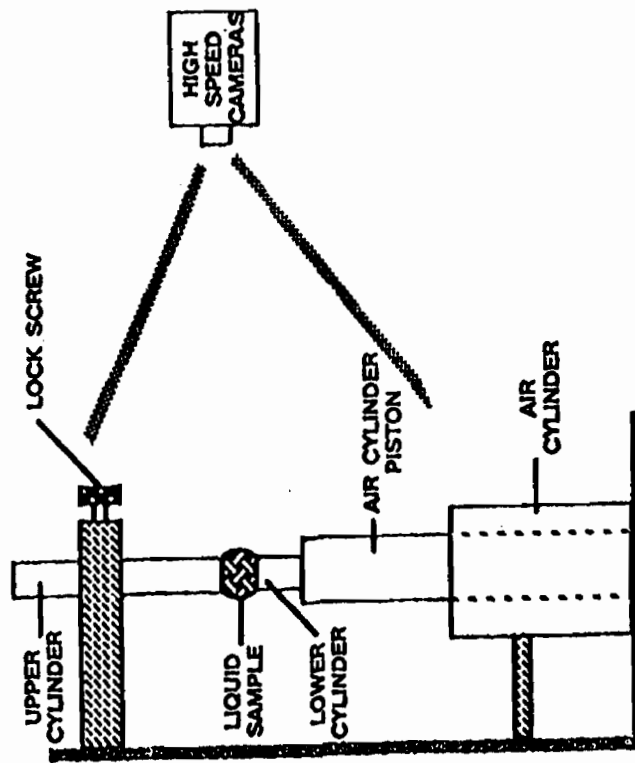


Figure 2

1045 SAMPLE SESSION # 102
 CYLINDER WEIGHT= .583 GRAMS
 RADIUS TIME CONSTANT= 1.333
 RADIUS CONSTANT= 1.2E-03
 CALCULATED ACCELERATION= 832.4 CM/SEC

TIME (SEC)	RADIUS (CM)	LIGAMENT STRESS (DYNE/CM ²)	ELONGATION RATE (1/SEC)	ELONGATIONAL VISCOSITY (POISE)
.04	.124	1355.6	68.6	22.1
.05	.109	2081.1	52.2	24.9
.06	.091	3041.9	32.3	22.2
.07	.081	3641.5	44.4	21.1
.08	.072	4647.5	44.4	104.5
.09	.064	5804.4	41	141.5
.10	.055	6121.2	36.5	187
.11	.045	6121.2	32.5	242.4
.12	.035	7028.6	32.3	309.7
.13	.025	12181.3	31.3	377.4
.14	.012	14207.8	28.6	478.6

1045 SAMPLE SESSION # 104
 CYLINDER WEIGHT= 1.652 GRAMS
 RADIUS TIME CONSTANT= 1.133
 RADIUS CONSTANT= 1.9E-03
 CALCULATED ACCELERATION= 981.2 CM/SEC

TIME (SEC)	RADIUS (CM)	LIGAMENT STRESS (DYNE/CM ²)	ELONGATION RATE (1/SEC)	ELONGATIONAL VISCOSITY (POISE)
.025	.124	400.2	50.6	4.4
.03	.1	673.1	75.5	8.9
.035	.084	1022	64.7	15.7
.04	.072	1450.4	56.6	25.8
.046	.063	1961.3	50.3	38.8
.05	.056	2557.3	45.3	56.4
.056	.05	3241.2	41.2	78.6
.06	.048	4019.1	37.7	108.3
.065	.042	4881.3	34.6	140
.07	.038	5841.9	32.3	180.4
.075	.035	6898.7	30.2	228.3
.08	.033	8033.6	28.3	284.3

1140 SAMPLE SESSION # 110
 CYLINDER WEIGHT= .583 GRAMS
 RADIUS TIME CONSTANT= .98
 RADIUS CONSTANT= 5E-02
 CALCULATED ACCELERATION= 364.4 CM/SEC

TIME (SEC)	RADIUS (CM)	LIGAMENT STRESS (DYNE/CM ²)	ELONGATION RATE (1/SEC)	ELONGATIONAL VISCOSITY (POISE)
.036	.123	7022.8	51.5	136.1
.04	.117	7778.8	48.5	158.7
.046	.104	9833.9	43.5	225.7
.05	.084	12124.2	39.1	309.2
.056	.085	14848.8	35.6	411
.06	.078	17406.8	32.8	532.6
.066	.072	20398.8	30.1	676.4
.07	.067	23818.9	27.9	843.6
.076	.063	27072	26.1	1038.9
.08	.059	30765.4	24.4	1258.3

1140 SAMPLE SESSION # 112
 CYLINDER WEIGHT= 1.652 GRAMS
 RADIUS TIME CONSTANT= .76
 RADIUS CONSTANT= 2E-03
 CALCULATED ACCELERATION= 691 CM/SEC

TIME (SEC)	RADIUS (CM)	LIGAMENT STRESS (DYNE/CM ²)	ELONGATION RATE (1/SEC)	ELONGATIONAL VISCOSITY (POISE)
.02	.136	7896.8	76	103.9
.026	.116	11331.8	60.7	183.1
.03	.1	14733.3	50.6	290.7
.036	.089	18685.1	43.4	429.7
.04	.078	23905	38	602.7
.046	.073	27433.7	33.7	812.1
.05	.068	32235.2	30.3	1060.3
.056	.063	37295.9	27.5	1349.5
.06	.059	42604.2	25.3	1681.7
.066	.055	48149.8	23.3	2059
.07	.052	53983.8	21.7	2483.3

BATTELLE SAMPLE SESSION # 113
 CYLINDER WEIGHT= .583 GRAMS
 RADIUS TIME CONSTANT= 1
 RADIUS CONSTANT= 8E-03
 CALCULATED ACCELERATION= 434.6 CM/SEC

TIME (SEC)	RADIUS (CM)	LIGAMENT STRESS (DYNE/CM ²)	ELONGATION RATE (1/SEC)	ELONGATIONAL VISCOSITY (POISE)
.04	.125	6016.5	49.9	120.3
.045	.111	7650.9	44.4	172.1
.05	.1	9478.9	40	236.9
.056	.09	11802.5	36.3	316.3
.06	.083	13721.7	33.3	411.6
.066	.076	16136.4	30.7	524.4
.07	.071	18746.9	28.5	658.1
.075	.068	21522.7	26.6	809.2
.08	.062	24594.2	24.9	982.1
.086	.058	27751.2	23.5	1179.4
.09	.055	31143.5	22.2	1401.4

BATTELLE SAMPLE SESSION # 115
 CYLINDER WEIGHT= 1.652 GRAMS
 RADIUS TIME CONSTANT= .98
 RADIUS CONSTANT= 5.4E-03
 CALCULATED ACCELERATION= 624.4 CM/SEC

TIME (SEC)	RADIUS (CM)	LIGAMENT STRESS (DYNE/CM ²)	ELONGATION RATE (1/SEC)	ELONGATIONAL VISCOSITY (POISE)
.022	.134	4268.2	78.1	56.2
.025	.121	5340.8	67	79.6
.03	.103	7297.3	55.8	130.6
.035	.091	9493.8	47.8	198.2
.04	.081	11918.6	41.9	284.4
.046	.073	14561.6	37.2	390.9
.05	.067	17415.1	33.5	519.5
.056	.062	20771.4	30.4	671.7
.06	.058	24724.5	27.9	849.3
.065	.054	29168.8	25.7	1053.6
.07	.051	34099.5	23.9	1286.3
.076	.048	39612	22.3	1546.8
.08	.045	45802.4	20.9	1843.8

Figure 3

IMPINGING JET DATA
(TAKEN AT 77 DEG. F)

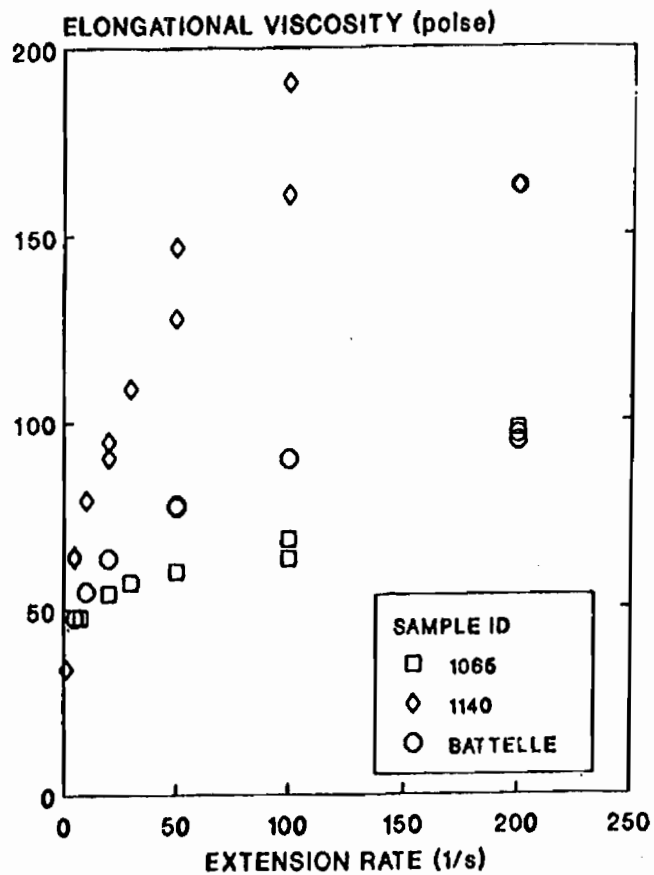


Figure 4

	Cylinder Weight (Grams)	Falling Cylinder Viscosity (Poise)	Impinging Jet Viscosity (Poise)
1066 Sample	.563	22.1	62.0
	1.562	4.4	65.0
1140 Sample	.563	136.1	137.4
	1.562	103.9	157.0
Battelle Sample	.563	120.3	77.8
	1.562	45.2	85.0

Figure 5

	Cylinder Weight (Grams)	Time Range For Constant Extension Rate (Seconds)	Calculated Extension Rate (1/sec)	2 mm Displacement Extension Rate (1/sec)
1065 Sample	.563	.025 - .045	69.3	66.6
	1.562	.008 - .028	88.9	90.6
1140 Sample	.563	.01 - .04	57.3	51.6
	1.562	.01 - .025	71.2	76.0
Battelle Sample	.563	.018 - .047	52.0	49.9
	1.562	.008 - .025	72.8	76.1

Figure 6

	Cylinder Weight (Grams)	Falling Cylinder Viscosity (Poise)	Impinging Jet Viscosity (Poise)
1065 Sample	.563	18.1	62.0
	1.562	4.4	65.0
1140 Sample	.563	97.5	137.4
	1.562	117.6	157.0
Battelle Sample	.563	102.0	77.8
	1.562	63.5	85.0

Figure 7

**FORMULATION OF PREFERENTIALLY SOLUBLE POLYMER SOLUTIONS
AND COMPARISONS OF THEIR FIRST NORMAL STRESS DIFFERENCE
AND EXTENSIONAL VISCOSITY**

Brian S. Ince and Wendel J. Shuely
U.S. Army Chemical Research, Development and Engineering Center
Aberdeen Proving Ground, MD 21010-5423

ABSTRACT

The viscoelastic properties of polymer solutions were enhanced by the formulation of preferentially soluble solutions in which a major comonomer component is nominally insoluble in the solvent. Further progress on the ability to predict and formulate preferentially soluble compositions will be reported. Research continued on comparisons of steady mode first normal stress difference and extensional viscosity of soluble and preferentially soluble polymer solutions in the semi-dilute regime.

INTRODUCTION

The objective was to identify liquids for preferentially soluble polymer solutions by utilizing Polymer Cohesion Parameter Diagram (PCPD) theory and liquid substituent trends. Since this was a continuing effort, previous research will only be referenced to avoid repetition¹.

EXPERIMENTATION

Polymer solutions in the semi-dilute regime were prepared at a concentration of 4.7 g/dL of solvent. The viscoelastic polymeric additive (VEPA) used was Acryloid K125, an acrylic terpolymer which is composed of the three monomers, methyl methacrylate (MMA), ethyl acrylate (EA), and butyl acrylate (BA) in mole ratios of 82:12:6 respectively². Solubility determinations were also made of solutions of each of the homopolymers poly(MMA), poly(EA) and poly(BA) in each of the test liquids. As a continuation of previous research, the liquids of interest were those in which the terpolymer, Acryloid K125 was soluble and its component homopolymers poly(EA) and/or poly(BA) were also soluble but the third component homopolymer poly(MMA) was insoluble. Solutions of Acryloid K125 in these liquids were then labeled as preferentially soluble or in the "Nonsolvent with 0.82+" solvent set because the major component homopolymer (82 mole %), poly(MMA) is insoluble in the liquid. Additionally, limiting viscosity number (LVN) and rheological measurements were performed to characterize solutions of Acryloid K125 in each of these preferential liquids.

RESULTS

The objective was to develop a systematic means of identifying preferentially soluble liquids. The PCPD concept was employed by overlaying the PCPD of Acryloid K125 and the PCPD of poly(MMA). The non-

overlap region outside of poly(MMA) but inside Acryloid K125 then defines the solvent parameter values of a preferential solvent. Since GD is a preferential solvent for Acryloid K125¹, the liquids of interest were aprotic organophosphorus liquids of two general types; dialkyl alkylphosphonates and trialkylphosphates. By increasing/decreasing the size of the alkyl substituents, additional preferential solvents were identified and tested to confirm the predictions and the updated liquid list is shown in Table 1. Table 1 shows the names and structures for GD and a series of aprotic model liquids in the "Non-solvent with 0.82+" solvent set. Column 1 shows the liquid name and code. Columns 2-5 show the four substituents on the central phosphorus atom. Table 1 compiles the previous 6 preferential solvents¹ in addition to the 4 new solvents identified by the PCPD-Overlap/Substituent-Trend method. The prediction capabilities have improved from 5 of 20 (5 preferential solvents determined from 20 solvents tested) to 4 of 4, by using the PCPD-Overlap/Substituent-Trend method.

TABLE 1

Names and Structures for GD and a Series of Aprotic Model Liquids in the "Nonsolvent /0.82+" Solvent Set	Structure:*			
	$\begin{array}{c} \text{R}'' \\ \\ \text{R}' - \text{P} = \text{X} \\ \\ \text{R} \end{array}$			
Liquid Name, Code	R	R'	R''	X
Phosphonates:				
Pinacolyl methylfluorophosphonate, GD	OPin	Me	F	O
Dibutyl methylphosphonate, DBMP	OBu	OBu	Me	O
Diethyl bromodifluoromethylphosphonate, DEBDFMP	OEt	OEt	MeBrFF	O
Diethyl 2-chloroethylphosphonate, DECEP#	OEt	OEt	EtCl	O
Diethyl cyanomethylphosphonate, DECNMP#	OEt	OEt	MeCN	O
Diethyl isocyanomethylphosphonate, DEICNMP#	OEt	OEt	MeNCO	O
Diethyl (methylthiomethyl)phosphonate, DEMENTP#	OEt	OEt	MeSMe	O
Phosphates:				
Tripropyl phosphate, TPPO	OPr	OPr	OPr	O
Tris (2-chloroethyl)phosphate, T(CE)PO	OEtCl	OEtCl	OEtCl	O
Triethyl thiophosphate, TEPS	OEt	OEt	OEt	S
* F - fluorine; Cl - chlorine; Br - bromine; O - oxygen; S - sulfur; C - carbon; N - nitrogen; Pin - pinacolyl or (3,3-dimethyl-2-butyl); Me - methyl; Et - ethyl; Pr -propyl; Bu - butyl				
# New preferential solvents				

Figure 1 shows a plot of first normal stress difference (FNSD) vs LVN with the 95% confidence interval. The x-axis represents LVN and the y-axis represents FNSD. Figure 1 represents the baseline correlation developed previously without preferentially soluble solutions.

New data added to the correlation plot include the 4 new preferential solvents which are poly(MMA) insoluble (see Table 1), 2 of which yielded results generally within the normal correlation 95% confidence interval (DECEP, DEMENTP). These 2 poly(MMA) insoluble organophosphorus solvents, coupled with the previously identified TEPS, have the following characteristics:

- 1) LVN values at the high end of the range, i.e., 2.13 - 2.44 relative to 1.27 - 2.48 (see Table 2).

2) The presence of sulfur molecules in 2 of the 3 non-poly(MMA) soluble liquids (DEMTMP, TEPS).

The majority of the preferentially soluble solution FNSD values cannot be displayed on the baseline correlation because the values are so much higher. Figure 2 graphically displays the increased FNSD in the 5 preferentially soluble solutions significantly above the correlation line, which appears essentially horizontal at this expanded FNSD y-axis scaling.

Note that these extremely high FNSD solutions display some time dependent behavior at the day-to-day level but show no hysteresis within the time span of the rheological experiment (hour). Solutions showing increasing FNSD with time are plotted as average values although the FNSD changes are small relative to the increase over the baseline. These two plots, Figures 1 and 2 are partially summarized in Table 2.

Table 2 shows the test liquids and their solubility classes, LVN ranges and FNSD ranges. The homopolymer solubility class is listed in column 1. Column 2 lists the LVN for the liquid with Acryloid K125 and column 3 lists the FNSD at 398 sec⁻¹ for 4.7 g/dL solutions of Acryloid K125 in each liquid. Three organophosphorus liquids in the poly(MMA) insoluble class fall below the upper 95% confidence interval, DECEP, DEMTMP and TEPS (Figure 1).

TABLE 2

List of Model Liquids and Their Solubility Classes, Limiting Viscosity Number (LVN) Ranges and First Normal Stress Difference (FNSD) Ranges		
Solubility Class	LVN Range, dL/g, at 25.0°C	FNSD Range, dyn/sq cm, at 398 sec ⁻¹ , 25.0 ± 2.0°C and 4.7 g/dL
Poly(MMA) Insoluble:	(1.27 - 2.48)	(4,000 - 12,000,000)
4-heptanone (4HP)	1.27	9,400
DBMP	1.47	70,000
DEICNMP	1.62	800,000
TPPO	1.67	525,000
DECNMP	1.89	12,000,000
GD	2.10	30,000
DECEP*	2.13	8,300
TEPS*	2.20	4,000
DEMTMP*	2.44	5,900
T(CE)PO	2.48	180,000
Poly(MMA) Soluble:	(1.42 - 3.03)	(1,420 - 12,200)
Proton Donating:	(2.50 - 4.08)	(100 - 20,000)

* FNSD below the baseline correlation 95% confidence interval.

The overall change of viscoelastic properties as a function of polymer-solvent interaction is shown in Table 3 by updating our previously published summary. A detailed description has been published². The previous ratios are left and the updated ratios are added for comparison. The increased viscoelasticity (Table 3, col 4: row 6 [12,000,000] vs row 3 [900,000]) is due to the most anomalously high solvent identified to date (DECNMP). Below the FNSD is listed the ratio from the average of all 9 preferentially soluble solutions (increasing from 96 to 3,000). The mean value for FNSD at 398 sec⁻¹ for the 9 preferential solutions, excluding GD, is in excess of 1.5E+06 dyn/sq cm, which is at least 2 orders of magnitude greater than FNSD for typical poly(MMA)-poly(EA)-poly(BA) solutions (see Table 3, row 6, col 2: 12,200).

TABLE 3

Solvent Effect Ranges and Ratios For The Rheological Properties of Polymer Solutions of Acryloid K125 at 4.7 ± 0.1 g/dL and $25.0 \pm 2.0^\circ\text{C}$				
Property	Solvent Set*			
	Within PMMA-PEA-PBA Soluble	Within Proton Donor	Within PEA-PBA Soluble	Between Proton Donor and PEA-PBA
<u>Previous:</u> LVN (dL/g)	3.03/1.27 = 2.4	4.08/3.36 = 1.2	2.12/1.27 = 1.7	4.08/1.27 = 3.2
Apparent Viscosity (poise), @ 10/sec	11.7/4.05 = 2.9	16.1/2.52 = 6.4	29.2/5.18 = 5.6	29.2/2.52 = 11.6
FNSD (dyn/sq cm), @ 398/sec	6800/1420 = 4.8	6660/100 = 67	900K/9400 = 96	900K/100 = 9000
<u>Updated:</u> LVN (dL/g)	3.03/1.42 = 2.1	4.08/3.36 = 1.2	2.48/1.27 = 2.0	4.08/1.27 = 3.2
Apparent Viscosity (poise), @ 10/sec	14.2/4.05 = 3.5	16.1/2.21 = 7.3	68.7/3.93 = 17.5	68.7/2.21 = 31.1
FNSD (dyn/sq cm), @ 398/sec	12200/1420 = 8.6	6660/100 = 67	12000K/4000 = 3000	12000K/100 = 120000
* PMMA - poly(MMA); poly(methyl methacrylate) PEA - poly(EA); poly(ethyl acrylate) PBA - poly(BA); poly(butyl acrylate) K - thousands				

INTRODUCTION TO EXTENSIONAL VISCOSITY STUDIES

Preferentially soluble solutions appear to produce anomalously high steady shear mode viscoelasticity as measured by FNSD. Initial studies are reported herein on preferentially soluble solutions and their extensional viscosities. Three studies are included:

- (A) The FNSD vs extensional viscosity correlations on completely soluble (poly(MMA), poly(EA), poly(BA)) polymer solutions,
- (B) The comparison of prototype and commercial versions of the opposed flow extensional viscometer for this same FNSD vs extensional viscosity correlation, and
- (C) The addition of a preferentially soluble polymer solution to the same correlation.

EXPERIMENTATION ON EXTENSIONAL VISCOSITY

Polymer solutions were prepared at a standardized concentration of 4.7 g/dL. The polymer used was Acryloid K125 and the liquids studied were diethyl malonate (DEM), methyl salicylate (MS), triethyl phosphate (TEPO) and tripropyl phosphate (TPPO). Steady mode determinations of FNSD were obtained. Elongational stress determinations of extensional viscosity were obtained, first on the prototype "opposed flow" rheometer and later on the B-site version of the commercial instrument. Measurements are underway to obtain both extensional and shear measurements on specimens from the

identical solution. Typical FNSD values have been substituted at identical concentrations for cases in which measurements are not yet complete.

RESULTS ON EXTENSIONAL VISCOSITY STUDIES

Plots of extensional viscosity data obtained from the prototype (Stanford University, Prof. G. Fuller) and from the commercial β -site instrument (Rheometrics, Model RFX) vs FNSD are shown in Figure 3. The prototype and the commercial solutions were of the same concentration and composition. One can see that the values of extensional viscosity are offset but generally parallel for both the prototype and the commercial elongational rheometer. Additionally, the correlation of extensional viscosity and FNSD, two measures of viscoelastic performance, appeared promising.

Note that the three solutions are conventional, not preferentially soluble, solutions. An example of a preferentially soluble solution (TPPO) with anomalously high FNSD is plotted on Figure 4 with the three previous solutions. One can again observe the extraordinarily high FNSD, seen on previous plots for TPPO. One can also observe that K125/TPPO also shows anomalously high extensional viscosity. The extension of the three point correlation from lower values is also shown, and the preliminary results suggest the extensional viscosity is proportionally lower than FNSD, although still anomalously high.

DISCUSSION

One can envision other copolymers with the capability to more easily formulate preferentially soluble polymer solutions. These would be a commercial series with systematically decreasing contents of one comonomer: e.g. the butadiene-acrylonitrile series, the styrene-butadiene series and the vinylchloride-vinylacetate series. These polymers have the disadvantage of being commercially available only at low molecular weight.

An example of a critical application of this investigation concerns the question of what type of model solution (simulant) provides an accurate solution for thickened GD. The answer could be a solution with similarly anomalously high viscoelasticity due to preferential solubility (e.g. thickened TPPO) or a normal, fully soluble solution (thickened DEM, etc). Other choices might also be devised such as fully soluble solutions with polymer concentration increased to provide viscoelastic properties equivalent to thickened GD. The improved prediction of liquid structures yielding preferentially soluble solutions demonstrates that these solutions are not that unusual and argues for development of equivalent model solutions. Conversely, the presence of several highly polar organophosphorus liquids in the poly(MMA) soluble class (Table 4) argues that anomalously high viscoelasticity is not a necessary property of methacrylate-organophosphorus systems.

CONCLUSIONS

The correlation of FNSD with extensional viscosity is promising and will be pursued.

Nine polymer solutions with anomalously high FNSD (and probably extensional viscosity) have been formulated.

PCPD overlap regions and substituent effects on dispersion parameters have improved the prediction of preferentially soluble polymer-liquid systems with the extraordinarily high viscoelastic properties (per unit concentration in the semi-dilute regime).

TABLE 4

Names and Structures for GD and a Series of Aprotic Model Liquids in the "Solvent w/0.82+" Solvent Set	Structure:*			
	$\begin{array}{c} R'' \\ \\ R' - P = X \\ \\ R \end{array}$			
Liquid Name, Code	R	R'	R''	X
Phosphonates:				
Diethyl methylphosphonate, DEMP	OEt	OEt	Me	O
Diethyl ethylphosphonate, DEEP	OEt	OEt	Et	O
Diethyl propylphosphonate, DEPP	OEt	OEt	Pr	O
Diethyl (ethylthiomethyl)phosphonate, DEETMP	OEt	OEt	MeSEt	O
Diethyl 2-bromoethylphosphonate, DEBrEP	OEt	OEt	EtBr	O
Diethyl chloromethylphosphonate, DECMP	OEt	OEt	MeCl	O
Dipropyl chloromethylphosphonate, DPCMP	OPr	OPr	MeCl	O
Diisopropyl methylphosphonate, DIPrMP	OIPr	OIPr	Me	O
Phosphates:				
Triethyl phosphate, TEPO	OEt	OEt	OEt	O
* Cl - chlorine; Br - bromine; O - oxygen; S - sulfur; Me - methyl; Et - ethyl; Pr -propyl; IPr - isopropyl				

REFERENCES

1. Shuely, Wendel J., and Ince, Brian S., CRDEC-SP-034, Correlation of Type and Degree of Polymer-Solvent Interactions with Several Rheological Properties of Polymer Solutions, Proceedings of the 1990 U.S. Army Chemical Research, Development and Engineering Center Scientific Conference on Chemical Defense Research, 13-16 November 1990, UNCLASSIFIED Report.
2. Shuely, Wendel J., and Ince, Brian S., "Rheological Properties of High-Molecular-Weight Poly[(methyl methacrylate)-co-ethylacrylate-co-butylacrylate] Solutions", in Polymers as Rheology Modifiers, ACS Symposium Series 462, edited by Schulz, Donald N., and Glass, J. Edward, 1991.

FIGURE 1

FNSD 0398 1/sec vs LUN @ 25 Deg C for a
(X 1E6) Series of Solvents with Acryloid K125

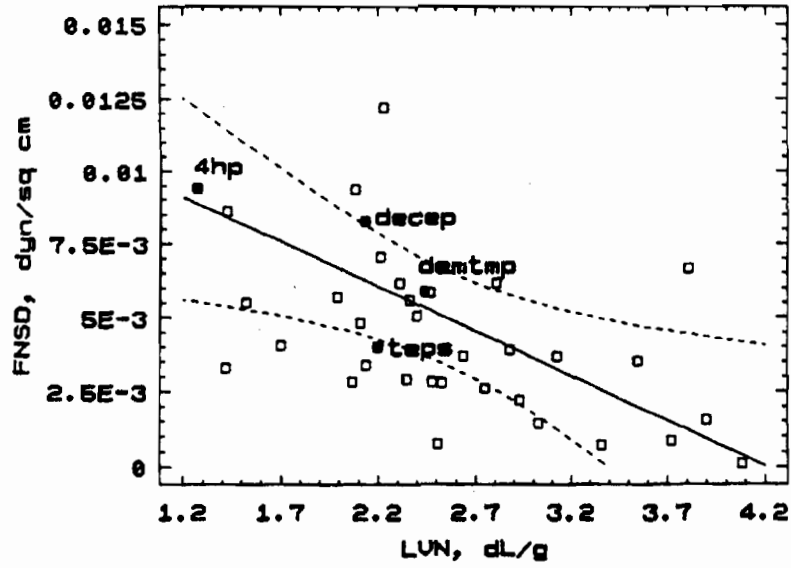


FIGURE 2

FNSD 0398 1/sec vs LUN @ 25 Deg C for a
(X 1E6) Series of Solvents with Acryloid K125

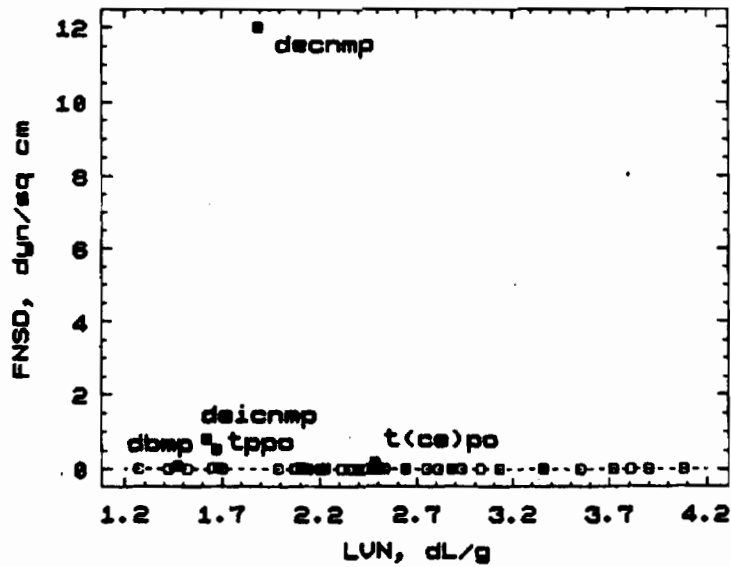


FIGURE 3

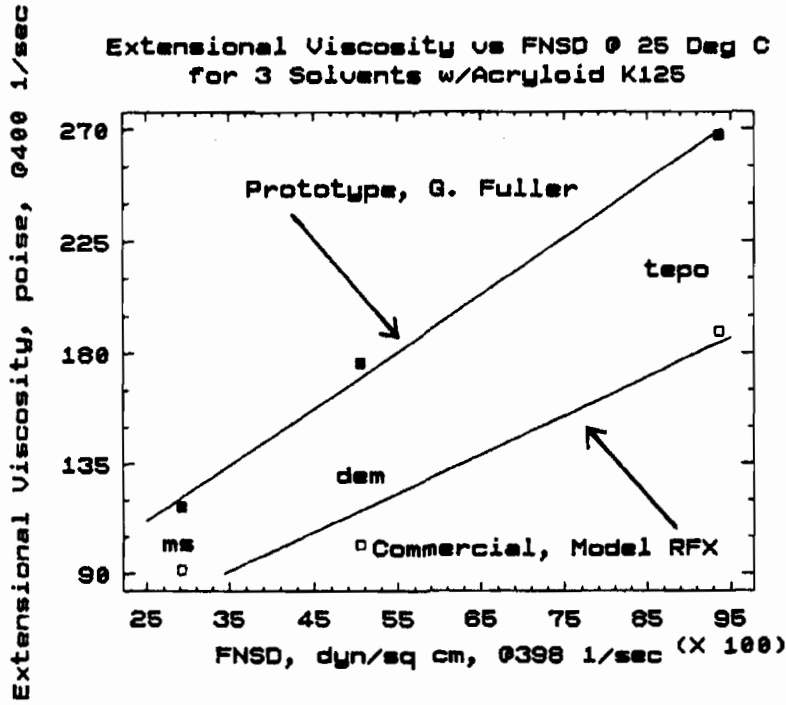
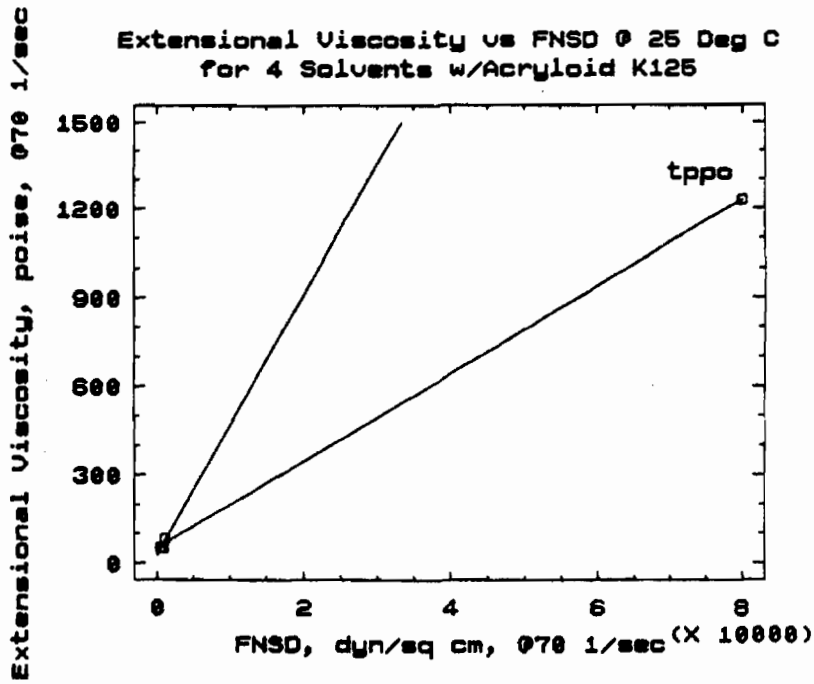


FIGURE 4



MAGNET ENHANCED OPTICAL FALLING NEEDLE/SPHERE RHEOMETER

Benjamin Chu and Jian Wang
Department of Chemistry, State University of New York at Stony
Brook, Stony Brook, NY 11794-3400

and

Wendel J. Shuely
Chemical Research, Development and Engineering Center
Aberdeen Proving Ground, MD 21010-5423

ABSTRACT

A magnet enhanced optical falling needle/sphere rheometer controlled with a PC computer has been developed on the basis of principles of falling needle/sphere viscometers and magnetorheometers. Such an arrangement has enabled this device to exhibit some unique features in addition to all the features of both falling needle/sphere viscometers and magnetorheometers. The crucial achievement of this device would lie on the enhanced ability of measuring the rheological properties of fluids in a remarkably wide viscosity range from a few centipoise to 10^7 centipoise (could be up to 10^{10} centipoise, which is beyond the upper limit of most commercial rheometers). Moreover, it provides the capability of measuring the viscosity of fluids at different shear rates in a small sealed glass vial over a large viscosity range.

INTRODUCTION

Falling ball viscometers (FBVs) and falling needle viscometers (FNVs) have been used widely to determine the viscosity of Newtonian fluids because of their fast and simple operations.¹ The theoretical expression for a falling ball in an unbounded Newtonian fluid has the form

$$\eta = \frac{d^2 g (\rho_s - \rho_l)}{18 U_s} = K_s \frac{\rho_s - \rho_l}{U_s} \quad (1)$$

where g is the acceleration of gravity, d is the ball diameter, $K_b (= d^2g/18)$ is a ball constant, ρ_s and ρ_l are the density, respectively, of the ball and of the liquid and U_∞ is the terminal velocity. For a Newtonian fluid, a remarkably simple relation of the fluid dynamic viscosity for a falling needle with the measured terminal velocity and the system geometry, similar to the falling ball, is given by²

$$\eta = \frac{g d^2 (\rho_s - \rho_l)}{8 U_\infty} [-(1 + \ln k)] = K_n \frac{\rho_s - \rho_l}{U_\infty}, \quad k < 0.033 \quad (2)$$

where $k (= d/D)$ is the ratio of the needle diameter(d) to cylindrical container diameter(D) and $K_n (= gd^2/8[-(1 + \ln k)])$ is a needle constant. By measuring a set of fluids of known viscosity, one can calibrate the constants K_b and K_n .

Both FBVs and FNVs are usually restricted to fluids of intermediate viscosity due to the poor measurement accuracy for low viscosity fluids or unacceptably high shear rates or long measuring time for high viscosity fluids. For example, if a stainless steel ball with a diameter of 3.2 mm takes 36.44 seconds to fall through 25 mm in a viscosity standard of 3.07×10^4 cP, it would take about 115 days to fall through the same distance in a fluid with a viscosity of $\sim 10^{10}$ cP. It would still need 29 days to make one measurement according to eq.(1) even if we were to enlarge the ball diameter to 6.4 mm.

In this article, we present a newly developed magnet enhanced optical falling needle/sphere rheometer, which could increase the viscosity range (could be up to 10^{10} centipoise) and render some excellent features not available in existing falling needle/sphere viscometers.

PRINCIPLE OF OPERATION

Figure 1 shows a schematic block diagram of the magnet enhanced optical falling needle rheometer (MOFNRR) (hereafter, we will only refer to the falling needle for simplicity). A 5 mW laser beam expanded by a lens ($f=50$ mm) illuminates the needle and projects an image of the needle on the position detector. The needle can be levitated by means of an electromagnetic coil, which produces the necessary magnetic force for keeping the needle in a null position as shown in Fig.1. The current flowing through the coil is controlled by a PC-286 computer according to the feedback information from the detector via the current amplifier-analog/digital board system.³ The glass sample cell mounted on a translational stage can be moved vertically by using a stepping motor. After the needle has been levitated to a preassigned null position, the current to the electromagnetic coil is shut off, the sample cell is moved upward at a

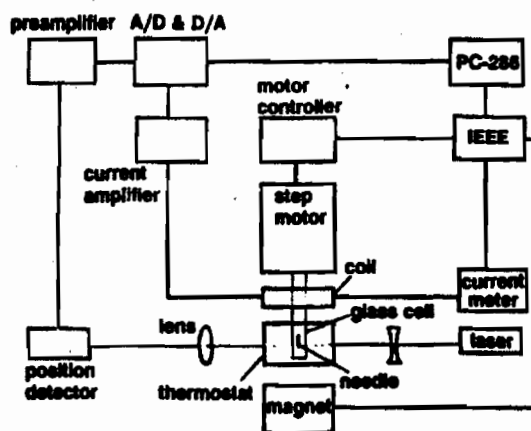


Figure 1. Schematic block diagram of the magnet enhanced optical falling needle rheometer. The DC/12 V magnet (Eriez, SL-4) has a maximum breakaway capacity of 750 lb and 38 Watts output.

certain speed over a distance of Δh (say, $20\mu\text{m}$), and at the same time, the lower electromagnet, which is located at ~ 20 mm below the sample cell is switched on. The needle position change under this field with respect to the null position is then recorded as a function of time. When the needle falls back to the null position, the sample cell will be moved upward by Δh again. In such a way, each run has a number of cycles over which the average falling velocity of the needle and its standard deviation can be calculated.

For Newtonian fluids, the needle velocity for each cycle can be precisely determined. As shown in Fig. 2, from t_0 to t_1 the sample cell is moved by a distance of Δh (controlled to $0.1\mu\text{m}$) while the needle falls down by a distance of Δh_1 . From t_1 to t_2 , the needle travels through a distance of Δh_2 , back to the null position, while the sample cell is in a rest status. For this cycle, the average needle velocity can be calculated as

$$U = \frac{\Delta h_1 + \Delta h_2}{(t_1 - t_0) + (t_2 - t_1)} = \frac{\Delta h}{t_2 - t_0} \quad (3)$$

For viscoelastic fluids, the needle velocity could be determined at each time t' ($t_0 < t' < t_2$) by calibrating the detector response with respect to the needle displacement, whereby we can detect whether the needle has reached the terminal velocity or the time it would take the needle to reach the terminal velocity as well as the time dependence of the velocity after the initial perturbation.

SAMPLE MATERIALS

The viscosity standards, purchased from Polyscience, Inc. and Cannon Instrument Co., were Newtonian fluids having a viscosity range from 10 to 5.2×10^6 cP at room temperature. The non-Newtonian liquid we used was a concentrated solution of a random copolymer, poly(isobutyl methacrylate-tert-butylaminoethyl methacrylate)(poly(iBMA-tBAEMA), in N,N-dimethylacetamide(DMAA) at a concentration of $C=0.16$ g/mL, where molecular entanglement and aggregations occurred. The weight-average molecular weight of poly(iBMA-tBAEMA) was 2.4×10^6 g/mole and the polydispersity index was large.⁴ All the

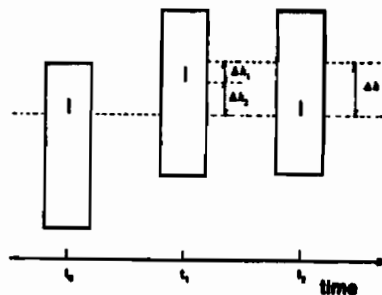


Figure 2. Principle of the optical falling needle experiment: Δh_1 is the distance the falling needle travels with respect to the medium during the time interval $(t_1 - t_0)$; Δh_2 is the distance the falling needle travels back to the null position with respect to the position detector in the time interval $(t_2 - t_1)$. $\Delta h (= \Delta h_1 + \Delta h_2)$ is the distance a sample cell moves during each cycle and is controlled by using a stepping motor to $0.1\mu\text{m}$ precision. t_0 is the starting time when the current to magnetic coil is shut off and the translational stage starts to move; t_1 is the time when the translational stage has moved over a distance Δh ; t_2 is the time when the needle returns to its null position. The average velocity of the falling needle can be calculated by $U = \Delta h / (t_2 - t_0)$.

viscosity measurements were performed at room temperature($25 \pm 0.5^\circ\text{C}$).

DISPLACEMENT DISTANCE RESOLUTION

The position sensitive detector(Silicon Detector Co., SD-380-23-21-051) in our MOFNR was equipped with a home-made preamplifier and a 12 bit/10 V analog-digital convertor which allowed the computer to read the voltage output from the detector with a precision of 2.5 mV. As the needle image was 9 times the needle size of 1 mm diameter, a needle position change of 1 μm could yield a signal output of 13.1 mV. The fluctuations of the detector signal caused mainly by the system electron noise was about 10 mV which corresponded to a needle displacement of 0.76 μm .

The translational stage-stepping motor assembly(Klinger, UT 100.50), which was employed to displace the sample cell had a step length of 0.1 μm and was controlled by a motor controller(Klinger, MC-4/MD-4) which possessed a rate range from 1 to 4000 step per second. If we consider all the errors involved in electronic interfaces and mechanical movements, a resolution of 1 μm could be guaranteed throughout the measurement.

NEWTONIAN FLUID MEASUREMENT

Figure 3 shows a typical measurement of a Newtonian viscosity standard of the highest viscosity we have found at room temperatures under natural gravity field by using a needle of 2.5 mm in diameter and 13 mm in length. By choosing a displacement distance of 10 μm , we were able to make a number of measurements over 1 minute. If we had observed the needle falling through a distance of 20 mm visually, it would have taken us *ca.* 2 hours to complete only one measurement, or *ca.* 10 hours to complete 5 measurements. If we consider a fluid of 4-order higher viscosity than that of this sample, the use of a conventional falling needle viscometer requiring an experimental time period of thousands of hours would be meaningless, while the use of the MOFNR requiring an experimental time period of only hours should be remarkably meaningful.

Figure 4 shows the linear relationship between the viscosity and the reciprocal of the needle velocity(U_∞) corrected by buoyancy which is proportional to the current(I) in the upper electromagnetic coil for a set of viscosity standards measured using a needle of 16 mm in length and 1 mm in diameter under the natural gravity field. The travel distance Δh of the sample cell for each cycle varied from 800 to 20 μm with the liquids becoming more viscous. The standard deviation for each sample measurement was $\sim 1\%$. It is important to emphasize here that a single needle could cover quite a few orders of the fluid viscosity. As shown in Fig.4, the needle has spanned a viscosity range of 4 orders of magnitude(from 10^0 to 1×10^4 cP). This large dynamic range could be considered as another important advantage over many existing viscometers. The Δh value could, in principle, be chosen arbitrarily as long as it leaves an elapsed time(~ 0.5 sec here) which is sufficiently large, allowing the computer to complete all communications with each device in one cycle. It was also tested that the choice of Δh did not present an appreciable effect on both the average needle velocity and the experimental precision. A typical measurement of a viscosity standard of 5910 cP under an enhanced gravity field with a fixed magnet voltage of 6 V is

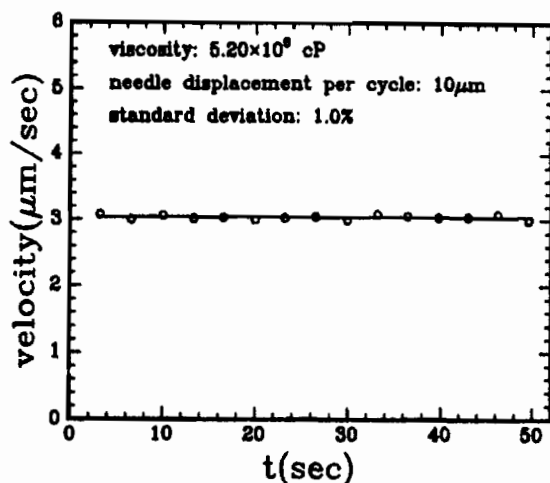


Figure 3. Velocity of a falling needle in a viscosity standard of 5.2×10^6 cP under natural gravity field. The travel distance was $10 \mu\text{m}$ per cycle and the motor speed was $200 \mu\text{m}/\text{sec}$.

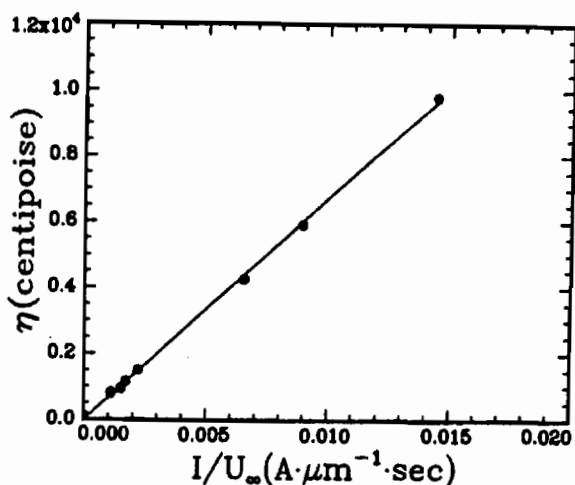


Figure 4. Plot of viscosity against the reciprocal of the velocity of the falling needle corrected by buoyancy in a set of viscosity standards under natural gravity field. The travel distance varied from $800 \mu\text{m}$ to $20 \mu\text{m}$ per cycle with the sample becoming more viscous.

shown in Fig.5 where the inset is a linear curve of viscosity versus the reciprocal of the needle velocity. As the extra magnetic force below was acting on the needle, the needle fell down faster. In our present arrangement with a magnet at full power (12 V), the velocity of the needle, which was 1 mm in diameter and 16 mm in length with an insert of a 3 mm long magnetic bar, was increased by one order of magnitude. If a larger size needle and a smaller clearance distance between the magnet and the needle were employed, a stronger effect on the needle velocity could be expected. The addition of an artificial magnetic field is useful, in particular, in the determination of rheological properties of polymer melts.

NON-NEWTONIAN FLUID MEASUREMENT

Another important feature of MOFNR is the ease of performing the rheological measurements, such as the shear rate dependent viscosity and the zero shear rate viscosity. By changing the magnetic field strength, the gravity field could be influenced and thus the velocity of a single needle could be altered. For non-Newtonian fluids, the viscosity is shear rate dependent. A log-log plot of viscosity versus shear rate is called a flow curve. Although the measurement of viscous properties of non-Newtonian fluids is a difficult experiment for a FNV, a successful method concerning the determination of the flow curves has been developed.²

In our MOFNR experiments, we changed the shear rate by changing the electromagnet voltage, i.e., we changed the value of the gravity acceleration constant instead of the value of needle density. By following the approach described in reference 2, we estimated the flow index and thus determined the flow curves. Figure 6 shows a flow curve of a random copolymer solution, poly(iBMA-tBAEMA) in DMAA at a concentration of 0.16 g/mL. The inset is the log-log plot of the acceleration of gravity versus terminal

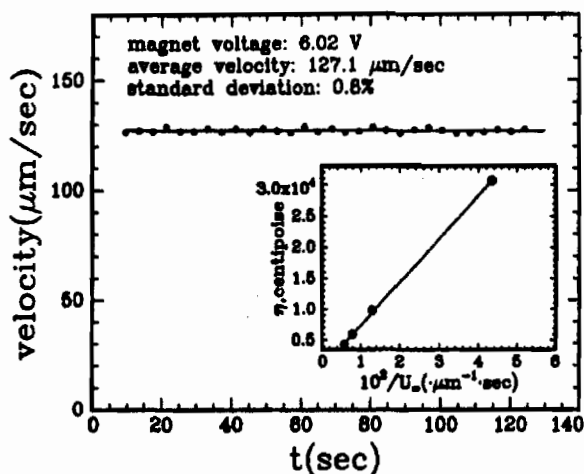


Figure 5. Velocity of the falling needle for each movement cycle under a fixed magnetic field in a viscosity standard of 5910 centipoise. The travel distance was 500 μm per cycle and the motor speed was 400 $\mu\text{m}/\text{sec}$. The inset is the plot of viscosity against the reciprocal of the velocity of the falling needle in a set of viscosity standards under this fixed magnetic field.

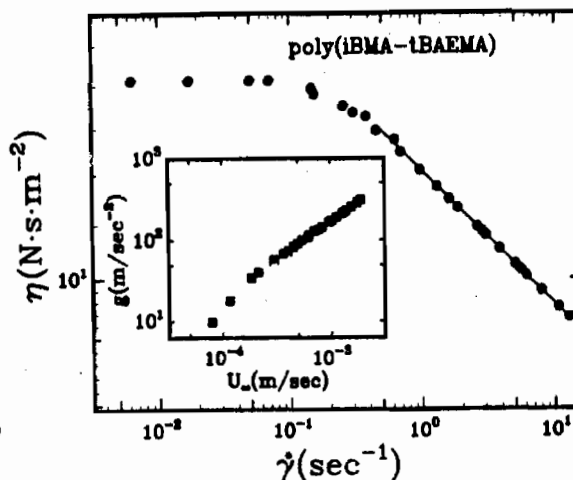


Figure 6. Flow curve of a random copolymer, poly(iBMA-tBAEMA), in DMAA at $C=0.16 \text{ g/mL}$. The system parameters are $k=d/D=0.1$, $R=0.005 \text{ m}$, $(\rho_s-\rho_l)=105.7, \text{ kg/m}^3$. The inset is the log-log plot of g versus terminal velocity. From the slope of the straight line section, the flow index n was estimated to be 0.91.

velocity, which allowed us to estimate the flow index². It should be noted that the strength of the MOFNR is in the lower shear rate region for polymer melts or the likes. For this reason, the MOFNR is particularly suitable for the determination of the zero shear rate viscosity.

VISCOELASTIC PROPERTY MEASUREMENT

The time dependent elastic modulus $G(t)$ can be related to the time dependent dynamic viscosity $\eta(t)$, which is measurable using the present instrument

$$\eta(t) = \int_0^t G(\tau) d\tau \quad (4)$$

If the elastic modulus can be described by a Maxwell model⁵ with a single relaxation time and a constant shear rate is applied to the needle, we have

$$\eta(t) = \int_0^t G(\tau) d\tau = \eta_\infty [1 - \exp(-t / \tau_r)] \quad (5)$$

where $\eta_\infty = G_0\tau_r$. Thus the relaxation time can be obtained by plotting a half-log plot of $\eta(t)$ against t . It is interesting to note that the MOFNR could work in different versions for different purposes. These functions can be implemented by simply using different softwares.

For example, the needle can be fixed in space while the medium is moving(i.e., magnetic needle rheometer); and the needle can be oscillated sinusoidally around the null position by an AC current coil(under construction) for dynamic viscoelastic measurements.

CONCLUSIONS

A magnet enhanced optical falling needle/sphere rheometer has been developed on the basis of principles of falling needle/sphere viscometers and magnetorheometers. This device has demonstrated some excellent features which could not be found in a single existing rheometer. The important advantages of this instrument over existing falling needle/sphere viscometers are as follows: (1) An extremely large viscosity range from the usual solvent viscosity(say, ~ 1.0 cP) to that of polymer melts(say, 10^{10} cP) is available with an experimental precision of $< 1\%$; (2) the measurement time could be reduced by about 4 orders of magnitude(e.g., from hours to seconds for a high viscosity fluid); (3) one single needle/sphere could cover a few orders of the viscosity range and two needles with appropriate densities could cover the whole viscosity range($1 \text{ cP} \leq \eta \leq 10^{10} \text{ cP}$); (4) only a small amount (~ 4 mL) of sample is needed; (5) the sample chamber can be sealed hermetically and is suitable for toxic fluids; (6) the instrument permits measurements of the shear rate dependence of viscosity using a single needle/sphere; (7) for non-Newtonian fluids, the viscoelastic behavior could be measured.

ACKNOWLEDGEMENT

We greatly acknowledge the U. S. Army Research Office(DAALO391G0040) for the support of this research and thank Professor Thomas F. Irvine, Jr. for several helpful discussions on non-Newtonian fluids and FNVs.

REFERENCES

- [1] Park, N. A. and Irvine, T. F., Jr., *Waerme-Stoffuebertrag.*, 1984, 18, 201.
- [2] Park, N. A., Ph.D. thesis, Mechanical Engineering Dept., State Univ. of New York, Stony Brook, NY, 1984.
- [3] Hilfiker, R., and Chu, B. and Shook, J., *Rev. Sci. Instrum.*, 1989, 60, 760, and references therein.
- [4] Chu, B., Wang, J. and Shuely, W. J., *Macromolecules*, 1990, 23, 2252.
- [5] Ferry, J. D., "*Viscoelastic Properties of Polymers*"(Wiley, New York, 1980).

BLANK

IX. MATERIALS

NOTE: Papers with the following titles were presented at the Conference but are not included in this document:

Simulation of Permeation from a Deposited Droplet

Control Material Formulation Development for MIL-STD-282 Static Diffusion Testing

Novel Elastomeric Materials for Chemical Protective Clothing

Chemical Agent Hardness of Transparent Polymers

A Preliminary Evaluation of Diamond-Like Carbon Coated Polycarbonate

BLANK

EQUILIBRIUM SOLUBILITY AND DIFFUSION COEFFICIENT MEASUREMENTS AND CORRELATIONS WITH PREDICTIVE PROPERTIES

Brian S. Ince and Wendel J. Shuely
U.S. Army Chemical Research, Development and Engineering Center
Aberdeen Proving Ground, MD 21010-5423

ABSTRACT

An experimental method for the measurement of equilibrium solubility, fractional extraction, and diffusion coefficient has been developed into a standardized test, specifically to provide rigorous data for a computerized materials database. Results on the further evaluation and validation of the method are provided. Investigations are underway that anticipate the future exploitation of databases to derive generalizations and trends on material-contaminant compatibility. Progress is reported on correlations to predict solubility and diffusion (Fickian and concentration-dependent) in materials and to rank material and liquid interactions.

INTRODUCTION

The development of standardized methods is critical to establishing a computerized knowledge base for chemically resistant and protective materials. Deviations from standardized methods prevent the use of computerized search-compare-rank capabilities of relational databases.

The standardization for measurements with toxic liquids and their interaction with materials is especially important since deviations from standard procedures are unavoidable for safety reasons. Standardized modifications are required that minimize toxic liquid volume and the manipulation of contaminated specimens; since every investigator could modify the procedures in a unique way to provide safe experimentation, non-comparable data could result. Further, once standardized methods and databases are established, the overall database contents can be analyzed for global trends in polymer-liquid (agent, decontaminant) interaction based on thermodynamic and transport principles.

The scope of the research presented here includes two areas. The first area includes the completion of validation studies on the experimental method that provide determination of the precision of the thermodynamic property, equilibrium solubility and the kinetic property, diffusion coefficient. These measurements were performed on one of four possible polymer-liquid systems based on contribution of volatility and sorption level to error. Thermoplastic fluoropolymers with low anticipated sorption were employed. These polymers were contributed by a TACOM/MTL (Dr. A. F. Wilde) program with interest in the chemical resistance ranking of the six materials.

The second area consists of initiating exploratory data analysis of the limited data set obtained as part of the method development.

Emphasized at this time are correlations of liquid-polymer sorption with phase diagram predictions and rationalization of diffusion coefficient trends based on molecular dimensions.

EXPERIMENTATION

PROCEDURES

The experimental method is documented in previous publications¹. These can be reviewed by surveying:

1. The diagram of weight change vs time during various phases of the experiment, noting points of equilibrium solubility and diffusion coefficient measurement.
2. The minimization of toxic liquid volume by use of smaller, 12 mm diameter (nominally dime sized) specimens.
3. The specimen mounting on a microbalance holder for continuous, unattended desorption measurements (requiring only two manipulations of a toxic specimen).

MATERIALS

The materials employed (Table 1) in the determination of precision consist of six thermoplastic fluoropolymers (Dr. A. F. Wilde, TACOM/MTL project).

TABLE 1

Fluoropolymer Classes, Structure Codes, Trademarks, Sources/Lots And Nominal Sample Thicknesses				
Fluoropolymer Class	Structure Code	Trademark	Source/Lot	Nominal Thickness
Perfluoroalkoxy resin	PFA	Teflon PFA	Du Pont/ 2000LP	0.018"
Poly(tetrafluoroethylene-co-hexafluoropropylene)	FEP	Teflon FEP	Du Pont/ 2000A	0.021"
Poly(ethylene-co-tetrafluoroethylene)	PETFE	Tefzel	Du Pont/ 2000LZ	0.019"
Poly(chlorotrifluoroethylene)	PCTFE	Aclar	Allied/ 22C	0.011"
Poly(chlorotrifluoroethylene)	PCTFE	Kel-F	3M Co./ 81	0.041"
Poly(chlorotrifluoroethylene)	PCTFE	Kel-F (heat treated)	3M Co./ 81	0.044"

RESULTS

METHOD PRECISION DETERMINATION

The evaluation of the contribution of liquid volatility and sorption level to errors in diffusion coefficient and equilibrium solubility are summarized in Table 2. The columns represent the level of polymer sorption (column 1) and the relative liquid volatilities of "low" and "high" (columns 2-3). The rows show the relative liquid sorption levels of "low" (row 1) and "high" (row 2). Each of the four elements of the matrix has entries that give general error levels expected for each system of that

volatility-sorption level. Examples of typical polymer-liquid systems for each case are also noted in each matrix element.

TABLE 2

Equilibrium Solubility and Diffusion Coefficient Relative Error Predicted For Polymer-Liquid Systems Over A Spectrum Of Liquid Volatility and Polymer Sorption		
Polymer Sorption:	Liquid Volatility: Low	Liquid Volatility: High
Low (Fickian)	Equilibrium Solubility: Med Diffusion Coefficient: Low Polymer-Liquid: GD/Fluorel*	Equilibrium Solubility: High Diffusion Coefficient: Med Polymer-Liquid: GB/ Thermoplastic Fluoropolymer
High	Equilibrium Solubility: Low Diffusion Coefficient: Med Polymer-Liquid: CEES*/Butyl	Equilibrium Solubility: Med Diffusion Coefficient: Low Polymer-Liquid: TCE*/Neoprene
* Fluorel - Similar to Viton A, Du Pont CEES - 2-chloroethyl ethyldisulfide TCE - Tetrachloroethylene		

The results of equilibrium solubility determinations for polymer-liquid systems hypothesized to be low sorbing are listed in Table 3. The 6 thermoplastic fluoropolymer trademarks are listed in column 1, followed by single repetition equilibrium solubility values for GD and HD (columns 2 and 4). Also included for comparison are candidate test simulant values provided by MTL investigators (Dr. A. F. Wilde).

TABLE 3

Equilibrium Solubility (25°C) Of Fluoropolymers with GD, HD and Two Of Their Simulants, DIMP and DCP				
Fluoropolymer Trademark, Lot	Equilibrium Solubility (Max % Mass Change):			
	GD	DIMP*	HD	DCP*
Teflon PFA, 2000LP	0.17	0.2	0.10	1.0
Teflon FEP, 2000A	0.15	0.1	0.49	0.6
Tefzel, 2000LZ	0.82	0.4	0.10	1.0
Aclar, 22C	0.13	≥8.1 @ 31 days	0.32	1.1
Kel-F, 81	0.28	0.27	0.64	-0.025
Kel-F, 81 (heat treated)	0.28 #	0.20	0.17	-0.02
* DIMP - Diisopropyl methylphosphonate DCP - 1,5-dichloropentane # Mean of 3 experimental runs				

All equilibrium solubility mass gain percentage values are less than 1% for all 6 thermoplastic fluoropolymers with GD and HD. This indicates that these materials have excellent resistance. Additionally, for the purpose of this study, these values would classify these thermoplastic fluoropolymers in the "low sorption" element on Table 2, above; GD and HD would fall into the low volatility and GB into the high volatility

elements. Therefore, these thermoplastic fluoropolymers provide one of the required elements for error classification for method validation studies of precision and accuracy (see Table 4).

A summary (Table 4) is shown of the precision as 95% confidence intervals for various classes of polymer/liquid error systems. Column 1 shows the polymer/solvent pair, column 2 shows the accuracy as a percentage of a comparable macrobalance value. Columns 3-4 show the mean values for equilibrium solubility and diffusion coefficient, and columns 5-6 show the 95% confidence for equilibrium solubility and diffusion coefficient. All the errors are reasonably low. The GD-thermoplastic fluoropolymer (GD/Kel-F 81) values should be noted for the low absolute error (0.74%), appropriate for the almost zero sorption level (0.28%). The relative error is, therefore, enormous (260%), as a consequence, and is an artifact of the ultra-low sorption value. Several other GD and HD equilibrium solubility precision levels are being determined and can be added to clarify the precision of very low sorbing systems.

TABLE 4

Accuracy (Relative to a Macrobalance) and Precision (Mean and 95% Confidence Interval, (CI)) of Equilibrium Solubility (EqS) and Diffusion Coefficient (DC) for A Series of Polymer/Solvent Pairs, Showing the Relative Error in Parentheses					
Polymer/Solvent*	Accuracy	Mean EqS, %	Mean DC, cm ² /sec	95% CI for EqS, %	95% CI for DC, cm ² /sec
Butyl/TCE	+1.85%	302.5	9.63E-08	10.18 (3.4%)	0.67E-08 (7.0%)
Butyl/CEESS	+1.23%	41.2	1.25E-08	1.31 (3.2%)	0.03E-08 (2.0%)
Neoprene/TCE	+2.76%	223.6	14.6E-08	5.14 (2.3%)	2.37E-08 (16.2%)
Kel-F, 81/GD, heat treated	ND	0.28	ND	0.74 (260%)	ND
* TCE - Tetrachloroethylene CEESS - 2-chloroethyl ethyldisulfide					

EXPLORATORY DATA ANALYSIS FOR SOLUBILITY AND DIFFUSION EFFECTS

In general, the research study is limited to the development of new experimental methods. Since the experimental method will be used to measure equilibrium solubility and diffusion coefficient values for a materials database, it is of interest to perform exploratory data analysis using the developmental data sets generated during method development to preview potential strategies for comprehensive evaluation of the overall database. The data sets were derived from experimental designs targeted at determining the effects of volatility and non-Fickian sorption levels on measurement errors, therefore, most data sets are incomplete with respect to a complete solubility or diffusion coefficient correlation.

EQUILIBRIUM SOLUBILITY CORRELATIONS WITH PHASE DIAGRAM PREDICTIONS

Rationale

Polymer Cohesion Parameter Diagrams (PCPD) have been extensively used in our research on polymer-liquid interactions². The simplified concept can be summarized as follows: Liquids with known solvent parameter

coordinates are employed to determine solubility as "miscibility-in-all-proportion" or sorption weight fractions. These coordinates are plotted to define regions of predicted solubility-insolubility or various swell regions for cross-linked polymers. As shown in the first example, Figure 1, the x-axis is total hildebrand solubility parameter and the y-axis is hydrogen bond index (from IR bond shifts; Crowley Index). The outer region represents areas of predicted insolubility. The boundaries define the soluble coordinates within the phase diagram.

The solvent parameter values for GD and HD have been determined for several systems of PCPD. The appropriate solvent parameters are plotted on Figure 1, for poly(isobutylene-co-isoprene), (butyl rubber). These predictions can then be compared with our equilibrium solubility measurements, employing the new standardized method. To allow comparisons, conversions were calculated between weight and volume fractions³ and different cross-link densities were scaled and normalized by referencing to common maximal sorbing calibration solvents⁴.

The scaling and normalizing is shown in Table 5. Column 1 shows the elastomer⁵ and column 2 shows the maximal solvent. Columns 3-5 show the change in volume-percent for each polymer/liquid pair, using three different data sources (Smithers/Beerbower/Exxon). Columns 6-7 show the ratios of the Smithers and the Exxon⁶ data respectively, to the Beerbower⁷ data. Beerbower was chosen as the denominator since it was the only source which contained data for all six elastomers. Note that a secondary solvent had to be selected for the Nitrile, Neoprene and SBR elastomers in order to compare all three data sources.

TABLE 5

Comparison of Standard Elastomer Crosslink Density for a Series of Standard Elastomer Types From Three Sources Using Maximal Sorbing Solvent Data						
Elastomer Type	Maximal Solvent#	Change in Volume Percent Swell:			Ratios of:	
		Smithers	Beerbower	Exxon	S/B	E/B
Butyl	TCE	218	197	220	1.11	1.12
Fluorel*	TBPO	360	430	ND	0.84	ND
Silicone	C-Tet	247	103	ND	2.40	ND
Nitrile	T-Cl-Et Benz	202 ND	305 195	ND 216	0.66 ND	ND 1.11
Neoprene	T-Cl-Et TCE	193 146	193 150	ND 148	1.00 0.97	ND 0.99
SBR	T-Cl-Et TCE	171 ND	205 187	ND 204	0.83 ND	ND 1.09
* Similar to Viton A, Du Pont. # TCE Tetrachloroethylene TBPO Tributyl phosphate C-Tet Carbon tetrachloride T-Cl-Et Tetrachloroethane Benz Benzaldehyde						

For butyl rubber (Figure 1), HD is predicted to be in the non-swell region and was measured to be ca. 6.5% volume swell, in the non-swell region. GD is predicted to be at ca. the 50% volume swell region and was measured at 6.8% volume swell, i.e., prediction should be in the non-swell

region. Similar predictions/experimental determinations were performed for five other polymers with GD and HD. These comparisons of predicted versus measured equilibrium solubility are summarized in Table 6. Column 1 lists the elastomer and column 2 shows the liquid. Column 3 shows the predicted region of the volume-percent swell map and column 4 shows the experimental change in volume-percent swell converted from percent weight-gain data. Column 5 describes the agreement/disagreement of the experimental data (column 4) with the predicted (column 3). Overall, HD predictions were correct in 5 of 5 polymers completed to date. GD predictions were correct in 3 of 6 polymers measured to date. Note, in some cases the availability of a PCPD is limiting and in other cases, the availability of measurements is limiting with respect to allowing comparisons.

TABLE 6

Comparison of PCPD Predictions with Sorption Results Based on Scaling of Elastomer Crosslink Density				
Elastomer Type	Liquid	Volume % Region of Swell Map	Experimental Change in Volume %	Agreement
Butyl	GD	ca. 50 non-swell	6.8	No
	HD		6.5	Yes
Fluorel*	GD	> 100 non-swell	378.1	Yes
	HD		4.2	Yes
Silicone	GD	50 - 100 non-swell	11.8	No
	HD		1.7	Yes
Nitrile	GD	50 - 100	109.2	Yes
	HD	> 100	220.4	Yes
Neoprene	GD	> 100	34.9	No
	HD	ca. 50	79.6	Yes
SBR	GD	ca. 50	65.7	Yes

* Similar to Viton A, Du Pont.

Evaluation of Predictions

The incorrect predictions are evaluated as follows. The comparison of 2-dimensional (2D) PCPD predictions with experimental sorption data for GD and HD demonstrates that:

- (1) All the PCPD predictions for HD are generally correct.
 - (2) The PCPD predictions for GD were correct for half the polymers.
- This difference in predictive accuracy can be evaluated by comparing the dipole moments. 2D-PCPD do not include a third polarity axis and, therefore, consist of an averaged value between dipole moments of 0 to 4 or around 2. The HD value of 1.8 is near the mid point of the 3-dimensional (3D) plane used to produce the 2D-PCPD. The GD value of 3.6 is extremely high, typical of organophosphorus compounds. Consequently, the GD coordinates are likely to be outside of the boundaries of the PCPD in the missing polarity axis, but would be projected forward to "within" the PCPD if only two dimensions are employed.

The use of 2D instead of 3D-PCPD leads to a conservative error in the selection of chemically protective or resistant polymer materials. One would predict GD "solubility" and reject a polymer and, therefore, arrive at safe-sided decisions about candidate materials. On the other hand, one would lose the availability of a certain fraction of suitable candidates.

This safe-sided error would not be of consequence unless only a few candidate materials existed for an application.

EXPLORATORY DATA ANALYSIS OF DIFFUSION COEFFICIENT CORRELATIONS TO MOLECULAR DIMENSION PARAMETERS

The evaluation of the diffusion coefficient data begins with the well documented and intuitively reasonable precept that molecules of smaller molecular cross-section (and sometimes smaller volume) diffuse more rapidly through polymeric chains than larger molecules. A second precept would limit this molecular size vs diffusion correlation to low volume fractions of liquid-in-polymer. That is, the polymer-liquid system is not swollen and is "Fickian". The transport of molecules through an even slightly swollen polymer matrix (i.e., over 10%) can be increased significantly.

For the limited data sets, we have plotted either molecular cross-section or molecular volume (x-axis) vs nominal Fickian diffusion coefficient (y-axis). The molecular cross-section was determined employing Stuart space-fill models. The diffusion coefficients were determined by our microbalance method.

The macroscopic trend in these plots should consist of a trend line from high diffusion coefficient, low molecular size to low diffusion coefficient, high molecular size (i.e., from upper left to lower right) as plotted in Figure 2. This trend is usually observed for a homologous series of liquids with similar low solubility and incrementally increasing molecular size via methylene segments. For the diverse set of molecular structure in these studies, this simple trend is rarely observed. About 7 diffusion coefficient vs molecular dimension relationships have been analyzed for about 7 different polymers; one example is provided below.

The plot (Figure 2) displays diffusion coefficient vs molecular volume for butyl rubber. The resulting regression fit is from low size and rapid diffusion to higher volume and slower diffusion, as expected. The individual liquids are noted with their equilibrium solubility values to identify non-Fickian systems and expected deviations from the molecular volume vs diffusion coefficient correlation. One can mark the data points with arrows indicating the direction of an expected Fickian diffusion coefficient, in the absence of high sorption. After the non-Fickian, high sorption adjustments, either GD or HD still appears to be anomalous.

RANKING OF MATERIALS BASED ON GD AND HD RESISTANCE

Although direct material evaluation is not an objective of this methodology study, one can demonstrate the future use of the method by ranking those materials employed in the process of developing the method, and this ranking is shown in Table 7 for the elastomers and fluoropolymers studied. Column 1 shows the material rank based on interaction with GD or HD. Columns 2-3 show the polymer and its equilibrium solubility with GD respectively, and Columns 5-6 show similar information for HD. In this updated summary of our previously reported results, we again show that GD and HD must be considered to have separate and unique interactions with elastomers. Qualitatively, about half sorb more HD than GD (and vice-versa). Quantitatively, no correlations exist.

COMPARISON OF EQUILIBRIUM SOLUBILITY

Dr. A. F. Wilde (MTL) procured specimens of thermoplastic fluoropolymers for TACOM, screened them with diisopropyl methylphosphonate (DIMP) and 1,5-dichloropentane (DCP), and sponsored our CRDEC investigation of diffusion coefficient and equilibrium solubility with GD and HD. The experimental design was configured to yield an equilibrium solubility and diffusion coefficient ranking of the 6 thermoplastic fluoropolymers with GD

and HD (Table 3) and in addition to yield a precision determination on the new experimental method for these anticipated low sorbing materials (Table 4). The studies of precision were combined and coordinated with a TACOM/MTL study of chemically resistant polymers. Fortunately, all of the thermoplastic fluoropolymers were resistant and are excellent candidates. Unfortunately, for the method precision validation study, the diffusion coefficient could not be measured because the low sorption weight was not within the sensitivity of the balance transducer.

TABLE 7

Ranking of Materials Interaction with GD and HD Based On Equilibrium Solubility (EqS), And Comparisons With DIMP and DCP						
Rank	Polymer	EqS, %		Polymer	EqS, %	
		GD	DIMP*		HD	DCP*
1	TFP*	< 1.0	< 1.0	TFP	< 1.0	≤ 1.1
2	Butyl	6.6	> 30	Fluorel*	2.7	14
3	Silicone	24.8	39	Aflas	3.0	6.3
4	Aflas	31.8	23	Silicone	6.1	26
5	Neoprene	41.9	54	EPDM	6.2	ND
6	SBR	48.6	33	Butyl	7.8	34
7	Nitrile	58.0	76	Neoprene	85.5	111
8	Hypalon	70.2	132	Nitrile	146.8	121
9	Fluorel	179.2	204	Hypalon	212.7	440
10	Hydrin	195.7	248	Hydrin	233.2	190
11	Vamac	219.4	195	SBR	ND	117
12	EPDM	ND	ND	Vamac	ND	374

* DIMP - Diisopropyl methylphosphonate
 DCP - 1,5-dichloropentane
 TFP - Thermoplastic Fluoropolymers, see Table 3.
 NOTE Aclar/DIMP value (>8%) in Table 3.
 Fluorel - Similar to Viton A, Du Pont.

The equilibrium solubility values for GD and HD reported here can be compared with candidate simulant values determined by Dr. A. F. Wilde, MTL (Table 7, columns 4 and 7). Since all GD and HD values are below 1%, the simulants can be evaluated by their deviations from predicting this low level of sorption. DIMP sorption in Aclar 22C is >8% vs about 0.13% for GD (Table 3). Therefore, DIMP would not be recommended for ranking all fluoropolymers. Since DIMP-GD values are similar for other fluoropolymers, DIMP might have some useful role for pre-established correlations. DCP and HD correlate well, as expected for polymers in which the lack of the hydrogen bond accepting sulfur atom would not have an influence.

CONCLUSIONS

Equilibrium solubility determinations with HD and GD found six thermoplastic fluoropolymers to sorb less than 1% after several months immersion. Therefore, all six appear to have excellent chemical resistance and can be recommended as candidate surface materials.

Analysis of the errors in the ASTM D471/543 method in terms of liquid volatility-sorption levels is a useful strategy.

The precision of the NBCCS ASTM D471/543 method has been determined for a new class of polymer-liquid volatility-sorption level. This low sorption, low volatility class is represented by the thermoplastic fluoropolymer with GD/HD. The absolute precision was less than $\pm 1\%$ as a 95% confidence interval. The relative error was anomalously high as a consequence of the very low sorption level ($< 0.3\%$). This new precision value, along with other relative precision values of $\pm 2-4\%$ for equilibrium solubility shows that the method has good precision for materials database data generation.

2D-PCPD reliably predict polymer/liquid interactions for liquids with moderate dipole moments of 1-3 debye (e.g. HD).

The use of 2D-PCPD instead of 3D leads to a conservative, safe-sided error in the selection of chemically protective or resistant polymer material for liquids with extremely high polarity (organophosphorus esters, G-agents). If available, 3D-PCPD are preferable.

The exploratory analysis of diffusion coefficient vs molecular dimension correlations suggests that GD and/or HD are not well-behaved with respect to nominal Fickian diffusion coefficient. The expected relationship is established with the addition of further liquids that expand the molecular dimension range. Further comparisons of molecular dimensions with concentration dependent diffusion coefficient or more limited ranges of Fickian diffusion coefficient might provide more promising correlations. In addition, the range might be too limited between the molecular dimensions and/or diffusion coefficients of GD and HD.

Data evaluation of material-agent data in the Chemical Defense Material Database should be pursued against established transport and thermodynamic principles as a validity check on the quality of the database and as a diagnostic tool.

REFERENCES

1. Shuely, Wendel J., and Ince, Brian S., CRDEC-SP-034, Evaluation of Standardized Experimental Methods for Measurement of Equilibrium Solubility and Diffusion Coefficient, Proceedings of the 1990 U.S. Army Chemical Research, Development and Engineering Center Scientific Conference on Chemical Defense Research, 13-16 November 1990, UNCLASSIFIED Report.
2. Shuely, Wendel J., and Ince, Brian S., CRDEC-SP-013, Development of Procedures for The Measurement of Vapor Sorption Followed By Desorption and Comparisons with Polymer Cohesion Parameter and Polymer Coil Expansion Values, Proceedings of the 1988 U.S. Army Chemical Research, Development and Engineering Center Scientific Conference on Chemical Defense Research, 15-18 November 1988, August 1989, UNCLASSIFIED Report.
3. ASTM D471-79, Standard Test Method for Rubber Property - Effect of Liquids.

4. Shuely, Wendel J., and Ince, Brian S., CRDEC-MS-896, Material Research Contributions to the Evaluation of Simulants: Scaling and Normalization to Allow Simulant-Agent Comparisons, Proceedings of the Fifth International Simulant Workshop, CRDEC, 5-7 March 1991, UNCLASSIFIED Report.

5. Wilde, Anthony F., MTL-TR-89-5, Standard Rubbers for Chemical Defence Research, Volume I: Formulation and Properties, January 1989, UNCLASSIFIED Report.

6. EXXON Elastomers Chemical Resistance Handbook, Exxon Chemical Company, U.S.A., 1974.

7. Beerbower, A., Kaye, L. A., and Pattison, D. A., "Picking the Right Elastomer to Fit Your Fluids", Chem. Eng. (NY), 74 (26), 118, 1967.

FIGURE 1

POLYMER COHESION PARAMETER DIAGRAM FOR POLY(ISOBUTYLENE-CO-ISOPRENE) RUBBER SHOWING THE SOLUBILITY PARAMETER AND HYDROGEN BOND INDEX COORDINATES FOR GD AND HD.

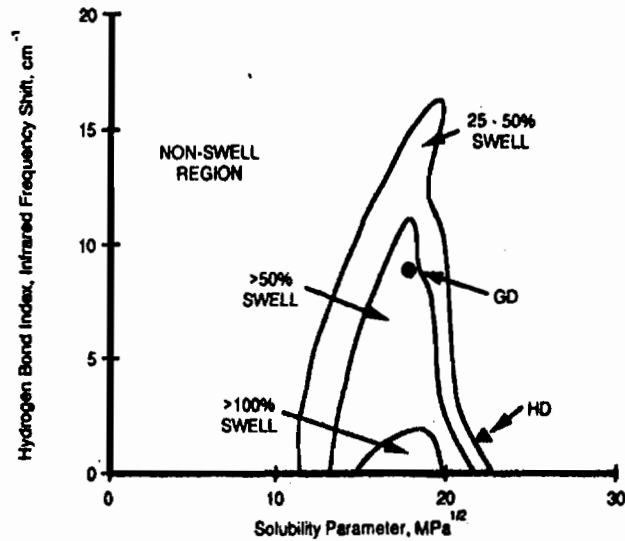
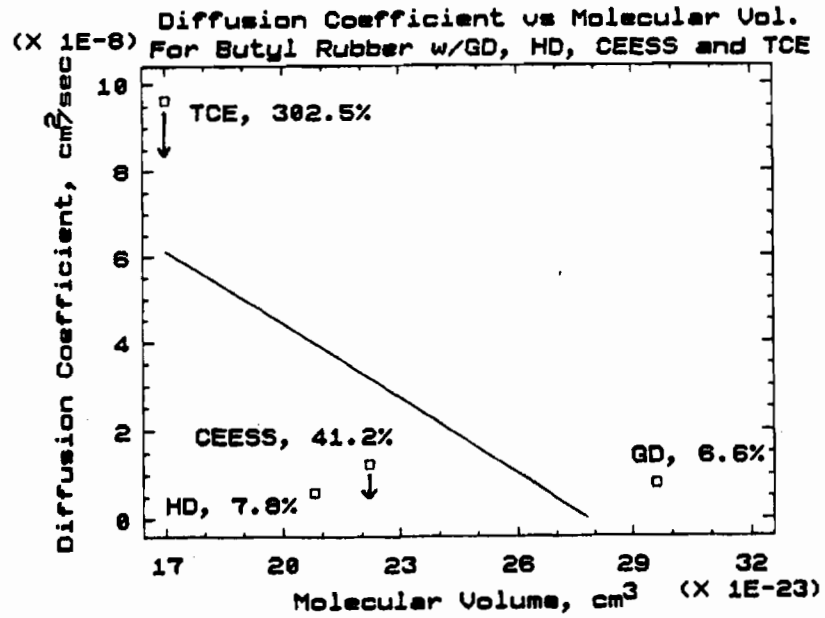


FIGURE 2



BLANK

376

RECENT DEVELOPMENTS IN THE FUNDAMENTALS OF GAS PERMEATION IN RUBBERY POLYMERS

C. Richard Desper

U.S. Army Materials Technology Laboratory, Watertown, MA

ABSTRACT

The ability to predict the gas permeation behavior in rubbery polymers requires knowledge of both the equilibrium solubility and of the diffusion constant. The methods for predicting the solubility and diffusion constants from first principles have been assessed. The dissolution process is best addressed by the methods of statistical mechanics, using the lattice-fluid equation of state. This treatment requires experimental PVT data on the pure components but not on mixtures, assuming ideal gas behavior. Departure from ideality would require knowledge of the χ interaction parameter. The diffusion part of the problem is best addressed by molecular dynamics simulation.

INTRODUCTION

In dealing with problems of chemical protection, it is desirable to have a way of predicting the permeability behavior for small molecules in a rubbery polymer, simply from first principles. This predictive capability would give one the capability of assessing the strengths and weakness of a given type of elastomer in terms of acting as a barrier for a CW agent, or in terms of its capacity for absorbing decontaminant molecules. The permeation problem divides into two parts, the solubility problem and the diffusion problem, which are amenable to different calculational approaches. The purpose of this paper is to review recent advances in such calculational approaches, and assess the most promising approaches in terms of the needs of the CW permeation problem.

Thermodynamics is the controlling factor for the solubility part of the problem. In this context, thermodynamics deals with the free energy considerations for mixing the small molecule with the matrix of rubbery polymer chains. This, in turn, concerns itself with entropic and enthalpic terms, but the details of the molecular shape, size, and motions are of interest only inasmuch as they affect these terms. Thus, molecular modeling is not particularly fruitful in terms of dealing with calculating the solubility of small molecules in a rubbery polymer. A more direct approach is preferable, involving evaluation of a few fundamental thermodynamic parameters experimentally, then relating these in turn to solubility, using the most appropriate theoretical approach. For the diffusion problem, on the other hand, the molecular modeling approach is quite relevant, since the molecular sizes,

shapes, and motions influence directly how a small molecule can move through a polymeric matrix.

THEORY OF SOLUBILITY OF SMALL MOLECULES IN RUBBERY POLYMER

The goal in this section is the prediction the solubility isotherms and, as a related factor, the partial molar volumes for small molecules in rubbery polymers. A recent paper of Pope, Sanchez, Koros, and Fleming¹ deals with this problem quite well, for the case in which the penetrating molecule is a gas. We shall examine this model as presented and in terms of a possible future extension.

The theory of Pope et al¹ is formulated in terms of the lattice-fluid (LF) equation of state, first proposed by Sanchez and Lacombe²⁻⁴, then modified by Sanchez^{5,6} specifically for polymer-gas systems, and is written:

$$\bar{\rho}^2 + \bar{P} + \bar{T} [\ln(1-\bar{\rho}) + (1-1/r) \bar{\rho}] = 0 . \quad (1)$$

In equation (1), $\bar{\rho}$, \bar{P} , and \bar{T} are reduced thermodynamic variables, that is, they are the ratios ρ/ρ^* , P/P^* , and T/T^* , respectively, of the ordinary density, pressure, and temperature quantities to the critical values of the same for the binary gas/polymer mixture. The variable r in this equation is the number of lattice sites occupied by the polymer. Pope et al¹ offer closed form equations for the evaluation of the critical pressure and temperature P^* and T^* of the binary mixture, in terms of the corresponding critical pressures and temperatures of the pure components, which, in turn, are obtained from PVT data on the pure components. [It should be noted at this point that component 1 is taken to be the gas, component 2 the polymer.]

This leaves the critical density $\bar{\rho}$ as the sole unknown in equation (1), which indicates that a solution is possible. However, an explicit solution is not obtained. It is useful at this point to recast this equation as an implicit equation in the reduced density:

$$\bar{\rho} = 1 - \exp[-\bar{\rho}^2/\bar{T} - \bar{P}/\bar{T} - (1-\phi_1/r_1)\bar{\rho}] . \quad (2)$$

In equation (2), $1/r$ is replaced by ϕ_1/r_1 , where ϕ_1 is the volume fraction of gas in the mixture, and r_1 is the number of lattice sites for each gas molecule. We are assuming that the corresponding term ϕ_2/r_2 is negligible in comparison to ϕ_1/r_1 due to the large value of r_2 , the polymer degree of polymerization.

For equilibrium, one must equate the chemical potential of gas in the gas phase with its chemical potential in the binary mixture. For brevity, these equations, [(5) through (9) in the paper] are omitted here. The additional parameters introduced in these equations are: M_1 , the gas molecular weight; ϕ_2 [$=1-\phi_1$], the polymer volume fraction; and χ , the Flory-Huggins interaction parameter, which, for ideal gases interacting with polymer may be written:

$$\chi = [(P_1^*)^{1/2} + (P_2^*)^{1/2}]^2 / RT . \quad (3)$$

We now have all we need for the solution of the problem, albeit not in closed form. For a given gas pressure (expressed as reduced pressure P_1^*), the resulting ϕ_1 (volume fraction of gas in the gas/polymer mixture) is found by iterative solution of three equations, readily accomplished using a computer. Using this ϕ_1 , the weight fraction w_1 of gas in the mixture may be calculated from:

$$w_1 = \phi_1 / [\phi_1 + \phi_2 (\rho_2^* / \rho_1^*)] \quad (4)$$

Pope et al¹ then proceed to solve for Henry's law constant k_H , applicable in the limit of low pressure, as the ratio of concentration of gas absorbed to partial pressure of component 1. In this equation, numbered (11) in the paper but omitted here, k_H^{-1} is written in terms of reduced densities and temperatures, along with (M_1/RT) , the aforementioned χ , and the gas critical molar volume v_1^* given by:

$$v_1^* = M_1 / \rho_1^* \quad (5)$$

It is important to remember, however, that the theory does much more than calculate the (inverse) Henry's Law constant for the low pressure limit: it calculates the nonlinear behavior at higher pressures as well.

If desired, the lattice-fluid approach also provides information about volumetric changes associated with gas sorption, in the form of the partial molar volume of gas penetrant, defined as:

$$\bar{v}_1 = (\partial v / \partial n_1)_{T, P, n_2} \quad (6)$$

[The subscripts indicate that temperature, pressure, and moles of polymer are held constant in the partial differentiation.] To evaluate this partial molar volume, a value of the isothermal compressibility β is needed, along with a value of $g_{v\phi 1}$, a mixed second partial derivative of the free energy. The authors provide equations for both of these quantities in terms of the critical and reduced temperature, pressure, and volume, along with r_1 and ϕ_1 . Again, the theory does not afford an explicit solution, but an iterative calculation is used to calculate values of the partial molar volume as a function of dissolved gas concentration.

COMMENTARY ON THE SOLUBILITY THEORY

Figure 1 shows a sorption isotherm, showing a comparison of the calculated gas uptake for ethylene in silicone rubber as a function of ethylene pressure. For a given ethylene gas pressure, the experimental volume fraction of gas sorbed is greater than the calculated value for the entire range of pressures. However, the theory shows the same upward curvature as the experimental data. Similar upward curvature appears in the data and theory for carbon dioxide (not shown here), while linear behavior is seen in both the experimental and predicted behavior for methane and nitrogen. Thus the LF theory follows the trends in the data qualitatively if not quantitatively. The trend towards curvature for carbon dioxide and ethylene sorption may be linked to the higher volumes of gas sorbed in the rubber for these two gases at a given pressure of gas. Thus the data goes to higher values of volume

fraction of gas sorbed for these two gases in the experimental pressure range of 0 to 70 atm. Accordingly, the gas concentrations in the mixed phase are much higher, entering concentration ranges where non-linear behavior begins, in contrast to the other two gases, which stay in the linear range of gas sorption versus pressure.

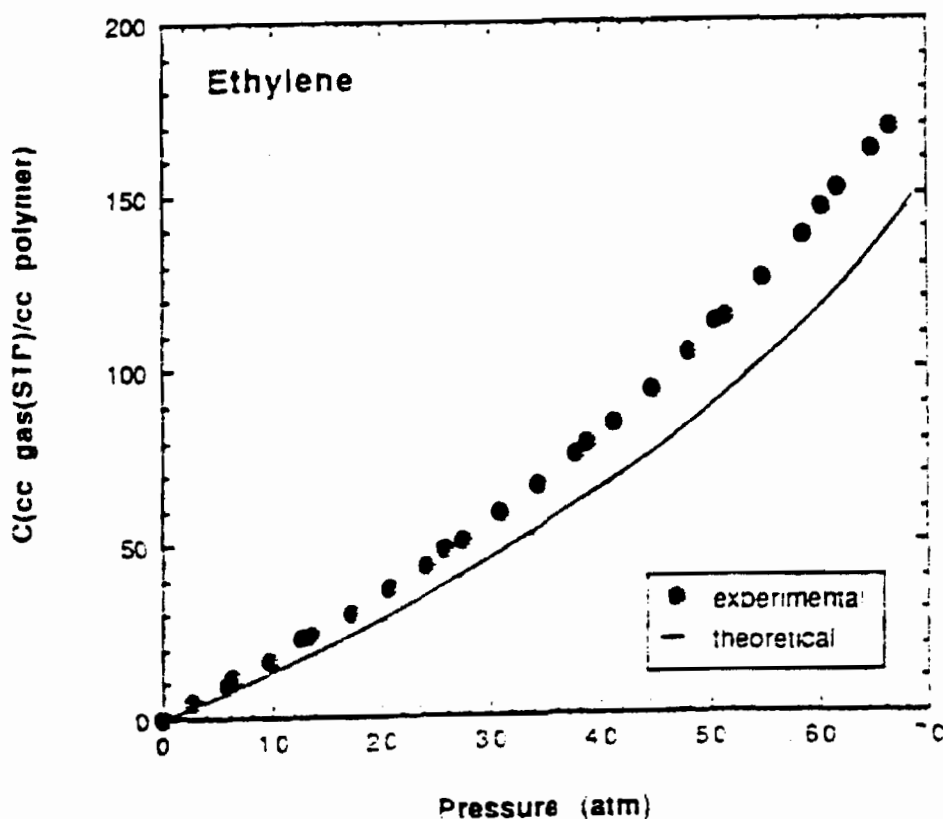


Figure 1. Comparison of theoretical predictions with experimental results for ethylene sorption in silicone rubber. Reprinted by permission from *Macromolecules*, 24, 1779-83, copyright 1991 American Chemical Society.

In terms of the inverse Henry's Law constant and the partial molar volume of the gas at infinite dilution, comparisons are shown between the LF theory and experimental values in Table 1. Excellent agreement is seen in terms of the partial molar volumes at infinite dilution. For the inverse Henry's Law constants, greater discrepancy is seen between the experimental and calculated value. Moreover, the discrepancy is systematic: in all instances the theoretical inverse Henry's Law constant is less than the experimental value by approximately 25%. This would suggest a common cause for

that discrepancy, and should be a subject for further inquiry. However, even with this discrepancy, the present results are quite useful for many purposes, particularly where differences on an absolute scale may not be as important as differences on a logarithmic scale.

TABLE 1.
Comparison of Calculated and Experimental Values of the
(Inverse) Henry's Law Constants and Infinite Dilution Partial Molar Volumes

Absorbing Polymer: Silicone Rubber				
<u>Gaseous Species</u>	$k_H^{-1}, \text{cm}^2 \text{ (STP) / cm}^3$ (polymer) · atm		$\bar{v}_1, \text{cm}^3 / \text{mol}$	
	<u>expt.*</u>	<u>theory</u>	<u>expt.#</u>	<u>theory</u>
ethylene	1.66	1.26	58.3	58.9
carbon dioxide	1.28	0.98	46.1	45.9
methane	0.43	0.33	52.2	49.8
nitrogen	0.12	0.09	49.7	49.4

* Error ±0.01 (After Pope et al¹) # Error ±0.1

EXTENSION TO VAPORS AND LIQUIDS

In the above discussion, we have referred to the permeant molecule as a gas. Since vapors and liquids are of great interest in terms of CW applications, it is appropriate to examine the limitations of the lattice fluid model. The question then becomes, at what point in the theory is it dependent upon the permeant molecule being a gas? In this regard, we find that, since reduced thermodynamic variables are used, referred to critical values, the gas itself need not be an ideal gas; in particular, it could be a vapor. The one area which could be a problem is in the gas-polymer interaction parameter χ_{12} . Sanchez⁶ offers the following expression for χ_{12} :

$$\Delta P_{12}^* \equiv RT \chi_{12} = [(P_1^* + P_2^* - 2\xi(P_1^* P_2^*)^{1/2})] \quad (7)$$

where the P^* values are reduced pressures and ξ is a dimensionless parameter controlling the combinatorial law. In particular, for non-polar gas and polymer, $\xi=1$ so the equation reduces to equation (2) above. In practice, χ_{12} may be determined experimentally using inverse gas chromatography.⁶

However, it is found, through application of the lattice-fluid equation, that the interaction parameter χ_{12} or equivalently, $\Delta P_{12}^* \equiv RT\chi_{12}$, is of secondary importance in establishing solubility. This is dramatically illustrated in quite recent data of Rodgers and Sanchez⁷. This paper deals with gas solubility in terms of the specific retention volume V_g in an inverse gas chromatography experiment, which is related⁷ to the inverse Henry's Law constant k_H^{-1} by:

$$V_g = k_H^{-1} (RT/M_1 \rho_2) \quad (8)$$

In this data, shown in part in Table 2, there are gross differences in the

ΔP_{12}^* values, even in terms of sign, between the experimental value and that calculated from equation (7). Nonetheless, the error between calculated and experimental retention volumes for inverse gas chromatography is quite acceptable, averaging 11.5% for one polymer and 22.2% for another. This indicates that the accuracy of ΔP_{12}^* is not critical for the calculation of V_g .

Values of the characteristic parameters (critical constants) for a variety of penetrant and polymer species have been tabulated by Sanchez and co-workers^{2,7,8}. Sanchez and Rodgers⁸ report good results for predicting gas solubility, except for alcohols and for non-polar/polar combinations of gas and polymer.

TABLE 2.
Comparison of Experimental and Calculated Values of Interaction
Parameter ΔP_{12}^* , and of Specific Retention Volume V_g

Penetrant	Polymer	ΔP_{12}^* (J/cm ³)		V_g (cm ³ /g) @ 543K		$\frac{V_g}{V_g^*}$, % Error
		expt.	theory	expt.	theory	
Benzene	PS*	8.15	4.64	1.82	1.91	5.2
Toluene	PS*	10.7	1.31	2.38	2.80	17.7
Ethylbenzene	PS*	5.01	1.37	3.13	3.37	7.6
Chlorobenzene	PS*	15.4	3.94	3.68	4.47	21.5
Bromobenzene	PS*	5.07	8.27	5.64	5.33	-5.5
Benzene	PPO#	-12.4	4.53	2.26	1.77	-21.7
Toluene	PPO#	-6.45	9.85	2.97	2.23	-24.8
Ethylbenzene	PPO#	-9.24	9.70	3.85	2.63	-31.8
Chlorobenzene	PPO#	-2.82	5.28	4.65	4.04	-12.9
Bromobenzene	PPO#	-10.4	1.98	6.85	5.51	-19.6

* PS: Polystyrene; # PPO: Poly(2,6 dimethyl phenylene oxide).

Avg. error in V_g : 11.5% for PS, 22.2% for PPO.

(After Rodgers and Sanchez⁷)

ESTIMATION OF DIFFUSION COEFFICIENTS

In contrast to the discussion of solubility theory, the molecular sizes, shapes, and motions have a direct bearing on the diffusion coefficients for small molecules in an amorphous polymer matrix, since the problem is a dynamic one rather than a thermodynamic one. In this regard, it is fruitful to apply computer molecular modeling, and in particular molecular dynamics simulation, to the diffusion problem. Such an approach has become feasible within the last few years only because of the increasing power of available computer systems. A group at the University of Cincinnati⁹ have studied the diffusion of small spherical molecules (CO₂, He, Ar) through rubbery amorphous polyethylene chains with some success. Their Monte Carlo approach (using a Cray computer) allows "jumping" of polymer and permeant segments to be followed every 25 picoseconds, diffusion being defined in terms of mean-squared displacements of segments from their original positions with time. The calculated results for CO₂ underpredict the activation energy (6 - 7.5 vs. 13.5 - 13.9 kJ/mol), while overpredicting the diffusion coefficients (17.8x10⁻⁹ vs. 4.44x 10⁻⁹ m²/s). The discrepancy is attributed to a defici-

ency in the polymer model itself, which exhibits a lower calculated density of 0.576 compared to an experimental value of 0.741 g/cm³. Nonetheless, the method shows great potential for the prediction of gas diffusion coefficients in polymers.

CONCLUSIONS

Recent advances on the theoretical front have improved our ability to predict the permeation behavior of small molecules in rubbery polymers. For the solubility part of the problem, the Lattice-Fluid (LF) theory of Sanchez and Lacombe²⁻⁶, as implemented by Pope et al.¹, has proven its capability of predicting Henry's Law coefficients to better than an order of magnitude, requiring only certain critical constants characteristic of the polymer and of the penetrant, but not of the combination. For the diffusion coefficient side of the problem, molecular dynamics computations using powerful computers offer great promise for the prediction of both coefficients and activation energies, but improvements in the basic model are needed to bring the results closer to experimental values.

REFERENCES

1. D. S. Pope, I. C. Sanchez, W. J. Koros, and G. K. Fleming, "Statistical Thermodynamic Interpretation of Sorption/Dilation Behavior of Gases in Silicone Rubber", Macromolecules, 24, 1779-1783 (1991).
2. I. C. Sanchez and R. H. Lacombe, "An Elementary Molecular Theory of Classical Fluids. Pure Fluids", J. Phys. Chem., 80, 2352-2362 (1967).
3. R. H. Lacombe and I. C. Sanchez, "Statistical Thermodynamics of Fluid Mixtures", J. Phys. Chem., 80, 2568-2580 (1967).
4. I. C. Sanchez and R. H. Lacombe, "Statistical Thermodynamics of Polymer Solutions", Macromolecules, 11, 1145-1156 (1978).
5. I. C. Sanchez, "Polymer Phase Separation", Encycl. Phys. Sci. Technol., 11, 1 (1987).
6. I. C. Sanchez, "Relationships Between Polymer Interaction Parameters", Polymer, 30, 471-475 (1989).
7. P. A. Rodgers and I. C. Sanchez, "Gas Solubility in Polymers and Blends", ACS Polymer Preprints, 32 (3), 392-393, (Aug. 1991).
8. I. C. Sanchez and P. A. Rodgers, "Solubility of Gases in Polymers", Pure & Appl. Chem., 62, 2107-2114 (1990).
9. S. Trohalaki, A. Kloczkowski, J. E. Mark, D. Rigby, and R. J. Roe, "Estimation of Diffusion Coefficients for Small Molecular Penetrants in Amorphous Polyethylene", in Computer Simulation of Polymers (R. J. Roe, Ed.), Prentice Hall, Englewood Cliffs, NJ, Ch. 17, 221-233 (1991).

BLANK

EMULSION COPOLYMERIZATION OF METHACRYLATES: A SCALE-UP STUDY

J.M. Park and J.W. Vanderhoff
Emulsion Polymers Institute
Lehigh University, Bethlehem, PA 18052

S.H. Hong
Research Directorate
U.S. Army Chemical Research, Development
and Engineering Center, APG, MD 21010-5423

Emulsion polymerization of methacrylate monomers with disparate reactivity ratios was studied. A quantitative study of the influence of reaction conditions, such as initiator and surfactant, on the physical properties of the laboratory size emulsion polymerization was completed. The properties were then correlated to the particle size of the latexes and molecular weight of the recovered polymers. Then, the reaction was scaled-up 10-fold. Thus, several runs of 5-L semi-continuous emulsion polymerization were performed and the properties of the resulting copolymers were compared. A pilot plant reaction (200-L size) was then carried out and the properties of the product were compared to those of smaller scale reactions.

1. Introduction

High molecular weight compositionally homogeneous viscoelastic poly(alkylaminoalkyl methacrylate-co-alkyl methacrylate), was prepared by emulsion copolymerization using water-soluble initiators¹. Emulsion polymerization is well suited to the preparation of high molecular weight polymers at rapid polymerization rates. As a first approximation, the rate of polymerization, R_p , and the number average degree of polymerization, X_n , are given by the following equations²:

$$R_p = k_p[M]nN \quad (\text{eqn 1})$$

$$X_n = 2k_p[M]nN/R_i \quad (\text{eqn 2})$$

where k_p is the rate constant for propagation, $[M]$ the concentration of monomer in the particles, n the average number of free radicals per

particle, N the total number of particles, and R_i the rate of free radical generation. Thus X_n can be increased by increasing N , increasing $[M]$, or decreasing R_i . Usually, high emulsifier concentrations give high values of N , while the value of $[M]$ is limited by the equilibrium swelling volume of the latex particles; low initiator concentrations and low polymerization temperatures give low R_i values. Therefore, the combination of high emulsifier concentration with a low initiator concentration and polymerization temperature should favor the formation of high molecular weight polymer.

Monomer-starved semi-continuous emulsion copolymerization was employed to ensure that the copolymers would be random and homogeneous in composition³. Here, the rate of polymerization is controlled by the rate of monomer addition; however, this gives low values of $[M]$, which means the molecular weight of the polymer would be limited. This limitation must be compensated for by increasing the value of N and decreasing that of R_i .

2. Experimental

Except where noted, the inhibitors were removed from the monomers used; the *t*-butylaminoethyl and isobutyl methacrylates (Rohm & Haas) were passed through an inhibitor removal column (Aldrich) prior to use. The emulsifier Triton X-405 (Rohm & Haas) and initiator sodium persulfate (Fisher Scientific) were used as received. Distilled deionized water was used for all polymerizations.

For semi-continuous polymerizations, 7% of the monomer mixture was emulsified at ambient temperature in the water containing the dissolved emulsifier and sodium persulfate initiator in a four-necked 500 mL round-bottom flask equipped with a stirrer, condenser, nitrogen inlet, and monomer inlet pump, heated to 60°C, and polymerized in batch to form the seed latex. The remaining 93% of the monomer mixture was then added continuously at a constant rate over a four hour period. After the monomer addition was completed, the polymerization was continued at 60°C to complete the polymerization. In some cases, the polymerization was carried out at 50 or 70°C. The final pH of the latexes was 9.40 to 9.60. The limiting viscosity numbers were measured in *N*-methyl-2-pyrrolidone utilizing Cannon-Ubbelohde viscometer. The latex particle sizes were determined by photon correlation spectroscopy (Nicomp Submicron Particle Sizer), the copolymer ratio by ¹³C nuclear magnetic resonance spectrometry, and the T_g by differential scanning calorimetry. Rheological properties of polymer solutions were measured with Rheometrics Fluid Rheometer model RFR-7800 with cone and plate geometry.

3. Results and Discussion

Table 1 shows the variation with polymerization time of the number- and volume-average particle size of the latex prepared by batch copolymerization in a stirred glass flask at 60°C. The number-average

Table 1. Particle Size in Batch Polymerization.

Sample #	Polymerization Time (min)	D _n (nm)	D _v (nm)	N, x 10 ⁻¹⁶
1	15	13	26	3.1
2	20	32	45	0.88
3	30	33	45	1.5
4	40	29	43	2.0
5	60	29	41	2.2
6	75	17	34	3.9
7	90	26	40	2.5
8	150	26	41	2.4
Final	420	28	44	1.9

particle size increased to 13 nm in 15 minutes and to 32 nm in 20 minutes, and remained constant thereafter (average 25 nm over the range 20 to 420 minutes). Similar results were observed for semi-continuous polymerizations carried out at 60°C and 70°C. Table 2 shows that the number-average particle size increased to constant values of 32 nm at 60°C and 26 nm at 70°C after 20 to 30 minutes, which were maintained throughout the remainder of the polymerization.

Table 3 gives the particle sizes corresponding to the number of polymer molecules calculated assuming a molecular weight of 1 megadalton and a copolymer density of 1.15 g/cm³. Thus, the 15-min batch polymerization sample (which has a number-average particle size of 13 nm) corresponds to a single copolymer molecule, and the succeeding samples (25 nm) to about 5 polymer molecules. Similarly, the semi-continuous copolymerizations showed the seed particles of both 60°C and 70°C polymerizations contained approximately two copolymer molecules. In other words, the first particles initiated comprised single copolymer molecules and these particles grew until they comprised about 5 to 10 copolymer molecules. And then, surprisingly, they stopped growing. This cessation of particle growth at an early conversion is most unusual^{4,5}. Usually, the particles continue to grow until the supply of monomers or free radicals is exhausted. If particle nucleation ceased early in the polymerization, the final latex would be of uniform size; if the particle nucleation continued for a longer time, the final latex would have a broad size distribution. The particle size distribution of these samples were relatively broad; the average polydispersity indexes were 1.54 for batch polymerization (Table 1) and 1.22 for the 70°C semi-continuous polymerization (Table 2).

Table 2. Particle Size in Semi-Continuous Polymerization.

Sample #	Polymerization Time (min)	Dn (nm)	Dv (nm)	N, x 10 ⁻¹⁶
60°C Polymerization				
1	seed	19	27	0.58
2	20	28	39	0.20
3	40	26	36	0.31
4	60	28	41	0.29
5	90	29	41	0.78
6	120	31	44	1.4
7	140	41	52	1.1
8	175	37	50	1.2
final	420	38	51	1.2
70°C Polymerization				
1	seed	18	27	0.58
2	30	28	37	1.0
3	60	21	36	2.9
4	90	24	40	2.1
5	105	25	39	2.5
6	130	19	35	3.7
7	160	34	45	1.8
final	420	34	46	1.7

The reason for the cessation of particle growth at this small size or early stage of the polymerization is not known. However, one possible explanation comprises a reversal of the mode of adsorption of the sulfated oligomeric radicals. The commonly accepted mechanism of initiation using persulfate initiator comprises the formation of sulfate ion-radicals in the aqueous phase, their slow propagation in the aqueous phase until they become surface-active and adsorb at the particle-water interface with the radical end oriented toward the monomer-polymer phase, and their rapid growth into the particle because of the high concentration of monomer. In the present system, the initial growth of the particles would give an increasing number of amino surface groups from the t-butylaminoethyl methacrylate units, so that an acid-base interaction between the surface amino groups and the sulfate groups of the oligomeric radicals would give a

Table 3. Calculated Number of Polymer Molecules Corresponding Spherical Particle Sizes.

Number of Copolymer Molecules	Spherical Size (nm)
1	14
2	18
3	20
5	24
10	30
20	38

reversed mode of adsorption, with the sulfate end oriented toward the particle surface and, therefore, the radical end toward the aqueous phase. They can not grow rapidly because of the low concentration of monomer in the aqueous phase. Moreover, they would be vulnerable to termination by oligomeric radicals or primary radicals from the aqueous phase. This termination would inhibit further polymerization within the particle, and thus, growth of the particle. Meanwhile, the nucleation of new particles would proceed continuously, so that the particles would be nucleated, grow to a given size and then stop growing. This cessation of particle growth is therefore termed limited growth emulsion polymerization. This proposed mechanism would give a surface layer of different composition from the particle interior, which would be consistent with the observations by transmission electron microscopy.

Table 4 shows the results of larger scale polymerizations including rheological properties (i.e., apparent viscosity and first normal stress difference (FNSD) of the dilute solutions at different shear rates). Eight 5-L polymerizations (designated as EPI-S5-01 to EPI-S5-08) gave good reproducibility but larger particle size (range of 50-55 nm) and lower LVN (range 1.47-1.90 dL/g) than smaller scale polymerizations. The pilot plant polymerization (designated as MT-303) resulted in the latex with smaller particle size (39 nm) and the copolymer showed a good LVN (1.78 dL/g). The NMR spectra of these copolymers showed the amount of IBMA incorporated into the copolymers was, in general, higher than the expected molar ratio of 75 %, although the polymerization experiments were all carried out with the 75:25 molar ratio mixture of IBMA:TBAEMA. One would expect TBAEMA to be fully incorporated into the copolymer system (i.e., 25 %) based on the reactivity ratio of the two monomers. However, the lower TBAEMA content may be attributed to the difference in water solubility of the two monomers. The apparent viscosity of 5-L samples was, generally, within an acceptable range, with the exception of sample EPI-S5-03. In the case of EPI-S5-03, which also showed the highest LVN among the 5-L samples, the apparent viscosity was unexpectedly high. The cause of this high viscosity is not clear. However, FNSD of the same sample was within an acceptable range. FNSD of all 5-L samples indicated that these samples have high

Table 4. Properties of the Methacrylate Copolymers Produced by Larger Scale Polymerizations.

Sample # Reference	LVN ^c (dL/g)	Dn (nm)	Monomer ^b Ratio		Solvent	Concn. (g/dL)	FMSD ^d (dyne/cm ²)			Apparent Viscosity (poise)				
			IBMA	TBAEMA			Shear Rate/sec.			Shear Rate/sec.				
							100	250	500	1000	12.5	25	50	
CMI-120	1.9	NA	77	23	Mix 1 ^d	2.0 ^e	155	530	1215	- ^f	2.1	2.0	1.9	1.7
					Mix 2 ^g	3.0	-	-	702	2296	4.9	3.2	2.8	2.4
						3.0	-	-	204	1722	2.8	2.7	2.5	2.3
						3.1	(68)	464	1232	2891	3.9	3.4	2.9	2.5
Scale-Up (5-L) Samples														
EPI-S5-01	1.47	50	79.0	21.0	Mix 1	2.0	427	878	1220	1329	2.3	2.0	1.6	1.4
					Mix 2	3.0	-	-	350	497	1.7	1.5	1.5	1.3
EPI-S5-02	1.58	50	83.0	17.0	Mix 1	2.0	(74)	229	476	570	1.9	1.8	1.6	1.4
					Mix 2	3.0	-	252	731	1663	3.4	2.9	2.4	2.2
EPI-S5-03	1.90	53	79.1	20.9	Mix 1	2.1	488	971	1489	2043	9.0	7.1	5.6	4.0
					Mix 2	3.0	(39)	364	1009	2310	5.9	4.8	4.1	3.5
EPI-S5-04	1.75	51	78.5	21.5	Mix 1	2.1	445	1062	1857	2760	4.9	4.3	3.7	3.0
					Mix 2	3.1	181	282	857	2055	4.2	3.6	3.1	2.7
EPI-S5-05	1.78	52	80.1	19.9	Mix 1	2.1	520	853	1391	1767	2.9	2.6	2.3	2.0
					Mix 2	3.0	-	324	893	2058	3.8	3.4	2.8	2.5
EPI-S5-06	1.50	55	78.7	21.3	Mix 1	2.1	125	351	724	988	2.0	1.9	1.7	1.6
					Mix 2	3.1	-	-	193	928	3.5	2.9	2.7	2.4
EPI-S5-07	1.72	53	82.2	17.8	Mix 1	2.0	115	373	766	1148	2.2	2.0	1.8	1.6
					Mix 2	3.0	-	(87)	544	1399	3.6	3.1	2.7	2.3
EPI-S5-08	1.73	53	79.4	20.6	Mix 1	2.0	181	608	1115	1399	2.7	2.4	2.1	1.9
					Mix 2	2.9	(40)	435	1111	2411	4.0	3.5	3.0	2.6
Pilot Plant (100-lb) Polymerization Sample (prepared by Morton International)														
MT-303	1.78	39	77.4	22.6	Mix 1	2.0	150	511	1034	1555	2.5	2.3	2.1	1.8
					Mix 2	3.0	-	280	824	1971	3.5	2.9	2.5	2.3

a. First Normal Stress Difference.
 b. Molar ratio of the monomers incorporated into the copolymer by C-13 NMR.
 c. Limiting viscosity number; measured at 25 °C in N-methylpyrrolidone.
 d. A proprietary organic solvent mixture.
 e. Estimated values from the measurements of 2 g/dL solutions at 20, 30, and 40 °C.
 f. Not observed.
 g. A proprietary organic solvent mixture.

enough viscoelasticity in the given solvents. Both apparent viscosity and FNSD of the MT-303 (pilot plant sample) were almost identical to those of the reference material, which indicated that the pilot plant polymerization was quite successful.

4. Conclusion

In summary, high molecular weight 25:75 poly(t-butylaminoethyl methacrylate-co-isobutyl methacrylate) has been prepared by semi-continuous emulsion copolymerization. The molecular weight of these copolymers were in the megadalton range, and the rheological properties of the solutions were satisfactory; however, the polymer molecules appeared to associate in solution, forming clusters in some organic solvents. The molecular weights did not vary as sensitively with reaction conditions, such as particle size of the latex, initiator concentration, and polymerization temperature, as expected. The particle sizes were inordinately small, and this was attributed to the rapid nucleation and growth of the particles to about 10 copolymer molecules, followed by cessation of growth. Therefore, this was termed "limited growth emulsion polymerization". The scale-up (to 5-L) resulted in samples with good reproducibility. And a successful pilot plant production was carried out.

Acknowledgement

Special thanks are extended to Dr. J. Kim of Morton International for carrying out the pilot plant emulsion copolymerization operation. The authors thank M. Potts and D. Dunn of MTL, W. Beaudry and L. Szafraniec of CRDEC, and M. Hu, I. Segall and H. Yu of Lehigh University for their help in characterizing copolymers. They also wish to express appreciation to W. Shuely and E. Jeffers of CRDEC for their support of this program.

Literature cited

1. Hong, S.H., "Review of Emulsion Polymerization: Optimization for the Production of Ultrahigh Molecular Weight Poly(Alkylaminoalkyl Methacrylate-co-Alkyl methacrylate)", CRDEC-TR-88146, UNCLASSIFIED Report, August 1988.
2. Smith, W.V. and Ewart, R.H., J. Chem. Phys., 16, 592 (1948).
3. Misra, S.C., Pichot, C., El-Aasser, M.S. and Vanderhoff, J.W., J. Polym. Sci., Polym. Chem. Ed., 21, 2383 (1983).
4. Medvedev, S.S., Zuikov, A.V., Gritskova, A. and Dudukin, V.V., Vysokomol. Soyed. (English transl.), A13, 1397 (1971).
5. Snuparek Jr., J. and Kleckova, Z., J. Appl. Polym. Sci., 29, 1 (1984).

BLANK

SOLVENT EFFECTS ON THE TENSILE PROPERTIES OF THERMOPLASTIC COMPOSITES

Vincent M. McHugh, Wendel J. Shuely, and Richard W. Brletich
U.S. Army Chemical Research, Development and Engineering Center

John M. Henshaw
University of Tulsa

The ability of a material to maintain fundamental mechanical properties after solvent exposure is a primary criterion for material selection in the Aircrew Protective Mask (ACPM) and in numerous military and commercial developmental items. An experimental design and material test methodology were developed and the tensile properties for candidate thermoplastic composite materials (TPCM) were determined as a function of solvent exposure. Solvent systems considered consisted of hygrothermal, standard, and developmental decontaminating solutions. The candidate TPCM investigated were: 3 Nylons (6/6, 6/10, and 6/12), PEEK, PPS, PET, PBT and a Liquid Crystal Polymer (LCP). Correlations were explored between changes in tensile properties and fundamental material properties, concurrent measurements of solvent effects, and performance properties. These studies were performed within the context of a concurrent engineering methodology.

INTRODUCTION

Previously published reports^{1,2} document the use of a Total Quality Design (TQD) approach to concurrent engineering for selection of chemically resistant TPCM as substitutes for aluminum in components of the ACPM. Decontaminability, low agent/decontaminant sorption and mechanical stability after solvent exposure were identified as some of the high priority requirements for candidate replacement materials. The agents to be considered are GD, HD, and VX; the decontaminants are a hygrothermal surfactant solution (HSS), DS-3 and DAM.

The scope of the investigation reported herein is limited to a study of the HSS decontaminant, which includes results for determination of tensile properties and weight and dimensional changes of the candidate TPCM tensile specimens as a function of exposure.

EXPERIMENTATION

The candidate TPCM are listed in Table 1. The ASTM standard identified for solvent resistance testing of TPCM is ASTM standard D543 (Standard Test Method for Resistance of Plastics to Chemical Reagents). To determine weight and dimensional changes for a molded or extruded plastic as a function of solvent exposure, according to ASTM D543, the investigator is instructed to use a 2 inch diameter disk with a thickness of 0.125 inches. ASTM standard D543 also provides a brief procedure for immersion of mechanical test specimens in solvents. After immersion the investigator is instructed to "determine the mechanical properties of identical non-immersed and immersed

specimens in accordance with the" appropriate standard method.

ASTM standard D638 (Standard Test Method for Tensile Properties of Plastics) was selected as the standard method for determining mechanical properties of the TPCM since the tensile strength of the candidate materials as a function of exposure to solvents was identified as a translated critical requirement for the ACPM. ASTM standard D638 requires the use of one of five different specimen types depending on various sample production configurations (sheet, plate, molded, tube or rod), plastic rigidity type as defined in ASTM standard D883 (rigid, semi-rigid or non-rigid), presence of reinforcement (highly orthotropic or isotropic), and "whether or not direct comparisons are required between materials in different rigidity cases." Since all of the candidate TPCM test specimens were injection molded, rigid, isotropically reinforced thermoplastics, the Type I specimen was selected; the thickness was 0.13 (\pm 0.02) inches.

In this investigation the advantages of both ASTM standards D543 and D638 were gained through the use of only the Type I tensile specimen. That is, a single specimen was used for determining plastic weight and dimensional changes as a function of solvent exposure as well as for measuring tensile property changes as a function of solvent exposure. In addition, the visible appearance of the test specimens was documented photographically before and after solvent exposure, and before and after tensile testing.

Before testing was initiated an overall experimental design was developed. The factors considered in this test design included: 1) total number of specimens available per sample, 2) the number of solvent exposure conditions (with "no solvent exposure" being considered as one type of condition), 3) day-to-day test variability (i.e. room temperature, room RH, instrument fluctuations, etc.), 4) operator-to-operator variability, 5) randomness of test specimen selection per sample, and 6) randomness of testing order.

A Sintech/6 Universal Test Machine was used for all tensile testing. Self-tightening wedge grips with serrated faces were used to grip the tensile test specimen, and a universal joint was used for specimen self-alignment. A computer-interfaced micrometer was used to measure the width and length of the test specimen gage section. Strain was measured using a 2 in (50% maximum strain) extensometer and the applied load was measured with a 10,000 pound capacity load cell. The test speed was 0.2 in/min. The ambient relative humidity and temperature at the time of testing were recorded.

The exposure solvent used in this phase of the investigations was the HSS decontaminant. The HSS (identified in TM 3-4240-312-12&P) is a solution of hot, distilled water (90 to 95 deg C) and liquid soap (type 1, NSN 8520-00-228-0598); a 1 volume percent soap solution was used.

All tensile specimens were injection molded by the plastic manufacturer. Specimens were randomly selected for testing and then conditioned for 168 (\pm 5) hours (7 days) at room temperature in a desiccator containing a saturated magnesium nitrate-hexahydrate salt solution (providing an atmosphere of ca. 50% RH at 25 deg C, see ASTM standard E104). Conditioning of test specimens before solvent exposure or tensile testing is specified in ASTM standards D543 and D638. The recommended temperature, %RH and length of time are, respectively, 23 (\pm 2) deg C, 50 (\pm 5) %RH, and >40 hours. The conditioning time of 168 hours was selected in order to allow testing on all five days of the work-week and, therefore, to ensure that conditioning times for all specimens were essentially constant. That is, a sample which started conditioning on a Monday was tested on the following Monday, etc.. ASTM standard D638 specifies that hygroscopic materials like Nylon 6/6 should not be conditioned before testing but should, instead, be tested "dry-as-molded." The nylon materials in this investigation were not tested "dry-as-molded" because the mask components would be exposed to ambient humidity.

After conditioning for 168 hours, specimens were individually removed from the desiccator and weighed on an analytical balance; length and width of the test specimen gage section were also measured. If a specimen was not going to be exposed to a solvent the tensile test was then performed. For solvent exposure tests, tensile specimens were immersed in the HSS for 30 minutes (private conversation with C. Grove, CRDEC). After the 30 minute exposure the tensile specimens were removed from the HSS, dried with a lint-free Kimwipe and immediately reweighed on the analytical balance. The length and width of the test specimen gage section were also immediately recorded and a photograph was taken for visual documentation of specimen condition. The tensile specimen was then returned to a ca. 50% RH desiccator and allowed to equilibrate to test temperature (i.e. room temperature) for 1 hour. (ASTM standard D543 states that the equilibration of the test specimen to test temperature shall be in another sample of the exposure solvent which is at test temperature. This was not done in this case since the total solvent exposure time was not to exceed 30 minutes). The total length of time between removal of tensile specimen from HSS and placement in the desiccator was <5 minutes. After conditioning for one hour the test specimen was then removed from the desiccator and reweighed; the length and width of the gage section were recorded and another photograph was taken. The specimen was then tested for tensile properties. A post-test photograph of all specimens was taken to document final visual appearance.

RESULTS

Table 2 summarizes the mean percent weight change for the nine candidate TPCM immediately after exposure to the HSS decontaminant. The first column identifies the material and the next column shows the mean percent weight change with a 95% confidence interval. The materials are listed in order of decreasing percent weight change. The Nylon 6/6 sample had the greatest percentage weight gain and the PPS and LCP samples actually had a decrease in weight after exposure to the HSS decontaminant.

Some specimens did not break within the gage section as required by ASTM standard D638 and other specimens slipped in the tensile grips yielding no data. Due to these two circumstances, the amount of "valid" test data for comparing overall tensile strength changes as a function of solvent exposure was limited. Therefore, an analysis of variance (ANOVA) was performed to evaluate "good breaks" versus "bad breaks" (inside versus outside the gage section). As a result, it was concluded that there was no statistically significant difference in tensile strength between those specimens which broke inside the gage section and those which broke outside the gage section. Subsequent pooling of data did increase the amount of "valid" data for evaluating a solvent effect on material tensile strength.

Table 3 summarizes the mean percent tensile strength change for eight of the nine candidate TPCM after exposure to the HSS decontaminant. (For one material, Nylon 6/12 [ICI], all unexposed specimens slipped in the tensile grips and provided no baseline data). The first column identifies the material and the next column shows the mean percent tensile strength change. The materials are listed in order of greatest positive percentage tensile strength change to greatest negative percentage tensile strength change. Therefore, the LCP appeared to have the greatest gain of tensile strength and the Nylon 6/6 appeared to have the greatest loss of tensile strength after exposure to HSS. However, an ANOVA of the tensile strength changes for all materials was completed and only the Nylon 6/6 showed a statistically significant change in tensile strength after exposure to the HSS.

The figure shows a plot of mean percent tensile strength change on the y-axis versus mean percent weight change on the x-axis for eight of the nine TPCM. The linear regression curve and 95% confidence intervals are also included. Based on the limited amount of data available to date there is a

direct correlation between percent weight gain in the TPCM and loss of tensile strength. There appears to be a corresponding increase in tensile strength for materials which essentially had no weight change after exposure to HSS decontaminant.

DISCUSSION

If ASTM procedures were strictly followed, without an appropriate statistical analysis, a large number of tests would have been considered invalid. However, the ANOVA performed on tensile results proved valuable in determination that there was no statistically significant difference between breaks in versus outside the gage section, allowing pooling of data sets. Future ANOVA will be used to evaluate strain data for validity.

The weight gain of some candidate materials after exposure to the HSS decontaminant is probably due to water sorption. The weight loss of other materials may be due to loss of polymer additives or fillers and/or removal of external dirt, grease, mold-releasing compound, etc.

The change in tensile strength for the TPCM after exposure to the relatively high temperature HSS decontaminant may be partially due to polymer annealing as a result of being heated near or above the thermoplastics glass transition temperature (T_g).

Additional tensile tests of unexposed specimens will be conducted in the course of completing the overall experimental design to evaluate the TPCM as a function of exposure to agents and the remaining decontaminants. This additional data may help to reduce the confidence intervals for the tensile strengths of unexposed specimens. This will help with the statistical analysis of tensile strength changes for materials after solvent exposure and statistically significant differences in tensile strengths for materials before versus after solvent exposure may be identified.

CONCLUSIONS

The use of ASTM standard D638 tensile specimens to (also) determine weight and dimensional changes per ASTM standard D543 allows for an optimized solvent sorption/tensile testing methodology. Thus, weight and dimensional changes of plastics, as a function of solvent exposure, can be determined using tensile specimens.

The data from this phase of the investigation show a direct correlation between weight and tensile change after exposure to the HSS decontaminant.

Of the materials investigated only Nylon 6/6 experienced a statistically significant reduction in tensile strength after exposure to the HSS decontaminant. In addition, Nylon 6/6 showed the greatest weight change after exposure to the HSS decontaminant. In general, all of the nylons (polyamides), which are hydrogen bond donors/acceptors, absorbed the greatest weight fraction of water. The remaining candidate materials, which are proton acceptors/non-donors absorbed insignificant amounts of water; further regression of separate data sets will be reported in the future.

ACKNOWLEDGEMENT

The authors would like to express their appreciation to Mr. Ron Crosier (CRDEC) for his expert assistance in the development of the experimental design and the statistical analysis.

REFERENCES

1. McHugh, Vincent M., Shuely, Wendel J., Brletich, Richard W., Henshaw, John M. and Munson-McGee, Stuart H. Total Quality Design (TQD) Methodology Applied to the Selection of Chemical Resistant Composites for Mask Components. CRDEC-SP-034. Proceedings of the 1990 U.S. Army Chemical Research, Development and Engineering Center Scientific Conference on Chemical Defense Research, 13-16 November 1990, UNCLASSIFIED Report.
2. McHugh, Vincent M., Shuely, Wendel J., Brletich, Richard W., Henshaw, John M. and Munson-McGee, Stuart H. Investigation of Novel Composite Material Manufacturing Science and Chemical Interaction Tests for Mask Component Materials. U.S. Army Chemical Research, Development and Engineering Center FY 90 In-House Laboratory Independent Research (ILIR) Annual Report, November 1990, UNCLASSIFIED Report.

Table 1. Summary of Candidate Thermoplastic Composite Materials for Replacement of Aluminum in Components of the Aircrew Protective Mask.

Nylon 6/6 (PA66) - DuPont, Inc. Zytel 70G-43L (43% chopped glass)

Nylon 6/10 (PA610) - ICI, Inc. Thermocomp QF-100-12 (60% glass fiber)

Nylon 6/12 (ICI PA612) - ICI, Inc. Thermocomp IF-100-10 (50% glass fiber)

Nylon 6/12 (Com PA612) - Comalloy, Inc. 640-3050N (50% glass fiber)

polyetheretherketone (PEEK) - Thermofil, Inc. K2-40NF-0100 (40% graphite fiber)

poly(phenylene sulfide) (PPS) - RTP Co. 1387-P1 (40% carbon fiber)

poly(ethylene terephthalate) (PET) - Comalloy, Inc. Comtuf 464N (55% glass fiber)

poly(butylene terephthalate) (PBT) - Thermofil, Inc. E1-45FG-0100 (45% chopped glass)

Liquid Crystal Polymer (LCP) - Hoechst-Celanese, Inc. Vectra A422 (40% carbon/glass fiber)

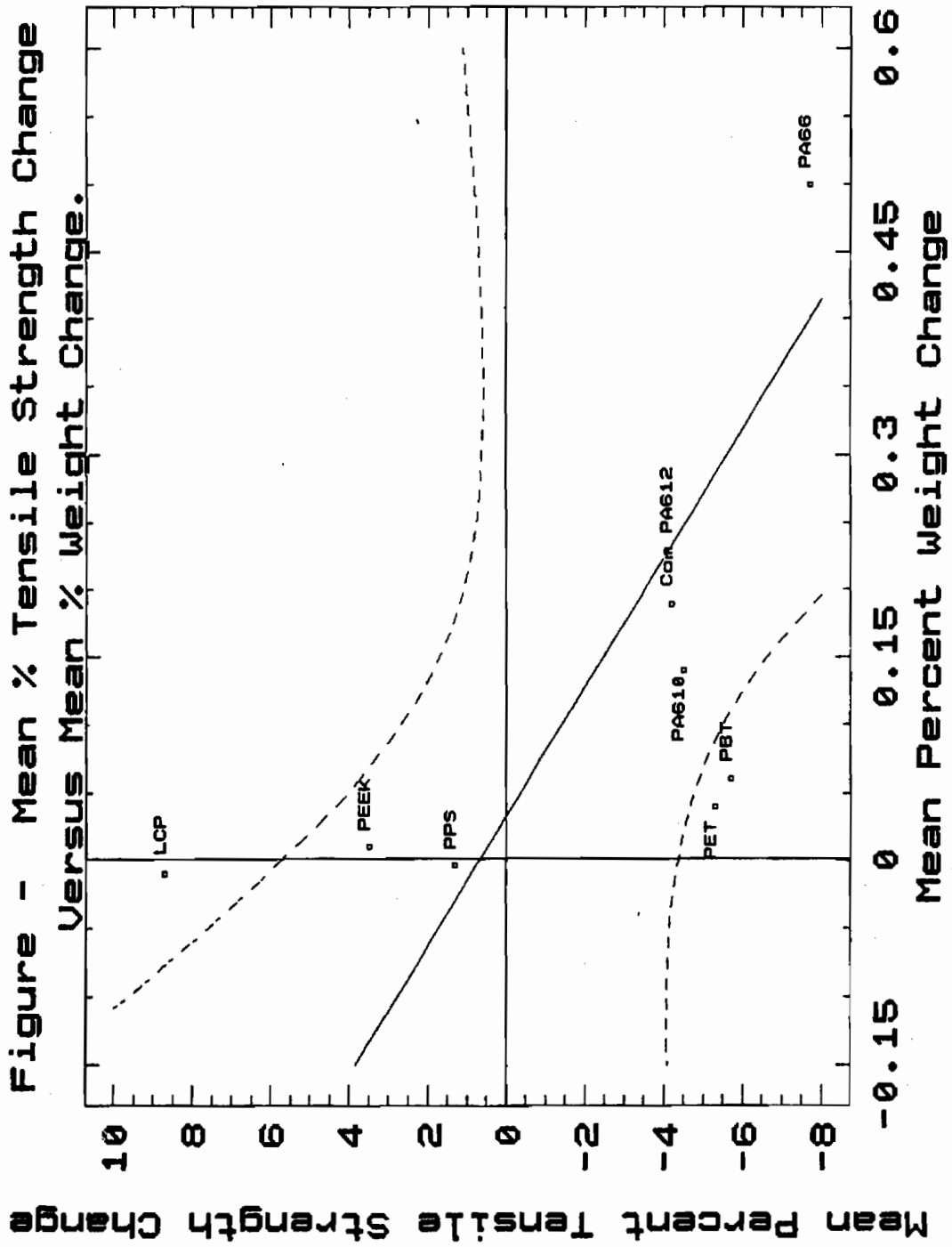
Table 2. Mean Percent Weight Change for 9 Candidate Thermoplastic Composite Materials After Exposure to a Hygrothermal Surfactant Solution Decontaminant (90-95 °C, 30 minutes).

<u>Material</u>	<u>Mean Percent Weight Change (95% CI)</u>
Nylon 6/6	+ 0.5 (\pm 0)
Nylon 6/12 (Comalloy)	+ 0.19 (\pm 0.01)
Nylon 6/10	+ 0.14 (\pm 0.01)
Nylon 6/12 (ICI)	+ 0.13 (\pm 0)
PBT	+ 0.06 (\pm 0.03)
PET	+ 0.04 (\pm 0)
PEEK	+ 0.01 (\pm 0)
Liquid Crystal Polymer	- 0.01 (\pm 0)
PPS	- 0.004 (\pm 0.002)

Table 3. Mean Percent Tensile Strength Change For Candidate Thermoplastic Composite Materials After Exposure to a Hygrothermal Surfactant Solution Decontaminant (90-95 °C, 30 minutes).

<u>Material</u>	<u>Mean Percent Tensile Strength Change</u>
Liquid Crystal Polymer	+ 8.7
PEEK	+ 3.5
PPS	+ 1.3
Nylon 6/12 (Comalloy)	- 4.2
Nylon 6/10	- 4.5
PET	- 5.3
PBT	- 5.7
Nylon 6/6	- 7.7

Figure - Mean % Tensile Strength Change Versus Mean % Weight Change.



BLANK

400

CORROSION BEHAVIOR STUDY OF TYPE II AND TYPE III ANODIZED Al 5052-0 IN AQUEOUS DS2 SOLUTIONS

Chester V. Zabielski and Milton Levy

U.S. Army Materials Technology Laboratory,
Watertown, MA 02172-0001

ABSTRACT

Corrosion studies utilizing both short-time electrochemical techniques and long-term immersion tests of Type II and Type III anodized Al 5052-0 and uncoated Al 5052-0 were carried out in 30 volume-percent DS2 aqueous decontaminating solution. Both electrochemical and immersion test data indicated that Type III anodized Al 5052-0 provided significantly greater resistance to degradation than Type II anodized Al 5052-0 or uncoated Al 5052-0.

INTRODUCTION

The System Engineering Division, U.S. Army Tank-Automotive Command, Warren, MI, requested U.S. Army Materials Technology Laboratory (MTL) assistance in assessing the corrosion resistance of two types of anodic coatings for the Al 5052-0 alloy housing cover of the Bradley turret drive system when exposed to the decontaminating agent DS2. The housing cover is presently treated with the Type III hard anodic coating in accordance with MIL-A-8625E. The General Electric Company, responsible for the turret drive system, has proposed as a cost savings measure, that the Type III hard anodic coating be replaced with the Type II conventional anodic coating produced from the sulfuric acid bath. The Corrosion Science Team at MTL has developed a technical data base for a variety of metals, alloys, and metal matrix composites listing their compatibility with DS2 and other decontaminating agents employing both short-term electrochemical and long-term immersion tests. However, data for the Al 5052-0 alloy and this anodically coated alloy had not been obtained. Accordingly, the objective of this program was to assess and compare the performance of Al 5052-0 when protected by either of the MIL-A-8625E Type II and Type III anodic coatings after exposure to DS2 decontaminating agent.

Prior experimental work at MTL¹ on the compatibility of aluminum alloys with DS2 showed that a marked increase in corrosion rate occurs when the DS2 agent is diluted with H₂O. It is reasonable to expect that moisture or water will be introduced into the DS2 agent in field service, particularly under combat conditions. As a consequence, an aqueous solution of DS2 was used in this study to represent a worst-case scenario.

Aluminum is essentially nonreactive near pH7, but its electrochemical activity in aqueous solutions increases rapidly on either side of this neutral point. The corrosion reaction on the acid side involves dissolution of aluminum with the evolution of hydrogen:



The reaction on the basic side forms aluminate anions and liberates hydrogen:

1. ZABIELSKI, C., LEVY, M., and SCANLON, J. *Corrosion and Corrosion Inhibition of Metals/Alloys in Methylphosphonic Difluoride and Decantaminating Solutions*. U.S. Army Materials Technology Laboratory, MTL TR 89-61, July 1989.



Factors that control metallic corrosion can be categorized as thermodynamic or kinetic. Thermodynamics determine the tendency to corrosion; i.e., whether or not a reaction is possible. The electrochemical principles of thermodynamics are those of reversible cells and standard potential. Application of these principles shows that most materials can react with their environments. The important engineering question is how fast will they react, which is the basis for the study of kinetics of corrosion reactions. Polarization techniques are particularly well suited for the study of corrosion reaction kinetics. These techniques are faster and more sensitive than conventional corrosion tests. They allow each of the partial processes in the corrosion reaction to be studied independently of the others. Polarization techniques have been used to study the effect of a variety of factors on the corrosion behavior of metals and alloys; i.e., the effects of composition, microstructure, heat treatment, and strength level. In potentiostatic polarization, by making the potential rather than the current the independent variable, it is possible to study the dissolution behavior of the alloy over its entire potential range.

In this study rapid potentiodynamic scans were performed over a very limited potential range (generally -100 to +100 mV from the corrosion potential) in order to determine the corrosion rate of the underlying alloy due to the microporosity and permeability of the oxide film. The long-term immersion tests performed provide supporting corrosion rate and oxide film data based on weight loss measurements and metallographic analysis. Immersion tests, weight loss, and metallographic studies were performed to determine the rates of anodized layer (oxide) degradation and dissolution and the rate of metal alloy corrosion.

Materials and Procedures

Two housing covers were provided by the General Electric Company of Pittsfield, MA. These housing covers were fabricated of annealed Al 5052-0 (SPEC QQ-A-250/8) and had a thickness of 0.090 ± 0.004 in. (2.29 ± 0.10 mm). Table 1 contains the nominal chemical analysis of the alloy in weight percent.

The first housing cover received a hard anodic coating in accordance with MIL-A-8625 Type III, Class 2, black and hot water seal $0.0025 + 0.0010$ or $- 0.0000$ in. ($0.0635 + 0.0254$ or $- 0.0000$ mm) thick. The second housing cover was given an anodic coating in accordance with MIL-A-8625, Type II, Class 2, black, 0.0004 in. (0.010 mm) minimum thickness.

The corrosion behavior of uncoated Al 5052-0, and the alloy coated with Type II and Type III anodized films, was studied by anodic and cathodic potentiostatic polarization techniques and by long-term immersion tests as a function of time at room temperature.

A Pyrex cell with a volume of one liter containing 500 ml of DS2 agent with water added was utilized for potentiodynamic scans. The composition of the DS2 decontaminating solution is shown in Table 2.

Table 1. CHEMICAL ANALYSIS FOR Al 5052-0

Si	Fe	Cu	Mn	Mg	Cr	Zn	Others		Al
							Each	Total	
0.25	0.40	0.10	0.10	2.2-2.8	0.15-0.35	0.10	0.05	0.15	Rem

NOTE: Composition in percent maximum unless shown as a range or minimum.

Table 2. DECONTAMINATING SOLUTION COMPOSITION

DS2	70 wt% Diethylenetriamine
	28 wt% Methyl Cellosolve (Ethylene Glycol Monomethyl Ether)
	2 wt% Sodium Hydroxide

NOTE: Previous work¹ showed that the maximum corrosion rate for aluminum alloys occurred in about 30 volume-percent DS2. As a consequence, this highly corrosive solution (pH 12) was utilized in this investigation.

The reference electrode was a saturated calomel electrode (SCE) separated by a glass bridge with a Vycor tip. The working electrode disc was contained in a polytetrafluorethylene holder and had an exposed surface area of 1.0 cm^2 . The electrochemical cell has been described in detail elsewhere.² In order to describe the anodic and cathodic processes, anodic and cathodic polarization measurements were made utilizing the potential sweep method of potentiodynamic polarization. The electrode potential was

2. LEVY, M. *Anodic Behavior of Titanium and Commercial Alloys in Sulfuric Acid*. *Corrosion*, v. 23, no. 8, August 1967, p. 237.

continuously changed at a constant rate of 5000 mV/hr, and current was simultaneously recorded. Corrosion rates in mils per year (mpy) were also obtained by extrapolation of Tafel slopes to the corrosion potential. For Al 5052-0 corrosion rate calculations, a density of 2.68 g/cm³ was utilized.

A 100 ml glass jar containing 80 ml of DS2 solution was utilized for immersion tests. The test specimen disc was contained in a polytetrafluorethylene holder which exposed a surface area of 1.0 cm². Measurements of total weight loss in mg/cm² were made versus immersion time in hours. The weight losses were converted to corrosion rates in mils per year. For the corrosion rate calculation for the anodized oxide layer, a density of 3.99 g/cm³ was utilized for aluminum oxide.

RESULTS AND DISCUSSION

Potentiodynamic Polarization - Uncoated Al 5052-0

Figure 1 shows a potentiodynamic scan for the uncoated alloy after ten minutes immersion in DS2 solution. Since the anodic and cathodic scans for the alloy after longer immersion times (not shown) were made within the same potential range, the curves were quite similar. The anodic curve shows active dissolution with no tendency to passivate and a maximum observed current density of ~1500 $\mu\text{A}/\text{cm}^2$. Table 3 lists the corrosion rates (mpy) for the uncoated alloy determined by extrapolation of the anodic and cathodic Tafel regions to the corrosion potential as a function of immersion time in the DS2 solution. The corrosion rates were high and ranged from 238 to 511 mpy.

Table 3. POTENTIODYNAMIC POTENTIAL RANGES, CORROSION POTENTIALS, TAFEL CONSTANTS, AND CORROSION RATES FOR UNCOATED Al 5052-0 IN 30 VOLUME-PERCENT DS2

Immersion Time (min)	Initial E to Final E (mV)	E _{corr} (mV)	E _{corr} Calc (mV)	Tafel Constant		i _{corr} ($\mu\text{A}/\text{cm}^2$)	Corr Rate (mpy)
				β_c (mV)	β_a (mV)		
10	-100 to 100	-1605	-1604.2	166.29	168.9	566.65	238.5
30	-100 to 100	-1597	-1596.98	192.2	310.98	823.2	346.4
60	-100 to 100	-1597	-1596.27	176.85	182.6	672.31	282.9
80	-100 to 0	-1596	nd				
100	-100 to 0	-1591	nd				
120	-250 to 250	-1585	-1582.8	317.21	343.63	1212.27	510.1
240	-250 to 250	-1573	-1571.02	320.9	345.4	1215.33	511.4

NOTE: nd = no data

Type II Anodized Al 5052-0

Figure 2 contains potentiodynamic scans for the Type II anodized alloy after different immersion times in DS2 decontaminating solution. Comparing these curves with that of the bare aluminum alloy in Figure 1, it is clear that the Type II anodic coating, after immersion times of 10 and 30 minutes, shifts the corrosion potential in the noble direction and significantly reduces the maximum observed current density from ~1500 $\mu\text{A}/\text{cm}^2$ to less than 30 $\mu\text{A}/\text{cm}^2$, which is typical of passivity. However, after immersion times of 60 to 240 minutes, there are marked changes; i.e., the corrosion potential and magnitude of the current density approach those of the uncoated alloy, indicative of dissolution of the protective anodic film. Corrosion rates extrapolated from the polarization curves in Figure 2 are contained in Table 4. The corrosion rates after 10 and 30 minutes of immersion, two and seven mpy, respectively, were much lower than those found for the uncoated alloy at identical times of immersion (see Table 3). Thus, the anodic protective layer was still present and effective. However, after 60 minutes of immersion time the corrosion rate markedly increased to 223 mpy, indicative of dissolution of the anodic layer. Longer immersion times resulted in higher corrosion rates reaching a maximum of 294 mpy which approached the corrosion rate of the uncoated alloy.

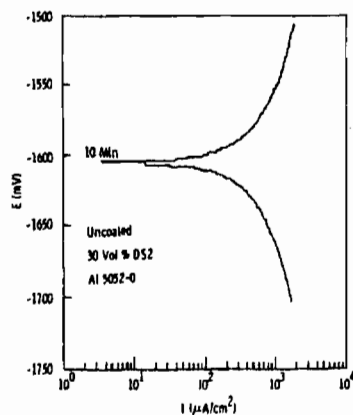


Figure 1. Potentiodynamic polarization curve of uncoated Al 5052-0 after 10 minutes immersion in 30 volume-percent DS2 at 25°C. Scan Rate: 1.388 mV/sec.

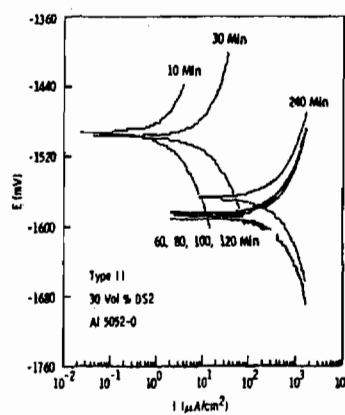


Figure 2. Effect of time of immersion on the potentiodynamic polarization behavior of Type II anodized Al 5052-0 in 30 volume-percent DS2 at 25°C. Scan Rate: 1.388 mV/sec.

Type III Anodized Al 5052-0

Figure 3 shows polarization curves for the alloy protected with the Type III hard anodic coating after immersion times of up to 120 minutes in DS2 solution. The anodic curves after 10, 30, and 60 minutes of immersion time are quite similar and are characterized by significantly more noble corrosion potentials and lower maximum observed current densities ($\sim 1 \mu\text{A}/\text{cm}^2$), indicative of the superior nature of the Type III hard anodic coating when compared to the Type II anodic coating. However, after 120 minutes of immersion time in DS2 solution, the corrosion potential became much more active and the maximum observed current density increased to $\sim 100 \mu\text{A}/\text{cm}^2$, which is still lower than the maximum observed current density of $\sim 1000 \mu\text{A}/\text{cm}^2$ developed for the Type II coating after the same immersion time. Extending the immersion time to 240 minutes served only to shift the corrosion potential in the more active direction to the same corrosion potential as the uncoated alloy. The maximum observed current density, however, remained at $100 \mu\text{A}/\text{cm}^2$ (see Figure 4), which is considered to be the limit for passivity. Further increases in immersion time up to 420 minutes (see Figure 5) produced no changes in either corrosion potential or maximum observed current density. Figure 6, which is a macrograph of the coated alloy surface taken after nine hours of immersion time, shows that a significant amount of the Type III hard anodic coating is still present. Corrosion rates for the Type III anodized Al 5052-0 extrapolated from the polarization curves of Figures 3, 4, and 5 are contained in Table 5. Corrosion rates of 0.22, 0.15, and 0.16 mpy are shown after 10, 30, and 60 minutes of immersion time, indicating a thicker and less porous anodized layer was present. Corrosion rates increased at longer immersion times, reaching a maximum of 49 mpy at 180 minutes of immersion time, and diminishing to 20 mpy at 540 minutes of immersion time. Nevertheless, these corrosion rates were markedly lower than those for the uncoated alloy and the Type II anodized alloy at comparable immersion times.

Table 4. POTENTIODYNAMIC POTENTIAL RANGES, CORROSION POTENTIALS, TAFEL CONSTANTS, AND CORROSION RATES FOR TYPE II ANODIZED Al 5052-0 IN 30 VOLUME-PERCENT DS2

Immersion Time (min)	Initial E to Final E (mV)	E_{corr} (mV)	$E_{\text{corr Calc}}$ (mV)	Tafel Constant		i_{corr} ($\mu\text{A}/\text{cm}^2$)	Corr Rate (mpy)
				β_c (mV)	β_a (mV)		
10	-100 to 100	-1523	-1492.33	187.86	554.1	5.0	2.1
30	-100 to 100	-1501	-1497.09	126.8	252.26	17.2	7.24
60	-100 to 100	-1588	-1586.13	167.21	169.59	529.86	222.9
80	-100 to 100	-1590	-1589.42	196.45	204.89	681.54	286.7
100	-100 to 100	-1592	-1591.13	166.38	172.1	555.77	233.8
120	-100 to 100	-1589	-1587.73	194.64	199.04	673.5	283.4
240	-100 to 100	-1568	-1567.5	199.74	207.76	699.39	294.3
250	-100 to 100	-1567	-1567.01	163.79	169.66	542.43	228.2

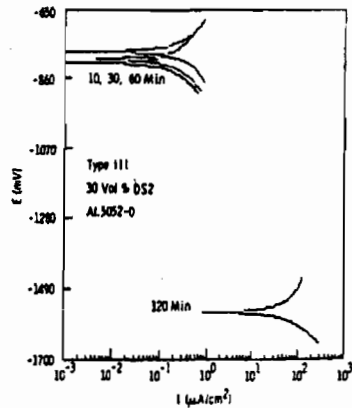


Figure 3. Effect of time of immersion up to 120 minutes on the potentiodynamic polarization behavior of Type III anodized Al 5052-0 in 30 volume-percent DS2 at 25°C. Scan Rate: 1.388 mV/sec.

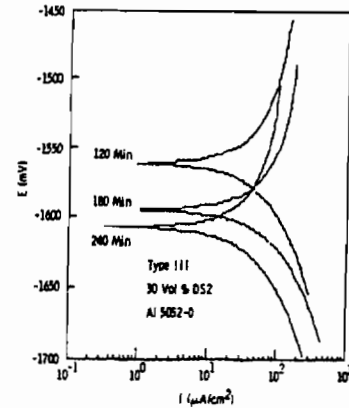


Figure 4. Effect of time of immersion from 120 to 240 minutes on the potentiodynamic polarization behavior of Type III anodized Al 5052-0 in 30 volume-percent DS2 at 25°C. Scan Rate: 1.388 mV/sec.

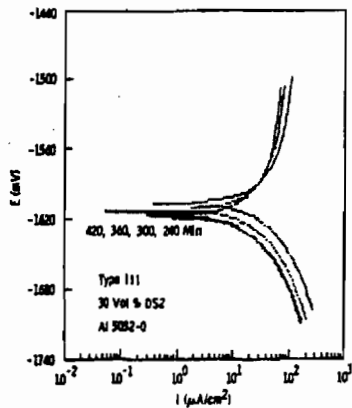


Figure 5. Effect of time immersion from 240 to 420 minutes on the potentiodynamic polarization behavior of Type III anodized Al 5052-0 in 30 volume-percent DS2 at 25°C. Scan Rate: 1.388 mV/sec.

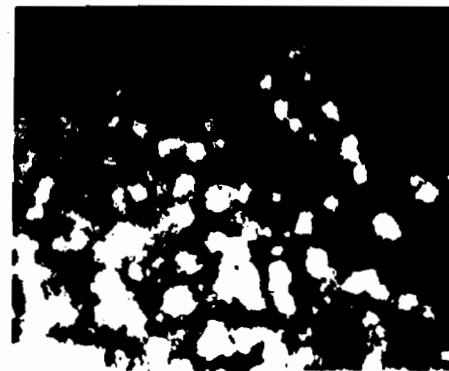


Figure 6. Degradation of Type III anodized Al 5052-0 coating after nine hours exposure to 30 volume-percent DS2 in polarization cell. Mag. 5X

Table 5. POTENTIODYNAMIC POTENTIAL RANGES, CORROSION POTENTIALS, TAFEL CONSTANTS, AND CORROSION RATES FOR TYPE III ANNOXIDIZED Al 5052-0 IN 30 VOLUME-PERCENT DS2

Immersion Time (min)	Initial E to Final E (mV)	E _{corr} (mV)	E _{corr} Calc (mV)	Tafel Constant		I _{corr} (μA/cm ²)	Corr Rate (mpy)
				β _c (mV)	β _a (mV)		
10	-100 to 100	-778	-774.93	299.54	304.22	0.53	0.22
30	-100 to 100	-800	-800.92	286.01	292.18	0.36	0.15
60	-100 to 100	-807	-812.92	284.65	380.07	0.39	0.16
120	-100 to 100	-1555	-1559.87	141.06	364.2	84.84	35.7
180	-100 to 100	-1588	-1593.59	128.57	434.51	115.73	48.7
240	-100 to 100	-1599	-1607	157.82	1073.82	99.07	41.6
300	-100 to 100	-1605	-1613.43	161.17	1218.68	78.75	33.1
360	-100 to 100	-1606	-1616.33	120.35	364.12	40.15	16.9
420	-100 to 100	-1610	-1617.41	117.17	320.68	35.71	15.0
540	-100 to 100	-1615	-1624.88	140.29	657.45	47.19	19.8

Long-Term Immersion Tests for Uncoated Al 5052-0

Figure 7 is a plot of total weight loss in mg/cm^2 versus hours of immersion for uncoated Al 5052-0 disc specimen exposing one square centimeter of surface area to the 30 volume-percent DS2 solution. The total weight loss in mg/cm^2 versus hours of immersion is shown in Table 6. A linear relationship is observed and the rate of weight loss is approximately constant at about $2.5 \text{ mg}/\text{cm}^2/\text{hr}$. The corresponding corrosion rate is 0.37 mils per hour (mph), 8.8 mils per day (mpd), or 3200 mpy.

Figure 8 shows the surface of an uncoated Al 5052-0 specimen prior to immersion at 5X magnification with machining marks evident. Figure 9 shows the same specimen surface after 12 hours immersion time. The machining marks have disappeared, reflecting the relatively large weight loss of the alloy due to corrosion.

Table 6. IMMERSION TIMES, DISC WEIGHTS, AND TOTAL WEIGHT LOSSES FOR UNCOATED Al 5052-0

Immersion Time (hour)	Disc Weight (grams)	Total Weight Loss (mg/cm^2)
0	1.0871	0.00
2	1.0805	6.66
4	1.0762	10.90
6	1.0711	16.00
8	1.0663	20.80
10	1.0622	24.90
12	1.0579	29.20

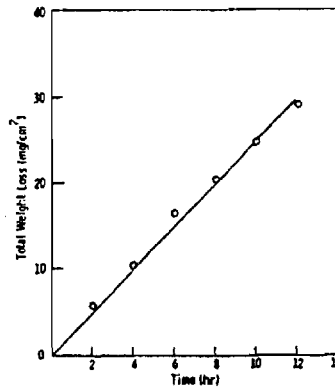


Figure 7. Effect of time of exposure on total weight loss for uncoated Al 5052-0 in 30 volume-percent DS2.



Figure 8. Presence of machining marks on surface of uncoated Al 5052-0 prior to immersion in 30 volume-percent DS2. Mag. 5X

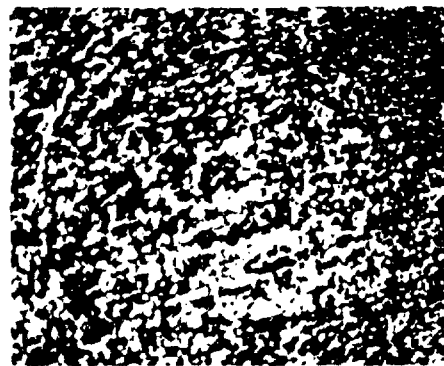


Figure 9. Disappearance of machining marks from surface of uncoated Al 5052-0 after 12 hours immersion in 30 volume-percent DS2. Mag. 5X

Type II Anodized Al 5052-0

Figure 10 plots total weight loss as a function of immersion time. The initial linear rate of increase of weight loss up to two hours of immersion time is high, and corresponds to a rate of weight loss of $7.5 \text{ mg}/\text{cm}^2/\text{hr}$ (see Table 7) and a corresponding corrosion rate of 0.74 mph, 17.8 mpd, and 6500 mpy, due to the rapid dissolution of the Type II anodized coating. After two hours immersion time the corrosion rate decreases to 0.45 mph, 10.8 mpd, or 3900 mpy, which is roughly equivalent to the corrosion rate of the

uncoated alloy. Metallographic examination, as shown in Figures 11 through 14, is consistent with the weight loss data. Figure 11 shows the surface of the as-received Type II black anodized Al 5052-0 disc at 5X magnification prior to immersion. Figures 12 and 13 show the now mottled gray anodized coating after one and one-and-one-half hours of immersion time, respectively. Figure 14 indicates that, after two hours of immersion time, the gray coating is no longer present.

Table 7. IMMERSION TIMES, DISC WEIGHTS, AND TOTAL WEIGHT LOSSES FOR TYPE II ANODIZED Al 5052-0

Immersion Time (hour)	Disc Weight (grams)	Total Weight Loss (mg/cm ²)
0	1.1582	0.00
0.5	1.1555	2.7
1	1.1515	6.7
1.5	1.1494	8.8
2	1.1431	15.1
4	1.1375	20.7
6	1.1309	27.3
8	1.1249	33.3

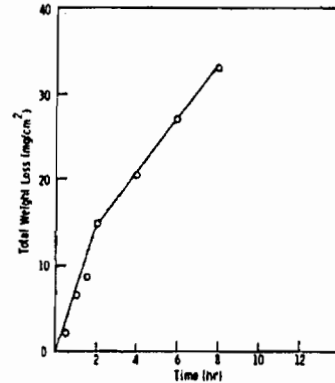


Figure 10. Effect of time exposure on total weight loss for Type II anodized Al 5052-0 in 30 volume-percent DS2.



Figure 11. Uniformly dyed black surface of as-received Type II anodized Al 5052-0 coating prior to immersion in 30 volume-percent DS2. Mag. 5X

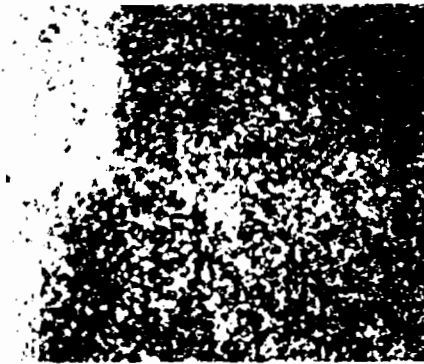


Figure 12. Mottled gray surface of degraded Type II anodized Al 5052-0 coating after one hour immersion in 30 volume-percent DS2. Mag. 5X



Figure 13. Mottled gray surface of degraded Type II anodized Al 5052-0 coating after 1.5 hours immersion in 30 volume-percent DS2. Mag. 5X

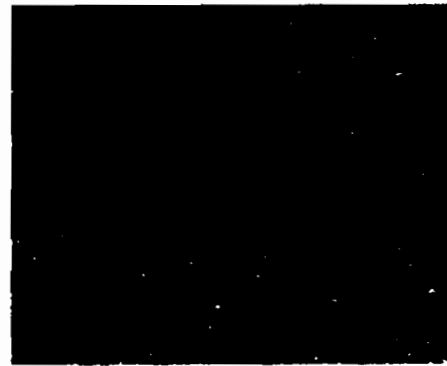


Figure 14. Uncoated metallic surface after complete dissolution of the Type II anodized Al 5052-0 coating after two hours immersion in 30 volume-percent DS2. Mag. 5X

Type III Anodized Al 5052-0

Weight loss data for the Type III anodized alloy is shown in Table 8, as well as in Figure 15. The initial relatively high dissolution rate of the Type III hard anodic coating diminishes significantly after eight hours immersion time. The rate of total weight loss and the corrosion rates are markedly below those for the Type II anodized Al 5052-0 and the uncoated alloy. These data are supported by the macrographs shown in Figures 16 through 19. Figure 16 shows the surface of the as-received Type III black anodized Al 5052-0 disc at 5X magnification prior to immersion. Figures 17, 18, and 19 show the progress of degradation of the coating after two, four, and eight hours immersion time in 30 volume-percent DS2 solution. Although some deterioration of the Type III anodized Al 5052-0 coating occurs at about two hours, most of the coating remains after eight hours of immersion time.

Table 8. IMMERSION TIMES, DISC WEIGHTS, AND TOTAL WEIGHT LOSSES FOR TYPE III ANODIZED Al 5052-0

Immersion Time (hour)	Disc Weight (grams)	Total Weight Loss (mg/cm ²)
0	1.2412	0.0
1	1.2378	3.4
2	1.2361	5.1
4	1.2309	10.3
6	1.2270	14.2
8	1.2249	16.3
14	1.2240	17.2
17	1.2229	18.3
20	1.2220	19.2
26	1.2220	19.2
32	1.2211	20.1
38	1.2209	20.3

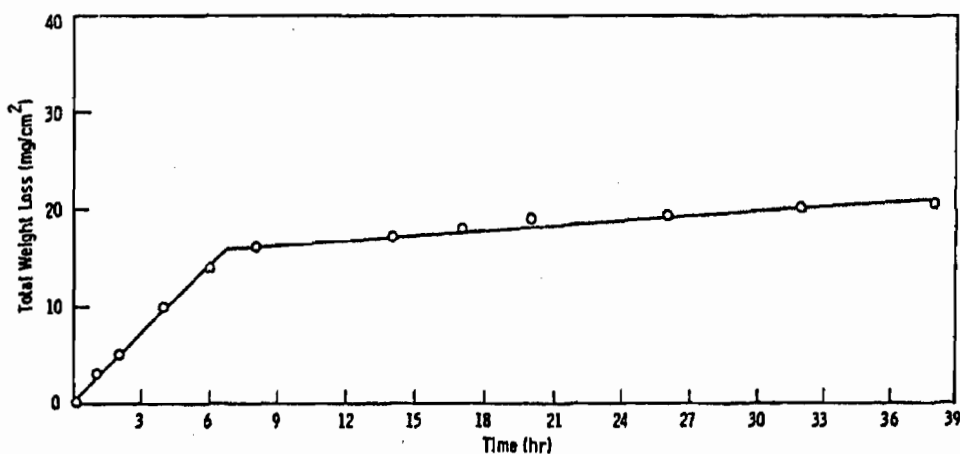


Figure 15. Effect of time of exposure on total weight loss for Type III anodized Al 5052-0 in 30 volume-percent DS2.

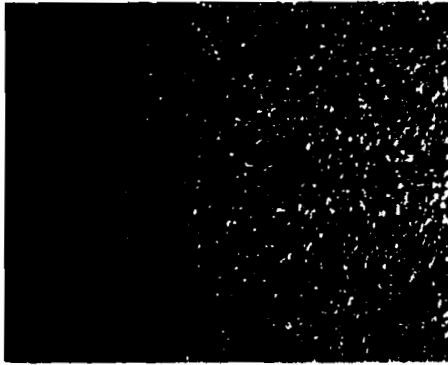


Figure 16. Uniformly dyed black surface of as-received Type III anodized Al 5052-O coating prior to immersion in 30 volume-percent DS2. Mag. 5X

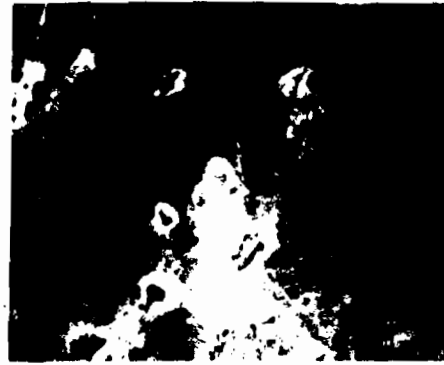


Figure 17. Degradation of Type III anodized Al 5052-O coating after two hours immersion in 30 volume-percent DS2. Mag. 5X



Figure 18. Degradation of Type III anodized Al 5052-O coating after four hours immersion in 30 volume-percent DS2. Mag. 5X

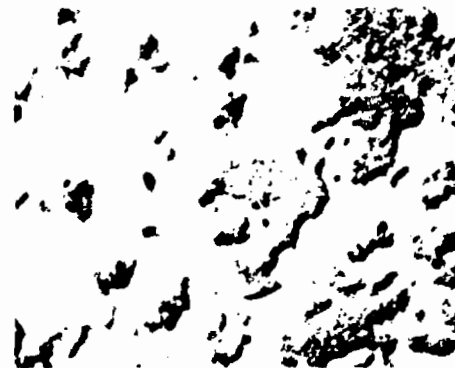


Figure 19. Degradation of Type III anodized Al 5052-O coating after eight hours immersion in 30 volume-percent DS2. Mag. 5X

CONCLUSIONS

The potentiodynamic polarization tests, the long-term immersion tests, and metallographic examination show:

- The uncoated alloy has a very high corrosion rate of greater than 200 mpy when exposed to the DS2 decontaminating solution and will require a protective coating.
- The Type II anodic coating dissolves after about one hour of exposure to DS2 solution, after which a corrosion rate equivalent to that of the uncoated alloy is observed.
- The Type III hard anodic coating was protective after two hours of exposure. Although some dissolution occurred thereafter, the coating was still present on the alloy surface after eight hours of exposure to DS2 solution. Weight loss and electrochemically determined corrosion rates were markedly lower than those of both the Type II coated alloy and the uncoated alloy.
- The performance of the Type III hard anodic coating was markedly superior to that of the Type II anodic coating in an aqueous DS2 solution representing the worst-case scenario and it is therefore recommended for the application.

BLANK

X. DECONTAMINATION

NOTE: Papers with the following titles were presented at the Conference but are not included in this document:

Complete Destruction of Agents in Microheterogeneous Solution and on Oxide Films (153)

Mechanistic Studies of the Reaction of Phenolates and Thiophenolates with 2-Chloroethyl Methyl Sulfide in Aprotic Solvents and Some Containing Water (157)

Exploration of Non-Enzymatic Broad Spectrum Catalysts for CW-Agent Decomposition (159)

BLANK

REACTION OF VX WITH CHLORAMINE-B

Yu-Chu Yang, Linda L. Szafraniec, William T. Beaudry, and J. Richard Ward

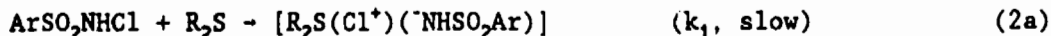
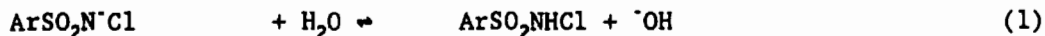
U.S. Army Chemical Research, Development and Engineering Center,
Aberdeen Proving Ground, MD 21010-5423.

ABSTRACT

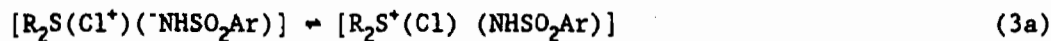
The nerve agent VX ((C₂H₅O)(CH₃)P(O)(SCH₂CH₂N[CH(CH₃)₂]₂) reacts with the sodium salt of N-chlorobenzenesulfonamide or Chloramine-B (CAB, C₆H₅SO₂N(Cl)Na), only in the presence of sufficient acid. In a solution of 0.01 M VX and 0.1 M CAB at pH of 10.5, hydrolysis was the only reaction observed at 21°C until sufficient acidic products were accumulated after a few days. The CAB was suddenly activated to rapidly oxidize the remaining VX. When 0.25 M H₂SO₄ was initially added to the same mixture, VX reacted completely in less than 15 minutes. In addition to the corresponding phosphonic and sulfonic acid products, sulfimides were also formed. The reaction follows a similar mechanism as that of the sulfides reported in the literature - the formation of the chlorosulfonium ion is the rate determining step followed by rapid hydrolysis and substitution reactions.

INTRODUCTION

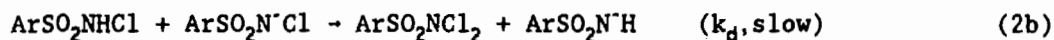
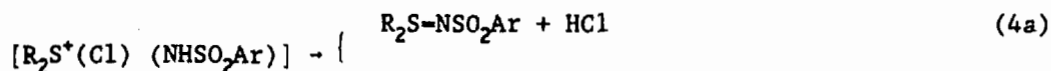
Chloramine-B (CAB, C₆H₅SO₂N(Cl)(Na)), the sodium salt of an N-chloro sulfonamide, has long been known for its effectiveness in detoxifying the chemical agent mustard (S(CH₂CH₂Cl)₂).¹ As shown in the two parallel, competitive paths in equations (1) thru (5a) as well as (1) thru (5b), a dialkyl sulfide (R₂S, R = CH₂CH₂Cl for mustard) rapidly reacts with CAB to form both mustard sulfoxide (O-S(CH₂CH₂Cl)₂) and the sulfimide addition product, (C₆H₅S(O)₂N-S(CH₂CH₂Cl)₂) at room temperature in aqueous solution.



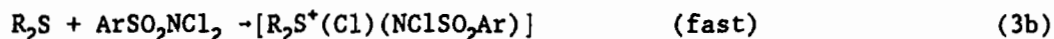
CSA



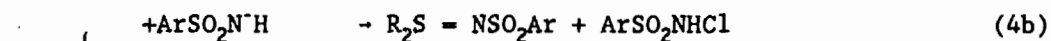
I



DCA



II



In the rate determining step (k_1), the protonated CAB, an N-chloro-sulfonamide (CSA), is the reactive component which provides both the oxidative chloronium ion, $[Cl^{+1}]$, and the protonated sulfonamide anion ($^-\text{NHSO}_2\text{Ar}$) to form the chlorosulfonium ion-pair intermediate I shown in eq (3a). This intermediate subsequently reacts quickly by two parallel paths to form the observed sulfimide and sulfoxide products. However, as shown in eq (2b), a competing path also exists. The CSA can disproportionate (k_d) to produce the highly reactive dichloramine-B (DCAB) which reacts as soon as it is formed to produce the chlorosulfonium ion intermediate II shown in eq (3b). The competitive formation of I and II is dependent on the relative magnitudes of k_1 and k_d with k_1 also dependent on the sulfide. For most sulfides, the overall rates were too fast to be measured in neutral to acidic solution, but could be measured in basic solution; the mechanism was reported to be acid-catalyzed.²

One of the U.S. Army fielded personal decon kits, the M280 system, uses about 0.2 M CAB and 5 wt% $ZnCl_2$ in an ethanol-water mixture to detoxify mustard instantaneously at pH 5 to 6. However, as shown in Table 1, the M280 system did not detoxify VX effectively; about 65% VX was still present after 21 hours.³ Oxidation of thiolates or thioates by N-chloro oxidants has previously been reported: Chloramine-T (CAT, $(CH_3)_6H_4SO_2N(Cl)(Na)$), was shown to oxidize thioate pesticides such as parathion (O,O-diethyl O-(4-nitrophenyl)-phosphorothionate) and malathion (S-(1,2-dicarbethoxyethyl) O,O-dimethyl phosphorothioate) in ethanol-water solutions at low pH.^{4,5} Furthermore, sodium dichloroisocyanurate (fichlor) was found to oxidize a stoichiometric amount of VX instantaneously to form the corresponding phosphonic and sulfonic acids at room temperature in a t-butyl alcohol-water mixture.⁶ In the same study, the VX analog, O,S-diethyl methylphosphonothiolate or DEMPT ($(CH_3)_2P(O)(OC_2H_5)(SCH_2CH_3)$), also reacted immediately with both CAB and fichlor in aqueous solution. The purpose of

this study was to investigate the apparently unique inertness of VX towards CAB and to determine if catalytic activation of CAB for reaction with VX is possible.

EXPERIMENTATION

^{31}P NMR was used to monitor the reactions of CAB and the thiolates at 21-22°C. For dilute solutions at 0.0005 M sulfide or thiolate, ^1H NMR was used to follow the rates in D_2O . The reaction products were identified by ^{31}P and ^{13}C NMR as well as GC/MS in the final solutions. Detailed experimental procedures have been reported in previous publications.³

RESULTS AND DISCUSSION

(1) Reactions of VX with CAB

As shown in TABLE 1, in neutral to basic solutions, no apparent reaction of VX and CAB was observed for at least the first 10 hours. During this period, only a small amount of VX was converted to the phosphonic acid (1, $(\text{CH}_3)_2\text{P}(\text{O})(\text{OC}_2\text{H}_5)(\text{OH})$) from cleavage of the P-S bond. In addition, the thioic acid of VX (2, $(\text{HO})\text{P}(\text{O})(\text{CH}_3)(\text{SCH}_2\text{CH}_2\text{N}(\text{CH}_3)_2)_2$) from cleavage of the P-O bond was not observed in any of the reaction mixtures containing excess CAB. In these solution mixtures, the oxidation product from the thioic acid, methylphosphonic acid (3, $(\text{CH}_3)_2\text{P}(\text{O})(\text{OH})_2$) was detected and positively identified by NMR.⁷

In acidic solutions, on the other hand, VX reacted with CAB completely in less than one hour. The reaction rates increased as the CAB and/or acid concentrations increased. As shown in TABLE 1, the stronger Lewis acid, AlCl_3 , was a better catalyst than the ZnCl_2 used in the M280 system. This indicated that the reaction of VX and CAB required a large amount of acid to activate one or both of the reactants. The thioic acid must be more reactive than VX and reacted as soon as it was produced from hydrolysis.

The reaction half-life of 0.01 M VX in 0.1 M CAB in the presence of 0.5 N $[\text{H}^+]$ is shown in FIGURE 1 to be 9 min. In the absence of any $[\text{H}^+]$, the CAB was eventually catalyzed by the acidic products generated from hydrolysis after 4 days. The reaction profile as followed by ^{31}P NMR is shown in FIGURE 2.

(2) Comparison with DEMPT.

As shown in TABLE 2, a neutral thiolate analog of VX, DEMPT, did not require the addition of acid for reaction with CAB in pure water. However, in D_2O where D^+ is a weaker catalyst than H^+ , a small amount of H^+ must be added to the reaction mixture for reaction to occur. The amount of acid required for DEMPT was smaller than that for VX in the same medium. Apparently the additional acid is required to protonate the basic nitrogen in VX.

TABLE 1 The Reaction of VX and Chloramine-B at 21-22°C

[VX], M	[CAB], M	Solvent	Reaction Time	VX	Composition by ³¹ P NMR, mol %		
					P(O)OH 1	P(O)(SR)OH 2	P(O)(OH) ₂ 3
0.02	0.00	H ₂ O	8 hr	80	7	9	0
0.02	0.02	H ₂ O	24 hr	74	13	5	2
0.01	0.10	H ₂ O	17 hr	78	11	0	3
0.02	0.02	t-BuOH-H ₂ O	24 hr	94	4	0	0
0.02	0.20	C ₂ H ₅ OH-H ₂ O	5 hr	76	18	0	0
		+5% ZnCl ₂ (M280)	21 hr	65	26	0	0
0.01	0.01	H ₂ O + 0.05 N [H ⁺]	7 min	51	49	0	0
			45 min	3	97	0	0
0.01	0.30	H ₂ O + 0.10 N [H ⁺]	2 min	15	70	0	0
			15 min	0	91	0	0
0.01	0.30	H ₂ O + 5% AlCl ₃	6 min	7	57	0	0
			15 min	0	74	0	0

TABLE 2 The Reaction of DEMPT and CAB at 21-22°C

[Thiolate], M	CAB, M	Solvent	Reaction Time	Composition by ¹ H and/or ³¹ P NMR mole%	
DEMPT				thiolate	Me(OEt)P(O)OH
0.01	0.00	H ₂ O	7 months	100	0
0.05	0.02	H ₂ O	5 min (final)	73	25
5 x 10 ⁻⁴	5 x 10 ⁻²	H ₂ O	47 min	34	66
			55 min	0	100
5 x 10 ⁻⁴	5 x 10 ⁻²	D ₂ O	18 hr	96	---
5 x 10 ⁻⁴	5 x 10 ⁻²	D ₂ O + 0.002 N [H ⁺]	4 hr	3	97
5 x 10 ⁻⁴	5 x 10 ⁻²	D ₂ O + 0.006 N [H ⁺]	< 2 min	0	92
VX					
5 x 10 ⁻⁴	5 x 10 ⁻²	D ₂ O + 0.006 N [H ⁺]	22 hr	73	---
			96 hr	10	90

SCHEME 1

Reaction Mechanism of VX and CAB in Acidic Solutions

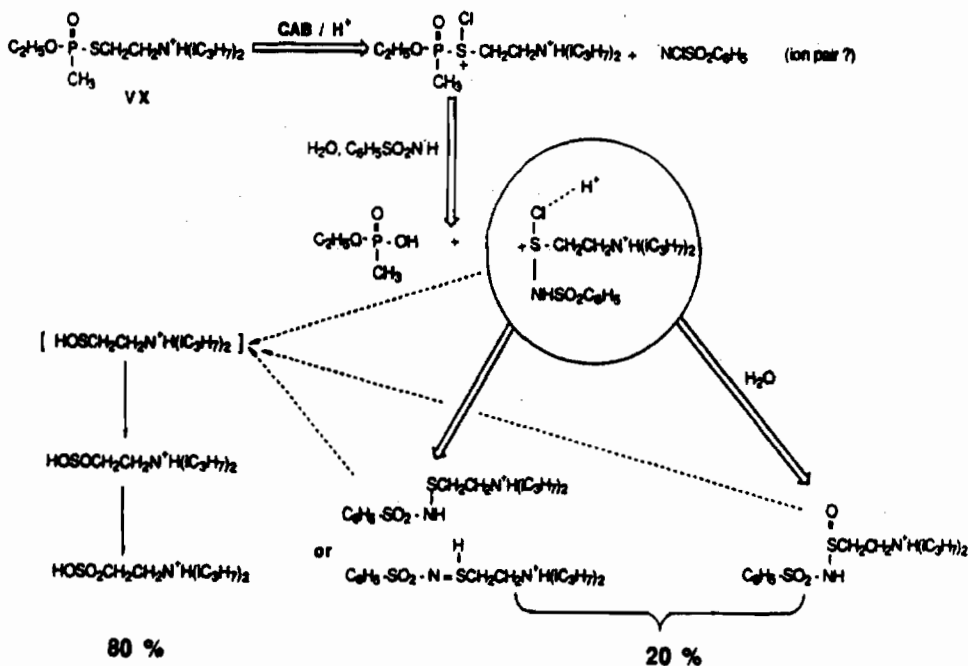


TABLE 3 Reaction of 2-Hydroxyethyl Sulfoxides and Chloramine-B (CAB) in D₂O at 21-22°C

Substrate	[CAB], M ^a	[H ⁺] or [OH ⁻], M ^b	pH ^b	t _{1/2} , min	Product Ratio by ¹ H NMR Imine/Sulfoxide, mole/mole
0.0005M HEES	0.015	0	8.9	<2	72/28
0.0005M HEPS	0.015	0	8.9	12	72/28
0.0005M HEFS	0.015	0.002 N [H ⁺]	4.9	<2	100/0
0.0005M HEPS	0.015	0.002 N [OH ⁻]	10.6	63	64/36
0.005 M HEPS	0.003	0	8.8	-	37/63 ^c

a. The active chlorine content in CAB is about 86%.
 b. The pH values were measured in solutions prepared with H₂O rather than D₂O.
 c. The final solution contains 41-42% of unreacted HEFS.

FIGURE 1 Reaction of VX and CAB in H₂SO₄

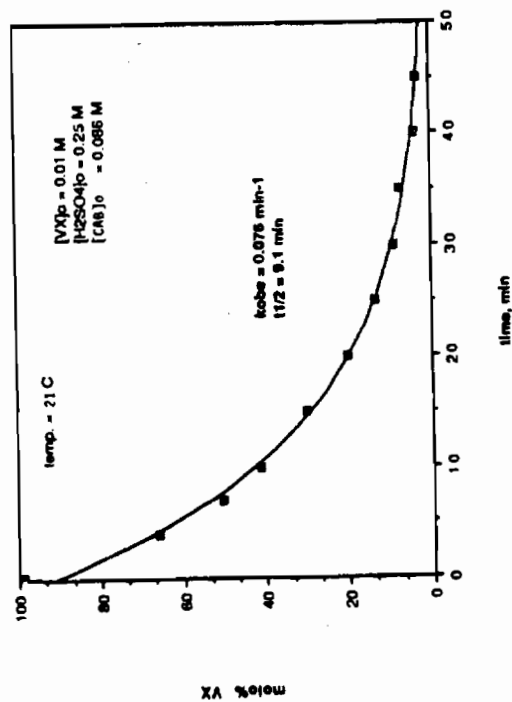
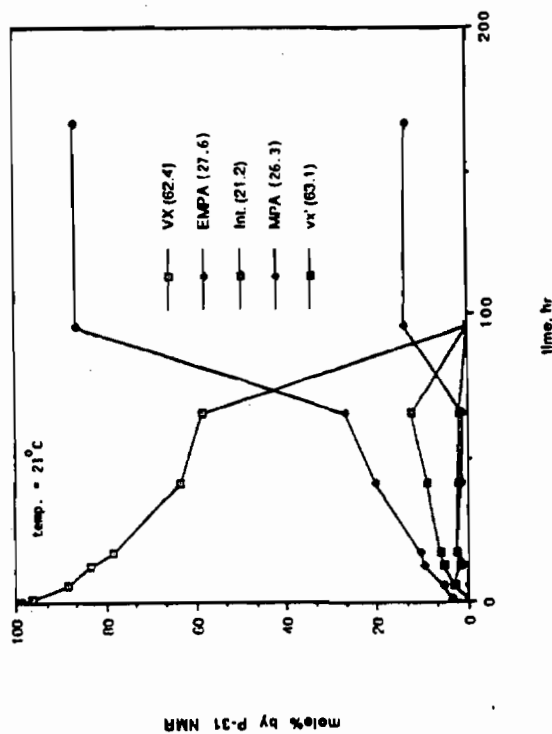


FIGURE 2 0.01M VX and 0.1M CAB in Water



(3) Reaction Products and Proposed Mechanism.

The reaction products of VX in an acidic solution are illustrated in SCHEME 1. Based on the structures of these products, a reaction mechanism of CAB with VX is proposed. Different from the sulfide-CAB reaction, oxidation of VX involves the cleavage of the P-S bond as soon as the chlorosulfonium ion is formed. The final sulfonic acid product is believed to be a result of the fast overoxidation of the transient sulfenic acid by CAB. No sulfone was ever detected from sulfide-CAB reactions.

(4) Comparison with the Reactions of 2-Hydroxyethyl Sulfides.

To confirm that the CAB oxidation of a sulfide is acid-catalyzed, the reaction of CAB with two water-soluble sulfides, 2-hydroxyethyl ethyl sulfide (HEES) and 2-hydroxyethyl phenyl sulfide (HEPS) were investigated in D_2O as a function of pH. As shown in TABLE 3, the reactions in basic solution were slower than in neutral and acidic solution. The exclusive imine product from HEPS also indicated that the concentration of the sulfonamide anion was higher in the presence of acid.

However, as shown in TABLE 2, a higher proton concentration is required for the thiolates than for the sulfides. In particular, the basic VX must be protonated in order to react with the protonated CAB. Furthermore, as discussed in (1), the thioic acid from hydrolysis at the P-O bond of VX,⁸ has been found to be a more reactive oxidation substrate and provides the necessary proton for rapid reaction with CAB. Therefore, at constant pH, the reactivity of CAB is also dependent on the oxidation potential of the sulfur atom. For the substrates investigated, the reactivity is found to follow the order, sulfide \gg thiolates. For the sulfides studied, the reaction rate of HEES is much faster than that of HEPS; and for the thiolates studied, the reaction rate of DEMPT is much faster than that of VX. As the reactivity of the substrate decreases, k_1 becomes smaller, thus k_d becomes more competitive (see eqs (2a) and (2b)). We believe that DCA is a more important reactant for VX than for the bivalent sulfides.²

SUMMARY

In aqueous solutions, CAB oxidation of sulfur-containing compounds is acid-catalyzed. The observed rate increases as H^+ or pH increases. At neutral pH and ambient temperature, bivalent sulfides are oxidized rapidly both in H_2O and in D_2O . DEMPT also reacts with CAB rapidly in water but requires the presence of sufficient proton for the same reaction to occur in D_2O . As for VX, no reaction has been detected either in H_2O or in D_2O ; a relatively high concentration of protons must be present to activate CAB as well as to protonate VX. It is recommended that the $ZnCl_2$ in the M280 system be replaced by $AlCl_3$ or by sufficient H_2SO_4 to keep the solution at a lower pH of 2 for effective detoxification of VX by CAB.

ACKNOWLEDGEMENT

The authors are grateful to Mr. Dennis K. Rohrbaugh of CRDEC for the identification of reaction products in the final mixtures by GC/MS and to Mr. Leonard J. Szafraniec of CRDEC for a sample of the thiolate, DEMPT.

REFERENCES

1. Campbell, M. M.; Johnson, G., Chem. Rev., 1978, 78, 65-79.
2. Ruff, F.; Kucesman, A., J. Chem. Soc., Perkin Trans. II, 1975, 509-519.
3. Szafraniec, L. L.; Beaudry, W. T.; Ward, J. R.; Rohrbaugh, D. K., "Reactions Between Chemical Agents and the Chemicals in the M280 Decontamination Kit" CRDEC-TR-134, Aberdeen Proving Ground, MD 21010-5423, January 1990, UNCLASSIFIED Report.
4. Padma, D. K.; Shaw, R. A.; Thakur, C. P.; Vasudeva Murthy, A. R.; Woods, M., Phosphorus, 1972, 2, 81-85.
5. Lakshminarayana, V., J. Agr. Food Chem., 1966, 14, 55-56.
6. Yang, Y.-C.; Szafraniec, L. L.; Beaudry, W. T.; Rohrbaugh, D. K., "Mechanism of VX Oxidation. II. Oxidation by Chlorine-based Oxidants", in Proceedings of the 1989 CRDEC Scientific Conference on Chemical Defense Research, Unclassified, Aberdeen Proving Ground, MD 21010-5423.
7. The structure was confirmed by undecoupled ^{31}P NMR.
8. Yang, Y.-C.; Szafraniec, L. L.; Beaudry, W. T.; Rohrbaugh, D. K., J. Am. Chem Soc., 1990, 6621-6627.

BLANK

MECHANISM OF DEHALOGENATION OF ALIPHATIC HALOCARBONS
SUCH AS HD BY $W_{10}O_{32}^{6-}$

Craig L. Hill and Daryush Sattari

Department of Chemistry, Emory University, Atlanta, GA 30322

ABSTRACT

A new mode of dehalogenation of aliphatic halocarbons in the presence of decatungstate has been identified. The two-electron reduced form of decatungstate, $W_{10}O_{32}^{6-}$ (1) reacts directly and thermally with some halocarbons, RX (X = chloride, as in HD, or bromide) to give the corresponding hydrocarbons, RH, dimers, RR, and other products. Competitive kinetics for the reaction of 1 with a range of halocarbons and structure-activity profiles for these reactions are compatible with either halogen atom abstraction or electron transfer as the rate-determining step in the dehalogenation mechanism.

INTRODUCTION

The effective decontamination of mustard (HD) remains an issue of considerable significance. Progress has been made in the development of oxidative as well as nucleophilic methods to destroy HD that might offer advantages over the reasonably effective but corrosive and nonselective conventional decon agents such as DS2 and STB.¹ We report another approach to the decontamination of halocarbons such as the primary chloride HD. It involves the use of a strongly reducing polyoxometalate, the two-electron reduced form of decatungstate, $W_{10}O_{32}^{6-}$ (1) (Figure 1). As 1 can be generated by reduction of $W_{10}O_{32}^{4-}$ with a number of reducing agents, the prospects for decontamination by catalytic dehalogenation using this system are good. Previous methods for the decontamination of CW agents and agent simulants by polyoxometalates principally relied on the oxidation or photooxidation properties of the oxidized forms of the compounds,² or the ability of some polyoxometalates to generate dehalogenating radicals in the presence of light,³ and not the reducing properties of the reduced forms.

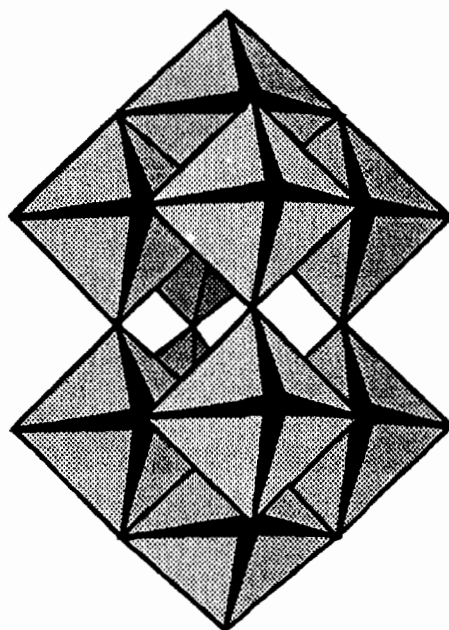


Figure 1. Structure of decatungstate (D_{4h} point group symmetry) in polyhedral notation: oxidized form = $W_{10}O_{32}^{4-}$; reduced form = $W_{10}O_{32}^{6-}$, **1**. In this notation each octahedron represents one MO_6 unit; the oxygen atoms are the vertices of the octahedra and the metal atoms are not directly seen.

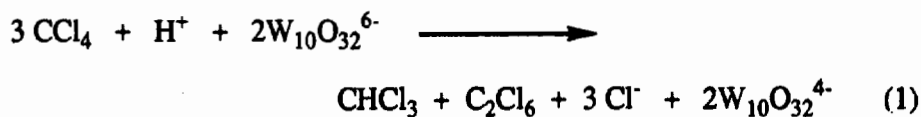
EXPERIMENTAL

The complex $Q_4W_{10}O_{32}$, was prepared by literature methods.⁴ UV-visible, IR and 1H NMR spectra were recorded on HP 8451A, PE 1430, and GE QE-300 instruments, respectively. Organic product distributions were quantified using a HP 5890 gas chromatograph (GC) equipped with a 25-m x 0.2-mm 5% phenyl methyl silicone capillary column and a HP 3390A integrator. Gas chromatographic/mass spectral analyses were also conducted to confirm product assignments. All reactions and syringe manipulations were done under argon. The same procedure was used in all competitive kinetics experiments where two alkyl halides were allowed to compete for the same amount of reduced polyoxotungstate (20 mM). In a typical reaction, 2-butanol (25 mg, 0.11 mM) was added to 3 ml of acetonitrile solution containing $Q_4W_{10}O_{32}$ (20 mM) and the subsequent solution degassed and irradiated ($\lambda = 320$ nm) for 20 min under argon. This led to reduction of $W_{10}O_{32}^{4-}$ to the blue reduced complexes $W_{10}O_{32}^{5-}$ ($\lambda_{max} = 780$ nm) and then **1** ($\lambda_{max} = 630$ nm).⁵ The reaction was initiated by adding a mixture of the halides (9 mmol of cyclohexyl bromide and 9 mmol of alkyl bromide) and internal standard (7×10^{-3} g of trimethylacetone) to the reaction mixture in one portion by syringe. The kinetic measurements were made in stirred solutions thermostated at 45°C by monitoring the disappearance of the organohalides.

The first aliquot was withdrawn immediately after addition of the alkyl halides. Aliquots were withdrawn at varying time intervals by removing ca. 0.8 ml of the reaction mixture by syringe and adding it to a vial open to the air. The vial was capped and shaken until the blue color disappeared. Samples were analyzed by GC. Five to eight aliquots were withdrawn in each kinetics experiment, and each aliquot was analyzed by GC three to four times. In a few cases some points were not reproducible. All results reported here have an error of ca. $\pm 10\%$.

RESULTS AND DISCUSSION

The reduced decatungstate, $W_{10}O_{32}^{6-}$, reacts directly with a range of halocarbons generating hydrocarbon, dimer, inorganic halide, and oxidized decatungstate, $W_{10}O_{32}^{4-}$, as the principal products. This is illustrated for halocarbon substrate = CCl_4 in eq 1. The source of the proton is the alcohol present. Since the reduced form of the complex can be generated in a host of



thermal and photochemical ways from the oxidized form of the complex, the prospects for facile catalytic decon processes based on eq 1 are quite reasonable. The reaction of 1 with several aliphatic chlorides and bromides including primary chlorides, as models for HD, all indicated successful dehalogenation so we proceeded immediately to probe the mechanism of the reaction.

Competitive kinetics methods were chosen as most appropriate for assessing the relative rates of reaction of different alkyl halides. The bromides were chosen over the chlorides for experimental reasons (availability, rate of reaction, etc.). Table I below summarizes not only the rates of reaction of 1 with structurally and electronically diverse alkyl bromides relative to cyclohexyl bromide but also the carbon-bromide bond energies and reduction potentials of these substrates. There are moderate correlations between rates and both the bond energies and the reduction potentials of the substrates. Although this rules out some mechanisms, it doesn't rule out others. A structure-activity profile is given in Figure 2. It is similar to one for radical abstraction and distinct from the ones for rate-determining carbonium or carbanion formation or concerted oxidative addition.

The relative rate of reaction the alkyl halides in these structure-reactivity studies would be expected to reflect, among other structural features, changes in the hybridization of the carbon atom attached to halogen in going from ground state to the rate-limiting transition state.⁶ The results above are compatible with a rate-determining dehalogenation process in the mechanism that is either radical halogen abstraction or electron transfer.

Other mechanisms are less likely. In some reductive dehalogenation systems, including that of Grignard reagent formation ($\text{Mg} + \text{RX} \rightarrow \text{RMgX}$), it is very

TABLE I
Relative Rates of Reaction with 1, Bond Dissociation Energies, and Redox Potentials for Representative Alkyl Halides.

RX	$k_{\text{RX}}/k_{\text{c-C}_6\text{H}_{11}\text{Br}}$	B.E. (Kcal/mol)	$E_{1/2}$ (V) ⁷
$(\text{CH}_3)_3\text{CBr}$	1.83	42.2	-2.19
$(\text{CH}_3)_3\text{CCH}_2\text{Br}$	0.32	-	-2.45
$n\text{-C}_5\text{H}_{11}\text{Br}$	0.76	50.5	-2.27
$n\text{-C}_6\text{H}_{13}\text{Br}$	0.89	39.2	-2.29
$\text{C}_6\text{H}_5\text{CH}_2\text{Br}$	1.56	50.5	-1.22
$c\text{-C}_4\text{H}_7\text{Br}$	0.40	-	-2.36
$c\text{-C}_5\text{H}_9\text{Br}$	1.14	43.7	-2.19
$c\text{-C}_6\text{H}_{11}\text{Br}$	1.00	46.1	-2.29
$c\text{-C}_7\text{H}_{13}\text{Br}$	1.20	-	-2.27

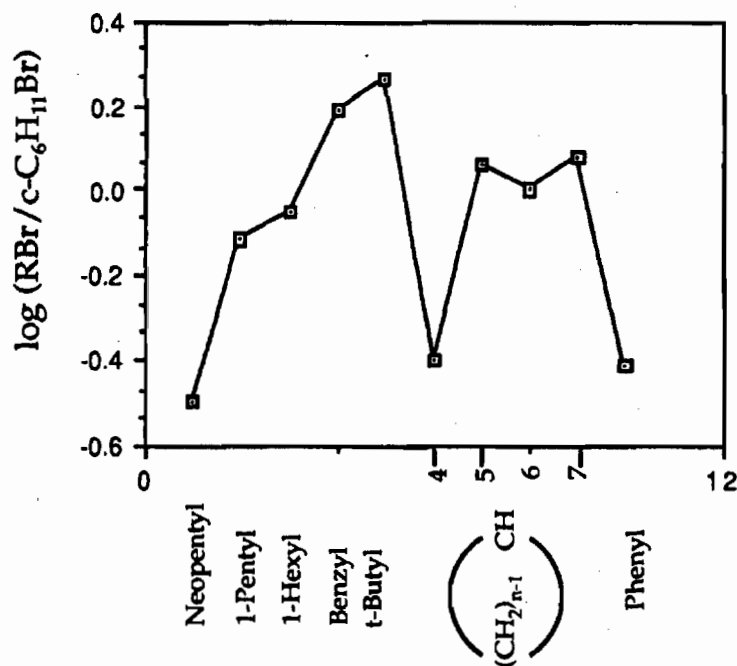
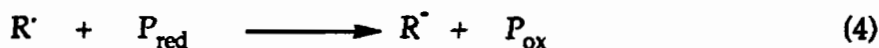
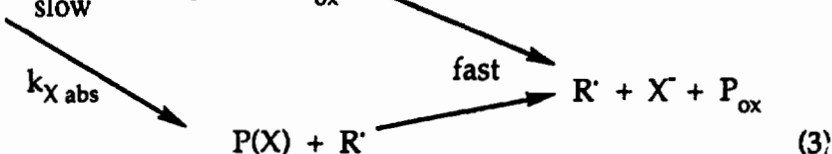
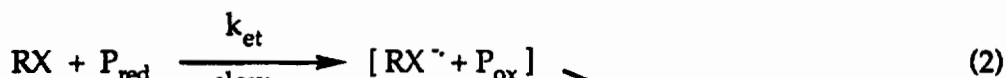


Figure 2. Structure-reactivity profile for the reaction of organic bromides with 1. The ring size of the cycloalkyl bromide is denoted by "n". All reactions were run in acetonitrile at 45°C under Ar.

hard to distinguish experimentally between electron transfer and atom abstraction. Note that both mechanisms lead to an intermediate radical -- atom abstraction produces radical directly; electron transfer produces one indirectly via an organohalide radical anion. It is further noted that the latter may represent a transition state or a very short lived intermediate (one with a shallow energy minimum). The elementary processes in the mechanism after the rate-determining step are all fast and well preceded. Reduction of halocarbon radicals by reduced polyoxometalates was first demonstrated by Ebersson.⁸

A mechanism compatible with all data garnered to date is summarized below, where $P_{ox} = W_{10}O_{32}^{4-}$ and $P_{red} = 1$ or $W_{10}O_{32}^{5-}$.



CONCLUSIONS

$W_{10}O_{32}^{6-}$ (1) reacts readily with some aliphatic halocarbons, RX , ($X = Cl^{\cdot-}$, as in HD, or $Br^{\cdot-}$) to give principally the corresponding hydrocarbons, RH , dimers, RR , and oxidized decatungstate, $W_{10}O_{32}^{4-}$. Kinetics and product studies are consistent with either halogen atom abstraction or electron transfer as the rate-determining step in the dehalogenation mechanism. Other mechanisms for carbon-halogen bond cleavage are very unlikely. The process can be rendered catalytic in $W_{10}O_{32}^{4-}$ in the presence of reducing agents. Organic compounds including as alcohols in the presence of light can function as the reducing agent.

ACKNOWLEDGEMENT

We thank the U.S. Army Research Office for support.

REFERENCES

- (1) (a) *Proc. 1988 U.S. Army CRDEC Conf. on Chem. Defense Res.* Vol I, sections I and XVIII, and references cited in each.
(b) Drago, R. S.; Barnes, M. J.; Davis, S.; Ramsden, J. H.; Bailey, C. L. *Proc. 1987 U.S. Army CRDEC Conf. on Chem. Defense Res.* Vol I, pp 103-109.
(c) Yang, Y.-C.; Szafraniec, L. L.; Beaudry, W. T.; Ward, J. R. *J. Org. Chem.* **1988**, *53*, 3293.
(d) Menger, F. M.; Elrington, A. R. *J. Am. Chem. Soc.* **1990**, *112*, 8201.
- (2) (a) Truitt, L.; Dorsey, R.; Hill, C. L. *Proc. 1988 U.S. Army CRDEC Conf. on Chem. Defense Res.*, pp 1079-1083. (b) Hill, C. L.; Faraj, M. *Proc. 1989 U.S. Army CRDEC Conf. on Chem. Defense Res.*, pp 131-134. (c) Chambers, R. C.; Hill, C. L. *J. Am. Chem. Soc.* **1990**, *112*, 8427 and references cited in each.
- (3) Sattari, D.; Hill, C. L. *Proc. 1990 U.S. Army CRDEC Conf. on Chem. Defense Res.*, See also the preliminary study: Sattari, D.; Hill, C. L. *J. Chem. Soc., Chem. Commun.* **1990**, 634.
- (4) Chemseddine, A.; Sanchez, C.; Livage, J.; Launay, J. P.; Fournier, M. *Inorg. Chem.* **1984**, *23*, 2609.
- (5) (a) Pope, M. T. *Heteropoly and Isopoly Oxometalates*; Springer-Verlag: Berlin, 1983. (b) Renneke, R. F.; Pasquali, M.; Hill, C. L. *J. Am. Chem. Soc.* **1990**, *112*, 6585.
- (6) (a) Ruchardt, C. *Angew Chem., Int. Ed. Engl.* **1970**, *9*, 830.
(b) Applequist, D.E.; Klug, J.H. *J. Org. Chem.* **1978**, *43*, 1729
- (7) Mann, C.K.; Barnes, K.K. "Electrochemical Reactions in Nonaqueous Systems" 1970, p 201.
- (8) Ebersson, L.; Ekstrom, M. *Acta Chem. Scand.* **1988**, *B42*, 101.

MICELLAR CHARGE EFFECTS ON SULFIDE OXIDATION

Andrei Blaskó, Clifford A. Bunton, Houshang Foroudian,
Tracey S. Taylor and Sallyanne Wright

Department of Chemistry, University of California,
Santa Barbara, CA 93106

ABSTRACT

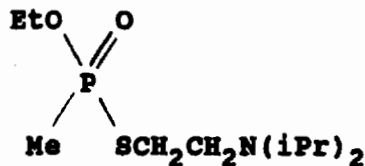
Reactions of periodate ion (IO_4^-) with di-n-propyl and di-n-butyl sulfide and 1-methoxy-4-(methylthio) benzene are inhibited by anionic micelles of sodium dodecylsulfate (SDS) but there is a residual reaction of micellar-bound substrate showing that IO_4^- is not completely excluded from the micellar surface. The concentration of IO_4^- at the micellar surface can be calculated by solving the Poisson-Boltzman equation and second order rate constants at the micellar surface are similar to those in water. The situation is very different for reaction in cationic micelles where second order rate constants at the micellar surface are much lower than in water. Oxidation of 2-chloroethyl phenylsulfide by HSO_5^- (in the form of OXONE) is inhibited, but not completely suppressed, by anionic alkanesulfonate micelles.

INTRODUCTION

Oxidation is a potentially useful method for decontamination of toxic sulfur compounds, e.g., Mustard and VX.¹⁻⁷



Mustard



VX

Oxidizing agents, including peroxymonosulfate ion (HSO_5^-) in the form of OXONE ($2\text{KHSO}_5 \cdot \text{KHSO}_4 \cdot \text{K}_2\text{SO}_4$), react readily with organic sulfides, but, because of the very low solubility of Mustard in water, it is desirable to use some solubilizing

agents,^{6,7} which can be a phase transfer catalyst, a micellized surfactant or a microemulsion. Oxidation of VX can take place at the amino group, which gives a toxic amine oxide, or more usefully at sulfur which leads to destruction of the agent.¹ Formation of the amine oxide is prevented by protonation of the amino group, so it is desirable to carry out oxidation in acidic solution, and the acidity of OXONE is very convenient in this respect.

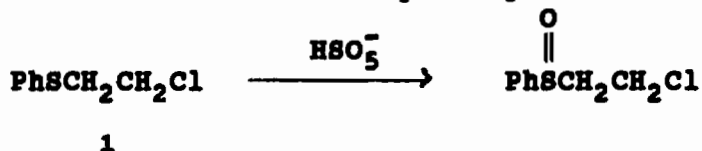
However, we now face a problem if we wish to use OXONE to destroy both Mustard and VX. Protonated VX is very soluble, and Mustard is almost insoluble, in water, so it is difficult to use aqueous OXONE for the rapid destruction of both these agents. One approach is to carry out the reactions in an aqueous cationic surfactant, or in a cationic microemulsion, because cationic micelles or microemulsion droplets will take up both the hydrophobic Mustard and the anionic peroxymonosulfate ion (HSO_5^-). Unfortunately this approach will be less satisfactory for VX. Cationic micelles and microemulsion droplets will repel protonated VX, which will stay in the aqueous medium away from HSO_5^- which will, as noted, be attracted by the cationic micelles.

We therefore considered the alternative approach of carrying out these reactions in anionic micelles which should take up both Mustard and protonated VX, but will repel peroxymonosulfate ion. Exclusion of HSO_5^- from anionic micelles will, of itself, inhibit the overall reaction and we set out to examine the probable extent of this inhibition for oxidation of organic sulfides.

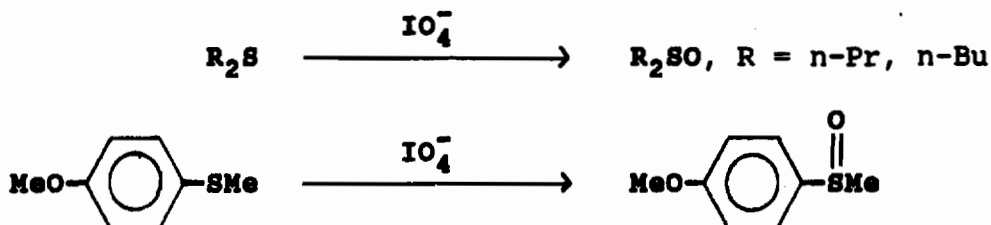
Rate effects of micelles and microemulsion droplets upon relatively slow bimolecular thermal reactions are controlled by two factors, (i) the transfer equilibria of the two reagents between water and the micelles or microdroplets because incorporation of the reactants at colloidal surfaces increases their local concentrations, which speeds reaction, and (ii) the second order rate constants in water and at the surface of a micelle or microdroplet. The model that treats water and colloidal self-assemblies as distinct reaction regions, i.e., as pseudophases, is the basis of most quantitative treatments of rates and equilibria in these assemblies. For many ionic reactions, e.g., of nucleophilic anions such as OH^- or iodobenzoate ions, second order rate constants are similar in water and at surfaces of cationic micelles, so the overall rate effect is governed largely by the concentration of reactants at the micellar surfaces.^{8,9} However, the situation is very different for oxidations of sulfides by either HSO_5^- or periodate ion (IO_4^-) in cationic micelles where second order rate constants at micellar surfaces are much lower than in water.^{2b,c} This unfavorable rate effect markedly offsets the concentration effect, and we postulated that unfavorable interactions between the transition state and cationic micellar head groups strongly inhibited reaction at the micellar surface. On this hypothesis reactions of sulfides with HSO_5^- or IO_4^- at the surface of anionic micelles should not be disfavored by interactions

between the transition state and micellar head groups, so we speculate that this effect may partially compensate for repulsion of the anionic oxidants HSO_5^- and IO_4^- . We note that organic sulfides, e.g., Mustard, and protonated VX, should be taken up readily by anionic micelles or microemulsion droplets.

We examined two sets of reactions. The first was oxidation of 2-chloroethyl phenylsulfide (1) by HSO_5^- in alkanesulfonate micelles or micelles modified by t-amyl alcohol. We



could only examine these data qualitatively because the presence of K_2SO_4 and KHSO_4 in OXONE complicates the use of quantitative treatments of micelle-ion interactions.¹⁰ The second reaction is oxidation by periodate ion where quantitative treatments can be applied.^{2b,c} The substrates were di-n-propyl and di-n-butyl sulfide (Pr_2S and Bu_2S) and 1-methoxy-4-(methylthio)benzene (ArSMe). The concentration of



IO_4^- at surfaces of spherical ionic micelles can be calculated by solving the Poisson-Boltzmann equation (PBE)¹⁰ so we hoped to be able to treat these data quantitatively and estimate second order rate constants at the surface of an anionic micelle. We had shown earlier that for sulfide oxidations in cationic micelles relative second order rate constants at micellar surfaces and in water were very similar for oxidations by HSO_5^- and IO_4^- .^{2b,c}

Although IO_4^- is not a practical oxidant for decontamination of toxic sulfides it is a very convenient model reagent for the study of rate effects of surfactants.

RESULTS

Oxidation by HSO_5^- . We used sodium decane- and dodecanesulfonate as anionic surfactants, because the low solubility of potassium dodecylsulfate precluded use of the readily available sodium dodecylsulfate (SDS). Potassium alkanesulfonates are slightly more soluble, but still we could use only dilute surfactant and HSO_5^- (as OXONE), although we reduced the solubility problem by adding either HClO_4 or NaClO_4 to OXONE so that most of the potassium ion was removed

as the sparingly soluble KClO_4 . We also carried out some reactions with added 5% t-amyl alcohol, which should increase solubility of the surfactant. The anionic surfactants have only small effects upon the overall reaction rates even though HSO_5^- should be partially excluded from the micellar surface due to coulombic repulsions.

Oxidation by IO_4^- . These reactions were followed in solutions of SDS with sodium periodate to avoid solubility problems due to the potassium form of the surfactant and we could therefore use a range of surfactant concentrations. Overall reaction rates decrease in SDS, but overall first order rate constants reach limiting values in 0.15 - 0.25 M SDS. It is convenient to consider in detail the oxidation of ArSMe where, in high [SDS], substrate is largely micellar bound and the overall first order rate constant is lower than that in water by a factor of ca. 30.

The concentration of IO_4^- within a discrete region at the micellar surface can be calculated by solving the PBE on the assumption that IO_4^- interacts coulombically with the anionic micelle.^{10b,11} The general treatment is that already applied to reactions of OH^- in SDS micelles and of H_3O^+ in cationic micelles. In all these systems there are unfavorable interactions between the micelle and co-ions but they are not sufficient to exclude coions completely from the micellar surface.^{10b-12} The surface electrical potential of the micelle depends upon its radius and surface charge density, and concentrations of surfactant and added electrolyte. The first order rate constant for overall reaction with respect to organic sulfide is given by:

$$k = \frac{k_w[\text{IO}_4^-]_w + k_2^m K_s [\text{SDS}_M] [\text{IO}_4^-]_\Delta}{1 + K_s [\text{SDS}_M]} \quad (1)$$

In equation (1) k_w and k_2^m are second order rate constants in water and at the micellar surface respectively, K_s is the substrate binding constant to micellized SDS (SDS_M) and $[\text{IO}_4^-]_w$ and $[\text{IO}_4^-]_\Delta$ are respectively molarities in the aqueous region and at the micellar surface in a shell of thickness, Δ .^{10,11} Values of k_w and K_s are obtained directly or by analogy with similar systems. Equation (1) is written for reaction followed under first order conditions with IO_4^- in excess over organic sulfide, but it can easily be modified to cover reaction followed with sulfide in excess over IO_4^- and it is convenient to follow this approach in some cases.^{2b,c}

An example of the data treatment is given in Table 1, with values of $[\text{IO}_4^-]_\Delta$ and k_2^m calculated for various [SDS]. Values in cationic micelles are included for comparison. These values depend upon the value of Δ , but not markedly so. The key points are that coions are not completely excluded from the micellar surface and k_2^m is not much lower than k_w . It is useful to consider the factors that control relative values of k_w and k_2^m and their implications for the development of

surfactant systems for decontamination, especially as regards micellar charge and charge density. Although IO_4^- is attracted to the surface of a CTACl micelle values of k_2^m are so low that overall reaction rates are slightly larger in SDS (0.2-0.25 M), even though IO_4^- is largely excluded from the micellar surface.

TABLE 1

Second Order Rate Constants And $[\text{IO}_4^-]_{\Delta}$ For Reaction Of ArSMe With NaIO_4 At Various [SDS].^{a, b}

[SDS] M	$10^4 [\text{IO}_4^-]_{\Delta}$, M	k_2^m , $\text{M}^{-1}\text{s}^{-1}$
0.10	2.20	0.68
0.15	3.45	0.52
0.20	4.87	0.31
0.25	6.52	0.28

^a $[\text{IO}_4^-]_{\text{T}} = 2.03 \times 10^{-3}$ M, $k_{\text{W}} = 1.55 \text{ M}^{-1}\text{s}^{-1}$, $\Delta = 4 \text{ \AA}$.
^bIn cationic micelles $k_2^m = 0.002 \text{ M}^{-1}\text{s}^{-1}$.

Micelles and Microemulsion Droplets as Reaction Media.

Values of k_2^m/k_{W} for oxidations of sulfides by IO_4^- are given in Table 2. It is important to recognize that overall reaction rates depend upon these rate constants and reactant concentrations in water and at micellar surfaces. There is a very striking effect of micellar charge upon k_2^m/k_{W} . Oxidations of organic sulfides by HSO_5^- and IO_4^- are sensitive to polarities of the reaction media and are speeded by media of high polarity.^{2b, c, 13} Polarities of micelles and microemulsion droplets are lower than that of water,¹⁴ and seem to be similar to polarities of hydrophilic alcohols. Therefore, based only on consideration of polarity, we predict $k_2^m/k_{\text{W}} < 1$. Polarities of anionic and cationic micelles are similar, so there is an additional rate effect which we believe depends on micellar charge.

TABLE 2

Second Order Rate Constants For Reactions Of Sulfides With IO_4^- In SDS Micelles.^a

Substrate	k_2^m , $\text{M}^{-1}\text{s}^{-1}$	k_2^m/k_{W}
Pr_2S	0.6-0.9	0.19-0.28
Bu_2S	0.3-0.4	0.09-0.12
ArSMe	0.3-0.7	0.19-0.45

^aIn cationic micelles $k_2^m/k_{\text{W}} = 0.004-0.005$ for Pr_2S and $0.0013-0.0017$ for ArSMe.

In the reaction of an organic sulfide with either HSO_5^- or

IO_4^- positive charge builds up on sulfur as an electron is transferred to the oxidant. The organic sulfide intercalates at the micellar surface so in the transition state there is an unfavorable electrostatic interaction between the partial positive charge on sulfur and cationic micellar head groups, but in an anionic micelle there will be a favorable interaction between sulfur and the micellar head groups.

These transition state effects of micellar charge are in the opposite direction to those depending on transfer equilibria because cationic micelles concentrate HSO_5^- and IO_4^- at their surfaces, and anionic micelles have the opposite effect.

Charge effects will be different for anionic nucleophiles and anionic electrophiles (oxidants), because for nucleophilic reactions negative charge is transferred from an anionic reagent to substrate at the micellar surface and is generally delocalized out to electronegative groups in the substrate, as in deacylation or dephosphorylation, for example.⁸⁻¹⁰ In these reactions micellar charge effects seem to be related to transfer equilibria rather than to transition state interactions.

How do these conclusions affect the selection of surfactant systems in decontamination? If we consider reactions of anionic nucleophiles, e.g., OH^- , oximates or iodosobenzoates,^{8-10,15} we will obtain the maximum concentration of the anionic nucleophile at the micellar surface by having cationic micelles of the highest charge density and the greatest coulombic affinity for anions. Addition of co-surfactants will decrease anion concentrations at the colloidal surface, although it may be useful in solubilizing a hydrophobic substrate. Transition state interactions will be less important than transfer equilibria.

The situation is very different for reactions of anionic oxidants, especially peroxyanions, because here transfer equilibria and transition state interactions are in opposition. The second order rate constant at the micellar surface should increase as we make a micelle less cationic, for example by adding cosurfactant, and this effect will offset the decreased concentration of anionic oxidant at the micellar surface.

Applying these principles to the destruction of both VX and Mustard by OXONE, or HSO_5^- , we conclude that the best system will not involve cationic micelles, which would not take up protonated VX, and would not give high reaction rates at the micellar surface. Instead it would be better to use a microemulsion or a cosurfactant-modified micelle based on an anionic surfactant which would take up both the hydrophobic, nonionic, Mustard, and the hydrophilic, cationic, protonated VX, because of coulombic attraction by the negatively charged colloid. The peroxyanion, e.g., HSO_5^- , would not be coulombically attracted, but the second order rate constant at the colloidal surface would be much higher than at a cationic surface (Table 2), which compensates for the relatively low concentration of oxidant at the surface.

The coulombic model allows us to estimate relative concentrations of co-ions in water and at the surface of an ionic micelle.^{10,11} The ion concentration gradient between the micellar and aqueous pseudophase is relatively low at high [surfactant] where the micellar surface electrical potential is low. For example, in our experiments we estimate that in 0.25 M SDS the concentration of IO_4^- in a 3 Å shell at the micellar surface is lower than that in water by a factor of 15, for 2×10^{-3} M stoichiometric IO_4^- , and the difference decreases if the shell width is increased, e.g., by a factor of 11 in a 4 Å shell.

EXPERIMENTAL

Materials. The sulfides and oxidants were commercial and were purified and used as described^{2b}. Alkanesulfonates were prepared from the alkyl bromide and Na_2SO_3 under nitrogen,¹⁶ and SDS was commercial material, purified as described.^{10b}

Kinetics. Reactions were followed spectrophotometrically at 235 nm for Pr_2S and Bu_2S , 260 nm for ArSMe and 250-270 nm for $\text{PhSCH}_2\text{CH}_2\text{Cl}$.

For oxidations by OXONE, HSO_5^- (10^{-3} M) was in excess over $\text{PhSCH}_2\text{CH}_2\text{Cl}$ (2×10^{-5} M) and for oxidation of ArSMe , IO_4^- (2×10^{-3} M) was in excess over ArSMe (10^{-4} M). For oxidations of Pr_2S and Bu_2S , sulfide (2×10^{-3} M) was in excess over IO_4^- (5×10^{-5} M). It was then necessary to convert observed first order rate constants with respect to IO_4^- (k_p) into first order rate constants with respect to sulfide (k_s) by using equation (2).

$$k_s = k_p[\text{IO}_4^-]/[\text{R}_2\text{S}] \quad (2)$$

These values of k_s were analyzed by using equation (1) with micellar parameters described earlier.^{2b,c} All reactions were followed in aqueous solution at 25.0°C.

CONCLUSIONS

Second order rate constants in the micellar pseudophase for sulfide oxidations by HSO_5^- or IO_4^- depend upon micellar charge. Cationic micelles incorporate and concentrate both sulfide and anionic oxidant, but this rate-enhancing effect is offset by unfavourable interactions between the transition state and the cationic headgroups of the micelle. Anionic micelles incorporate the sulfide, but not the anionic oxidant, which remains largely in the water. However, interactions between the transition state and the anionic headgroups do not disfavor reaction. As a result there is a significant contribution from reaction in the micellar pseudophase, despite the low concentration of anionic oxidant at the micellar surface.

Addition of cosurfactant decreases surface charge density

and should decrease binding of reactive anions by cationic micelles and increase that by anionic micelles as well as changing second order rate constants at the surface of the colloidal assembly. This strategy should help to optimize development of surfactant-based systems for oxidation of both Mustard and protonated VX by reactive peroxyanions.

ACKNOWLEDGEMENT

Support of this work by the U.S. Army Research Office is gratefully acknowledged. Tracey S. Taylor was a student apprentice supported by the Academy of Applied Science.

REFERENCES

1. Y.-C. Yang, L. L. Szafraniec, W. T. Beaudry and D. K. Rohrbaugh, *J. Am. Chem. Soc.*, 112, 6621 (1990).
2. (a) R. Bacaloglu, A. Blaskó and C. A. Bunton, Proc. 1988 Conference on Chemical Defense Research, 1989, p. 27; (b) C. A. Bunton, A. Blaskó and H. Foroudian, 1990 Conference on Chemical Defense Research; (c) R. Bacaloglu, A. Blaskó, C. A. Bunton and H. Foroudian, *J. Phys. Org. Chem.*, in press.
3. J. Bielowski and J. E. Casida, *J. Agri. Food Chem.*, 36, 610 (1988) and ref. cited.
4. D. R. Leslie, W. T. Beaudry, L. L. Szafraniec and D. K. Rohrbaugh, *J. Org. Chem.*, 56, 3459 (1991).
5. Y.-C. Yang, L. L. Szafraniec, W. T. Beaudry and F. A. Davis, *J. Org. Chem.*, 55, 3664 (1990).
6. J. H. Ramsden, R. S. Drago and R. Ridley, *J. Am. Chem. Soc.*, 111, 3958 (1989).
7. F. M. Menger and A. R. Elrington, *J. Am. Chem. Soc.*, 112, 8201 (1990).
8. (a) K. Martinek, A. K. Yatsimirski, A. V. Levashov and I. V. Berezin, in "Micellization, Solubilization and Microemulsions", K. L. Mittal, Ed., Plenum, New York, 1977, vol. 2, p. 488; (b) L. S. Romsted, ref. 8a, p. 509; (c) L. S. Romsted, in "Surfactants in Solution", K. L. Mittal and B. Lindman, Eds., Plenum, New York, 1984, vol. 2, p. 1015; (d) C. A. Bunton and G. Savelli, *Adv. Phys. Org. Chem.*, 22, 213 (1986).
9. F. Quina and H. Chaimovich, *J. Phys. Chem.*, 83, 360 (1979).
10. (a) C. A. Bunton and J. R. Moffatt, *J. Phys. Chem.*, 90, 538 (1986); (b) C. A. Bunton, M. M. Mhala and J. R. Moffatt, *ibid.*, 93, 7851 (1989).
11. A. Blaskó, C. A. Bunton, C. Armstrong, W. Gotham, Z.-M. He, J. Nickles and L. S. Romsted, *J. Phys. Chem.*, 95, 6747 (1991).
12. H. Chaimovich, R. M. V. Aleixo, I. M. Cuccovia, D. Zanette and F. H. Quina, in "Solution Behavior of Surfactants", K. L. Mittal and E. J. Fendler, Eds., Plenum, New York, 1982, vol. 2, p. 949.
13. F. Ruff and A. Kucsman, *J. Chem. Soc. Perkin Trans. II*,

683 (1985).

14. (a) C. Ramachandran, R. A. Pyter and P. Mukerjee, *J. Phys. Chem.*, 86, 3198 (1982); (b) C. A. Bunton and F. de Buzzaccarini, *ibid.*, 85, 3139 (1981).
15. (a) R. A. Moss, K. W. Alwis and G. O. Bizzigotti, *J. Am. Chem. Soc.*, 105, 681 (1983); (b) R. A. Moss, K. Y. Kim and S. Swarup, *ibid.*, 108, 788 (1986); (c) R. A. Mackay, F. R. Longo, B. L. Knier and H. D. Durst, *J. Phys. Chem.*, 91, 961 (1987).
16. (a) R. M. Reed and H. V. Tartar, *J. Am. Chem. Soc.*, 57, 570 (1935); (b) C. A. Bunton, L. S. Romsted and G. Savelli, *ibid.*, 101, 1253 (1979).

BLANK

ACTIVATION OF H_2O_2 USING CO-CATALYSTS IN N-METHYLPYRROLIDINONE SOLVENT

Russell S. Drago* and Douglas E. Patton
University of Florida
Department of Chemistry
Gainesville, Florida 32611

ABSTRACT

The activation of H_2O_2 in the oxidation of several mustard and VX simulants has been investigated at ambient conditions using several co-catalyst systems in N-methylpyrrolidinone. When various materials are added, which have the ability to react with H_2O_2 to form peroxyacids, the complete oxidation of n-butyl sulfide and the near complete oxidation of diphenyl sulfide are observed. In these oxidative systems, both the reaction times for complete oxidation and the selectivities to sulfoxide or sulfone can be varied by using transition metal catalysts and by varying the amount of H_2O_2 . The oxidation of the VX simulant, Monitor (O,S-dimethylphosphoramidothioate) is effected using these co-catalyst systems.

INTRODUCTION

In recent years, the oxidative decontamination of chemical agents has received increasing attention.¹ Yang and co-workers investigated the oxidative detoxification of phosphonothiolates using several peroxygen compounds. Mechanistic studies indicate the oxidation of the sulfur in O,S-dimethyl phosphoramidothioate is the initial step.

Since aqueous H_2O_2 is relatively inexpensive, of low equivalent weight, environmentally clean, and easy to handle, this oxidant would be very attractive in the oxidative decontamination of chemical agents, such as mustard and VX. As shown in the oxidation of various organic substrates, transition metal catalysts activate the oxidant to effect oxidation of the substrate.² Another method for H_2O_2 activation involves synthesizing the peroxyacids³ of acetic, m-chlorobenzoic and formic acids and employing them in stoichiometric oxidations.

In this paper, we investigate transition metal and peracid precursors as catalysts for the H_2O_2 activation in the oxidation of simulant compounds for mustard and VX.

RESULTS AND DISCUSSION

The activation of H_2O_2 by transition metal catalysts in the oxidation of the mustard simulant, n-butyl sulfide, was investigated in a solvent system consisting of N-methylpyrrolidinone (NMP) and H_2O under ambient conditions. While the uncatalyzed homogeneous reaction showed no oxidation products, the use of $FeSO_4 \cdot 7H_2O$ as a catalyst led to an 11% conversion to sulfoxide after 1 hour. The low conversions based on H_2O_2 suggests that the metal-catalyzed decomposition of the peroxide (Class IV Fenton chemistry)⁴ is a major problem with these catalysts. Similar behavior was observed with $Co(hfacac)_2$ and $CoDMPCl_2$ (DMP = 2,9-dimethyl-1,10-phenanthroline) leading to low conversions. Metal catalysts were sought that either bound H_2O_2 (Class IV B) or reacted to form metal-oxo complexes (Class III)⁴ in order to obtain a more efficient use of the oxidant. Using NMP as the solvent, the catalysts, $Pd(OAc)_2$ (OAc = acetate) and $SnCl_2 \cdot 2H_2O$, resulted in sulfoxide conversions of 4% and 5%, respectively. The employment of $Mo(O)_2(acac)_2$ (acac = acetylacetonate) resulted in a 42% conversion to sulfoxide. Total oxidation of the mustard simulant was obtained using the catalyst, $V(O)(pic)_2$ (pic = pyridine-2-carboxylate), in 2 hours. $RuCl_3 \cdot 3H_2O$ was a very efficient catalyst for the oxidation of n-butylsulfide oxidizing 75% to sulfoxide and 20% to the sulfone in five minutes using a 1:3 substrate to H_2O_2 system. The above results are explained by the tentative classifications of runs 1 to 5, 7, 8, 11 and 12 to Class IV A, run 6 to Class III (metal oxo, oxygen atom transfer) with a possible Class IV A component) and runs 9, 10 and 13 to Class IV B (nucleophilic attack on coordinated peroxide).

Effective activation of H_2O_2 resulted with the addition of glacial acetic acid to the 50:50 NMP/water solvent system, yielding the complete oxidation of the substrate in 30 minutes. The use of a metal catalyst in this system showed no improvement in the rate of oxidation. Decreasing the amount of glacial acetic acid resulted in lower activity. Peroxyacetic acid is the suggested active peroxy-intermediate in this system.

The substitution of maleic anhydride, for acetic acid resulted in a more potent system for the oxidation of mustard simulants. Increasing the amount of maleic anhydride to 1.6M and decreasing the amount of H_2O_2 from $4.9 \times 10^{-1}M$ to $1.6 \times 10^{-1}M$ led to 100% selectivity to sulfoxide with a 100% yield in 14 hours. The molar ratio of substrate to H_2O_2 was 1:1 in this reaction using NMP as the solvent. The efficient use of H_2O_2 in this homogeneous simulant oxidation is an exciting result. Increasing the amount of H_2O_2 to $4.9 \times 10^{-1}M$ resulted in the complete oxidation of the sulfide to sulfone in 1 hour. Both the reaction completion time and the selectivity can be varied by varying the amount of H_2O_2 .

An evaluation of the use of metal catalysts with the maleic anhydride/ H_2O_2 system was performed in an attempt to increase the rate of oxidation. In the reaction utilizing a 1:1 substrate to H_2O_2 molar ratio

(i.e. $1.6 \times 10^{-1} \text{M}$ in each), the use of $\text{SnCl}_2 \cdot 2\text{H}_2\text{O}$ ($1.6 \times 10^{-2} \text{M}$) gave 100% selectivity to sulfoxide with a 100% yield in 10 hours (compared to 14 hours in the absence of tin). The use of $\text{Pd}(\text{OAc})_2$ led to lower activity than tin leading to 39% in 1 hour with no increase observed at longer times. Increasing the concentration of H_2O_2 up to $4.9 \times 10^{-1} \text{M}$ in these metal-catalyzed systems resulted in formation of both sulfoxide and sulfone. The catalyst, $\text{SnCl}_2 \cdot 2\text{H}_2\text{O}$, gave a 100% yield of sulfone in 1 1/2 hours, while $\text{Pd}(\text{OAc})_2$ gave a mixture of sulfoxide (42%) and sulfone (58%) in 1 hour.

$\text{RuCl}_3 \cdot 3\text{H}_2\text{O}$ was evaluated as a catalyst in the oxidation of n-butyl sulfide using the maleic anhydride/ H_2O_2 system. A study involving the variation of the amount of H_2O_2 was conducted with this system employing a catalyst concentration of $1.6 \times 10^{-2} \text{M}$. The use of a 1:3 substrate to H_2O_2 molar ratio oxidized the substrate in 5 minutes to sulfoxide (34%) and sulfone (66%). In the 1:2 substrate to H_2O_2 system, the oxidation of the substrate produced sulfoxide (68%) and sulfone (32%) in 5 minutes. When the molar ratio of substrate to H_2O_2 was 1:1, only sulfoxide formed, but only 53% of the H_2O_2 was used productively. The system is very active. No increase in product is observed at longer times indicating that the peroxide has been decomposed. Decreasing the amount of catalyst to $1.6 \times 10^{-3} \text{M}$ yielded a corresponding decrease in the rate of oxidation but more efficient use of the peroxide resulted. Experiments were designed to demonstrate that maleic anhydride was catalytic in this reaction. A 1:1 substrate to H_2O_2 ratio was studied at ambient conditions but their molarity was increased twenty fold. A very exothermic reaction occurred with complete oxidation of the mustard simulant, n-butyl sulfide, in 5 minutes.

An evaluation of the maleic anhydride/ H_2O_2 oxidative system using a less reactive mustard simulant, diphenyl sulfide, was performed. A complete oxidation of the substrate to sulfoxide (14%) and sulfone (86%) was observed in one hour. The use of a metal catalyst gave similar results.

Oxidative systems involving H_2O_2 activation were extended to the VX simulant compound, Monitor (O, S-dimethyl phosphoramidothioate). The oxidation of this substrate was investigated using $[\text{Ru}(\text{dmp})_2(\text{H}_2\text{O})_2][\text{PF}_6]_2$ (dmp = 2,9-dimethyl-1,10-phenanthroline) and H_2O_2 in CH_3CN . After 24 hours of reaction, ^{31}P NMR showed the appearance of 3 resonances in addition to the substrate resonance. Approximately 40% of the substrate was reacted via the oxidative-hydrolysis of the $-\text{SCH}_3$ and/or $-\text{NH}_2$ functional groups. Symmetrical and unsymmetrical pyrophosphate formation was observed.

Utilization of the maleic anhydride/ H_2O_2 system resulted in the complete oxidation of the VX simulant. ^{31}P NMR showed the loss of the $-\text{SCH}_3$, $-\text{NH}_2$, and/or $-\text{OCH}_3$ functionalities without any toxic pyrophosphate formation. Adding the metal catalyst, $\text{RuCl}_3 \cdot 3\text{H}_2\text{O}$, to the maleic anhydride/ H_2O_2 system resulted in incomplete oxidation of the substrate because of competing metal-catalyzed H_2O_2 decomposition.

CONCLUSION

Metal complex and acid anhydride-H₂O₂ in NMP have been employed in the oxidative destruction of both mustard and VX simulant compounds. In the metal-catalyzed oxidation of n-butyl sulfide with H₂O₂, V(O)(pic)₂ and RuCl₃·3H₂O exhibited the best activity. Even though the addition of acetic acid to the H₂O₂ system led to an increase in substrate oxidation, another peroxyacid precursor, maleic anhydride, has been found to yield a more potent oxidizing system in the oxidation of mustard simulants. Furthermore, this system has been shown to be catalytic in maleic anhydride with efficient use of H₂O₂ in a 1:1 substrate to H₂O₂ system. In the oxidation of the VX compound, Monitor, the activation of H₂O₂ by metal-catalysts is also demonstrated. The most effective catalyst for this simulant is maleic anhydride/H₂O₂, which gave no toxic pyrophosphate formation.

TABLE I

Catalytic Oxidations of n-Butyl Sulfide Using H₂O₂ in
the Presence of Metal Catalysts (1:3 substrate to H₂O₂ ratio 1.6 x 10⁻¹M)

Run	Catalyst (M)	Time (min)	Products (%)
1 ^a	none	5	none
	(0)	30	none
		60	none
2 ^a	FeSO ₄ ·7H ₂ O (1.0 x 10 ⁻²)	5	none
		30	none
		60	none
4 ^a	Co(dmp)Cl ₂ (1.6 x 10 ⁻³)	5	R ₂ SO (4)
		30	R ₂ SO (4)
		60	R ₂ SO (4)
6 ^b	RuCl ₃ ·3H ₂ O (1.6 x 10 ⁻²)	5	R ₂ SO (75)
			R ₂ SO ₂ (20)
		30	R ₂ SO (75)
			R ₂ SO ₂ (20)
		60	R ₂ SO (75)
			R ₂ SO ₂ (20)
7 ^a	V(O)(acac) ₂ (1.0 x 10 ⁻²)	5	none
		30	none
		60	none

9 ^a	Mo(O) ₂ (acac) ₂	5	R ₂ SO	(9)
		30	R ₂ SO	(26)
	(1.0 x 10 ⁻²)	60	R ₂ SO	(35)
10 ^a	Mo(O) ₂ (acac) ₂	5	R ₂ SO	(4)
		30	R ₂ SO	(25)
	(1.0 x 10 ⁻³)	60	R ₂ SO	(42)
13 ^b	V(O)(pic) ₂	5	R ₂ SO	(59)
			R ₂ SO ₂	(7)
	(1.6 x 10 ⁻²)	30	R ₂ SO	(79)
			R ₂ SO ₂	(12)
		60	R ₂ SO	(81)
			R ₂ SO ₂	(17)
	120	R ₂ SO	(77)	
		R ₂ SO ₂	(23)	

^a Runs I - V and VII - X were run with the following amounts under ambient conditions:

Substrate (1.6 x 10⁻³ moles)
H₂O₂ (4.9 x 10⁻³ moles, 30% aqueous solution)
NMP (5.0 ml)
H₂O (5.0 ml)

^b Runs I, VI, and XI - XIII were run with the following amounts under ambient conditions:

Substrate (1.6 x 10⁻³ moles)
H₂O₂ (4.9 x 10⁻³ moles, 30% aqueous solution)
NMP (10 ml)

TABLE II

Catalyzed Oxidations of 1.6×10^{-1} M di-n-butylsulfide at 1:3 Substrate to H_2O_2 (10 ml of NMP and 30% aqueous H_2O_2 (-0.5 ml) were used in all systems)

Run	MA (M)	H_2O_2 (M)	Metal (M)	Time (min)	Products (%)
1	1.6M	4.9×10^{-1}	none	5	R ₂ SO (62)
				30	R ₂ SO (38) R ₂ SO ₂ (62)
				60	R ₂ SO ₂ (100)
2	1.6M	4.9×10^{-1}	Pd(OAc) ₂ (1.6×10^{-1})	5	R ₂ SO (58)
				30	R ₂ SO (79) R ₂ SO ₂ (21)
				60	R ₂ SO (42) R ₂ SO ₂ (58)
3	1.6M	4.9×10^{-1}	SnCl ₂ ·2H ₂ O (1.6×10^{-2})	5	R ₂ SO (65)
				15	R ₂ SO (84) R ₂ SO ₂ (16)
				30	R ₂ SO (42) R ₂ SO ₂ (58)
				60	R ₂ SO (16) R ₂ SO ₂ (84)
				90	R ₂ SO ₂ (100)
4	1.6M	4.9×10^{-1}	RuCl ₃ ·3H ₂ O (1.6×10^{-2})	5	R ₂ SO (34) R ₂ SO ₂ (66)
				30	R ₂ SO (16) R ₂ SO ₂ (84)
				60	R ₂ SO ₂ (100)

ACKNOWLEDGEMENT

The authors acknowledge the support of this research by the U.S. Army Research Office through Grant #26914-CH. We thank Dr. Yu Chu Yang, Dr. Linda Szafraniec and their co-workers for their experimental assistance and useful discussions and Mr. Michael J. Naughton for his assistance in obtaining the ^{31}P NMR spectra.

REFERENCES

- (a) Edgewood Arsenal Special Report EO-SR-74001 Vol. 1, 1974, p. 47.
(b) Yang, Y. C.; Szafraniec, L. L.; Beaudry, W. T.; Ward, J. R. J. Org. Chem. 1988, 53, 3293.
(c) Yang, Y. C.; Szafraniec, L. L.; Beaudry, W. T.; Rohrbaugh, D. K. J. Am. Chem. Soc. 1990, 112, 6621.
- (a) Pralus, M.; Lecoq, J. C.; Schirmann, J. P. In "Fundamental Research in Homogeneous Catalysis"; Tsutsui, M., Ed.; Plenum: New York, 1979; Vol. 3, p. 327.
(b) Sheldon, R. A.; Kochi, J. K. "Metal-Catalyzed Oxidation of Organic Compounds"; Academic: New York, 1981.
(c) Mimoun, H. In "The Chemistry of Functional Groups, Peroxides"; Patai, S., Ed.; Wiley: New York, 1982; p. 463.
(d) Proceedings of the 1989 U.S. Army Chemical Research, Development and Engineering Center Scientific Conference on Chemical Defense Research, Williams, J. D.; Bouillon, G.; Lick, C.; Schank, K. 1990, CRDEC-SP-024, p. 123.
- In "The Chemistry of Functional Groups, Peroxides"; Patai, S., Ed.; Wiley: New York, 1982; p. 279.
- Drago, R. S. Submitted for Publication.

BLANK

MECHANISM OF THE HYDROLYSIS OF ORGANOPHOSPHINATES CATALYZED BY
COPPER (II) N,N,N',N'-TETRAMETHYLETHYLENEDIAMINE (CuTMED)

Masato Nakashima and David M. Alabran
U.S. Army Natick Research, Development and Engineering Center
Natick, MA 01760

In order to identify the mechanism of copper complex catalyzed hydrolysis of a G agent simulant, p-nitrophenyl methylphenylphosphinate (I), we have made kinetic studies of CuTMED catalyzed hydrolysis of (I) and its analogues spectrophotometrically. The analogues are p-methoxyphenyl methylphenylphosphinate (II), p-nitrophenyl ethylphenylphosphinate (III), and p-nitrophenyl isopropylphenylphosphinate (IV). At room temperature, the relative values of $\log((\text{pseudo first order rate constants at pH 7})/(\text{CuTMED}))$ were determined to be 0 (I), -3.7 (II), -0.76 (III), and -3.1 (IV). It is concluded that the catalyst works by electron withdrawal from the phosphorus and that large substituents on phosphorus sterically retard the reaction.

We have been using p-nitrophenyl methylphenylphosphinate (I) as a G agent simulant to study various substances as potential hydrolytic catalysts¹. Here we are reporting the catalytic effect of CuTMED toward (I) and related phosphinates. It has been known that the complex is an effective catalyst toward DFP², a phosphate, and GB³, a phosphonate. If the complex is found to be an effective catalyst for the phosphinate as well, such a finding will suggest the similarity in the catalytic mechanism among the esters of these phosphorus acids. One can take advantage of such a similarity to study the kinetic substituent effects on the phosphinate to infer the detail of the catalytic mechanism not only of the phosphinate but of phosphonate and phosphate.

Para substituted phenyl alkylphenylphosphinates (X-Ar-OP(O)R(Ph)) have structural features useful in studying the substituent effects that can readily be related to analogous systems in organic esters. Also their low but appreciable solubility in water allows one to follow the hydrolytic kinetics easily by the usual UV - vis spectrophotometric technique.

We have chosen to investigate (I), paramethoxyphenyl methylphenylphosphinate (X = MeO and R = Me) (II), paranitrophenyl ethylphenylphosphinate (X = NO₂ and R = Me) (III), and paranitrophenyl isopropylphenylphosphinate (X = NO₂ and R = iPr) (IV). The first two compounds were synthesized in-house and the others were obtained from Ash Stevens Inc.

The results of the hydrolysis of the phosphinates are summarized in Table 1.

TABLE 1.

CuTMED catalyzed hydrolysis of phosphinates at pH 7

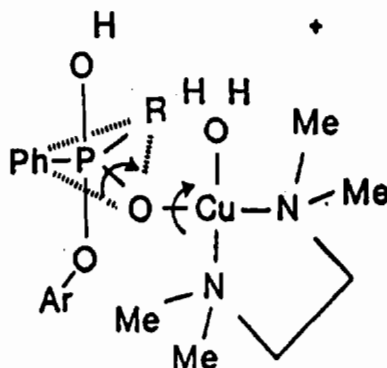
SUBSTRATE substituents X, R	(CuTMED) mM	k 1/Min	k' = k/(CuTMED) 1/Min/M	log(k'/k _I ')	log(k/k _I)
I nitro, methyl	0.101	0.191	1890	0	0
	0.05	0.11	2200		
	0	0.0025	—		
II methoxy, methyl	5.0	0.002	0.4	-3.7	-1.8
	0	4 x 10 ⁻⁵	—		
III nitro, ethyl	1.0	0.35	345	-0.76	-1.2
	0	0.00015	—		
IV nitro, i-propyl	1.0	0.0016	1.6	-3.1	-2.8
	0	4 x 10 ⁻⁶	—		

The hydrolysis of phosphinates was carried out in a pH 7 buffer solution containing 0.05M piperazine-N-N'-bis(2-ethanesulfonic acid) (PIPES) and 0.15 M NaClO₄. The catalytic hydrolysis rate constants of I and II showed that the kinetic polar substituent effect is very large. Roughly speaking, they give the Hammett rho⁺ value of 3.7, the difference between the Hammett sigma values of p-nitro and p-methoxy being approximately 1. The large rho⁺ value implies an interaction of two reactants with opposite charges. The kinetic substituent effect of R shows a steric retardation in going from methyl, ethyl, to isopropyl. Both of the substituent effects are in the same direction as in the saponification of simple organic esters by Bac2 mechanism.

The following figure shows a transition state structure that is consistent with these observations:

FIGURE 1.

Transition state of CuTMED-catalyzed hydrolysis of phosphinate



The function of the copper is to reduce electron density from the displacement center P through $=O$ to facilitate nucleophilic attack, as has been suggested in the case of GB³.

The transition state picture shows that the steric effect of alkyl groups is on the approach of nucleophile to the P analogous to the organic ester saponification mechanism. However, one must note that the copper complex moiety is also a large group, which can sterically interact with the nucleophile. The group that can come in contact with the nucleophile is a ligand cis to the phosphinate oxygen; it can be a TMED amino group or a water molecule. Any one of these ligands can position itself close to the nucleophile through rotation around the two bonds, P - O - Cu, as indicated by arrows in Fig. 1. The interaction between the nucleophile and the ligand should be an important factor affecting the reaction rate. Martell et al.³ has suggested that in the hydrolysis of GB, a copper tridentate chelate, such as Cu(hydroxyethylethylenediamine), is a much less effective catalyst than CuTMED because of such a steric hindrance. Presently our data do not warrant any further speculation.

Other mechanisms can be imagined besides the one described here. One is nucleophilic attack by a water molecule instead of that by an OH⁻. Considering a large ρ^+ value, the contribution of this path is probably small. Kinetic measurements as a function of pH will certainly show this. Another mechanism is one that involves a formation of an intermediate with a structure same as that of the transition state shown above.

CONCLUSION

It is concluded that CuTMED is an effective hydrolytic catalyst for phosphinates. Its catalytic effect is due to its ability to reduce electronic density on the phosphorus to facilitate the nucleophilic attack. The kinetic substituent effects showed the same pattern as the saponification of organic esters by Bac2 mechanism. The role of the water molecule as a third ligand of the copper complex is yet to be studied.

REFERENCES

1. Frederick M. Robbins, Raymond E. Andreotti, Charles T. Woodbury, Rosa Linda Bagalawis, and Louis J. Piscitelle, NATICK/TR-91/021L, April 1991, AD B154615
2. R. C. Courtney, R. L. Gustafson, S. J. Westerback, H. Hyttiainen, S. C. Chaberek, Jr., and A. E. Martell, J. Am. Chem. Soc., 79, 3030 (1957)
3. Richard L. Gustafson and Arthur E. Martell, J. Am. Chem. Soc., 84, 2309 (1962)

BLANK

DEVELOPMENT OF THE CANADIAN REACTIVE SKIN DECONTAMINANT LOTION

J. Garfield Purdon,
Defence Research Establishment Suffield,
PO Box 4000, Medicine Hat, Alberta, Canada, T1A 8K6

Abstract

Although the Fuller's Earth Decontaminating Mitt is an effective broad-spectrum skin decontaminant, its disadvantages include dust and non-destruction of CW agents. In-house and contract research has developed a reactive skin decontaminant (RSD) lotion which achieves chemical destruction of a wide range of CW agents, is non-toxic, easy to apply and economical. An overview of the live-agent in-vitro screening, toxicological examinations, reaction and product characterisation, and materials compatibility studies is presented. The item, which was deployed during the Persian Gulf conflict, is now commercially manufactured impregnated on towellettes and packaged in foil pouches.

Introduction

In the area of protection of skin against Chemical Warfare (CW) agents, the traditional approaches have been to use reactive creams, ointments or lotions, e.g., the US M5 and M258A1 Kits and the UK Anti-Gas ointment, or a reactive or adsorptive powder, e.g. Fuller's Earth (FE) and Dutch Powder. Ointments have been the only items which might be used as protective devices (i.e., in place before contamination of the skin) while powders dominate the decontamination approach. Previous attempts at developing new decontaminants and barriers have encountered difficulties in irritation to skin or eyes, in means of application, in retention or removal, in interference with other equipment, and in agent specificity.

Powders are effective in the laboratory but, in practice, troops often find them difficult to use effectively and to remove after use. Among these, FE has been demonstrated to be a non-toxic effective absorber of classical CW agents. Its main attraction hinges on its non-specific high capacity absorbency for liquids and gases; it is applicable to all liquid agents since the removal process is one of physicochemical absorption. It is economical to obtain and can be packaged in bags, dispensing pads and mitts. The FE decontaminating mitt is and has been a standard Canadian Forces (CF) issue for decontamination of skin and personal protective equipment such as masks, gloves, boots and clothing. Variations of the FE mitt are also standard issue in the UK and AS army inventories although the specific method of application differs from country to country.

In spite of the fact that FE can be used effectively, it does have some disadvantages as a skin decontaminant including those in Table 1. Chief among these is the fact that it doesn't destroy agents and it creates a dust problem. Because of these deficiencies research was initiated to develop a

chemically-reactive formulation. The Reactive Skin Decontaminant or RSD is replacing FE as a skin decontaminant in the CF but FE will continue to find application as an operational decontaminant for protective clothing and, for the time being, as a personal equipment decontaminant.

TABLE 1.

Disadvantages Of Fullers Earth

- | | |
|---|--|
| - Only Absorbs Agents/No Chemical Destruction | - Can Obscure Vision in the Mask |
| - Deployment is Slow | - Affected By Moisture |
| - Requires Training For Maximum Effectiveness | - Cannot Be Used Prophylactically |
| - Can Cause Skin, Eye and Nose Irritation | - Logistical Load |
| - May Cause Outlet Valve Mask Leakage | - Cannot readily remove particulates |
| - Creates a Dust Problem in Confined Areas | - Can render instrumentation inoperative |
| | - Incompleteness of coverage |
| | - Adheres to surface |
| | - Difficult to remove from air |

Development of the Reactive Skin Decontaminant

The RSD has its origin in research directed at developing a dual-purpose barrier cream/skin decontaminant which could be applied either before a suspected attack as a protective device and/or (re)applied after as a skin decontaminant. The advantages of the RSD include fast chemical destruction of agents, easy application and removal, compatibility with skin, eyes and protective gear, and low toxicity. Since it is a lotion, the RSD stays in place after application and, being a liquid, provides complete coverage. It avoids the dusting problems of FE and, because it destroys agents, does not have to be removed immediately. The lotion base is completely miscible with water so that subsequent showering or washing will readily remove the non-toxic residual lotion.

The major areas of research and development are summarized in Table 2.

TABLE 2.

R & D Areas For The Reactive Skin Decontaminant Project

Synthesis	Toxicity (Products)	Field Trial - Concept-of-Use
Complexation Constants	Review of Toxicity	- User Preference
Screening (<u>In-Vitro</u>)*	Chronic Skin Irritation*	Final Specifications
Screening (<u>In-Vivo</u>)	Skin Absorption (Active Salt)	Storage Stability
Solubility Limits	Mask/Glove Compatibility*	Gulf War
Formulation Studies	CAM Compatibility	Barrier Applications
Window-of-Use	Draft Specifications	Wound Decontamination
Determinations of Reaction Mechanisms*	Quality Assessment	Personal Equipment Decontamination
Product Identification*	Methodology	
Toxicity/Toxicology (Formulation)*	Reactive Capacity/Reactivity test	

Obviously, only a few key areas can be discussed at this time and these are denoted by asterisks. The initial approach was based on complexation of alkali metal ions using compounds known as crown ethers and cryptands. It was reasoned that complexation of the cation of a salt in a non-aqueous solvent might produce a very reactive nucleophile. In this way, nucleophiles powerful enough to destroy CW agents, yet which avoided the highly corrosive effects normally observed with in-service decontaminants, might be found. Investigation initially led to a four-component system consisting of a potassium nucleophile salt, a complexation compound, a thickener and a

solvent. Among the nucleophiles which displayed significant promise were potassium phenoxide and the potassium salts of several simple oximates including acetophenone oxime, acetone oxime and diacetyl monoxime. Solvent systems included chemicals such as alcohols, dioxolane, tetraglyme, dimethoxyethane, and polyethylene glycol (PEG)-related compounds.

The in-vitro effectiveness of these nucleophiles in two such solvent systems is evident in experiments (Table 3) in which an eight-fold excess of active ingredient and, optionally, an equivalent amount of complexer were reacted at ambient with CW agents for five minutes. In some systems, small amounts of water, indicated as bracketed percentage values, had to be added to achieve dissolution of the salt. It is clear that solvent has a profound effect on the reactivity in tetraglyme, the dimethyl ether of tetraethylene glycol, supporting higher conversions and that the higher the complexation ability ([222]>18C6>none), the more reactive is the "naked" anion formed.

=====

TABLE 3.

Effectiveness Of Selected Nucleophile/Complexer Combinations Against Agents

Nucleophile	Solvent	Decontamination (%) at (8:1)			Decontamination (%) (18C6 8:8:1)			Decontamination (%) ([222] 8:8:1)		
		HD	VX	GD	HD	VX	GD	HD	VX	GD
Phenoxide	Ethanol	6	26	100	47	16	100	49	46	100
Phenoxide	Tetraglyme	100	100	100	-	-	-	100	100	100
2,3-Butanedione Monoximate	Ethanol	3	17	100	36	17	100	39	30	100
2,3-Butanedione Monoximate	Tetraglyme	86	100	100	- (3%)	83 (3%)	100 (3%)	100 (1%)	100 (1%)	100 (1%)
Acetone Oximate	Ethanol	12	21	100	12	36	100	36	52	100
Acetone Oximate	Tetraglyme	insol	insol	insol	100 (2.5%)	100 (2.5%)	100 (2.5%)	100 (2%)	100 (2%)	100 (2%)
Acetophenone Oximate	Ethanol	10	21	100	17	33	100	20	43	96
Acetophenone Oximate	Tetraglyme	insol	insol	insol	100 (3%)	100 (3%)	100 (3%)	100 (4%)	100 (4%)	100 (4%)

Although complexers proved to be useful for identification of candidate nucleophiles, their cost and the need for stoichiometric amounts and extensive toxicological examination necessitated their replacement by straight-chain analogues. The roles of complexer and solvent were at this point combined in polyethylene glycol (PEG) dimethylethers and the potential field item would be a three-component system. Although effective in in-vitro studies and in-vivo trials against CW agents, the combination based on tetraglyme with Cab-O-Sil™ as a thickener proved to be unsuitable as it dried out and flaked off skin. Also, despite its advantages of supporting high reactivity, tetraglyme is not a good solvent for these salts. Addition of water seemed contraindicated so PEG monomethyl ethers (MPEGs) were added to the tetraglyme. Some of these results are given in Table 4. In this study, it was also shown that an increase in the proportion of monomethyl ether in the solvent leads to some decrease in the overall reactivity. The eventual solvent/complexer/thickener of choice was a mixture of MPEGs which possess the desirable features of the simpler solvents, the thickener, and the complexers but is compatible with eyes, skin and painted surfaces, and is more economical. Based on in-vivo and in-vitro studies, two promising candidate barrier cream systems were identified; one containing potassium phenoxide, the other potassium 2,3-butanedione monoximate (KBDO). For reasons of stability, compatibility with skin and eyes, etc., the oximate salt became the candidate of choice.

TABLE 4.

Effectiveness Of Oximates In Tetraglyme/2-Glycol MME Against Agents

Nucleophile	Ratio salt/agent	2-Glycol MME in Tetraglyme (% v/v)	Decontamination (% in 5 mins)		
			HD	VX	GD
2,3-Butanedione Monoximate	8:1	14	20	90	100
"	25:1	32	45	100	100
"	8:1	10		99	
Acetone Oximate	8:1	30	57	96	100
"	25:1	45	97	100	100
"	8:1	15		100	
Acetophenone Oximate	8:1	14	85	100	100
"	25:1	16	100	100	100
"	8:1	10		100	

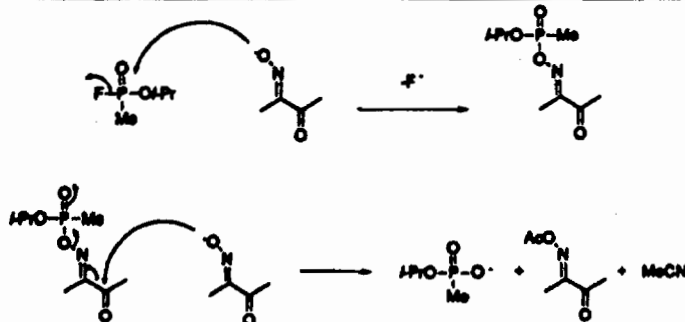
At this point, the CF requested that emphasis be placed on provision of a skin decontaminant only which meant that lower molecular weight solvent homologues could be used to provide a less viscous lotion. *In-vivo* testing of a decontaminant using the new carriers (PEGs/MPEGs) was performed including studies designed to define the window-of-use as a CW agent decontaminant and comparative studies with other formulations and approaches. In all studies, it was evident that the formulations are effective against nerve agents and mustard. In fact, even the base media provided a degree of effectiveness.

The final formulation is a solution of KBDO (1.25m) in a mixture of MPEGs, number average molecular weight 550 daltons, with 10% w/w water added to suppress the freezing point and improve the formulation spreadability. Water does introduce some penalty in reactivity but the formulation is still very reactive and sufficient to meet the requirements. To mediate the pH, there is about 6% of the free oxime in the formulation.

For nerve agents, the initial step in the decontamination reaction (Figure 1) is the formation of the phosphorylated oxime. The major final product of KBDO and GB in deuterated chloroform is, however, O-acetyl 2,3-butanedione monoxime, apparently formed by the reaction of the phosphorylated oxime. Other identified products include acetonitrile and the phosphonate anion. Although earlier simulant studies in anhydrous toluene indicated the stoichiometry between KBDO and agent to be 2:1,

FIGURE 1.

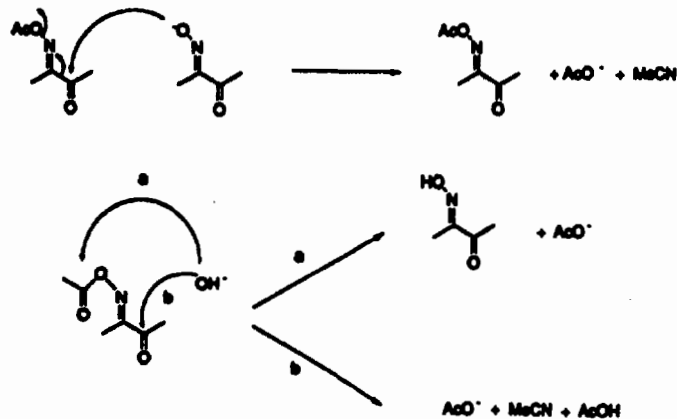
Reaction of 2,3-Butanedione Monoximate and GB



recent simulant studies in MPEG 550/water suggest that the stoichiometry is, in fact, less than 2:1. Although additional reactions between the acetylated oxime and KBDO (Figure 2) may occur under certain conditions,

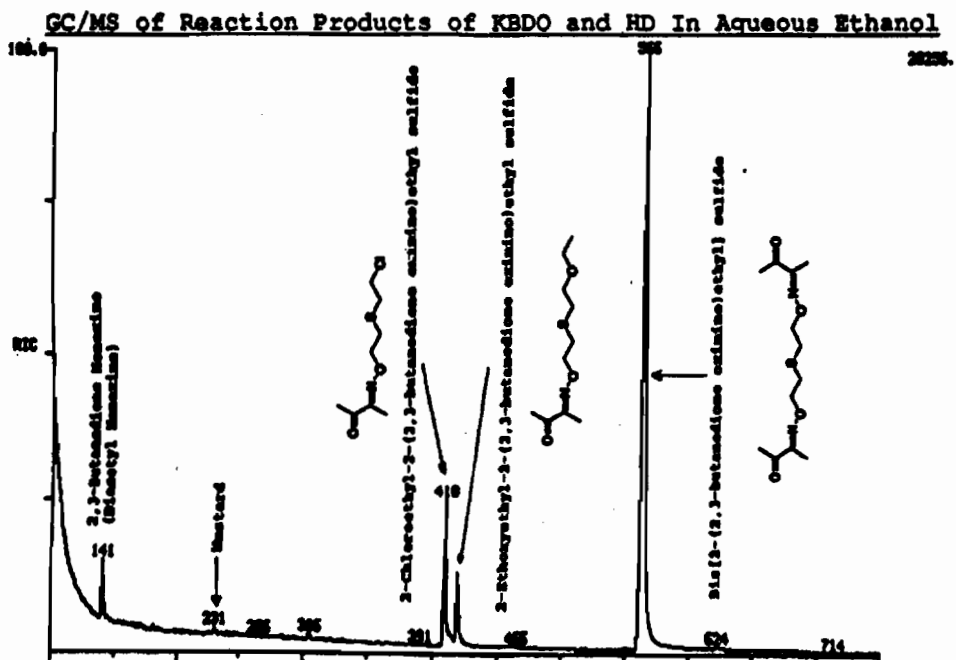
FIGURE 2.

Possible Fates of Acetylated Oximes



chain disproportionation of KBDO does not appear to occur in this solvent system. GC/MS spectra have been generated for the products of KBDO with all nerve agents and HD in simple homologues of the RSD solvent, such as methoxyethanol. Efforts are underway to investigate and further characterize the reaction products in the actual RSD using LC/MS. The GC/MS of a fraction from the product mixture of reaction of KBDO with HD in aqueous ethanol is shown in Figure 3. It is interesting to note the presence of mono- and

FIGURE 3.



di-O-alkyl 2,3-butanedione monoxime substitution products of mustard in 89% yield. Also noteworthy is the presence of the tentatively-identified ethoxy/oximino derivative indicating that the reaction is susceptible to solvent intervention. LC/MS studies of the reactions in fully-formulated RSD are planned to see if this substitution is maintained and if alkoxy derivatives are likewise generated.

Demonstration of low toxicity of the decontamination products is critical to the success of any formulation. The systemic toxicity of nerve agent reaction product mixtures was investigated in rats. In addition to demonstrating that the RSD is effective against the nerve agents, the study clearly established that the products have low toxicity even with direct injection.

Any skin decontaminant must not be toxic or irritate skin with extended contact such as under a protective mask. Toxicity examinations have been carried out using several animal species. First, the low toxicity of KBDO was established in a test series covering intraperitoneal, dermal and oral toxicities. Injections of 10 mL/kg body weight of KBDO in aqueous saline were administered to Sprague-Dawley Albino rats and New Zealand White rabbits. For rats, the acute intraperitoneal LD₅₀ toxicity was moderate (405 mg/kg) whereas for the rabbit, the toxicity was relatively low (1175 mg/kg). The same administrations of KBDO yielded significantly lower acute oral toxicities ranging from 950 to 2225 mg/kg. In both intraperitoneal and one oral examination, notable increases in serum potassium levels were considered to be a significant factor in the mortalities. In acute dermal toxicity studies, KBDO, slightly moistened by saline, was administered to at least 10% of the body areas on abraded and intact occluded skin. For both species, the LD₅₀s were greater than 2000 mg/kg and there was no indication that serum potassium levels played a factor. Thus, the active ingredient is considered as being safe for use as a skin decontaminant. The base medium contains MPEGs of molecular weight average 550; our specifications ensure that the levels of potentially toxic low molecular weight homologues are kept at a minimum.

Several skin and eye irritation examinations have been performed on New Zealand White rabbits and guinea pigs, and a chronic skin test has been carried out on humans. In contrast to the previous series, the base media was either the same as or very similar to the RSD. In all cases, including a 21-day chronic irritation and sensitization study trial with humans, the formulation was considered as non-irritating with no sensitization. In the human trial, no changes in serum haematology or biochemical variables were observed. It is noted that the solvent in these tests, being MPEG in nature, is a complexer of potassium whereas the saline solutions and pastes in the toxicity trials are not.

In order to further reduce the threat to personnel, it is highly desirable that the lotion can be left in place under the mask and gloves. To address the compatibilities, an examination of the effect of exposure of rubber samples from both the olive- and the black-coloured Canadian C4 respirators and the protective glove to continuous challenges from various formulations of the RSD and barrier cream was performed. Following removal of the formulations, tensile stress, tensile strength, ultimate elongation and tear strengths were determined by standard ASTM methods. The data indicate that exposure of these materials to the various formulations including RSD/MPEG550 for continuous 96-hr periods does not appear to have any significant effect on the rubber properties.

There remain several areas in which some experimental work is required. These include identification and distribution of decontamination products using the final RSD formulation by LC/MS, characterisation of storage stability by accelerated aging, development of a reactive capacity/reactivity assessment method, and estimation of the extent, if any, of absorption of KBDO through skin. Past experience indicates that the

formulation is effective for a period of over two years without special storage precautions. In addition to the completed assessment procedures for the starting ingredients and the concentration of total oxime in the final formulation, a specific reactivity test for KBDO in RSD is being developed. Finally, studies are underway to determine the extent of absorption of KBDO into occluded intact and abraded skin in live rabbits.

During the Persian Gulf War, some 190 L were formulated in-house and under contract and deployed in 100-mL flip-top cosmetic bottles. The initial commercial item, rushed into production due to the Persian Gulf, is very close in appearance to the planned final form of the item. RSD is impregnated on a towellette and sealed in a foil pouch similar to that used for the FE mitt; each towellette is considered to be a single application and is intended to be discarded after use.

CONCLUSIONS

When the final testing is completed and the product specifications and assessment methodology put in place, our efforts to develop a new skin decontaminant will be completed but that will not be the end of the story. Since the active ingredient of the RSD and related compounds are effective against traditional CW agents, it is natural that they be considered for application to other areas of decontamination. Future studies will investigate application to wound decontamination for which no current satisfactory procedure is available, to decontamination of personal equipment such as protective masks, gloves, boots and gear, and as a protective skin barrier to be applied when there is a danger of exposure to or contact with CW agents.

BIBLIOGRAPHY

- Casselman, A.A. and Bannard, R.A.B., "The Effectiveness of the Potassium Phenoxide - Tetraglyme System In-Vitro As a Decontaminant for CW Agents", DREO Report No. 875, November 1983.
- Casselman, A.A., Bannard, R.A.B., Purdon, J.G. and Bovenkamp, J.W., "An Examination of Macrocyclic Ether-Alkali Metal Complexes and Quaternary Ammonium Salts as Decontaminants for Chemical Warfare Agents in Non-aqueous Solvents. Part II (U)", DREO Report No. 888, November 1983.
- Casselman, A.A., Mah, R., and Bannard, R.A.B., "The Effectiveness of Three Potassium Oximates and Potassium Phenoxide in Tetraglyme/Diethylene Glycol Monomethyl Ether Systems as In-Vitro Decontaminants for Chemical Warfare Agents (U)", DREO Report No. 905, August 1984.
- Bide, R.W., Armour, S.J., Sawyer, T.W., Parker, D. and Risk, D., "Comparison of Three Skin Decontaminant Systems for Activity Against G and H Agents (U)", Suffield Memorandum No. 1265, October 1988.
- Sawyer, T.W., Birmingham, M.T., Hansen, A.S., and Boulet, C.A., "Toxicity of Phosphorylated Oximes When Injected Subcutaneously Into Mice (U)", Suffield Report No. 509, March 1989.
- Bide, R.W., Sawyer, T.W. and Parker, D., "Efficacy of the Proposed Reactive Skin Decontaminant Lotion Against Challenge by GD, VX and HD (U)", Suffield Report No. 516, March 1989.
- Purdon, J.G. and Casselman, A.A., "Reactive Skin Decontaminant - Respirator/Glove Materials Compatibility (U)", Suffield Memorandum No. 1311, January 1990.
- Dunn, E.J. and Miller, R.K., "Substitution of Chloride Ion in Bis(2-Chloroethyl) Sulfide (HD) by Various Oxygen Anions (U)", DREO TN 90-9, January, 1990.
- Boulet, C.A. and Hansen, A.S., "Reactions of Oximes and Nerve Agents. NMR Analysis of the Reaction Products of GB and Potassium 2,3-Butanedione Monoximate (U)", Suffield Memorandum No. 1323, April 1990.

BLANK

Characterization of the Microemulsion Aggregate by
Luminescence and Electrochemical Techniques

*P. L. Cannon, Jr.^a *S. M. Garlick,^b S. D. Christesen,^a
N. M. Wong,^d A. C. Novelli,^e F. R. Longo,^{a,c} R. A. Mackaya^a

- a U.S. Army Chemical Research, Development and
Engineering Center, Aberdeen Proving Ground, MD 21010-5423
- b Geo-Centers, Inc., Fort Washington, MD 20744
- c Drexel University, Philadelphia, PA 19104
- d National Research Council Fellow, U. S. Army CRDEC, Aberdeen
Proving Ground, MD 21010-5423
- e Lab. IMRCP, Université Paul Sabatier, 31 062 Toulouse, France

* Co-First Author to whom correspondence should be addressed.

ABSTRACT

We have systematically examined microemulsions as potential media for chemical degradation of toxic substances, and we have undertaken a variety of physicochemical studies designed to characterize their microstructure. Luminescence quenching has been used to determine aggregation numbers for CTAB, CTAC, and SDS microemulsion systems. Static luminescence quenching studies are apparently not applicable to most of the microemulsion systems that we have studied. Our data, however, indicate that time-resolved luminescence quenching studies give valid results for solutions with aggregation numbers up to ~200. Electrochemical techniques, cyclic voltammetry and chronocoulometry, have been employed to determine the diffusion coefficients of oil and water soluble electroactive probes located in various microstructural regions of these microemulsions. For those probes that

provide a measure of the aggregate diffusion coefficient, the luminescence and electrochemical results exhibit a good correlation.

INTRODUCTION

We have examined microemulsions (μE) as media for the iodobenzoate (IBA) catalyzed degradation of the nerve agent simulant, *p*-nitrophenyldiphenyl phosphate (PNDP).¹⁻⁶ In order to understand the reactivity control effected by these media, we have initiated studies designed to provide information concerning the microproperties, or more precisely, the nanoproperties, (e.g., aggregation numbers, radii, and net charge of the microemulsion droplets) in the systems in which we have measured degradation rate constants. In this paper, we report the aggregation numbers determined by luminescence quenching techniques and the microaggregate diffusion coefficients determined by electrochemical techniques, namely, cyclic voltammetry (CV) and chronocoulometry (CC).

Luminescence probes have been used successfully in both steady-state and time-resolved luminescence quenching techniques to measure the mean aggregation number (N , the average number of surfactant molecules per aggregate) in micellar and microemulsion media. In the steady-state or static method, developed by Turro and Yekta⁷ and by Yekta, Aikawa and Turro⁸ to determine micelle aggregation number, the following assumptions⁹ are implied: (1) donor and quencher molecules must be associated primarily with the micelles, (2) the residence time of the donor and quencher molecules in the micelles must be longer than the unquenched lifetime of the donor, (3) there are independent Poisson distributions of the donors and quenchers over the aggregates, (4) the immediate deactivation route of excited donor is quenching by an acceptor, (5) the micelles are monodisperse, and (6) the luminescence lifetime of the donor is independent of the quencher concentration, and, therefore, dynamic collisional quenching does not occur.

When donor and quencher reside in the same aggregate, the intensity (I) of probe luminescence follows the relationship

$$I = I_0 \exp \frac{[M]}{[Q]} \quad (1)$$

where I_0 is the luminescence intensity in the absence of added quencher (Q) and M is the concentration of aggregates. When static quenching occurs, a plot of $\ln (I/I_0)$ vs [Q] yields a straight line whose slope is proportional to N .

Lifetime measurements must be available to determine the applicability of the steady-state technique as the plot of $\ln (I/I_0)$ vs [Q] will appear linear even in cases where the technique is not theoretically valid and should not be used to estimate N .

For larger aggregates, where the static luminescence quenching method fails, a time-resolved method has been reported by Infelta, Grätzel and Thomas¹⁰ and by Infelta.¹¹ As with the steady-state technique, both probe and quencher are assumed to be totally associated with the aggregate and independently distributed according to Poisson statistics. However, the measured lifetime of the luminescence probe in the presence of quencher depends on the quencher concentration. Infelta, Grätzel, and Thomas proposed Equation 2 to describe the kinetics of luminescence quenching in micellar systems.¹⁰

$$I(t) = I(0) \exp \{-A_2 t - A_3 (1 - \exp(-A_4 t))\} \quad (2)$$

When both donor and quencher are immobile (relative to the aggregate), A_2 equals $1/\tau_0$, A_3 equals η , and A_4 equals k_q . $I(0)$ and $I(t)$ are the

luminescence intensity at zero time and at time t , τ_0 is the lifetime of the donor in the absence of quencher, k_q is the first order rate constant for luminescence quenching in a micelle containing one quencher, and η is the average number of quencher molecules per aggregate, $[Q]/[M]$.^{11,12} Substitution yields:

$$I(t) = I(0) \exp\{-t/\tau_0 + \eta(\exp(-k_q t) - 1)\} \quad (3)$$

The luminescence decay curve of the donor is fit to Equation 3 by adjusting the parameters I_0 , k_q , and η .

There are several reports on the application of the static and time-resolved luminescence quenching techniques to micelles.¹²⁻¹⁹ Llanos, Lang, Strazelle and Zana²⁰ and Llanos, Lang, and Zana^{21,22} have studied the effects of compositional changes on the aggregation numbers in microemulsions prepared from anionic surfactants. Almgren, Grieser, and Thomas²³ have measured aggregation numbers in sodium lauryl sulfate / *n*-pentanol / dodecane /water microemulsions using the static quenching method.⁷ Almgren and Löfroth¹² calculated aggregation numbers and quenching constants from single-photon counting data and steady state luminescence measurements in sodium dodecyl sulfate/1-pentanol microemulsions and swollen micelles.

We have analyzed luminescence quenching data by both static and time-resolved techniques, and present results for six stable microemulsion systems and for three microemulsion systems not apparently at equilibrium. In addition, we include data for two microemulsion systems whose luminescence decay curves appear to follow a single exponential decay; neither of these systems is amenable to analysis using either technique.

Diffusion coefficients of electroactive species are obtained from diffusion-controlled electrochemical reactions through the examination of the

dependence of the faradaic current on the applied potential . Doping a microemulsion with an electroactive species that is only soluble in the oily interior of the microdroplet yields a measured current that depends only on the rate at which the microdroplet vehicle moves to the electrode surface. Hence, it is possible to obtain the diffusion coefficient and the hydrodynamic radius of a microdroplet from electrochemical experiments.

In cyclic voltammetry (CV), the peak current, i_p , is given by the Randles-Sevcik equation:

$$i_p = (2.69 \times 10^5) n^{3/2} A C_o D_o^{1/2} v^{1/2} \quad (4)$$

where n , A , C_o , D_o , and v are the number of electrons, the electrode area, the bulk concentration of the electroactive species, the diffusion coefficient and the potential scan rate, respectively. By calibrating the electrode area with a species of known diffusion coefficient, the value of D_o can be obtained.

In chronocoulometry (CC), a trace of charge transferred, Q_d , versus $t^{1/2}$ (time) is linear as predicted by the integrated form of the Cottrell equation:

$$Q_d = (2 n F A D_o^{1/2} C_o t^{1/2}) / \pi^{1/2} \quad (5)$$

where F and t are the Faraday and the time, respectively. In the single-potential step chronocoulometric experiment, the potential is instantaneously increased, and held at this voltage for a time period equal to the pulsewidth, t_o . In a double-potential step chronocoulometric experiment, the potential after the first step is decreased to a lower value, and held there for an additional t_o . Data from a double-potential step experiment yields plots of Q_d versus $t^{1/2}$ when $t < t_o$ and plots of Q_d' versus Θ (Anson plot) when $t > t_o$ where Q_d' is defined as $Q_d(t_o) - Q_d(t)$, and Θ is $t_o^{1/2} + (t - t_o)^{1/2} - t^{1/2}$. Slopes of a plots of Q_d versus $t^{1/2}$ and of Q_d' versus Θ are proportional to the diffusion coefficient. For a diffusion-controlled process, these plots are co-linear.

The choice of the electroactive probe is the key to obtaining meaningful data. According to Chokshi, Qutubuddin and Hussam,²⁴ who have recently discussed this problem, the electroactive probe must: (1) minimize the disruption in the nature of the microemulsion aggregate, (2) undergo diffusion-controlled charge transfer at the electrode surface, (3) be non-polar in oil-in-water systems, and (4) not be significantly adsorbed onto the electrode surface. Of course, the probe must be electrochemically reactive within the potential range governed by the electrode material and the microemulsion medium. Ferrocene meets these requirements in many microemulsions and we employ it as the probe in our studies.

Using a polarographic method, Mackay²⁵ obtained microdroplet radii (in anionic and cationic microemulsions) comparable to those determined by all angle x-ray scattering, quasi-elastic light scattering and luminescence quenching.¹⁹ (It should be noted that, while these probes (alkylpyridinium ions) were polar, their long (C₁₂ - C₁₆) alkyl chains assured that they were anchored in the "oil" aggregate.)

Recently Qutubuddin²⁶ reported diffusion coefficients and microdroplet radii from cyclic and rotating disc voltammetry experiments for CTAB/*n*-butanol microemulsions. Rusling, Wang and Owlia²⁷ observed that the apparent diffusion coefficients determined from cyclic voltammetry decrease with increasing concentration of electroactive probe; this was explained in terms of changes in the mole fractions of the bound and unbound electroactive probe.

We have previously examined the suitability of numerous microemulsions as media for nucleophilic degradation of phosphate esters. The second order rate constants (25°C) for IBA catalyzed degradation were previously reported¹⁻⁶ for the microemulsions for which we now report the

results of luminescence quenching and electrochemical experiments. The microemulsion compositions are given in Table 1.

EXPERIMENTAL PROCEDURE

Materials

Cetyltrimethylammonium bromide (CTAB) and *n*-hexadecane (HEX) were purchased from Aldrich or Sigma Chemical Co. Cetyltrimethylammonium chloride (CTAC) was purchased from Eastman Kodak as a dry chemical and from Akzo Chemie America as a 29% aqueous solution (Arquad 16-29). 1-Methyl-2-pyrrolidinone (MP) was received as a gift from BASF Corporation. 1-Cyclohexyl-2-pyrrolidinone (CHP) was received from Virginia Chemicals as experimental material. Sodium dodecyl sulfate (SDS), Adogen[®] 464, 4-*tert*-butyltoluene (*t*-BuTOL), *n*-dodecane (DDEC) and 9-methylanthracene (MeA) were obtained from Aldrich. Toluene (TOL) was purchased from Baker. Tris (2,2'-bipyridine-*N, N'*)-ruthenium (2+) dichloride hexahydrate (Probe 1) was obtained from GFS Chemicals, and tris (4,7-diphenyl-1,10-phenanthroline-*N*¹,*N*¹⁰)-ruthenium (2+) dichloride hexahydrate (Probe 2), and tetrasodium tris [[(1,10-phenanthroline-4,7-diyl) bis (benzenesulfonato)] (2⁻) -*N, N'*] ruthenate (4⁻) decahydrate (Probe 3) were synthesized.²⁸ All other chemicals were reagent grade and were used as supplied except for *N, N*-dimethylformamide (DMF), which was dried over 4Å molecular sieves before use. The aqueous phase (AQ) used in the microemulsions was 0.03M sodium tetraborate decahydrate at pH 9.2 in glass-distilled, deionized water.

μ E	% CTAB	CoS	% CoS	Oil	% Oil	% AQ	N
1	4.5	DEF	4.5	TOL	1.0	90.0	118 \pm 15
2	4.5	1-BuOH	4.5	HEX	1.0	90.0	153 \pm 20
3	4.5	MP	4.5	TOL	1.0	90.0	173 \pm 22
4	8.0	MP	8.0	TOL	4.0	80.0	194 \pm 39
5	4.5	DMF	4.5	TOL	1.0	90.0	246 \pm 16
6	4.5 CTAC	Ad	4.5	HEX	1.0	90.0	452 \pm 57
7	4.5	DIPF	4.5	TOL	1.0	90.0	277 \pm 166
8	4.5	CHP	4.5	t-BuTOL	1.0	90.0	335 \pm 130
9	5.53 SDS	1-PeOH	10.28	DDEC	5.14	79.05	489 \pm 302
10	8.0	CHP	13.5	TOL	4.0	74.5	-----
11	8.9	1-BuOH	9.1	HEX	2.0	80.0	-----

Table 1. Microemulsion compositions and aggregation numbers determined by time-resolved luminescence quenching experiments.

Luminescence

Steady-state luminescence data were collected on a computer-controlled Perkin Elmer MPF-66 Fluorescence Spectrophotometer using a xenon lamp source. The sample turret was thermostatted at 25.0 °C. Corrected excitation and emission spectra were collected in the ratio mode with a spectral bandpass of 1.5 to 1.8 ± 0.1 nm. An MPF-66 OBEY program, SCOUT, was used to determine the maximum excitation and emission wavelengths for the donor molecules. The slit widths for samples containing quencher were adjusted to give intensity readings of approximately 25% of the maximum intensity observed for samples without quencher.

Time-resolved luminescence data were collected at 90° using a Spex Model 1403 monochromator with a RCA 31034A photomultiplier tube (PMT). The donor was excited using the doubled output from a Spectra-Physics Quanta-Ray Model DCR-2A Nd:YAG laser. The monochromator was set at the emission wavelength of the donor with the bandpass set at 1 nm. The output of the PMT was digitized at 20 ns intervals using a LeCroy Model TR8828C transient recorder. The data were analyzed using customized least square routines written in Asyst[®] 29 to model the data to Equation 3. The short laser pulse width (10 ns) gave essentially instantaneous Rayleigh scattering from the sample thus defining $t = 0$ and eliminating the need to deconvolute the incident laser pulse.

For the luminescence measurements, 3 ml of microemulsion was placed in a fluorimetry cuvette and 20 μ l of a 2.0×10^{-3} M to 7.2×10^{-3} M solution of probe 1 or 3 dissolved in water or probe 2 dissolved in MP was added to give a final solution concentration of donor between 1.2×10^{-5} to 4.5×10^{-5} M. Since dissolved oxygen quenches probe luminescence, the microemulsions were purged with nitrogen for 15 minutes (measured luminescence intensity

maximized at ≈ 12 minutes purge time). Ten (static) or 25 (time-resolved) μl aliquots of a 6.16×10^{-2} M solution of quencher, 9-methylanthracene, dissolved in acetonitrile were then added to give a final quencher concentration between 2.033×10^{-4} to 1.003×10^{-3} M, after which the microemulsion was again purged for 3 minutes.

Electrochemistry

Electrochemical measurements were conducted using an M273/96 Potentiostat/Galvanostat interfaced to an IBM PS/2 Model 70-E61 microcomputer, employing EG&G Princeton Applied Research (PAR) M270 V3.00 Electrochemical Software, on microemulsions (μE) 1 to 6 and 8 to 11, Table 1. The electrochemical cell included a PAR G0197 glassy carbon working electrode, a silver-silver chloride reference electrode and a platinum wire auxiliary electrode. Appropriate IR compensation by positive feedback was applied in all experimental determinations. Temperature was controlled to $26 \pm 0.5^\circ\text{C}$.

Cyclic voltammetric studies were conducted in the staircase mode. For microemulsions μE 's 1 to 5 and 8 to 11 currents were sampled at 25% of the pulse width and for μE 6 at 50%, since, in this medium, the oxidation of ferrocene was characterized by a lower heterogeneous transfer rate constant. Chronocoulometric studies were conducted in the double potential step mode with a pulse width (t_p) of 10 seconds. The raw data was corrected for background charge before the determination of the diffusion coefficients from Q_d vs $t^{1/2}$ plots.

The electrochemical areas of working electrodes were determined by CV and CC in aqueous solutions of 1.0 M KCl and 4.0 mM $\text{K}_4\text{Fe}(\text{CN})_6$. The literature value of the diffusion coefficient of $\text{Fe}(\text{CN})_6^{4-}$ under these conditions is

$0.632(\pm 0.003) \times 10^{-5} \text{ cm}^2/\text{s}$ at 25°C .³⁰ The areas of the three glassy carbon electrodes used in this study ranged from 0.075 to 0.081 cm^2 .

RESULTS AND DISCUSSION

It is assumed that all the surfactant above the critical micellization concentration (cmc), which, for all practical purposes, is all of the surfactant, is associated with the droplets of the microemulsion. This may not be true and surfactant organized into micelles may co-exist with the microemulsion aggregates. Although the amount of surfactant, if any, in the form of co-existing micelles is not known, it must be an extremely small fraction, otherwise, our phosphate ester hydrolysis studies would have yielded much higher rate constants. (Second order hydrolysis rate constants measured in micellar solutions are greater than the corresponding rate constants in microemulsion media by 2 to 3 orders of magnitude.) For CTAB, CTAC, and SDS, the cmc values are $9.2 \times 10^{-4} \text{ M}$,³¹ $1.3 \times 10^{-3} \text{ M}$,³¹ and $2 \times 10^{-3} \text{ M}$,^{23,32} respectively, and were negligible by comparison to total surfactant concentrations ranging from ≈ 0.12 to 0.22 M .

Luminescence

Luminescence probes 1 and 3 are water soluble while probe 2 is insoluble in water but soluble in oils. Luminescence from probe 1 is effectively quenched in SDS micelles and in μE 9, however no quenching is observed in μE 's 3 or 4 or in CTAC micelles. Luminescence from probe 2 or 3 is efficiently quenched in all 11 microemulsions, and in SDS and in CTAC micelles. Comparison of visible spectra of probes 1 or 3 obtained in micellar or in microemulsion media employing anionic or cationic surfactants to probe spectra

obtained in water, changes in peak location and shape indicate probe interaction or binding with the aggregates. It has been suggested that these ruthenium donor complexes exhibit strong binding to anionic micelles due to hydrophobic interaction of the ligands with the micellar hydrocarbon core. In addition, any repulsive forces exhibited by similarly charged aggregates and complexes are diminished by the diffuseness of the charge of the donor.³³ Aggregation numbers determined using probes 2 or 3 were found to agree within the uncertainty of the measurement. Probe 1 was used in an SDS microemulsion (μE 9) to duplicate the measurement reported by Almgren and Löfroth.¹²

Steady state studies of a 0.045 M SDS micellar system with Probe 1 gave an aggregation number of 60.5 ± 3.0 , in close agreement with the value of Turro and Yekta⁷ of 60 ± 2 . In addition, this method was applied to solutions of CTAC in 0.02 M phosphate buffer, pH 8.0, 0.08 M NaCl, using Probe 3 (Table 3). Measured aggregation numbers agree ($\pm 10\%$) with the values calculated from electrochemical measurements reported by Mackay, Dixit, Agarwal and Seiders.³⁴

The results of the static measurements in the microemulsions, whose compositions are given in Table 1, are presented in Table 2. The aggregation data are averages of between 2 to 4 different determinations and are reported as the mean \pm (the standard deviation). The donor lifetimes were functions of quencher concentration in all microemulsions tested, and decreased as the quencher concentration increased. These results indicate that the steady-state luminescence quenching technique is not valid for any of the systems examined.

When the time resolved luminescence technique was applied to μE 1-6, reproducible results (i.e. small standard deviations) were obtained, with good

<u>[CTAC]</u>	<u>N_s</u>	<u>$k_{IBA}(\text{Ms})^{-1}$</u>
1×10^{-3}	10	54
6×10^{-3}	98 ± 11	156
1×10^{-2}	113 ± 4	180

Table 3. Aggregation numbers for several CTAC solutions determined by steady state luminescence quenching measurements. Second order rate constants for the catalytic hydrolysis of PNDP are included.

fits of the data to Equation 3. In these systems, the excited probe luminescence in the presence of quencher exhibits an apparent double exponential decay. Immediately after excitation, the decay from aggregates containing one or more quencher molecules dominates, with the luminescence decreasing rapidly and depending on the quencher concentration. At longer times, the luminescence intensity is dominated by emission from aggregates without quencher, and the excited probe lifetime approaches τ_0 . Luminescence decay traces for μE 4, containing different quencher concentrations, are shown in Figure 1. Systems 1-6 are probably thermodynamically stable, as evidenced by the fact that measured values of N did not change significantly over a time period of 100 hours. For μE 's 7, 8, and 9 which were studied at 24 hours and at 100 hours after preparation, the apparent mean aggregation number changed dramatically, indicating unstable systems. Calculated values of N were irreproducible and imprecise. The mean aggregation number for μE 9 was reported by Almgren¹² to be 313 in comparison to the value of 292 which we found 24 hours after preparation. Measured at 100 hours, however, N had increased to 833. For μE 's 7 and 8, the aggregation number was 285 and 141 respectively at 100 hours.

Equation 3 could not be solved satisfactorily with data obtained for μE 's 10 and 11; $\ln I$ vs t plots of these data were linear, indicating single exponential decay, which is expected for quenching in homogeneous media without aggregates. However, the presence of aggregates of some kind was indicated by the presence of Tyndall scattering in these solutions. Inspection of Equation 3 reveals that it predicts a single exponential decay for small values of k_q . In other words, if,

$$I(t) = I(0) \exp\{-t/\tau_0 + \eta(\exp(-k_q t) - 1)\} \quad (3)$$

and $\exp(-k_q t)$ approximates to $(1 - k_q t)$ for small values of k_q , then,

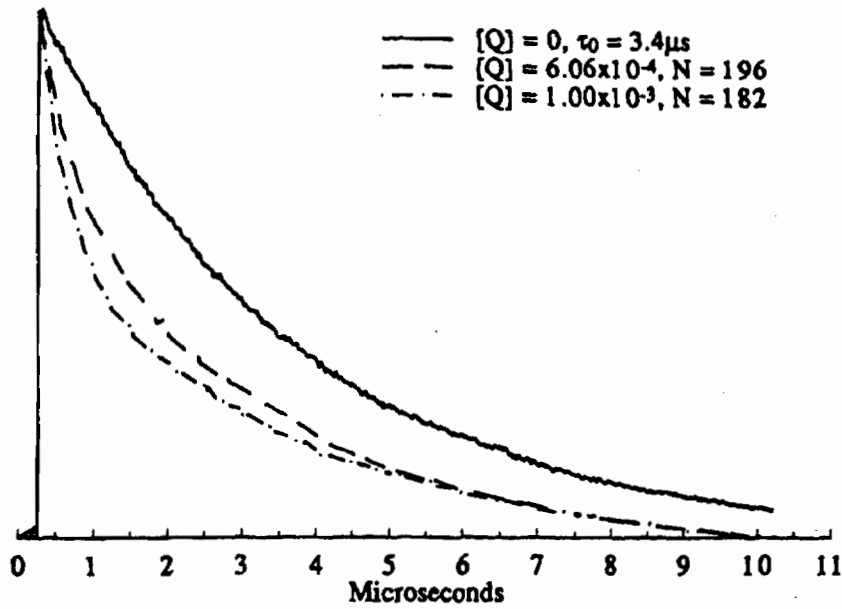


Figure 1. Luminescence decay curves of Probe 3 in $\mu\text{E } 4$; (—) $[\text{Q}] = 0$, $\tau_0 = 3.4 \mu\text{s}$, $R^2 = 0.9991$; (---) $[\text{Q}] = 6.06 \times 10^{-4}$, $N = 196$, $R^2 = 0.9985$; (- · - · -) $[\text{Q}] = 1.00 \times 10^{-3}$, $N = 182$, $R^2 = 0.9996$.

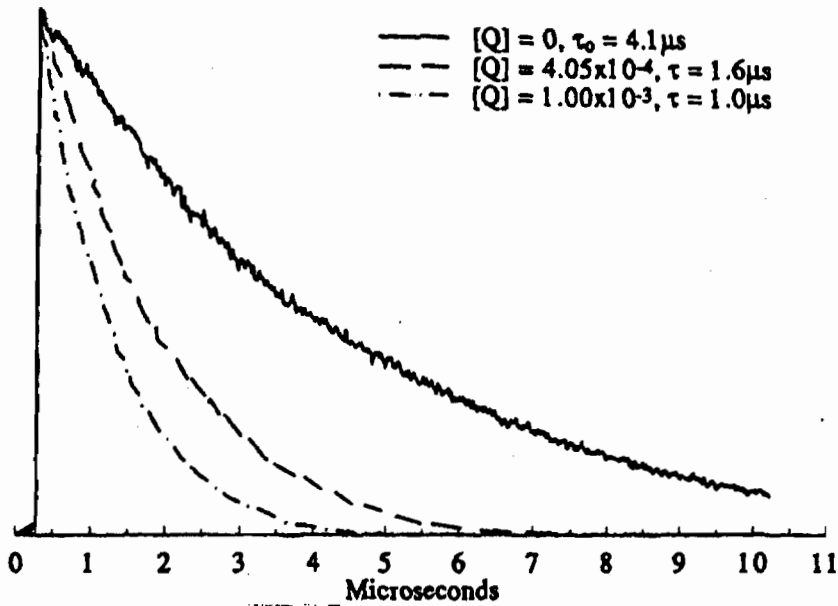


Figure 2. Luminescence decay curves of Probe 3 in $\mu\text{E } 10$; (—) $[\text{Q}] = 0$, $\tau_0 = 4.1 \mu\text{s}$, $R^2 = 0.9983$; (---) $[\text{Q}] = 4.05 \times 10^{-4}$, $\tau = 1.6 \mu\text{s}$, $R^2 = 0.9983$; (- · - · -) $[\text{Q}] = 1.00 \times 10^{-3}$, $\tau = 1.6 \mu\text{s}$, $R^2 = 0.9987$.

$$I(t) \sim I(0) \exp(-t/\tau_0 - \eta k_q t) \quad (3a)$$

$$\text{and} \quad \sim I(0) \exp-t(1/\tau_0 + \eta k_q) \quad (3b)$$

$$\sim I(0) \exp-t(1/\tau_0 + k_q [Q]/[M]) \quad (3c)$$

By correlation with an unquenched system, where, for any decay,

$$I(t) = I(0) \exp(-t/\tau) \quad (6)$$

comparison of the exponentials of the right sides of Equations 3c and 6 shows that:

$$1/\tau = 1/\tau_0 + \eta k_q \quad (7)$$

$$\text{and:} \quad \tau_0/\tau = 1 + k_q \tau_0 [Q]/[M] \quad (8)$$

Equation 8 is the Stern-Volmer relationship for collisional quenching.³⁵ Plots of τ_0/τ vs $[Q]$ for μE 's 10 and 11 do indeed yield straight lines over the range of quencher concentrations used (Figure 3). Since these two systems exhibited Tyndall scattering, this result is probably indicative of large aggregates containing 1 or more quencher molecules. In μE 10, assuming a Poisson distribution of quenchers among the aggregates, if $\eta \approx 2.5$ (barely adequate to fit the intensity:time data to Equation 3) then less than 10 % of the aggregates will contain no quenchers ($P_0 \approx 0.08$) and N would have to be ~ 1375 for $[Q] = 4 \times 10^{-4}$. This approach is obviously not quantitative but it does give some estimate of how large the aggregates might be. For μE 's 10 and 11, the time-resolved luminescence data can tell us that the structures are large (i.e. have many surfactant molecules associated with them), but cannot provide us with aggregation numbers.

Results of our studies suggest that the time-resolved luminescence quenching technique to determine N may accurately be applied only to micellar media or to small microemulsion aggregates. When the time-resolved luminescence quenching technique is employed to determine aggregation numbers in microemulsion media containing large aggregates, precise results,

i. e., good fits of intensity:time data to Equation 3, are not obtained. Decreasing the percentage of surfactant and increasing the percentage of AQ produces microemulsions with smaller aggregates or swollen micelles which are likely to yield systems that will fit the model described by Equation 3. It may be noted that, simply diluting a given microemulsion composition with aqueous buffer does not significantly change the aggregation number (compare μE 's 3 and 4).

Aggregation numbers determined from steady-state measurements agree with aggregation numbers determined from time-resolved measurements for μE 's 1, 2, 3, and 4. However, as mentioned above, the steady-state data are not valid, since donor lifetimes in these microemulsions are a function of quencher concentration.

Electrochemistry

We have estimated the diffusion coefficients of the microemulsion aggregates from data obtained by electrochemical methods. Diffusion coefficients for molecules of ordinary size in aqueous medium are of the order of 10^{-5} to 10^{-6} cm^2/s . For instance, the value of D_0 for ferrocene, as determined by chronopotentiometry in acetonitrile at 25°C , is 2.4×10^{-5} cm^2/s ,³⁶ whereas the values of D_0 for ferrocene in the microemulsions examined in this study are of the order of 10^{-7} cm^2/s . The Stokes-Einstein Equation relates diffusion coefficient to the radius of a molecule:

$$\text{radius} = kT / (6\pi\eta D) \quad (9)$$

where k is the Boltzmann constant, T is the absolute temperature, and η is the viscosity coefficient (0.98×10^{-3} Ns/m^2 for pure water at 23°C). As can be seen from examination of Equation 9, this indicates that the radius of the electroactive species and/or the viscosity are different in microemulsions. We have assumed that the ferrocene, since it is non-polar, is strongly associated with the

microaggregates present in the microemulsion and, as a simplification, the aqueous medium retains the viscosity of pure water. The ferrocene has lost its translational degrees of freedom and moves with the microaggregate, thus forming a giant electroactive species with $n = 1$. The electrochemical measurements then yield the diffusion coefficients and diameters of the microaggregates.

Ferrocene appears to undergo quasi-reversible electrochemical oxidation in the microemulsions (1 to 6 and 8 to 11) which we have studied by cyclic voltammetry and chronocoulometry. This is borne out by examination of a typical CV trace, Figure 4, for ferrocene (2 mM) in μ E 1 at a scan rate of 20 mV/s. Note that the cathodic peak current is lower than the anodic peak current, with a separation of ~ 110 mV between the peak potentials. The anodic peak potential and the separation between the anodic and cathodic peaks increases with sweep rate. These are all characteristics of a non-Nernstian system. The chronocoulometric results also indicate quasi-reversible behavior of ferrocene in all μ E's except 1 and 10, data from a double-potential step experiment yields plots of Q vs $t^{1/2}$ and Q_d' vs Θ , that are not co-linear. Figure 5a is a typical, double-potential step chronocoulomogram from data taken in μ E 1 at a pulsewidth of 10 seconds. A plot of this data as charge, Q , vs $t^{1/2}$ is linear as shown in Figure 5b. The intercept of this plot is the sum of the capacitive charge on the double layer and the faradaic component involved in the oxidation of any adsorbed species. The Anson plot, also shown in Figure 5b, is displaced and not co-linear, indicating that a homogeneous chemical reaction precedes the cathodic reaction.³⁷

Figure 6 shows plots of D_0 values derived from CV and from CC measurements vs ferrocene concentration over a range from 0.5 to 2.5 mM in μ E 6. As expected from previous studies,^{27,38} the diffusion coefficients appear

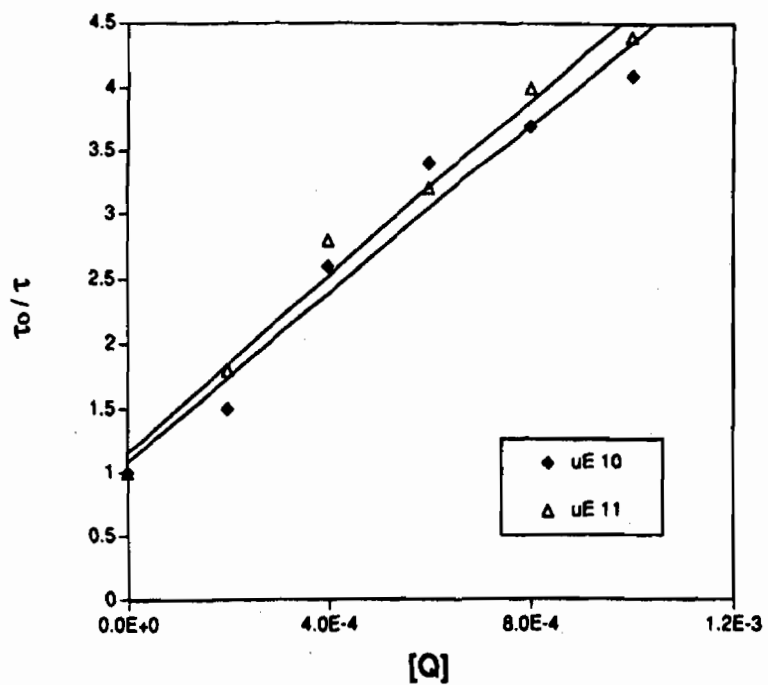


Figure 3. Stern-Volmer plots for $\mu\text{E 10}$ and $\mu\text{E 11}$. Slopes are 3271 M^{-1} ($R^2 = 0.9629$) for $\mu\text{E 10}$ and 3429 M^{-1} ($R^2 = 0.9827$) for $\mu\text{E 11}$.

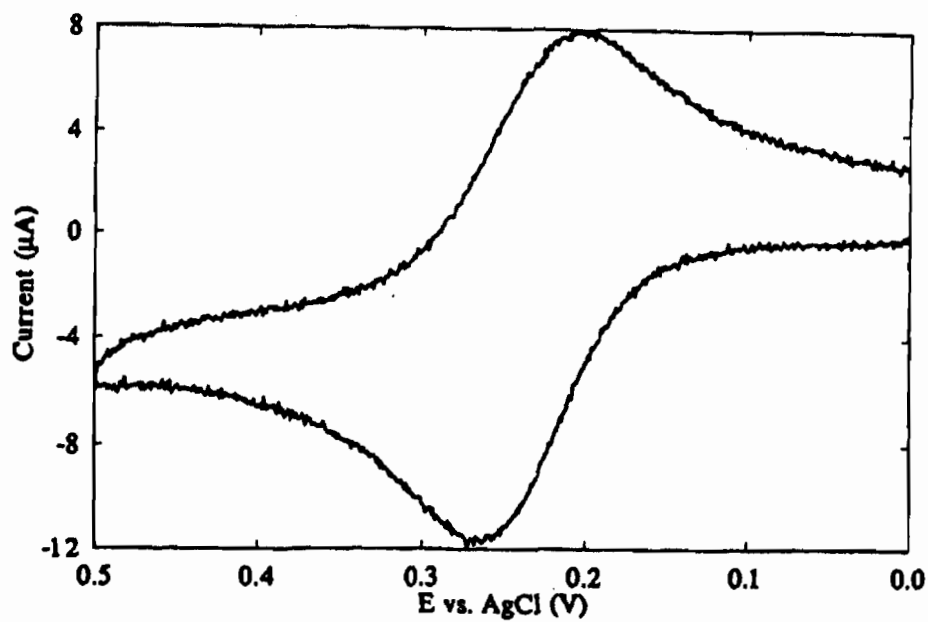


Figure 4. The cyclic voltammogram of ferrocene (2 mM) in $\mu\text{E 1}$. Several aspects of this trace indicate that the electrochemical process is quasi-reversible.

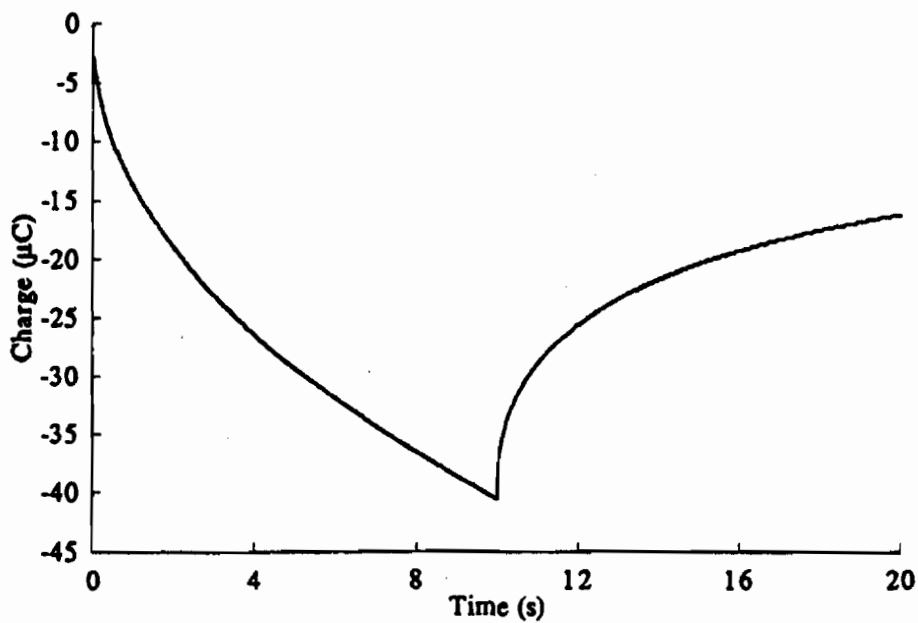


Figure 5a. A double-potential step chronocoulomogram, Q vs time, taken in $\mu\text{E } 1$ at a pulsewidth of 10 seconds.

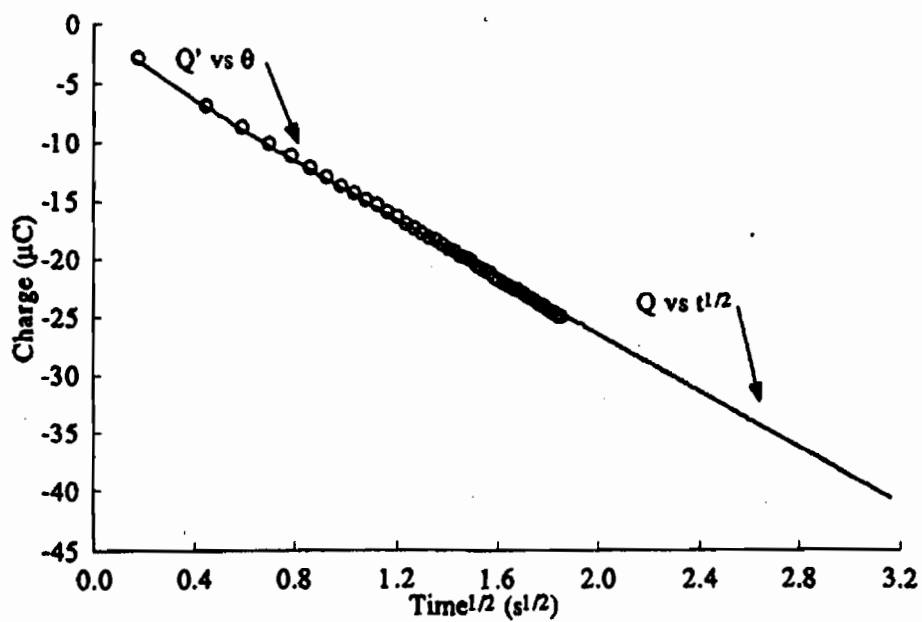


Figure 5b. A plot of Q vs $t^{1/2}$ with Anson plot overlay for $\mu\text{E } 1$ from a double-potential step chronocoulometry experiment (see Figure 5a for conditions.)

to decrease and level off as the concentration of the probe increases. We take the level-off values as the actual diffusion coefficients. In general, analogous plots for systems $\mu\text{E}1$ to 5 and 8 to 11 also exhibit the same characteristics.

The cyclic voltammogram (Figure 7) of $\mu\text{E} 6$, containing 2 mM ferrocene, demonstrated interesting behavior. At 500 mV/s, a very prominent anodic peak is observed and no cathodic peak, while at 20 mV/s the cathodic peak is quite evident. This indicates that a fast, homogeneous reduction by a contaminant proceeds during the anodic sweep. when the homogeneous reductant is consumed the electrochemical reaction is observed. Therefore, there is no cathodic peak at 500 mV, but it is present at lower scan rates. Examination of the composition of $\mu\text{E} 6$ (Table 1) shows that it is the only one of our microemulsion systems containing Adogen 464 which may contain an amine contaminant from its synthesis; amines can act as sources of homogeneous reductant. In the double-potential step chronocoulometric experiment in $\mu\text{E} 6$, plots (Figure 8) of both Q and Θ (the Anson plot) versus $t^{1/2}$ are overlaid to indicate that this occurs.

Examination of the overlaid Anson plot of data for ferrocene in $\mu\text{E} 9$ indicates that the electrode process is under mixed control; see Figure 9. Identical examination of $\mu\text{E} 10$ shows that ferrocene oxidation, subjected to double- potential step chronocoulometry, is diffusion-controlled; see Figure 10.

CONCLUSION

As mentioned, (vide supra) our object is to understand how microemulsion media affect reactivity, and we have thoroughly investigated the hydrolysis of phosphate esters in numerous microemulsion systems including

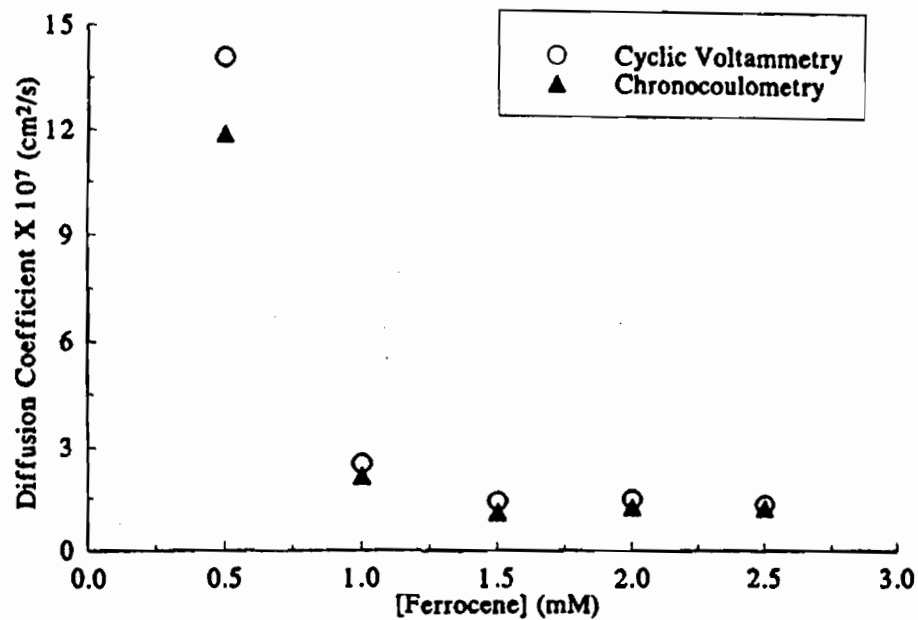


Figure 6. Plots of D_0 values derived from CV and from CC measurements vs ferrocene concentration over a range of 0.5 to 2.5 mM in $\mu E 6$.

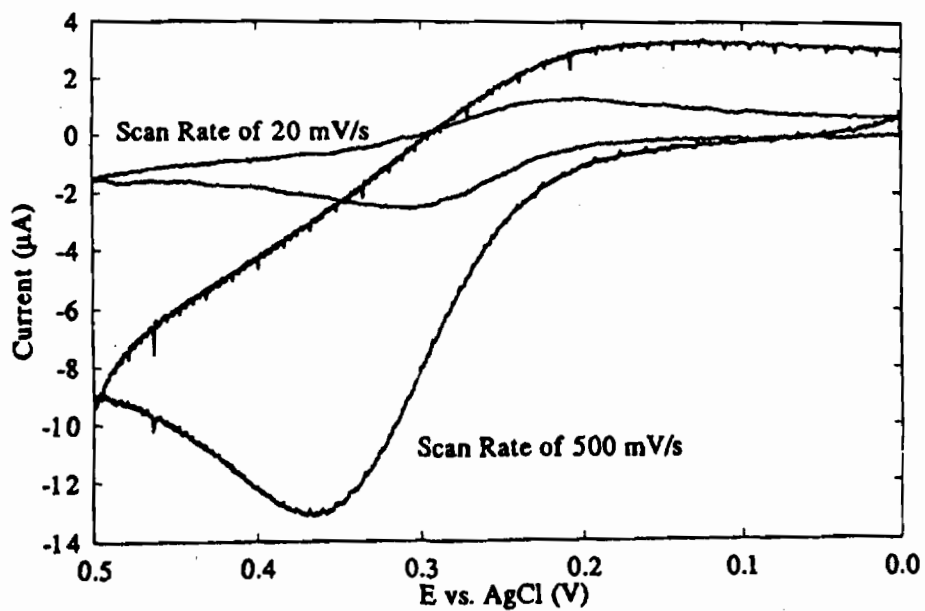


Figure 7. Cyclic voltammograms for 2.0 mM ferrocene in $\mu E 6$ at sweep rates of 20 and of 500 mV/s.

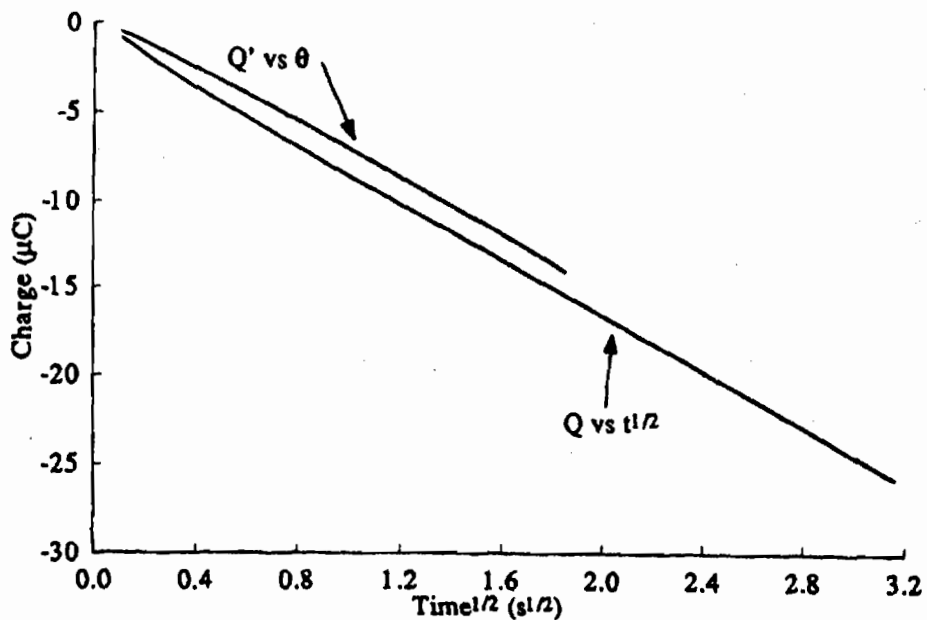


Figure 8. A plot of Q vs $t^{1/2}$ with Anson plot overlay for $\mu\text{E } 6$ from a double-potential step chronocoulometry experiment with a pulsewidth of 10 seconds.

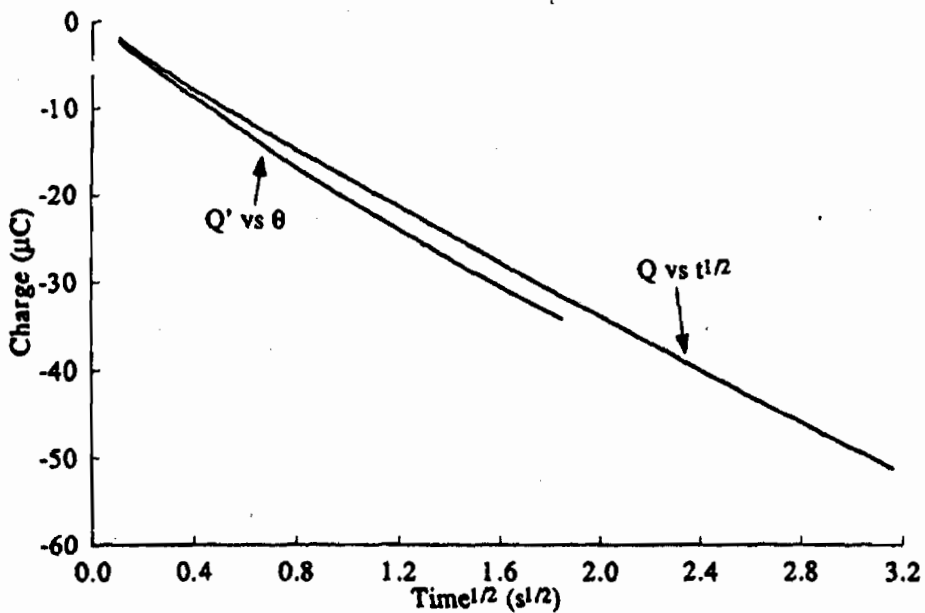


Figure 9. A plot of Q vs $t^{1/2}$ with Anson plot overlay for $\mu\text{E } 9$ from a double-potential step chronocoulometry experiment with a pulsewidth of 10 seconds.

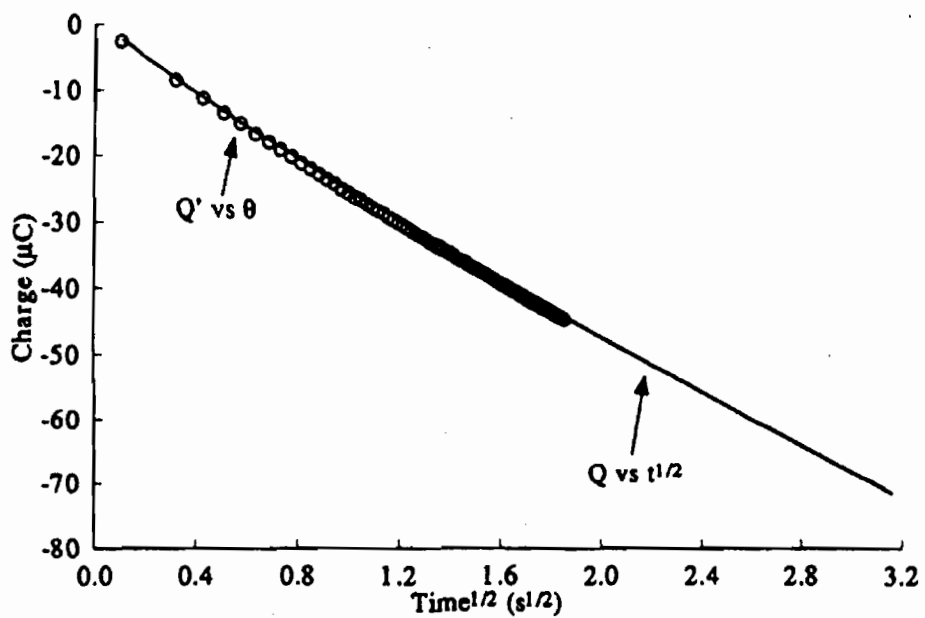


Figure 10. A plot of Q vs $t^{1/2}$ with Anscn plot overlay for μE 10 from a double-potential step chronocoulometry experiment with a pulsewidth of 10 seconds.

those examined in this work. Hence, our luminescence and electrochemical studies represent the initiation of a search for structure/reaction relationships.

Table 2 summarizes all of the relevant results of our studies. The diffusion coefficients, D_0 , extracted from the CV studies agree reasonably well with those from CC. In order to test the consistency of the luminescence and the electrochemical data, we estimated the diameters of the microemulsion aggregates from the CV-determined diffusion coefficients using the Stokes-Einstein Equation (Equation 9) and compared them with the diameters determined from the aggregation number, N_D . (To calculate aggregate diameter from N_D , assumptions must be made; we assumed that all of the organic substances present in the media reside in the microemulsion aggregates. In addition, we estimated the density of the microdroplets to be 0.8g/cm^3 and the overall density of the microemulsion to be $\sim 0.95\text{g/cm}^3$.) Examination of our results shows that the diameters estimated from the three types of measurements are fairly consistent, the worst case being the values obtained from studies in $\mu\text{E } 6$, in which we have already indicated that an unusual irreversible process occurs in our electrochemical studies.

Although we are fairly certain that the reactivity enhancement of the microemulsions is due to the reagent concentrating effect of the interfacial area, there appears to be no simple correlation between the iodosobenzoic acid catalyzed hydrolysis of phosphate esters and aggregation number. The lack of correlation is probably due to the fact the interfacial area is enormous and, therefore, its magnitude is not a rate limiting factor. For instance, our calculations show that for $\mu\text{E } 2$, the interfacial area available in one dm^3 of microemulsion is $\sim 10^9 \text{cm}^2$. The fraction of interfacial area occupied in an ordinary hydrolysis study is negligible in comparison. We are now attempting to determine the dependence of the rate constant on microaggregate charge

$D_0 \times 10^7 \text{ (cm}^2/\text{s)} \pm 15\%$

Diameter (Å)

μE	CV	CC	$\tau_0 \times 10^6 \text{ (s)}^a$	$k_q \text{ (} \times 10^6 \text{) / s}$	Ns	Nd	CV	Nd
1	5.05	5.02	3.4±0.3	1.5±0.2	115±30	116±17	97.2	71.9
2	5.93	5.97	3.9±0.2	1.6±1.0	151±22	138±29	85.0	76.2
3	7.10	7.13	5.0±0.1	1.0±0.1	156±18	186±16	68.8	84.2
4	3.02	3.90	3.0±0.5	1.8±0.3	174±14	184±20	161	84.2
5	3.51	4.21	4.2±0.5	0.9±0.1	124±47	244±14	142	89.3
6	1.36	1.26	3.8	0.31	221±28	443±78	363	107.7
7	—	—	4.3±0.4	0.33±0.20	135±15	208±173 ^c	—	95.5
8	4.90	6.52	4.0±0.3	0.11±0.04	110±1	374±103 ^c	100.7	106.6
9	1.06	b	0.71±0.01	1.6±0.2	142±16	292±66 ^c	463.5	110.6
10	5.34	b	4.3±0.2	—	271±21	—	91.8	—
11	3.53	3.95	4.8±0.2	—	364±32	—	140	—

a. Lifetime of probe 3 (μE 1-8; 10, 11); lifetime of probe 1 (μE 9).

b. The data indicated that the system was highly irreversible with respect to chronocoulometric investigation.

c. From data taken 24 hours after preparation of the medium; system may not have been at equilibrium.

Table 2. Microemulsion aggregation numbers and aggregate diameters determined by static and dynamic luminescence quenching experiments, and by electrochemical techniques of cyclic voltammetry and chronocoulometry.

and zeta potential, since it is fairly clear that the charge has a pronounced effect on the rate of ester hydrolysis in surfactant systems.^{5,6,39}

REFERENCES

1. Mackay, R.A., Longo, F.R., Knier, B.L., and Durst, H.D., *J. Phys. Chem.*, **91**, 861-864 (1987).
2. Knier, B.L., Durst, H.D., Burnside, B.A., Mackay, R.A., and Longo, F.R. *J. Solution Chem.*, **17**, 77-81 (1988).
3. Burnside, B.A., Szafraniec, L.L., Knier, B.L., Durst, H.D., Mackay, R.A., and Longo, F.R., *J. Org. Chem.*, **53**, 2009-2011 (1988).
4. Burnside, B.A., Knier, B.L., Mackay, R.A., Durst, H.D., and Longo, F.R., *J. Phys. Chem.*, **92**, 4505-4510 (1988).
5. Mackay, R.A., Burnside, B.A., Garlick, S.M., Knier, B.L., Durst, H.D., Nolan, P.M., and Longo, F.R., *J. Disp. Sci. Technol.*, **9**, 493-510 (1989).
6. Garlick, S.M., "Chemical and Physical Studies in Microemulsion Media, University Microfilms International, Ann Arbor, MI, (1990).
7. Turro, N.J. and Yekta, A., *J. Am. Chem. Soc.*, **100**, 5951- 5952 (1978).
8. Yekta, A., Aikawa, M., and Turro, N.J., *Chem. Phys. Lett.*, **63**, 543-548 (1979).
9. Lofroth, J-E.; Almgren, M. "Surfactants in Solution, Volume 1", edited by Mittal, K. L. and Lindman, B. Ed.; Plenum Press: New York, 1984; pp 627-643.
10. Infelta, P.P., Gratzel, M., and Thomas, J.K., *J. Phys. Chem.*, **78**, 190-195 (1974).
11. Infelta, P.P., *Chem. Phys. Lett.*, **61**, 88-91 (1979).
12. Almgren, M. and Lofroth, J-E., *J. Coll. Int. Sci.*, **81**, 486-499 (1981).
13. Almgren, M. and Swarup, S., "The Size of Sodium Dodecyl Micelles With Various Additives: A Fluorescence Quenching Study," in "Surfactants in Solution, Volume 1", edited by Mittal, K.L. and Lindman, B., Plenum Press: New York, 1984; pp. 613-625.
14. Kajiwara, T.; Thomas, J. K. *J. Phys. Chem.*, **76**, 1700-1706 (1972).
15. Turro, N. J.; Lee P. C. C. *J. Phys. Chem.*, **86**, 3367-3371 (1982).
16. Aikawa, M.; Yekta, A.; Yurro, N. J. *Chem. Phys. Lett.*, **68**, 285-290 (1979).

17. Aikawa, M.; Yekta, A.; Liu, J-M.; Turro, N. J. Photochem. and Photobiol., **32**, 297-303 (1980).
18. Atik, S. S.; Nam, M.; Singer, L. A. Chem. Phys. Lett., **67**, 75-80 (1979).
19. De Schryver, F. C. 4th Interim Report # DAJA 45-84-C-0012, U. S. Army, European Research Offices of the U. S. Army, 1985.
20. Llanos, P., Lang, J., Strazelle, C., and Zana, R., J. Phys. Chem., **86**, 1019-1025(1982).
21. Llanos, P., Lang, J., and Zana, R., J. Phys. Chem., **86**, 4809-4814 (1982).
22. Llanos, P., Lang, J., and Zana, R., J. Phys. Chem., **88**, 819-822 (1984).
23. Almgren, M., Grieser, F., and Thomas, J.K., J. Am. Chem. Soc., **102**, 3188-3193 (1980).
24. Chokshi, K., Qutubuddin, S., and Hussam, A., J. Coll. Int. Sci., **129**, 315-321 (1989).
25. Mackay, R.A. and Hermansky, C., J. Phys. Chem., **85**, 739-744 (1981).
26. Chokshi, K.; Qutubuddin, S.; Hussam, A. J. Colloid Interface Sci., **129** 31-26 1989
27. Rusling, J. F., Wang, Z., and Owlia, A., J. Colloids and Surfaces, **48**, 173-184 (1990).
28. Durst, H.D., Longo, F.R., Garlick, S.M., Haddaway, K.G., U.S. Army CRDESCS Chemical Defense Research, 39-46 (1990).
29. ASYST Software Technology, Inc. 100 Corporate Woods, Rochester, NY 14623.
30. Von Stackelberg, M., Pilgram, M., and Toome, V., Z. Elektrochem, **57**, 342-351 (1953).
31. Rosen, M.J., "Surfactants and Interfacial Phenomena," Wiley Interscience, New York, 1978, p 96.
32. Hayase, K. and Hayano, S., J. Coll. Int. Sci., **63**, 446-451 (1978).
33. Hauenstein, B. L. Jr., Dressick, W. J., Buell, S. L., Demas, J. N., DeGraff, B. A., J. Am. Chem. Soc., **105**, 4251-4255 (1983).
34. Mackay, R. A.; Dixit, N. S.; Agarwal, R.; Seiders, R. P. J. Disp. Sci. Tech., **4**, 397-407 (1983).

35. Lakowicz, J.R., "Principles of Fluorescence Spectroscopy," Plenum Press, New York, 1986, pp 257-301.
36. Kuwana, T., Bublitz, D. E., and Hoh, G., J. Am. Chem. Soc., **82**, 5811-5817 (1960)
37. Anson, F. C., and Osteryoung, R. A., J. Chem. Ed. **60**, 293 - 296 (1983).
38. Personal communication by S. Qutubuddin, Case Western Reserve University.
39. Garlick, S. M., Burnside, B. A., Mackay, R. A., Knier, B. L., Durst, H. D., Nolan, P. M., Haddaway, K. G., Longo, F. R., Proc. U. S. Army CRDEC Chem. Def. Res. 3 - 10 (1988).

BLANK

THE HYDROLYTIC KINETICS OF MUSTARD SIMULANTS IN POLYMER SOLUTIONS

Lawrence C. Cerny and Elaine L. Cerny
Utica College of Syracuse University
Utica, N.Y. 13502

A variety of pyrrolidiones have been used as cosurfactants in the formation of microemulsions. In the present investigation, the polymeric analog, polyvinylpyrrolidone (PVP), has been used. These polymers are commercially available with molecular weights of 10000, 40000, 160000 and 360000. Therefore at a given polymer concentration, there is a several-fold increase in solution viscosity as the molecular weight increases. Also, in mixtures of water and acetone, the molecular size of the PVP changes because this mixture is similar to a Theta-solvent in which polymer-solvent interactions are minimized. The hydrolytic kinetics of 2-chloroethyl ethyl sulfide, 2-chloroethyl methyl sulfide and 2-bromoethyl phenyl sulfide were followed conductrimetrically. The parameters investigated include: the PVP concentration, solution viscosity and the conditions of the Theta-solvent. The results of these experiments illustrate the effect of the polymeric species on the kinetics.

INTRODUCTION

Previous studies from this laboratory examining the hydrolytic kinetics of mustard simulants investigated the role of the dielectric constant of the solvent, solutions of biological polymers such as collagen and gelatin, as well as other naturally occurring compounds including poi, starch and hemoglobin. Since most biological polymers are difficult to characterize and have certain variations in their molecular characteristics which depend upon the source from which they were obtained, the current study extends the earlier investigation to commercially available materials.

A well-characterized polymer-solvent system offers several advantages. Most commercially available polymers have well-known molecular weights or molecular weight distributions. These polymers also provide a molecular architecture, that is, they can be random coils, branched chains or even rods. Also by changing the polymer concentration, it is possible to control the viscosity of the solution. This of course, can modify the diffusion of the reacting species. There is one other feature of a polymer-solvent system which is commonly overlooked. This is the concept of the ideal solution. In polymer chemistry this is known as the "Theta"-condition. A "Theta"-solvent is one in which the polymer-solvent interactions are minimized or are nonexistent. This takes place at a fixed temperature for the system, called the "Theta"-temperature.

In the current study, we report the hydrolytic kinetics for several mustard simulants using a random coil polymer, polyvinylpyrrolidone, and a highly branched polymer, dextran.

EXPERIMENTAL

Chemicals and Materials

The bromo phenyl ethyl sulfide, chloro ethyl ethyl sulfide and chloro ethyl methyl sulfide were obtained from the Fairfield Chemical Company. The acetone and methyl alcohol were analytical reagent grade and were used without further purification. The polyvinylpyrrolidone (PVP) were generously supplied to us by BASF Corporation. The dextran was purchased from the Pharmacia Company. The polymeric characterization of the polymers is given in Table 1 and supplied to us by the companies.

TABLE 1

Characterization of Polymers

	Number Average Molecular Weight, M_n	Weight Average Molecular Weight, M_w
<u>Polyvinylpyrrolidone</u>		
PVP-90	360,000	1,100,000
PVP-30	10,000	45,000
Plasadone	10,000	15,000
PVP-PF-12	1,300	2,900
<u>Dextran</u>		
T-500	276,000	502,000

Equipment

The kinetic studies were followed by the increase in the rate of conductivity of the HCl in the reaction mixture. Accurate measurements were made with a YS 1 Model 35 Conductance

Meter and monitored by a Heath Strip Chart Recorder using calibrated conductivity cells. The rate constants were determined using a non-linear regression analysis¹.

All viscosity measurements were made in a calibrated Cannon-Ubbelohde semimicro dilution viscometer placed in water bath controlled to within ± 0.01 C of the desired temperature. In no case was a kinetic energy correction necessary.

The concentrations were made by weight. Each substrate was dissolved in freshly distilled acetonitrile at a concentration of 10%. The initial concentration for all kinetic studies were less than 8×10^{-4} M. For these polymers, the solvent was doubly distilled water.

Determination of Theta Conditions

A. Modified Elias Procedure. In order to specify a convenient Theta temperature for PVP, a combination of the method of Elias^{2,3} and its modification by Cornet and Van Ballegovijen⁴ was used. Two fractions of PVP (PVP-90 and PVP-30) were dissolved in water at various polymer concentrations and then filtrated with acetone, at 25 C, until a cloud point occurred. A plot of log percent acetone versus log volume fraction of polymer was made and the critical water-acetone solution composition was found by extrapolation to a volume fraction of polymer equal to unity. This is shown in Figure 1.

B. Flory Method. The Theta temperature for dextran in a proposed Theta solvent (40.5% methanol, 59.5% H₂O by volume) was determined by the usual Flory method. A series of fractions of a wide molecular weight range polymer were dissolved in the solvent mixture, and appropriate corrections were made for volume change upon mixing. Several dilutions were then made for each of the fractions and the temperature of the solution was varied until the solutions became cloudy. This precipitation temperature was plotted versus polymer concentration expressed in weight percent and the maximum of this curve was the consolute temperature. The reciprocals of the consolute temperatures for each of the fractions were then plotted versus the reciprocal square roots of the molecular weight, and the resulting straight line extrapolated to infinite polymer molecular weight yielding $1/T_{\theta}$. This is shown in Figure 2.

C. Light Scattering. An independent verification of the dextran Theta temperature found using the Flory method was achieved through the use of the second virial coefficient obtained from light-scattering measurements. Measurements on three dextran samples ranging in weight average molecular weight from 76,000 to 238,000 were made at several temperatures and the values of the second virial coefficient A_2 thus obtained were plotted versus temperature, as shown in Figure 3. The temperature for which $A_2=0$ is the Theta temperature and was found to be 33 C, in excellent agreement with the temperature of 34 C found by the precipitation method.

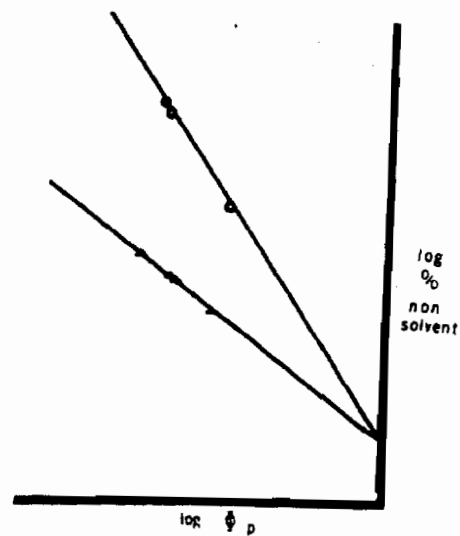


FIG. 1. Determination of solvent mixture from precipitation measurements.

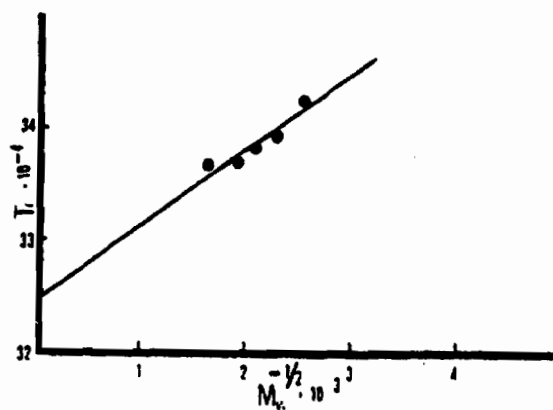


FIG. 2. Determination of the θ temperature from precipitation measurements.

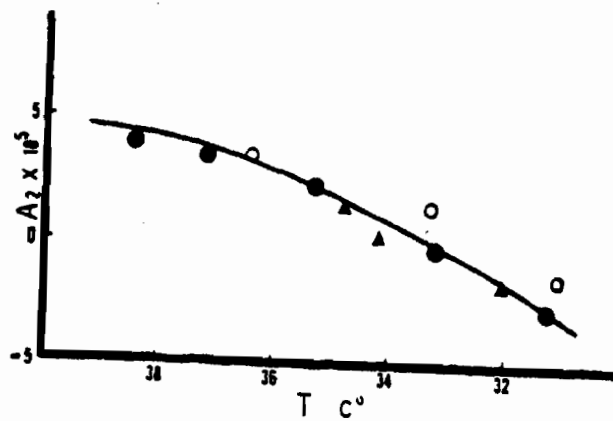


FIG. 3. Evaluation of θ temperature from light scattering. ●—228,000; ○—209,000; ▲—370,000.

RESULTS

The Theta conditions for PVP are at 25C in a mixed solvent (65% by volume acetone and 35% by volume water). For Dextran, the Theta conditions are in a mixed solvent (40.5% by volume methanol and 59.5% by volume water) at 34C.

The results of the kinetic data are presented in Table 2. The dielectric constants for the two Theta solvents (acetone and water) and (methanol and water) are calculated to be 44.1 and 62.4, respectively. It does not appear that they play a major role in the kinetics. As expected, the viscosity of the solution is strongly dependent upon the molecular weight of the polymer. In a Theta-solvent, the polymer molecule assumes its smallest configuration. This is also reflected in the reduced values of the viscosity. One of the problems that exists with the PVP is the high degree of heterogeneity of the samples, that is, the ratio of the weight average molecular weight to the number average molecular weight. These ratios range from 1.5 to 4.5. As a result, it is difficult to isolate the effect of the polymer additions in detail. However, the presence of the polymer on the kinetics is evident. If fractionated polymers were used, their contribution could be easily defined. The molecular architecture of the polymer species is very important in the hydrolytic kinetics. This is shown by the role played by a random coil from a linear polymer when compared with highly branched molecules.

CONCLUSIONS

This preliminary investigation indicates that combining the role of the dielectric constant of the solvent with the addition of a polymer may serve as a possible decontaminant for mustard simulants. The important conclusions indicate that:

- 1) The molecular architecture of the polymeric specie plays a crucial role in the kinetics;
- 2) In a Theta-solvent, the addition of a polymer alters the rate of reaction; its effect is dependent upon the molecular weight of the polymer;
- 3) The viscosity of the medium can be controlled by the type of polymer used and its molecular weight;
- 4) It should be possible to formulate an ideal (Theta) polymer system with a biocompatible polymer such that one of the solvents in the mixture would evaporate leaving a protective polymer film.

TABLE 2

SUMMARY OF KINETIC DATA

SUBSTRATE: Bromo phenyl ethyl sulfide

Solvent	Polymer	k(min ⁻¹)	t _{1/2} (min)	Relative Viscosity	Temp
θ-solvent Acetone + H ₂ O	None	0.019	36.5	1.330	25C
θ-solvent Acetone + H ₂ O	1.75% PVP-90	0.00925	74.9	4.315	25C
θ-solvent Acetone + H ₂ O	1.75% PVP-30	0.0145	47.8	1.779	25C
θ-solvent Acetone + H ₂ O	1.75% PVP Plasadone	0.0182	38.1	1.759	25C
θ-solvent Acetone + H ₂ O	1.75% PVP PF-12	0.00320	216.7	1.411	25C
H ₂ O	5% PVP-90	No Reaction	---	4.918	25C
H ₂ O	1.75% PVP-90	0.0131	52.9	4.826	25C
H ₂ O	1.75% PVP-30	0.0149	46.5	1.389	25C
H ₂ O	1.75% PVP PF-12	0.0295	23.5	1.091	25C
θ-solvent MeOH + H ₂ O	NONE	0.311	2.23	---	34C
θ-solvent MeOH + H ₂ O	1.75% Dext T-500	0.264	2.63	---	34C
θ-solvent Acetone + H ₂ O	NONE	0.0195	35.7	---	34C
θ-solvent Acetone + H ₂ O	1.75% PVP-90	0.0106	65.8	---	34C
SUBSTRATE: Chloro ethyl ethyl sulfide					
θ-solvent Acetone + H ₂ O	NONE	0.0214	32.5	1.330	25C
θ-solvent Acetone + H ₂ O	1.75% PVP-90	0.01	69.3	4.432	25C
H ₂ O	1.75% PVP-90	0.22	3.15	4.700	25C
SUBSTRATE: Chloro ethyl methyl sulfide					
θ-solvent Acetone + H ₂ O	NONE	0.0119	58.2	1.330	25C

TABLE 2-CONTINUED

Solvent	Polymer	k(min ⁻¹)	t _{1/2} (min)	Relative Temp Viscosity
θ-solvent Acetone + H ₂ O	1.75% PVP-90	0.0082	84.6	4.198 25C
H ₂ O	1.75% PVP-90	0.35	2.00	4.808 25C

REFERENCES

- 1) Physical Chemistry on a Microcomputer J. H. Noggle, Little, Brown and co., Boston, 1985, p.145.
- 2) H. G. Elias, Makromal. Chem. 33, 140 (1959).
- 3) H. G. Elias, Makromal. Chem. 50, 1 (1961).
- 4) C. F. Cornet and H. Van Ballegovijen, Polymer (London), 7, 293 (1965).

BLANK

XI. COMPUTATIONAL CHEMISTRY

NOTE: Papers with the following titles were presented at the Conference but are not included in this document:

Conformational Analysis of Oligopeptides: Molecular Dynamics versus Monte Carlo Techniques

Calculation of Electronic Spectra with the Valence Effective Hamiltonian Method

Integration of the AVS Visualization Environment into Chemical Defense Research: Investigation of Alpha-2 Adrenergic Agonists

BLANK

PBI HYDRATION STUDY IN THE DEVELOPMENT OF METHODOLOGY FOR THE MOLECULAR MODELING OF MECHANICAL PROPERTY TRENDS

Nancy E. Iwamoto
Chemistry Division, Research Department
Naval Weapons Center, China Lake, CA

ABSTRACT

Polybenzimidazole (PBI) is a polymer of high aromatic character with exceptionally high thermal stability. Because of these characteristics, it is of interest as a component in high temperature resistant composite materials. However, PBI absorbs water up to 18% by weight, which also degrades stiffness properties of the material. Molecular modeling has been used in order to understand the water absorption characteristics of PBI and its effect on short strain stiffness.

INTRODUCTION

Studies of the effects of hydration on polymeric materials has long been of interest because of moisture dependent changes on their mechanical properties. PBI is among an important class of high performance polymers with high thermal stability and mechanical strength but whose mechanical properties diminish with moisture uptake.¹ Because PBI exhibits water retention characteristics similar to natural fibers, it has been used as a comfortable alternative to natural fibers for protective clothing such as flight suits, helmets, and fire-fighting protective gear. It has also found usefulness in composite materials where high strength and resistance to thermal degradation is necessary. Stabilization of the hydration characteristics of the material would be desirable in order to stabilize mechanical responses of the material. Although hydration studies of PBI have been performed in the past,² mechanistic studies on the effects of structure on stiffness have not been done.

Because of these concerns, molecular dynamics was used to study water absorption characteristics of PBI. This study addresses both the effects of substitution on the hydration tendencies in PBI and the development of a method to study structural and matrix effects on the mechanical properties of polymers from the molecular level.

A standard commercial molecular modeling package (obtained from Biosym Technologies, Inc.) was used in this study. This package consisted of a Newtonian molecular mechanics/dynamics algorithm running on a CRAY X-MP and a front-end graphics package running on a Silicon Graphics workstation.

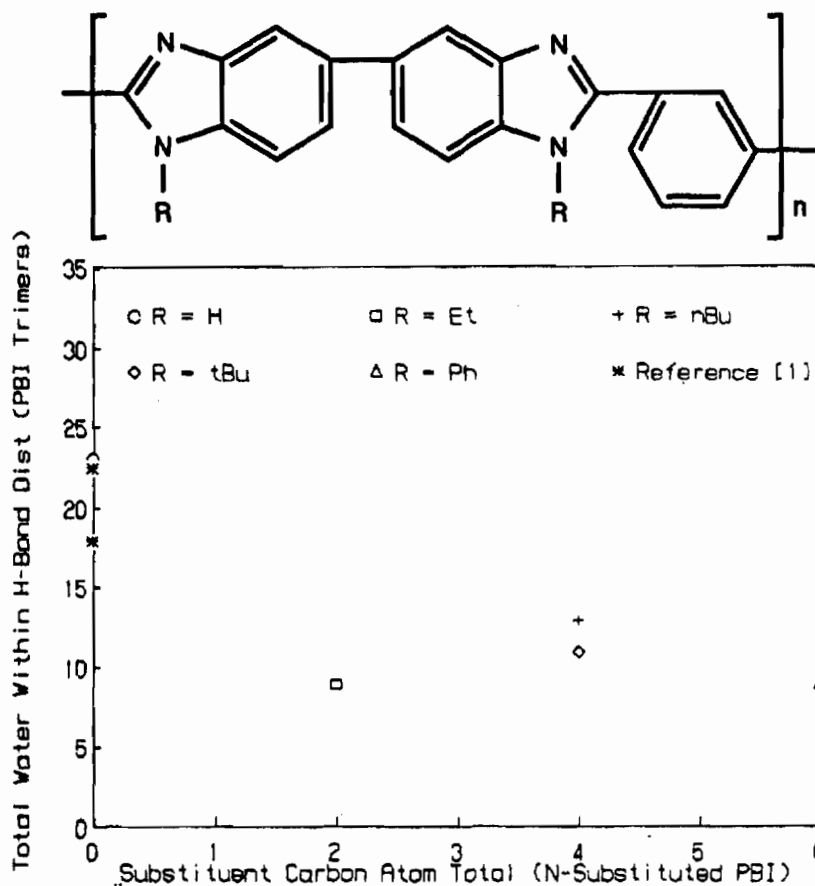
RESULTS AND DISCUSSION

The basic model consisted of two linear strands of an oriented PBI trimer which was subsequently surrounded by an initial five angstrom layer of water. The amine hydrogens were replaced with ethyl, butyl, t-butyl, and phenyl groups to study substituent effects. All

trimer models were minimized to convergence before temperature and stress dynamics were calculated. The oriented trimer model was used in order to simulate PBI in its strongest and most typical oriented form, in fibers and composites. Placement of the strands was arbitrary but kept constant for all substituent forms. PBI length was kept short to keep computer time to a minimum. The minimized models were compared by looking for water migration within hydrogen bonding distance.

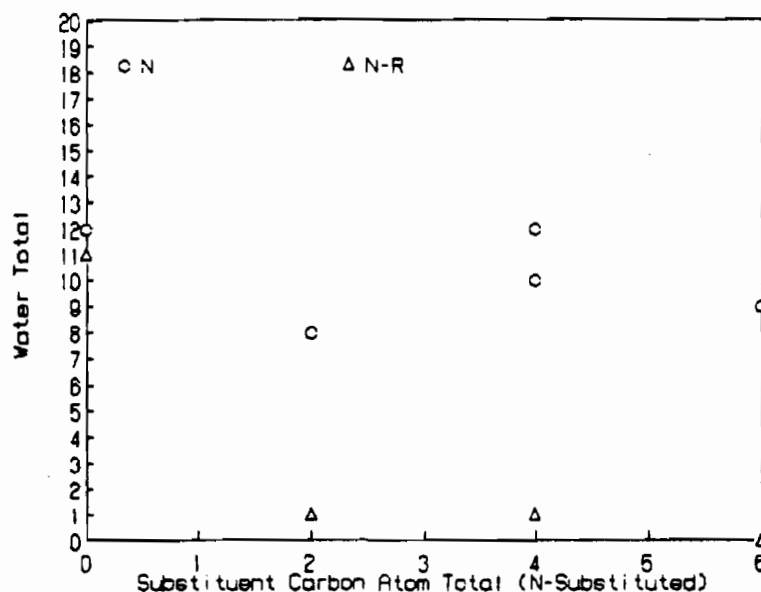
The tendency toward hydration was estimated by determination of those water molecules equilibrated within hydrogen bonding distance of the chains, Figure 1. The model indicated affinity of water by only the imidazole nitrogen groups, with 23 water molecules equilibrated

FIGURE 1
Hydration Tendencies in PBI and Substituted Forms.



within hydrogen bonding distance in the unsubstituted case (R = H). This was directly comparable to the amount found in the literature at 23 water molecules calculated for 18% water by weight, and 20 water molecules calculated for 15% water by weight. The amount of water dropped by about half with amine substitution. The origin of this drop was explained by comparison of the hydrogen-bond target atoms (Figure 2). Upon substitution, water was excluded from the substituted (amine) side of the monomers. However the opposite (imine) side retained the same amount of water as in the unsubstituted molecule. Therefore simple substitution appeared to help eliminate hydration tendencies in PBI, but did not eliminate it completely.

FIGURE 2
Location of H-Bonded Water



The stress response of hydrated and unhydrated forms of unsubstituted PBI was also simulated at room temperature in order to better understand the causes of modulus (or short strain stiffness) degradation in hydrated PBI. The stress simulations were repeated on the substituted forms in order to predict the effect of both substitution and hydration on stiffness. The models were first equilibrated at 300°K, followed by an NOE push which separated the strands along their axis in order to simulate a linear tensile force.

By comparison of the energy profiles obtained from the NOE dynamics, indications of the source of modulus loss were obtained. For example, upon application of stress on unhydrated, unsubstituted PBI, the model indicated that the molecule must first pass through an energy barrier. This energy barrier totally disappeared upon hydration, using a 5 Å initial layer. The extent of the energy barrier loss was found to depend upon the amount of water used in the model (Figure 3). Such comparisons suggest that the initial energy barrier contributes to stiffness, which is lost upon hydration.

Upon N-substitution of the hydrated PBI (still using a 5 Å water layer), some of the energy barrier was restored in comparison to unsubstituted PBI. The amount of restoration was estimated by calculation of the ratio of the energy barrier to the distance traveled (or "pushed" in the NOE simulation) for the unsubstituted case to a similar ratio in the substituted models (Table 1). It was found that while there is no large difference between hydration tendencies of ethyl and butyl substituted, there is a larger energy barrier to distance ratio restored (compared to the unsubstituted case) in heavily hydrated n-ethyl as opposed to n-butyl. The smallest ratio was found restored in t-butyl and phenyl (Figure 4, Table 1). These trends suggest that the free volume influence of the side chains on stiffness is as important as the compounding influence of hydration.

FIGURE 3
Energy Profiles of PBI and Hydrated Models

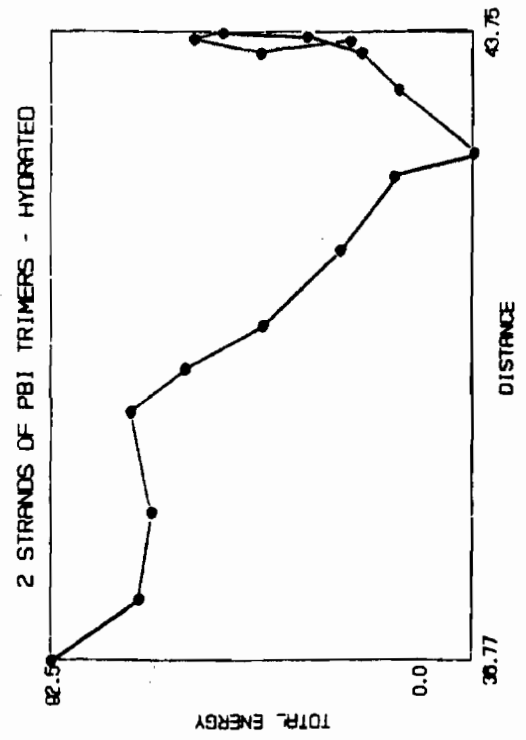
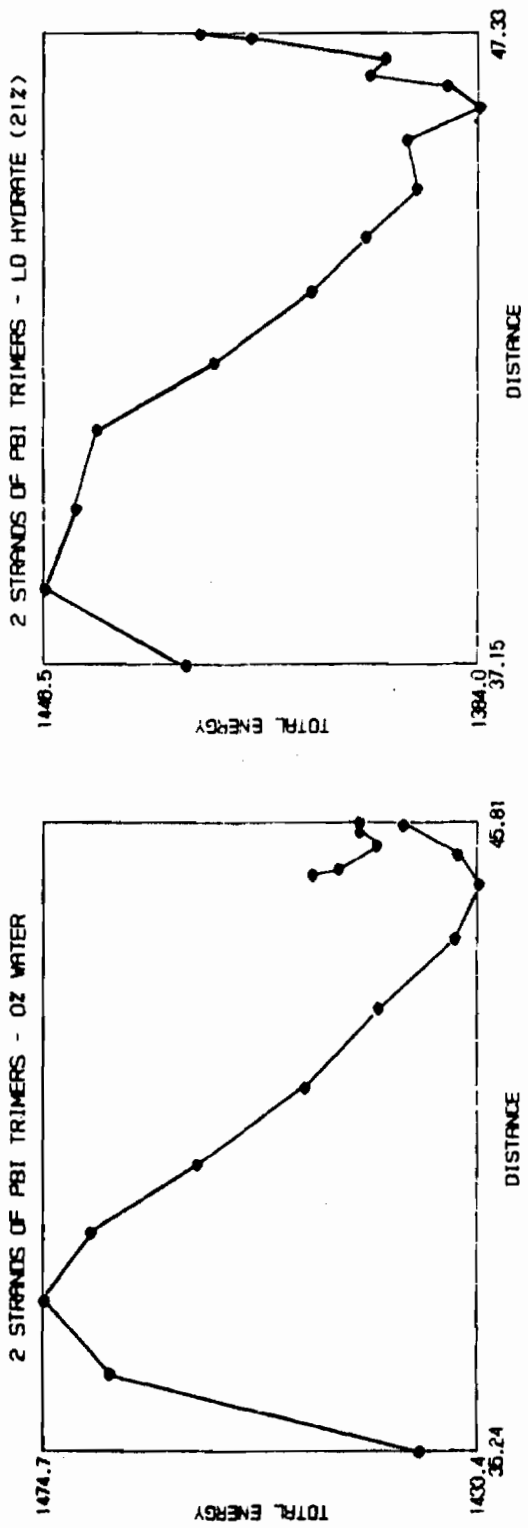
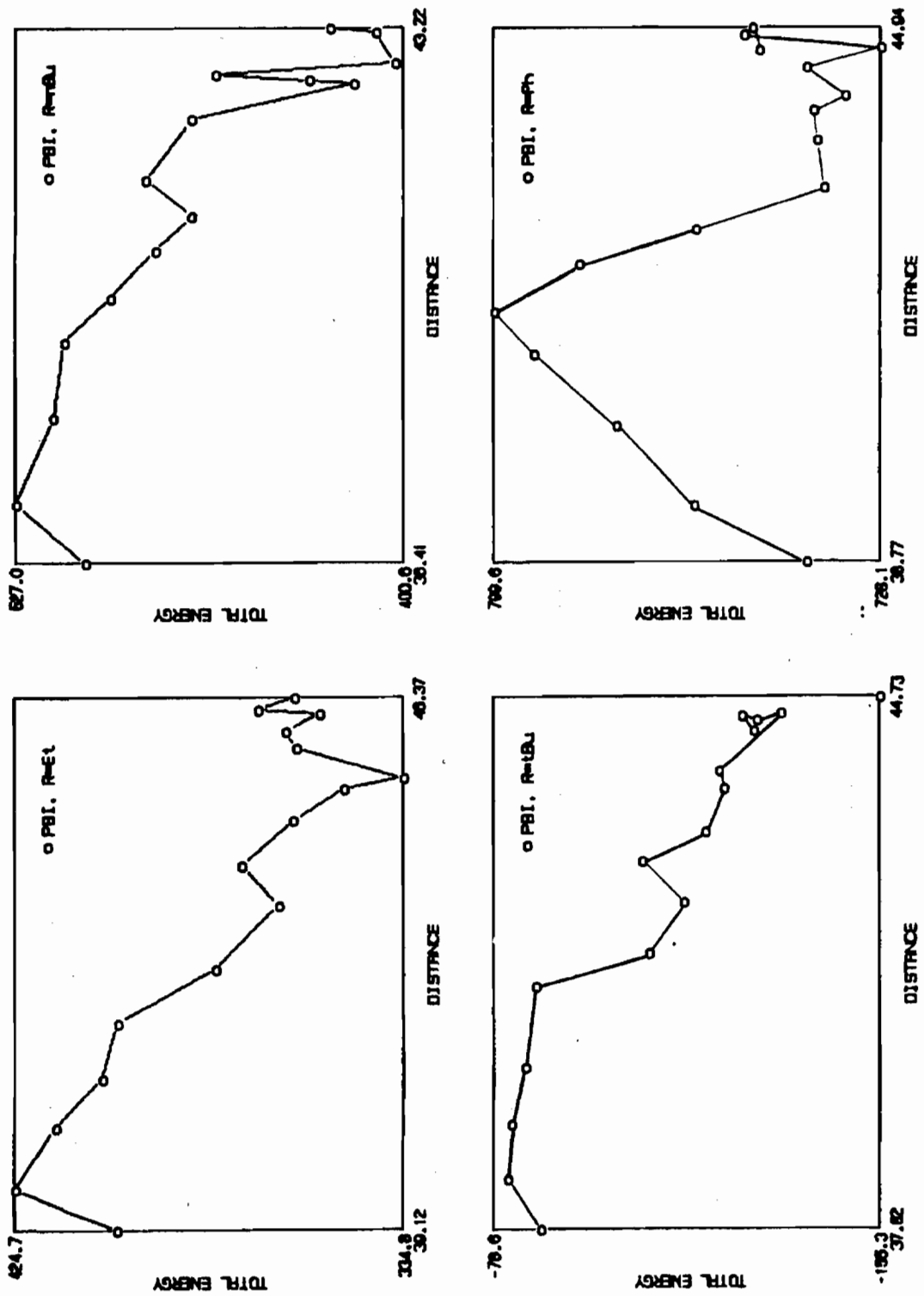


FIGURE 4
Energy Profiles of Substituted PBI—Fully Hydrated



The stiffness trends with substitution for the unhydrated counterparts were similar to the hydrated cases in that ethyl group gave among the largest energy to distance ratio. However, the t-butyl group showed anomalous stiffness behavior depending upon its hydration state. The trends also indicated that phenyl substitution could make the polymer more flexible than expected regardless of hydration. Interestingly, hydration of the substituted cases generally showed an increase in the energy barrier to distance ratio in comparison to their unhydrated cases. This may indicate that hydration can be a significant cohesive contributor in substituted PBI polymers, so should not be completely eliminated. This may be additionally important since extensive hydrogen bonding is found in unsubstituted PBI.²

TABLE I
Energy Barrier to Distance Ratios

Substituent R =	Hydrated, kcal/Å	Unhydrated, kcal/Å
Ethyl	40.2	12.46
n-Butyl	29.9	9.33
t-Butyl	10.0	14.5
Phenyl	19.8	5.70
H	...	14.0

An additional study was done on the stress response of two strands of a randomly oriented PBI decamer. The random orientation was simulated by initial generation of a phi-psi map to define specific probable dihedral angles, then generation of the polymers based upon random building using the defined dihedral angles. The decamers were subsequently hydrated by several different amounts of water, and the energy profiles compared. The decamers showed a similar trend to hydration as the trimers, Figure 5, showing loss of the initial energy barrier with increasing amounts of water.

In order to quantitate stiffness trends, the initial slopes of the trimer and decamer energy curves were determined and compared to modulus changes (percent changes in modulus) upon hydration found in the literature.¹ The calculated trends of the models were slightly higher than the experimental (Figure 6). However, when the trimer model was repeated using more frequent intermediate steps, the calculated degradation in stiffness became closer to that of experimental data (see "PBI trimer, refined" points in Figure 6).

CONCLUSION

Molecular modeling was used in order to understand small strain behavior in hydrated PBI. The study properly predicted the extent and location of hydration tendencies in unsubstituted and substituted PBI. From dynamic models calculated by stressing the molecules, an initial energy barrier in the energy profiles was lost with hydration. Such degradation could be a source of stiffness or modulus loss in hydrated PBI. The barrier was also found to be restored, even in heavily hydrated PBI, by substitution. However, the energy profiles also suggested that substitution may also contribute to losses in mechanical stiffness.

FIGURE 5
Energy Profiles of Amorphous Decamer Medals with Varying Water Content

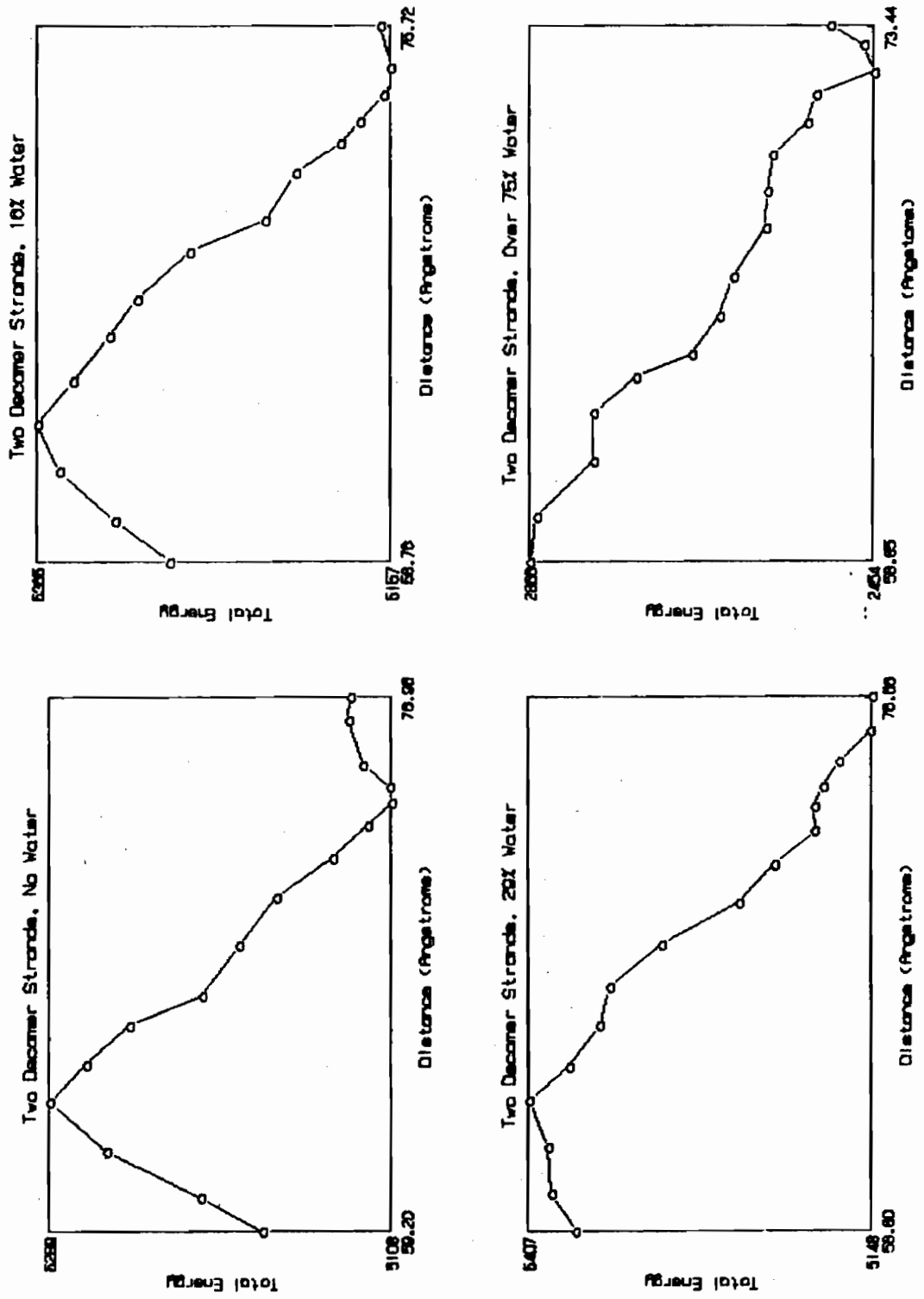
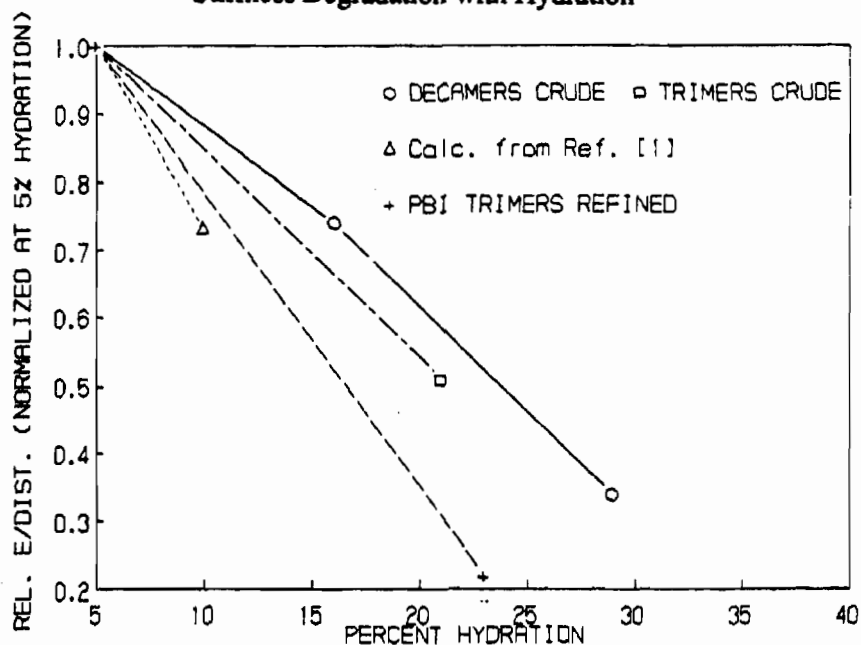


FIGURE 6
Stiffness Degradation with Hydration



REFERENCES

- Alan Buckley, D. E. Stuetz, G. A. Serad; *Encyclopedia of Polymer Science and Engineering*, Vol. 11; 1988, John Wiley & Sons; pp. 512-601.
 - Leo R. Belohlav; *Die Angewandte Makromolekulare Chemie*, 40/41 (1974), 465.
 - Joseph R. Leal; *Modern Plastics*; August 1975, 60.
- Gaetano Guerra, Soonja Choe, David J. Williams, Frank E. Karasz, William J. MacKnight; *Macromolecules*, 21 (1988), 231.
 - P. Musto, F.E. Karasz, W.J. MacKnight; *Polymer*, 30 (1989), 1012
 - Eberhard W. Neuse, Mohamed S. Loonat; *Macromolecules*, 16 (1983), 128.

STRUCTURE SEDATIVE ACTIVITY RELATIONSHIPS OF ALPHA2 ADRENERGIC COMPOUNDS

William P. Ashman, Todd M. Nelson, and Brian H. Meehan
Chemometric / Biometric Modeling Branch
Physics Division, Research Directorate
U.S. Army Chemical Research, Development and Engineering Center
Aberdeen Proving Ground, MD

ABSTRACT: A series of detomidine like arylalkyl imidazoles and compounds known to be agonists at the alpha 2 adrenergic receptor were studied to identify structural, electrostatic, and physicochemical parameters related to sedative activity. Semi-empirical (AM1,PM3) quantum chemical calculations determined the lowest energy conformations and electrostatic parameters of each compound. A molecular modeling analysis for compound/ 'proposed adrenoceptor pharmacophore' interaction provided additional features for analysis.

Multiple regression analysis identified each compound's octanol/water partition coefficient, the electrostatic charge around a specific nitrogen region of the molecule, the position of a proton in relationship to a proposed binding site on the adrenoceptor pharmacophore, and the presence of specific compound functional groups to be correlated with sedation.

INTRODUCTION

The adrenergic system is made up of a variety of receptor subtypes that have been differentiated into two main categories, alpha 1 and alpha 2 (1,2,3). The physiological responses of compounds interacting on the system varies from increases and decreases in cardiovascular functions (i.e., heart rate, blood pressure) and in respiratory functions, to the ability to cause sedation and anesthesia. Timmermans (4) and Savola (5) have discussed the classification and mechanisms of action of compounds on the various types of adrenergic receptors. Ruffolo (6) has discussed structure-activity relationships (SAR) specifically with the alpha 2 adrenergic system. Alpha 2 adrenergic agonists can be potent sedatives (7,8). Most important, unlike opiate anesthetics, sedation and anesthesia are produced by adrenergics without the unwanted side effect of respiratory depression. Because of this capability, a molecular modeling and theoretical chemistry study was initiated to develop structure-sedative/ anesthetic activity relationships.

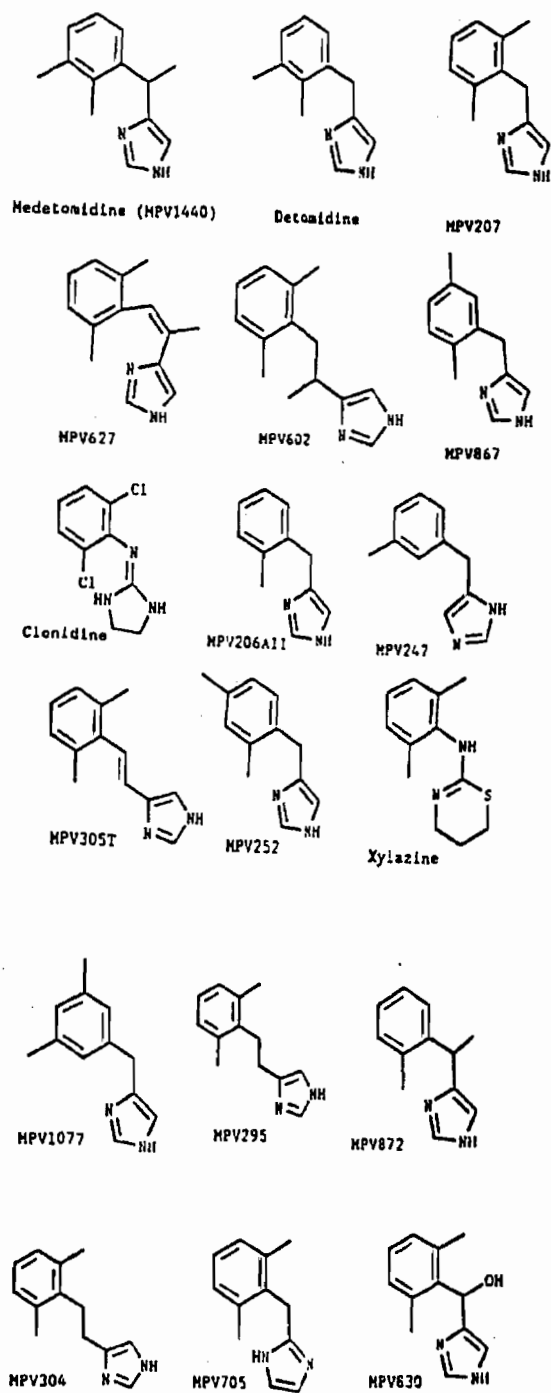


Figure 1

EXPERIMENTAL

COMPOUNDS AND SEDATIVE ACTIVITY. Savola (5) reported on the sedative effects of a series of Medetomidine derivatives (Figure 1). Sedative activity was measured as pST10, the log dose to cause the loss of righting reflex for 10 minutes in new born chicks after intermuscular injection (5). The drug was administered in (0.2 ml/100g) increments and the sleeping time was measured. The doses were determined graphically from the log dose response curve (5).

THEORETICAL CHEMISTRY AND MOLECULAR MODELING. The U.S. Army Chemical Research, Development and Engineering Center's Molecular Modeling, Analysis and Display System (MMADS) (9) was used to incorporate the structures, to calculate the minimum energy 3-dimensional conformations and the semi-empirical MOPAC (PM3, AM1)(10) electronic parameters, and to perform the molecular modeling analysis.

Literature searches were made for steric (geometric), physicochemical and electronic parameters that were related to adrenergic agonist and alpha 2 adrenergic sedative activity. Studies (1,3-7,11-15) suggested specific structural and functional requirements as common to the agonists.

Allinger's MM2 (16) molecular mechanics program was used to establish the initial conformations. Molecular modeling was performed using the MM2 conformations and additional 3-dimensional analyses were performed using MOPAC AM1 and PM3 generated 3-dimensional conformations of the compounds and the protonated forms of the molecules.

A study (17) of alpha 2 receptor agonist compounds defined a pharmacophore model of the alpha 2 adrenoceptor and the molecular modeling techniques employed. Using MMADS and a Techtronix 4105 color graphics terminal, each PM3 and AM1 compound conformation was superimposed on the corresponding AM1 or PM3 model to measure the distance between the nitrogen and proton of the compound to the proposed interaction region of the pharmacophore. The resultant distances were used in the SAR analysis.

DISCUSSION

In developing SAR models, one must identify those steric (geometric), physicochemical, and electrostatic parameters which relate to the resultant activity. These parameters define the transport of the compound to the active site on the adrenoceptor and the corresponding

Studies as noted above have identified specific compound interatomic geometric distances as important to agonist activity. Figures 2 and 3 illustrate these distances.

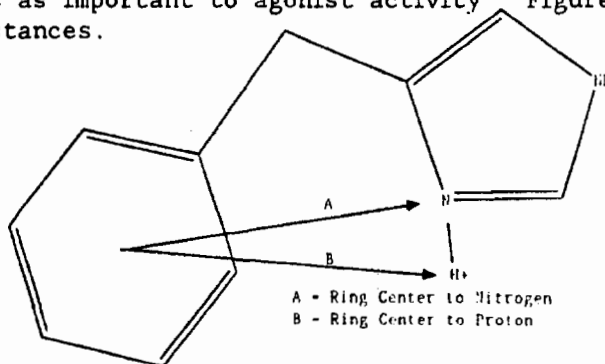


Figure 2

Plane Coplaner with the Phenyl Ring

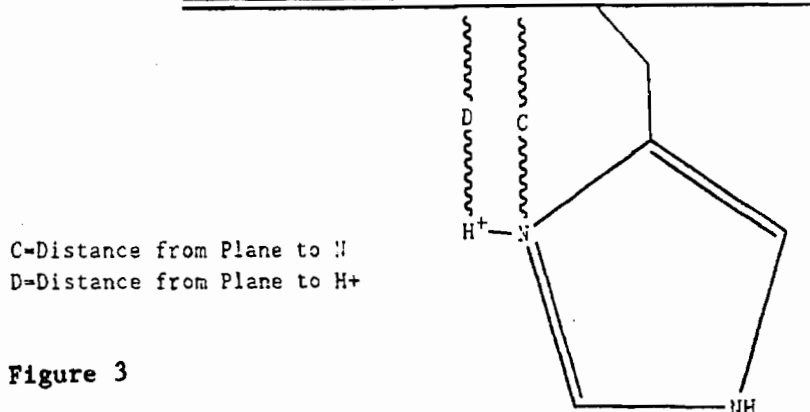


Figure 3

Electrostatic parameters analyzed included charge on the nitrogen plus proton that are proposed to interact at the adrenoceptor, and the compound's dipole moment. Physicochemical parameters analyzed included octanol/water partition coefficient and molar refraction.

Regression analyses were performed using Minitab (18). Initial analysis resulted in the above parameters not being highly correlated. Therefore, additional parameters were identified for analysis. The proposed AM1 and PM3 alpha 2 receptor pharmacophores were used as a compound/receptor interaction template and each compound was superimposed on it; and the distances from the nitrogen and the proton of the compound to the proposed site for their interaction were measured. Figure 4 illustrates the distances (E,F). Additionally, the substitutions on the phenyl ring were noted, (a) presence of a methyl group on position 2 and 3 and (b) presence of a methyl group on position 5, and were used as indicator variables related to sedative activity. Table 1 gives the parameters used in the multiple regression analyses.

Agonist- Adrenoceptor Pharmacophore Interaction Distance Measurements

Compound Overlaped with Pharmacophore

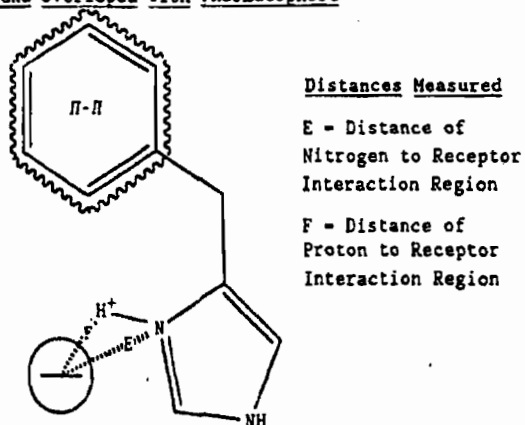


Figure 4

Initially, two compounds not of the detomidine series, clonidine and xylazine, were included in the analysis. However, no high correlation was obtained. Therefore, they were removed from the analysis. Table 2 gives correlations obtained.

AM1											
CI	SEDATION	LOG P	CEN-NDIS	CEN-H+	PLAN-N	PLAN-H+	CHARGE	DIPOLE	AREC-N	AREC-H+	2,3-CH3
1440	6.35	2.80	5.07	5.54	-1.10	-0.28	0.18	11.861	1.37	0.41	1
1	5.80	2.50	5.15	5.67	-1.57	-0.86	0.17	12.564	1.92	1.22	1
207	5.81	2.54	5.11	5.66	-1.50	-0.80	0.17	11.831	2.02	1.44	0
627	5.69	3.46	5.85	5.57	0.00	0.58	0.17	14.300	0.61	0.54	0
602	5.64	2.79	5.81	5.53	0.11	-0.78	0.18	15.151	0.50	0.68	0
867	5.60	2.54	5.12	5.66	-1.67	-0.99	0.17	12.485	2.17	1.64	0
206	5.48	2.13	5.12	5.66	-1.80	-1.15	0.17	11.508	2.09	1.53	0
247	5.47	2.21	5.09	5.64	-1.47	-0.78	0.17	12.120	1.86	1.16	0
305	5.44	3.35	6.12	6.08	0.10	0.80	0.18	14.691	0.57	1.09	0
252	5.38	2.52	5.12	5.66	-1.66	-0.99	0.17	12.734	2.11	1.56	0
1077	4.88	2.34	5.10	5.65	-1.77	-1.13	0.17	13.162	2.09	1.44	0
295	4.88	2.73	5.91	5.75	-0.84	-0.47	0.18	15.626	0.99	0.89	0
872	4.83	2.37	5.12	5.61	-1.11	-0.35	0.18	11.138	1.40	0.56	0
304	4.57	2.87	6.49	6.73	-3.89	-3.22	0.17	16.925	4.37	3.73	0
705	4.49	1.19	5.09	5.62	-1.56	-0.88	0.16	7.997	1.91	1.11	0
830	3.90	1.49	5.06	5.51	-1.50	-0.74	0.21	10.418	2.70	2.61	0

PM3										
ID	SEDATION	CALCLOGP	LOG P	AREC-N	AREC-H+	MOLREF	CHARGE	DIPOLE	2,3-CH3	5-CH3
1440	6.35	3.867	2.80	1.138	0.218	62.73	0.56	12.146	1	0
1	5.80	3.468	2.50	1.683	1.191	58.10	0.56	12.861	1	0
207	5.81	3.468	2.54	1.382	0.727	58.10	0.55	11.973	0	0
627	5.69	3.543	3.46	0.442	1.254	70.16	0.55	14.778	0	0
602	5.64	4.396	2.79	0.474	1.322	67.37	0.56	15.350	0	0
867	5.60	3.468	2.54	1.336	0.700	58.10	0.55	12.624	0	1
2	5.55	1.220	0.80	0.495	0.573	58.14	0.81	11.534	0	0
206	5.48	2.819	2.13	1.288	0.624	53.46	0.56	11.659	0	0
247	5.47	2.819	2.21	1.252	0.365	53.46	0.56	12.262	0	0
305	5.44	3.453	3.35	0.871	1.718	65.52	0.56	15.079	0	0
252	5.38	3.468	2.52	1.354	0.697	58.10	0.56	12.871	0	0
3	5.08	0.900	1.00	0.874	0.721	66.66	0.23	6.246	0	0
1077	4.88	3.468	2.52	1.337	0.525	58.10	0.56	13.303	0	1
295	4.88	3.997	2.73	0.682	1.340	62.73	0.57	15.851	0	0
872	4.83	3.218	2.37	1.006	0.470	58.10	0.56	11.329	0	0
304	4.57	4.526	2.87	3.520	2.856	67.37	0.58	17.173	0	0
705	4.49	3.468	1.19	1.303	0.425	58.10	0.54	8.429	0	0
830	3.90	1.561	1.49	2.092	2.153	59.63	0.61	10.526	0	0

CI - Compound identification number.
 SEDATION - Log dose reflecting a 10 minute loss of righting reflex in new born chicks.
 LOG P - Octanol / water partition coefficient (experimental).
 CEN-NDIS - Distance from center of planar ring to the nitrogen (A).
 CEN-H+ - Distance from center of planar ring to the proton (B).
 PLAN-N - Distance from the nitrogen [above (+) or below (-)] to the plane of the planar ring (C).
 PLAN-H+ - Distance from the proton [above (+) or below (-)] to the plane of the planar ring (D).
 CHARGE - Charge of the nitrogen plus proton environment (AM1 or PM3 electronic units).
 DIPOLE - Dipole Moment.
 AREC-N - Distance from the alpha2-receptor pharmacophore interaction site to the compound nitrogen (E).
 AREC-H+ - Distance from the alpha2-receptor pharmacophore interaction site to the compound proton (F).
 2,3-CH3 - Indicator variable: presence of methyl group in positions 2 and 3 of phenyl ring.
 5-CH3 - Indicator variable: presence of methyl group in position 5 of phenyl ring.
 MOLREF - Molar refraction.
 CALCLOGP - Calculated octanol / water partition coefficient.

*** Distance measurements are in Angstrom units.

Table 1 Data Matrix of Sedation Activity and Parameters ***

TABLE 2

RESULTS OF REGRESSION ANALYSES OF SEDATIVE ACTIVITY OF DETOMIDINE-LIKE COMPOUNDS

AM1

SEDATION = 7.12 + 0.457 LOG P - 0.236 AREC-H+ + 0.700 2,3 CH3 - 15.8 CHARGE

n=16 Rsq = .72 s = .3830

SEDATION = 6.95 + 0.438 LOG P - 0.286 AREC-H+ + 0.638 2,3 CH3 - 14.0 CHARGE

n=15 Rsq = .745 s = .3767

SEDATION = 7.18 + 0.426 LOG P - 0.287 AREC-H+ + 0.613 2,3 CH3 - 14.9 CHARGE

n=14 Rsq = .756 s = .3817

SEDATION = 4.24 + 0.635 LOG P - 0.308 AREC-H+ + 0.405 2,3 CH3

n=10 Rsq = .777 s = .4062

PM3

SEDATION = 3.96 + 0.703 LOG P - 0.484 AREC-H+ + 0.596 2,3 CH3 - 0.200 5-CH3

n=16 Rsq = .788 s = .333

SEDATION = 4.07 + 0.712 LOG P - 0.551 AREC-H+ + 0.508 2,3 CH3 - 0.293 5-CH3

n=15 Rsq = .849 s = .290

SEDATION = 4.09 + 0.717 LOG P - 0.571 AREC-H+ + 0.489 2,3 CH3

n=14 Rsq = .902 s = .230

SEDATION = 4.05 + 0.737 LOG P - 0.567 AREC-H+ + 0.467 2,3 CH3

n=10 Rsq = .941 s = .209

Compound MPV872, which has an asymmetric carbon, was removed for the analyses n=15 and n=14. Compound MPV1077, which has methyl substituents in position 3,5 of the phenyl ring, was removed in n=14. The regression analysis identified that (a) the Log P, that could relate to the transport of the compound to the site and also the lipophilic nature of the active site, (b) the distance of the proton of the compound to the interaction region of the pharmacophore model, that could reflect the electrostatic compound/receptor interaction (in the series studied the PM3 charges calculated were similar (Table 1), and (c) the presence of methyl groups in positions 2 and 3 of the phenyl ring, that could identify a possible lipophilic area for compound interaction, correlated with sedative activity.

CONCLUSIONS

Molecular modeling and SAR multiple regression analyses have identified steric, physicochemical and electrostatic parameters related to sedative activity of a series of detomidine-like compounds. The results of this study can be used in designing new alpha 2 adrenergics having sedative activity. In analyzing the 3-dimensional conformations of alpha 2 agonists, it is recommended to use the protonated form of the molecule.

ACKNOWLEDGEMENTS

The authors would like to acknowledge Byron Bloor of UCLA, Duane Miller of Ohio State, Fu-Lian Hsu, Christopher Cramer and Alexander Mickiewicz of CRDEC for their collaboration and helpful insights into the chemistry and physiology of the alpha 2 adrenergic system.

REFERENCES

1. van Zwieten, P. A., and Timmermans, P. B., *Advances in Drug Research*, Vol 13, pp 209-254, 1984.
2. Bylund, D. B., and Ray-Prenger, C., *The Journal of Pharmacology and Experimental Therapeutics*, Vol 251 (2), pp 640-644, 1989.
3. Kobinger, W., *Archives of Pharmacology*, Vol 332, pp 113-123, 1986.
4. Timmermans, P. B., and van Zwieten, P., *Journal of Medicinal Chemistry*, Vol 25 (12), pp 1389-1401, 1982.
5. Savola, J., *Acta Universitatis Ouluensis, Series D, Medica No. 147, Pharmacologica Et Physiologica No. 25*, 1986.
6. Ruffolo, R. R., Jr., De Marinis, R. M., Wise, M., and Hieble, J. P., *The Alpha 2 Adrenergic Receptors*. Edited By Limbird, L. E., Humana Press. Clifton, New Jersey, pp 115-187, 1988.
7. Scheinin, M., Kallio, A., Koulu, M., Viikari, J., and Scheinin, H., *British Journal of Clinical Pharmacology*, Vol 24, pp 443-451, 1987.
8. Bloor, B., and Flacke, W. E., *Anesth Analg*, Vol 41, pp 741-745, 1982.
9. Leonard, J. M. and Famini, G. R., CRDEC-TR-89030, January 1989.
10. Stewart, J. P., FJSRL-TR-88-007, December 1980.
11. DeBarnardis, J. F., Kerkman, D. J., Arendsen, D. L., Buckner, S. A., Kyncl, J. J., and Hancock, A. A., *Journal of Medicinal Chemistry*, Vol 30, pp 1011-1017, 1987.
12. Gupta, S. P., *Chemical Reviews*, Vol 89 (8), pp 1765-1800, 1989.
13. Hancock, A. A., Kyncl, J. J., Martin, Y. C., and DeBarnardis, J. F., *Journal of Receptor Research*, Vol 8 (1-4), pp 23-46, 1988.
14. Kier, L.B., *Journal of Pharmacology and Experimental Therapeutics*, Vol. 164, No. 1, pp 75-81, 1968.
15. Lloyd, E.J. and Andrews, P.R., *Journal of Medicinal Chemistry*, Vol. 29, No. 4, pp 453-462, 1986.
16. Allinger, N. L. and Yuh, Y.H., *QCPE*, Vol 13, p 395, 1980.
17. Ashman, W. P., Mickiewicz, A. P., and Nelson, T. M., CRDEC- TR- Submitted for publication, October 1991.
18. Minitab, Release 7, Minitab Inc., Data Tech Industries, Valley Forge, Pa. 1989.

BLANK

SOME INTERRELATIONS OF THE HEATS OF FORMATION OF ISOSTERIC
AND ISOELECTRONIC OXYGEN AND FLUORINE COMPOUNDS

Carol A. Deakyne

Department of Chemistry, Eastern Illinois University,
Charleston, IL 61920.

Andrew D. Fant, Deborah L. Kunkel and Joel F. Liebman*

Department of Chemistry and Biochemistry, University
of Maryland, Baltimore County Campus, Baltimore, MD 21228.

ABSTRACT

We have investigated the heats of formation of isosteric and isoelectronic hydroxo and fluoro species by examination of the results of experiment, intuition, and quantum chemical calculations. In particular, using AM1 semiempirical quantum chemical calculations we have derived the equation

$$\begin{aligned}\delta\Delta H_f(g) &= 1/n[\Delta H_f(H_mX(OH)_n, g) - \Delta H_f(H_mXF_n, g)] \\ &= -23.024EN(X) + 61.899, r^2 = 0.874, \# \text{ pts.} = 26\end{aligned}$$

for X = H, B, C, N, O, Al, Si, P, S and Cl and m + n = 1, 3, 4, 3, 2, 3, 4, 3, 2 and 1 with n > 0.)

The chemistry of fluorine is among the most diverse of the nonmetals^{1,2}. Because fluorine is small, steric effects are minimal. However, its electronic effects are often counterintuitive because fluorine is highly electronegative and so electron withdrawing, but it is also electron donating and so stabilizes electron deficient centers such as trivalent boron and carbenium ions. The reactivity patterns of fluorinated species range from those that are highly oxidizing and thus corrosive such as the element and KrF₂ (which is an even

better fluorinating agent than F_2 itself) to the essentially inert CF_4 and polytetrafluoroethylene. Relatedly, while some fluorinated species are seemingly nontoxic such as SF_6 and perfluoroalkanes, while others such as fluoroacetic acid, "Sarin", perfluoroisobutylene and S_2F_{10} are highly toxic. Fluorine in its capacity as a highly powerful oxidant has been profitably used in bomb calorimetry where oxygen has proven inadequate. The comparatively weak F-F bond and strong "almost anything else-F" bond aids the combustion process. However, combustion of fluorinated organic compounds is not a simple process in that their combustion in oxygen results in some CF_4 and so there must have been cleavage of C-F bonds during the oxidation process.

The current study discusses the energetics of fluorine-containing species, in particular, their heats of formation. A particularly simple rule of thumb discussed by Benson³, Woolf⁴ and Liebman⁵ spoke of a constant difference of the heats of formation of the oxygen species $X(OH)_n$, and their isosteric and isoelectronic fluorinated analogs⁶, XF_n . More precisely, Benson³ briefly commented that HO- and F- groups are a "homothermal" pair having noted that the heats of formation of solid bisulfates and fluorosulfate salts are nearly identical. That is, for these well-defined classes of salts,

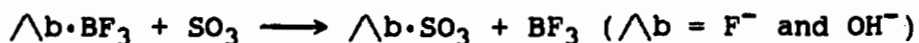
$$\delta\Delta H_f(s) = \Delta H_f(X(OH)_n, s) - \Delta H_f(XF_n, s) \approx 0 \text{ kcal mol}^{-1}.$$

Woolf⁴ extended this equality and additionally suggested equating the heats of formation of $X(OH)_n$ species with $n \geq 2$ and the corresponding oxo-containing "anhydrides" + H_2O . For example, he compared NO_2^+ and NF_4^+ salts, phenol with fluorobenzene, the octet-obeying triphenylarsine oxide with the hypervalent arsorane difluoride. Liebman⁵ limited his attention to only organic compounds containing neither any metal nor metalloids and so only the phenol, fluorobenzene comparison "qualified". However, careful consideration was made of the phase of the species and the effect of hydrogen bonds in the condensed phase of the oxygen-containing compounds was assessed. In agreement with Woolf, it was suggested that the heats of formation in the condensed phase are nearly the same for the hydroxo and fluoro compounds, while there is a difference of 6 kcal mol^{-1} per F in the gas phase. As to obviate complications from these hydrogen bonds (eg. their number and strength) and from any lattice effects because of size differences (eg. the Madelung energies of crystalline salts), we opt in the current study to consider only gas phase species here. In addition, this allows us to compare the results from experiment, intuition, and quantum chemical calculations.

To begin with, it is "obvious" that there cannot be a constant heat of formation difference between hydroxo and fluoro compounds. More precisely, consider the species H_2O and HF. Their heats of formation⁷ are -57.8 and $-65.1 \text{ kcal mol}^{-1}$, a difference of $7.3 \text{ kcal mol}^{-1}$ and quite close to the

above difference of 6 kcal mol⁻¹. Since we do not expect the H-F and H-OH bond strengths do be the same, thermochemical reasoning (a la Hess' law) suggests that the species OH and F will not have the same heat of formation difference. And indeed, they do not -- the values are 9.3 and 19.0 kcal mol⁻¹ and a difference of -8.7 kcal mol⁻¹. We do not expect the electron affinities of OH and F to be the same. Equivalently, we do not expect the heats of formation of OH⁻ and F⁻ to be the same and so it is not obvious what their difference will be. From ref. 7, we find the relevant numbers are -32.7, -59.5, and 26.8 kcal mol⁻¹. Encouragingly, the difference found⁶ for the highly ionic NaF and NaOH ("tight ion pairs") is 20.1 kcal mol⁻¹, quite comparable to the value just given for the free anions. Relatedly, the ionization potentials of F and OH are significantly different and so the heats of formation of OH⁺ and F⁺ is now -111.6 kcal mol⁻¹. While we know of no salt or ion pair containing either ion, we may compare the heats of formation of their "fluorides", namely FOH and F₂, -23 kcal mol⁻¹, and of their "hydroxides", namely HOOH and FOH, -9 kcal mol⁻¹. Our qualitative analysis suggests that the difference of heats of formation of isosteric and isoelectronic hydroxo and fluoro compounds is most negative when X is most electronegative and conversely, the difference is most positive when X is most electropositive.

What can we say about the difference for arbitrary X? There is distressingly little experimental data for the heats of formation for most the species of interest (see refs. 4, 7 and 8) -- we can only surmise the inertness of some fluorinated species and excessive reactivity of others has impeded thermochemical measurements. We also note that many desired hydroxo compounds (indeed, most), do not exist but instead readily dehydrate (eg. C(OH)₄) or rearrange (eg. P(OH)₃ spontaneously isomerizes to HP(O)(OH)₂.) Quantum chemical calculations are not affected by extremes of refractory or reactivity behavior of the substance of interest. Nonetheless, the computationally inclined chemist still has to pick and choose her/his species that will be studied. We have opted to compare the heats of formation of a well-defined set of isosteric and isoelectronic hydroxo and fluoro compounds. In principle *ab initio* calculations can be performed, but these give total energies and not heats of formation. For example, an earlier study of Deakynne and Liebman⁹ obtained the total energies of the isoelectronic species BF₄⁻, BF₃OH⁻, FSO₃⁻ and HSO₄⁻ as part of a study comparing the Lewis acidities of BF₃ and SO₃. However, it was deemed necessary to employ these total energies in the exchange reaction



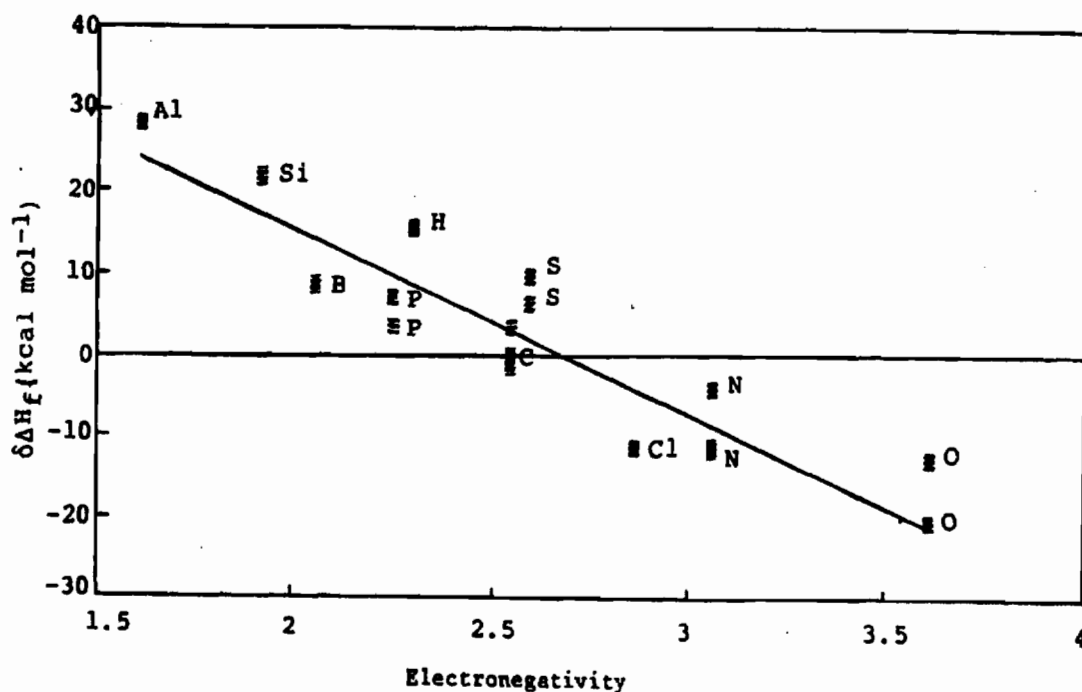
and then to interrelate calculated reaction energies and heats (at 298K) by including numerous "correction terms"

$$\Delta H_{298} = \Delta E^{\text{elec}} + \Delta E^{\text{vib}}_{298} + \Delta E^{\text{rot}}_{298} + \Delta^{\text{trans}}_{298} + \Delta(PV)_{298}$$

We have not opted to use this approach for the current study because it is too computationally extensive, but instead have employed AM1 semiempirical calculations¹⁰ with the MOPAC program package¹¹. We now present in Figure 1 the differences of the calculated heats of formation on a per OH and F basis, $\delta\Delta H_f(g) = 1/n[\Delta H_f(H_mX(OH)_n, g) - \Delta H_f(H_mXF_n, g)]$, as a function of electronegativity (from ref. 12). To simplify the figure, we use the elemental symbol regardless of the "degrees of hydrogenolysis", ie. m and n, for each central element X.

FIGURE 1

AM1 calculated normalized heats of formation of hydroxo and fluoro species vs. electronegativities (from ref. 12).



We present below the "actual numbers", where "XOH" and "XF" refer to the normalized heats of formation of the hydroxo and fluoro species for central the atom X = H, B, C, N, O, Al, Si, P, S and Cl, but now presenting them in the order of increasing electronegativity¹², namely Al, Si, B, P, H, C, S, Cl, N and O. To stipulate the degree of "hydrogenolysis", we use a "*" accompanying the central atom symbol. For example, Al*3 refers to AlF₃ and Al(OH)₃ and the AM1 calculated heat of formation is divided by 3. Relatedly, AlH*2 and AlH₂* refers to normalized heats of formation for AlH(OH)₂ and AlHF₂, AlH₂OH and AlH₂F. We also present in this table the desired difference of the heats of formation on this "per" basis, XOH-XF = $\delta\Delta H_f(g)/n$, the explicit value of EN(X), and the range of values of this difference found for all of the various degrees of "hydrogenolysis" for each of element X.

TABLE 1

Encouragingly, we find there is a chemically -- and statistically -- meaningful relation between the normalized differences of heats of formation¹³ and electronegativity¹⁴:

$$\begin{aligned} \delta\Delta H_f(g) &= 1/n[\Delta H_f(H_mX(OH)_n, g) - \Delta H_f(H_mXF_n, g)] \\ &= -23.024EN(X) + 61.899, \quad r^2 = 0.874, \quad \# \text{ pts.} = 26 \end{aligned}$$

CONCLUSIONS

In summary, we find there is a chemically and statistically meaningful relation between the heats of formation of isoelectronic and isosteric hydroxo and fluoro compounds that depends on the electronegativity of the central atom. As such, we have a convenient method for estimating desired thermochemical quantities.

ACKNOWLEDGEMENT

The authors wish to thank the UMBC Academic Computer Services for assistance and generous gifts of computer time. J.F.L. also wishes to thank the UMBC Designated Research Initiative Fund for a Special Research Initiative Support award that allowed his research group to gain co-ownership of its own computer and A.D.F. extends his gratitude for the funding that allowed him to participate in this project. In addition, C.A.D. and J.F.L. acknowledge numerous discussions on fluorine chemistry, electronegativity and quantum chemical calculations with Leland C. Allen, and all four of us wish to dedicate this study to him on the occasion of his 65th birthday.

TABLE 1

Normalized heats of formation of hydroxo and fluoro species "XOH" and "XF", the difference of these quantities, the electronegativities for each X, and the range of values for the difference with the various degrees of "hydrogenolysis".

X	XOH	XF	XOH-XF	EN	range
Al*3	-66.33	-95.28	28.94	1.613	0.69
AlH*2	-67.96	-96.21	28.25		
AlH ₂ *	-63.14	-91.49	28.35		
Si*4	-74.20	-95.49	21.29	1.916	0.90
SiH*3	-72.47	-93.63	21.16		
SiH ₂ *2	-68.37	-90.73	22.06		
SiH ₃ *	-64.14	-85.79	21.65		
B*3	-81.72	-90.73	9.00	2.051	0.89
BH*2	-83.10	-91.21	8.11		
BH ₂ *	-73.40	-82.03	8.63		
P*3	-72.90	-76.32	3.42	2.253	3.61
PH*2	-67.62	-71.43	3.81		
PH ₂ *	-72.90	-76.32	3.42		
H*	-59.24	-74.28	15.04	2.300	
C*4	-57.76	-56.40	-1.36	2.544	5.35
CH*3	-57.85	-57.50	-0.35		
CH ₂ *2	-57.23	-58.04	0.81		
CH ₃ *	-57.03	-61.02	3.99		
S*2	-41.93	-51.03	9.10	2.589	3.35
SH*	-40.04	-45.79	5.75		
Cl*	-21.76	-10.53	-10.23	2.869	
N*3	-24.92	-13.34	-11.58	3.066	7.71
NH*2	-23.05	-11.94	-11.11		
NH ₂ *	-16.67	-12.80	-3.87		
O*2	-35.23	-22.58	-12.65	3.610	7.85
OH*	-15.29	5.25	-20.51		

REFERENCES AND FOOTNOTES

- [1] Note "The Journal of Fluorine Chemistry" and the American Chemical Society Division of Fluorine Chemistry. These are unique in that we know of no other element, save carbon, for which there is a specialized journal and ACS division.
- [2] Three recent relevant research monographs are:
- a) "Fluorine-containing Molecules: Structure, Reactivity, synthesis and Applications" (ed. J.F. Liebman, A. Greenberg and W.R. Dolbier, Jr., VCH, Weinheim, 1988).
- b) "Selective Fluorination in Organic and Bioorganic Chemistry" (ed. J.T. Welch, American Chemical Society, Washington, DC, 1991).
- c) J.T. Welch and S. Eswarakrishnan, "Fluorine in Bioorganic Chemistry" (John Wiley & Sons, New York, 1991).
- [3] S.W. Benson, Chem. Rev., 78, 23 (1978).
- [4] A.A. Woolf, a) Adv. Inorg. Chem. Radiochem., 24, 1 (1981), b) J. Fluor. Chem., 11, 307 (1978), 20, 627 (1982) and 32, 453 (1986).
- [5] J.F. Liebman, in ref. 2a, Chapter 12.
- [6] Two groups are isosteric if they are the "same" size. The adjective "isoelectronic" refers to two groups if they have the same number of electrons and the same number of "heavy" (ie., nonhydrogen) atoms.
- [7] All heats of formation in this paper, unless otherwise explicitly mentioned, are from S.G. Lias, J.E. Bartmess, J.F. Liebman, J.L. Holmes, R.D. Levin and W.G. Mallard, "Gas-Phase Ion and Neutral Thermochemistry", J. Phys. Chem. Ref. Data, 17 (1988), Supplement 1.
- [8] These numbers are derived from the data in D.D. Wagman, W.H. Evans, V.B. Parker, R.H. Schumm, I. Halow, S.M. Bailey, K.L. Churney and R.L. Nuttall, "The NBS Tables of Chemical Thermodynamic Properties: Selected values for inorganic and C₁ and C₂ organic substances in SI units", J. Phys. Chem. Ref. Data, 11 (1982), Supplement 2. We note that the difference in aqueous solution (at infinite dilution) is 24.4 kcal mol⁻¹.
- [9] C.A. Deakne and J.F. Liebman, J. Mol. Struct. (Theochem), 234, 343 (1991).
- [10] M.J.S. Dewar, E.G. Zoebisch, E.F. Healy, J.J.P. Stewart, J. Amer. Chem. Soc., 107, 3902 (1985).
- [11] J.J.P. Stewart, QCPE #405.
- [12] We have used the "spectroscopic" electronegativity values of L.C. Allen, J. Amer. Chem. Soc., 111, 9003 (1989).
- [13] We have not explicitly contrasted experimental and calculated heats of formation. Most differences are under 4 kcal mol⁻¹, the sole exceptions are SF₂, for which the experimental value is considered unreliable (John T. Herron, personal communication), and, enigmatically, the "normal" HF and CH₃OH.
- [14] We admit that we overestimated the stabilization for X = Na and the destabilization for X = F, but these elements have nearly the extreme values of electronegativity. We also note that both F⁻ and F₂ are generally misdescribed by chemical theory, eg. AM1 "predicts" a heat of formation of -22.5 kcal mol⁻¹ while Hartree-Fock theory "predicts" F₂ to be unbound.

BLANK

AB INITIO QUANTUM CHEMICAL INVESTIGATIONS OF SOLUTE/SOLVENT POLARITY AND HYDROGEN-BONDING PARAMETERS

Peter Politzer*, Jane S. Murray and Tore Brinck

Department of Chemistry
University of New Orleans
New Orleans, LA 70148

ABSTRACT

Analysis of the electrostatic potential $V(r)$ that the nuclei and electrons of a molecule create in the surrounding space can provide quantitative insight into its interactions with other molecules. For several families of molecules, we have demonstrated that good relationships exist between (a) electrostatic potential minima and the *solvent* and *solute* hydrogen-bond-acceptor parameters β and $\beta_{\frac{1}{2}}^H$, and (b) the surface electrostatic potential maxima and the *solvent* and *solute* hydrogen-bond-donor parameters α and $\alpha_{\frac{1}{2}}^H$. We have further shown that $V(r)$ computed on a molecular surface defined by the 0.001 electron/bohr³ contour of the electronic density provides an effective basis for defining a molecular polarity index. Good relationships exist between our polarity values and the solvatochromic polarity/polarizability parameters, as well as with bulk dielectric constants.

INTRODUCTION

The electrostatic potential $V(r)$ in the space around a molecule, defined rigorously by eq. (1), is an effective tool for interpreting and predicting chemical reactive behavior.¹⁻⁴ Z_A is the

$$V(r) = \sum_A \frac{Z_A}{|R_A - r|} - \int \frac{\rho(r') dr'}{|r' - r|} \quad (1)$$

charge on nucleus A, located at R_A ; $\rho(r)$ is the molecular electronic density function. The sign of $V(r)$ in any particular region depends upon whether the effects of the nuclei or the electrons are dominant there. Thus an approaching electrophile, such as a hydrogen to be donated in a hydrogen bond, will initially be attracted to those regions in which $V(r)$ is negative, and particularly to the points where $V(r)$ has its most negative values (the local minima, V_{\min}).

Using $V(r)$ to predict sites susceptible to nucleophilic attack is not as straightforward as for electrophilic, due to the fact that $V(r)$ maxima are found only at the positions of the nuclei;⁵ they reflect the magnitudes of the nuclear charges and cannot be assumed to indicate relative reactivities toward nucleophiles. However we have demonstrated that when $V(r)$ is examined on three-dimensional molecular surfaces significantly removed from the nuclei, then buildups of positive potential do reflect relative affinities for nucleophiles.⁶⁻¹²

Analysis of a molecule's electrostatic potential can provide quantitative, as well as qualitative, insight into its interactions with other systems. In this work, two applications will be discussed:

- 1) correlations between *solvent* and *solute* hydrogen-bond-donor and acceptor parameters and the calculated molecular electrostatic potential^{9,11-13}, and
- 2) the development of a polarity scale using surface electrostatic potentials.¹⁴

CORRELATIONS BETWEEN *SOLVENT* AND *SOLUTE* HYDROGEN-BOND-DONOR AND -ACCEPTOR PARAMETERS

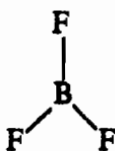
Solvent parameters obtained through linear solvation energy relationships (LSER)¹⁵⁻¹⁹ have been used to quantify the manner in which various solvents influence a particular property of a given *solute*. The initial LSER studies by Kamlet *et al* examined how different solvents affect the spectroscopic properties of selected solutes, and resulted in a set of three solvatochromic solvent parameters: π^* , α and β .¹⁵⁻¹⁹ π^* is viewed as reflecting both the polarity and the polarizability of a solvent,¹⁷⁻¹⁹ while α and β are interpreted as measures of its ability to donate or accept a proton, respectively, in *solvent-solute* hydrogen bonding.^{15,16,19}

More recently, Abraham *et al*,²⁰⁻²³ following upon work by Taft *et al*,²⁴ have developed *solute* scales of relative hydrogen bond acidities (α_H^+) and basicities (β_H^+). These were taken to be linear functions of the equilibrium constants for the formation of 1:1 complexes between the *solute* molecule and a given reference base or acid, respectively, in CCl_4 .

We have shown earlier that the solvatochromic *solvent* parameters α and β correlate well with the calculated electrostatic potentials associated with the solvent molecules. β , which measures hydrogen bond accepting ability, correlates with the magnitudes of the most negative potentials, V_{min} , in the vicinities of heteroatoms,^{11,13} while α , the hydrogen-bond-donor parameter, varies directly with the maximum positive values on the molecular surfaces near the hydrogens, $V_{\text{S,max}}$.^{9,11} More recently we have shown that there are also close relationships between the electrostatic potential and the *solute* hydrogen-bond-acidity and -basicity parameters, α_H^+ and β_H^+ .¹²

DEVELOPMENT OF A POLARITY SCALE USING SURFACE ELECTROSTATIC POTENTIALS

Molecules are generally classified as being nonpolar if they have zero dipole moment, and polar otherwise. Thus BF_3 (I), which is planar, is termed nonpolar, even though each B-F bond individually can be anticipated to have considerable polarity. *p*-Dinitrobenzene (II) is also in the nonpolar category despite having a very significant degree of charge separation within the molecule, as is seen from its electrostatic potential.¹⁴ An analogous example is *s*-tetrazine (III), for which the electrostatic potential shows highly negative regions above the nitrogen lone pairs, separated by a strongly positive one above the ring and the hydrogens.²⁵ III has been observed to form dimers and also complexes with other molecules (including HCl , H_2O and C_2H_2),²⁶⁻²⁸ in which the relative orientations are such as to allow the positive regions on one to interact with the negative on the other. There are clearly numerous examples attesting to the fact that a zero-dipole-moment molecule may have considerable charge separation, which may play an important role in determining its properties.



I



II



III

Some insight into the charge separation can of course be obtained from the magnitudes of the multipole moments. However we believe that it may be useful to have a more direct quantitative measure of it, and that a reasonable basis for this would be the molecular electrostatic potential $V(\mathbf{r})$, which is a physical manifestation of the distribution of electronic and nuclear charge.

We suggest that a meaningful measure of charge separation is given by the quantity Π defined by eq. (2):

$$\Pi = \frac{1}{A} \int_S |V(\mathbf{r}) - \bar{V}_S| dS \quad (2)$$

The integral represents the total amount by which the electrostatic potential on the molecular surface deviates from its average value, \bar{V}_S ; this is divided by the surface area A in order to permit comparisons between molecules of different sizes.

For practical convenience, eq. (2) can be written in the form,

$$\Pi = \frac{1}{n} \sum_{i=1}^n |V_i(\mathbf{r}) - \bar{V}_S| \quad (3)$$

where $V_i(\mathbf{r})$ is the potential at the i^{th} point on the surface and $\bar{V}_S = \frac{1}{n} \sum_{i=1}^n V_i(\mathbf{r})$. As n increases,

eq. (3) approaches eq. (2). We propose eq. (3) as the working formula for the charge separation (or polarity) index Π , which can be viewed as the average deviation of the electrostatic potential on the molecular surface.

It follows from eq. (3) that any spherically-symmetric system, such as a ground state atom,^{29,30} has $\Pi = 0$, since $V(\mathbf{r}) = V(\mathbf{r}) = \bar{V}_S$ for any surface of any radius r . Increasing charge separation will correspond to increasingly positive values of Π .

We have computed Π for about 40 molecules of various types,¹⁴ using STO-3G optimized geometries and calculating $V(\mathbf{r})$ at the STO-5G level.^{31,32} The points on the surface were determined by establishing a square grid; the shortest distance between points was 0.28 bohr, although we have ascertained that Π changes by only 1% after a distance of 0.80 bohr. For a molecule of the size of cyclohexane, the 0.28-bohr grid corresponds to about 6,000 points on the 0.001 electrons/bohr³ surface. We found that using the 0.002 surface produces slightly larger Π values, but they correlate extremely well with the 0.001 results; the correlation coefficient is 0.99, confirming that the relative magnitudes are essentially unaffected. In this work we present Π computed on the 0.001 surface.

In Table 1 are listed our calculated Π values for a group of twenty-five solvents,¹⁴ along with the corresponding π^* parameters,¹⁹ dielectric constants,^{33,34} and calculated STO-5G and experimental dipole moments³³. The Π values in this table range from 2.2 to 21.6 kcal/mole, for cyclohexane and water, respectively.

We have found a good linear relationship between Π and π^* when ketones and disubstituted amides are excluded from the data set.¹⁴ In addition there is a linear relationship between Π and the dielectric constant when strongly associating solvents (water and the amides) and weakly associating solvents (acetic acid, methyl acetate) are excluded from the data set.¹⁴

Table 1. Some calculated, experimentally-determined and derived properties of some solvents.

Molecule	Π (kcal/mole)	π^*a	ϵ^b	$\mu_{calc.}$ (Debye)	$\mu_{exp.}^d$ (Debye)
cyclohexane	2.2	0.00	2.02 (20)	0.00	0.00
toluene	4.6	0.54	2.38 (25)	0.27	0.36
carbon tetrachloride	4.8	0.28	2.24 (20)	0.00	0.00
benzene	4.9	0.59	2.28 (20)	0.00	0.00
diethyl ether	6.7	0.27	4.34 (20)	1.21	1.15
acetophenone	7.2	0.90	17.39 (25)	1.96	3.02
tert-butanol	7.7	0.41	10.9 (25)	1.49	
chlorobenzene	8.0	0.71	5.71 (20)	1.92	1.69
2-butanone	8.1	0.67	18.5 (20)	2.02	2.03
tetramethylurea	8.1	0.83		1.43	
pyridine	8.5	0.87	12.30 (25)	2.08	2.19
2-propanol	8.7	0.48	18.3 (25)	1.50	1.66
acetone	9.4	0.71	20.7 (25)	2.00	2.88
ethanol	10.1	0.54	24.30 (25)	1.48	1.69
dimethylacetamide.	10.1	0.88	37.80 (25) ^c	2.35	3.81
dimethylformamide	11.1	0.88	37 (25) ^c	2.41	3.82
nitrobenzene	12.3	1.01	34.82 (25)	4.09	4.22
methanol	12.8	0.60	33.62 (25)	1.56	1.70
acetic acid	12.9	0.64	6.15 (20)	0.84	1.74
methyl acetate	15.3	0.60	6.68 (25)	3.08	1.72
acetonitrile	17.1	0.75	36.2 (25) ^c	3.14	3.92
formamide	18.1	0.97	109 (20)	2.38	3.73
dimethylsulfoxide	19.1	1.00	46.60 (25) ^c	4.45	3.96
nitromethane	19.9	0.85	35.9 (30) ^c	3.24	3.46
water	21.6	1.09	80.37 (20)	1.75	1.85

^a π^* values are taken from reference 19.

^b Dielectric constants are taken from reference 33 unless marked otherwise.

^c Dielectric constant taken from reference 34.

^d Dipole moments are taken from reference 33.

CONCLUSIONS

Our *ab initio* quantum chemical studies discussed in this work illustrate the usefulness of the molecular electrostatic potential as a tool in the study of intermolecular interactions. Our relationships between *solvent* and *solute* hydrogen-bond-donor and -acceptor parameters and the calculated electrostatic potential confirm that the latter, which refers to the molecule in the gas phase, can be quantitatively related to its tendency to hydrogen bond in solution, whether as part of a solvent interacting with a solute or as a solute molecule forming a 1:1 complex with a reference system. Our proposed polarity (or charge separation) index Π , based on surface electrostatic potential calculations, has been presented and discussed briefly in relation to derived and experimentally-determined solvent properties and parameters.

ACKNOWLEDGEMENT

We greatly appreciate the support of this work by the Office of Naval Research through contract #N00014-91-J-1897.

REFERENCES

1. E. Scrocco and J. Tomasi, *Adv. Quantum Chem.* **11**, 115 (1978).
2. P. Politzer and K. C. Daiker, in *The Force Concept in Chemistry*, D. M. Deb, editor, Van Nostrand Reinhold Co., 1981, ch. 6.
3. P. Politzer and D.G. Truhlar, eds., *Chemical Applications of Atomic and Molecular Electrostatic Potentials*, Plenum Press, New York, 1981.
4. P. Politzer and J. S. Murray, in *Reviews of Computational Chemistry*, K. B. Lipkowitz and D. B. Boyd, eds., VCH Publishers, New York, 1991, ch. 7.
5. R. K. Pathak and S. R. Gadre, *J. Chem. Phys.* **93**, 1770 (1990).
6. P. Sjoberg and P. Politzer, *J. Phys. Chem.* **94**, 3959 (1990).
7. J. S. Murray, P. Lane and P. Politzer, *J. Mol. Struct. (Theochem)* **209**, 163 (1990).
8. J. S. Murray, P. Lane, T. Brinck, P. Politzer and P. Sjoberg *J. Phys. Chem.*, **95**, 844 (1990).
9. J. S. Murray and P. Politzer *J. Org. Chem.*, **56**, 6699 (1991).
10. P. Lane, J. S. Murray and P. Politzer, *J. Mol. Struct. (Theochem)*, in press.
11. J. S. Murray, T. Brinck, M. E. Grice and P. Politzer, *J. Mol. Struct. (Theochem)*, in press.
12. J. S. Murray and P. Politzer, *J. Chem. Res.*, in press.
13. J. S. Murray, S. Ranganathan and P. Politzer, *J. Org. Chem.* **56**, 3734 (1991).
14. T. Brinck, J. S. Murray and P. Politzer, *J. Mol. Phys.*, submitted.
15. M. J. Kamlet and R. W. Taft, *J. Am. Chem. Soc.* **98**, 377 (1976).
16. R. W. Taft and M. J. Kamlet, *J. Am. Chem. Soc.* **98**, 2866 (1976).
17. M. J. Kamlet, J.-L. M. Abboud and R. W. Taft, *J. Am. Chem. Soc.* **99**, 6027 (1977).
18. J.-L. M. Abboud, M. J. Kamlet and R. W. Taft, *J. Am. Chem. Soc.* **99**, 8325 (1977).
19. M. J. Kamlet, J.-L. M. Abboud, M. H. Abraham and R. W. Taft, *J. Org. Chem.* **48**, 2877 (1983).
20. M. H. Abraham, P. P. Duce, P. L. Grellier, D. V. Prior, J. J. Morris and P. J. Taylor, *Tetrahed. Letters* **29**, 1587 (1988).
21. M. H. Abraham, P. L. Grellier, D. V. Prior, J. J. Morris, P. J. Taylor, C. Laurence and M. Berthelot, *Tetrahed. Letters* **30**, 2571 (1989).
22. M. H. Abraham, P. L. Grellier, D. V. Prior, P. P. Duce, J. J. Morris and P. J. Taylor, *J. Chem. Soc. Perkin Trans. II*, 699 (1989).
23. M. H. Abraham, P. L. Grellier, D. V. Prior, J. J. Morris and P. J. Taylor, *J. Chem. Soc. Perkin Trans II*, 521 (1990).
24. R. W. Taft, D. Gurka, L. Joris, P. von R. Schleyer and J. W. Rakshys, *J. Am. Chem. Soc.* **91**, 4801 (1969).

25. Politzer, P., Murray, J. S., Seminario, J. M. and Miller, R. S., *J. Mol. Struct. (Theochem)*, submitted.
26. C. A. Haynam, D. V. Brumbaugh and D. H. Levy, *J. Chem. Phys.* **79**, 1581 (1983).
27. C. A. Haynam, C. Morter, L. Young and D. H. Levy, *J. Phys. Chem.* **91**, 2519, 2526 (1987).
28. C. L. Morter, Y. R. Wu and D. H. Levy, *J. Chem. Phys.* **95**, 1518 (1991).
29. G. Delgado-Barrio and R. F. Prat, *Phys. Rev. A* **12**, 2288 (1975).
30. J. K. Nagle, *J. Am. Chem. Soc.* **112**, 4741 (1990).
31. M. J. Frisch, M. Head-Gordon, H. B. Schlegel, K. Raghavachari, J. S. Binkley, C. Gonzalez, D. J. Defrees, D. J. Fox, R. A. Whiteside, R. Seeger, C. F. Melius, J. Baker, R. Martin, L. R. Kahn, J. J. P. Stewart, E. M. Fluder, S. Topiol and J. A. Pople, *GAUSSIAN 88*, Gaussian Inc., Pittsburgh, PA, 1988.
32. The programs for computing and plotting properties on surfaces defined in terms of the molecular electronic density were written by Per Sjoberg and Tore Brinck.
33. *Handbook of Physics and Chemistry*, 3rd Ed., The Chemical Rubber Co., Cleveland, 1968.
34. E. M. Kosower, *An Introduction to Physical Organic Chemistry*, Wiley & Sons, New York, 1968.

Model of the Active Site Spectroscopy of the Rhodanese Enzyme

M.Krauss
Biotechnology Division
National Institute of Standards and Technology
Gaithersburg, Md.20899

Abstract

The activated form of the sulfur-transferase enzyme, rhodanese, has a sulfur atom bound to the Cys-247 thiol side-chain to form a disulfide bond. An absorption band has been observed at 330nm and attributed to this bond. Ab initio model calculations confirm that the absorption is due to the disulfide anion. Excitation energies calculated by a simplified ab initio first-order configuration interaction (FOCI) method is shown to compare well with more accurate procedures for the in vacuo model compounds. Spectral shifts are reported with the FOCI method including a model of the electrostatic potential of the protein residues close to the active site. Ionic residues near the active site are shown not to have a substantial influence which suggests that they also do not directly effect the direct reaction of the anionic substrate and disulfide active site. The largest shift in the spectra and in stabilizing the disulfide bond arises from the local residues of the D helix.

1. Introduction

Rhodanese is an enzyme that transfers sulfur in a two-step reaction from a donor such as thiosulfate to convert cyanide into the less toxic thiocyanate (1). The first reaction step creates a sulfur substituted rhodanese by adding a sulfur atom to the E-CH₂S⁻ thiolate side chain at the Cys-247 residue creating a disulfide anion, E-CH₂SS⁻. Cyanide then abstracts the outer sulfur in the second step to form thiocyanate. The x-ray structure of both the sulfur-free and sulfur-substituted enzyme has been reported and used to suggest a mechanism (2,3). In both steps of the reaction anionic substrates approach an anionic active center on the Cys-247 residue. Two cationic residues, Lys-249 and Arg-186, are located at the entrance to the active site and their coulombic attraction was suggested to 'facilitate' the reaction (2). However, it was also noted that there are ten putatively charged residues within 13Å of the thiol group of Cys-247 and the net effect of these fields on the pK of the thiol group is calculated to be small (2,4). This suggests the mechanism is more complicated than the direct interaction of the anionic substrate and enzyme thiol or disulfide active center. The most direct theoretical method is to evaluate the transition states for both reactions in the presence of the reaction field (5) of the protein. The transition state calculation is in a preliminary stage and is not discussed today. We are also considering probes of the electronic structure in addition to the pK of the thiol group to map the electrostatic potential throughout the active site. One that lends itself to both theoretical and experimental analysis is the spectra of the S-S⁻ bond at the active site. This paper presents a study of the effect of the electrostatic fields of the protein on the spectra of rhodanese that supports the conclusion that the ionic residues in

the active site do not play an electrostatic role in reducing the activation energy of the anionic rhodanese reactions.

A weak band appears at 330nm when rhodanese is treated with thiosulfate (6) and is associated with the formation of the S-S⁻ bond. Excitation energies and transition probabilities have been determined for the neutral compounds, HSSH and CH₃SSH, the anions, HSS⁻ and CH₃SS⁻, and the neutral radicals, HSS and CH₃SS (7). The theoretical results predict a first transition for the model compound, CH₃SS⁻, at 365.4nm and a second transition at 277.4nm as seen in Table 1. The experimental band is relatively narrow with a width of about 20nm. The in vacuo result for CH₃SS⁻ supports the assignment of the absorption band in rhodanese considering the protein field shift which is examined below. The calculation method which is described briefly below can calculate excitation spectra of amino-acid radicals and ions relatively easily using ab initio methods. The accuracy has been checked against large scale configuration interaction calculations and for the neutral molecules with experiment (7).

2. Method

Excitation energies are calculated with first-order configuration interaction (FOCI) calculations using the GAMESS system of codes (8). The FOCI method includes all configuration excitations among valence orbitals that significantly contribute to the ground and excited states being calculated. As long as there is no valence-Rydberg mixing the valence space can be improved by iterating on the natural orbital vectors of the FOCI solution. Compact effective potentials are used to accurately eliminate core orbitals (9). Excitation energies are presented for two excited states in Table 1. The in vacuo energies represent excitation energies for model compounds using coordinates obtained from the protein data bank for sulfur-substituted rhodanese (2) and for self-consistent-field (SCF) energy-gradient optimized geometries. There is an appreciable red-shift when the methyl group is substituted for hydrogen but the transition is still dominated by the S-S bond orbitals and HSS⁻ is used for the present calculation for ease of calculation.

The CEP-31G basis set (9) is of double zeta quality and is augmented by two polarization functions on the sulfur atom to account for the polarization of the sulfur atoms. The FOCI calculation included two additional valence orbitals beyond the occupied orbitals in the dominant ground state SCF wave-function. Experimentation with the FOCI found that one valence orbital dominates but two were included to insure convergence. For this preliminary study only the electrostatic field of various elements of the protein were included as point charges (10). Previous studies of the effect of the protein fields on the pK shift of the active site thiolate have identified important components of the rhodanese (4). As noted before the charged residues have a small effect and the dominant interactions are the neighboring intersecting D and E helices together with the local hydrogen bonds to the thiolate. Essentially we have looked at the same components but decomposed some of the groups to focus on apparently important residues. Only overall neutral interactions were examined since polarization effects were not included at this time.

3. Results and Discussion.

Only the D helix substantially shifts the spectra. Even here the dominant effect is due to the closest residue, Thr-252. A 15nm shift to the blue is predicted. This accompanies a 40 kJ/mol stabilization of the SS^- bond by the helix field. Adding three more residues of the D helix contributes a slight additional shift of 3nm to the blue suggesting a cooperative effect. However, this is smaller than the large cooperative helix effect that has been predicted (2,11). On the other hand, the H-bonding residues (2), Lys-249, Gly-250, Val-251, and Ser-274 slightly destabilize SS^- by 4 kJ/mol and only shift the spectra by 2nm. The active site salt bridges, Arg-186, Glu-193, Arg-248, Glu-71, Arg-182, Asp-180, destabilize SS^- by 3 kJ/mol but produce a blue shift of 8nm. However if two additional charge residues, Lys-249 and Asp-272, are added, the shift reduces to about 3nm. Assuming the shifts are additive, a blue shift of about 20nm is predicted. Relative to the calculated absorption wavelength for the model compound CH_3SS^- , this would yield a predicted wavelength of 345nm in reasonable agreement with observation (6) considering the simplicity of the present calculation.

The conclusion to be drawn from these results is that the ionic residues as a group have a small interaction with the disulfide anion. Added to the weak effect on the Cys-247 pK, this supports the contention that the ionic residues do not reduce the coulombic repulsion between the anionic reactants by their electrostatic interactions. We are now examining other possibilities for the cationic groups at the active site entrance. Desolvation of the entering substrate is apparent in the observation of a Michaelis intermediate between the enzyme and thiosulfate (12). Such binding would alter the pK relationships among the reactants and residues that could allow for a proton transfer that dramatically alters the reaction and transition state behavior. This is now being examined.

The suggestion that the D and E helices play an important role in the stabilization of the sulfur-substituted rhodanese (2,4) is supported by these calculations. Only a part of the helix interaction was examined here and with only a part of the electrostatic potential. A more accurate representation of this potential is possible with a reaction field treatment and is being considered. The local H-bond interactions and the Thr-252 residue from helix D are represented only by fields and their proximity to the sulfur atom requires a test using an all-electron model representation of the H-bonds and the other close interactions.

References.

1. Westley, J. *Advan. Enzymol.* 1973, 39, 327.
2. Ploegman, J.H.; Drent, G.; Kalk, K.H.; Hol, W.G.J. *J. Mol. Biol.* 1979, 127, 149.
3. Hol, W.G.J.; Lijk, L.J.; Kalk, K.H. *Fund. Appl. Toxicol.* 1983, 3, 370.
4. Gilson, M.K.; Honig, B.H. *Proteins: Struct. Funct. Genet.* 1988, 3, 32.
5. Garmer, D.R.; Stevens, W.J.; Basch, H.; Krauss, M. mss in prep.
6. Agro, A.F.; Federici, G.; Giovagnoli, C.; Cannella, C.; Cavallini, D. *Eur. J. Biochem.* 1972, 28, 89.
7. Krauss, M.; Roszak, S. mss. in prep.
8. Schmidt, M.W.; Baldrige, K.K.; Boatz, J.A.; Jensen, J.H.; Kokeski, S.; Gordon, M.S.; Nguyen, K.A.; Windus, T.L.; Elbert, S.T. *GAMESS, QCPE Bulletin* 1990, 10, 52.
9. Stevens, W.J.; Basch, H.; Krauss, M. *J. Chem. Phys.* 1984, 81, 6026.
10. Weiner, S.J.; Kollman, P.A.; Case, D.A.; Singh, U.C.; Ghio, C.; Alagona, G.; Profeta, S. Jr.; Weiner, P.A. *J. Am. Chem. Soc.* 1984, 106, 765.
11. Hol, W.G.J.; Van Duijnan, P.T.; Berendsen, H.J.C. 1978, *Nature* 273, 443.
12. Mintel, R.; Westley, J. *J. Biol. Chem.* 1966, 241, 3381.

Table 1. Effect of the protein field on the SS⁻ spectra

A. vacuo			
protein	28640	37530	cm ⁻¹
R(S-S)	349.2	265.8	nm
optimized	28277	35392	
HSS ⁻	353.6	282.6	
optimized	27368	36049	
CH ₃ SS ⁻	365.4	277.4	
B. H-bonds residues Lys-249, Val-251 S ^g ; Gly-250, Ser-274 S			
	28749	38070	
	347.3	262.7	
D. active site salt bridges Arg-186, Glu-193, Arg-248, Glu-71, Arg-182, Asp-180			
	29320	38564	
	341.1	259.3	
E. D + Lys-249, Asp-272			
	28908	38263	
	345.9	261.4	
F. residues 252-254 helix d; H-bond residues 249, 250, 251, 274			
	29918	38474	
	334.3	259.9	

BLANK

COMPUTER MODEL FOR THE SPECTRAL PREDICTIONS OF NERVE AGENTS

Hendrik F. Hamerka
Department of Chemistry
University of Pennsylvania
Philadelphia, PA 19104-6323

James O. Jensen
U.S. Army Chemical Research
Development and Engineering Center
Aberdeen Proving Ground, MD 21010-5423

ABSTRACT

We present the 6-31G* optimized geometries and the corresponding vibrational frequencies of the three nerve agents sarin, soman and tabun. Subsequently we correct the computed frequencies of the three molecules by multiplying the computed frequencies by previously derived correction factors. We compute the 6-31G* optimized geometries and vibrational frequencies of methylphosphonic difluoride and methylphosphonofluoridic acid in order to derive correction factors for the P-F stretching and bending vibrational frequencies.

INTRODUCTION

We are interested in predicting the vibrational infrared and Raman spectra of the nerve agents by making use of our recently acquired improved computing capability and of recently introduced improved software. The nerve agents are awkward to deal with in a laboratory environment and there are certain advantages to studying them by purely theoretical means.

We base our theoretical studies on the use of the Gaussian 90 Program package¹. We make use of the closed shell Hartree Fock option with the 6-31G* basis set. We first derive the 6-31G* optimized geometries of the molecules and then we compute the corresponding vibrational frequencies with their infrared and Raman intensities. The margin of error of these computed frequencies is of the order of 10%.

In order to improve the accuracy of the theoretical frequency predictions we multiply the 6-31G* computed frequencies by empirical correction factors. These correction factors are derived by computing the vibrational frequencies of a group of similar molecules and by comparing the computed frequencies with the available experimental data. The correction factors are then used for making accurate predictions for those molecules where experimental information is not available and where it is difficult to obtain.

The key feature of our approach to the prediction of vibrational frequencies is the use of different correction factors for different vibrational modes. This refinement reduces the error in the computer generated frequency predictions to about 1% from an error of about 3% when one universal correction factor is used for all different vibrational modes. The procedure has been applied to a group of alcohols and ethers², a group of sulfides and mercaptans³ and a group of amines^{4,5}. Recently we presented computations on a group of methylphosphonates⁶, the results of this study are relevant to our present work on the nerve agents.

COMPUTATIONS

The three nerve agents are known either by the abbreviated names GA, GB and GD or by their German names. The simplest of the three has the code name GB, the German name sarin and the chemical name isopropyl methyl phosphonofluoridate, its formula is $\text{CH}_3\text{P}(\text{O})(\text{F})(i\text{C}_3\text{H}_7)$. The second one, code name GD, may be derived from sarin by replacing three hydrogens in one of the isopropyl methyl groups by three methyl groups. Its German name is soman and its formula is $\text{CH}_3\text{P}(\text{O})(\text{F})\text{O}(\text{CH}_3)\text{CHC}(\text{CH}_3)_3$. The third nerve, code name GA, has the German name tabun, the chemical name ethyl n,n-dimethylphosphoramidocyanidate and the formula $\text{C}_2\text{H}_5\text{OP}(\text{O})(\text{CN})\text{N}(\text{CH}_3)_2$.

We computed the 6-31G* optimized geometries and the corresponding vibrational frequencies of sarin, soman and tabun. The geometries, are described in a recently published Technical Report⁷.

In order to find a set of correction factors for the nerve agents we make use of our recent work on the methylphosphonates. These are molecules with the general formula $\text{CH}_3\text{P}(\text{O})(\text{OR})_2$; we considered the four cases with $\text{R}=\text{H}$, $\text{R}=\text{CH}_3$, $\text{R}=\text{C}_2\text{H}_5$ and $\text{R}=(i\text{C}_3\text{H}_7)$. The methylphosphonates are similar to the three nerve agents, at least parts of the molecules are. We derived a set of 6-31G* frequency correction factors for the methylphosphonates and these correction factors are applicable to the majority of the vibrational modes in the nerve agents.

Some of the vibrational modes in the nerve agents are not accounted for by our work on methylphosphonates, in particular the C-F stretch and bend modes and the vibrations involving the CN group in tabun. In order to derive correction factors for the C-F vibrational modes we computed the 6-31G* geometries and frequencies for two similar molecules for which experimental information is available. These two molecules are methylphosphonic difluoride, $\text{CH}_3(\text{PO})\text{F}_2$, and methylphosphonofluoridic acid $\text{CH}_3(\text{PO})\text{FOH}$. The results of these computations are presented elsewhere⁷, they allow us to derive correction factors for the C-F stretch and bend modes. We also list the average value of the correction factors. We use this average value in those situations where no specific information is available.

RESULTS

We use the correction factors of Table 1 for a theoretical prediction of the vibrational frequencies of the three nerve agents sarin, soman and tabun. The results are summarized in Table 2. We discuss the molecules separately in the following three sections.

Sarin

The four phosphorus bonds in sarin form a slightly distorted tetrahedron. One half of the molecule resembles diisopropyl methylphosphonate⁶ and the other half resembles methylphosphonic difluoride⁷. We first computed the 6-31G* optimized geometry of sarin and then the corresponding vibrational frequencies. The values in Table 2 were obtained by multiplying by the correction factors listed in Table 1. We also computed the IR and Raman intensities⁷ but we do not list them here due to lack of space.

The strongest and most important IR absorption lines are the P-O stretch at 1000 wave numbers, the P=O stretch at 1282, the P-F stretch at 844, the P-C stretch at 780 and the three P-CH₃ modes at 912, 914 and 929 wave numbers. The C-H stretch frequencies range from 2868 to 2966 wave numbers and the C-H bend frequencies range from 1330 to 1463 wave numbers, the latter two groups of frequencies are of little

TABLE 1.
Correction factors for vibrational modes in nerve agents.

Assignment	correction
P-O-C stretch	0.883
P=O stretch	0.901
P-C stretch	0.930
C-H stretch	0.893
P-F stretch	0.903
P-CH ₃ rock	0.892
C-PO ₃ wag	0.922
O-P-O bend	0.907
O ₂ P=O bend	0.928
P-F bend	0.936
C-H bend	0.884
C-C bend	0.899
average	0.907

importance for identification purposes.

Soman

The soman molecule is derived from sarin by replacing the three hydrogen atoms in one of the isopropyl CH₃ groups by methyl groups. The soman molecule is the largest of the three nerve agents. Its geometry is very similar to the sarin structure⁷. The vibrational frequencies are listed in Table 2, they were obtained by multiplying the 6-31 G* computed frequencies by the correction factors of Table 1.

The soman molecule has a total of 75 vibrational frequencies, we do not list the lowest 15 frequencies because their assignments are ambiguous and they are not important for identification purposes. The substitution of the CH₃ group in sarin by the C(CH₃)₃ group in soman affects some of the vibrational frequencies but it has remarkably little effect on some of the others. For example, the 6-31G* computed P-F stretch frequencies are 844 and 843 in the two molecules, the P=O stretch frequencies are both 1282 and the P-O stretch frequencies are 1000 and 999, respectively. The vibrational spectra of sarin and soman differ in the vibrational modes that are localized in the C₃H₇ and in the C₃H₄(CH₃)₃ groups both in the number of lines and in the frequencies. But even those parts of the vibrational spectra are quite similar for the two molecules, the C-H stretch frequencies in sarin vary from 2868 to 2966 and in soman they vary from 2859 to 2965 wave numbers.

Tabun

The tabun molecule contains a CN and an amine group, its structure is somewhat different from sarin and soman but its toxic effects are quite similar. We first computed the 6-31G* optimized geometry and the corresponding vibrational frequencies, the results are presented elsewhere⁷.

In order to derive the corrected vibrational frequencies we have to introduce some additional assumptions since the 6-31G* correction factors for the vibrational modes involving the cyano and the amino groups are not available² (Our previous work on amines was based on

TABLE 2.

Comparison of theoretical and experimental infrared frequencies of sarin, soman and tabun.

sarin		soman		tabun	
exp	corr	exp	corr	exp	corr
461.7	455	430.7	429	434.6	418
484.9	490	441.4	456	449.1	?
-	-	-	-	469.4	477
510.0	507	509.1	509	510.0	525
-	-	532.3	524	607.7	611
-	-	-	-	715.1	710
731.5	748	752.8	762	733.4	764
781.8	780	807.0	793	792.4	790
845.6	844	844.7	843	850.5	?
-	-	870.8	860	875.6	?
927.9	929	907.5	911	965.6	944
-	-	923.0	925	-	-
-	-	989.8	989	-	-
1022.6	1000	1021.7	999	1008.1	982
1114.5	1101	1050.7	1052	1045.8	1062
1134.8	1129	1081.6	1076	1190.9	1184
1146.4	?	1120.3	1114	1252.8	1274
1181.1	1181	1152.2	?	1289.6	1285
1304.0	1282	1216.1	1214	1330.2	1325
1327.3	1330	1302.1	1282	1400.8	1413
1422.1	1415	1326.3	1341	1467.5	1464
1468.4	1463	1368.9	1359	2203.5	?
-	-	1388.2	1391	2344.7	2350
-	-	1469.5	1460	-	-
-	-	1484.9	1476	-	-

the use of the 3-21 G basis set and the results are not applicable to the present situation). We first assumed that the carbon and nitrogen atoms behave in a similar fashion so that we may take the C-N stretch and bend correction factors equal to the corresponding C-C values. For those frequencies for which no information was available we took the average value of 0.907 of Table 1.

The tabun molecule is characterized by the presence of a cyano group bonded to the phosphorus atom. This group may be identified by its characteristic C=N stretch frequency at 2350 wave numbers. The other two frequencies characteristic for the cyano group occur at 611 and 710 wave numbers. The CN group moves as one entity relative to the phosphorus atom in both cases and we could assign both frequencies to a P-C stretch mode. The 710 line is the more intense of the two IR lines, it is more clearly localized in the P-C bond than the 611 motion which extends also to the P=O bond.

The tabun molecule also contains a dimethylamine group which is characterized by a C-N-C bond mode and by two C-N stretch modes. The corresponding frequencies are at 982 for the bond mode and at 1184 and 1325 wave numbers for the N-C stretch modes. All three have fairly substantial IR intensities.

Additional strong IR absorption lines belong to the P=O and P-O-C stretch modes, the corresponding frequencies are very similar to the corresponding sarin and soman values. We do not list the many C-H stretch modes of tabun since they are not relevant for identification purpose.

CONCLUSIONS

It should be noted that the experimental data in Table 2 were not available to us until after we made our theoretical predictions⁸. The comparisons in Table 2 offers therefore a good illustration of the accuracy of a set of theoretical predictions.

From a practical point of view we observe that it is quite difficult to differentiate between sarin and soman by measuring and analyzing the IR or Raman spectra of the two molecules because all the characteristic strong IR absorption lines are found at very similar frequencies. However, it is not really that essential to differentiate between the two molecules since their toxic effects are quite similar and all precautions and treatment procedures against sarin and soman are identical.

ACKNOWLEDGMENT

This work was supported by the Chemical Research, Development and Engineering Center (Dr. James O. Jensen) under the auspices of the U.S. Army Research Office Scientific Services Program administered by Battelle (Delivery Order 2327, Contract No. DAAL 03-86-D-0001).

REFERENCES

1. M.J. Frisch, M. Head-Gordon, H.B. Schlegel, K. Raghavachari, J.S. Binkley, C. Gonzalez, D.J. DeFees, D.J. Fox, R.A. Whiteside, R. Seeger, C.F. Melius, J. Baker, R.L. Martin, L.R. Kahn, J.J.P. Stewart, E.M. Fluder, S. Topiol and J.A. Pople, Gaussian 90, Gaussian Inc., Pittsburgh, Pennsylvania (1990).
2. H.F. Hameka, Theoretical Prediction of Structures and Infrared Frequencies II. Alcohols and Ethers, *J. of Molecular Structure, (Theochem)* **226** (1991), 241-249.
3. H.F. Hameka, S.L. Emery, G.R. Famini, J.O. Jensen, J.M. Leonard and D.J. Reutter, Theoretical Prediction of Vibrational Infrared Frequencies I. Mercaptans and Sulfides, Phosphorus, Sulfur and Silicon **53** (1990), 373-388.
4. H.F. Hameka, G.R. Famini, J.O. Jensen and E.I. Newhouse, Computations of Vibrational Infrared Frequencies of Selected Amines, CRDEC-CR-041, U.S. Army Chemical research, Development and Engineering Center, Aberdeen Proving Ground, MD, Jan. 1990, Unclassified Report.
5. H.F. Hameka, G.R. Famini, J.O. Jensen and J.L. Jensen, Theoretical Prediction of Vibrational Infrared Frequencies of tertiary Amines, CRDEC-CR-101, U.S. Army Chemical Research, Development and Engineering Center, Aberdeen Proving Ground, MD, Febr 1991, Unclassified Report.
6. H.F. Hameka, A.H. Carrieri and J.O. Jensen, Calculation of the Structure and the Vibrational Infrared Frequencies of some Methylphosphonates, Phosphorus, Sulfur and Silicon, in press.
7. H.F. Hameka and J.O. Jensen, Theoretical Prediction of the Infrared Spectra of Nerve Agents, CRDEC-CR-000, U.S. Army Chemical Research, Development and Engineering Center, Aberdeen Proving Ground, MD, xxx 1992, Unclassified Report, in press.
8. S.L. Emery, Private communication.

BLANK

540

THEORETICAL PREDICTION OF VIBRATIONAL CIRCULAR DICHROISM SPECTRA
OF HEXOSES IN LINEAR FORM

Daniel Zeroka^{1a}, James O. Jensen^{1b}, Arthur H. Carrieri^{1b},
and Janet L. Jensen^{1b}

ABSTRACT

A very important objective of the Detection Directorate at CRDEC is the remote detection of biological materials in the field. One line of thinking currently being followed, is the recognition that sugars are distinguishing features of biological materials. This study reports on the theoretical prediction of the VIBRATIONAL CIRCULAR DICHROISM (VCD) spectra of the chiral molecules consisting of the eight hexoses in linear form. The procedure involves the optimization of geometries at the 3-21 G level using Gaussian 90 and the subsequent determination of normal mode frequencies and rotational strengths based on the method of P.J. Stephens, which is incorporated in the CADPAC version 4.2 program. All calculations were done on STARDENT 3000 computers. Key results reported include: optimized structures, normal mode frequencies and rotational strengths.

1. INTRODUCTION

This report represents a continuation of previous work (2,3) in the area of the theoretical prediction of the vibrational circular dichroism (VCD) spectra of chiral molecules. The work is a part of a long-term project of the Detection Directorate at CRDEC to be able to detect biological materials in the field. The plan is to relate the VCD spectrum of a molecule to the (1,4) matrix element of the Mueller matrix (4,5), which corresponds to a transformation matrix between an incident Stokes vector and a scattered Stokes vector. A procedure to determine all 16 elements of the Mueller matrix (4,5) by a two laser phase sensitive experiment is currently being developed by one of the coauthors (AHC).

The line of thinking followed in this report is to recognize that sugars are distinguishing features of biological materials. Sugars are chiral molecules and are optically active. In the absence of applied fields optical activity arises from chirality which exists when a molecule is not superimposable on its mirror image - or more specifically a molecule must not possess any improper-rotation axes to be optically active. Molecules which are optically active interact differently with left circularly polarized (LCP) and right circularly polarized (RCP) radiation. Circular dichroism is the difference in the absorption of LCP and RCP radiation by an optically active

sample. Only a handful of workers are currently involved in VCD measurements and theoretical predictions. A sampling of some research groups is represented by references (6-15). Instrumentation was developed in the early 1970's but only recently has commercial instrumentation become available. Here, the difference in absorptivity of a sample between LCP and RCP radiation is plotted as a function of wavenumber. A rotational strength, which corresponds to a difference in absorptivity of a sample between LCP and RCP radiation, can be positive or negative and the intensities are not related to the infrared and Raman intensities. The essential points to be studied in this investigation are frequencies, magnitudes of intensities and signs of intensities.

2. STEPHENS' FORMULATION OF THE ROTATIONAL STRENGTH

P. J. Stephens (6,7) has developed a theory for the determination of the rotational strength of a vibrational transition $g \rightarrow e$, $R(g \rightarrow e)$, for a chiral molecule. The formulation involves the determination of the rotational strength of a vibrational transition $g \rightarrow e$, $R(g \rightarrow e)$, for a chiral molecule

$$R(g \rightarrow e) = \sum_{\beta} \text{Im}[\langle g | (\mu_{e1})_{\beta} | e \rangle \langle e | (\mu_{mag})_{\beta} | g \rangle] \quad (1)$$

$$[\beta = x, y, z]$$

where g and e are ground and excited states and μ_{e1} and μ_{mag} are electric and dipole moment operators. The derived equation for the rotational strength can be expressed in terms atomic polar tensors and atomic axial tensors. Details on the formulation of the rotational strengths corresponding to given vibrational transitions can be found in references (6,7) or (2,3).

3. HEXOSES

The task undertaken on this project was the prediction of the vibrational circular dichroism spectra (VCD) of the D enantiomers of the hexoses (sugars with 6 carbon atoms). There are 8 such sugar molecules (16) with molecular formula $C_6H_{12}O_6$: aldose, altrose, glucose, mannose, idose, gulose, talose, and galactose. In this report we have considered these molecules in a linear configuration. Studies on the cyclic forms of these sugars will follow. The calculations have proceeded in the following stepwise manner:

- (1) based on previous geometries of 5 carbon sugars a reasonable starting geometry of D-allose was obtained and used in an optimization using the Gaussian 90 (17-20) electronic structure program.
- (2) frequencies and rotational strengths were obtained by running CADPAC version 4.2 (21).
- (3) by suitable change of dihedral angles starting geometries were devised for the other D-enantiomers. Steps (1) and (2) were repeated for each of the 8 D-enantiomers of the hexoses.

The calculations on the sugars, at this point, have been carried out at the

3-21G level. This level was selected because past experience indicates very reasonable optimized structures are found as compared to experimental structures. As is well known with ab initio determination of vibrational motion, the vibrational frequencies are typically too high by roughly 10 per cent - e.g. the C-H stretch predicted for 3-21 G level calculations multiplied by a scaling factor of 0.89, found empirically, is in very good agreement with experimental data (22).

The work on this project that has been done up to this time is the following:

- (1) the optimized geometry at the 3-21G level of calculation of the 8 D-hexoses have been determined and
- (2) the prediction of VCD spectral parameters, wavenumbers and rotational strengths of the 8 hexoses (vide supra) have been determined.

Our objectives are the following:

- (1) develop the VCD parameters (frequency and rotational strengths) in the range $800-1200\text{ cm}^{-1}$ that indicate transitions of high rotational strength and predict the correct sign.
- (2) develop the VCD parameters as accurately as possible, within a procedure that is computationally reasonable, for sugars in order that the results can be dovetailed into the experimental program on Mueller Matrix Spectroscopy directed by one of the authors (AHC).

Attention was focussed on sugar molecules with six carbon atoms (16). Because of space limitations the results for all molecules cannot be reported here. Therefore we report the calculated frequencies, rotational strengths and optimized geometries for only one molecule, arbitrarily selected as D-allose, in Tables 1 and 2.

Through examination of given spectral ranges, it is possible to scan the frequencies and rotational strengths in Table 2 to predict at which frequency a maximum rotational strength should be observed. The key points to note are the following:

- (1) The calculation is sensitive, because of the nature of the quantum mechanical operators involved - namely the angular momentum, to the choice of origin of the coordinate system. Comparisons in the literature at present find better agreement with the choice of origin as the center of mass of the molecule. Very key to the calculation is the level of the calculation. As mentioned our calculations are carried out at the 3-21G level, the origin chosen was the center of mass. The gauge origin used is the distributed origin, following the recommendation of Stephens.
- (2) The inaccuracies that result will be manifest in
 - force field generated
 - atomic polar tensor
 - atomic axial tensor

It is appropriate to point out that the size of the basis set for a 3-21G level of calculation is given by $22n$ where n corresponds to the molecular formula

(CH₂O)_n. For the hexoses the basis set size is 132, which is a fairly large basis set by today's standards. Note that the ab initio unscaled frequencies will be somewhat high (roughly about 10 %) compared to experimental frequencies.

The following work, in progress, is designed to continue the project toward the generation of a library of theoretically predicted VCD spectra:

- (1) Investigate the hexoses in ring configurations.
- (2) Label the modes of vibration for all molecules that were studied and compare with experimental data or other calculations where available.
- (3) Investigate the use of scaled force field and their effects on calculated frequencies, atomic polar tensors and atomic axial tensors and their subsequent effect on rotational strengths.
- (4) Investigate larger basis set calculations, such as 6-31G or 6-31G*, using the 3-21G optimized structures as starting geometries. In order to obtain quantitative accuracy in the prediction of the VCD spectrum of a molecule, some form of scaling is definitely needed. However, if the main intent of the calculations is to predict the transitions of high rotational strength and their correct signs then 3-21G seems to be an adequate level to do the calculations at based on the small set of molecules that have been studied up to this point in time.

4. SUMMARY

This study represents continuing work toward the goal of generating theoretically predicted VCD spectra of sugars as well as other chiral molecules. The approach involves the use of Stephens' theoretical formulation of the rotational strength and the use of Gaussian calculations at the 3-21G level. It should be emphasized that the key assumptions being used are:

- (1) use of Stephens' theoretical formulation and
- (2) use of Gaussian 3-21G level of calculation.

The level of calculation affects the frequencies, atomic polar tensor, atomic axial tensor, and thereby the rotational strength. It is worth noting that the VCD rotational strength is quite sensitive to small changes in molecular conformation. Thermal averaging must be taken into account when internal rotational motion is possible.

Since in this study the hexoses in the linear form have been studied no direct comparison with experimental VCD of hexoses can be made at this time. Studies on the hexoses in cyclic form are in progress and a comparison with experiment will be made in a future report.

REFERENCES

1. (a) Department of Chemistry 6, Lehigh University, Bethlehem, PA 18015-3172.
(b) U.S. Army Chemical Research, Development and Engineering Center, Aberdeen Proving Ground, MD 21010-5423.
2. D. Zeroka, G.R. Famini, J.O. Jensen, A.H. Carrieri, and C.F. Chabalowski, "Theoretical Prediction of Vibrational Circular Dichroism Spectra", CRDEC-CR-063 Report (1990).
3. D. Zeroka, G.R. Famini, J.O. Jensen, A.H. Carrieri and C.F. Chabalowski, "Theoretical Prediction of Vibrational Circular Dichroism Spectra", Proceedings of 1989 U.S. Army Chemical Research, Development and Engineering Center Scientific Conference on Chemical Defense Research 14-17 November 1989 (Aberdeen Proving Ground, MD; August, 1990) pp 181-189.
4. H. Mueller, *J. Opt. Soc. Am.* **38**, 661 (1948).
5. C. F. Bohren and D. F. Huffman, "Absorption and Scattering of Light by Small Particles", Wiley-Interscience, New York (1983), Chapters 2 and 3.
6. P.J. Stephens, *J. Phys. Chem.* **89**, 748-52 (1985).
7. P.J. Stephens and M.A. Lowe, *Ann. Rev. Phys. Chem.* **36**, 213-41 (1985).
8. M.G. Paterlini, T.B. Freedman and L.A. Nafie, *J. Am. Chem. Soc.* **108**, 1389 (1986).
9. R. D. Amos, N. C. Handy, K. J. Jalkanen and P. J. Stephens, *Chem. Phys. Letters*, **133**, 21-26 (1987).
10. K. J. Jalkanen, P. J. Stephens, R. D. Amos and N. C. Handy, *Chem. Phys. Letters*, **142**, 153-58 (1987).
11. K. J. Jalkanen, P. J. Stephens, P. Lazzerti and R. Zanasi, *J. Chem. Phys.* **90**, 3204-13 (1989).
12. P. L. Polavarapu, B. A. Hess, Jr., L. J. Schaad, D. O. Henderson, L. P. Fontana, H. E. Smith, L. A. Nafie, T. B. Freedman and W. M. Zuk, *J. Chem. Phys.* **86**, 1140-46 (1987).
13. H. Dothe, M. A. Lowe and J. S. Alper, *J. Phys. Chem.* **92**, 6246-49 (1988).
14. J. S. Alper and M. A. Lowe, *J. Chem. Phys.* **121**, 189-97 (1988).
15. R.A. Shaw, H. Wieser, R. Dutler, A. Rauk, *J. Am. Chem. Soc.* **112**, 5401-5410, (1990).
16. A. L. Lehninger, "Biochemistry", Worth Publishers, New York (1970).
17. J. S. Binkley, M. J. Frisch, D. J. DeFrees, K. Raghavachari, R. A. Whiteside, H. B. Schlegel, E. M. Fluder and J. A. Pople, "Gaussian 86", Department of Chemistry, Carnegie-Mellon University, Pittsburgh, PA.

18. M. J. Frisch, "Gaussian 86 User's Manual", Department of Chemistry, Carnegie-Mellon University, Pittsburgh, PA (1984).
19. W. J. Hehre, L. Radom, P. von R. Schleyer and J. A. Pople, "Ab Initio Molecular Orbital Theory", John-Wiley, New York (1986).
20. T. Clark, "A Handbook of Computational Chemistry", Wiley-Interscience, New York (1985).
21. R. D. Amos, "The Cambridge Analytical Derivative Package Publication", CCP 1/84/4 SERC, Daresbury Laboratory, Daresbury, Warrington WA4 4AD (1984).
22. H. F. Hamerka, S. L. Emery, G. R. Famini, J. O. Jensen, J. M. Leonard and D. L. Reutter, "Computation of Vibrational Frequencies in Mercaptans, Alcohols, and Sulfides", CRDEC-TR-069 Report (1989).

Table 1. Optimized Geometry for D-Allose [CHO-HCOH-HCOH-HCOH-HCOH-CH₂OH] Based on 3-21G Level of Calculation. [The total energy = -679.532701306 a.u. and the dipole moment = 2.133612 D.]

geometrical coordinate	value of geometrical coordinate
$r(C_1-C_2)$	1.5087 A
$r(C_3-C_2)$	1.5203 A
$r(C_3-C_4)$	1.5178 A
$r(C_1-H_5)$	1.0789 A
$r(C_1-O_6)$	1.2113 A
$r(C_3-O_7)$	1.4242 A
$r(C_3-H_8)$	1.0827 A
$r(O_7-H_9)$	0.9710 A
$r(C_3-H_{10})$	1.0837 A
$r(C_3-O_{11})$	1.4346 A
$r(O_{11}-H_{12})$	0.9690 A
$r(C_4-H_{13})$	1.0785 A
$r(C_4-C_{14})$	1.5210 A
$r(C_4-O_{15})$	1.4440 A
$r(O_{15}-H_{16})$	0.9692 A
$r(C_{14}-H_{17})$	1.0823 A
$r(C_{14}-C_{18})$	1.5265 A
$r(C_{14}-O_{19})$	1.4481 A
$r(O_{19}-H_{20})$	0.9699 A
$r(C_{18}-H_{21})$	1.0765 A
$r(C_{18}-H_{22})$	1.0746 A
$r(C_{18}-H_{23})$	1.4550 A
$r(O_{23}-H_{24})$	0.9661 A
$\phi(C_3-C_2-C_1)$	109.237 °
$\phi(C_4-C_3-C_2)$	113.625 °
$\phi(H_5-C_1-C_2)$	115.307 °
$\phi(O_6-C_1-C_2)$	121.147 °
$\phi(O_7-C_2-C_3)$	109.212 °
$\phi(H_8-C_2-C_3)$	108.660 °
$\phi(H_9-O_7-C_3)$	108.955 °
$\phi(H_{10}-C_3-C_2)$	109.622 °
$\phi(O_{11}-C_3-C_2)$	105.202 °
$\phi(H_{12}-O_{11}-C_2)$	107.646 °
$\phi(H_{13}-C_4-C_3)$	109.240 °
$\phi(C_{14}-C_4-C_3)$	116.579 °
$\phi(O_{15}-C_4-C_3)$	103.778 °

geometrical coordinate	value of geometrical coordinate
$\phi(\text{H}_{16}-\text{O}_{15}-\text{C}_4)$	107.042 °
$\phi(\text{H}_{17}-\text{C}_{14}-\text{C}_4)$	110.141 °
$\phi(\text{C}_{18}-\text{C}_{14}-\text{C}_4)$	114.774 °
$\phi(\text{O}_{19}-\text{C}_{14}-\text{C}_4)$	103.205 °
$\phi(\text{H}_{20}-\text{O}_{19}-\text{C}_{14})$	107.269 °
$\phi(\text{H}_{21}-\text{C}_{18}-\text{C}_{14})$	113.183 °
$\phi(\text{H}_{22}-\text{C}_{18}-\text{C}_{14})$	108.938 °
$\phi(\text{H}_{23}-\text{C}_{18}-\text{C}_{14})$	107.111 °
$\phi(\text{H}_{24}-\text{O}_{23}-\text{C}_{14})$	104.193 °
$\tau(\text{C}_4-\text{C}_3-\text{C}_2-\text{C}_1)$	171.203 °
$\tau(\text{H}_5-\text{C}_1-\text{C}_2-\text{C}_3)$	55.100 °
$\tau(\text{O}_6-\text{C}_1-\text{C}_2-\text{C}_3)$	-124.325 °
$\tau(\text{O}_7-\text{C}_2-\text{C}_3-\text{C}_4)$	50.484 °
$\tau(\text{H}_8-\text{C}_2-\text{C}_3-\text{C}_4)$	-71.004 °
$\tau(\text{H}_9-\text{O}_7-\text{C}_2-\text{C}_3)$	4.007 °
$\tau(\text{H}_{10}-\text{O}_3-\text{C}_2-\text{C}_1)$	51.127 °
$\tau(\text{O}_{11}-\text{C}_3-\text{C}_2-\text{C}_1)$	-67.836 °
$\tau(\text{H}_{12}-\text{O}_{11}-\text{C}_3-\text{C}_2)$	187.321 °
$\tau(\text{H}_{13}-\text{C}_4-\text{C}_3-\text{C}_2)$	-71.560 °
$\tau(\text{C}_{14}-\text{C}_4-\text{C}_3-\text{C}_2)$	51.078 °
$\tau(\text{O}_{15}-\text{C}_4-\text{C}_3-\text{C}_2)$	-190.447 °
$\tau(\text{H}_{16}-\text{O}_{15}-\text{C}_4-\text{C}_3)$	187.696 °
$\tau(\text{H}_{17}-\text{C}_{14}-\text{C}_4-\text{C}_3)$	-69.166 °
$\tau(\text{C}_{18}-\text{C}_{14}-\text{C}_4-\text{C}_3)$	57.433 °
$\tau(\text{O}_{19}-\text{C}_{14}-\text{C}_4-\text{C}_3)$	-187.465 °
$\tau(\text{H}_{20}-\text{O}_{19}-\text{C}_{14}-\text{C}_4)$	200.976 °
$\tau(\text{H}_{21}-\text{C}_{18}-\text{C}_{14}-\text{C}_4)$	-72.454 °
$\tau(\text{H}_{22}-\text{C}_{18}-\text{C}_{14}-\text{C}_4)$	49.312 °
$\tau(\text{H}_{23}-\text{C}_{18}-\text{C}_{14}-\text{C}_4)$	-196.623 °
$\tau(\text{H}_{24}-\text{O}_{23}-\text{C}_{14}-\text{C}_4)$	224.575 °

Table 2. Calculated Wavenumbers $\bar{\nu}$ and Rotational Strengths R for D-Allose [CHO-HCOH-HCOH-HCOH-HCOH-CH₂OH] Based on 3-21G Level Optimized Geometry.

$\bar{\nu}$ (cm ⁻¹)	R (x 10 ⁻⁴⁴ esu ² cm ²)
52.59	14.710
64.85	-16.555
103.06	18.665
143.19	-39.354
158.54	18.545
167.54	-8.769
210.28	44.743
263.56	17.824
292.37	11.132
311.20	60.635
320.94	-88.576
334.37	-7.591
352.29	-20.802
367.38	-1.531
455.12	-29.528
460.35	-71.927
522.69	90.392
554.17	80.522
590.32	11.152
602.16	59.302
654.85	-38.471
692.47	-75.077
802.00	-38.208
827.93	-51.259
890.53	-15.821
928.25	-14.187
964.86	131.950
1037.10	-37.785
1089.92	163.110
1110.71	-235.750
1129.18	-15.280
1141.91	81.167
1162.17	-17.818
1188.22	89.104
1204.47	-119.73
1246.31	-25.781
1288.53	-19.950
1354.50	152.130
1364.71	40.903
1391.41	104.280
1398.47	-90.794

$\tilde{\nu}$ (cm ⁻¹)	R (x 10 ⁻⁴⁴ esu ² cm ²)
1439.73	-55.255
1453.75	-48.573
1483.17	30.799
1500.26	-18.187
1506.69	5.050
1512.44	-18.719
1518.71	-0.882
1525.40	17.372
1572.11	-8.048
1578.42	26.216
1587.42	24.669
1669.45	3.816
1903.68	0.068
3217.48	14.326
3236.11	-52.773
3243.74	41.509
3278.94	-2.267
3293.21	-2.952
3297.96	-9.403
3360.94	6.792
3821.55	5.886
3844.74	5.269
3862.83	3.909
3865.66	-4.044
3875.82	1.918

POSTER SESSIONS

BLANK

XII. PROTECTION POSTERS

BLANK

Barrier Properties of Matrices for Reactive Systems - A Reactivity Probe

John W. Halliday¹ and John E. Walker¹

ABSTRACT

The dynamics and perhaps the efficacy of the interaction between chemical agents and reactive or catalytic sites immobilized in a host matrix, e.g., Cu^{2+} in the biopolymer chitosan, is moderated by the barrier properties of the matrix. The present study compares these permeative characteristics for two matrices - chitosan with Cu^{2+} and chitosan without Cu^{2+} . Transport of agent surrogates through these matrices is facilitated by maintaining them at a high degree of hydration, i.e., equilibration at 100% relative humidity. The chemical agent surrogate dimethyl methyl phosphonate (DMMP) is used to determine and compare basic transport properties for these two matrices with minimal potential for reaction between the permeant and matrix. To probe transport properties with a possibility for reaction between the permeant and the Cu^{2+} reactive site, the reaction surrogate for G-type agents, diisopropyl fluorophosphinate (DFP), is used. Transport of DFP through the chitosan matrix serves as a self-hydrolysis blank against which results from the reactive system can be contrasted. Those results show that the steady-state flux for the DFP/reactive system is almost an order of magnitude less than for the nonreactive blank. Detailed comparison of results, e.g., shape of transport curves, for DFP and DMMP permeation through the same film and through different films indicates a larger interfilm variation than a basic difference in transport properties between the two surrogates. These results provide evidence for other than surface reactivity in this reactive system.

INTRODUCTION

Reactive centers can be deployed in many different ways. They may be incorporated into a resin, covalently bound to a substrate, or simply physically dispersed in a host matrix. It is often difficult to assess the efficacy of the reactive center itself independent of factors which moderate the reactant's accessibility to the reactive center. For example, barrier properties of the host matrix, i.e., the rate at which the reactant (permeant) can approach the reactive center (permeability), may literally render the interaction diffusion limited and consequently restrict the viability of reaction mechanisms for a specific detoxification process. For essentially impermeable matrices, reactivity is restricted to the surface. Thus, the barrier characteristics of the host matrix combined with the degree of homogeneity of dispersion of the reactive center in that matrix define the time-dependent challenge profile for a given permeant. It is the dynamics relative to that profile which determine the efficacy of the reactive system and in terms of which factors affecting the reactivity should be evaluated. For the work reported on here, the matrix (chitosan) is the source of chelating ligands for the reactive

¹ Soldier Science Directorate, U.S. Army Natick RD&E Center, Natick, MA 01760-5020

center (Cu^{2+}) which hydrolyzes G agents. For the purposes of this study, the Cu^{2+} - chitosan system is deployed as a very thin cast film (ca. 0.05mm) and the agent surrogate challenge is applied in the form of small droplets.

Chitosan at ordinary conditions of relative humidity (<80%) is a relatively good barrier against the permeation of G agent surrogates. It is, therefore, difficult to assess the reactivity or catalytic activity of the Cu^{2+} center, since the challenge surrogate does not get much beyond the surface. It is also difficult to assess moisture requirements in maintaining the hydrolytic activity of the system when changing the degree of hydration also changes the barrier properties of the matrix and, hence, the overall challenge profile for the surrogate agent. The basis of the present work is a study of the permeability of both reaction surrogates.

EXPERIMENTAL

Chitosan and Cu^{2+} - chitosan films were prepared (1) in a cast form and dried while being pressed between two plates for a minimum of 72 hours. These films were then equilibrated in a 100% relative humidity (RH) chamber, again for a minimum of 72 hours. For the permeation experiment, a film was removed from the RH chamber, rapidly mounted in the permeation cell, and the cell attached to the apparatus shown in Figure 1.

Measures taken to preserve the hydration of the sample included: (1) bubbling the purging air stream on the detection side of the cell through water and (2) suspending a water-saturated plug of cotton ca. 0.5 cm above the sample surface (inset, Figure 1) on the challenge side of the cell. The sample was equilibrated in this configuration for a minimum of three hours prior to the start of the permeation run. The sample was challenged with permeant by removing the stopper capping the cell (with the cotton plug attached), depositing a $3.5 \mu\text{L}$ droplet from a syringe held ca. 1 cm above the film surface, and immediately restoppering the cell. The permeant flux exiting the film on the other side was measured using mass spectrometric techniques.

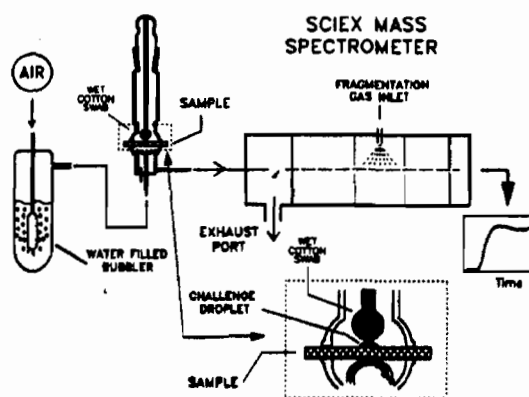
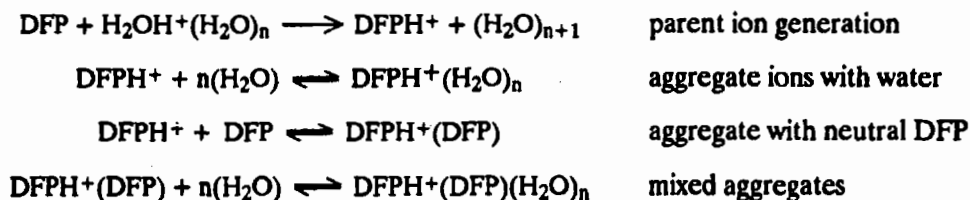


Figure 1. Apparatus for measuring permeation of agent surrogates through films.

A Sciex^(R) mass spectrometer operating with an Atmospheric Pressure Chemical Ionization (APCI) front end was used to measure the exit flux. The APCI process (used in the positive ion mode, appropriate to the phosphonate surrogates) results in a series of ions indicative of the presence of trace quantities of the permeant in the purging air stream. In addition to the primary ion (parent) resulting from proton transfer from the APCI reactive ion, $\text{H}_2\text{O}^+(\text{H}_2\text{O})_n$, additional aggregate ions involving water and neutral surrogate molecules are formed. The reactions and equilibria involved are summarized generically in Table 1 using DFP as an example. The specific species produced and their intensities depend on the particular surrogate and its concentration in the ionization region.

Table 1.

Formation of observable ions in APCI detection of DFP. Analogous ions can be formed for DMMP.



There are interesting aspects of the ion chemistry involved which are outside the scope of the present considerations. The practical result of this ion chemistry is the partitioning of the total ion intensity among several species. The transport curve is obtained by summing the intensities of the contributing ions. This approach is illustrated in Figure 2. For DFP, the major contributing ions are DFPH^+ , $\text{DFPH}^+(\text{DFP})$, and $\text{DFPH}^+(\text{H}_2\text{O})$; for DMMP, analogous ions are involved. The primary ion generation reaction, e.g., the $\text{DFP} - \text{H}_2\text{O} + (\text{H}_2\text{O})_n$ reaction, resembles a titration. Figure 3 shows the depletion of APCI reactive water ions, $\text{H}_2\text{O} + (\text{H}_2\text{O})_n$, for $n = 1, 2,$ and 3 ($m/e = 37, 55,$ and 73 , respectively) as the permeant flux increases. For high concentrations of permeant, the dynamic response range can be exceeded as the reactive ion concentration is totally depleted. The supposition of the APCI process that the permeant is a trace component in the purging airstream also risks violation (high permeant concentrations perturb the ion chemistry) under these conditions. For these reasons, some transport curves involving DMMP may be slightly distorted in the approach to steady-state region. Since there is no preferential reactivity (the normalized curves for $n = 1, 2$ and 3 superimpose, Figure 3) among the reactive water ions, the $n = 1$ ($m/e = 37$) ion intensity is measured in every permeation run as a indication of whether or not the detection limit restrictions are violated.

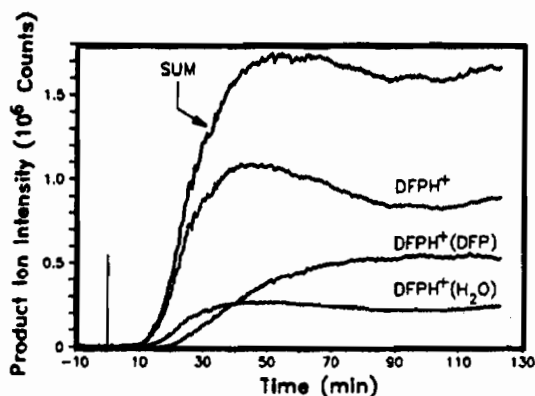


Figure 2. Intensity correlating with permeant concentration in the purging airstream is distributed among several ionic species. These separate intensities are summed to give the transport curve. This figure illustrates the process for a DFP run.

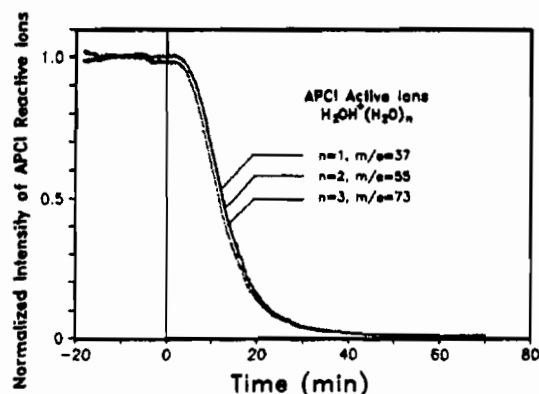


Figure 3. Depletion of APCI reactive ions in a DMMP - chitosan permeation run.

After completion of a permeation run, the sample is removed from the cell and its thickness measured using a micrometer. Film thicknesses were reasonably uniform at 0.05 ± 0.01 mm (< 1 mil) for all films used in this study. In addition to construction of transport curves as indicated in Figure 2, plots of flux normalized to the steady-state value are constructed using data for the first 120 minutes. These standard-scale normalized plots are used in evaluating and comparing the shapes and breakthrough characteristics of the transport curves.

RESULTS AND DISCUSSION

Transport curves can be evaluated using several criteria. The steady-state permeation rate, the breakthrough behavior, and the general shape of the curve are some criteria commonly used. The steady-state flux is perhaps the most useful comparative index for evaluating reactivity. Breakthrough behavior, e.g., the onset of physical breakthrough or the time to reach 50% of the steady-state flux, and the shape of the transport curve, particularly the area between physical breakthrough and steady state, will be used in more qualitative comparisons, such as assessment of intersample variations and differences in transport behavior between DFP and DMMP.

The steady-state values for transport of DFP and DMMP through chitosan and Cu-chitosan matrices are summarized in Table 2. The transport curves are of the general shape exemplified in Figures 4 - 6.

Table 2.

Steady state flux values for transport of reactive (DFP) and unreactive (DMMP) agent surrogates through chitosan and Cu-chitosan matrices.

Permeant	Steady State Exit Flux ¹	
	Chitosan	Cu-Chitosan
DMMP	3×10^6	3.5×10^6
DFP	1.8×10^6 (*) ²	1.0×10^6
	1.1×10^6	0.35×10^6 (1) ²
		$< 0.02 \times 10^6$ (2) ²
		0.03×10^6 (3) ²
DMMP (rechallenge)	3.5×10^6 (*) ²	2.8×10^6 (1) ²
		3.5×10^6 (2) ²
		3.1×10^6 (3) ²

1. Steady state flux is in instrument counts
2. Parentheses, e.g., (*), (1), (2), (3), denote matching pairs in the rechallenge experiments.

In several instances films initially challenged with DFP and the transport curve measured were rechallenged with DMMP. In these cases, the DFP exit flux reached a level low enough that DMMP could be applied without danger of exceeding the detection limit or compromising the ion chemistry. In Table 2 such experiments are labelled as DMMP (rechallenge) in the first column. Matching pairs in the rechallenge scheme are identified by indices enclosed in parentheses. Because the rechallenge is at a site physically close to the original DFP challenge site (and therefore to exactly the same film) and because the experimental conditions are identical, such experiments provide a strong basis for interpreting the DFP transport either in terms of reactivity or as some basic difference in the matrix transport properties.

While there is variability in the steady-state fluxes observed for transport of DFP through a Cu-chitosan matrix, the values are generally lower than for DFP transport through chitosan. Comparison of Figures 4 and 6 shows that the breakthrough and ascent to steady-state times are comparable for DFP in both the Cu-chitosan and chitosan matrices. Therefore DFP transport through chitosan is a reasonable self-hydrolysis blank against which transport through Cu-chitosan can be contrasted. The single high value (1.0×10^6 counts) for DFP through Cu-chitosan is difficult to explain. The breakthrough behavior and shape of the curve is consistent with that generally observed in this study and was not abnormal in any way other than exhibiting a high steady-state flux. Local inhomogeneities in Cu distribution, small matrix defect(s), or subtle aging effects are possible explanations. Coincidentally, the DFP - Cu-chitosan values are listed in the order in which they were run; therefore films showing the much lower DFP transmission rates, i.e., higher reactivity, had been equilibrated longer at high RH. The results from the DMMP rechallenges show consistent behavior, including the steady-state flux values, and no indication of abnormal transport behavior. This evidence, together with similar results from the DMMP initial challenge experiments, mitigates against gross differences in the degree of matrix hydration as an explanation for variation in the DFP results. Such differences would be reflected in the breakthrough behavior for DMMP as well, a difference which is not observed. Reactivity, however, may be influenced by water distribution effects

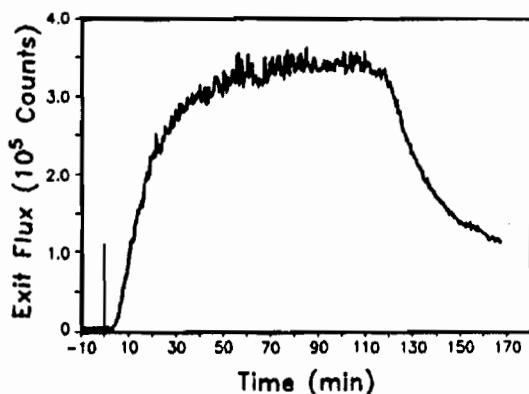


Figure 4. Transport curve for DFP through Cu-chitosan, including a desorption region. Reduction in steady-state flux compared to that observed for transport through chitosan (Figure 6) is indicative of reaction within the matrix.

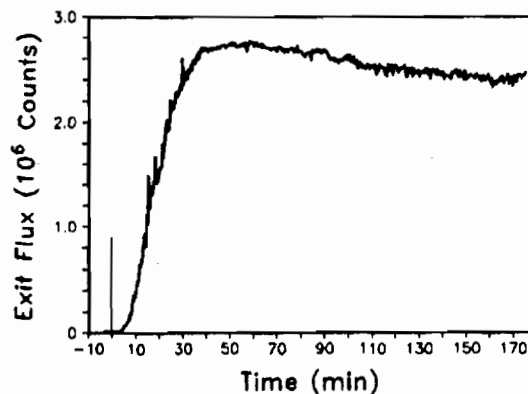


Figure 5. Transport curve for DMMP through Cu-chitosan - a rechallenge of the same film used in Figure 4. Experiments of this type are a confirmation that the basic transport properties of the matrix have not changed.

not necessarily related to matrix hydration (more of a *bound* type water) that would not be as readily reflected in the transport behavior but would be important in defining or enhancing the efficacy of the reactive center. Such effects may establish a balance between stoichiometric and catalytic reaction modes, the shifting of which would affect only the DFP transport.

Evaluation of the transport curves using the standard scale normalized plots shows that the variations observed correlate neither with basic differences in transport behavior between the two types of matrices nor with differences between the two surrogates. As Figures 4 and 5 illustrate (using the unnormalized versions of the transport curves but plotted on the same time scale), the breakthrough behavior and general shape of the initial part of the curves are similar for both DFP and DMMP in the same sample, i.e., a rechallenge experiment. Figure 6 also serves to illustrate a slight variation in breakthrough behavior that is commonly observed. Therefore, dissimilar behavior is more likely related to small intersample variations (degree of hydration, perhaps) than to basic differences attributable to matrix or surrogate type.

While the effect of the degree of hydration is the topic of a future study, it should be pointed out that prior investigation of the barrier properties of chitosan and Cu-chitosan at ambient RH (ca. 50%) show both matrices to be good barriers. The physical breakthrough time for DMMP is greater than 50 hours. Experiments with DFP under the same conditions are more equivocal due to self-hydrolysis and the long times involved. Studies by Walker *et al.* (2) indicate a dramatic change in reactivity/transport around 80% RH.

CONCLUSIONS

The premise underlying the work presented here is that transport behavior of an agent *through* a reactive system is determined by two processes: (1) interaction of the agent with the reactive center resulting in detoxification, and (2) the fundamental barrier properties of the host matrix governing permeation/diffusion of molecules of that size/shape irrespective of their potential reactivity. In systems for which the host matrix is a very good barrier, the agent - reactive center interaction is restricted to the surface. For systems in which the matrix is an extremely poor barrier, reaction centers within the matrix become accessible. In such cases, the transport rate through the matrix defines the agent challenge profile for the reactive centers; it is this profile which is important in assessing the protective or detoxification capacity of such systems.

As this study has shown, well-hydrated chitosan and Cu-chitosan are very poor barriers to both reactive (DFP) and nonreactive (DMMP) agent surrogates. A good indication of the reactivity of DFP in the Cu-chitosan system is obtained from contrasting the steady-state transport flux with that of a suitable reference. The blank chosen was chitosan equilibrated at the same RH as the Cu-chitosan (ca. 100%). Since both DFP and DMMP transport through chitosan and Cu-chitosan occurs on a comparable time scale (they have similar physical breaktimes and rates of approach to

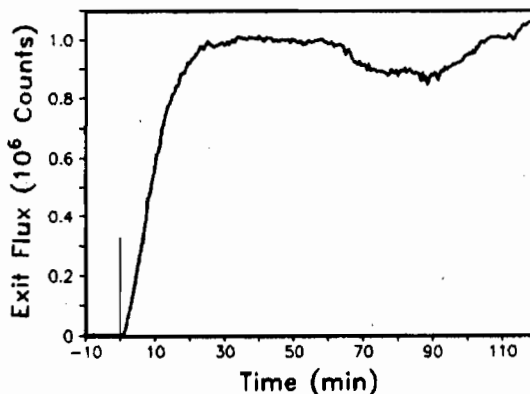


Figure 6. Transport curve for DFP through chitosan. The steady-state flux (ca. 1.0×10^6) from this type of experiment is the *self-hydrolysis blank* for transport of DFP through Cu-chitosan, e.g., Figure 4.

steady state), DFP transport through chitosan is a suitable self-hydrolysis (matrix hydrolysis) blank. With these considerations in mind, the DFP steady-state transport through Cu-chitosan is substantially lower than for the blank, indicating that reaction has taken place within the film.

That the degree of this reduction varies dramatically and may be associated with aging effects prompts speculation about the nature of the reactive site and, at least for a hydrolysis reaction, its special requirements. The DMMP results showed, from the perspective of an inert permeant, that the barrier properties did not grossly vary. The ability, in several instances, to rechallenge a film with DMMP following a DFP run and to observe normal barrier transport behavior lends special credence to this position.

Qualitative comparison of transport curve shapes, including breakthrough behavior, indicates that the comparatively small variations that are seen can be attributed to sample variations rather than any fundamental differences between type of matrix or surrogate agents.

The mass spectrometric detection employed resulted in very precisely defined transport curves. These curves will be used in performance model development, which will make this general transport behavior approach an effective and informative reactivity probe.

REFERENCES

1. Robbins, F.M., Walker, J.E., Andreotti, R.E., Evans, G., and Woodbury, C., "A Catalytically Active Metal Ion - Polymer Complex" (U), U.S. Army Science Conference, October 1988.
2. Walker, J., Robbins, F., Andreotti, R., Woodbury, C., and Alabran, D., "Moisture Requirements for Chemical Agent Inactivation by Catalytic Protective Systems", NATICK/TR-91/005L, December 1990, AD B151 784.

BLANK

REMOVAL OF DIETHYL SULFIDE FROM BREATHING AIR BY THE NRL-1000L OXIDATION CATALYST

Vasgen A. Shamamian
Applied Research Corporation, 8201 Corporate Dr.
Landover, MD 20785

Kim W. Pierson¹, and D. S. Y. Hsu
Code 6114, Chemistry Division, Naval Research Laboratory,
Washington D. C., 20375-5000

Abstract

The complete removal of 1000 ppm diethyl sulfide from breathing air has been studied. We employ a temperature controlled reactor (25-500°C) in which we mix upstream a variety of gases at atmospheric pressures, pass them over the 60-80 mesh catalyst at high flow rates, and continually sample the effluent with an electron impact ionization quadrupole mass spectrometer. Complete destruction of diethyl sulfide is achieved at the catalyst temperatures of 320 and 360°C for the entire duration of a typical experiment (4-5 hours) when pure oxygen and breathing air are used, respectively. Below the destruction temperature, the decrease in the diethyl sulfide parent ion is complemented by a commensurate increase in the mass spectrometer intensities for SO₂ and CO₂.

Introduction

The present state of technology for the removal of chemical warfare (CW) agents from breathing air relies primarily on the activated charcoal adsorbers and chromium impregnated, carbon catalysts. The inherent problem associated with this air purification system is its relatively short exposure lifetime and deactivation under humid conditions.² As an alternative to adsorption, catalytic oxidation has been shown to be an effective means of reducing toxic automobile emissions,^{3,4} and its suggested military application toward collective protection has been the subject of recent research activity.^{5,6} Unlike auto exhausts, however, the need for complete catalytic deactivation of CW agents is imperative due to their high toxicity at extremely low concentrations. The objective of our research effort is to develop and test new candidate catalysts for the complete oxidative removal of CW agents.

The NRL-1000 oxidation catalyst has been shown to remove both perfluoropropene and monochlorodifluoromethane from low pressure streams of

air.^{7,8} We have adapted our experimental apparatus to accommodate a flowing, fixed bed, atmospheric reactor. As our first test case system, we have chosen the oxidation of diethyl sulfide. Our reasons for this choice are twofold. Diethyl sulfide (Et₂S) is a non-chlorinated simulant for mustard agents, and provides a means for testing the catalyst against sulfur poisoning. More importantly, the oxidation of Et₂S is a model system where extensive kinetic studies have been performed by Rossin.^{9,10,11}

Experimental

The apparatus used in this work has been described previously in detail.¹² A schematic representation of the atmospheric reactor modifications is displayed in Figure 1. Briefly, air (or O₂) and diethyl sulfide are mixed upstream of the reactor using individual mass flow controllers and the head pressure measured with a capacitance manometer (MKS Instruments). The reactor is a quartz tube 0.5" in diameter and 6" in length. Approximately 5" downstream of the inlet, a quartz frit is sealed into place. The catalyst is placed against the frit and secured in place with a plug of quartz wool, leaving a preheat zone of 4" which is loosely packed with short pieces of quartz tubes. This design allows for uniform heating along the length of the reactor. A chromel-alumel thermocouple is placed on the downstream side and in physical contact with the quartz frit backstop. The heating elements are resistive coils encased in a clamshell ceramic oven insulated with ceramic cloth. Operating temperatures attainable with this configuration are between 25° and 700°C, although the temperature was rarely raised above 500°C. A bypass line allows us to isolate the reactor and analyze the feed gas directly. A small portion of the reactor effluent is directed to the detector through a precision metering valve. The detector is a two stage differentially pumped quadrupole mass spectrometer (QMS) employing electron impact as an ionization scheme (Extranuclear). Typical quiescent residual gas pressures in the QMS chamber are 2.0×10^{-8} torr. The pressure rises one order of magnitude during operation. Mass ion currents are multiplexed, digitized and stored on a dedicated microcomputer, using a program written by one of the authors (KWP). Time, temperature, and up to 10 mass ion intensities are averaged and recorded. Transit time of argon through reactor from flow valve to detector is 5-7 seconds.

One gram of catalyst (U.S. Standard Sieve 60-80 mesh) is prepared by degassing for 8 hours at 50°C. It is then calcined in O₂ at 425°C for 30 minutes and reduced in H₂ at 225°C for an additional 30 minutes. The catalyst is then stored in vacuum until used. Unfortunately, the oxidation state of the catalyst at this time is not known. Methods of pretreatment have been shown to have a strong influence on the efficacy of oxidation catalysts and we intend to pursue this aspect further.¹³

The diethyl sulfide (98%) was obtained from Aldrich and subjected to freeze pump thaw degassing. The liquid was then vacuum evaporated into a large ballast volume and pressurized with He to generate a 4.25% mixture. The flow rates of the He/ Et₂S mixture was then set at 14 SCCM and the breathing air flow rate at 595 SCCM to generate a 1000 ppm mixture feed gas, yielding a weight to flow ratio of $W/F = 2 \times 10^6$ g cat sec/mol.

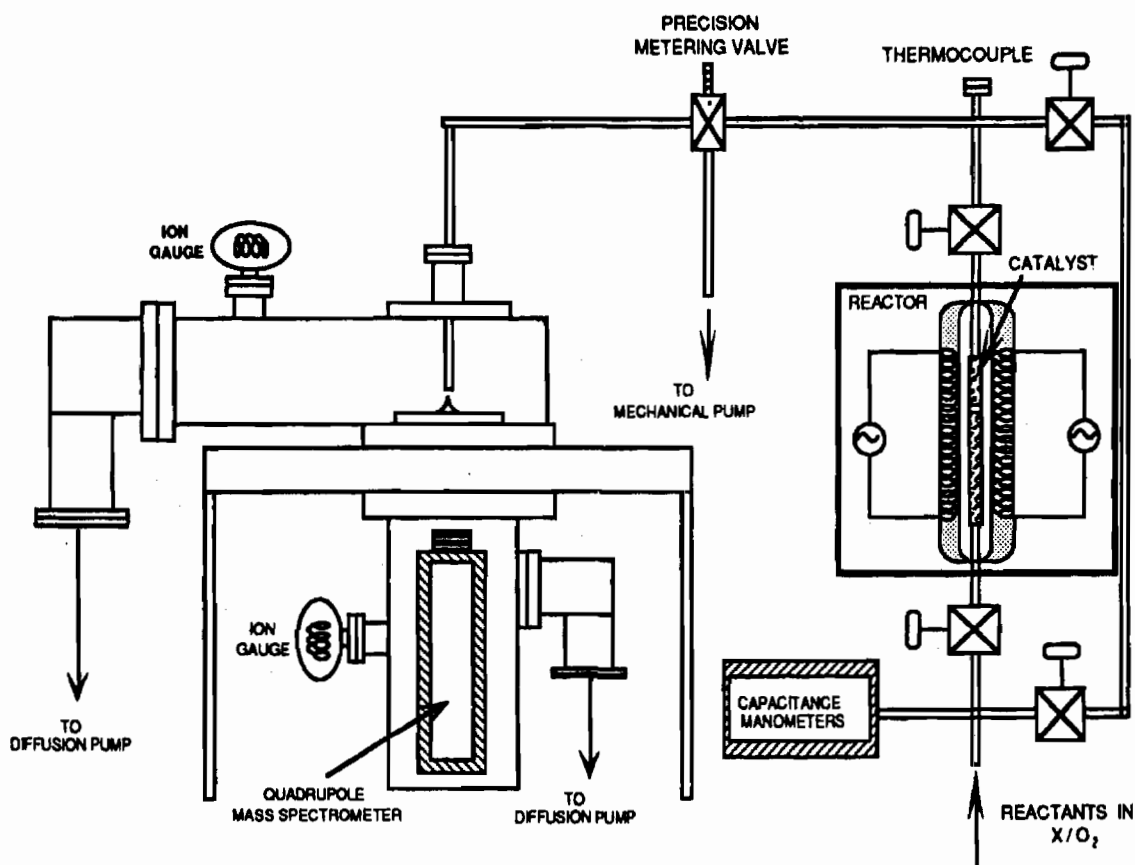


Figure 1: Schematic representation of apparatus.

Results and Discussion

One unique aspect of this experimental arrangement is that we may identify reactant and product species *in situ*. For example, in bypassing the reactor, we are able to identify any potential impurities in the feed mixture, which may have been introduced intentionally or unintentionally. Similarly, the mechanistic pathway to complete oxidation may be ascertained by monitoring the temperature dependence of partially oxidized species in the reactor effluent. To illustrate our point, we show in Figure 2a a portion of the mass spectrum obtained by diverting the feed gas directly to the QMS. It shows peaks at $m/e=90$, 75, and 61 amu corresponding to the parent ion and first two fragments of diethyl sulfide namely $\text{CH}_3\text{CH}_2\text{SCH}_2^+$ and $\text{CH}_3\text{CH}_2\text{S}^+$. Also, there are peaks at $m/e=62$ and 47 amu that we attribute to the dimethyl sulfide impurity. At $m/e=64$ and 48 are trace amounts of one of the oxidation products, SO_2 and its first fragment SO , and partial oxidation products EtO^+ and EtOH^+ at 45 and 46 respectively. Concerned about reactions catalyzed by the vessel walls, the relative intensities of the impurity peaks with respect to the Et_2S parent ion were monitored daily, with no change over the lifetime of the $\text{Et}_2\text{S}/\text{He}$ mixture. (note the presence of Ar and CO_2 at 40 and 44 amu respectively, which are significantly abundant in breathing air.) Figure 2b shows the effluent of

the reactor held at 400°C. The principal products in this mass range are CO₂ and SO₂.

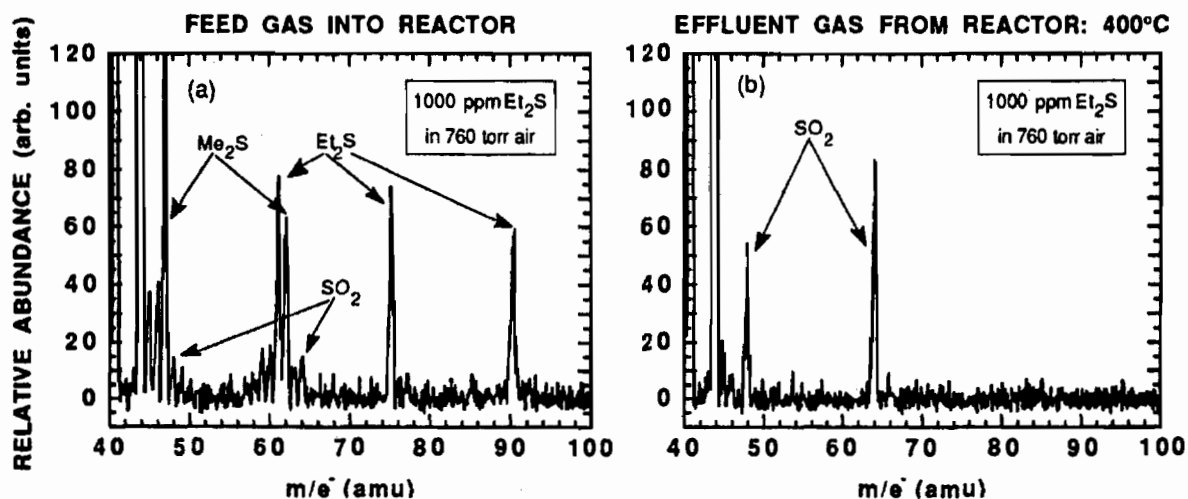


Figure 2: Mass Spectrum of feed gas and reactor effluent. Reactor temperature: 400°C

We have investigated the role of adsorption on the catalyst. The pristine catalyst is held at a temperature below the oxidation threshold, (220°C) and challenged by 1000 ppm of diethyl sulfide in continuous flow. We then monitor the emergence of diethyl sulfide in the effluent as a function of time. This procedure is then repeated for the catalyst at the destruction temperature, 360°C. The results are summarized in Figure 3a. After 80 minutes of exposure at 220°C, we see threshold to break-through. The column continues to adsorb Et₂S until 3.75 hours at which point complete passivation is achieved, *i.e.*, the inlet and exhaust fluxes of Et₂S are equal.

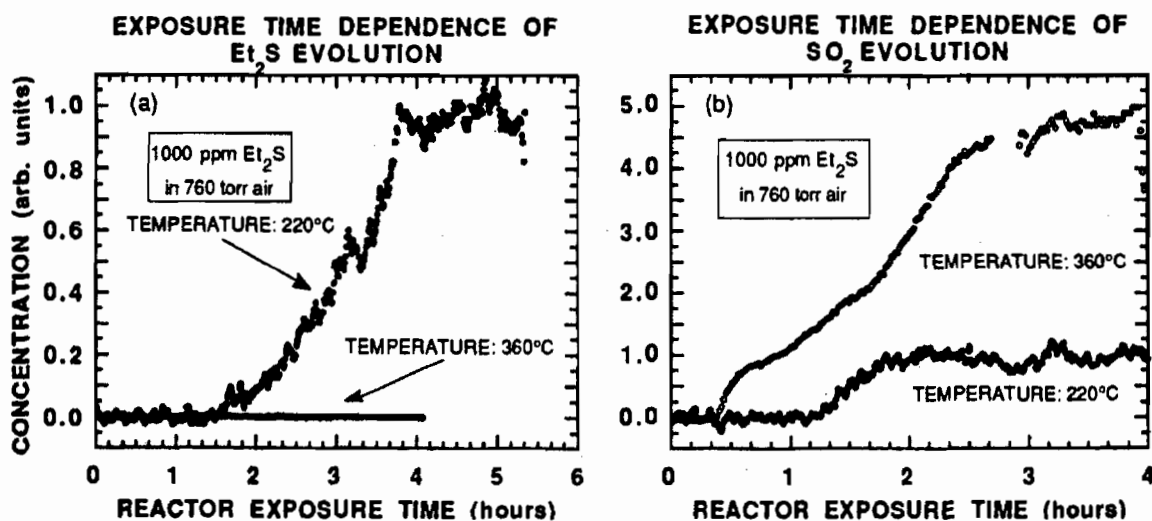


Figure 3: Exposure time dependence of reactant and product evolution in reactor effluent

Simultaneous to the diethyl sulfide measurements, we observe the breakthrough of SO_2 , and this is displayed in Figure 3b. At temperatures below the destruction threshold, the retention time of SO_2 corresponds to the same value of Et_2S , 80 min, indicating efficient adsorption of reactants and/or products by the catalyst/support system. At elevated temperatures, the retention time of SO_2 is reduced to 10 minutes as one might expect, however, the system still requires more than 4 hours to reach steady state evolution of SO_2 . This suggests at higher temperatures, there is significant adsorption/desorption-diffusion of reactants and products on the pristine catalyst.⁹ There is also evidence which suggests Et_2S or its decomposition products undergoes irreversible sticking. Used catalyst, when re-calcined at 360°C , continues to evolve small amounts of SO_2 , indicating some cleaning, but upon re-exposure to Et_2S , products immediately appear in the effluent without the delay observed in the case of the pristine (unexposed) catalyst. Carbon and Sulfur are also observed in the XPS analysis of the used catalyst.

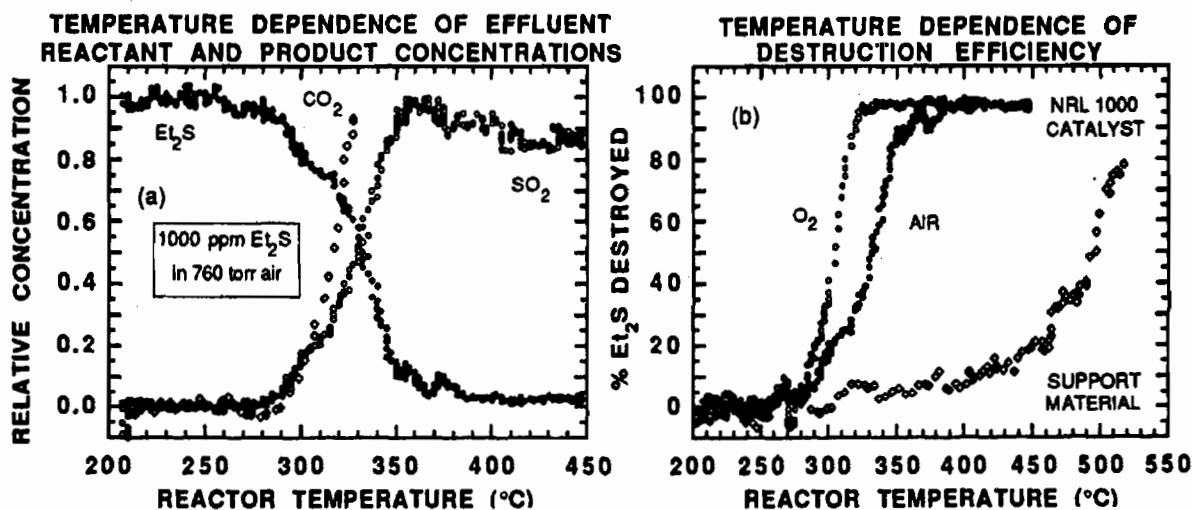


Figure 4: Temperature dependence of destruction efficiency of catalyst

Despite these large adsorption effects, the passivated catalyst remains active in the temperature range between 250 - 450°C . The temperature dependence of its oxidation efficiency is shown in Figure 4a. As expected, we show a commensurate rise in the product (CO_2 and SO_2) concentrations with respect to the decrease in Et_2S in the reactor effluent. The threshold to oxidation occurs at 250°C and complete destruction is achieved by 360°C . These temperature dependences were reproducible after repeated heating/cooling cycles and exposures in excess of 17 hours. Finally, we investigate the contribution of the support material toward oxidation. In this experiment, we activated and passivated the support in the same manner as the catalyst/support system. Figure 4b compares the destruction efficiency of the catalyst with the support material. Figure 4b shows less than 10% contribution to the overall destruction fraction from the support in the same temperature as the catalyst. Significant oxidation begins at temperatures above 450°C , and even at 520°C only 80% of the Et_2S is destroyed. We also show that replacing air with pure O_2 has

the effect of reducing the destruction temperature to 320°C. We attribute this to simple equilibrium effects.

Conclusions

We report the removal of 1000 ppm diethyl sulfide from breathing air by the NRL-1000 catalyst. The principal means of removal of Et₂S is via catalytic oxidation, producing H₂O, CO₂, and SO₂ as products. Complete oxidation is attained at 360°C in air and at 320°C in pure oxygen. The support shows 10% contribution to oxidation at these temperatures. The pristine catalyst/support system initially shows significant adsorption of reactants and products. Sulfur has been shown to hinder the efficacy of supported metal oxidation catalysts,^{14,15} and we feel that, at low temperatures, the same is true with this system. However, the exposed catalyst/support does show continued, reproducible catalytic activity upon prolonged exposure to Et₂S.

References

1. N.R. C. Postdoctoral Fellow
2. J. A. Rossin, E. Petersen, D. Tevault, R. Lamontagne, and L. Isaacson, "Effects of Environmental Weathering on the Properties of ASC Whetlerite," *Carbon* **29**, 197 (1991)
3. J. J. Spivey, "Complete Catalytic Oxidation of Volatile Organics," *Ind. Eng. Chem. Res.* **26**, 2165 (1987)
4. B. K. Cho, "Performance of Pt/Al₂O₃ Catalysts in Automobile Engine Exhaust with Oscillatory Air/Fuel Ratio," *Ind. Eng. Chem. Res.* **27**, 30 (1988)
5. R. W. Baier, W. M. Graren, H. D. Linhardt, R. C. Oliver, D. L. Peters, and S. W. Weller, "Final Report: Feasibility Study of Catalytic Methods of Air Purification," U. S. Army CRDEC Publication No. C-2767, Aberdeen, MD, 1964
6. G. R. Lester and G. C. Joy, "Low Temperature Air Purification Catalysts," *Proc. 1990 Sci. Conf. on Chem. Defence CRDEC*, Aberdeen, MD, 1987
7. D. S. Y. Hsu and P. Nazario-Gonzalez, "Destruction of Perfluoropropene over the NRL-1000 Oxidation Catalyst," *Proc. 1990 Sci. Conf. on Chem. Defence CRDEC*, Aberdeen, MD, 1990
8. P. Nazario-Gonzales and D. S. Y. Hsu, "Catalytic Oxidation of Monochlorodifluoromethane (Freon 22) over the NRL-1000 Oxidation Catalyst," *Proc. 1990 Sci. Conf. on Chem. Defence CRDEC*, Aberdeen, MD, 1990
9. J. A. Rossin, "Effects of Pre-treatment Conditions on the Activity of a 1% Pt/Al₂O₃ Catalyst," *J. Mol. Catal.* **58**, 363 (1990)
10. J. A. Rossin, "Complete Catalytic Oxidation of Diethyl Sulfide over a 1% Pt/Al₂O₃ Catalyst: Effects of Mass Transfer on Reactivity," *Proc. 1989 Sci. Conf. on Chem. Defence CRDEC*, Aberdeen, MD, 1989
11. J. A. Rossin, "Complete Catalytic Oxidation of Diethyl Sulfide over a 1% Pt/Al₂O₃ Catalyst: Effects of Mass Transfer on Reactivity," *Ind. Eng. Chem. Res.* **28**, 1562 (1989)
12. C. S. Dulcey, M. C. Lin, and C. C. Hsu, *Chem Phys. Lett.* **115**, 481 (1985)
13. J. A. Rossin, *J. Mol. Catal.* **58**, 363 (1990)
14. J. T. Kummer, "Laboratory Experiments Evaluating the Effects of S and Cu on Pt-Al₂O₃ Auto Exhaust Oxidation Catalysts," *J. Catal.* **38**, 166 (1975)
15. C. F. Cullis and B. M. Willat, "The Inhibition of Hydrocarbon Oxidation over Supported Precious Metal Catalysts," *J. Catal.* **86**, 187 (1984)

BLANK

XIII. SYNTHESIS AND PROPERTIES POSTERS

BLANK

PREDICTING LIQUID DENSITIES OF ORGANIC COMPOUNDS
I. HALOGENATED AND OXYGENATED

Gerry O. Wood and Travis B. Weaver
Los Alamos National Laboratory
Mail Stop K-486, Los Alamos, NM 87545

Abstract

A new model has been developed and applied for correlating and predicting liquid densities near 20 °C. While extensive tabulations of liquid densities exist, there are many exotic and highly toxic chemicals not included for obvious reasons. The products of liquid density and molecular weight were found to be linear functions of number and types of carbon atoms in the molecule. Increments provided by halogens and oxygens were best described by quadratic functions. Oxygen increments were independent of types of functional groups, including polar and hydrogen bonding molecules.

I. Introduction

In developing a mathematical model that could be used to predict adsorption capacities of carbon beds for organic vapors, liquid densities were needed as input. Although extensive tabulations of liquid densities exist,^{1,2} not all of the hundreds of thousands of possible organic compounds are included. Furthermore, look-up tables are not very efficient for computer calculations.

Methods of calculating liquid densities at various temperatures have been developed.^{2,3} However, these require input of physical data, such as critical temperatures and pressures, and/or a reference experimental density at some temperature. Again, such data are available for only some liquids. The goal of the efforts reported here was to find a way of estimating liquid densities from a minimum of information.

We were interested, at least initially, only in liquid densities near normal ambient temperatures. The CRC Handbook of Chemistry and Physics lists densities for many liquids, usually

at 20 °C.¹ We used values reported within the 19-25 °C range.

II. Empirical Correlations for Hydrocarbons

Figure 1 shows plots of liquid densities versus number of carbon atoms for saturated and unsaturated straight and branched chain hydrocarbons. We found that when liquid density times molecular weight (LDxMW) was plotted against number of carbon atoms, the results converged into a linear correlation (Figure 2). Intuitively, it would be expected that density would be proportional, rather than inversely proportional to molecular weight. However, the latter produced a function independent of 1) number of hydrogen atoms and 2) types of bonds in a hydrocarbon molecule.

When this approach was applied using data for purely cyclic and aromatic hydrocarbons, similar results were obtained (Figures 3 and 4). However, the slope of the LDxMW versus number of carbon atoms plot was higher. This is reasonable, since a cyclic structure is more compact and would result in greater density. The LDxMW values for hydrocarbons containing both straight/branched carbons and cyclic/aromatic carbons were intermediate, as would be expected.

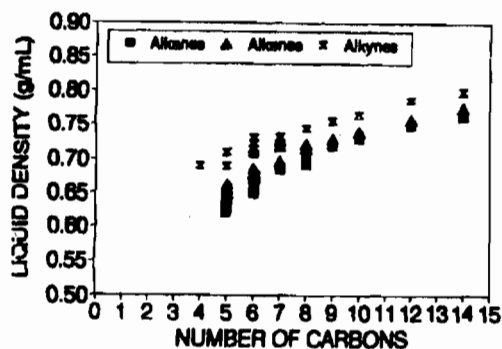


Figure 1.

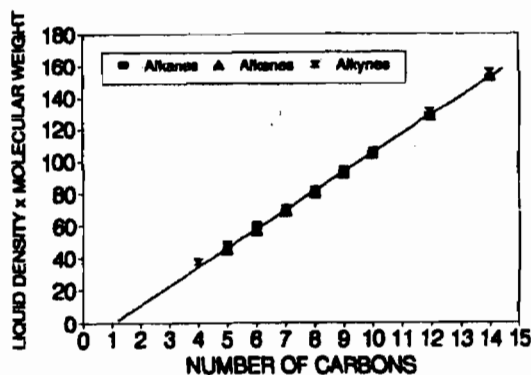


Figure 2.

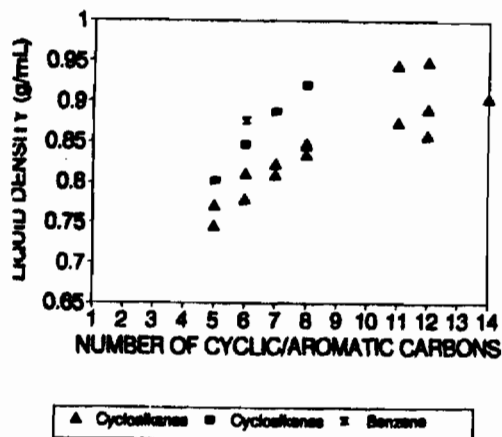


Figure 3.

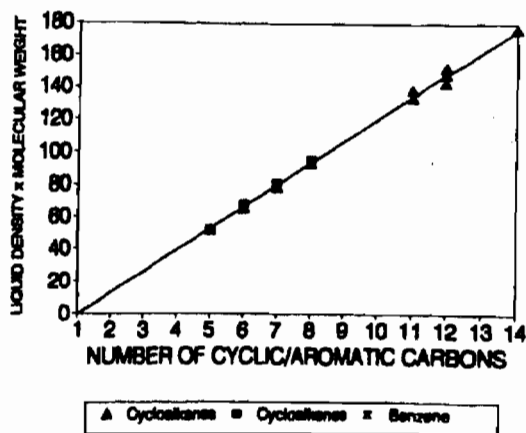


Figure 4.

Using these empirical relationships, densities of 105 hydrocarbons (46 straight/branched, 20 cyclic/aromatic, and 39 mixed) were correlated to give:

$$\text{Liquid Density (g/mL)} = \frac{(11.639 \cdot C + 13.803 \cdot CC - (12.104 \cdot C + 17.128 \cdot CC))}{(C + CC) \cdot MW}$$

where C is the number of carbons not part of a ring, CC is the number of cyclic carbons, and MW is molecular weight. The correlation constants were obtained by fitting this equation using a nonlinear curve fitting program (SYSTAT from SYSTAT, Inc., Evanston, IL) on an IBM-PC compatible desktop computer. The standard deviation of 105 experimental points from this correlation was 0.017 g/mL. Calculated and experimental densities are compared in Figure 5.

III. Extension to Halocarbons

The next step was to observe the effect on liquid densities of replacing hydrogen atoms on hydrocarbons with chlorine atoms. Figure 6 shows that chlorines shift the intercept, but do not affect the slope, of the LDxMW vs C plot. This shift is more than linear with the number of chlorine atoms. The same result was observed for chlorinated cyclic and aromatic hydrocarbons.

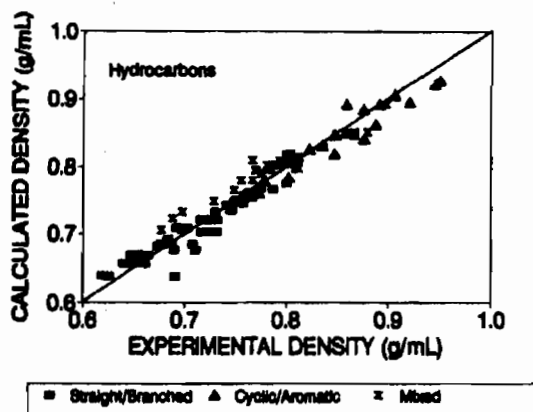


Figure 5.

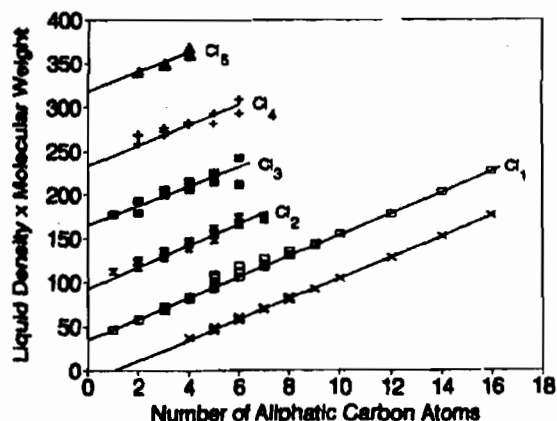


Figure 6.

The correlation equation was extended to include the number of a second heavy atom, X:

$$\text{Liquid Density (g/mL)} = \frac{(11.639 \cdot C + 13.803 \cdot CC + S \cdot X + Q \cdot X^2 - (12.104 \cdot C + 17.128 \cdot CC + I \cdot X))}{(C + CC + X) \cdot MW}$$

Correlation coefficients S, Q, and I for fluorocarbons, chlorocarbons, bromocarbons, and iodocarbons are listed in Table 1. Standard deviations of the data fits ranged from 0.043 g/mL for fluorine, the lightest halogen, to 0.113 g/mL for iodine, the heaviest.

TABLE 1.

Liquid Density Coefficients for Hydrocarbons

Class	Number of Data	Coefficients			Standard Deviation (g/mL)
		S	Q	I	
Straight/ Branched (C)	105	11.639	0	12.104	0.017
		13.803	0	17.128	
Cyclic/ Aromatic (CC)					
Oxygenated	172	21.523	1.486	3.658	0.052
Fluorinated	22	51.522	-0.417	166.160	0.043
Chlorinated	126	52.720	3.036	31.032	0.054
Brominated	56	85.567	34.472	-127.687	0.095
Iodinated	33	131.644	102.962	-170.761	0.113

Figures 7-10 show comparisons of calculated and experimental densities. Note: The correlations do not yet include mixed halocarbons, e.g., chlorofluorocarbons.

IV. Extension to Oxygenated Hydrocarbons

Unlike halogens, oxygen atoms can be incorporated into hydrocarbon structures in a variety of functional groups, forming alcohols, aldehydes, ketones, esters, ethers, acids, and epoxides. These classes of oxygenated compounds exhibit wide differences in polarity and hydrogen bonding, which would be expected to significantly affect liquid density. Figures 11 and 12 show the surprising result that liquid densities of oxygenated hydrocarbons can again be correlated by structure alone, ignoring polarity and hydrogen bonding properties.

The effect of multiple oxygens in straight/branched chain hydrocarbons is shown in Figure 13 to be similar to that seen for chlorine. Intercepts of LDxMW versus C are shifted more than linearly for increasing numbers of oxygen atoms; the slope is essentially unchanged.

Correlation coefficients given in Table 1 were obtained using densities for 172 oxygenated hydrocarbons, representing the classes of compounds listed above. The standard deviation of the fit was 0.052 g/mL. Figure 14 shows a graphical comparison of calculated and experimental values. Note: The correlations do not yet include compounds where oxygen is incorporated into a ring structure.

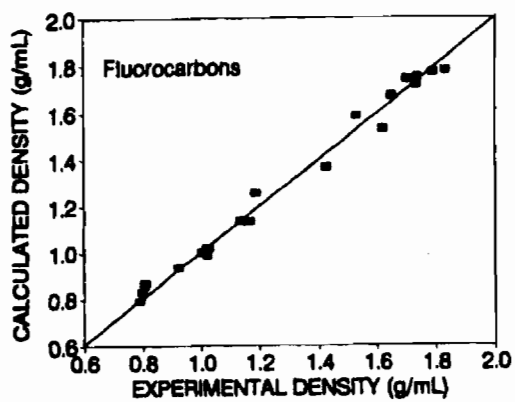


Figure 7.

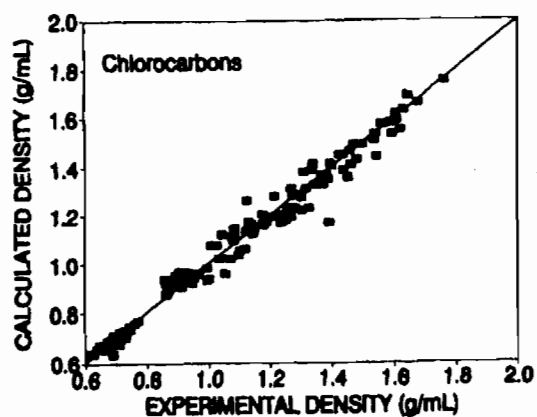


Figure 8.

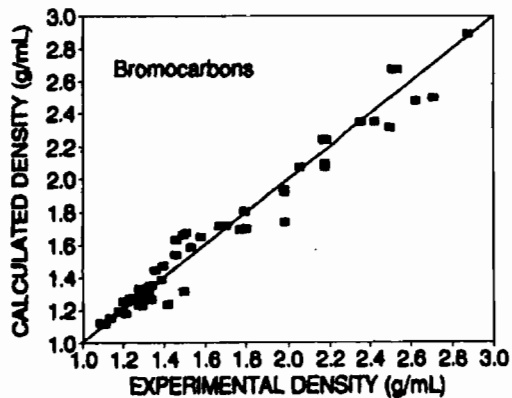


Figure 9.

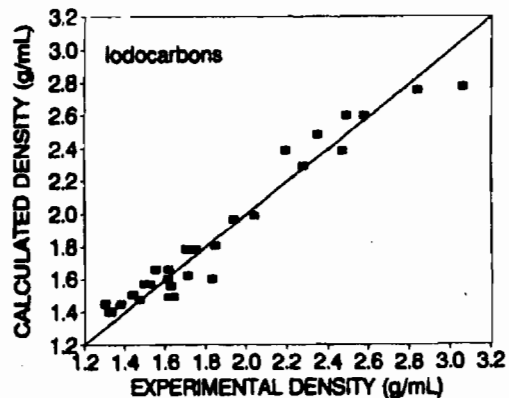


Figure 10.

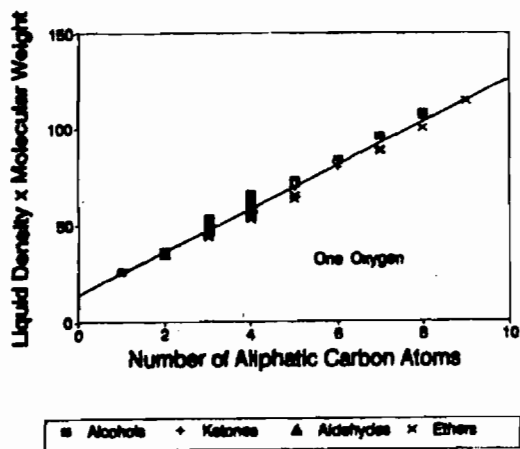


Figure 11.

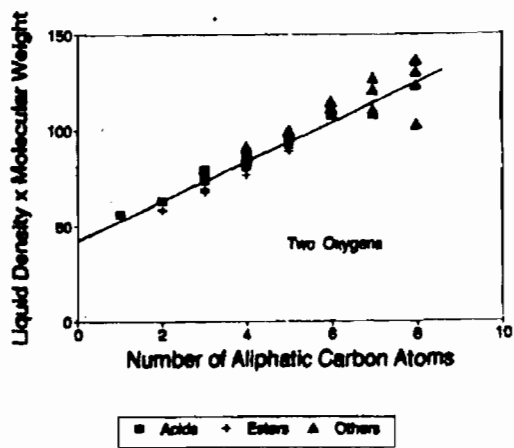


Figure 12.

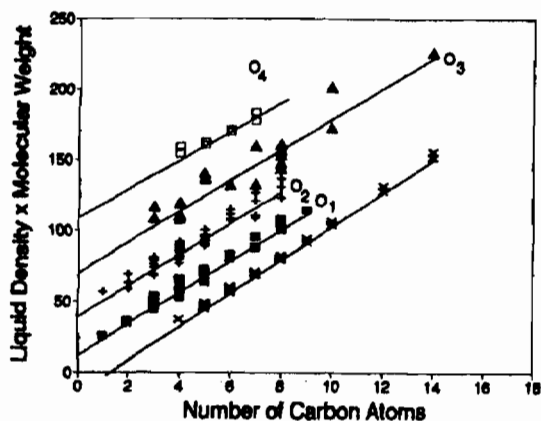


Figure 13.

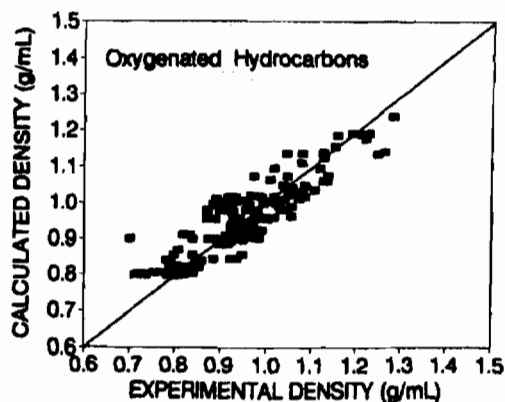


Figure 14.

CONCLUSIONS

Correlations have been developed for estimating densities of liquids near 20 °C. The only information that needs to be known is: 1) carbon atom number and type (cyclic or not) and 2) other heavy atom number and type (F, Cl, Br, I, O). Effects of polarity and hydrogen bonding have not been observed in these correlations, but may provide second-order improvements in these estimates. Applications of these correlations include: 1) Checking reported densities. [Some suspicious values have been found in Reference 1.] 2) Calculating unknown densities, such as for exotic or highly toxic liquids. 3) Calculating by computer other properties, such as carbon adsorption capacity, that require liquid density as input. [This avoids the inefficient use of look-up tables.]

REFERENCES

1. Weast, R. C., ed., CRC Handbook of Chemistry and Physics, 67th Edition, pp C42-C553, CRC Press, Inc., Boca Raton, Florida (1987).
2. Reid, R. C., J. M. Prausnitz, and B. E. Poling, The Properties of Gases & Liquids, Fourth Edition, McGraw-Hill Book Co., New York (1987).
3. Lyman, W. J., W. F. Reehl, and D. H. Rosenblatt, Handbook of Chemical Property Estimation Methods, Chapter 19, McGraw-Hill Book Company (1982).

RELATIONS BETWEEN NUCLEOPHILICITY AND ACIDITY OF OXIMES

Frédéric Guir
Direction des Recherches, Etudes et Techniques
Centre d'Etudes du Bouchet, B.P. N° 3
91710 Vert-le-Petit, France

François Terrier
Ecole Nationale Supérieure de Chimie de Paris
Laboratoire de Physicochimie des Solutions
11 rue Pierre et Marie Curie
75231 Paris Cedex 05, France

The acidity (pK_a) of several families of oximes and the nucleophilicity of their oximate ions ($\log k$, where k is the rate constant of the reaction of the oximate ions of the oximes with *p*-nitrophenyl acetate) were measured. No satisfactory Brønsted line can be drawn on plotting the statistically corrected $\log k$ values versus the statistically corrected pK_a values. A levelling off of the nucleophilicity of oximate ions is observed at $pK_a > 8$, i.e. for $pK_a > 8$ the reactivity of oximate ions does not increase any more with pK_a . As a consequence of this, the oximes showing the highest level of reactivation of Ache inhibited by organophosphorus compounds (a reactivation process based upon a nucleophilic displacement) have a pK_a in the range 7.5 - 8, which allows a fairly good degree of ionisation at the physiological pH (7.8) and the highest expression of the nucleophilicity of their oximate ions. Finally the measure of the pK_a of an oxime is a good indicator of the nucleophilicity and the reactivating power of its oximate ion.

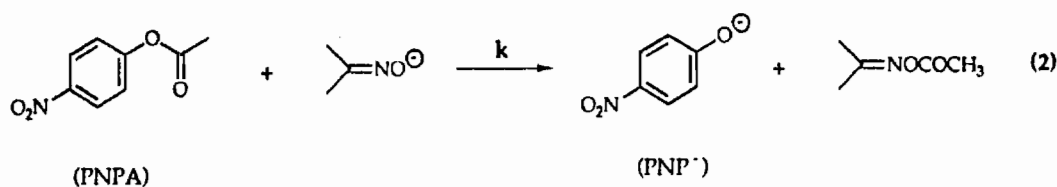
INTRODUCTION

The choice of a new oxime used as a reactivator of organo-phosphorus compounds inhibited Acetylcholinesterase (Ache) is obviously based on biological tests. But as far as a nucleophilic displacement of the phosphorylated enzyme by an oximate ion is thought to take place during the reactivating process of Ache, it seemed interesting to characterize the nucleophilicity of the oxime and its behaviour in relation with its acidity, in order to see if any relationship between nucleophilicity and acidity can be drawn and if a quite simple measurement of acidity (pK_a) could lead to a primary assessment of the reactivating potency of an oxime.

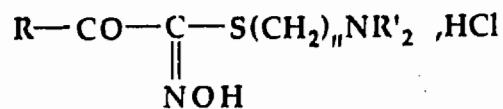
METHODOLOGY

The acidity of oximes was measured at 25°C by standard potentiometric methods using aqueous oximate buffer solutions with various [oximate]/[oxime] ratios, the ionic strength, I, being maintained at 0.1M by adding KCl as needed.

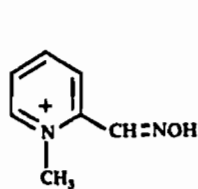
The nucleophilicity of the oximate ions was measured through the rate constant *k* of the nucleophilic displacement of the oximate ion towards a model electrophile namely *para*-nitrophenylacetate (PNPA). This constant *k* was deduced from the initial rates of appearance of *p*-nitrophenate anions in series of experiments which were conducted with a large excess of PNPA over the concentration of the various oximate ions.



Reaction of oximate ions with PNPA

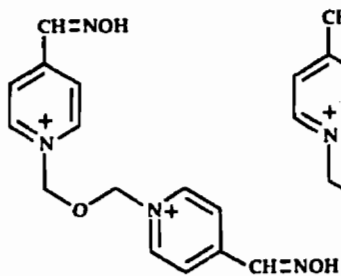


- | | | |
|-------------|----------------------------|-------------------|
| 11a: | $n = 2, R = 4-NO_2C_6H_4$ | $R' = C_2H_5$ |
| 11b: | $n = 2, R = CH_3$ | $R' = C_2H_5$ |
| 11c: | $n = 2, R = C_6H_5$ | $R' = C_2H_5$ |
| 11d: | $n = 2, R = 4-CH_3OC_6H_4$ | $R' = C_2H_5$ |
| 11e: | $n = 2, R = 4-CH_3OC_6H_4$ | $R' = CH_3$ |
| 11f: | $n = 2, R = 4-CH_3OC_6H_4$ | $R' = (CH_3)_2CH$ |
| 11g: | $n = 3, R = 4-CH_3OC_6H_4$ | $R' = CH_3$ |



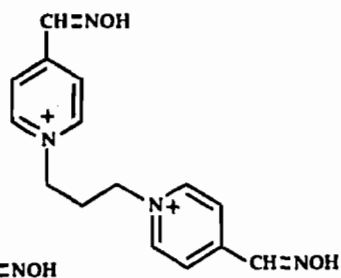
2-PAM

1



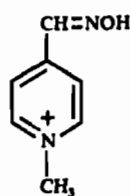
Toxogonine

2



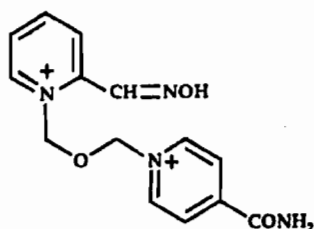
TMB 4

3



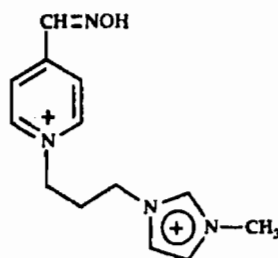
4-PAM

4



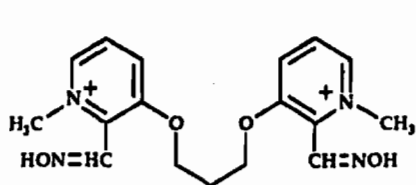
HI-6

5



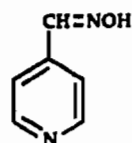
CEB 1574

6



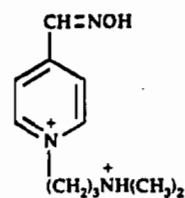
R-665

7

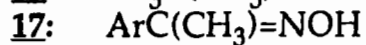
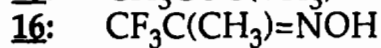
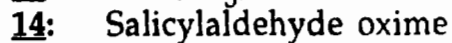
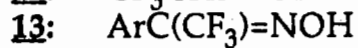
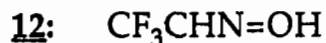
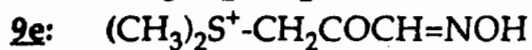
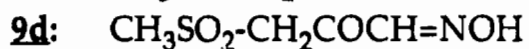
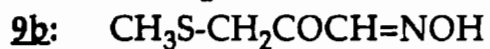
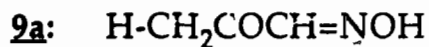


4-PA

8



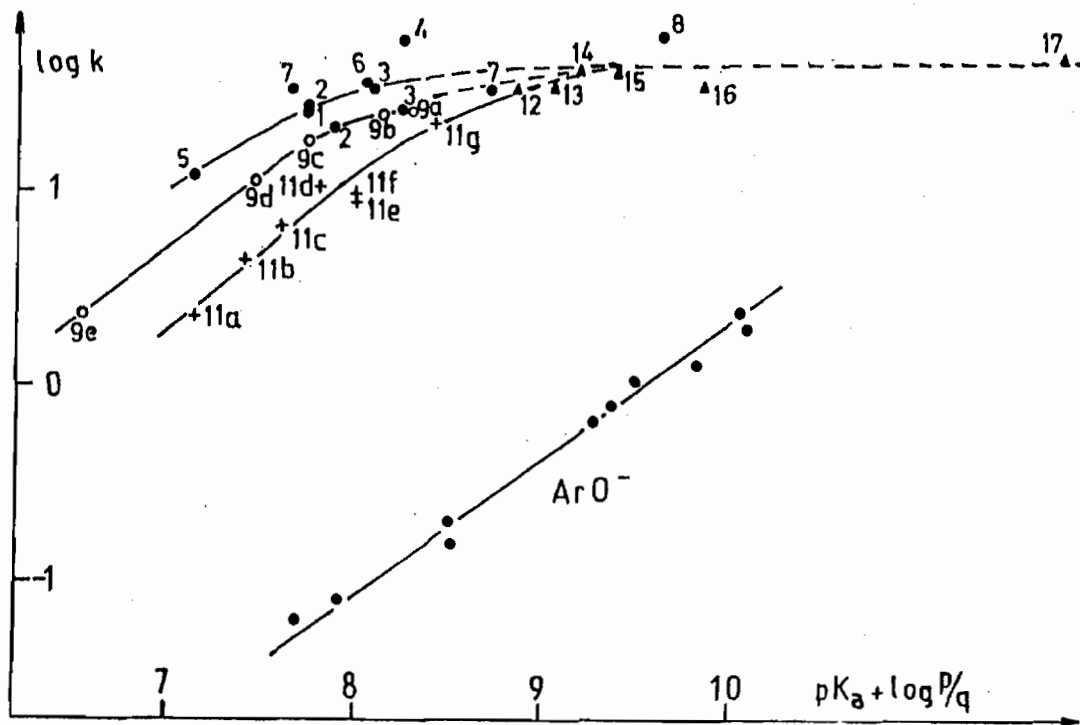
10



pK_a values and kinetic parameter for the reactions of mono- and di-oximate ions derived from 1-8 with PNPA in aqueous solution.

Parent oxime	N°	pK _{a1}	pK _{a2}	K ₁ /dm ³ mol ⁻¹ s ⁻¹	K ₂ /dm ³ mol ⁻¹ s ⁻¹
HI 6	5	7.13 7.28		11.8	
R665	7	7.33	9.02	34.5	63.3
Toxogonine	2	7.46 7.54,7.55	8.17 8.12,8.20	22.3,20.74	37.2,39.6
2-PAM	1	7.75 7.68,7.92,7.99,8		25 16	
TMB 4	3	7.79 7.78,7.99	8.55 8.61,8.68	32.1	48
CEB 1574	6	8.05		35	
4-PAM	4	8.27 8.55		61	
Pyridine-4-carbaldehyde oxime	8	9.55 9.65		65.63	

Brönsted plot for the reactions of oximate ions and phenoxide anions with PNPA in aqueous solutions at T=25°C.



DISCUSSION

No satisfactory Brønsted line can be drawn on plotting the statistically corrected $\log k$ values for the reactions of the various mono- and di-oximate ions of 1-8 with PNPA versus the corresponding statistically corrected pK_a values (Figure 1). Nevertheless Figure 1 shows the two different linear Brønsted plots of similar slope corresponding to a β_{nuc} value of *ca.* 0.7 analogous to that for the phenoxide reactions that were defined for the reactions of moderately basic oximate ions of general structure 9 and 11 with PNPA. However, a very important feature which emerges from Figure 1 is that these plots start to curve at around pK_a 8 with the observed curvature fitting, apparently well, the data previously obtained for a number of structurally different and more basic oximate ions (pK_a 8-11). Since we have suggested that this levelling off in the reactivity is typical for the behaviour of all relatively basic oximate ions, it is interesting to find that the data obtained for 1-8 support this idea. While the reactivity of the less basic pyridiniumcarbaldoximate ions studied is slightly higher than that of similarly basic species in series 9 and 11, it is clear that the reactivity of most basic pyridinium aldoximate ions tends to level off to about the same limit as all other basic oximate species, including the oximate ion derived from the neutral pyridinecarbaldehyde oxime 8. This levelling off effect is thought to be due to a strong requirement for desolvation of oximate ions before their nucleophilic attack can proceed.

CONCLUSIONS

The pyridinium aldoxime family has a chemical reactivity greater than any other oximes family but their nucleophilicity behaves at higher pK_a the same way as other oximes do: a levelling-off effect in their reactivity is also reached at $pK_a > 8$. This effect is a key-element in a quick assessment process of the efficiency of an oximate ion as an antidote of nerve agents poisoning. Even if the reactivating efficiency implies good biochemical properties, a strong nucleophilicity of the oximate ion is required. At the reactivation pH (7.8), the saturation of reactivity around $pK_a = 8-8.3$ shown by the Brønsted plot, indicates that good reactivating oximes should be found with a pK_a close to 8 which combines a strong nucleophilicity with a sufficient ionisation at the reactivation pH. This is the case of all oximes currently used as Ache reactivator apart from HI 6. Finally the measure of the pK_a of a new oxime represents a primary assessment test of its reactivating potency through its location on the Brønsted plot.

REFERENCES

Non-linear Brønsted correlations: Evidence for a levelling off in the reactivity of oximate ions in aqueous solution.

F. Terrier, P. MacCormack, E. Kizilian, J-C. Hallé, P. Demerseman, F. Guir and C. Lion; *J. Chem. Soc. Perkin Trans. 2*, 1991, p. 153-158.

BLANK

SOME PHYSICOCHEMICAL AND PHARMACOLOGICAL CHARACTERISTICS OF
1-SUBSTITUTED-4-PHENYL-4-PIPERIDINOLS AND THEIR ESTERS

James W. King¹, William R. Hydro², and W. James Lennox³

ABSTRACT

The title esters, generally referred to as prodines, are known for their analgetic potency. Their duration of activity has been presumed to depend on the *in vivo* rates of N-dealkylation, hydrolysis of the ester linkage, and likely, *para*-hydroxylation of the 4-phenyl moiety. To investigate the influence of "simulated" physiological conditions on compound stability, a series of 1-cinnamyl substituted-4-phenyl-4-propionoxypiperidinium chlorides, 1-(3-phenylpropyl)-4-phenyl-4-propionoxypiperidinium chlorides and 1-benzoylethyl substituted-4-phenyl-4-piperidinols and the latter's propionate esters were examined at pH 7.38 and 37°C in aqueous alcohol. The 1-benzoylethyl compounds undergo an incomplete N-dealkylation whereas the 1-cinnamyl and 1-phenylpropyl series are unaffected even after a prolonged time period; the rate of ester hydrolysis in all series is extremely slow under these conditions. The pKa values for a number of compounds in the series were determined; subsequently, their octanol/water partition coefficients were calculated.

INTRODUCTION

In the study of series of compounds with pharmacological activity(s) of interest, the prudent investigator will consider the effect of metabolism as it relates to alteration of the compound or as it affects the nature of the activity. A primary aspect of such considerations is the pKa of the compound as it determines the extent of ionization at physiological pH and thus dictates to some extent physiological transport properties, nature of drug-receptor interaction, metabolic lability, etc. Further, octanol/water partition coefficients often reveal transport potential or indicate water and lipid propensities *in vivo*. It was the objective of the studies reported herein to bring these and other considerations to bear on series of phenylpiperidine-type analgesics, known collectively as prodines, for the purpose of understanding the influence of substituents on their bioactivity. Such knowledge

could then be applied in the design of new compounds with improved or selected physicochemical and/or pharmacological characteristics.

Lednicer has recently discussed the synthesis and analgesic activity of the phenylpiperidines and related compounds.⁴ The prototype in these series is meperidine (I), a compound still widely prescribed for pain relief more than 50 years after its discovery. The prodines, with the general structure II, are reversed esters of I, and because of the steric hindrance afforded by the phenyl and piperidine rings, less prone to hydrolysis, as will be shown below.



A second and more obvious difference is the substituent on the nitrogen. In the prodine series, the benzoylethyl, cinnamyl, and phenylpropyl groups have been prominent and are included herein.

In addition to ester hydrolysis as a means of deactivation of the prodines (the free piperidinols are generally devoid of significant analgetic activity⁵) the potential for *in vivo* N-dealkylation has been suggested and was one of the objects of this study.^{6,7} The principal remaining metabolic lability of these compounds is *para*-hydroxylation of the phenyl rings; this aspect is beyond the scope of this report.

In an initial study such as this, the determination of the parameters noted above would be undertaken in water solution with dilute acid or base being used to titrate the compounds for pK determination or to maintain pH in hydrolysis or dealkylation studies. However, compound insolubility required the addition of alcohol to effect solubility. Under these circumstances, the conditions cannot be said to simulate those *in vivo*; nevertheless, the ultimate import of such information mandated its generation.

METHODOLOGY

A. Materials and Equipment

The compounds used in this study were prepared in these Laboratories.⁸⁻¹³ A Beckman Model 76 pH meter was used for measurement in pK determinations and a Beckman Model K Automatic Titrator was used in the pH-stat mode for kinetic experiments. Water-jacketed reaction cells with pH electrodes were maintained at $37.2 \pm 0.2^\circ \text{C}$ under nitrogen. The reaction solution (50% aqueous ethanol) was stirred with a magnetic stirrer and a microburette was used to add acid or base as appropriate; pK values were determined from a plot of titrant volume *vs* pH.

B. Conduct and Analysis of Kinetic Studies.

The behavior of the esters or alcohols in aqueous alcohol solution was monitored by a pH-stat set to maintain pH 7.38 after initial adjustment of the solution to pH 7.4. The kinetic data was assumed to be first order since hydroxide ion was held constant. The rate constants were determined by an expression given by Laidler.¹⁴

C. Partition Coefficients.

The logarithm of the octanol/water partition coefficients were calculated manually by following published procedures.^{15,16} A computerized method is now available commercially.¹⁷

D. Pharmacology.

The bioactivity data noted in the tables herein was developed using standard pharmacological screening methods.¹⁸

RESULTS

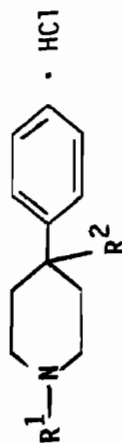
The results of the experimentation performed as noted above are shown in the accompanying tables.

DISCUSSION

A general perusal of Tables 1-5 indicates that no direct relationship exists between pKa and bioactivity of the prodines, assuming, of course, little change in the pKa's if extrapolated to actual physiological conditions. The same can be inferred regarding the partition coefficient data. This is not to suggest that a mathematical model incorporating pKa, partition coefficient and bioactivity could not be derived, but such is beyond the scope of this report. What the data does show is that the 1-(2-benzoyl-ethyl) substituent is labile under mild conditions while the 1-cinnamyl and 1-phenylpropyl type compounds are extremely stable and not N-dealkylated. This is because the former is subject to a reverse Michael reaction that cannot take place with the latter substituents. In fact, addition of phenylhydrazine to a typical hydrolysis mixture of the 1-(2-benzoyl-ethyl)-4-phenyl-4-propionoxypiperidinium chloride, gave 1,3-diphenyl-2-pyrazoline, thus confirming the dealkylation reaction. Also, addition of phenyl vinyl ketone (prepared by dry distillation of 2-benzoyl-ethyl-dimethylamine as described by Young and Roberts¹⁹) to a typical hydrolysis mixture containing 4-phenyl-4-propionoxypiperidinium chloride, and monitored by pH-stat, required the neutralization of liberated acid. Further, 1-propionyl-4-phenyl-4-piperidinol was isolated from a typical hydrolysis mixture after 24 hours.

TABLE 1

Physicochemical Parameters - Esters

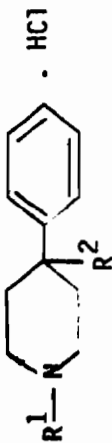


EA No.	R ¹	R ²	pKa	CLOGP*
2221	Benzoyl ethyl	Propionoxy	6.8	2.62
2236	4-Methoxybenzoyl ethyl	-do-	6.83	2.71
2392	3-Nitrobenzoyl ethyl	-do-	6.90	-
2422	Benzoyl ethyl	Acetoxy	6.90	-
2228	4-Fluorobenzoyl ethyl	Propionoxy	6.65	2.76
2464	Benzoyl propyl	-do-	7.30	-
3287	4-Chlorobenzoyl propyl	-do-	7.28	-
2219	Cinnamyl	-do-	7.00	3.62
2230	4-Fluorocinnamyl	-do-	6.94	3.76
2240	2-Chlorocinnamyl	-do-	6.63	4.21
2475	2-Nitrocinnamyl	-do-	6.51	3.39
2535	3-(1-Naphtho)-2-propenyl	-do-	7.50	4.77
2393	Cinnamyl	Cinnamoxy	6.85	-
3480	Hydrogen	Propionoxy	8.92	-
2265	Benzyl	-do-	6.83	-
3367	2-Propenyl	-do-	7.15	-
3306	3-(4-Fluorophenyl)-3-hydroxypropyl	-do-	7.96	2.80
3439	Phenylpropyl	-do-	7.36	4.02
3387	4-Chlorophenylpropyl	-do-	7.36	4.73
3407	4-Methylphenylpropyl	-do-	7.39	4.47

* Calculated as the free base

TABLE 2

Pharmacological Data - Esters

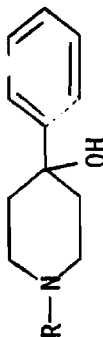


EA No.	MICE			MONKEYS		
	LD 50 (mg/kg)	MED 50 (mg/kg)	AFD 50*	LD (mg/kg)	MED (Prostration) (mg/kg)	No Effect (mg/kg)
2221	12.6	0.0063	0.492	0.03	0.005	0.001
2236	15.8	ca 0.1	0.740	--	--	0.1
2392	20.0	0.56	--	--	0.01	--
2422	12.6	0.023	--	--	--	0.001
2228	14.1	0.005	0.014	0.03	0.01	0.001
2464	28.2	0.0178	--	--	--	--
3287	20.0	0.316	--	--	--	--
2219	17.8	0.0158	--	0.03	0.02 Collapse	--
2230	20.0	0.00032	--	--	0.01 Signs	--
2240	31.6	0.56	0.238	0.25	0.05	0.01
2475	28.2	0.000056	0.001	0.1	0.05	0.01
2535	56.2	0.178	4.128	0.15	0.1	0.01
2393	178	5.6	--	--	--	0.1
3480	44.7	0.178	--	--	--	0.1
2265	22.4	>0.1<0.32	--	--	--	0.1
3367	44.7	0.178	--	--	--	--
3306	--	--	1.327	--	--	--
3439	25.1	0.0178	0.155	0.1	--	0.01
3387	17.8	0.0178	0.758	--	--	--
3407	28.2	0.00562	1.393	0.1	--	0.01

* Analgesic ED 50, micromoles/kg

TABLE 3

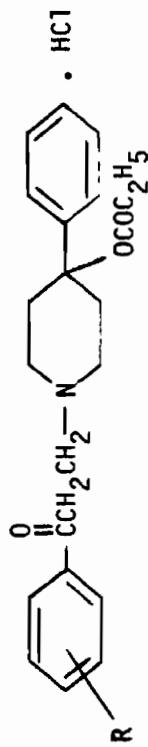
Physicochemical and Pharmacological Parameters - Alcohols



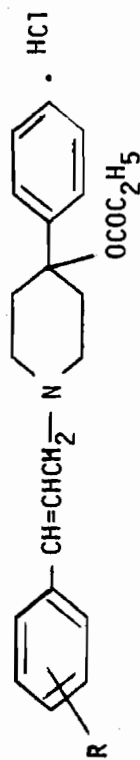
EA No.	R ¹	pKa	LD 50 (mg/kg)	MED 50 (mg/kg)
3171	Benzoylethyl	6.38	11.2	3.2
2227	4-Fluorobenzoylethyl	6.46	15.8	2.5
2362	4-Bromobenzoylethyl (HCl Salt)	7.05	44.7	5.6
2235	4-Methoxybenzoylethyl	6.43	40	>0.1 < 0.32
3364	2-Fluorobenzoylethyl	6.47	17.8	1.78
3309	4-Chlorophenylpropyl	6.28	-	-
2615	2-Chlorophenylpropyl	6.19	17.8	0.75
2216	3-Phenyl-3-hydroxypropyl	5.60	44.7	ca 3.2
2217	3-(4-Fluorophenyl)-3-hydroxypropyl	6.06	40	>1.0 < 3.2
2389	Benzoylpropyl	5.63	25	1.78
3525	2-Benzoyl-2-Methylethyl (HCl Salt)	7.45	17.8	1.78
2237	Benzoyl (HCl Salt)	7.87	15.8	ca 1.0
2218	Cinnamoxyl	6.30	8.9	ca 1.0
2405	2-Nitrocinnamyl	6.43	-	-
2407	3-Nitrocinnamyl	6.72	-	-
2442	2-Chlorocinnamyl	6.71	8.9	1.78
3441	4-Methylcinnamyl	6.26	17.8	1.78

TABLE 4

Relative Rates of N-Dealkylation - Esters



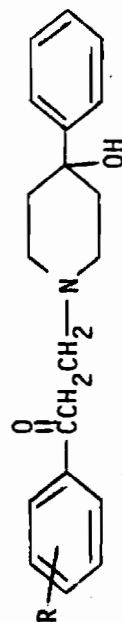
EA NO.	R	Hammett σ for R	Time (t_0) to half Acid Consumption (minutes)	K	Average % Cleared at Equilibrium
2236	4-Methoxy	-0.27	28	0.77 ± 0.15	40
2221	Hydrogen	0.00	14	1.68 ± 0.06	49
2228	4-Fluoro	+0.06	10	2.39 ± 0.27	43
2392	3-Nitro	+0.71	4	7.8 ± 1.0	56



2219	Hydrogen	0.00	-	ca. 0	ca. 0
2230	4-Fluoro	+0.06	-	ca. 0	ca. 0
2475	2-Nitro	-	-	ca. 0	ca. 0

TABLE 5

Relative Rates of N-Dealkylation - Alcohols



EA No.	R	Hammett σ for R	Time (t_0) to Half Acid Consumption (minutes)	K	Average % Cleaved at Equilibrium
2235	4-Methoxy	-0.27	40	0.29 ± 0.01	22
3171	Hydrogen	0.00	29	0.55 ± 0.08	28
2227	4-Fluoro	+0.06	21	0.62 ± 0.02	24
2362	4-Bromo	+0.23	6	2.11 ± 0.34	26
3631	3-Fluoro	+0.34	11	1.83 ± 0.08	37
2391	3-Nitro	+0.71	3.5	8.1 ± 1.4	58

The fact that dealkylation is only partial is seen in the data of Table 4, and in general, the behavior of the esters and the precursor alcohols is quite similar (Table 5). Hydrolysis of the ester linkage is also a relatively slow process. Treatment of the 1-(2-benzoyl-ethyl) compound with excess aqueous alcoholic base at 60° C, gave only 42% hydrolysis of the propionoxy linkage in 7 hours. Hydrolysis of 1-cinnamyl-4-phenyl-4-propionoxypiperidinium chloride and 1-benzyl-4-phenyl-4-propionoxypiperidinium chloride was attempted at 37° C in 50% methanolic potassium chloride solution to which was added diluted blood serum. The mixture containing the former compound was monitored for 23 hours (pH-stat) and the latter for more than 3 days. No conclusive evidence of hydrolysis appeared in either event.

CONCLUSIONS

Under "pseudo-simulated" physiological conditions, the title esters are stable to hydrolysis. Partial N-dealkylation of the esters and precursor alcohols takes place only in the case of the 1-(2-benzoyl-ethyl)-substituted compounds, where a reverse Michael reaction is possible. Neither pKa nor partition coefficient values of the esters appear to correlate directly with the specifically observed pharmacological indices; however, this data may find justification in a structure/property-bioactivity model.

ACKNOWLEDGMENTS

The authors are grateful to Mrs. Barbara C. LaGrange for her assistance in composing this report. We are pleased to note the technical contributions of Dr. Richard J. Sundberg and Mr. R.C. Smith. We shall always be indebted to the late Dr. F.W. Hoffmann for his leadership and teaching. We thank Mr. C. Parker Ferguson, Chief, Organic Chemistry Branch, and Dr. John F. Weimaster for their interest and continuing support. We especially appreciate the enthusiastic tolerance and encouragement of Mr. Joseph D. Williams, Program Coordinator for Research Directorate and the Conference.

REFERENCES

1. U.S. Army Chemical Research, Development and Engineering Center (CRDEC), Aberdeen Proving Ground, Maryland 21010-5423.
2. Formerly a senior research chemist, Organic Chemistry Branch, Chemical Division, Research Directorate, CRDEC; now retired.

3. Present address: U.S. Army Medical Research Institute of Chemical Defense, Aberdeen Proving Ground, MD 21010-5425.

4. D. Lednicer. Central Analgetics. John Wiley and Sons, Inc., New York, NY. 1982. p. 173 ff.

5. A.F. Casey and A.H. Beckett. 4-Alkoxy piperidines Related to Reversed Esters of Pethidine. J. Pharm. Pharmacol. 13, 161 T (1961).

6. A.H. Beckett, A.F. Casey, and H.J. Harper. Analgesics and Their Antagonists. Some Steric and Chemical Considerations. Part III. The Influence of the Basic Group on the Biological Response. J. Pharm. Pharmacol. 8, 874 (1956).

7. A.F. Casey, et al. Chemistry and Pharmacology of 4-Alkoxy piperidines Related to Reversed Esters of Pethidine. J. Med. Pharm. Chem. 4, 535 (1961).

8. D.H. Wadsworth, et al. CRDLR 3152. Compounds of the α -Prodine Type. I. The Preparation of Several 1-Cinnamyl-4-phenyl-4-piperidinols and Their Esters. January 1963. UNCLASSIFIED Report.

9. D.H. Wadsworth, R.L. Hively, and F.W. Hoffmann. CRDLR 3157. Compounds of the α -Prodine Type. II. The Preparation of Several 1-(2-Benzoyl ethyl)-4-phenyl-4-piperidinols and Their Esters. Preparation of Several 1-Substituted-4-phenyl-1,2,3,6-tetrahydro pyridines. January 1963. UNCLASSIFIED Report.

10. D.H. Wadsworth, et al. CRDLR 3166. Compounds of the α -Prodine Type. III. The Preparation of Several 1-Substituted-4-aryl-4-Piperidinols and Their Esters. January 1963. UNCLASSIFIED Report.

11. A.E. Schiavone, et al. CRDLR 3193. Compounds of the α -Prodine Type. IV. Preparation and Reactions of Several 1-Substituted-4-phenyl-piperidinols and Their Esters. November 1963. UNCLASSIFIED Report.

12. W.R. Hydro. EC-TR-74099. Compounds of the α -Prodine Type. V. Preparation of 1-Substituted Homologs and Analogs of 1-Benzoyl ethyl-1-phenyl-4-piperidinols. Reduction of Keto Esters to the Corresponding Hydroxy Esters. March 1975. UNCLASSIFIED Report.

13. W.R. Hydro and R.J. Sundberg. EC-TR-74100. Compounds of the α -Prodine Type. VI. The Synthesis and Reactions of 4-Phenyl-4-propionoxypiperidinium Chloride. March 1975. UNCLASSIFIED Report.

14. K.J. Laidler. Chemical Kinetics. McGraw-Hill Book Company, Inc. New York, NY. 1950. p. 21.
15. A. Leo, C. Hansch, and D. Elkins. Partition Coefficients and Their Uses. Chem. Rev. 71 (6), 525-616 (1971).
16. C. Hansch. A Quantitative Approach to Biochemical Structure-Activity Relationships. Accts. Chem. Res. 2 (8), 232-239 (1969).
17. Daylight Chemical Information Systems, Inc., 18500 Von Karman, STE #450, Irvine, CA 92715.
18. Edgewood Arsenal Research Laboratories SOP 70-3. The Search for and Selection of Toxic Chemical Agents for Weapons Systems. 1 June 1967. UNCLASSIFIED Document.
19. W.G. Young and J.D. Roberts. Allylic Rearrangements. II. Some Addition Reactions of Butenylmagnesium Bromide. J. Am. Chem. Soc. 68, 649 (1946).

BLANK

SYNTHESIS AND BIOACTIVITY OF 2-(α -HYDROXY-*p*-ALKOXYBENZYL)
AND 2-ALKOXYARYLAMINO ANALOGS OF ETONITAZENE (CS-4640)

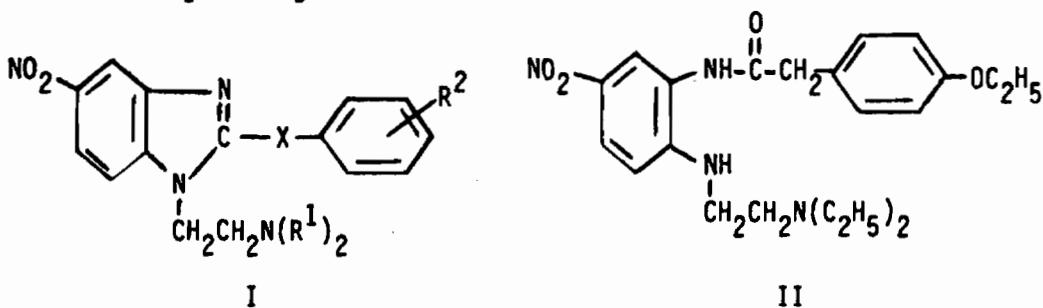
James W. King,¹ James P. Cleveland,² and W. James Lennox³

ABSTRACT

Etonitazene [1-(2-diethylaminoethyl)-2-(*p*-ethoxybenzyl)-5-nitrobenzimidazole] is an opioid analgesic in a class of compounds whose potency appears to be sensitive to minor structural changes. However, the literature reports that changing the 2-position substituent to an α -hydroxy-*p*-ethoxybenzyl group increases analgesic potency by a factor of 5 and therapeutic index by more than two orders of magnitude. A series of analogs of the latter compound was prepared for comparison of LD50 and MED50 values. In a similar manner, 2-*N*-acyl-substituted-alkoxyanilino analogs were prepared and like biological parameters determined. Evaluation of the resulting data in conjunction with limited analgesic ED50 values evinced no improvement in potential efficacy as compared to Etonitazene.

INTRODUCTION

Some of the structural factors influencing the analgesic activity of Etonitazene [1-(2-diethylaminoethyl)-2-(*p*-ethoxybenzyl)-5-nitrobenzimidazole] (I: X = -CH₂-, R¹ = C₂H₅, R² = 4-C₂H₅O-) have been previously discussed.⁴ The importance of an alkoxyaralkyl function (as compared to an alkyl substituent) at the 2-position was demonstrated. Also noted was the reported potentiating effect, on potency and therapeutic index, of placing an hydroxyl group on the methylene bridge (I: X = -CH(OH)-).⁵ In respect to the latter observation, our objective was to not only prepare a sample of this compound for evaluation but to assess the influence of the "bridge hydroxyl" on the pharmacological activity of Etonitazene analogs. The principal method of synthesis followed that previously established, *viz.*, the reaction of an appropriately substituted aniline with the alkoxyaralkylimino ester prepared from the corresponding nitrile.⁶⁻⁸ In the present case, cyanohydrins were prepared from the appropriate aldehydes and subsequently converted to the corresponding imino esters.



The seminal work of Hunger and his colleagues also addressed the synthesis of anilino analogs (I: X = -NH- or -N(acyl)-) as well as those with various groups on the side-chain nitrogen (I: R¹).⁹⁻¹³ Our objective in these cases was also to prepare analogs for evaluation which would assist in defining structural pharmacology across the series. Again, reported synthesis procedures were employed for preparation of the compounds.

An ancillary consideration in the present effort involved a report that the amide (II) was a more potent analgesic than Etonitazene itself.¹⁴ Inasmuch as a sample purported to be this material had been received by the Organic Chemistry Branch under a data exchange agreement, it was necessary to compare it chemically and pharmacologically with a sample of known origin and purity.

METHODOLOGY AND EXPERIMENTATION

Synthesis of Cyanohydrins

The substituted aralkylcyanohydrins required for the preparation of their corresponding imino esters were prepared either by the direct addition of HCN to a solution of the appropriate aldehyde in the presence of a catalytic amount of ammonium hydroxide, or by treatment of the aldehyde sulfite addition product with KCN in the presence of ammonium chloride.¹⁵ The former method is generally cleaner and more easily worked up; however, greater care must be exercised than with the latter method and all operations carried out in a fume hood.

Synthesis of the Substituted α -Hydroxy Benzimidazoles

The appropriate cyanohydrins were converted to their corresponding imino esters in a manner similar to that described for the substituted acetonitrile precursor in the Etonitazene preparation; these esters were subsequently treated with "Hippchen's amine" to give the requisite benzimidazole.⁶ An alternate method is based on a synthesis demonstrated in the case of the 2-alkyl substituted benzimidazoles, i.e., reaction of an alkoxyarylacetic acid with the amine, usually under melt conditions.⁴ The feasibility of this route in the present instance was demonstrated by treating mandelic acid with the substituted amine to give the benzimidazole (EA 5155).

Synthesis of the Substituted Anilino Benzimidazoles

These compounds were prepared by the condensation of the suitably substituted 4-nitro-*o*-phenylenediamine and the appropriately substituted carbodiimides or isothioureas.^{13,16}

Synthesis and Cyclization of 4-Nitro-2-(p-ethoxyphenylacetyl-amino)-N-(2-diethylaminoethyl)aniline

The title compound (a new sample of EA 4232) was prepared under contract on a 0.06 mole scale in 25% yield by treatment of 2-(2-diethylaminoethyl)-4-nitroaniline in DMF solution with excess p-ethoxyphenylacetyl chloride.¹⁷ The product gave a melting point of 121-125°; an undocumented source gave m.p. 116-117°. A sample of this material in refluxing methanol was monitored by thin-layer chromatography (TLC) for 56 hours. At seven hours there was a significant amount of Etonitazene present; at 19 hours the cyclization appeared essentially complete and ultimate work-up gave the product in 72% yield. In a related experiment, the methoxy analog (EA 4910) (m.p. 121-125°) of the title compound was heated in vacuo at 158° for three hours.¹⁸ Work-up of the residue gave 1-(2-diethylaminoethyl)-2-(p-methoxybenzyl)-5-nitrobenzimidazole (EA 4835), m.p. 76-78°, in 79% yield.

Pharmacological Screening

Standard methods were used for determining the bioactivity data in mice.¹⁹

RESULTS

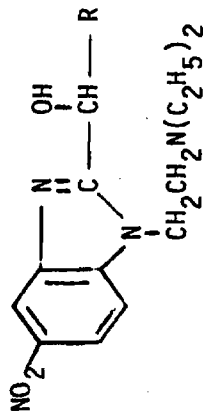
Tables 1, 2, and 3 exhibit the pharmacological screening data. Where available, the analgesic ED50's are noted also. In addition to the tabular data, screening for new EA 4232 (vide supra), the purported sample received under the data exchange agreement, and mixtures with Etonitazene were screened for bioactivity in mice concurrently with the chemical investigations. The bioactivity results, along with thin-layer chromatographic and ultra-violet analyses, and the experimental results noted above, left no doubt that EA 4232 is not an analgesic of the same order as Etonitazene, if at all. Because of the former compounds' propensity to cyclize with heat or in solution and in view of the analytical data, we suggested that the sample as received was a mixture of the noted amide and cyclized product; ultimately, the proponent stated that his sample contained about 18% Etonitazene.

DISCUSSION

Perhaps the most desirable characteristic of a physiologically active compound with potential for medical use is that its activity be highly specific. The specificity is often judged on the basis of its potency in reference to a particular effect. Thus, the data in Table 1 may be compared to morphine sulfate which has an LD50 of 220 mg/kg, a MED50 of 1.8 mg/kg, and an analgesic ED50 of 5.6 mg/kg. The problem with Etonitazene is that although it has 1000 times the potency of morphine as an analgesic, it may be no less a respiratory depressant (this appears to be the mechanism of death in primates); however, there is some question as to whether it had

TABLE 1

Summary of Primary Screening Data in Mice - α -Hydroxy Analogs

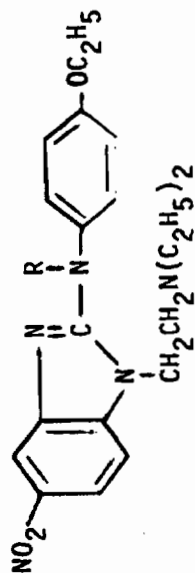


R	EA Code No.	LD50 (mg/kg)	MED50 (mg/kg)	Analgesic ED50 (mg/kg)
phenyl	5155	56	0.56	-
4-ethoxy-phenyl (b)	5270	63	0.001	0.032
2-ethoxy-phenyl (a)	4165	31.6	1.78	-
3-methoxy-4-ethoxy-phenyl (c)	5006	56	0.056	0.56
3,4,5-trimethoxy-phenyl (b)	5033	ca. 100	18	-
Etonitazene (free base) (d)	4941	54	≤0.001	0.0056

a) screened as the monohydrochloride
 b) screened as the dihydrochloride tetrahydrate
 c) screened as the dihydrochloride monohydrate
 d) included for comparison

TABLE 2

Summary of Primary Screening Data in Mice - Alkoxyarylamino Analogs

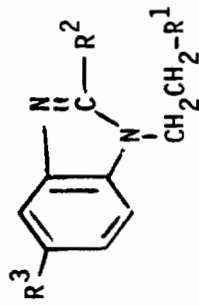


R	EA Code No.	LD50 (mg/kg)	MED50 (mg/kg)	Analgesic ED50 (mg/kg)
H-	4916	56	0.32	1.8
$\text{CH}_3\text{C}(=\text{O})-$	2664	32	0.0032	-
	4937	ca. 20	0.018	0.056
$\text{CH}_2=\text{CH}(\text{CH}_2)_8\text{C}(=\text{O})-$	4986	> 20	5.6	nil
Etonitazene (free base)*	4941	54	≤ 0.001	0.0056

* included for comparison

TABLE 3

Summary of Primary Screening Data in Mice - Miscellaneous Analogs



EA Code No.	R ¹	R ²	R ³	LD50 (mg/kg)	MED50 (mg/kg)
4129	diallylamino	4-ethoxybenzyl	5-NO ₂	100	0.56
4059	diethylamino	α-dimethylamino-methyl-4-ethoxybenzyl	-do-	22	0.056
3473	methyl(diethyl)-ammonium	4-ethoxybenzyl	-do-	-	-
3536	diethyl(hydroxyethyl)-ammonium	-do-	-do-	-	-
4113	diethylamino	-do-	5-CF ₃	> 20	0.56
4177	-do-	-do-	5-CH ₃ O	18	0.013
4245	-do-	-do-	5-NH ₂	3.2	0.178
4557	-do-	-do-	5-CO ₂ H	100	5.6

a fair evaluation in human studies. An apocryphal report suggests that it was employed in one instance after major surgery when the patient had already received maximum dosage of opioid-type analgesics, and heroic measures were required to prevent a disaster. As for the "hydroxy bridge" analog (EA 5270), there appears to be little difference between it and the parent, based on our screening results.

The isosteric alkoxyarylamino analogs of Etonitazene are shown in Table 2; based on the available data, the most interesting is the N-acetyl (EA 2264). This compound was obtained from a commercial source by the late Dr. F.W. Hoffmann, a former chief of the Organic Chemistry Branch. With a MED50 (minimum effective dose for any pharmacological index among about 180 in our screen) of 0.0032 mg/kg, this compound might be expected to have an analgesic effect at a low dose level - provided comparison of known tabular parameters is valid, as implied to an extent for other compounds in Tables 1 and 2. From a chemical as well as pharmacological aspect, EA 4937, with its N-cyclopropylcarboxy substituent (equivalent to a vinylcarboxy function) is unusual in that the MED50 is significantly lowered in respect to the -NH- parent. The N-(10-undecenoyl) analog is unusual for its absence of activity; there is an implication that a chain-length effect is operable when comparing it to the N-acetyl compound.

Table 3 shows principally compounds in which the side-chain amino function of Etonitazene was varied. The diallylamino analog was suggested by the late Dr. Benjamin Witten, a former chief of the Organic Chemistry Branch, as an attempt to mimic the effect of N-allylating morphine, thereby giving the opioid antagonist nalorphine. Again, in the absence of analgesic data, the success of this approach cannot be determined; however, the effect on the absolute LD50 and MED50 values as compared with Etonitazene is unmistakable - they are significantly higher. The quaternary analogs (EA 3473 and EA 3536) were originally prepared in a futile attempt to increase the water solubility of Etonitazene. The presence of a bridge dimethylaminomethyl group (EA 4059) apparently has little effect on the noted parameters. The remainder of the compounds in this table were prepared under contract at the direction of Dr. T.C. Simmons, a former chief of the Organic Chemistry Branch, now retired;¹⁷ their synthesis was subsequently reported.²⁰

CONCLUSIONS

On the basis of available though somewhat incomplete data, potential challenges to the analgesic efficacy of Etonitazene (CS 4640) by a number of its analogs have not been substantiated. Previous general observations that its known pharmacological responses are quite sensitive to structural changes are now more firmly established. A comparison of the known pharmacological data across the series of analogs suggests that additional analgesic

evaluations are warranted to provide a more complete basis for structure-activity considerations. Further, the d- and l- isomers of the hydroxy-bridged parent (EA 5270) should be resolved to determine if all the analgesic activity is attributable to one isomer. Etonitazene can be prepared cleanly in one step and in good yield from 4-nitro-2-(p-ethoxyphenylacetyl-amino)-N-(2-diethylaminoethyl)aniline (EA 4232).

ACKNOWLEDGEMENTS

The authors are grateful to Mr. C. Parker Ferguson, Chief, Organic Chemistry Branch, and Dr. John F. Weimaster for their support permitting the documentation of this research. We thank most heartily Mrs. Barbara LaGrange for her assistance in composing this report. We are fondly indebted to Mr. Joseph D. Williams, Program Coordinator for the Research Directorate and this conference, for his enthusiastic support of our research and his forbearance of our lack of temporal rectitude.

REFERENCES

1. U.S. Army Chemical Research, Development and Engineering Center, Aberdeen Proving Ground, MD 21010-5423.
2. Present address: Eastman Chemical Company, Kingsport, TN 37660.
3. Present address: U.S. Army Medical Research Institute of Chemical Defense, Aberdeen Proving Ground, MD 21020-5425.
4. J.W. King, J.P. Cleveland, and W.J. Lennox. Synthesis and Bioactivity of 2-Alkyl Analogs of Etonitazene (CS-4640). CRDEC-SP-034. Proceedings of the 1990 U.S. Army CRDEC Scientific Conference on Chemical Defense Research. UNCLASSIFIED Report. pp. 633-639.
5. G. Haberland. German Patent 1,176,661 (1964) and British Patent 943,569 (1963).
6. R.R. Irino, J.W. King, and T.C. Simmons. Chemical Warfare Laboratories Technical Memorandum 13-12. The Preparation of 1-(2-Diethylaminoethyl)-2-(p-ethoxybenzyl)-5-nitrobenzimidazole Hydrochloride (CS 4640). February 1960. UNCLASSIFIED Report.
7. J.K. Humphrey and S.R. Kramer. Chemical Research and Development Laboratories Technical Memorandum 31-126. Bench Scale Synthesis of CS-4640. 15 May 1962. UNCLASSIFIED Report.
8. T.P. Dawson, L. Katzoff, T.C. Simmons, and R.J. Salzman. Chemical Research and Development Laboratories Technical Report CRDLR 3178. Preparation of CS4640. October 1963. UNCLASSIFIED Report.

9. A. Hunger, J. Kebrle, A. Rossi, and K. Hoffman. Experientia **13**, 400 (1957). (Chem. Abstr. 52, 7289i).
10. A. Hunger, J. Kebrle, A. Rossi, and K. Hoffman. Helv. Chim. Acta **43**, 800 (1960). (Chem. Abstr. 54, 24677d).
11. A. Hunger, J. Kebrle, A. Rossi, and K. Hoffman. Helv. Chim. Acta **43**, 1032 (1960). (Chem. Abstr. 55, 519h).
12. A. Rossi, A. Hunger, J. Kebrle, and K. Hoffman. Helv. Chim. Acta **43**, 1046 (1960). (Chem. Abstr. 55, 521a).
13. A. Hunger, J. Kebrle, A. Rossi, and K. Hoffman. Helv. Chim. Acta **44**, 1272 (1961). (Chem. Abstr. 56, 2436h).
14. T.C. Simmons. Private communication.
15. A. Weissberger and E. Dym. Ann. **502**, 74-85 (1933) (Chem. Abstr. 27, 3468⁴).
16. K. Hoffman, A. Hunger, J. Kebrle, and A. Rossi. U.S. Patent 3,000,898 (1961).
17. Natural Products Laboratory, Research Triangle Institute, Durham, NC. Contract No. DA18-035-AMC-130(A).
18. K. Hofmann. Imidazole and Its Derivatives. Part 1, in The Chemistry of Heterocyclic Compounds (A. Weissberger, ed.). Interscience Publishers, Inc. New York, NY. 1953. p. 264 ff.
19. Edgewood Arsenal Research Laboratories SOP 70-3. The Search for and Selection of Toxic Chemical Agents for Weapons Systems. 1 June 1967. UNCLASSIFIED Document.
20. F.I. Carroll, R.W. Handy, J.A. Kepler, and J.A. Gratz. J. Heterocycl. Chem. **4**(2), 262-267 (1967).

BLANK

XIV. DETECTION POSTERS

BLANK

THE IDENTIFICATION AND DETECTION OF URINARY METABOLITES OF SULPHUR MUSTARD

Robin M Black, Keith Brewster, Ray J Clarke, Joy L Hambrook, John M Harrison,
David J Howells and Robert W Read

Chemical and Biological Defence Establishment, Porton Down, Salisbury,
Wiltshire SP4 0JQ, U.K.

ABSTRACT

Urinary metabolites were investigated following i.p. injection of sulphur mustard in the rat. Nine metabolites were isolated by HPLC and identified by mass spectrometry. Major metabolites were thiodiglycol sulphoxide, mono- and bis- N-acetylcysteine conjugates of mustard sulphoxide or sulphone, and two methylthio/methylsulphinyl derivatives resulting from the further action of β -lyase on cysteine conjugates. Excretion profiles were investigated for the hydrolysis products thiodiglycol and thiodiglycol sulphoxide and two β -lyase metabolites, following cutaneous application of sulphur mustard in the rat. Hydrolysis products were excreted over a more prolonged period than were β -lyase metabolites.

INTRODUCTION

Sulphur mustard, [1,1'-thiobis(2-chloroethane)] is one of the oldest of the currently declared CW agents and has been manufactured and stockpiled in considerable quantities by a number of countries during and since the 1914-1918 war. Most recently it was used during the Iraq-Iran conflict¹. Whilst there is an extensive literature on the toxicology and mechanism of action of sulphur mustard², there is a paucity of information on its fate in biological systems. In particular, a knowledge of the metabolites excreted in urine is required for the development of analytical methods for the retrospective confirmation of mustard poisoning in victims of chemical attacks.

Two previous investigations established that conjugation with glutathione was a major factor in determining the metabolic fate of sulphur mustard, and was of greater importance than hydrolysis^{3,4}. However, the results reported differed substantially with regard to the metabolites derived from glutathione conjugation. On the basis of chromatographic properties and dilution assays, Davison *et al.*³ concluded that the major urinary metabolite, following iv. administration of sulphur mustard, was the unoxidised bis-conjugate of mustard with glutathione, accounting for around 45% of the urinary metabolites. They also reported that a further 14% was accounted for by thiodiglycol and its acid-labile conjugates. Using similar methodology, but ip. administration, Roberts and Warwick⁴ reported that the major metabolite in urine, after acid

hydrolysis, was the bis-cysteinyl conjugate of mustard sulphone, and that intact glutathione conjugates were not excreted. They also demonstrated that about 15% of the metabolites were similar to those excreted following ip. administration of thiodiglycol, although the identification of these metabolites derived from hydrolysis was not established. However, the limited chromatographic and spectroscopic techniques available at that time must cast uncertainty on some of these earlier findings.

In this paper we report the isolation and identification of urinary metabolites using HPLC and mass spectrometry, following ip. administration of sulphur mustard in the rat. Excretion profiles were determined for two groups of these metabolites, those derived from hydrolysis and those resulting from the glutathione/ β -lyase pathway, following cutaneous application of mustard.

MATERIALS AND METHODS

Chemicals

The syntheses of ^{13}C and ^{35}S -labelled sulphur mustard⁵, and all standard compounds used for comparison with isolated metabolites are described elsewhere⁶. A doubly labelled injection stock comprising [^{13}C], [^{35}S] and non-labelled mustard was prepared in propylene glycol-ethanol (1:1, v/v) to give a mustard concentration of 20 $\mu\text{mol/ml}$ at the required specific activity and with an overall [^{12}C]:[^{13}C] mustard ratio of approximately 1:1.

Animals and dosage

Male albino Porton strain rats weighing ca. 250-300 g were used in animal studies. Labelled mustard was administered by ip. injection using freshly prepared stock solutions at a dose of 20 $\mu\text{mol/kg}$ (3.18 mg/kg). The injection volume was typically ca. 1 ml/kg. Urine was collected over 24 h with immediate cooling to -3°C and stored at -20°C until analysis.

Isolation of metabolites

The 24 h urine from each of four rats was pooled and the metabolites purified and isolated by HPLC. Analytical and preparative HPLC were carried out using a Gilson HPLC system; full details are given elsewhere⁷. Initial fractionation of bulk urine was performed using a Dynamix C-18, 8 μm preparative column, 25 cm x 21.4 mm i.d. Thereafter, analytical and preparative chromatography were performed using a variety of 4.6 mm i.d. reversed phase and ion exclusion columns. Solvents were typically mixtures of methanol or acetonitrile and water plus 0.1% trifluoroacetic acid. On-line radiochemical monitoring during chromatography was performed using a Packard Trace II Model 7150 radioactivity monitor fitted with a heterogeneous flow cell assembly, positioned in-line after the column and before the UV detector.

Identification of metabolites

Isolated fractions were analysed by mass spectrometry using a VG7070 EQ mass spectrometer fitted with a standard VG thermospray - PlasmasprayTM LC-MS interface. Fractions were initially examined by combined LC-MS using an LKB HPLC system under isocratic conditions and flow rates 0.5-1.0 ml/min. A glow discharge was used for ionisation (PlasmasprayTM ionisation), with or without ammonium acetate buffer, depending on the quality of the spectra obtained. 0.5 M Ammonium acetate was added at 0.2 ml/min via a T-piece inserted before the probe. Additional mass spectral information was obtained using desorption chemical ionisation (DCI) with ammonia or isobutane as reagent gas, and from collision induced dissociation of selected ions, obtained under ammonia DCI conditions, in those cases where identification was uncertain. Structural assignments were confirmed by comparison with authentic synthetic standards.

Quantitative determination of hydrolysis and β -lyase metabolites

Sulphur mustard ($2 \mu\text{mol}$, $318 \mu\text{g}$) was applied over 6 h to a 1 cm^2 area of the shaved back of groups of 3 or 4 rats as described previously⁸. Urine was collected and stored as described above, 24 h before dosing, at 6 h and 24 h after the start of the application and at further 24 h intervals up to 8 days. Thiodiglycol and thiodiglycol sulphoxide were initially determined in separate groups of 3 rats using GC-MS as reported previously^{9,10}. Using a different group of 4 rats, the excretion of the combined hydrolysis products, after reduction with titanium trichloride to the single analyte thiodiglycol, was compared to excretion of the combined β -lyase metabolites (B and D), similarly reduced to the single analyte 1,1'-sulphonylbis[(1-methylthio)ethane]¹¹.

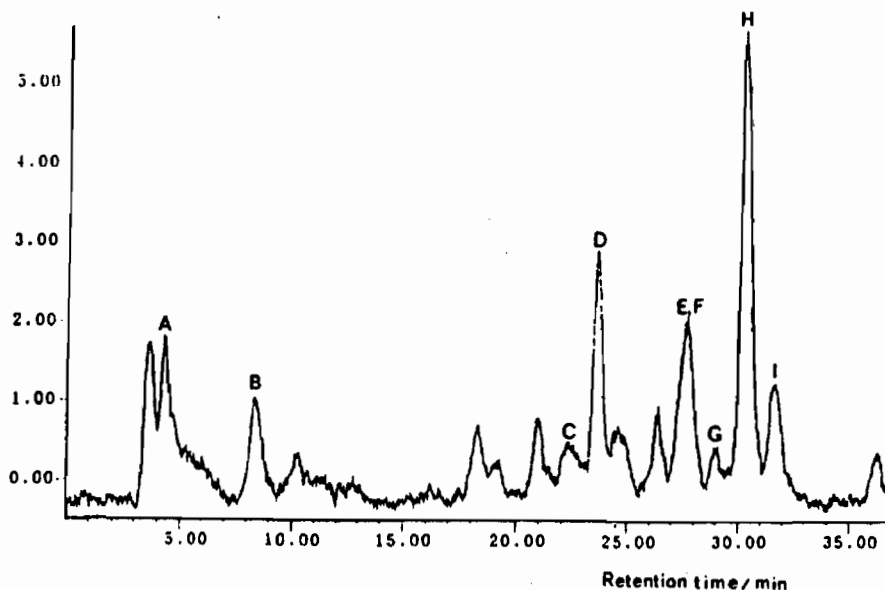
RESULTS

Isolation and identification of metabolites

Approx. 60% of the applied dose of sulphur mustard was excreted in the 24 h urine and was distributed amongst many metabolites. A typical radiochromatogram, obtained using a C-18 column, is shown in Fig 1.

FIGURE 1

Radiochromatogram of 24 h urine following ip. administration of sulphur mustard



None of the peaks was completely resolved and chromatography under different conditions usually revealed an alternative metabolic profile. Nine metabolites, labelled A to I, were isolated and identified; structures are shown in Fig 2. A summary of plasmaspray mass spectra is shown in Table 1. The use of doubly-labelled mustard in conjunction with HPLC-MS analysis ensured that only those ions appearing as doublets were used in the initial interpretation of mass spectra. The mass spectra of several of the metabolites, were noticeably variable in respect of the relative abundances of parent and fragment ions, presumably due to thermal degradation and/or

FIGURE 2

Structures of metabolites A to I and putative metabolic pathways

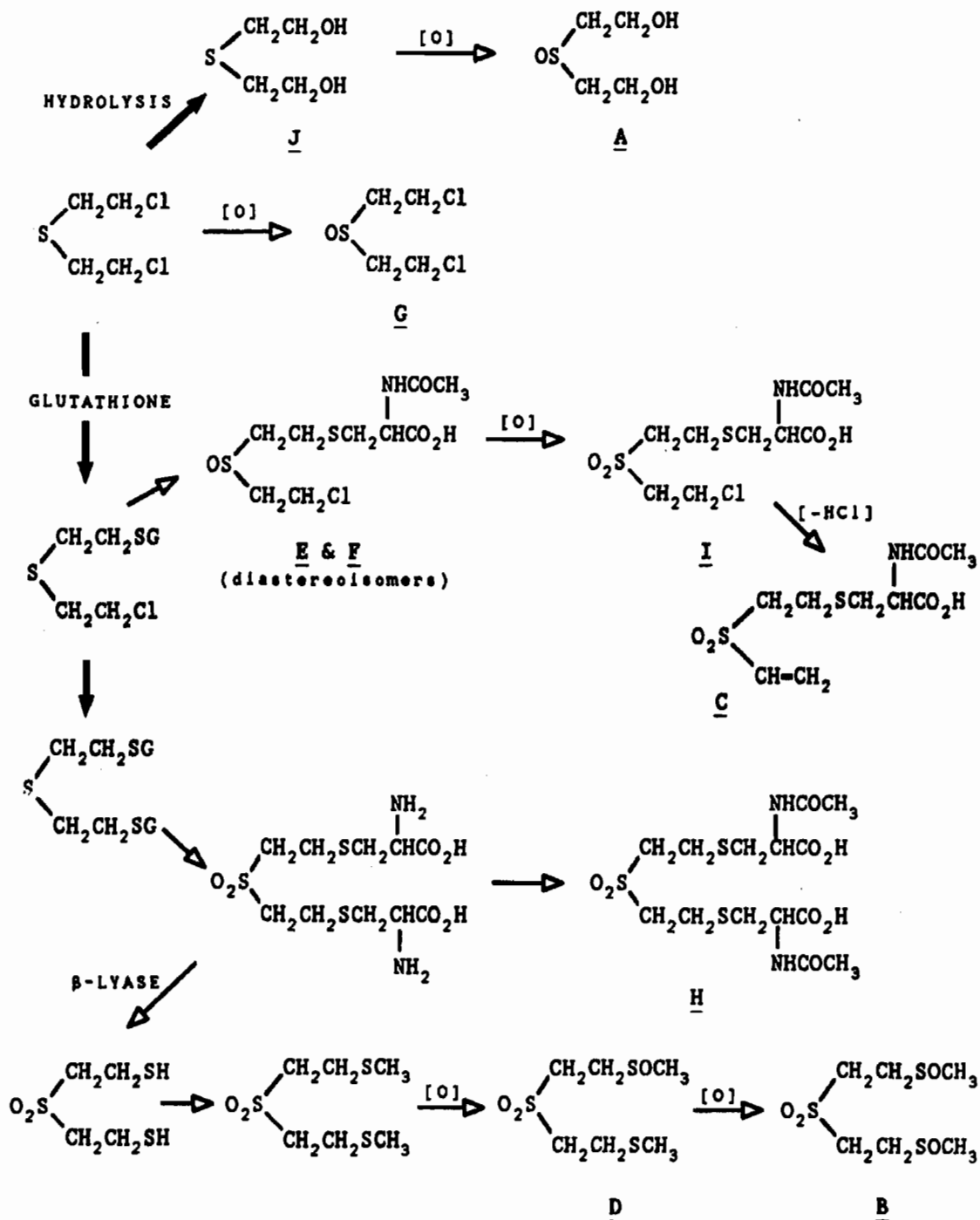


TABLE 1.

Summary of plasm spray mass spectra of isolated metabolites.

Metabolite	m/z (percent relative abundance)		Fragment ions
	[M+NH ₄] ⁺	[M+H] ⁺	
A	160/156 (10)	143/139 (100)	
B	268/264		204/200, 187/183, 140/136
C	303/299	286/282	181, 164, 147, 130
D	252/248 (100)	235/231 (32)	188/184 (24)
E		306/302 (5)	252/248 (probably metabolite D), 192/190 (100), 182/178, 158/154, 141/137
F		306/302 (7)	287/283, 270/266, 192/190, 173/169, 158/154, 141/137 (100)
G	196(8)/194(50) 192 (100)	179(3)/177(26) 175 (42)	
H			334/330 (4), 320/316 (10), 250/246 (3), 226/224 (5), 181 (15), 164 (20), 149/147 (42), 132/130 (100)
H methyl ester I		477/473 (1)	300/296 (3), 178 (34), 144 (100)
		324/320 (22) 322/318 (55)	286/282 (100), 192/190 (9), 155/151 (37), 132/130 (100)

* Indicates no ammonium acetate.

matrix effects. A more detailed discussion of mass spectral data is given elsewhere⁷. The metabolic profile could vary markedly from rat to rat, for example the relative intensity of metabolite A (thiodiglycol sulphoxide) was greater in the metabolic profile from some rats than in the one shown.

Putative metabolic pathways are shown in Figure 2. The primary metabolic transformations result from a competition between reaction with glutathione, hydrolysis and a minor amount of direct oxidation on sulphur to give mustard sulphoxide (metabolite G). Most of the oxidation on sulphur probably occurs after the initial reactions with nucleophiles. The bis-N-acetylcysteine conjugate of mustard sulphone (metabolite H) was identified as a major metabolite and all of the metabolites isolated were oxidised on the mustard sulphur atom. Our results are therefore more consistent with those of Roberts and Warwick⁴, who also used ip. administration, than with those of Davison et al.³. A hitherto unrecognised pathway for mustard metabolism is the formation of metabolites B and D, assumed to be formed via the further action of the enzyme β -lyase on cysteine conjugates (see Fig 2). This alternative pathway for the degradation of glutathione conjugates has received increasing attention in recent years¹². An important observation, from the viewpoint of retrospective identification of mustard poisoning, is that the major excretion product arising from the hydrolysis of sulphur mustard is thiodiglycol sulphoxide and not the initial hydrolysis product thiodiglycol.

Excretion profiles of hydrolysis products and β -lyase metabolites

The calculated half lives of elimination for the hydrolysis products and β -lyase metabolites, and the amounts excreted over 8 days, expressed as a percentage of the applied cutaneous dose, are shown in Table 2. Free thiodiglycol excreted over 8 days accounted for < 0.3% of the dose. Treatment of urine with hydrochloric acid increased levels of thiodiglycol by up to 1000%, but even after acid treatment the amount excreted accounted for only 1-1.5% of the applied dose in 3 rats, an average of 1.4% of the absorbed dose allowing for 95% uptake⁶.

TABLE 2

Results of quantitative excretion studies

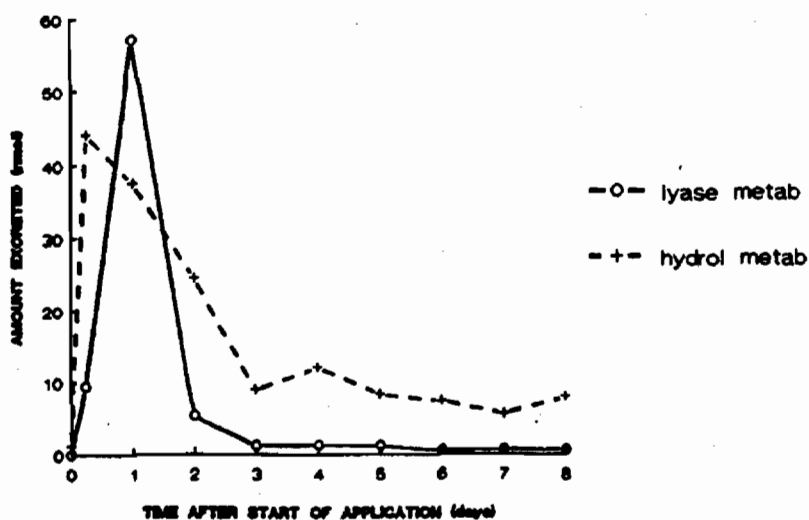
Excretion product in urine	Half-life of elimination	% applied dose over 8 days
Thiodiglycol	2.4 days	0.24
Thiodiglycol (after HCl treatment)	1.7 days	1.3
Thiodiglycol sulphoxide	1.9 days	3.8
Hydrolysis products (after $TiCl_3$ treatment)	1.9 days	7.8
β -Lyase metabolites (after $TiCl_3$ treatment)	1.6 days	3.9

mean data for 3 or 4 rats

Thiodiglycol levels in rat urine before dosing were < 1 ng/ml. Thiodiglycol sulphoxide accounted for a higher percentage of the applied dose, 3.4 - 4.3% in 3 rats, supporting the results of the metabolism study. However, a complicating factor was the detection of low levels of the sulphoxide (2-10 ng/mL) in the 24 h urine collected before dosing. Appropriate controls eliminated the possibility that these arose from contamination of equipment. Similar background levels have been observed in human urine. The mean urinary excretion profiles of the combined hydrolysis products and β -lyase metabolites, determined in 4 rats after treatment of urine with acidic titanium trichloride, are shown in Fig 3.

FIGURE 3

Excretion profiles of hydrolysis products and β -lyase metabolites after cutaneous administration of sulphur mustard (mean data 4 rats)



There was a considerable variation between rats although the general pattern of excretion remained similar. The recovery of hydrolysis products over 8 days varied from 3.7 to 13.6%; the recovery of β -lyase metabolites varied from 2.5 to 5.3%. The most notable difference was the much sharper decline in the excretion of the β -lyase products. The concentrations of the hydrolysis products in urine after 8 days, detected as thiodiglycol, were in the range 43-88 ng/mL, compared with levels of β -lyase products of 2-26 ng/mL. The prolonged later phase of elimination of hydrolysis products may be due, in part, to the slow turnover/breakdown of proteins, nucleic acids etc. which may form esters with mustard (e.g. aspartic and glutamic acid residues). Consistent with the results for thiodiglycol sulphoxide, low levels of reduced hydrolysis products, in the range 7-15 ng/ml, were detected in rat urine before dosing. No background levels (< 2 ng/mL) of β -lyase products were detected in rat urine, or in normal human urine.

CONCLUSIONS

Many urinary metabolites of sulphur mustard are excreted in the rat; nine were isolated and identified. The majority of metabolites result from an initial competition between reaction with glutathione and hydrolysis. The bis-N-acetylcysteine conjugate of mustard sulphone was a major metabolite. Cysteine conjugates may be further metabolised via β -lyase to methythio/methylsulphinyl derivatives. Thiodiglycol sulphoxide is the major excretion product resulting from hydrolysis. Quantitative determinations of excretion over 8 days, following cutaneous application of sulphur mustard, indicated that hydrolysis products were excreted over a longer period than were β -lyase metabolites. However, from the viewpoint of retrospective confirmation of mustard poisoning, the detection of hydrolysis products is complicated by the presence of low background levels of thiodiglycol sulphoxide in normal human urine.

REFERENCES

1. U.N. Security Council Reports S-16433, S-17911, S-20134 (1984-1988).
2. Somani S M and Babu S R, *Int J Clin Pharmacol, Therapy and Toxicol.*, 27 419-435 (1989).
3. Davison C, Rozman R S and Smith P K, *Biochem Pharmacol.* 7 65-74 (1961).
4. Roberts J J and Warwick G P, *Biochem Pharmacol.* 12 1329-1334 (1963).
5. Harrison J M, *J Labelled Cpds and Radiopharm.*, XXIX 1175-1080 (1991).
6. Black R M, Brewster K, Clarke R J and Harrison J M, *Phosphorus, Sulphur and Silicon* (submitted).
7. Black R M, Brewster K, Clarke R J, Hambrook J L, Harrison J M. and Howells D J, *Xenobiotica* (submitted).
8. Hambrook J L, Harison J M, Howells D J and Schock C, *Xenobiotica* (in press).
9. Black R M and Read R W, *J Chromatogr.* 449 261-270 (1988).
10. Black R M and Read R W, *J Chromatogr.* 558 393-404 (1991).
11. Black R M, Clarke R J and Read R W, *J Chromatogr.* 558 405-414 (1991).
12. Elfarra A A and Anders M W, *Biochem Pharmacol.*, 33 3729-3732 (1984).

BLANK

CHARACTERIZATION OF BACTERIA BY OXIDATIVE PYROLYSIS-GAS CHROMATOGRAPHY-MASS SPECTROMETRY

Philip B. Smith¹, and A. Peter Snyder²

¹GEO-CENTERS INC., 10903 Indian Head Highway, Ft. Washington, MD
20744 and ²U.S. Army Chemical Research, Development and Engineering
Center, Aberdeen Proving Ground, MD 21010.

ABSTRACT

Three different bacterial species were analyzed using a quartz tube pyrolysis GC-MS system under oxidative and non-oxidative pyrolysis conditions. Differences in their lipid composition made it possible to distinguish between the three bacterial species by visual examination of appropriate data plots. However, the results obtained after oxidative pyrolysis were indistinguishable from those obtained following non-oxidative pyrolysis. The lipid biomarker was clearly observed in a commercial bacterial insecticide which contained *Bacillus thuringiensis* and inert filler, 6:94% w/w, respectively.

INTRODUCTION

Analysis of fatty acid composition by gas chromatography has found widespread application as an aid to the rapid identification and classification of microorganisms. The utility of this approach has been advanced by the use of pyrolysis as a sample introduction technique, eliminating the need for time consuming extractions. A quartz tube pyrolysis gas chromatograph mass spectrometer (Py-GC-MS) system was constructed, and the equipment configured to permit the analysis of bacteria under a variety of different conditions including both oxidative and non-oxidative pyrolysis.

EXPERIMENTAL

The Py-GC-MS equipment consisted of a Pyroprobe Model 122 power supply, a platinum coil probe, a modified pyrolysis reactor/GC interface (Chemical Data Systems, Oxford, PA) a Hewlett Packard 5890 II gas chromatograph (Palo Alto, CA) and a Finnigan-MAT 700 Ion Trap (San Jose, CA). The bacterial samples (20-50 μ g) were pyrolysed in the pulsed mode at 1000°C for 20s. The pyrolysis reactor/GC inlet system was maintained at 300°C. The GC column (5m x 0.32mm i.d. DB-1) was operated with He carrier gas at 100 cm/s linear velocity, and temperature programmed from 100°C to 300°C at 30°C/min and then held at 300°C. Spectra were accumulated over a 100-650 amu range at a rate of 1 scan/s for 12 min. Under oxidative pyrolysis conditions, the reactor was equilibrated with the atmosphere for 120s before insertion of the sample. Immediately following insertion, the sample was pyrolysed, and after completion of the pyrolysis pulse, a stream of helium was directed through the reactor unit flushing the pyrolysate into the GC injector and onto the column. Under non-oxidative conditions the pyrolysis reactor containing the sample was flushed with helium for 60s before the pyrolysis event.

RESULTS

The Total Ion Chromatograms (TICs) obtained from *Bacillus subtilis* following pyrolysis under oxidative and non-oxidative conditions were virtually indistinguishable, and are presented in Figure 1. The early region (0-6 min.) of the chromatograms contain non-informative low molecular weight compounds and pyrolytic fragments; the lipid components of the bacteria elute from the GC column at 6-9 min. The integrated mass spectra for the lipid region of the two chromatograms are reproduced in Figure 2 and are essentially identical. Further data analysis, including comparison of reconstructed ion chromatograms (RICs) for selected diagnostic lipid ions, and their corresponding extracted mass spectra, revealed no differences between the two sample treatments. An identical analysis of the results obtained with two other bacteria, *Staphylococcus albus* and *Pseudomonas fluorescens* also revealed no differences between oxidative and non-oxidative pyrolysis. However differences in the lipid composition of the three bacterial species permitted their discrimination by visual examination of the integrated mass spectra for the lipid region of the chromatogram.

The total ion chromatogram (TIC) obtained with DiPel 2X, a commercial bacterial insecticide consisting of 6.4% *Bacillus thuringiensis* and 93.6% inert filler, is reproduced in Figure 3. Because of elevated background signals, the lipid components of the bacteria are not readily apparent from a visual inspection of the TIC. However, several of the ions characteristic for bacterial-derived lipid

components (m/z 299, 313, 522, 536, 550, 564, 578) are clearly visible in the mass spectra obtained from the relevant region of the TIC.

CONCLUSIONS

Despite fairly extensive data analysis, there was no discernable difference in the analytical information following either oxidative or non-oxidative pyrolysis. The ability to obtain useful analytical information following pyrolysis in air minimizes instrumental constraints, and offers a considerable logistical advantage, eliminating the requirement for bottled helium. Furthermore, our findings might indicate that the large amount of published reference data already obtained under non-oxidative conditions is readily applicable to an oxidative, pulsed pyrolysis system. The results obtained from DiPel 2X indicate that despite the presence of a 15 fold excess of other material, useful diagnostic information could be obtained using the system outlined above.

Figure 1. Py-GC-MS Total Ion Chromatograms of *Bacillus subtilis*.

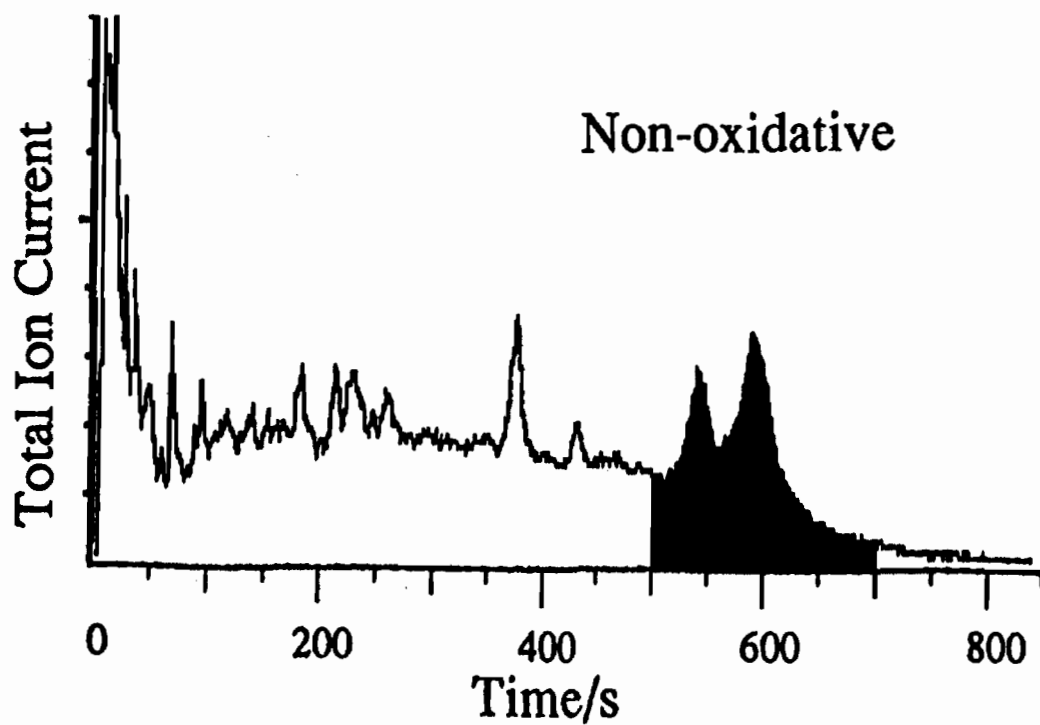
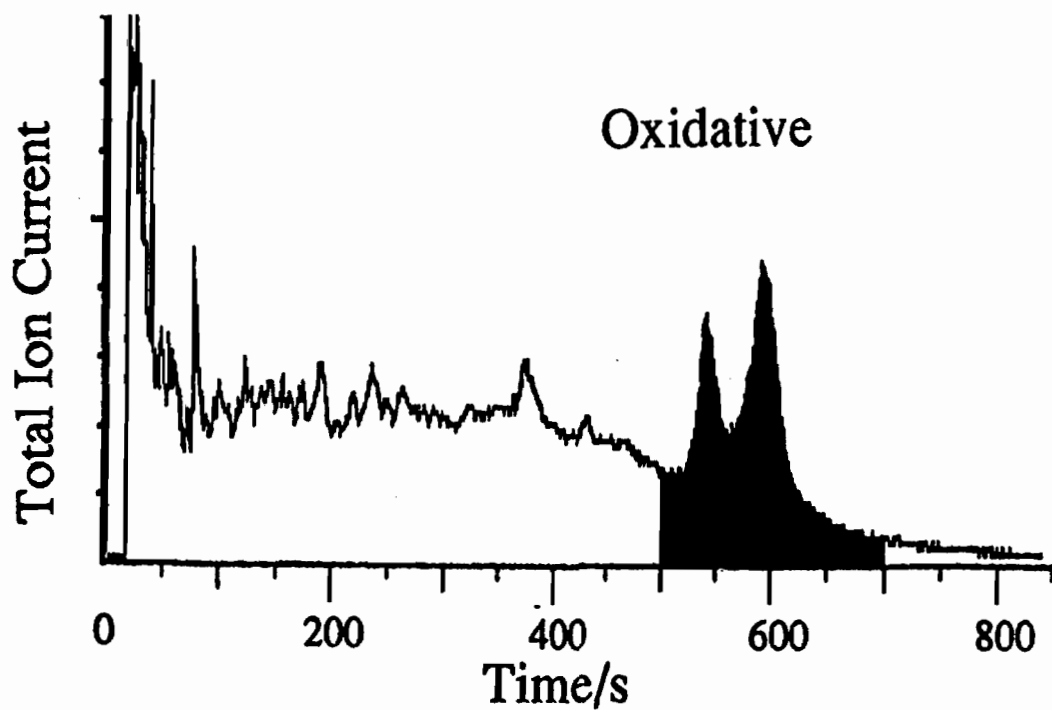


Figure 2. Py-GC-MS Mass Spectra of Total Lipid content of *Bacillus subtilis*.

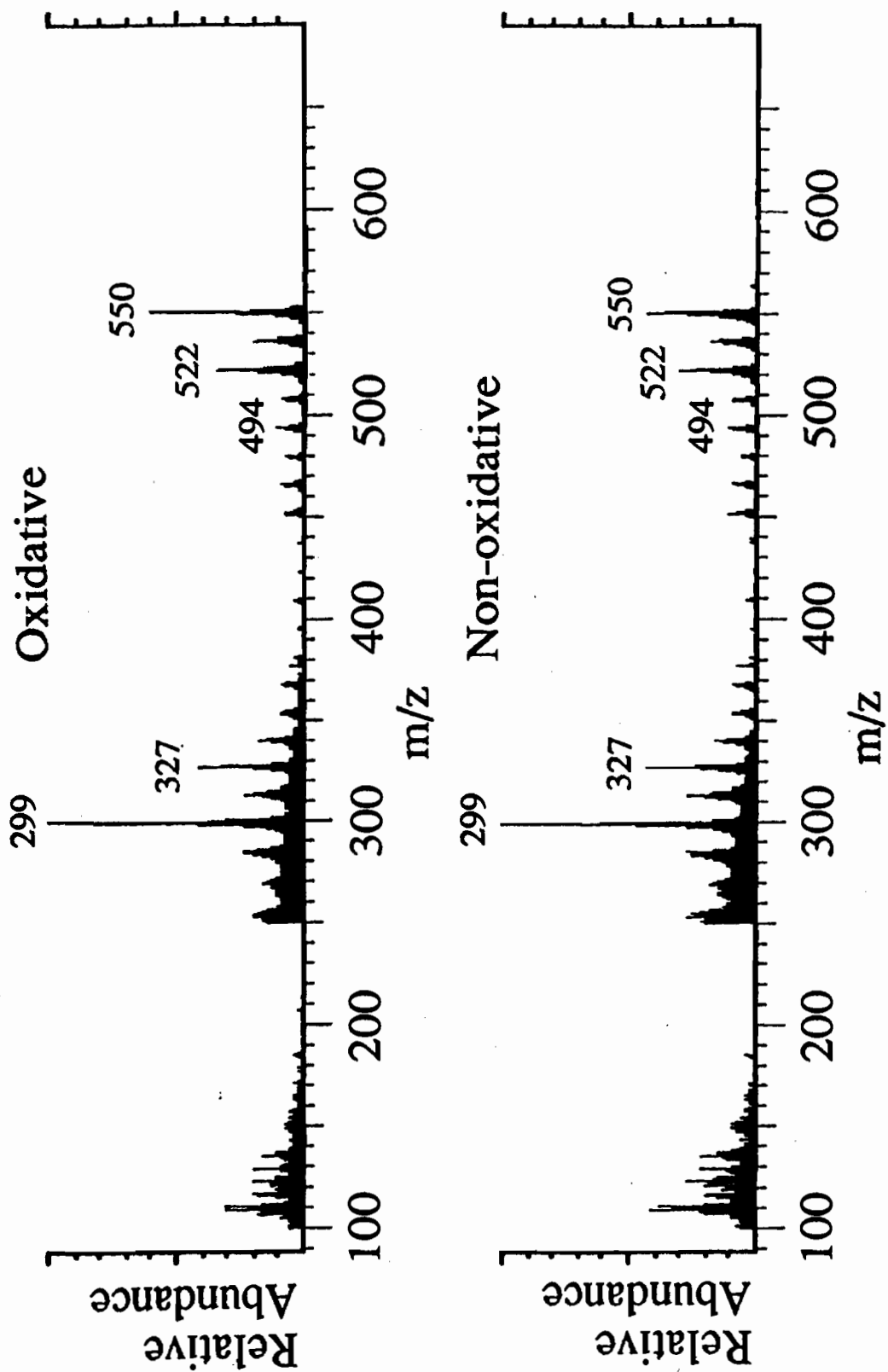
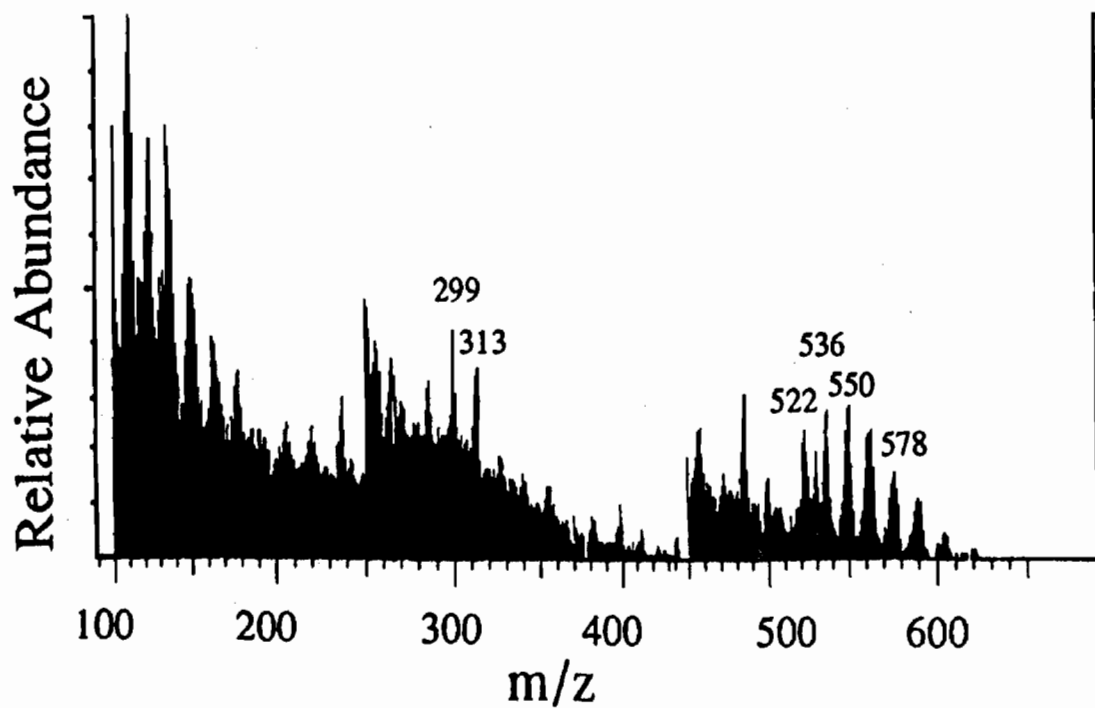
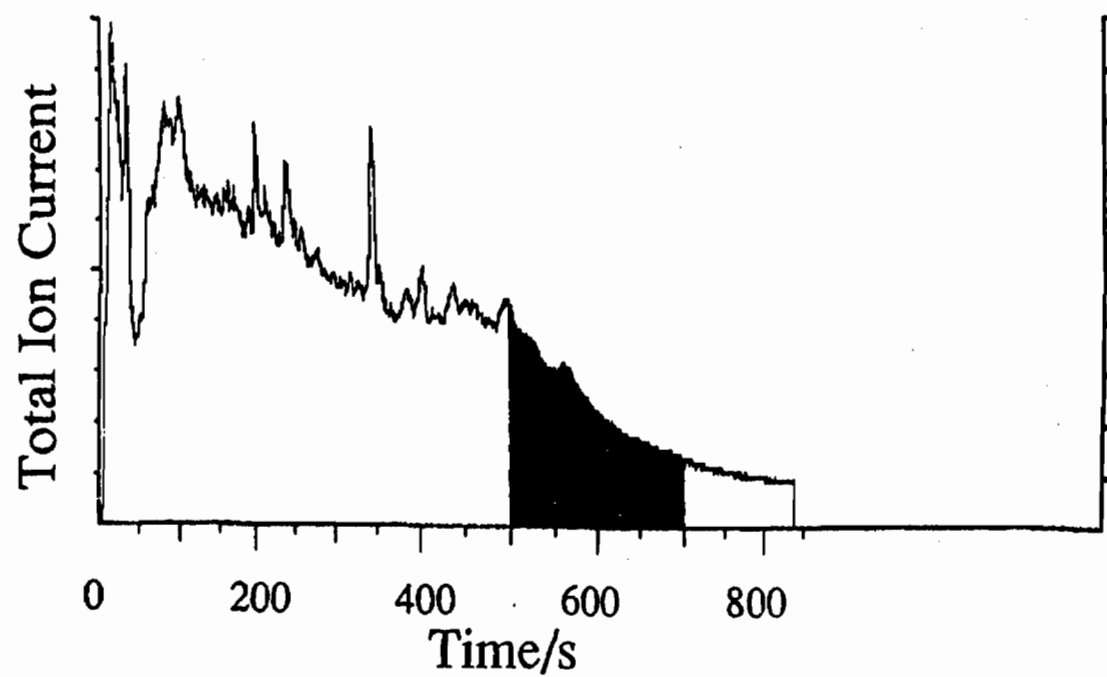


Figure 3. Py-GC-MS Total Ion Chromatogram (upper trace), and Py-GC Mass Spectra of Total Lipid content of DiPel 2X.



Tradeoff Analysis of Nonradioactive Source Alternatives for the XM22 Automatic Chemical Agent Alarm

JOSEPH E. ROEHL, Environmental Technologies Group
1400 Taylor Avenue, P.O. Box 9840
Baltimore, MD 21284-9840
Funded by: CRDEC

Abstract

Ion Mobility Spectrometry (IMS) has been chosen by CRDEC as the portable chemical detector technology of the future. It overcomes many of the problems with previous technologies including: combining nerve agent and blister agent detection with one device, elimination of wet chemicals requiring minimal maintenance, and automated microprocessor controlled operation. In spite of its advantages IMS does have a drawback in that it requires a ^{63}Ni radioactive source. Although the source is a beta emitter sealed in a closed cell it requires special handling and record keeping and causes a logistics burden. This paper describes a CRDEC funded task in the XM22 Full Scale Development (FSD) program to replace the ^{63}Ni source with a nonradioactive alternative. The paper will describe a systems tradeoff analysis based on XM22 requirements.

Introduction

The XM22 system is a portable chemical warfare (CW) agent detector based on IMS¹. Figure 1 illustrates the XM88 detector which forms the heart of the XM22 system. The XM88 detector is a fully automated microprocessor controlled IMS. A sampling system draws air into the unit from the ambient air. The sampling system consists of a heated membrane inlet. The ambient air inlet is meant to approximate the human respiration rate and is nominally 1.7 liters/minute. The inlet is a membrane inlet and isolates ambient air from air internal to the system. A recirculating loop of dry air passes behind the membrane and into the IMS cell.

The IMS Process

The IMS cell has two functions: to separate chemical agents from atmospheric constituents and common background materials, and to detect the chemical agents at part per billion levels. Figure 2 illustrates the IMS process. An ionization source is required in the reaction tube to create ions which ultimately ionize target chemicals. Once target chemicals are ionized they are drawn down a drift tube by an electric field where they impact a plate and are amplified to form Ion Mobility Spectra. IMS spectra are digitized and used as the basis of the alarm decision.

Radioactive Source - Pros and Cons

The goal of the research is to design and demonstrate an alternative XM88 detector with a nonradioactive ionization source. The payoff from this work is an XM88 detector without the costs associated with storage and operation of an instrument using a controlled radioactive source. The source poses no radiation hazard once sealed within the XM88 detector cell module; however, a potential remains for migration of active nickel material outside the cell due to corrosion and/or flaking of the source. Smear tests are required every six months to monitor for flaking. Consequently, use of this material causes significant storage, logistics, and maintenance burdens under routine storage and training conditions. The ^{63}Ni radioactive source used in the XM88 detector does, however, have some advantages which are hard to match using an alternative ionization source:

- a. the radioactive source requires no power,
- b. the source is extremely rugged,
- c. the source requires a minimum of volume and weight, and
- d. since the half-life of the source is 100 years it poses no reliability problem.

Any satisfactory alternative source must contend with these advantages to offer a viable alternative. In addition, CRDEC has considerable operating experience with and data on the radioactive source. This experience and information will have to be duplicated with a nonradioactive source.

Nonradioactive Source History

In most work reported in the literature, IMS uses 15 mCi ^{63}Ni foil as an ionization source. This source is usually identical in design to the source commonly used in electron capture detectors. Electron capture detectors are used in many gas chromatograph applications common to chemical laboratories and are not usually considered a problem in a laboratory environment. Because radiation source handling and control procedures are already in place in laboratories using this technology, use of a radioactive source in laboratory IMS has not often created safety concerns.

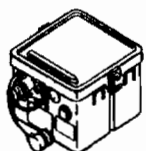
Despite the more common use of IMS with a ^{63}Ni source, significant prior work^{2,3} has been reported on the application of IMS to a number of analytical problems where the ionization scheme using ^{63}Ni is not optimal. For example, Shumate and Hill⁴ have used a corona spray source in an IMS detector for a liquid chromatograph. In Environmental Technologies Group, Inc.'s (ETG) commercial experience with an IMS using a membrane inlet and a ^{63}Ni source, it has proven difficult to detect light hydrocarbons. Photoionization is under investigation as a promising alternative in these conditions⁵.

In addition to research studies in other areas using a nonradioactive source, the Chemical Research, Design and Engineering Center (CRDEC) has funded several research studies using IMS with a nonradioactive source to detect CW agents. The most relevant studies to the XM88 detector have been performed by ETG using a thermionic bead source⁶ and by PCP Inc.⁶ using a photoionization source. The ETG source has been demonstrated with CW agents and the PCP source has been demonstrated with simulants. There is minimal risk that an alternate ionization source cannot be developed which will detect all of the CW agents. There is more risk that an alternate source will prove unacceptable for the XM88 detector application because of engineering considerations such as power, size or operational life.

Overview of Previous Work

Over 475 articles were reviewed in support of this analysis. These articles are summarized in a bibliography⁷ prepared as part of the project. Only a small number of these articles dealt directly with IMS. This work may be divided into:

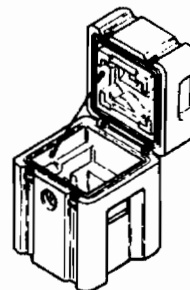
THE XM88 DETECTOR, WHICH FORMS THE HEART OF THE XM22 SYSTEM, IS A SELF-CONTAINED AIR SAMPLING SYSTEM BASED ON ION MOBILITY SPECTROMETRY (IMS)



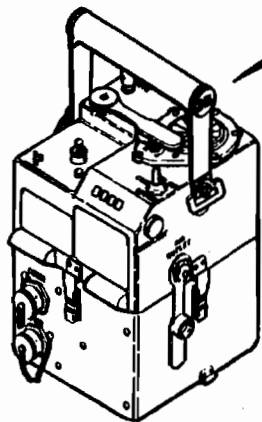
BATTERY BOX



M42 ALARM



TRANSIT CASE



XM88 DETECTOR

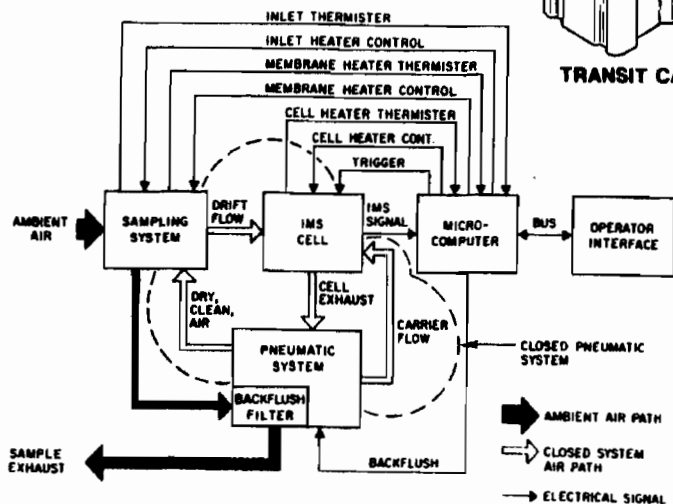


FIGURE 1. XM22 automatic chemical agent alarm

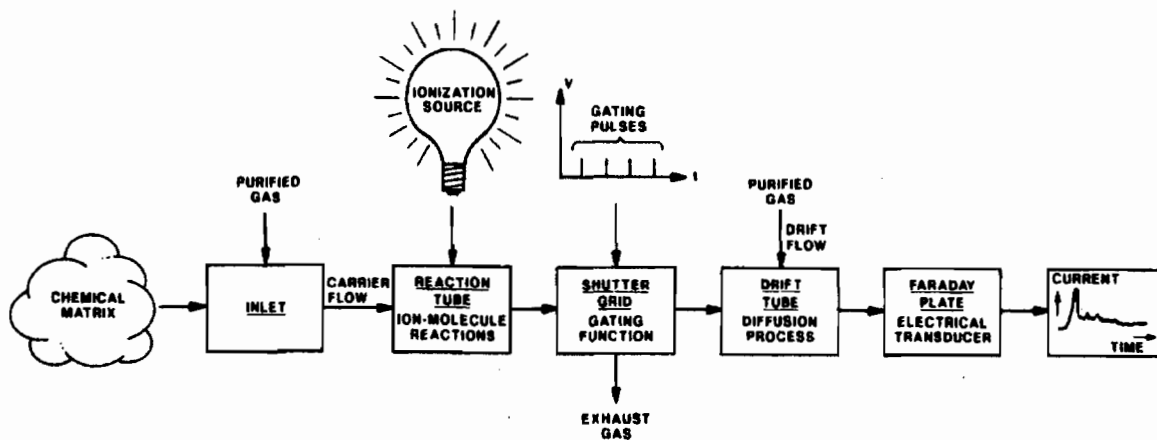


FIGURE 2. Block diagram of IMS process

a. Work on applications other than chemical warfare agent detection^{9,10,11,12}.

b. Work specifically funded by CRDEC on chemical warfare agents and simulants using IMS.

Work funded by CRDEC on CW agent detection included the following projects.

The Thermionic Emitter.

Development of a nonradioactive source based on a thermionic emitter was funded by CRDEC as part of the XM22 and auxiliary equipment AD program⁹.

The thermionic emitter source material chosen was beta-alumina heated by a nicrome filament. The source was actually installed in an AD XM88 detector and tested with chemical agents. Sources were manufactured at ETG. The mounting configuration of the thermionic emitter in the AD IMS cell is illustrated in Figure 3.

Two problems developed with the heated beta-alumina source which made it unacceptable for XM22 and auxiliary equipment. The source did not produce a consistent signature for lewisite and there was an unacceptable tradeoff between the source power requirement and life expectancy. A heated beta-alumina source drawing 1.0 Watt (W) of electrical power would last about one day. Extending the source life requires substantial additional power; this additional power is not available to the XM88 detector when operating on battery power.

Photoionization IMS (PIMS).

CRDEC funded a two phase study using a photoionization lamp as an ionization source for a commercial IMS. Simulants and alternate chemistries were used^{9,13}. These studies utilized a D.C. Krypton filled lamp (Scientific Services Model 109) to ionize the gas sample.

Laser Ionization.

Laser ionization source work is presented in a CRDEC report prepared by the U.S. Army Ballistic Research Laboratory¹⁴. This work utilized laser radiation at 25 nanometers (nm) to ionize DMMP and diisopropyl methylphosphonate (DIMP). The unique characteristic of a laser, coherent light, was not required to ionize the molecules; the laser was used only as a bright, pure source of ultraviolet (UV) light.

PIMS phase II.

This work is presented in CRDEC-CR-88082, Tandem Ion Mobility Spectrometer for Chemical Agent Detection, Monitoring, and Alarm Phase II. This work was a followed the phase I work described in PIMS and confirmed the utility of a krypton source¹³.

Honeywell XM22 and auxiliary equipment experimental development (XD) work.

Honeywell developed a corona discharge device for ionizing mustard in an IMS experimental development (XD) prototype design, instead of the ETG approach using a membrane inlet. This corona discharge source was not meant to replace the radioactive source. Instead, the corona discharge element was used in front of the IMS cell with a radioactive source. Honeywell's experimental source consisted of a wire in a cylinder with a high voltage applied across the elements. The source was not required to operate the IMS device and proved less reliable than a membrane inlet. This corona discharge source is not comparable to other sources used behind the membrane to replace a radioactive source. Information on this

source is available from CRDEC.

Summary of CRDEC-funded work.

ETG has found a limited amount of literature on nonradioactive IMS sources used for CW agent and simulant detection. Conclusions drawn from the work described in the literature are: the thermionic bead has received the most thorough testing with CW agents, and photoionization appears to be a primary source candidate for a portable instrument. Honeywell's work did not provide useful information on a corona discharge source used internal to an IMS cell and behind a membrane.

Systems Tradeoff Analysis Results

Table 1 contains the matrix used to calculate the tradeoff scores for each alternative source considered in the tradeoff analysis. Resulting total scores are included. The highest scores were obtained from the evaluation of the corona discharge^{4,8,9,10} and photoionization techniques.

Variable scores ranged from zero to ten based on the evaluators confidence that a source would meet the XM22 and auxiliary equipment requirement for that variable. A score of ten was assigned if the evaluator had a high confidence that the source would meet the requirement for that variable, and a score of zero was assigned if the evaluator was confident that the source would not meet that variable's requirement. The tradeoff score matrix clearly indicates that work must be done early in the laboratory phase of the nonradioactive source development program to demonstrate the CW agent response characteristics of the two chosen sources. Reviewers found no literature on the CW agent sensitivity of any source aside from ETG's work on the thermionic bead, which did not produce consistent results for lewisite. Some sources, such as inductively coupled plasma and microwave induced plasma, were judged highly unlikely to give a satisfactory response to CW agent based on the literature review.

Elimination of all but six sources was relatively easy from a cursory examination of the literature. For example, several sources are physically large, require kilowatts of power, and are only used for elemental analysis. Because the XM88 detector has limited power resources, the number of techniques considered for nonradioactive ionization can be narrowed. Only those techniques used under atmospheric pressure conditions and consuming less than 1.0 Watt of power qualify as alternative sources. Techniques fulfilling these criteria are as follows:

- a. Glow discharge (in helium)
- b. Corona discharge
- c. Liquid metal source
- d. Electrospray/ion spray
- e. Thermionic emission
- f. Photoionization

Of the techniques listed above, only the corona discharge and photoionization techniques are considered as good ionization sources for the XM22 and auxiliary equipment.

A key discriminator used to eliminate sources was the need for expendables. Glow discharge, liquid metal, and electrospray techniques were eliminated due to expendable requirements. Thermionic emission is the only source not to demonstrate satisfactory detection of a CW agent, but it was the only source for which agent data was available.

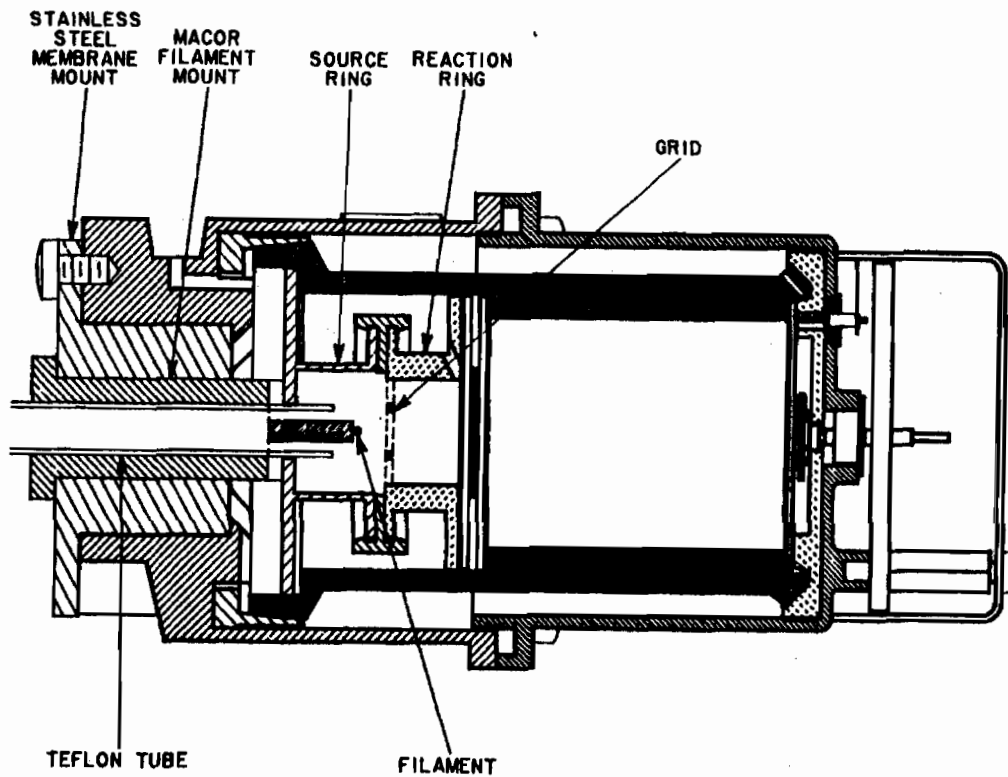


FIGURE 3. *Cross section of IMS cell with alkali source*

TABLE I. Tradeoff analysis of candidate sources based on the XM88 requirements

REQUIREMENT	WT.	SOURCES EXAMINED IN STUDY																
		CONDA DISCHARGE	PHOTOMIZATION	ARCSPARK	TOWERSD DISCHARGE	GLOW DISCHARGE	CAPILLARY ARC	PLASMA JET	ALUMI DOPED DISCHARGE	LIQUID METAL SOURCE	CAPILLATION	ELECTROSPRAY	FIELD EMISSION/IONIZATION	THERMOGRAVY	SURFACE IONIZATION	THERMIONIC EMISSION	INDUCTIVELY COUPLED PLASMA	MICROWAVE INDUCED PLASMA
Operate in three mission roles	10	8	8	0	0	5	0	0	0	8	0	10	0	0	0	0	0	0
Agent response	10	5	5	5	5	0	5	5	5	5	3	5	5	5	5	0	0	0
Sensitivity	10	5	5	5	5	0	5	5	5	5	5	5	5	5	5	0	0	0
Specificity	10	5	5	5	5	0	5	5	5	5	5	5	5	5	5	0	0	0
Response to physical state	10	5	5	5	5	0	5	5	5	5	5	5	5	5	5	0	0	0
Interferences	10	5	5	5	5	0	5	5	5	5	5	5	5	5	5	0	0	0
Repeated challenges	10	5	5	5	5	0	5	5	5	5	5	5	5	5	5	0	0	0
Maintainability	10	5	10	0	5	5	5	0	0	0	0	0	0	0	0	0	0	0
Transportability	10	10	8	0	10	10	0	10	10	10	5	10	10	10	10	10	10	0
Shelf life	8	10	10	10	10	10	10	10	10	10	10	10	10	10	10	10	10	10
Size (form factor)	8	10	8	2	8	5	0	5	10	5	5	5	5	5	10	0	0	0
Weight	8	10	8	2	8	5	0	5	10	5	5	5	5	5	10	0	0	0
Power supply	8	8	8	0	10	5	0	0	5	5	10	10	10	10	10	0	0	0
Nuclear survivability	10	8	8	5	5	5	5	5	5	5	5	5	5	5	5	5	5	5
Protected operator	8	10	0	5	5	5	5	5	5	5	5	5	5	5	5	5	5	5
Safety	10	8	8	0	10	5	0	0	10	5	10	10	10	10	10	0	0	0
Computer resources	8	10	8	5	5	5	5	5	5	5	5	5	5	5	5	5	5	5
Two sensitivity modes	2	8	10	10	10	10	10	10	10	10	10	10	10	10	10	10	10	10
Life cycle cost	8	8	8	0	5	2	2	2	10	10	2	2	10	5	10	5	0	0
Hardware changes	8	9	5	0	2	2	2	2	0	2	0	2	2	2	5	5	0	0
Software changes	5	9	8	5	5	5	5	5	5	5	5	5	5	5	5	0	0	0
XM88 detector module changes	5	9	8	0	0	0	0	0	5	5	5	5	5	5	5	0	0	0
IMS cell module changes	2	9	9	0	5	5	0	0	5	5	5	5	5	5	5	0	0	0
Additional modules	5	10	10	0	0	5	0	0	5	5	0	0	5	5	5	0	0	0
Total score:		1,448	1,406	651	1,079	892	337	641	1,031	1,191	896	1,062	1,071	1,046	1,065	1,176	270	270

Corona discharge and photoionization are very close in the tradeoff analysis. Corona discharge does not require an alternate chemistry, but the corona discharge needle is unlikely to be as reliable as the photoionization source.

Two Sources Chosen for Further Development

The two sources chosen for further development are illustrated in Figure 4. Both will be adapted to existing IMS cells for laboratory testing.

The corona discharge source will consist of a thin needle in the reaction region located where the radioactive source ring is now located. The corona discharge requires a source of high direct current (dc) voltage delivered at low current. Shumate and Hill² used an electrical connection through a resistor from the cell bias supply for the corona's power source. A similar arrangement may not be possible for the XM88 detector application, but this illustrates the low power requirement of the source. A major advantage of the corona discharge source is that this source produces reactant ions very similar to the radioactive source. In this respect the source is well understood. A primary concern with the corona discharge source is life expectancy. Sources become pitted over time, decreasing in efficiency.

The second approach, most similar to the PIMS, uses a photoionization source such as a krypton lamp. A major advantage of this approach is the long life expectancy of the lamp (5000 hours). The disadvantage of the photoionization technique is that an alternate chemistry, such as benzene, is required and this chemistry will require optimization during CW agent laboratory work.

Corona discharge and photoionization source prototypes will be built and tested in the laboratory during the next phase of the XM22 and auxiliary equipment FSD program.

Block Diagram

Figure 5 illustrates a block diagram of a nonradioactive source subsystem for the XM88 detector developed during systems analysis. The ionization source, approximately at the center of the diagram, is the heart of the subsystem. This ionization source mounts mechanically near the reaction tube of the IMS cell. In the XM88 detector this mechanical mounting is of concern due to shock and vibration requirements. The source is powered by the nonradioactive source power supply, converting the nominal 28 Volts (V) available to the XM88 detector into the voltage and waveform required to drive the source. Additional control electronics trigger the source. Where possible, the XM88 detector microprocessor controls the source and implements the built-in-test (BIT) function required by that source. Unlike the nonradioactive source, the radioactive source did not require a separate BIT function.

A separate support software module is required to modify the algorithm training software. Minor modifications may be required to the pneumatic system to change flow rates. In addition, there will be modifications to the logistics support package, including RAM.

Current XM22 and auxiliary equipment capabilities used to support nonradioactive source development.

ETG plans to minimize the cost of nonradioactive source development by utilizing existing XM22 and auxiliary equipment development facilities. Facilities key to success of the nonradioactive source program are the IMS-mass spectrometer (upgraded for the nonradioactive source development task), the VAX computer facility, the real-time data acquisition system developed

during the redesign phase of the XM22 and auxiliary equipment AD program, the CW agent laboratory, the microprocessor development laboratory, and the environmental test chambers.

The IMS-mass spectrometer facility will be used to identify simulant and CW agent peaks found in the IMS signature when the new IMS cell is challenged. Peaks must be identified to ensure that the CW agent detection algorithm keys from features related to CW agent chemistry instead of test artifacts. Since the XM88 detector algorithm is entirely empirical this IMS-mass spectrometer testing ensures the accuracy of CW agent detection. ETG purchased a new quadrupole mass spectrometer to upgrade the laboratory specifically in support of the nonradioactive source test program.

The VAX computer facility with the existing XM22 and auxiliary equipment data base will be used to store and process nonradioactive source data. Data is easily catalogued and sorted with existing Government-owned software on this equipment.

Efforts to ensure that the nonradioactive source can be implemented.

To meet implementation requirements of the task, the nonradioactive source will be moved from the laboratory to fieldable prototypes in a short period of time. For this reason it is important to maintain a practical engineering approach to the nonradioactive source program. The nonradioactive source program has a research and development subtask; however, the overall program is geared to an engineering solution. Focusing on the XM22 and auxiliary equipment application requirements from the beginning of the program and discarding options that may be interesting but would not easily fit into the existing XM22 and auxiliary equipment is the key to successful implementation.

Minimization of modifications to the existing XM88 detector.

Throughout the nonradioactive source development effort care will be taken to minimize the impact of nonradioactive source modifications on the overall XM22 and auxiliary equipment. Existing budgets for power, size, and weight will be as closely adhered to as possible. Since a baseline XM88 detector already exists performance specifications are well defined and baseline test results are available for reference.

Any nonradioactive source will require energy, most likely electrical power. The nonradioactive source will require additional physical space in the XM88 detector, additional support electronics, and software modification to the XM88 detector microprocessor. A cursory analysis of the current baseline XM88 detector and upgrades to be made during the FSD program indicates room for growth in the existing detector design. Technology has improved since the XM88 detector was originally designed, and both new batteries and a redesigned microprocessor board will be available during the FSD program to free up space in the XM88 detector box and provide additional power. One strategy to be used during the nonradioactive development task involves taking advantage of changes in the existing baseline design whenever possible to minimize the design impact.

Conclusions.

The nonradioactive source development plan assumes that no CW agent detection or interference rejection performance can be sacrificed when modifying the XM88 detector with a nonradioactive source. However, there are engineering areas where some flexibility must be assumed. Any reasonable alternative to a radioactive source will require additional electrical power. Minor growth in the volume of space used by the XM88 detector may be required (the

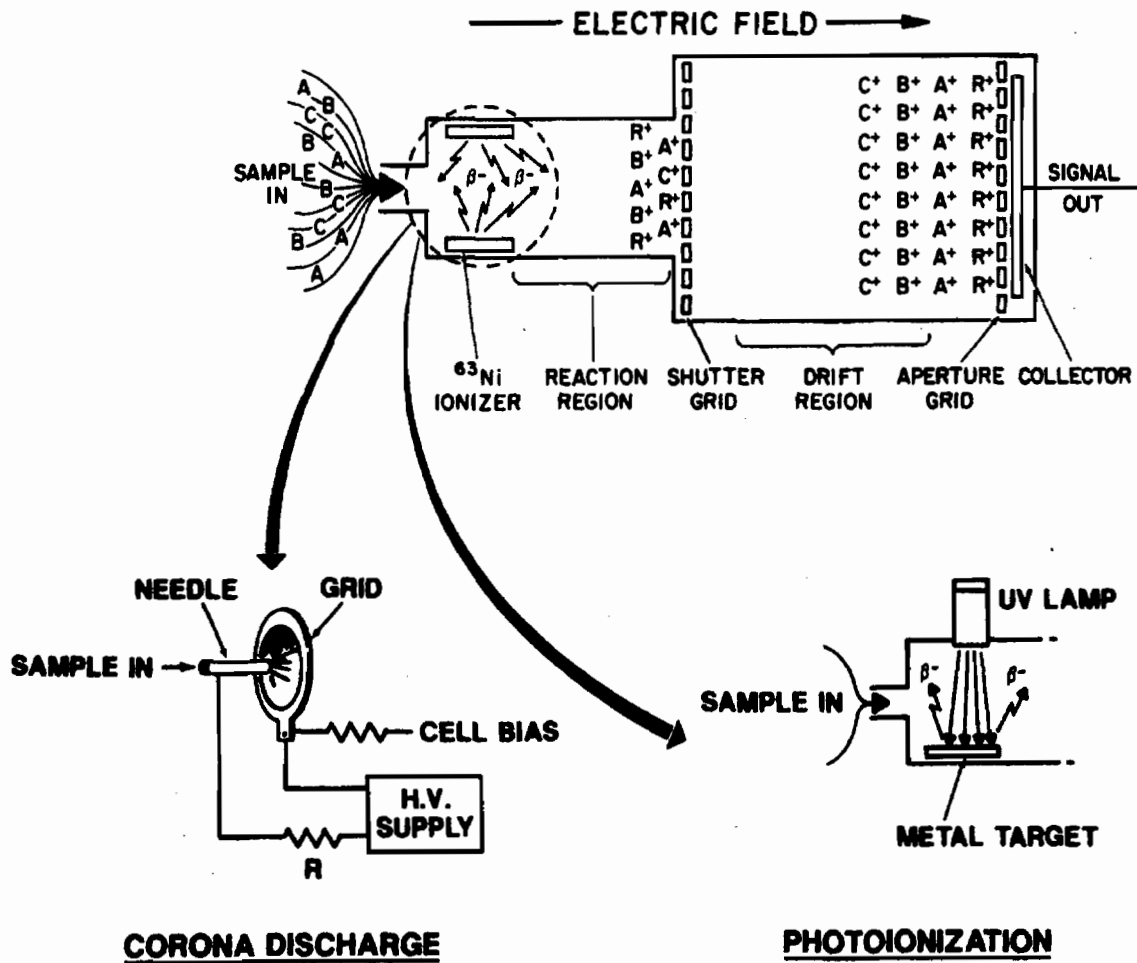


FIGURE 4. Alternate sources chosen for further development

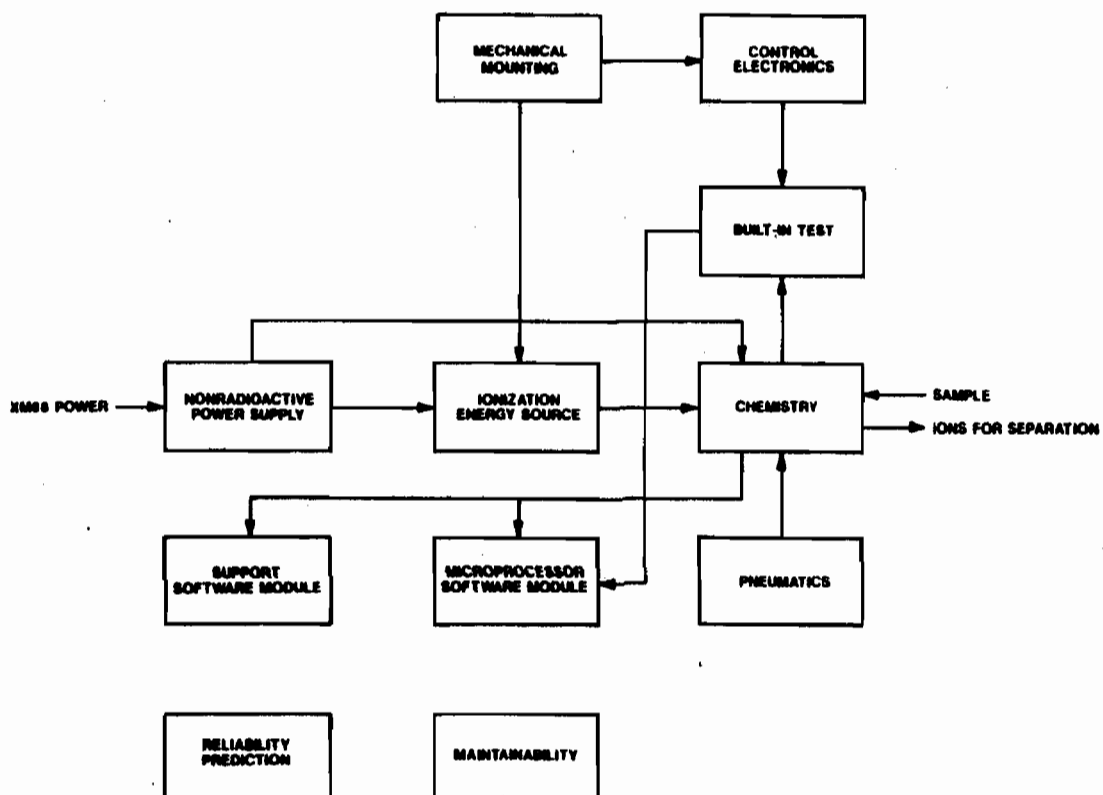


FIGURE 5. Nonradioactive source block diagram

current XM88 detector uses less space than required by its specifications).

A nonradioactive source may only marginally diminish reliability of the XM22 and auxiliary equipment. Since part of the detector reliability is related to interference rejection it is possible there will be reliability tradeoffs. The new source must not introduce a greater hazard than the radioactive source. Finally, the nonradioactive source must not complicate the logistics plan for XM22 and auxiliary equipment.

14. Laser Ionization/Ion Mobility Spectrometry of Diisopropyl Methylphosphonate, CRDEC-TR-102 prepared by U.S. Army Ballistic Research Laboratory.

REFERENCES

1. Roehl, J.E., "Microprocessor Controlled Chemical Detection and Alarm System Based on Ion Mobility Spectrometry", IEEE Transactions on Industrial Electronics, 32, 108, 1985.
2. Eiceman, G.A., "Advances in Ion Mobility Spectrometry: 1980-1990", Critical Reviews in Analytical Chemistry, 22 (1,2).
3. Roehl, J.E., "Environmental and Process Applications for Ion Mobility Spectrometry", Applied Spectroscopy Reviews, 26 (1&2), 1-57, 1991.
4. Shumate and Hill, "Coronaspray Nebulization and Ionization of Liquid Samples for Ion Mobility Spectrometry", Analytical Chemistry, Vol. 61, 1989, pp 601-69-06.
5. Spangler, Kim, Epatien, Campbell, Carrico, "IMS/MS Studies on Chemical Warfare Agents using Alkali Reactant Cations", Paper, Proc. 1988 U.S. Army CRDEC Scientific Conference on Chemical Defense Research, USACRDEC, APG, MD, August 1989.
6. Stimac, Wernlund, Cohen, "Photoionization - Ion Mobility Spectrometer (PIMS) for Real Time Chemical Agent Detector", Final Report CRDC-CR-84012, U.S. Army CRDEC, APG, MD, January 1984.
7. Bibliography of Atmospheric Pressure Ionization Technology, EIR 1987, prepared as an Appendix to Monthly Progress Report, XM22 Full-Scale Development Contract, Contract DAAA15-90-C0030.
8. Scott A. McLuckey, Gary L. Glish, Keiji G. Asano, Barry C. Grant, "Atmospheric Sampling Glow Discharge Ionization Source for the Determination of Trace Organic compounds in Ambient Air", Analytical Chemistry 1988, 60, 2220-2227.
9. Lawson, Mathieu, "Discharge Ionization Detector", U.S. Patent No. 4,975,648, December 4, 1990.
10. Look, "Discharge Ionization Detector", U.S. Patent No. 4,789,783, December 6, 1988.
11. Sofer, Zhu, Lee, Antos, Lubman, "An Atmospheric - Pressure Glow Discharge Ionization Source", Applied Spectroscopy, Volume 44, No. 8, 1990.
12. Balm, Eatherton, Hill, "Ion Mobility Detector for Gas Chromatography with a Direct Photoionization Source", Analytical Chemistry, 1983, 55, 1761-1766.
13. Stimac, Cohen, Wernlund, "Tandem Ion Mobility Spectrometer for Chemical Agent Detection, Monitoring, and Alarm - Phase II", Contractors Report CRDEC-CR-88082, CRDEC, APG, MD, August 1988.

BLANK

**TRIAZINE DERIVATIVES AS POTENTIAL MICROSENSOR COATINGS
FOR THE DETECTION OF AIRBORNE CONTAMINANTS**

Alan R. Katritzky, and Jamshed N. Lam*

*Center for Heterocyclic Compounds, Department of Chemistry,
University of Florida, Gainesville, FL 32611-2046, USA.*

Research Funded by: **CRDEC**

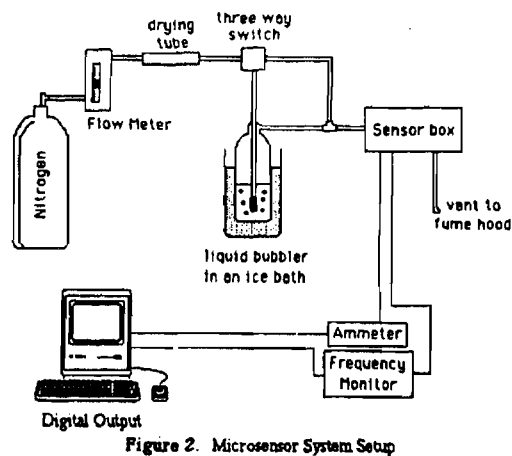
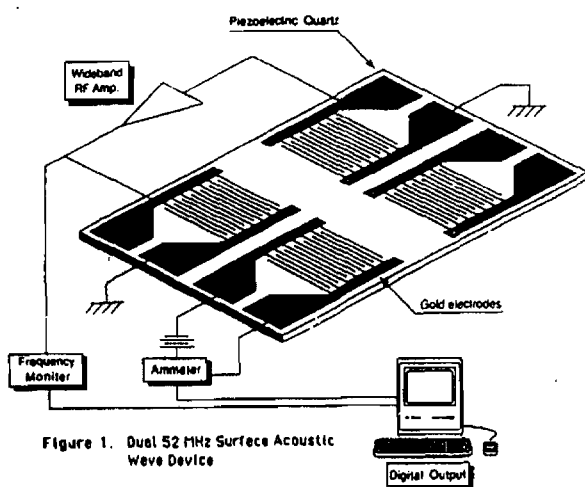
ABSTRACT: New compounds were tested as coatings for Surface Acoustic Wave (SAW) and chemiresistor devices in an attempt to obtain selective detection and reversible monitoring of chemical warfare agent simulants.

1,3,5-Triazine derivatives were spray coated onto SAW and chemiresistor devices and exposed to vapors of chloroethyl ethyl sulfide (CEES), dimethyl methylphosphonate (DMMP) and water. Changes in chemiresistor and SAW responses were monitored and recorded via computer controlled data acquisition techniques. All the derivatives tested showed little or no chemiresistor or SAW responses to water vapor. The largest reversible chemiresistor response to DMMP vapor was observed with a dicarboxylic acid. The largest SAW response to DMMP was with a dithione while a dichlorooctylthio derivative showed the largest response to CEES.

INTRODUCTION

The need to design instruments to detect airbourne contaminants has increased rapidly in recent years. Gas chromatographic mass spectroscopy (GC/MS), which has been used for the detection of atmospheric pollutants, is rapidly being displaced by smaller and more sensitive instruments. The need to detect contaminants in parts per million (ppm) concentrations for gas leaks, chemical warfare (CW) agents and illicit drug manufacture makes a GC/MS or some other large monitoring device impractical.

Microelectronics and computer design has lead to the fabrication of selective and sensitive vapor detectors which are small in size and are applicable to military, industrial and environmental use. The microsensors devices available for such uses are chemiresistor,^{1,2} surface acoustic wave (SAW)³⁻⁵ and bulk-wave piezoelectric quartz crystal sensors.⁶ The chemiresistor and SAW devices are both manufactured from piezoelectric quartz with an interdigital electrode array (usually gold) lithographically fabricated onto the surface of the quartz crystal.¹ It is this similarity between the two devices that allows resistance (chemiresistor) and frequency (SAW) measurements to be conducted simultaneously⁷ (Figure 1). The principles of operation of SAW devices^{3,8} as well as those of chemiresistors¹ have been previously described in detail. Details of the system used in our laboratory and modes of operation (Figure 2) have been published in two reviews by our group^{9,10} and will not be discussed here.



A variety of compounds have been used as coatings for SAW and bulk piezoelectric devices.^{9,10} However, the lack of a systematic approach for the identification and development of new microsensors coatings and thus an inability to predict coatings of high selectivity and sensitivity impedes the use of this technology on a commercial scale. Work in our laboratory involves a rapid and preliminary screening of heterocyclic derivatives and examines the behavior of various classes of compounds in an attempt to utilize these microsensors to their

fullest potential. A few heterocyclic systems tested so far include benzimidazole,¹¹ pyridine and pyrylium,¹² thiadiazole,¹³ nicotinamide,¹⁴ acridinium betaines,¹⁵ and phosphorus,¹⁶ derivatives. Hopefully, acquisition of such data will provide valuable insight to the vapor/coating interactions and afford a better understanding of the effects of various functional groups on the device responses. Herein, we report our most recent findings: the responses of a variety of trisubstituted-1,3,5-triazines to DMMP (a nerve-agent simulant), CEES (a sulfur-mustard-gas simulant) and water (an interferant).

EXPERIMENTAL

Simultaneous chemiresistor and SAW measurements were performed while exposing the device (in turn) to water, CEES and DMMP vapors. The results are usually reproducible to within 5%. The dual 52 MHz surface acoustic wave apparatus used (Microsensor Systems, Inc.), has been described in detail elsewhere.^{9,11,15}

The resonant frequency was monitored with a digital frequency counter, Phillips Model PM 6674 universal frequency counter (550 MHz). The conductivity measurements were made by the application of a 1-V bias to either of the two remaining electrodes, and measurement of the current. The precision current to voltage converter used consisted of an operational amplifier and a switch selectable feedback resistor.

Both SAW and chemiresistor data acquisition was controlled by an Apple II computer with an IEEE-488 interface, connected to the frequency counter and electrometer (Keithley 617 Programmable Electrometer).

The coatings were dissolved in a volatile organic solvent, typically spectroscopic grade chloroform, and the device was spray-coated with an air brush using dry nitrogen as the propellant. The coating thickness was monitored via the frequency counter until a frequency shift of *ca* 50 kHz was obtained. The frequency shifts caused by the coating were recorded as an indication of coating thickness. Vapor challenges were generated by passing a regulated flow of nitrogen through the neat liquid at 0 °C, in a vapor bubbler equipped with a gas dispersion tube. The flow rate over the device was controlled with a flow meter and was determined to be 7.5 mL/min using a bubble meter. Absolute concentrations of vapor challenge were calculated by methods described previously.¹⁵ Thus at 0 °C, the vapor pressures of DMMP, CEES and water afforded concentrations of 5.2 g m⁻³, 30.7 g m⁻³ and 4.8 g m⁻³ respectively.

Initially the system was purged with nitrogen for 5 min to establish a baseline curve. The device was then exposed to the vapor for 40 min and this was followed by a nitrogen purge for 50-60 min. If a response was irreversible, the SAW device was cleaned and recoated before exposure to the next vapor challenge.

The SAW devices used were rinsed between runs with acetone, and this was followed by ultrasonic cleaning for 15 min in spectroscopic grade isopropanol.

All compounds mentioned here have been fully characterized and details are available.¹⁷

RESULTS AND DISCUSSION

The compounds 1-4 (Figure 3) were then tested as microsensor coatings towards vapor challenges of DMMP, CEES and water. Surface acoustic wave and chemiresistor measurements were recorded simultaneously using a dual 52 MHz surface acoustic wave device. The coated device was exposed (in turn) to water, CEES and DMMP vapors (Table 1). The frequency shifts were calculated by subtracting the lowest frequency recorded during vapor exposure from the initial (baseline) frequency. Resistance changes were calculated by dividing the initial resistance by the lowest resistance recorded over the same period. A value close to unity thus denotes no change. The low signal to noise ratio in SAW device enables small frequency changes to be detected quite readily. Typically, for a SAW delay line operating in the frequency range of 30-300 MHz, mass changes of the order of 10^{-9} g can be detected. However, for chemiresistor devices, a 100 fold change is required for a compound to be considered a good coating.

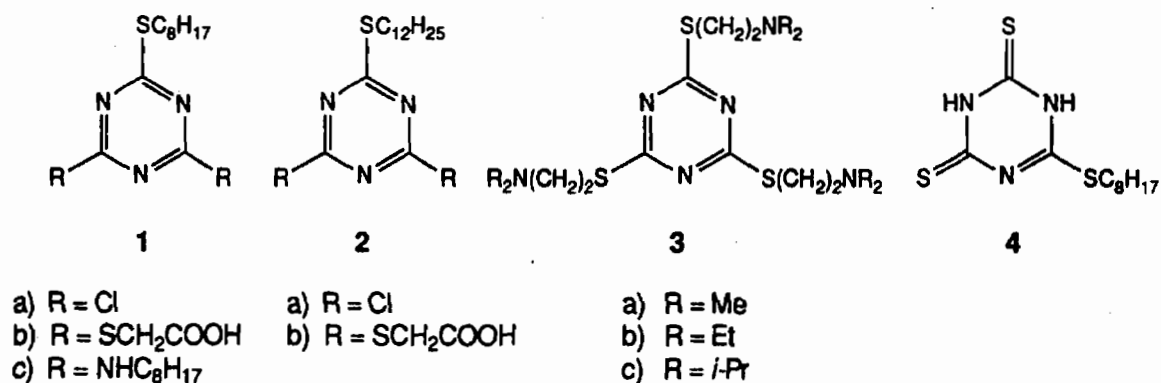


Figure 3. Triazines Tested

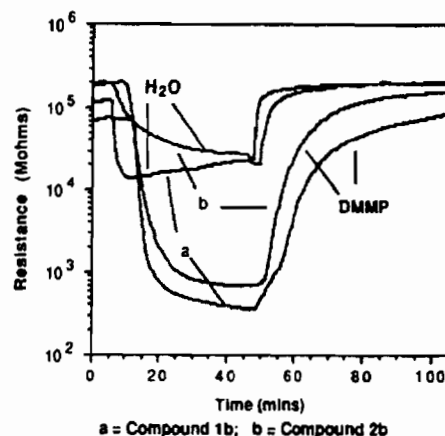
Table 1. Response of 2,4,6-Trisubstituted-1,3,5-triazines to Vapor Challenges.

Cmpd.	Coating mass (kHz)	Resistance Change (Factor)			Frequency Shift (kHz)		
		DMMP	CEES	H ₂ O	DMMP (kHz)	CEES (kHz)	H ₂ O (kHz)
1a	52	37.0	34.0	1.0	4.1	18.1	0.3
1b	47	351.0	11.9	8.5	27.2	2.7	1.0
1c	55	1.0	1.0	1.1	2.5	1.9	0.3
2a	50	5.2	37.4	1.0	4.1	4.9	0.3
2b	55	283.0	2.4	8.0	17.4	1.3	0.7
3a	48	1.0	1.0	1.4	2.6	9.6	2.2
3b	54	15.0	6.4	2.0	2.0	6.0	0.1
3c	53	20.8	22.3	1.8	2.1	11.4	0.8
4	56	126.9	3.9	1.0	52.6	2.8	2.8

A large reversible resistance change (351 fold) was observed to DMMP with 2,4,-dicarboxymethylthio-6-octylthio-1,3,5-triazine (**1b**) as the coating. The corresponding dodecylthio analog (**2b**) also showed a comparable resistance change (283 fold). This large resistance change is not surprising since with the presence of two carboxylic acid moieties, one would expect some interaction with an ester functionality. What is surprising though is the fact that both these coatings showed a comparatively very low response to water vapor (Figure 4). Furthermore, both (**1b**) and (**2b**) displayed good frequency responses to DMMP (27.2 and 17.4 kHz, respectively) indicating that there was a mass loading (absorption) effect. A large resistance change with a low frequency change would have implied a surface effect.

The largest resistance change (37.4 fold) for CEES vapor was observed with 2,4-dichloro-6-dodecylthio-1,3,5-triazine (**2a**). The octylthio compound (**1a**) also gave a high response (34.0 fold) to CEES and showed a similar response (37 fold) to DMMP vapor. Interestingly, the dodecylthio derivative (**1a**) did not show a comparable challenge to the DMMP vapor. The highest responses to water vapor were with the dicarboxylic acids (**1b**) and (**2b**) (Figure 4). However, the much higher response to DMMP vapors would still make these derivatives good chemiresistor coatings for the detection of DMMP vapors.

The greatest SAW frequency response was with the dithione (**4**) which displayed a frequency shift of 52.6 kHz for DMMP and showed good discrimination by affording a small response to CEES and water vapor (Figure 5). Furthermore, it was 90% reversible. Consequently, this makes it a very good coating for a SAW device towards the detection of DMMP in the presence of CEES and water vapor. A sharp change in frequency when the vapor is turned on and off is shown in Figure 6. After purging the system with nitrogen for 5 mins. (to establish a baseline frequency), the vapor was repeatedly turned on for 5 min. intervals and turned off for 2 min. intervals over a period of 40 min. The on/off times were then changed to 10 mins and 5 mins respectively for a further 60 mins. The graph displays a second order absorption (with a correlation factor of 0.992) and a second order desorption (with a correlation factor of 0.997). The dicarboxylic acids (**1b**) and (**1c**) also showed good selectivity by displaying a large response only to DMMP vapor. For CEES vapor, the largest response was with the dichlorooctylthio compound (**1a**) with low responses towards DMMP and water, thus displaying potential as a coating for the detection of CEES. However, the dodecyl derivative (**2a**) showed poor responses to all three vapors.



a = Compound 1b; b = Compound 2b
Figure 4. Chemiresistor responses for exposure to DMMP and water vapors

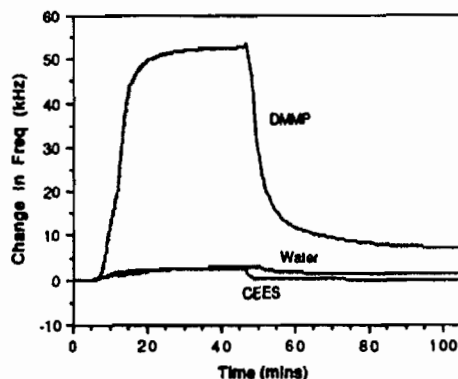


Figure 5. Frequency response of (4) vs time, for exposure to vapor.

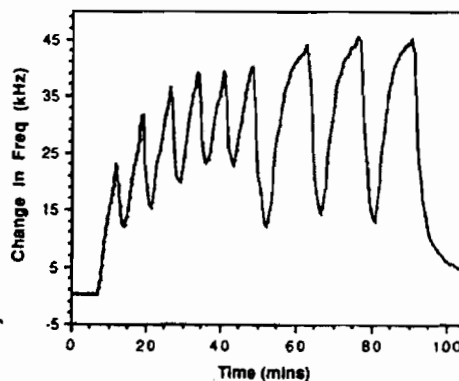


Figure 6. Frequency response of (4) vs time for periodic vapor exposure to DMMP (on/off time interval 5/2 min till $t = 48$, then 10/4 till $t = 90$).

CONCLUSIONS

In all cases, where a high response was seen to DMMP or CEES vapor there was a low response to water vapor. This is encouraging since it indicates a low interference by humidity. The moderate to good solubility of these triazine derivatives in chloroform caused no unfound difficulties in the spraying of these coatings. The relatively low volatility (as indicated by a baseline drift of ca. 1 kHz/h which is normal in a laboratory environment without a sensor temperature control), indicated a negligible tendency to vaporize when exposed to air and the possibility of a reasonable lifetime as a coating since the responses were reversible.

The coating thicknesses were relatively the same for all the triazines challenged. Although a thicker coating would display a larger response due to the greater number of sorption sites, there are other factors such as shear modulus, film mass density etc. that come into play. The vapor diffusion rate and device response times are closely related.³ As a result, a highly dense coating would hinder easy diffusion of the analyte and the corresponding response time would also be greater. It is for this reason that we have chosen not to study coating thickness versus response amounts and response times.

REFERENCES

1. H. Wohltjen, W. R. Barger, A. W. Snow, and N. L. Jarvis, *IEEE Trans. Elect. Dev.*, **1985**, ED-32(7), 1170.
2. T. E. Edmonds and T. S. West, *Anal. Chim. Acta*, **1980**, 117, 147.
3. H. Wohltjen, *Sensors Actuators*, **1984**, 5, 307.
4. C. T. Chuang, R. M. White, and J. J. Bernstein, *IEEE Electron. Device Lett.*, **1982**, EDL-3(6), 145.
5. A. Venema, E. Nieuwkoop, M. J. Vellekoop, M. S. Nieuwenhuizen, and A. W. Barendsz, *Sensors Actuators*, **1986**, 10, 47.
6. W. H. King, Jr., *Anal. Chem.*, **1964**, 36, 1735.

7. A. W. Snow, W. R. Barger, M. Klusty, H. Wohltjen, N. L. Jarvis, *Langmuir*, **1986**, *2*, 513.
8. M. S. Nieuwenhuizen and A. W. Barendsz, *Sensors Actuators*, **1987**, *11*, 45.
9. A. R. Katritzky and R. J. Offerman, *Crit. Rev. Anal. Chem.*, **1989**, *2*, 83.
10. A. R. Katritzky and G. P. Savage, *Rev. Heteroatom Chem.*, **1990**, *3*, 160.
11. A. R. Katritzky, G. P. Savage, J. N. Lam, and M. Pilarska, *Chem. Scr.*, **1989**, *29*, 197.
12. A. R. Katritzky, G. P. Savage, M. Pilarska, and Z. Dega-Szafran, *Chem. Scr.*, **1989**, *29*, 235.
13. A. R. Katritzky, G. P. Savage, and M. Pilarska, *Chem. Scr.*, **1989**, *29*, 317.
14. A. R. Katritzky, G. P. Savage, M. Pilarska, N. S. Bodor, and M. E. Brewster, *Chem. Scr.*, **1989**, *29*, 319.
15. A. R. Katritzky, R. J. Offerman, J. M. Aurrecochea, and G. P. Savage, *Talanta*, **1990**, *37*, 911.
16. A. R. Katritzky, G. P. Savage, R. J. Offerman, and B. Pilarski, *Talanta*, **1990**, *37*, 921.
17. A. R. Katritzky, J. N. Lam, and H. M. Faid-Allah, *Talanta*, **1991**, *38*, 535.

BLANK

FEASIBILITY OF DRONE-PORTABLE ION MOBILITY SPECTROMETRY

Neil S. Arnold, Henk L.C. Meuzelaar, Jacek Dworzanski and Paul Cole
University of Utah Center for Micro Analysis & Reaction Chemistry
Salt Lake City, UT 84112

A. Peter Snyder
U.S. Army Chemical Research, Development and Engineering Center
Aberdeen Proving Ground, MD 21010

ABSTRACT

The feasibility of telemetry based, drone-portable IMS (ion mobility spectrometry) and GC/IMS (gas chromatography/-ion mobility spectrometry) for real-time detection and monitoring of atmospheric concentrations of target vapors in otherwise inaccessible locations has been demonstrated using primarily "off the shelf" technology. The test configuration involved a Graseby Ionics CAM (Chemical Agent Monitor) with an ASP type PC interface, a Compaq 386 mother-board with 1 Mbyte RAM, two H-Cubed Corp. and Tekk Corp. digital radio transmitter and receiver sets, CoSession (Triton Technology) communications software and a remote, 386 level computer workstation. On-board system components weigh <15 lbs and use <30 W of battery power. Preliminary test results indicate the feasibility of transmitting ion mobility data at up to 9600 baud, corresponding to approximately 20 spectra per minute. Typical range of the tested transceiver system is 1-2 miles. Potential applications include military or law enforcement operations as well as environmental and industrial screening or monitoring.

BACKGROUND

The conventional role of a human operator in the realm of field portable ("fieldable") analytical instrumentation is threefold: (1) to carry the apparatus; (2) to perform measurements (i.e., actually operate the device); and (3) to evaluate the data. Increasingly, the last two tasks are being supported (if not completely taken over) by microcomputers. This trend threatens to reduce the human role to that of the device "carrier". Although the carrier role makes excellent sense in situations where the primary function of the fieldable instrument is to provide personal protection, the obvious limitations and vulnerability of the human body

suggest that more appropriate means of carrying a fieldable device should be considered for most other applications. In contrast to properly designed and constructed mechanical devices, the unprotected human body cannot fly, function in oxygen-deprived environments, be exposed to poisonous or corrosive chemicals, extreme heat, pressure or radiation and is vulnerable to a wide range of mechanical injuries. This seriously restricts the potential operational envelope of portable detection devices unless suitable mechanical alternatives can be developed, e.g., in the form of unmanned autonomous vehicles (UAV's).

Depending on the task at hand such UAVs may be primarily air, land or water based, may range from dumb drones (e.g., under direct remote control of human operators) to truly autonomous, smart robotic vehicles. Potential military, as well as nonmilitary (DEA, EPA, NASA) uses of UAVs for chemical/biological detection and monitoring purposes have multiplied rapidly during the past few years. Nevertheless, with the exception of recent CRDEC work on passive IR detection aboard small flying drones¹, very little work has been reported yet.

Ion mobility spectrometry (IMS) is an especially attractive candidate method for UAV based applications in view of its small size, weight and power requirements, its high degree of computerization for instrument control functions as well as data evaluation, and its advanced level of "fieldability engineering" (e.g., with regard to ruggedness, shelf life, operational simplicity and low maintenance requirements). Particularly the recently introduced, hand-portable GC/IMS (combined gas chromatography/ion mobility spectrometry) instrumentation², which promises markedly improved specificity, dynamic range and quantitative performance, would seem to be near ideal for drone-portable detection and monitoring applications.

In view of the high level of activity in all fields involved, e.g., GC/IMS, UAV, computer and communications technologies, the authors deemed important to employ "off-the-shelf" hardware and software rather than to mount a development program doomed to be outdated by the fast pace of developments in these fields. Consequently, the following two objectives were outlined at the start: (1) to expand the operational envelope of IMS and GC/IMS technology through the development of drone-portable systems, and (2) to design, assemble and test such systems using off-the-shelf, commercially available modules and components, where possible.

INSTRUMENTAL APPROACH

Several design parameters, identified as critical to the achievement of our primary objectives, need to be mentioned.

- a) Total weight of the on-board system components should be less than 25 lbs in order to permit the use of small relatively inexpensive flying drones. For instance, when using "blimp" type dirigibles, a 25 lb payload dictates a dirigible in the 15-20 m³ range.

- b) Total power requirements of the on-board modules should preferably be less than 25 watt, resulting maximally in a 50 watt hour energy requirement for a typical 2 hour flight. This permits the use of standard high performance power packs such as lithium sulfur dioxide batteries. Alternatively, under suitable ambient light conditions such low power requirements can be readily satisfied by means of a few square feet of high efficiency solar panel, e.g., mounted on the wing and/or hull structures of flying drones. This is especially attractive when considering longer duration, (e.g., 3-4 hr) flights.
- c) Ruggedness should be adequate for the demanding operational environment aboard a small, unheated flying platform. Here the dirigible blimp concept offers obvious advantages since the oversized engine needed to lift and propel a small plane and its payload tends to generate strong mechanical vibrations as well as electromagnetic noise. Naturally, weather considerations play a major role when trying to develop a drone-portable instrument package. Operation in subzero temperatures as well as under turbulent atmospheric conditions requires an even higher level of ruggedness and is currently impossible and the concept of a miniaturized all-weather, day-and-night deployable flying drone is unlikely to become reality before the end of this century.
- d) Finally, assuming that telemetry based systems (see Figures 1b and c) are generally preferable over self-contained data processing and recording systems (Figure 1a) because of the lack of real time information and the potential for catastrophic data loss inherent to the latter, minimum data transmission needs are estimated to be in the 2400-9600 baud range for IMS as well as GC/IMS applications.

The various system modules and components selected by the authors are listed in Table 1. Although an attempt was made to use only "off the shelf" available hardware and software, the Graseby Ionics EVM (Environmental Vapor Monitor), the GC/IMS module shown in Figure 2, is a special pre-production prototype. Also the Tekk 9600 baud transceiver represents an incompletely tested, new model selected on the basis of experiments with two other Tekk transceiver sets, the model KS-900 (1200 baud, UHF), and the model TS-200 (1200 baud, VHF), both with built-in modems but lacking the more sophisticated communication protocols of the Tekk 9600 (according to the company's specifications). Earlier tests with a 2400 baud digital transceiver, without modem, manufactured by H-Cubed Corporation¹ convinced the authors of the desirability of using advanced modem communication protocols to eliminate (or at least strongly reduce) electromagnetic noise interference.

Although, in principle, one could develop special communications software with built-in noise rejection capabilities, the above described strategy of using "off-the-shelf" software and hardware modules limited our options to commercially available communication software packages such as Carbon Copy, PC Anywhere or Co-Session, all of which had been tested previously at UUMARC (University of Utah Center for Micro Analysis & Reaction Chemistry). Among these three packages, Co-Session was selected for drone-portable IMS

and GC/IMS applications because of its ability to download data simultaneously with the remote data acquisition.

The choice of the microcomputer, a Compaq portable LTE 386/20e was based entirely on size, weight and power requirement considerations as well as on the availability of an IO bus extender (which is assured to be completely stripped of its voluminous and heavy plastic housing). Moreover, both hard disk and display screen can be turned off by software commands to limit in flight power consumption. A suitable UAV system has been developed by H-Cubed Corporation for CRDEC and has been successfully demonstrated while carrying the 15 lb FTIR instrument package for up to 3 hours at a payload power consumption level of 28 W. Standard features of this light weight, low cost, UAV have been described elsewhere³ and include digital transceiver control of the avionics hardware and an on-board video camera (or camcorder) with video telemetry transceiver. Consequently, a remote human operator can receive a continuously updated birdseye view of the terrain below, thus facilitating precise maneuvering and terrain-responsive navigation.

Although the EVM (or similar (GC)/IMS system) has not yet been tested aboard the UAV shown in Figure 3, no special weight and/or size problems are anticipated. In fact, the most uncertain element of the proposed approach probably lies within the area of mechanical vibrations and electromagnetic stability. If actual flight tests encounter particularly severe obstacles in this regard then the use of a dirigible ("blimp") type UAV may need to be considered as a possible alternative.

PRELIMINARY GC/IMS TEST RESULTS

Using an automated vapor sampling (AVS) device of the type shown in Figure 4, developed at UUMARC (US patent 4,970,905) and also built into the Graseby Ionics EVM under special licensing agreements with FemtoScan Corporation (Salt Lake City, Utah), a mixture of 4 phosphonate simulants was tested. The overall test configuration was comparable to that depicted in Figure 1b, except that the two transceivers were replaced by a direct twisted wire pair cable connection between the RS232 ports of both microcomputer workstations. Consequently, only the GC/IMS system (a specially constructed breadboard prototype), the ASP board and the Co-Session communication software were involved in this test.

The "waterfall display" type representation of the GC/IMS data in Figure 5, as recorded by the remote workstation, shows excellent picture quality at an effective IMS scanning rate of approx. 3 seconds per spectra.

At the time of writing, laboratory testing of various wireless configurations (e.g., involving the Tekk 9600 baud transceivers with built-in modem functions) continues at UUMARC. Consequently, the practical feasibility of drone-portable GC/IMS with real-time, wireless data transmission, while using off-the-shelf modules and components, remains to be demonstrated with particular emphasis on establishing an interference-free, fast telemetry link and on performing actual flight tests using a small airplane or dirigible type flying UAV.

CONCLUSIONS

It appears feasible to assemble drone-portable IMS and GC/MS systems using off-the-shelf, commercially available components provided an on-board computer system is used for data reduction and pre-processing in order to bring data transmission rates within the range of currently available telemetry equipment. Presently available computer and telemetry modules account for more than 50% of the on-board weight, size and power projections. Besides further reductions in weight, size and power requirements, there is a need for additional evaluation of potential sources of mechanical and electrical interference.

ACKNOWLEDGEMENTS

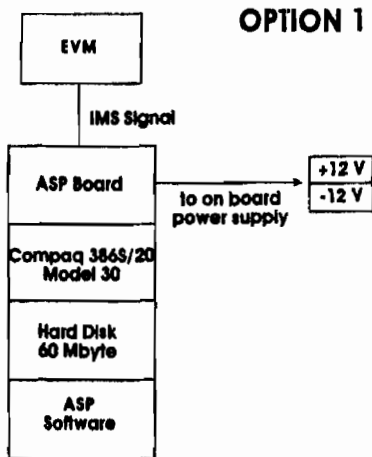
The authors wish to thank Graseby Ionics Ltd., H-Cubed Corporation and Tekk Corporation for their kind assistance in providing technical information and illustrations describing recently developed prototype systems.

REFERENCES

1. Kroutil, R.T., et al. Proceedings of the 1990 CRDEC Scientific Meeting, in press.
2. Meuzelaar, H.L.C., Kim, M.-G., Arnold, N.S., Urban, D.T., Kalousek, P., Snyder, A.P., "Man-portable Gas Chromatography/Ion Mobility," Proceedings of the 1990 CRDEC Scientific Meeting, in press.
3. U.S. Army Armament, Munitions and Chemical Command, "UAV Passive Chemical Detection System," Aberdeen Proving Grounds, MD 21010.

TABLE 1
SELECTED COMPONENTS

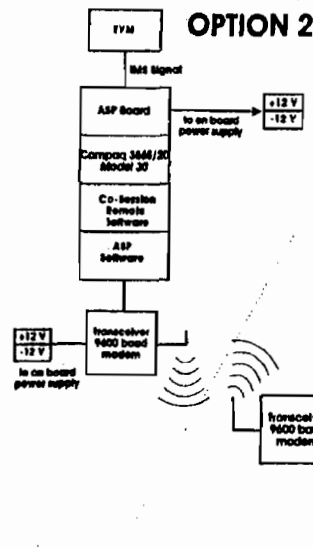
On-board Component	Manufacturer/ Model	Weight	Power Consumption	Dimensions
EVM	Graseby Ionics	7 lbs (inc. battery)	4-12 W (self-supplied)	21.4" x 3.2" x 8"
ASP Board	Graseby Ionics	.54 lbs	.6 - 5 W	9" x 5.5" x .9"
Transceiver	Tekk VHF 9600 baud	.6-.95 lbs.	1-12 W	2.8" x 1.9" x 6.9"
Compaq Computer	Compaq 386 s/20 Model 30	7.7 lbs (inc. battery)	6-13 W (self-supplied)	2.2" x 11" x 8.5"
+ 12 V Powerpack	Saft BA5590/U	2.25 lbs inc. on Drone	96 Watt-hours (2A, + 12 V, 2A,-12 V)	5" x 4.4" x 2.45"



Option 1. All on-board GC/IMS/COMP system (with hard disk data recording) e.g. flying a predetermined grid pattern while recording location and time.

Advantage:
 * simplicity and low cost

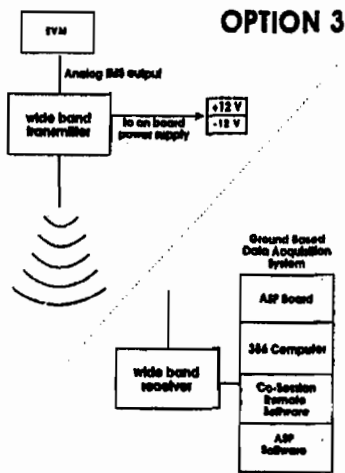
Disadvantage:
 * no real-time info
 * potential for accidental data loss
 * heavy on-board computer needed
 * need for advanced positioning technology



Option 2. On-board GC/IMS/COMP system with telemetry (VHF transceiver) connection to remote PC ground station.

Advantage:
 * back-up data recording (2 places)

Disadvantage:
 * potential electronic data transmission interference
 * heavy on-board computer needed



Option 3. On-board GC/IMS system with wide band telemetry transceiver to remote PC ground station.

Advantages:
 * low weight and power requirements

Disadvantages:
 * reliable wide band telemetry not yet routinely available
 * no back-up data recording

Figure 1. Schematic diagrams illustrating three possible configurations for drone portable GC/IMS. Option 2 is most promising for its data security with on-board storage and real-time observation.

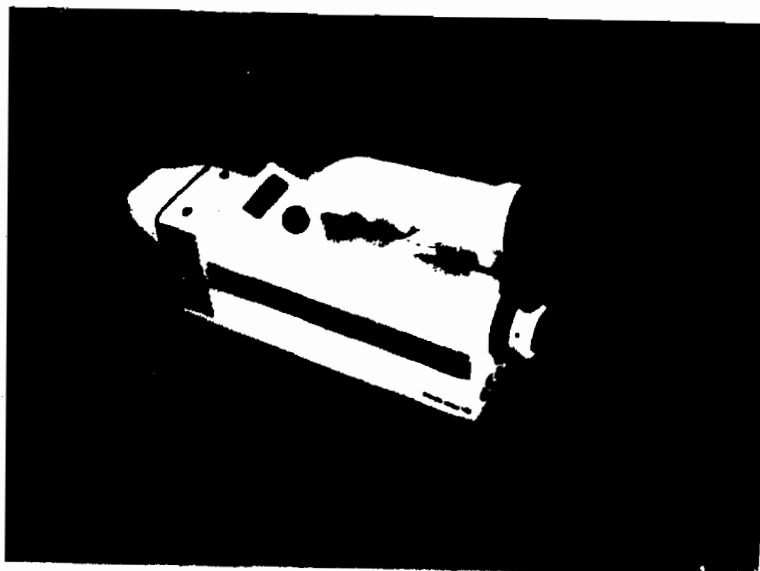


Figure 2. Photograph of prototype GC/IMS module (EVM, Graseby Ionics Ltd.).

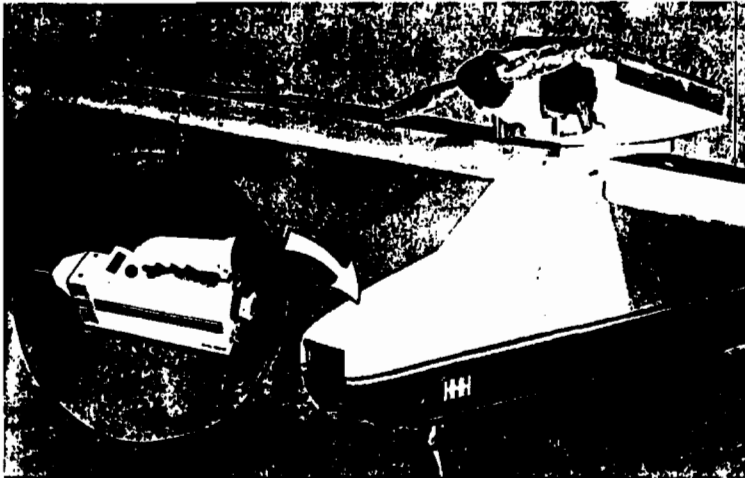


Figure 3. UAV "drone" with EVM module inset.

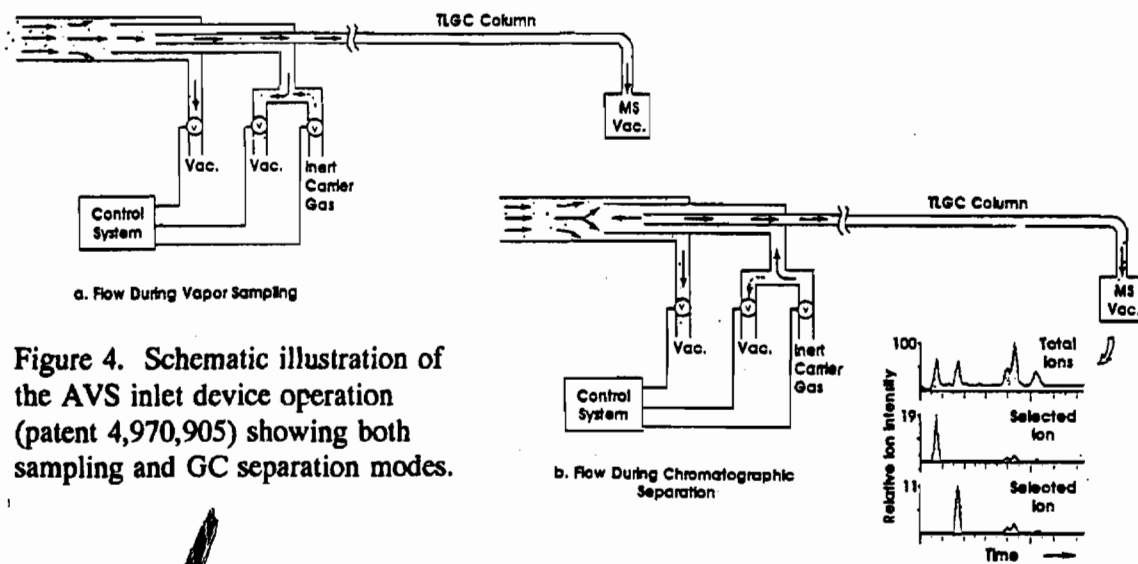


Figure 4. Schematic illustration of the AVS inlet device operation (patent 4,970,905) showing both sampling and GC separation modes.

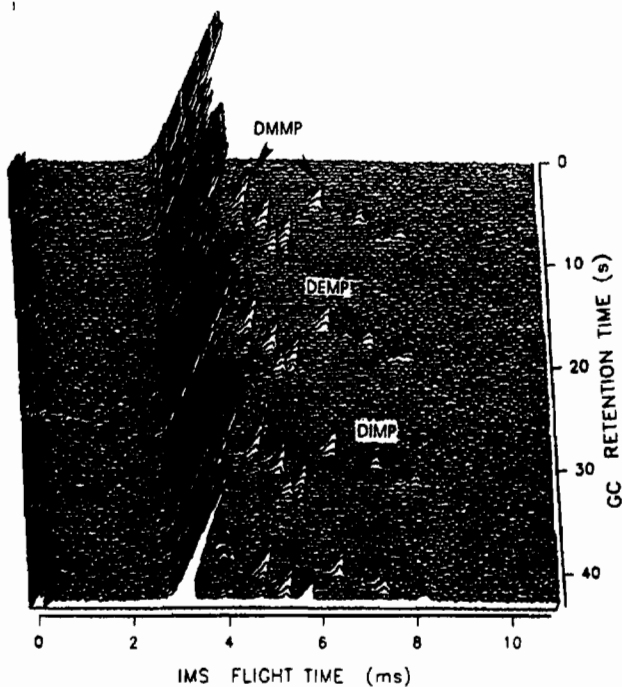


Figure 5. "Waterfall" display of three successive vapor samples and subsequent GC separations of a mixture of four alkyl phosphonate simulants. The vertical axis (surface profile height) indicates the IMS cell signal intensity.

BLANK

MATERIEL TEST FACILITY

(MTF)

PARAMETRIC CONTROL

AND

HAZARD CONTAINMENT

BY

Gary R. Bodily

Frank D. Anderson

ABSTRACT

The Materiel Test Facility (MTF), now under construction at DPG is designed to test large test items in chemical environments. To meet this mission the MTF must be able to meet the technical requirements of the test while providing absolute protection for human life, the environment, and government facilities. Central to meeting these objectives is the control system that runs the building. This system must monitor the building continuously. If a problem arises, such as equipment failure, the operator must be alerted and appropriate action initiated to contain the problem. This is critical while chemical agent operations are in progress. The program must also maintain a test environment within set limits. These limits may be static (time invariant) or dynamic (time varying) in nature. This paper describes the control system and its function that will allow the MTF to meet these requirements.

BACKGROUND

The Materiel Test Facility (MTF) is a new toxic agent facility under construction at U.S. Army Dugway Proving Ground (DPG). In this facility a state-of-the-art test facility, military equipment will be exposed to toxic agents.

Appendix A contains a simplified MTF fact sheet describing MTF equipment.

The multipurpose room will be used to test various toxic agents (i.e., GA, GB, GD, VX, H, HL, and L). Other agents that may be used for specific applications.

The multipurpose room will have controls that allows operation of the room 24 hours per day with pressure with temperature (150°F to -50°F), and Relative Humidity RH (5% to 95%) are fully controlled through the MTF control system.

The agent transfer room has the repository for agent storage. It will have two chemical fume hoods on either side of the access door.

In the closed system chamber testing will be done on smaller items.

The pressures inside the agent areas will be maintained through the pollution abatement system. The pollution abatement system consists of the

Thermal Decon Furnace (TDF) and an independent filter systems. Depending on concentration inside the multipurpose chamber the flow will be directed through either the TDF or the filter system.

CONTROL HARDWARE DESCRIPTION

The MTF will have real time monitoring 24 hrs. a day 7 days a week that will be logged on a PC mini net, this monitoring will be through out the facility.

The MTF control system consists of the Genesis™ (Reference 1) control software program. This program communicates with two high performance programmable controllers (HPPC) (Reference 2). These controllers are a double "hot" redundant system, either one or the other will run the facility. The HPPCs communicate with through five Serial Interface Modules (SIM) that access the I/O boards. The HPPCs, SIMs, and I/O boards together makeup the Program Logic Controller (PLC). See Figure 1

The PLC has a SIM in each container that controls the Discrete and the Analog signals for each container, There are a total of five containers in the MTF facility. The PLC has expansion capabilities of up to 16 SIMs which allows for future expansion.

CONTROL REQUIREMENTS

During operation all equipment must operate together properly in order to meet the operational requirements.

A control system must meet two requirements:

1. Contain hazards inherent in testing.
2. Meet time dependent test criteria.

HAZARD CONTAINMENT

Hazards are a fact of life at the MTF. In fact we will routinely generate environments that are hazardous according to any standard. We will determine how other equipment will react in these environments.

Before a hazard containment system can be identified, engineered, or tested, a through analysis of MTF operations and equipment failure modes needs to be completed.

In the list that follows we have not discussed all possible failures. In each case, the failure that could cause a hazard containment fault will be identified. The hazard that could be released or generated will be described, and the methods to contain the hazard will be explained.

OPERATOR INTERFACE

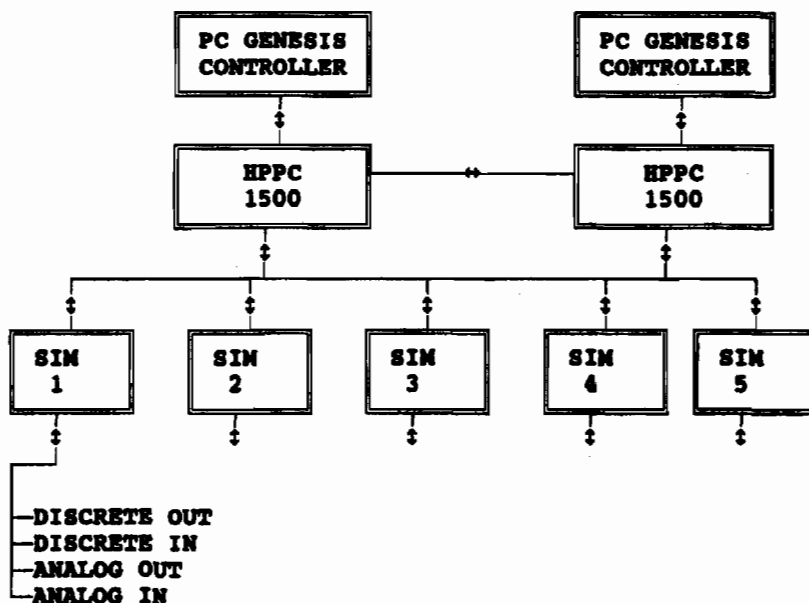


FIGURE 1 PLC (Flow Chart)

NO FAILURE

DESCRIPTION OF FAILURE

The first mode of operation that is considered is the basic no-fault mode. In this mode, no failure has occurred, however a hazard could still exist. This mode of operation will be used as a baseline situation to examine all other failure modes.

HAZARD DESCRIPTION

The most common hazard in the MTF will be the release of chemical agents in the various test chambers/fixtures.

HAZARD CONTAINMENT

To preclude agent migration, the MTF uses the following safety measures:

1. Chamber Insulation. Between each test chamber in the MTF are heavy industrial doors. These doors designed with an inflatable butyl rubber seal that can be inflated to seal the room.
2. Pressure Control. To ensure no agent-laden air leaves the containment facilities we always keep the agent chambers at a lower pressure than their airlocks. We also keep the airlocks at a negative pressure compared to the secondary containment areas.

FAILURE COMMERCIAL POWER

DESCRIPTION OF FAILURE

Loss of commercial line power.

HAZARD

Possible Agent release due to loss of engineering controls.

CONTAINMENT

After an interruption in line power the critical load of the MTF is taken over by an Uninterruptable Power Source (UPS). There is a five second delay before an emergency generator automatically starts and restores power to the MTF.

PRESSURE SENSOR FAILURES

DESCRIPTION OF FAILURE

Loss of signal to the PLC

HAZARD

There are many areas that have pressure sensors. If one should fail this could cause a possible structural damage to the facility. This damage is caused by the PLC trying to maintain a negative pressure because of the faulty sensor. If the facility failed this would cause a loss of engineering controls that could result in a release of agent.

CONTAINMENT

This hazard could be resolved by:

Installation of a redundant pressure sensor in the multipurpose test chamber. This could then be monitored through the PLC and determined as to which one to use by the operator.

Monitoring the sensors and comparing them to predictions made by an internal model (Reference 3).

PLC SHUTDOWN (Leaving only one active)

DESCRIPTION OF FAILURE

This failure is described as a shut down of Active PLC 1 or PLC 2. See Figure 1 For flow chart of PLC configuration.

HAZARD

None, however, backup redundancy is compromised.

CONTAINMENT

This is an automatic transfer from one HPPC to the HPPC however there is a alarm signal that is sent to the operators station notifying that only one HPPC is active. The facility remains up without any "bump" in the transfer.

PARAMETRIC CONTROL

The second function of the control system is parametric control of test conditions. Parametric control implies that we are concerned with the time dependent, or time varying control of test conditions.

The MTF is setup to provide control over the environment in all areas of the building. The agent areas, administrative areas, etc. each have to be controlled to keep the temperature, RH, and pressures within comfort safety limits.

We will describe the control options available by using the temperature control problem as our example. A simple feedback system will be described and then expanded to include other important control features. The control of other systems are developed in a similar manner.

Figure 2 diagrams the flow of information in the physical system. In other words, the Heater Control Valve (HCV) position will affect the system (Sys) in some manner and produce an output T.



Figure 2, physical block diagram.

It is the value of T that we are interested in. If T is too high or too low, we want to modify HCV to bring it into specifications.

A control diagram that will control the temperature is shown in Figure 3.

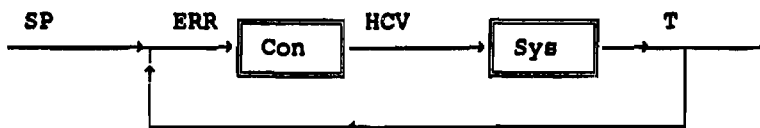


Figure 3, Basic Feedback Control

As you can see the temperature (T) and set point (SP) are compared and an error (ERR) is produced. The error tells how far T is from the desired temperature, i.e. the set point.

A control system (Con) takes the error signal (Sys) and produces an output signal (HCV) that will control the system.

If we have chosen the control system properly, the HCV will soon reach a value where T is at the desired temperature and ERR becomes zero.

It now becomes a simple matter to set the temperature. We simply change the set point.

If this was our only difficulty the control problem would be solved. However, Figures 2 and 3 are simplifications of the real world. We have other factors that influence the temperature. For example, if we have an air handling unit (AHU) that turns on, the heat content of the air entering the system will change the temperature. This situation is portrayed in Figure 4.

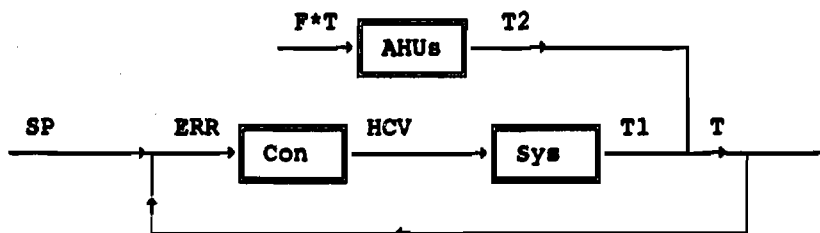


Figure 4, Block Diagram of Indicated Interference

Notice that now the temperature can be changed by means other than the control system we have put in place. This secondary means of changing the temperature can change in such a way as to never allow the controller to catchup.

Another problem comes is that our controller has to wait for an error to appear and grow before it takes action. This lag of response means that we must leave the test specifications for a period of time. If the air handling unit changes fast enough, we may never meet the required test conditions.

To reduce the difficulties caused by these auxiliary disturbances, we need to monitor the changes that will cause these temperatures to fluctuate. This accomplished by adding an additional controller AHUc this will then cancel out the influence of T2 resulting in a constant temperature

All of the PID loops will have to be modeled in a similar Manner after construction has been completed.

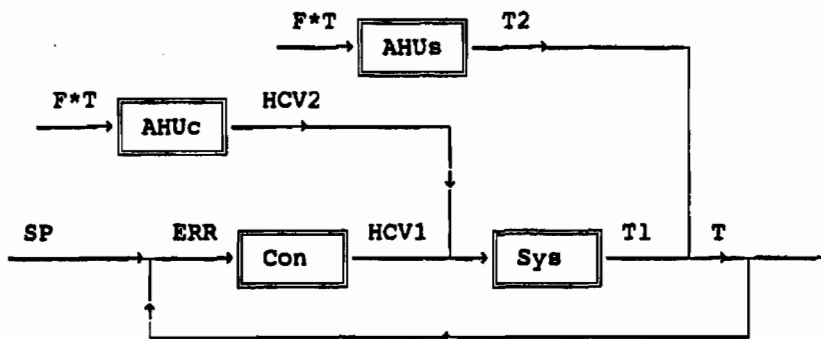


Figure 5, TEMPERATURE CONTROL EXAMPLE

CONCLUSIONS

The control program envisioned for the MTF will be able to provide protection and meet test requirements. To achieve this objective, a through analysis of all possible hazards needs to be conducted. Based on this analysis automatic control logic needs to be incorporated into the control program to respond to all hazards. This logic will be tested thoroughly before the facility comes on line. All operational parameters of the building needs to be modeled. This modeling will consist of analytical and empirical modeling. Based on this modeling, failures can be detected even if an instrument fails, or an instrument is not available. This modeling will be used to predict performance of the MTF, and allow test conditions to be met as accurately as possible.

TABLE OF NOMENCLATURE

AI	- Air Handling unit
CON	- Controller
DPG	- U.S. Army, Dugway Proving Ground
ERR	- Error
HCV	- Heat Control Valve
HPPC	- High Performance Programmable Controller
MTF	- Materiel Test Facility
PID	- Proportional Integral Derivative
PLC	- Program Logic Control
SIM	- Serial Interface Module
SP	- Set Point
SYS	- System
T	- Temperature
TDF	- Thermal Decon Furnace
UPS	- Uninterrruptable Power Source

REFERENCES

1. "Genesis Control User's Reference Guide", ICONICS, Inc., 1989.
2. "APL Programming Manual", WESTINGHOUSE ELECTRIC CORP., Aug. 1985.
3. D'Azzo John J. and Houpis, Constanine H., "Linear Control System Analysis and Design", McGraw-Hill Publishing Company, USA, 1988.

APPENDIX A, MATERIEL TEST FACILITY FACT SHEET

MULTIPURPOSE TEST CHAMBER

50' L X 50' W X 30' H
+150°F to -50°F
Stainless Steel Construction
High Agent Concentration
Air Tight Chamber
13,000 CFM Purge
Humidity Control
16' W X 24' H Door
Bridge Crane (sealed)
Pneumatically Sealed Air-locks

AGENT TRANSFER ROOM

25' L X 25' W X 30' H
5,300 CFM purge
Pneumatically Sealed Air-locks
2 - Fume Hoods
Agent Repository

CLOSED SYSTEM CHAMBER

25' L X 25' W X 30' H
5,300 CFM purge
Pneumatically Sealed Air-locks
Env. Controlled Glove Box
-65 °F to 125 °F
5% to 90% RH

THERMAL DECON FURNACE

1,800 °F
37,800 CFM
3 - 100 HP fans
5 - sec residence time

FILTER SYSTEM

0 to 34,600 CFM
2 - 150 HP variable speed fans

UPS SYSTEM

Maintains Critical Load
30 Minute Backup

SECURITY

Controlled Entry Point
Self-contained facility
Emergency Generator
Double Perimeter Fence
Intrusion Detection System

BACKUP GENERATOR

1 MW power
5 sec response
Electrically Heated Heads

PROPANE TANKS

3 - 15,000 gallon tanks
40,500 Gallon Total Max. Cap.

BOILERS

2 - 25/125 Psi Boilers
250 Hp
8,600 #/hr steam

SERVICE AIR

2 - 300 SCFM Screw Comp.
1 - 1,400 gal. rec. tank
1 - 1,600 gal. rec. tank

LIFE SUPPORT/INSTRUMENTATION AIR

2 - 150 SCFM Carbon Ring Comp.
1 - 2,100 gal. air rec. tank
1 - 1,200 gal. air rec. tank

GENERAL

1,546 Instruments
21 - Supply/Exhaust Fans
10 - Process Fans
5 - Duct Fans
2 - Cooling Tower Pumps
2 - BFW Pumps
2 - Heat-exchanger Pumps
1 - Water Service Pump
1 - 15,000 Turbo Exhaust

VACUUM SYSTEM

Filtered Exhaust
2 - 100 SCFM vac. pumps
40 IWG

SPENT DECON TANKS

3 - 5,000 gal. tanks
3 - 40 gpm pumps
3 - 30 gpm pumps

IMMUNO-CAM: THE DETECTION OF BACTERIA USING AN IMMUNOASSAY TECHNIQUE COMBINED WITH THE CHEMICAL AGENT MONITOR (CAM)

David A. Blyth¹, Maryalice Miller², John A. Parsons¹
and A. Peter Snyder²

¹GEO-CENTERS, INC., 10903 Indian Head Highway, Ft. Washington, MD 20744, ²U.S. Army Chemical Research, Development and Engineering Center, Aberdeen Proving Ground, MD 21010-5423

Abstract

An immunoassay technique has been modified so that the end product is not a colour change (as in a conventional ELISA assay) but the evolution of a vapour. The vapour is then detected by CAM, a chemical agent monitor that is already in service with NATO armed forces. The method is an extension of the previously reported BIO-CAM technique, but because it employs antigen/antibody reactions it is inherently more specific and therefore potentially more useful for field application.

Bacillus cereus organisms (a simulant for *B. anthracis*) have been detected in a suspension containing 10^3 - 10^4 bacteria per ml, this result being very competitive with current technologies. Another antigen interrogated was lipopolysaccharide endotoxin, a surface marker of *Haemophilus influenza* and pneumonia bacteria.

Introduction

Intracellular and extracellular enzymes have traditionally provided microbiologists with a means for the identification of the parent microorganism¹⁻⁵. In many instances the enzyme is made to react with a substrate that will cause a colour change, detected either visually or by spectrophotometric analysis. BIO-CAM⁶ showed that a substrate could be chosen that would give a vapour product that could be readily detected by an appropriate sensor, in this case the Chemical Agent Monitor (CAM). The advantage of using CAM is twofold, first the instrument is in wide scale of issue throughout NATO armed forces. Secondly, it employs the principle of ion mobility spectrometry (IMS) which is the sensor employed in the 'chemical side' of the 6.2 XD

chemical/biological (CB) detector programme currently being pursued by Detection Directorate. The implication of this latter fact is that it opens up the possibility of using IMS as the sensor for both chemical and biological components in the detector.

The principle used in BIO-CAM was simple and effective but was limited in that the method probed the intracellular enzymes of the microorganism (and depended on the fact that such an organism had available enzymes). This meant that a time-delay was introduced to allow diffusion of the reactants through the cell wall. This delay time was about 20 min. when probing the *E. coli* enzyme beta-galactosidase. It was also realised that specificity of the method could be improved if an antibody/antigen reaction could be used, and further, it may be possible to label the antibody with an appropriate enzyme thus making the enzyme directly accessible to the added substrate, eliminating the delay time.

With these factors in mind, the principle of Immuno-CAM was established based on an antigen/antibody reaction and with a detectable vapour as the final product. One great advantage of the system is that virtually any agent of biological origin can be targeted using the appropriate antibody. Most of the work described here was carried out using *B. cereus* organisms as the target antigen, since from an identification point-of-view, it simulates *B. anthracis*. The enzyme to be attached to the antibody was beta-galactosidase and the substrate ortho-nitrophenylgalactoside (ONPG). The enzyme would then cleave the ONPG to form ortho-nitrophenol (ONP), a vapour which was subsequently detected by CAM in the negative ion (H) mode.

Unfortunately, it was not possible at this time to obtain the beta-galactosidase enzyme directly attached to the antibody specific to the lipopolysaccharide found in *B. cereus* or *B. anthracis*. A secondary antibody had to be employed which although complicating the reaction chain, did have the advantage of introducing some degree of signal amplification.

Experimental

The complete immunoassay 'ladder' is represented schematically step-by-step in Figure 1.

Step 1.

Antigen is adsorbed onto a surface by immersing a polystyrene 'paddle' into the bacterial suspension overnight. The area involved was 1.5 cm². Upon removal the paddle was rinsed in washing buffer solution.

Step 2.

The paddle was immersed in a monoclonal antibody, specific to the lipopolysaccharide found in *B. cereus*, for 1 hr. Upon removal the paddle was washed in buffer, immersed in blocking solution for 1 hr, and then given a final rinse in buffer. At this stage all adsorption sites should be occupied by either antibody or blocking agent.

Step 3.

The paddle was immersed in a secondary antibody, biotinylated goat anti-mouse, which will selectively attach itself to the monoclonal antibody, leaving exposed several biotin sites on each secondary antibody. The paddle was again washed.

Step 4.

In this step the β -galactosidase enzyme is added to the 'ladder' by immersing the paddle in a solution of β -galactosidase labelled streptavidin. The streptavidin binds strongly to the several biotin sites on each molecules effectively giving an amplification factor in the number of exposed enzyme sites available to react with the vapour producing substrate.

Step 5.

At this stage the ONPG substrate was added to the paddle to produce the ONP vapour. Before adding the ONPG, the paddle had folded over it a 1 cm² of Kimwipe tissue. Past experience had shown that the tissue facilitated the spread of a small drop of liquid into a thin film evenly covering the paddle surface, and did not inhibit nor delay the evolution of the ONP vapour from the liquid film. Immediately after the ONPG had been added to the paddle, its handle was broken off and the paddle sealed into a specially designed vapour sampler prior to sampling by CAM.

The vapour sampler, shown in Figure 2, consisted of two parts, a 5.7 ml volume pot which held the paddle, and a pot holder which fitted over the inlet nozzle of CAM. When the pot was partially inserted into its holder, it became sealed and vapour could start to build up. At this time CAM was able to sample ambient air as normal. When the pot was fully inserted into the holder the ambient air flowing directly into CAM was cut off, and CAM sampled ambient air via the pot, picking up any vapour that may be present.

The variation of the CAM output signal with varying dilutions of bacteria suspensions was determined. As a cross reference for these procedures, the same dilutions were used to run an Enzyme Linked Immunosorbent Assay (ELISA) in parallel with the Immuno-CAM.

Results

The ortho-nitrophenol (ONP) vapour produced as the detectable product of the immunoassay produces both monomer and dimer in a negative ion mobility spectrum. In the present study we were only interested in the lower vapour concentrations, thus the height of the monomer peak with a mobility of $1.7 \text{ cm}^2 \text{ sec}^{-1} \text{ volt}^{-1}$ was taken as the CAM output signal.

Two minutes was required for equilibrium conditions to be reached. At this time, the vapour was sampled by CAM. Figure 3 shows a sequence of spectra taken over a period of 1 min. The height of the first peak was taken as the CAM output. Over the duration of the sequence shown, the signal dropped only a small amount, since what was being measured was the near steady output of vapour from the paddle. The significance of this result is that integration of the peak areas (or alternatively use of a vapour pre-concentrator) could provide an enormous signal that would allow detection of low vapour concentrations.

Figure 4 is a plot of CAM output signal obtained from bacteria suspensions of different concentrations. The plot is characteristically sigmoid in style, and suggests a limiting sensitivity 10^3 - 10^4 organisms per ml. Also in the figure is a plot of the ELISA run using the same series of suspensions. The normal sigmoid curve was obtained with the limit of detection being between 10^4 and 10^5 organisms per ml. In neither titration was there any measure of the actual number of bacteria adsorbed on the surface of the paddle - only of the number concentration of the suspension into which the paddle had been immersed. It is this latter figure which is relevant, since the suspension will be a direct consequence of sampling from the atmosphere.

Discussion

A comparison of the two plots of Figure 4 show that the sensitivity of the present Immuno-CAM concept compares favourably to a standard laboratory ELISA technique. This is very encouraging when it is considered that the present Immuno-CAM procedure and hardware are not optimised: for example, the paddles, instead of being specially sensitized polystyrene surfaces, were nothing more than McDonalds coffee stirrers which were used as an expedient until the size, shape and material of a more suitable reaction surface could be found. [Some conventional materials such as cellulose nitrate were not applicable to Immuno-CAM because of self vapour absorption.] Neither the reagents nor reaction times have been optimised, but it is known that it is not necessary to immerse the paddles in antigen overnight, and that the immersion times may be reduced (e.g. - 2 hrs.). An investigation into these parameters will be included in the next phase of the work. Another subject for investigation is the possibility of shortening the immuno-assay by eliminating Steps 3 and 4 and attaching the enzyme directly to the primary antibody. What the results do show, however, is that the use of an immunoassay technique combined with an ion

mobility vapour sensor can detect the presence of organisms with a realistic sensitivity in a time frame of minutes.

CONCLUSIONS

A conventional immunoassay technique has been modified so that the end product is not a colour change but the evolution of vapour. The vapour is then detected using the Chemical Agent Monitor CAM. By this means it has been shown possible to adapt CAM, an instrument in a wide scale of issue throughout NATO armed forces, to the detection of bacteria.

ACKNOWLEDGMENT

The authors wish to thank Linda G. Jarvis for the preparation of this manuscript.

REFERENCES

1. EPA, AWWA, Standards Methods for the Examination of Water and Wastewater, 16 Ed., American Public Health Assoc.; Washington, D.C. (1985).
2. J. S. Newman and R. T. O'Brien, *Appl. Microbiol.* **30**, 584-588 (1975).
3. U. Bachrach and Z. Bachrach, *Appl. Microbiol.* **28**, 169-171 (1974).
4. J. R. Wilkins, R. N. Young and E. H. Boykin, *Appl. Environ. Microbiol.* **35**, 214-215 (1978).
5. P. Cady, S. W. Dufour, J. Shaw and S. J. Kreager, *J. Clin. Microbiol.* **7**, 265-272 (1978).
6. A.P. Snyder, M. Miller, D. M. Davis, G. A. Eiceman, D. A. Blyth and J. A. Parsons, Proceedings of 1990 U.S. Army Chemical Research Development and Engineering Center Scientific Conference on Chemical Defense Research, 13-16 November 1990.

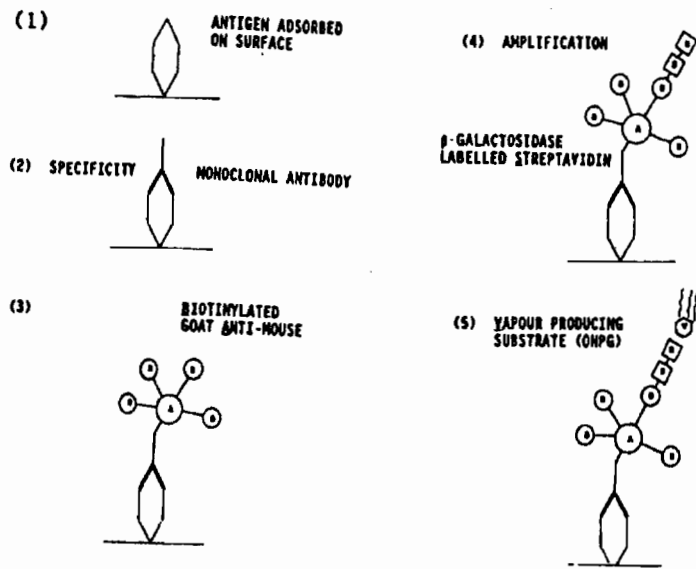


Figure 1. Principle of Immuno-CAM

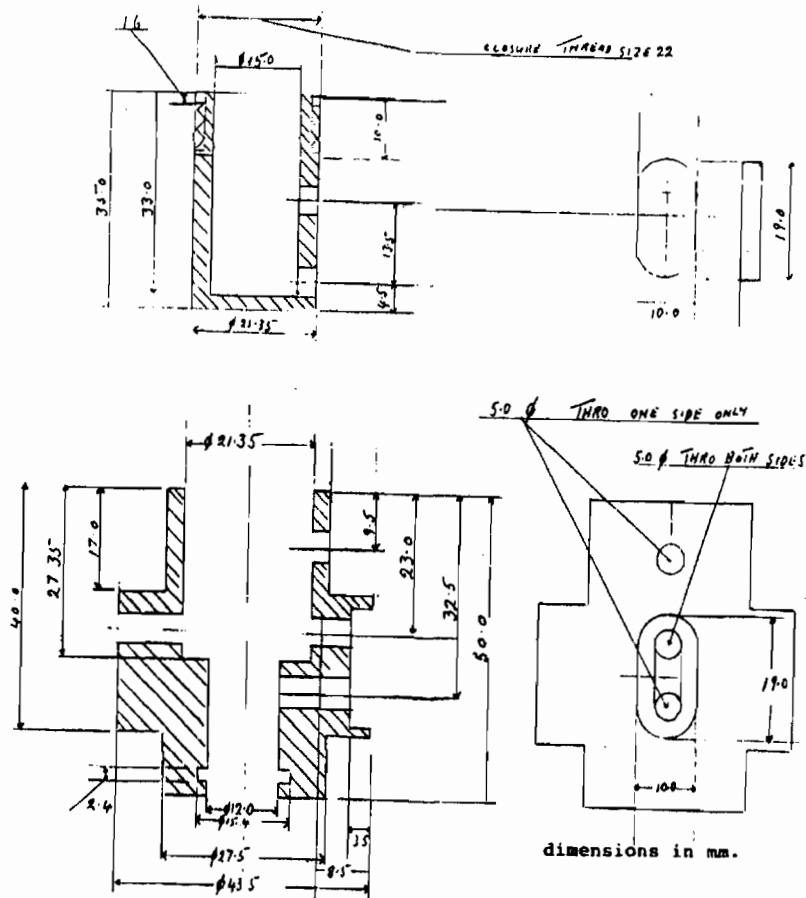


Figure 2. Vapour Sampler for Immuno-CAM

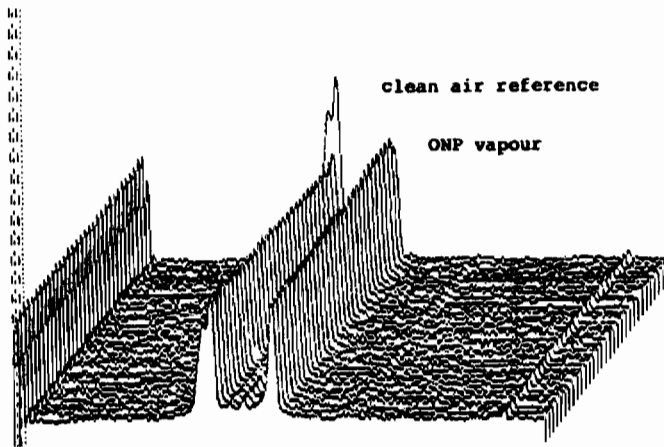


Figure 3. Sequence of Mobility Spectra Showing Steady Output from Immuno-CAM

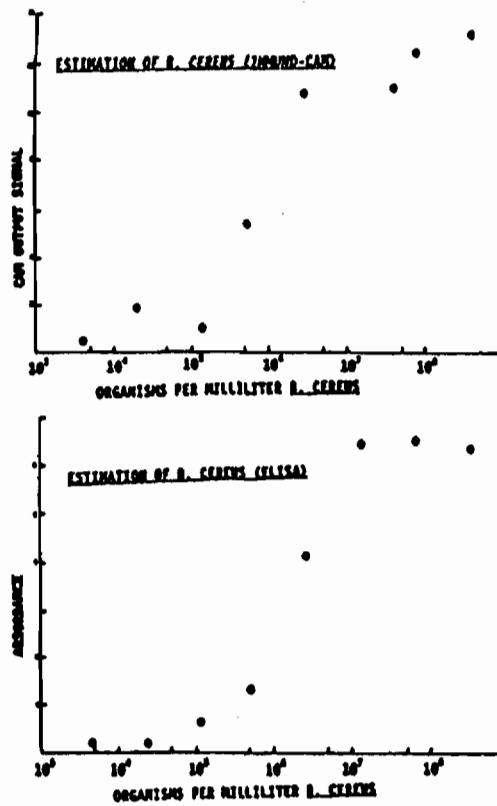


Figure 4. Estimation of *B. cereus* using Immuno-CAM and ELISA

BLANK

**DETECTION AND IDENTIFICATION OF O-ETHYL S-[2-DIMETHYLAMINOETHYL]
METHYLPHOSPHONOTHIOATE DEGRADATION PRODUCTS BY
CHEMICAL IONIZATION MASS SPECTROMETRY**

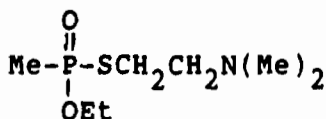
Dennis K. Rohrbaugh
Research Directorate
U.S. Army Chemical Research, Development and Engineering Center
Aberdeen Proving Ground, MD 21010-5423

ABSTRACT

Because of recent multinational chemical weapon treaty verification efforts there is renewed interest in the detection of Schedule 1 compounds and their degradation products. In this study we apply methane chemical ionization (CI) capillary column gas chromatography/ mass spectrometry (GC/MS) to successfully identify 18 degradation products resulting from the degradation of O-ethyl S-[2-dimethylaminoethyl] methylphosphonothioate. Products are identified for both storage under an inert atmosphere and after exposure to the atmosphere. Under inert conditions degradation occurs primarily to a mixture of pyrophosphonates, thiolamine, and phosphonothioates containing 1, 2 and 3 sulfur atoms. Exposure to the atmosphere results in oxidation to disulfides.

INTRODUCTION

Recent multinational interest in chemical weapon treaty verification has renewed interest in the detection of chemical warfare agents and their degradation products, particularly organophosphorus compounds. The objective of this study is to provide a suitable method of detection for these compounds and to provide information on the types of degradation products formed to aid in treaty verification. Many of these compounds are difficult to analyze by conventional electron ionization (EI) mass spectrometry because extensive fragmentation occurs under these conditions. In this study we apply methane chemical ionization GC/MS to identify 18 products resulting from the degradation of O-ethyl S-[2-dimethylaminoethyl] methylphosphonothioate.



Products are identified for both storage under an inert atmosphere and after exposure to the atmosphere.

METHODS

Mass spectra were obtained on a Finnigan model 5100 GC/MS equipped with a fused silica 15 m x 0.25 mm ID SE-54 capillary column (J&W Scientific). Injection temperature was 200°C, GC/MS interface temperature was 220°C and the oven was programmed from 60°C to 260°C at 10°C/min. 0.01 µl of sample was injected with a split ratio of 50:1. The CI reagent gas was methane with an internal source pressure of 0.6 Torr. The mass range was scanned from 60 to 450 amu at a rate of 1 scan per second.

RESULTS AND DISCUSSION

Figure 1 illustrates the GC/MS CI total ion chromatogram obtained for a sample of O-ethyl S-[2-dimethylaminoethyl] methylphosphonothioate after storage under inert conditions. 18 compounds were observed. The identification of each of these compounds for storage under inert (nitrogen) and atmospheric conditions is listed in Table 1.

FIGURE 1

Methane CI GC/MS Chromatogram of O-Ethyl S-[2-Dimethylaminoethyl] Methylphosphonothioate After Storage Under Inert Conditions

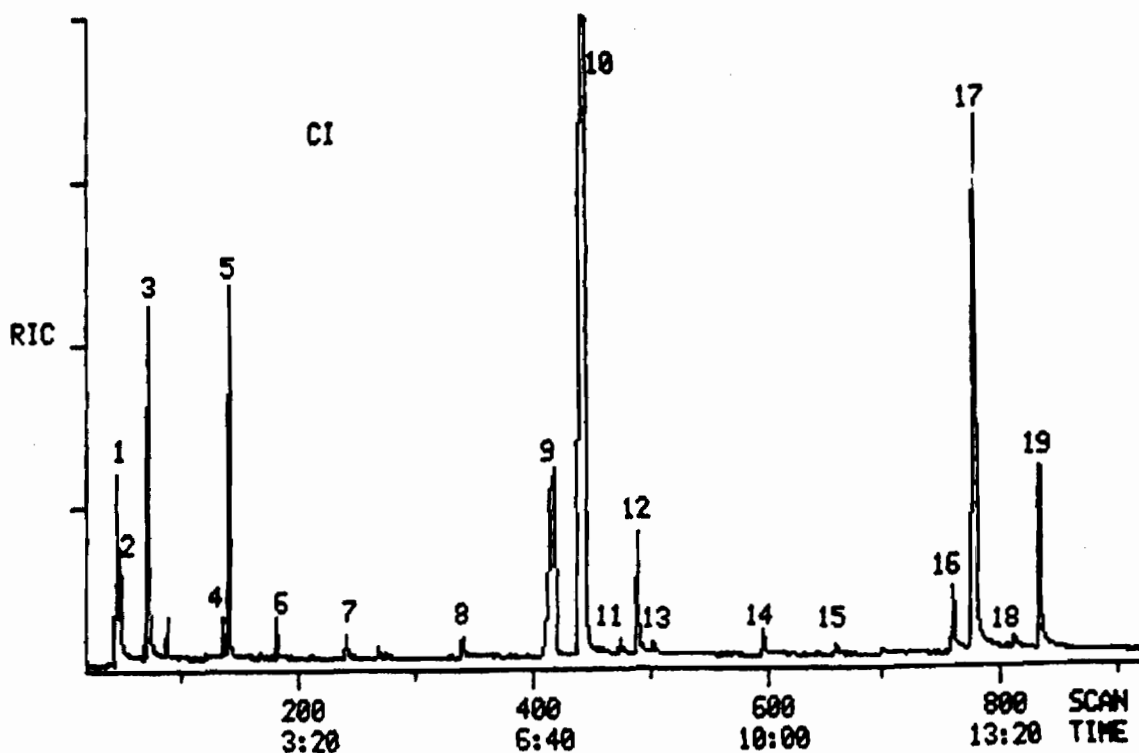


TABLE 1

O-Ethyl S-[2-Dimethylaminoethyl] Methylphosphonothioate
 Degradation Products Observed During Storage Under
 Inert and Atmospheric Conditions

PEAK NO.	R.T. (MIN)	COMPOUND	GC/MS AREA %	
			INERT STORAGE	ATMOSPHERIC STORAGE
<u>AMINES</u>				
1	0.8	Me ₂ NEt	2.6	1.0
<u>THIOLS</u>				
3	1.2	Me ₂ NCH ₂ CH ₂ SH	5.9	14.4
8	5.7	Me ₂ NCH ₂ CH ₂ SCH ₂ CH ₂ SH	0.5	0.1
<u>SULFIDES</u>				
2	0.8	$\begin{array}{c} \text{S} \\ \diagup \quad \diagdown \\ \text{CH}_2 - \text{CH}_2 \end{array}$	4.4	2.1
4	2.3	Me ₂ NCH ₂ CH ₂ SEt	0.8	1.0
<u>DISULFIDES</u>				
12	8.2	Me ₂ NCH ₂ CH ₂ SSCH ₂ CH ₂ NMe ₂	2.2	26.0
18	13.6	Me ₂ NCH ₂ CH ₂ SCH ₂ CH ₂ SSCH ₂ CH ₂ NMe	0.4	1.5
<u>PHOSPHONATES</u>				
5	2.4	$\begin{array}{c} \text{O} \\ \\ \text{Me}-\text{P}-\text{OEt} \\ \\ \text{OEt} \end{array}$	4.9	3.7
6	3.0	$\begin{array}{c} \text{O} \\ \\ \text{Me}-\text{P}-\text{NMe}_2 \\ \\ \text{OEt} \end{array}$	0.6	2.5
7	4.0	$\begin{array}{c} \text{O} \\ \\ \text{Me}-\text{P}-\text{SEt} \\ \\ \text{OEt} \end{array}$	0.4	0.3

TABLE 1 (CONTINUED)

O-Ethyl S-[2-Dimethylaminoethyl] Methylphosphonothioate
 Degradation Products Observed During Storage Under
 Inert and Atmospheric Conditions

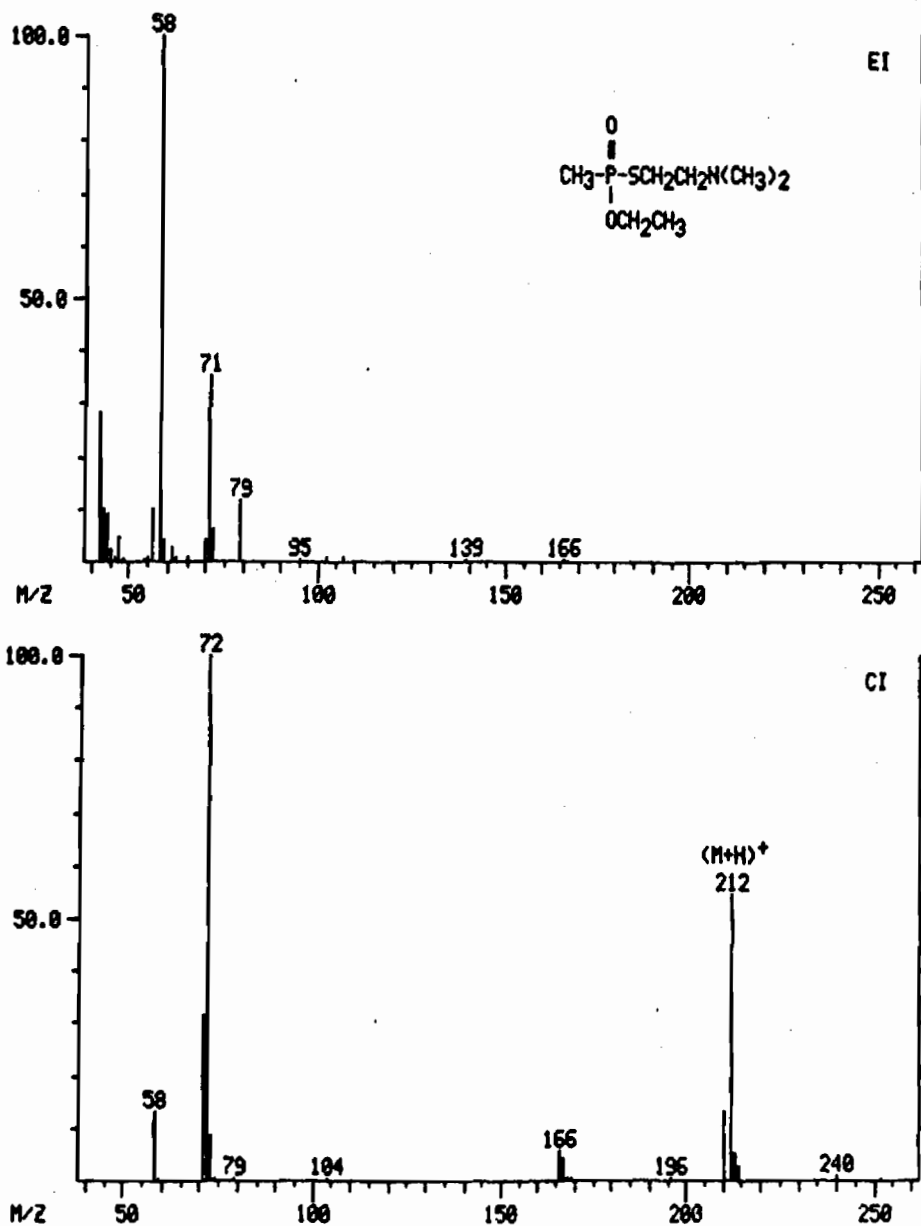
PEAK NO.	R.T. (MIN)	COMPOUND	GC/MS AREA %	
			INERT STORAGE	ATMOSPHERIC STORAGE
10	7.4	$\begin{array}{c} \text{O} \\ \parallel \\ \text{Me}-\text{P}-\text{SCH}_2\text{CH}_2\text{NMe}_2 \\ \\ \text{OEt} \end{array}$	40.7	25.8
13	8.4	$\begin{array}{c} \text{S} \\ \parallel \\ \text{Me}-\text{P}-\text{SCH}_2\text{CH}_2\text{NMe}_2 \\ \\ \text{OEt} \end{array}$	0.2	-
14	10.0	$\begin{array}{c} \text{O} \\ \parallel \\ \text{Me}-\text{P}-\text{SCH}_2\text{CH}_2\text{NMe}_2 \\ \\ \text{SEt} \end{array}$	0.6	-
15	11.0	$\begin{array}{c} \text{S} \\ \parallel \\ \text{Me}-\text{P}-\text{SCH}_2\text{CH}_2\text{NMe}_2 \\ \\ \text{SEt} \end{array}$	0.3	-
16	12.7	$\begin{array}{c} \text{O} \\ \parallel \\ \text{Me}-\text{P}-\text{SCH}_2\text{CH}_2\text{SCH}_2\text{CH}_2\text{NMe}_2 \\ \\ \text{OEt} \end{array}$	1.7	2.3
17	13.0	$\begin{array}{c} \text{O} \\ \parallel \\ \text{Me}-\text{P}-\text{SCH}_2\text{CH}_2\text{NMe}_2 \\ \\ \text{SCH}_2\text{CH}_2\text{NMe}_2 \end{array}$	16.7	-
19	13.9	$\begin{array}{c} \text{S} \\ \parallel \\ \text{Me}-\text{P}-\text{SCH}_2\text{CH}_2\text{NMe}_2 \\ \\ \text{SCH}_2\text{CH}_2\text{NMe}_2 \end{array}$	4.9	1.9
<u>PYROPHOSPHONATES</u>				
9	3.8	$\begin{array}{c} \text{O} \quad \text{O} \\ \parallel \quad \parallel \\ \text{Me}-\text{P}-\text{O}-\text{P}-\text{Me} \\ \quad \\ \text{OEt} \quad \text{OEt} \end{array}$	11.4	13.5
11	7.9	Unknown	0.6	-

As shown in Table 1, under inert storage conditions degradation occurs primarily to a mixture of pyrophosphonates, thiolamines and phosphonothioates containing 1, 2 and 3 sulfurs. Exposure to the atmosphere results in considerable oxidation to disulfides.

A comparison of EI and CI spectra for the phosphonothioate shown in Figure 2 illustrates the usefulness of CI for the identification of these compounds.

FIGURE 2

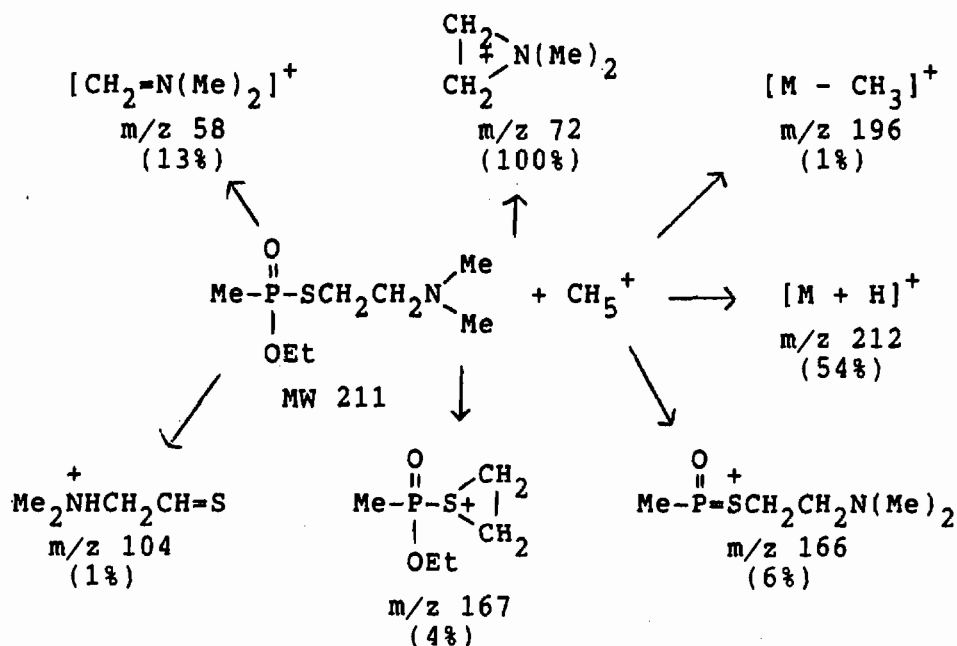
EI and Methane CI Mass Spectra of O-Ethyl S-[2-Dimaminoethyl] Methylphosphonothioate



A fragmentation scheme for the phosphonothioate is shown in Figure 3.

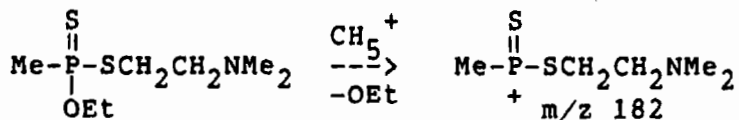
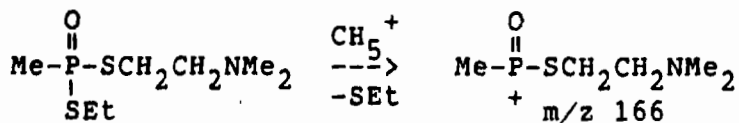
FIGURE 3

Methane CI Fragmentation Pathways For O-Ethyl S-[2-dimethylaminoethyl] Methylphosphonothioate



As shown in Figure 2, identification of phosphonothioates is difficult on the basis of EI information alone because no molecular ion is observed. In addition, all products containing the dimethylaminoethyl group have similar EI spectra dominated by a fragmentation ion at m/z 58, corresponding to $[Me_2N=CH_2]^+$. Less intense ions observed at m/z 71 and m/z 42 can be accounted for by the fragmentation structures $[Me_2NCH=CH_2]^+$ and $[CH_2=N=CH_2]^+$, respectively.

Methane chemical ionization provides the necessary molecular ion information necessary to identify these compounds. Protonated molecular ions were observed for all 18 compounds. In addition, valuable information is obtained from the fragmentation ions to aid in structure elucidation. For example, the ion shown in Figure 3 at m/z 167 is useful for determining the number of sulfur atoms in the molecule. This ion will appear at m/z 167, 183 or 199 depending upon whether the molecule contains 1, 2 or 3 sulfur atoms, respectively. The fragmentation ion at m/z 166 is useful for determining the sulfur distribution as shown in the following example for dithioates:



CONCLUSIONS

Methane chemical ionization GC/MS is an excellent technique for the detection of the degradation products produced during the breakdown of O-ethyl S-[2-dimethylaminoethyl] methylphosphonothioate. This technique provides both molecular ion and fragmentation information to aid in the identification of these compounds. 18 degradation products were identified. Under inert storage conditions degradation occurs primarily to a mixture of pyrophosphonates, thiolamine, and phosphonothioates containing 1, 2, or 3 sulfur atoms. Exposure to the atmosphere results in considerable oxidation to disulfides. This information will be useful to aid in the detection of Schedule 1 compounds for the treaty verification program.

BLANK

GF DETECTION USING ION MOBILITY SPECTROMETRY

Donald B. Shoff and Lynn D. Hoffland
U.S. Army Chemical Research, Development and Engineering Center
Aberdeen Proving Ground, MD 21010-5423

ABSTRACT

GF vapor was analyzed using an Ion Mobility Spectrometry (IMS) coupled to a Mass Spectrometer and with a handheld IMS, the Chemical Agent Monitor (CAM). The reduced mobility (k_0) and ion-molecule identity were determined for the detected ions. Acetone and water were used as the reagents (reactant ions) in this study. The IMS signature of GF was compared to that of the structurally related agent GD (Soman). GF was detected and the CAM "alarmed" at appropriate vapor concentrations.

INTRODUCTION

Ion Mobility Spectrometry (IMS) is an analytical technique in which sample molecules are drawn into a reaction region where they are collisionally ionized at or near atmospheric pressure through proton transfer or attachment to reactant ions present in the reaction region.¹ The resultant ions are pulsed into a drift region, moving down the drift region under the influence of a weak electric field. The time-of-flight current (number density) of these ions through the drift region is measured by a collection grid and electrometer at the opposite end of the drift region. Ionic velocities, determined from the times-of-flight, are directly proportional to the electric field strength and the proportionality constant is the ionic "mobility". Mobility is a characteristic of each ionic species according to the ion's effective size. Reduced mobility (k_0) is the mobility corrected for the drift gas at 1 atmosphere and 0°C. Several papers describing IMS are available.²⁻⁵

This study involves IMS analysis of the chemical warfare agent GF (cyclohexyl methylphosphonofluoridate). The mass resolved reduced mobilities for the ions formed in the ion mobility spectrometer were determined using both acetone and water reactant ions.

The reduced mobilities of the GF ions were compared to those of GD which were previously obtained. Because of the structural similarities between GF and GD, it was expected that the IMS response would be comparable.

EXPERIMENTAL

INSTRUMENTATION

IMS/MS

An Ion Mobility Spectrometer/Mass Spectrometer (IMS/MS)(PCP Inc. MMS-290) equipped with a Nicolet 1280 computer was used for data acquisition (Figure 1). Primary ionization was provided using a 12.5 mCi ^{63}Ni (beta particles) sealed ionization source. The MMS-290 is capable of collecting data in four modes for positive and negative ion detection. The IMS mode is used to obtain digital signal averaged IMS spectra. In the Mass Spectral mode, the shutter grid is held open and a mass spectra of all ionic species is taken. The Integral Ion mode is similar to the IMS mode but with the mass spectrometer used "unresolved" as the ion collector. In this mode the mass spectrometer can be set to allow the detection of ions with masses greater than a preset value. In the Tuned Ion mode, as in the Integral Ion mode, the shutter grid operates and the mass spectrometer is used as the collector, but the mass spectrometer is set to detect only one particular mass. This allows the mobility of specific ions to be determined. During this experiment, with GF, only positive ions were analyzed.

The IMS/MS was operated at 30-35°C. The sample vapor was introduced to the IMS through a heated teflon tube. Acetone vapor (50 ppb) was added to the IMS to mimic the response using the CAM (in which acetone is intentionally added as a reagent).

CAM

The Chemical Agent Monitor (CAM) was a standard CAM produced by Graseby Ionics, Ltd. Signals from the CAM were processed using a Graseby Advanced Signal Processing board installed in an IBM PC/AT computer. The CAM operates at ambient temperature and pressure.

Operating Parameters of IMS/MS and CAM

IMS/MS

drift gas: air
source: 12.5 mCi ^{63}Ni
drift region length: 10 cm.
drift field: 215 V/cm
shutter width: 0.2 ms

drift gas flow: 500 cc/min
reaction region length: 5 cm.
IMS cell temp: 30-35°C
mass range: 10-439 amu
polarity: positive

CAM

drift gas: air
source: 10.5 mCi ^{63}Ni
drift region length: 3.8 cm
drift field: 200 V/cm.

drift gas flow: ca. 500 cc/min
reaction region length: 2.2cm.
cell temp. ambient: 25°C
membrane temp: 70°C

MATERIALS

The GF was obtained locally and was determined by ^{31}P and ^{13}C Nuclear Magnetic Resonance and Gas Chromatography to be 97% pure. An acetone permeation tube, supplied by Analytical Instrument Development, Inc., had a certified permeation rate of 193 ng/mln at 50°C. The chemicals were used as obtained without further purification.

METHODS

Vapor Generation

The GF vapor concentrations were generated using a Q₅ Vapor Dilution Apparatus.⁶ The vapor concentration was started at a low level and increased until a suitable signal was obtained with the IMS. The dilution and carrier gases to the Q₅ were both from the same source of air, purified and dried by 13X molecular sieve and Drierite, respectively. The acetone vapor was generated by a permeation device held at a constant temperature; the acetone vapor was mixed in the air supplying the Q₅.

Vapor was introduced to the IMS/MS through a heated teflon inlet tube at a rate of 200 cc/min. A separate outlet port was provided on the Q₅ to allow direct sampling for the CAM.

IMS Ion Identification

Because operating parameters in the CAM are difficult to measure, the reduced mobility of ions observed in CAM spectra cannot be accurately determined. To correlate the mass resolved mobility spectra of the IMS/MS and the mobility spectra of the CAM, the "drift time ratio", T_d, method is employed. The ratio of the drift time of the peak of interest to the drift time of the reactant ion peak (RIP) ($T_d = T_{(peak)} / T_{(RIP)}$) is nearly independent of cell parameters thus allowing good comparisons between mobility spectra of different instruments. The identification of ions formed in the CAM is determined in this manner (see Table 1).

RESULTS

IMS/MS with Acetone Reactant Ion Peak (RIP)

The IMS spectra in Figure 2 are for GF at three concentrations. The spectra show three distinct peaks for which k₀ values are 1.84, 1.35, and 1.11 cm²/V·s. The mass spectra (Figure 3) shows the major ions present to be 117, 239, and 361 daltons. Mass resolved mobility spectra (tuned ion mode) were obtained for these three masses. The tuned ions (Figure 4) were used to make the mass assignments and species identification in Table 1.

Table 1. Ion Identification with Acetone Reactant Ion

Species	Masses	k ₀	IMS		CAM	
			T _d	Ratio	T _d	Ratio
H ⁺ (acetone) ₂ ·N ₂	117,145	1.84	24.04	1.00	7.34	1.00
H ⁺ Acetone-GF	239	1.35	32.70	1.39	9.922	1.35
H ⁺ (GF) ₂	361	1.11	40.10	1.67	12.15	1.66

CAM

The multiple spectra shown in Figure 5 represents the GF concentration decay in the CAM after a 30-second exposure to a 1 ppm vapor concentration. The three peaks shown were identified by comparison of drift time ratios to the spectra taken using the IMS/MS (see Table 1).

IMS/MS with Water Reactant Ions

Upon completion of experiments using acetone as the reactant ion, the acetone source was removed from the IMS/MS. The spectra shown in Figure 6 are of GF at three concentrations using water as the RIP. As with the acetone experiments, there are three predominant peaks in the IMS spectra. In this case the mobilities reported are 2.07, 1.49, and 1.11 $\text{cm}^2/\text{V}\cdot\text{s}$. The difference in mobilities for the first agent peak can be directly attributed to the absence of acetone in the IMS. The mass spectra in Figure 7 shows the predominant masses to be 73, 101, 199, 227, and 361 daltons. Tuned ion data (Figure 8) confirms the identities shown in Table 3.

Table 3. Ion Identification with Water Reactant Ion

Species	Masses	k_o	T_d	Ratio
$\text{H}^+(\text{H}_2\text{C})_n \cdot (\text{N}_2)_n$	73,101	2.07	21.66	1.00
$\text{H}^+\text{GF} \cdot (\text{H}_2\text{O})_n \cdot (\text{N}_2)_n$	199,227	1.49	30.08	1.39
$\text{H}^+(\text{GF})_2$	361	1.11	40.10	1.87

Comparison of GF and GD IMS Signatures

GF and Pinacolyl methylphosphonofluoridate (GD) have similar molecular structures, molecular weights (180 and 182, respectively), and, as expected, similar IMS signatures. This similarity accounts for the CAM's "bar" response even though it is not specifically programmed to detect GF. Figure 9 shows the IMS spectra for both GF and GD using acetone as the RIP. In both cases, the first agent peak is an acetone-agent complex ion with a reduced mobility of 1.35 $\text{cm}^2/\text{V}\cdot\text{s}$. The second agent peak for both compounds is a dimer ($\text{H}^+(\text{GF})_2$ and $\text{H}^+(\text{GD})_2$) with a reduced mobility of 1.11 $\text{cm}^2/\text{V}\cdot\text{s}$.

CONCLUSIONS

Cyclohexyl methylphosphonofluoridate (GF) is easily detected using IMS technology. GF has been shown to cause the Chemical Agent Monitor (CAM), which is programmed for the detection of Pinacolyl methylphosphonofluoridate (GD), to alarm. Because of the similarity in mobility it was also found that discrimination between GF and GD using IMS would prove difficult. Further investigations should include alternate reactant ion chemistry and higher temperature IMS studies.

REFERENCES

- (1) Eiceman, G.A., Shoff, D.B., Harden, C.S., Snyder, A.P., Martinez, P.M., Fleisher, M.E., and Watkins, M.L., "Ion Mobility Spectrometry of Halothane, Enflurane, and Isoflurane Anesthetics in Air and Respired Gases," *Analytical Chemistry*, **61**, 1093, 1989.
- (2) Spangler, G.E., and Cohen, M.J., in Plasma Chromatography, Carr, T.W. (Ed.), Plenum Press, New York, 1984, Chap. 1.
- (3) Werlund R.F., in Plasma Chromatography, Carr T.W. (Ed.), Plenum Press, New York, 1984, Chap. 8.
- (4) Eiceman, G.A., Blyth, D.A., Shoff, D.B., and Snyder, A.P., "Screening of Solid Commercial Pharmaceuticals Using Ion Mobility Spectrometry" *Analytical Chemistry*, **62**, 1374, 1990.

- (5) Eiceman, G.A., Shoff, D.B., Harden, C.S., and Snyder, A.P., "Fragmentation of Butyl Acetate Isomers in the Drift Region of an Ion Mobility Spectrometer" *Int. J. Mass Spectrom. Ion Processes*, **85**, 265, 1988.
- (6) Instruction Manual for the Installation, Operation, and Maintenance of Dilution Apparatus, Q₅; Report No. 136-300-52E, PAD, EA, APG, MD, May 3, 1976.

Figure 1 IMS/MS

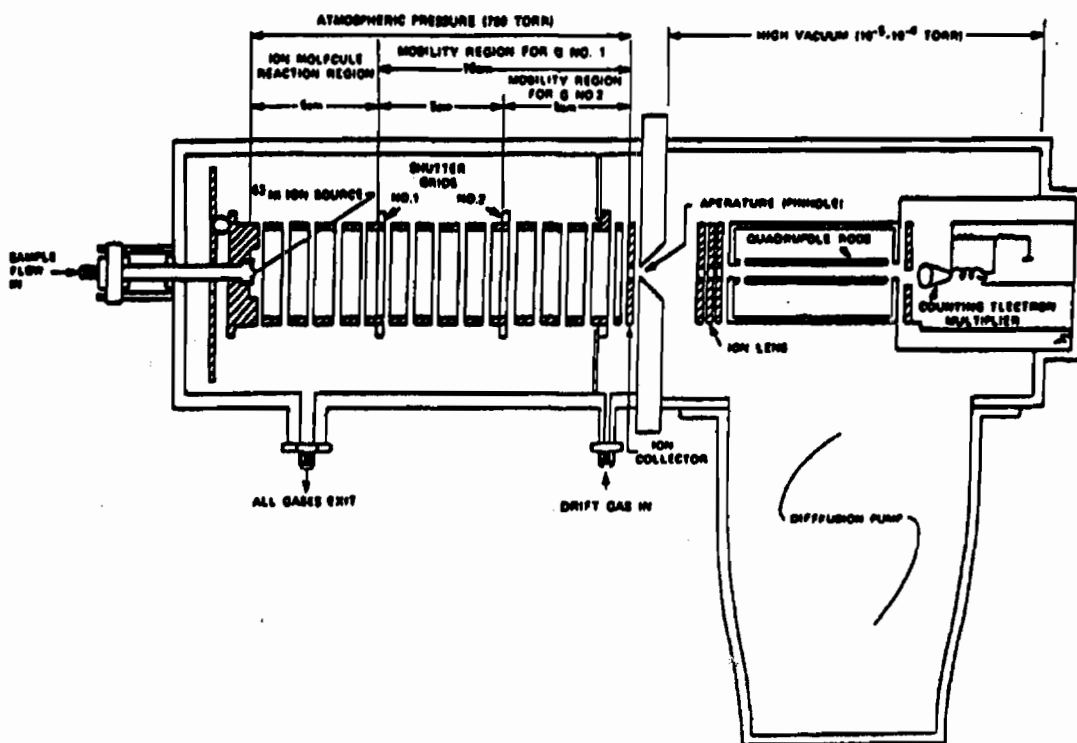


Figure 2 GF Ion Mobility Spectrum with Acetone RIP

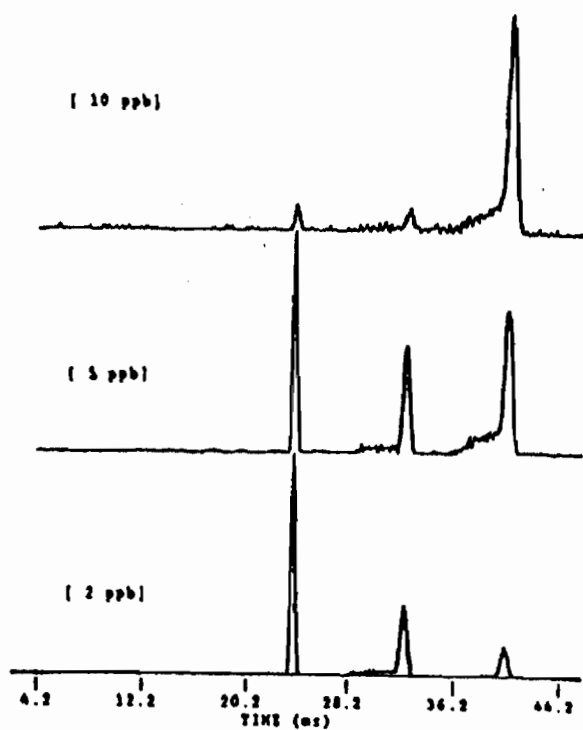


Figure 3 Mass Spectrum of GF with Acetone RIP

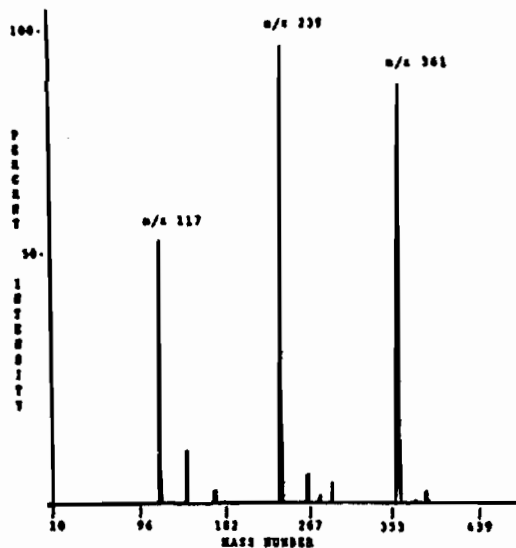


Figure 4 Mass Resolved Mobility Spectra with Acetone RIP

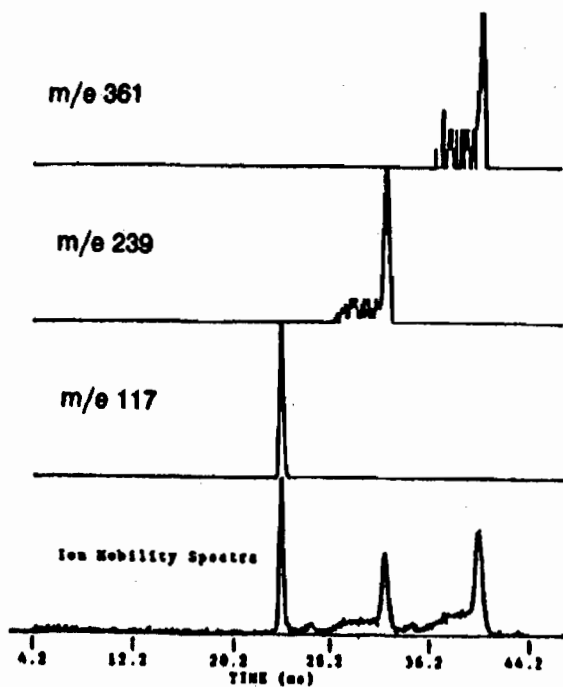


Figure 5 CAM Recovery from 1ppm GF Exposure

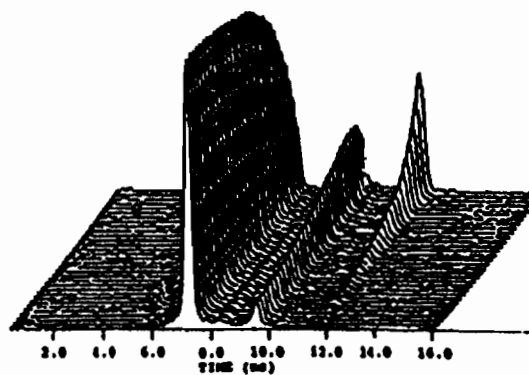


Figure 6 GF Ion Mobility Spectrum with Water RIP

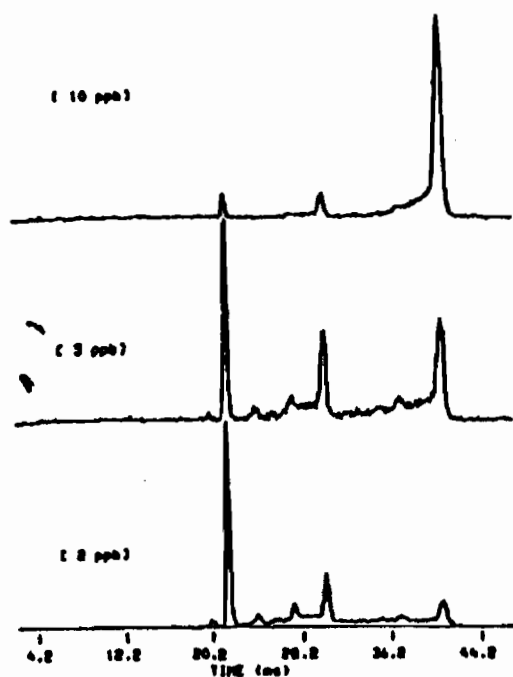


Figure 7 Mass Spectra of GF with Water RIP

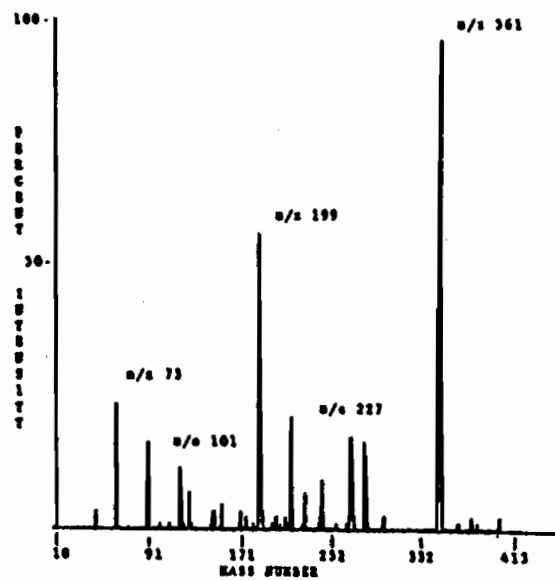


Figure 8 Mass Resolved Mobility Spectra with Water RIP

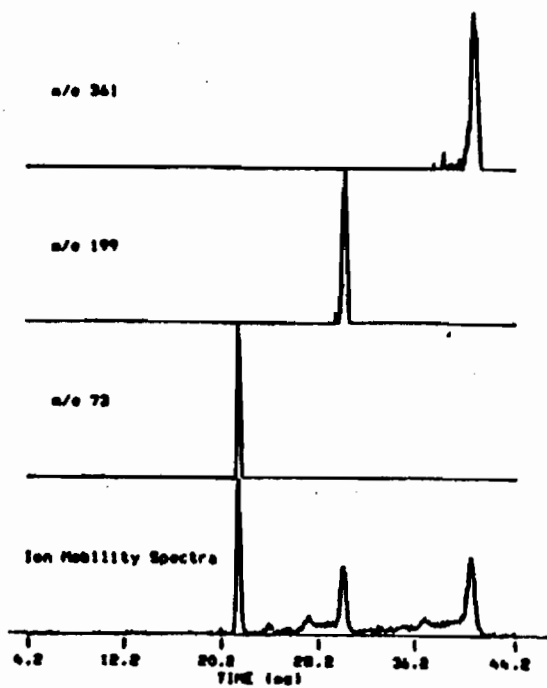
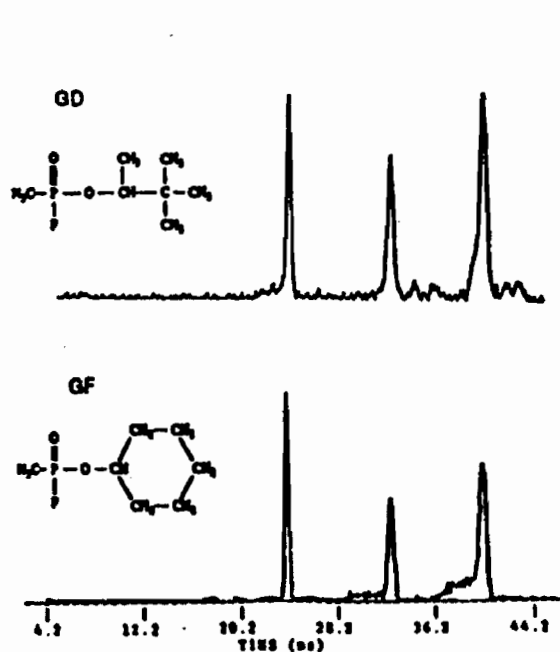


Figure 9 GD and GF Ion Mobility Spectra with Acetone RIP



BLANK

XV. TOXICOLOGY POSTERS

BLANK

INHIBITION OF SULFUR MUSTARD-INCREASED PROTEASE ACTIVITY BY NIACINAMIDE, N-ACETYL-L-CYSTEINE OR DEXAMETHASONE

Fred M. Cowan, Clarence A. Broomfield and William J. Smith

Biochemical Pharmacology Branch
U.S. Army Medical Research Institute of Chemical Defense
Aberdeen Proving Ground, MD 21010-5425, USA

The pathologic mechanisms underlying sulfur mustard-induced skin vesication are as yet undefined. Papirmeister et al. have postulated a biochemical mechanism for sulfur mustard-induced cutaneous injury involving DNA alkylation, metabolic disruption and enhanced proteolytic activity. We have previously utilized a chromogenic peptide substrate assay to establish that human peripheral blood lymphocytes exposed to sulfur mustard exhibited enhanced proteolytic activity. In this study, compounds known to alter the biochemical events associated with sulfur mustard exposure or to reduce protease activity were tested for their ability to block the sulfur mustard-increased proteolysis. Treatment of cells with niacinamide, N-acetyl-L-cysteine, or dexamethasone resulted in a decrease of sulfur mustard-increased protease activity. Complete inhibition of sulfur mustard-increased proteolysis was achieved by using protease inhibitors (antipain, leupeptin and 4-(2-aminoethyl)-benzenesulfonyl fluoride). These data suggest that therapeutic intervention in the biochemical pathways that culminate in protease activation or direct inhibition of proteolysis might serve as an approach to treatment of sulfur mustard-induced pathology.

INTRODUCTION

Sulfur mustard (HD) is a chemical warfare blistering agent for which neither the mechanism of action nor an antidote is known. Papirmeister et al. (1) have postulated a biochemical mechanism for HD-induced cutaneous injury involving the sequelae of DNA alkylation and NAD⁺ depletion which results in metabolic disruption and enhanced proteolytic activity. The hypothesized HD increased protease activity is proposed to cause cutaneous degradation, setting the stage for inflammatory infiltration and blister formation (1). Cell cultures of human peripheral blood lymphocytes (PBL) assayed using chromogenic protease substrates have been utilized as an *in vitro* model to demonstrate HD-increased proteolysis (2). In this study compounds known to alter the biochemical events associated with HD exposure or reduce protease activity were tested to determine their ability to affect the HD-increase proteolytic activity. For example, niacinamide prevents HD-induced NAD⁺ depletion and reduces HD cytotoxicity *in vitro* (3). N-acetyl-L-cysteine increases cellular glutathione levels which may react with some of the HD reducing its concentration and thereby decreasing HD cytotoxicity (4). The corticosteroid dexamethasone induces the synthesis of both plasminogen activator and the naturally occurring protease inhibitor plasminogen activator inhibitor, with the net result being inhibition of protease activity (5). The actions of these compounds and known protease inhibitors on increased protease activity in HD-exposed human PBL were determined *in vitro*.

MATERIALS AND METHODS

Reagents: RPMI 1640 tissue culture medium (GIBCO, Grand Island, NY) was used for cell washing and assays. Sulfur mustard (HD, 2,2'-dichlorodiethyl sulfide) with a purity of >98% was obtained from the Chemical Research, Development and Engineering Center, Aberdeen Proving Ground, MD. All protease substrates and protease inhibitors were obtained from Boehringer Mannheim Biochemicals, Indianapolis, IN. Niacinamide, N-acetyl-L-cysteine, Histopaque ($d = 1.077$) and trypan blue were purchased from Sigma, St. Louis, MO. Dexamethasone was obtained from Aldrich Chemical Company, Inc., Milwaukee, WI.

Lymphocytes: Human peripheral blood lymphocytes (PBL) in cell cultures were employed as an *in vitro* model for HD toxicity (6). PBL were collected by venipuncture from healthy normal volunteer donors under an approved human use protocol and maintained under sterile conditions. PBL were isolated by buoyant density centrifugation (7) using Histopaque and resuspended in RPMI 1640. Cell counts were done with trypan blue on a hemacytometer.

Sulfur Mustard Exposure: Cells in 25 cm² tissue culture flasks were exposed to 0.01 to 0.5 mM HD. The flasks were maintained at room temperature in a fume hood for 1 hr to allow venting of volatile agent and then transferred to a CO₂ incubator at 37° C for a total incubation time of 16 hr.

Chromogenic Peptide Substrate Protease Assay (CPSPA): The use of small proteolysis sensitive peptides coupled to p-nitroaniline (pNA) (8) was adapted for protease assay by micro-plate reader (Bio-Rad, Richmond, CA) (2). The chromogenic peptide, when cleaved by protease, releases pNA producing a change in absorbance measured spectrophotometrically at 405 nm (8). The assay can detect protease at ng/ml levels, e.g., 50 ul of 100 ng/ml of trypsin assayed with 50 ul of 2.5 mM chromozym TRY substrate for 1 hr yielded an absorbance of 0.602 ± 0.036 . HD-exposed and untreated control PBL in cell culture were harvested by centrifugation. Assay samples containing 10⁶ to 10⁷ lymphocytes resuspended in 50 ul RPMI 1640 tissue culture media were added to each well of a 96 well flat bottom tissue culture plate. Fifty ul of protease detection peptide substrate (2.5 mM substrate in H₂O) was added to each well, in a total volume of 100 ul, and placed inside a CO₂ incubator at 37° C for 1 hr. Fifty ul of assay supernates were removed to a micro-titer plate to eliminate PBL background, and absorbance readings were made on a micro-plate reader at 405 nm using media/substrate controls as blank values.

Peptide Substrates: The following Boehringer Mannheim Biochemicals' Chromozym substrates (enzyme specificity) were used; t-PA (plasminogen activator), PL (plasmin), TRY (trypsin), TH (thrombin), PK (plasma kallikrein), X (Factor Xa), U (urokinase), GK (glandular kallikreins), PCa (Protein C) and XIIa (Factor XII). While a particular protease may have a preference for a given substrate, cross reaction with other substrates is often observed.

Protease Inhibitor: The concentration of protease inhibitor incubated with assay samples was 400 ug/ml unless otherwise stated. Protease inhibitors used were antipain, APMSF, aprotinin, bestatin, chymostatin, leupeptin, pepstatin, E-64 (1 mg/ml), EDTA (1 mg/ml), and phosphoramidon (4 mg/ml).

Data Analysis: All data points in the chromogenic assays for treatment compounds were derived from quadruplicate samples, whereas substrate "finger prints" and protease inhibitor studies were assayed in duplicate. Data are expressed as mean of absorbance or percent of control. Individual group significance was determined by Student's t-test and data are presented with standard errors.

RESULTS

Treatment with niacinamide (10^{-3} M) 1 hr after or with N-acetyl-L-cysteine (10^{-2} M) or dexamethasone (10^{-7} M) 24 hr prior to HD exposure resulted in decreases of 39%, 33% and 42% respectively in HD-increased protease activity (Figure 1). However, the protective effects of these three compounds were never complete and often variable. For example, two PBL donors demonstrated different responses to 10 μ M niacinamide that seemed to be dependent on HD dose (Figure 2). Treatment with 10 μ M niacinamide 1 hr after HD exposure resulted in a variable response with niacinamide only inhibiting protease activity in donor A at the 0.5 high dose, whereas in donor B inhibition occurred at the 0.05, 0.1 and 0.5 mM doses. Niacinamide did not inhibit HD-increased protease in either donor at the 0.01 mM sulfur mustard low dose. In untreated control PBL from 3 donors, niacinamide did not significantly affect protease activity, N-acetyl-L-cysteine decrease protease activity in donors 1 and 2, and dexamethasone activated protease in donor 3 (Figure 3).

The protease inhibitors antipain, APMSF, aprotinin, bestatin, chymostatin, leupeptin, pepstatin, E-64, EDTA, and phosphoramidon were incubated with assay samples and compared to untreated controls (Figure 4). Complete inhibition of sulfur mustard-increased proteolysis was consistently achieved by antipain, APMSF and leupeptin. Data presented in this study were obtained from individual donors and were representative of activities seen in studies repeated at least twice.

Assay of protease with 2.5 mM of ten different protease substrates, i.e., t-PA, PL, TRY, TH, PK, X, U, GK, PCa and Xlla, produces a pattern of reactivity characteristic of a specific protease, e.g., trypsin (100 ng/ml) or plasmin (2 μ g/ml) (Figure 5). When comparing relative absorbances, the patterns of substrate hydrolysis for trypsin and plasmin were clearly different from that of HD-increased proteolysis (Figure 6).

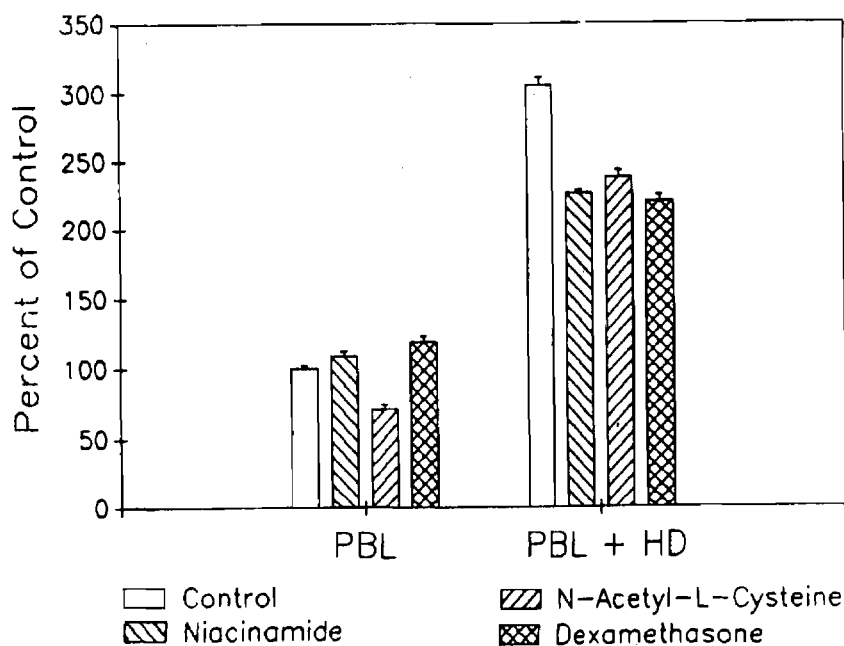


Figure 1. Effect of treatment compounds on HD-increased protease. Human PBL, 16 hr post-exposure to HD, were assayed with 2.5 mM chromozym TH. Treatment with niacinamide (10^{-3} M) 1 hr after or with N-acetyl-L-cysteine (10^{-2} M) or dexamethasone (10^{-7} M) 24 hr prior to HD exposure resulted in decreases of 39%, 33% and 42% respectively of HD-increased protease activity.

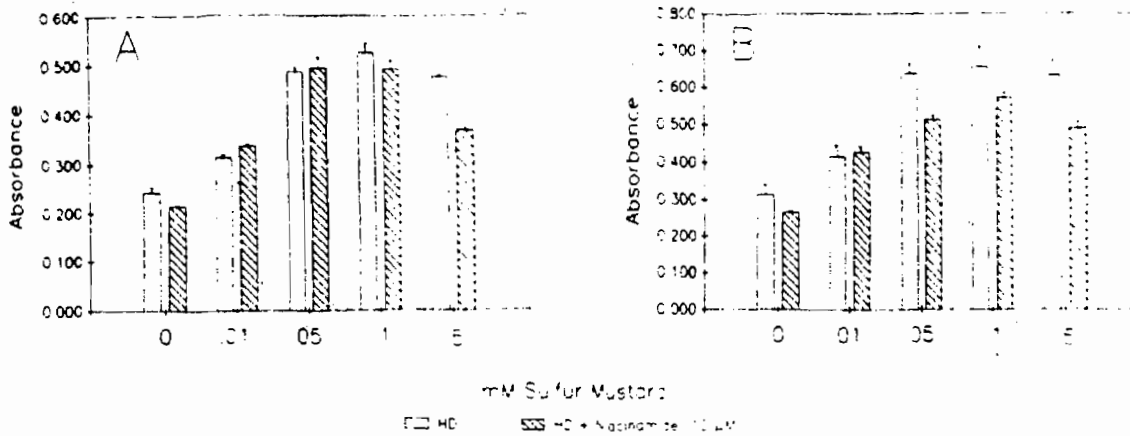


Figure 2. Effect of niacinamide on HD-increased protease in two PBL donors. Human PBL 16 hr post exposure to HD were assayed with chromozym TH. Treatment with 10 μM niacinamide 1 hr after HD exposure resulted in a variable response with niacinamide only inhibiting protease activity in donor A at the 0.5 high dose, while in donor B inhibition occurred at the 0.05, 0.1 and 0.5 doses.

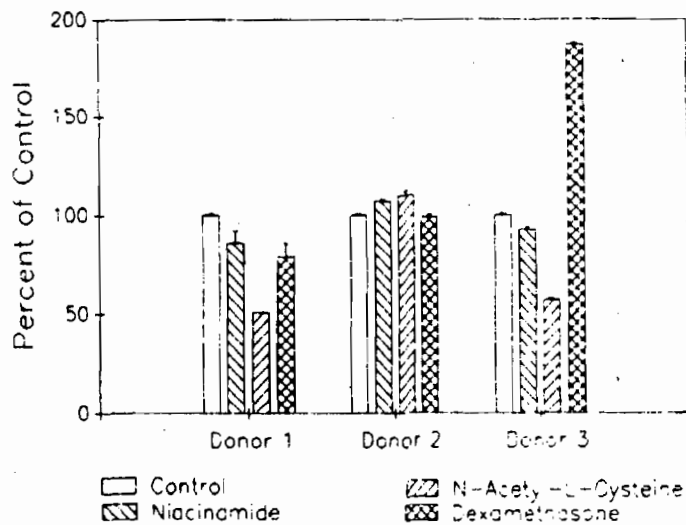


Figure 3. Effect of treatment compounds on untreated control PBL. Control PBL not exposed to HD were assayed with chromozym TH. Niacinamide did not significantly affect protease activity, N-acetyl-L-cysteine reduced protease activity in donors 1 and 2, and dexamethasone increased proteolysis in donor 3.

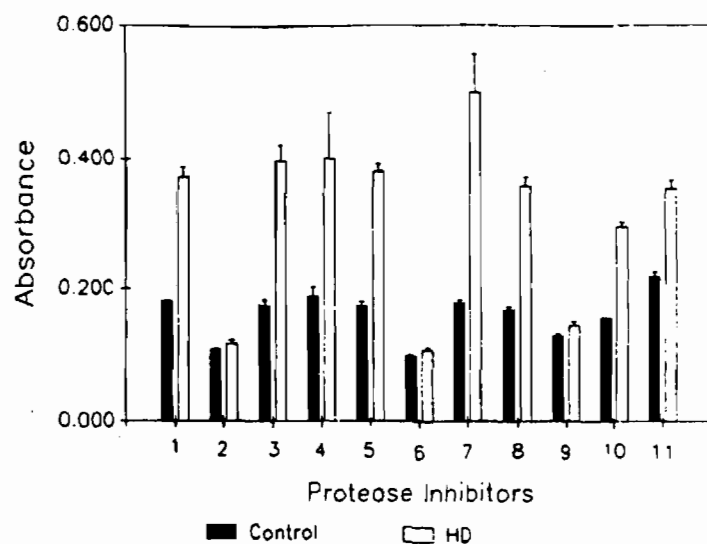


Figure 4. Effect of protease inhibitors on HD-increased protease. Human PBL 16 hr post exposure to HD were assayed by CPSPA with chromozym TH. Untreated control and HD-exposed PBL (1) and like samples incubated with the protease inhibitors (2)antipain, (3)bestatin, (4)chymostatin, (5)E-64, (6)leupeptin, (7)pepstatin, (8)phosphoramidon (9)APMSF, (10)EDTA and (11)aprotinin were assayed. Significant inhibition was seen only with (2)antipain, (6)leupeptin and (9)APMSF.

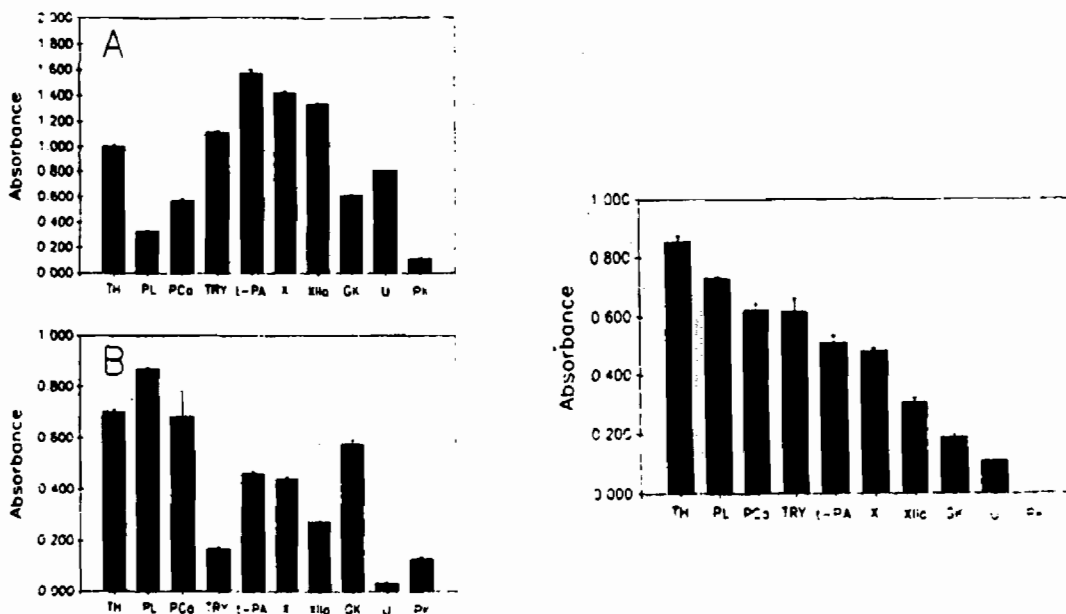


Figure 5. Chromozym substrate proteolysis with trypsin and plasmin. Trypsin (A) [100 ng/ml] or plasmin (B) [2 ug/ml] were assayed with 2.5 mM chromozym substrates.

Figure 6. Chromozym substrate proteolysis by HD-increased protease. Human PBL 16 hr post exposure to HD were assayed with 2.5 mM chromozym substrates to determine substrate specificity of HD-increased protease activity.

DISCUSSION

Niacinamide, N-acetyl-L-cysteine, dexamethasone, and several protease inhibitors reduced protease activity in HD-exposed human PBL. The ability of the protease inhibitors antipain, APMSF and leupeptin completely to abolish proteolysis while chymostatin failed to inhibit proteolytic activity due to HD exposure indicates that the enzyme activity is mediated by serine protease(s) not of the chymotrypsin type (Instructions "Protease Inhibitor Kit" Boehringer Mannheim Biochemical, Indianapolis, IN.). Additionally, multiple substrate proteolysis "finger prints" may be useful in identifying potential sulfur mustard-increased protease(s). The sulfur mustard-enhanced protease substrate "finger print" does not match either trypsin or plasmin, which further indicates that neither a trypsin-like enzyme nor plasmin are a major component of HD-increased proteolysis in human PBL.

The reduction of HD-increased protease by the three potential treatment compounds niacinamide, N-acetyl-L-cysteine and dexamethasone may involve their known activities. Niacinamide prevents HD-induced NAD⁺ depletion which may restore some normal metabolic activities (1,3) and reduce induction of proteolytic activity. N-acetyl-L-cysteine increases cellular glutathione levels which may provide alternative sites other than DNA for HD alkylation, hence blocking the initial event that leads to enhanced proteolytic activity (1,4). The corticosteroid dexamethasone induces the synthesis of both plasminogen activator and the naturally occurring protease inhibitor plasminogen activator inhibitor, with the net result being inhibition of protease activity (5).

Unlike protease inhibitors, the protective effects of compounds with action on metabolic pathways, i.e., niacinamide, N-acetyl-L-cysteine or dexamethasone, were never complete and often variable. The variability of response was noted even in untreated control PBL where N-acetyl-L-cysteine inhibited and dexamethasone occasionally increased proteolytic activity. The variability of response to treatment compounds for protection against sulfur mustard-increased protease was not totally unanticipated, since variable responses to sulfur mustard in PBL from different donors *in vitro* (2) and sensitivity of individuals to sulfur mustard *in vivo* (9) have been previously reported.

HD-increased proteolysis in PBL may reflect mechanisms of HD pathology and potentially provide an *in vitro* model to predict efficacy of therapeutic intervention for HD toxicity. This conclusion is supported by the protective action of niacinamide on HD associated cytotoxicity *in vitro* (3) and the *in vivo* observation that niacinamide has been shown to reduce HD-induced microvesicle formation in hairless guinea pigs (10). However, further testing is required to better characterize HD-increased protease and confirm the role of proteolysis in HD-induced vesication.

CONCLUSIONS

Human PBL exposed to sulfur mustard (HD) demonstrate increased proteolytic activity that is cell associated and of the serine protease class. Niacinamide, an inhibitor of poly(ADP-ribose) polymerase, lowers the proteolytic activity as would be postulated by Papirmeister et al. The HD-increased protease activity could also be reduced by N-acetyl-L-cysteine, a precursor of glutathione, and dexamethasone. The protective effects of niacinamide, N-acetyl-L-cysteine and dexamethasone were never complete and often variable. Complete inhibition of proteolysis was consistently achieved by the protease inhibitors antipain, APMSF and leupeptin. HD-increased proteolysis in PBL may reflect mechanisms of HD-pathology and potentially provide an *in vitro* model to predict the efficacy of therapeutic intervention for HD toxicity.

References

1. PAPIRMEISTER, B., GROSS, C.L., MEIER, H.L., PETRALI, J.P. AND JOHNSON, J.B. (1985). Molecular basis for mustard-induced vesication. *Fund. and Appl. Toxicol.* 5:S134-S149.
2. COWAN, F.M., BROOMFIELD, C.A. AND SMITH, W.J. (1991). Effect of sulfur mustard on protease activity in human peripheral blood lymphocytes. *Cell Biol. and Toxicol.* 7, 239-248.
3. MEIER, H.L., GROSS, C.L. and PAPIRMEISTER, B. (1987). 2,2'-Dichloroethyl sulfide (sulfur mustard) decreases NAD⁺ in human leukocytes. *Toxicol. Lett.* 39, 109-122.
4. SMITH, W.J. and GROSS, C.L. (1991). Early events in the pathology of sulfur mustard *in vitro*: Approaches to intervention. Proceedings of the NATO, Panel VIII Meeting, Grenoble, France. 1991.
5. OIKARINEN, A., HOYHTYA, M. and JARVINENY M. (1990). Dexamethasone-induced plasminogen activator inhibitor: characterization, purification, and preparation of monoclonal antibodies. *Dermatol. Res.* 282, 153-158.
6. SMITH, W.J. SANDERS, K.M., GALES, Y.A. AND GROSS, C.L. (1991). Flow cytometric analysis of toxicity by vesicating agents in human cells *in vitro*. *J.Toxicol. Cutan. and Ocular Toxicol.* 10, 33-42.
7. BOYUM, A. (1968). Separation of leucocytes from blood and bone marrow. *Scand J. Clin. Lab. Invest.* 21 (suppl 97):1-106.
8. FRIBERGER, P. (1982). Chromogenic peptide substrates. *Scand. J. Clin. Lab. Invest.* 42 (Suppl 162):1-98.
9. TRAGER, F.C. (1991). [Letter] Chemical sensitivity. *Chemical & Engineering News.* 69:4.
10. YOURICK, J.J., CLARK, C.R. and MITCHELTREE, L.W. (1991). Niacinamide pretreatment reduces microvesicle formation in hairless guinea pigs cutaneously exposed to sulfur mustard. *Fund. and Appl. Toxicol.* In press.

BLANK

DISSOCIATION OF OPIATE-INDUCED SEDATION AND RESPIRATORY DEPRESSION IN FERRETS BY OPIATE ANTAGONIST COADMINISTRATION: POTENTIAL PHARMACOLOGICAL MECHANISMS

R. Mioduszewski and S. Reutter, U.S. Army Chemical Research, Development and Engineering Center, Aberdeen Proving Ground, MD

Respiratory depression can be minimized during opiate-induced sedation/anesthesia by coadministration of opiate antagonist. This study examined pharmacodynamic/kinetic changes associated with such unusual dissociation of effects. Opiate agonist (sufentanil) and antagonist (nalmeferene) were intravenously coadministered to ferrets in a cocktail ratio which optimized sedation, but minimized respiratory depression. Post-injection plasma concentrations of the cocktail components were measured by radioimmunoassay. The opiate cocktail rapidly induced limited duration sedative/ anesthetic effects with minimal respiratory depression. Patterns of sufentanil plasma distribution and clearance were altered by large doses of agonist and by nalmeferene coadministration. Likewise, nalmeferene decreased sufentanil bioavailability and selectively increased its plasma threshold for apnea. It is hypothesized that the observed dissociation of opiate sedative/anesthetic and respiratory depressant effects results from nalmeferene coadministration which may induce dose-dependent changes in the pharmacodynamic/kinetic profiles of sufentanil.

INTRODUCTION

Previous studies in the rat¹ and ferret^{2,3} have suggested that dissociation of opiate-induced sedative and respiratory depressing effects is feasible by coadministration of opiate agonists with antagonists. Pharmacological effects of opiate agonist plus antagonist cocktails can differ from those of their individual components. Because the adverse respiratory effects of these formulations is minimized, they may potentially serve as a safer method for inducing sedative/anesthetic responses.

Although, little is known about the mechanisms by which this is accomplished, opiate antagonist-induced alterations in opiate pharmacodynamics and pharmacokinetics is possible. Pharmacodynamic mechanisms may involve competition and displacement of opiate agonist by antagonist at their common receptor sites within the "effect" compartments of the central nervous system (CNS). The net effect of these interactions may result in increased threshold plasma concentrations required for opiate-induced responses. Pharmacokinetic mechanisms may also be involved such that opiate uptake, distribution and clearance is directly or indirectly affected by the opiate antagonist. Both mechanisms involve opiate antagonist-induced changes in "bioavailability" of the opiate agonist.

One of the purposes of the present study was to examine potential changes in the pharmacodynamics and pharmacokinetics of sufentanil (opiate agonist) which may occur with coadministration of the potent, and long lasting opiate antagonist, nalmeferene.

MATERIALS AND METHODS

At least one week after recovery from surgical implantation of a vascular access port into the jugular vein, ferrets were weighed and injected with a bolus of one of seven doses (4 ferrets/dose) of sufentanil alone or coadministered with nalmefene. A constant molar ratio of sufentanil:nalmefene (15:1) was used in this study. Venous blood samples (approximately 1.9 ml) were collected at 2, 10, 30 and 60 minutes after injection for measurement of plasma concentrations of test compounds. Onset and duration of opiate effects (akinesia, catalepsy, loss of righting, light anesthesia, apnea and oxygen consumption) were monitored up to 60 min following treatment, as described previously³. Plasma samples were analyzed for sufentanil and nalmefene concentrations by sensitive and specific radioimmunoassay (RIA) procedures at Harris Laboratories, Inc., Lincoln, NE.

Sufentanil, N- (4- (methoxymethyl) - 1 - [2- (2-thienyl) ethyl] - 4 - piperidiny]) - N - phenylpropanamide - 2 - hydroxy -1,2,3- propane- tricarboxylate, and Nalmefene, 17- (cyclopropylmethyl)- 4,5 -epoxy-3,1,4 -dihydroxymorphinan-6-methylene. HCl were provided by the Organic Chemistry Branch, CRDEC, APG, MD Purity of test compounds was greater than 99% by NMR with elemental analysis and TLC.

An Oxymax™ system (Columbus Instruments, Columbus, OH) was used to monitor the effects of test compounds on respiratory frequency and oxygen consumption, including the severe state of respiratory depression defined here as apnea. Apnea was considered to occur when all signs of breathing stopped for at least 10 sec on at least two occasions within a one minute measurement period. Respiratory measurements were made 20 -60 minutes following dosing.

Areas under plasma sufentanil concentration-time curves were calculated by trapezoidal summation. Intergroup differences were statistically analyzed with the Mann-Whitney U test as described in Talarida and Murray⁷. The effects of dose and treatment on oxygen consumption, and dose and time on plasma sufentanil concentrations were analyzed by analysis of variance; differences between means were analyzed with the Student Neuman Keuls test⁷. Differences were considered significant when the probability was less than 0.05.

RESULTS

As reported previously³, coadministration of nalmefene with sufentanil (1:15) resulted in what may be considered a "dissociation" of sufentanil-induced sedative/anesthetic and severe respiratory depression potency, Table 1. Nalmefene coadministration shortened the duration but did not significantly delay the onset of opiate-induced sedative/anesthetic effects³. In contrast, nalmefene coadministration completely prevented apnea (Table 1) and significantly improved oxygen consumption in ferrets treated with relatively high doses (100 - 1000 ug/kg) of sufentanil, Figure 3.

Table 1. Potency of Sufentanil with and without Nalmefene coadministration. Median effective dose, and 95% confidence limits.

Clinical Sign	Median Effective Dose (ug/kg) (95 % C . L .)	
	Sufentanil	Sufentanil + Nalmefene (15:1)
Akinesia	2.0 (0.9 - 4.0)	4.7 (2.1 - 10.5)
Catalepsy	2.4 (0.8 - 7.2)	4.7 (2.1 - 10.5)
Loss of Righting	7.8 (2.5-24.5)	52.2 (14.0-191.0)
Anesthesia	9.1 (3.5-25.9)	10.0 (3.3-315.0)
Apnea	9.1 (3.2-25.5)	No apnea observed
Lethality	285.0 (52.2-1,564.5)	No lethality observed

Concentrations of sufentanil in plasma declined rapidly following bolus injections of 1 - 316 ug/kg; an exponential decline appeared from the first sampling period (2 min) to the last sampling period (60 min), Figure 1. However, at very high doses (1000-3160 ug/kg), maximum concentrations were seen at 10 min in all ferrets (regardless of nalmefene coadministration); sufentanil plasma concentrations declined comparatively slowly thereafter, especially in the absence of nalmefene

coadministration, Figure 1.

Log areas under sufentanil plasma concentration-time curves, either with ($r = 0.99$) or without ($r = 0.99$) nalmefene, were best fit to log doses of sufentanil by a second order linear regression, Figure 2. Coadministration of nalmefene with sufentanil significantly lowered the areas under the sufentanil plasma concentration-time curves generated at higher doses, Figure 1 and Table 2. Nalmefene coadministration appeared to have the greatest effect on sufentanil plasma concentration beginning at 30 min after both were injected, Figure 1. This appears to correlate with significant improvement in respiration (V_{O_2}) beginning at the same time period, Figure 3.

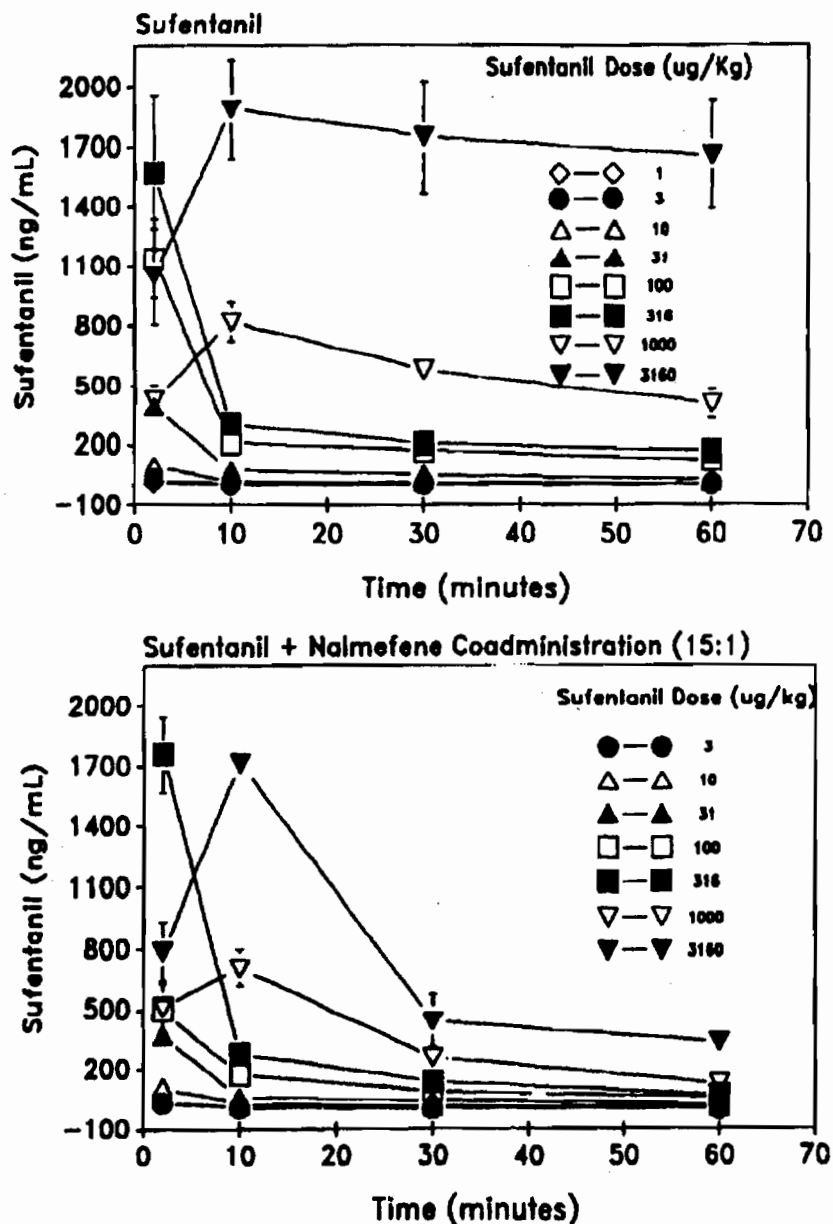


Figure 1. Sufentanil concentrations from 2 to 60 minutes following bolus intravenous injections of various doses of Sufentanil or Sufentanil + Nalmefene coadministration (15:1) in ferrets.

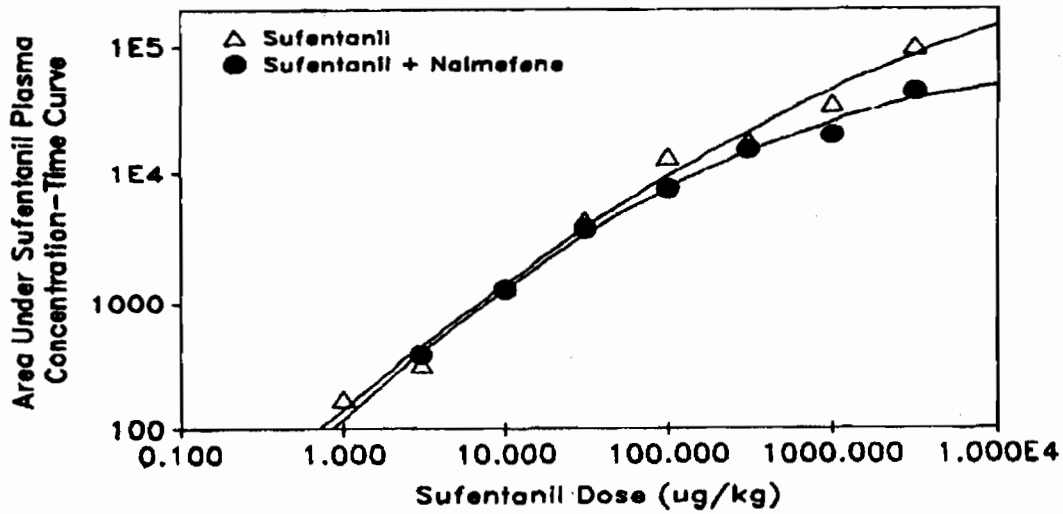


Figure 2. Areas under the sufentanil plasma concentration-time curve (2-60 minutes) associated with dose of Sufentanil or Sufentanil + Nalmefene coadministration in ferrets.

Table 2. Effects of dose and Nalmefene coadministration on areas under Sufentanil plasma concentration-time curves (calculated between 2 and 60 min after treatment). Mean areas under the curve \pm standard deviation.

Dose (ug/kg)	Area Under Sufentanil Plasma Concentration-Time Curve	
	Sufentanil	Sufentanil+ Nalmefene (15:1)
1	176.4 \pm 19.2	-
3	321.7 \pm 19.9	383.3 \pm 26.2
10	1341.3 \pm 19.9	1289.5 \pm 83.9
31	4246.3 \pm 33.4	3705.6 \pm 429.0
100	13624.4 \pm 1253.7	7603.3 \pm 476.7*
316	18119.0 \pm 5029.2	15461.3 \pm 715.3
1000	34557.2 \pm 3897.3	20322.8 \pm 2233.8*
3160	99206.3 \pm 14434.2	42692.1 \pm 3120.9*

* $P < 0.05$ vs. Sufentanil

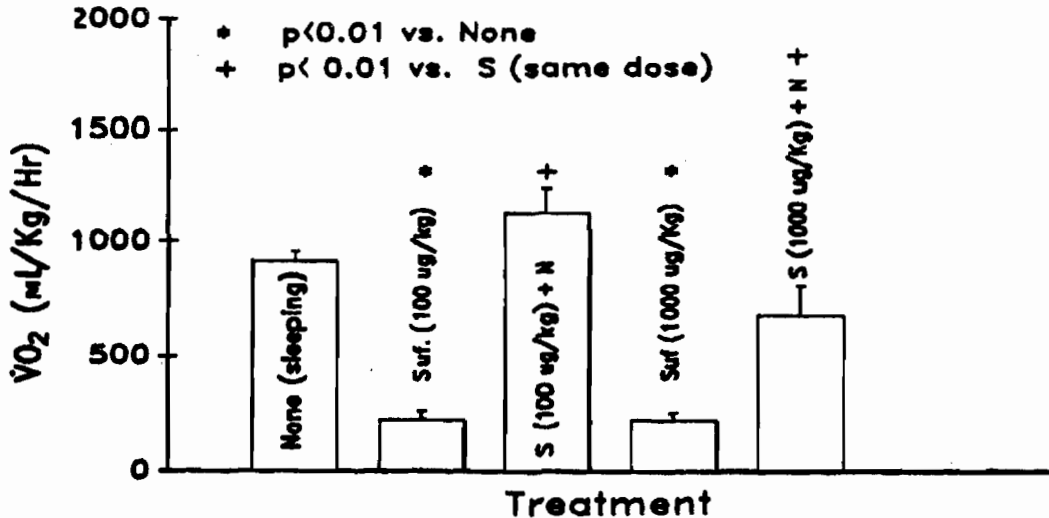


Figure 3. Ferret oxygen consumption (VO_2) at 25 minutes following treatment with different doses of Sufentanil (S), Sufentanil + Nalmefene (S+N) 15:1, or during untreated sleep.

Mean "threshold" plasma concentrations of sufentanil for various opiate-induced responses were determined from the incidence of various categorical signs of opiate effects at each blood sampling period and its associated plasma concentration of sufentanil for all doses, Table 3. Nalmefene coadministration with sufentanil was associated with disproportionately higher threshold plasma sufentanil concentrations for apnea than for sedative/anesthetic effects (Table 3).

Table 3. Threshold plasma concentrations of Sufentanil associated with sedative/anesthetic and adverse respiratory effects in ferrets treated with a bolus intravenous injection of Sufentanil or Sufentanil + Nalmefene coadministration. Mean concentrations (ng/mL) \pm standard deviation.

Response	Threshold Plasma Concentrations of Sufentanil (ng/mL)	
	Sufentanil	Sufentanil + Nalmefene (15:1)
Akinesia	13.0 \pm 3.9	42.9 \pm 6.2
Catalepsy	20.8 \pm 5.3	42.9 \pm 6.2
Light Anesthesia	20.8 \pm 5.3	42.9 \pm 6.2
Loss of Righting	27.9 \pm 2.2	91.1 \pm 5.9
Apnea	51.0 \pm 2.6	>1755.0 \pm 189.0 *

* No apnea was noted at or below the average peak plasma concentration of sufentanil (1755 ng/mL) measured in this study.

DISCUSSION

Narcotic antagonists, such as nalmefene, naltrexone or naloxone, have three main clinical applications: 1) diagnosis of addiction, 2) prophylactic treatment of narcotic abuse, and 3) emergency treatment of narcotic overdose. Each of these is based upon the belief that such compounds displace previously assimilated opiates from their receptor sites and/or, if administered prior to narcotic intake, will preclude narcotic agonist activity at those sites.⁸ It is very likely that in the present study, the opiate antagonist, nalmefene, competed with sufentanil for opiate receptor binding sites in some "differential" manner so as to preclude respiratory but not sedative/anesthetic effects. Relatively large elevations in sufentanil plasma threshold concentrations (Table 3) for apnea vs. those for sedative effects support the hypothesis that opiate antagonist effects are mediated at the level of the opiate receptor, i.e., through an alteration in sufentanil pharmacodynamics. However, further speculation on such complex receptor-level mechanisms is beyond the scope of this study. Perhaps the mechanisms by which antagonists influence opiate agonist effects may not be limited to receptor sites; pharmacokinetic factors can determine the bioavailability of drugs, and thus influence the course of their clinical effects.

Hug and Murphy¹² reported that approximately 95 percent of a therapeutic dose of fentanyl is eliminated from plasma within the first five minutes after injection. However, extremely high doses such as the two highest levels used in the present study, may temporarily saturate the "central" group (lung, heart and brain) of uptake compartments. Bjorkman et al.,¹⁴ reported that after an initial draining of injected fentanyl from the plasma compartment, drug that has circulated through the system reappears in the compartment. With fentanyl, this recirculation is slow enough to give a visible secondary peak in the fentanyl plasma concentration-time curve. Perhaps, at extremely high doses of sufentanil, recirculation would also be comparatively slow. According to Bailey and Stanley¹⁵, the clinical effects of small doses of sufentanil are likely to be terminated by redistribution to the peripheral compartment (muscle, fat). With larger doses, plasma concentrations of sufentanil are not rendered sub-therapeutic by redistribution, due to relative saturation of the peripheral compartment. In this instance, hepatic biotransformation is responsible for termination of clinical effect. The slower elimination of sufentanil from plasma at the highest two doses (Figure 1) may also be the result of such

mechanisms.

Under conditions of prolonged hypercapnia or hypoxia, drug absorption, distribution, and metabolism can be altered ¹⁶. Sufentanil is a basic drug (pKa is about 8.0), ¹⁷ and increases in blood pH shift the equilibrium to favor the unionized moiety; the reverse may be true of respiratory acidosis ¹⁸. Hug and Murphy ¹¹ found decreased binding of fentanyl to plasma proteins with acidemia in dogs. Acidemia-induced decreases in sufentanil binding to plasma proteins could also account for increased deposition of sufentanil in storage compartments and possibly resulting in the unusual pattern of changes in plasma sufentanil concentrations (from the two highest doses) with time in the present study.

The exact mechanisms by which nalmefene improved respiratory function could also involve physiological parameters not measured in the present study. For example, nalmefene could have reversed sufentanil-induced decreases in blood flow to highly perfused compartments such as lung, liver and kidneys, and thus limited its CNS bioavailability which, in turn, would limit further respiratory effects. Nalmefene has been reported to improve aortic blood pressure, cardiac output, and blood flow to the myocardium in dogs with experimental congestive heart failure ¹⁰. Nalmefene may, therefore, indirectly limit sufentanil bioavailability as a result of its stimulation of blood flow.

CONCLUSIONS

The mechanisms by which nalmefene can alter the profile of sedative vs. respiratory responses to sufentanil appears to involve a complex interaction of receptor, pharmacokinetic and other secondary physiological parameters. Differentiation of "causes" and "effects" would require additional studies which are designed to address such questions. Hopefully, the findings of the present study will stimulate new questions to consider in defining opiate agonist and antagonist interactions.

REFERENCES

1. Mioduszewski, R. and Farrand, R., Pharmacological Effects of Carfentanil in Rats: Influence of Adjuvant Coadministration. CRDEC-TR-041, 1989.
2. Mioduszewski, R., Reutter, S. and Berg, D., Pharmacological Effects of Opiate Agonist and Antagonist Coadministration in Ferrets. CRDEC-TR-182, May 1990
3. Mioduszewski, R., Reutter, S., Crowley, R., and Pullen, R., Dissociation of Opiate-Induced Sedation and Respiratory Depression By Coadministration of Opiate Antagonist in Ferrets. Submitted for Publication, 1990 .
4. Mesina, J., Syvina, T., Hotaling, L., Peauet-Goad, M., and Fox, G. A Simple Technique for Chronic Jugular Catheterization in Ferrets. Laboratory Animal Science 38:89-90, 1988.
5. Michiels, M., Hendriks, R. and Heykants, J., Radioimmunoassay of the new opiate analgesics alfentanil and sufentanil. Preliminary pharmacokinetic profile in man. J. Pharm. Pharmacol. 35:86-93, 1983.

6. Dixon, R., Hsiao, J., Taafe, W., Hahn, E., and Tuttle, R., Nalmefene: Radioimmunoassay for a New Opioid Antagonist. J. Pharmaceutical Sci. 73 (11): 1645-1646, 1984.
7. Tallarida, Ronald and Murray, Rodney, eds. A Manual of Pharmacologic Calculation With Computer Programs, 2nd edition, Springer-Verlag, 1987.
8. Langguth, P. Khan, P.J., and Garrett, E.R., Pharmacokinetics of Morphine and Its Surrogates XI: Effect of Simultaneously Administered Naltrexone and Morphine on the Pharmacokinetics and Pharmacodynamics of Each in the Dog. Biopharmaceutics of Drug Disposition 11:419-444 (1990).
9. Garrett, E.R., Shyu, W.C., and Ulubelen, Pharmacokinetics of Morphine and Its Surrogates VII: Naloxone and Naloxone Conjugate Pharmacokinetics in Dogs as a Function of Dose and as Affected by Simultaneously Administered Morphine. J. Pharm. Sci. 75: 1127 (1986).
10. Liang, C.S., Imai, N., Stone, C.X., Woolf, P.D., and Tuttle, R.R., The Role of Endogenous Opioids in Congestive Heart Failure: Effects of Nalmefene on Systemic and Regional Hemodynamics in Dogs. Circulation 75 (2): 443-451, 1987.
11. Hug, C. C., and Murphy, M. R., Fentanyl Disposition in Cerebrospinal Fluid and Plasma and Its Relationship to Ventilatory Depression in the Dog. Anesthesiology 50:342-349, 1979.
12. Hug, C. C., and Murphy, M.R., Tissue Redistribution of Fentanyl and termination of Its Effects in Rats. Anesthesiology 55:369-375, 1981.
13. Bovill, J.G., Sebel, P.S., and Blackburn, C.L., Kinetics of Alfentanil and Sufentanil: A Comparison, Anesthesiology 55: A174, 1981.
14. Bjorkman, S., Stanski, D.R., Verotta, D. and Harashima, H., Comparative Tissue Concentration Profiles of Fentanyl and Alfentanil in Humans Predicted from Tissue/Blood Partition Data Obtained in Rats. Anesthesiology 72:86-873, 1990.
15. Bailey, P. and Stanley, T. The Pharmacology of Intravenous Narcotic Anesthetics. In: Miller, R.D., Ed, "Anesthesia". New York: Churchill Livingstone, 1981; pp.745-797.
16. Shook, J.E., Watkins, W.D. and Camporesi, E.M., Differential Roles of Opioid Receptors in Respiration, Respiratory Disease, and Opiate-induced Respiratory Depression. Am. Rev. Respir. Dis. 142:895-909, 1990.
17. Hug, C.C., "Clinical Application of a Narcotic Antagonist: Nalbuphine," in Opioids in Anesthesia, Ed. F. G. Estafanous, Butterworth Publishers, Boston, 1984.
18. Ainslie, S. G., Eisele, J. H., and Corkill, G., Fentanyl Concentrations in Brain and Serum during Respiratory Acid-Base Changes in the Dog. Anesthesiology 51: 293-297, 1979.

BLANK

THE FATE OF SULFUR MUSTARD AFTER INTRAVENOUS INTOXICATION IN RATS

A. Maisonneuve, I. Callebat, L. Debordes, L. Coppet
Centre d'Etudes du Bouchet, BP n°3, 91710 VERT LE PETIT-FRANCE

ABSTRACT : The aim of this work is to investigate the biodisposition of a powerful vesicant : Sulfur Mustard (2,2'-dichlorodiethyl sulfide, SM). To rats is administered an intravenous dose of free and ¹⁴C-SM (10 mg/kg). Blood levels of intact SM are analyzed by CG-FID and revealed a rapid distribution phase followed by a slow elimination phase. SM is still detected 8 hr after the intoxication. The major route of elimination of radioactivity is urine and accounts about 70% of the dose during the first 24 hr. After 4 days, cumulative excretion in urine represented about 80% of the dose. Tissue distribution has shown a widely repartition of radioactivity in organism ; highest tissue levels were found in elimination and transformation organs.

INTRODUCTION

Among the vesicants, sulfur mustard, (Bis(2-chloroethyl) sulfide, Mustard gas, Yperite), is known as one of the most dangerous toxic warfare. Since its use during the different World Wars I and II, its injuries have been described. More recently, its toxicity and its insidiousity have been still demonstrated at the time of Iran-Irak conflict. In spite of these facts, no therapeutic means are developed and actually known (1).

To our knowledge, the most part of works is directed towards the characterizations of injuries and the explanations of toxic mecanisms of sulfur mustard (2). Only very few reviews described the processes of sulfur mustard toxicokinetic. Moreover, these informations were published in the years 40-60 and most of them about metabolism and excretion of sulfur mustard : after intravenous (IV) administration, urine was found as the primary route of excretion for rats, mices, rabbits and humans (3, 4). The same results were obtained after intraperitoneal (IP) administration (5). Urinary metabolites were described after IV or IP intoxications (4, 6). If for Davison et al. the main metabolites, after intravenous SM administration, are glutathione-bis-chloroethyl sulfide conjugates, for Roberts et al., it is cysteine-bis(β -chloroethyl) sulfone after intraperitoneal SM administration. Thiodiglycol was found in the urines of Iran-Irak war victims (7, 8, 9, 10). Distribution of radiolabeled sulfur mustard was related, after percutaneous or intravenous administrations, with whole body autoradiography. High level of radioactivity, without quantisation of radioactivity, is observed in elimination organs (3, 11, 12, 13, 14). Drasch et al. (15) reported the recovered concentrations of mustard gas, 7 days after an exposure, in the tissues of an iranian victim.

As the toxicodynamic is influenced by the toxicokinetic data, a comprehensive study on biodisposition of sulfur mustard is necessary to progress towards the interpretations of its toxicity. Thus, it is important to investigate and to put together, in a same study, blood kinetic, urinary and faecal excretions, tissue and organ distributions of sulfur mustard. The purpose of this work is to determine the biological fate of sulfur mustard in rats after intravenous intoxication of this toxic. For the first time, the blood toxicokinetic with determination of kinetic parameters (volume of distribution, clearance) is described. Urinary and faecal excretions, following ^{14}C -sulfur mustard administration, are determined. The complete repartition of sulfur mustard and/or its metabolites in the tissues (muscle, fat, skin and carcass), in the organs (liver, kidney, heart, intestine, lung, brain...) and in blood are described after intravenous intoxication of ^{14}C -sulfur mustard in rats. These data have allowed to establish the kinetic distribution of mustard gas in all the tissues and organs.

For the whole study, an intravenous administration mode is chosen to reflect an inhalation intoxication. A 10 mg sulfur mustard or ^{14}C -sulfur mustard dose /kg is given to male Wistar rats via the femoral vein to investigate the disposition of toxic. 10 mg/kg corresponds to threefold LD_{50} (determined on 14 days).

TOXICOKINETIC STUDIES

A liquid-liquid extraction procedure coupled with GC-FID analysis is validated for quantisation of intact sulfur mustard in blood. For the first time, the disappearance of sulfur mustard from blood, from 5 min to 8 hr, has been studied after intravenous sulfur mustard injection (via the femoral vein). The disposition of sulfur mustard, (fig. 1.), is characterized by a biexponential decline. The distribution phase is rapid with a $t_{1/2\alpha} = 5,56$ min and the elimination phase is slow and longer than one with a $t_{1/2\beta} = 3,59$ hr. Toxicokinetic parameters derived from the blood concentrations data are summarized in the table 1. It is important to notice that sulfur mustard is a persistent toxic in the systemic circulation, $11,90 \pm 1,72$ ng/ml was still detected 8 hr after intravenous intoxication to rats.

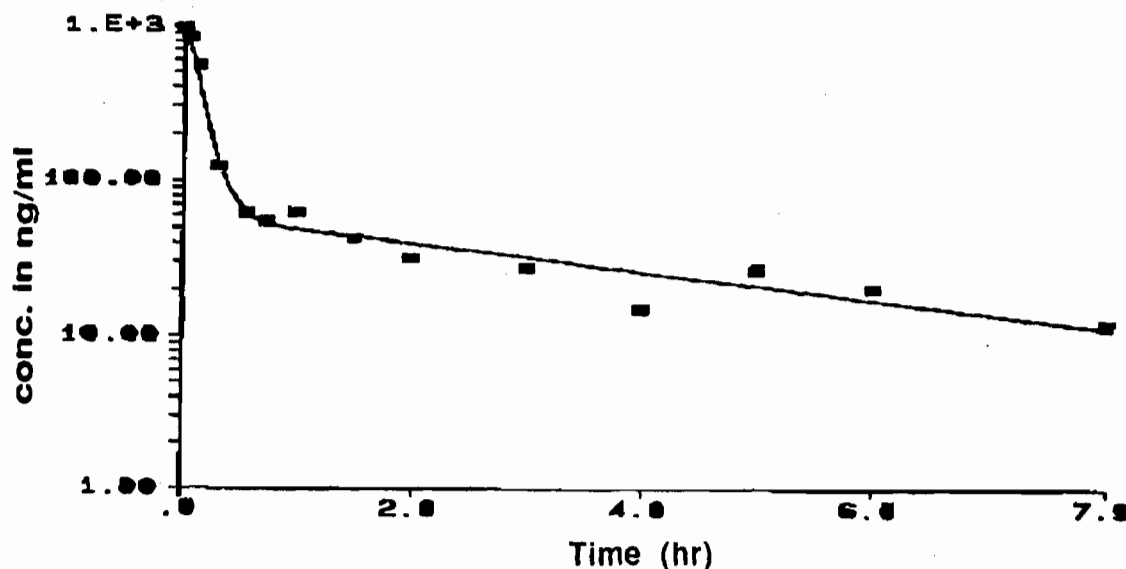


FIG.1.
Representative blood concentration-time profile of sulfur mustard in the rat following its intravenous administration at 10mg/kg.

AUC (ng/ml)	Cl (ml/hr)	Vdss (l/kg)	t _{1/2α} (mn)	t _{1/2β} (hr)
410,69	21037,1	74417,29	5,56	3,59
A (ng/ml)	α (h ⁻¹)	B (ng/ml)	β (h ⁻¹)	
1293,53	7,47	45,84	0,1929	

TABLE 1.
Toxicokinetic parameters of sulfur mustard after intravenous administration (10mg/kg) to wistar rats. (Model : two exponential, data fitted using weighted least squares algorithm
weighting factor : 1/sd)

URINARY AND FAECAL EXCRETIONS

Fig.2. illustrates the pattern of elimination of radioactivity in urine and faeces. $79,5 \pm 8,55 \%$ of the applied dose is recovered in urine at 96 hr. Most of the radioactivity, $64,5 \pm 7,54 \%$, are recovered in the first 24 hr. Then, some residual rate are eliminated until 96 hr. Faecal excretion represented less than 3 % of the administered radioactivity. In the first urinary fraction 0-3 hr, several metabolites have been separated on TLC plates. It appears three major radioactive lines and at least seven minor radioactive lines. No glucuroconjugued or sulfoconjugued products have been detected.

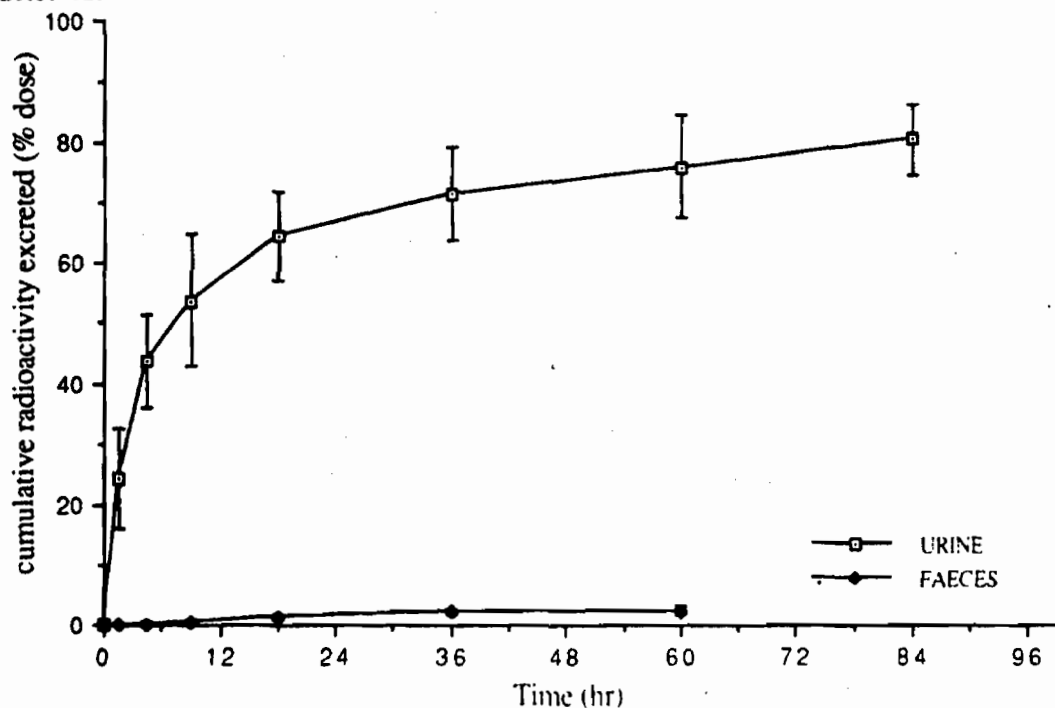


FIG.2.
Cumulative elimination of carbon 14 level 96 hr after administration of an intravenous dose of 10 mg/kg sulfur mustard in urine and faeces. Values are mean \pm sd n=7 male rats.

TISSUE AND ORGAN DISTRIBUTIONS

The results of the complete tissue distribution from 2 min to 96 hr are shown a widely repartition of radioactivity in all organs and tissues of rats after ¹⁴C-sulfur mustard administration (fig.3-4-5). Most of the radioactivity is located in the kidney, liver, lung which are the elimination

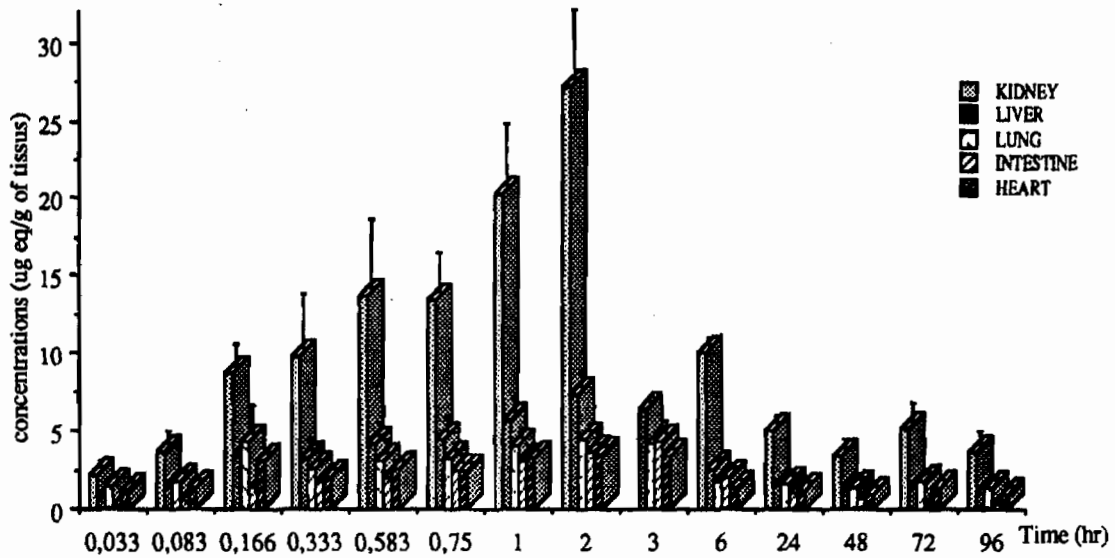


FIG. 3. Concentrations of radioactivity in organs after ¹⁴C-sulfur mustard intravenous intoxication (10 mg/kg)

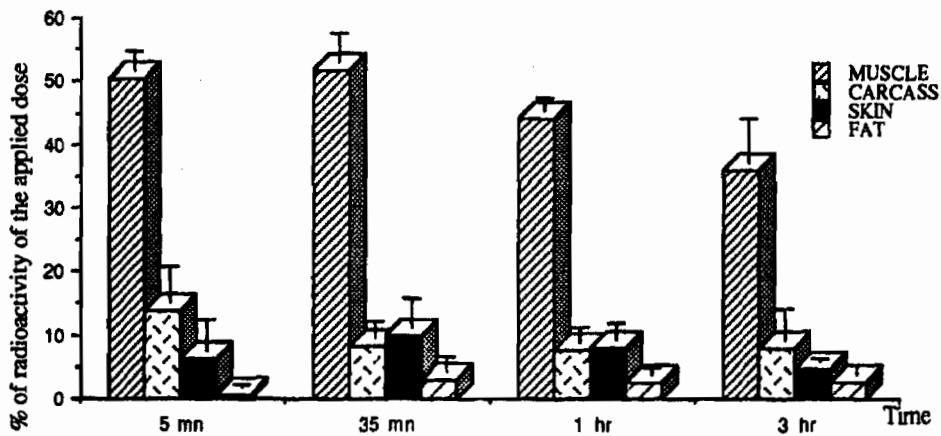


FIG. 4. Repartition of the radioactivity in the tissues after ¹⁴C-sulfur mustard intravenous intoxication (10 mg/kg dose)

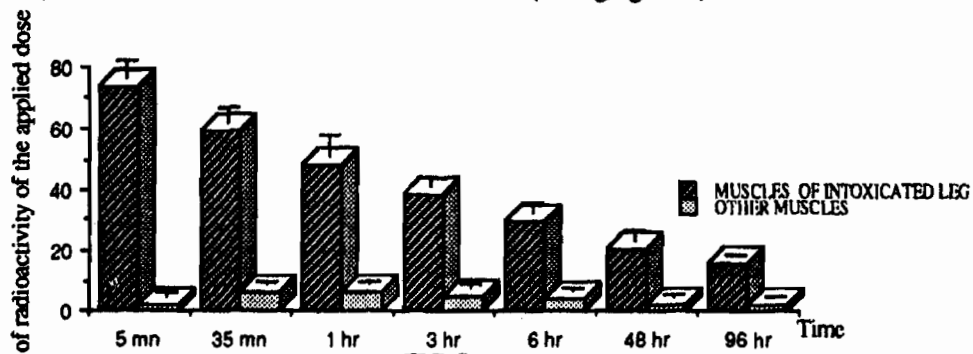


FIG. 5. Repartition of radioactivity between the muscles at the site of intoxication (leg) and the other muscles after 10mg/kg ¹⁴C-sulfur mustard intoxication.

and transformation organs. The maximum of accumulation of radioactivity in the organs is reached two and three hours after the intravenous injection. Then the radioactivity decreased slowly from tissues after 24 hr of intoxication. The total percentage of the applied dose, from every added organs, not exceeded 4 % of the applied dose for the duration of the experiment (96 hr). These slight values of percentage are not representative of the injected dose. Among organs or tissues, no preferential site of storage is demonstrated, but a retention site is observed in the leg receiving the toxic dose. It is important to notice that the radioactivity is found in a preferential aponevros tissue, comparatively to the opposite leg. The same retention is obtained with a smaller dose 500 µg/kg. Via the jugulaire, an alternative route of injection, no higher values in the lung is observed as expected, but the maximum of radioactivity is recovered in the muscles. The kinetic of sulfur mustard in blood showed, after a climax point at 1 hr, a decrease until a constant level, and an increase at 48 hr.

CONCLUSIONS

This paper brings together the comprehensive toxicokinetic data, as blood concentrations of sulfur mustard-time curve, urinary and faecal excretions, the complete quantitative tissue and organ distributions after 10 mg/kg free or radiolabeled sulfur mustard intravenous intoxication (via the femoral vein).

Intact sulfur mustard appears as a persistent toxic in the systemic circulation. It is detected 8 hr after its administration. ¹⁴C-sulfur mustard blood concentrations time-curve has showed a second increase between 48 to 72 hr, phenomenon that Young et al. (11, 12, 13) have already observed and interpreted as a hemoconcentration.

In addition to the widely distribution in all the organs, a local uptake is observed in the leg receiving the sulfur mustard dose. The poor blood flow of the femoral vein may involve the immobilization of toxic in this region. Physically, a consequence of this fact is the transcapillary transport of toxic throughout the space. Moreover, sulfur mustard is a small molecule, PM = 159 g and is liposoluble. The main target, in the intoxicated leg, is the aponevros tissue ($30,4 \pm 8,74$ % of the administered dose at 35 mn).

This accumulation could be assimilated with results obtained after cutaneous toxic absorption (18). A similar accumulation is obtained after a smaller dose 500 µg/kg. In spite of this retention of one part of the injected dose, most of the applied dose, $64,5 \pm 7,54$ %, is accounted in urine, very early, for the first 24 hr. This fact is in agreement with the results described by Hambrook et al. (5) after IV or IP intoxications. Whereas, 3 days are necessary, according these authors, to recover the most part of the absorbed dose after cutaneous application (16).

Due to the electophilic property of the ethylensulfonium ion, sulfur mustard reacts with nucleophilic compounds such as DNA, RNA and macromolecules (17). The interactions between sulfur mustard and the components of the skin or of the tissue of leg are perhaps different. The comparison between the different metabolites in each route of intoxication could give new findings. However via the jugular intoxication, another kinetic distribution is revealed.

Contrary to it was expected in the fat, no more than $3,07 \pm 2,27$ % of the radioactivity were found, after intravenous sulfur mustard administration via the femoral vein ; but $9,80 \pm 4,75$ % of the radioactivity were accounted in the subcutaneous fat .

REFERENCES

1. L. J WILLEMS : Clinical management of mustard gas casualties.
Ann. Med. Milit. (Belg) 3 (suppl.), 1-61. (1989).
2. B. PAPIRMEISTER, A.J. FEISTER, S.I. ROBINSON, R.D. FORD : Medical Defense Against Mustard Gas : toxic mechanisms and pharmacological implications.
CRC Press, Boca Raton, FL pp 79-88. (1991).
3. J.C. BOURSNEILL, J.A. COHEN, M. DIXON, G.E. FRANCIS, G.D. GREVILLE M. NEEDHAM, A. WORMALL : Studies on mustard gas ($\beta\beta'$ -dichlorodiethyl sulphide) and some related compounds. 5. The fate of injected mustard gas (containing radioactive sulphur) in the animal body.
Biochem. J. 40, 756-764. (1946).
4. R. DAVISON, R.S. ROZMAN, P.K. SMITH : Metabolism of bis- β -chloroethyl sulfide (sulfur mustard gas).
Biochem Pharmacol, 7, 65-74, (1961).
5. J.L. HAMBROOK, J.M. HARRISON, D.J. HOWELLS, R.F. METCALFE : The fate of mustard and its metabolites in animals. The urinary and faecal excretion of S35 Labelled sulfur mustard(R).
Note technique n°460, (1986).
6. J.J. ROBERTS, G.P. WARWICK : Studies of the mode of action of alkylating agents-VI. The metabolism of bis-2-chloroethylsulphide (mustard gas) and related compounds.
Biochem. pharmacol., 12, 1329-1334, (1963).
7. E.R.J. WILS, A.G. HULST, A.L. DE JONG, A. VERWEIJ, H.L. BOTER : Analysis of thiodiglycol in urine of victims of an alleged attack with mustard gas.
J. Anal. toxicol., 9, 254-257, (1985).
8. E.R.J. WILS, A.G. HULST, J. VAN LAAR : Analysis of thiodiglycol in urine of victims of an alleged attack with mustard gas, Part II.
J. Anal. Toxicol., 12, 15-19, (1988).
9. VYUDILIK W. : Detection of mustard gas bis(2-chloroethyl)-sulfide in urine.
Forensic science international, 28, 131-136, (1985).
10. W. VYUDILIK : Detection of bis(2 chloroethyl)-sulfide (yperite) in urine by high resolution gas chromatography-mass spectrometry.
Forensic science international, 35, 66-71, (1987).
11. L. YOUNG : A study of the action of liquid mustard gas on the rat. University of Toronto, Canada, Report N°. 6. Cited in : Anslow W.P., Houck C.R., 1946, Systematic Pharmacology and Pathology of Sulfur and Nitrogen Mustards. In Chemical Warfare Agents, and Related Chemical Problems. Parts III-VI. Summary Technical Report of Division 9, National Defense Research Committee of the Scientific Research and Development, Washington, D.C. DTIC N°. AD-234 249, (1942).

12. L. YOUNG : Biochemical Experiments with Mustard Prepared from Radioactive Sulphur. University of Toronto, Canada, Report N° 2, Report N°8, C.P. 26. Cited in : Anslow W.P., Houck C.R., 1946, Systematic Pharmacology and Pathology of Sulfur and Nitrogen Mustards. In Chemical Warfare Agents, and Related Chemical Problems. Parts III-VI. Summary Technical Report of Division 9, National Defense Research Committee of the Office of Scientific Research and Development, Washington, D.C. DTIC No. AD-234-249, (1942).
13. L. YOUNG , J.A. McCARTER, EDSON M., E. ESTOK : Biochemical Experiments with Mustard Gas Prepared from Radioactive Sulphur. V. The systemic Distribution of S^{35} at Different Times after Application of Radioactive Mustard Gas to the skin of the Rat. University of Toronto, Canada, Report N° 17, C.P. 75. Cited in : Anslow W.P., Houck C.R., 1946, Systemic Pharmacology and Pathology of Sulfur and Nitrogen Mustards. In chemical Warfare Agents, and Related Chemical Problems. Parts III-VI. Summary Technical Report of Division 9, National Defense Research Committee of the Office of Scientific Research and Development, Washington, D.C. DTIC N°. AD-234 249, (1944).
- 14 C.J. CLEMEDSON, H. KRISTFFERSSON, O B. SORB, S. ULLBERG : Whole body autoradiographic studies of the distribution of sulphur 35-labeled mustard gas in mice. Acta Radiol. Ther. 1, 314-320. (1963).
15. G. DRASH, E. KRETSCHMER, G. KAUERT, L. VON MEYER : Concentrations of mustard gas (bis(2 chloroethyl)sulfide) in the tissues of a victim of a vesicant exposure. Journal of Forensic Sci. (JF SCA) 32(6), 1788-1793. (1987).
16. J.L. HAMBROOK, D.J. HOWELLS, C. SCHOCK : The fate of mustard and its metabolites in animals. 3 The urinary and faecal excretion of ^{35}S by the rat after cutaneous application of ^{35}S -labelled sulphur mustard. C.D.E. , T.P. n° 525, (1989).
17. T.A. CONNORS : Mechanism of Action of 2-Chloroethylamine Derivatives, Sulfur Mustards, Epoxides and Aziridines. Antineoplastic an Immuno Supressive Agent II. (Ac. Sartorelli & D.G. Johnseds). 18-34. (1975).
18. B. RENSHAW : Mechanisms in Production of Cutaneous Injuries by Sulfur an Nitrogen Mustards. In Chemical Warfare Agents, and Related Chemical Problems. Parts III-VI. Summary Technical Report of Division 9, National Defense Research Committee of the Office of Scientific Research and Development, Washington, D.C. DTIC n°. AD-234-249, (1946).

BLANK

INCREASED PROTEOLYTIC ACTIVITY IN HUMAN EPITHELIAL CELLS
FOLLOWING EXPOSURE TO SULFUR MUSTARD

William J. Smith, Fred M. Cowan, and Clarence A. Broomfield

Biochemical Pharmacology Branch, USAMRICD, APG, MD

ABSTRACT

In an attempt to define the biochemical basis of sulfur mustard-induced vesication, we have previously shown that human lymphocytes respond to sulfur mustard exposure with an increase in proteolytic activity. Since the basal epidermal cell is a major target of sulfur mustard *in vivo*, we studied the ability of sulfur mustard to elicit protease activity in two types of human epithelial cells in culture, normal human epidermal keratinocytes (HEK) and HeLa, the human epithelioid carcinoma cell line. Using a chromogenic substrate assay, we determined that exposure of either epithelial cell type to sulfur mustard and its monofunctional analogue, chloroethyl ethyl sulfide (CEES), resulted in significantly increased proteolytic activity when measured 24 hours after exposure. In HEK, 100 μM CEES resulted in 150% of control protease activation, while 50 μM sulfur mustard gave comparable proteolytic activation. In HeLa, markedly higher concentrations of CEES (5 mM) or sulfur mustard (500 μM) were required to achieve the same level (150%) of activation.

The observation that protease activity can be increased in epithelial cells following exposure to both monofunctional and bifunctional alkylating agents supports the hypothesis of Papirmeister et al. (Fundam Appl Toxicol 5:S134,1985) on the role of proteases in vesication and suggests that further characterization of this activity might lead to a therapeutic approach for sulfur mustard-induced skin vesication.

INTRODUCTION

Sulfur mustard (HD, 2,2'-dichlorodiethyl sulfide) is a chemical warfare agent for which there is no known antidote. After 50 years of research, the basic mechanisms of action resulting in vesication are not yet understood. One hypothesis (1) suggests a linkage between DNA alkylation and protease production. The hypothesized HD-increased protease activity is proposed to cause cutaneous degradation, setting the stage for inflammatory infiltration and blister formation.

The principal area of cutaneous mustard damage is at the epidermal basal cell layer, and histologically, the separation of the epidermal-dermal junction supports the suggestion of localized protease activation (2). Skin organ culture fluids from HD-exposed rabbits, when assayed with synthetic peptide substrates, displayed increased trypsin-like and chymotrypsin-like proteolytic activity in both developing and healing lesions (3), but evidence was not provided which established these proteases to be causal for blister formation.

Other reports from our laboratories have established that human peripheral blood lymphocytes provide a useful *in vitro* system for studying the activation of proteases following HD exposure (4,5). In the present study, human epithelial cells in culture were exposed to the alkylating agents HD or chloroethyl ethyl sulfide (CEES) and proteolytic activity measured.

METHODS

Reagents: Minimum Essential Medium (MEM) containing gentamicin (50 µg/ml) was used for cell washing and assay. MEM supplemented with 5% fetal bovine serum was used for overnight incubations. All tissue culture reagents were from Sigma, St. Louis, MO with the exception of Keratinocyte Growth Medium (KGM) from Clonetics, San Diego, CA. HD with a purity of >98% was obtained from the Chemical Research, Development and Engineering Center, Aberdeen Proving Ground, MD. Chloroethyl ethyl sulfide (CEES) was obtained from Aldrich Chemicals, Milwaukee, WI.

Cells: HEK (Clonetics) and HeLa (ATCC, Rockville, MD) cultures were maintained in 75 cm² flasks in KGM or MEM at 37°C in 5% CO₂. When the cultures became 80% to 90% confluent, cells were removed with trypsin-EDTA. After removal, the cells were placed in a conical tube containing trypsin-neutralizing solution, and centrifuged at 250 X g for 10 minutes. Cells were resuspended in 10 ml of media for cell counts and initial viability determinations.

Alkylating Agent Exposure: HEK and HeLa cells in 24 well tissue culture plates were exposed to 0.1 to 1 mM CEES, or 0.05 to 0.5 mM HD. The plates were maintained at room temperature in a fume hood for 1 hr to allow venting of volatile agent, and then transferred to a CO₂ incubator and incubated at 37° C for a total incubation time of 4 to 24 hr.

TESTSKIN, a human living skin equivalent, (Organogenesis, Cambridge, MA) was exposed to liquid dilutions of HD in 6-well assay trays. After incubation at 37°C in 5% CO₂ for 16 hours, 4 mm punch biopsies were taken and placed in wells of a 96-well plate.

Chromogenic Peptide Substrate Protease Assay (CPSPA): The use of small proteolysis sensitive peptides coupled to p-nitroaniline (pNA) (6) was adapted for protease assay by micro-plate reader (Bio-Rad, Richmond, CA) as previously described (4,5).

Alkylating agent-exposed and untreated control cell cultures were harvested by centrifugation. Cells and supernates were assayed separately for protease activity. Assay samples (50 ul), of supernate or 10^5 to 10^6 cells resuspended in MEM (50 ul), were added to a 96 well flat bottom tissue culture plate. Fifty ul of protease detection peptide substrate (1 - 2.5 mM in H₂O) was added to each well. Absorbance readings were made at times from 10 min to 4 hrs depending on the protease activity of each cell culture.

Peptide Substrates: Chromozym TRY (Carbobenzoxy-vayl-glycl-arginine-4-nitranilide acetate) is used for detection of proteases with trypsin-like activity; Chromozym TH (Tosyl-glycyl-prolyl-arginine-4-nitranilide acetate) for detection of proteases with thrombin-like activity. (Boehringer Mannheim Biochemicals, IN.).

Data Analysis: All data points in the chromogenic assays were derived from quadruplicate samples and expressed as mean of percent of control with standard error. Results were tested by analysis of variance. Individual group significance was determined by Student's t-test.

RESULTS

Increased protease activity (150 - 300% of control) after alkylating agent exposure was associated with both HEK (Figure 1) and HeLa (Figure 2). This activity was not detected in cell culture supernates. CEES, a chemical compound capable of causing DNA alkylation and metabolic disruption similar

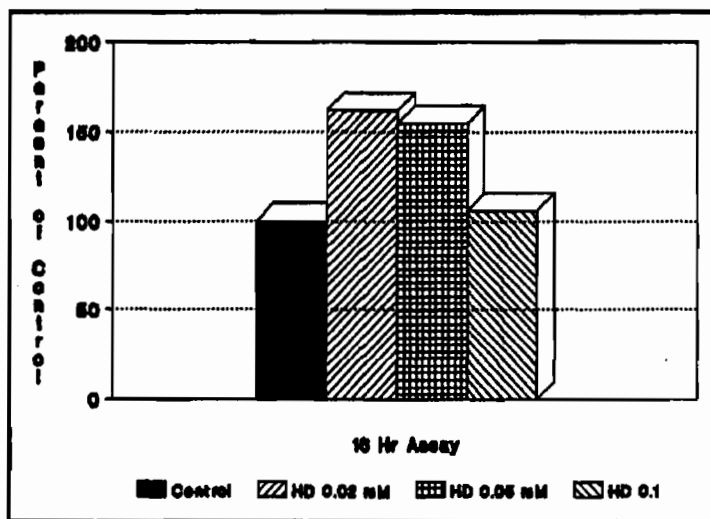


Figure 1. HEK 16 hour post exposure to HD (0.02, 0.05, and 0.1 mM) were assayed for protease activity using 2.5 mM Chromozym TH as described in METHODS.

to HD (7), resulted in increases in activation of protease similar to those observed in HD-treated cells (Data not shown). However, higher concentrations of CEES were required to increase protease activity. This observation is similar to that seen for the cytotoxic potential of CEES compared to HD (7).

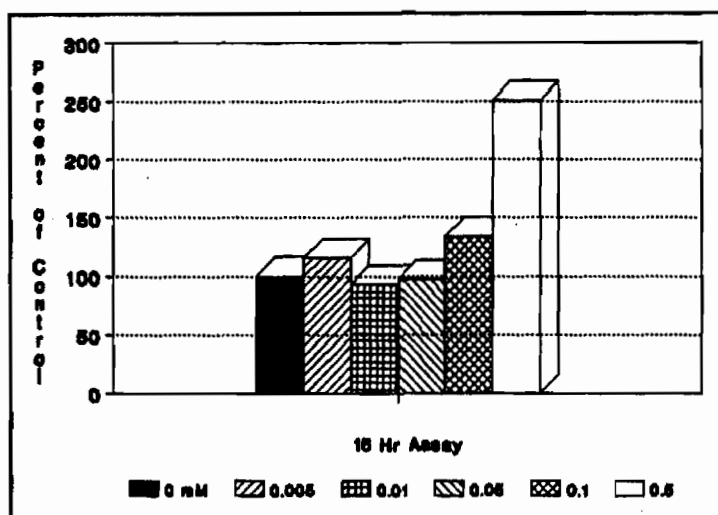


Figure 2. HeLa cells 16 hour post exposure to HD (0.005-0.5 mM) were assayed for protease activity using 2.5 mM Chromozym TH as described in METHODS.

Exposure of the human living skin equivalent, TESTSKIN, to HD resulted in very high levels of proteolytic activity (500-600% of control) and some activity could be detected in the biopsy supernates (Figure 3).

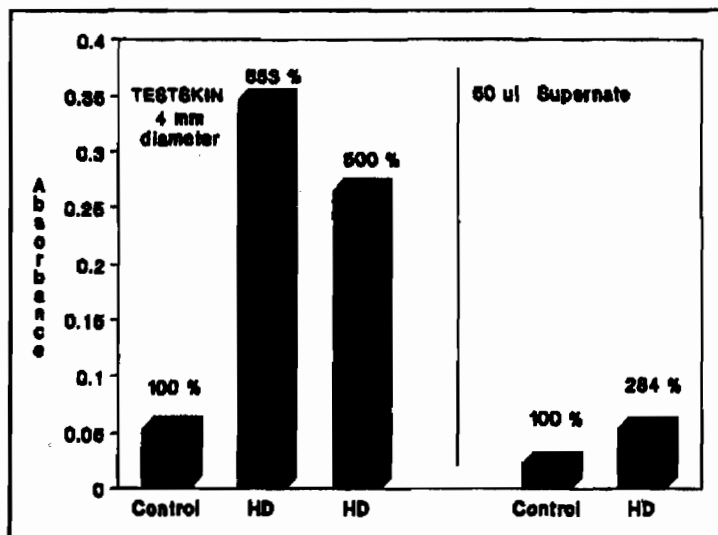


Figure 3. TESTSKIN 16 hour post exposure to HD (0.5 mM) were assayed for protease activity using 2.5 mM Chromozym TH as described in METHODS.

DISCUSSION

Enhanced protease activity in human epithelial cells by HD or CEES demonstrates that these alkylating agents can cause an increase of protease activity in cells related to those found *in vivo* at the epidermal-dermal junction. The HD-increased protease in epithelial cells consists, at the minimum, of serine protease(s) which may be cell associated, since increased protease activity could not be detected in cell culture supernates.

The increased protease activity in human epithelial cells exposed to HD, demonstrated in this study, provides experimental evidence that proteolytic activation might be a consequence of HD toxicity. This assay system should provide a useful means of fully characterizing the HD-associated proteolytic activity.

CONCLUSION

Both monofunctional (CEES) and bifunctional (HD) alkylating agents increase proteolytic activity in human epithelial cells in culture. This activity is associated with the cells and not detected in supernates. Exposure of the organotypic skin equivalent, TESTSKIN, results in considerably higher protease activation and at this high level results in protease being released into the medium. These cellular and organotypic assays support the hypothesized activation of protease by skin epithelium and should be useful in understanding the mechanisms of HD-induced vesication and the development of therapeutic interventions.

REFERENCES

1. PAPIRMEISTER, B., GROSS, C.L., MEIER, H.L., PETRALI, J.P. AND JOHNSON, J.B. (1985). *Fund. and Appl. Toxicol.* 5:S134-S149.
2. PAPIRMEISTER, B., GROSS, C.L., PETRALI, J.P. AND MEIER, H.L. (1984). *J. Toxicol. Cutan. and Ocular Toxicol.* 3:395-410.
3. HIGUCHI, K., KAJIKI, A., NAKAMURA, M., HARADA, S., PULA, P.J., SCOTT A.L. AND DANNENBERG, A.M. (1988). *Inflammat.* 12:311-334.
4. COWAN, F.M., BROOMFIELD, C.A., AND SMITH, W.J. (1991). *Cell Biol & Toxicol* 7:239-248, 1991.
5. COWAN, F.M., BROOMFIELD, C.A., AND SMITH, W.J. (1991). Accompanying Article. *Proceedings of the CRDEC Scientific Conference*, November, 1991.
6. FRIBERGER, P. (1982). *Scand. J. Clin. Lab. Invest.* 42 (Suppl 162):1-98.
7. SMITH, W.J., SANDERS, K.M., GALES, Y.A. AND GROSS, C.L. (1991). *J. Toxicol. Cutan. and Ocular Toxicol.* 10:33-42, 1991.

BLANK

SULFUR MUSTARD-INDUCED ALTERATIONS OF DNA STRUCTURE AND KINETICS
IN PROLIFERATING HUMAN CELLS IN CULTURE

William J. Smith, K. Michael Sanders, James E. Caulfield
and Clark L. Gross

Biochemical Pharmacology Branch, USAMRICD, APG, MD.

ABSTRACT

Sulfur mustard (2,2'-dichlorodiethyl sulfide, HD) was the major cause of chemical casualties in World War I, and its use in recent combat situations continues to result in numerous civilian and military casualties. Despite decades of research, the mechanism by which HD induces vesication is not known and no effective antidotes are available. Since the replicating basal epidermal cell is a major target of HD-induced vesication, we used human epidermal keratinocytes (HEK), human epithelial tumor cells (HeLa), and actively proliferating human peripheral blood lymphocytes (PBL) as *in vitro* model systems to investigate the biochemical sequelae of HD-induced injury.

HD exposure of all three proliferating cell types resulted in inhibition of cell cycle progression in the early S phase. HD treatment of mitogen-activated PBL resulted in a higher cytotoxicity in those cells in S phase. Blockage of replicative progression through the cell cycle as measured by flow cytometry and inhibition of ³H-thymidine uptake was also observed. Alterations in DNA structure following HD were detected through changes in uptake of DNA specific fluorescent dyes. These alterations suggested that DNA repair processes were active in cells for at least 24 hours after HD exposure. Niacinamide (1mM), which has been shown to protect resting PBL from the effects of HD, protected HEK against the cytotoxic effects of HD for 24 hours. However, this protection waned when cell growth was allowed to proceed for up to 72 hours after HD. Niacinamide protected activated PBL against the cytotoxic effects of HD for 24 hours. This protection then decreased, but did not completely disappear, by 72 hours after exposure.

Proliferating human cells in culture were sensitive models for studying the toxic effects of HD. This sensitivity was studied through both loss of cellular viability and changes in cellular DNA. Our data suggest, for the first time, that a window of opportunity exists for therapeutic intervention into DNA repair processes following HD. Further studies of the effects of HD on cellular DNA should point the way to a therapeutic approach to both short-term (vesicating) and long-term (mutagenic) pathologies induced by HD.

INTRODUCTION

Sulfur mustard (HD) is an alkylating agent that has been shown to have mutagenic (1,2), cytotoxic(3), and vesicating (4) properties. Its use in combat situations has resulted in lethal, incapacitating, and disfiguring injuries. The principal incapacitating injuries come from the vesicating capacity of HD, i.e., production of skin blisters.

Despite decades of medical research, the mechanism by which HD induces vesication is not known and no effective antidotes are currently available. In 1985, Papirmeister *et al.* (5) proposed a hypothesis delineating the following events for the generation of HD-induced pathology: HD alkylates DNA, DNA strand breaks occur, poly(ADP-ribose)polymerase is activated and utilizes cellular NAD⁺ as substrate, NAD⁺ is depleted, glycolysis is inhibited, hexose monophosphate shunt is activated, proteases are released, and pathology results. Since the basic tenet of this hypothesis is the formation of cellular damage through the interaction of HD with the DNA of the cell, an understanding of the association between HD exposure and damage at the level of cellular DNA should lead to a better comprehension of the mechanism of HD-induced pathology and could aid in the design of prophylactic and therapeutic compounds against the HD lesion.

METHODS

Reagents:

The lymphocyte studies used RPMI 1640 containing gentamicin (50 µg/ml) for cell washing and RPMI 1640 supplemented with 5% fetal bovine serum (RPMI-FBS) for final cell suspension and assay. All tissue culture reagents were from Sigma Chemical Co., St. Louis, MO. Buoyant density isolations were performed using Histopaque (Sigma, St. Louis, MO).

Keratinocyte studies used HEK, Keratinocyte Growth Medium (KGM), trypsin-EDTA, and trypsin neutralizing solution from Clonetics Corporation (San Diego, CA).

HD (2,2'-dichlorodiethyl sulfide, mustard gas) was obtained from the Chemical Research, Development and Engineering Center, Aberdeen Proving Ground, MD. The following chemicals were purchased from commercial sources: RNase A from Boehringer Mannheim (Indianapolis, IN), propidium iodide (PI), dextran T-500, and Concanavalin A (Con A) from Sigma (St. Louis, MO).

PI was dissolved in RPMI 1640 at 20 µg/ml for use in viability studies and at 250 µg/ml in 5% triton X-100 for DNA staining. RNase (1 mg/ml) was added to the DNA staining solution when needed (6).

Lymphocyte Isolation:

Human PBL were isolated from whole blood obtained by venipuncture from volunteers under an approved human use protocol. One ml of 6% dextran was added per 10 ml of blood to expedite red blood cell sedimentation. After allowing sedimentation for 30 minutes at 37°C, the white cell rich supernate was collected, layered onto Histopaque (d-1.077), and centrifuged at 450 X g for 20 minutes. The mononuclear cell layer was harvested, washed twice in RPMI, and centrifuged at 250 X g for 10 minutes. The isolated PBL were resuspended in RPMI-FBS for cell counting, and initial cell viability

determinations were performed by trypan blue dye exclusion. Con A activation of the cells was accomplished by incubating the PBL for 24-72 hours at 37°C in RPMI-FBS containing Con A at a final concentration of 5 µg/ml.

Keratinocyte Culture System:

HEK cultures were maintained in 75 cm² flasks in KGM at 37°C in 5% CO₂. When the HEK cultures became 80% to 90% confluent, cells were removed with trypsin-EDTA. After removal, the cells were placed in a conical tube containing trypsin-neutralizing solution, and centrifuged at 250 X g for 10 minutes. Cells were resuspended in 10 ml of KGM for both cell counts and initial viability determinations.

HeLa Cell Cultures:

HeLa cultures were obtained from the American Type Culture Collection (Rockville, MD) and maintained in either Earle's Minimum Essential Media or RPMI 1640 with 5% fetal bovine serum (Sigma) and 50 µg/ml gentamicin (GIBCO, Grand Island, NY). Trypsinization and counting were conducted as with HEK.

Microplate Preparation:

PBL were resuspended in RPMI-FBS at 4 X 10⁶ cells/ml, and 50 µl/well dispensed into 96-well microtest plates (Falcon, Oxnard, CA) to yield a final concentration of 2 X 10⁵ cells/well. RPMI-FBS and HD (1 - 600 µM) were added to the wells to yield a final volume of 200 µl/well. The plates were vented in a fume hood for 1 hour to exhaust volatile agent. They were then incubated at 37°C for 0-72 hours in 5% CO₂ after which time they were prepared for flow cytometric analysis.

HEK or HeLa cells (1 X 10⁵ cells/well) were placed in the wells of a 24-well plate in a total volume of 1 ml. The plates were incubated for 24 hours. The media was discarded, and fresh media containing HD was added to a final volume of 1 ml. The plates were vented for 1 hour and incubated for 24-96 hours as described above.

Niacinamide Studies:

Immediately prior to the addition of HD to the test plates, niacinamide in media was added to the appropriate wells to a final concentration of 1 mM.

Flow Cytometry:

PBL. PI in RPMI was added to each well to yield a final concentration of 6 µg/10⁶ cells. After 3 minutes at room temperature, the plates were placed on a Multiple Sample Delivery System (MSDS, Coulter Electronic, Hialeah, FL) attached to an EPICS C flow cytometer (Coulter) for viability analysis. The flow cytometer operates with a 5 watt argon laser generating a 488 nm line at 200 mW. The MSDS permits automatic sampling of all wells of the 96-well plate.

Immediately after conclusion of the viability analysis, 50 µl of PI in triton X-100 was added to each well, and the plate was returned to the MSDS for cytometric analysis of DNA.

Data analysis was performed using the EASY2 computer system with cell viability analyzed using the Intgra program and DNA histogram analysis by the Paral program (Coulter).

HEK or HeLa. To determine epithelial cell viability by propidium iodide

(PI), the supernatant media containing the non-attached dead cells were collected in 12 x 75 mm tubes. Cells were trypsinized from the wells, pooled in the respective tubes containing supernatant cells and trypsin neutralizing solution, and centrifuged at 250 X g for 10 minutes. The pellet was resuspended in 1 ml of medium and PI (1 μ g) was added. After 3 minutes at room temperature, viability determinations were performed on the flow cytometer. Immediately after PI viability determinations, DNA cell cycle analysis was conducted by adding PI-triton to each tube, and the samples were analyzed on the flow cytometer. Data analysis was performed as with the PBL.

RESULTS

Viability Studies

For all cell lines studied, the viability results (data not shown) were consistent with those previously reported by our laboratories (7,8). Niacinamide had a protective effect against the cytotoxicity of HD for the first 24 hours after exposure but this effect waned within 72 hours in all proliferating cells, i.e. mitogen-stimulated PBL, HEK, HeLa (7,8,9).

Disruption of Cell Cycle Kinetics

PI is a fluorescent dye which intercalates into the structure of DNA and binds stoichiometrically. The amount of dye taken up per cell increases as dividing cells progress through the replicative cell cycle. Flow cytometric analyses of dividing cells produce fluorescent histograms which represent the full spectrum of DNA content seen in these populations. A typical DNA histogram for control PBL is shown in Figure 1. These cells were evenly distributed throughout the cell cycle. DNA histograms of HD-exposed PBL indicated that the cell cycle was blocked in the late G1/early S phase (Figure 1). HeLa cells,

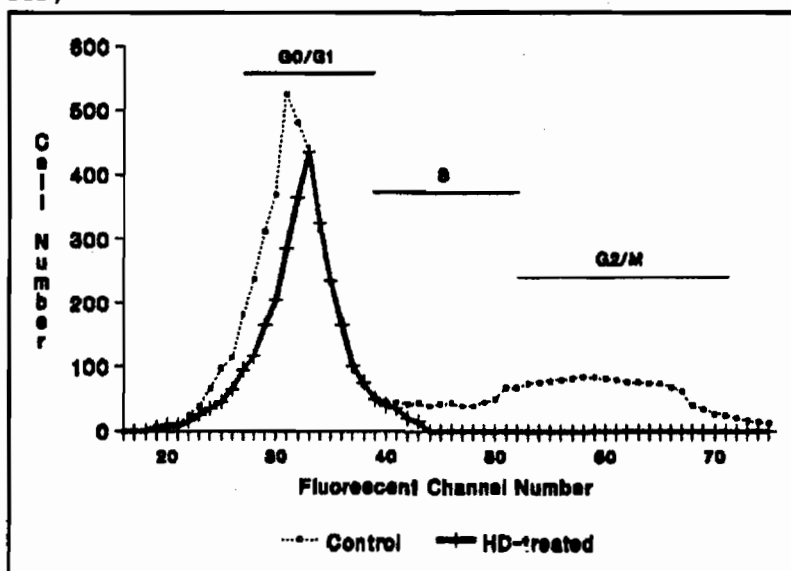


Figure 1. Blockage of PBL in S phase of the cell cycle by HD (100 μ M). DNA histograms were determined 24 hours after exposure by flow cytometric analysis of PI-triton staining as described in METHODS.

derived from a human epithelial tumor, showed a similar blockage in early S phase (Figure 2). These observations are identical to those previously reported using HEK (7).

The blockage of Con-A stimulated PBL cell cycling could also be demonstrated by a inhibition of uptake of ^3H -thymidine, a necessary precursor of DNA synthesis, 48 hours after activation (Figure 3). Neither this thymidine uptake blockage nor cell cycle progression as seen by flow cytometry could be prevented by treatment with 1 mM niacinamide (Data not shown).

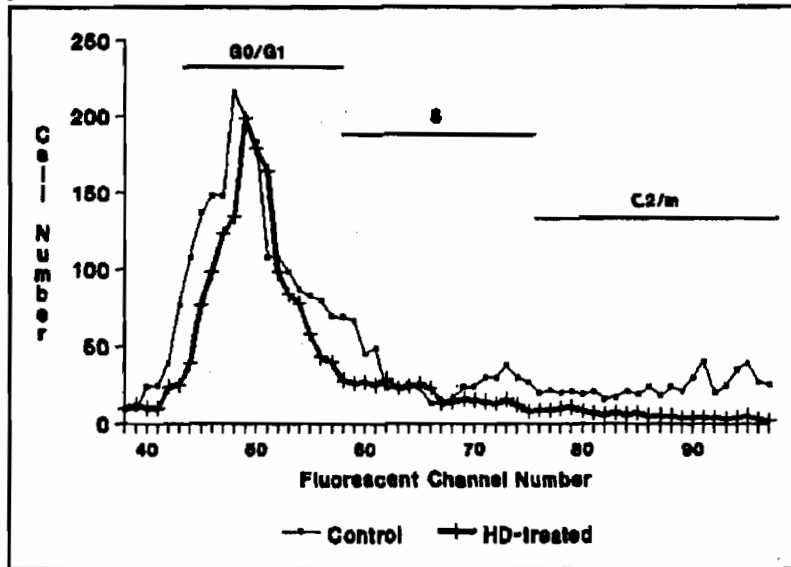


Figure 2. Blockage of HeLa cells in S phase of the cell cycle by HD (100 μM). DNA histograms were determined 24 hours after exposure by flow cytometric analysis of PI-triton staining as in METHODS.

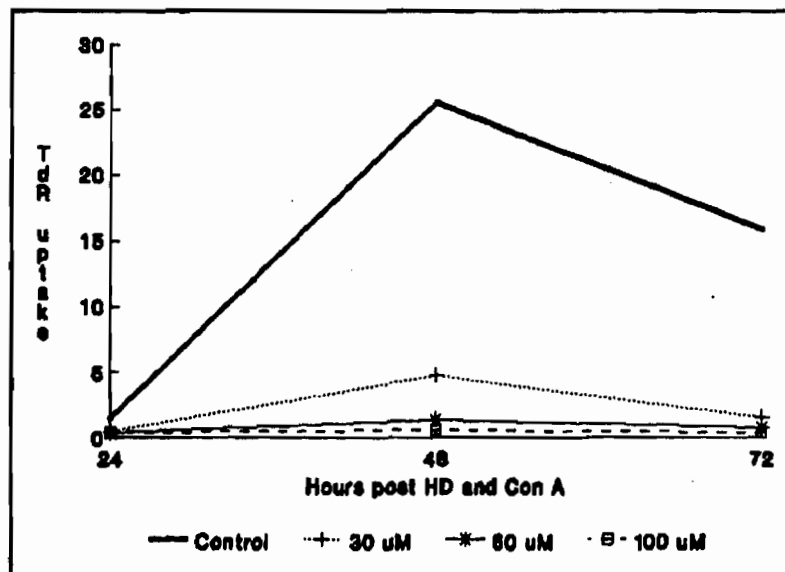


Figure 3. Uptake of ^3H -thymidine by lymphocytes at various times after Con A activation with treatment by HD.

Structural Modifications to the DNA

In contrast to the fluorescent histograms generated from dividing cell populations, uptake of PI by the diploid DNA of resting PBL resulted in the detection of a single fluorescent peak. This peak was normally distributed and highly reproducible, varying less than 1 or 2 fluorescent channels in replicate samples. Within 4 hours following exposure to HD, and more markedly at 24 hours post-exposure, the treated cell DNA exhibited a distinct shift to the right, indicating increased dye uptake (Figure 4). By 48 hours, no dye uptake could be detected, suggesting that the DNA had collapsed upon itself and was beyond repair.

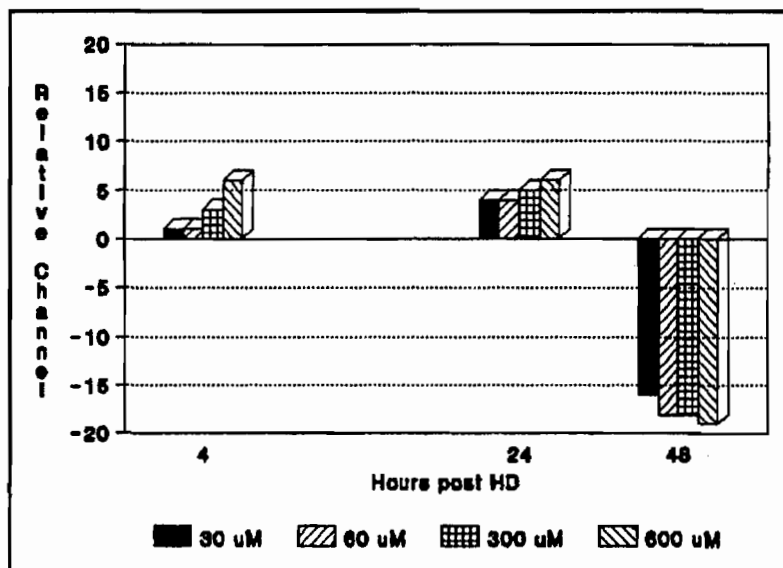


Figure 4. Shift of the peak diploid DNA fluorescent channel in HD-treated PBL as compared to controls. Lymphocytes were treated with HD, and the cellular DNA was stained by PI-Triton and peak positions determined with Paral software. Right shift of fluorescent peak indicates increased dye uptake possibly due to active repair processes.

DISCUSSION

Proliferating cells allowed investigations into the effects of HD alkylation on cellular progression through the cell cycle. HD blocked cell cycling of both Con A-stimulated PBL and HeLa in the early S phase in a manner analogous to that previously seen in HEK (7). Along with the demonstration that cells in the S phase of the cell cycle were the most sensitive to the cytotoxic effects of HD (7,8), the data suggest that therapeutic approaches to HD should be directed towards maintaining cells in the G1 phase. This strategy would allow repair of DNA before the HD-exposed cells attempt DNA replication in the S phase. A class of reversible inhibitors of the cell cycle, which work in the G1 phase, has recently been described (9).

Shifts in peak DNA fluorescent channel following HD exposure provide

important information as to the repair capacity of alkylated DNA. Increased dye uptake at 24 hours post-exposure strongly suggests that the DNA is still undergoing repair processes. Since at 48 hours the lack of dye uptake suggests non-vital DNA, it can be assumed that failure to therapeutically interdict in the cellular DNA repair activities will be accompanied by loss of cell viability and subsequent pathology. On a more positive note, however, the DNA activity present at 4 and 24 hours after HD suggests an expansion of the therapeutic window for intervention well past the time formerly believed possible. Further studies of this phenomenon are required to confirm the association with active DNA repair processes. Once such an association is confirmed, specific inhibitors or promoters of repair can be utilized to alter the cytotoxicity of HD.

CONCLUSIONS

The S phase of the cell cycle is particularly sensitive to the toxic action of HD, as demonstrated by increased cytotoxicity of cells exposed to HD in S phase and block of the cell cycle at the G1/S interface by high doses of HD. The use of propidium iodide, an intercalating dye, allows demonstration of DNA structural changes following exposure to HD. These structural changes may reflect DNA repair activities being active as late as 24 hours post HD. Therapeutic interventions which hold the HD damaged cells in G1 phase should minimize the extent of HD injury and should allow for enhancement of DNA repair activity.

REFERENCES

1. CAPPIZZI, R.L., SMITH, W.J., FIELD, R.J. AND PAPIRMEISTER, B. (1973). *Mutation Res* 21: 6.
2. ROZMIAREK, J., CAPPIZZI, R.L., PAPIRMEISTER, B., FURMAN, W.H. AND SMITH, W.J. (1973). *Mutation Res* 21: 13.
3. SMITH, W.J., SANDERS, K.M., GROSS, C.L. AND MEIER, H.L. (1988). *Cytometry Suppl* 2: 21.
4. VEDDERS, E.B. (1925). in The Medical Aspects of Chemical Warfare. Baltimore, MD, Williams and Wilkins Co. pp. 125-166.
5. PAPIRMEISTER, B., GROSS, C.L., MEIER, H.L., PETRALI, J.P., AND JOHNSON, J.B. (1985). *Fund. App. Toxicol.* 5: S134-S149.
6. TAYLOR, I.W. (1980). *J Histochem Cytochem* 28: 1021-1024.
7. SMITH, W.J., SANDERS, K.M., GALES, Y.A., AND GROSS, C.L. (1991). *J Toxicology: Cutaneous and Ocular Toxicology* 10: 33-42.
8. SMITH, W.J., COWAN, F.M., CLARK, O.E., MARTENS, M.E., AND GROSS, C.L. (1991). *Proc of the 1991 Medical Defense Bioscience Review*. pp 33-40. (DTIC # AD B158 588).
9. SMITH, W.J., GROSS, C.L., CHAN, P., AND MEIER, H.L. (1990). *Cell Biology and Toxicology*. 6: 285-291.
10. SMITH, W.J., SANDERS, K.M., GROSS, C.L. AND MEIER, H.L. (1988). *Proc of the NATO RSG-3, Panel VIII Meeting, Washington, DC*, : 87-97.
11. HOFFMAN, B.D., HANAUSKE-ABEL, H.M., FLINT, A., AND LALANDE, M. (1991). *Cytometry* 12: 26-32.

BLANK

720

ENZYMATIC CYANIDE DETOXIFICATION

Sidney A. Katz and Harry Salem

CRDEC, Toxicology Division, SMCCR-RST, Aberdeen Proving Ground, MD 21010-5423

ABSTRACT

Continuing research efforts at CRDEC are directed to the development of chromium-free sorbants for agent AC (HCN) to replace the current Whetlerite (ASC carbon) formulation. The possibility of using a commercially available nitrilase to detoxify HCN enzymatically was investigated. A potentiometric assay was developed, the pH and temperature optimums of the enzyme were determined, and the enzymatic detoxification of HCN was evaluated. The rate at which the commercially available enzyme detoxified HCN was too slow to protect military personnel from the toxic effects of agent AC. The enzyme may, however, be useful in the detoxification of HCN in wastewaters.

BACKGROUND

Over three years ago, the Center for Disease Control¹ issued a letter expressing concern about the inhalation of chromium-containing dust particles from gas mask canisters filled with Whetlerite, and recommending replacement of the Whetlerite in such canisters with a chromium-free sorbant. Military research centers and their civilian contractors are developing alternate impregnants. Five possible candidate impregnants for a chromium-free carbon have been identified², and the performance of a carbon impregnated with copper-zinc-TEDA formulation most nearly met all current specifications for ASC carbon³. The incorporation of an immobilized nitrilase into the gas mask canister for the enzymatic decomposition of cyanide may demonstrate sufficient activity toward agent AC to qualify as another alternative to the chromium impregnant.

Cyanidase is an enzyme derived from fermentation organisms. It is a nitrilase, EC3.5.5.1, that catalyzes the hydrolysis of hydrogen cyanide to ammonium formate:



Cyanidase is commercially available from NOVA NORDISK in Denmark⁴ as an immobilized product identified as SP 379.

OBJECTIVES

The purpose of this project is: (1) to determine the temperature and pH optimums for the degradation of hydrogen cyanide by SP 379, and (2) to determine the effectiveness with which SP 379 degrades hydrogen cyanide.

SAFETY CONSIDERATIONS

To minimize inhalation hazards, the use and storage of cyanide was restricted to a hood where the average open face velocity was 43 cfm, and the average velocity at the operating height was 84 cfm. Skin absorption and ingestion hazards were minimized by the use of gloves and automatic pipette devices. The amount of cyanide present in the working environment at any given time was limited to 100 mL of 1.0×10^{-1} molar potassium cyanide solution. The waste cyanide solutions were oxidized to cyanate solution with an excess of ammoniacal copper sulfate solution⁵ at the completion of each measurement:



POTENTIOMETRIC ENZYME ASSAY

Katz and his coworkers^{6,7,8,9,10} developed the direct potentiometric assay of enzyme

activity with ion selective electrodes over a quarter century ago. Landis and his colleagues have applied such measurements to the enzymatic degradation of some fluorophosphate choline esterase inhibitors similar to agents GB and GD^{11, 12, 13, 14, 15}. These measurements made with the fluoride ion selective electrode served as the basis for monitoring the DFPase-catalyzed hydrolysis of the fluorine to phosphorus bonds in the choline esterase inhibitors.

The cyanide ion sensitive electrode was applied to monitoring the cyanidase-catalyzed hydrolysis of agent AC.

The potential developed by an Orion model 94-06 cyanide ion selective electrode relative to an Orion model 90-02 double junction reference electrode was measured with an Orion digital "IONALYZER", model 701A. Daily calibrations were made by injecting 11 successive 0.10 mL aliquots of a 1.002×10^{-1} M standard reference solution of potassium cyanide into 100 mL of a 1.00×10^{-2} M sodium hydroxide solution or into 100 mL of a 1.00×10^{-2} M phosphate buffer solution and recording the potential developed by the cyanide ion sensitive electrode after 1.0 minutes of stirring at constant speed in a thermostated water bath. The electrode demonstrated a "Nernstian" response under most conditions. Day-to-day reproducibility was usually within 2 millivolts under a given set of pH and temperature conditions. A typical calibration curve is shown in figure 1.

The potential-concentration data were evaluated by linear regression. Correlation coefficients of at least "two nines" were obtained, and the intercepts and slopes were stored in a program for calculating the concentrations of cyanide ion remaining in the system from the potentials recorded during the cyanidase-catalyzed hydrolysis.

Cyanidase activity was evaluated from the rate of change in cyanide ion concentration remaining in the system per unit mass of SP 379 added to the system. This was accomplished by injecting 1.00 mL of 1.002×10^{-1} M potassium cyanide solution into 100 mL of phosphate buffer containing a known mass of SP 379. The system was mixed with a constant speed stirrer during the hydrolysis, and the system was maintained at constant temperature in a thermostated water bath while the investigation was in progress. Measurements with the cyanide ion selective electrode were used to determine the cyanide ion concentration remaining in the system. To minimize erosion of the electrode, these measurements were made periodically rather than continually. The activity of cyanidase was calculated as the number of micromols of hydrogen cyanide hydrolyzed per minute per gram of SP 379 thirty minutes after the injection of the standard potassium cyanide solution.

pH OPTIMUM

The pH optimum of SP 379 was evaluated from measurements of cyanidase activity in 1.00×10^{-2} M phosphate buffers with pH values of 4.95, 6.88, 7.20, 7.56, 8.02, 8.82, 9.50, and 11.33. One gram of SP 379 suspended in 100 mL of phosphate buffer was mixed with the constant speed stirrer in the water bath thermostated at 25°C for five minutes to establish thermal equilibrium. Exactly one mL of 1.002×10^{-1} M potassium cyanide solution was quickly injected into the system, and residual cyanide concentrations were determined every ten minutes for one hour by potentiometric measurements with the cyanide ion selective electrode. Maximum activity was observed in the systems buffered at pH 7.58. The effect of pH on cyanidase activity is summarized in figure 2.

TEMPERATURE OPTIMUM

The temperature optimum of SP 379 was evaluated by measuring cyanidase activity in 1.00×10^{-2} M, pH 7.58 phosphate buffer at temperatures of 20, 25, 30, 35, and 40°C. One gram of SP 379 was suspended in 100 mL of 1.00×10^{-2} M, pH 7.58 phosphate buffer, and stirred at constant speed in the thermostated water bath to establish thermal equilibrium. Exactly one mL of 1.002×10^{-1} M potassium cyanide solution was quickly injected into the system, and the

residual cyanide ion concentrations were determined every ten minutes for one hour by potentiometric measurements with the cyanide ion selective electrode. Maximum activity was observed in the systems thermostated at 35°C. The effect of temperature on cyanidase activity is summarized in figure 3.

DEGRADATION OF HYDROGEN CYANIDE

The degradation of hydrogen cyanide by SP 379 was evaluated by repetitive measurements on cyanide concentration during the course of the cyanidase-catalyzed hydrolysis at pH 7.58 and 35°C. A measured mass of SP 379 was suspended in 100 mL of 1.00×10^{-2} M pH 7.58 phosphate buffer and stirred at constant speed in a water bath thermostated at 35° for five minutes to establish thermal equilibrium. Exactly one mL of 1.002×10^{-1} M potassium cyanide solution was injected into the suspension, and the concentration of cyanide remaining in the system was determined at ten minute intervals for one hour from potentiometric measurements with the cyanide ion selective electrode. Results for the degradation of hydrogen cyanide by SP 379 at pH 7.58 and 35° C are summarized in table 1.

The tabulated results indicate a loss of hydrogen cyanide in the absence of cyanidase. This may be due to a non-enzymatic decomposition. Charlot¹⁶ has reported that such a decomposition takes place slowly in cold water and more rapidly in hot water. The loss of hydrogen cyanide from the solution to which no cyanidase was added could also be due to volatilization. Whatever the cause, this loss adds to the uncertainty in quantitatively evaluating the degradation of hydrogen cyanide by SP 379. Qualitatively, the rate of degradation appears to increase with the amount of SP 379 added to the system.

QUALITY ASSURANCE

Quality assurance consisted of the daily preparation of eleven-point calibration curves for pCN versus the potential of the cyanide ion selective electrode, and confirmation of the calibration at least twice during the working day. No alternate methods of measurement were applied to the quality assurance process. No SRM's or CRM's were available for confirming the results obtained from the potentiometric method. Whenever it was possible to do so, a given experiment was conducted in replicate to validate the results.

Calibration curves were quite reproducible. The extremes of the linear regressions for the calibration data at pH 7.58 and 35°C are presented in table 2 along with recovery data for the corresponding calibration checks.

table 2:

QUALITY ASSURANCE FOR THE POTENTIOMETRIC DETERMINATION OF CYANIDE

	maximum	minimum
<u>calibration curve</u>		
intercept	363.4 mv	358.6 mv
slope	63.4 mv/pCN	61.5 mv/pCN
<u>recovery</u>		
3.006×10^{-4} M	3.48×10^{-4} M	2.89×10^{-4} M
6.012×10^{-4} M	6.56×10^{-4} M	6.07×10^{-4} M

DISCUSSION

The data presented in table 1 reflect the effectiveness with which SP 379 catalyzed the degradation of hydrogen cyanide. The reaction appears to be much too slow to be of value in offering protection against the toxic effects of hydrogen cyanide. This material may, however, be useful for detoxifying cyanide wastes in the pH range of 7 to 8 and at temperatures between 25° and 40°C.

CONCLUSIONS

The SP 379 catalyzed degradation of hydrogen cyanide appears to be too slow to be of value in the protection of military personnel from the toxic effects of agent AC. SP 379 is not useable as an additional alternative to the chromium impregnant in ASC carbon.

REFERENCES

1. Bender, T.R., letter to respirator manufacturers dated 13 May 1988.
2. Groose, J.E., Doughty, D.T., and Wagner, N.J., "Development of a Chromium-Free Impregnated Carbon for Absorption of Toxic Agents - Phase I", CRDEC-CR-089, US AAMCC, APG, MD, October 1990.
3. Doughty, D.T., "Development of a Chromium-Free Impregnated Carbon for the Absorption of Toxic Agents - Phase II", CRDEC-CR-090, US AAMCC, APG, MD, October 1991.
4. Bioindustrial Group, NOVO Industri A/S, Novo Alle, 2880 Bagsvaerd, Denmark.
5. Welcher, F.J. and Hahn, R.B., Semimicro Qualitative Analysis, D. van Nostrand Co., Inc., Princeton, 1960, p. 256.
6. Katz, S.A. and Rechnitz, G.A., *Z. Anal. Chem.*, 1963, 196:248-251.
7. Katz, S.A., *Anal. Chem.*, 1964, 36:2500-2501.
8. Cowans, J.A. and Katz, S.A., *J. Chem. Educ.*, 1965, 42:553.
9. Katz, S.A. and Cowans, J.A., *Biochem. Biophys. Acta*, 1965, 107:605-608.
10. Hughes, R.D., Katz, S.A., and Stubbins, S.E., *Enzymologia*, 1969, 36:332-334.
11. Landis, W.G., Savage, R.E., and Hoskins, F.C.G., *J. Protozool.*, 1985, 32:517-519.
12. Landis, W.G., Haley, M.V., and Johnson, D.W., *J. Protozool.*, 1986 33:216-218.
13. Landis, W.G., Durst, H.D., Savage, R.E., Haley, D.M., Haley, M.V., and Johnson, D.W., *J. Appl. Toxicol.*, 1987, 7:35-41.
14. Landis, W.G., Anderson, R., Durst, H.D., James, J., Chester, N.A., Haley, M.V., Johnson, D.W., and Tauber, R.M., "The organofluorophosphate hydrolases of *Tetrahymena thermophila* and *Rangia cuneata*", Proceedings of the CRDEC Conference on Chemical Defense Research, M.D. Rousa, ed., CRDEC-SP-7007, APG, MD, 1987.
15. Landis, W.D., Anderson, R., Chester, N.A., Haley, M.V., and Johnson, D.W., "The organophosphate acid anhydrase system of the clam, *Rangia cuneata*", Proceedings of the CRDEC Conference on Chemical Defense Research, M.D. Rousa, ed., CRDEC-SP-88013, APG, MD, 1987.
16. Charlot, G., Qualitative Inorganic Analysis, Methuen and Co., London, 1954, p. 310.

Figure 1: Calibration Curve for Cyanide Ion Selective Electrode

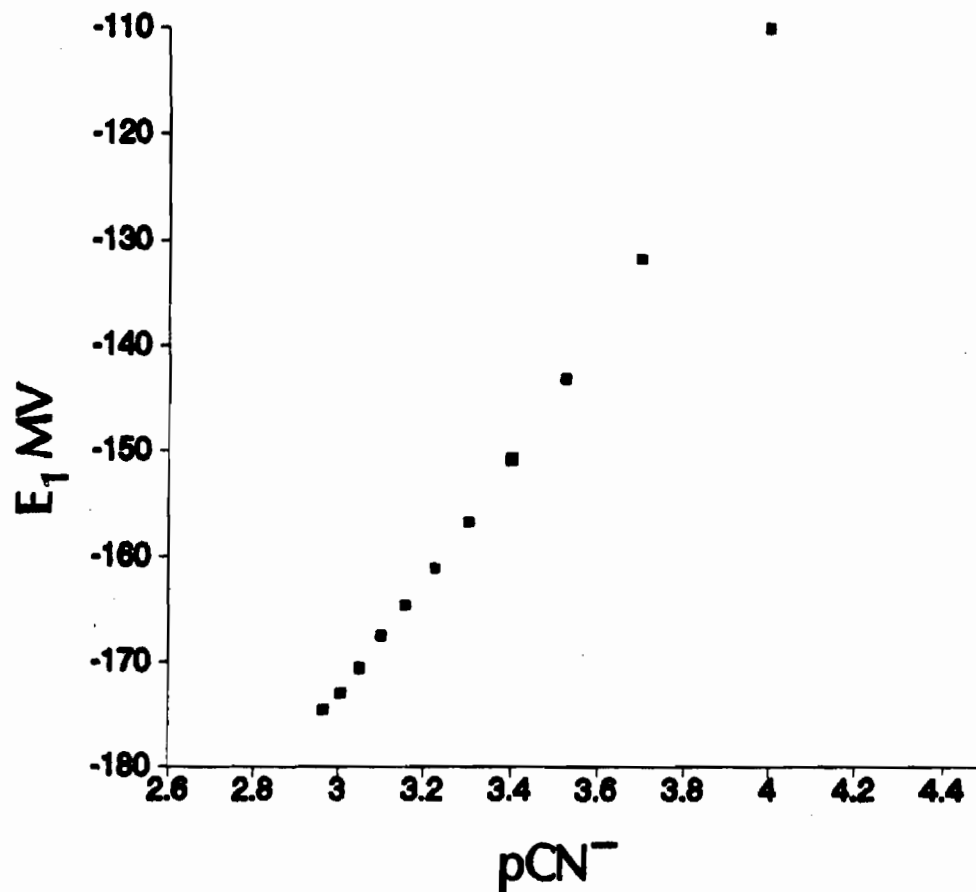


Figure 2: Cyanidase pH
Optimum

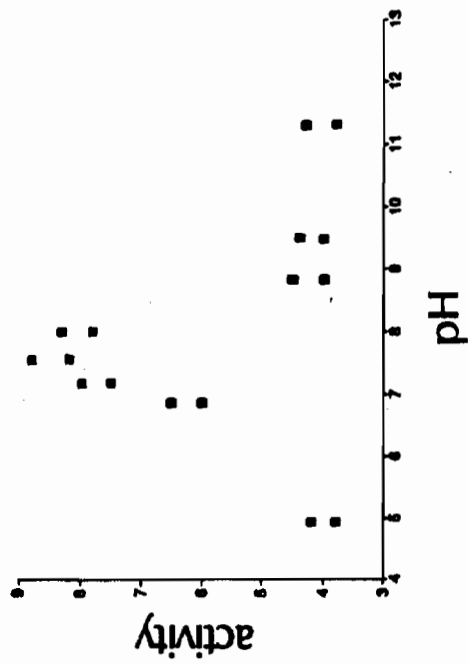


Figure 3: Cyanidase Temperature
Optimum

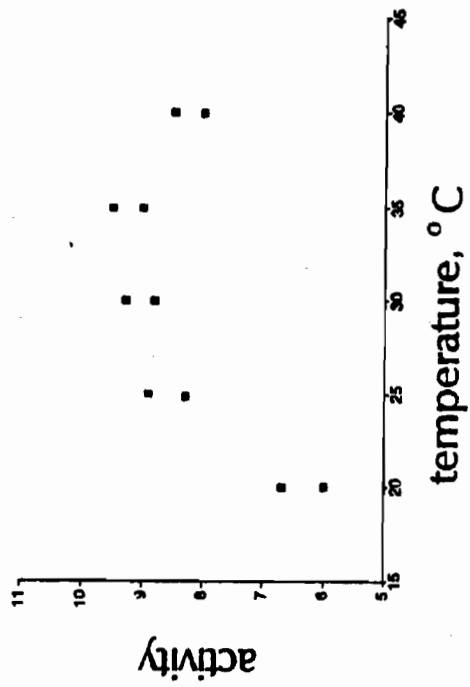


TABLE 1: DEGRADATION OF HYDROGEN CYANIDE BY SP 379

mass SP 379	percent hydrolyzed after t minutes					
	t=10	t=20	t=30	t=40	t=50	t=60
<u>none</u>						
B/04-1	0.0	17.5	33.0	44.8	--	--
B/05-1	6.2	33.9	38.9	40.6	47.7	54.8
B/07-1	3.6	24.4	35.6	46.3	56.2	62.1
B/11-1	9.1	26.8	36.3	45.2	53.2	60.8
B/12-1	11.4	22.0	36.0	45.1	54.0	60.3
<u>0.1 gram</u>						
0.1/04-1	5.5	31.0	49.7	65.8	76.1	83.8
0.1/12-1	4.5	27.9	44.5	58.6	69.0	77.1
<u>0.5 gram</u>						
0.5/05-1	14.0	42.4	66.0	81.9	91.2	95.3
0.5/11-1	33.2	60.2	78.1	88.9	94.4	97.4
<u>1.0 gram</u>						
1.0/05-1	53.8	79.9	91.4	95.9	97.5	98.3
1.0/07-1	38.5	73.3	90.8	96.7	98.2	98.8
1.0/07-2	57.7	87.5	96.1	98.0	98.7	99.0
1.0/11-1	48.9	80.0	92.1	96.6	98.1	98.8
<u>2.0 gram</u>						
2.0/11-1	57.0	87.7	96.1	98.1	98.8	99.2
2.0/12-1	71.0	90.3	96.2	98.1	98.8	99.1

ALL SYSTEMS INITIALLY CONTAINED 100 MICROMOL OF KCN IN 100 ML OF
 PH 7.58 1.00×10^{-2} MOLAR PHOSPHATE BUFFER AT 35° C

BLANK

XVI. BIOTECHNOLOGY POSTERS

BLANK

FIELD EMISSION SCANNING ELECTRON MICROSCOPY OF THE INTERACTION
OF CLOSTRIDIUM DIFFICILE WITH HUMAN EMBRYONIC INTESTINAL CELLS

Sheila Wood and Erica Petersen
U.S. Army Chemical Research, Development and Engineering Center
Aberdeen Proving Ground, MD 21010-5423

An in vitro assay system, consisting of monolayers of human embryonic intestinal cells (HEI) and Clostridium difficile (C. difficile), was used to observe interactions of microorganisms with the cell surface and cytoplasm. Tests were performed using Toxin B positive C. difficile Strain 938, and Toxin B negative Strain 789, harvested from casamino acids agar (CAS), and CAS containing subinhibitory concentrations of clindamycin (CAS-CL). Adherence to the surface and internalization into HEI cells was quantified at 30, 60, and 90 min. Cryopreserved and freeze-fractured preparations were made at 60 min and observed for adherence and internalization using field emission scanning electron microscopy. Quantitative microorganism determinations, confirmed by the observed microorganism activity, harvested from CAS and CAS-CL, revealed their capability to adhere to and/or enter HEI cells. The Toxin B producer, Strain 938, harvested from CAS-CL entered the cytoplasm and remained intact within it.

Introduction

Clostridium difficile (C. difficile), the etiologic agent of pseudomembranous colitis, unpredictably colonizes the bowel of certain hospitalized patients following the administration of antibiotics or during the course of a hospital stay.¹ Enterotoxins produced by this microorganism are capable of damaging the bowel mucosa;² but until now, it has not been determined whether [as with microorganisms such Escherichia coli (E. coli)] adhesive factors help this microorganism colonize and proliferate before toxin production.³⁻⁷

Previous studies using the hamster model clarified some assumptions about proper conditions for colonization. In the hamster, diet, colonization, and competition for colonization sites, were shown to affect the outcome of an experimentally induced infection. More specifically, administration of a high

percentage of protein in the diet (or total food deprivation for several days) hampered the animal's ability to resist establishment of C. difficile cecitis in the presence or absence of antibiotics.⁸ Also, when antibiotics were administered during the course of a high percentage protein diet, experimental lifespans were shortened compared to the administration of antibiotics or increased protein alone. Evidence suggests a synergistic action of diet with antibiotics.^{4,8}

Indirectly, a colonization mechanism has been elucidated in the following experiments. The presence of a nonpathogenic strain in C. difficile in the bowel, before challenge with a pathogenic strain, protected the bowel from colonization.^{1,2,9,10} This protection was shown not to be immunologic but resulted from exclusion of the pathogenic strain from mucosa.¹¹ Although increased survival time of cefoxitin-treated hamsters was observed when prior treatment with a noncytotoxic strain was employed, no protection was seen when cytotoxic and noncytotoxic strains were administered simultaneously. These observations show that attachment sites were blocked by nonpathogenic variants.⁸ Colonization appears to be site dependent and may be influenced by the selective production of cell wall components resulting from microbial consumption of available nutrients.^{5,12}

This in vitro study notes the effects of a high percentage of protein in the growth media and exposure to clindamycin on the behavior of C. difficile on human embryonic intestinal (HEI) cells. The role of selected nutrients and clindamycin in the predisposition of C. difficile to attach to cell surfaces, enter, and survive within HEI cells is shown. A combination of selected nutrients and the presence of clindamycin, in addition to the microenvironment, may be critical to the development of pseudomembranous colitis. As no valid explanation for relapse has yet been postulated, one explanation that must be considered is survival within nonphagocytic cells in response to selected microbial nutrients and clindamycin.

Materials and Methods

Organisms Used. Clostridium difficile strains, isolated from the patient population at the Medical College of Virginia Commonwealth University (Richmond, VA), include C. difficile Strain 938 from a symptomatic adult and C. difficile Strain 789 isolated from an asymptomatic child. Assays for the production of Toxin B⁷ showed that Strain 938 caused rounding of HEI cells in 24 hr, and Strain 789 did not cause rounding after 48 hr. Rounding was inhibited by C. difficile antitoxin obtained from Dr. Tracey Wilkins, Virginia Polytechnic Institute and State University (Blacksburg, VA).

Identification was based on the appearance of the colony, fluorescence under a 366-nm lamp, gram stain morphology, the absence of lipase or lecithinase, and gas-liquid chromatography profiles. The C. difficile isolates had minimum inhibitory concentrations of 1.0 ug/mL clindamycin when tested by agar dilution susceptibility.¹³

Organism Preparation for Adherence Assay. Microorganisms were grown on casamino acids agar (CAS) consisting of 1% casamino acid (DIFCO Labs, Detroit, MI), 2% agar (DIFCO), and 0.5% sheep blood (Flow Labs, McLean, VA). To expose the organisms to subinhibitory concentrations of clindamycin, 0.05 ug/mL clindamycin was added to the CAS media. Organisms were harvested at 48 hr in Eagle's minimal essential media (MEM) (Flow Labs) containing 1% fetal calf serum (FCS) (GIBCO, Grand Island, NY), pH 5.5, washed once, and resuspended in MEM 1% FCS.

Tissue Cells Used. Human embryonic intestinal cells #CCL6 were obtained from the American Type Culture Collection (Rockville, MD). They were maintained in HAM's F12 medium (GIBCO) containing 10% FCS (GIBCO) and penicillin/streptomycin (DIFCO), 50 units and 50 ug/mL, respectively. Three washes with media containing no antibiotics were performed prior to the assay.

Assay for Cytotoxigenicity. Procedures for the determination of cytotoxigenicity were followed as previously described.⁷ Briefly, the cytotoxin assay tested supernatant dilutions from each microorganism for rounding of HEI cells from 4 to 48 hr after inoculation. If rounding was observed, and this rounding was blocked using antitoxin to Toxin B, then the organisms were considered cytotoxigenic.

Adherence Assay. The adherence assay was performed using C. difficile grown on CAS as previously described. Earlier studies measured adherence of seven different isolates under five different conditions, in duplicate.⁷ Briefly, microorganisms were inoculated onto cell monolayers, incubated anaerobically on a rotating platform for 15 min at 37°C, washed, stained with Giemsa stain, and read. The percentage of cells (number of cells out of 100 with adherent microorganisms) with microorganisms adhering was calculated. Areas with low background adherence were chosen for these counts.

To determine whether adherence depended on microbe viability, viable and nonviable microorganisms were used initially. Viable C. difficile were taken from CAS plates, which had been incubated anaerobically for 48 hr. Nonviable microorganisms were taken from blood agar plates, which had been stored aerobically for 3 days. Subcultures from aerobic plates failed to produce growth when plated on sheep blood agar (SBA) and incubated anaerobically at 37°C for 48 hr.

Internalization Assay. Adherence assay procedures were followed with several exceptions: assays were carried out in 24-well Falcon plates (BDMS); confluent monolayers were inoculated with approximately 5×10^5 organisms; five wells per test condition were harvested; and incubation was in gas pak pouches (BDMS) generating an anaerobic environment. At 30, 60, and 90 min, monolayers were washed to remove loose microorganisms, and a 1% solution of Triton X100 was placed on the monolayer and incubated at room temperature for 5 min. After 5 min, the microorganisms were harvested, dilutions were made, and microorganisms were subcultured to SBA and incubated anaerobically for 48 hr at which time colony counts were established. To the same 24-well tissue culture plate, in different test wells, clindamycin at 10 ug/mL was added to kill any microorganisms attached to the monolayer surface. After incubation in an anaerobe pouch for 90 min, these test wells were washed to remove dead organisms, and a 1% solution of Triton X100 was added for 5 min. The microorganisms were harvested, diluted, and plated on SBA for subsequent colony counts. To determine the percentage of internalized microorganisms, a ratio of internalized organisms to total cell associated organisms $\times 100$ was obtained. Microorganisms 789 and 938, harvested from CAS and CAS containing subinhibitory concentrations of clindamycin (CAS-CL), were used.

Field Emission Scanning Electron Microscopy, Cryopreservation, and Freeze Fracture. The adherence assay was performed as previously described.⁷ Preparations were rinsed in buffer and fixed in 3% gluteraldehyde at room temperature after a 60-min incubation at 37°C. Cryopreservation (Strain 938, CAS) in liquid nitrogen was performed, and etching was used to achieve clarity of the image. Freeze fracture (Strain 938, CAS-CL) was performed by freezing the coverslip containing the cell/microorganism layer in liquid nitrogen, then manually fracturing the coverslip inside a cold chamber.

Results

Cytotoxigenicity Assay. The in vitro assay for the presence of Toxin B showed rounding of 100% HEI cells at 24 hr by Strain 938 which was blocked with C. difficile antitoxin. Strain 789, however, caused no rounding of HEI cells after 48 hr.

Adherence Assay. Adherence assays previously performed, in duplicate, on seven different isolates gave an average of 60% cells with microorganisms attached. The preparative adherence assay performed prior to this set of experiments showed 62 and 67% attachment for Strains 938 and 789, respectively. In preliminary experiments comparing attachment of viable microorganisms to attachment of nonviable microorganisms, only viable microorganisms attached, which indicated that an active process was at work in the attachment phenomena.

Internalization Assay. As seen in Figure 1, the ratio of internal to total cell associated organisms was highest with Strain 938 harvested from CAS-CL at 60 min. Data from the in vitro adherence assay was substantiated by reproducibility of the in vitro results (data not shown) and electron micrograph results.

Field Emission Scanning Electron Microscopy. In Figure 2, the cryopreserved freeze-fractured preparation of Strain 938 harvested from CAS-CL, shows intact microorganisms within HEI cells. Microorganisms are shown with arrows.

CONCLUSIONS

Adults develop C. difficile associated colitis following the administration of antibiotics; whereas, infants harbor C. difficile in the bowel but rarely show signs of disease. In addition, historical data has shown that intravenous and intramuscular administration of antibiotics are associated with the development of pseudomembranous colitis; but, a direct correlation of disease symptoms to dose does not exist.¹⁴ Pre-disposing environmental conditions in the bowel, which are indirectly related to antibiotic administrations, have been implicated in the development of pseudomembranous colitis. These conditions include disruptions in the protective layer of the bowel, selected antibiotic administration, changes in health or nutritional status of the host, food deprivation, and a designated diet or change in diet.¹⁰ Changes in the organism instead of in the environmental conditions in the bowel have not yet been considered. Organism changes in response to growth conditions cannot be discounted as contributive to the development of pseudomembranes.

Initial results, presented here, suggest a direct effect of available nutrients (amino acids) and clindamycin on the microorganisms. Entrance into, and survival within, HEI cells occurred with Toxin B producer, Strain 938, when harvested from media containing amino acids and clindamycin. When grown on CAS containing no clindamycin, levels of internalization and survival were not as great.

Adhesins have been implicated as an important initiating factor in colonization by enterotoxigenic E. coli.¹⁵ In the case of C. difficile, such an adhesin may play a role in disease production by serving as the initial anchor to the intestinal epithelium. Response of the microorganism to an environmental signal and/or regulatory control and its role in disease production remain to be determined.¹⁵⁻¹⁷

FIGURE 1

Internalization of C. difficile by Human Embryonic Intestinal Cells. Ratio of internalized microorganisms versus total cell associated microorganisms at 30, 60, and 90 min.

**Clostridium difficile Internalization Comparison
30, 60, 90 Minutes**

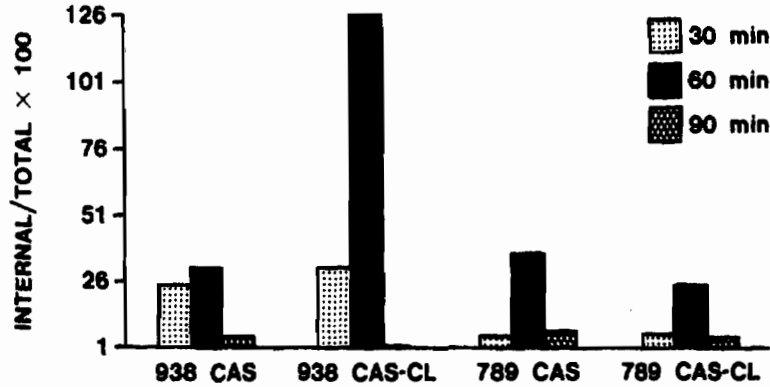


FIGURE 2

FESEM of a Freeze-Fractured Preparation of C. difficile, Harvested from CAS-CL. Organisms are numerous and appear unharmed.



ACKNOWLEDGMENTS

The authors acknowledge Dr. Bill Wergin and the members of the electron microscopy facility at the U.S. Department of Agriculture (Beltsville, MD) for the use of their facilities, and also Deryck J. Mills, Applications Engineer for Oxford Instruments (Oxford, England), for his instructive help in instrument use.

REFERENCES

1. Borriello, S.P., Larson, H.E., Honour, P., and Barclay, F.E., "Antibiotic Associated Diarrhea and Colitis," In Clinical Research Center Report, Medical Research Council, London, England, pp 96-98, 1982.
2. Borriello, S.P., "Clostridium difficile and Gut Disease," In Microbes and Infections of the Gut, Blackwell Scientific Publications, Oxford, England, pp 327-346, 1983.
3. Finley, B.B., Heffron, F., and Falkow, S., "Epithelial Cell Surfaces Induce Salmonella Proteins Required for Bacterial Adherence Invasion," Science Vol. 243, pp 940-941 (1989).
4. Freter, R., "Mechanisms of Association of Bacteria with Mucosal Surfaces," In Adhesion and Microorganism Pathogenicity, Pitman Medical Publishers, London, England, pp 36-55, 1981.
5. Hu, P.C., Cole, R.M., and Huang, Y.S., "Mycoplasma pneumoniae Infection: Role of a Surface Protein in the Attachment Organelle," Science Vol. 216, p 313 (1982).
6. Levine, M.M., "Adhesion of Enterotoxigenic Escherichia coli in Animals and Humans," In Adhesion and Microorganism Pathogenicity, Pitman Medical Publishers, London, England, pp 142-160, 1981.
7. Wood-Helie, S.J., Dalton, H.P., and Shadomy, S., "Hydrophobic and Adherence Properties of Clostridium difficile," Eur. J. Clin. Microbiol Vol. 5, pp 441-445 (1986).
8. Silva, J., Fekety, R., Werk, C., Ebrifgt, J., Cudmore, M., Batts, D., Syrjamaki, C., and Lukens, J., "Inciting and Etiological Agents of Colitis," Rev. Infect. Dis. Vol. 6, pp S214-S220 (1984).
9. Borriello, S.P., and Barclay, F.E., "Clostridium difficile Infection Protection by Prior Colonization with Nonpathogenic Strains," In Models of Anaerobic Infection, Martinus Nijhoff Publishers, Boston, MA, pp 239-240, 1984.

10. Lee, A., "Normal Flora of Animal Intestinal Surfaces," In Adsorption of Microorganisms to Surfaces, Wiley and Sons, New York, NY, pp 145-173, 1980.
11. Wilson, K.H., and Sheagren, J.N., "Antagonism of Toxigenic Clostridium difficile," J. Infect. Dis. Vol. 147, pp 733-736 (1983).
12. Woese, C.R., Maniloff, J., and Zablen, L.B., "Phylogenic Analysis of the Mycoplasmas," Proc Natl Acad Sci USA Vol. 77, p 494 (1980).
13. The National Committee for Clinical Laboratory Standards, Reference Agar Dilution Procedure for Antimicrobial Susceptibility Testing of Anaerobic Bacteria, Vol. 5, pp 25-29, National Institute of Health, Bethesda, MD, 1985.
14. Tedosco, F.J., Barton, R.W., and Alpers, D.H., "Clindamycin Associated Colitis: A Prospective Study," Ann Intern Med Vol. 81, pp 429-433 (1974).
15. Finley, B.B., Heffron, F., and Falkow, S., "Epithelial Cell Surfaces Induce Salmonella Proteins Required for Bacterial Adherence and Invasion," Science Vol. 243, pp 940-941 (1989).
16. Isberg, R.R., Voorhis, D.L., and Falkow, S., "Identification of Invasion: A Protein that Allows Enteric Bacteria to Penetrate Culture Mammalian Cells," Cell Vol. 50, pp 769-778 (1987).
17. Miller, J.F., Mekalanos, J.J., and Falkow, S., "Coordinate Regulation and Sensory Transduction in the Control of Bacterial Virulence," Science Vol. 243, pp 916-921 (1989).

DETECTION OF THRESHOLD NUMBERS OF *ESCHERICHIA COLI* AND
PSEUDOMONAS AERUGINOSA USING A HAND-HELD DETECTION DEVICE

Sheila J. Wood and Jared M. Veronick
U.S. Army Chemical Research, Development and Engineering Center
Aberdeen Proving Ground, MD 21010-5423

Minimum colony forming units per milliliter (CFU/mL) of *Escherichia coli* and *Pseudomonas aeruginosa* were determined by the bioluminescent generation of light which was monitored in a hand-held detection device, the Monolight 100. Light energy resulted from the interaction of luciferin and adenosine triphosphate (ATP) in the presence of luciferase and magnesium. *E. coli* and *Ps. aeruginosa* were detectable at 1×10^5 CFU/mL and 3.6×10^3 CFU/mL, respectively. The Monolight 100 was useful for detection but required tedious and meticulous techniques, difficult to execute in the field.

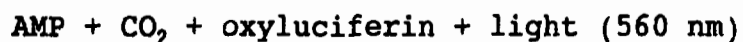
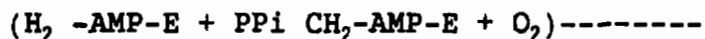
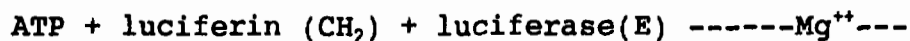
Introduction

Methods for detection of the presence of microbial flora from water are numerous and varied.¹ The ability to perform such detection in the field, without the aid of laboratory facilities, is highly dependent on the method and type of detection device. This investigation describes an approach to detection of microorganisms based on the presence of adenosine triphosphate (ATP). A well established interaction with ATP, based on light generation, using luciferin/luciferase was monitored. Reference values were obtained using the photon counting capability of Beckman LS 1801 scintillation counter.² Lower limits of detection were determined by comparison to an ATP standard in both the Beckman instrument and a field device, the Monolight 100. A critical analysis of the possible use of the Monolight 100 as a field device for detecting microorganisms in environmental samples was generated.

The ability to use a hand-held device for detection of threshold levels of microorganisms, depends on the ability of that device to give results similar to those obtained in a laboratory setting. The number of organisms detected per milliliter serves as the measurement parameter. The feasibility of use of the Monolight 100 for detection of bacteria is

assessed in this report. It should be noted that when testing samples obtained from the environment, one must consider interfering variables, such as temperature, pH, and ionic variations, age and storage of the reagents, and consistency of technique.³

Detection, based on the reaction illustrated below, results in the use of approximately one molecule of ATP by one molecule of luciferase to produce one photon of light.³



Materials and Methods

Reagents Used. Reagents for detection of ATP were obtained from Analytical Luminescence Laboratory, San Diego, CA. The reagents, marketed for use in bioluminescence systems, result in light emission from interaction with ATP. Hi-Intensity Firelight^R (luciferin-luciferase), Hepes buffer with Mg⁺⁺, and Extralight^R (a bacterial cell wall permeating reagent) were used. ATP, lyophilized in 10 ug quantities, was reconstituted in Hepes buffer, pH 7.75, resulting in a concentration of 1.97 x 10⁻⁵M. One hundred microliters of the preparation contained 1.97 x 10⁻⁹ moles of ATP.²

Dilutions of stock ATP were made in Hepes buffer. Plotted values of concentration vs. light emission formed the basis for comparison of unknowns. Threshold amounts of ATP in microorganisms were determined by correlation to the number of moles of ATP present.

Hi-Intensity Firelight was reconstituted with five mLs of Hepes buffer, pH 7.75, inverted to mix and stored at 4°C until use. To avoid loss of reagent integrity, each microorganism ATP determination was obtained shortly following generation of an ATP standard curve. Background determinations were made by measuring the light emitted from reagents used in the assay preparations. Background luminescence values were subtracted from each unknown value prior to plotting results.³

Accuracy and reproducibility of bioluminescent measurements depends on a consistent injection technique for luciferin-luciferase delivery. The peak height and integration of the readings suffer in accuracy if not injected with very similar delivery strokes (force). To ensure this type of delivery, the Monolight 100 is equipped with a syringe delivery feature. When performing injections by hand, practice is recommended to ensure reproducibility.⁴

Specifications of the Monolight 100. The Monolight 100 was designed for use in the field. It is portable and can operate on either conventional electrical circuitry or batteries. Some valid uses of the instrument include monitoring water samples for the presence of unacceptably high levels of microorganisms, and simply detecting the presence of ATP in a sample.⁴

Light detection is accomplished by a silicon diode within the instrument. The instrument has a spectral range of 300-900 nm and a sensitivity of 100 femtomoles ($1 \times 10^{-13}\text{M}$) of ATP, using specified reagents. Reagent is dispensed using a repeatable Hamilton dispenser, capable of dispensing 100 uL into 100 samples per hour. The signal of the Monolight 100 may be set to integrate at 10 second or 40 second intervals. The signal is displayed digitally or may be connected to a strip chart recorder (8 volt full range, analog output). The dynamic range is 4 decades, from 0.00 to 200 with autoranging. The source of power for the Monolight 100 is AC 117/220V (50/60Hz or 20W) or a 6 volt rechargeable battery that allows up to six hours of operation on a full charge. The size of the instrument is 10 x 18 x 18 cm and it weighs 1.1 kg.⁴

Operation of the Monolight 100. Carefully measured 4 mL amounts of prepared sample were pipetted into a test cuvette (12 x 75 mm) and placed in the counting chamber. The injection nozzle was locked into place at the opening of the test cuvette to prevent room light from interfering with the sample read. To begin analysis, the start button prompted the instrument to establish baseline at zero. The injection light then indicated the appropriate time to dispense reagent using the repeating dispenser. Reproducible injections were essential for accurate readings. A series of readings was digitally displayed every 2.5 seconds for a time period of 40 seconds per sample read.⁴

Preparation of Reagents. Hi-Intensity Firelight was reconstituted with 5 mL Hepes buffer, pH 7.75 on day 1 of the experimentation and stored at 4°C until use. The Extralight was prepared ahead for use and was stored at 4°C. ATP was reconstituted with Hepes buffer and prepared at concentrations of 0.10, 0.01, 0.001, 0.0001, and 0.00001 ug/mL. In preparation for the assay, 200 uL of each dilution was placed in 9.5 mL buffer with 200 uL Extralight and 200 uL of sample. To 4 mL of this preparation, 100 uL of luciferin/luciferase reagent was added immediately prior to reading.

Preparation of Organisms. The following stock concentrations of organisms were used: E. coli at 5.0×10^8 , 5.0×10^6 , 5.0×10^5 , 5.0×10^4 , and 5.0×10^3 CFU/mL. Pseudomonas aeruginosa at 1.8×10^9 , 1.8×10^7 , 1.8×10^6 , 1.8×10^5 , 1.8×10^4 , and 1.8×10^3 CFU/mL.

Performance of the Assay. Establishment of an ATP curve provided a basis for comparison of sample results. Background light emission was established by measuring the light emitted from reagent preparations without ATP. Prior to graphically representing the data, background values were subtracted from test values.

Upon establishment of background light emission, microorganism preparations were tested, background luminescence reads subtracted from microorganism reads, and results represented graphically. Positive signals were targeted as those producing higher amounts of luminescence than background reads. The number of moles of ATP in microorganism samples was estimated by correlation of light emitted to the concentration of ATP responsible for emitting approximately the same amount of light energy.

Results

Lower limits of detection using the Monolight 100 are displayed in Figures 2 and 3. The organisms chosen for evaluation, Escherichia coli and Pseudomonas aeruginosa, were detectable at 1.0×10^3 CFU/uL and 3.6×10^3 CFU/mL, respectively. This corresponds to a concentration of 0.2 to 2 ng/mL ATP, as shown in Figure 1a. Microorganisms at concentrations less than 1×10^3 produced signals approaching background. Therefore, interpretation of positive results became ambiguous at this level, as seen more clearly in Figure 1b.

Baseline reference values were established on a Beckman LS 1801 using the photon counting mode. ATP threshold concentrations between 0.02 and 0.2 ng/mL and microorganism sensitivity of 5×10^4 CFU/mL for E. coli, 3.6×10^3 CFU/mL for Pseudomonas aeruginosa gave definitive positive signals. The detection limits were slightly lower when using the Monolight 100.

CONCLUSIONS

The method described in this technical report uses an enzyme system for indirect detection of microorganisms by monitoring the presence of ATP. Although known as one of the more sensitive detection methods, bioluminescence determinations are fraught with a number of problems. The ensuing discussion will provide a critical evaluation of the usefulness of the Monolight 100 for detection of microorganisms in the field, on the basis of reagent stability, ease of use, lower limits of detection, and validity of signal.

Consideration #1: Materials needed for valid evaluations include ATP at several concentrations, buffer solutions, pipettes, 12 x 75 mm clean tubes, luciferin-luciferase reagents, a clean and loaded Hamilton repeating syringe for dispensing reagent.

Consideration #2: Experiments conducted in a controlled laboratory environment were not without problems. ATP standards, necessary for adequate completion of the experiments were stable for a maximum of one week following reconstitution. The luciferin-luciferase reagent was stable for several days at 4°C after reconstitution and was stable for one day at room temperature. In addition to being temperature sensitive, this reagent is also light sensitive. An ATP standard curve must be performed each day for accurate determination of the number of ATP molecules present. This procedure is lengthy and time consuming in itself. A necessity for quick response, precludes the usefulness of the instrument for instant response.

Consideration #3: The Monolight 100 was found to be extremely sensitive but unpredictable. The meticulous and tedious measuring and injecting methods required acute attention to detail. The use of this instrument in a laboratory environment was difficult and problematic. The Hamilton repeatable dispenser requires acute attention to the amount of reagent being dispensed and to the force of the injection. Even with proper external delivery, there is no method of ensuring that the reagent is properly injected and mixed within the sample. The Monolight 100 is capable of detecting significant levels of microorganisms with adequate sensitivity, but poor reproducibility. Reproducibility issues are a function of reagent stability and the inherently poor operating parameters of the instrument.⁵

Consideration #4: It has been shown that there is greater variability in reads when using glass tubes compared to plastic tubes. According to the study done by Lequin⁶, five glass tubes and five plastic tubes were exposed to various light sources for different time intervals and distances. The results showed that glass tubes have a C.V. of 12% and plastic tubes have a C.V. of 2%. Results using glass tubes are therefore more difficult to interpret. The manufacturer of the Monolight 100 (International Light, Inc.) not only refers to glass tubes in the instruction manual but also distributes glass tubes for use with the instrument.⁴

FIGURE 1a

Nanograms/mL ATP vs. light units as monitored by the Monolight 100. Concentrations of 0.002, 0.02, 0.2, and 2.0 ng/mL were measured. Readings over a 40 second interval minus background were graphed to establish an ATP concentration vs. light emission standard curve. This was used to estimate the amount of ATP in bacterial samples.

Light Emission: ATP Standard Curve

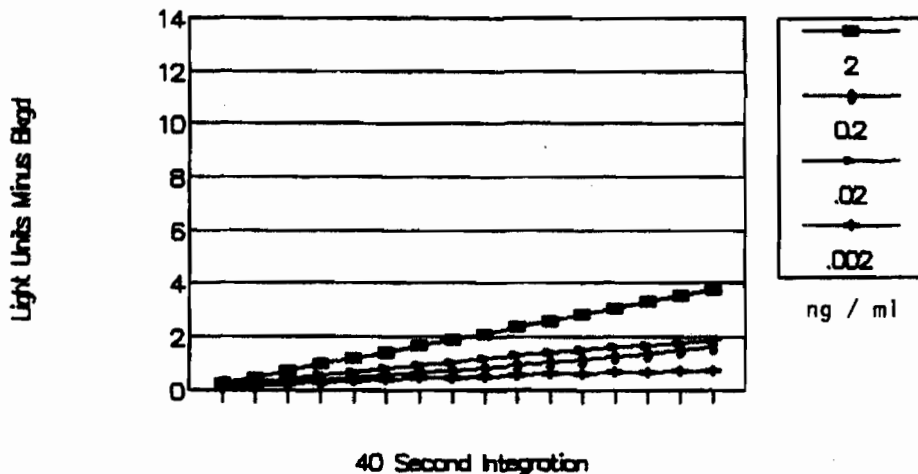


FIGURE 1b

Exploded view of the ATP curve to illustrate minor response differences in low concentrations.

Light Emission: ATP Standard Curve

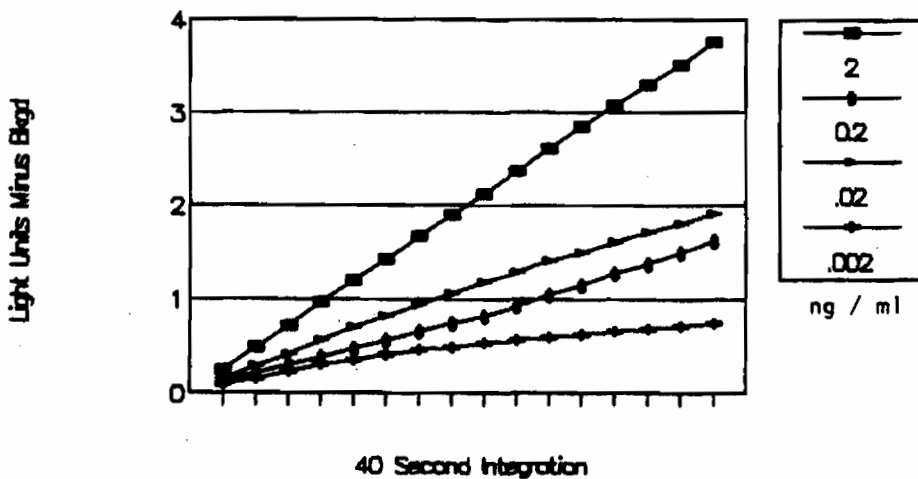


FIGURE 2

Colony forming units per mL of Escherichia coli represented by the amount of ATP present. The number of moles of ATP was based on the luciferin/luciferase and measured by the Monolight 100.

Light Emission of E.coli

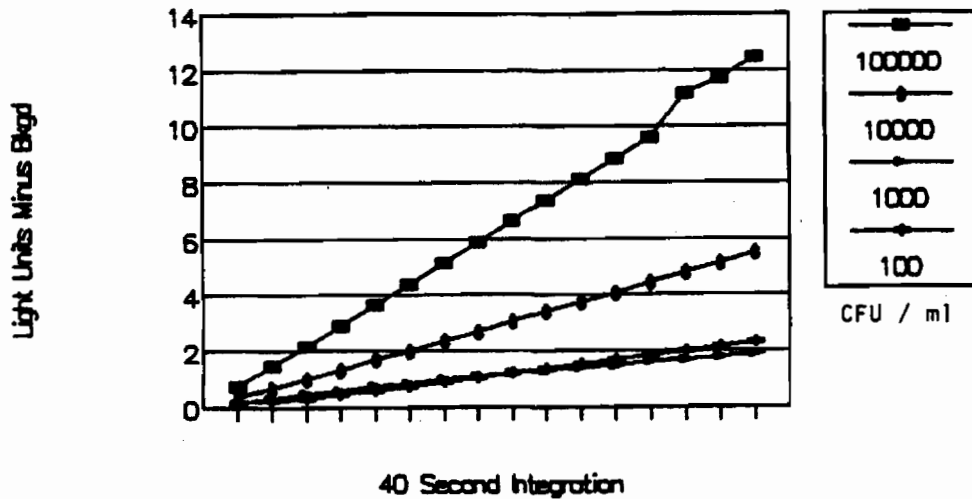
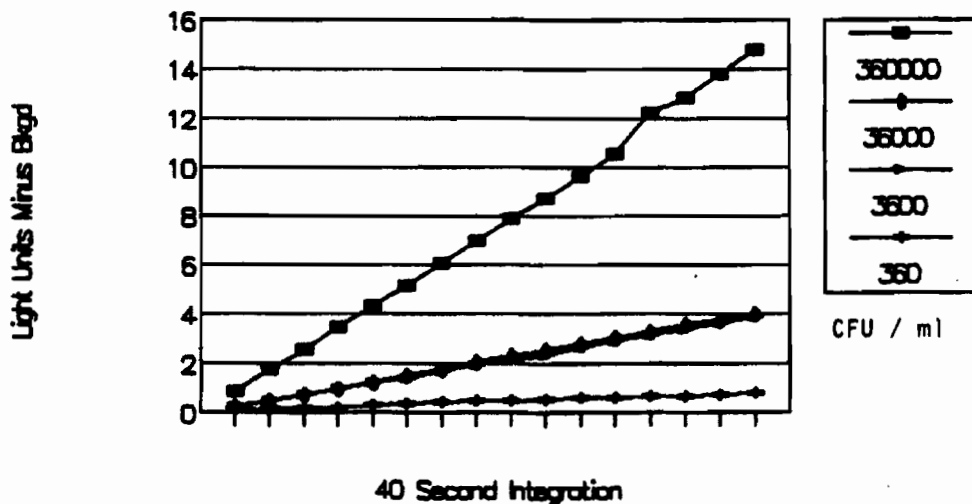


FIGURE 3

Colony forming units per mL (CFU/mL) of Pseudomonas aeruginosa represented by the amount of ATP present. The number of moles of ATP was based on the luciferin/luciferase reaction and measured by the Monolight 100.

Light Emission of P.aeruginosa



REFERENCES

1. Kricka, Larry, J., "Clinical and Biochemical Applications of Luciferases and Luciferins," Analytical Biochemistry, Vol. 175, pp 14-21, (1988).
2. Beckman Instrument Inc., Irvine, CA, 1985. Beckman Ls 1801, 3801, 5801, Series Liquid Scintillation Systems Operating Manual.
3. Analytical Luminescence Laboratory, San Diego, CA, 1990. Product Information Sheet, Catalog #1128, and #2800.
4. International Light Inc., Newburyport, MA. Instruction Manual, Monolight 100 Portable Luminescence Photometer.
5. Schram, E., and Janssens, J., "Effect of Dilution and Other Factors on the Behavior of Standard Firefly Luciferase Reagents," In Bioluminescence and Chemiluminescence, Ed. Turner, G.K., CRC Press, Boca Raton, FL, pp 539-542, 1985.
6. Lequin, Rudolf, M., "Luminescence of Glass and Plastic Tubes Exposed to Various Light Sources," In Bioluminescence and Chemiluminescence, Ed. Turner, G.K., CRC Press, Boca Raton, FL, pp 447-450, 1985.

DETERMINATION OF A UNIQUE EPITOPE BINDING SITE FOR A
COMPLEMENT-LYSIS-ENHANCING MONOCLONAL ANTIBODY, 3D12,
ON THE GALACTOSE ADHERENCE LECTIN OF ENTAMOEBA
HISTOLYTICA, USING BIACORE

Sheila J. Wood
U.S. Army Chemical Research, Development and Engineering Center
Aberdeen Proving Ground, MD 21010-5423

William Petri, Jr.
University of Virginia, Health Sciences Center
Charlottesville, VA

Mechanisms of pathogenicity used by Entamoeba histolytica to invade the bloodstream and cause liver abscess, include complement mediated lysis. Although pathogenic strains of E. histolytica become involved in immune functions by (1) activation of the alternate complement pathway, (2) binding of the C9 component of complement, and (3) depletion of active complement mediated hemolysis, the organism is not eliminated from the body by complement induced lysis. Monoclonal antibody (mAb) 3D12 was produced to target molecules responsible for lysis resistance. Binding of mAb 3D12 to the galactose-specific surface lectin, circumvented resistance to C5b-9 complement lysis. The epitope position on the adherence lectin for mAb 3D12 was mapped using BIAcore. Epitope specificity of mAb 3D12 is unique and separate from six previously characterized monoclonal antibodies and plays a role in enhancing complement mediated lysis of E. histolytica.

Introduction

BIAcore™ (Pharmacia Biosensor, Piscataway, N.J.) uses surface plasmon resonance to detect changes in a sensor surface as bio-molecular reactions occur. Changes in light reflection are a direct result of changes in mass occurring at the sensor surface. The reaction surface can be made biospecific by immobilizing the ligand of choice onto a derivatized dextran layer. Controlled sequential injections of reactants makes it possible to measure each binding event using no molecular labels.¹

A reaction surface is prepared in BIAcore by covalent coupling of a ligand to a derivatized matrix of dextran located on a sensor chip. This reaction surface, attached to a 50nm gold surface, is supported by glass. Monochromatic light, directed at the metal surface, is reflected by total internal reflectance. Concomitantly, evanescent wave energy from within the metal surface is generated and results in a portion of minimally reflected light. The change in the angle of minimally reflected light is a direct result of mass changes on the metal surface. This change is monitored electronically and recorded graphically as reactions occur. A response, expressed as resonance units (RU), of 1000 roughly corresponds to 1 ng per mm^2 attached monoclonal antibody. Other corresponding weights may vary with the protein used, depending on its complexity.²

E. histolytica causes parasitic infections worldwide and approximately 110,000 deaths per year. It is found in South and Central America, Africa, India, and the United States and surpassed only by malaria and schistosomiasis as parasitic causes of death.² A search of DOD technical report summaries revealed 82 citations for studies performed in at least 8 different countries.³ In addition, 25 unclassified U.S. government DA, DF, and DN projects were documented.⁴

E. histolytica carries a 170 kDa adherence lectin responsible for causing disease. The lectin inhibits C5b-9 complement activity on pathogenic strains. A recently generated monoclonal antibody, 3D12, partially decreased inhibition by the adhesin and increased amebic susceptibility to lysis in the presence of normal human serum. When purified human complement, C5b-9, was added, lysis increased threefold. This lysis was not reproduced when heat inactivated (complement-free) serum was used. MAb 3D12 served to neutralize circumvention of lysis by the amebic surface. It was shown using immunoprecipitation and Western blots that mAb 3D12 recognized the 170 kDa subunit of the adherence lectin.⁵

The objectives of this study were to more clearly define pathogenic mechanisms of E. histolytica by 1) structuring an affinity profile for the binding of 6 monoclonal antibodies to the adherence lectin, 2) substituting mAb 3D12 to estimate its point of attachment in reference to the other 6 monoclonal antibodies, and 3) target portions of the adherence lectin that are responsible for circumvention of complement mediated immune elimination in pathogenic strains.

Materials and Methods

Purified adherence lectin, purified monoclonal antibodies and mAb 3D12 in ascites fluid were obtained from Dr. William Petri, Jr., University of Virginia, Charlottesville, Va. Buffers used in the procedures included immobilization buffer, (10mM sodium acetate, pH 5.0), running buffer, HBS, (10mM Hepes,

150mM NaCl, 3.4mM EDTA, and 0.05% surfactant P20, pH 7.4), and HBS with no salt. Standard immobilization techniques for attachment of amino groups to a carboxyl rich surface were used. The reagents, n-hydroxysuccinimide, n-ethyl-n'-(dimethylamino-propyl) carbodiimide, and 1.0 M ethanolamine hydrochloride, pH 8.5, were supplied by Pharmacia Biosensor. In addition, rabbit anti-mouse Fc antibody was supplied by Pharmacia Biosensor.

Purified lectin was used at a concentration of 50 ug/mL in immobilization buffer for attachment to the dextran surface. Purified monoclonal antibodies were used at concentrations of 20 ug/mL and added in succession for three separate runs to ensure reproducibility of stacking response. In addition, the order of injection of the antibodies was varied to establish a relative sequence of lowest to highest quantity attachers.

Due to the reluctance of purified mAb 3D12 to attach to lectin, preparations of mAb 3D12 in ascites fluid were tested for their propensity to bind to antigen. For this set of experiments, the attachment base was varied. Rabbit anti-mouse Fc (RAM-Fc) antibody was immobilized to the dextran surface and used to capture 3D12 from the ascites fluid. Following a wash step and blocking of all unreacted sites of RAM-Fc by an unrelated antibody, antigen was introduced. This prepared the surface for performing a stacking response using all seven monoclonal antibodies and RAM-Fc as a base.

Results

A resonance response of 12571 RU was obtained from immobilization of antigen which served as a base for monoclonal antibody attachment. Figure 1 shows the relative stacking response of purified preparations of the monoclonals. MAb 3D12 did not attach in its purified form. The graph represents an average of 3 values for each monoclonal from three separate runs. When the order of injection of the monoclonals was varied, the same relative stacking response was obtained. (Data not shown)

Figure 2 shows a change in response when mAb 3D12 was included in the sequence. Using RAM-Fc as a base, mAb 3F4 was used to capture antigen and the remaining 6 monoclonals were successively added. The graph shows lower relative binding of mAbs 7F4 and 8A3, and higher relative binding of mAb 3D12. In Figure 3, the relative order of binding, highest to lowest responder, shows that mAb 3D12 partially displaces both mAbs 8A3 and 7F4.

FIGURE 1

Stacking response of purified monoclonal antibodies on the adherence lectin of Entamoeba histolytica.

**Monoclonal Stacking on Purified Antigen
Order - Highest Responder to Lowest**

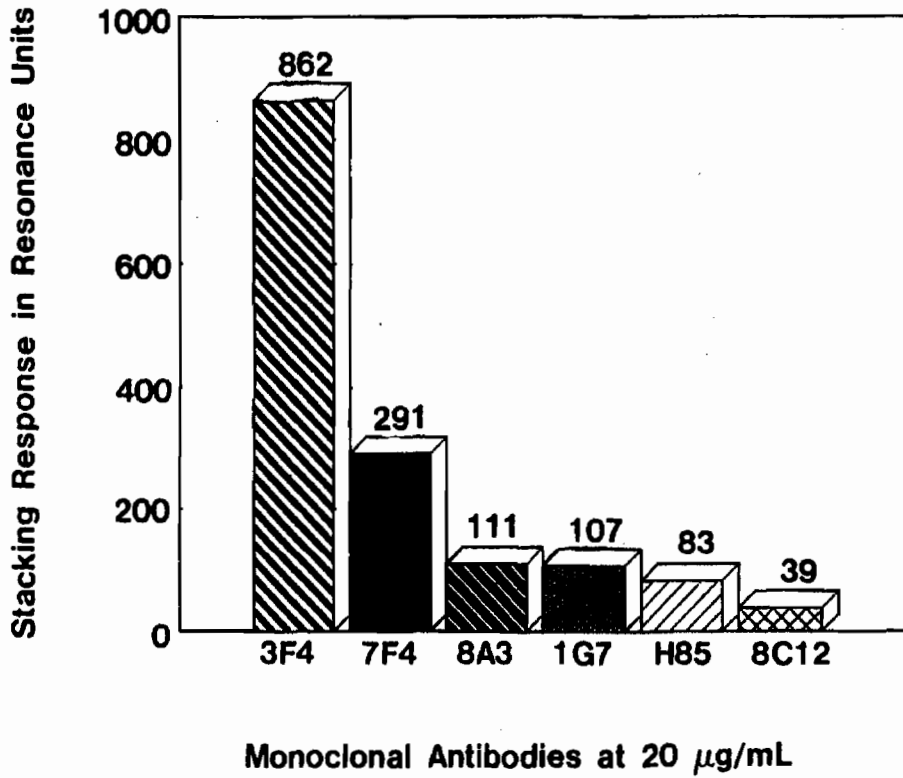


FIGURE 2

Change in relative stacking response with the addition of mAb 3D12.

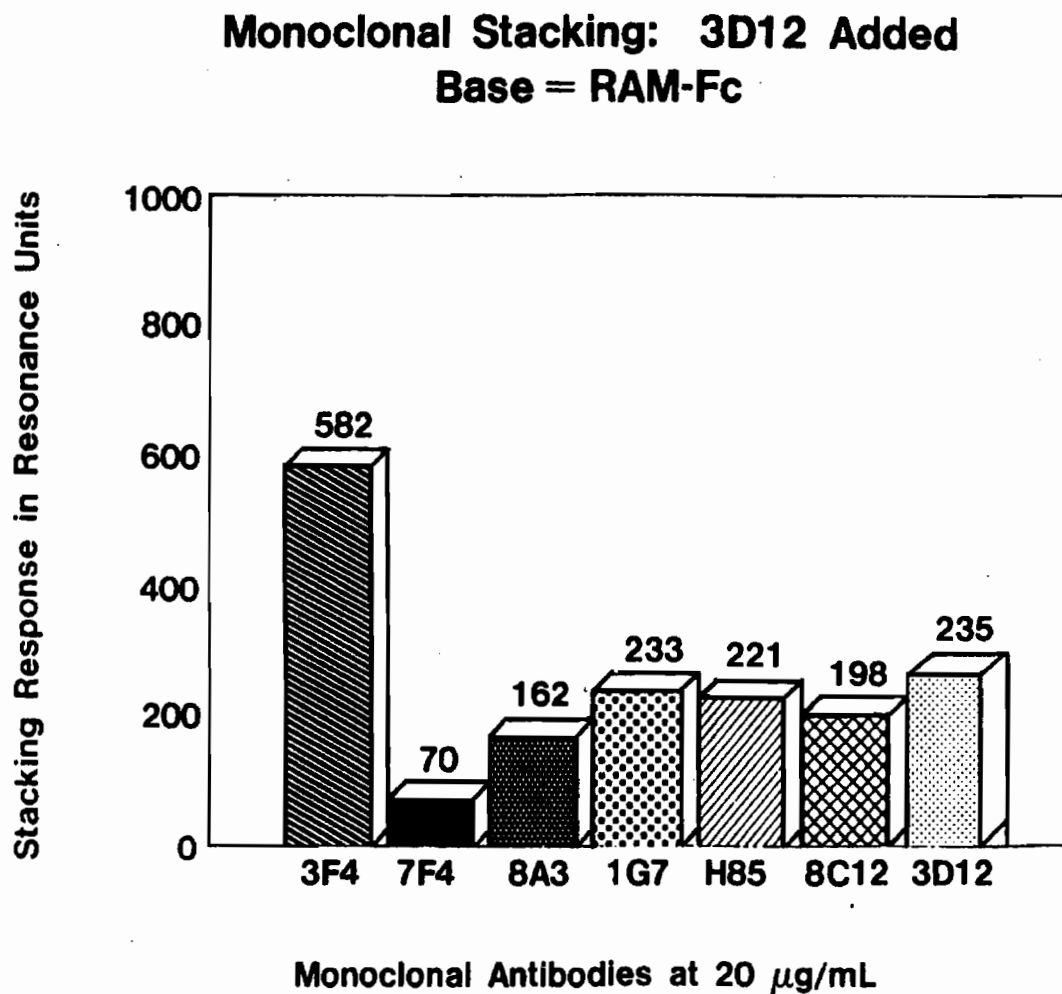
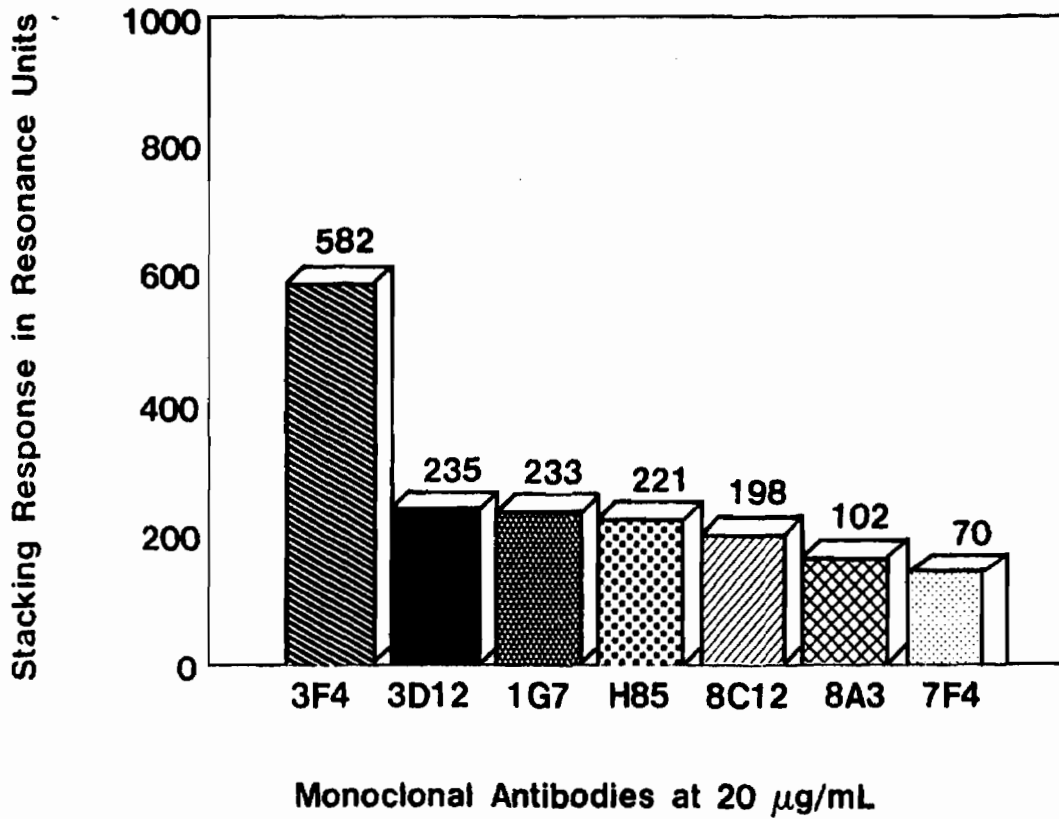


FIGURE 3

Displacement in the stacking order of mAbs 8A3 and 7F4 by mAb 3D12. The binding site appears to be between epitopes 2 and 3.

**Monoclonal Stacking: 3D12 Added
Order - Highest Responder to Lowest**



CONCLUSIONS

Results show partial circumvention of binding of mAbs 8A3 and 7F4 to lectin by mAb 3D12. This suggests a unique binding site for mAb 3D12 at position 2.5, that is, between epitopes 2 and 3. This data correlates well with data obtained by Dr. Petri on partial obviation of lectin-mediated lysis protection in the presence of mAb 3D12. If mAb 3D12 has partial homology to mAbs 8A3 and 7F4, then perhaps portions of epitopes 2 and 3, bind the C5b-9 complex, serving to protect pathogenic strains from lysis. Another possibility is a separate binding site for C5b-9 between epitopes 2 and 3, and, still another possibility, the ability of mAb 3D12 to change the binding configuration for C5b-9, which changes its activity and renders the amoebae more susceptible to lysis.

The naturally occurring sequence of epitopes on the adherence lectin is shown below.

epitopes	1	2	3	4	5	6
mAbs	3F4	8A3	7F4	8C12	IG7	H85
			3D12			

The projected attachment area of mAb 3D12, i.e., the area of the lectin responsible for circumvention of elimination by the immune system, is between epitopes 2 and 3.

REFERENCES

1. Pharmacia Biosensor AB. Application notes 102, 201, 202.
2. Petri, W.A. Jr. "Invasive Amebiasis and the Galactose-Specific Lectin of *Entamoeba histolytica*." ASM News Vol. 57, pp 299-306 (1991)
3. Technical Report Summaries, Defense Technical Information Center, Cameron Station, Alexandria, VA. Search Control No. FF011N. October 9, 1991.
4. Work Unit Summaries, Defense Technical Information Center, Cameron Station, Alexandria, VA. DTIC Report No. FF013J. October 9, 1991.
5. Braga, L.L., Eacker, S., Pahn, C., Wiedmer, T.W., McCoy, J.J., Sims, P., and Petri, W. Jr. "A Monoclonal Antibody to the Galactose Adhesin of *Entamoeba histolytica* Abrogates Amebic Resistance to Lysis by the Human Complement C5b-9 Membrane Attack Complex." Submitted to Science, October, 1991.

BLANK

754

THE USE OF PROTEASE INHIBITORS IN THE PURIFICATION OF SQUID ORGANOPHOSPHOROUS ANHYDRASE

Karla Kopec-Smyth and Devayani Eswaran
GEO-Centers, Inc. 100903 Indian Head Highway, Ft. Washington, MD 20744

Jeffrey R. Deschamps and Keith B. Ward
Naval Research Laboratory, Washington, DC 20375

The purification of organophosphorous acid (OPA) anhydrase (EC 3.8.2.1) from the hepatopancreas of *Loligo pealei* requires a laborious, multistep procedure to obtain an homogeneous enzyme population. Enzyme preparations which show a single, unambiguous N-terminal sequence also show multiple bands on isoelectric focusing gels. It is possible that the multiple forms of the enzyme observed by isoelectric focusing are proteolytic artifacts of the purification. Therefore, we assayed for the presence of proteases and tested nine protease inhibitors for their ability to inhibit proteolysis in fresh homogenates of hepatopancreas and optic ganglion tissues. On a small scale, chymostatin was the best inhibitor, and reduced the protease activity in hepatopancreas and optic ganglion preparations by 49% and 72%, respectively. A mixture of the four inhibitors chymostatin, bestatin, E-64, and leupeptin, inhibited the proteases in hepatopancreas homogenates by 72% as compared to homogenate with no inhibitors present. A mixture of chymostatin, bestatin and leupeptin inhibited the proteases in optic ganglion homogenates by 82%. Interestingly, PMSF, an inhibitor commonly used in OPA anhydrase purification, reduced only 2% of the protease activity in hepatopancreas homogenate and 35% of the protease activity in optic ganglion homogenate. In large scale purifications of the enzyme, these mixes of inhibitors were found to be only 30% effective in eliminating protease activity. DFP was tried and found to be an excellent inhibitor of proteases in hepatopancreas. None of the inhibitors had any effect on the activity of OPA anhydrase in the homogenates. Contrary to expectation, the use of multiple inhibitors or DFP did not result in the isolation of a more homogeneous enzyme preparation, but did allow for the isolation of another form of OPA anhydrase.

Hepatopancreas tissue obtained from the squid *Loligo pealei* is an excellent source of the enzyme organophosphorous acid (OPA) anhydrase (1). The hepatopancreas, however, is a digestive gland which secretes proteases as well as other enzymes used in digestion (2). Protease inhibitors must be used during the isolation of any protein from such a tissue in order to curtail the activity of the proteases so that the protein of interest can be isolated intact. Phenyl methyl sulfonyl fluoride (PMSF) is a common protease inhibitor which has been used in the purification of OPA anhydrases (3). However, squid hepatopancreas OPA anhydrase purified in the presence of PMSF shows multiple bands on isoelectric focusing gels and laborious purification is required to obtain small quantities of a single species of the enzyme. Since many experiments, such as crystallization and X-ray diffraction studies, require large amounts of highly purified

homogeneous enzyme populations, it is necessary to understand, and if possible eliminate, the source of the heterogeneity observed in preparations of OPA anhydrase. Therefore, we examined homogenates of hepatopancreas and optic ganglion tissues for protease activity and the effectiveness of a variety of inhibitors in eliminating the protease activity. Purifications done in the presence and absence of protease inhibitors are compared.

MATERIALS AND METHODS

Protease activity was assayed spectrophotometrically using resorufin-labeled casein (Boehringer Mannheim) as the substrate and homogenates of the squid tissue as the source of the proteases. Resorufin-labeled peptides produced from the casein by the action of proteases are soluble during precipitation with trichloroacetic acid whereas intact casein precipitates. The amount of resorufin-labeled peptides produced is followed at 574 nm and is equivalent to the proteolytic activity present in the sample. Frozen squid hepatopancreas or optic ganglion was thawed and lightly homogenized in 50 mM sodium phosphate, 50 mM NaCl, 0.05% azide, pH 7.2 and allowed to stand overnight at 4° C. The homogenate was centrifuged at 10000 x g for 60 minutes and the supernatant decanted. The clarified homogenate (0.2 ml) was incubated with 50 µl of a 0.4% resorufin-labeled casein solution in 50 µl of incubation buffer (0.2 M Tris, .02 M CaCl₂, pH 7.8), with enough squid homogenization buffer and inhibitors to make a total volume of 400 µl. Samples were incubated for 4 hours at 37° C and stopped by the addition of 5% trichloroacetic acid (480 µl). Samples were incubated for an additional 10 minutes at 37° C and centrifuged for 5 minutes in a microfuge (Eppendorf). 400 µl of supernatant was mixed with 600 µl of assay buffer (0.5M Tris, pH 8.8) and absorbance was measured at 574 nm. Inhibitors tested were antipain (0.05 mg/ml), 4-amidinophenyl-methanesulfonylfluoride (APMSF) (0.04 mg/ml), aprotinin (0.01 mg/ml), bestatin (0.04 mg/ml), chymostatin (.1 mg/ml), E-64 (0.5 mg/ml), leupeptin (0.5 µg/ml), pepstatin (0.7 µg/ml), phosphoramidon (0.3 mg/ml) (Boehringer Mannheim), and diisopropyl fluorophosphate (DFP) (Sigma).

All HPLC was performed using a Beckman System Gold controller equipped with model 114M pumps and a model 168 diode array detector. Size exclusion chromatography was accomplished on an FPLC system (Pharmacia).

Hepatopancreas and optic ganglion tissue was dissected from fresh *Loligo pealei* (obtained from a local seafood wholesale distributor) and stored at -20° C. Typically, a 100 gram sample of frozen squid hepatopancreas tissue was thawed and lightly homogenized in a Waring blender with an equal volume of 50 mM sodium phosphate, 50 mM NaCl (Sigma), pH 7.5, and protease inhibitors as indicated. After standing for 1 hour at 4° C, the crude preparation was centrifuged at 10,000 x g for 80 min. The supernatant was adjusted to 45% saturation with ammonium sulfate (Research Plus, absolute grade), stirred for 1 hour at 4° C, and then centrifuged at 40,000 x g for 60 minutes. The resulting supernatant was brought up to 80% ammonium sulfate saturation, stirred overnight in the cold, and centrifuged at 40,000 x g for 60 minutes. Calcium chloride was added to both ammonium sulfate solutions to a final concentration of 1 mM. The pellet was dissolved in 50 mM Tris, pH 7.5, 100 mM NaCl, and chromatographed on a Sephacryl S-200 superfine (Pharmacia) size exclusion column (2.5 x 60 cm) equilibrated in the same buffer at a flow rate of 0.5 mL/minute. The pooled fractions containing OPA anhydrase were concentrated in a stirred cell (Amicon) using a Diaflow YM10 ultrafiltration membrane (Amicon).

After the Tris buffer was exchanged for 50 mM sodium phosphate, pH 7.0, by repeated dilution and concentration in an ultrafiltration cell, the concentrated size pool was further purified on a Toyo Soda DEAE-5PW column (21.5 mm ID x 15 cm). Solvents used for DEAE HPLC

were distilled water (Buffer A) and 0.1 M sodium phosphate, 1.0 M sodium chloride, pH 6.8 (Buffer B). Elution conditions were isocratic at 0.5% B for 4 minutes, 0.5% B to 25% B in 64 minutes, and 25% B to 95% B in 40 minutes. Fractions containing OPA anhydrase were pooled and concentrated using a stirred cell and a Centricon-10 (Amicon) to a final volume of 300 μ L. The concentrate was diluted to 1.5 ml with 2.5 M ammonium sulfate in 0.1 M sodium phosphate, pH 5.85 (Buffer A). A Beckman CAA-HIC column was equilibrated in 98% Buffer A and 2% Buffer B (0.1 M sodium phosphate, pH 5.85). Hydrophobic interaction chromatography (HIC) was performed using a shallow gradient: 2% B (2 minutes), 2% to 30% B (32 minutes), hold at 30% B (1 minute), 30% to 40% B (10 minutes), hold at 40% B for 1 minute. The concentrated OPA anhydrase solution from the HIC step was diluted to 1.5 ml with 20 mM sodium acetate, pH 5.00. The sample was then applied to an Altex Spherogel - TSK SP-5PW cation exchange column (7.5 mm x 7.5 cm). The column was equilibrated in 2% B (0.1 M sodium acetate, 1.0 M NaCl, pH 5.00). Solvent A was distilled water. Initial conditions were held for eight minutes post injection. Separation was achieved with a gradient from 2% B to 50% B in 30 minutes, 50% B to 100% B in 10 min. Fractions were collected directly into tubes containing 0.05 ml of 1.0 M Tris, pH 7.5.

RESULTS AND DISCUSSION

A variety of inhibitors were evaluated for their ability to inhibit proteolytic activity in crude homogenates of squid hepatopancreas and optic ganglion tissues (figure 1). Chymostatin was the best inhibitor in both tissues, inhibiting 49% and 72% of protease activity in hepatopancreas and optic ganglion respectively. Chymostatin is an inhibitor of alpha-, beta-, gamma-, and delta-chymotrypsin. Bestatin, an aminopeptidase inhibitor, was capable of inhibiting 17% of protease activity in hepatopancreas and 36% in optic ganglion. E-64 (cysteine protease inhibitor) and leupeptin (serine and cysteine protease inhibitor) could inhibit protease activity by 21% in hepatopancreas and 34% in optic ganglion. Antipain, an inhibitor of trypsin and cathepsins, was 45% effective in optic ganglion. APMSF, a commonly used inhibitor, inhibited only 2% of the protease activity in hepatopancreas homogenates.

Mixtures of these inhibitors were tried to observe their combined effects on protease activity. A mixture of chymostatin, bestatin, E-64, and leupeptin (mix 1) worked the best in homogenates of hepatopancreas by inhibiting 72% of the protease activity (figure 2). A mixture of chymostatin, bestatin and leupeptin (mix 2) could inhibit 82% of proteases present in optic ganglion homogenate. None of the inhibitors tried could inhibit the activity of SHOPA anhydrase (data not shown).

Although inhibitor mix 1 could inhibit protease activity by 72% in a small sample of the crude homogenate, actual purifications done using large quantities of starting material showed different results. Purifications done in this manner showed only a 30% decrease in protease activity as compared to a purification done with no inhibitors added in the first three steps of the procedure (figure 3). These first three steps are critical, since the highest concentrations of proteases are found here (figure 4). Thus, we tried adding 10 mM DFP to a sample of each purification step and observed the protease activity in each sample. Although SHOPA anhydrase is quite capable of degrading DFP, the DFP was still able to inhibit protease activity by 68% in the homogenate, 97% in the 45% ammonium sulfate supernatant, and by 65% in the 75% ammonium sulfate pellet as compared to the purification done in the absence of protease inhibitors. SHOPA anhydrase is purified away from proteases during the HIC step in the purification.

A purification of SHOPA anhydrase was done in the presence of DFP in order to see if a more homogeneous population of purified SHOPA anhydrase could be attained. SHOPA

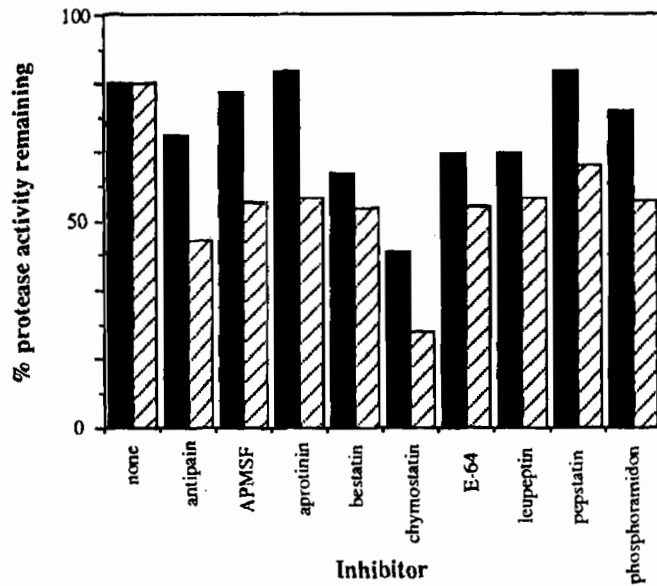


Figure 1. Effect of protease inhibitors on protease activity in hepatopancreas (■), and optic ganglion (▨) homogenates

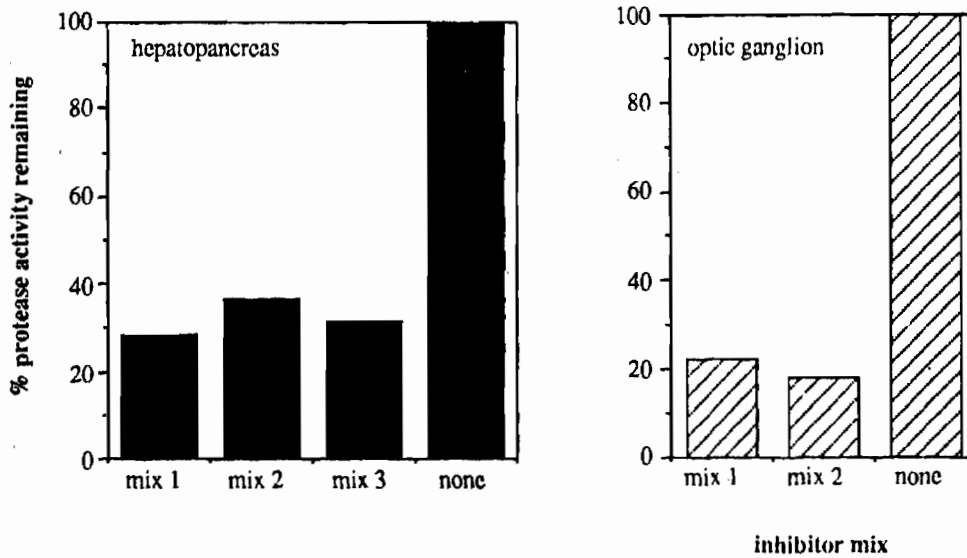


Figure 2. Effect of mixtures of inhibitors on proteases in hepatopancreas (■) and optic ganglion (▨) homogenates. For hepatopancreas, mix 1 is chymostatin, bestatin, E-64 and leupeptin; mix 2 is mix 1 plus phosphoramidon; and mix 3 is chymostatin, bestatin, E-64, leupeptin and APMSF. For optic ganglion, mix 1 is chymostatin, antipain, leupeptin, and bestatin; mix 2 is chymostatin, bestatin and leupeptin.

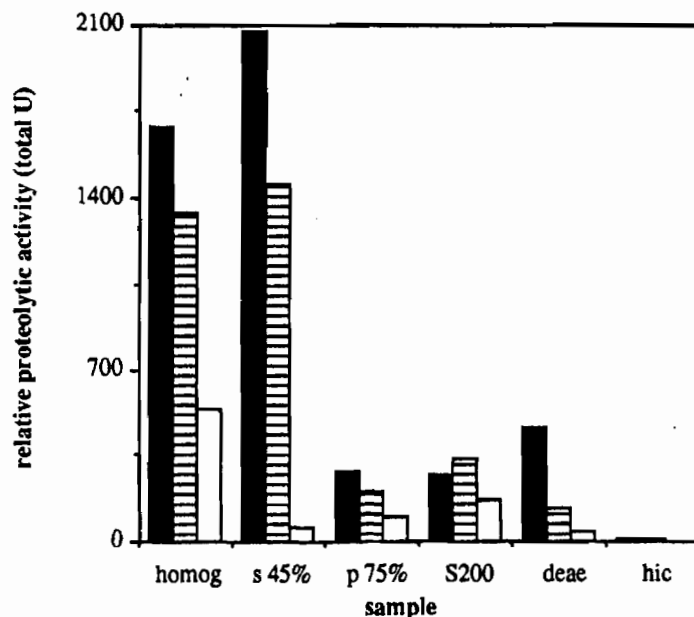


Figure 3. The effect of protease inhibitors on the total protease activity at various stages in the purification of SHOPA anhydrase. Homogenate is the crude homogenate of the hepatopancreas after centrifuging out cellular debris. s45% is the supernatant after a 45% ammonium sulfate precipitation. p75% is the pellet after a 75% ammonium sulfate precipitation. The S200 fraction is the pool of SHOPA anhydrase activity after size exclusion chromatography on Sephacryl S200 superfine. The deae fraction is the pooled SHOPA anhydrase activity after anion exchange HPLC on a Toyosoda DEAE 5PW column. The hic fraction is the pooled SHOPA anhydrase activity after hydrophobic interaction chromatography HPLC on a Beckman CAA-HIC column. The columns are no inhibitors added (■), inhibitor mix 1 added (▨), and inhibitor mix 1 plus 10 mM DFP (□) added to each step of the purification.

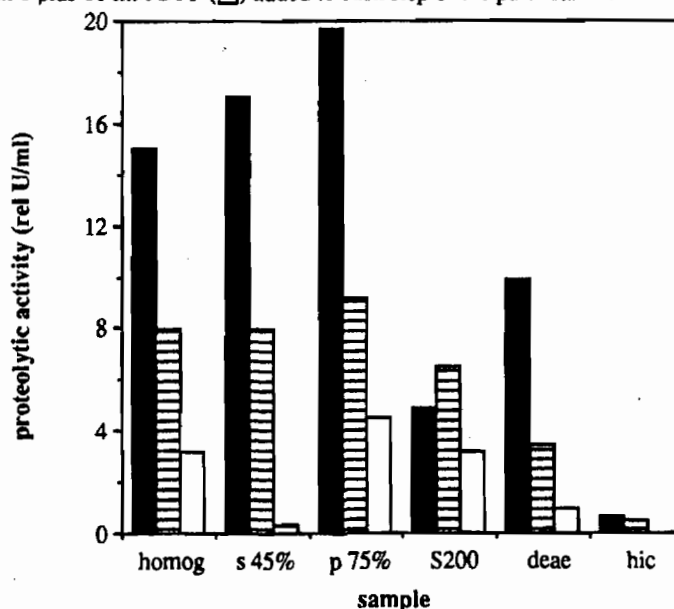


Figure 4. The concentration of proteases in hepatopancreas at various stages in the purification of SHOPA anhydrase and the effect of protease inhibitors. The columns are no inhibitor added (■), inhibitor mix 1 added (▨), inhibitor mix 1 plus 10 mM DFP (□) added to each step in the purification.

anhydrase purified through through the cation exchange step typically has a specific activity of 320 U/mg, shows five closely resolved bands on isoelectric focusing gels.(figure 5) and gives an unambiguous N-terminal sequence analysis (data not shown). Continuing the purification results in fewer bands on isoelectric focusing gels, but also shows a decrease in specific activity. Lane 1 in figure 5 shows SHOPA anhydrase (209 U/mg) which was purified one step further past the cation exchange column. Lane 2 in figure 5 shows cation exchange HPLC-purified SHOPA anhydrase (320 U/mg). The addition of DFP (lane 3, figure 5) or mix 1 of the protease inhibitors (lane 4, figure 5) during the purification of SHOPA anhydrase did not result in fewer bands observed in isoelectric focusing experiments. The same number of bands were observed in either case in spite of the fact that DFP was a more effective inhibitor. These data suggest that the heterogeneity observed on isoelectric focusing gels is not due to proteolysis but arise from some other source. Isoenzyme variants and alternative post translational processing are two possibilities for the heterogeneity observed for SHOPA anhydrase. The addition of the protease inhibitor DFP did allow for the isolation of another SHOPA anhydrase which was clearly resolved from the main activity by cation exchange HPLC (figure 6). This enzyme had a specific activity of 7.6 U/mg and a pI range of 5.03 - 5.21, whereas the main activity peak had a specific activity of 320 U/mg and a pI range of 4.79 - 5.14.

CONCLUSIONS

The best inhibitor for the proteases found in hepatopancreas tissue is the serine protease inhibitor DFP. SHOPA anhydrase purified in the presence of DFP showed heterogeneity similar to enzyme purified in the presence of less effective or no inhibitors, indicating that the variants of SHOPA anhydrase are not artifacts of proteolysis. The presence of DFP during purification of the SHOPA anhydrase did allow for the isolation of another enzyme form with similar pI but very low specific activity.

REFERENCES

1. Garden, J.M., Hause, S.K., Hoskin, F.C.G. and Roush, A.H. (1975) *Comp. Bioch. Physiol.* 52C, 95-98
2. Barnes, Robert D. "Invertebrate Zoology", W.B. Saunders Co. Philadelphia pg 421-423
3. Deschamps, J.R. and K.B. Ward. (1987) *Proceedings of the 1986 U.S. Army Chemical Research, Development and Engineering Center Scientific Conference on Chemical Defense Research (CRDEC-SP-87008)*, pp. 959- 964

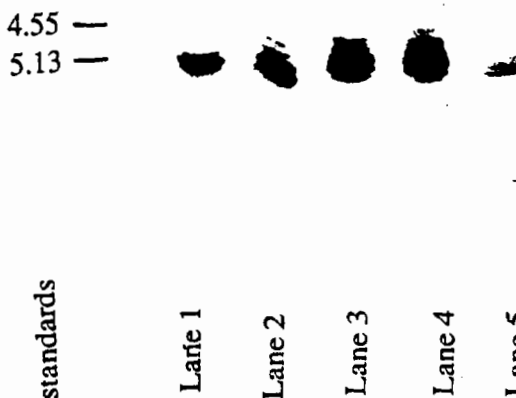


Figure 5. Isoelectric focusing gel of purified SHOPA anhydrase (0.7 $\mu\text{g}/\text{lane}$). Lane 1, SHOPA anhydrase (209 U/mg) which was purified one step further than lane 2; Lane 2, cation exchange HPLC-purified SHOPA anhydrase (320 U/mg); Lane 3, SHOPA anhydrase purified in the presence of DFP; Lane 4, SHOPA anhydrase purified in the presence of inhibitor mix 1; Lane 5, SHOPA anhydrase 2 (7.6 U/mg), isolated in the presence of DFP.

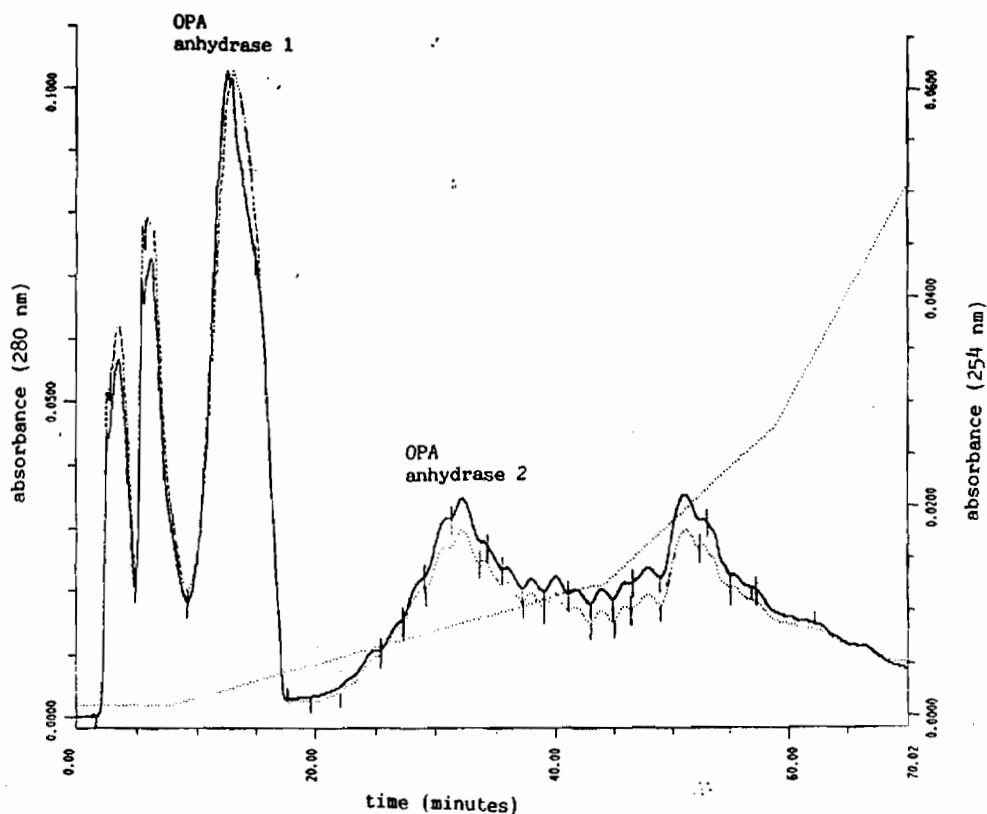


Figure 6. Purification of SHOPA anhydrase by cation exchange HPLC. Buffer A: distilled water, Buffer B: 0.1 M sodium acetate, 1.0 M sodium chloride, pH 5.00. Column was equilibrated at 2% B and held for 8 minutes post injection. Gradient ran from 2% B to 20% B in 35 minutes, 20% B to 45% B in 15 minutes and 45% B to 90% B in 15 minutes. Flow rate was 1 ml/minute.

BLANK

IMMUNOCHEMICAL AND NUCLEIC ACID SCREENING OF BACTERIA FOR ORGANOPHOSPHATE-DEGRADING ENZYMES

Tu-chen Cheng, Joseph J. DeFrank, Maryalice N. Miller,
Danielle K. Vervier and Heather S. Heitz
U. S. Army Chemical Research, Development and Engineering Center
Aberdeen Proving Ground, MD 21010-5423

ABSTRACT

It is of considerable importance to be able to identify new organophosphate-degrading enzymes from microorganisms which grow in extreme environments such as high salt (halophiles) or high temperature (thermophiles). Recently, a stable organophosphorus acid anhydrase (OPAA-2), with the highest catalytic activity yet reported against GF, GD and GB, was purified from a halophilic bacterial isolate *Alteromonas* sp. JD6.5. The gene for this agent-degrading enzyme has been cloned into *Escherichia coli*. In order to identify other sources of similar enzymes as well as elucidate their natural function, various other Alteromonads, halophiles and thermophiles were screened. Anti-OPAA-2 antibodies were reacted with cell lysates of these organisms and formed several different protein patterns in Western blot analysis. An oligonucleotide derived from the N-terminal amino acid sequence of OPAA-2 and from the cloned gene were also used as probes to identify cross-hybridizing DNA and RNA sequences from these same organisms. The similar antibody reactivity, nucleic acid hybridization patterns and enzymatic activity in these different organisms suggest that the proteins detected and the nucleic acid sequences identified are those of related enzymes.

INTRODUCTION

Organophosphorus acid (OPA) anhydases are a class of enzymes which hydrolyze P-X bonds of organophosphorus compounds. These enzymes are found in such diverse organisms as squid⁽¹⁾, protozoa⁽²⁾, clam⁽³⁾ mammals⁽⁴⁾ and soil bacteria⁽⁵⁾. OPA anhydases from these sources exhibit different substrate specificity, sensitivity to metal ions or inhibitors, molecular weight and cellular distribution. The native biological role of OPA anhydrase is not yet known. Diisopropyl fluorophosphate (DFP) is a common substrate used to screen for OPA anhydrase activity. The defluorination capability of these enzymes play a significant role in detoxification of G-type nerve agents and cholinesterase inhibitors.

As we reported previously⁽⁶⁾, an OPA anhydrase (OPAA-2) from halophile JD6.5, tentatively identified as a species of *Alteromonas*, has been purified to homogeneity with a molecular weight of 60,000. Halophile JD6.5 possesses at least two OPA anhydrase activities. The predominant enzyme, OPAA-2 which accounts for nearly 90% of total activity can be separated from OPAA-1 by DEAE-Sephacel chromatography. The first 10 N-terminal amino acids of OPAA-2 have been sequenced. Furthermore, polyclonal and monoclonal antibodies against this enzyme have been prepared. Using these antibodies and an oligonucleotide derived from partial N-terminal sequence of OPAA-2 as probes, a gene encoding an OPA anhydrase was cloned and identified on a 4 Kb KpnI DNA fragment⁽⁷⁾. In addition to DFP, OPAA-2 was shown to have high specific activity against GD (Soman), GB (Sarin) and GF (cyclohexyl methylphosphonofluoridate), and a chromo-genic analog of DFP, NPEPP (p-nitrophenyl-ethyl)-phenylphosphate).

Recently, we found that the crude extracts of other halophilic and thermophilic JD series and a number of *Alteromonas* species obtained from the ATCC (American Type Culture Collection, Rockville, Md.) have a wide range of enzyme activities against DFP, GD, GA and GF. The strains of JD series have not yet been identified. All these strains were shown to have various degrees of activity on different chromogenic substrates for phosphodiesterase, acid or alkaline phosphatase⁽⁸⁾. In the present study, we used OPAA-2 antibodies and an oligonucleotide derived from its N-terminal amino acid sequence as probes to see whether common sequences could be found from these various bacterial sources with similar functional enzymes. These probes should be useful for the identification, purification and cloning of new enzymes with similar function.

EXPERIMENTAL PROCEDURES

Organism and Cultivation:

The halophilic and thermophilic JD species bacteria were isolated by Dr. DeFrank and the *Alteromonas* species were provided by the Department of Microbiology, University of Maryland (originally from ATCC). All halophile JD species (6.5, 26.1, 28.3, 30.3), and *A. espejiana*, *A. haloplanktis*, *A. macleodii*, *A. nigrifaciens* and *A. undina* were grown on HM medium (50 g NaCl, 10 g MgSO₄, 10 g proteose peptone, 6 g yeast extract, 5 g casamino acids, 2.5 g HEPES per liter, pH 6.5). *A. citrea*, *A. luteoviolaceae* and *A. rubra* were grown on Instant Ocean Medium (38 g Instant Ocean, 5 g proteose peptone, and 1 g yeast extract per liter, pH 7.0). *A. colwelliana* and *A. putrefaciens* were grown on 278 medium (24 g NaCl, 10 g proteose peptone, 0.7 g KCl, 7 g MgSO₄, 5.3 g MgCl₂, 3 g yeast extract per liter, pH 7.2). Thermophiles JD100, JD200 and JD300 were grown on TH medium (2 g NaCl, 7 g yeast extract, 5 g tryptone, 5 g neopeptone and 10 ml Wolin salts solution per liter, pH 6.8). Except for the thermophiles which were grown at 65 °C, all strains were grown at 30 °C in an incubator shaker. Cells were harvested by centrifugation (7,500×g) for 10 minutes.

Enzyme Assay:

OPA anhydrase activity against DFP or GF was routinely assayed by monitoring fluoride release with an ion-specific electrode⁽⁶⁾. The reaction mixture contained 500 mM NaCl, 50 mM Bis-Tris Propane, pH 7.2, 3 mM DFP or GF (in isopropanol), 1 mM MnCl₂ and 5-50 µl of enzyme solution in a total volume of 2.5ml. Assays were routinely run at 25°C in a thermostatically controlled vessel with stirring. One unit of OPA anhydrase activity catalyzes the release of 1.0

μ mole of F^- per minute at 25°C. Specificity activity is expressed as units per milligram of protein.

Enzyme activity against GD or GA (10 mM each) were monitored by ^{31}P NMR at 161.9 MHz. The assays were conducted in the same reaction mixture as for DFP except in the absence of manganese due to the paramagnetic nature of this metal. The NMR analysis was conducted in 1 ml volume containing 0.25 mg/ml crude enzyme protein at 18°C. All results are corrected for spontaneous hydrolysis activity determined under identical conditions.

Crude Cell Extract Preparation and Protein Determination:

Harvested cells were resuspended in 10 BM buffer (10 mM Bis-Tris Propane, 0.1 mM $MnCl_2$, pH 7.2 at a ratio of 3 ml of buffer for each gram of cells. The cells were disrupted by passage through a French pressure cell (SLM Aminco) at 16,000 psi. Cellular debris was removed by centrifugation (46,000xg) for 30 minutes at 4°C. In all cases, the OPA anhydrase activity was found in the supernatant. The Commassie Protein Assay Reagent (Pierce) was used for determination of total protein concentration with bovine serum albumin (BSA) as the standard.

Preparation of Polyclonal and Monoclonal Antibodies:

Preparation of polyclonal and monoclonal antibodies against OPAA-2 from JD6.5 were obtained as previously described⁽⁷⁾. Biotinylated rabbit anti-rat IgG conjugated to horseradish peroxidase (rat Extravidin staining kit, Sigma) was used to identify antibodies specific for OPA anhydrases in a standard enzyme-linked immunoassay⁽⁷⁾.

Western Blot Analysis of OPA Anhydrases:

For each sample tested, 150 μ g of protein from the crude cell extract was mixed with an equal volume of 2x loading buffer [0.125 M Tris, pH 6.8, 4% sodium dodecyl sulfate (SDS), 100 mM dithiothreitol (DTT) 10% glycerol and 0.025% bromophenolblue], incubated for 3 minutes at 100 C and layered on a 7.5% SDS-polyacrylamide gel according to Laemmli⁽⁹⁾. The gel was run at 80 mA until the tracking dye was 1-2 cm from bottom of the gel. Prestained marker proteins (GIBCO BRL) were included on each gel. After SDS-polyacrylamide gel electrophoresis (SDS-PAGE), the proteins were electrophoretically transferred to a nitrocellulose filter (MicronSep) using the polyblot transfer system (American Bionetics). The nitrocellulose blot was preincubated with TBS (50 mM Tris-HCl, pH 7.5, 0.5 N NaCl) containing 2% BSA for 2 hours. The 1:1000 (v/v) polyclonal antiserum or 1:5 (v/v) monoclonal antibody (MAB#6) was added and incubated for an additional 2 hours. The cross-reacting proteins were then detected with biotinylated rabbit antibody to rat IgG and avidine-peroxidase (Sigma; rat Extravidin staining kit). After final wash with TBS (50 mM Tris-HCl, pH 7.5, 0.5 M NaCl), the bound peroxidase was detected by incubating with 30 mg 4-chloro-1-naphthol (dissolved in 10 ml methanol) in 50 ml TBS containing 0.03% hydrogen peroxide. When the color has developed to the desired intensity, the reaction was stopped by rinsing the filter in deionized water for several minutes, changing the water at least twice.

Dot Blot Analysis of Total RNA from Various Bacterial Strains:

High molecular weight genomic DNA from various bacterial strains were prepared by the method of Davis et al⁽¹⁰⁾. Total RNA from these same source was extracted by the method of Puissant and Houdebine⁽¹¹⁾. DNA or RNA from each bacterial strain was applied to nitro-

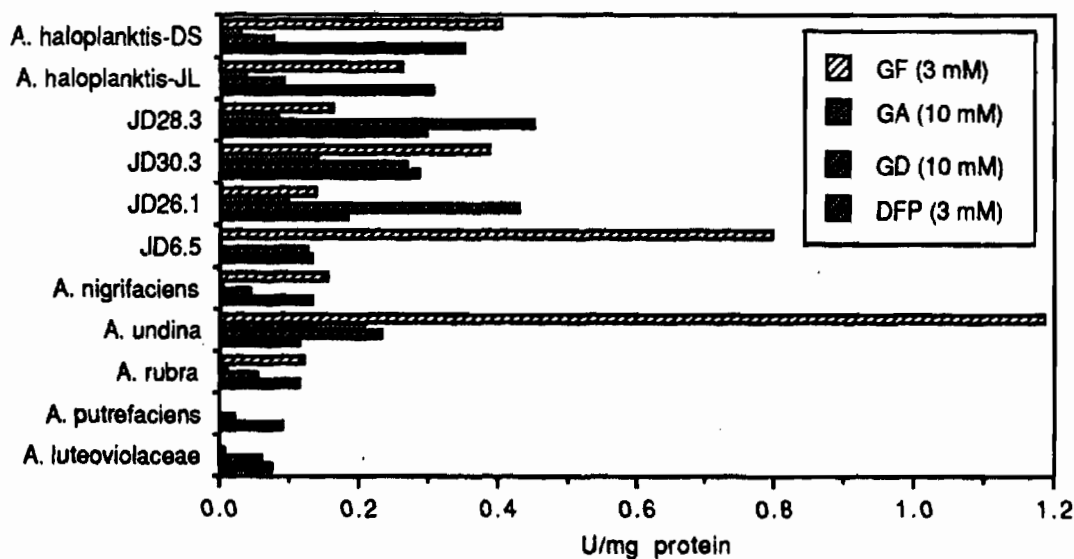
cellulose membrane by the method of Thomas⁽¹²⁾. DNA or RNA sequences corresponding to the N-terminal of the OPAA-2 enzyme were detected by hybridization with a photobiotinylated 20 mer probe. The presence of probe sequence was detected by hybridization of the blot with the a photobio-tinylated 20-base oligomer derived from partial N-terminal sequence of OPAA-2. The preparation of this phototinyated oligonucleotide probe followed the procedure as described by Denman and Miller⁽¹³⁾.

RESULTS

OPA Anhydrase activity of Various Bacterial Strains:

The crude extracts of the bacterial strains listed here have a broad range of substrate specificity. Most significantly, they were found to have varying degrees of enzyme activity against GD, GA and GF. In Figure 1, the order of organisms was based on the DFP hydrolysis activity in the absence of Mn^{2+} . The two highest enzyme activities against GD were found in crude enzyme extracts from *A. undina* and JD26.1. Extracts from *A. undina* and JD28.1 also had high enzyme activity against GA. The purified enzyme (OPAA-2) obtained from JD6.5 was previously shown to possess good activity against GB⁽⁷⁾. In addition, the crude enzyme extracts from JD6.5, JD26.1, *A. undina* and *A. haloplanktis* were shown to contain high enzyme activity against GF. For comparison, all the assays shown in Figure 1 were conducted in the absence of Mn^{2+} due to the high background of NMR analysis with this metal ion. Since most of these enzymes require Mn^{2+} , it can be expected that the hydrolysis of these G-agents will be considerably higher. The results indicate that these bacterial strains are potential enzyme sources for G-agent decontamination.

Figure 1. Substrate Specificity of Various Bacterial Strains



*DFP and GF: activity determined by fluoride electrode at pH 7.2

**GD and GA: activity determined by ³¹P NMR at pH 7.2

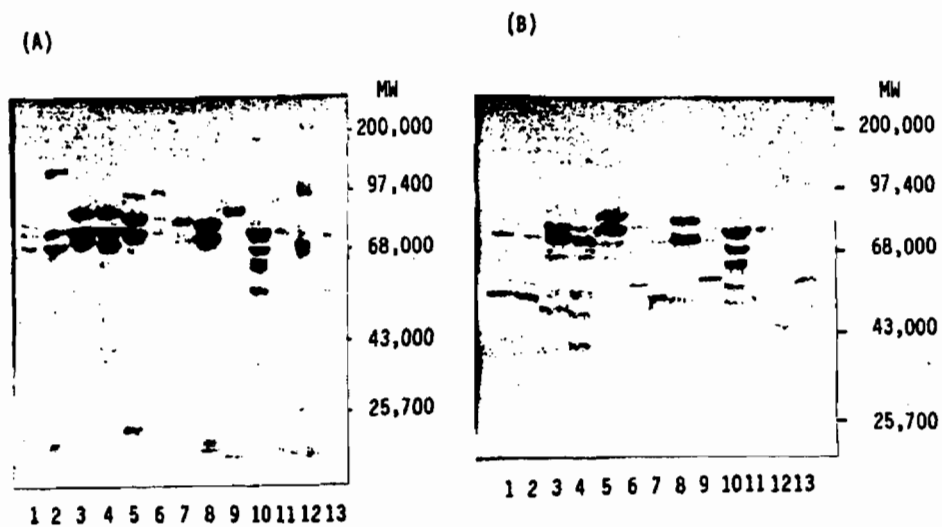


Figure 2. Western blot analysis of various JD-series halophiles and *Alteromonas* species. The lysate samples (150 µg each) were subjected to SDS-PAGE and blotted onto nitrocellulose membrane and probed with A) monoclonal antibody or B) anti-serum. Lane 1, *A. haloplanktis*-DS; Lane 2, *A. haloplanktis*-JL; Lane 3, JD28.3; Lane 4, JD30.3; Lane 5, JD26.1; Lane 6, JD6.5; Lane 7, *A. nigrilaciens*; Lane 8, *A. undina*; Lane 9, *A. rubra*; Lane 10, *A. putrefaciens*; Lane 11, *A. luteoviolaceae*; Lane 12, pre-stained protein molecular weight markers; Lane 13, JD6.5 (250 µg).

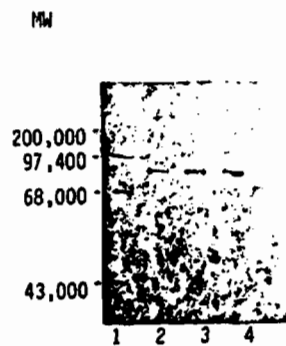


Figure 3. Western blot analysis of various JD-series thermophiles. The lysate samples (150 µg each) were subjected to SDS-PAGE and blotted onto nitrocellulose membrane and probed with monoclonal antibody. Lane 1, pre-stained protein molecular weight markers; Lane 2, JD100; Lane 3, JD200; Lane 4, JD300.

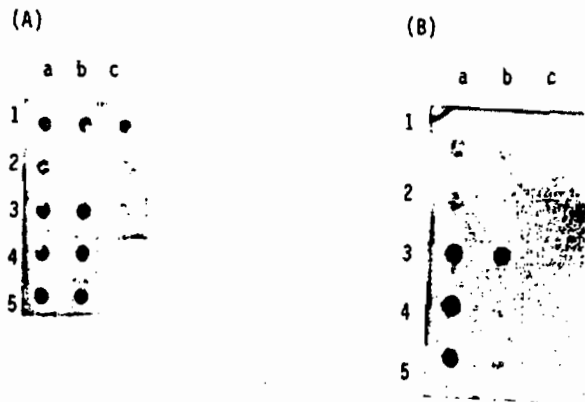


Figure 4. DNA and RNA dot blot screening of complementary nucleotide sequence of OPA anhydrases in various bacterial strains using a photobiotinylated oligonucleotide probe. Solutions containing 5 μ g of DNA or RNA from each sample were applied to a nitrocellulose membrane. The DNA (A) or RNA (B) membrane was then washed and probed with photobiotinylated oligonucleotide, followed by streptavidine-alkaline phosphatase and chromogenic substrate, as described in the *Experimental Procedures*. Column a: Lane 1. *A. haloplanktis*-DS; Lane 2. *A. haloplanktis*-JL; Lane 2. JD28.3; Lane 4. JD30.3; Lane 5. JD26.5. Column b: Lane 1. JD6.5; Lane 2. *A. nigrifaciens*; Lane 3. *A. undina*; Lane 5. *A. rubra*; Lane 6. *A. putrelaciens*. Column c: Lane 1. *A. luteoviolaceae*; Lane 2. *E. coli* BB4.

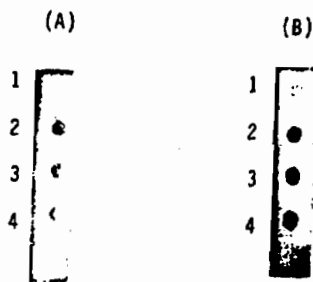


Figure 5. DNA or RNA dot blot analysis of nucleotide sequence of OPA anhydrases in various thermophiles. The experimental procedures were identical to that described in Figure 3. A) DNA blot; B) RNA blot. Lane 1, *E. coli* BB4; Lane 2, JD100; Lane 3, JD200; and Lane 4, JD300.

The three thermophile strains (JD100, JD200, and JD300) were also found to have high enzyme activity against GD. Interestingly, JD100 was the only strain that was shown to have no DFP-hydrolyzing activity.

Cross-reactivity of JD6.5 OPAA-2 Antibodies with Various Bacterial Lysates:

In order to determine whether monoclonal and polyclonal antibodies raised against OPAA-2 can cross-react with crude extract from the above bacterial strains, equal amounts of enzyme extract from each sample were subjected to Western analysis after SDS-PAGE. As seen in Figure 2, these antibodies showed considerable cross-reactivity with all the extracts. Several additional bands were seen when probed with polyclonal serum (Fig. 2b). The patterns revealed that the number, molecular weight and intensity of proteins from all these strains were varied. No protein bands were observed in *E. coli* HB101 and yeast DBY747 which are known to have trace or no enzyme activity against DFP. Interestingly, an identical single band was detected by monoclonal antibody in extracts from thermophiles JD100, JD200 and JD300 (Fig. 3). The molecular weight of this protein band was estimated at approximately 85,000 which is comparable to that observed from Sephacel S-200 chromatograms with their partially purified enzymes. The results suggest that OPA anhydrases from all these strains (halophile or thermophile JD series and *Alteromonas* species) may share common structural domains. Since these strains also contain various amounts of phosphodiesterases, acid or alkaline phosphatases⁽⁸⁾, the possibility of antibody cross-reacting with these functionally related enzymes or other unrelated cellular proteins can not be excluded.

Screening of Specific Nucleotide Sequences of Genomic DNA and Total RNA:

To further demonstrate the cross-reactivity of OPA anhydrases from these various bacterial strains, a photobiotinylated 20-base oligonucleotide, complementary to the 4-10 N-terminal amino acid sequence of OPAA-2, was used as a probe to investigate its specific binding to high molecular weight DNA and total RNA isolated from various organisms in this study. In this experiment, DNA and total RNA from each sample was spotted onto a nitrocellulose membrane and then hybridized with the biotinylated probe. Binding of probe sequence to the dot blots was then detected by using a streptavidin-alkaline phosphatase conjugate, nitroblue tetrazolium (NBT) and 5-bromo-4-chloro-3-indoylphosphate (BCIP)⁽¹³⁾. The results of screening DNA and total RNA from various cultures are shown in Figure 4. Positive color reactions indicating the presence of the probe sequence were found in DNA from most of bacterial strains, although intensity varied (Fig. 4a). The signal is absent in the control *E. coli* cells. In the RNA dot blot (Fig. 4b), a strong signal was observed on total RNA from all the JD series, *A. undina* and the two *A. haloplanktis* strains. The probe also produced similar signal intensity in the three thermophiles, JD100, JD200 and JD300 in both DNA and RNA blots (Fig. 5). However, the probe did not hybridize to total RNA isolated from control *E. coli* cells. Strikingly, the intensity of the binding response in RNA dot blot was proportional to the GD-hydrolyzing activity of JD6.5, JD26.1, JD28.3, JD30.3, *A. undina*. and *A. haloplanktis* strains (see Figure 1).

DISCUSSION

In this report, antibodies and an oligonucleotide derived from the N-terminal amino acid sequence of OPAA-2 were used as tools to screen for new OPA anhydrases from other bacterial sources. Using these antibodies in Western analyses, the results showed that the number, molecular weight and intensity of proteins from different bacterial strains were varied. The results suggest that microorganisms with high levels of OPA anhydrase activity can be

recognized of by their unique binding properties. However, such findings do not exclude the possibility of cross-reactivity with other functionally related cellular enzymes such as phosphodiesterases, acid or alkaline phosphatases or totally unrelated proteins (8). In conjunction with this study, DNA and RNA dot blot analyses were used to screen for a OPA anhydrase gene and its transcript in each sample with an oligonucleotide probe complementary to the partial 5'-terminal sequence of JD6.5 OPAA-2. Cross-reaction found in such screening clearly demonstrated that the OPA anhydrases from various strains may share a similar 5' end sequence.

Even though the chemical and physical properties of the bacterial OPA anhydrases are varied, the similarity of enzyme activity against various G-agents, protein patterns of antibody reactivity, and cross-hybridization of OPAA-2 5'-terminal sequence suggest that their sequences may be highly homologous. This similarity is found in a wide range of bacterial strains, including halophiles and thermophiles. On the basis of this data, it is postulated that these enzymes may originate from a common ancestral gene. The availability of antibodies and an oligonucleotide probe described here should facilitate the identification, purification, cloning and sequencing of new OPA anhydrase genes from these sources. Most important, these enzymes are potentially useful for non-corrosive decontamination of G-type agents and protection against cholinesterase inhibitors. A comparison of the sequences and activities of these enzyme should also provide considerable insight into their structure-function relationship.

REFERENCES

1. Attaway, H., Nelson, J. O., Baya, A. M., Voll, M. J., White, W. E., Grimes, D. J., and Colwell, R. R. *Appl. Environ. Microbiol.* **53**:1685-1689 (1987)
2. Landis, W. G., Durst, H. D., Savage, R. E., Jr., Haley, D. M., Haley, M. V., and Johnson, D. W. *J. Appl. Toxicol.* **7**:35-41 (1987)
3. Anderson, R. S., Durst, H. D., and Landis, W. G. *Comp. Biochem. Physiol.* **91C**:575-578 (1988)
4. Losch, V. H., Losch K., Haselmeyer, K. H., Chemnitius, J. M., and Zech, R. *Arzneim-Forsch* **32 (II)**:1523-1529 (1982)
5. Hoskin, F. C. G., and Rousch, A. H. *Science* **215**:1255-1257 (1982)
6. DeFrank, J. D., and Cheng, T-c. *J. Bacteriol.* **173**:1938-1943 (1991)
7. Cheng, T-c., and DeFrank, J. D. In: *Proc. of the 1990 Scientific Conference on Chemical Defense Research*, Research Directorate; U.S. Army Armament, Munitions and Chemical Command, Aberdeen Proving Ground, Md. (1991)
8. Cheng, T-c., Miller, M.N., and DeFrank, J. J. *CRDEC-TR-256*, U.S. Army Chemical Research, Development and Engineering Center, Aberdeen Proving Ground, Md (1991)
9. Laemmli, U. *Nature* **227**:680-685 (1970)

10. Davis, L. G., Dibner, M. D. and Battey, J. F. *In: Basic Methods in Molecular Biology*, Elsevier, NY, 44-46 (1986)
11. Puissant, C., and Houdebine, L. M. *BioTechniques* 8:148-149 (1990)
12. Thomas, P. *Proc. Natl. Acad. Sci., U. S. A.* 77:5201-5205 (1980)
13. Denman, R. B. and Miller, D. L. *BioTechniques* 7:138-141 (1989)

BLANK

ANALYSIS OF PROTEINS BY ON-LINE HPLC ELECTROSPRAY MASS SPECTROMETRY

Philip B. Smith¹ and A. Peter Snyder²,
¹GEO-CENTERS INC., 10903 Indian Head Highway, Ft. Washington, MD 20744
and ²U.S. Army Chemical Research, Development and Engineering Center,
Aberdeen Proving Ground, MD 21010

ABSTRACT

A series of proteins varying in molecular weight from 16,950 to 66,000 Da were analyzed by Electrospray Ionisation mass spectrometry (ESI-MS) and by on-line gradient elution HPLC ESI-MS. Significant increases in the quality of the mass spectra, accompanied by an increase in the overall sensitivity were observed in the mass spectra obtained with on-line gradient elution HPLC-ESI-MS, compared to those obtained with direct ESI-MS.

INTRODUCTION

Direct coupling of a gradient elution HPLC to an electrospray ionisation (ESI) mass spectrometer offers considerable advantages for the analysis of large biomolecules. These include rapid removal of low molecular weight contaminants, ease of automation, and considerable economies of time and sample handling compared to off-line chromatographic separations. The ability to perform on-line HPLC ESI-MS would be of particular value in monitoring the progress and composition of enzymatic or chemical digests, which are routinely generated during the analysis of large biomolecules. However, the varying composition of the mobile phase produced by a gradient elution system, and the high flow rates necessary for an efficient chromatographic separation, may seriously compromise the performance of the mass spectrometer. A series of proteins were analyzed both by direct ESI-MS and by on-line gradient elution HPLC ESI-MS, and the results compared, in order to evaluate the utility of on-line gradient elution HPLC ESI-MS for the analysis of large biomolecules.

EXPERIMENTAL

Electrospray mass spectra were obtained on a Sciex API III triple quadrupole mass spectrometer using the articulated Ionspray® (pneumatically assisted electrospray) interface (Thornhill, Canada). Mass analysis was performed using the first quadrupole (q1), operated at unit resolution, and scanned in 0.1 Da increments. Equine myoglobin, *S. aureus* V8 protease, and Human serum albumin were obtained from Sigma (St. Louis, MI) and dissolved in an aqueous solution containing 5% trifluoroacetic acid to give a final concentration of 1 µg/µl. The samples were introduced either directly into the Ionspray® interface using an infusion pump at a flow rate of 5 µl/min, or following on-line HPLC separation, by connecting the HPLC column eluent to the Ionspray® interface with a fused silica transfer line. The protein solutions (10 µl) were injected onto a C8 HPLC column (2.1 x 30 mm) which was eluted with a linear gradient of acidified aqueous acetonitrile (10-70% over 25 min) at a flow rate of 25 µl/min with an Applied Biosystems 140B dual syringe pump (Foster City, CA).

RESULTS

The full scan mass spectra for equine myoglobin following direct ESI-MS and HPLC ESI-MS are reproduced in Figures 1 and 2 respectively, and expanded regions of these spectra in Figures 3 and 4 respectively. The mass spectra contain the characteristic bell-shaped series of the multiply protonated molecular ions, each peak in the series differs from the next one by the sequential addition of a proton. The mass spectrum obtained following the direct introduction of the sample, contains in addition, several satellite peaks closely associated with each of the protonated ions, appearing in the mass spectrum at slightly higher mass to charge ratios than the protonated series. These adduct ions are formed from the replacement of one or two of the protons with a sodium or potassium ion, and have a deleterious effect on the overall sensitivity, the signal to noise ratio, and the peak width. The accuracy and precision of the overall molecular weight determination will also be reduced if these satellite peaks are not adequately resolved from the protonated series. These satellite peaks were absent in the mass spectra for equine myoglobin obtained with on-line HPLC.

Similar results were obtained with the other two proteins investigated; in all cases the removal of alkaline metal salts and other low molecular weight contaminants by the on-line HPLC, decreased the amount of "chemical noise" in the mass spectra, and resulted in narrower peak widths and significantly higher S/N ratios for the protonated series.

CONCLUSIONS

Significant increases in the quality of the mass spectra, accompanied by an increase in overall sensitivity, were observed in the mass spectra obtained with on-line gradient elution HPLC-ESI-MS, compared to those obtained with direct ESI-MS. These results indicate that the initial concerns that the high flow rates and altering composition of the mobile phase necessary for efficient chromatography would compromise the performance of the mass spectrometer were unfounded, and clearly demonstrate the utility of on-line HPLC ESI-MS.

Figure 1. ESI Mass Spectrum of Myoglobin.

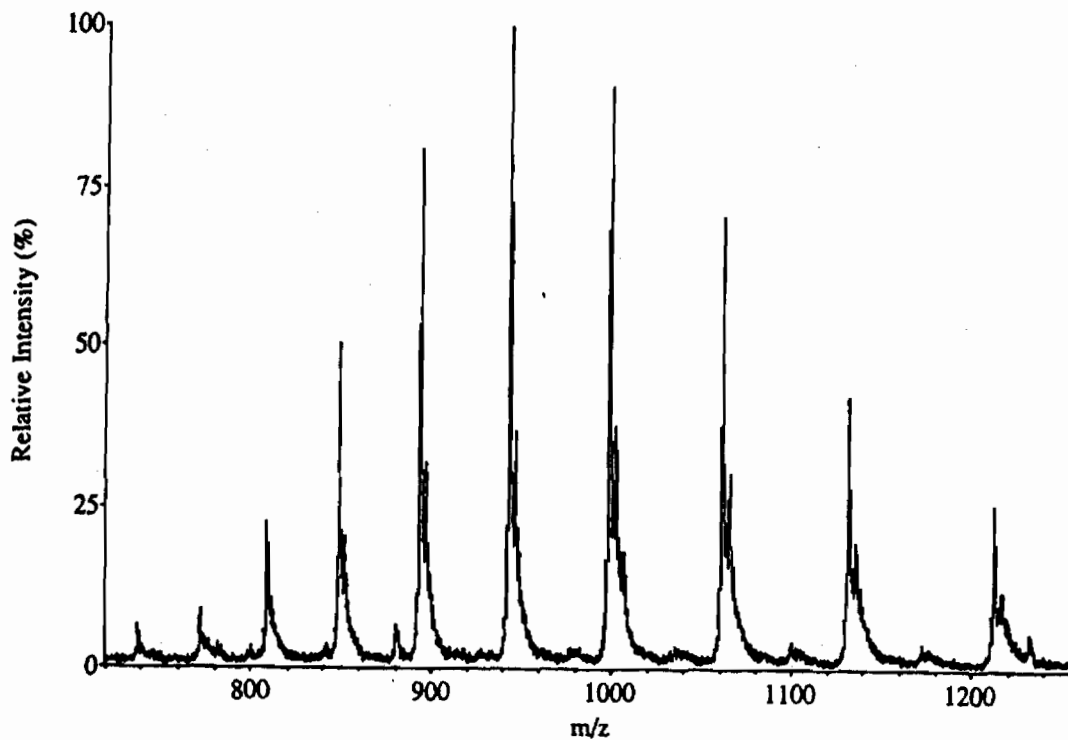


Figure 2. HPLC ESI Mass Spectrum of Myoglobin.

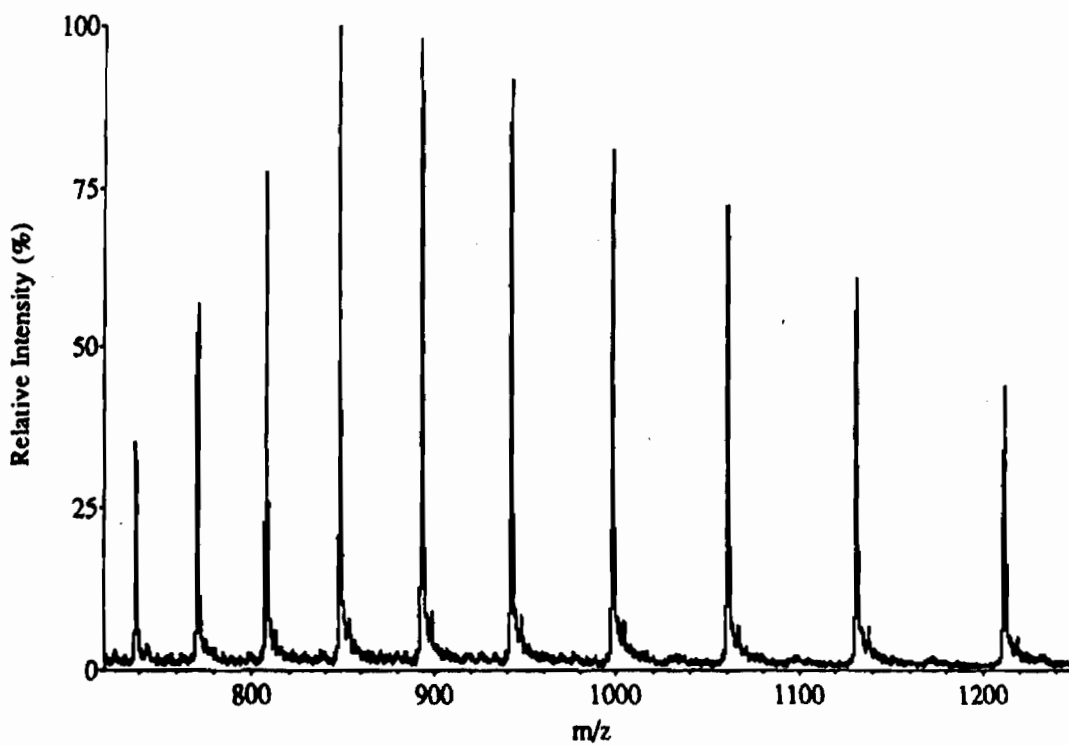


Figure 3. Partial ESI Mass Spectrum of Myoglobin.

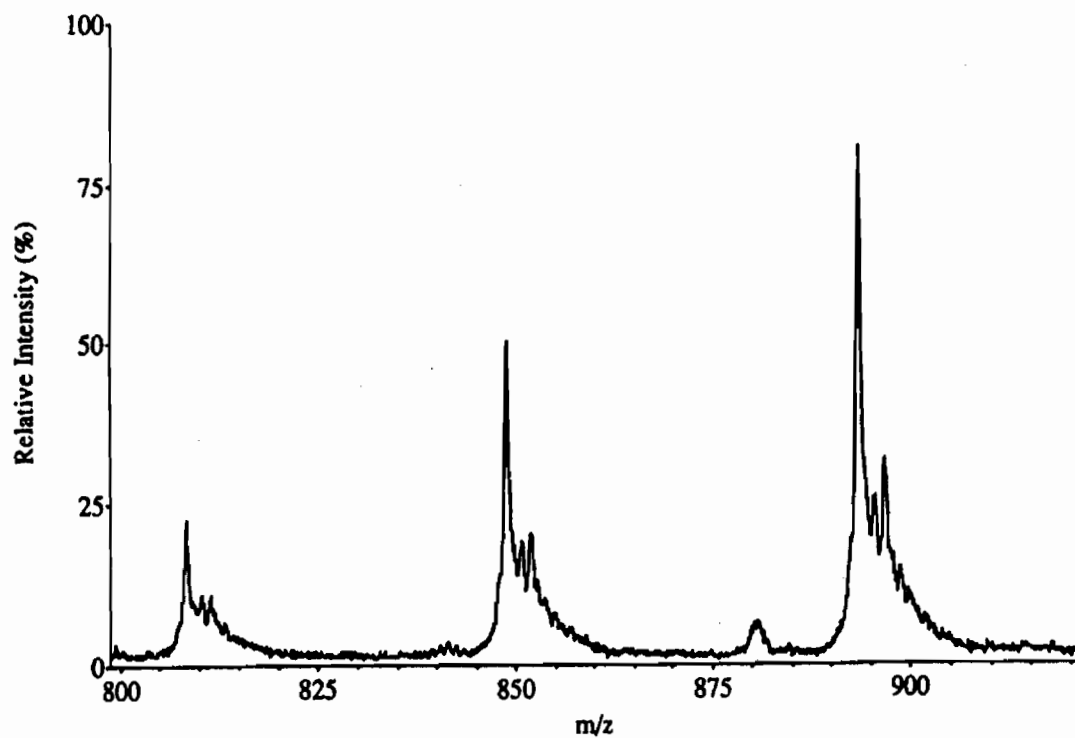
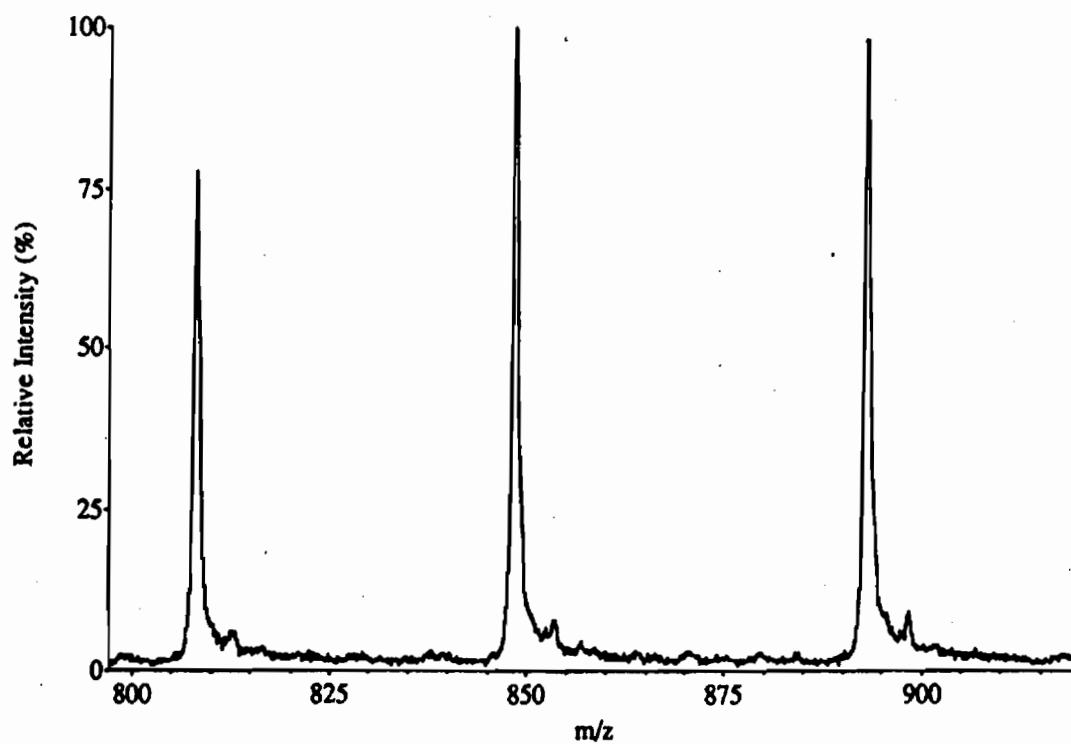


Figure 4. Partial HPLC ESI Mass Spectrum of Myoglobin.



BLANK

ANTIBODY-BASED FIBER OPTIC EVANESCENT WAVE SENSOR

D.E. Menking, K.R. Rogers, J. Heitz, and R.G. Thompson
US Army Chemical Research, Development & Engineering Center
Aberdeen Proving Ground, MD 21010-5423

D.G. Menking
Science and Technology Corp.
Hampton, VA 23666

M.E. Eldefrawi
University of Maryland School of Medicine
Baltimore, MD 21201

ABSTRACT

The fiber optic evanescent wave sensor uses the evanescent wave to excite fluorophores just outside the waveguide boundary. The resulting fluorescence is trapped and transmitted back up the fiber. Purified Rabbit immunoglobulin G (IgG) was immobilized on the surface of quartz fibers by adsorption or covalent binding and probed with fluorescein isothiocyanate labeled Goat anti-rabbit antibody (FITC-aR). The IgG density was quantitated by ¹²⁵I-Protein A binding. For covalent binding, fibers were silanized and activated with glutaraldehyde. There was no significant difference in initial rates and total binding between regular (non-silanized) and silanized fibers. Specific binding of FITC-aR was inhibited by non-labeled Goat anti-rabbit (aR). This system is being used as a model for the development of other antibody-antigen detection systems.

INTRODUCTION

Biological molecules bind very selectively to specific target sites within their native environments. Biosensors take advantage of this bio-affinity by immobilizing the target sites on various transductive devices and converting biomolecular interactions on the surface into electrical or optical signals. Capacitance, fiber optic, ChemFET, and potentiometric devices have been designed and tested using receptors and antibodies as the sensor coating. (1-4) In the present study, we developed a model antibody system using IgG immobilized on the surface of quartz rods. When FITC-aR was perfused across the IgG immobilized fiber, FITC-aR bound to the IgG producing a fluorescent signal that was directly proportional to the amount of antigen bound. Perfusion of fibers with increasing amounts of unlabeled aR also decreased the signal, due to competition for the same binding sites.

Protein A, isolated from Staphylococcus aureus, was used to quantitate the amount of protein on the fiber. Since Protein A binds to the Fc region of the antibody, it may be used to probe a number of immunoglobulin molecules.

MATERIALS AND METHODS

Apparatus

A fiber optic evanescent wave sensor, designed and built at ORD, Inc. was used for all experimentation. The instrument included the items as indicated in the schematic (Figure 1). The quartz fibers, 1 mm in diameter with polished ends, were obtained from ORD, Inc. The flow cell allowed the center 47 mm of a 60 mm long fiber to be immersed in 46 μ l which was exchanged every 14 sec.

Antibody purification

Rabbit IgG was purified by gel filtration chromatography on a Sephacryl S-300 column (bed height: 94 cm, flow rate: 0.5 ml/min) equilibrated with 0.1 M phosphate buffered saline (PBS) pH 6.8, and eluted with the same buffer. Eluant was monitored for absorbance at 280 nm and fractions containing the protein were pooled.

Fiber preparation

Quartz fibers were first acid cleaned and then silanized after the method of Weetal.(5) Silanized fibers were then activated by incubating in glutaraldehyde (3%) for 90 min, followed by incubation in 50 μ g/ml solution in PBS (pH 7.4) for 30 min, 4^o C.

Fluorescent measurements

After immobilizing the IgG, the fiber was placed in the flow cell of the instrument and perfused for 5 min with PBS containing bovine serum albumin (BSA) (0.1 mg/ml) to eliminate nonspecific binding. The fiber was then perfused with FITC-aR in PBS/BSA. Between experiments, the flow cell was washed in 1% SDS for 2 min followed by PBS for 10 min. Initial rates were determined graphically from tracing of the millivolt response vs time.

¹²⁵I-Protein A binding

Rabbit IgG was immobilized on silanized fibers as previously described, pretreated with BSA, and incubated with ¹²⁵I-Protein A (specific activity-0.3 Ci/mmol, New England Nuclear) for 15 min. This represents the time required for the fibers to reach equilibrium in the sensor. Silanized fibers without IgG were also incubated for determination of nonspecific binding. Fibers were washed in three passages of PBS and radioactivity was counted.

RESULTS

Literature reports indicate that covalent immobilization of protein to fibers is preferred to passive adsorption due to the stable linkage that is formed and greater half-life of the sensor's responsiveness. Comparison between the covalent immobilization of IgG via the silanization procedure employed in this paper and passive adsorption of IgG onto bare fibers revealed no significant difference in either initial or maximum binding when probed with FITC-Protein A (Table 1). Unless otherwise stated, all subsequent experiments were performed using covalent immobilization.

FITC-labeled aR ($0.5 \mu\text{g/ml}$) bound nonspecifically to silanized fibers, however, with the addition of BSA there was an 83% decrease in maximum binding. IgG coated fibers, pretreated with BSA and perfused with FITC-aR in PBS/BSA yielded a maximum fluorescent asymptote over 200% of that obtained with the uncoated fiber (Figure 2). Perfusion of IgG-coated fibers with increasing ratios of FITC-aR to unlabeled aR resulted in inhibition of the initial rate. With this competition type assay, we were able to detect unlabeled aR at the nanomolar level (Figure 3). These data suggest that the binding of the FITC-aR to IgG coated fibers is the result of specific binding of the aR to the IgG, rather than to the fiber itself.

The IgG coated fibers bound FITC-Protein A in a concentration-dependent manner. Fibers incubated 30 min with $50 \mu\text{g/ml}$ IgG bound $31 \text{ fmol } ^{125}\text{I-Protein A sites/fiber}$. Comparison of $^{125}\text{I-Protein A}$ and FITC-Protein A binding to fiber-immobilized IgG yielded similar slopes (Figure 4).

DISCUSSION

Fiber silanization produces a more stable immobilization by covalently linking the protein to the surface. The amount of biological material that binds to the fiber appears to be dependent on several factors: the choice of silanization technique/crosslinker used, and the type of biomolecule used. The lack of difference we observed between non-silanized and silanized fibers may be due to the choice of an aqueous method of silanization and the use of a glutaraldehyde activator. With aqueous silanization, lower amine loading occurs than when organic solvents are used, although the surface is reported to be more uniform. Preliminary experiments using organic solvent silanization with (3-mercaptopropyl)-trimethoxysilane (MTS) and N-(γ -maleimido-butyryloxy)succinimide (GMBS) as a crosslinker yielded nearly twice the maximum binding compared with non-silanized fibers (unpublished data). Rogers reports the passive adsorption of 29 fmol/mm^2 of nicotinic acetylcholine receptor onto non-silanized fibers. (6)

Binding of fluorophores within the evanescent wave zone produces a fluorescent signal that is detected by the evanescent wave sensor. FITC-aR alone binds to the quartz fibers but this binding is almost entirely eliminated in the presence of 0.1 mg/ml BSA. In the presence of BSA, binding of FITC-aR on IgG coated fibers was 200% greater than on uncoated fibers. Co-treatment of fibers with labeled and unlabeled aR showed competition-like inhibition of FITC-aR. It may, therefore, be concluded that the observed

fluorescence in the BSA-treated fibers is due to specific binding of FITC-a: to the IgG.

When probed with ^{125}I -Protein A, the silanized fibers bound 0.6 fmol/mm^2 Rabbit IgG. This value, compared with Bhatia's report (7) of 6 fmol/mm^2 for immobilized IgG, may be due to a shorter fiber incubation time. The fiber optic evanescent wave sensor has the advantages of ease of use and reagent preparation. It is anticipated that new assays may be developed very quickly, since purification of antibodies and FITC-labeling of the antigen are the only steps required for each new assay. Fiber optics are not subject to interference problems, have a rapid response time, and are very versatile for developing new assays.

REFERENCES

1. Tromberg, B.J., Sepaniak, M.J., Vo-Dinh, T. and Griffin, G.D. "Fiber-Optic Chemical Sensors for Competitive Binding Fluoroimmunoassay," Anal. Chem. Vol. 59, pp 1226-1230 (1987).
2. Anderson, F.P and Miller, W.G. "Fiber Optic Immunochemical Sensor for Continuous, Reversible Measurements of Phenytoin," Clin. Chem. Vol. 34/7, pp 1417-1421 (1988).
3. Eldefrawi, M.E., Sherby, S.M., Andreou, N., Mansour, A., Annau, Z., Blum, N.A. and Valdes, J.J. "Acetylcholine Receptor-Based Biosensor," Analytical Letters, Vol. 21(9), pp 1665-1680 (1988).
4. Schultz, J.S. "Biosensors," Scientific American, Vol. 265(2), pp 64-69 (1991).
5. Weetal, H.H., "Covalent Coupling Methods for Inorganic Support Materials," Methods of Enzymology, Vol. 44, pp 134-148 (1977).
6. Rogers, K.R., Valdes, J.J. and Eldfrawi, M.E., "Acetylcholine Receptor Fiber-Optic Evanescent Fluorosensor," Analytical Biochemistry, Vol. 182, pp 353-359 (1989).
7. Bhatia, S.K., Shriver-Lake, L.C., Prior, K.J., Georger, J.H., Calvert, J.M., Bredehorst, R. and Ligler, F.S. "Use of Thiol-Terminal Silanes and Heterobifunctional Crosslinkers for Immobilization of Antibodies on Silica Surfaces," Analytical Biochemistry, Vol. 178, pp 408-413 (1989).

Table 1. Comparison of Silanized and Non-Silanized Fibers

IgG incubation concentration	Silanized fibers		Non-silanized fibers	
	initial rate (mv/min)	total mv	initial rate (mv/min)	total mv
0.5 $\mu\text{g/ml}$	83	133	88	150
5 $\mu\text{g/ml}$	113	225	175	150
50 $\mu\text{g/ml}$	325	925	325	1150

SCHEMATIC PRESENTATION OF THE OPTICAL SYSTEM USED TO MEASURE FLUORESCENCE

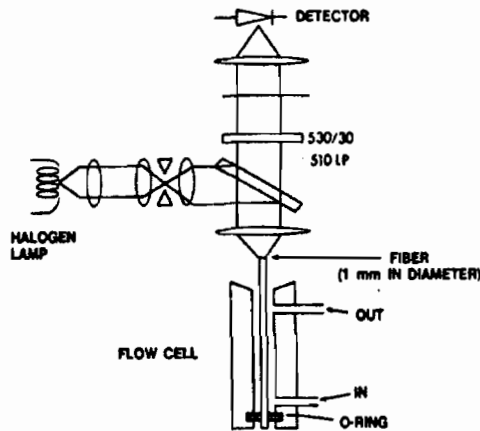


FIGURE 1.

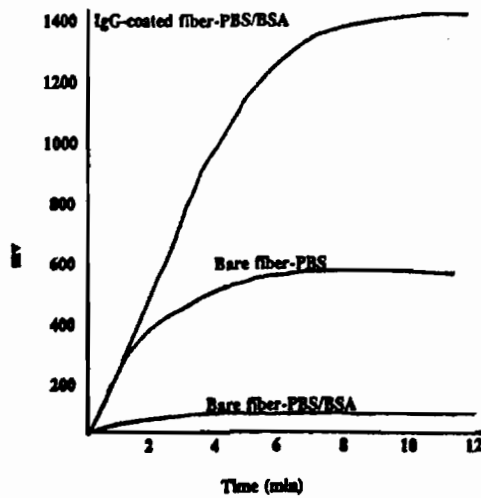


FIGURE 2. Specificity of FITC-aR for IgG

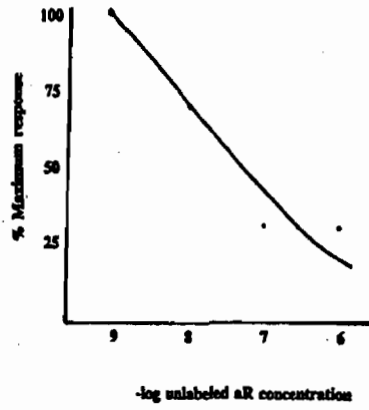


FIGURE 3. Inhibition of FITC-aR binding by unlabeled aR

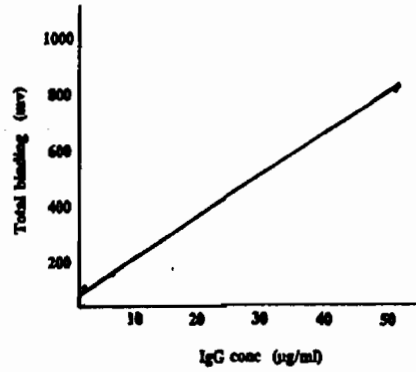


FIGURE 4a. Binding of FITC-Protein A to IgG

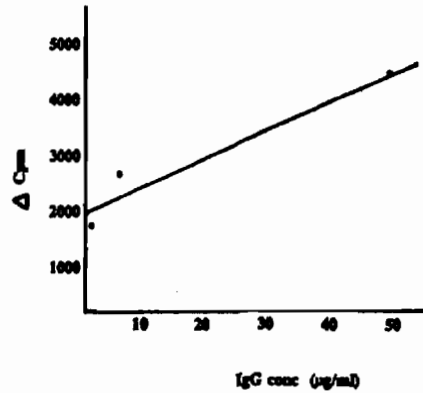


FIGURE 4b. Binding of ¹²⁵I-Protein A to IgG

RETROVIRAL VECTORS: TOOLS TO EXPRESS ENZYMES ACTIVE AGAINST SULFUR MUSTARD

Marc Boidot-Forget, Vincent Ramisse and Joëlle Lemaire
Laboratory of Molecular Toxicology
Centre d'Études du Bouchet, BP n°3, 91710 Vert-le-Petit, France

Abstract

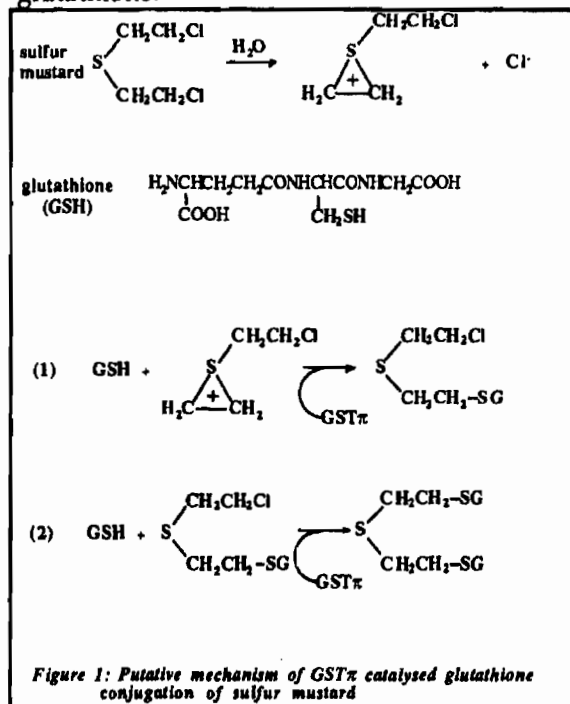
Various enzymes were studied as potential tools to detoxify *in vivo* chemical species. To do this, retroviral vectors were constructed encoding either human glutathione S-transferase π (GST π) or catalase. GST are able to detoxify electrophilic compounds through glutathione conjugation. Catalase is able to destroy hydrogen peroxide produced during oxygenated radicalar reactions, such as those occurring in radiolysis. Constructs were optimised for both titre and enzymic expression. Cultured mammalian cell lines were infected with these constructs and submitted to the action of several chemical agents (sulfur mustard, nitrogen mustards, peroxides). Constructs expressing high levels of GST π afforded protection against sulfur mustard (resistance factor: 2). Catalase constructs afforded protection against hydrogen and organic peroxides (resistance factor: 2 to 20).

Introduction

Retroviral vectors can be used as a tool to express various enzymes in mammalian cells. Such an expression might favourably alter, depending on which enzyme is being used, the ability of a cell to withstand a chemical onset. The vectors presented here encode either glutathione S-transferase or catalase.

Glutathione S-transferase (GST) vectors

GST are enzymes which can metabolize many xenobiotic compounds, either electrophilic or hydrophobic, thus rendering them more prone to elimination and as a rule decreasing their cytotoxicity. Conjugation takes place between an electrophilic region in the molecule and the thiol moiety of glutathione.

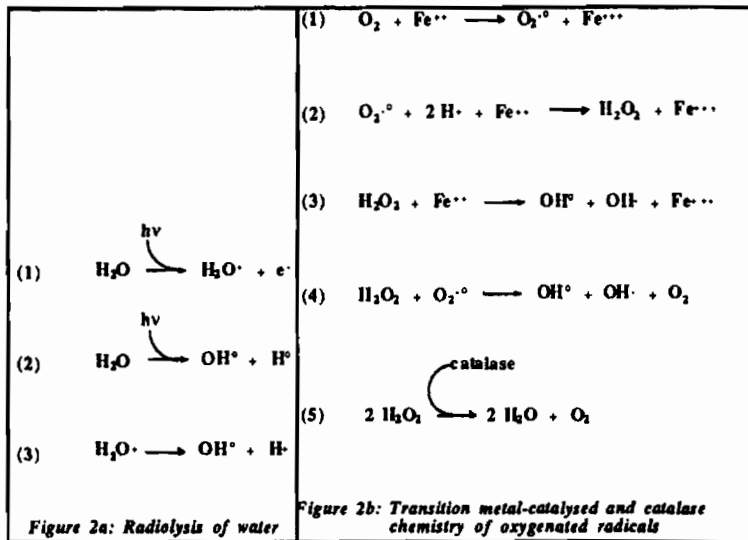


Sulfur mustard is a very electrophilic molecule. It can react with proteins, nucleic acids, coenzymes, lipids in a living cell. Some cell lines isolated from tumours which had previously been treated with nitrogen mustards used as chemotherapeutic agents, and which have become resistant to these agents, show markedly increased levels of certain classes of GST, and especially one called GST π . This has prompted us to test GST π (3) (gift of Dr. Masami Muramatsu, University of Tokyo, Japan) as a candidate enzyme to detoxify sulfur mustard. Fig. 1 shows the structure of sulfur mustard, its activated form, glutathione and the putative GST π catalysed reactions between both molecules. We have used retroviral vectors as a versatile tool to

obtain high enzymic expression levels in a large proportion of the target population.

Catalase constructs

During an irradiation as high energy photons enter a cell they create in its aqueous and oxygenated environment oxygenated free radicals which are the mediators of the observed cytotoxic phenomena (fig. 2a). Hydrogen peroxide is an intermediate species in the transition metal catalysed Fenton and Haber-Weiss pathways of production of hydroxyl radicals (reactions 3 and 4 in fig. 2b).



Catalase is an enzyme able to dismutate hydrogen peroxide without production of activated by-products (reaction 5 in fig. 2b). We have thus constructed catalase encoding vectors and tested the effect of catalase overexpression on hydrogen and organic peroxides toxicity with the aim of afterwards testing it on irradiation. Two genes have been used, one encoding rat liver

catalase (2) (rCAT; gift of Dr. Shuichi Furuta, Shinshu University, Japan) the other one human catalase (1) (hCAT; gift of Dr. Graeme I. Bell, Howard Hughes Medical Institute, University of Chicago, USA).

Methodology

Retroviral vectors were constructed according to standard protocols (4, 6). Mammalian cells were cultured in Dulbecco's modification of Earle's medium containing 10% foetal calf serum. Constructs were introduced by calcium phosphate transfection into PA317 cells (5), which are murine cells bearing a packaging-defective virus supplying in *trans* all viral proteins. Supernatant from these cells were used to infect target cells. After G418 (neomycin analog) selection resistant clones were scored to assess viral titre. Resistant clones were then pooled and lysed to determine mean enzymic expression. GST activity was monitored spectrophotometrically with 1-chloro-2,4-dinitrobenzene as a substrate. Catalase was monitored with hydrogen peroxide as a substrate. Enzymic activity was normalised by total protein amount. Cells were plated in 96-well microplates at 1.5×10^3 cells per well for J8 measurements and 10^4 for J3. One day later they were exposed to the toxic substance (in serum free medium for mustards), incubated at 37°C for two hours, rinsed and replenished with medium. Three (J3) or eight (J8) days after, the amount of cells per well was measured by MTT method. Toxicity was measured by the toxic concentration yielding 50% growth inhibition (IC_{50}). Protection factor was defined as the ratio of IC_{50} for infected *vs.* uninfected cells.

Virus production and gene expression

GST constructs

The structure of the vectors is depicted in fig. 3. **LTR** means long terminal repeat; it encompasses the viral promoter, signals for RNA processing, reverse transcription and integration. Ψ stands for the region necessary for viral RNA packaging into virions. **neo** is the gene encoding neomycin resistance, **hygro** the one for hygromycin resistance. **SV** is simian virus 40 early promoter. Fig. 4 shows the highest titre for each construct, as measured by *neo* resistant clones, as well as the mean enzymic expression. Some configurations, such as those with an internal cytomegalovirus promoter (**CMV**) give a high yield of enzymic expression but a lesser titre of viral particles, whereas others give the reverse situation, higher titre but poorer expression (compare for instance F38 vs. F34, or F80.12 vs. F79). A compromise has to be struck between these two factors.

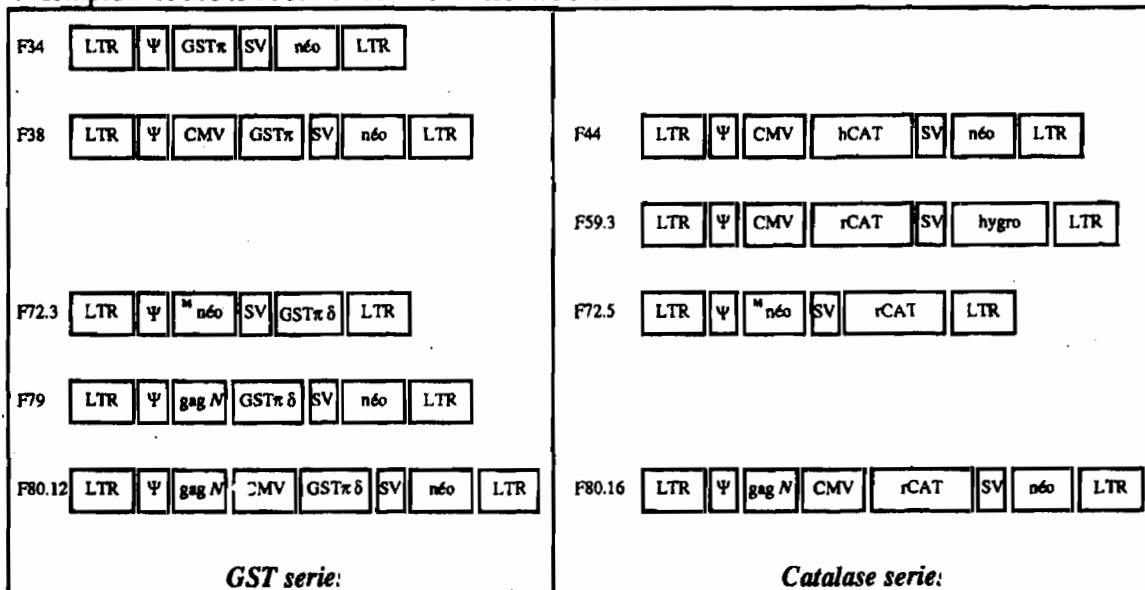
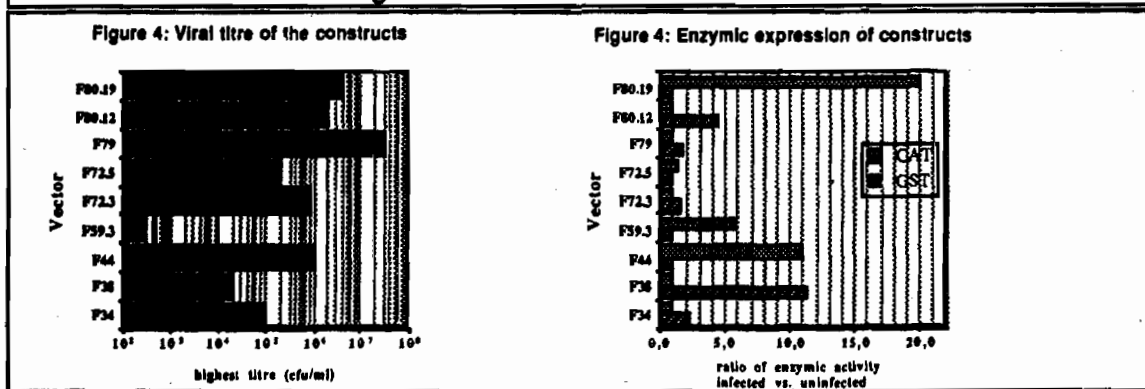


Figure 3: structure of the vectors



Catalase constructs

All catalase constructs expressed more readily catalase than did homologous GST ones, but the same pattern arose: enhancement of titre meant a decrease in gene expression.

Effects on cytotoxicity

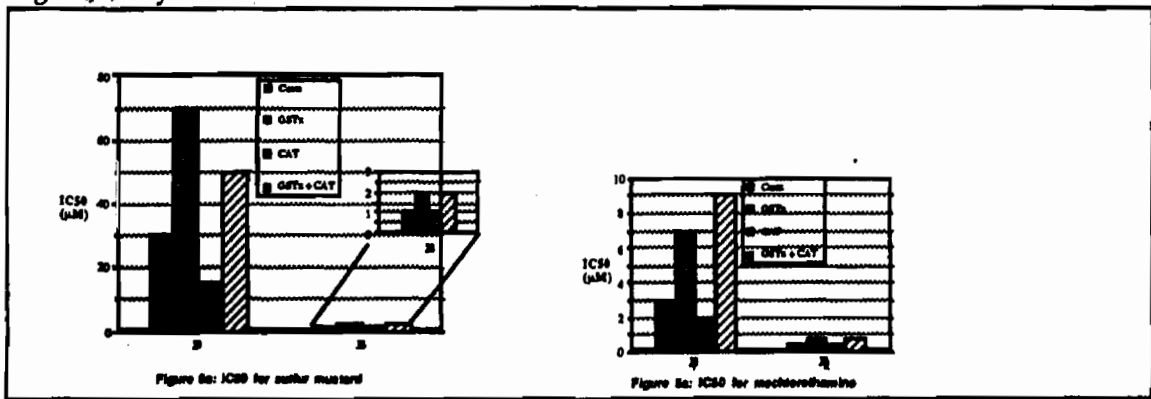
Uninfected cells (costs), cells infected by F38 and producing GST π , cells infected by F44 and producing catalase, and cells doubly infected with F38 and F59.3 producing both GST π and catalase were treated with sulfur and nitrogen mustards, or with hydrogen and cumene peroxides.

Table 1 shows the enzymic activities of the cells used in cytotoxicity measurements. It must be noted that the GST π level is very high in both F38 and (F38+F59) cells (exaltation ratio 20 to 30), whereas catalase is very high only in F44 cells (ratio 170), and but moderately elevated in (F38+F59) cells (ratio 3).

Table 1: enzymic activity of the cells used in the IC₅₀ experiment

	GST activity (nmol.min ⁻¹ .mg ⁻¹)	catalase activity (μ mol.min ⁻¹ .mg ⁻¹)
costs	80	1.0
costs/F38 (GST π)	1700	1.5
costs/F59 (CAT)	100	170
costs/(F38+F59) (GST π + CAT)	2300	3.2

Fig. 5a shows the IC₅₀ for sulfur mustard and nitrogen mustard (mechlorethamine), fig 5b for peroxides. Table 2 shows the protection factors afforded by GST π and catalase after three (J3) and eight (J8) days.



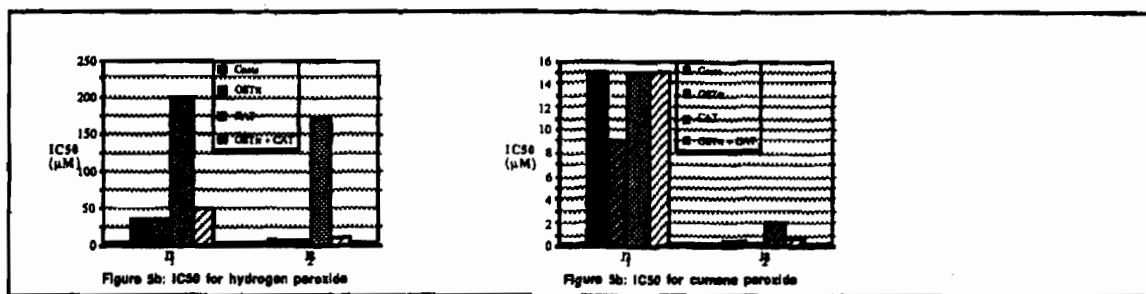


Table 2: protection factors (ratio of IC₅₀)

	GSTπ		CAT		GSTπ + CAT	
	J3	J8	J3	J8	J3	J8
sulfur mustard	2.3	2.0	0.5	1.0	1.7	2.0
nitrogen mustard	2.3	1.6	0.7	0.8	3.0	1.6
hydrogen peroxide	1.0	1.0	5.7	21	1.4	2.2
cumene peroxide	0.6	0.3	1.0	6.7	1.0	2.3

Discussion

As can be seen from fig. 5 and table 2 which summarizes it, expression of GSTπ in costs cells does confer them a resistance to mustard treatment, both after three days and after eight days. Catalase expression was of no avail against these two chemicals, and coexpression of GSTπ and catalase afforded mustard resistance, although not higher than that obtained with GSTπ alone, thus ruling out any synergistic effect. Expression of catalase conferred resistance against both hydrogen and cumene peroxide. The extent of resistance was higher after eight days than it was after three days, suggesting long-term effects of peroxides. Indeed, there was no protection at all for cumene peroxide after three days whereas a notable resistance could be measured after eight days. Coexpression of GSTπ and catalase did not afford any further protection; the extent of protection against peroxides in (GSTπ+CAT) cells is even lower than the one in CAT cells. However it should be noted that the catalase coexpressed in the cells was the rat enzyme, and at a much lower level than the human one expressed in cells with catalase only (cf. table 1).

CONCLUSIONS

We have shown that retroviral vectors encoding two enzymes, either GST π or catalase, were able to transduce in cultured cells a phenotype of resistance to mustards or peroxides. We have thus in hand a tool with which we can investigate cytotoxic mechanisms for several toxic agents. The use of this approach may give us an insight into the toxic phenomena. If it lives up to its expectations, i.e. if infection of mammalian cells *in vitro* provides them with a very strong protection factor, which is not yet the case, it will be extremely interesting to use these expression vectors in a whole animal. The success of such an approach *in vivo* might provide us with totally new ways of therapy.

Bibliography

- 1- Bell, G. I., Najarian, R. C., Mullenbach, G. T. and Hallewell, R. A. (1986). cDNA sequence coding for human kidney catalase. *Nucleic Acids Res.*, **14**, 5561-5562.
- 2- Furuta, S. and Hayashi, H. (1990). Purification and properties of recombinant rat catalase produced in *Escherichia coli*. *J. Biochem. (Tokyo)*, **107**, 708-713.
- 3- Kano, T., Sakai, M. and Muramatsu, M. (1987). Structure and expression of a human class π glutathione-S-transferase messenger RNA. *Cancer Res.*, **47**, 5626-5630.
- 4- Karn, J., Watson, J. V., Lowe, A. D., Green, S. M., *et al.* (1989). Regulation of cell cycle duration by *c-myc* levels. *Oncogene*, **4**, 773-787.
- 5- Miller, A. D. and Buttimore, C. (1986). Redesign of retrovirus packaging cell lines to avoid recombination leading to helper virus production. *Mol. Cell. Biol.*, **6**, 2895-2902. (ATCC CRL 9078)
- 6- Sambrook, J., Fritsch, E. F. and Maniatis, T. (1989). *Molecular Cloning: a laboratory manual*. Cold Spring Harbour Laboratory.

BLANK

**USE OF SURETY EXEMPT-DILUTE GD STOCK SOLUTION TO DETERMINE
INITIAL (ZERO ORDER) HYDROLYSIS RATES BY OPA ANHYDRASE
PREPARATIONS**

Johnnie M. Albizo and Joseph W. Hovanec

Research Directorate, U.S. Army Chemical Research, Development
and Engineering Center Aberdeen Proving Ground, MD 21010 -5423

ABSTRACT

A fluoride ion specific electrode method, utilizing 0.01 M stock GD solution in isopropanol and a multi-point calibration procedure, was devised to determine initial (zero order) hydrolysis rates by organophosphorus acid (OPA) anhydrase preparations in the presence and in the absence of Mn(II) ion. The method was developed to enable research workers to screen OPA anhydrase preparations for GD hydrolyzing activity in laboratories certified only for conducting dilute G-agent operations. All data was recorded through direct connection to a personal computer. Standard linear regression techniques were used to obtain calibration curves and zero order kinetics. Fluoride calibration curves were linear from 2.5×10^{-7} M to 2.0×10^{-4} M with a correlation coefficient of 0.998 and a slope efficiency of 0.962. Zero order kinetics were observed between 2 and 10 minutes. The percent standard deviation was 1.9% for GD hydrolysis in 0.05 M bis-tris-propane buffer pH 7.2 and 6.5% for GD hydrolysis by OPA anhydrase. Reaction velocities in terms of moles GD hydrolyzed per minute were 2.77×10^{-7} in buffer alone, 5.59×10^{-7} with 0.002 M Mn(II), 5.6×10^{-3} /mg protein OPA anhydrase, and 1.39×10^{-2} /mg protein OPA anhydrase with 0.002 M Mn(II). OPA anhydrase activity was found to decrease each time the dilute enzyme preparation was re-frozen and re-thawed.

INTRODUCTION

The fluoride ion specific electrode¹, which reportedly quantifies fluoride

concentrations as low as $1 \times 10^{-6} \text{ M}^2$ has been a useful tool for monitoring the release of fluoride from toxic flouride-containing organophosphorus compounds undergoing hydrolysis catalyzed by organophosphorus acid anhydrases in buffered aqueous solutions³⁻⁶.

Because of the large number of samples frequently screened, only the initial phase of the hydrolysis process is monitored. During that initial phase, which only lasts a few minutes, the rate of substrate hydrolysis is independent of substrate concentration — hence the term zero order kinetics applies.

Where possible, workers routinely use a simulant such as diisopropyl-fluorophosphate (DFP) for the more highly toxic chemical agents such as GD (pinacolyl methyl phosphonofluoridate). When DFP is used as the substrate, the working stock concentration is sufficiently high that initial rate (zero order) kinetics can be observed at fluoride concentrations above $1 \times 10^{-6} \text{ M}$ fluoride.

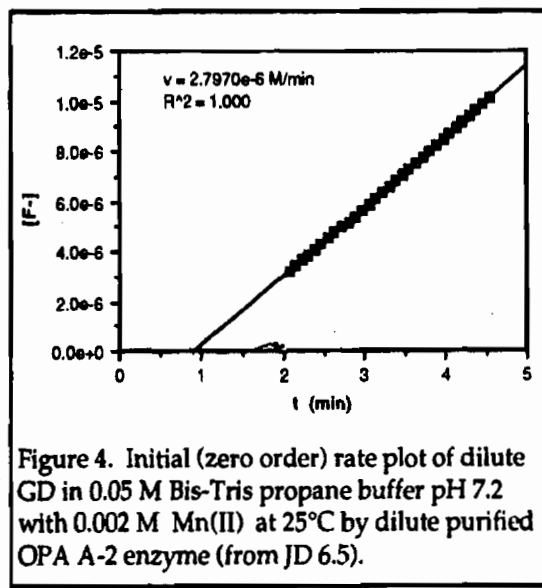
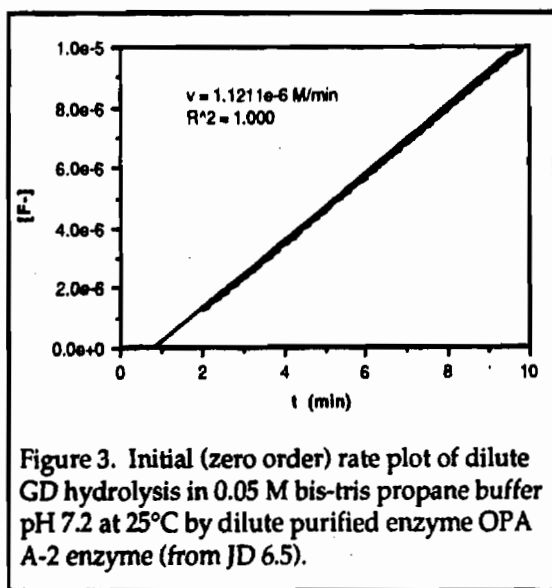
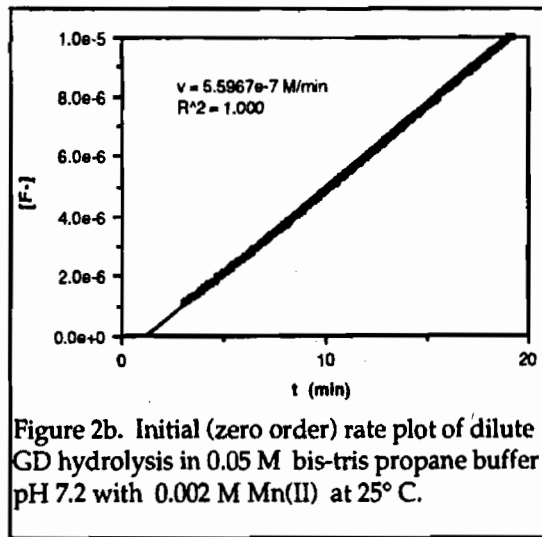
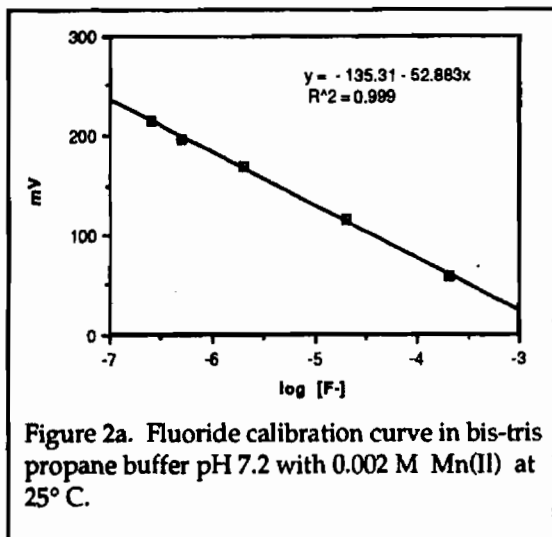
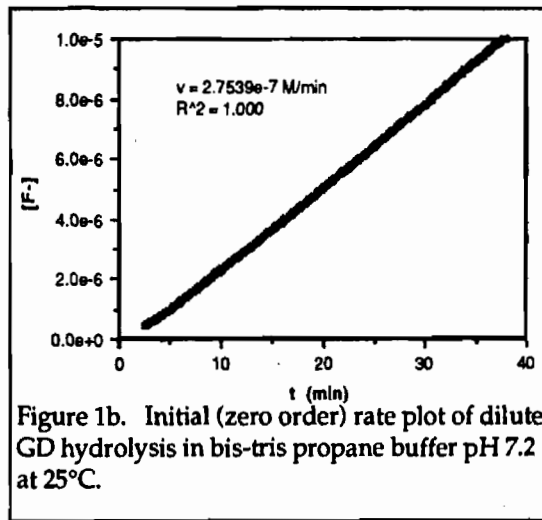
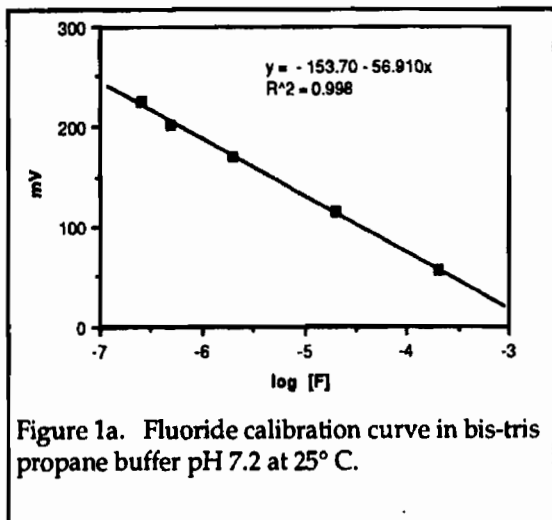
We seek to reduce some of the safety and surety hazards that would be incurred with the use of neat highly toxic chemical agents, such as GD, when used as substrates in conducting hydrolysis studies. Accordingly, the objective of this study is to document zero order kinetics using dilute working GD stock solutions to assay OPA anhydrase preparations by fluoride ion specific electrode methodology. Attainment of this objective requires the quantitation of fluoride at concentrations below the $1 \times 10^{-6} \text{ M}$ lower limit previously reported².

MATERIALS AND METHODS

Dilute GD working stock solution: Neat GD (99% purity) was diluted with anhydrous isopropanol to prepare volumetrically 10 ml of 0.01 M dilute GD working stock solution. Two ml quantities of the dilute GD working stock solution were pipeted into each of five 2-ml glass micro sample vials (Wheaton) fitted with teflon-lined plastic screw caps. These dilute GD working stock solutions were stored, doubly contained, under lock and key at 4° C in an approved dilute surety agent storage room until needed for conducting OPA anhydrase assays. All work with dilute GD was conducted in an approved dilute surety agent chemical fume hood located in an approved dilute surety agent laboratory.

Flouride calibration curves: Fluoride standards in 0.05 M bis-tris propane pH 7.2 were prepared fresh daily with and without 0.002 M MnCl_2 . The fluoride electrode (Orion model 96-09-00) was calibrated before each series of assays using a multipoint calibration procedure⁷ in conjunction with a pH meter (Fisher Accumet model 925). The molarity of fluoride standards used in calibrating the electrode were; $2.5 \times 10^{-7} \text{ M}$, $5.0 \times 10^{-7} \text{ M}$, $2.0 \times 10^{-6} \text{ M}$, $2.0 \times 10^{-5} \text{ M}$, and $2.0 \times 10^{-4} \text{ M}$. Standard linear regression techniques were used to construct calibration curves.

OPA anhydrase working stock: Purified OPA A-2 enzyme from bacteria (JD 6.5) was diluted 1:5 in 0.05 M bis-tris propane buffer pH 7.2. The dilute enzyme was stored at 4° C prior to conducting assays and subsequently frozen and thawed prior to conducting further assays.



Initial rate (zero order) kinetic assays: Enzyme assays were conducted in triplicate. Five ml of 0.05 M bis-tris propane buffer pH 7.2 was pipeted into a thermostatically controlled (25° C) glass reaction vessel containing a fluoride electrode that had been subjected to a 5-point calibration procedure⁷. Five μ l of dilute OPA A-2 enzyme was added using a micropipet (Gilson Pipetman model P-20). In some assays, 100 μ l of 0.1 M MnCl₂ in distilled water solution, was added. After allowing the mixture to stir magnetically for 3 minutes, 100 μ l of dilute GD working stock solution was added. Data was recorded directly through a personal computer (Mcintosh Plus). Standard linear regression analysis techniques were used to determine zero order kinetics.

RESULTS

Fluoride calibration curves were linear from 2.5×10^{-7} to 2.0×10^{-4} M fluoride in 0.05 M bis-tris propane buffer pH 7.2 at 25° C (Fig. 1a). The initial (zero order) reaction rate for GD hydrolysis in 0.05 M bis-tris propane buffer pH 7.2 at 25° C was 2.75×10^{-7} moles per minute (Fig. 1b).

Fluoride calibration curves were linear from 2.5×10^{-7} to 2.0×10^{-4} M fluoride in 0.05 M bis-tris propane buffer pH 7.2 with 0.002 M Mn(II) at 25° C (Fig. 2a). The initial (zero order) reaction rate for GD hydrolysis in 0.05 M bis-tris propane buffer pH 7.2 with 0.002 M Mn(II) at 25° C was 5.59×10^{-7} moles/minute (Fig. 2b).

The initial (zero order) reaction rate of GD hydrolysis by dilute purified OPA A-2 enzyme (from JD 6.5) in bis-tris propane buffer pH 7.2 at 25° C was 1.12×10^{-6} moles GD hydrolyzed/minute (Fig. 3.).

The initial (zero order) reaction rate of GD hydrolysis by purified dilute OPA A-2 enzyme (from JD 6.5) in bis-tris propane pH 7.2 with 0.002 M Mn(II) at 25° C was 2.79×10^{-6} moles GD hydrolyzed/minute (Fig. 4.).

The hydrolytic activity of dilute purified OPA A-2 enzyme (from JD 6.5) decreased against GD each time the dilute purified enzyme was re-frozen and re-thawed according to fluoride ion specific electrode assay in bis-tris propane buffer pH 7.2 at 25° C (Fig. 5.).

Mn(II) (0.002 M) doubled the initial (zero order) hydrolysis rate of dilute GD in 0.05 M bis-tris propane buffer pH 7.2

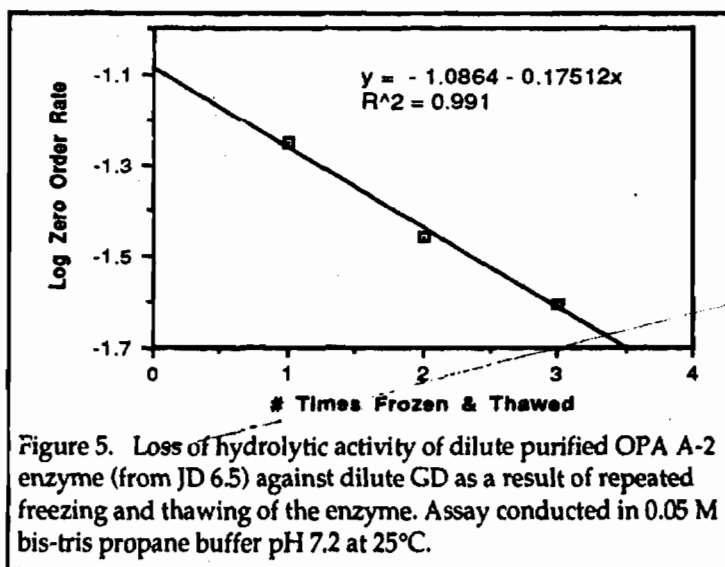


Figure 5. Loss of hydrolytic activity of dilute purified OPA A-2 enzyme (from JD 6.5) against dilute GD as a result of repeated freezing and thawing of the enzyme. Assay conducted in 0.05 M bis-tris propane buffer pH 7.2 at 25° C.

at 25°C. Mn(II) (0.002 M) Increased the activity of dilute purified OPA A-2 enzyme by a factor of 2.5 in 0.05 M bis-tris Propane buffer pH 7.2 at 25°C (Table 1).

Table 1. Summary of the effect of 0.002 M Mn(II) on the initial (zero order) hydrolysis rate of dilute GD by dilute purified OPA A-2 enzyme (from JD 6.5) in 0.05 M bis-tris propane buffer pH 7.2 at 25° C.

<i>Conditions</i>	<i>Moles GD Hydrolyzed/min/mg OPA A-2 Enzyme Protein</i>
GD in Buffer	2.77×10^{-7} (no enzyme protein)
GD in Buffer + Mn[II]	5.59×10^{-7} (no enzyme protein)
GD in Buffer + OPA A-2	5.60×10^{-3}
GD in Buffer + OPA A-2 + Mn[II]	1.39×10^{-2}

[% standard deviation in the presence of enzyme was 6.5 %]

DISCUSSION

Because of productivity considerations, it is desirable to use initial rates (zero order) hydrolysis kinetic assays to screen large numbers of OPA anhydrase preparations for hydrolytic activity against fluoride-containing organophosphorus compounds when using the fluoride ion specific electrode method.

Furthermore, because of safety and surety considerations, it is desirable to start with dilute working stock solutions when evaluating the hydrolysis of highly toxic chemicals such as GD.

Imposition of the combined specific requirements of conducting initial rate (zero order) kinetic assays using the fluoride electrode and using a dilute working stock solution of toxic fluoride-containing compound as starting material, requires linear quantitation of fluoride below the 1×10^{-6} M lower limit advertised by the manufacturer of the fluoride ion specific electrode.²

We were successful in quantifying fluoride at concentrations as low as 2.5×10^{-7} M by using pre-calibrated microliter pipets and by using a 5-point electrode calibration procedure.⁷ This methodology will enable other workers to evaluate the comparative effectiveness of hydrolytic materials against highly toxic fluoride-

containing organophosphorus compounds, such as GD, in laboratories certified for conducting dilute agent operations.

CONCLUSIONS

Dilute GD (2mg/ml) stock solution can be used to determine zero order kinetics while screening OPA anhydrase for hydrolytic activity using a fluoride ion specific electrode. The method will enable researchers to screen OPA anhydrase enzyme preparations against GD in laboratories only certified for dilute agent work.

REFERENCES

1. Frant, M. S., and J. W. Ross. "Electrode for sensing fluoride ion activity in solution." *Science* 1966, 154, 1553-1555.
2. Instruction Manual, fluoride electrode model 96-09-00, Orion Research Inc. 1983, pages 9,12.
3. Hoskins, F. C. G., and Roush, A. H. "Hydrolysis of nerve gas by squid type diisopropyl phosphorofluoridate hydrolyzing enzyme on agarose resin." *Science* 1982, 215, 1255-1257.
4. Landis, W.G., R. E. Savage, and F. C. G. Hoskin. "An organofluorophosphate hydrolyzing activity in *Tetrahymena thermophila*." *J. Protozool.* 1985, 32, 517-519.
5. Chettur, G., J. J. DeFrank, F. C. Gallo, F. C. G. Hoskin, G. Mainer, F. M. Robins, K. E. Steinmann, and J. E. Walker. "Soman-Hydrolyzing and detoxifying properties from a thermophilic bacteria." *Fundam. appl. toxicology* 1988, 11, 373-380.
6. DeFrank, J. J., and T. C. Cheng. "Purification and properties of an organophosphorus acid anhydrase from a halophilic bacterial isolate." *J. Bacteriology* 1991, 173, 1938-1943.
7. Instructions, Fisher Accumet model 925 pH meter, catalog No. 13-636-925 & 926, Fisher Scientific Pages 35-36, Part No. 67870, Published 3/87.

XVII. ENVIRONMENTAL STUDIES POSTER

BLANK

DETECTION OF THIODIGLYCOL AND ITS SULFOXIDE AND SULFONE
ANALOGUES IN ENVIRONMENTAL WATERS BY
HIGH PERFORMANCE LIQUID CHROMATOGRAPHY

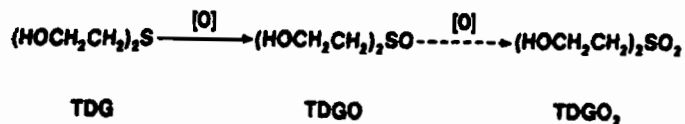
Paul C. Bossle, Michael W. Ellzy and John J. Martin
U.S. Army Chemical Research, Development and Engineering
Center, Aberdeen Proving Ground, MD 21010-5423

ABSTRACT

A new method is described to directly and simultaneously separate and quantitate trace amounts of 2,2'-thiodiethanol (thiodiglycol) (TDG) and its oxidative derivatives 2,2'-sulfinyldiethanol (TDGO), and 2,2'-sulfonyldiethanol (TDGO₂) in surface water and seawater. Separations in this study were carried out on an ion exclusion column at 35° C using an isocratic mobile phase consisting of 100 mM perchloric acid. Detection and quantitation of TDG, TDGO, and TDGO₂ were by ultraviolet (208 nm) and pulsed amperometric detection. The working platinum electrode potentials were E₁ = 0.30V; E₂ = 1.25V; E₃ = -0.10V, where E₁ was the sampling voltage, and E₂ and E₃ the cleaning and regenerating voltages, respectively. Detection limits for TDG, TDGO, and TDGO₂ were in the 40 to 80 nanogram range.

INTRODUCTION

2,2'-Thiodiethanol, commonly known as thiodiglycol (TDG), is oxidized gradually in water to relatively stable 2,2'-sulfinyldiethanol (TDGO) and possibly, under the influence of sunlight, to 2,2'-sulfonyldiethanol (TDGO₂)¹. Therefore, any methodology for detecting trace quantities of TDG in environmental waters should of necessity also include the simultaneous detection of TDGO and TDGO₂.



Current U.S. Army Chemical Research, Development and Engineering Center (CRDEC) methodology for the trace analysis of TDG in environmental waters uses high performance liquid chromatography (HPLC). An environmental water sample is injected directly into the liquid chromatograph and the TDG is separated from the environmental matrix on a reverse phase C-18 column. TDG is quantitated with combined ultraviolet (UV) (208 nM), electrochemical (EC) (+970 mV), and fluorine-induced sulfur chemiluminescence (SCL) detection.^{2,3}

This methodology cannot be used for analyzing TDGO and TDGO₂. TDGO and TDGO₂ are not separated on a C-18 reverse phase column and are not amenable to EC and SCL detection. TDGO₂ has no significant absorption at 208 nM and, therefore, is not amenable to UV detection at trace concentration levels.

A HPLC method is described here to directly separate, detect, and quantitate TDG, TDGO, and TDGO₂ at trace levels in water. They are separated on an ion exclusion column, and upon elution, are detected and quantitated using combined UV and pulsed amperometric detection (PAD). The feasibility of this method for the analysis of surface water and seawater is demonstrated.

MATERIALS AND METHODS

1. Chemicals.

Water used in this study was distilled and deionized (10-14 meq/cm) using the Barnstead Nanopure II System (Barnstead/Sybron, Boston, MA). Analytical grade perchloric acid was obtained from Mallinckrodt Chemical Works (St. Louis, MO). TDG was obtained from Aldrich Laboratories (Milwaukee, WI). TDGO was obtained from Chem Service, Inc. (West Chester, PA). TDGO₂ was prepared in-house and gave analytical data consistent with its chemical structure.⁴ Simulated seawater was prepared from "Instant Ocean" (Aquarium Systems, Incorporated, Mentor, OH) according to the directions provided by the supplier.

2. Instrumentation.

Chromatography was performed using a Model 2120i Ion Chromatograph (Dionex Corporation, Sunnyvale, CA) equipped serially with both a variable wavelength UV detector and a Dionex Model PAD-1 pulsed amperometric detector operating with a platinum working electrode. Samples were introduced by an air-activated valve injector with a 200 uL sample loop. This system was connected to a Model 4270 Recorder-Integrator (Dionex Corporation) that measured UV and pulsed amperometric

detector response in terms of peak area. The UV spectrum of TDGO₂, and TDGO, and TDG, were obtained on a Cary Model 17-D (Varian Corporation, Sunnyvale, CA).

3. Chromatographic Procedure.

Ion-exclusion separations were performed using these chromatographic parameters: column, Dionex HPICE-AS1; column temperature, 35° C; eluent, 100 nM perchloric acid; and flow rate, 1 mL/min. The UV detection of TDG and TDGO was carried out at the 208 nM wavelength (0.05 AUFS). Pulsed amperometric detection was determined at an output range of 1000 nanoamps. The working electrode potentials used were $E_1 = 0.30V$, $E_2 = 1.25V$, $E_3 = -0.10V$, where E_1 was the sampling voltage, and E_2 and E_3 the cleaning and regenerating voltages, respectively, and the duration of these potentials were 60, 60, and 240 milliseconds, respectively.

Stock solutions of TDGO₂, TDGO, and TDG were injected onto the column and retention times of 7.90, 10.00, and 21.80 minutes, respectively, were determined. TDGO₂, TDGO, and TDG peak fractions of the eluent were evaporated to dryness using a nitrogen steam at ambient temperature, and identified by mass spectrometry. Calibration curves were obtained by injecting a known concentration (100, 200, 400, 1000, 2000, 4000, and 10,000 ng/mL) of each of the three compounds in deionized distilled water into the chromatograph in triplicate and measuring both the UV and pulsed amperometric detector response obtained.

4. Sample Preparation.

Both a surface water and a simulated seawater sample were spiked with TDGO₂, TDGO, and TDG at a concentration level of 1000 ng/mL. The samples were filtered and then injected, along with unspiked samples, into the liquid chromatograph.

RESULTS AND DISCUSSION

Retention (and separation) of analytes on an ion-exclusion column is by a mixed hydrogen bonding, reverse phase, and steric exclusion mode mechanism. TDGO₂, TDGO, and TDG, being small, nonionic molecules, are highly retained on the column. Large ionic species that are prevalent in environmental waters, however, are unretained and are eluted in the void.

Pulsed amperometric detection which uses multiple potentials applied in a repeating sequence is quite successful in electrochemically detecting glycols such as TDGO₂, TDGO, and TDG. The hydroxyl groups are oxidized and detected at the first potential (0.30V); a second step provides the potential where

reaction products are removed (1.25V); and the third step regenerates the electrode at a negative potential (-0.10V). The platinum working electrode surface, therefore, remains clean with no loss of detection sensitivity over time.

The feasibility of this method for analyzing TDGO₂, TDGO, and TDG in environmental waters was demonstrated with spiked surface water and simulated seawater. Using pulsed amperometric detection, peak areas for all three species in the standard and spiked surface water chromatograph (Figure 1a, 1b) are similar

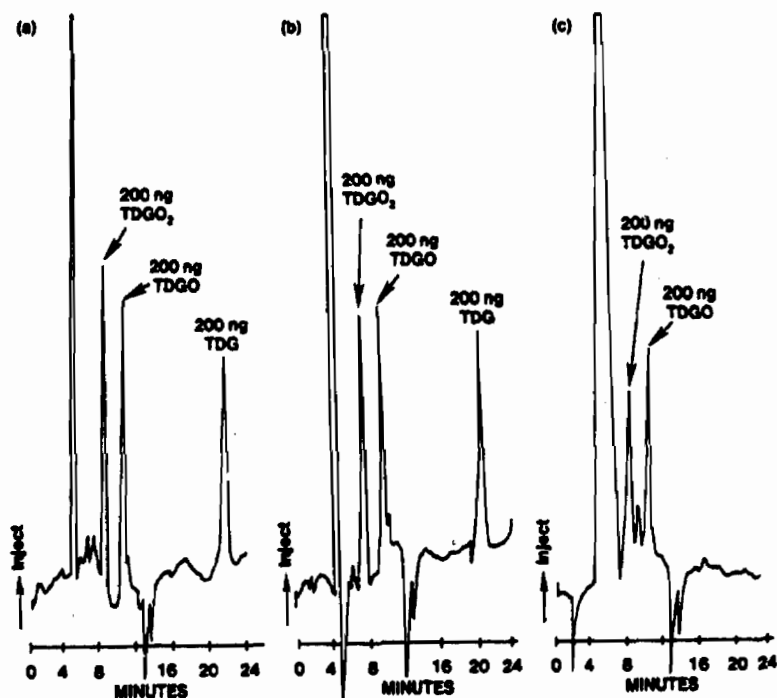


FIGURE 1. Ion-Exclusion Separation - Pulsed Amperometric Detection Chromatograms of (a) Standards, (b) Spiked Surface Water, and (c) Spiked Simulated Seawater

since the detection signal is a function of the halfwave potential of the glycol moiety. While the chromatogram of the spiked surface water (Figure 1b) was free of matrix interference, the spiked simulated seawater sample has first to be passed through a cartridge containing a strong cation exchanger (Ag⁺ form) which removed interfering halide ions but retained TDG. The TDGO₂ and TDGO peaks in the chromatogram of the treated spiked simulated seawater (Figure 1c) are now free of matrix effects. Using UV detection, the optimal signal-to-noise ratio for TDG and TDGO was observed at a wavelength of 208

nM where TDG and TDGO have relatively strong molar absorptivities of 1415 and 1271, respectively. In comparison, TDGO₂ absorbs weakly ($\epsilon = 185$) (Figure 2a). The peaks of TDGO and TDG in the spiked surface water and simulated seawater chromatograms (Figures 2b, 2c) are free of matrix effects.

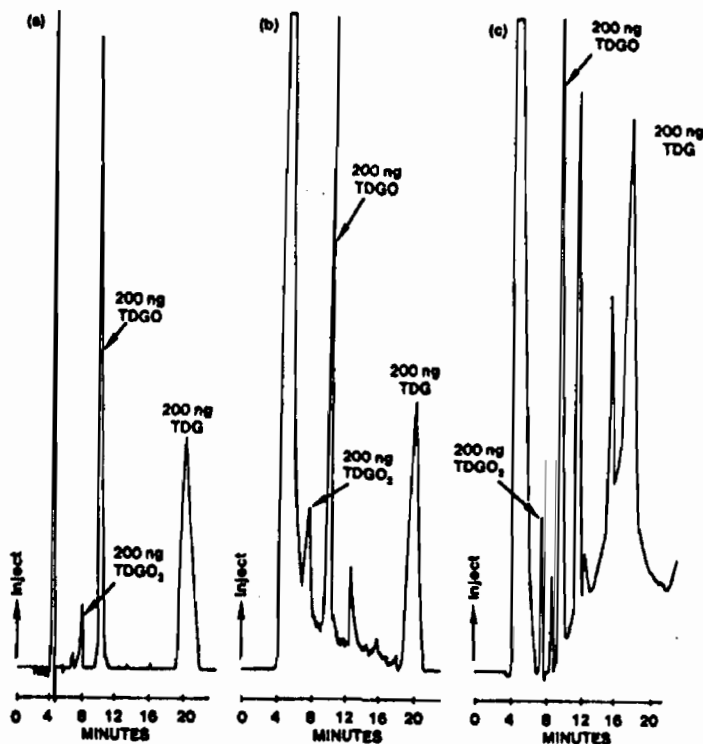


FIGURE 2. Ion-Exclusion Separation-Ultraviolet Detection Chromatograms of (a) Standards, (b) Spiked Surface Water, and (c) Spiked Simulated Seawater

TDGO₂, TDGO, and TDG each responded linearly (correlation coefficient >0.99) to pulsed amperometric detection of an injected range of 20-2000 ng. The minimum quantifiable detection limit for all three species was approximately 40 ng (S/N = 3). TDGO and TDG also responded linearly to UV detection (correlation coefficient >0.99) over the same concentration range with detection limits for both species being approximately 80 ng (S/N = 3).

CONCLUSION

Ion exclusion chromatography with combined pulsed amperometric and UV detection is a rapid and direct method for analyzing TDGO₂, TDGO, and TDG in water in quantities as low as 40 ng. The feasibility of this method for analyzing surface water and seawater is demonstrated.

REFERENCES

1. Ivey, J. P. and Haddad, P. R., Determination of Dimethylsulphoxide Using Ion-Exclusion Chromatography with Ultraviolet Absorption Detection, J.Chromatogr, 391, 309-314 (1987).
2. Bossle, P. C., Hallowell, S. F., Reutter, D. J., and Sarver, E. W., Analysis of 2,2'-Thiodiethanol, A Water Soluble Alkyl Sulfide in Aqueous Matrices, J.Chromatography, 330, 388-391 (1985),
3. Bossle, P. C., Ellzy, M. W., and Martin, J. J., Application of Chemiluminescence for the Detection of Thiodiglycol in Aqueous Matrices Using High Performance Liquid Chromatography, CRDEC-TR-219, U.S. Army Chemical Research, Development and Engineering Center, Aberdeen Proving Ground, MD, UNCLASSIFIED Report.
4. Levin, I. M., Oxidation of Sulfides by Benzoyl Peroxide, J.Prakt.Chem., 127, 77-91 (1930).

XVIII. NMR INVESTIGATIONS POSTERS

BLANK

METAL-ION PROMOTED OXIDATION OF DIMP

D. Ralph Leslie, Materials Research Laboratory, DSTO,
Melbourne, Australia and J. Richard Ward, U.S. Army
Chemical Research, Development and Engineering Center,
Aberdeen Proving Ground, MD

ABSTRACT

Oxone rapidly decontaminates VX by means of sulfur oxidation. G-agents, such as sarin or soman, are difficult to oxidize, and all means to decontaminate sarin or soman are based on hydrolysis. In order to see if oxone might have utility as a general decontaminant, experiments were run to see if the ability of oxone to destroy organophosphorus esters could be enhanced with transition-metal catalysts.

It was shown that decomposition of the G-agent simulant, diisopropyl methylphosphonate (DIMP), was promoted in oxone solution by the presence of low valent metal ions such as cobalt (II), chromium (III), or manganese (II). The reaction is initiated by radical formation from decomposition of persulphate. The radical chains may be terminated by dimerization of SO_4^- ; by other reactions forming O_2 ; or by reduction of the radical to sulphate ion by low valent metal ion. The radical can also reduce the oxidized metal ion back to the original low valent state, providing a path for turnover of the metal ion.

INTRODUCTION

Decontamination of equipment exposed to chemical warfare agents is necessary for its further, unrestricted operation. Ideally, the decontamination process should be rapid and not compromise the integrity of equipment. The standard U.S. Army decontamination solution, DS2, rapidly reacts with the classical agents to yield products that are not hazardous to personnel.¹ However, concern has been expressed regarding the incompatibility of this formulation with a range of material and also problems associated with its storage.²

A major obstacle to overcome in developing a replacement for DS2 is the requirement for the decontaminant to react with diverse classes of organic compounds, including vesicants such as 2-chloroethyl sulfides, amines, and organophosphorus nerve agents. Even within these broad classifications, the reactivity of compounds varies considerably.⁴

Recent investigations by Yang et al have demonstrated that aqueous solutions of Oxone (a commercial mixture of potassium hydrogen monoperoxysulfate, potassium hydrogen sulfate and potassium sulfate) react rapidly with VX to yield products that do not exhibit the acute toxicity associated with VX.⁵ The reaction proceeds via oxidation of the phosphonothiolate sulfur by oxygen transfer, with subsequent hydrolysis of the original S-alkyl moiety. Solutions of Oxone are acidic (pH ~ 2, 0.01 M) which, although aiding the solubilization of VX, prevents its application for general decontamination. G agents are not directly oxidized by peroxymonosulfate and are relatively stable in acidic solution. Rapid hydrolysis of G agents may be effected by increasing the pH of the solution, however, the peroxymonosulfate anion is unstable in alkaline solution.⁶

An alternate approach to include reactivity towards G agents in an Oxone-based decontamination system would be to modify the mechanism by which Oxone acts as an oxidant. The ability of hydrogen peroxide to oxidize organic substrates is greatly enhanced by the addition of low-valence metal ions to solution.^{7,8} Fenton's reagent, a mixture of hydrogen peroxide and ferrous ion, is the most thoroughly studied metal ion-peroxide oxidizing agent.

The purpose of this study is to identify whether a Oxone/metal ion system analogous to Fenton's reagent exists, and if it would have application to the decontamination of equipment exposed to chemical warfare agents. Metal ion-induced radical formation from peroxymonosulfate anion may occur via two possible pathways.⁹ The radical products could then react with organic substrates.



A variety of radicals have been shown to react with esters of methylphosphonofluoridates via abstraction of hydrogen from the alcohol moiety.¹⁰ Thus, we have chosen to study the reaction of diisopropyl methylphosphonate (DIMP) in solutions of peroxymonosulfate and metal ions as the secondary alcohol moieties of DIMP are the same as that in the nerve agent, GB.

EXPERIMENTAL

Materials

Oxone was as technical grade product purchased from Aldrich and used as received and was determined to contain 87% of the theoretical amount of KHSO₅ by titration in water against standard sodium thiosulfate with KI as indicator. Concentrations of Oxone cited in the report are not corrected. Diisopropyl

methylphosphonate (DIMP) was a technical grade sample containing 7% by weight of water. Metal salts were analytical reagent grade and were used as supplied. Distilled water was used for solution preparations.

Oxidation Reactions

Reactions were performed at room temperature and solutions were prepared by adding standard solutions of reagents to 3 ml screw-cap glass vials. A typical reaction involved addition of appropriate aliquots of Oxone, diisopropyl methylphosphonate and metal ion solutions and distilled water to a vial using adjustable pipettes. After mixing, approximately 1 ml of the solution was transferred to a 5mm o.d. NMR tube and reactions monitored using ^{31}P NMR spectroscopy.

Product Identification

A solution of oxone (230 mg, 0.34 mmol), DIMP (68mg 0.35 mmol) and $\text{CrCl}_3 \cdot 6\text{H}_2\text{O}$ (54 mg, 0.20 mmol) in 5 ml of distilled water was heated at 50°C for 2 days, after which it was extracted once with CCl_4 . ^{31}P and ^{13}C spectra were recorded of the reaction mixture and the CCl_4 extract after addition of sufficient d_6 -benzene to allow locking of the spectrometer. The CCl_4 extract was also subjected to GC/MS analysis. (Need to add GC/MS data somewhere.)

Instrumentation

NMR spectra were obtained with either a Varian XL-200 or a Varian VXR-400S FTNMR system. The spectra were recorded at room temperature (18-21°C) without field stabilization. ^{31}P spectra were recorded at 81 MHz (XL-200) using a 62 ppm spectral width, 30° pulse angle, 1.6 sec acquisition time, 0.5 sec pulse delay and gated WALTZ decoupling. Chemical shifts are reported relative to external H_3PO_4 and are reproducible to ± 0.1 ppm. Typically, 500-100 transients were accumulated for each spectrum. Digital integration of peak areas in the ^{31}P spectra were used to obtain semi-quantitative information for estimating the extent of reaction. The error in the integration of individual spectra may be as large as $\pm 5\%$ of the total phosphorus response. ^{13}C spectra were recorded at 50 MHz (XL-200) or 100 MHz (VXR-400S) with a spectral width of 250 ppm, 40° pulse angle, 1.0 sec acquisition time, 2.5-3.0 sec pulse delay and full WALTZ decoupling. Chemical shifts were referenced to external tetramethylsilane in chloroform.

Gas Chromatography/Mass Spectrometry (GC/MS) was performed using a Finnigan model 5100 GC/MS in the chemical ionization mode. Methane (0.6 Torr internal source pressure) was used as the reagent gas. The instrument was equipped with a 25 m x 0.25 mm i.d. fused silica GB-1 capillary column (Foxboro/Analabs, North Haven, CT). The injection port temperature was 210°C, and the oven was programmed from 60-278°C at 10°C/min. The mass range was scanned from 60-450 amu at a rate of 1 scan/sec.

RESULTS AND DISCUSSION

By virtue of its composition ($2\text{KHSO}_5 \cdot \text{KHSO}_4 \cdot \text{K}_2\text{SO}_4$), solutions of Oxone are strongly acidic. Even so, under the conditions used in this study, the contribution of acid catalyzed hydrolysis to the loss of reactant is negligible.¹¹ The effects of various metal ions on the hydrolysis of DIMP in Oxone solution was monitored in a series of screening experiments. The metal ions were chosen to represent a range of oxidation potentials.¹² The conversion of DIMP to hydrolyzed products was measured within 3 hours of solution preparation and again after 6 days. The presence of Cr^{III} , Mn^{II} or Co^{II} markedly promotes the hydrolysis of DIMP in Oxone solution (Table 1). Control experiments demonstrated that in the absence of Oxone, the metal ions did not catalyze hydrolysis of DIMP in acidic solution. Fe^{II} and Ag^{I} provide no enhanced reactivity, although both of these ions are reported to promote the formation of reactive radicals in Oxone solution.^{9,13} In order to clarify the mechanism by which the low valence ions, Cr^{III} , Mn^{II} and Co^{II} , enhance the hydrolysis of DIMP in Oxone solutions, a series of reactions in Cr^{III} /Oxone solutions was monitored. The choice of Cr^{III} as the metal ion was largely dictated by the quality of the ^{31}P NMR spectra of the reaction solutions. The ^{31}P NMR linewidths in solutions containing either Mn^{II} or Co^{II} were (after oxidation) extremely broad. While allowing distinction of DIMP from hydrolysis products, quantitation of the spectra was less accurate than with Cr^{III} as the metal ion.

TABLE 1. Hydrolysis of DIMP in Oxone/Metal Ion Solutions^a

Metal Ion	Hydrolysis (%) ^b		Couple	E°, V ^c
	3 hrs	6 days		
Fe ^{II}	0	0	Fe ^{II} --> Fe ^{III} + e ⁻	0.68
Cr ^{III}	30	30 ^d	2Cr ^{III} + 7H ₂ O --> Cr ₂ O ₇ + 6e + 14H ⁺	1.33
Mn ^{II}	30	37 ^e	Mn ^{II} --> Mn ^{III} + e ⁻	1.51
Co ^{II}	86	96	Co ^{II} --> Co ^{III} + e ⁻	1.84
Ag ^I	0	0	Ag ^I --> Ag ^{II} + e ⁻	1.99
--	0	2		--

^a 0.05M Oxone, 0.001 M (Metal ion), 0.01 M DIMP

^b Fraction of ³¹P response corresponding to phosphonic acids.

^c Ref 12

^d Distinctive color of Cr (VI) in solution after reaction.

^e Oxidation to Mn^{IV} (MnO₂) or Mn^{VII} (MnO₄⁻) not considered to have occurred as distinctive precipitate or pink coloration was not evident.

From the screening experiments (Table 1), it is clear that the effect of added metal ions was largely manifested in a short period after the solutions were prepared. Thereafter, subsequent reaction was considerably slower even though active oxidant remained in solution (detected by starch/iodide paper). Further reaction was initiated by addition of the metal ion to the partially reacted solution (Table 2). When repeated with a higher concentration of chromium (III), the distinctive color of chromium (III) faded and changed to orange, characteristic of chromium (VI).¹⁴ Cr^{VI} is ineffective in promoting hydrolysis of DIMP in oxone solution. No hydrolysis of DIMP in 0.05 M Oxone solution containing 0.005 M Cr^{VI} was evident 6 days after solution preparation.

The influence of Cr^{III}, Oxone and DIMP concentration on the hydrolysis of DIMP is summarized in Tables 3-5. The conversion of DIMP reaches a maximum at a Cr^{III} concentration of approximately 0.005 M (Table 3), while DIMP conversion against Oxone concentration has a minimum (Table 4). Finally, the amount

of DIMP that reacts is seen to increase with increasing concentration of DIMP (Table 5).

TABLE 2. Hydrolysis of DIMP Promoted by Chromium (III)-Oxone Solution

Time, days	% Hydrolysis of DIMP	Additions after Analysis
0	0	1.0 umole Cr ^(III)
1 ^a	30	
6	30	1.0 umole Cr ^{III}
7	40	1.0 umole Cr ^{III}
8	63	

^a Concentration after first additions 0.05M, oxone, 0.01M DIMP, and 0.001M chromium (III)

TABLE 3

Percentage of DIMP Hydrolyzed as a Function of Chromium (III) Concentration^a

Percent Hydrolyzed ^b	Chromium (III), M
33	0.0025
64	.0050
68	.010
55	.015
37	.020

^a 0.01 DIMP in 0.053M Oxone

^b After 24 hours

Table 4
 Percentage of DIMP Hydrolyzed as a Function of
 Oxone Concentration

Percentage Hydrolyzed ^b	Oxone, M
16	0.005
10	.01
32	.02
48	.03
67	.05

^a 0.01M DIMP in 0.005 M Chromium (III)

^b After 24 hours

Table 5
 Hydrolysis of DIMP as a Function of
 Initial DIMP Concentration^a

DIMP Hydrolyzed, umoles/ml ^b	DIMP, M
2.7	0.005
4.9	.010
6.8	.015
9.6	.020

^a 0.053M Oxone in 0.005M chromium (III)

^b After 24 hours

TABLE 6.

³¹P NMR Parameters of Species Present in DIMP/Oxone/Cr^{III} Solution

³¹ p	¹ H Coupling	Assignment
33.54	q,t ² J _{PCH} = 17.3 Hz, ³ J _{POCH} = 7.9 Hz	DIMP
34.91	-----	CDIMP ^a
35.39	-----	CDIMP ^a
30.34	q,d ² J _{PCH} = 17.1 Hz, ³ J _{POCH} = 8.6 Hz	IMPA
29.95	q ² J _{PCH} = 17.5 Hz	MPA
29.47	q,d ² J _{PCH} ~ 17 Hz ³ J _{POCH} ~ 8 Hz	CIMPA ^{a,b}
27.74 ^c	q,t ² J _{PCH} ~ 17.5 Hz, ³ J _{POCH} ~ 8 Hz	DIMP
28.52c	q,t ² J _{PCH} ~ 18 Hz ³ J _{POCH} ~ 8 Hz	CDIMP ^a
29.28c	q,t ² J _{PCH} ~ 18 Hz ³ J _{POCH} ~ 8 Hz	CDIMP ^a

^a See text for structure assignment.

^b CIMPA = 1-chloromethylethyl 1-methylethyl methylphosphonic acid

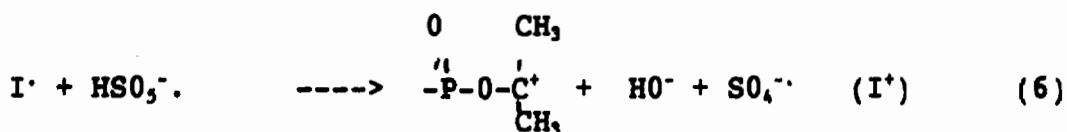
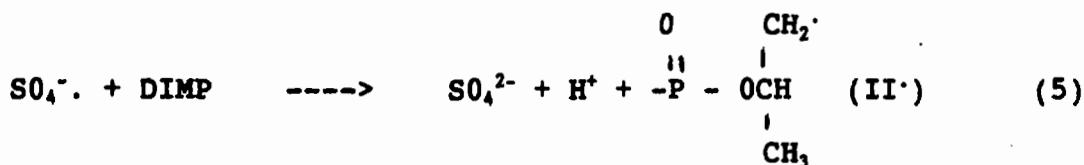
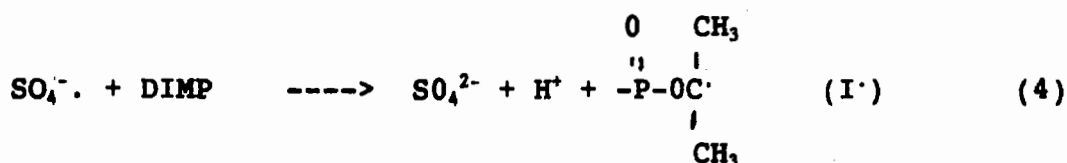
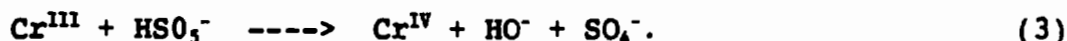
^c Chemical shifts in CCl₄/d₆-benzene.

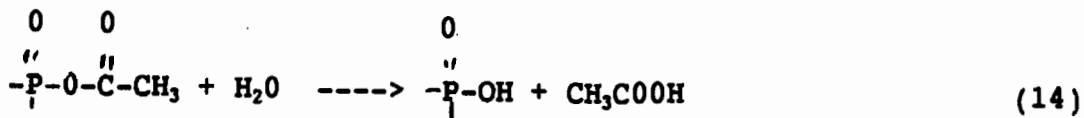
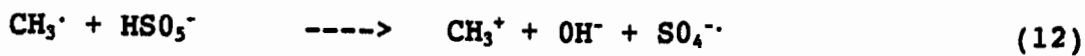
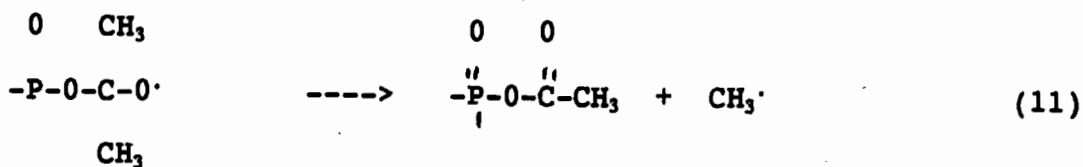
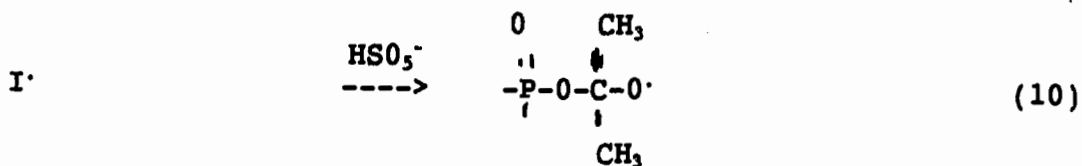
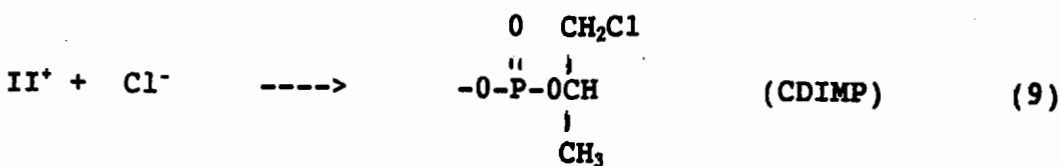
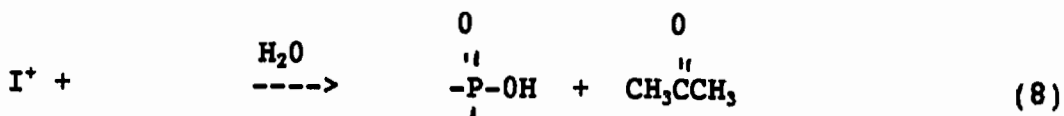
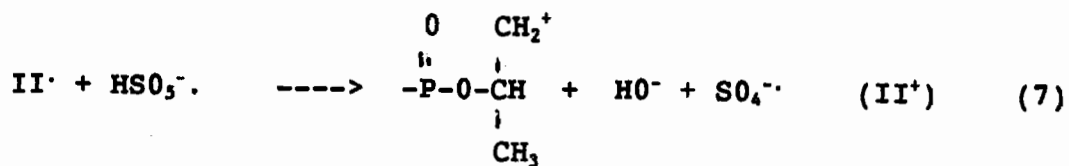
The behavior of the DIMP/Oxone/Cr^{III} system can be explained if the reactions are initiated by Cr^{III} induced decomposition of monoperoxysulfate to give a reactive radical as shown in equations 1 or 2. Neither Cr^{III} nor Oxone alone results in the accelerated hydrolysis observed when both are present. In addition, products formed in which a methyl hydrogen is replaced by a chlorine atom cannot be adequately explained by an alternate mechanism.

Formation of the identified products (Table 6) is accommodated by reactions 3 to 14. The decomposition of peroxymonosulfate is presumed to yield the sulfate radical anion and hydroxide (equation 8) rather than sulfate and hydroxyl radical in accordance with the work of Gilbert and Stell,⁹ who found that the Ti^{III} promoted decomposition followed this course.

On the other hand, the thermodynamically preferred products of the decomposition are SO_4^{2-} and $\text{HO}\cdot$,⁹ and it is possible that the hydroxyl radical is formed in the presence of Cr^{III} . In either case, the observed products are consistent with a radical initiated process.

HSO_5^- is an extremely strong one-electron oxidant of radicals, more powerful than $\text{S}_2\text{O}_8^{2-}$ or H_2O_2 .⁹ Thus the fate of I \cdot and II \cdot is expected to be oxidation to the corresponding carbonium ions, I $^+$ and II $^+$. Once formed by oxidation of I \cdot , I $^+$ will rapidly hydrolyze to ultimately yield IMPA and acetone, a minor product from the reaction. Trapping of II $^+$ by chloride yields the diastereomeric product, CDIMP. Acetic and formic acids, which were identified in the reaction, do not form via further oxidation of acetone. In a control experiment, acetone was reacted with HSO_5^- and Cr^{III} at 50°C for 20 hrs, after which the distinctive color of chromium (VI) appeared. Neither of the carboxylic acids were detected in solution by ^{13}C NMR at this time or after a further 60 hrs. Formation of these products may occur according to reaction 10 - 14, which is analogous to the previously proposed reaction of oxygen conjugated radicals derived from alcohols or ethers with HSO_5^- .⁹ The predominance of acetic and formic acids over acetone indicate that reaction 15 is favored over 11. Rapid oxidation of the methyl radical to CH_3^+ , with concomitant reaction with water would yield methanol. $\text{HSO}_{15}^-/\text{Cr}^{\text{III}}$ was shown in a control experiment to oxidize methanol to formaldehyde and formic acid.





Thus, the hydrolysis of DIMP is initiated by Cr^{III} promoted decomposition of peroxymonosulfate to produce a reactive radical species. The efficiency of reaction of the hydroxyl radical (and therefore H_2O_2) with organic substrates in Fenton's system is dependent upon the metal ion concentration.

Our observations of the $\text{Cr}^{\text{III}}/\text{HSO}_5^-$ system do not indicate whether there is turnover of the metal ion. Certainly, Cr^{VI} does not oxidize HSO_5^- , simultaneously providing a low-valent chromium species (analogous to equation 21 for Fenton's system) initiating further decomposition of HSO_5^- to form reactive radicals (equation 7). Turnover of Cr^{III} must rely upon reduction of the higher-valent chromium ions (Cr^{IV} , Cr^{V}) by intermediate radicals.

Evidence of chromium turnover cannot be obtained from the stoichiometry of reactions in the $\text{HSO}_5^-/\text{Cr}^{\text{III}}/\text{DIMP}$ system. Oxidation of Cr^{III} can provide three equivalents of $\text{SO}_4^{\cdot-}$ (equation 2). Each radical then initiates a chain sequence (equations 4-7 and 10-12). The fate of the radical species is not limited to the reactions shown in these equations and the chain may be terminated by a number of plausible reactions. The radical chains may be terminated by dimerization of $\text{SO}_4^{\cdot-}$ to form $\text{S}_2\text{O}_8^{\cdot-}$; other reactions forming oxygen; or oxidation of low-valent ions to form sulphate ion.

The effectiveness, or lack thereof, displayed by the metal ions other than chromium (III) in promoting hydrolysis of DIMP as reported in Table I deserve comment. Since iron (II) reacts rapidly with HSO_5^- ($k_2 = 3 \times 10^4 \text{ M}^{-1}\text{s}^{-1}$),⁹ one might be surprised by the lack of evidence for reaction between DIMP and $\text{SO}_4^{\cdot-}$ in the presence of $\text{Fe}(\text{II})$. However, it is likely that Fe^{II} also reacts rapidly with $\text{SO}_4^{\cdot-}$ and acts as a scavenger⁹, while iron (III) is too weak a reducing agent to react with HSO_5^- to regenerate Fe^{II} . Mill and co-workers¹⁵ showed that Fe^{II} in the presence of H_2O_2 could promote decomposition of O-ethyl S-ethyl methylphosphonothioate, presumably through formation of $\cdot\text{OH}$. The lack of reactivity of DIMP in the presence of iron (II) is further indirect evidence that iron (II) reacts with HSO_5^- to form OH^{\cdot} and $\text{SO}_4^{\cdot-}$ rather than OH^{\cdot} and $\text{SO}_4^{\cdot-}$.

The lack of reactivity in the $\text{Ag}^+/\text{HSO}_5^-$ system has a simpler explanation. While Ag^+ has been reported to catalyze the decomposition of HSO_5^- , the proposed mechanism requires the presence of $\text{S}_2\text{O}_8^{2-}$ as a co-catalyst.¹² The role of $\text{S}_2\text{O}_8^{2-}$, which has a more positive oxidation potential than HSO_5^- (2.0 compared to 1.44 v) is to oxidize Ag^{I} to Ag^{II} . The oxidation potential for the $\text{Ag}^{\text{I}}/\text{Ag}^{\text{II}}$ couple is the most negative of the metal ions studied.

Mn^{II} and Co^{II} are both effective in promoting hydrolysis of DIMP in Oxone solution. With Mn^{II} , the conversion of DIMP is similar to Cr^{III} and does not warrant further comment.

The effectiveness of Co^{II} is far greater than Cr^{III} or Mn^{II} . Calculation of the stoichiometry of the reaction reveals that after 3 hours, the ratio of DIMP reacted per mole of Co^{II} is 8.6. For Cr^{III} , under the same conditions, this ratio is only 1.0, after correction for the greater number of electrons involved in oxidation of Cr^{III} to Cr^{VI} . The radical chain path is therefore much longer with cobalt (II) as the initiator, rather than chromium (III) or manganese (II). One reason for this may be that cobalt (III) is a sufficiently strong oxidizing agent to oxidize HSO_3^- to HSO_4^- , which decomposes to form O_2 and SO_4^{2-} as well as serve to regenerate cobalt (II). Edwards¹⁶ established that cobalt (II) was the most efficient metal-ion catalyst for the decomposition of Caro's acid.

CONCLUSIONS

1. Hydrolysis of the G-agent simulant, DIMP, in oxone solution is promoted by the presence of low-valent metal ions. The reaction is initiated by radical formation from decomposition of HSO_3^- to form, by analogy with other systems, OH^- and SO_4^{2-} .

2. No effort has been made to optimize the metal ion/oxone system with respect to the most important parameter in decontamination applications of the chemistry, conversion of the phosphonate ester to hydrolysis products. Nevertheless, the following observations are pertinent regarding the potential of metal ion/peroxide systems as decontamination solutions. The desired reactions are initiated by decomposition of the peroxide. The presence of organic species in metal ion/peroxide systems has accurately been described by others^{9,15} as providing a trap for radicals, which otherwise would react to liberate O_2 , and in the case of HSO_3^- , the dimer $\text{S}_2\text{O}_8^{2-}$. Consequently, solutions of this type cannot be stored. The peroxy compound and metal ion must be mixed after, or at best, immediately before the addition of organic species to the reaction. The efficiency of the system, as measured by the extent of reaction of added substrates will vary greatly, depending on the efficiency of the substrate to trap radicals as well as the presence of other species in solution. In a practical application, there is very little control over potential contaminants.

ACKNOWLEDGEMENTS

The authors are grateful to D.K. Rohrbaugh of the Chemistry Division, Research Directorate, CRDEC for obtaining mass spectra.

LITERATURE CITED

1. W.T. Beaudry, L.L. Szafraniec, D.K. Rohrbaugh, and D.R. Leslie, "Reactions of CW Agents in DS-2," Proceedings of the 1990 Chemical Defense Research Conference, November 1990.
2. GAO Report NSIAD-90-10 "Hazardous Materials - DOD Should Eliminate DS2 from It's Inventory of Decontaminants" April 1990.
3. R.L. Gustafson, S. Chabarek, and A.E. Martell, "A Kinetic Study of the Copper (II) Chelate-catalyzed Hydrolysis of Isopropyl Methylphosphonofluorideate (sarin)," J. Am. Chem. Soc., **84**, 2300 (1962).
4. J. Epstein, J.J. Callahan, and V.E. Bauer, "The Kinetics and Mechanisms of Hydrolysis of Phosphonothiolates in Dilute Aqueous Solution," Phosphorus, **4**, 157 (1974).
5. Y. Yang, L.L. Szafraniec, W.T. Beaudry, and Dennis K. Rohrbaugh, "Oxidative Detoxification of Phosphonothiolates," J. Am. Chem. Soc., **112**, 6621 (1990).
6. R.J. Kennedy and A.M. Stock, "The Oxidation of Organic Substances by Potassium Peroxymonosulphate," J. Org. Chem., **25**, 1901 (1960).
7. R.A. Sheldon and J.K. Kochi, Metal-Catalyzed Oxidations of Organic Compounds, Academic Press, NY 1981.
8. C. Walling, "Fenton's Reagent Revisited," Acc Chem Res, **8**, 125 (1975).
9. B.C. Gilbert and J.K. Stoll, "Mechanisms of Peroxide Decomposition. An ESR Study of the Reactions of the Peroxomonosulphate Anion (HOOSO_3^-) with Ti (III), Fe (II), and alpha-Oxygen Substituted Radicals," J. Chem Soc. Perkins Trans. **2**, **1990**, 1281.
10. S. Preis, Z. Oser, L.M. Kindley, H.E. Podall, and G.L. Braude, "Studies of Free Radical Initiated Oxidation of G Agents," final report contract DA-18-035-AMC-287(A), August 1966.
11. R.F. Hudson and L. Keay, "The Hydrolysis of Phosphonate Esters," J. Chem Soc., **1956**, 2463.
12. R. Weast and D. Lide, CRC Handbook of Chemistry and Physics, ed., CRC Press, Inc., Boca Raton, FL. 1989.
13. R.C. Thompson, "Catalytic Decomposition of Peroxymonosulphate in Aqueous Perchloric Acid by the Dual Catalysts Ag^+ and $\text{S}_2\text{O}_8^{2-}$ and by Co^{2+} ," Inorg Chem, **20**, 1005 (1981).

14. C. Altman and E.L. King, "The Mechanism of Exchange of Chromium (III) and Chromium (VI) in Acidic Solution," J. Am Chem Soc, 83, 2825 (1961).

15. T. Mill, T. Pettit, A. Richardson, and W. Haag, "New Concepts for Aqueous Decontamination: Catalytic Decontamination of CW Agents Using Peroxygen Compounds," CRDEC-CR-055, November 1989.

16. D.L. Ball and J.O. Edwards, "The Catalysis of the Decomposition of Caro's Acid," J. Phys. Chem., 62, 343 (1958).

DMMP-TC REACTION STUDY

Leonard J. Szafraniec, Linda L. Szafraniec and V. Bruce May
U.S. Army Chemical Research, Development and Engineering Center
Aberdeen Proving Ground, Maryland 21010-5423

ABSTRACT

³¹P NMR was used to characterize the intermediate compounds formed during the pyridine catalyzed reaction to produce methylphosphonic dichloride (DC) from dimethyl methylphosphonate (DMMP) and thionyl chloride (TC) at elevated temperatures. It was determined that methyl methylphosphonochloridate (MMPC), P,P'-dimethyl dimethyldiphosphonate (symmetrical pyro), and mixed pyros are produced in significant quantities early in the reaction but are rapidly converted to DC as the chlorination approaches completion. Inverse addition (DMMP added to TC) or the lack of pyridine catalyst in the reaction mixture likewise resulted in the initial formation of pyro compounds. The MMPC intermediate was found to have a half-life of 53.2 hr at 21.5 °C whereas the symmetrical pyro degraded less than 4% after 167 hr at the same temperature.

INTRODUCTION

During 1983 and 1984, the reaction of thionyl chloride (TC) with dimethyl methylphosphonate (DMMP) to produce methylphosphonic dichloride (DC) was extensively studied by both Olin Chemicals¹ and Crawford and Russell, Inc.² Work done by these contractors was concerned primarily with maximizing the yield for batch-wise production of DC. Although the formation of various intermediates was noted by both contractors, no efforts were made to quantitate either the amounts or the lifetimes of the various species present. Consequently, the present study was undertaken to identify these intermediates and to determine their concentrations as a function of time during the course of the reaction.

A total of five laboratory experiments on the DMMP-TC reaction were conducted. The first three of these experiments were designed to follow plant time, temperature, and reactant addition as closely as possible, and to provide data on the decomposition of the major intermediates in situ at ambient temperature. Experiments to determine the effects of chlorinating without the catalyst present and of altering the order of addition of the reactants also were conducted.

EXPERIMENTAL SECTION

General Procedure. All syntheses of DC were carried out in a 100-ml, three-neck, conical flask fitted with an addition funnel, thermometer, condenser (Hopkins coil), nitrogen inlet, and a magnetic stirrer. The condenser was cooled to 4.4 °C by a Lauda RC-64 Refrigerating Circulator/Bath and was connected to a series of traps which protected the system from the atmosphere and provided a positive pressure of 0.3 psi. The reaction flask was purged with dry nitrogen and then charged with 25.0 g DMMP and 1.60 g of pyridine. This mixture was heated in an oil bath to an internal temperature of 80 +/- 4 °C. TC was added dropwise to the stirred reaction mixture. An addition rate of ca. 6.6 ml/0.5 hr was maintained throughout the 3 hr addition period. In Runs 1 and 3, the additions were made without interruption. In Run 2, the addition was made more portionwise so that the addition was stopped ca. 4 min before a sample was removed for analysis. After completing the TC addition, the reaction mixture was maintained at 85 +/- 3 °C for at least an additional 2 hr. Samples of the reaction mixture were removed at 30 min intervals for immediate analysis using ³¹P FTNMR. Glass pipettes which had been flame dried and flushed with nitrogen were used in transferring the reaction mixture to the 5-mm o.d. NMR tubes which had been similarly dried.

The procedure used for Run 4 was almost identical to that described above except that the pyridine catalyst was not added to the DMMP at the beginning of the run. After the reaction had proceeded for 6.4 hrs, 0.4 g of pyridine was added to the mixture which had been allowed to cool to 65 °C. After the addition, the reaction mixture was heated and held at 87 +/- 2 °C for 45 min.

Run 5 was conducted in a manner similar to that described above for Runs 1-3 except that the DMMP was added dropwise over a 3 hr period to a stirred mixture of the TC and pyridine. Also, the temperature of the reaction mixture for the first 2.75 hr did not exceed 80 °C.

Decomposition Studies. Two samples from the reaction mixture of Run 3 which contained the methyl methylphosphonochloridate (MMPC, 2, Table 1) and the P,P'-dimethyl dimethyldiphosphonate (sym pyro, 3) near their respective maximum concentrations were placed into 5-mm o.d. Pyrex NMR tubes, sealed with Parafilm, and maintained at 21.5 °C for one week. These samples were monitored periodically using ³¹P FTNMR to determine the rate of disappearance of the two intermediates.

RESULTS

Plant Simulation. The results of the first 3 experiments (fig. 1-3) revealed that the concentration of the intermediate 2 maximized between 1.0 and 1.5 hr after the start of the reaction and that it could represent as much as 37% of the reaction mass. It was also found that 3 formed in relatively large amounts (ca. 50% of the reaction mass) maximizing between 0.5 and 1.0 hr. In addition, several other pyro compounds were observed by ³¹P NMR during the course of the reaction. With the exception of the cyclic trimer, 7, the individual mixed pyro and linear trimer compounds could not be quantitated due to overlapping peaks in the NMR spectrum. The total concentration of these mixed pyros and trimers, including 7, peaked between 1.0 and 1.5 hr and, at times, exceeded 70% of the reaction mass.

Reaction Without Catalyst Present. The results of the run without pyridine catalyst present are shown in fig. 4. The intermediates, consisting

almost completely of pyro compounds, accounted for greater than 70 % of the reaction mass. Addition of a fractional charge (25%) of catalyst after the reaction had stabilized in composition fully converted these pyros to DC.

Inverse Addition Reaction. The inverse addition reaction in which DMMP was added to the TC and pyridine catalyst also resulted in the initial formation of the pyro compounds. The concentration of 3 reached a maximum of ca. 50% at 1.25 hr, and the concentration of the mixed pyros and trimers maximized at ca. 2.25 hr at ca. 23%. In this reaction, 2 reached a maximum of 54% at 2.75 hr (see fig. 5).

Stabilities of the Intermediates, 2 and 3. Intermediate 2 was found to have a half-life of 53.2 hr at 21.5 °C in the reaction mixture (see fig. 6). The ³¹P NMR spectra indicated that the chloro-ester, 2, was reacting with the mixed pyro compounds to form the cyclic trimer, 7. On the other hand, the sym pyro, 3, was quite stable degrading less than 4% after 167 hr at 21.5 °C (see fig. 7).

DISCUSSION

The chemical reactions involved in producing DC from the catalyzed DMMP-TC process are numerous and not completely understood. However, rational equations can be written which account for the presence of the observed intermediates. Several of these equations are shown in table 1. Based on our observations, we believe the process to produce DC proceeds in the following manner. Upon addition of TC to DMMP, 2 (eq. 1) is formed exothermally. This compound, however, does not accumulate in the early stages of the process because it reacts rapidly with DMMP to form 3 (eq. 2). The concentration of 3 increases and is observed in the ³¹P NMR spectrum as the earliest major intermediate. This compound immediately starts to compete with DMMP for 2 which gives rise to the trimer, 4, (eq. 3). Longer chain pyro compounds also can form by this same reaction. The length of these pyro compounds is apparently dependent on temperature and the rate of TC addition. Compounds 3 and 4 then react with TC to form the monochloro pyro compounds, 5 and 6, respectively (eqs. 4 and 5). These two compounds continue to react with either DMMP or 3 to give additional longer chain pyro compounds or react with TC to give the symmetrical dimethyldiphosphonyl chloride or trimethyltriphosphonyl chloride. Since there is evidence in the ³¹P NMR spectra for the presence of a cyclic trimer, 6 probably also cyclizes to give 7 as shown in eq. 6.

The number of possible reactions in the early stages of the DMMP-TC process is potentially large; however, almost all appear to consist of P-O-C cleavage or P-O-P formation. In the latter phase of the reaction, after all of the DMMP has reacted to give various pyro compounds, the major reactions become cleavage of P-O-P bonds. It is at this phase that 2 appears to accumulate in the reaction mixture primarily from the reaction shown in eq. 7. Additional 2 can also form from the reaction of TC with other pyro compounds still having a terminal methoxy group. In the final phase of the process, with no 3 nor DMMP with which to react, 2 is finally converted to DC as shown in eq. 8. The major portion of the DC which is formed, however, comes from the reaction of the catalyzed TC on the various pyro compounds including 7, as shown in eqs. 9 and 10.

CONCLUSIONS

Quantitative measurement of the species present during the DMMP-TC reaction showed that methyl methylphosphonochloridate, P,P'-dimethyl dimethyldiphosphonate and mixed pyro compounds are produced in significant quantities early in the reaction but are rapidly converted to DC as the chlorination approaches completion. Inverse addition of the reactants also results in the initial formation of pyro compounds as does the lack of pyridine catalyst in the reaction mixture. However, addition of even a fractional charge of catalyst fully converts the pyros to DC.

At ambient temperature (21.5 °C), the methyl methylphosphonochloridate was found to have a half-life of 53.2 hr whereas the P,P'-dimethyl dimethyldiphosphonate degraded less than 4% after 167 hr.

REFERENCES

1. Olin Chemicals, Contract No. DAAK11-84-C-0005, Methyl Phosphonic Dichloride Project, Final Comprehensive Report. June 1984.
2. Crawford and Russell, Inc., Contract No. DAAK11-83-C-0094, MPOD Commercial Facility for the Production of Methylphosphonic Dichloride, Final Report. June 1984.

TABLE 1

Equations Involved in the Formation of DC from DMMP and TC.

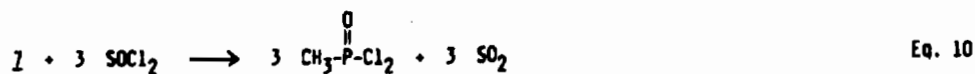
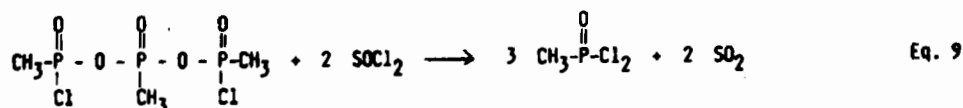
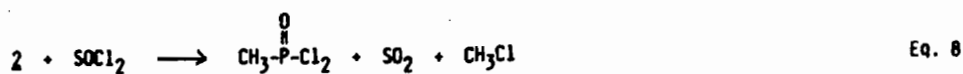
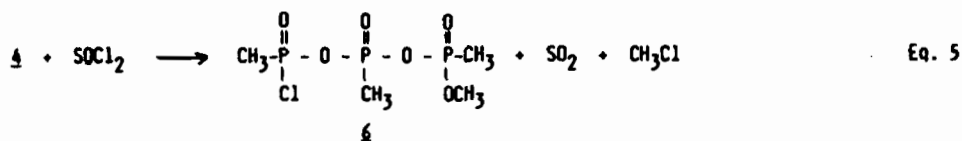
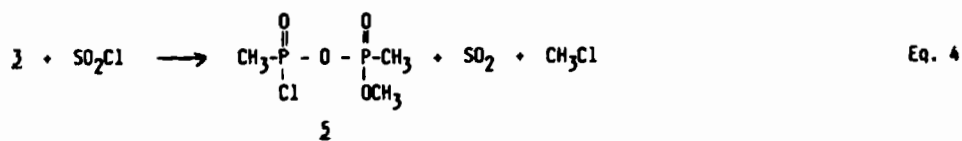
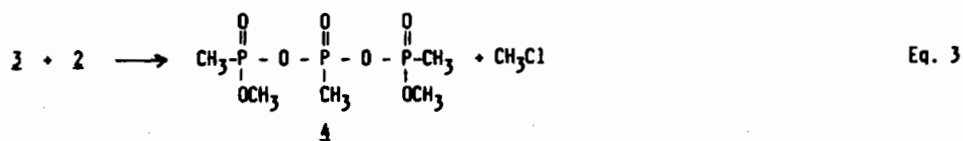
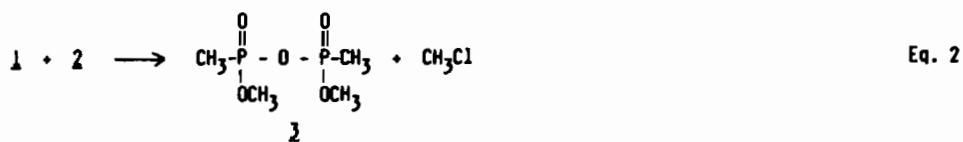
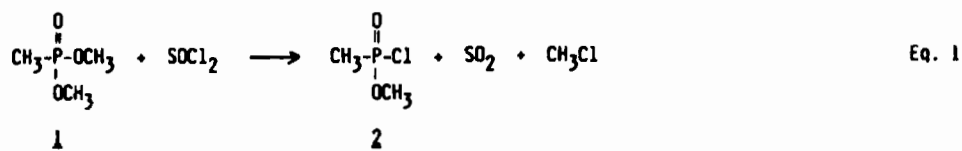


FIGURE 1

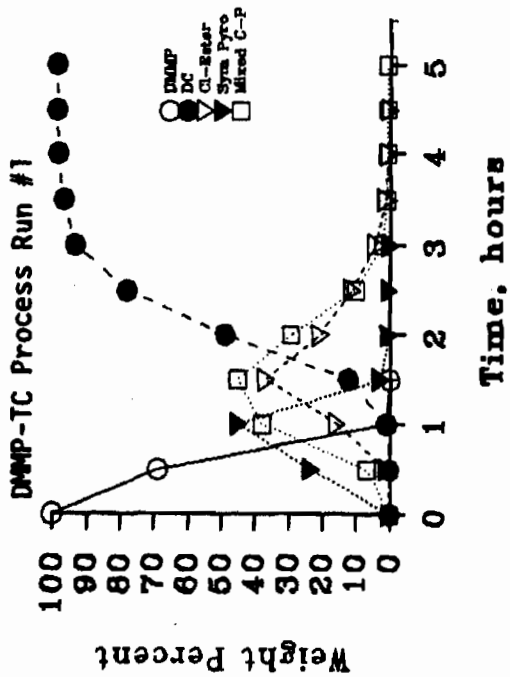


FIGURE 2

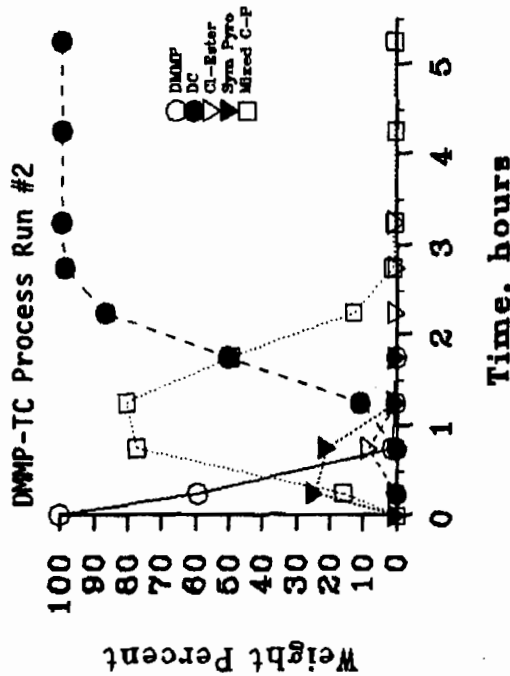


FIGURE 3

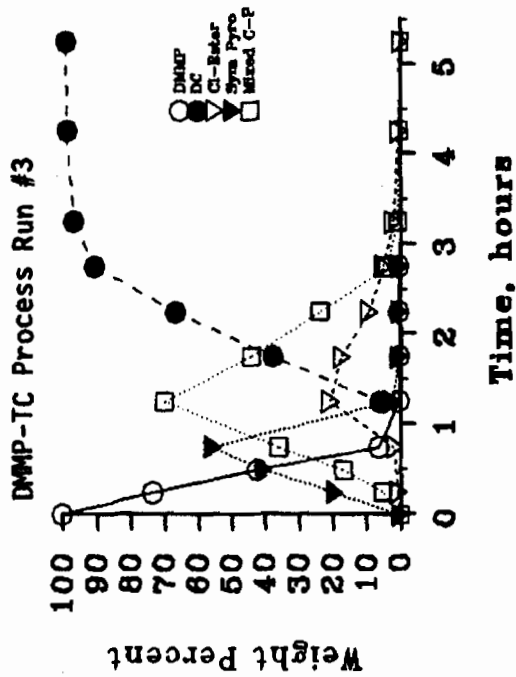
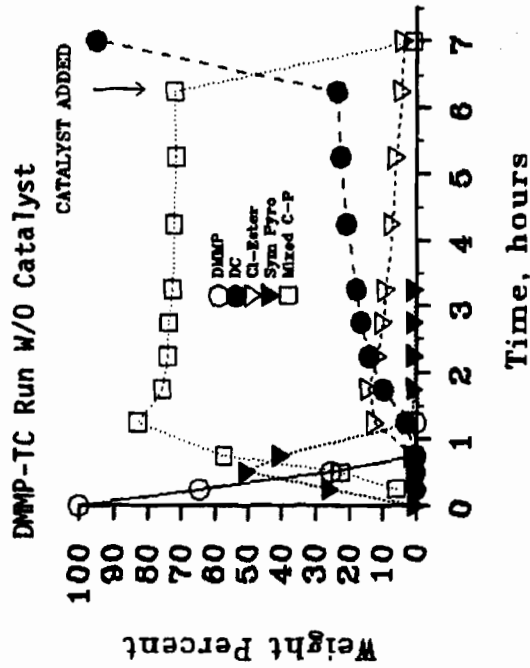
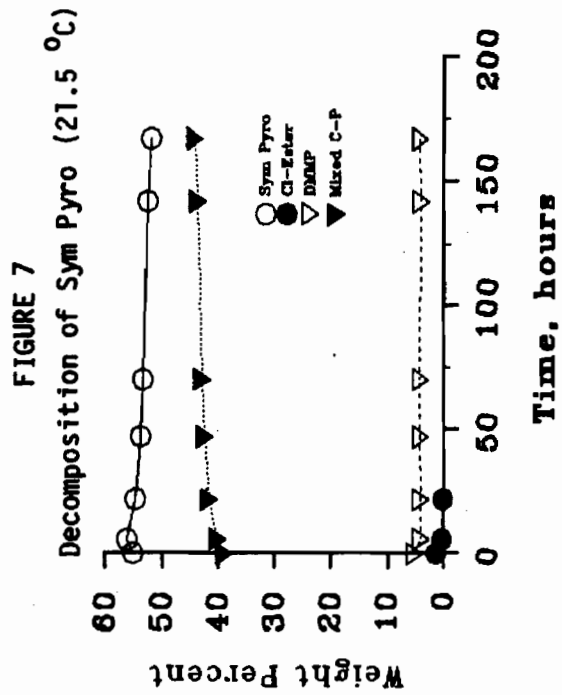
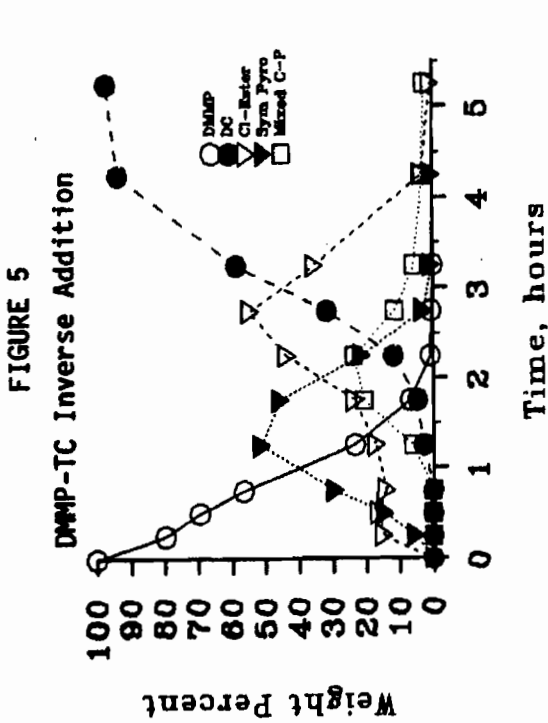
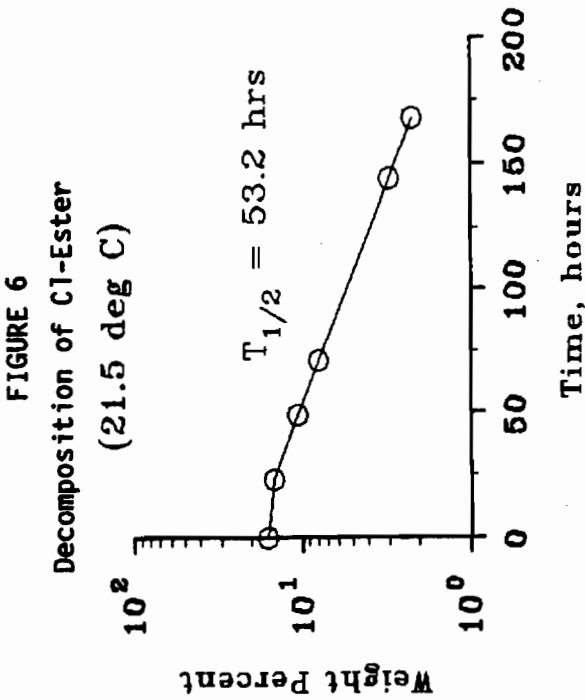


FIGURE 4





BLANK

830

DIFFUSION OF SMALL FLUORINATED MOLECULES IN POLYMERIC MEDIA
STUDIED VIA HIGH-RESOLUTION SOLID-STATE ^{19}F NMR SPECTROSCOPY

Paul J. Toscano,* E. James Schermerhorn, John Waechter,
Peiguang Zhou, and Harry L. Frisch
Department of Chemistry, State University of New York at
Albany, Albany, NY 12222

ABSTRACT

High-resolution solid-state ^{19}F NMR spectroscopy was employed in order to assess diffusion constants for hexafluorobenzene (HFB) and 3,5-bis(trifluoromethyl)aniline (TFMA) in commercial polystyrene (PS) and butyl rubber (BR) films. The results for the TFMA/PS system corroborate those obtained previously via resonant nuclear reaction analysis.

INTRODUCTION

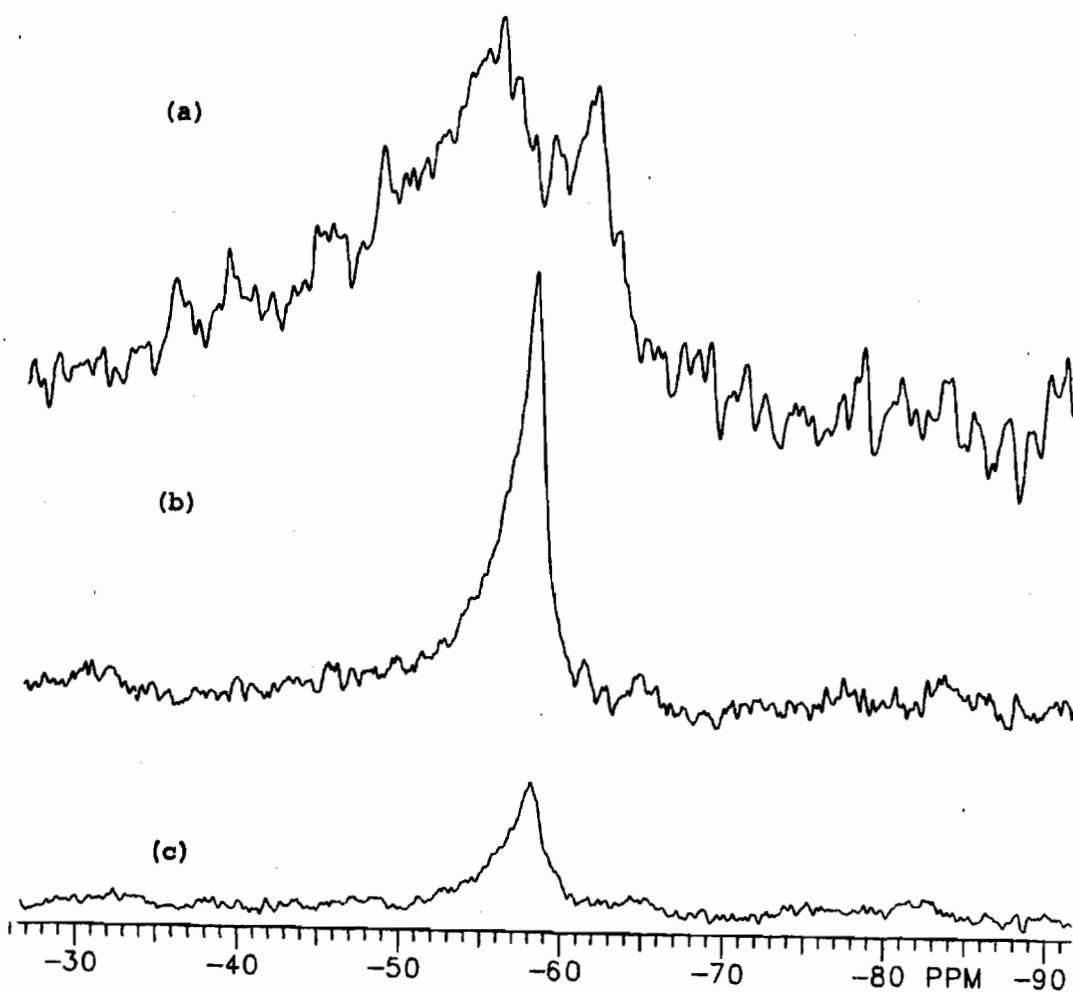
Previously, we have demonstrated the value of ^{31}P and ^{19}F magic-angle spinning (MAS) NMR spectroscopy to the detection of dual-mode sorption of small phosphorus^{1,2} and fluorine² containing molecules by commercial polystyrene (PS), a glassy polymer. That is, the NMR method was able to distinguish between (at least) two distinct types of physically sorbed species having relatively free and constrained motional properties, respectively. In this contribution, we report upon our continued investigations regarding the application of high-resolution solid-state NMR methods to the study of the sorption of small molecules in polymeric media. Specifically, we describe the use of ^{19}F solid-state NMR spectroscopy for the purpose of determining diffusion (desorption) coefficients in the hexafluorobenzene (HFB)/PS, 3,5-bis(trifluoromethyl)aniline (TFMA)/PS and HFB/butyl rubber (BR) systems.

EXPERIMENTAL SECTION

Properties of the PS film (Opticite 320, Dow Chemicals) and the methods of its doping have been reported elsewhere.¹ The doped PS films had T_g 's of 106.5°C (HFB) and 103.5°C (TFMA), respectively, and thus were glassy polymers. DSC measurements were accomplished on a TA Instruments 2000/55SX system. Films of butyl rubber (Polysar Rubber Corp., $T_g = -74^\circ\text{C}$) were cast from THF solution on smooth glass surfaces.

FIGURE 1

^{19}F NMR Spectra of the TFMA/PS System: (a) Static (11,155 scans); (b) MAS (before desorption; 12,691 scans; spin rate 7.3 kHz); (c) MAS (after 25.5 h of desorption; 10,756 scans; spin rate 7.0 kHz). All spectra have 60 Hz line broadening and are printed at the same absolute intensity.

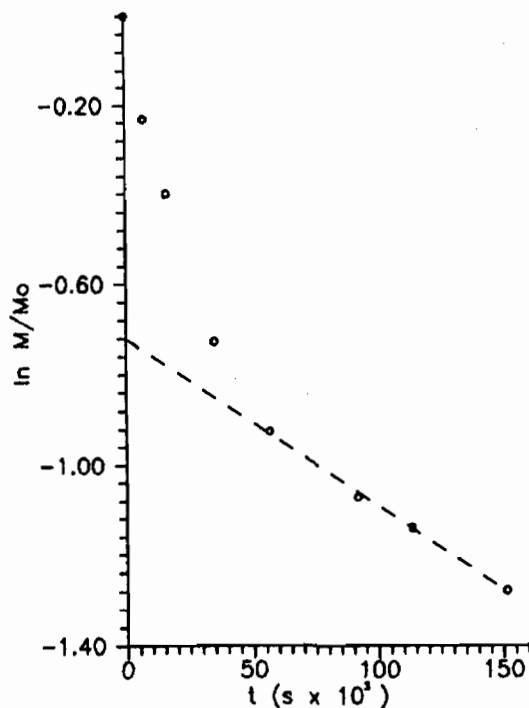


The doped films were cut quickly into small pieces and loaded into standard rotors for the NMR experiments. MAS and static ^{19}F NMR spectra were collected in the single-pulse mode (5.0 μs pulse, 100 kHz window, 5.0 s repetition) on a Varian XL-300 spectrometer (282.203 MHz) and referenced with respect to external CFCl_3 . Rotors were opened to ambient atmosphere for appropriate periods of time and spectra were obtained to assess desorption; integration of absolute signal intensity determined the relative amount of sorbent remaining in the polymer as a function of time.

DISCUSSION

Static and MAS ^{19}F NMR spectra of TFMA-doped PS film are depicted in Fig. 1a and 1b, respectively. Though anisotropic, the MAS spectrum appears to be a superposition of broad (-57.2 ppm) and relatively narrow (-58.1 ppm) signals, suggesting dual-mode sorption of the TFMA molecules. Fig. 1c illustrates a typical spectrum after the polymer film was exposed to air in order to allow desorption of sorbent. Fig. 2 summarizes the desorption data with a plot of the \ln of remaining sorbed material vs. time.

FIGURE 2. Desorption Data for the TFMA/PS System



At longer time periods, the behavior becomes linear with slope = $-\frac{D\pi^2}{l^2}$ where D is the diffusion coefficient and l is

the thickness of the film.³ With the slope determined by linear correlation analysis to be -3.71×10^{-6} (correl coeff = 0.993) and l being 5.1×10^{-3} cm, we calculate $D = 1.0 \times 10^{-11}$ cm²/s. This value for D is gratifyingly close to that of 1.2×10^{-11} cm²/s determined by Umezawa et al.⁴ by the method of resonance nuclear reaction analysis for the TFMA/PS system.

The ¹⁹F NMR spectrum of the HFB/PS system (Fig. 3a), when spinning rate is reduced, clearly exhibits three signals. The very sharp signal (-162 ppm) can be assigned to surface sorbed material,⁵ while the less narrow signal (-152.5 ppm) and the broad spinning sideband manifold (isotropic signal at -153 ppm as determined by variation of the spin rate) can be assigned to dual-mode sorbed HFB species. Figs. 3b and 3c illustrate the desorption of HFB as a function of time. An analysis entirely analogous to that for the TFMA/PS system above, gives a slope of -1.28×10^{-4} (correl coeff = 0.999) and $D = 3.4 \times 10^{-10}$ cm²/s. Figs. 3b and 3c also illustrate the apparent equilibration of the surface sorbed HFB concentration with time; the intensity of the small sharp resonance at -162 ppm remained essentially constant after the initial exposure to ambient atmosphere.

The HFB/BR system presented a different challenge. The magic-angle spinning process caused the pieces of doped butyl rubber film to uniformly redistribute themselves into a hollow cylinder with outer radius (R_o) of 0.20 cm and inner radius (R_i) of 0.12 cm. Fig. 4 shows the ¹⁹F NMR spectra for HFB/BR under nonspinning and MAS conditions. In each spectrum, one symmetrical signal occurs at -153.4 ppm (line widths are 665 and 260 Hz, respectively). At short time periods, desorption from the hollow cylinder is approximately linear with respect to $t^{1/2}$.⁶ A plot of relative weight loss of HFB vs. $[t/(2R_o - 2R_i)^2]^{1/2}$ (Fig. 5)⁷ bears this out; the slope ($D^{1/2}$) is 1.33×10^{-4} . Thus, D is 1.8×10^{-8} cm²/s, about two orders of magnitude greater than for the HFB/PS case.

CONCLUSIONS

High-resolution ¹⁹F NMR spectroscopy has been utilized to measure diffusion constants of small, fluorinated molecules in glassy (polystyrene) and rubbery (butyl rubber) polymers. The technique was applicable to diffusion in both thin films and hollow cylindrical samples. The diffusion constant for the 3,5-bis(trifluoromethyl)aniline/polystyrene system was determined by the NMR method was essentially identical to that found by resonant nuclear reaction analysis and was about an order of magnitude less than the diffusion constant for the hexafluorobenzene/polystyrene system. On the other hand, diffusion in the hexafluorobenzene/butyl rubber system was approximately two orders of magnitude greater than the latter number for the glassy polymer.

FIGURE 3

¹⁹F NMR Spectra of the HFB/PS System: (a) MAS (before desorption; 7,646 scans; spin rate 3.2 kHz); (b) MAS (after 40 m of desorption; 13,185 scans; spin rate 6.6 kHz); (c) MAS (after 45 m of desorption; 2,971 scans; spin rate 6.8 kHz). All spectra have 30 Hz line broadening and are printed at the same absolute intensity.

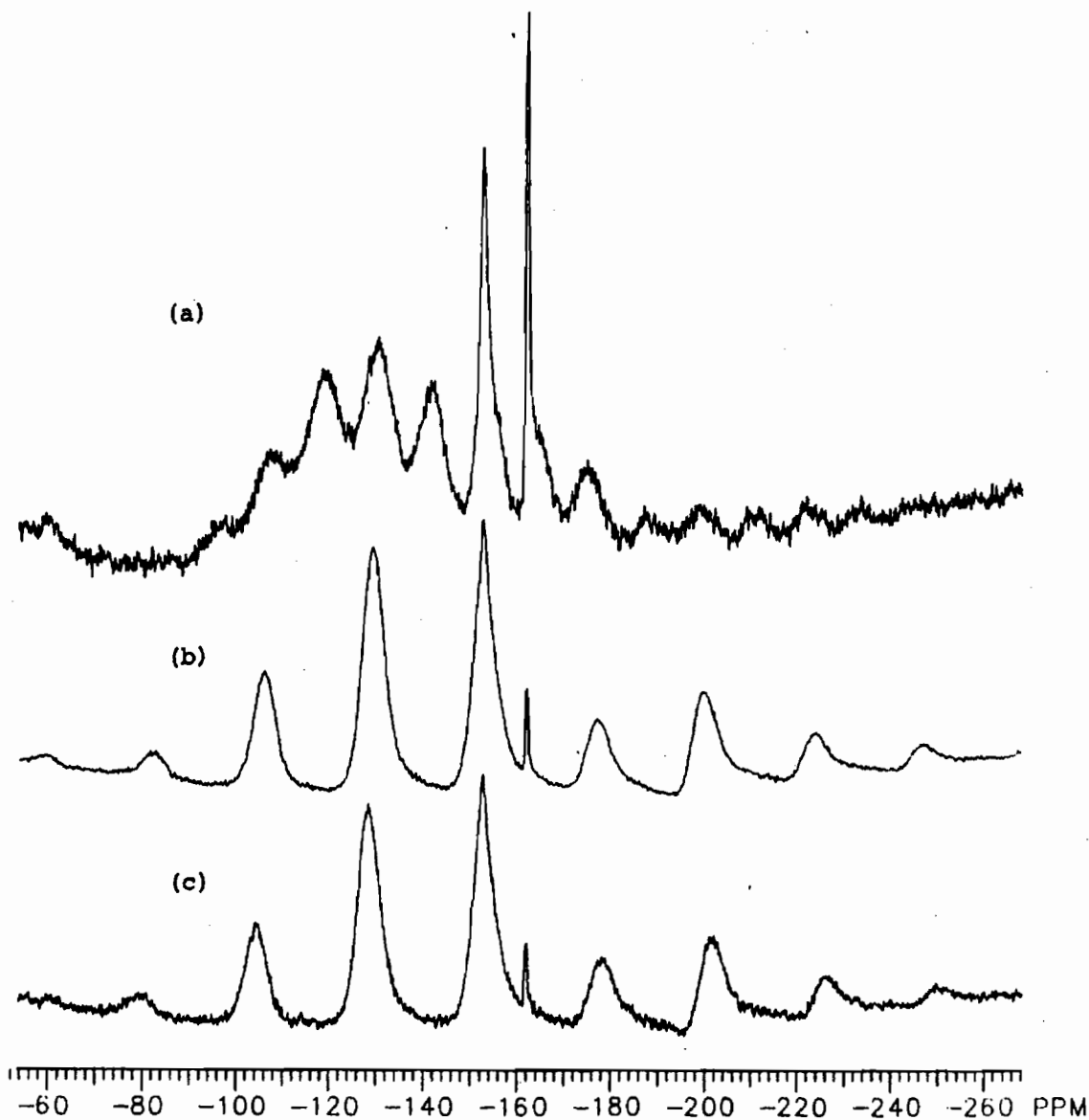


FIGURE 4

^{19}F NMR Spectra of the HFB/Butyl Rubber System: (a) Static (300 scans); (b) MAS (300 scans; spin rate 7.3 kHz). Both spectra have 10 Hz line broadening and are printed at the same absolute intensity.

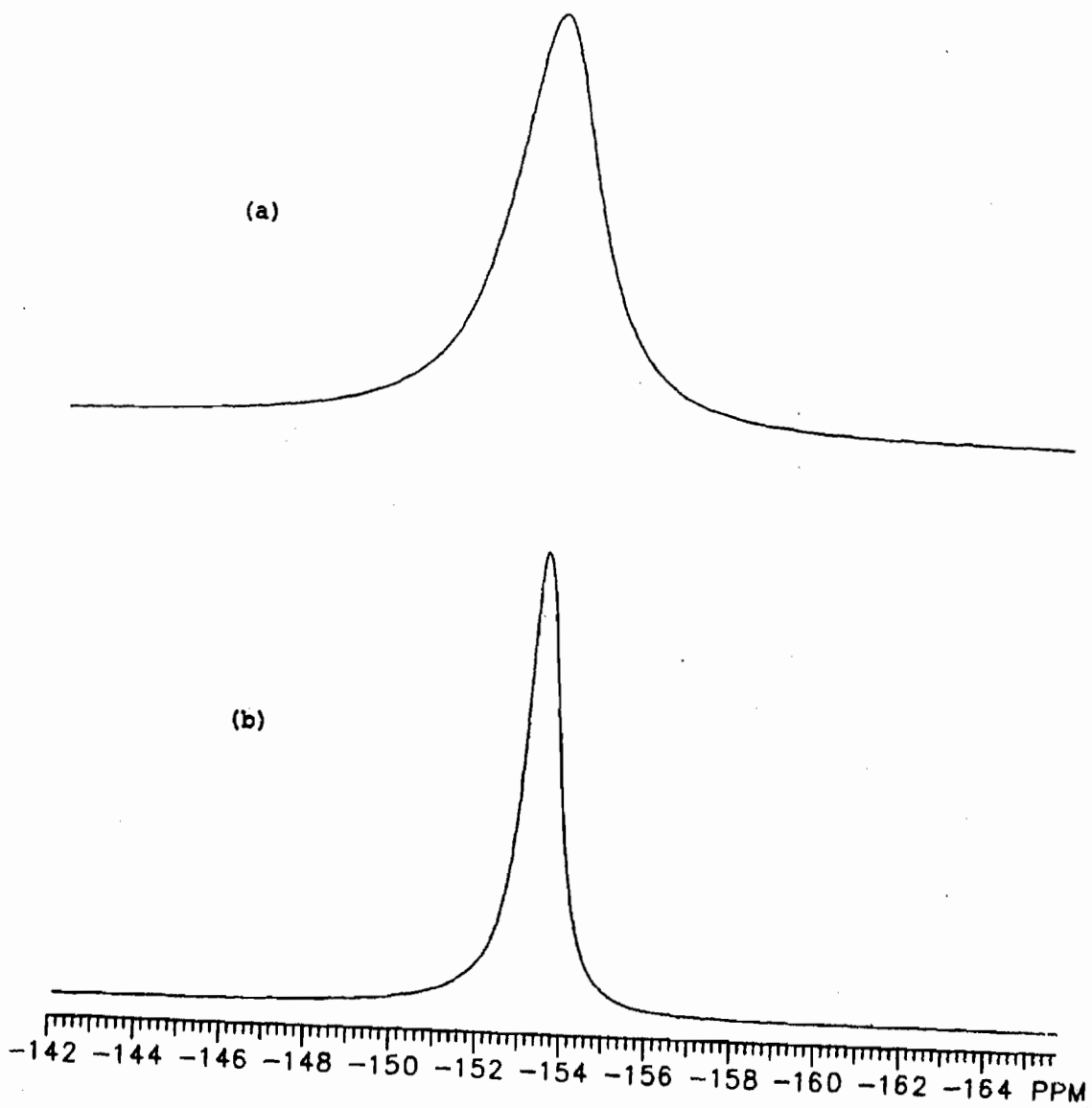
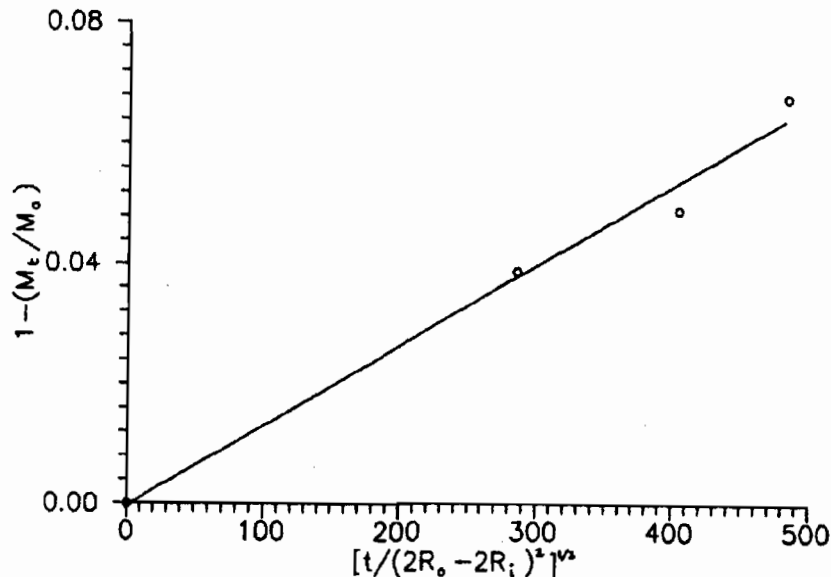


FIGURE 5. Desorption Data for the HFB/Butyl Rubber System



ACKNOWLEDGMENTS

We thank DARPA (Grant DAAL03-88-K-0198 administered by the U.S. Army Research Office) for their generous support.

REFERENCES

1. P. J. Toscano and H. L. Frisch, J. Polym. Sci. Polym. Chem. **29**, 1219 (1991)
2. P. J. Toscano and H. L. Frisch, Proceedings of the 1990 U.S. Army CRDEC Scientific Conference on Chemical Defense Research, in press.
3. J. Crank, "The Mathematics of Diffusion", 2nd Edn., Clarendon Press, Oxford, 1975; Chap. 4.
4. K. Umezawa, W. M. Gibson, J. T. Welch, K. Araki, G. Barros, and H. L. Frisch, J. Appl. Phys. in press.
5. The resonance at -162 ppm was previously erroneously assigned to desorbed HFB.²
6. J. Crank, "The Mathematics of Diffusion", 2nd Edn., Clarendon Press, Oxford, 1975; Chap. 5.
7. The factor of two in the denominator arises from the fact that the outer surface of the cylinder is essentially impenetrable.

BLANK

STRUCTURE DETERMINATION OF COMPOUND 34

D. Ralph Leslie

Materials Research Laboratory, Ascot Vale, Victoria, Australia
and

Linda L. Szafraniec, Dennis K. Rohrbaugh and Leonard J. Szafraniec
U.S. Army Chemical Research, Development and Engineering Center
Aberdeen Proving Ground, Maryland 21010-5423

ABSTRACT

Compound 34 is an indicator used in the M19 CBR sampling and analyzing kit for detection of G-agents. For the past 25+ years, numerous discrepancies have existed in both the chemical name and the chemical structure of this compound. One- and two-dimensional NMR experiments together with mass spectrometry and derivatization and degradation of the actual material resulted in an unequivocal assignment of the structure.

Compound 34 is an N-phenyl-para-phenylenediamine with ethoxy and sulfonic acid substituents. NMR showed that the sulfonic acid group is on the ring with the $-NH_2$ moiety and that it is meta to this group. The ethoxy is on the other ring, ortho to the NH(phenyl) moiety. Therefore, the correct chemical name for Compound 34 is either 5-amino-2(2'-ethoxyphenyl)aminobenzenesulfonic acid or 4-amino-2'-ethoxy-2-sulfo diphenylamine.

INTRODUCTION

Compound 34 was studied in the early 1950's and found to be an excellent colorimetric indicator for G-agents when used in conjunction with sodium pyrophosphate peroxide in the Schoenemann reaction.^{1,2} Today, Compound 34 is a reagent in the M19 CBR Agent Sampling and Analyzing Kit³ which was fielded in the Persian Gulf to be used under projects Desert Shield and Desert Storm. The kit is used to detect and identify CW agents, to perform preliminary processing of suspect CBR samples and to delineate contaminated areas.

A review of the literature over the past 25+ years revealed discrepancies in the nomenclature for Compound 34; 8 similar, but different, names were found and 3 different structures were reported. Recent discussions with personnel both in Detection Directorate and Research Directorate showed that there are still many misconceptions regarding the structure of Compound 34. Consequently, a rigorous investigation was undertaken using one- and two-dimensional nuclear magnetic resonance (NMR) techniques together with mass spectrometry to study Compound 34 and two of its derivatization/degradation

products. The results of this investigation have allowed us to assign the structure of Compound 34 unambiguously.

EXPERIMENTAL SECTION

Compound 34 (a purplish-blue solid) was obtained from Detection Directorate and used as received. N-Acetyl-N'-(2'-ethoxyphenyl)-1,4-diaminobenzene was prepared by the desulfonation of Compound 34 in 50% H₂SO₄ at 190 °C with subsequent acetylation using acetic anhydride at ambient temperature, and N,N'-diacetyl-5-amino-2(2'-ethoxyphenyl)aminobenzenesulfonic acid was prepared by refluxing Compound 34 in acetic anhydride, then allowing the solution to stand overnight before freeze-drying.

The ¹H and ¹³C NMR spectra were obtained using a Varian VXR-400S superconducting FTNMR system operating at 400 MHz for ¹H and 100 MHz for ¹³C. Spectra were obtained at probe temperature (ca. 21 °C) and quantitative information was obtained via digital integration of the spectral regions of interest. The two-dimensional experiments (COSY, HETCOR and NOESY) were performed using the standard Varian VNMR software.

The electron ionization (EI) and chemical ionization (CI) mass spectra were obtained on a Finnigan Model 5100 GC/MS using a Direct Insertion Probe (DIP). The quartz tube probe was heated from 60-500 °C at 120 °/min. The source temperature was 120 °C, and the CI reagent was methane at a source pressure of 0.6T. The mass range was scanned from 40-450 amu for EI and from 60-450 amu for CI at 1 scan/sec.

RESULTS AND DISCUSSION

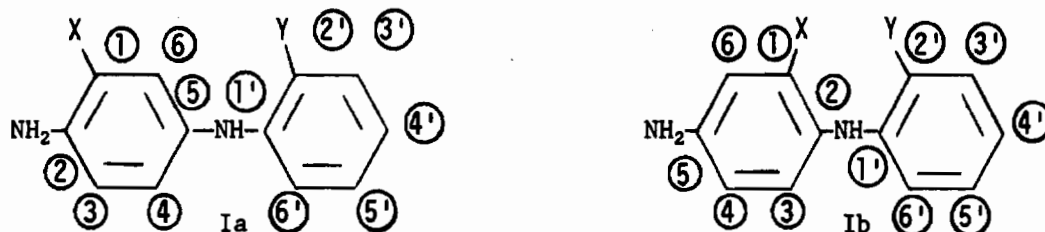
¹H NMR. Compound 34 is reported to be an N-phenyl-para-phenylenediamine with ethoxy and sulfonic acid substituents.¹⁻³ Integration of its ¹H spectrum in dmsO-d₆ (figure 1) revealed that Compound 34 contains 7 aromatic protons and one ethoxy group (CH₃: δ1.33, triplet, J=7.0 Hz; OCH₂: δ4.01, quartet, J=7.0 Hz). In addition, 3 resonances corresponding to slowly exchanging protons are present, one of which (δ3.43) arises from the water in the solvent. Integration of the other resonances indicates that one corresponds to a single proton (δ8.66) and is assigned as the proton on the secondary amine, while the number of protons represented by the other resonance (δ9.69) varies from 2-3 between solutions. Presumably, this corresponds to the primary amino group exhibiting a variable degree of protonation by the sulfonic acid moiety. Thus, the gross detail of the ¹H NMR spectrum is consistent with an N-phenyl-para-phenylenediamine substituted with an ethoxy moiety plus one other substituent containing an acidic exchangeable proton.

The ¹H COSY spectrum was used to provide the through-bond connectivities of the aromatic ¹H nuclei of the sample. Two isolated aromatic spin systems containing 3 and 4 protons are readily identified. Analysis of the 3 spin system shows it to be a 1,2,5-substituted benzene ring. Thus, H₆ is meta to a single hydrogen, H₄ (J_{H₄-H₆}=2.6 Hz), which in turn is ortho to H₃ (J_{H₄-H₃}=8.7 Hz). The second aromatic ring is easily identified as having substituents in the 1 and 2 positions. The 2 resonances of this spin system that are resolved are not coupled to each other, but do have more than one coupling. Thus, the substituents on this ring are ortho.

A consistent feature of all the names for Compound 34 is that each indicates the presence of the N-phenyl-para-phenylenediamine moiety. Although not yet proven, this structural feature is presumed correct. Thus, 2 arrangements are possible (Ia and Ib) when combining the 2 ring systems

indicated by the ^1H spectrum. A homonuclear nOe (nuclear Overhauser enhancement) experiment was used to determine a through-space connection between the CH_2 of the ethoxy group and one of the aromatic spin systems. Irradiation of $\delta 4.01$ induced an enhancement of the methyl resonance ($\delta 1.33$) and the aromatic resonance at $\delta 7.00$, previously assigned as H_3 , of the 4 spin ring system. Thus, the identity of substituent Y in Ia and Ib is established as ethoxy.

^{13}C NMR. The ^{13}C NMR spectrum and the ^1H - ^{13}C 2-D heteronuclear correlated (HETCOR) spectra are consistent with both structures proposed by analysis of the ^1H spectra. The ^{13}C spectrum contains resonances for each chemically distinct carbon in Compound 34; one methyl ($\delta 14.7$) and one methylene ($\delta 64.0$) for the ethoxy group, 7 aromatic methines and 5 aromatic quaternary carbons.



The number of directly bonded hydrogens on each carbon was determined using the APT experiment (Attached Proton Test). The directly coupled HETCOR experiment (see table 1) allows facile assignment of all but 2 of the aromatic methine resonances ($\delta 120.6$ and 121.3). The remaining methine resonances and those of the quaternary carbons are assigned from the long range HETCOR experiment (see table 1). From the previously assigned methine resonances, it is apparent that the strongest long range correlations correspond to coupling with protons on meta carbons. Thus, the resonances at $\delta 122.7$, 124.4 and 113.0 all exhibit strong correlations to their meta protons. In addition, much less intense correlations with ortho protons are evident for C_3 and C_4 . C_6 shows an even less intense correlation with its para hydrogen (H_3). The ^{13}C resonances at $\delta 120.6$ and 121.3 have a single, strong correlation with H_3 and H_6 , respectively. These are assumed to arise from correlations with meta hydrogens and allow unambiguous assignment of the resonances to C_5 , ($\delta 120.6$) and C_4 , ($\delta 121.3$).

The only aromatic methine resonance not exhibiting a long range C-H correlation is that at $\delta 116.3$ (C_6). In the ^1H -coupled ^{13}C spectrum, the lines of the corresponding doublet are the broadest, reflecting the presence of a number of unresolved long range couplings. The intensity of the resonance for C_6 in the long range HETCOR experiment will, therefore, be divided among a number of correlations which, although present, do not exceed the noise level and are not detected. The intensity of correlations to individual proton resonances is also diminished if the ^1H signal has a large number of homonuclear couplings.⁴ In this instance, the missing correlation is to H_4 , which is coupled to 3 other ^1H nuclei.

Working from the observation that the strongest correlations correspond to couplings with meta hydrogens, assignment of the quaternary carbon resonances is straightforward. See Table 1. The strong (meta) correlations of the resonances at $\delta 131.2$, 140.0 and 148.6 provide for their unequivocal assignment as C_1 , C_2 and C_2' , respectively. The meta correlations to H_4 and H_5 are weaker than expected, and the correlation between C_2' and H_4 is below

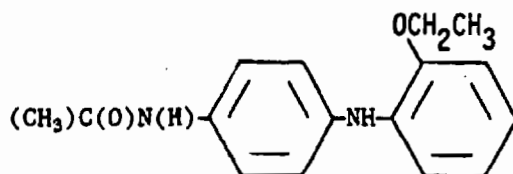
the noise level. The low intensity of correlations to extensively coupled ^1H nuclei was discussed above.

The unassigned resonances (δ 120.8 and 134.5) must correspond to C_1 and C_5 , both of which should, and do, display a strong (meta) correlation with H_3 and a weak (ortho) correlation with H_6 . The δ 134.5 resonance also has a weak (presumably ortho) correlation with H_4 and is, therefore, assigned as C_5 . Thus, the resonance at δ 120.8 is that of C_1 . These assignments may be reversed, but would require that the para correlation between C_1 and H_4 be stronger than the ortho correlation between C_5 and H_4 . The only para correlation observed in the experiment (C_6 and H_3) is much less intense than the ortho correlations.

^1H Homonuclear nOe. Differentiation between Ia and Ib as the correct structure for Compound 34 may be achieved by establishing the through-space relationship of the NH_2 protons with the aromatic protons of the phenylenediamine ring. In theory, a homonuclear nOe experiment with irradiation of the NH_2 protons should provide this relationship. In practice, interpretation of this experiment is ambiguous. Irradiation of the NH_2 resonance also causes saturation of the secondary amine proton and water resonances, indicating exchange of protons between the 3 environments. Thus, although 2 resonances (H_4 and H_6) are enhanced by irradiation of the NH_2 indicating Ib as the correct structure, it is possible that the interaction is with either the NH_2 or the NH protons. In order to obtain the through-space relationship between the NH_2 and the aromatic ring, the NH_2 group was acetylated. Amide protons do not exchange, and an nOe experiment with irradiation of the amide proton would provide the required information. (See below).

MS Characterization. The EI and CI mass spectra of Compound 34 were obtained. The spectra indicate that desulfonation occurs under MS conditions. The EI base peak at m/z 228 corresponds to the molecular weight of the desulfonated product, and the ions at m/z 64 and 48 represent the spectrum of SO_2 . Similarly, the CI base peak at m/z 229 corresponds to the protonated molecular ion of the desulfonated product, and the ion at m/z 65 represents the protonated molecular ion of SO_2 . Structural assignments for the CI fragmentation products were made.⁵

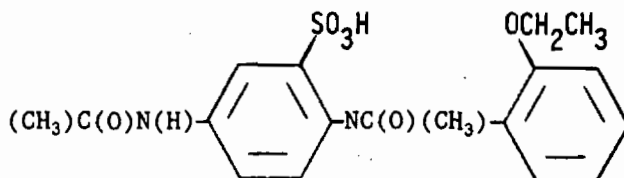
Desulfonated/Acetylated Compound 34 (II). In order to confirm the earlier homonuclear nOe experiment that indicated that the ethoxy group was on the ring by itself (structure I, Y=ethoxy), Compound 34 was desulfonated. This desulfonated product was acetylated to obtain a pure compound (II) that was identified by its ^1H and ^{13}C NMR spectra and its EI and CI mass spectra.⁵



Two 4-spin systems in the aromatic region of the ^1H spectrum can be identified in the ^1H and ^1H COSY spectra. The para and ortho substitution patterns indicated for the 2 aromatic rings in structure II are confirmed by analyzing

the couplings within each of the spin systems. The 1,2-disubstituted ring exhibits the same complex pattern as that observed for the ethoxy substituted ring in Compound 34 whereas the 1,4-disubstituted ring shows the typical AA'XX' pattern (δ 7.02 and 7.42). Thus, both the position of the ethoxy group on the ring by itself and the assumed para relationship of the amino groups in the N-phenyl phenylenediamine moiety of Compound 34 are firmly established.

Acetylated Compound 34 (III). The acetylated product of Compound 34 (III) was identified by its ^1H and ^{13}C NMR spectra and its EI and CI mass spectra.⁵ Two features of the ^1H spectrum warrant comment. Firstly, corresponding to each major peak is a smaller resonance (ca. 20%) with the same multiplicity. A similar duplication of peaks is also apparent in the ^{13}C spectrum. The most reasonable interpretation of this feature is that slow exchange between the syn and anti regio-isomers of the secondary amine acetamide results in separate spectra for each isomer. Heating the sample to 80 °C causes coalescence of each pair of peak, confirming that the resonances in each pair



III

are linked by exchange. Secondly, there appear to be 3 acetate groups in the sample as indicated in both the ^1H and ^{13}C spectra. In all other respects, the spectra are consistent with the N,N'-diacetamide, III. The extra acetate group arises from the presence of one equivalent of acetic acid that is not removed by freeze-drying. An increase in the intensity of the resonance at δ 1.90 in the ^1H spectrum and those at δ 21.1 and 172.0 in the ^{13}C spectrum after addition of acetic acid to the sample allowed assignment of these resonances.

The position of the sulfonic acid substituent in III was determined by establishing a through-space connection for the amide proton with protons on the aromatic ring. Irradiation of the amide ^1H resonance (δ 10.08) provided enhancement of the aromatic proton resonances at δ 7.98 (H_6) and 7.69 (H_4). Clearly, both H_6 and H_4 are ortho to the NHC(O)CH_3 moiety. A NOESY experiment, the 2-D version of the nOe experiment, was also performed. The nOe correlations between the amide proton resonance and those of H_4 and H_6 are also observed in this experiment. In addition to nOe correlations, NOESY spectra exhibit cross peaks between resonances linked by chemical exchange. Strong correlations, therefore, are present between each of the resonances of the major regio-isomer of III and its smaller counterpart resonance for the minor regio-isomer. This experiment complements the elevated temperature spectrum; both demonstrate exchange between the major and minor species (regio-isomers) in solution.

Determination of the arrangement of substituents in III was also possible by analysis of the long range ^1H - ^{13}C correlations involving the amide proton. The 2-D long range HETCOR spectrum exhibits correlations between this proton and 2 protonated carbon resonances (C_4 and C_6). Thus, this acetamide substituent has 2 ortho hydrogens, further confirming III as the product obtained from diacetylation of Compound 34. The correct structure for Com-

pound 34 is, therefore, 5-amino-2(2'-ethoxyphenyl)aminobenzenesulfonic acid or 4-amino-2'-ethoxy-2-sulfo diphenylamine, IV.

CONCLUSION

Compound 34 is an N-phenyl-para-phenylenediamine with ethoxy and sulfonic acid substituents. NMR showed that the sulfonic acid group is on the ring with the $-NH_2$ moiety and that it is meta to this group. The ethoxy is on the other ring, ortho to the NH(phenyl) moiety. The structure of Compound 34 (IV) is shown below along with the 1H and ^{13}C NMR assignments.

	<u>1H Assignments</u>		<u>^{13}C Assignments</u>
<p style="text-align: center;">IV</p>	-	1	120.8
	-	2	140.0
	7.34 (J=8.7)	3	115.0
	7.17 (J=8.7, 2.6)	4	124.4
	-	5	134.5
	7.70 (J=2.6)	6	122.7
	9.69	NH_3^+	-
	8.66	NH	-
	1.33 (J=7.0)	CH_3	14.7
	4.01 (J=7.0)	CH_2	64.0
	-	1'	131.2
	-	2'	148.6
	7.00	3'	113.0
	6.88	4'	121.3
6.89	5'	120.6	
7.28	6'	116.3	

REFERENCES

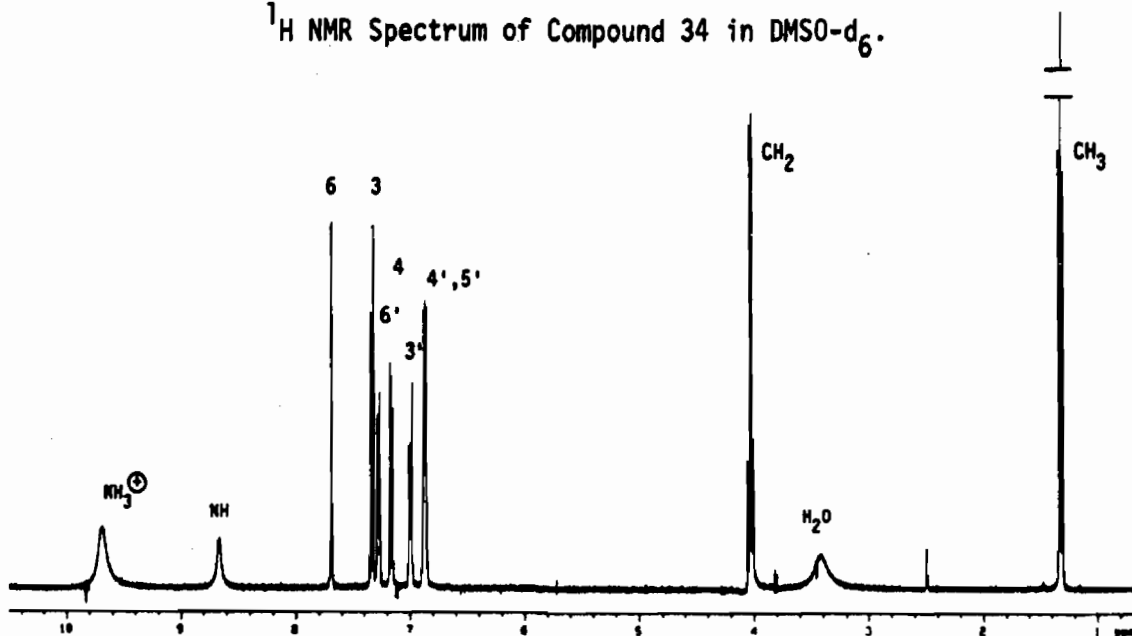
1. Kramer, D. N. "Use of the Schonemann Reaction in the Analysis and Detection of AC and CK", CRLR 194, Interim Report Project 4-08-04-009, Chemical Corps, Chemical and Radiological Laboratories, Army Chemical Center, MD. 11 June 1953, UNCLASSIFIED Report.
2. Kramer, D. N. "Improved Detector-Tube Test for G-Agents", CRLR 270, Interim Report Project 4-08-04-022 and 4-08-04-008, Chemical Corps, Chemical and Radiological Laboratories, Army Chemical Center, MD. 27 January 1954, UNCLASSIFIED Report.
3. Operator's Manual, Sampling and Analyzing Kit, CBR Agent, M19, TM 3-666-5-205-1011, Headquarters, Department of the Army, September 1966.
4. Sanders, J.K.M. and Hunter, B. K. Modern NMR Spectroscopy, Oxford University Press, New York, NY, 1987, p. 105.
5. Leslie, D. R., Szafraniec, L. L., Rohrbaugh, D. K. and Szafraniec, L. J. "Structure Determination of Compound 34", CRDEC Technical Report in Press, MS 845, 1991, UNCLASSIFIED Report.

TABLE 1
 ^1H - ^{13}C Correlations for the Aromatic Resonances in Compound 34.

Delta ^{13}C , ppm	Directly Coupled Correlations	Long-Range Correlations	Assignment
113.0 (d)	7.00 ($\text{H}_{3,}$)	6.88 (s, $\text{H}_{4,}$ or $\text{H}_{5,}$)	$\text{C}_{3'}$
115.0 (d)	7.34 ($\text{H}_{3'}$)	7.17 (w, $\text{H}_{4'}$)	C_3
116.3 (d)	7.28 ($\text{H}_{6,}$)	-	$\text{C}_{6'}$
120.6 (d)	6.88 ($\text{H}_{4,}$ or $\text{H}_{5,}$)	7.00 (s, $\text{H}_{3,}$)	$\text{C}_{5'}$
121.3 (d)	6.88 ($\text{H}_{4,}$ or $\text{H}_{5,}$)	7.28 (s, $\text{H}_{6,}$)	$\text{C}_{4'}$
122.7 (d)	7.70 ($\text{H}_{6'}$)	7.17 (s, $\text{H}_{4'}$)	C_6
124.4 (d)	7.17 (H_4)	7.34 (v.w., H_3)	C_4
		7.70 (s, $\text{H}_{6'}$)	
120.8 (q)	-	7.34 (w, H_3)	C_1
		7.70 (w, $\text{H}_{6'}$)	
131.2 (q)	-	7.00 (s, $\text{H}_{3,}$)	$\text{C}_{1'}$
		7.28 (w, $\text{H}_{6,}$)	
134.5 (q)	-	6.88 (w, $\text{H}_{4,}$ or $\text{H}_{5,}$)	C_5
		7.34 (s, H_3)	
		7.70 (w, $\text{H}_{6'}$)	
		7.17 (w, $\text{H}_{4'}$)	
140.0 (q)	-	7.17 (s, H_4)	C_2
		7.70 (s, $\text{H}_{6'}$)	
148.6 (q)	-	7.28 (s, $\text{H}_{6,}$)	$\text{C}_{2'}$
		7.00 (w, $\text{H}_{3,}$)	

d = doublet, q = quaternary carbon
s = strong, w = weak, v.w. = very weak

FIGURE 1
 ^1H NMR Spectrum of Compound 34 in DMSO-d_6 .



BLANK

846

XIX. MATERIALS POSTERS

BLANK

JET ENGINE DISSEMINATION OF MICROENCAPSULATED AEROSOLS

Mark A. Guelta and Hugh R. Carlon
U.S. Army Chemical Research, Development and
Engineering Center, Aberdeen Proving Ground, MD
Research Funded by: CRDEC

The presence of jet turbine engines in battlefield environments has increased dramatically over the past few decades. The role of these engines has also broadened from units to power aircraft to ground based units for powering vehicles, auxiliary power units, smoke generators and decontamination equipment. Concern has grown over the jet engines threat potential for delivering chemical and biological materials. The results of this program demonstrate, the potential threat of jet engine dissemination of aerosols containing microencapsulated materials. The microcapsules produced in this study consisted of starch or gelatin shell materials surrounding a oil core. By adapting readily available hardware to allow injection of microcapsule emulsions into jet engine exhaust gases we are able to produce microcapsules in the respirable size range. Fill rates for encapsulated materials are estimated as high as 80 percent with dissemination concentrations of 160 mg/m³ under test conditions.

Introduction

Aerosolized materials have been employed in battlefield environments for years. These aerosols have usually been in the form of smoke obscurants designed to mask troop and military vehicle movements from visual, infrared and other types of remote detection. Other types of potentially threatening battlefield aerosols include those of a chemical or biological nature. Part of the Chemical Research Development and Engineering Center's (CRDEC) mission is to evaluate the threat of deployment of these types of aerosols by our adversaries. Threat assessment includes the application of available hardware and technology required to deliver offensive aerosols and development of strategies to defend ourselves against these threats.

A recently identified potential threat is the dissemination of microencapsulated aerosols. As commercial use of microcapsules becomes more widespread so does the availability of technology required to generate them. The types of microcapsules produced have become broader and more complex. At the same time techniques are becoming more standardized. The

techniques and technology used commercially can easily be adapted for military purposes. As early as 1964 Anderson and Butz¹ demonstrated the potential for encapsulating biological materials (i.e. E. coli). Stockham² in 1967 reported the ability of microcapsule shell materials to protect biologicals from the effects of ultraviolet radiation. Nash, et al³ demonstrated several possible methods for delivery of encapsulated materials in gelatin bomblets and as a spray dried aerosol.

Proven methods for generation of microcapsules fall into two general categories, chemical and mechanical. Chemical methods include complex coacervation, polymer-polymer incompatibility and in situ polymerization. Mechanical methods include spray drying, fluidized bed and solvent evaporation. Of these processes spray drying is perhaps the least complex and has the easiest field application. This paper will concentrate on the application of a single spray drying technique to disseminate microcapsules made of food grade materials with a small jet engine.

Materials and Equipment

The microemulsion was prepared using food grade materials. The emulsion consisted of soybean oil droplets suspended in water. A starch shell material (Capsul Starch) was dissolved in the water along with a shell modifier (maltodextrin) and an emulsifier (tween 20).

The standard recipe used in these test consisted of:

Distilled Deionized Water	69.9 %
Capsul Starch	17.08 %
Maltodextrin	1.26 %
Tween 20	0.84 %
Soybean oil	10.9 %

Equipment:

Gaulin Model 31M Laboratory Homogenizer
Cole Palmer high speed mixer
Noel Penny NPT 100 Jet Turbine Engine
TSI APS 3310 Aerodynamic Particle Sizer
TSI Model 3302 Capillary Diluter
Olympus BH-2 Phase contrast microscope
Test Cloch
Cyclone sampler

The Cole Palmer high speed mixer and Gaulin homogenizer was used to mix and breakup the microcapsule emulsion. The Noel Penny jet engine was used to supply emulsion breakup, drying and dilution air. The APS 3310 Particle Sizing Analyzer was used to measure aerodynamic particle size of the microcapsules at the sampling point. An Olympus microscope was used to identify the presence of a core material in the microcapsules. A test Cloche is a half circular tunnel made of galvanized metal ribs with heavy plastic material covering the entire length of the tunnel. The tunnel is 4.27 meters wide at the base, 29.3 meters in length, and 2.24 meters in height. The cloche has a wall on each end containing sliding doors which open to a cross sectional area of 3.04M². The exhaust from the jet was directed into

one end of the cloche. The APS particle sizer was placed at the other end of the cloche 26 meters from the jet exhaust nozzle.

Methods

Emulsion Preparation

1. 4500 gms of distilled deionized water was placed into mixing vessel.
2. While stirring at approx. 1000 rpm with the mechanical stirrer, slowly add 1100 gms of capsule starch.
3. After capsule starch is mixed completely add 108 gms of maltodextrin and 54 gms of tween 20. Let shell solution mix for 30 minutes. Stir at a speed that mixes as little air as possible into the shell solution.
4. While continuing to mix add 702 gms of soybean oil containing 0.005 % by wt. series blue dye. Mix until oil is broken uniformly into drops which are barely discernable with your eye.
5. Process the emulsion through the homogenizer at a pressure setting of 2000 psi. A single test generally consists of four complete batches of emulsion. Each batch is ran through the homogenizer four times each.
6. A sample of the emulsion was routinely examined under the Olympus microscope at a magnification of 400X. Examination consistently revealed that oil droplets were below the microscope resolution and therefore less than 1.0 micron in diameter. There was also a undetermined amount of undissolved shell material.

Dissemination

Dissemination was accomplished by pumping the emulsion from the nalgene bottle through a flowmeter set to 1 LPM. The emulsion was introduced into the end of the jet exhaust nozzle through a stainless steel pipe with an end opening of 4.5 mm (figure 1). The high velocity of the jet exhaust, 260 M/sec at 30,000 RPM's, causes a shearing action sufficient to break the emulsion into droplets of approximately 20-50 microns in diameter. Each droplet contains all the constituents of the emulsion formula. The heat from the jet engine also serves to evaporate the water from the emulsion leaving a starch shell incasing a soybean oil core. Jet exhaust temperature at the nozzle varies from 500° to 540°C.

The velocity of the jet exhaust entering the cloche doorway also entrains dilution air at a rate of 14:1. Air velocity and temperature in the cloche quickly stabilizes. Air velocity slows to 2.4 M/sec at an engine speed of 30,000 rpm's. Temperature inside the cloche also stabilizes after the first 10 meters, the point where complete mixing of jet exhaust and entrained dilution air is complete. This final temperature is very dependant on ambient air conditions. Typical temperatures can vary from 25° to 60°C.

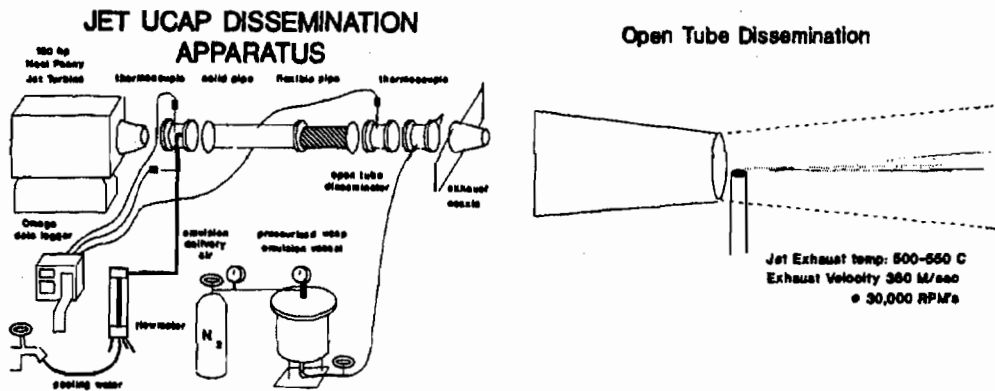


Figure 1. Jet Engine emulsion dissemination setup.

Sampling

Samples of the microcapsules were taken at a point at the far end of the cloche, 26 meters away from the jet exhaust nozzle. Samples were taken using several instruments, the principle instrument being the TSI APS 3310. The APS 3310, previously described by Remiarz et al.⁴ and Chen⁵, is a popular instrument for scientists measuring the aerodynamic size of airborne particles. The instrument operates on the principle that a particle's change in velocity in an accelerating flow field is related to its aerodynamic diameter. Changes in acceleration are related to a particles aerodynamic drag and particle density. Corrections for particle density are made in the aerodynamic size calculations (Wang and John⁶). The inlet of the APS was fitted with hardware to reduce the inlet size. This reduction in size allows matching of the APS inlet velocity to that of the cloche air stream to achieve isokinetic sampling.

Samples were also taken with probe samplers containing membrane filters and with a cyclone sampler. These samplers allow collected microcapsules to be examined using light and scanning electron microscopy. Anderson impactor samplers were also used for particle sizing, however, for the purpose of brevity they will not be discussed in this article.

RESULTS

Figure two is a typical printout from the APS particle sizer. The APS automatically calculates and prints count(CMD), surface(SMD) and mass median(MMD) diameters. The particular run displayed is from test date 1 Nov. 1991. The microcapsule emulsion was disseminated at an engine speed of 30,000 rpm's. Dissemination conditions were:

Ambient Temperature 16°C
Cloche Air Temperature 41°C

Exhaust Gas Temperature 524-528°C
Relative Humidity 80%

During the Nov. 1 test 20 individual size measurements were taken with the APS. Because engine speed was constant there was very little drift in particle distribution. CMD ranged from 1.102 µg to 1.123 µg, MMD ranged from 4.813 µg to 5.440 µg.

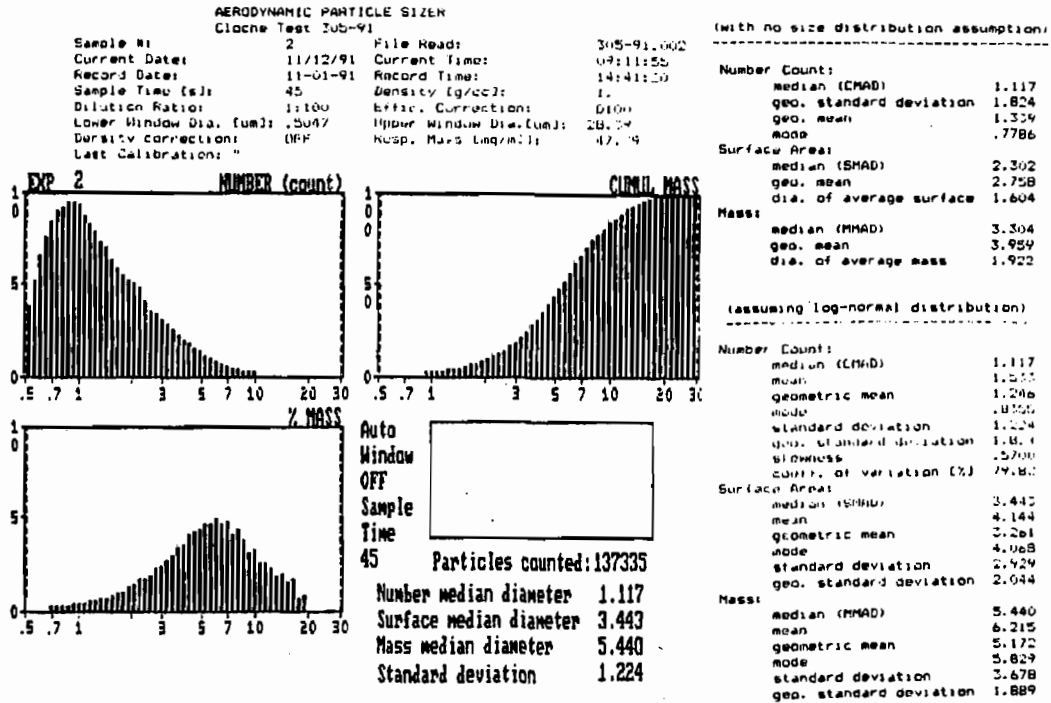


Figure 2. Sample printout from the APS from dissemination test 1 Nov. 91.

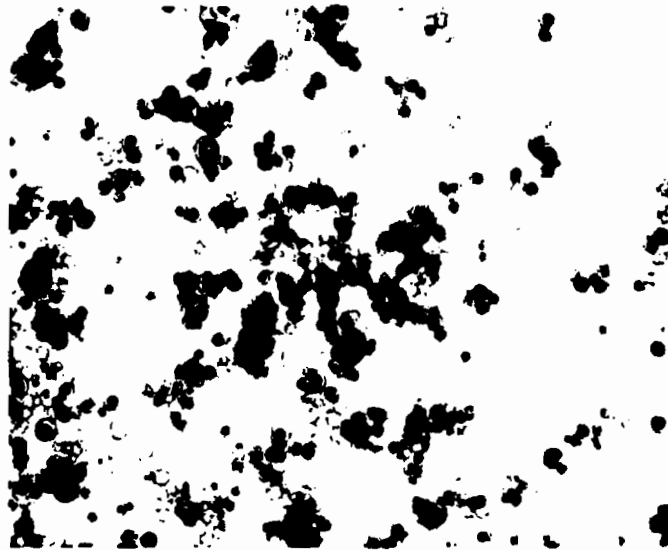


Figure 3. Photomicrograph of microcapsules with visible core material taken using light microscopy with 200X magnification. Capsule size range is 7.0-12.0 μm (2mm = 10 μg).

Microcapsules collected in the cyclone were observed using light microscopy. The addition of small amounts of oil soluble dye made core identification possible with the light microscope (figure 3). Surface analysis of the microcapsules was accomplished using Scanning Electron Microscopy (SEM).

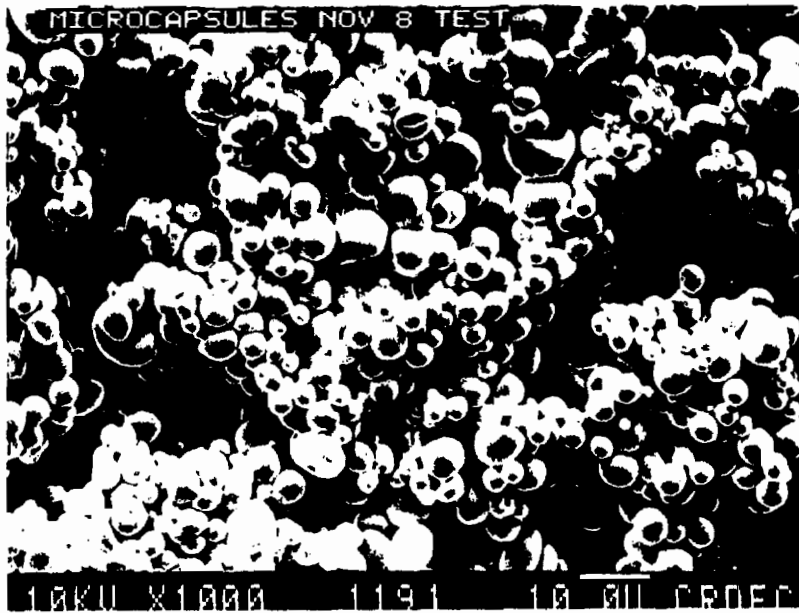


Figure 4. SEM photograph of microcapsules taken at 1000x magnification.

CONCLUSIONS

We have demonstrated that microcapsules consisting of a soybean oil core surrounded by a starch shell can be made and disseminated using a relatively simple technique powered by jet engine exhaust. We feel this technique and the principles used can be upscaled to larger systems. Even though figure 2 represents a particle distribution from a single test with a MMD of 5.4, other tests have proven we can control the MMD by altering dissemination parameters and emulsion formulations. The parameter with the most influence on final microcapsule size is the initial drop breakup size at the nozzle. This breakup size is controlled primarily by the velocity of the jet exhaust, the emulsion surface tension and viscosity. It is understandable that varying the jet exhaust velocity dramatically changes the breakup size. Our testing also indicated that the level of emulsifiers in the microcapsule formulation plays an important role in determining initial drop size.

In the size range of 3.0-10.0 microns core material is estimated to be present in as high as 80 percent of the microcapsules. Although imaging the capsules is difficult, the photo in figure 3 clearly shows the presence of the dyed core material. Estimation of percent filled is difficult using this method, our claim of 80 percent filled is actually qualitative.

The SEM and light photomicrographs show the capsules to be nearly spherical. The SEM photo shows that the surface of the capsules is relatively smooth although some of the capsules are slightly collapsed. Even though the stress on the capsule walls is high in the SEM environment, the capsule shell material shows no cracking or porous areas. Rosenberg et al⁷ also observed this collapse in spray dried microcapsules made of ethylcaprylate core material and gum arabic. We agree with them in that dissemination temperatures cause an expansion of the core material during

the drying process, leaving voids when the capsule cools. Increasing the concentration of shell material in the emulsion can increase shell thickness thereby reducing incidence of collapse and leakage of core material. Lowering dissemination temperatures can also decrease the occurrence of voids within the capsule.

We believe this method of dissemination to be practical in battlefield environments and hence could pose a real threat to unprotected personnel. Although the microcapsules produced are relatively innocuous we believe its possible to produce microcapsules with a chemical or biological payload. Its also possible that encapsulation may prolong the viability of the core material as well as disguise it from sophisticated sensing equipment. Further research is needed to determine the viability of this technology and the threat level posed. This research should include challenges to detection and protection equipment and development of viable countermeasures.

ACKNOWLEDGEMENTS

The authors would like to thank Teresa Richardson and Ron Grieb for emulsion preparation and dissemination, Bob Jolliffe for microcapsule collection and Dottie Paterno for SEM analysis.

REFERENCES

1. Anderson, J.L. and Butz, D., "Encapsulation of Viruses," TR WL-TR-64-167, AFWL Kirkland Air force Base, New Mexico, AD 620 833, August 1965.
2. Stockham, J.D., "Dissemination Properties of Encapsulated Particles," TR AFATL-TR-67-18 IIT Research Institute, Chicago, IL, 1967.
3. Nash, J.H., Blomquist, A.W., and Cooney, W.J., "Dissemination Properties of Encapsulated Particles," TR-AFATL-TR-67-95, Litton Systems, Inc., 1967.
4. Remiarz, R.J., Agarwal, J.K., Quant, F.R. and Sem, G.J., "Real-Time Aerodynamic Particle Size Analyzer," Proc. Int. Symp. on Aerosols in Mining and Industrial Work Environments 879-895, Minneapolis, edited by V.A. Marple and B.Y.H. Lui, Ann arbor Science, MICH (1981).
5. Chen, B.T., Cheng, Y.S. and Yeh, H.C., Aerosol Sci. Technology, 4:89-97 (1985).
6. Wang, HC. and John W., "Particle Density Correction for the Aerodynamic Particle Sizer," Aerosol Science and Technology, 6:191-198 (1987).
7. Rosenberg, M., Talmon, Y., and Kopelman, I.J., "The Microstructure of Spray Dried Microcapsules," Food microstructure 7, 15-23 (1988).

BLANK

NEW TEST METHODS FOR NBC SURVIVABILITY

P.S. Grasso, P.L. Cannon, Jr.

U.S. Army Chemical Research, Development and Engineering Center, Aberdeen Proving Ground MD.

Abstract- Two research test methods were adopted in order to investigate the survivability of electronic components and coatings. A thermal image acquisition system, planned for use in the testing of electronic components for operational survivability after chemical exposure, is described. Through the use of pyroelectric infrared and video cameras, sections of printed circuit boards containing components of interest, can be marked as 'Regions of Interest' (ROI) for automated thermal monitoring in order to study the component failure process. Follow-up studies of the damaged board lead to an understanding of the failure modes and assist in design of more chemically survivable electronic circuits. In an attempt to better understand the conformal coating failure process, an electrochemical impedance spectroscopy system (EIS) was added to our test capabilities. Since this method measures both impedance, and capacitance of the substrate, we are able to study the dynamics of chemical attack on coatings without altering the normal physical and chemical processes leading to coating failure. A number of coatings exposed to DS-2 were tested using this method. Several coatings which appear to be survivable using the standard "Y" board resistive test do not appear as resistant, using the EIS method. The EIS method is intended for the study of changes in the electrical properties of materials, while the "Y" board method is an operational test which uses much lower challenge levels, and only measures changes in bulk resistivity resulting from single droplet application.

DESCRIPTION OF SYSTEMS

1. Thermal Image Acquisition System

The thermal image acquisition system is intended to acquire analog thermal image data, digitize it, and when specified temperature changes have occurred, save the data on a hard disk for future analysis. Analysis includes the generation of thermal profiles and statistical distributions based on pixel intensity. Thermal images can be colorized according to pixel intensity so that thermal features can be more easily identified. Failure points will be studied using other methods such as scanning electron microscopy (SEM), to determine which critical material properties were altered in the coating. This information guides us in selecting standard test methods which must be conducted to assess the nuclear, biological, and chemical (NBC) survivability of coatings. This infrared (IR) technology is currently in use by the electronics industry for nondestructive quality control testing of printed circuit boards. A reference thermal

mask is used to isolate defective boards while under power. Even underlying short circuits in multiple layer boards can be spotted using this technique. Our challenge is to determine if we can locate component failure points through the thermal pattern created by chemical interactions with the conformal coating. The entire circuit board can now be chemically exposed and monitored while operating under normal conditions. It will thus be possible to see component failure due to the interactive degradation of sub-components on the printed circuit board. The combination of IR image analysis, scanning electron microscopy, and electrochemical impedance spectroscopy (EIS) allows us to spot failure points and processes. This information can then be used to determine vulnerabilities, suggest methods to improve survivability in existing systems, and identify the best materials of construction for new equipment.

The image acquisition system is capable of digitizing and processing data from video tape signals, or from visual and infrared (IR) camera signals. Video and IR images can be superimposed (mixed) as required. Event trapping, the collection of data when threshold temperature conditions are achieved, can be limited to previously established regions of interest. Event trapping is based on either an absolute or relative (%) change in pixel intensity (temperature) from a pre-exposure mask.

If the target emissivity is known, it will be possible to relate pixel intensity to temperature, using the dual temperature reference source. This system has an emittance of approximately 1, and allows variable temperature on two isolated plates. These two plates can then be calibrated to the dial setting, the observed pixel intensity, and the observed temperature. While circuit boards will not have an emittance of 1, only relative temperature changes will be required to establish the effects of chemical interaction with the conformal coating.

The major system components are related to four basic functions:

- (1) Data Acquisition
- (2) Data Storage and Processing
- (3) Data Output
- (4) System Control Interface.

DATA ACQUISITION-The data acquisition system acquires the analog IR and video signals for processing by the data storage and processing system. These cameras are housed in a remote controlled stainless steel structure which has pan, tilt and camera control through the remote control unit mounted in the system rack. The video camera window is glass, while the IR window is germanium with a diamond coating. This design will allow for camera operations in a toxic chemical environment without contamination of the cameras. Mirror systems were considered, however stray IR pickup was considered a major potential problem.

The IR camera operates in the 8-14 micron wavelength range, has a thermal sensitivity of less than 0.15 degrees Celsius ($^{\circ}\text{C}$), and provides a picture resolution of 250 pixels over the picture height. The use of a pyroelectric Vidicon tube eliminates the need for external cooling which simplifies experimental operations in the hood. The germanium optics selected is a 22 mm, f 0.7 lens which allows for a wide range of focal distances.

BLOCK DIAGRAM FOR THERMAL IMAGE SYSTEM

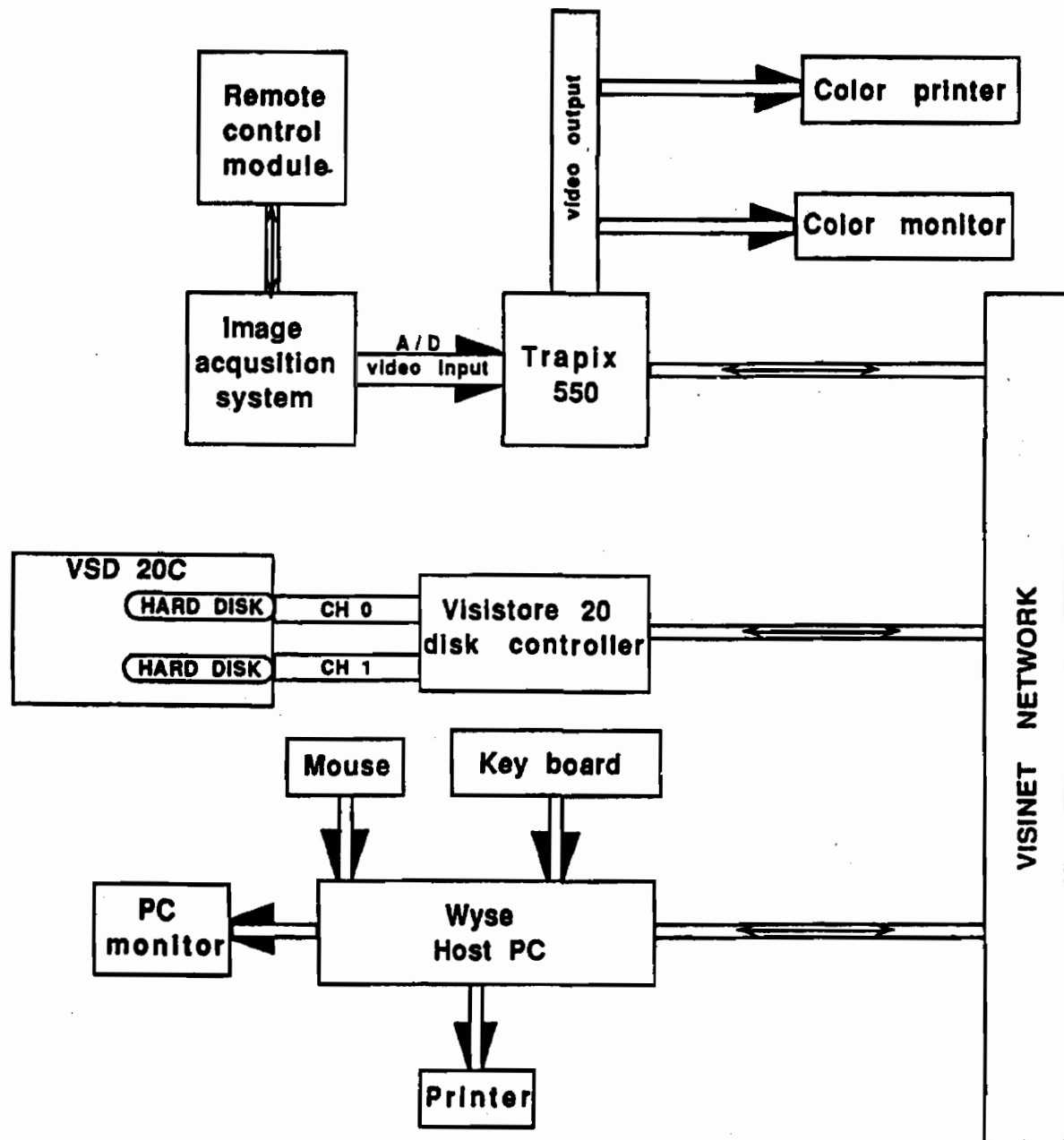


Figure 1

The black and white video camera is secured above the IR camera. A custom beveled mount above the IR camera permits the video camera to focus on the same field of view as the IR camera. This feature allows identification of thermal features of interest, and creation of regions of interest based on electronic component locations. The resolution achieved is 600 horizontal TV lines over the picture height, with a signal to noise ratio of 56 db, and requires a minimum of 0.2 lux illumination. The 25 mm lens allows for IR/visual overlay from 12 to 30 inches.

An external dual temperature reference source has internal heating and cooling for the two independently controlled plates (targets). Dial settings can be related to temperature settings and controlled to within +/- 0.75 °C. The adjustable target range is from +80 to -20 °C about ambient. A flexible target holder (neck) allows great ease in positioning the reference source under the camera's field of view.

The cameras and the dual temperature reference source are controlled from a remote control module located in the main control console. This module allows the operator to align and focus the cameras over the desired field of view and to control the temperature range on the dual temperature reference source. All camera focusing, light sensitivity, and mixing functions can be controlled from this module.

DATA STORAGE/PROCESSING- The image processor acquires, digitizes, and transports data, using instructions in look-up tables programmed with the host interface computer. Images are acquired at 15 frames pre second. The internal memory of 8Mb, stores 32 (512X512X8) image planes (8 bits per pixel). Both video tape and camera data can be acquired and processed. Look-up tables are used to generate pseudo color for the IR images, to compress gray scales for optimal contrast, to create regions of interest, and for many other functions. Data is stored on a 1.6 Gb, data storage component with an 8 bit dual digital disk system operating at 15 frames per second with a sustained data transfer rate of 4.6 Mb per second. The minimum sample time for event trapping, at these transfer rates, is 1.5 seconds.

DATA OUTPUT- Data output is to a 19 inch high-resolution color display monitor and a RGB color printer operating off the monitor signal. Both high resolution color transparencies and hard copies, up to 17 inches in length, can be printed.

SYSTEM CONTROL INTERFACE- A WYSE 286 personal computer (PC) serves as the interface computer used to program the data acquisition system. This computer is equipped with a 5 1/4 inch, 1.2Mb floppy drive and a 40 Mb hard drive which holds the interfacing and operating software. A dot matrix printer is used to document input commands, and general statistical pixel data output from the data acquisition system. Access to the data acquisition system is controlled through a security port device.

IR SYSTEM SUMMARY- As shown in Figure 1, "System Block Diagram", image data is acquired through the infrared and visual cameras, which are adjusted prior to testing with an independent remote control module. The Trapix image processor controls all image processing operations after receiving run instructions from the host computer. Image data is moved along the VISINET network to the 1.6 Gb hard drive disk and the host PC. The outputs from the image processor are sent in RGB (Red Green Blue) format to the 19 inch monitor and the color

AC IMPEDANCE TEST OF CONFORMAL COATINGS

FAILURE TIME WITH DS2 EXPOSURE

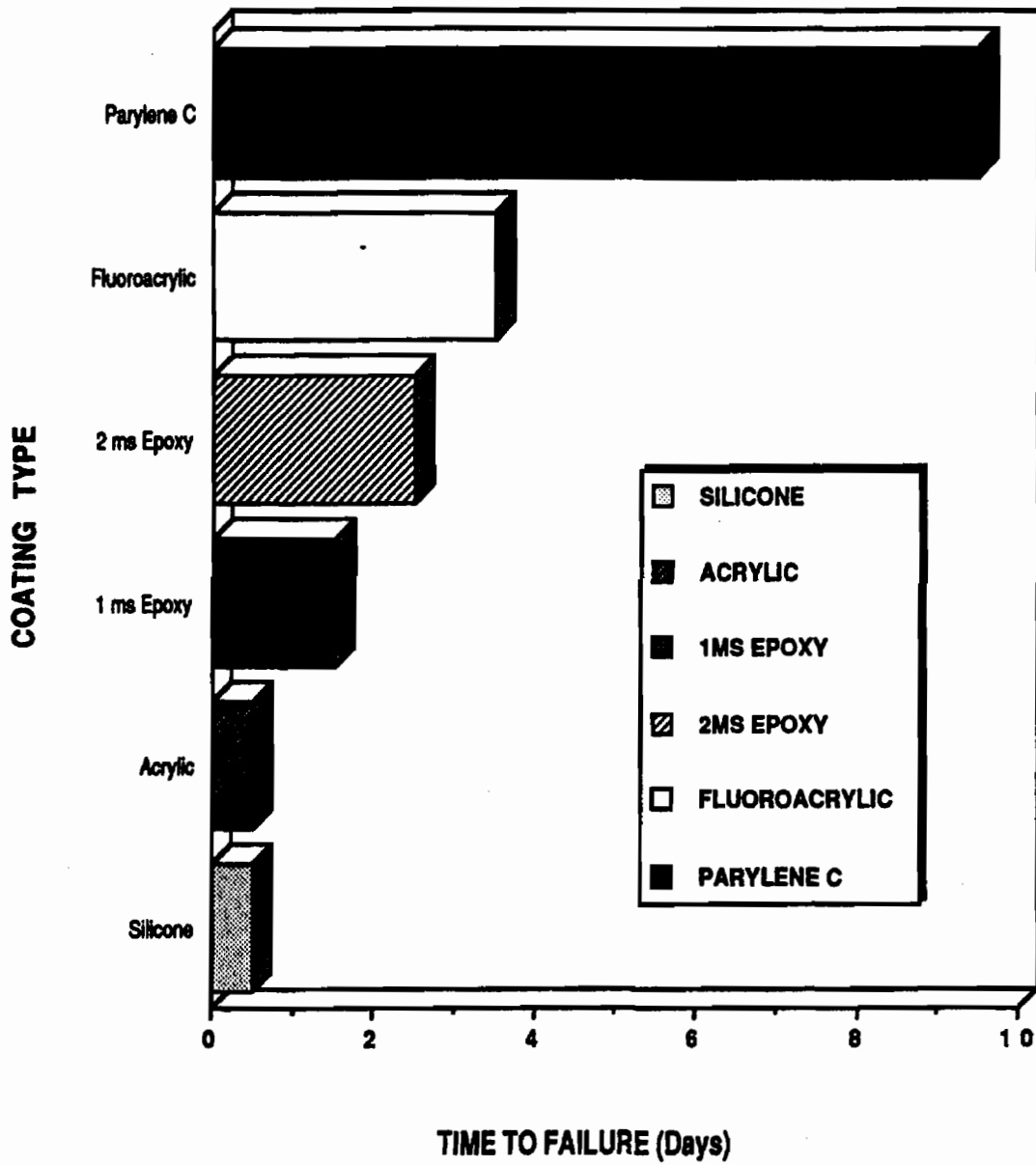


Figure 2

printer. The 1.6 Gb hard disk drive consists of two, 781 Mb disk assemblies accessed through channel modules 0 and 1.

2. Electrochemical Impedance Spectroscopy

The EIS technique is an electrochemical method that accurately and quickly measures the impedance and capacitance of protective coatings. Through an understanding of the equivalent circuit formed by the coating, solution, and metallic substrata, it is possible to follow the failure process of the coating and the resulting corrosion at the metallic interface. The method employs a potentiostatic circuit which applies a short duration, alternating potential superimposed over a larger DC potential, across the solution/ coating/ metallic substrata system for a wide range of frequencies, while measuring the resulting alternating current that flows as a result of the applied voltage.

A number of copper plates coated with military standard conformal coatings used on electronic printed circuit boards were tested with decontamination solution (DS-2) to determine the long term coating hardness to this chemical challenge. It was also possible to estimate the magnitude of ambient water uptake into the coating, which occurred prior to actual testing, through DS-2 and coating interface studies. Pore resistance, coating capacitance, and alternating current phase changes are determined with Bode, Nyquist, Randles admittance, and real impedance plots.

Experience has shown that if the pore resistance of a coating is less than 10^6 ohms, the coating no longer provides adequate protection to the metallic substrata. Under these conditions the coating is said to be in failure. Four of six coatings exposed to DS-2 challenge failed in two days or less. One coating failed after three days, and one coating lasted for at least 30 days. These results are summarized in figure 2. It should be noted that the coatings appear to be intact by visual inspection. This technique is very sensitive to changes in the coatings, and SEM methods are normally required to see the failure path detected by these EIS procedures.

An alternate test method which applies a constant voltage across two parallel conductors coated with military standard conformal coatings, and measures the current to compute the bulk resistivity of the coating between the conductors has shown similar results to the EIS method just described. This "Y" board method is intended to look at more realistic exposures to coatings, and determine if the coating can survive a droplet challenge and be reused. Two coatings which do not pass the EIS long term exposure test do pass the "Y" board test. Clearly the EIS methods are more sensitive in determining material compatibility and hardness, while the "Y" board test provides estimates of operational survivability, when exposure conditions can be determined. Both methods have an important use; the intended purpose of the test method must be remembered when interpreting the resulting data.

CONCLUSIONS

The thermal image acquisition system provides a simple and rapid means to monitor circuit board performance after chemical exposure. This component test method can be used to determine component survivability under realistic challenges, and to aid in locating the failure

path and process. This information when combined with results from other analytical techniques like SEM, aids the developer of test methods in the identification of the most appropriate material properties which need to be described. The EIS system provides comprehensive data on the failure process of coatings and when combined with other analytical techniques like SEM, also allows for the determination of the failure process, and identification of critical material properties. These materials-effects test methods are key elements of our ongoing effort to develop new and improved procedures for assessing NBC material survivability.

BLANK

XX. DECONTAMINATION POSTERS

BLANK

ADSORPTION OF MUSTARD FROM A CHLOROFLUOROCARBON SOLVENT
USING A MACRORETICULAR STRONG ACID RESIN

James H. Buchanan¹, Dennis K. Rohrbaugh¹,
Philip W. Bartram² and Noel C. DiBona³

ABSTRACT

Currently, chlorofluorocarbons (CFC), used as decontaminants in the Nonaqueous Equipment Decontamination System (NAEDS), are purified in a series of steps involving mixing with sodium hypochlorite, decanting, distillation, and cooling. Experiments were performed to determine the feasibility of using adsorption as an alternate method for purification. An experimental, macroreticular, strong acid resin, Amberlite XE-393, was evaluated in 1,1,2-trichloro-1,2,2-trifluoroethane (CFC-113) contaminated with 1% bis(2-chloroethyl) sulfide (HD). The adsorption efficiency of the resin was evaluated at room temperature with constant stirring in glass reaction vials. Liquid samples were taken at ten minutes, two hours, and four hours. Adsorption efficiencies were evaluated at resin concentrations of 10%, 15% and 20%. Analysis by gas chromatography using a flame ionization detector indicated HD adsorption of 40%, 67% and 72% for the three respective concentrations after ten minutes; 60%, 91% and 95% after two hours; and 62%, 92% and 95% after four hours.

INTRODUCTION

The NAEDS was developed to provide the U.S. Army the capability to remove chemical agent contamination from electronics, avionics, and other items sensitive to conventional decontaminating solutions.

The present NAEDS design includes a CFC spray which removes the contaminant from the item. The CFC solvent/agent solution is processed by mixing with sodium hypochlorite in an in-line mixer. The solvent is then separated from the aqueous hypochlorite by decanting and finally distilled. The NAEDS was developed for use in NBC hardened facilities. Therefore, the size and weight of the system were not critical. By demonstrating that the purification system could be replaced by a small adsorption column, the usefulness of the NAEDS technology could be significantly extended.

Two major criteria were considered in evaluating the adsorption system. First, the rate of sorption of threat chemical warfare agents from the contaminated CFC solvent must be significantly greater than the rate of sorption of the CFC solvent. Second, the rate of agent desorption from the column material should be significantly less than the rate of sorption. These partitioning characteristics were addressed in these "static" tests.

Comparative evaluation of various particle structures can be based on factors such as capacity and rate of sorption. Recent advances by researchers in related fields have led to formulations that combine sorptive and reactive properties into a single material. Catalytic substituents are available on, or can be incorporated into, a wide spectrum of particle structures. Each provides one or more sets of intermolecular forces for retaining contaminants. Once retained, the chemical warfare (CW) agents can be detoxified by the reactive substituents of the particles.

A literature review suggested that a macroreticular strong acid resin, such as Amberlite XE-393, would effectively sorb and decontaminate organophosphorus CW agents. Basic research focused on the development of decontaminating coatings, recommended sulfonic acid catalysts on a hydrophobic polymer particle. Shuely and McHugh found that adsorptive, macroreticular particles functioned well in retaining contaminants⁴.

In their evaluation of candidate materials to remove undesired contaminants from flowing air streams, Maroldo and coworkers⁷ reported strong acid, high surface area, ion exchange resins to have very good dynamic adsorption capacity for the G-agent simulant, diisopropyl fluorophosphate, under dry and humid (80% RH) conditions. In addition, acid catalyzed hydrolysis was observed under humid conditions.

This report is the second in a series of reports describing the results of research studies aimed at purification of agent contaminated CFC using state-of-the-art sorption technologies. It focuses on the initial research studies designed to determine the feasibility of removing HD from the NAEDS solvent, CFC-113, using the macroreticular strong acid resin, Amberlite XE-393. The initial report⁶ indicated that XE-393 was extremely effective (greater than 99.9%) in removing VX from VX-contaminated CFC-113. Results will be used to design a small scale adsorption column directed toward eventual replacement of the present NAEDS purification system.

EXPERIMENTAL

The HD sample (Lot No. HD-U-6216-CTF-N-1) used in these experiments was obtained from the Chemical Agent Standard Analytical Reference Material Program at CRDEC. Originally synthesized in August 1986 and determined to be 97.3% (w/w) pure by multinuclear NMR spectroscopy, this particular sample was recently monitored with no degradation detected. Impurities were identified by GC/MS and matched by order of elution to GC results.

The CFC-113 solvent was obtained from E.I. Dupont de Nemours. GC analysis resulted in an area % purity of 99.99 with the only impurity eluting 12 seconds before the main peak. Amberlite XE-393 (Lot 84/0079), an experimental polydivinylbenzene ion exchange resin, was supplied by Rohm and Haas Company, Philadelphia, PA. The black spherical resin beads, with a surface area of 410 m²/g, a proprietary average pore size, and a 20/50

mesh range, were used as received. Detailed characteristics were previously determined by Nene and coworkers. Amberlite is a registered trademark of Rohm and Haas Company or one of its subsidiaries or affiliates.

An HP 5880A GC equipped with an FID was used in this study. The analysis of HD was accomplished using a 30 meter fused silica capillary column (0.32 mm ID) with a 0.25 μ m film of methylsilicone (SE-30). The carrier gas was helium split at a 50:1 ratio. Pressure controlled (47 KPa) column flow resulted in a calculated helium flow of 22.7 cm/sec (1.1 mL/min) based on the retention gap (2.2 minutes) obtained for methane at 40 °C. Detector make-up flow was helium at a rate of 23 mL/min. The injection port temperature was 225 °C and the detector temperature was 300 °C. The column oven temperature was programmed from 75 to 275 °C at 20 °C/min and held at 275 °C for 10 minutes. The combustion gases were hydrogen and air, at 32 and 420 mL/min, respectively. The septum purge flow was adjusted to 1 mL/min. A Hamilton 7001SN microliter syringe was used to manually inject 1.0 μ L sample volumes. Area integration of the resulting chromatographic peaks was accomplished electronically.

PROCEDURE

To determine the adsorption efficiency of Amberlite XE-393 resin, a master dilution of HD in CFC-113 was prepared. To 100 μ L (127.1 mg) of HD, 10 mL of CFC was added volumetrically. This solution was transferred to a glass reaction vial containing a small, teflon-coated magnetic stirbar, and sealed with a teflon-lined silicone septum and an aluminum crimp cap. This 1% (v/v) HD solution served as both the experimental sample for resin adsorption testing and as the master standard for further dilution and calibration in the concentration range of interest. This concentration was calculated to be the maximum agent concentration challenged by the NAEDS.

Duplicate samples were prepared by the addition of 2.0 mL of the master standard solution (1% HD in CFC) to each of two 10 mL glass reaction vials containing a small, cylindrically shaped, teflon-coated, magnetic stirbar and 200 mg of Amberlite XE-393 resin. The vials were sealed with a teflon-lined silicone septum and an aluminum crimp cap. The mixtures were stirred at 500 rpm. Stirring was interrupted after 10 min, 2 hrs, and 4 hrs to enable sampling of the liquid with a Hamilton 7001SN microliter syringe. For each sampling, a 5/8-inch, 25 gauge stainless steel needle was used to vent the sample to assure exactly 1.0 μ L of liquid was withdrawn. All work was performed at room temperature (25 \pm 1 °C) in an air atmosphere.

Duplicate samples were also prepared to determine the effect of resin concentration on the adsorption efficiency of Amberlite XE-393 resin with HD-contaminated CFC. The procedure described above was used to prepare samples with 15% (300 mg) and 20% (400 mg) Amberlite XE-393 resin.

A series of dilutions were prepared volumetrically from the 1% HD in CFC master standard. A 1.0 μ L aliquot of each was injected manually into the GC to generate a calibration curve. Duplicate dilutions were made for HD at 0.10% in CFC-113 since a distinct difference in detector response was noted. Excellent reproducibility (\pm 1%) was obtained for sample concentrations in this range.

Quantitative analysis of HD in CFC was accomplished using gas chromatography. A calibration curve was generated relating HD area counts to a known concentration of HD in CFC-113. HD area counts obtained for experimental samples of unknown HD concentration which had been exposed to the resin in the solvent were quantitated based on this linear relationship.

The FID Minimum Detectable Level (MDL) for HD was determined to be 1 ng with a signal of better than twice the noise level for a 1.0 μ L injection of HD in CFC. This corresponds to 0.0001% (v/v) concentration of HD in CFC. Since 1% HD in CFC was chosen as the starting concentration for adsorption testing with Amberlite XE-393, the described procedure detected HD at the MDL after 99.99% had been adsorbed.

RESULTS AND DISCUSSION

Table 1 presents a summary of the data obtained for this series of static adsorption experiments carried out using a concentration of 10 mL of HD per liter of CFC solvent. Samples "E" and "F" contained 10% Amberlite XE-393 resin, sample "G" had 15% and sample "H" had 20%.

The rate of HD adsorption is depicted graphically in Figure 1. The rate of HD adsorption by Amberlite XE-393 resin appears to be significantly greater than the rate of CFC adsorption and the rate of HD desorption from the resin material appears to be significantly less than the rate of HD adsorption.

Table 1. HD Adsorption by Amberlite XE-393 Resin in CFC-113 Solvent

Time	Percent HD Adsorbed by Amberlite XE-393 Resin			
	10% Resin Sample "E"	10% Resin Sample "F"	15% Resin Sample "G"	20% Resin Sample "H"
10 min	40.2	39.5	67.1	72.1
2 hours	60.8	59.4	91.1	95.3
4 hours	61.5	62.2	92.4	95.3
23 hours	62.6	ND	ND	ND

ND = Not Determined.

The rate of HD adsorption is most significant during the initial stages for each of the three resin concentrations tested. During the first ten minutes of the experiment with 10% resin, 40% of the HD initially present in the CFC mixture had been retained by the resin. After two hours, an additional 20% had been adsorbed. Little, if any, additional HD adsorption was observed after 23 hours.

The first report in this series indicated that all of the VX initially present in the CFC-113 mixture was adsorbed and retained after 2 - 4 hours⁶. The HD data indicated that the capacity of Amberlite XE-393 resin to adsorb and retain HD was significantly less than its capacity to adsorb and retain VX. A comparison of HD and VX adsorption rate data for CFC mixtures containing 10% Amberlite XE-393 resin is given in Figure 2.

Since the capacity of Amberlite XE-393 resin to adsorb and retain HD appeared significantly less than its capacity to adsorb and retain VX, experiments were performed to determine the effect of various resin concentrations on the HD adsorption rate. HD adsorption results, for resin concentrations of 10%, 15%, and 20% (Table 1), show a similar trend. Specifically, it appeared that the most significant amount of HD adsorption occurred in early stages of exposure to the resin regardless of resin concentration. For the tests with 15% and 20% resin, approximately 70% of the HD initially present was adsorbed in ten minutes. It took nearly two hours for the resin to adsorb the next 25% of HD at both resin levels. Insignificant changes in HD adsorption were observed from two to four hours.

A significant increase in both the rate of HD adsorption and the capacity of the resin to adsorb and retain HD was observed when the resin concentration was increased from 10% to 15%. However, the increase in HD adsorption rate and resin capacity was not nearly as significant when the resin concentration was increased from 15% to 20%. The effect of resin concentration on HD adsorption rate is depicted graphically in Figure 1.

The major HD impurity, dithiane, was totally adsorbed in less than two hours, regardless of resin concentration. The only HD impurities not totally adsorbed after four hours (20% resin) were two six-carbon, chlorinated sulfides.

No evidence of resin induced CFC decomposition or contamination was detected in a control sample. The major CFC impurity detected by gas chromatography was preferentially adsorbed by Amberlite XE-393 resulting in a recovered product of greater purity. This purification⁶ process was previously presented in the initial report of this series.

The 1% agent concentration in CFC was chosen since it appears to be the maximum theoretical threat that the NAEDS might encounter. Amberlite XE-393 efficiently removed HD from contaminated CFC in a timely manner under the "static" conditions of this experiment. Continued evaluation of this adsorption material for removal of other threat chemical warfare agents from contaminated CFC will be accomplished.

Transformation of the demonstrated potential of this resin for CFC purification into a practical operating system should eventually include a series of column experiments in which breakthrough times, fate of agents on the resin, resin regeneration and other relevant issues are addressed.

CONCLUSIONS

The following conclusions can be drawn from this work.

a. Amberlite XE-393, a macroreticular, strong acid resin, purified HD-contaminated 1,1,2-trichloro-1,2,2-trifluoroethane by removal of HD to the 0.05% (500 ppm) level. The HD adsorption efficiency was greater than 95%.

b. The most significant amount of HD adsorption occurred in the first ten minutes of exposure to the resin, regardless of resin concentration.

c. The rate of HD adsorption by Amberlite XE-393 resin is significantly accelerated by an increase in resin concentration.

d. The capacity of Amberlite XE-393 resin to adsorb HD is significantly increased by a slight increase in resin concentration.

REFERENCES

- 1 Research Directorate, Chemical Research, Development and Engineering Center, Aberdeen Proving Ground, Maryland 21010-5423.
- 2 Physical Protection Directorate, Chemical Research, Development and Engineering Center, Aberdeen Proving Ground, Maryland 21010-5423.
- 3 Research, Development and Engineering Support Directorate, Chemical Research, Development and Engineering Center, Aberdeen Proving Ground, Maryland 21010-5423.
- 4 Shuely, Wendel J. and McHugh, Vincent M., Development of Decontaminating Coatings Employing Sulfonic Acid Catalysts Bonded to Macroreticular Sorbent Particles, CRDEC-TR-88113, U.S. Army CRDEC, Aberdeen Proving Ground, MD, July 1988, UNCLASSIFIED Report.
- 5 Maroldo, Stephen G., Holy, Norman L., Kaufell, Louis A., Langenmayr, Eric J., and Smith, Rebecca L., "High Surface Area Ion Exchange Resins As Adsorbents for Air Purification", In Proceedings of the 1987 U.S. Army CRDEC Scientific Conference on Chemical Defense Research, CRDEC-SP-88013, April 1988, Unclassified Report.
- 6 Buchanan, James H., Rohrbaugh, Dennis K., Bartram, Philip W. and DiBona Noel C., "Adsorption of Agent from a Chlorofluorocarbon Solvent Using a Macroreticular Strong Acid Resin", in Proceedings of the 1990 U.S. Army CRDEC Scientific Conference on Chemical Defense Research, CRDEC-SP-034, November 1991, Unclassified Report.
- 7 Nene, Dilip M., Kopchick, Richard M., Brendley, William H., Koals, Michael A., Shuely, Wendel J., and McHugh, Vincent M. Composition, Formulation Method, Test Development, and Performance Evaluation Investigations of Sorptive/Catalytic Self-Decontaminating Coatings, CRDEC-TR-88112, U.S. Army CRDEC, Aberdeen Proving Ground, MD, July 1988, UNCLASSIFIED Report.

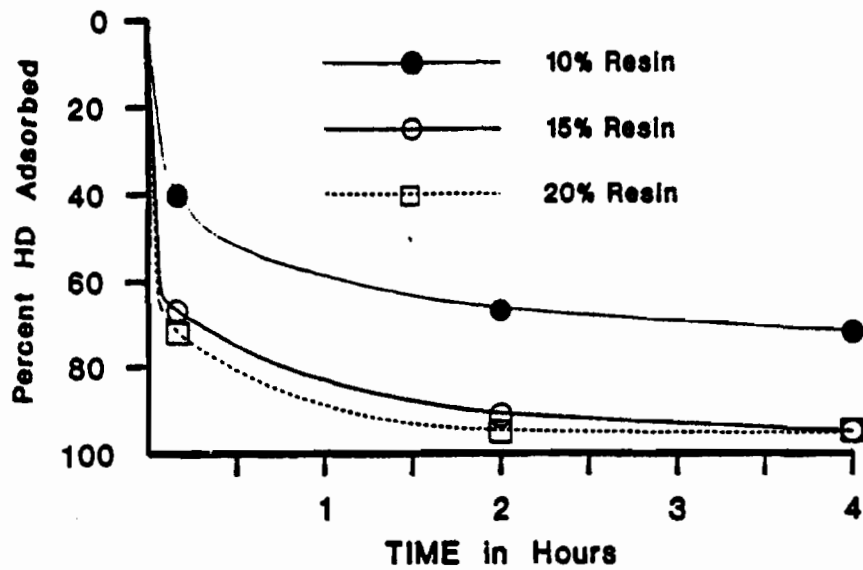


Figure 1. Effect of Resin Concentration on HD Adsorption Rate.

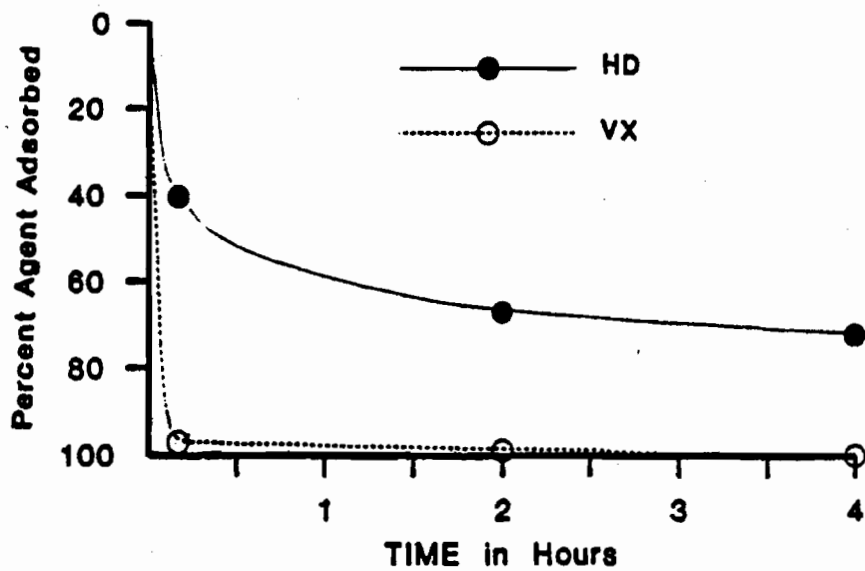


Figure 2. Comparison of HD and VX Adsorption Rates.

BLANK

OXIDATIONS OF ALKENES CATALYZED BY A MN(III) PORPHYRIN AND CATIONIC POLYMER LATEXES

Weiming Zhu and Warren T. Ford*

Department of Chemistry, Oklahoma State University, Stillwater, Oklahoma 74078

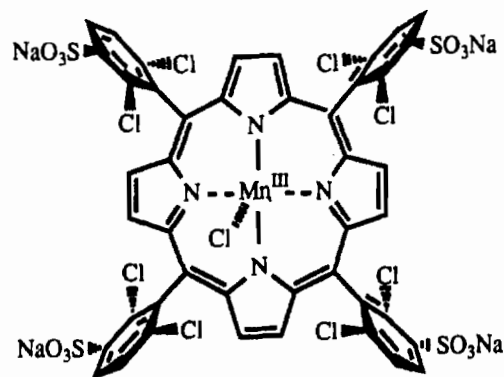
Three types of cationic polymer latexes were prepared by emulsion copolymerization of vinylbenzyl chloride, divinylbenzene and a third monomer, vinyl octadecyl ether, styrene, or *n*-decyl methacrylate, followed by quaternization with trimethylamine. The latexes had 44-71 nm diameters and polydispersity indices of 1.06-1.10. Vinyl octadecyl ether did not copolymerize but hydrolyzed under the polymerization conditions to produce 1-octadecanol, which as a coemulsifier gave highly viscous latexes. The tetraanion 5,10,15,20-tetrakis-(2,6-dichloro-3-sulfonatophenyl)porphinatomanganese(III) chloride bound irreversibly to the cationic latexes and was an active catalyst for oxidations of alkenes by sodium hypochlorite and potassium peroxymonosulfate in the absence of added organic solvent. The porphyrin catalyst in the latexes was more active than in solution. Porphyrin catalysis gave epoxides concurrently with competing uncatalyzed hypochlorous acid oxidations to complex mixtures of allylic chlorides, allylic alcohols, α,β -unsaturated ketones, and chlorohydrins.

INTRODUCTION

Polymer latexes have potential as catalyst supports because their $<1 \mu\text{m}$ sizes may avoid mass transfer and intraparticle diffusional limitations to reaction kinetics. There are many examples of large polymer particles as catalyst supports, but in most cases of reasonably fast chemical reactions, slow mass transfer of reactants to the particle surface or slow intraparticle diffusion of reactants or products makes the overall reactions slower than those catalyzed by the same active species in solution. Diffusional limitations have been demonstrated clearly with polymer-supported phase transfer catalysts.¹ In 1984 we showed that quaternary phosphonium ions on colloidal polystyrene supports provided faster rates of reaction of cyanide ion with benzyl bromide than on conventional polystyrene beads, but that the usual phase transfer catalysis conditions were impractical because of fast coagulation of the charged colloidal particles by the aqueous electrolyte solution.² However, colloidal polymers have proved to be viable catalyst supports for a variety of oxidation and hydrolysis reactions in which high electrolyte concentrations are not required.³⁻¹¹ Although the colloidal catalysts are more difficult to recycle than large beads, they can be ultrafiltered, or coagulated and redispersed, for repeated use.

One example of latex catalysis is the epoxidation of styrene by sodium hypochlorite at room temperature catalyzed by 5,10,15,20-tetrakis-(2,6-dichloro-3-sulfonatophenyl)porphinatomanganese(III) chloride (**MnPor**) bound to anion exchange latexes.⁷ Metalloporphyrins have been studied extensively as oxidation catalysts in attempts to mimic and to understand the mechanism of action of the natural oxygenases such as the cytochromes P-450.¹²⁻¹⁷ Our latex-hypochlorite conditions that produced high yields of styrene oxide, however, gave only low yields of epoxides from aliphatic alkenes.⁷ We have reinvestigated the oxidations of aliphatic alkenes with latex-bound **MnPor** at 40 °C using latexes containing fewer

quaternary ammonium ion repeat units and more aliphatic or aromatic hydrocarbon repeat units than those used for the epoxidation of styrene, in order to sorb more of the alkenes into the reactive catalyst phase.



MnPor

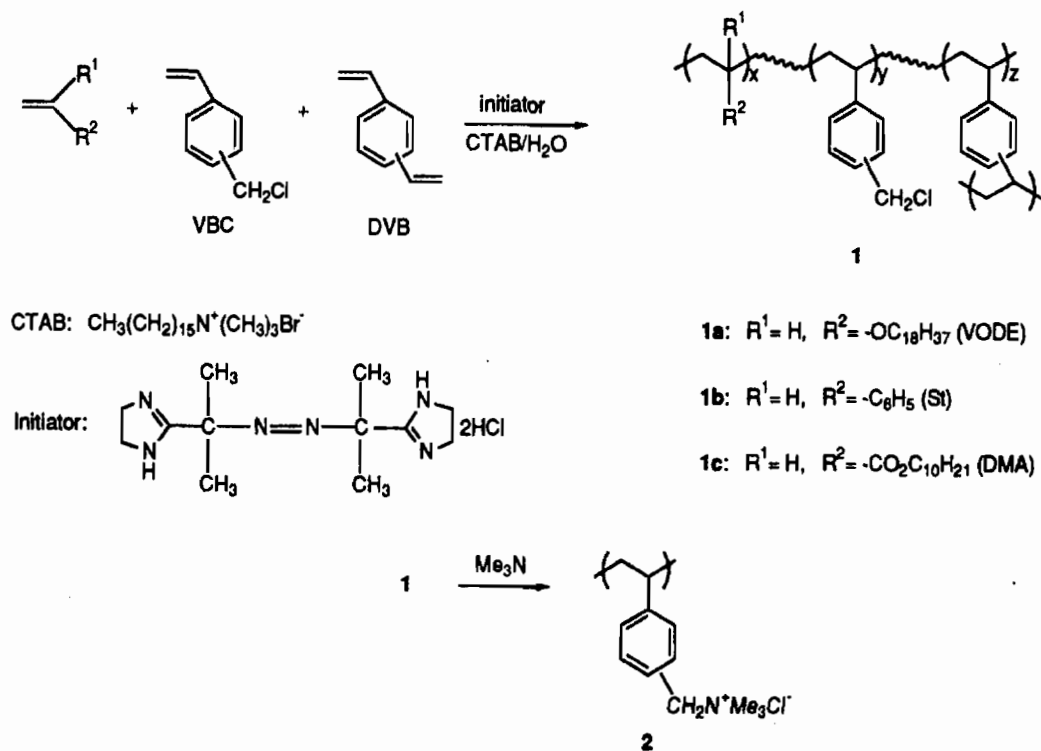
RESULTS AND DISCUSSION

Preparation of Latexes

Cationic latexes were prepared by two steps as shown in Scheme 1: Emulsion copolymerization of vinylbenzyl chloride (VBC), divinylbenzene (DVB), and a third monomer (vinyl octadecyl ether, styrene, or *n*-decyl methacrylate) with 2,2'-azobis(*N,N*-dimethyleneisobutyramidine) dihydrochloride as the initiator and cetyltrimethylammonium bromide as a surfactant produced latexes that were quaternized by treatment with 25 wt % aqueous trimethylamine. The emulsion polymerizations were performed by both batch and semicontinuous methods. The quaternization of chloromethylene groups from VBC was carried out in an ordinary round bottom flask at 40-60 °C with a condenser or in a stainless steel vessel at 60 °C under elevated pressure due to trimethylamine (bp 2.9 °C). The higher pressure conditions gave higher conversion. The quaternized latexes were ultrafiltered to remove impurities derived from surfactant and initiator, and analyzed by chloride-selective electrode titration to contain 1.72-4.09 mequiv of Cl⁻/g of the dried latex, which corresponds to 53-89% conversion of the VBC units. Details of latex preparations are available from the authors.

The polymerizations in which we attempted to use vinyl octadecyl ether (VODE) as a comonomer produced highly viscous latexes a puzzling result at first. Later we found from the following evidence that the high viscosity was due to 1-octadecanol produced by hydrolysis of the VODE under the polymerization conditions. (1) We recovered 1-octadecanol by extracting the latex with dichloromethane. (2) A CP-MAS ¹³C NMR spectrum of the extracted latex contained no long chain aliphatic carbon signals, which proves that VODE did not polymerize. (3) Deliberate addition of 1-octadecanol to a quaternized latex, prepared from styrene, VBC, and DVB, gave a highly viscous dispersion. Fatty alcohol coemulsifiers are known to produce highly viscous emulsions.¹⁸ The failure of VODE to copolymerize with styrene derivatives is not surprising, but there are reports of copolymerizations of alkyl vinyl ethers and styrene in bulk,¹⁹ and we speculated that the emulsion method might lead to higher copolymer reactivity, because the VODE in a growing latex particle might be concentrated near the particle surface.

SCHEME I



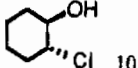
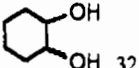


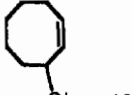
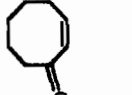
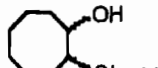

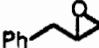
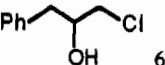
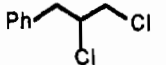
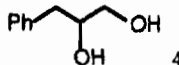
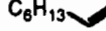
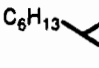
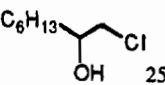
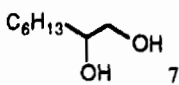
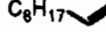
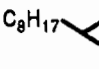


Oxidations with NaOCl

Oxidations of cyclooctene, cyclohexene, 1-octene, allylbenzene and 1-decene with NaOCl catalyzed by latex bound MnPor were carried out at 40 °C for 5 h. The anionic MnPor was quantitatively bound to the cationic latexes, since no porphyrin could be detected in ultrafiltrates.⁷ The resulting red colloidal catalysts were used to perform the reactions in triphase mixtures of water, particles, and organic reactants. The results in Table I show complex mixtures of oxidation products. Cyclohexene reacted fastest, giving 97 % conversion, while only 10 % 1-decene was converted after 5 h. Conversion of alkene and epoxide yield increased with NaOCl concentration. The latex compositions had little influence on the oxidation of cyclooctene, and latex bound MnPor was more active than MnPor in solution (41% vs. 15% conversion).


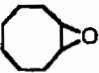
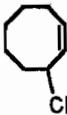

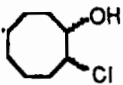
Several key results of oxidations of cyclooctene reported in Table II are important for our understanding of these reactions: (1) In the absence of MnPor, oxidation still gave several products, but only 2 mol percent of cyclooctene oxide (expt 1 of Table II). (2) The MnPor raised the yield of the epoxide, but did not affect the yields of other products (expt 2). Lower concentration of NaOCl gave slightly less epoxide (expt 3), and one hour reaction produced lower yields than five hour reaction (expt 4). (3) Highly basic media (pH ≥13) resulted in selective epoxidation (expt 5).

TABLE I
Oxidation of Alkenes with NaOCl^a

Alkene	Conv (%)	Products (mol %)				
	97	 55	 10	 32		
	47	 16	 13	 4	 14	
	39	 25	 6	 4	 4	
	39	 7	 25	 7		
	10	 4				

^a All experiments were carried out at 40° C for 5 h by using 0.35 mmol of alkene, 0.52 mmol of NaOCl, 6.91×10^{-4} mmol of Mn porphyrin, and 13.5 mg of latex L-3 containing 0.038 mmol N⁺Cl⁻ sites in 1.64 mL of aqueous mixture. The ratio N⁺/Mn was 55.

TABLE II
Product Distribution from the Oxidation of Cyclooctene^a

Expt	Mn por (μ M)	NaOCl (M)	pH	 (mol %)	 (mol %)	 (mol %)	 (mol %)	 (mol %)
1	-	0.32	10.3	68	2	13	2	15
2	0.42	0.32	10.3	53	16	13	4	14
3	0.42	0.27	10.3	64	11	13	2	10
4 ^b	0.42	0.27	10.3	87	3	4	1	5
5 ^c	0.34	0.22	≥ 13	75	25	-	-	-

^a Experiments were done under conditions reported in Table I unless noted otherwise.

^b This experiment was performed for 1 h.

^c pH was adjusted by addition of 2.0 mL of 1 N NaOH.

We interpret the NaOCl oxidation results as follows: (1) The relative reactivities in Table I are normal for reactions of cyclohexene, cyclooctene, and 1-alkenes with electrophilic reagents. (2) The lesser reactivity of 1-decene than of 1-octene in Table I is likely due to lesser solubility of the longer chain alkene in water and in the latex. Solubility differences may also be responsible for some of the other reactivity differences. The solubility of cyclohexene in water at 25 °C is 2.6×10^{-3} M,²⁰ while that of 1-decene is estimated to be 1.5×10^{-6} M.²¹ (3) The latex phase is the site of epoxidation catalyzed by MnPor, since all MnPor is bound to the particles. The latex phase is also the site of a major part of the HOCl reactions, since all of the oxidations proceed faster in the presence of the latex. The quaternary ammonium latex acts as a phase transfer catalyst which binds ClO⁻ and the MnPor catalyst as an anion exchange resin, and as a sorbent for HOCl and the alkene. High local concentrations of reactants and catalyst in the latex lead to faster reactions than in water in the absence of latex. We found previously that polystyrene gels are oxidized by NaOCl under similar phase transfer catalysis conditions,²² Thus it is likely that the latexes in this study were partly chlorinated and oxidized, although we did not analyze recovered polymers. (4) The MnPor catalyzes formation of epoxide but is not necessary for the formation of the other oxidation products, as shown in Table II. As proposed before an oxo Mn(V) porphyrin is likely a reactive intermediate.¹²⁻¹⁷ (5) All of the oxidation products except epoxide are formed primarily from hypochlorous acid (HOCl) without involvement of the Mn Por. Although only about 5.4×10^{-4} M HOCl (pK_a 7.53) is present initially in the pH 10.3 sodium hypochlorite solution, the HOCl is highly reactive. At pH >13 (expt 5 in Table VI) the HOCl reactions are suppressed and only epoxide is formed.

Other Oxidizing Agents

Aqueous potassium monoperoxysulfate (KHSO₅) at pH 1.5 oxidized cyclooctene with high conversion and high selectivity for epoxide. Commercial KHSO₅ (DuPont OXONE) was analyzed to contain KHSO₅·KHSO₄·K₂SO₄ in relative molar amounts of 1.73:1.0:1.34. In a more acidic solution (pH 0.3), diol rather than epoxide was produced by ring opening hydration of cyclooctene oxide. Although we tried many combinations of KHSO₅, substrate, latex quantity and water, and even addition of the surfactant cetyltrimethylammonium bromide, the latex coagulated during every reaction. Since a solution of 0.31 M KHSO₄ and 0.10 M K₂SO₄ (ionic strength = 0.61 M, the same as that in the oxidation mixture) did not coagulate the latex particles, apparently the KHSO₅ is responsible for the coagulation.

In a control experiment we discovered that KHSO₅ oxidizes alkenes efficiently even in the absence of latex and in the absence of any metalloporphyrin catalyst. Aqueous KHSO₅ produces epoxides of many alkenes at pH ≥6.6 and diols in acidic aqueous mixtures.²³ The latex-free, catalyst-free conditions are useful synthetically, whereas the oxidations reported in this paper are not.

CONCLUSIONS

Cationic polymer latexes about 50 nm in diameter can be prepared by emulsion polymerization of vinylbenzyl chloride, divinylbenzene and a third monomer, vinyl octadecyl ether (VODE), styrene or *n*-decyl methacrylate, with a water-soluble azo-amidine initiator and CTAB as surfactant, and subsequent quaternization with trimethylamine. The VODE does not copolymerize, but hydrolyzes to produce 1-octadecanol, which causes high viscosity in the

dispersions. The water-soluble anionic manganese(III) porphyrin can be ionically bound to the cationic latex to form a colloidal porphyrin catalyst for the oxidation of alkenes in the absence of added organic solvent. The porphyrin catalyst is more active in the latex than in solution. The latex acts as both a carrier of reactants and a phase transfer catalyst, and its exact composition has little effect on the oxidations.

ACKNOWLEDGMENT

This research was supported by U.S. Army Research Office. We thank Dr. Frank McEnroe of Conoco, Inc., for the solid state ^{13}C NMR spectra and Dr. H. Turk for the manganese porphyrin.

REFERENCES

1. M. Tomoi and W. T. Ford, *Adv. Polym. Sci.*, **55**, 49 (1984).
2. M. Bernard, W. T. Ford, and T. W. Taylor, *Macromolecules*, **17**, 1812 (1984).
3. M. Hassanein and W. T. Ford, *J. Org. Chem.*, **54**, 3106 (1989).
4. H. Turk and W. T. Ford, *J. Org. Chem.*, **53**, 460 (1988).
5. W. T. Ford, R. S. Chandran, and H. Turk, *Pure Appl. Chem.*, **60**, 395 (1988).
6. R. S. Chandran, S. Srinivasan, and W. T. Ford, *Langmuir*, **5**, 1061 (1989).
7. H. Turk, W. T. Ford, *J. Org. Chem.*, **56**, 1253 (1991).
8. H. Kitano, Z.-H. Sun, and N. Ise, *Macromolecules*, **16**, 1306 (1983).
9. Z. Sun, C. Yan, and H. Kitano, *Macromolecules*, **19**, 984 (1986).
10. K. Arai, J. Sugita, and Y. Ogiwara, *Makromol. Chem., Rapid Commun.*, **7**, 427 (1986). K. Arai, Y. Maseki, and Y. Ogiwara, *Makromol. Chem., Rapid Commun.*, **7**, 655 (1986).
11. J. H. Kim, M. S. El-Aasser, A. Klein, and J. W. Vanderhoff, *J. Appl. Polym. Sci.*, **35**, 2117 (1988).
12. T. J. McMurray and J. T. Groves, *Cytochrome P450: Structure, Mechanism, and Biochemistry*, P. R. Ortiz de Montellano, Ed.; Plenum Press: New York, 1986, chapter 1.
13. K. A. Jorgensen, *Chem. Rev.*, **89**, 431 (1989).
14. T. Mlodnicka, *J. Mol. Catal.*, **36**, 205 (1986).
15. B. Meunier, *Bull. Soc. Chim. Fr.*, 578 (1986).
16. D. Mansuy, *Pure Appl. Chem.*, **59**, 759 (1987).
17. T. C. Bruice, *Aldrichim. Acta*, **21**, 87 (1988).
18. J. H. Schulman and E. G. Cockbain, *Trans. Faraday Soc.*, **36**, 651 (1940).
19. G. Akazome, S. Sakai, Y. Choshi, and K. Murai, *Kobunshi Kagaku*, 478-558. *Chem. Abstr.*, **55**, 22901e-22902h (1961).
20. C. McAuliffe, *J. Phys. Chem.*, **70**, 1267 (1960).
21. This value was estimated from 1-octene and an assumed decrease of solubility by a factor of 4 per additional CH_2 group: C. Tanford, *The Hydrophobic Effect*, Wiley: New York, 1973, pp 4-8.
22. S. Mohanraj and W. T. Ford, *Macromolecules*, **19**, 2470 (1986).
23. W. Zhu and W. T. Ford, *J. Org. Chem.* in press.

TESTS OF A REACTANT-LOADED DECONTAMINATING POLYMER POWDER AGAINST CW AGENTS AND THICKENED SIMULANTS

Nolan Tillman, Mark S. Kaplan, Gary M. Russo

Advanced Chemical Technologies Group
Federal Systems Division
Eastman Kodak Company
Rochester, NY 14650-2156

ABSTRACT

A polymer-based decontaminating powder mixture, consisting of a cross-linked, cationic latex blended with Oxone[®] and sodium iodosobenzoate, was tested against thickened 2-chloroethyl ethyl sulfide (CEES) and 4-nitrophenyl hexanoate (NPH), simulants for mustard oxidation and G-agent hydrolysis, respectively. Solvent extraction and quantitative GLC was used to monitor simulant reaction with time. The powder was found to be about as reactive against thickened simulants as unthickened simulants. Tests at Calspan with HD showed activity comparable to CEES, but tests with GD or VX detected no reaction of the agent. Thus, our simulant studies accurately predicted the results for HD oxidation, but not for GD hydrolysis.

INTRODUCTION

Our research seeks to develop decontamination technologies that effectively destroy CW agents without being toxic, environmentally hazardous, or caustic threats in themselves. For example, a sorptive, decontaminating powder or coating should rapidly sorb an agent to eliminate the vapor or contact threat of the agent, and then chemically degrade it *in situ* to innocuous biproducts.

We have previously described results showing that "dry" cationic latex polymer powders containing oxidants or the hydrolysis catalyst NaIBA (sodium iodosobenzoate) chemically destroyed either the G-agent simulant NPH (4-nitrophenyl hexanoate) or the mustard simulant CEES (2-chloroethyl ethyl sulfide).^{1,2} Other investigators have published results on catalytic hydrolysis of 4-nitrophenyl diphenyl phosphate in aqueous dispersions and latexes of cationic polymers with either covalently bound³ or dissolved⁴ iodosobenzoates. We report here on testing of a NaIBA and oxidant loaded powder with (a) thickened simulants, and (b) agents GD, HD and VX.

EXPERIMENTAL METHODS

Preparation of Decontamination Powder

A multicomponent, decontaminating powder was formulated containing the following components (in wt %):

- 44% Polymer solids
- 29% Oxone®
- 18% NaHCO₃
- 7% Sodium iodobenzoate (NaIBA)
- 2% NaOH

The polymer component was a cationic, crosslinked latex containing 49.5% styrene monomer, 49.5% of a vinylbenzyl trialkylammonium monomer, and 1% divinylbenzene as a crosslinking agent.^{1,2} All the components, except for the Oxone®, were freeze dried together, to form a fine, free-flowing powder. Then the Oxone (active ingredient: KHSO₅, used as supplied from Aldrich), was added by grinding it with the powder in an agate mortar and pestle.

Preparation of Thickened Simulants

CEES (2-chloroethyl ethyl sulfide) was thickened by mixing 4.75 g of CEES with 0.25 g (5% by weight) of K-125 polymer (copolymer of 82% methyl methacrylate, 12% ethyl methacrylate, and 8% butyl methacrylate, kindly supplied by Fred Longo of CRDEC) in a 4-dram screw cap vial. The simulant was placed on a roll mill with a stir bar for 24 hours, during which time the polymer dissolved completely to form a slightly cloudy solution.

NPH was thickened in the same manner with 2.5% K-125 and rolled for 2 hours, to form a very viscous simulant.

Challenge-Extraction of Decontamination Powder with CEES and Thickened CEES

Experiments were conducted under ambient conditions (23 °C and ≤ 35% R.H.). The powder was weighed into 100 mg samples in 4-dram screw cap vials. Each sample was challenged with 10.0 μL of CEES or thickened CEES, a small stir bar was added, and the vials were recapped. The samples were stirred for the duration of the challenge time. Samples were worked-up by adding, after varying challenge times, 6.0 mL of diethyl ether. After mixing for 1.5 minutes, 10.0 μL of a 40% v/v solution of diethyl malonate (DEM) in 1,1,1-trichloroethane was added as an internal standard. Then an aliquot of the solution was removed by pipetting through a plug of glass wool, and placed in a septum-capped vial.

Challenge-Extraction of Decontamination Powder with NPH and Thickened NPH

Thickened NPH was too viscous to transfer with a microliter syringe, so challenge sizes were measured by weighing on an analytical balance to the nearest milligram.

The powder was weighed into 100 mg samples in 4-dram screw cap vials and placed in a high humidity chamber and preconditioned for 24-48 hours at ≥ 76% R.H and 23 °C.

The samples were then capped and moved to a weighing station. A total of 50 mg of NPH or thickened NPH was weighed into the vials. The vials were re-capped and agitated for about 1.0 minute to mix powder and simulant. Samples were handled in groups of six, with time $t = 0$ min taken as approximately the average time at which the vials were challenged (each group took about 7 minutes to challenge). Thus, the time of challenge reported for a sample is accurate to approximately ± 5 minutes. The samples were then returned to the high humidity chamber and stirred until $t = 0.5$ h. Stirring was then stopped, but samples were left to stand in the chamber for the duration of the challenge time.

Samples were worked-up by adding, after varying challenge times, 3.0 mL of diethyl ether and stirring for 1.0 h. Then 50 μL of 8% w/v 1,4-di-terbutylbenzene (DTBB) in 1,1,1-trichloroethane was added (4.0 mg of DTBB) as an internal standard. After a brief swirling, an aliquot of the solution was removed by pipetting through a plug of glass wool to remove suspended particulates, and placed in a small, septum-capped vial.

Quantitative GLC

The samples were analyzed for unchanged NPH or CEES recovered by capillary GLC using the internal standard technique with a flame ionization detector. Chromatograms were recorded and electronically integrated. Peak areas of extracted NPH and DTBB or CEES and DEM were compared with a calibration curve of ratios determined for authentic, standard solutions containing varying amounts of simulant and a constant amount of internal standard.

Testing of Decontamination Powder With HD, GD and VX

Testing of the decontamination powder with HD, GD and VX was performed at Calspan Corporation, Advanced Technology Center, using methods similar to those described in detail above for testing with thickened simulants. 100 mg powder samples were challenged with agent and extracted with diethyl ether at the end of the challenge time. Quantitative GLC was performed using a flame photometric detector. Butyl sulfone added to ether extracts after extraction served as an internal standard with HD. No internal standard was used with VX or GD, and absolute integrated peak areas were used to quantify the amount of residual agent remaining.

RESULTS AND DISCUSSION

The recovery of simulant from decontamination powder samples challenged with either CEES or NPH is shown in Figures 1 and 2, respectively. Powder samples of 100 mg size were challenged with either 10 μL of neat CEES or thickened CEES or 40 μL of neat NPH or thickened NPH. The amount of residual simulant at varying times after challenge was determined by extracting samples with diethyl ether and analyzing the extracts by quantitative GLC. The results for thickened simulants are overlaid on the results for unthickened simulants. Testing of samples with CEES was done under ambient conditions. The tests with NPH were performed under high-humidity conditions in an environmental chamber. Prior work showed that the rate of NPH hydrolysis under in such "dry" powders strongly increased with increasing relative humidity.¹

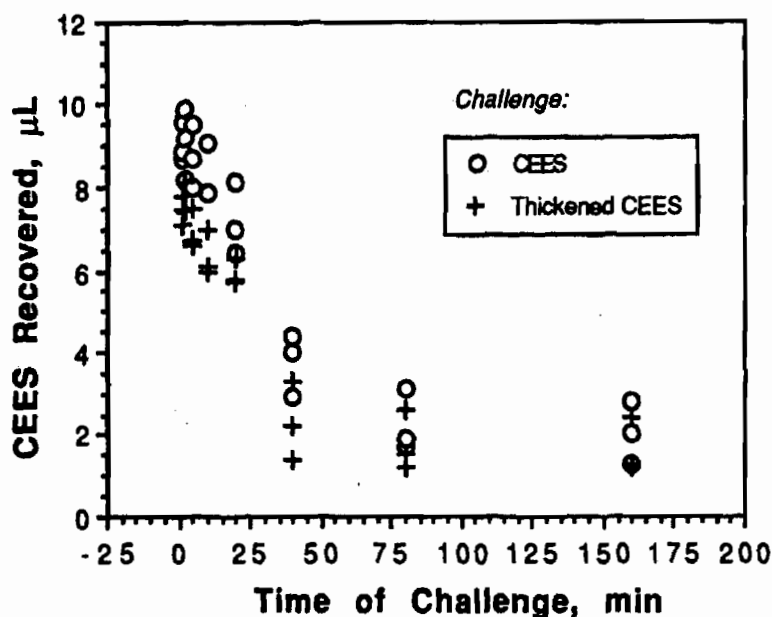


Figure 1. Recovery of unreacted CEES, applied neat or thickened, from 100 mg decontamination powder samples challenged with 10.0 μL simulant under ambient conditions.

The points for recovery of CEES or NPH from thickened challenges closely overlay the points for unthickened simulants. Thus, within experimental error, this multiply-loaded powder formulation appears to be as active against thickened simulants as unthickened simulants. We observed destruction of 8 μL of CEES in ≤ 2 hours and 40 μL of NPH by 100 mg of powder. Chemical destruction of the agent simulants has been further confirmed by monitoring the appearance of simulant reaction products, which form at the same rates as simulants are destroyed. Up to 50% of 2-chloroethyl ethyl sulfoxide (based on CEES reacted) was detected, as well as up to 50% yields of hexanoic acid and 4-nitrophenol formed from NPH.

Tests of this decontamination powder with HD indicated that destruction of 10.0 μL of HD by 100 mg of powder occurred rapidly in ≤ 3 hours, the minimum challenge time evaluated (Figure 3). The lower limit of detection on the flame photometric detector employed was 3.0 μL of HD, but the evidence showed that extensive oxidation of HD by this powder occurred.

However, when challenged with 40.0 μL of GD or 10.0 μL of VX, significant agent destruction was not seen (Figure 3). Although we had no reason to believe that VX would react (prior work with Malathion suggested only that very slow hydrolysis may be occurring), the failure to observe any GD hydrolysis was surprising.

Literature results have shown recently that accurate simulation of the rate of G-agent hydrolysis in micellar solutions is difficult. The greater hydrophobicity of typical simulants, such as 4-nitrophenyl diphenyl phosphate and NPH, than G agents results in greater partitioning of the simulants into the micellar phase, in close proximity to the catalytic sites at the surface of the micelle particles.⁵ As a result, simulant hydrolysis is

faster than agent hydrolysis. We postulate that a similar explanation may account for our failure to detect GD hydrolysis in the powder described here.

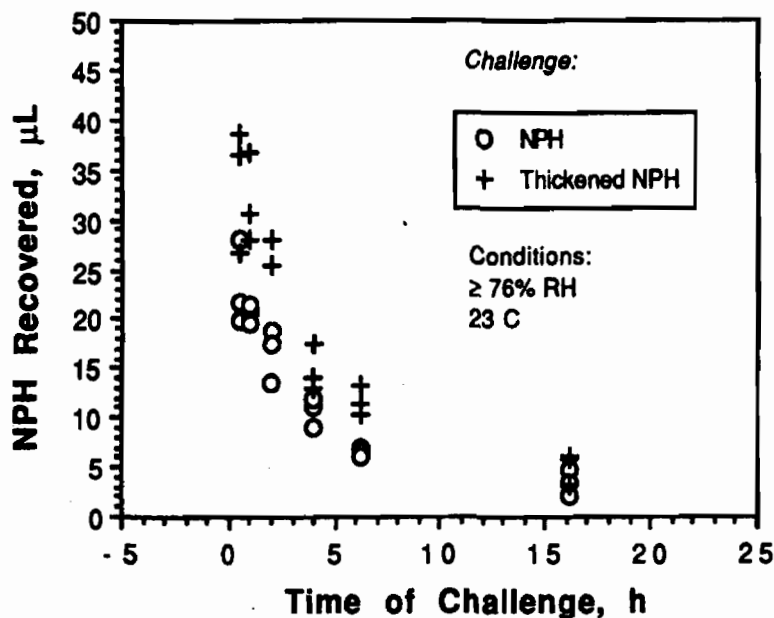


Figure 2. Recovery of unreacted NPH, applied neat or thickened, from 100 mg decontamination powder samples challenged with 40.0 µL simulant. Conditions: $\geq 70\%$ RH and 23 °C.

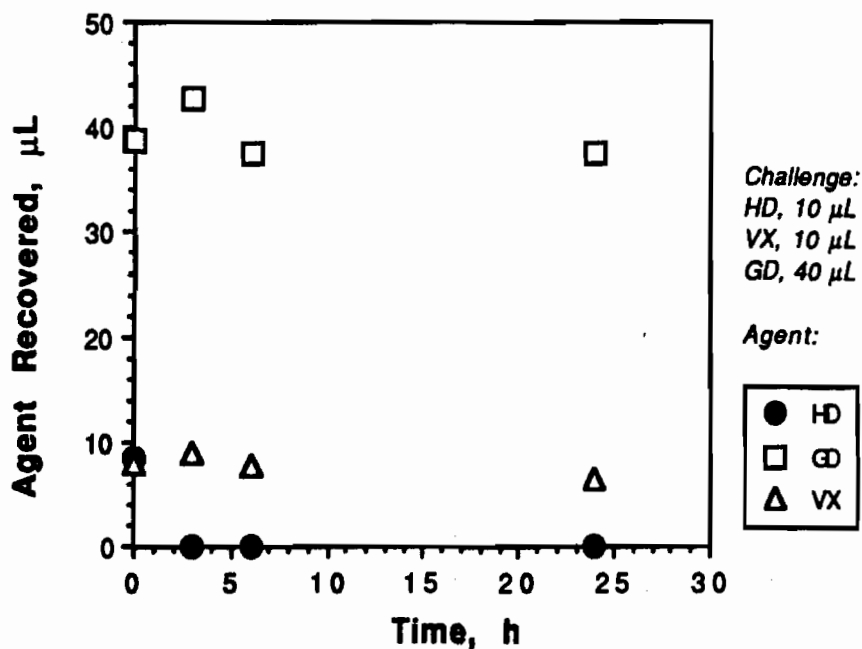


Figure 3. Recovery of unreacted agent from 100 mg decontamination powder samples challenged with HD, VX or GD. Each point represents the average of three samples.

CONCLUSIONS

A direct comparison of a multiple decontaminant-loaded (7% NaIBA/29% Oxone) powder based on a cationic latex polymer was challenged with either thickened or unthickened simulants. The results did not show significant differences in the rate of either CEES oxidation or NPH hydrolysis between thickened or unthickened simulants. Tests with live agents detected oxidation of HD, but no oxidation of VX or hydrolysis of GD. Agent tests could be performed on only a limited number of samples, so additional work is needed to confirm this result and establish more quantitative correlations of simulant and agent results. This result points out the need for caution in extrapolating from simulants to live agents in the testing of decontamination materials.

ACKNOWLEDGEMENTS

This research was funded by Eastman Kodak Company, based on previous work funded by the U.S. Army Advanced Concepts and Technology Committee (Joseph V. Pistrutto, COR [CRDEC]). Testing with HD, GD and VX was performed Calspan's Advanced Technology Center, Buffalo NY. We thank Thomas McMahon and David Mangino of Calspan for conducting the agent tests described here, and for helpful discussions.

REFERENCES

- (1) Tillman, N.; Speaker, L. M. S.; Kaplan, M. S.; Russo, G. M.; Wolf, B. L.; Whitt, T.; Rowley, L. A. "Reactive Polymeric Materials For Decontamination: Catalytic Hydrolysis of NPH by Iodosobenzoate-Containing Polymeric Materials," *1990 Scientific Conference on Chemical Defense Research*, U.S. Army Chemical Research, Development and Engineering Center, Edgewood MD, November 1990.
- (2) Tillman, N.; Speaker, L. M. S.; Kaplan, M. S.; Russo, G. M.; Wolf, B. L.; Whitt, T.; Rowley, L. A. "Reactive Polymeric Materials For Decontamination: Sorption and Oxidation of CEES by Polymer-Supported Reactants," *1990 Scientific Conference on Chemical Defense Research*, U.S. Army Chemical Research, Development and Engineering Center, Edgewood MD, November 1990.
- (3) Moss, R. A.; Chung, Y.-C. "An Efficient Iodosobenzoate-Functionalized Polymer for the Cleavage of Reactive Phosphates," *Langmuir* 6, 1614-1616 (1990).
- (4) Ford, W. T.; Yu, H. "Hydrolysis of p-Nitrophenyl Diphenyl Phosphate Catalyzed by IBA in Cationic Latexes," *1990 Scientific Conference on Chemical Defense Research*, U.S. Army Chemical Research, Development and Engineering Center, Edgewood MD, November 1990.
- (5) Leslie, D. R. "A Quantitative Description of the Effect of Cetyltrimethylammonium Bromide on the 2-Iodosylbenzoate-Catalysed Hydrolysis of Active Esters and Related Compounds," *Aust. J. Chem.* 42, 2119 (1989).

REMOVAL OF THICKENED MUSTARD FROM PAINTED TEST PANELS BY LIQUID SYSTEMS

Yu-Chu Yang¹, J. Richard Ward¹, Kurt Görgens², and Manfred Zillmer²

ABSTRACT

More than 40 reactive and nonreactive liquid systems have been systematically evaluated for their effectiveness in removing thickened mustard from the surfaces of test panels. On panels with nonsorptive paint, high efficacy is achieved by nonreactive systems that rapidly solubilize the thickened mustard. Addition of reactants to these systems does not change the results. Chemical reaction alone does not remove the thickened mustard when the solvent fails to solubilize it rapidly. Consequently, solubilization is both sufficient and necessary for achieving high efficacy. One exception was noted: High efficacies were measured for aqueous bleach solutions by way of vigorous reactions only at the mustard-water interface. On panels with sorptive paint into which mustard has penetrated, however, a better decon efficacy is obtained with the addition of a reactant.

INTRODUCTION

While the solubilities of mustard (HD) and a number of polymers in organic solvents are available,^{3,4} the efficiencies of these solvents to remove mustard thickened with such polymers from the surface of painted test panels has not been systematically determined. In particular, the performances of solvent mixtures such as the aqueous solutions of polar organic solvents in removing thickened mustard (THD) are poorly understood. For the same solvent, it is suspected that the efficiency of removal may be different from that determined in a test tube in the absence of a solid surface. Recently, J.W. Hovanec and coworkers⁵ have initiated a program to measure the rate of solution of THD in aqueous solutions of N-alkyl 2-pyrrolidinones, which are solvent candidates of a new liquid decon system under development. It will be useful to compare their results with the efficacy of THD removal from the surface of painted test panels.

It has been perceived that mustard is best removed from a surface by first dissolving in a solvent followed by reacting with a reactant in the solvent. However, a number of field decontaminants are reactive aqueous solutions such as HTH (High Test Hypochlorite) slurries. In these systems, the first dissolution step does not occur. Therefore, we attempt to also investigate decon efficacies of a series of reactants including Ca(OCl)₂ in aqueous solutions. Our purpose is to determine which reactants can ensure an efficient removal solely by a fast chemical reaction at the interface of the thickened mustard and the aqueous solution containing the reactant.

Previous panel tests have shown that mustard, and particularly thickened mustard, could not be satisfactorily removed by water alone.⁶ Any increase in the rate of agent removal should directly reflect the reaction at the HD-water interface. A comparison of the reactants in organic solvents is also desirable but less accurate. The solvent itself is expected to remove a major portion of the mustard from the surface regardless of the presence of a reactant.

In this paper, the results of three series of panel tests are summarized. In the first series, organic solvents are tested for their decon efficacies. Next, aqueous solutions of polar organic solvents are tested to compare the changes in decon efficacies as a result of the decrease in solvent polarity. In the last series, a range of reactants dissolved in aqueous solutions are examined. Since those solutions cannot dissolve the thickened mustard, the measured amount of mustard removed from the panel should only reflect the extent of the chemical reactions.

All the above tests are performed on panels covered with nonsorptive (hardened) paint. On sorptive paint, on the other hand, HD or THD penetrated into the paint and was made more difficult to remove. For the purpose of comparison, test results on a sorptive paint, (i.e., alkyd painted panels) are also presented.^{7,8}

EXPERIMENTATION

To reduce the number of variables, all the panels tested are painted by the same epoxy resin paint which is resistant to HD penetration.⁸ Control experiments showed that indeed all the HD or THD was present on the surface without any loss as a result of diffusion into the paint layers during the contamination period of 3 hours. Since panel tests are usually procedure-, equipment-, and operator-dependent, it is recommended that data interpretation should focus on the trend, but not on the absolute value.

Each test panel was of a surface area of 12.6 cm² (diameter = 4 cm) and contaminated with 10 ul HD or THD at a surface contamination density of 10 g/m². The panel was contaminated for three hours. About 4 ml of a liquid decontaminant was added to each panel contained in a weighing bottle of about the same cross-sectional area as the panel. After the panel was exposed to the decontaminant for 30 minutes, the panel was removed from the liquid, rinsed with distilled water, and dried with a paper towel. Any mustard left on the panel was extracted in 6.3 ml n-heptane overnight. The n-heptane extract was analyzed by GC (FPD detector with sulfur filter) for quantitative determination of the residual mustard left on the panel. The detection limit by the above procedure was 0.01 g/m² HD. The procedure described above was depicted in Figure 1. For each test condition, at least four experiments were conducted on four separate but identical panels. As shown in Tables 1 to 4, reproducibility was very good for most of the tests.

HD was thickened with 10% (by weight) Parlon S300 (chlorinated polyisoprene) polymer powder. This THD looked viscous and was as adhesive to the surface of the panels as a glue. For comparison, the panels were contaminated with three types of mustard samples: regular (technical)

HD at greater than 95% purity; with 10% thickener (THD, 10%); and THD with 50% thickener (THD, 50%). The latter THD sample was prepared by evaporating the THD, 10%, on the panel for 3 hours under the hood. About 70% of the HD was evaporated; consequently the thickener content was increased to about 50%. Note that the surface contamination density of THD, 10% was 10 g/m² but that of THD, 50% was reduced to only 2-3 g/m². The analyzed contamination densities of both THD samples on two sets of 8 panels are shown below. These results were obtained by extracting the THD samples directly from the panels with n-heptane for about 18 hours; and by analyzing the extracts for HD contents.

Analyzed Contamination Density, g/m² HD

THD, 10%	9.4	9.4	10.0	10.4
THD, 50%	2.8	1.8	2.3	2.6

RESULTS AND DISCUSSION

Non-Reactive Systems

As shown in Table 1, both HD and THD (10%) were removed efficiently by a broad class of organic solvents ranging from pure hydrocarbons to alcohols and polar, aprotic solvents with solubility parameters (δ) ranging from 7 to 13. However, the N-ethyl 2-pyrrolidinone (NEP) was relatively less efficient in removing both HD and THD of 10% thickener. The more polar solvents could remove the THD of 50% thickener better than the nonpolar hydrocarbons. The 90% ethanol-NEP mixture was among the best in removing the THD samples. (Such organic solvent mixtures offer the flexibility in adjusting both the boiling and freezing points of the mixture.) The result demonstrated that the removal was very efficient in the absence of any chemical reaction.

However, as shown in Table 2, the aqueous solutions of most of the organic solvents listed in Table 1 were less effective in removing THD. In particular, the 50% ethanol solution, performed as poorly as water. On the other hand, the efficiency of 50% CH₃CN was only slightly reduced relative to the pure solvent. The 70% NEP solution was better than the 30% NEP solution in removing THD, particularly at 50% thickener content. Apparently, the solubilities of both HD and the thickener were important in determining the efficiency of the removal.

It is important to note that when water alone was used, about 95% of the HD was removed simply by the physical contact with water but not by dissolving in water. (HD is only sparingly soluble in water.) Furthermore, the same degree of HD removal was obtained by using an aqueous 0.2 M NaCl solution. This indicated that there was no reaction of HD with water because HD hydrolysis was very slow in the presence of 0.2 M [Cl⁻].⁹ The removal of THD 10% by water was reduced to about 70-80% and reduced to almost 0 for THD 50% thickener at 2-3 g/m² contamination density. Consistent with previous test results⁶, the addition of 5% surfactant was effective for HD but ineffective for THD removal. An emulsion consisting of water droplets in a continuous C₂Cl₄ phase, on the other hand, was as good as pure C₂Cl₄. In summary, the removal of THD was more efficient in less polar solvent systems.

Reactive Systems

A series of reactive solutions was tested subsequently. As shown in Table 3,¹⁰ all hydrolysis/substitution reactions¹¹ were too slow to expedite mustard removal. Only those reactants containing active chlorine could remove mustard effectively. The relative strength appeared to be $\text{Ca}(\text{OCl})_2 > \text{NaOCl} \gg \text{Fichlor} (\text{C}_3\text{N}_3\text{O}_3\text{Cl}_2\text{Na})$. Chloramine B ($\text{C}_6\text{H}_5\text{SO}_2\text{NClNa}$) was not reactive enough to remove mustard from the surface although it was reported to react with mustard instantaneously in a homogeneous solution containing ethanol.¹²

For THD 10%, all the reactants, with the possible exception of $\text{Ca}(\text{OCl})_2$, failed the test. Therefore, in developing alternate aqueous reactive systems, it may be necessary that the reactivity of the new reactant match that of $\text{Ca}(\text{OCl})_2$ in order to remove mustard by interfacial reaction alone. On the other hand, based on the results discussed above, a reactant need not be as reactive as $\text{Ca}(\text{OCl})_2$ if an organic solvent is present to dissolve HD or THD rapidly.

Next, the reactions in a series of less polar solutions were examined. These solutions by themselves were found less effective in removing mustard or thickened mustard. Any improvement in the removal should reflect the effectiveness of the chemical reaction. It was found that in most cases the addition of reactants did not improve the degree of removal significantly. On the contrary, in a number of cases (16 versus 15; 18 versus 17; and 21 versus 19) in Table 3,¹⁰ the presence of the reactants even made THD removal far less efficient. Therefore, one tends to conclude that except for hypochlorite salts, agent removal from a surface was controlled by solubilization but not affected by reactivity. Many highly reactive compounds for mustard had no effect on its removal from a surface unless a solvent that could rapidly dissolve mustard was used. Panel test results provided a good indication on how well the thickened mustard dissolved in the liquid, but could not reflect the rate of the chemical reaction.

Removal of HD From Alkyd Painted Panels

Finally, to illustrate how decon efficacy is influenced by the type of the paint, panels covered with alkyd paint were also tested. It was observed that HD penetrated into the alkyd paint during contamination more rapidly than other agents. To remove the agent from the paint lattice and achieve deliberate decon (less than 0.01 g/m² residual agent), both a solvent that can penetrate into the paint and a reactant that is carried into the paint by the solvent are required. Solvents that penetrate the paint could usually penetrate the thickener as well.

As shown in Table 4, a significant amount of mustard was removed by an equal-volume mixture of ethanol and NEP. The addition of the NaOC_2H_5 reactant to the same solvent mixture improved the removal further such that the residual mustard was below the detection limit. However, the alkyd paint was damaged by the NEP component in the solvent. The epoxy resin, on the other hand, remained intact after exposure to the same solution. The residual HD after decontamination with a 10% $\text{Ca}(\text{OCl})_2$ solution represented the total amount of HD that penetrated into the paint during the 3 hour residence time.

CONCLUSIONS

When the test panels are coated with non-sorptive paint such as the epoxy resin, both mustard and thickened mustard can be removed efficiently by all the organic solvents as well as most of the aqueous solutions of polar organic solvents tested. Decon efficacy increases as the polarity of the solvent decreases.³ The presence of a reactant in these solvents is not necessary. Furthermore, measured efficiencies of removal cannot reflect the reactivities of the reactants in these solutions. Thickened mustard cannot be removed by aqueous solutions containing reactants except the aqueous solution of $\text{Ca}(\text{OCl})_2$. When the test panels are coated with a sorptive paint such as alkyd, an organic solvent that can penetrate into the paint and a reactant carried by the solvent are necessary to remove HD efficiently¹³. The aqueous solution of $\text{Ca}(\text{OCl})_2$ can only remove the HD on the surface of the paint but not the HD in the paint.

Figure 1

Schematic Procedure of the Panel Test

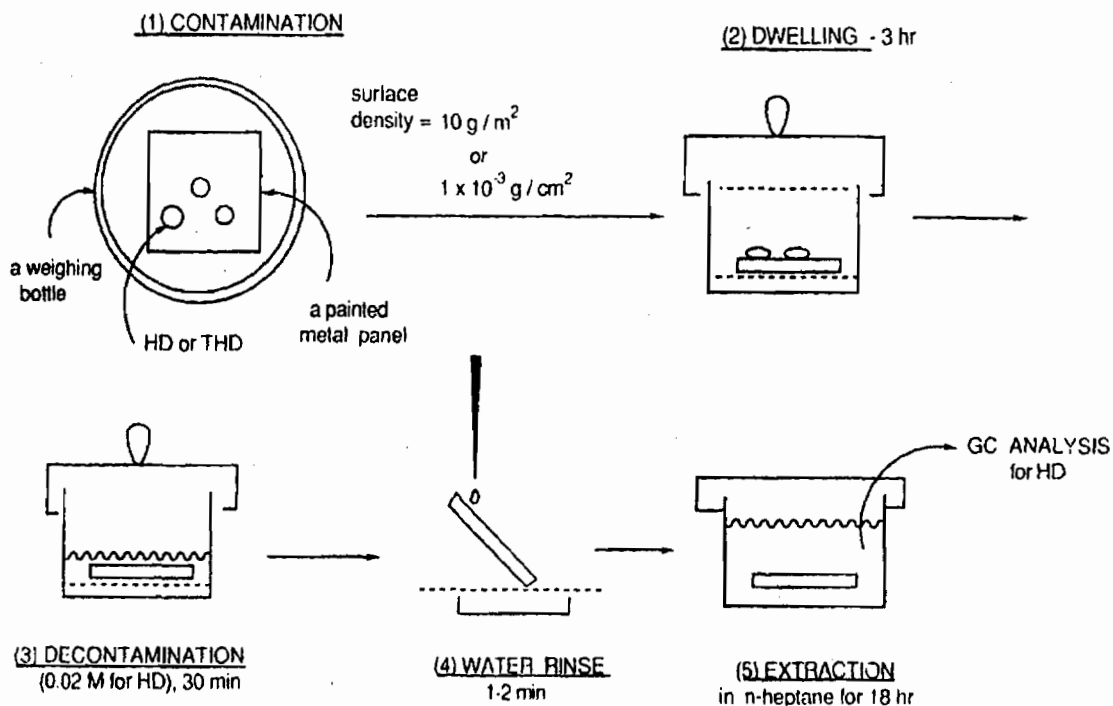


Table 1

Removal of Mustard from Epoxy Painted Panels by Organic Solvents^a

Organic Solvents	Agent	Residual HD, g/m ²			
1. C ₂ H ₅ OH ($\delta = 12.7$) ^b	HD ($\delta = 10.7$) ^b	0.02	0.03	0.05	0.02
	THD, 10% ^c	0.01	0.01	0.01	0.01
2. n-Butanol ($\delta = 11.4$)	THD, 10%	0.01	0.04	0.02	0.03
	THD, 50% ^d	0.10	0.03	0.01	0.12
3. CH ₃ CN ($\delta = 11.8$)	HD	0.01	0.01	0.01	0.01
	THD, 10%	0.02	0.03	0.02	0.02
4. DMF ^e ($\delta = 12.1$)	THD, 10%	0.04	0.11	0.05	0.04
	THD, 50%	0.07	0.07	0.08	0.07
5. n-hexane ($\delta = 7.3$)	THD, 10%	0.01	0.01	0.01	0.02
	THD, 50%	0.35	0.17	0.24	0.01
6. Xylene ($\delta = 8.8$)	THD, 10%	<0.01	<0.01	<0.01	<0.01
	THD, 50%	0.22	0.20	0.08	0.24
7. C ₂ Cl ₄ ($\delta = 9.3$)	THD, 10%	<0.01	<0.01	<0.01	<0.01
	THD, 50%	<0.01	<0.01	<0.01	<0.01
8. NEP ^f ($\delta = 11.3$) ^g	HD	0.20	0.16	0.19	0.22
	THD, 10%	0.20	0.18	0.14	0.23
	THD, 50%	0.10	0.05	0.06	0.05
9. 90% C ₂ H ₅ OH + 10% NEP (X _E = 0.95) ^f	THD, 10%	0.02	0.02	0.02	0.02
	THD, 50%	0.01	<0.01	<0.01	<0.01
10. 50% C ₂ H ₅ OH + 50% NEP (X _E = 0.66) ^f	THD, 10%	0.15	0.21	0.34	0.10

Table 2

Removal of Mustard From Epoxy Painted Panels by Aqueous Solutions^a

Aqueous Solutions	Agent	Residual HD, g/m ²			
1. H ₂ O ($\delta = 23.4$) ^b	HD ($\delta = 10.7$) ^b	0.49	0.03	0.36	0.59
	THD, 10% ^c	3.1	2.0	1.5	2.5
	THD, 50% ^d	2.5	2.1	3.0	2.7
2. 0.2 M NaCl	HD	0.48	0.43	0.52	0.45
	THD, 10%	1.0	0.48	0.68	0.76
	THD, 50%	2.1	2.2	1.9	2.7
3. 5% surfactant ^b	HD	0.01	0.01	0.01	0.01
	THD, 10%	1.0	0.48	0.68	0.76
	THD, 50%	2.1	2.2	1.9	2.7
4. 30% N-ethyl 2- pyrrolidinone (NEP) (X _w = 0.94) ^f	THD, 10%	0.48	0.38	1.27	0.37
	THD, 50%	1.5	1.2	1.5	1.9
5. 70% N-ethyl 2- pyrrolidinone (NEP) (X _w = 0.73)	THD, 10%	0.19	0.16	0.10	0.09
	THD, 50%	---	0.07	0.12	0.15
6. 50% C ₂ H ₅ OH (X _w = 0.77)	HD	0.09	0.10	0.08	0.15
	THD, 10%	2.7	3.4	4.4	3.9
7. 50% CH ₃ CN (X _w = 0.74)	HD	0.10	0.14	0.14	0.18
	THD, 10%	0.15	0.09	0.07	0.07
8. W/O Emulsion ^f	THD, 10%	0.01	0.01	0.01	0.01
	THD, 50%	0.01	0.01	0.01	0.01

Table 4

Removal of Mustard From Alkyd and Epoxy Painted Panels^{a,k}

<u>Decontamination Solution</u>	<u>Agent</u>	<u>Residual HD, g/m²</u>				
1. German Emulsion ^a	HD	<0.01	0.05	0.02	0.02	0.02
2. 10% Ca(OCl) ₂ in water	HD	0.66	0.59	1.31	0.63	1.50
3. NEP-C ₂ H ₅ OH ^b (50 VOL%)	HD	0.41	0.47	0.42	0.42	0.42
	THD, 10% ^c	0.15	0.21	0.34	0.10	----
4. 3% NaOC ₂ H ₅ NEP-C ₂ H ₅ OH ^{d,i}	HD	<0.01	<0.01	<0.01	<0.01	<0.01
	THD, 10% ^c	0.03	0.03	0.03	0.04	---

*Notes for Tables 1-4:

a. Surface contamination is 10 g/m² HD or THD. Each data point is the result from an individual panel. The detection limit for residual HD is 0.01 g/m².

b. δ , solubility parameter, is a measure of the H-bonding strength of the solvent.

c. HD thickened by 10% (by weight) Parlon S300 - a chlorinated polyisoprene powder.

d. The 10 g/m² THD with 10% Parlon S300 on the surface of a panel was evaporated for 3 hours under the hood; one 2-3 g/m² was left on the surface. The weight of the thickener in each droplet was consequently increased to about 50%.

e. DMF is dimethylformamid. The paint at the edge of each panel was softened by contact with DMF for 30 minutes.

f. X_E is mole fraction of ethanol; NEP is N-ethyl 2-pyrrolidinone.

g. Literature value for N-methyl 2-pyrrolidinone (NMP).

h. The sodium salt of an alkyl (C₉ to C₁₃) aryl sulfonate.

i. X_w is mole fraction of water in the binary aqueous mixture.

j. The W/O Emulsion was composed of 10% NaCl, 74% water, 15% C₂CL₄, and 1% emulsifier (IHF). This composition is the same as that of the German Emulsion (C8) with the reactive component Ca(OCl)₂, substituted by the same weight of the unreactive NaCl.

k. All panels are painted with alkyd except for tests with THD, 10%. In these tests, the panels are covered with epoxy resin.

l. The alkyd paint was damaged.

REFERENCES

1. U.S. Army CRDEC, SMCCR-PPD, APG, MD 21010-5423.
2. WWD BW ABC Schutz, Postfach 1320, 3042 Munster, Germany.
3. Buckles, M.F. "CW Visicants: Selected Values for the Physical Properties of H, T, and Q." (U) CRLR-542, Special Report, Project No. 4-08-016-01, 3 July 1956, UNCLASSIFIED Report.
4. Armour, S. J. and Gauthier, M. D. "Rheological Properties of Polymer Solutions. Part III: Polymer/Agent Solutions." (U) Suffield Report No: 363, June 1983. PCN #: 13E10. CONFIDENTIAL Report.

5. Hovanec, J. W.; Albizo, J. M., Henderson, V. D., Dissolution Studies of Thickened Agent and Simulants in Mixtures of Water, N-Alkyl Pyrrolidinones and Surfactants, in Proceedings of the 1990 U.S. Army CRDEC Scientific Conference in Chemical Defense Research, U.S. Army CRDEC, Aberdeen Proving Ground, in press.

6. Jones, W. E., et al, Engineering and Development Support of General Decon Technology for the U.S. Army's Installation Restoration Program, Task 5. Facility Decontamination, Contract No. DAAK11-80-C-0027, U.S. Army Toxic and Hazardous Materials Agency (THAMA), Aberdeen Proving Ground, MD, July 1982, UNCLASSIFIED Report.

7. Thompson, J. H.; Schwartz, M., "Evaluation of the Resistance of Standard Air Force Paint to Liquid Toxic Agent Sorption," ARCSL-TM-79016, 1979, UNCLASSIFIED Report.

8. Thompson, J. H.; Day, S. E.; Schwartz, M.; Keck, C. H., "Development of a Chemical Agent Resistant Coating," ARCSL-TM-80017, 1980, UNCLASSIFIED Report.

9. Bartlett, P. D.; Swain, C.G., "Kinetics of Hydrolysis and Displacement Reactions of β , β' -Dichlorodiethyl Sulfide (Mustard Gas) and of β -chloro- β' -Hydroxydiethyl Sulfide (Mustard Chlorohydrin)," J. Am. Chem. Soc., 1949, 71, 1406-1415.

10. Table 3 is available as Supplementary Material.

11. Yang, Y. -C.; Szafraniec, L. L.; Beaudry, W. T.; Ward, J. R., "Kinetics and Mechanisms of the Hydrolysis of 2-chloroethyl sulfides," J. Org. Chem., 1988, 53, 3293-3297.

12. Szafraniec, L. L.; Beaudry, W. T.; Ward, J. R.; Rohrbaugh, D. K.; "Reactions Between Chemical Agents and the Chemicals in the M280 Decontamination Kit," CRDEC-TR-134, Aberdeen Proving Ground, MD 21010-5423, January 1990, UNCLASSIFIED Report.

13. Similar results were observed from tests with the M280 Individual Equipment Decon Kit (see reference 12). On porous surfaces, physical (nonreactive) removal accounted for over 95% of the total agent removal; but addition of a reactant added a small, but statistically significant increase in decon efficiency.

DETERMINATION OF THE CRITICAL MICELLE CONCENTRATIONS OF CTAB IN WATER/1-ALKYL-2-PYRROLIDINONE MIXTURES

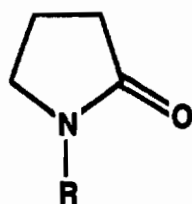
J.W. Hovanec and J.M. Albizo
U. S. Army Chemical Research, Development and Engineering Center,
Aberdeen Proving Ground, MD

Abstract

1-Alkyl-2-pyrrolidinones have been identified as potentially useful components in liquid decontaminants. Mixtures of 1-ethyl-2-pyrrolidinone (EtP), 1-cyclohexyl-2-pyrrolidinone (cHP) with water can promote the rate of dissolution of polymerically thickened agent simulant. This process is enhanced by the addition of cationic surfactants. The critical micelle concentration of hexadecyltrimethylammonium bromide (CTAB) was measured in these mixtures using the hydrolysis rate of p-nitrophenyl acetate (PNPA). As cationic micelles are formed, the rate of PNPA hydrolysis is increased. Plots of these rates against $\log [\text{CTAB}]$ show typical cmc curves. The log of the cmc of CTAB in water/EtP mixtures varies nearly linearly with [EtP]. With cHP however, the same plot exhibits a maximum at about 20% cHP indicating that the system behavior may be more complex than simple micelle formation.

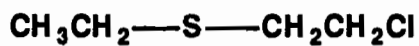
Introduction

The process of decontamination with a liquid decontaminant occurs in two discrete steps: the dissolution of the agent by the liquid and its chemical degradation by the reactive components therein. While the bulk of decon research has been directed at increasing reactivity, it is frequently the dissolution step which is rate controlling in the overall decon process. Earlier, we reported a study¹ in which the rate of dissolution of thickened 2-chloroethyl ethyl sulfide (CEES) in various mixtures of 1-alkyl-2-pyrrolidinones and water was measured (see figure 1 for chemical structures). It was observed that the addition of small amounts of either of two cationic surfactants, CTAC or Variquat K300, significantly enhanced this dissolution process (figure 2). It was speculated that this enhanced

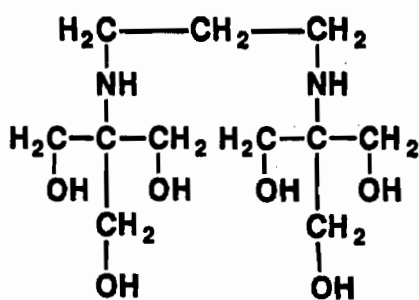


1-Alkyl-2-Pyrrolidinone

R= Methyl, MeP
Ethyl, EtP
Cyclohexyl, cHP



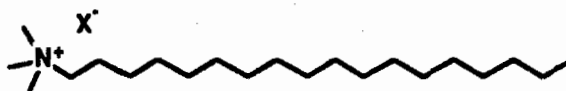
**2-Chloroethyl Ethyl Sulfide
(CEES)**



"bis-tris-Propane"



**Dicoco Dimethylammonium Chloride
(Sherex Variquat K300)**



X = Cl⁻: Cetyltrimethylammonium Chloride (CTAC)
X = Br⁻: Cetyltrimethylammonium Bromide (CTAB)

Figure 2. Structures and nomenclature of chemicals used in this study.

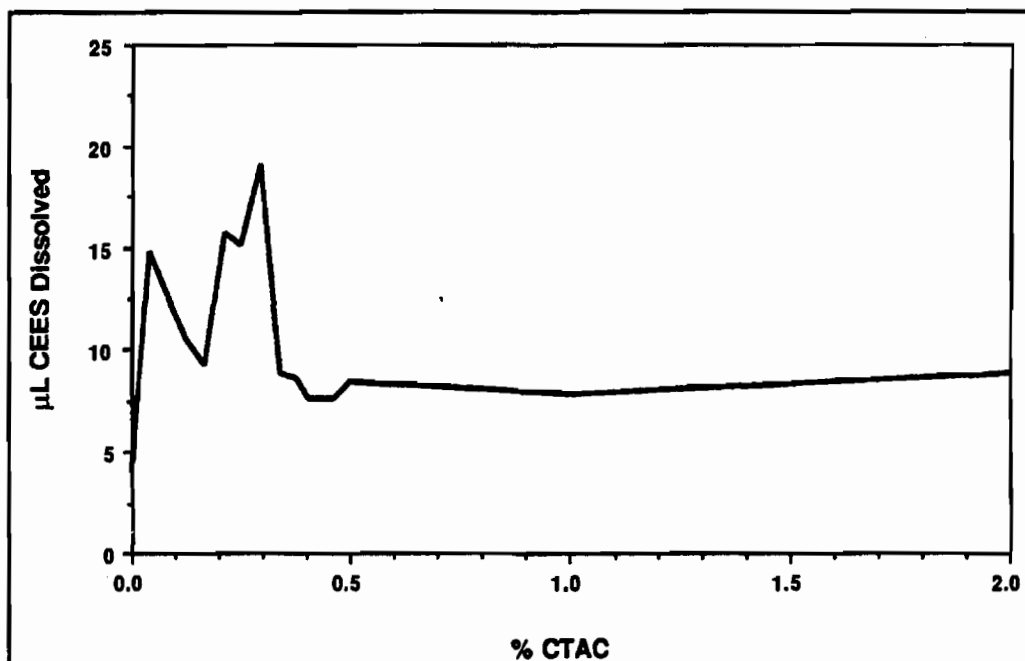


Figure 2. The rate of dissolution of thickened CEES in a mixture of 60% water, 13.3% EtP and 26.7% cHP with varying amounts of CTAC.

dissolution is due to the formation of micelles which then preferentially concentrate 1-cyclohexyl-2-pyrrolidinone.

In this study, we undertook to measure the critical micelle concentrations of CTAB in water/pyrrolidinone mixtures. This was done by utilizing the acceleration of the rate of ester hydrolysis in the presence of cationic micelles. In this study, the substrate chosen was p-nitrophenyl acetate (PNPA).

Experimental

Materials: All chemicals were obtained from commercial sources and used without further purification. Earlier studies² with CTAB showed no differences in hydrolysis rates with recrystallized vs. unpurified surfactant.

Preparation of Solutions: The aqueous portion of the mixtures consisted of 0.05 M bis-tris propane buffer. This was mixed with the pyrrolidinone in the desired ratio (w/w). The resultant mixture was used to prepare a 5% stock solution of CTAB (w/v). Intermediate concentrations of CTAB were obtained by mixing varying amounts of the CTAB stock and buffer/pyrrolidinone solutions.

Measurement of Hydrolysis Rates: A stock solution of 0.02 M PNPA was prepared in 1-ethyl-2-pyrrolidinone. The reaction was initiated by adding 10 μL of this solution to 1.00 mL of buffer/pyrrolidinone/CTAB solution in a cuvette. The absorbance at 400 nm was recorded as a function of time. In practice, we could measure seven reactions simultaneously. The data was acquired by computer and the pseudo-first-order rate constants determined using a non-linear regression method, "KORE", developed by Swain.³⁴

Results and Discussion

In all cases, acceptable first-order kinetics for PNPA hydrolysis were observed. The rates were plotted as a function of $\log [\text{CTAB}]$ to produce curves such as that shown in figure 3. Such curves are typical of a cmc determinations⁵: at CTAB concentrations below the cmc, no change is observed but as micelles are formed, the hydrolysis rate increases due to

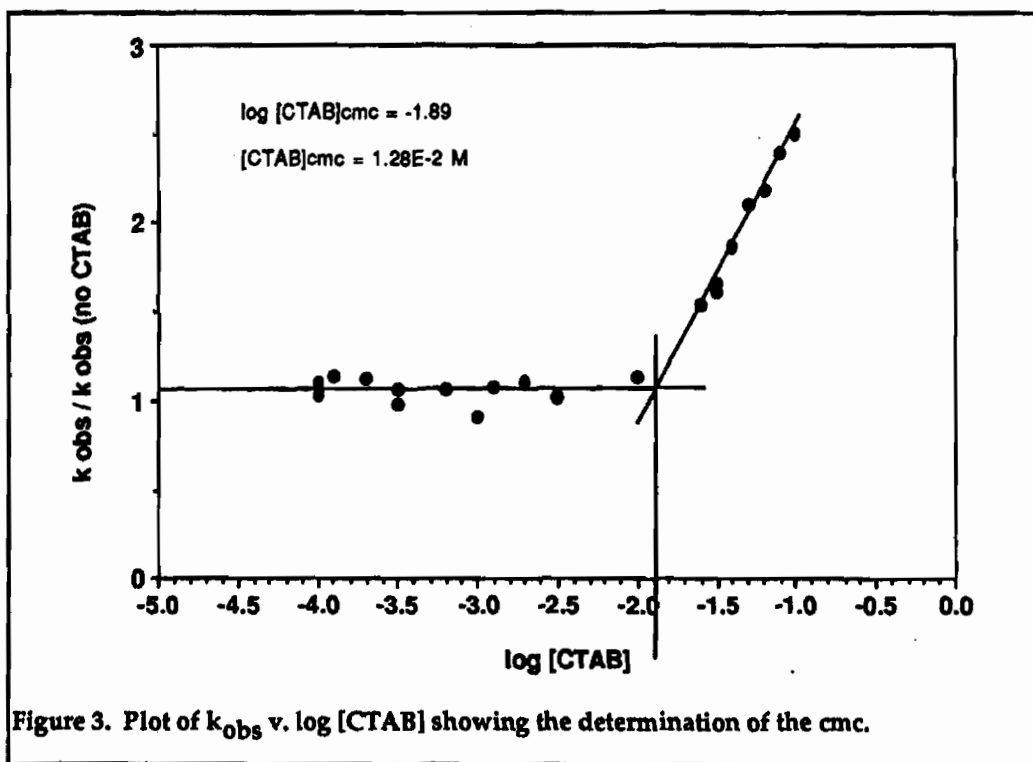


Figure 3. Plot of k_{obs} v. $\log [\text{CTAB}]$ showing the determination of the cmc.

micellar catalysis. By passing a straight line through the two regions of the curve, the cmc can be obtained (as the x-value at the point of intersection).

The cmc's were obtained for mixtures of 1-ethyl-, 1-methyl- and 1-cyclohexyl-2-pyrrolidinones with buffer in the range of 0-50%. The results are plotted in

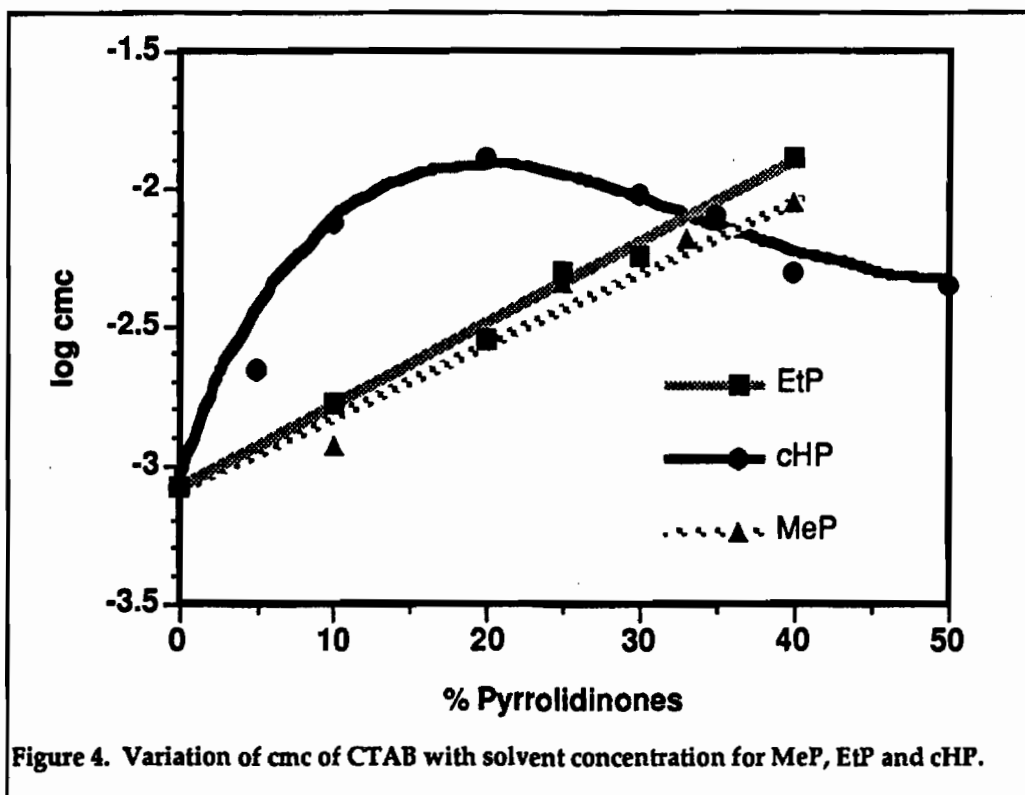


figure 4. As the fraction of pyrrolidinone increases, the polarity of the mixture decreases. Ordinarily, one would expect the cmc of an ionic surfactant to increase since the environment in the continuous phase becomes less incompatible with the hydrophobic tails of the surfactant.⁵ This is indeed what is observed with 1-ethyl- and 1-methyl-2-pyrrolidinone.

With 1-cyclohexyl-2-pyrrolidinone, however, an unusual observation is made. The apparent cmc of CTAB seems to increase rapidly with increasing cHP, as expected up to about 20% solvent. At that point, the cmc decreases with increasing solvent concentration. One still observes what appears to be micellar catalysis of PNPA hydrolysis in these mixtures which indicates that some cationic aggregate must be forming at a well-defined CTAB concentration. Furthermore, there is no discontinuity in the $\log [\text{CTAB}]_{\text{cmc}}$ vs % Pyrrolidinone curve which might indicate that reverse micellization had occurred. It has been speculated that some of the cHP may be present in the form of surfactant-stabilized microdrops which are larger than micelles. If so, they cannot not be very large since the mixtures remain optically clear.

A primary purpose of this study was to compare the cmc of CTAB in these mixtures with the concentration of CTAC which produces the best dissolution results. Referring back to figure 2, one sees that maximum

dissolution occurs at ~0.3% CTAC or 9.4 mM. The log of this value is -2.03 which, as one can see in figure 4, is very close to the $[CTAB]_{cmc}$ in both 40% EtP/water and 40% cHP/water. This observation is not consistent with the original hypothesis that the dissolution process is accelerated by the formation of micelles. If that were the case, there would not be any significant improvement in dissolution (figure 1) until the cmc is reached. At surfactant concentrations above the cmc, the improvement should remain steady or decrease only slightly. What we observe, however is a very different behavior. The improvement in thickened CEES dissolution occurs with amounts of CTAC which appear to be well below the cmc while at values just slightly above the cmc, the improvement decreases precipitously. Such behavior may be due to the localization of the surfactant at the interface between the solution and the thickened agent. As surfactant concentration reaches the cmc, some of the surfactant molecules move away from this interface and into the bulk phase of the solution where they no longer assist the dissolution process.

Conclusions

The addition of CTA'X' to mixtures of water, EtP and cHP will improve their ability to dissolve thickened CEES. Using the catalysis of ester hydrolysis as an indicator, it can be demonstrated that CTAB forms cationic aggregates at discrete surfactant concentrations in these mixtures. These aggregates are assumed to be classical spherical micelles except in the case of 20-50% cHP in water where the behavior does not follow normal patterns. Comparison of the cmc data and the previously obtained dissolution data on thickened mustard simulant indicates that the optimal effect of the surfactant occurs at concentrations below the cmc.

References

1. J. W. Hovanec, J.M. Albizo and V.D. Henderson, "Dissolution Studies of Thickened Agent and Simulants in Mixtures of Water, N-alkyl Pyrrolidinones and Surfactants.", CRDEC Scientific Conference on Chemical Defense Research, Nov. 1990.
2. R.A. Mackay, et al., *J. Phys. Chem* 1987, 91,861.
3. C.G. Swain, M.S. Swain and L.F. Berg, *J. Chem. Inf. Comput. Sci.* 1980, 20, 47.
4. J.W. Hovanec and J.R. Ward, *Computers and Chemistry* 1985, 9, 23.
5. D. Meyers, *Surface Science and Technology*, VCH Publ. Inc., N.Y., 1988, Ch. 2.

COVALENT ATTACHMENT OF ORGANIC "HANDLES" TO POLYOXOMETALATES WITH OXIDATIVE DECONTAMINATION ACTIVITY

Gyu-Shik Kim and Craig L. Hill
Department of Chemistry, Emory University, Atlanta, GA 30322

ABSTRACT

In context with immobilizing polyoxometalates with oxidative decontamination activity on fibers that can be woven into garments, we have succeeded in covalently derivatizing polyoxotungstates of Keggin class with organic groups. Keggin polyoxometalates catalyze the decontamination of HD and other cw agents under thermal or photochemical conditions. The formulas of the new complexes are $[\text{PhP}(\text{O})]_2\text{PW}_{11}\text{O}_{39}^{3-}$ (1) and $[\text{PhP}(\text{O})]_2\text{SiW}_{11}\text{O}_{39}^{4-}$ (2). The X-ray structure of the $n\text{-Bu}_4\text{N}^+$ salt of 1 has minimal (2-fold rotational) disorder and shows that the two divalent $\text{PhP}(\text{O})^{2+}$ groups are bonded to the 4 oxygen atoms that define the "hole" in the Keggin lacunary. ^{31}P and ^{183}W NMR confirms that the same structure (C_3 symmetry) exists in solution.

INTRODUCTION

Early transition metal-oxygen anion clusters, or polyoxometalates for short, have a range of systematically alterable properties including redox potentials, acidities, solubilities, polarities, and so on that make them of potential value in decontamination methodologies. Previous work from our laboratory or in collaboration with CRDEC demonstrated that some polyoxotungstates, such as $\text{W}_{10}\text{O}_{32}^{4-}$, could rapidly and catalytically destroy VX, HD, and G cw agents and agent simulants under aerobic photochemical conditions.¹ Other polyoxometalates have been demonstrated to be capable of catalytically destroying HD analogues thermally² or photochemically, even under anaerobic conditions.³ In context with the goal of making self decontaminating clothing, we report here the synthesis and characterization of redox active polyoxometalates that are covalently derivatized with organic groups. Since such derivatized polyoxometalates should have catalytic activity for decontaminating cw agents under various conditions and should be capable of attachment to a variety of fibers, this constitutes a modest first step in making polyoxometalate-immobilized catalytically decontaminating

fibers and clothing. In this initial investigation, PhP(O)^{2+} groups have been attached to the lacunary heteropolyundecatungstates, $\text{X}^{n+}\text{W}_{11}\text{O}_{39}^{(12-n)-}$ ($\text{X}^{n+} = \text{P}^{5+}, \text{Si}^{4+}$, Figure 1), and the product complexes characterized by FTIR, NMR (^1H , ^{31}P , ^{183}W) and X-ray crystallography.

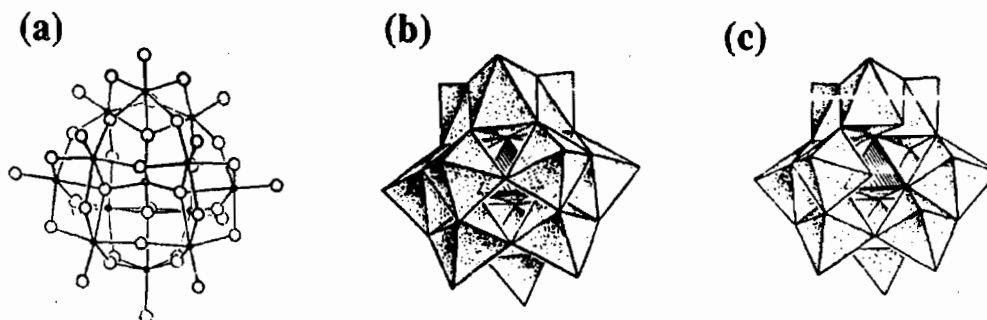


Figure 1. The Keggin structure of $\text{X}^{n+}\text{W}_{12}\text{O}_{40}^{(8-n)-}$ in (a) ball-and-stick, (b) polyhedral representations and (c) its' lacunary structure of $\text{X}^{n+}\text{W}_{11}\text{O}_{39}^{(12-n)-}$ in polyhedral representation.

EXPERIMENTAL

Methods and Materials. All chemicals were commercially available reagent grade and used as received. Elemental analyses were conducted by Atlantic Microlab., Inc. (Norcross, Georgia) for C, H, and N, and by E+R Microanalytical Lab., Inc. (Corona, New York) for the elements other than C, H, and N. Infrared spectra were obtained as KBr pellets on a Nicolet Model 510M FTIR Spectrophotometer. ^1H and ^{31}P NMR spectra were recorded with General Electric QE-300 and IBM WP-200SY FT spectrometers at 300 and 81 MHz, respectively. ^{183}W NMR spectra were recorded with IBM WP-200SY and GE GN-500 spectrometers at 8.34 and 20.83 MHz, respectively. ^1H , ^{31}P and ^{183}W NMR chemical shifts are referenced to $(\text{CH}_3)_4\text{Si}$, 1.0 % trimethylphosphate (TMP), and 2.0 M Na_2WO_4 in D_2O , respectively. In the case of ^{31}P and ^{183}W NMR spectra referencing was achieved by the substitution method. Chemical shifts downfield from the reference are reported as positive (+ δ). Sodium or potassium salts of $\text{X}^{n+}\text{W}_{11}\text{O}_{39}^{(12-n)-}$ ($\text{X} = \text{P}, \text{Si}$) were prepared following literature procedures⁴ and converted to appropriate tetraalkylammonium salts.

$[(n-\text{C}_4\text{H}_9)_4\text{N}]_2\text{H}[\text{PhP(O)}]_2\text{PW}_{11}\text{O}_{39}$, 1. To the heated acetonitrile solution of $\text{Q}_4\text{Na}_3\text{PW}_{11}\text{O}_{39}$ (1.00 g in 20 mL CH_3CN , hereafter Q denotes tetrabutylammonium cation for simplicity) at 60°C was added dropwise 2 equivalents of PhP(O)Cl_2 in 5 mL of acetonitrile over a period of 10 minutes. The flask was sealed with a rubber septum and stirred without further

heating. After 3 hrs of stirring a pale yellow precipitate began to form. The mixture was stirred for an additional hr and the solid was separated on a filter paper, washed with a 20-mL portion of ether and air-dried to give a pale yellow microcrystalline solid. Typical yield ranges from 20 - 30%. IR (1300 - 400 cm^{-1}): 1138 (m), 1119 (s), 1073 (m), 1063 (m), 1040 (w), 1024 (w), 991 (s), 977 (vs), 882 (s), 828 (vs), 744 (m, sh), 693 (w, sh), 594 (w), 575(w), 528 (w), 514 (w). ^1H NMR (CD_3CN): δ 0.94 (t, 12H), 1.34 (sextet, 8H), 1.58 (quintet, 8H), 3.07 (t, 8H), 7.60 (m, 3H), 8.07 (quartet, 2H). ^{31}P NMR (CD_3CN): δ 17.20 (s), -15.94 (s). Anal calcd for $\text{C}_{44}\text{H}_{83}\text{N}_2\text{O}_{41}\text{P}_3\text{W}_{11}$: C, 15.49; H, 2.45; N, 0.82; Na, 0.00; P, 2.72; W, 59.28. Found: C, 15.57; H, 2.31; N, 0.81; Na, 0.16; P, 3.06; W, 59.04. ^{183}W NMR (8.34 MHz, 0.17 M in CDCl_3) of tetradecylammonium salt: δ -83.0 (s, br, 2W), -99.5 (s, br, 3W), -111.0 (s, br, 2W), -190.0 (s, br, 2W, FWHH (full-width-at half-height) = 43 Hz), -215.3 (d, br, 2W, $^2J_{\text{W-O-P}} \approx 27$ Hz, FWHH = 58 Hz). The first three downfield peaks show FWHH = ~ 30 Hz.

$\text{Q}_3\text{H}[\text{PhP}(\text{O})]_2\text{SiW}_{11}\text{O}_{39}$, 2. To $\text{Q}_4\text{K}_4\text{SiW}_{11}\text{O}_{39}$ (3.11 g, 0.818 mmole) in 50 mL acetonitrile was slowly added 2 equivalents of $\text{PhP}(\text{O})\text{Cl}_2$ dropwise with vigorous stirring. The mixture was stirred for 4 days and then filtered through fine glass frit. The pale yellow filtrate was diluted with 150 mL of water to form pale yellow sticky solid. The supernatant was decanted and the solid redissolved in 50 mL of acetonitrile and then reprecipitated using 200 mL of absolute ethanol. The solid isolated was reprecipitated from 50 mL acetonitrile solution by adding 250 mL methanol. A 1.82 g (61% yield) of white microcrystalline solid was obtained. IR (1300 - 400 cm^{-1}): 1139 (m), 1085 (m), 1069 (m, sh), 1041 (vw), 1011 (w), 976 (s), 914 (vs), 812 (s), 741 (sh), 697 (sh), 648 (w), 593 (w), 572 (w), 549 (w), 538 (w). ^1H NMR (CD_3CN): δ 8.08 (m, 2H, *o*- C_6H_5), 7.55 (m, 3H, *m,p*- C_6H_5), 3.12 (t, 12H), 1.61 (quintet, 12H), 1.40 (sextet, 12H), 0.96 (t, 18 H). ^{31}P NMR (CD_3CN): δ 15.21 (s). Anal calcd for $\text{C}_{60}\text{H}_{119}\text{N}_3\text{O}_{41}\text{P}_2\text{SiW}_{11}$: C, 19.74; H, 3.28; N, 1.15. Found: C, 20.10; H, 3.26; N, 1.21. 20.83 MHz ^{183}W NMR (0.25 M in CD_3CN) of tetrahexylammonium salt: δ -79.9 (s, 2W), -106.1 (s, 1W), -109.6 (s, 2W), -113.8 (s, 2W), -154.0 (d, 2W, $^2J_{\text{W-O-P}} = 14$ Hz), -197.2 (d, 2W, $^2J_{\text{W-O-P}} = 26$ Hz), along with smaller intensity peaks at -97.8 (s), -101.3 (s), -123.5 (s), -151.2 (d, $^2J_{\text{W-O-P}} = 14$ Hz), -191.6 (d, $^2J_{\text{W-O-P}} = 26$ Hz) with an approximate integration ratio of 2:2:2:2:2. A missing peak with intensity 1 was presumed to be hidden under one of the stronger intensity peaks.

RESULTS AND DISCUSSION

Synthesis. The title compounds $\text{Q}_2\text{H}[\text{PhP}(\text{O})]_2\text{PW}_{11}\text{O}_{39}$, 1, and $\text{Q}_3\text{H}[\text{PhP}(\text{O})]_2\text{SiW}_{11}\text{O}_{39}$, 2, were prepared by the reaction of the lacunary precursors with phenylphosphonyldichloride in acetonitrile solution. The typical yields range from 20% to 30% for 1 and from 60 to 80% for 2. The

discrepancy in yield may reflect the greater stability of $\text{SiW}_{11}\text{O}_{39}^{8-}$ compared to that of $\text{PW}_{11}\text{O}_{39}^{7-}$.

Vibrational Study. The FTIR spectra of **1** and **2** show several bands in the P-O stretching⁵ region of 1000 - 1150 cm^{-1} . **1** shows two more P-O stretches at 1119 and 1063 cm^{-1} which arise from the central PO_4 moiety which are absent in **2**. The 56 cm^{-1} splitting arising from the central PO_4 moiety of **1** is comparable to the 54 cm^{-1} splitting for the precursor $\text{PW}_{11}\text{O}_{39}^{7-}$ which strongly suggests that the central PO_4 moiety is not much perturbed by the attached organic groups. The organic groups bind through only four oxygens compared to the interaction of 5 oxygens in the transition metal-substituted polyoxoundecatungstates complexes (TMSP's) in which central PO_4 are more perturbed through the interaction with transition metals.⁶

NMR Study. ^{31}P NMR chemical shifts of the central PO_4 of the $(\text{Na})\text{PW}_{11}\text{O}_{39}^{6-}$, **1**, and $\text{PW}_{12}\text{O}_{40}^{3-}$ in acetonitrile show a progressive trend, i.e., δ -14.61, -15.94 and -17.58. This may have relevance with the changes in electronic and structural parameters in these closely related compounds. The anion, $(\text{Na})\text{PW}_{11}\text{O}_{39}^{6-}$, is expected to have the least compact structure, $\text{PW}_{12}\text{O}_{40}^{3-}$ possessing the most compact structure, and **1** in between but more like $(\text{Na})\text{PW}_{11}\text{O}_{39}^{6-}$. The overall anionic charges are 6-, 3-, 3- in going from $(\text{Na})\text{W}_{11}\text{O}_{39}^{6-}$ to **1** to $\text{PW}_{12}\text{O}_{40}^{3-}$, which parallel the trend in chemical shifts. Although two $\text{PhP}(\text{O})^{2+}$ groups are attached to the $\text{PW}_{11}\text{O}_{39}^{7-}$ to form **1**, the anion is expected to possess a more open structure compared to the $\text{PW}_{12}\text{O}_{40}^{3-}$ Keggin structure.

^1H and ^{31}P NMR spectra of **1** in deuterated acetonitrile show only one type of the $\text{PhP}(\text{O})^{2+}$ group. ^{31}P NMR spectrum of **1** in deuterated acetonitrile shows two peaks; one peak at δ 17.20 and the other at δ -15.94. The peak at δ 17.20 is due to the phosphorus of the $\text{PhP}(\text{O})^{2+}$ group and that at δ -15.94 is due to the central phosphorus atom of the anion. ^{183}W NMR spectrum of the tetradecylammonium salt in CDCl_3 shows 5 lines with 2:3:2:2:2 intensity ratio (Figure 2). Accidental overlap of the two peaks with 2:1 intensity ratio gave the observed integration ratio of 2:3:2:2:2 consistent with C_5 symmetry. The most upfield peak at δ -215.3 ppm shows $^2J_{\text{W-O-P}} = 27$ Hz splitting and the second most upfield peak is broader than the three downfield peaks which suggests the peak is not resolved due to the low S/N. The ^{183}W NMR data taken together with ^1H , ^{31}P NMR data strongly suggest the anion **1** retains true C_5 symmetry in solution. This point was later confirmed even in solid state by single crystal X-ray structure determination on **1** (vide infra).

The ^1H , ^{31}P NMR spectra of the compound **2** as tetrabutylammonium and tetrahexylammonium salts also show only one type of the $\text{PhP}(\text{O})^{2+}$ group for the major product suggesting a solution species with C_5 symmetry just as compound **1**. Interestingly, the ^{183}W NMR spectrum shows a second

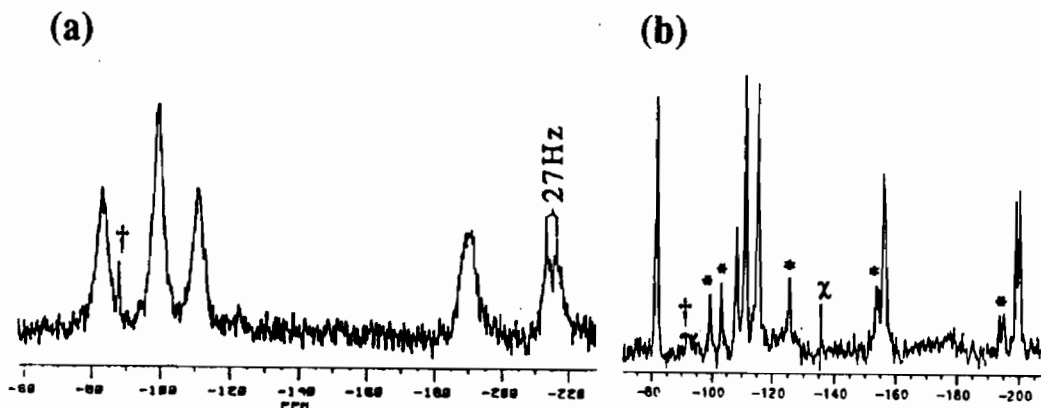


Figure 2. ^{183}W NMR spectra of (a) tetradecylammonium salt of 1 in CDCl_3 , and (b) tetrahexylammonium salt of 2 in CD_3CN , * denotes β isomer and χ arising from instrumental artifact. † denotes $\text{XW}_{12}\text{O}_{40}^{n-}$.

species along with the major species (Figure 2). The major species shows a pattern of 2:1:2:2:2:2 with the two most upfield peaks split by the phosphorus of the phenylphosphonyl groups. The $^2J_{\text{W-O-P}}$ values are 14 and 26 Hz, respectively, of which the value of 26 Hz is the similar value observed for the tetradecylammonium salt of 1. We assign the major species as an α -anion with C_s symmetry. The minor species shows 2:2:2:2:2 with the two most upfield peaks split into two with exactly the same $^2J_{\text{W-O-P}}$ as those of the major species. We assign this as one of the β isomers (either β -1 or β -3) with C_s symmetry. Presumably one peak with intensity 1 is accidentally degenerate with one of the stronger intensity peaks.

It is interesting to note that the ^{183}W NMR spectrum of the $\text{Q}_4(\text{CpTi})\text{PW}_{11}\text{O}_{39}$ in acetonitrile shows merely a 40 ppm range dispersion of the peaks which is comparable to that of the precursor.⁷ This suggests that the magnetic environment of the organic functionalized $\text{XW}_{11}\text{O}_{39}^{n-}$ compounds is much more perturbed than those of the TMSF complexes or organometallic fragment-bearing PW_{11} compounds.

X-ray Structure of $\text{Q}_2\text{H}[\text{PhP}(\text{O})]_2\text{PW}_{11}\text{O}_{39}$. The X-ray structure determinations of the lacunary compounds derived from the Keggin compounds suffer from minor to severe orientational disorder.⁸ For example, the X-ray structure of α - $(\text{Me}_4\text{N})_4\text{Na}_2\text{HPW}_{11}\text{O}_{39}$ suffers from the two-fold disorder and that of α - $\text{K}_8\text{SiW}_{11}\text{O}_{39}$ from 12-fold disorder.

X-ray structure of $[\text{PhP}(\text{O})]_2\text{PW}_{11}\text{O}_{39}^{3-}$ is shown in Figure 3. The anion is two-fold disordered due to the crystallographically imposed orientational disorder in the crystal lattice. Figure 3 shows two possible orientations of the central PO_4 moiety in the anion. The X-ray structure is actually the average of the two orientations. However the bonding connectivity of the two $\text{PhP}(\text{O})_2^+$

and dimensions are clear. The two $\text{PhP}(\text{O})_2^+$ groups bind to the vacant hole site through the four bridging oxygens which were the terminally bound oxygens for the lacunary $\text{PW}_{11}\text{O}_{39}^{7-}$ anion (see Figure 1). The two oxygens of $\text{PhP}(\text{O})_2^+$ groups are 2.72 Å apart which is just within van der Waals contact with each other.

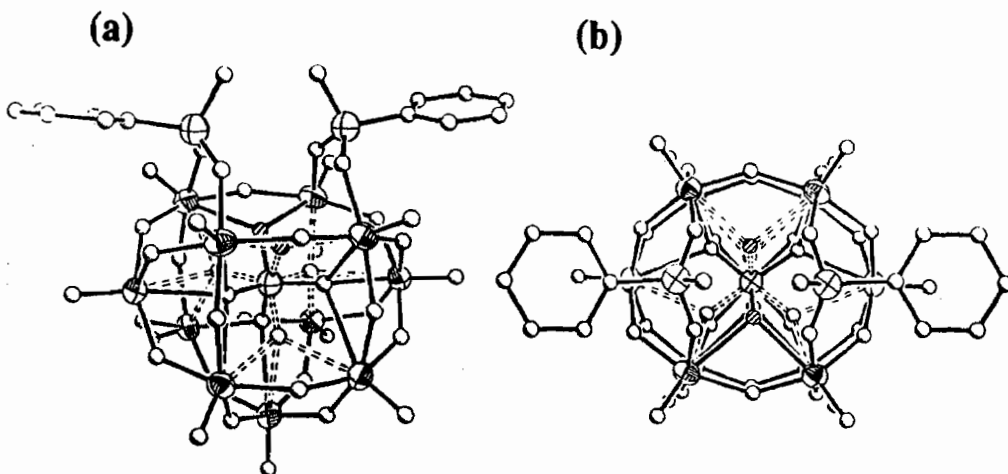


Figure 3. X-ray structure of 1 (a) side view and (b) top view looking down through 2-fold rotation axis. Note the 2-fold disordered PO_4 positions.

CONCLUSIONS

Polyoxometalates of the Keggin type have been functionalized with phenylphosphonyl groups. Two of these organic derivatized compounds, 1 and 2, have been prepared and fully characterized by various spectroscopic methods. A single crystal X-ray structure determination of 1 shows clearly the binding geometry of the organic groups.

ACKNOWLEDGEMENT

We thank the U.S. Army Research Office for financial support and Dr. Robert Jones of this department for running 20.83 MHz ^{183}W NMR spectra.

REFERENCES

1. Truitt, L.; Dorsey, R.; Hill, C. L. *Proc. 1988 U.S. Army CRDEC Conf. on Chem. Defense Res.*, pp 1079-1083.
2. Hill, C. L.; Faraj, M. *Proc. 1989 U.S. Army CRDEC Conf. on Chem. Defense Res.*, pp 131-134.

3. Chambers, R. C.; Hill, C. L. *J. Am. Chem. Soc.* **1990**, *112*, 8427.
4. (a) Brevard, C.; Schimpf, R.; Tourné, G.; Tourné, C. M. *J. Am. Chem. Soc.* **1983**, *105*, 7059. (b) Tézé, A.; Hervé, G. *J. Inorg. Nucl. Chem.* **1977**, *39*, 999. (c) Ginsberg, A. P. Ed. *Inorg. Synth.* **1990**, *27*, 89-90.
5. (a) Rocchiccioli-Deltcheff, C.; Thouvenot, R.; Frank, R. *Spectrochim. Acta*, **1976**, *32A*, 587. (b) Rocchiccioli-Deltcheff, C.; Fournier, M.; Frank, R. *Inorg. Chem.* **1983**, *22*, 207.
6. (a) Zonnevjlle, F.; Tourné, C. M.; Tourné, G. F. *Inorg. Chem.* **1982**, *21*, 2742. (b) Rocchiccioli-Deltcheff, C.; Thouvenot, R. *J. Chem. Res. (S)*, **1977**, 46.
7. Gansow, O.; Ho, R. K.C.; Klemperer, W. G. *J. Organometallic Chem.* **1980**, *187*, C27.
8. (a) Brown, G. M.; Noe-Spirlet, M. -R.; Busing, W. R.; Levy, H. A. *Acta Cryst.* **1977**, *B33*, 1038. (b) Fuchs, J.; Thiele, A.; Palm, R. *Z. Naturforsch.* **1981**, *36b*, 544.

BLANK

**ADSORPTION OF VX AND TBP BY VARIOUS
SORBENTS IN 1,2-DICHLOROETHANE**

J.H. Buchanan and S.H. Hong
Research Directorate
Chemical Research, Development and Engineering Center
APG, MD 21010-5423.

Experiments were carried out to observe the partitioning characteristics of VX and its simulant tributyl phosphate (TBP) between sorbent resins and a solvent. The extraction solvent chosen was 1,2-dichloroethane (DCE) because it is a good solvent for liquid contaminants and readily available. Other characteristics considered were its volatility, retention time in gas chromatography (GC), and purity. First, the calibration curve was established by injecting solutions made of known quantities of contaminant and DCE. The partitioning experiment was performed by stirring the liquid mixture with a sorbent and the resulting liquid was injected into GC. After 5 minutes of stirring, some sorbents showed sorption capacities of up to 60 % of TBP from the original solution. This experiment was repeated with VX and the results were compared.

1. Introduction

Many different materials can be used in a basic soldier skills decontamination operation and/or a hasty decontamination operation. The objective of this research is to investigate materials and procedures for these purposes; specifically, to develop a standard method for evaluating materials that sorb and retain chemical warfare agents (CWA's). The ideal method should be simple enough to be used for screening different materials with simulants, ranking and recommending high performance sorbents for detailed evaluation.

Experiments were planned to observe the partitioning characteristics of liquids in sorbent resins and a solvent.

The extraction solvent chosen was DCE because it is (1) a good solvent for liquid contaminants and (2) suitable for the experimental conditions. For example, it has characteristics such as good volatility (not too high, but high enough) and good retention time (well separated from the o-ethyl-S-(2-diisopropylaminoethyl) methylphosphonothiolate (VX) or TBP region). It was also readily available with high purity.

2. Experimentation

2.1 Materials.

The solvent, DCE, was obtained from Aldrich Chemical Company (lot number 02116BV). GC analysis using a flame ionization detector (FID) resulted in an area % purity of 99.99. The major impurity was identified as 1,1,2-trichloroethane by electron impact gas chromatography/mass spectrometry (GC/MS). Five minor impurities were detected by GC. No impurities were detected in the TBP or VX region of the chromatogram.

The TBP simulant was obtained from Ashland Chemical Co., a division of Ashland Oil Incorporated (Columbus, Ohio); no lot number was available. The purity of the TBP sample was determined to be 99.1% by GC. The FID chromatogram of neat TBP is Figure 1.

The VX sample (Lot No. VX-U-8132-CTF-N) used in these experiments was obtained from the Chemical Agent Standard Analytical Reference Material (CASARM) Program at the U.S. Army Chemical Research, Development, and Engineering Center (CRDEC). Originally synthesized in June 1988 and determined to be 96.8 area % pure by multinuclear Nuclear Magnetic Resonance (NMR) Spectroscopy, this particular sample was recently monitored (³¹P, ¹³C, January 1991) with no degradation detected. Both GC and GC/MS data were obtained from a 1% solution of VX in DCE. The GC determined purity of the neat VX sample was 94.0% by area using a FID. The FID chromatogram of neat VX is shown as Figure 2.

2.2 Equipment.

An HP 5880A GC equipped with an FID was used in this study. The analysis of VX was accomplished using a 30 meter fused silica capillary column (0.32 mm ID) with a 0.25 μm film of methylsilicone (Alltech Econocap Series SE-30). The carrier gas was helium split at a 50:1 ratio. Pressure controlled (47 Kpa) column flow resulted in a calculated helium flow of 22.7 cm/sec (1.1 mL/min) based on the retention gap (2.2 minutes) obtained for methane at 40 °C. Detector make-up flow was helium at a rate of 23 mL/min. The injection port temperature was

Figure 1. GC Chromatogram of Neat TBP.

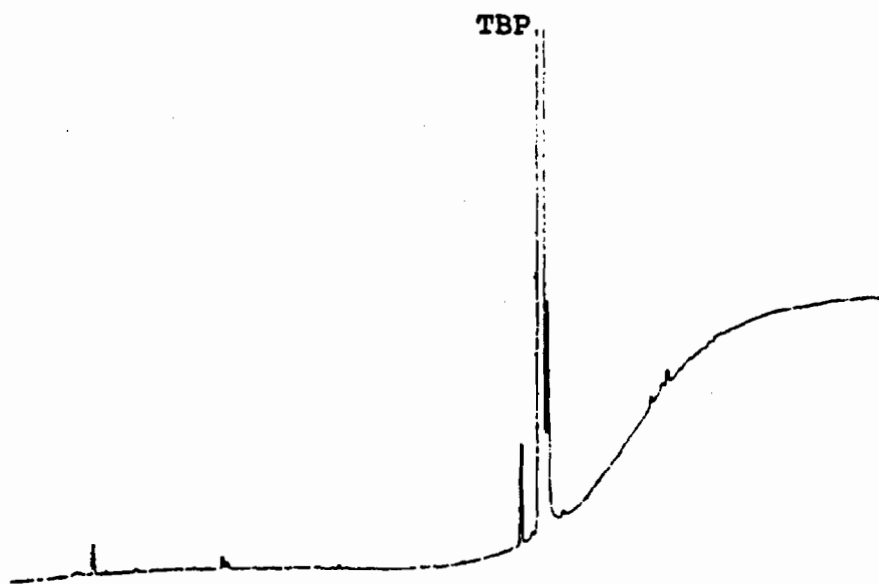
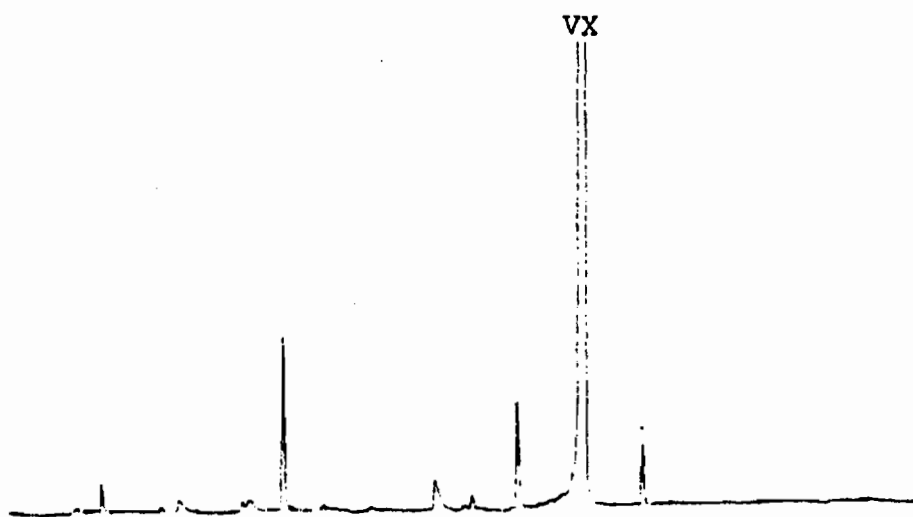


Figure 2. GC Chromatogram of Neat VX.



225 °C and the detector temperature was 300 °C. The column oven temperature was programmed from 75 to 275 °C at 20 °C/min and held at 275 °C for 10 minutes. The combustion gases were hydrogen and air, at 32 and 420 mL/min, respectively. The septum purge flow was adjusted to 1 mL/min. A Hamilton 7001SN microliter syringe was used to manually inject 1.0 µL sample volumes. Area integration of the resulting chromatographic peaks was accomplished electronically.

2.3 Experimental Procedure.

2.3.1 Sample Preparation.

To determine the adsorption efficiency of various sorbing materials, a master dilution of TBP in DCE was prepared. To 100 µL (101.01 mg) of TBP, 10 mL of DCE was added volumetrically. This solution was transferred to a 10 mL glass reaction vial containing a small, teflon-coated magnetic stirbar, and sealed with a teflon-lined silicone septum and an aluminum crimp cap. This 1% (v/v) TBP solution served as both the experimental sample for sorption material testing and as the master standard for further dilution and calibration in the range of interest.

Experimental samples were prepared by the addition of 1.8 mL of the master standard solution (1% TBP in DCE) to a 10 mL glass reaction vial containing a small, cylindrically shaped, teflon-coated, magnetic stirbar and 180 mg of candidate sorbent. The vials were sealed with a teflon-lined silicone septum and an aluminum crimp cap. The mixtures were stirred at 500 rpm. Stirring was interrupted after 5 minutes to enable sampling of the liquid with a Hamilton 7001SN microliter syringe. For each sampling, a 5/8-inch, 25 gauge stainless steel needle was used to vent the sample to assure exactly 1.0 µL of liquid was withdrawn. All work was performed at room temperature (25 ± 1 °C).

Identical procedures were used to prepare samples containing VX, DCE and candidate sorbent materials for testing.

2.3.2 Calibration.

A series of additional dilutions (0.75, 0.5 and 0.25%) were prepared volumetrically from the 1% TBP in DCE master standard. A 1.0 µL aliquot of each was injected manually into the GC using the previously described operating conditions. Duplicate injections were made for all dilute TBP solutions.

Quantitative analysis of TBP in DCE was accomplished using GC. A calibration curve was generated relating TBP area counts to a known concentration of TBP in DCE. The TBP area

counts obtained for experimental samples of unknown TBP concentration which had been exposed to sorbents in the DCE solvent were quantitated based on this linear relationship. Figure 3 graphically illustrates the calibration curve used for this purpose. Calibration data is presented in Table 1.

The amount of VX sorbed by various candidate materials was determined in an identical manner. The peak area from each experiment was then compared to the VX calibration data (also shown in Table 1 and in Figure 3) and % sorption was calculated.

2.3.3 Minimum Detectable Level.

The FID Minimum Detectable Level (MDL) for VX was determined to be 10 ng with a signal of better than twice the noise level for a 1.0 μ L injection of VX in DCE. This corresponds to 0.001% (v/v) concentration of VX in DCE. Since 1% VX in DCE was chosen as the starting concentration for sorption testing, the described procedure could detect VX at the MDL after 99.9 % had been sorbed.

3. Results and Discussion

The first phase of the investigation was carried out with the simulant TBP. The peak area from each experiment was compared to the calibration curve and % sorption was calculated (Table 2). The result indicated that some of the resins tested showed as much as (or, in some cases, more than) activated carbon (Charcoal). Also, the grinding of the charcoal (thus, the particle size) did not influence the sorption property under the given conditions. Among the resins tested, the Rohm and Haas Amberlite XE-393 resin showed best sorbing performance. The Rohm and Haas XE-555 resin includes XE-393 resin as one of its components, and one would instinctively assume that it will show some sorbency based on the performance of XE-393 resin. However, the result showed no sorption by XE-555 resin. The reason for this anomaly is not known at this time.

The second phase of the investigation, with the CWA VX, was then carried out. The results are also shown in Table 2. The last column "VX vs TBP" shows the difference in sorption properties of VX and TBP by the sorbents used. The + sign indicates the particular sorbent sorbed more VX than TBP, - sign indicates less VX, and = sign little difference. The () represents the cases where the difference is within the estimated experimental error. In general, the sorbents tested with VX were chosen because they showed some sorption of TBP. The adsorption of VX was greater than or equal to the adsorption of TBP for all sorbents tested with the exceptions of charcoal and Rohm and Haas XAD-2 resin. Also, even though

TABLE 1. CHROMATOGRAPHIC CALIBRATION STANDARDS FOR VX AND TBP IN DCE

<u>Dilu- tion</u>	<u>VX Standard Preparation</u>	<u>VX</u>		<u>Total DCE (mL)</u>	<u>VX Concentration (%)</u>				<u>GC Area Counts VX</u>
		<u>mg</u>	<u>μL</u>		<u>v/v</u>	<u>w/v</u>	<u>w/w</u>	<u>PPM</u>	
1	100 μL=101.01mg + 10.0mL DCE	101	100	10.0	1.00	1.01	0.80	10,000	903.5
2	0.3mL dil.#1 + 0.1mL DCE	3.03	3.00	0.4	0.75	0.76	0.60	7,500	677.4
3	0.5mL dil.#1 + 0.5mL DCE	5.05	5.00	1.0	0.50	0.51	0.40	5,000	469.3
4	0.2mL dil.#3 + 0.2mL DCE	1.01	1.00	0.4	0.25	0.25	0.20	2,500	230.1
5	0.1mL dil.#4 + 0.9mL DCE	0.25	0.25	1.0	0.025	0.025	0.020	250	30.8

<u>Dilu- tion</u>	<u>TPB Standard Preparation</u>	<u>TBP</u>		<u>Total DCE (mL)</u>	<u>TBP Concentration (%)</u>				<u>GC Area Counts TBP</u>
		<u>mg</u>	<u>μL</u>		<u>v/v</u>	<u>w/v</u>	<u>w/w</u>	<u>ppm</u>	
1	250 μL=246.91mg + 10.0mL DCE	247	250	25.0	1.00	0.99	0.79	10,000	1259.2
2	0.3mL dil.#1 + 0.1mL DCE	2.96	3.00	0.4	0.75	0.74	0.59	7,500	932.3
3	0.2mL dil.#1 + 0.2mL DCE	1.98	2.00	0.4	0.50	0.50	0.39	5,000	615.8
4	0.2mL dil.#3 + 0.2mL DCE	0.99	1.00	0.4	0.25	0.25	0.20	2,500	343.0

Figure 3a. Linear Relationship between GC Peak Area and TBP Concentration.

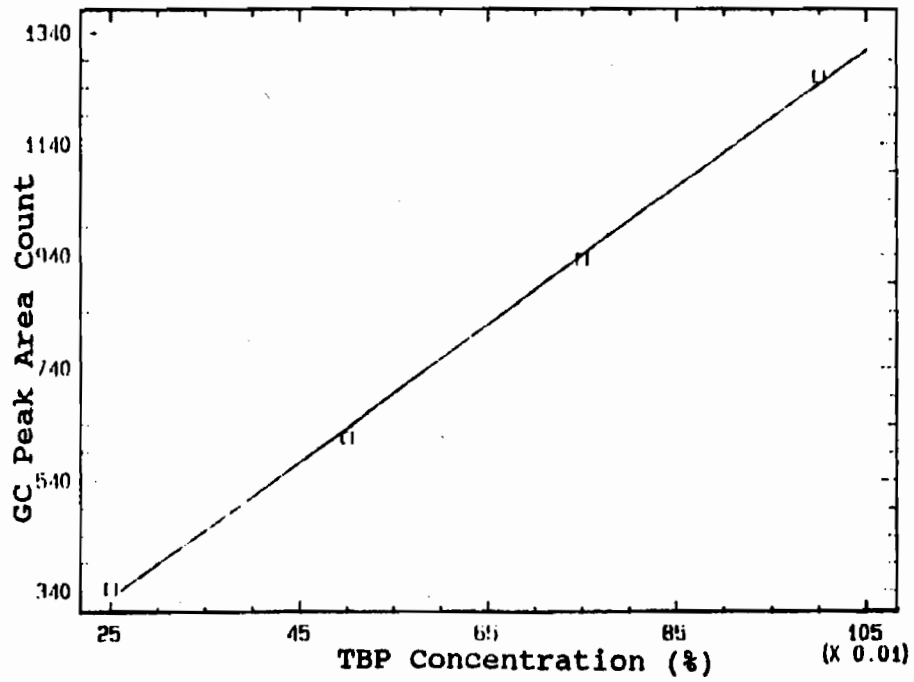


Figure 3b. Linear Relationship between GC Peak Area and VX Concentration.

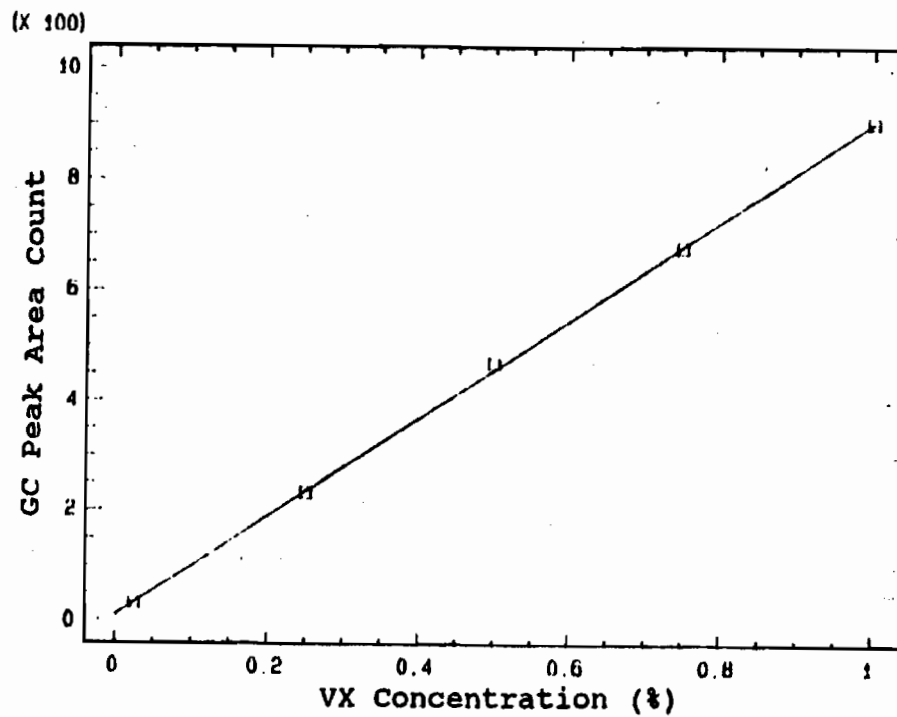


Table 2. Results of Partitioning/Analysis by GC Study of Selected Sorbents with TBP and VX.

Run #	Sorbent	TBP		VX		VX versus TBP
		Peak Area	% Sorbed	Peak Area	% Sorbed	
1	DC PolyTrap ¹	1166.8	7	423.5	7	(=)
2	R&H XAD-2	1125.5	10	897.4	0	(-)
3	R&H XAD-7	1254.4	--			
4	R&H XAD-16	1510.5	--			
5	R&H XE-393	449.6 423.3	65 67	15.2	99	+
6	R&H XE-555	1364.9	--	248.2	73	+
7	SPILL-X-A	1441.4	--			
8	SPILL-X-S	1305.0	--			
9	CDS AS-094-346-0	1168.0	7	733.0	19	+
10	CDS AS-095-346-0	1288.6	--			
11	CDS AS-096-346-0	1480.8	--			
12	CDS AS-097-346-0	1444.5	--			
13	DOW HCR-W2-H	1265.5	--			
14	DOW XUS-40323	1344.1 1337.3	-- --			
15	Dowex M-33	1154.4	8			
16	Dowex M-41-CL	1350.5	--			
17	XN-1010	1069.7	15	676.0	26	+
18	C-150	1126.6	10			
19	Resintech	1076.7	14			
20	Activated Carbon	1144.8	9	982.1	0	(-)
21	Ground Activated Carbon	1138.7	9			
22	Sodium/Calcium Borosilicate Glass	1322.9	--			
23	Fullers Earth	1124.0	10			

(cont.)
 Table 2. Results of Partitioning/Analysis by GC Study of Selected Sorbents with TBP and VX.

Run #	Sorbent	TBP		VX		VX versus TBP
		Peak Area	% Sorbed	Peak Area	% Sorbed	
24	GAF ACP-1001	968.1	23	574.7	37	+
25	GAF CD-260	1333.8	--	861.6	5	(+)
26	GAF Gantrez S-95	1173.2	6	827.8	9	(+)
27	GAF Gantrez AN-169	1365.5	--			

1. Only 5 wt % of sorbent material was used.

it did not show any sorption of TBP, the Rohm and Haas XE-555 resin showed very high sorption (73%) of VX. Among the resins shown some promise is the GAF ACP-1001 resin. This is a copolymer of acrylic acid and 1-vinyl-2-pyrrolidone. When the structure of the copolymer was altered to have one more acidic group in each repeating unit, i.e., copolymer of maleic acid and 1-vinyl-2-pyrrolidone (GAF CD-260), the sorption was reduced in both TBP and VX. As in the case of TBP, the Rohm and Haas Amberlite XE-393 resin showed best sorbing performance (99%) with VX.

4. Conclusion

In summary, it was shown that the amount of VX or TBP sorbed by various resins could be determined quantitatively by GC analysis. Among the resins tested, the Rohm and Haas XE-393 resin showed most sorbing for both VX and TBP under the experimental conditions. In most cases, VX was sorbed more than TBP under these conditions.

BLANK

**KINETICS OF THE HYDROLYSIS OF A MODEL PHOSPHORUS ESTER
BY DS2 DECONTAMINANT SORBED ONTO DOW-CORNING POLYTRAP RESIN
MONITORED BY NMR**

S.H. Hong
Research Directorate
Chemical Research, Development and Engineering Center
APG, MD 21010-5423

P-31 NMR experiments were performed to observe reactions of a model liquid (DMMP) with a decontamination agent (DS2) presorbed onto Dow-Corning PolyTrap sorbent. This sorbent is porous enough and exhibits liquid-like mobility such that a liquid probe can be used and solid state NMR is not required. The preliminary study showed that the hydrolysis reaction can be followed by this method, however, the transesterification reaction products could not be distinguished due to the small chemical shifts. Then, the kinetics of the hydrolysis reaction was followed by P-31 NMR. From the experimental data, assuming 1st order reaction kinetics, a rate constant of 0.0021/min was obtained.

1. Introduction

Many sorbent materials can be used to remove chemical warfare agents (CWA's) from a contaminated surface, and thus eliminate the immediate threat. However, the sorbed agent may present a hazard later if it remains as a CWA in the sorbent matrix. This is why reactive components are included in a sorbent resin, and the effectiveness of the sorbent decontaminant depends on (1) how fast the liquid is sorbed into the applied resin from the contaminated surface and (2) how effectively the sorbed liquid undergoes reaction with the reactive component of the sorbent. The latter, i.e., the fate of the CWA in the reactive sorbent matrix was the main subject of this study. Thus, objectives of this study were (1) to develop methods for detecting interactions between CWA's and sorbents and (2) to develop methods for direct detection of molecular destruction of CWA's in/on reactive sorbents.

The phosphorus ester, dimethyl methyl phosphonate (DMMP), was utilized for this study as a G-type CWA simulant. The possible reactions between DMMP and the components of the DS2 decontaminant, as shown in Figure 1, consist of two types, i.e., hydrolysis and transesterification. The phosphorus peak of the hydrolysis product showed a reasonably large change in chemical shift from that of DMMP (ca. 10 ppm), while the transesterification product showed a very small change in chemical shift (2-3 ppm)¹. Also, the hydrolysis reaction, caused by hydroxide ions (OH⁻), is the slower of the two.

Dow-Corning PolyTrap resin is a very porous material, with a high sorption capacity, and the liquid sorbed onto the resin exhibits a liquid-like flow property so that a liquid probe can be used for NMR spectrometry. The reactive component, the liquid decontaminant DS2, was presorbed onto the resin.

2. Experimental

Dow-Corning PolyTrap resin, presorbed with DS2 at different levels, was obtained from Physical Protection Directorate of CRDEC (L. Kanaras) and was used as received. The phosphorus ester DMMP was obtained from Aldrich Chemical Company and was used as received.

A Varian FX-80 NMR spectrometer was used with 10 mm diameter sample tubes. The samples were prepared in the following manner: the Dow-Corning PolyTrap resin, presorbed with DS2, was placed in a 10 mm NMR tube followed by an addition of DMMP. The mixture was agitated with a stainless steel wire to insure adequate mixing. The ³¹P NMR spectra were taken with an external standard (H₃PO₄).

3. Results and Discussion

A preliminary study was conducted to verify that there is no interaction between DMMP and the sorbent without DS2. The ³¹P spectrum obtained showed no such interaction and thus served as a reference. Then, experiments were performed to observe the mixing characteristics of liquids on the sorbent (Dow-Corning Polytrap). Several acid-base indicators were screened and Alizarine (0.1% Methanol solution) was chosen for these experiments. Thus, a simulant (acetic acid) was added dropwise to the sorbent/DS2 with Alizarine (blue) and the color change of the indicator Alizarine (to yellow) was noted. These preliminary tests showed that the mixing by diffusion alone is a very slow process. However, mixing time was shortened significantly by proper agitation (with a stainless steel wire).

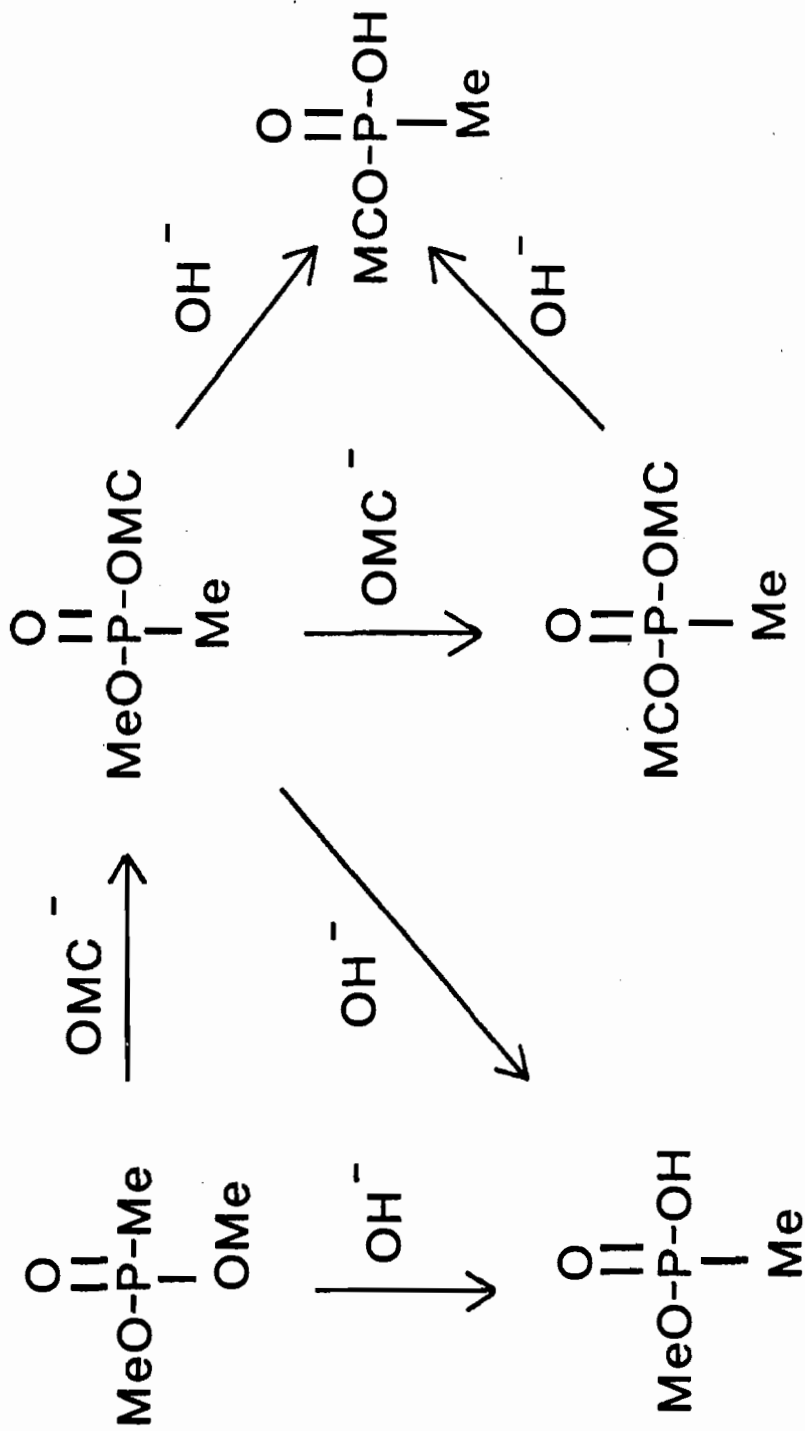


Figure 1. Schematic Diagram of Possible Reactions Between DMMP and DS2 Decontaminant.

The results from the ^{31}P NMR experiments with the model liquid (DMMP) and DS2 decontaminant sorbed onto the Dow-Corning PolyTrap resin are given in Figure 2 and Table 1. Figure 2 shows a typical ^{31}P NMR spectra: the peak at around 30 ppm represents phosphorus of DMMP while the peak at around 20 ppm represents that of hydrolysis product. It should be noted that the transesterification products can not be distinguished under these experimental conditions, and only the hydrolysis reaction can be followed. For the detection of the transesterification reaction, the possibility of using other simulants is under consideration. The ratio of these two peaks varied throughout the reaction due to the conversion of DMMP into the hydrolysis products (Table 1). From these experimental data, assuming 1st order reaction kinetics, a rate constant of 0.0021/min was obtained. By comparison, other CRDEC researchers reported a rate constant of 0.0066/day for the hydrolysis of a similar phosphorus compound, also assuming 1st order kinetics².

Table 1. Results of ^{31}P NMR of DMMP with DS2 in PolyTrap resin.

Time (min)	Percentage of Phosphorus	
	without Hydroxy groups	with Hydroxy groups
20	98.1	1.9
60	90.8	9.2
100	82.6	17.4
140	72.9	27.1
180	70.3	29.7
240	67.0	33.0
300	58.3	41.7
360	49.1	50.9
420	43.6	56.4
480	35.4	64.6

4. Conclusion

The hydrolysis reaction of DMMP with DS2 sorbed onto the Dow-Corning PolyTrap resin was followed by regular FT-NMR analysis with a liquid probe. However, the transesterification reaction products could not be distinguished due to the small chemical shifts.

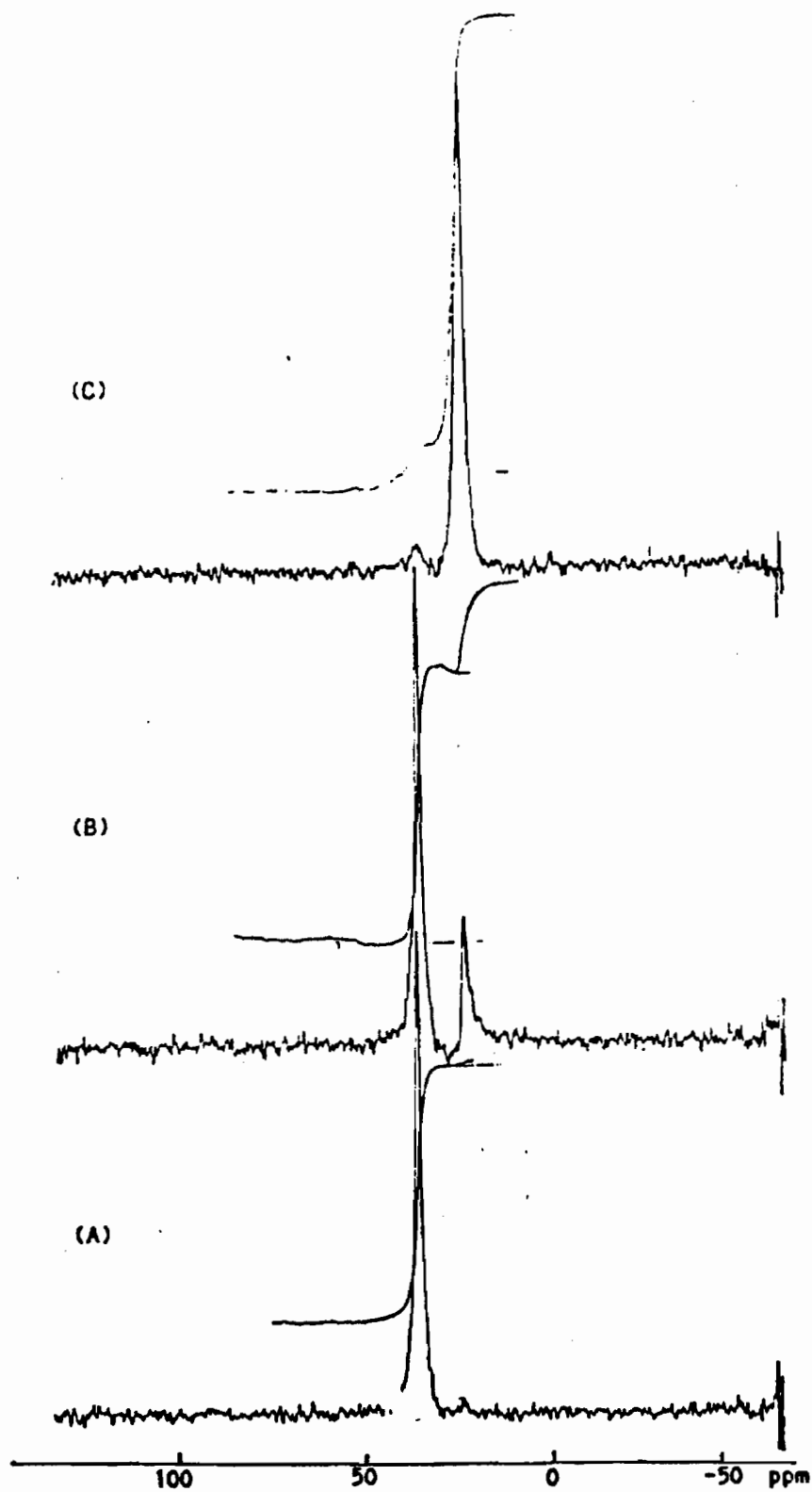


Figure 2. ^{31}P NMR Spectra of DMP in Dow-Corning Polytrap loaded with DS2. (A) 15 min, (B) 140 min and (C) 1 Day after mixing.

ACKNOWLEDGEMENT

The author thanks Mr. William Beaudry and Mrs. Linda Szafraniec for their help with NMR, Messrs. Ralph Leslie, Wendel Shuely and Vincent McHugh for many helpful discussions, and Mr. Louis Kanaras for his support of this program.

Literature Cited

1. Leslie, D.R., Beaudry, W.T. and Szafraniec, L.L.; "Sorption and Reaction of Chemical Agents by a Mixed Sorptive/ Reactive Resin", CRDEC-TR-292, October 1991, UNCLASSIFIED Report.
2. Szafraniec, L.L., Beaudry, W.T., Szafraniec, L.J. and Ward, J.R.; "Substituent Effect in the Hydrolysis of Sarin" in Proceedings of the 1988 U.S. Army Chemical Research, Development and Engineering Center Scientific Conference on Chemical Defense Research, CRDEC-SP-013, August 1989, UNCLASSIFIED Report.

AUTOXIDATION OF 2-MERCAPTOETHANOL CATALYZED BY COBALT(II) PHTHALOCYANINETETRASULFONATE ON COLLOIDAL PARTICLES

Sunkara Haribabu and Warren T. Ford*

Department of Chemistry, Oklahoma State University, Stillwater, Oklahoma 74078

Cobalt(II) phthalocyaninetetrasulfonate (CoPcTS) is a highly active catalyst in aqueous media for the autoxidation of thiols to disulfides, and cationic polymers further enhance the activity. In this work we tested a variety of cationic polymer supports for the CoPcTS-catalyzed autoxidation of 2-mercaptoethanol in aqueous dispersions at 25 °C. The order of activities was cationic polyelectrolytes >> cationic polymer colloids > cationic colloidal silica ≈ aqueous solution > ion exchange resins. Spectroscopic studies indicate that the high activity of the polyelectrolytes correlates with their ability to aggregate the CoPcTS.

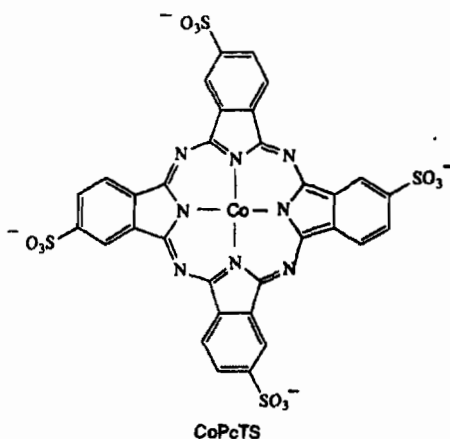
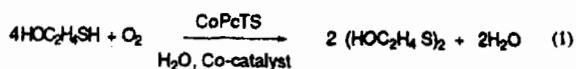
INTRODUCTION

The principal aim of using polymer and silica-supported catalysts in liquid dispersions is to attain the selectivity of homogeneous catalysts along with the recoverability of heterogeneous catalysts. With large particle polymer and silica supports rates of catalyzed reactions often depend on mass transfer and intraparticle diffusion, so we are investigating colloidal particle supports to overcome these transport limitations to activity. We have bound cobalt catalysts quantitatively to polymer latexes¹ for oxidation of 1-decanethiol,² 2,6 di-*tert*-butylphenol,^{3,4} and tetralin⁵ in aqueous dispersions. We have also used colloidal silica bound sulfonic acid catalysts for hydrolysis of diazinon and triphenylmethyl fluoride.⁶ The activities of these colloidal catalysts for oxidation of water insoluble organic substrates exceed their activities in aqueous solution, probably due to high local concentrations of both the organic substrates and the catalyst in the active catalyst phase.

Autoxidation of thiols is important both in industry for the sweetening of petroleum^{7,8} and in biological systems.^{9,10} For autoxidation of thiols in aqueous media cobalt(II) phthalocyaninetetra(sodium sulfonate) (CoPcTSNa₄) is the most active catalyst known.^{11,12} Researchers at Eindhoven have reported that many cationic polymers such as poly(vinylamine) and ionenes further enhance the activity of CoPcTS for thiol autoxidation.¹³⁻²⁶ The cationic polymer effects are ascribed to high concentration of the thiolate anion in the polymer domains,^{13,14} and suppression of formation of the inactive μ -peroxo dimer of CoPcTS.¹⁵ Since in the presence of ionenes (polyquaternary ammonium salts) CoPcTS is aggregated²³ and highly active, aggregated CoPcTS is thought to be the most active form of the catalyst. A large decrease in rate of thiol oxidation when 2,4-ionene/CoPcTS is immobilized on a macroporous resin is likely due to a combination of slow mass transfer of reactants and inhomogeneity of the active sites in the polymer particles.²⁴ Recently, CoPcTS was bound to a cationic latex prepared by emulsion polymerization of styrene and divinylbenzene using a block copolymer of styrene and quaternized 4-vinylpyridine as a surfactant.²⁶ The activity of the latex-bound CoPcTS was greater than that of the analogous soluble polymer-bound CoPcTS and that of

CoPcTSNa₄ in the absence of cationic polymer. In this paper we report the catalytic activities of CoPcTS bound to colloidal particles for autoxidation of 2-mercaptoethanol to 2,2'-dithiodiethanol (Scheme 1) and compare the activities with those of soluble poly(tetraalkylammonium) salts and conventional anion exchange resins.

SCHEME I



RESULTS

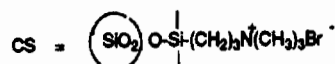
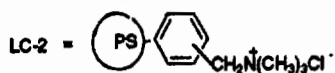
Catalyst Preparation

The polymers used are shown in Scheme 2. Aminated 2,4-ionene was prepared from 1,4-dibromobutane and excess N,N,N',N'-tetramethylethylenediamine. Colloidal silica (CS) was prepared by hydrolysis and condensation of tetraethyl orthosilicate using a sol-gel process,^{28,29} surface modified with (3-bromopropyl)trimethoxysilane, and converted to the cationic colloid by treatment with trimethylamine. Aqueous CoPcTSNa₄ solution was added to the surface modified silica sol to achieve a mol ratio N⁺/Co = 500. This dispersion was ultrafiltered twice. The absence of blue CoPcTS in the filtrate revealed that CoPcTS was bound quantitatively to the particles. Previously we showed that CoPcTS binds quantitatively to latex particles LC-1 and LC-2.^{2,3} Ion exchange resins with bound CoPcTS were prepared by treating the resin particles with excess aqueous CoPcTSNa₄ solution, filtering, washing and vacuum drying the resin particles before use. CoPcTS did not bind quantitatively to the anion exchange resins. The concentrations of unbound CoPcTSNa₄ were determined spectrophotometrically, and the percents of CoPcTS bound to resin particles are reported and compared with those of colloidal particles in Table I. The macroporous IRA-904 binds more CoPcTS than the microporous IRA-420C. The particle sizes and halide ion contents of the colloidal particles and anion exchange resins are reported in Table II.

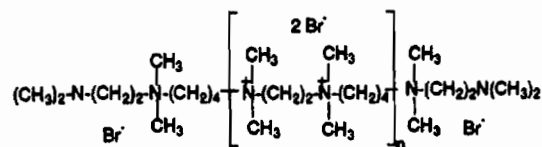
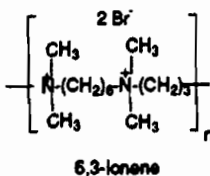
SCHEME II

Co-Catalysts

Colloidal Particles:



Soluble Polyelectrolytes:



Anion Exchange Resins: IRA 420 C, IRA 904

Aminated 2,4-Ionene

TABLE I
Percent CoPcTS Bound to Particles

co-catalyst bound to resins	N ⁺ /Co	Percent CoPcTS
LC-1	10	100
LC-2	4	100
CS	500	100
IRA-420C	500	42
IRA-904	500	97
IRA-904	4	20

TABLE II
Particle sizes and halide ion contents of the colloidal and resin particles

co-catalyst	d _n , μm ^a	mequiv of X ⁻ /g solids
LC-1	0.056	0.17
LC-2	0.067	3.81
CS	0.082	0.07
IRA-420C	519	3.80
IRA-904	541	2.6

^a Number average diameter of 50 particles

Autoxidation of 2-Mercaptoethanol

Kinetics of autoxidation of 2-mercaptoethanol catalyzed by CoPcTS bound to cationic polymers and by aqueous CoPcTSNa₄ in pH 9.2 borate buffer were measured at 25.5 °C. Zero order rate constants expressed in mL of dioxygen per minute were obtained from gas buret measurements of volume of dioxygen consumed vs. time. The autoxidation in the absence of any cationic polymer was slower and had a long induction time not observed with 6,3-ionene or latex LC-1.

To test for mass transfer limitations of the overall reaction rates, the reaction was conducted with varied magnetic stirring speeds. Stirring improves mass transfer of reactants to polymer-supported phase transfer catalysts.³⁰ Increased stirring speed increased the rate of oxidation of 2-mercaptoethanol catalyzed by CoPcTS bound to 6,3-ionene, but has no effect with CoPcTS bound to latex particles LC-1. The reaction rates in the presence of 6,3-ionene increased linearly with the concentration of CoPcTS from 4.9×10^{-8} to 1.96×10^{-7} M at N⁺/Co = 500 and at a constant 2500 rpm stirring.

Previously van Welzen found that rates of oxidation of 2-mercaptoethanol catalyzed by CoPcTS bound to polyelectrolyte depend on many experimental parameters, such as pH, ionic strength, stirring speed, concentration of substrates and polymer, and charge density of the polyelectrolyte.^{19,20,25} We determined the activity of CoPcTS in the presence of colloidal particles at slightly less than 1 atm of dioxygen and 2500 rpm stirring. Rate constants in the presence of soluble and insoluble cationic polymers are reported in Table III.

TABLE III
Activities of CoPcTS Catalysts for Autoxidation of 2-Mercaptoethanol^a

Catalyst	N/Co	Amount (mg)	Induction time (min)	k _{obs} mL/min	Turnovers (mol of O ₂ /mol of Co) s ⁻¹
CoPcTSNa ₄			145	0.044	2.9
6,3-ionene	500	0.95	0	2.248	147.0
Aminated 2,4-ionene	500	0.92	0	2.893	190.4
CS	500	70.0	0	0.048	3.2
LC-1	10	0.56	4	0.102	6.7
LC-1	500	28.3	0	0.158	10.4
LC-2	500	1.29	5	0.104	6.7
LC-2	10970	28.3	15	0.070	4.6
IRA-420C	1260	13.0	60	0.030 ^b	0.5
IRA-904	500	8.1	55	0.083 ^b	1.4
IRA-904	500	8.1	0	0.051 ^{b,c}	0.8

^a All experiments were carried out at 25.5 °C under O₂ pressure of 720 mm of Hg with 2500 rpm stirring of 100 mL of a mixture containing 0.032 M 2-mercaptoethanol and 0.98×10^{-7} M CoPcTS at pH 9.2.

^b Concentration of CoPcTS was 3.92×10^{-7} M and stirring speed was 2000 rpm.

^c The dispersion was mixed with a platform shaker instead of a magnetic stirrer.

DISCUSSION

German and co-workers^{16-23,25} have investigated thoroughly kinetics of autoxidation of thiols catalyzed by CoPcTS in aqueous solutions of cationic polyelectrolytes. The reaction is thought to proceed according to eqs. 2 and 3 with eq. 2 rate-limiting. Based on the observed Michaelis-Menten kinetics, they proposed a mechanism in which the cationic polyelectrolyte binds the thiolate ion, and the thiolate ion is oxidized. Observations of zero-order kinetics for consumption of far more than two mols of mercaptoethanol per mol of dioxygen in all cases prove that eq. 3 cannot be rate-limiting in our experiments.



We have confirmed the exceptionally high activity of the cationic polyelectrolytes 6,3-ionene and aminated 2,4-ionene discovered by the Eindhoven researchers. Their catalytic activities are one to two orders of magnitude greater than those of any of our cationic colloidal particles. Binding the reactive thiolate⁻¹ anion and the CoPcTS⁻⁴ anion to a cationic polymer overcomes the electrostatic repulsion that slows such reactions in solution.

Macroporous (Amberlite IRA-904) and microporous (IRA-420C) anion exchange resins as supports have particle sizes 10^4 times larger than the colloidal supports. Unlike the colloidal supports, the anion exchange resins did not bind CoPcTS quantitatively. The macroporous IRA-904 had greater capacity for CoPcTS than the microporous IRA-420C. The partial failure to bind CoPcTS must be due to N^+ sites located in the cross-linked networks that are inaccessible to the large CoPcTS tetraanion. The lower catalytic activities of CoPcTS bound to resin particles than CoPcTS bound to colloidal particles and aqueous CoPcTSNa₄ suggest that the reactions catalyzed by CoPcTS bound to ion exchange resin particles are partly limited by intraparticle diffusion of reactants or products in the large particles. It also implies that there are no intraparticle diffusional limitations to the reaction rates catalyzed by CoPcTS bound to colloidal particles. Similarly low activity of CoPcTS bound to Sephadex ion exchange resins compared with soluble CoPcTSNa₄ has been reported for autoxidation of 2-mercaptoethanol and 1-butanethiol in aqueous and nonaqueous media.³³

Polystyrene latex having only surface sites (LC-1) is a more active co-catalyst for oxidation of 2-mercaptoethanol than the latex having ion exchange sites throughout the particles (LC-2). Cationic colloidal silica has lower activity than the polystyrene latexes probably due to coagulation of the silica dispersion under the oxidation conditions.

Why are the latex particles so much less active than the ionenes? We expected high catalytic activity with the highly substituted ion exchange latex particles LC-2. We now believe that the lower activity is due to monomeric rather than aggregated CoPcTS in the latex. Aqueous CoPcTS exhibits two absorption maxima in the visible spectrum at 663 nm and 626 nm due to monomeric and dimeric (or aggregated) CoPcTS respectively.^{36,37} The absorption spectrum of CoPcTS in the presence of ionenes shows aggregation of phthalocyanines (λ_{max} 620-622 nm).²³ The high reaction rates with ionene stabilized CoPcTS are attributed to aggregation of CoPcTS, the active site for autoxidation of thiol, by the highly charged, flexible

ionene polymer. The absorption spectra of CoPcTS in the presence of latex particles (LC-2) at pH 9.0 under dioxygen free conditions, shows more monomeric (670 nm) and less aggregated phthalocyanine with increase in the amount of latex particles from 0.009 to 0.056 mg.³⁸ The catalytic activities of CoPcTS bound to latex particles resemble the activities of CoPcTS in the presence of polysoap-type ionenes such as 2,10-ionene rather than 2,4-ionene. The 2,10-ionene also stabilizes CoPcTS in its monomeric form, as our latex LC-2 does, and its activity is much less than that of CoPcTS on 2,4-ionene.

Although colloidal particles have much lower activity than soluble cationic polyelectrolytes for the CoPcTS-catalyzed autoxidation of mercaptoethanol, they do possess higher activity than aqueous CoPcTSNa₄, and other heterogeneous catalysts. Our investigation supports the previous conclusion of German and co-workers that an aggregated form of CoPcTS is the most active species for autoxidation of 2-mercaptoethanol. The results suggest that latex bound CoPcTS will be much more active if we can find a latex that promotes aggregation of the CoPcTS.

CONCLUSIONS

The ionene cationic polyelectrolytes have much higher activity than any colloidal or macroscopic polymer particle supports for co-catalysis of autoxidation of mercaptoethanol with CoPcTS as primary catalyst. Due to the transport limitations CoPcTS bound to commercial ion exchange resins is less active than CoPcTS in aqueous solution, whereas CoPcTS bound to colloidal polymer supports shows moderately higher activity.

ACKNOWLEDGMENT

This research was supported by the US Army Research Office. We thank H. Turk and M. Hassanein for the latex samples.

REFERENCES

1. W. T. Ford, R. S. Chandran, M. Hassanein, and H. Turk, U. S. Patent, 5,011,956, 1991.
2. M. Hassanein and W. T. Ford, *J. Org. Chem.*, **54**, 3106 (1989).
3. H. Turk and W. T. Ford, *J. Org. Chem.*, **53**, 460 (1988).
4. W. T. Ford, R. S. Chandran, and H. Turk, *Pure Appl. Chem.*, **60**, 395 (1988).
5. R. S. Chandran, S. Srinivasan, and W. T. Ford, *Langmuir*, **5**, 1061 (1989).
6. R. D. Badley and W. T. Ford, *J. Org. Chem.*, **54**, 5437 (1989).
7. R. R. Frame, U.S. Patent 4,298,453 (to UOP Inc.), 1981.
8. A. A. Oswald and T. J. Wallace, *The Chemistry Organic Sulfur Compounds*, N. Kharasch and C. Y. Meyers, Eds., Pergamon, London, 1966, vol. 2, chapter 8.
9. D. S. Tarbell, *Organic Sulphur Compounds*, N. Kharasch, Ed., Pergamon, London, 1961, vol. 1, chapter 10.
10. P. C. Jocelyn, *Biochemistry of the SH Group*, Academic, London, 1972, chapter 4.
11. P.-S. K. Leung and M. R. Hoffmann, *J. Phys. Chem.*, **93**, 434 (1989)
12. P.-S. K. Leung and M. R. Hoffmann, *Environ. Sci. Technol.*, **22**, 275 (1988).

13. J. Zwart, H. C. van der Weide, N. Broker, C. Rummens, G. C. A. Schuit, and A. L. German, *J. Mol. Catal.*, **3**, 151 (1977-78).
14. J. H. Schutten, and J. Zwart, *J. Mol. Catal.*, **5**, 109 (1979).
15. J. H. Schutten, P. Piet, and A. L. German, *Makromol. Chem.*, **180**, 2341 (1979).
16. W. M. Brouwer, P. Piet, and A. L. German, *J. Mol. Catal.*, **22**, 297 (1984).
17. W. M. Brouwer, P. Piet, and A. L. German, *J. Mol. Catal.*, **31**, 169 (1985).
18. W. M. Brouwer, P. Piet, and A. L. German, *J. Mol. Catal.*, **29**, 335 (1985).
19. W. M. Brouwer, P. Piet, and A. L. German, *Polym. Bull.*, **8**, 245 (1982).
20. A. M. van Herk, A. H. J. Tullemans, J. van Welzen, and A. L. German, *J. Mol. Catal.*, **44**, 269 (1988).
21. A. M. van Herk, K. H. van Streun, J. van Welzen, and A. L. German, *Brit. Polym. J.*, **21**, 125 (1989).
22. J. van Welzen, A. M. van Herk, H. Kramer, and A. L. German, *J. Mol. Catal.*, **59**, 291 (1990).
23. J. van Welzen, A. M. van Herk, H. Kramer, T. G. L. Thijssen, and A. L. German, *J. Mol. Catal.*, **59**, 311 (1990).
24. K. H. van Streun, J. Meuldijk, and A. L. German, *Angew. Makromol. Chem.*, **173**, 119 (1989).
25. K. H. van Streun, P. Piet, and A. L. German, *Eur. Polym. J.*, **23**, 941 (1987).
26. K. H. van Streun, R. Tennebroek, P. Piet, and A. L. German, *Makromol. Chem.*, **191**, 2181 (1990).
27. J. H. Weber and D. H. Busch, *Inorg. Chem.*, **4**, 469 (1965).
28. R. D. Badley, W. T. Ford, F. J. McEnroe, and R. A. Assink, *Langmuir*, **6**, 792 (1990).
29. W. Stöber, A. Fink, and E. Bohn, *J. Colloid Interface Sci.*, **26**, 62 (1968).
30. W. T. Ford and M. Tomoi, *Adv. Polym. Sci.*, **55**, 49 (1984).
31. L. S. Romsted, *Solution Behavior of Surfactants*, K. L. Mittal and E. J. Fendler, Eds. Plenum, New York, 1982, pp. 1015-1068.
32. F. H. Quina, and H. Chaimovich, *J. Phys. Chem.*, **83**, 1844 (1979).
33. C. A. Bunton, and G. Savelli, *Adv. Phys. Org. Chem.*, **22**, 213 (1986).
34. A. Skorobogaty, and T. D. Smith, *J. Mol. Catal.*, **16**, 131 (1982).
35. W. T. Ford, and H. Yu, *Langmuir*, **7**, 615 (1991).
36. L. C. Gruen, and R. J. Blagrove, *Aust. J. Chem.*, **26**, 319 (1973).
37. Y. Yang, J. R. Ward, and R. P. Seiders, *Inorg. Chem.*, **24**, 1765 (1985).
38. H. Turk, Ph. D. Dissertation, Oklahoma State University, 1989.

BLANK

XXI. COMPUTATIONAL CHEMISTRY POSTER

BLANK

PREDICTING OXIDATION SIMILARITIES
BETWEEN VX AND POTENTIAL SIMULANTS
BY SEMIEMPIRICAL MOLECULAR ORBITAL CALCULATIONS

George Famini and Philip Bartram
U.S. Army Chemical Research, Development and Engineering Center
Aberdeen Proving Ground, Maryland 21010-5423

ABSTRACT

In an attempt to discover new, more efficient decontamination methods, one major reaction pathway (oxidation) of the chemical agent VX has received renewed interest in the last several years. One impediment to this work has been the lack of a suitable fairly nontoxic simulant. This report examines the progress made to identify suitable simulants via computational means and describes two materials that are predicted to be useful for reaction pathway studies.

INTRODUCTION

Because VX is a potent inhibitor of the enzyme acetylcholinesterase (AChE), severe restrictions on its use in laboratory experimentation have been imposed. The need to study the reactivity of VX with experimental decontaminants has created a need for VX simulants that possess similar properties and/or activities as the agent, but are nontoxic.

The U.S. Army Chemical, Research, Development and Engineering Center (CRDEC) has been the lead organization for the development and use of chemical agent simulants (conversation with William White, Research Directorate, CRDEC, May 1990). To promote the use of simulants, and to provide a centralized library for simulant properties, CRDEC created and maintains the Chemical Agent Simulant Data Center.¹

Simulants are chosen for either physical or reactive similarities to the agents. Finding simulants that mimic the VX susceptibility to either oxidation or nucleophilic substitutions has not been very successful. In this paper, we have approached this problem by comparing the electronic properties believed to be important in oxidation and the size and shape of computer generated electrostatic potential maps to compare the thio-sulfur and amino-nitrogen in VX with either/or both groups in the simulants.

Semiempirical calculations and geometry optimization were accomplished with Modified Neglect of Diatomic Differential Overlap (MNDO) algorithm in MOPAC v5.0 computer program.^{2,3} Graphical displays of structures and electrostatic potentials were produced using Chemical Biological Modeling Branch's Molecular Modeling, Analysis and Display System (MMADS).⁴ The pattern recognition program ARTHUR (Informetrix, Incorporated, Seattle, WA) was used to predict the hierarchical clustering of the electronic properties using Euclidean distance criteria.

THE POTENTIAL SIMULANTS

The following chemicals were investigated as possible simulants for O-ethyl S-(2-diisopropylaminoethyl) methylphosphonothiolate (VX).

- o Simulant 1, O-methyl-S-methyl aminophosphorothiolate
- o Simulant 2, O-methyl-S-methyl-N-acetyl amidophosphorothiolate
- o Simulant 3, O-ethyl-O-chlorobromophenyl-S-propyl phosphorothiolate
- o Simulant 4, O-ethyl-S-ethyl methylphosphonothiolate
- o Simulant 5, bis (O-ethyl)-S-ethyl phosphorothiolate
- o Simulant 6, bis (O-methyl)-chlorophenyl phosphorothiolate
- o Simulant 7, triethyl phosphate

The simulants, except O,S-diethyl methylphosphonothiolate (EA-5533) are pesticides.⁵ Research Directorate, CRDEC, (conversation with Leonard Szafraniec, May 1990), synthesized EA-5533.

OXIDATION OF VX

The products of VX oxidation depend upon the solvents, oxidants, and pH used. In t-butanol or 50% aqueous t-butanol solution, one mole of oxygen from a reactive oxidant reacts with one mole of VX to form the N-oxide. This compound decomposes to O,S-Diethyl methylphosphonothiolate by the Cope reaction. The half-life of the E_i mechanism can be reduced in a 1:1 by volume benzene/butanol solution. In a 50% aqueous t-butanol solution, the N-oxide product reacts further with an excess of oxidant at the thio-sulfur to form the sulfoxide followed by hydrolysis at the electrophilic phosphorous atom. In these solvents oxidation of the thio-sulfur occurs only after the formation of N-Oxide. The difference in nucleophilicity (this difference in nucleophilicity is very subtle) is most likely due to electron-donating and electron-attracting groups in VX. The amino-nitrogen is made more nucleophilic by the electron-donating isopropyl groups, and the thio-sulfur less nucleophilic due to the electronegative phosphoryl oxygen. In t-butanol, VX is oxidized with excess oxidant to the sulfoxide with subsequent formation of the pyrophosphate. The sulfoxide product will rearrange to form the corresponding phosphinyl-oxysulphenate, which oxidizes further at the sulfur atom.⁶

APPLICATION OF THEORETICAL CHEMISTRY

Computational Chemistry has become an important tool for the experimentalist. However, although computational methods have been used to predict physical and biological properties, predictions of chemical reactivity have not been as successful.^{7,8,9} Theoretical methods allow for the facile computation of numerous electronic properties of molecules that can infer reactivity that can be used to further compute reaction related properties. In effect, the ground state electronic and steric attributes are used to predict qualitatively how well a reaction can occur.

A problem in the application of molecular orbital calculations is deciphering the large volume of electronic data generated. Two approaches

were used in this paper to compare the oxidation of VX with oxidation of some potential simulants. The first approach utilized hierarchical clustering techniques to find the compound that best matches those electronic properties that are expected to influence oxidation. The second approach used State-of-the-Art display capabilities to convert the numerical data into molecular graphic predictors (electrostatic potential maps). The electrostatic potential has been used successfully to assess the reactivity of a molecule.^{10,11}

COMPUTATIONAL PROCEDURE

All geometry optimizations and calculations of electronic properties were performed using the Modified Neglect of Diatomic Differential Overlap (MNDO) algorithm as contained in MOPAC v5.0 on a Stardent Titan Superworkstation. Graphical display of the electrostatic potentials and molecular structures was done using the Molecular Modeling Analysis and Display System (MMADS) program. The pattern recognition program, ARTHUR, was used to perform all hierarchical clustering.

RESULTS AND DISCUSSION

The approach in this paper was to compare the nucleophilicity of the VX thio-sulfur and the amino-nitrogen to similar functional groups in the simulants. This method compared the molecular electrostatic potential of the Highest Occupied Molecular Orbitals (pairs of electrons available for bonding). Electrostatic potential differences between VX and the simulants were compared. As the molecular electrostatic potential maps (MEP) approach exact overlap, the more likely the reactivities will be similar. Also, comparisons between VX and the simulants were accomplished by calculating and matching the theoretical electronic properties using pattern recognition methods.

HIERARCHICAL CLUSTERING

Five electronic properties (Table 1) for VX and the seven simulants were calculated by the MNDO algorithm. The electronic properties calculated were:

- o ΔH_f - the heat of formation
- o qN - the charge on the nitrogen atom
- o qS - the charge on the sulfur atom
- o E_{HOMO} - the energy of the Highest Occupied Molecular Orbital (HOMO) of nitrogen atom
- o E_{HOMO} - the HOMO energy of sulfur atom

When simulants did not contain a tertiary amino group, an oxygen atom similar in position and energy was evaluated.

Four dendrograms were produced by the pattern recognition package ARTHUR. The first dendrogram considered all five electronic properties. This dendrogram showed simulant 2 to be the best match for VX with simulants 3, 6, 5, 1, and 4 equally poor second choices. The second dendrogram compared four

Table 1. MNDO Electronic Properties

Compound	ΔH_f	q_N	E_{MON}	q_S	E_{MOS}
VX	-88.27250	-.491	-9.28092	-.1484	-10.08184
1	-90.55617	-.4180	-11.72019	-0.0926	-10.5271
2	-129.12229	-.5719	-11.35572	-.1436	-10.42774
3	-123.78412	-.4318*	N/A	0.0108	-10.68290
4	-103.2689	-.4671*	-11.64209	-.0890	-10.10128
5	-154.7065	-.4793*	-11.82132	-.0437	-10.50167
6	-115.91889	-.4736*	-11.89751	+0.0927	-10.62988
7	-209.08610	-.4998*	-11.93752	-.4998*	-11.93752

*Charge on selected oxygen atom

ΔH_f = Heat of formation
 q_N = Charge on nitrogen atom
 E_{MON} = Energy of highest occupied molecular orbital of nitrogen
 q_S = Charge on sulfur atom
 E_{MOS} = Energy of highest occupied molecular orbital of sulfur

Simulant 1, O-Methyl-S-methyl aminophosphorothiolate
 Simulant 2, O-Methyl-S-methyl-N-acetyl amidophosphorothiolate
 Simulant 3, O-Ethyl-O-chlorobromophenyl-S-propyl phosphorothiolate
 Simulant 4, O-Ethyl-S-ethyl methyl phosphonothiolate
 Simulant 5, Bis(O-Ethyl)-S-ethyl phosphorothiolate
 Simulant 6, Bis(O-methyl)-S-chlorophenyl phosphorothiolate
 Simulant 7, Triethyl phosphate

electronic properties, the HOMO energies of sulfur and nitrogen and the formal charges on sulfur and nitrogen. The dendrogram indicated that simulant 2 was again the best choice with simulants 1, 3, 4, 5, and 6 poor second choices. The third dendrogram compared the formal charges and orbital energies of sulfur atoms. Simulant 4 was now the best match for VX. Simulants 1, 2 and 5 were the second choices and simulants 3 or 6 the third choice. The fourth dendrogram, compared the formal charge and the molecular orbital energies of nitrogen atoms or oxygen atoms in cases where no nitrogen atoms were present. The best simulant for nitrogen oxidation was simulant 2. All other simulants were poor second choices. Simulant 7, triethyl phosphate, was included in the study only as a reference.

ELECTROSTATIC POTENTIALS

Relative reactivity between similar functional sites due to attraction and repulsion of point charges was predicted by electrostatic potentials. Molecular electrostatic potentials were calculated using a modified coulombic expression as shown in equation 1.

$$V_{app} = \sum_A \frac{q_a}{R_A - r} \quad (1)$$

V_{app} is the approximate electrostatic potential

q_a is the formal charge on atom A

R_A is the position of the atom

r is the electron at point r

Electrostatic potential maps (MEPs) for VX and the seven potential simulants were generated by the computer. The significant plane shown was the phosphorus/sulfur/nitrogen or the phosphorus/sulfur/oxygen region represented by solid contour lines for the phosphorous atom and broken contour lines for nitrogen, sulfur and/or oxygen atoms. The simulants that best fit the oxidative reactivity of VX had sulfur contour lines similar in shape and size. MEPs for VX, simulant 2, and simulant 4 are shown as figures 1, 2, and 3 respectfully.

Computer generated electrostatic potential difference maps were also made between VX and each of the simulants. The simulants that had the best electrostatic overlaps resulted in difference maps with the smallest negative lobe. Electrostatic overlap maps were made for both sulfur and nitrogen comparisons.

Examination of sulfur overlaps revealed that simulant 4 (EA 5533), figure 4, was the best match for VX sulfur reactivity. No other simulants appeared to have close reactivity.

Examination of nitrogen overlaps showed that the best match for oxidation at the amino-nitrogen is simulant 2, O-methyl-S-methyl-N-acetyl amidophosphorothiolate, figure 5.

SUMMARY

Seven thiolates containing a P-S bond were evaluated to determine if any were suitable as VX simulants for oxidation studies. Using semiempirical molecular orbital methods, five theoretically determined electronic properties were evaluated with the assistance of a mathematical algorithm. Comparisons were also made between VX and the potential simulants by overlapping their electrostatic contour maps. Results showed that no one simulant could serve as a simulant for oxidation at both the VX thiolo-sulfur and the amino-nitrogen. Simulant 4, EA 5533, was the best match for thiolo-sulfur oxidation. Simulant 2, O-methyl-S-methyl-N-acetyl amidophosphorothiolate, was the best choice for amino-nitrogen oxidation. Simulant 2 was the single best choice when all five electronic properties were considered. A ranking of the simulants is summarized in Table 2.

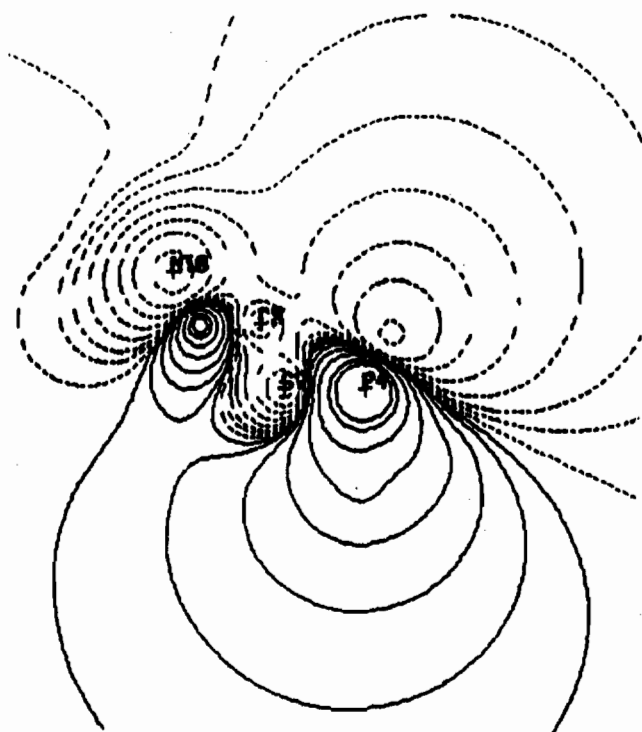


Figure 1. Electrostatic Map/VX

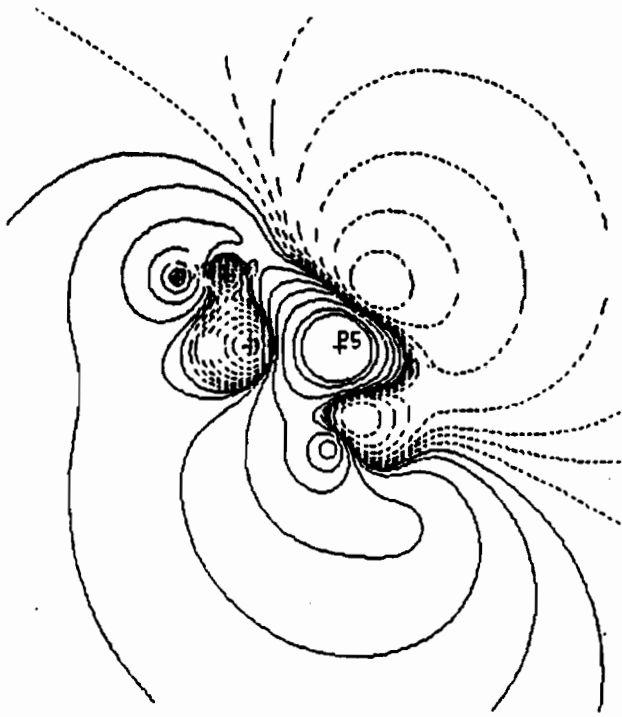


Figure 2. Electrostatic Map/
Simulant 2

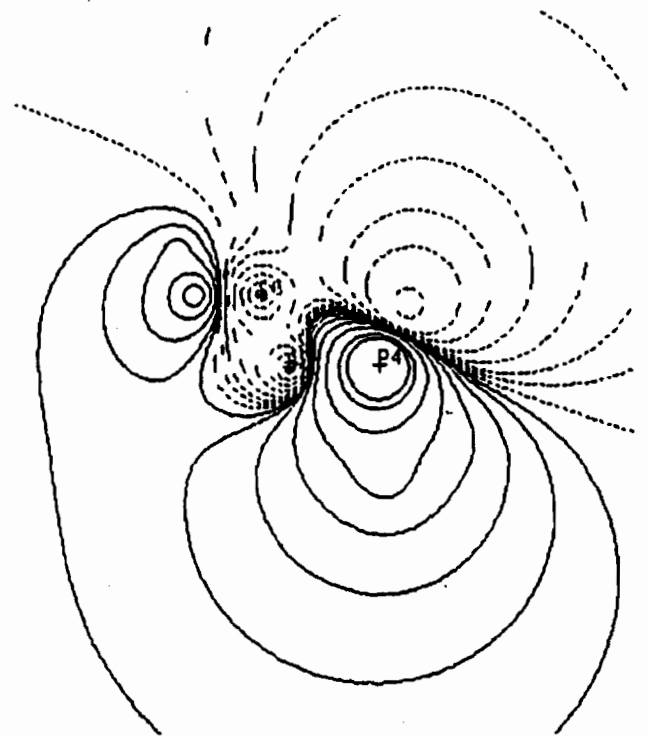


Figure 3. Electrostatic Map/
Simulant 4

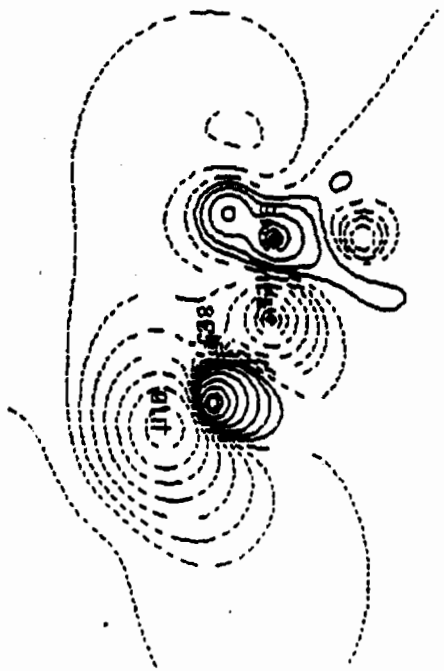


Figure 4. Difference Map/VX and
Simulant 4, S Overlap

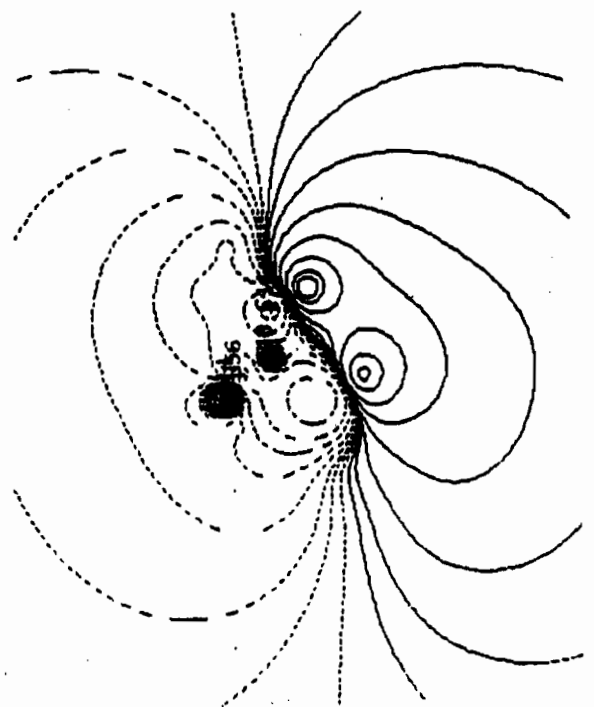


Figure 5. Difference Map/VX and
Simulant 2, N Overlap

Table 2.

SIMULANT RANKING

RANK	FIVE ELECTRONIC PROPERTIES ^a	FOUR ELECTRONIC PROPERTIES ^b	TWO ELECTRONIC PROPERTIES ^c	TWO ELECTRONIC PROPERTIES ^d	MEP
1	2	2	4	2	Simulant 4, Sulfur, Simulant 2, Nitrogen
2	3, 6, 5, 1, 4	1, 3, 4, 5, 6	1, 2, 5		

^a H_F, qN, qS, E_{HOMO} of S, N

^b E_{HOMO} of Sulfur and Nitrogen, qN, qS

^c E_{HOMO} of S, qS

^d E_{HOMO} of N, qN, qO

LITERATURE CITED

1. Coon, P.A., Famini, G.R., White, W.E., and Thornton, R.C., Data Base Users' Guide for the Chemical Agent Simulant Data Center, CRDEC-SP-88032, U.S. Army Chemical Research, Development and Engineering Center, Aberdeen Proving Ground, MD, November 1988, UNCLASSIFIED Report.
2. Dewar, M.J.T., and Thiel, W., "Ground States of Molecules 38. The MNDO Method," J. Am. Chem. Soc. Vol. 99, p 4899 (1977).
3. Steward, J.J.P., MOPAC Manual (5th Edition), FJSRL-TR-88-0007, U.S. Air Force Academy, Colorado Springs, CO, December 1988, UNCLASSIFIED Report.
4. Leonard, J.M., and Famini, G.R., A User's Guide to the Molecular Modeling, Analysis, and Display System (MMADS), CRDEC-TR-030, U.S. Army Chemical Research, Development and Engineering Center, Aberdeen Proving Ground, MD, January 1989, UNCLASSIFIED Report.
5. Eto, M., Organophosphorus Pesticides: Organic and Biological Chemistry, CRC Press, Cleveland, OH, 1974.
6. Yang, Y.-C., Szafraniec, L.L., Beaudry, W.T., and Rohrbaugh, D.K., "Oxidative Detoxification of Phosphonothiolates," J. Am. Chem. Soc. Vol. 112, pp 6621-6627 (1990).
7. Kamlet, M.J., and Taft, R.W., "Linear Free Energy Relationships. Local Empirical Rules or Fundamental Laws of Chemistry," Acta. Chem. Scand. Vol. 1339, pp 611-628 (1985).
8. Hansch, C., "A Quantitative Approach to Biochemical Structure Activity Relationships," Acc. Chem. Res. Vol. 2, p 232 (1969).
9. Famini, G.R., Using Theoretical Descriptors in Structural Activity Relationships, V. A Review of the Theoretical Parameters, CRDEC-TR-085, U.S. Army Chemical Research, Development and Engineering Center, Aberdeen Proving Ground, MD, July 1989, UNCLASSIFIED Report.
10. Famini, G.R., "A Computational Comparison of the Electronic Properties of G Agents with Selected Reaction Simulants," In Proceedings of the 1989 U.S. Army Chemical Research, Development and Engineering Center Scientific Conference on Chemical Defense Research, 14-17 November 1989, CRDEC-SP-024, U.S. Army Chemical Research, Development and Engineering Center, Aberdeen Proving Ground, MD, August 1990, UNCLASSIFIED Report.
11. Politzer, P., and Truhlar, D., Chemical Applications of Molecular Electrostatic Potentials, Plenum Press, New York and London, 1981.

BLANK

XXII. INDEXES

BLANK

INDEX A

AUTHORS FOR PAPERS IN THESE PROCEEDINGS

Alabran, D.M.	445	Cowan, F.M.	683, 707
Albizo, J.M.	793, 895	Czarnik, A.W.	149
Anderson, F.D.	649		
Anholt, R.H.	219	Dabbs, J.A.	209
Arnold, N.S.	641	Davis, V.J.	25
Ashman, W.P.	507	Deakyne, C.A.	515
		Debordes, L.	699
Banks, H.	141	DeFrank, J.J.	235, 763
Bartram, P.W.	867, 935	Deitz, V.R.	49
Beaudry, W.T.	267, 289, 413	Deschamps, J.R.	755
Black, R.M.,	609	Desper, C. R.	377
Blaskó, A.	427	DiBona, N.C.	867
Bloor, B.C.	177	Dill, K.	283
Blyth, D.A.	657	Drago, R.S.	437
Bodily, G.R.	649	Dworzanski, J.	641
Boidot-Forget, M.	785		
Bomalaski, S.H.	65	Eldefrawi, M.E.	779
Bossle, P.C.	801	Ellzy, M.W.	801
Boyd, V.L.	283	Eswaran, D.	755
Brady, A.B.	3		
Brewster, K.	609	Famini, G.	935
Brinck, T.	523	Fant, A.D.	515
Brltich, R.W.	393	Feller, D.R.	83, 91
Broomfield, C.A.	683, 707	Ferguson, C.P.	97, 109
Brozena, A.	135	Fielder, D.	135
Buchanan, J.H.	867, 909	Fikes, L.E.	149
Buettner, L.C.	3	Ford, W.T.	875, 925
Bunton, C.A.	427	Foroudian, H.	427
		Fox, A.	163
Caldwell, W.M.	257	Friday, D.K.	3, 17
Caltebat, I.	699	Frisch, Harry L.	831
Cannon, P.L., Jr.	457, 857		
Carlile, D.L.	3	Gareau, Y.	75
Carlson, H.R.	849	Garlick, S.M.	457
Carrieri, A.H.	541	Gee, S.J.	209
Caulfield, J.E.	713	George, C.	83
Cerny, E.L.	489	Görgens, K.	887
Cerny, L.C.	489	Grasso, P.S.	857
Chadha, S.	169	Green, C.E.	209
Cheng, T.-C.	763	Griest, W.H.	257
Christesen, S.D.	457	Gross, C.L.	713
Chu, B.	355	Guelta, M.A.	849
Clarke, K.J.	41	Guir, F.	579
Clarke, R.J.	609		
Cleveland, J.P.	597	Halliday, J.W.	555
Clewell, H.J., III	193	Hallowell, S.F.	159, 283
Cole, P.	641	Hambrook, J.L.	609
Coppet, L.	699	Hameka, H.F.	535

Haribabu, S.	925	Longo, F.R.	457
Harrison, B.	75		
Harrison, J.M.	609	Mackay, R.A.	457
Harvey, S.	241	Maisonneuve, A.	699
Heitz, H.S.	763	Martin, J.J.	801
Heitz, J.	779	Matsumoto, K.	91
Henshaw, J.M.	393	Matta, J.E.	337
Hepner, D.J.	317	Matuszko, J.S.	25
Heyl, M.J.	159	Matuszko, R.A.	17, 25
Hill, C.L.	421, 901	May, V. B.	823
Ho, C.-h.	257	McGown, E.L.	283
Hoffland, L.D.	673	McGrath, J.J.	201
Hong, S.H.	385, 909, 919	McHugh, V.M.	393
Hong, S.S.	83, 91	Meehan, B.H.	507
Hovanec, J.W.	793, 895	Menking, D.E.	779
Howe, G.B.	33	Menking, D.G.	779
Howells, D.J.	609	Meuzelaar, H.L.C.	641
Hsu, D.S.Y.	563	Miller, D.D.	83, 91
Hsu, F.-L.	83, 91	Miller, M.C.	299
Hydro, W.R.	585	Miller, M.N.	657, 763
		Mioduszewski, R.J.	185, 691
Ince, B.S.	347, 365	Molnar, J.W.	317
Iwamoto, N.E.	499	Munavalli, S.	97, 109
		Murray, J.S.	523
Jankowski, S.	119		
Jarnot B.M.	193	Nakashima, M.	445
Jensen, J.L.	541	Nelson, T.M.	507
Jensen, J.O.	535, 541	Nelson, W.H.	169
Johnson, M.P.	149	Norman, B.H.	75
		Novelli, A.C.	457
Kaplan, M.S.	881	Nusca, M.J.	325
Karwacki, C.J.	49		
Katrizky, A.R.	633	O'Connor, R.J.	283
Katz, S.A.	721	Owicki, J.C.	227
Kilian, J.P.	65		
Kim, C.	177	Padwa, A.	75
Kim, G.-S.	901	Parce, J.W.	227
King, J.W.	585, 597	Park, J.M.	385
Knadle, S.A.	209	Parsons, J.A.	657
Kopec-Smyth, K.	755	Patton, D.E.	437
Krauss, M.	529	Penski, E.C.	127
Kunkel, D.L.	515	Petersen, E.	731
		Petri, W., Jr.	747
Lam, J.N.	633	Pierson, K.W.	563
Lamontagne, R.A.	17, 25	Politzer, P.	523
Lee, P.S.	201	Purdon, J.G.	449
Lemaire, Joëlle	785		
Lennox, W. J.	585, 597	Quin, L.D.	119
Leslie, D. R.	809, 839		
Lester, G.	41	Ramisse, V.	785
LeValley, S.E.	209	Ramsey, R.S.	257
LeVan, M. D.	9	Read, R.W.	609
Levy, M.	401	Rehrmann, J.A.	49
Liebman, J.F.	515	Reutter, D.J.	159

Reutter, S.A.	185, 691	Tom, R.	41
Rodriguez, A.	75	Toscano, P.J.	831
Roehl, J.E.	623	Tyson, C.A.	209
Rogers, K.R.	779	Tytus, R.P.	337
Rohrbaugh, D.K.	97, 109, 665, 839, 867	Vanderhoff, J.W.	385
Romstedt, K.L.	83, 91	Veronick, J.M.	739
Rossman, D.I.	97,109	Vervier, D.K.	763
Russo, G.M.	881		
Salem, H.	721	Wada, H.G.	227
Sanders, K.M.	713	Waechter, J.	831
Sattari, D.	421	Wagner, G.W.	289
Savage, C.	235	Walker, J.E.	555
Schermerhorn, E. J.	831	Wang, J.	355
Schreck, R.M.	201	Ward, J.R.	275, 289, 413, 809, 887
Shamamian, V.A.	563	Ward, K.B.	755
Shoff, D.B.	673	Weaver, T.B.	573
Shuey, W.J.	347, 355, 365, 393	Weber, D.J.	309, 317
Smith, P.B.	617, 773	Winn, D.T.	149
Smith, W.J.	683, 707, 713	Wong, N.M.	457
Snyder, A. P.	617, 641, 657, 773	Wood, G.O.	573
Snyder, D.A.	219	Wood, S.J.	731, 739, 747
Sommerville, D.R.	337	Wright, S.	427
Sperry, J.F.	169	Wu, X.-P.	119
Spivey, J.J.	33		
Stinagle, G.W.	33	Yang, Y.-C.	413, 887
Sweger, R.W.	149	Yokoe, H.	219
Sybert, E.M.	247		
Szafraniec, L.J.	275, 823, 839	Zabielski, C.V.	401
Szafraniec, L.L.	267, 275, 413, 823, 839	Zeroka, D.	541
		Zhou, Peiguang	831
Taylor, T.S.	427	Zhu, W.	875
Terrier, F.	579	Zillmer, M.	887
Thompson, R.G.	779		
Tillman, N.	881		

BLANK

950



INDEX B

ORGANIZATIONS OF AUTHORS IN THESE PROCEEDINGS

Allied-Signal Aerospace Company	41	Science and Technology Corporation	779
Allied-Signal Research and Technology	41	SRI International	209
Applied Research Corporation	563	State University of New York at Albany	831
Armstrong Laboratories (ALCFTO)	65	State University of New York at Stony Brook	355
Armstrong Laboratory (AL/OET)	193		
Centre d'Etudes du Bouchet	579, 699, 785	Texas Tech University Health Sciences Center	201
Chemical and Biological Defence Establishment	609	The Ohio State University	83, 91, 149
Clark Atlanta University	75		
Clemson University	283	UCLA School of Medicine	177
Defence Research Establishment Suffield	449	U.S. Army Ballistic Research Laboratory	317, 325
Drexel University	457	U.S. Army Chemical Research, Development and Engineering Center	3, 49, 83, 91, 97 109, 127, 135, 141, 159, 185 235, 241, 267, 275, 283, 289 299, 309, 317, 337, 347, 355 365, 385, 393, 413, 457, 507 535, 541, 585, 597, 617, 641 657, 665, 673, 691, 721, 731 739, 747, 763, 773, 779, 793 801, 809, 823, 839, 849, 857 867, 887, 895, 909, 919, 935
Duke University Medical Center	219		
Eastern Illinois University	515	U.S. Army Materials Technology Laboratory	377, 401
Eastman Chemical Company	597	U.S. Army Materiel Test Facility	649
Eastman Kodak Company	881	U.S. Army Medical Research Institute of Chemical Defense	585, 597, 683, 707, 713
Ecole Nationale Supérieure de Chimie de Paris	579	U.S. Army Natick Research, Development and Engineering Center	445, 555
Emory University	75, 421, 901	Université Paul Sabatier	457
Environmental Technologies Group	623	University of California	427
General Motors Research Laboratories	201	University of Florida	437, 633
Geo-Centers, Inc.	3, 17, 25 49, 97, 109, 457 617, 657, 755, 773	University of Maryland	247, 515
Lehigh University	385, 541	University of Maryland School of Medicine	779
Letterman Army Institute of Research	283	University of Massachusetts	119
Los Alamos National Laboratory	573	University of New Orleans	523
Materials Research Laboratory	809, 839	University of Pennsylvania	535
Molecular Devices Corporation	227	University of Rhode Island	169
National Institute of Standards and Technology	529	University of South Carolina	163
Naval Research Laboratory	17, 25, 83 563, 755	University of Tulsa	393
Naval Weapons Center	499	University of Utah Center for Micro Analysis & Reaction Chemistry	641
Oak Ridge National Laboratory	257	University of Virginia	9, 747
Oklahoma State University	875, 925	Utica College of Syracuse University	489
Research Triangle Institute	33		
Rothe Development Corporation	65	WWD BW ABC Schutz	887

BLANK

XXIII. APPENDIXES

BLANK

APPENDIX A
LIST OF ATTENDEES

Mr. Herbert S. Aaron
US Army CRDEC
ATTN: SMCCR-RSC-O
APG, MD 21010-5423

Dr. George F. Adams
US Army BRL
ATTN: SLCBR-IB-I
APG, MD 21005-5060

Mr. Sanjay Agarwel
Research Triangle Institute
919/541-8024

Mr. Johnnie M. Albizo
US Army CRDEC
ATTN: SMCCR-RSB
APG-EA, MD 21010-5423
301/671-2761

Dr. Robert Allen
Dept of Veterans Affairs
Environmental Medicine and
Public Health
810 Vermont Avenue NW
Washington, DC 20420
202/535-7193

Mr. Mark Althouse
US Army CRDEC
ATTN: SMCCR-DDT
APG, MD 21010-5423

Mr. H. Juergen Altmann
WWDBW ABC-Schutz
Postfach 1320
Humbold Str
Munster, D-3042
GERMANY
495192126208

Dr. Robert R.H. Anholt
Duke University Medical Center
Dept of Neurobiology
P.O. Box 3209
Durham, NC 27710
919/684-8859

Mr. William P. Ashman
US Army CRDEC
ATTN: SMCCR-RSP-C
APG, MD 21010
301/671-3518

Mr. Vincent D. Auber
US Army CRDEC
ATTN: SMCCR-PPD
APG, MD 21010-5423
301/671-5645

Dr. Mira M. Bagdasarian
Michigan State University
Department of Microbiology
S-110 Plant Research Laboratory
East Lansing, MI 48824
517/353-8619

Dr. James A. Baker
US Army CRDEC
ATTN: SMCCR-PPD
APG, MD 21010-5423
301/671-5621

Dr. Harold D. Banks
US Army CRDEC
ATTN: SMCCR-RS-O
APG, MD 21010-5423
301/671-2131

Mr. James D. Barden
Kaman Sciences Corp.
Defense Systems Division
2560 Huntington Avenue
Suite 200
Alexandria, VA 22303
703/329-7116

Dr. Steven Baskin
USAMRICD
ATTN: SGRD-UV-PB
APG, MD 21010
301/671-2378

Dr. William T. Beaudry
US Army CRDEC
ATTN: SMCCR-RSC-P
APG, MD 21010-5423
301/671-3863

Mr. Thomas Bein
David Taylor Research Center
Code 2721
Annapolis Laboratory
Annapolis, MD 21402
301/267-2159

Dr. Herman P. Benecke
Battelle Columbus Labs
505 King Avenue
Columbus, OH 43201
614/424-4457

Mr. Frederic Berg
CRDEC
APG, MD
410/671-5634

Mr. T. D. Biggs
U.S. Army CRDEC
ATTN: SMCCR-RSL
APG, MD 21010-5423
301/671-5949

Mrs. Karen J.P. Binney
US Army FSTC
ATTN: IAAIF-RBA
220 Seventh Street NE
Charlottesville, VA 22901-5396
804/980-7808

Dr. Amnon Birenzvig
US Army CRDEC
ATTN: SMCCR-RSL
APG, MD 21010
301/671-4248

Dr. Robin M. Black
Chemical & Biological Defence
Establishment
Porton Down
Salisbury, Wiltshire, SP4 0JQ
UNITED KINGDOM
980610211201

Mr. William C. Blanchard
Blanchard & Co., Inc.
27 Glen Alpine Road
Phoenix, MD 21131
301/592-7507

Dr. Byron C. Bloor
UCLA School of Medicine
Department of Anesthesiology
10833 Le Conte Avenue
Los Angeles, CA 90024-1778
213/825-7582

Mr. David A. Blyth
Geo-Centers Inc.
Gunpowder Branch
P.O. Box 68
APG, MD 21010-0068
301/671-2416

Mr. Gary R. Bodily
US Army Dugway Proving Ground
ATTN: STEDP-JOD-A
Dugway, UT 84022-5000
801/831-3371

Dr. Anthony A. Boiarski
Battelle Memorial Institute
505 King Avenue
Columbus, OH 43201-2693
614/424-4778

MAJ Susan H. Bomalski
USAF Armstrong Laboratory
CFTO
Sustained Operations Branch
Brooks AFB, TX 78235-5000
512/536-3814

Mr. Noah Borenstein
Rohm and Haas Company
727 Norristown Road
Spring House, PA 19477
215/641-7240

Dr. Paul C. Bossle
US Army CRDEC
ATTN: SMCCR-RSL
APG, MD 21010-5423
301/671-3957

Mr. Donald R. Bowie
US Army CRDEC
ATTN: SMCCR-RSC-P
APG, MD 21010-5423
301/671-3171

Ms. Amanda B. Brady
Geo-Centers, Inc.
Gunpowder Branch
P.O. Box 68
APG, MD 21010-0068
301/671-4621

MAJ David J. Braitman
US Army Medical Rsch & Dev Cmd
ATTN: SGRD-PLA
Fort Detrick
Frederick, MD 21702-5012
301/663-7567

Dr. Ernest H. Braue, Jr.
USAMRICD
ATTN: SGRD-UV-DB
Bldg E3081
APG, MD 21010-5425
301/671-4373

Dr. William H. Brendley, Jr.
Rohm & Haas Company
Independence Mall West
Philadelphia, PA 19105
215/592-2093

Dr. Alan H. Brittain
Graseby Ionics
Odhams Trading Estate
St. Albans Road
Watford, Herts, WD2 5JX
UNITED KINGDOM
923-244464

Dr. Clarence A. Broomfield
USAMRICD
Attn: SGRD-UV-PB
APG, MD 21010
301/671-2626

Mr. Russell P. Brown
Naval Surface Warfare Center
ATTN: H-31
Dahlgren, VA 22448-5000
703/663-8621

Ms. Ann Brozena
US Army CRDEC
ATTN: SMCCR-RSC-P
APG, MD 21010-5423
301/671-3833

Mr. Joe L. Brumfield
Naval Surface Warfare Center
Code H305
Dahlgren, VA 22448-5000
703/663-8621

Mr. James H. Buchanan
US Army CRDEC
ATTN: SMCCR-RSC-P
APG, MD 21010-5423
301/671-2366

Mr. Leonard C. Buettner
US Army CRDEC
ATTN: SMCCR-RST-E
APG, MD 21010
301/671-4822

Mr. Joseph K. Bunting
PMI Technology
815 Middleground Blvd.
Newport News, VA 23606
804/873-3832

Prof. Clifford A. Bunton
UCSB
Department of Chemistry
Santa Barbara, CA 93106
805/893-2605

Dr. Luke A. Burke
Rutgers University
Dept of Chemistry
Camden, NJ 08102
609/757-6158

Mr. Brent R. Busey
US Army CRDEC
ATTN: SMCCR-DDT
APG, MD 21010-5423
301/671-5580

Mr. Lee E. Campbell
CRDEC
SMCCR-QAO-C
APG, MD 21010
410/671-3555

Ms. Donna A. Cannella
US Army CRDEC
ATTN: SMCCR-RS
APG, MD 21010-5423
301/671-3250

Mr. Paul L. Cannon, Jr.
US Army CRDEC
ATTN: SMCCR-RSC-C
APG, MD 21010-5423
301/671-3719

Ms. Donna L. Carlile
US Army CRDEC
ATTN: SMCCR-RSC-A
APG, MD 21010
301/671-4621

Dr. John C. Carpin
US Army CRDEC
ATTN: SMCCR-RST-E
APG, MD 21010-5423

Mr. Mark E. Carr
Gentex Corporation
Chemical Defense Products
P.O. Box 315
Carbondale, PA 18407
717/282-8511

Dr. Michael M. Carrabba
EIC Laboratories, Inc.
111 Downey Street
Norwood, MA 02062
617/769-9450

Dr. George D. Case
Resource Technologies Group, Inc.
400 Mississippi Street
Morgantown, WV 26505
304/291-6706

Mrs. Elaine L. Cerny
Utica College of Syracuse Univ.
Dept of Chemistry
Utica, NY 13502
315/792-3091

Prof. Lawrence C. Cerny
Utica College of Syracuse Univ.
Dept of Chemistry
Utica, NY 13502
315/792-3091

Dr. Cary F. Chabalowski
BRL
SLC BR-IB-1
APG, MD 21005-5066
301/278-6095

Dr. James P. Chambers
Univ. of Texas at San Antonio
Division of Life Sciences
Brain Res. Lab of Biochemistry
San Antonio, TX 78249
512/691-5477

Dr. Ronald T. Checkai
US Army CRDEC
ATTN: SMCCR-RST-E
APG, MD 21010
301/671-2036

Dr. Tu-Chen Cheng
US Army CRDEC
ATTN: SMCCR-RSB
E3220, Rm 209
APG, MD 21010
301/671-3972

Mr. Kes Chesonis
US Army Belvoir RD&E Center
ATTN: STRBE-VO
Fort Belvoir, VA 22060-5606
703/664-5889

Dr. Steven Christesen
US Army CRDEC
ATTN: SMCCR-RSL-S
APG, MD 21010-5423
301/671-2437

Dr. Benjamin Chu
SUNY at Stony Brook
Dept of Chemistry
Stony Brook, NY 11794-3400
516/632-7928

Mr. Gregory D. Clark
Howard University
Chemistry Department
P.O. Box 90795
Washington, DC 20010
202/806-7678

Dr. Daniel R. Coleman
CMS Research Corporation
200 Chase Park South
Suite 100
Birmingham, AL 35244
205/733-6900

Dr. Conrad G. Collins
Advanced Materials Inc.
1608 Justin Road
Metairie, LA 70001
504/835-3951

Dr. Kenneth R. Collins
US Army CRDEC
ATTN: SMCCR-RSC-P
APG, MD 21010-5423
301/671-3171

Mr. William H. Collins
US Army CRDEC
ATTN: SMCCR-RS
Bldg E3330
APG, MD 21010-5423
301/671-4144

Dr. Joseph A. Corella
MSA Research
P.O. Box 429
Pittsburgh, PA 15230
412/967-4329

Mr. Fred M. Cowan
USAMRICD
ATTN: SGRD-UV-PB
APG, MD 21010-5425
301/671-2847

Ms. Ilene A. Crabb
University of MD Baltimore County
Dept of Chemistry & Biochemistry
Baltimore, MD 21228
301/455-2491

Mr. Victor A. Crainich, Jr.
Chemical Delivery Systems, Inc.
P.O. Box 292677
Kettering, OH 45429
513/434-0572

Dr. Christopher J. Cramer
US Army CRDEC
ATTN: SMCCR-RSP-C
APG, MD 21010-5423
301/671-3518

LT Ruth A. Cresson
AFRC (NAVMIC 1313)
1430 Wright Street
Madison, WI 53704
608/262-2791

Dr. Donald T. Cronce
NAVSWC
Code H31
Dahlgren, VA 22448-5000
703/663-8621

Prof. Anthony W. Czarnik
Ohio State University
Department of Chemistry
120 West 18th Avenue
Columbus, OH 43210-1173
614/292-4531

Dr. Dennis M. Davis
US Army CRDEC
ATTN: SMCCR-RSL
APG, MD 21010-5423
301/671-2437

Dr. Franklin A. Davis
Drexel University
Dept of Chemistry
32nd & Chestnut Streets
Philadelphia, PA 19104
215/895-2647

Mr. Charles K. Dawsen, III
GEO Centers
301/442-1955

Dr. Joseph J. DeFrank
US Army CRDEC
ATTN: SMCCR-RSB
APG, MD 21010-5423
301/671-3972

Dr. Adarsh Deepak
Science and Technology Corp.
101 Research Drive
Hampton, VA 23666
804/865-1894

Dr. Victor R. Deitz
Naval Research Laboratory
Code 6170
Washington, DC 20375
202/767-2334

Dr. Jeffrey R. Deschamps
Naval Research Laboratory
Code 6030
Bldg 35
Washington, DC 20375-5000
202/767-0656

Dr. C. Richard Desper
US Army Laboratory Command
ATTN: SLCMT-EMP
Materials Technology Laboratory
Watertown, MA 02172-0001
617/923-5391

Mr. Remon J. Dihu
IIT Research Institute
Chemistry Department
10 West 35th Street
Chicago, IL 60616
312/567-4270

Dr. David T. Doughty
Calgon Carbon Corporation
P.O. Box 717
Pittsburgh, PA 15230-0717
412/787-6602

Prof. Russell S. Drago
University of Florida
Chemistry Department
Gainesville, FL 32611
904/392-6043

Mr. William J. Drumgoole
US Army CRDEC
ATTN: SMCCR-RSP-B
Bldg E5951
APG, MD 21010
301/671-2326

Dr. Daniel J. Ehntholt
Arthur D. Little, Inc.
15 Acorn Park
Cambridge, MA 02140
617/864-5770

Dr. Mohyee E. Eldefrawi
University of Maryland
School of Medicine
Dept of Pharmacology & Exp Therapy
655 W. Baltimore Street
Baltimore, MD 21201
301/328-3564

Dr. Janon F. Embury
US Army CRDEC
SMCCR-RSP-B
APG, MD 21010-5423
410/671-2543

Mr. Elmer H. Engquist
Battelle Edgewood Operations
2113 Emmorton Park Road
Suite 200
Edgewood, MD 21040
410/676-0200

Mr. Erik E. Engwall
US Army Materials Tech Lab
ATTN: SLCMT-EMP
Watertown, MA 02172
617/923-5348

Dr. Joseph Epstein
Environmental Technologies Group
4020 Essex Road
Baltimore, MD 21207
301/486-2793

Mr. Craig Falci
ORD
Washington, DC 20505
703/351-2136

Dr. George R. Famini
US Army CRDEC
ATTN: SMCCR-RSP-C
APG, MD 21010
410/671-2670

Mr. Andrew D. Fant
University of MD Baltimore County
Dept of Chemistry & Biochemistry
Baltimore, MD 21228
301/455-2190

Ms. Angela Farenwald
SMCOR-RSP
APG, MD 21010
301/671-3438

Ms. Michele M. Farris
Geo-Centers Inc.
Gunpowder Branch
P.O. Box 68
APG, MD 21010-0068
301/671-3311

Dr. Paul D. Fedele
US Army CRDEC
ATTN: SMCCR-RSP-P
APG, MD 21010-5423
301/671-2262

Mr. C. Parker Ferguson
US Army CRDEC
ATTN: SMCCR-RSC-O
Research Directorate
APG, MD 21010-5423
301/671-1901

Mr. Foy E. Ferguson
US Army CRDEC
ATTN: SMCCR-RSL-A
Analytical Research Division
APG, MD 21010
301/671-2560

Dr. John C. Fernando
University of Maryland
Dept of Pharmacology
655 West Baltimore Street
Baltimore, MD 21201
301/328-4295

Dr. John M. Ferriter
US Army CRDEC
ATTN: SMCCR-MU
APG, MD 21010-5423
301/671-2225

Mr. Donald Fielder
US Army CRDEC
ATTN: SMCCR-RSC-P
APG, MD 21010-5423
301/671-3833

Prof. Warren T. Ford
Oklahoma State University
Chemistry Department
419 Physical Science
Stillwater, OK 74078
405/744-5946

Dr. Alvin Fox
University of South Carolina
School of Medicine
Dept of Microbiology & Immunology
Columbia, SC 29208
803/733-3288

Mr. James G. Freedy
US Army CRDEC
Berger Bldg #3549
Rm 135B
APG, MD 21010-5423
301/671-5985

Dr. Mary Freeman
Kaman Sciences Corp.
2560 Huntington Avenue
Alexandria, VA 22303
703/329-7106

Dr. David K. Friday
Geo-Centers Inc.
Gunpowder Branch
P.O. Box 68
APG, MD 21010-0068
301/671-4377

Dr. Benedict J. Gallo
US Army Natick RD&E Center
ATTN: STRNC-YMT
Soldier Science Directorate
Natick, MA 01760-5020
508/651-5505

Ms. Stephanie M. Garlick
Geo-Centers, Inc.
Gunpowder Branch
P.O. Box 68
APG, MD 21010-0068
301/671-2131

Mr. Kurt D. Gerdes
Navy Clothing & Textile Rsch Fac
P.O. Box 59
Natick, MA 01760-0001
508/651-4785

Dr. Robert G. Ghirardelli
US Army Research Office
Chemical & Biological Sciences Div
Box 12211
Research Triangle Pk, NC 27709-2211
919/549-4209

Dr. Albert Gomezplata
ECO
513 Powell Drive
Annapolis, MD 21407
301/849-8231

Dr. Nat Gordon
4990 Sentinel Drive #301
Bethesda, MD 20816
301/229-1997

Dr. Michael Graetzel
Ecole Polytechnique Federale
Institut de chimie physique II
Ecublens
Lausanne, CH-1015
SWITZERLAND
0216933112

LTC Richard C. Graham
United States Military Academy
Department of Chemistry
West Point, NY 10996
914/938-3904

Mr. Paul Grasso
US Army CRDEC
ATTN: SMCCR-RSC-C
APG, MD 21010
301/671-3719

Ms. Phyllis A. Gray
US Army CRDEC
SMCCR-RSL
APG, MD 21010-5423
301/671-2560

Dr. Bernard S. Green
The Hebrew University of Jerusalem
School of Pharmacy
Dept of Pharmaceutical Chemistry
P.O. Box 12065
Jerusalem, 91120
ISRAEL

Mr. Clark L. Gross
USAMRICD
ATTN: SGRD-UV-PB
Bldg E3100
APG, MD 21010-5425
301/671-2847

LTC Martin Grumrine
703/697-3090

Mr. Mark A. Guelta
US Army CRDEC
ATTN: SMCCR-RSP-P
APG, MD 21010-5423
301/671-2608

Dr. Frederic Guir
l'Establissement Technique Central
de l'Armement
Centre d'Etudes du Bouchet
B.P. No. 3 - Le Bouchet
91710 Vert Le Petit,
FRANCE
33169908409

Mr. Devender K. Gulliani
RD&E Center
VATICK
508-651-5484

MAJ Dallas C. Hack
USAMRIID
Virology Division, Bldg 1425
Fort Detrick, MD 21702-5011
301/663-7655

Mr. Ronald C. Hallendorff
AMCCOM
AMSMC-RT
Rock Island, IL 61299
309/782-4551

Ms. Susan Hallowell
US Army CRDEC
ATTN: SMCCR-RSL
APG, MD 21010
301/671-2107

Dr. Hendrik F. Hamerka
University of Pennsylvania
Department of Chemistry
1503 Argyle Road
Berwyn, PA 19312
215/898-8303

Mr. James T. Hanley
Research Triangle Institute
P.O. Box 12194
Research Triangle Pk, NC 27709
919/541-5811

Mrs. Carol S. Hansen
US Army CRDEC
ATTN: SMCCR-RSP-A
APG, MD 21010-5423
301/671-4048

SPC Lavon Harbor
CRDEC
SMCCR-RSB
APG, MD 21010
301/671-2586

Dr. Peter M. Harvey
US Army Dugway Proving Ground
ATTN: STEDP-MT-C-T
Dugway, UT 84022-5000
801/831-5846

Dr. Steve Harvey
US Army CRDEC
ATTN: SMCCR-RSB
Bldg E3220, Rm 215
APG, MD 21010-5423
301/671-3972

Mr. Jude J. Height
US Army CRDEC
ATTN: SMCCR-RSL
APG, MD 21010-5423
301/671-4265

Mr. David J. Hepner
US Army BRL
ATTN: SLCBR-LF-A
Bldg 120
APG, MD 21005-5066
301/278-4103

Mr. Raymond E. Herd
US Army CRDEC
ATTN: SMCCR-RSL-A
APG, MD 21010
301/671-2620

Dr. James J. Hickman
SAIC
MS 2-3-1
1710 Goodridge Road
McLean, VA 22102
703/734-4078

Dr. Donald A. Hirst
HQ USAF/TXSG
Patrick AFB, FL 32925
407/494-2531

Dr. Chuen Huei Ho
Oak Ridge National Laboratory
Analytical Chemistry Division
P.O. Box 2008
Oak Ridge, TN 37831-6120
615/483-8331

Dr. Lynn D. Hoffland
US Army CRDEC
ATTN: SMCCR-RSL
APG, MD 21010
301/671-3129

Prof. Robert R. Holmes
Univ of Massachusetts
Dept of Chemistry
LGRTA 102
Amherst, MA 01003
413/545-2422

Dr. S. S. Hong
Ohio State University
College of Pharmacy
Columbus, OH 43210
614/292-1228

Dr. Seok H. Hong
US Army CRDEC
ATTN: SMCCR-RSC-P
Bldg E3300
APG, MD 21010-5423
301/671-2721

Dr. Marwan C. Houalla
University of Pittsburgh
Department of Chemistry
P.O. Box 67
Parkerson Avenue
Pittsburgh, PA 15260
412/624-8302

Dr. Barton L. Houseman
Goucher College
Chemistry Department
Towson, MD 21204
301/337-6313

Mr. Joseph W. Hovanec
US Army CRDEC
ATTN: SMCCR-RSC-C
APG, MD 21010
301/671-2671

Mr. Gary B. Howe
Research Triangle Institute
P.O. Box 12194
Research Triangle Pk, NC 27709
919/541-8028

Mr. Thomas A. Hrastich
PM-ALSE
ATTN: SFAE-AV-LSE
4300 Goodfellow Blvd.
St. Louis, MO 63120-1798
314/263-3574

Dr. Alex J. Hsieh
US Army MTL
ATTN: SLCMT-EMP
Watertown, MA 02172
617/923-5348

Dr. Chen C. Hsu
US Army CRDEC
ATTN: SMCCR-PPC
APG, MD 21010-5423
301/671-5788

Dr. David S.Y. Hsu
Naval Research Laboratory
Code 6114
Washington, DC 20375-5000
202/767-2742

Dr. Fu-Lian Hsu
US Army CRDEC
ATTN: SMCCR-RSC-O
APG, MD 21010-5423
301/671-2131

Dr. Paul F. Hudrlik
Howard University
Department of Chemistry
Washington, DC 20059
202/806-7678

Mr. Joseph Huerta
US Army CRDEC
ATTN: SMCCR-RSP-A
APG, MD 21010
301/671-2158

Dr. Richard Hutte
Sievers Instruments, Inc.
1930 Central Avenue
Suite C
Boulder, CO 80301
303/444-2009

Dr. Rodney D. Ice
Eagle-Picher Industries
200 Ninth Avenue NE
Miami, OK 74354
918/542-1801

Mr. Brian S. Ince
US Army CRDEC
ATTN: SMCCR-RSC-P
Bldg E3330
APG, MD 21010-5423
301/671-1902

Mr. Louis Isaacson
Geo-Centers, Inc.
10903 Indian Head Highway
Ft. Washington, MD 20744
301/292-1010

Dr. Nancy Iwamoto
Naval Weapons Center
Code 3858
Chemistry Division
China Lake, CA 93555
619/939-1609

Mr. Edward M. Jakuboushi
MRICD
671-3607

CPT Bruce M. Jarnot
USAF Armstrong Laboratory
AL/OET
Wright Patterson AFB, OH 45433-6573
513/255-5150

Ms. Linda G. Jarvis
Geo-Centers, Inc.
Gunpowder Branch
P.O. Box 68
APG, MD 21010-0068
301/671-2560

Dr. N. Lynn Jarvis
Microsensor Systems, Inc.
6800 Versar Center
Suite 118
Springfield, VA 22151
703/642-6919

Dr. James O. Jensen
US Army CRDEC
ATTN: SMCCR-RSP-C
APG, MD 21010-5423
301/671-5665

Ms. Janet E. Jensen
US Army CRDEC
ATTN: SMCCR-DDT
APG, MD 21010
301/671-3518

Ms. Kim Jodaro
SMCCR-IN
671-4345

Dr. Carroll K. Johnson
Oak Ridge National Laboratory
MS 6197, Bldg 4500N
Chemistry Division
Oak Ridge, TN 37831
615/574-4975

Mr. Robert V. Jolliffe
US Army CRDEC
ATTN: SMCCR-RSP-P
APG, MD 21010
301/671-3756

Mr. Elijah G. Jones
PM for Rocky Mountain Arsenal
ATTN: AMXRM-LSA
Bldg 741
Rocky Mountain Arsenal
Commerce City, CO 80022-2180
303/289-0194

Ms. Paulette Jones
US Army CRDEC
ATTN: SMCCR-PPC
Bldg E3160
APG, MD 21010-5423
301/671-5771

Dr. Daniel D. Joseph
University of Minnesota
Dept of Aerospace Eng & Mechanics
110 Union St., SE
107 Akerman Hall
Minneapolis, MN 55455
612/625-0309

Louis Kanaras
US Army CRDEC
APG, MD 21010
301/671-5647

Dr. Mark S. Kaplan
Eastman Kodak Company
5/82A RL
Rochester, NY 14650-2156
716/722-1303

Mr. Chris J. Karwacki
US Army CRDEC
ATTN: SMCCR-PPC
APG, MD 21010
301/671-5704

Mr. Ronald J. Kassel
US Army CRDEC
ATTN: SMCCR-RSC-O
APG, MD 21010-5423
301/671-4224

Prof. S. A. Katz
Rutgers University
Department of Chemistry
3rd Street & Penn Walk
Camden, NJ 08102-6233
609/757-6142

Mr. Lionel Katzoff
CRDEC
APG, MD 21010
410/671-5569

Mr. Frank W. Kelly
GEOMET Technologies Inc.
8577 Atlas Drive
Gaithersburg, MD 20877
301/963-3993

Dr. James W. King
US Army CRDEC
ATTN: SMCCR-RSC-O
APG, MD 21010-5423
301/671-3482

Mr. Harold Klapper
US Army CRDEC
ATTN: SMCCR-RSC-P
APG, MD 21010
301/671-2265

Mr. Alec A. Klinghoffer
Geo-Centers, Inc.
Gunpowder Branch
P.O. Box 68
APG, MD 21010-0068
301/671-3311

Mr. Jerry J. Klug
Donaldson Company Inc.
P.O. Box 1299
Minneapolis, MN 55440
612/887-3531

Dr. Michael A. Koals
Rohm and Haas Company
Specialty Purifications
Independence Mall West
Philadelphia, PA 19105
215/592-2953

Dr. George B. Koelle
University of Pennsylvania
Dept of Pharmacology
Medical School
Philadelphia, PA 19104-6084
215/898-8418

Dr. Philip G. Koga
ETG, Inc.
1400 Taylor Avenue
P.O. Box 9840
Baltimore, MD 21204
301/321-5312

Mr. Jan E. Kolakowski
US Army CRDEC
ATTN: SMCCR-RSL-A
Bldg E3330, Rm 75
APG, MD 21010
201/671-2755

Ms. Karla Kopec-Smyth
Naval Research Laboratory
Code 6030
Bldg 35
Washington, DC 20375
202/767-0656

Dr. Morris Krauss
Nat Inst of Standards & Technology
Biotechnology Division
Bldg 221, Rm B256
Gaithersburg, MD 20899
301/975-2598

Dr. Thaiya Krishnamurthy
US Army CRDEC
ATTN: SMCCR-RSL
APG, MD 21010-5423
301/671-3957

Dr. P. N. Krishnan
US Army CRDEC
ATTN: SMCCR-RSP-C
APG, MD 21010
301/671-3158

Dr. Robert Kroutil
US Army CRDEC
ATTN: SMCCR-RSL
APG, MD 21010-5423
301/671-2437

Mr. A. J. Kubis
U.S. Army CRDEC
ATTN: SMCCR-RSL
APG, MD 21010-5423
410/671-5702

Dr. Thomas J. Kulle
US Army CRDEC
ATTN: SMCCR-PPI
APG, MD 21010-5423
301/671-2519

Ms. Deborah L. Kunkel
University of MD Baltimore County
Dept of Chemistry & Biochemistry
Baltimore, MD 21228
301/455-2491

Dr. Jamshed N. Lam
University of Florida
Department of Chemistry
403 Leigh Hall
Gainesville, FL 32611-2046
904/392-0554

Mr. Robert A. Lamontagne
Naval Research Laboratory
Code 6182
4555 Overlook Avenue SE
Washington, DC 20375-5000
202/767-2312

Dr. Doron Lancet
Weizmann Institute of Science
Dept of Membrane Rsch & Biophysics
Rehovot, 76100
ISRAEL

SPC Harbor Lavon
SMCCR-RSB
301/671-2586

Mr. Charles M. Lawson
US Army CRDEC
ATTN: SMCCR-PPC
APG, MD 21010-5423
301/671-5690

Gen Andre LeBlanc
Etablissement Technique Central
de l'Armement
Centre d'Etudes du Bouchet
B.P. No. 3
91710 Vert le Petit,
FRANCE
33169908215

Prof. M. Douglas LeVan
University of Virginia
Dept of Chemical Engineering
Thornton Hall
Charlottesville, VA 22903-2442
804/924-6279

Dr. Joseph Leonard
Stardent Computer Inc.
6 New England Technical Center
521 Virginia Road
Concord, MA 01742

Dr. George R. Lester
Allied-Signal Inc.
50 E. Algonquin Road
P.O. Box 5016
Des Plaines, IL 60017-5016
708/391-3314

Mr. Bruce Lewbart
US Army CRDEC
ATTN: SMCCR-SPS-E
APG, MD 21010-5423
301/671-3022

Mr. David Leyz
USAMRICD
SGRD-UV-PB
APB, MD 21010
410/671-3525

Prof. Joel F. Liebman
University of MD Baltimore County
Dept of Chemistry & Biochemistry
Baltimore, MD 21228
301/455-2549

Mr. J. Michael Lochner
US Army CRDEC
ATTN: SMCCR-RSL
APG, MD 21010-5423
301/671-2730

Dr. S. Randolph Long
US Army CRDEC
ATTN: SMCCR-RSL
APG, MD 21010
301/671-2437

Dr. Frederick R. Longo
US Army CRDEC
ATTN: SMCCR-RSC-C
APG, MD 21010-5423
301/671-3719

Dr. Alfred H. Lowrey
Naval Research Lab
Lab for the Structure of Matter
Code 6030
Washington, DC 20375
202/767-6383

Prof. Ponzy Lu
University of Pennsylvania
Department of Chemistry
Philadelphia, PA 19104-6323
215/898-4863

Prof. David M. Lubman
University of Michigan
Dept of Chemistry
930 North University Avenue
Ann Arbor, MI 48109-1055
313/764-1669

Dr. Leonard J. Luskus
USAF AL/CFTO
Brooks AFB
San Antonio, TX 78235-5000
512/536-3126

Mr. John J. Mahle
US Army CRDEC
ATTN: SMCCR-RSC-A
APG, MD 21010
301/671-3753

Ms. Georgia Maitland
ICD
410/671-5103

Mr. Charles K. Mann
Florida State University
Department of Chemistry
Tallahassee, FL 32306-3006

Dr. Stephen G. Maroldo
Rohm and Haas Co.
727 Norristown Road
Bldg 10
Springhouse, PA 19477
215/641-7318

Dr. Philip G. Marsh
Teledyne CME
P.O. Box 7244
Mountain View, CA 94039-7244
408/962-6917

Mr. John J. Martin
US Army CRDEC
ATTN: SMCCR-RSL-M
APG, MD 21010-5423
301/671-2663

Dr. Kazu Matsumoto
Ohio State University
College of Pharmacy
500 West 12th Avenue
Columbus, OH 43210
614/292-1224

Mr. Richard A. Matuszko
Geo-Centers, Inc.
10903 Indian Head Highway
Ft. Washington, MD 20744
202/767-2332

Dr. Barry W. Maule
Ministry of Defence
PD/LWS, Rm 2127
St. Christopher House
Southwark Street
London, SE1 0TD
UNITED KINGDOM
719211788

COL Edward W. Mayer
United States Military Academy
Department of Chemistry
West Point, NY 10996
914/938-3908

Mr. Thomas H. Mayness
5109 Leesburg
Suite 414
Falls Church, VA 22041
703/671-0400

Prof. Richard E. McCarty
The Johns Hopkins University
Department of Biology
Baltimore, MD 21218
301/516-7330

Mr. Skye McClain
University of Connecticut
Dept of Chemistry
Box U60
215 Glenbrook Road
Storrs, CT 06268
203/486-4719

Dr. Michael J. McCreery
USAMRICD
ATTN: SGRD-UV-DA
APG, MD 21010-5425
301/671-2851

Dr. James J. McGrath
Texas Tech University
Health Sciences Center
School of Medicine
Department of Physiology
Lubbock, TX 79430
806/743-2520

Mr. Vincent M. McHugh
US Army CRDEC
ATTN: SMCCR-RSC-P
Bldg E3300, Rm 224
APG, MD 21010-5423
301/671-2721

Mr. Gene McIlvaine
Brunswick Corporation
Defense Division
Deland, FL 32724
904/736-1700

Dr. Samuel P. McManus
University of Alabama in Huntsville
MSB C-206
School of Graduate Studies
Huntsville, AL 35899
205/895-6002

Mr. D. P. (Bob) McQuire
Brunswick Corporation
Defense Division
Deland, FL 32724
904/736-1700

Ms. Caryn F. Mee
USA MTL
ATTN: SLCMT-EMP
Watertown, MA 02172
617/923-5288

Mr. Darrel E. Menking
US Army CRDEC
ATTN: SMCCR-RSB
APG, MD 21010-5423
301/671-3398

Mrs. Deborah G. Menking
US Army CRDEC
ATTN: SMCCR-DDT
APG, MD 21010-5423
301/671-5575

Dr. Millard M. Mershon
USAMRICD
ATTN: SGRD-UV-DA
Bldg E3100
APG, MD +1010-5425
301/671-2851

Dr. Henk L.C. Meuzelaar
University of Utah
Center for Micro Analysis and
Reaction Chemistry
214 EMRL, Bldg 61
Salt Lake City, UT 84112
801/581-8431

Dr. Elias K. Michaelis
University of Kansas
Dept of Pharmacology & Toxicology
Lawrence, KS 66045

Prof. Robert G. Michel
University of Connecticut
Department of Chemistry
215 Glenbrook Road
Storrs, CT 06269-3060
203/486-3143

Mr. Alexander P. Mickiewicz
US Army CRDEC
ATTN: SMCCR-RSP-C
APG, MD 21010-5423
301/671-3688

Dr. Duane D. Miller
Ohio State University
College of Pharmacy
Div. of Medicinal Chem & Pharmacol
500 West 12th Avenue
Columbus, OH 43210
614/292-9206

Mr. Miles C. Miller
US Army CRDEC
ATTN: SMCCR-RSP-A
APG, MD 21010-5423
301/671-4048

Dr. Robert J. Mioduszewski
US Army CRDEC
ATTN: SMCCR-RST-C
APG, MD 21010
301/671-4101

Ms. Patricia R. Miskelly
PM for Chemical Demilitarization
ATTN: SAIL-PMM-M
Bldg E-4517
APG, MD 21010-5401
301/671-4213

Dr. Andrzej W. Miziolek
US Army Ballistic Research Lab
ATTN: SLCBR-IB-I
APG, MD 21005-5066
301/278-6157

LTC David H. Moore, PhD
USAMRDC
ATTN: SGRD-PLE
Fort Detrick
Frederick, MD 21701-5012
301/663-2161

Mr. Ted Moran
USAMRICD
ATTN: SGRD-UV-YY
APG, MD 21010-5425
301/671-2803

Dr. Robert E. Morris
Coppin State College
Department of Natural Sciences
2500 W. North Avenue
Baltimore, MD 21216
301/333-7832

Mr. Robert W. Morrison
US Army CRDEC
ATTN: SMCCR-PPC
APG, MD 21010-5423
301/671-5689

Dr. Shekar Munavalli
Geo-Centers, Inc.
Gunpowder Branch
P.O. Box 68
APG, MD 21010-0068
301/671-2819

Dr. James S. Murday
Naval Research Laboratory
Code 6100
Washington, DC 20375-5000
202/767-3026

Dr. Masato Nakashima
US Army Natick RD&E Center
ATTN: PEB, FPSD, SSD
Natick, MA 01760-5020
508/651-5515

Prof. Wilfred H. Nelson
University of Rhode Island
Department of Chemistry
Pastore Hall
Rm 201A
Kingston, RI 02881
401/792-2498

Dr. A. S. Nogueroles
Colorado School of Mines
Chemistry & Geochemistry Dept
Golden, CO 80401
303/273-3610

Dr. Patrick Nolan
US Army CRDEC
SMCCR-MU
APG, MD 21010-5423
410/671-3313

Mr. Thaddeus J. Novak
US Army CRDEC
ATTN: SMCCR-RSC-C
APG, MD 21010-5423
301/671-2369

Mr. Michael J. Nusca
US Army BRL
ATTN: SLCBR-LF-A
APG, MD 21005
301/278-2057

Mr. Richard J. O'Connor
US Army CRDEC
ATTN: SMCCR-RSC-P
APG, MD 21010-5423
301/671-3863

Dr. Raymond T. O'Donnell
SUNY Oswego
Chemistry Department
Oswego, NY 13126
315/341-3048

Ms. Kate K. Ong
US Army CRDEC
ATTN: SMCCR-DDT
APG, MD 21010-5423
301/671-5566

Dr. John C. Owicki
Molecular Devices Corp.
Menlo Oaks Corporate Center
4700 Bohannon Drive
Menlo Park, CA 94025
415/322-4700

Mr. Cataldo A. Palladino
MSA Research
P.O. Box 429
Pittsburgh, PA 15230
412/967-4152

Dr. Donna Palmer
Battelle
505 King Avenue
Columbus, OH 43201-2693
614/424-5369

Mrs. Dorothea Paterno
US Army CRDEC
ATTN: SMCCR-RSP-P
APG, MD 21010
301/671-4466

Mr. Elwin C. Penski
US Army CRDEC
ATTN: SMCCR-RSC-P
APG, MD 21010-5423
301/671-3953

Dr. William A. Petri, Jr.
Univ Virginia School of Medicine
Department of Medicine
MR4 Bldg, Rm 2115
Charlottesville, VA 22908
804/924-5621

Mrs. Tina M. Phaneuf
Navy Clothing and Textile
Research Facility
P.O. Box 59
Natick, MA 01760-0001
508/651-4785

Mr. Carl Phillips
US Army CRDEC
SMCCR-RST-E
APG, MD 21010
410/671-4694

Mr. Michael R. Phillips
Brunswick Corporation
Defense Division
Deland, FL 32724
904/736-1700

Mr. Joseph V. Pistritto
US Army CRDEC
ATTN: SMCCR-RSC-C
APG, MD 21010-5423
301/671-3614

Mr. Stephen G. Pleva
US Army CRDEC
SMCCR-RSL-M
APG, MD 21010-5423
301/671-2255

Dr. Peter Politzer
University of New Orleans
Dept of Chemistry
Lakefront Campus
New Orleans, LA 70148
504/286-6850

Dr. Edward J. Poziomek
Univ of Nevada - Las Vegas
Environmental Research Center
4505 South Maryland Pkwy.
Las Vegas, NV 89154-4009
702/739-3382

Dr. Christopher L. Prince
Phyton Catalytic
175 Langmuir Laboratory
95 Brown Road
Ithaca, NY 14850-1257

Mr. Robert Przeslawski
Drexel University
215/784-0637

Dr. J. G. Purdon
Defense Research Est. Suffield
Protection Science
Box 4000
Medicine Hat
Alberta, T1A 8K6
CANADA
403/544-4106

Dr. Louis D. Quin
University of Massachusetts
Dept of Chemistry
Lederle Graduate Research Tower A
Amherst, MA 01003
413/545-2318

Dr. Krishna S. Rajan
IIT Research Institute
Chemistry Department
10 West 35th Street
Chicago, IL 60616
312/567-4262

Dr. Chitoor K. Ramachandran
US Army Dugway Proving Ground
ATTN: STEDP-JOD
Dugway, UT 84022-5000
801/831-3371

Mr. Michael D. Rausa
HQ LABCOM
ATTN: AMCLD-O
2800 Powder Mill Road
Adelphi, MD 20783-1145
202/394-3860

Dr. Radharaman Ray
USAMRICD
SGRD-UV-PB
Bldg E3100
APG, MD 21010-5425
301/671-3074

Mr. Louis P. Reiff
US Army CRDEC
SMCCR-RSC-O
APG, MD 21010-5423
301/671-2495

Dr. Dennis J. Reutter
US Army CRDEC
SMCCR-RS
APG, MD 21010-5423
410/671-2840

Dr. Sharon Reutter
US Army CRDEC
ATTN: SMCCR-RST-C
APG, MD 21010-5423
301/671-2686

Mr. James M. Reynolds
Lehigh University
Seeley G. Mudd Bldg #6
Bethlehem, PA 18015
215/758-5980

Mr. Dennis Riffin
DNA/RAAE
703/325-1631

Ms. Patti J. Riggs
EAI
Suite J
Continental Drive
Abingdon, MD
410/676-1449

Dr. Donald Rivin
US Army Natick RD&E Center
Natick, MA 01760-5019
508/651-4392

Mr. Ron Robbins
US Army CRDEC
SMCCR-DDT
APG, MD 21010-5423

Dr. Donald H. Robertson
US Army Natick RD&E Center
ATTN: SSD
Kansas Street
Natick, MA 01760-5020
508/651-5201

Dr. Augusto Rodriguez
Clark Atlanta University
J.P. Brawley at Fair Street
Atlanta, GA 30314
404/880-8750

Dr. Joseph E. Roehl
Environmental Technologies Group
1400 Taylor Avenue
P.O. Box 9840
Baltimore, MD 21284-9840
301/321-5304

Mr. Dennis K. Rohrbaugh
US Army CRDEC
ATTN: SMCCR-RSC-P
APG, MD 21010-5423
301/671-2366

Mr. David I. Rossman
US Army CRDEC
ATTN: SMCCR-RSC-O
APG, MD 21010-5423
301/671-2819

Mr. Thomas E. Rosso
CRDEC
APG, MD 21010
410/671-3812

Mr. Leonard C. Rowe
PM for Chem Demil
ATTN: SAIL-PMT-E
Bldg E4585
APG, MD 21010-5401
301/671-1456

Dr. Glenn O. Rubel
US Army CRDEC
ATTN: SMCCR-RSP-B
APG, MD 21010-5432
301/671-2395

Mr. Joseph M. Ruder
AiResearch-Los Angeles Division
Allied-Signal Aerospace Co.
Dept 93-129, M/S T-41
2525 W. 190th Street
Torrance, CA 90509
213/512-4379

Mr. James F. Rusling
University of Connecticut
Department of Chemistry
Box U-60
215 Glenbrook Road
Storres, CT 06269-3060
203/486-4909

Dr. Alan Russell
University of Pittsburgh
Chemical & Petroleum Eng Dept
1235 Benedum Hall
Pittsburgh, PA 15216

Mr. Gary M. Russo
Eastman Kodak Company
5/82A RL
Rochester, NY 14650-2156
716/477-6433

Ms. Maria C. Sadusky
Geo-Centers, Inc.
Gunpowder Branch
P.O. Box 68
APG, MD 21010-0068
301/671-4847

Prof. Mahmoud A. Saleh
Texas Southern University
Department of Chemistry
3100 Cleburne
Houston, TX 77004
713/639-1912

Dr. Harry Salem
US Army CRDEC
ATTN: SMCCR-RST
APG, MD 21010-5423
301/671-3034

Mr. John B. Samuel
US Army CRDEC
Attn: SMCCR-RSC-P
APG, MD 21010-5423
301/671-2366

Ms. Janis W. Schlager
USAMRICD
SGRD-UV-VA
APG, MD 21010
301/671-2591

Mr. John J. Schlager
USAMRICD
SGRD-UV-PA
APG, MD 21010
301/671-3836

Dr. Richard Schreck
GM Research Labs
Biomedical Science Department
Technical Center
Warren, MI 48090-9055
313/986-1742

Mrs. Janis K.D. Seegar
US Army CRDEC
ATTN: SMCCR-EM
APG, MD 21010-5423
301/671-4912

Dr. Donald P. Segers
Southern Research Institute
2000 Ninth Avenue South
P.O. Box 55305
Birmingham, AL 35255-5305
205/581-2664

Dr. Reginald P. Seiders
USARDSG-UK
P.O. Box 65
FPO, NY 09510
44714094485

MAJ Robert M. Serino
US Army CRDEC
ATTN: SMCTE-XO
APG, MD 21010-5423
301/671-3044

Dr. Vasgen A. Shamamian
Naval Research Laboratory
Code 6110, Bldg 207
4555 Overlook Avenue SW
Washington, DC 20375-5000
202/767-2674

Dr. M. Shih
USAMRICD
ATTN: SGRD-UV-VA
Bldg E3100
APG, MD 21010-5425
301/671-2591

Mr. Donald B. Shoff, Jr.
US Army CRDEC
ATTN: SMCCR-RSL
APG, MD 21010-5423
301/671-3194

Mr. Wendel J. Shuely
US Army CRDEC
ATTN: SMCCR-RSC-P
Bldg E3300
APG, MD 21010-5423
301/671-4125

Mr. William Shulman
US Army CRDEC
ATTN: SMCCR-SPS-E
APG, MD 21010-5423
301/671-2380

Dr. Gary D. Sides
CMS Research Corporation
200 Chase Park South
Suite 100
Birmingham, AL 35244
205/733-6900

Dr. Robert E. Sievers
Cooperative Institute for Research
in Environmental Sciences
University of Colorado
Campus Box 216
Boulder, CO 80309-0216
303/492-7943

Mr. Melvin Silverman
ALL-BAN ENT
315 Tartan Green Court
Joppa, MD 21085
301/679-4476

Mr. Achille Silvestri
US Army CRDEC
Berger Laboratory
APG, MD 21010
301/671-5563

Mr. Laurence E. Slivon
Battelle
505 King Avenue
Columbus, OH 43201
614/424-4274

Mr. J. Richard Smith
USAMRICD
Analytical Chemistry Branch
Bldg E3100, Rm 33
APG, MD 21010-5425
301/671-2591

Dr. Philip B. Smith
Geo-Centers, Inc.
Gunpowder Branch
P.O. Box 68
APG, MD 21010-0068
301/671-2560

Dr. William J. Smith
USAMRICD
ATTN: SGRD-UV-PB
APG, MD 21010-5425
301/671-2847

Dr. A. Peter Snyder
US Army CRDEC
ATTN: SMCCR-RSL
APG, MD 21010-5423
301/671-2416

Mr. Douglas R. Sommerville
US Army CRDEC
ATTN: SMCCR-RSP-P
Bldg E3160
APG, MD 21010-5423
301/671-4348

Dr. Ralph B. Spafford
Southern Research Institute
Physical Chemistry Division
P.O. Box 55305
2000 Ninth Avenue South
Birmingham, AL 35225-5305
205/581-2219

Dr. Glenn E. Spangler
Environmental Tech Group, Inc.
1400 Taylor Avenue
Baltimore, MD 21284-9840
301/321-5261

Mr. David W. Squire
System Planning Corporation
1500 Wilson Boulevard
Arlington, VA 22209-2454
703/351-8780

Mr. Ralph J. Steger
US Army CRDEC
ATTN: SMCCR-DDT
Bldg E3549
APG, MD 21010-5423
301/671-5567

Dr. Joseph R. Stetter
Transducer Research, Inc.
999 Chicago Avenue
Naperville, IL 60540
708/357-0004

Mr. Gary A. Stickle
US Army CRDEC
ATTN: SMCCR-PPC
APG, MD 21010-5423
301/671-5778

Mr. Peter J. Stopa
US Army CRDEC
ATTN: SMCCR-DDT
APG, MD 21010-5423
301/671-5578

Adam N. Stroup
CRDEC
SMCCR-RSB
APG, MD 21010
410/671-3792

Mr. Edward W. Stuebing
US Army CRDEC
ATTN: SMCCR-RSP-B
APG, MD 21010-5423
301/671-3089

Mr. Arthur K. Stuempfle
US Army CRDEC
ATTN: SMCCR-RSP
APG, MD 21010-5423
301/671-2651

Mr. Larry M. Sturdivan
US Army CRDEC
ATTN: SMCCR-RSP-C
APG, MD 21010-5423
301/671-4144

Mr. Steven L. Suib
University of Connecticut
U-60
Department of Chemistry
Storrs, CT 06269-3060
203/486-2797

Mr. Kenneth Sumpter
CRDEC
SMCCR-RSL-A
APG, MD 21010
410/671-2984

Mr. Edward M. Sybert
University of Maryland
Engineering Research Center
Wind Tunnel Building
College Park, MD 20742
301/405-3908

Mr. Leonard J. Szafraniec
US Army CRDEC
Attn: SMCCR-RSC-O
APG, MD 21010
301/671-4126

Mrs. Linda L. Szafraniec
US Army CRDEC
ATTN: SMCCR-RSC-P
APG, MD 21010-5423
301/671-3863

Dr. William C. Tacon
Battelle
505 King Avenue
Columbus, OH 43201-2693
614/424-4483

Dr. David E. Tevault
US Army CRDEC
ATTN: SMCCR-RSC-A
APG, MD 21010-5423
301/671-3753

Dr. C. Thiriot
l'Establissement Technique Central
de l'Armement
Centre d'Etudes du Bouchet
B.P. No. 3 - Le Bouchet
91710 Vert Le Petit,
FRANCE
33169908257

Mr. Joseph H. Thompson
US Army CRDEC
ATTN: SMCCR-PPD
APG, MD 21010

Dr. Sandra Thomson
US Army CRDEC
ATTN: SMCCR-RST-I
APG, MD 21010-5423
301/671-4821

Dr. Nolan T. Tillman
Eastman Kodak
Federal Systems Division
Bldg 82A/Mail Code 02156
Research Labs
Rochester, NY 14650-2156
716/477-5037

Mr. Robert Tom
AiResearch-Los Angeles Division
Allied-Signal Aerospace Co.
Dept 93-129, M/S T-41
2525 West 190th Street
Torrance, CA 90509
213/512-4385

Prof. Paul J. Toscano
SUNY - Albany
Department of Chemistry
Albany, NY 12222
518/442-3127

LT John A. Totzke
NTIC 1313
1430 Wright Street
Madison, WI 53704-4192
414/734-0320

Dr. Shirley R. Tove
U.S. Army Research Office
ATTN: SLCRO-DB
P.O. Box 12211
Research Triangle Pk, NC 27709-2211
919/549-4344

Dr. Gerard Trouiller
l'Establissement Technique Central
de l'Armement
Centre d'Etudes du Bouchet
B.P. No. 3 - Le Bouchet
91710 Vert Le Petit,
FRANCE
33169908262

Prof. Chun-che Tsai
Kent State University
Department of Chemistry
214 Williams Hall
Kent, OH 44242-0001
216/672-2989

Mr. Abe Turetsky
US Army CRDEC
ATTN: SMCCR-RSC-C
APG, MD 21010-5423
301/671-2357

Dr. Charles A. Tyson
SRI International
Toxicology Laboratory
333 Ravenswood Avenue
Menlo Park, CA 94025
415/859-4711

Mr. Raymond P. Tytus
US Army CRDEC
ATTN: SMCCR-RSP-P
APG, MD 21010-5423
301/671-3594

Dr. Joseph Urban
University of Delaware
Department of Chemistry
Newark, DE 19711

Dr. James J. Valdes
US Army CRDEC
ATTN: SMCCR-RSB
APG, MD 21010-5423
301/671-3564

Mr. Jacques J.G.M. van Bokhoven
TNO Prins Maurits Laboratory
P.O. Box 45
2280 AA
Ryswyk, - 2280 AA
NETHERLANDS
3115843500

Dr. David L. Venezky
Naval Research Laboratory
Code 6170
Surface Chemistry Branch
Washington, DC 20375-5000
202/767-3550

Mr. Joseph J. Vervier
US Army CRDEC
ATTN: SMCCR-RS
APG, MD 21010-5423
301/671-3250

Dr. Kent J. Voorhees
Colorado School of Mines
Dept of Chemistry
Golden, CO 80401
303/273-3616

Dr. George W. Wagner
US Army CRDEC
ATTN: SMCCR-RSC-P
APG, MD 21010-5423
301/671-3863

Mr. Tommy L. Waldrup
Tech Ops Div/DLRC
Bldg 1080, Rm 149
McClellan AFB, CA 95652
916/643-5313

Ms. Helen M. Walker
US Army CRDEC
ATTN: SMCCR-RSC-P
APG, MD 21010
301/671-2531

Mr. John E. Walker
US Army Natick RD&E Center
ATTN: STRNC-YSP
Soldier Science Directorate
Kansas Street
Natick, MA 01760-5020
508/651-4374

Ms. Charlotte C. Wang
U.S. Army CRDEC
ATTN: SMCCR-RSC-A
APG, MD 21010-5423
301/671-4822

Dr. J. Richard Ward
US Army CRDEC
ATTN: SMCCR-RSC
APG, MD 21010
301/671-2719

Mr. Daniel J. Weber
US Army CRDEC
ATTN: SMCCR-RSP-A
APG, MD 21010-5423
301/671-2158

Dr. William A. Weigand
University of Maryland
Dept of Chemical Engineering
Chem & Nuclear Engineering Bldg
College Park, MD 20742
301/405-1916

Mr. John F. Weimaster
US Army CRDEC
ATTN: SMCCR-RSC-O
APG, MD 21010-5423
301/671-4148

Dr. Stephen T. Wellinghoff
Southwest Research Institute
Chemistry & Chemical Eng Division
6220 Culebra Road
San Antonio, TX 78238
512/522-3084

Dr. Randy Wentsel
US Army CRDEC
ATTN: SMCCR-RST-E
APG, MD 21010
301/671-2036

Mr. Thomas E. Wenzel
David Taylor Research Center
Code 2833
Annapolis Laboratory
Annapolis, MD 21402-5067
301/267-2461

Dr. Christopher E. Whalley
US Army CRDEC
ATTN: SMCCR-RST-E
APG, MD 21010-5423
301/671-4716

Dr. William E. White
US Army CRDEC
ATTN: SMCCR-RSP-P
APG, MD 21010
301/671-3058

Dr. James R. Wild
Texas A&M University System
Dept of Biochemistry & Biophysics
College Station, TX 77843-2128
409/845-9459

Dr. Anthony F. Wilde
US Army Materials Tech Lab
ATTN: SLCMT-EMP
Polymer Research Branch
Watertown, MA 02172
617/923-5147

Mr. Joseph D. Williams
US Army CRDEC
ATTN: SMCCR-RS
APG, MD 21010-5423
301/671-2849

Mr. Richard Wittstruck
USAETDL
LABCOM
908/544-3319

Dr. Ngai Wong
US Army CRDEC
Attn: SMCCR-RSC-C
APG, MD 21010-5423
301/671-2369

Dr. Gerry Wood
Los Alamos National Laboratory
MS K-486
Los Alamos, NM 87545
505/667-9824

Dr. Sheila Wood
US Army CRDEC
ATTN: SMCCR-RSB
APG, MD 21010
301/671-2247

Dr. Jeffrey R. Wyatt
Naval Research Lab
Code 6110
Washington, DC 20375
202/767-3244

Dr. Yu-Chu Yang
US Army CRDEC
ATTN: SMCCR-PPD
APG, MD 21010-5423
301/671-5917

Dr. Chester V. Zabielski
Materials Technology Laboratory
ATTN: SLCMT-EMM
Watertown, MA 02172-0001
617/923-5332

Prof. Daniel Zeroka
Lehigh University
Department of Chemistry
S.C. Mudd Bldg #6
Bethlehem, PA 18015-3172
215/758-3479

Mr. Alan W. Zulich
US Army CRDEC
ATTN: SMCCR-DDT
APG, MD 21010-5423
301/671-5573

BLANK

**APPENDIX B
AGENDA**

**1991 U.S. Army Chemical Research, Development and Engineering Center
SCIENTIFIC CONFERENCE ON CHEMICAL DEFENSE RESEARCH**

19-22 November 1991

**Edgewood Area Conference Center
Aberdeen Proving Ground, Maryland**

Tuesday, 19 November 1991

- 0800 REGISTRATION
Post Conference Center (Seminar Building)
- 0900 OPENING SESSION
Welcome and Opening Remarks
- 0915 KEYNOTE ADDRESS
"Operation Desert Storm from a Soldier-Scientist Point of View"
Captain Christopher J. Cramer, U.S. Army Chemical Research, Development
and Engineering Center
- 0945 Presentation of Army Research and Development Achievement Awards
Congratulatory Remarks
- 1015 BREAK
- 1030 Overviews by Award Recipients
- 1100 Future Directions in the Chemical and Biological Basic Research Program
Joseph J. Vervier, U.S. Army Chemical Research, Development and Engineering Center
- 1115 Administrative Announcements
Lisa H. McCormick, Science and Technology Corporation
- 1130 LUNCH

Tuesday, 19 November 1991

SESSION 1 - PROTECTION

Moderator: *Joseph W. Hovanec*, U.S. Army Chemical Research, Development and Engineering Center

Conference Center

- 1310 Development of Air Purification Systems (1)
D.E. Tevault, J.J. Mahle and L.C. Buettner, U.S. Army Chemical Research, Development and Engineering Center; *D.K. Friday*, Geo-Centers, Inc.
- 1330 Adsorption Equilibria for Simulant Vapors on 13X Molecular Sieve (2)
A.B. Brady and D.K. Friday, Geo-Centers, Inc.; *D.L. Carlile and L.C. Buettner*, U.S. Army Chemical Research, Development and Engineering Center
- 1350 Single Component Isotherm Measurement with the Cahn Microbalance (3)
C.C. Wang, L.C. Buettner and D.L. Carlile, U.S. Army Chemical Research, Development and Engineering Center; *D.K. Friday*, Geo-Centers, Inc.
- 1410 Multicomponent Adsorption Equilibria for Vapors of Hydrocarbons and Water on Activated Carbons (4)
M.D. LeVan, University of Virginia
- 1430 Prediction of Binary Vapor Adsorption for a Hexane/Water Mixture on Activated Carbon (5)
R.A. Matuszko and D.K. Friday, Geo-Centers, Inc.; *R.A. Lamontagne*, Naval Research Laboratory
- 1450 BREAK
- 1510 Characterization of the Armored Vehicle Environment (6)
J. Matuszko and R. Lamontagne, Naval Research Laboratory; *R. Matuszko and V. Davis*, Geo-Centers, Inc.
- 1530 Experimental Studies in Pressure Swing Adsorption (7)
L.C. Buettner and J.J. Mahle, U.S. Army Chemical Research, Development and Engineering Center; *D.K. Friday and A.B. Brady*, Geo-Centers, Inc.
- 1550 Pressure Swing Adsorption (PSA) Performance Prediction Model (8)
N. Sundaram and D.K. Friday, Geo-Centers, Inc.; *J.J. Mahle*, U.S. Army Chemical Research, Development and Engineering Center
- 1610 Pressure Drop and Cyanogen Chloride Breakthrough Time for Beds of ASC Carbon with Nonuniform Cross-Sectional Area (9)
R.A. Newton, R.W. Morrison and R.C. Grue, U.S. Army Chemical Research, Development and Engineering Center
- 1630 Use of X-Ray Photoelectron Spectroscopy to Characterize Reactions on Activated Carbons (10)
M.M. Farris and J. Rassin, Geo-Centers, Inc.
- 1650 Adsorption Properties of Superactivated Carbons (11)
D. Rivin and C. Kendrick, U.S. Army Natick Research, Development and Engineering Center

Tuesday, 19 November 1991

SESSION 1A - SYNTHESIS & PROPERTIES (CONCURRENT)

Moderator: *Harold D. Banks*, U.S. Army Chemical Research, Development and Engineering Center

Chapel Annex

- 1330 The Cycloaddition Reactions of Sulfonated Dienes with Enamines, Ynamines, Amidines and Thioformamides - New Routes Towards Heterocycles (24)
A. Padwa, Y. Garreau, B. Harrison and B.H. Norman, Emory University; *A. Rodriguez*, Clark Atlanta University
- 1350 Synthesis, Isolation, Characterization and σ_2 -Adrenergic Activity of the Optical Isomers of 4-[1-(1-Naphthalenyl)Ethyl]-1*H*-Imidazole (25)
S.S. Hong, D.D. Miller, K. Matsumoto, K.L. Romstedt and D.R. Feller, The Ohio State University; *F.-L. Hsu*, U.S. Army Chemical Research, Development and Engineering Center; *C. George*, Naval Research Laboratory
- 1410 σ_2 -Adrenergic Activity of a New Series of Analogs of 4-[1-(1-Naphthalenyl)Ethyl]-1*H*-Imidazole (26)
K. Matsumoto, S.S. Hong, K.L. Romstedt, D.R. Feller and D.D. Miller, The Ohio State University; *F.-L. Hsu*, U.S. Army Chemical Research, Development and Engineering Center
- 1430 Novel Reactions of the S-S and C-S Bonds (27)
S. Munavalli, Geo-Centers, Inc.; *D.I. Rossman, D.K. Rohrbaugh and C.P. Ferguson*, U.S. Army Chemical Research, Development and Engineering Center
- 1450 Unusual Reactions of the Di- and Trisulfides with Grignard Reagents (28)
S. Munavalli, Geo-Centers, Inc.; *D. I. Rossman, D.K. Rohrbaugh and C.P. Ferguson*, U.S. Army Chemical Research, Development and Engineering Center
- 1510 BREAK
- 1530 Phosphorylation of OH Groups on Various Solids by Low-Coordination Phosphorus Species (29)
L.D. Quin, X.-P. Wu and S. Jankowski, University of Massachusetts
- 1550 Chemical Properties Update - Theory, Statistics, and Experimental Methods (30)
E.C. Penski, U.S. Army Chemical Research, Development and Engineering Center
- 1610 Subambient Applications of Differential Thermal Analysis for Determination of Vapor Pressure (31)
A. Brozana and D. Fielder, U.S. Army Chemical Research, Development and Engineering Center
- 1630 Chemoselective Transformations of Functionalized Piperidines (39)
H.D. Banks, U.S. Army Chemical Research, Development and Engineering Center
- 1650 Preassociating σ -Nucleophiles (38)
A.W. Czarnik, The Ohio State University

Wednesday, 20 November 1991

SESSION 2 - DETECTION

Moderator: *S. Randolph Long*, U.S. Army Chemical Research, Development and Engineering Center

Conference Center

- 0800 The Use of Ammonia as a Reagent in an Ion Mobility Spectrometer (40)
D.B. Shoff, U.S. Army Chemical Research, Development and Engineering Center
- 0820 Detection of Agents Using the Sulfur Chemiluminescence Detector (41)
S. Hutte and J.D. Ray, Sievers Instruments, Inc.; *R.E. Sievers*, University of Colorado
- 0840 Current Status of a Fraunhofer Line Discriminator (FLD) for the Characterization of Chemical Simulant Clouds (42)
D. Bodrero and R. Watson, U.S. Army Dugway Proving Ground
- 0900 Detection of Nonvolatiles Via Liquid Injection into Atmospheric Pressure DC and RF Glow Discharge Sources and Pulsed Time-of-Flight Mass Spectrometry (43)
D. Lubman, J. Zhao, S. Michael, M. Chien and C. Ma, The University of Michigan
- 0920 Detection Strategies for Treaty Verification: A Fieldable System for Sampling and Analysis of CW (44)
S.F. Hallowell, M.J. Heyl and D.J. Reutter, U.S. Army Chemical Research, Development and Engineering Center
- 0940 BREAK
- 1000 Color-Change-Based Detection of Bacterial Toxins (45)
D. J. Morr , Purdue University; R.D. Ice and J. Boone, Eagle-Picher Research Laboratories
- 1020 Characterization of an Unknown Polypeptide from *Naja Naja atra* (Chinese) (46)
T. Krishnamurthy, D. Hyashi, A.J. Kubis, J.G. Freedy and T.D. Biggs, U.S. Army Chemical Research, Development and Engineering Center
- 1040 Biodetection of Bacteria by Pyrolysis and Mass Spectrometry (47)
A. Fax, University of South Carolina
- 1100 Recognition of Chemical Markers for Biodetection in GC/MS Data: Feature Selection, Fingerprinting, and Discriminant Analysis (48)
S.L. Morgan and A. Fax, University of South Carolina
- 1120 UV Resonance Raman Rapid Detection and Identification of Single Bacterial Cells (49)
S. Chadha, W.H. Nelson and J.F. Sperry, University of Rhode Island

Wednesday, 20 November 1991

SESSION 2A - PROTECTION (CONCURRENT)

Moderator: *David Tevault*, U.S. Army Chemical Research, Development and Engineering Center

Chapel Annex

- 0800 Reaction Kinetics for the Oxidation of Hexafluoropropylene over a 3%Pt/Al₂O₃ Catalyst (12)
A.A. Klinghoffer and J.A. Rossin, Geo-Centers, Inc.
- 0820 Catalytic Oxidation of Hydrogen Cyanide Vapor (13)
G.B. Howe, J.J. Spivey and G.W. Stinagle, Research Triangle Institute
- 0840 Catalytic Oxidation of GD over a Monolithic Pt/TiO₂ Oxidation Catalyst (14)
R. Tom, Allied-Signal Aerospace Company; *G. Lester*, Allied-Signal Research and Technology
- 0900 Role of Tertiary Amines in Whetlerite Formulations (15)
V.R. Deitz, Geo-Centers, Inc.; *C.J. Karwacki and J.A. Rehrmann*, U.S. Army Chemical Research, Development and Engineering Center
- 0920 Aerosol Challenge Tests of Chemical Protective Ensembles (16)
J. Hanley, Research Triangle Institute
- 0940 Relationship Between Direct Skin Exposure to Methyl Salicylate (MeS) Vapor and Subsequent Vapor Carry-Through (17)
S.H. Bomalski and J. Kilian, U.S. Air Force Armstrong Laboratory
- 1000 BREAK

SESSION 2B - TOXICOLOGY (CONCURRENT)

Moderator: *Harry Salem*, U.S. Army Chemical Research, Development and Engineering Center

Chapel Annex

- 1020 Sedative, Hemodynamic and Ventilatory Effects of Four Different σ_2 -Andrenergic Agonists in Awake Chronically Instrumented Mini-Swine (66)
B.C. Bloor and C. Kim, University of California, Los Angeles
- 1040 Effects of Sufentanil and Nalmefene on Ferret Brainstem Responses: Dynamic Changes Do Not Mirror Plasma Levels (67)
S. Reutter and R. Mioduszewski, U.S. Army Chemical Research, Development and Engineering Center
- 1100 Evaluation of Chloropentafluorobenzene (CPF_B) as a CW Intake Training Simulant (68)
B.M. Jarnot, U.S. Air Force Armstrong Laboratory
- 1120 Effect of Altitude on Toxic Gas Uptake: CO Inhalation in Healthy Adult Volunteers (69)
J.J. McGrath, R.M. Schreck and P. Lee, Texas Tech University
- 1140 The Toxicology of Chromium (70)
S.A. Katz and H. Salem, U.S. Army Chemical Research, Development and Engineering Center

- 1200 Interspecies Differences in Response to Amphetamine, Acetaminophen, Trichloroethylene and Sodium Thiosulfate (71)
C.A. Tyson, C.E. Green, S. Knadle, S.J. Gee, J.A. Dabbs and S.E. LeValley, SRI International

Wednesday, 20 November 1991

1300-1700

SESSION 3 - POSTERS

Starke Recreation Center

Overviews of Other Department of Defense Chemical Defense Research Programs

Naval Research Laboratory/Office of Naval Research
Robert A. Lamontagne

U.S. Army Materials Technology Laboratory
Caryn F. Mee

U.S. Army Natick Research, Development and Engineering Center
Donald H. Robertson

BIOTECHNOLOGY POSTERS

A Monoclonal Antibody Against *Entamoeba Histolytica* Neutralizes Complement Resistance (92)
W. Petri, Jr. and L. Braga, University of Virginia; S. Wood-Helie, U.S. Army Chemical Research, Development and Engineering Center

Field Emission Scanning Electron Microscopy of the Interaction of *Clostridium Difficile* with Human Embryonic Intestinal Cells (93)
S. Wood-Helie and E. Petersen, U.S. Army Chemical Research, Development and Engineering Center

Detection of Threshold Numbers of *Escherichia Coli* and *Pseudomonas Aeruginosa* Using a Hand-Held Detection Device (94)
S. Wood-Helie and J.M. Veronick, U.S. Army Chemical Research, Development and Engineering Center

Determination of a Unique Epitope Binding Site for a Complement-Lysis-Enhancing Monoclonal Antibody, 3D12, on the Galactose Adherence Lectin on *Entamoeba Histolytica* Using BIAcore™ (95)
S. Wood-Helie, U.S. Army Chemical Research, Development and Engineering Center; W. Petri, Jr., University of Virginia

A High Resolution Tandem Mass Spectrometer (96)
T. Krishnamurthy, U.S. Army Chemical Research, Development and Engineering Center

Disulfide Bridges in a Cardiotoxin (97)
T. Krishnamurthy, K. Hyashi, J.G. Freedy, A.J. Kubis and T.D. Biggs, U.S. Army Chemical Research, Development and Engineering Center

Biopolymer Facility (98)
T. Krishnamurthy, U.S. Army Chemical Research, Development and Engineering Center

Characterization of Conotoxins (99)

T. Krishnamurthy, J.G. Freedy, A.J. Kubis, T.D. Biggs and J. Brzezinski, U.S. Army Chemical Research, Development and Engineering Center

The Use of Protease Inhibitors in the Purification of Squid Organophosphorous Acid Anhydrase (100)

K. Kopec-Smyth, D. Eswaran, J.R. Deschamps and K.B. Ward, Geo-Centers, Inc. and Naval Research Laboratory

Immunochemical and Nucleic Acid Screening of Bacteria for Organophosphate-Degrading Enzymes (101)

T.-C. Cheng, J.J. DeFrank, M.N. Miller, D.K. Vervier and H.S. Heitz, U.S. Army Chemical Research, Development and Engineering Center

An Anticholinesterase Biosensor System Based on Silicon Detector Potentiometry (102)

J.C. Fernando and M.E. Eldefrawi, University of Maryland School of Medicine; *K.R. Rogers and J.J. Valdes*, U.S. Army Chemical Research, Development and Engineering Center

Analysis of Proteins by On-Line HPLC Electrospray Mass Spectrometry (103)

P.B. Smith, Geo-Centers, Inc.; *A.P. Snyder*, U.S. Army Chemical Research, Development and Engineering Center

Immobilization of CW-Agent-Specific OPA-Anhydrase on Fabrics (104)

K.S. Rajan and S. Mainer, IIT Research Institute

Expression of Erabutoxin a Gene in *Escherichia Coli* Cultivated in Pilot Fermentor (105)

P. Silvestre, M.A. Labarre and P. Binder, Centre d'Etudes du Bouchet, France

Antibody-Based Fiber Optic Evanescent Wave Sensor (106)

D.E. Menkin, J. Heitz, R.G. Thompson, U.S. Army Chemical Research, Development and Engineering Center; *D.G. Menking*, Science and Technology Corporation; *M.E. Eldefrawi*, University of Maryland School of Medicine

Retroviral Expression of Detoxifying Enzymes in Mammalian Cells (107)

M. Boidot-Forget, Centre d'Etudes du Bouchet, France

DFP'ASE Synthesis by Diverse Microbes in Fermentor Batch Culture (108)

B.J. Gallo, U.S. Army Natick Research, Development and Engineering Center

Use of Surety Exempt-Dilute GD Stock Solution to Determine Initial (Zero Order) Hydrolysis Rates by OPA Anhydrase Preparations (109)

J.M. Albizo and J.W. Hovanec, U.S. Army Chemical Research, Development and Engineering Center

COMPUTATIONAL CHEMISTRY POSTERS

Studies in the Application of the Molecular Dynamics/Free Energy Perturbation Method to Model Systems for Acetylcholine/Acetylcholine Receptor (183)

J.J. Urban and G.R. Famini, U.S. Army Chemical Research, Development and Engineering Center

Theoretical Descriptors for the Potency of Substituted Cocaine; Relative Inhibition of Dopamine Uptake (184)

A.H. Lowrey, Naval Research Laboratory; *G.R. Famini*, U.S. Army Chemical Research, Development and Engineering Center

Predicting Oxidation Similarities Between VX and Potential Simulants by Semiempirical Orbital Calculations (185)
G.R. Famini and P.W. Bartram, U.S. Army Chemical Research, Development and Engineering Center

Rotational Barriers in Model Compounds of Polyvinyl Chloride (186)
P.N. Krishnan and R.E. Morris, Coppin State College; *G.R. Famini and J.O. Jensen*, U.S. Army Chemical Research, Development and Engineering Center; *L.A. Burke*, Rutgers University

Modeling Metabolic Pathways: A Graph-Theoretic Approach (187)
E. Gifford and C.-C. Tsai, Kent State University; *M. Johnson*, The Upjohn Company

Predicting Polymer Properties Using the Rotational Barrier (188)
R.E. Morris, Coppin State College; *G.R. Famini*, U.S. Army Chemical Research, Development and Engineering Center

DECONTAMINATION POSTERS

Adsorption of Mustard from a Chlorofluorocarbon Solvent Using Macroreticular Strong Acid Resins (162)
J.H. Buchanan, D.K. Rohrbaugh, P.W. Bartram and N.C. DiBona, U.S. Army Chemical Research, Development and Engineering Center

Oxidations of Alkenes Catalyzed by a Mn(III) Porphyrin and Cationic Polymer Latexes (163)
W. Zhu and W.T. Ford, Oklahoma State University

Tests of a Reactant-Loaded Decontaminating Polymer Powder Against Agents and Thickened Simulants (164)
M.S. Kaplan, G.M. Russo and N. Tillman, Eastman Kodak Company

Investigation of Additives to Improve Auto-Release of Coatings for Decontamination (165)
B.K. Huelle and S.T. Wellinghoff, Southwest Research Institute

Removal of Thickened Mustard from Painted Test Panels by Liquid Systems (166)
Y.-C. Yang and J.R. Ward, U.S. Army Chemical Research, Development and Engineering Center; *K. Goergens and M. Zillmer*, WWDBw ABC-Schutz, Germany

Determination of the Critical Micelle Concentrations of CTAB in Water/1-Akyl-2-Pyrrolidinone Mixtures (167)
J.W. Hovanec and J.M. Albizo, U.S. Army Chemical Research, Development and Engineering Center

Decontamination Trials Using Forced Hot Air (168)
H.-J. Altmann, WWDBw ABC-Schutz, Germany

Covalent Attachment of Organic "Handles" to Polyoxometalates with Oxidative Decontamination Activity (169)
C.L. Hill and G.-S. Kim, Emory University

Adsorption of VX and TBP by Various Sorbents in 1,2-Dichloroethane (170)
J.H. Buchanan and S.H. Hong, U.S. Army Chemical Research, Development and Engineering Center

Kinetics of the Hydrolysis of a Model Phosphorus Ester by DS2 Decontaminant Sorbed Onto Dow-Corning Polytrap Resin Monitored by NMR (171)
S.H. Hong, U.S. Army Chemical Research, Development and Engineering Center

Autoxidation of 2-Mercaptoethanol Catalyzed by Co(II) Phthalocyaninetetrasulfonate and Cationic Polymers (172)

S. HariBabu and W.T. Ford, Oklahoma State University

DETECTION POSTERS

The Identification and Detection of Urinary Metabolites of Sulphur Mustard (50)

R.M. Black, K. Brewster, R.J. Clarke, J.L. Hambrook, J.M. Harrison, D.J. Howells and R.W. Read, Chemical and Biological Defence Establishment, United Kingdom

Fiber Optic Immune Sensor for the Detection of Anticholinesterases (51)

N.A. Anis, K.R. Rogers and M.E. Eldefrawi, University of Maryland School of Medicine; *J.J. Valdes*, U.S. Army Chemical Research, Development and Engineering Center

Compact Raman Spectroscopy Instrument for Chemical Contamination Monitoring (52)

M.M. Carrabba, EIC Laboratories, Inc.

Characterization of Bacteria by Oxidative Pyrolysis-Gas Chromatography Mass Spectrometry (53)

P.B. Smith, Geo-Centers, Inc.; *A.P. Snyder*, U.S. Army Chemical Research, Development and Engineering Center

Tradeoff Analysis of Nonradioactive Source Alternatives for the XM22 Automatic Chemical Agent Alarm (54)

J.E. Roehl, Environmental Technologies Group, Inc.

Triazine Derivatives as Potential Microsensor Coatings for the Detection of Airborne Contaminants (55)

A.R. Katrizky and J.N. Lam, University of Florida

Feasibility of Drone-Portable Ion Mobility Spectrometry (56)

N.S. Arnold and H.L.C. Meuzelaar, University of Utah; *A.P. Snyder*, U.S. Army Chemical Research, Development and Engineering Center

Parametric Control and Hazard Containment (57)

G.R. Bodily, U.S. Army Dugway Proving Ground

Detection of Bacteria Using the Vapour Formed by an Immunological Reaction (58)

D.A. Blyth and J.A. Parsons, Geo-Centers, Inc.; *A.P. Snyder and M.C. Miller*, U.S. Army Chemical Research, Development and Engineering Center

Detection and Identification of O-Ethyl S-[2-Dimethylaminoethyl] Methylphosphonothioate Degradation Products by Chemical Ionization Mass Spectrometry (59)

D.K. Rohrbaugh, U.S. Army Chemical Research, Development and Engineering Center

Synthesis and Properties of a Polymeric VX Simulant (60)

G.D. Sides, CMS Research Corporation

Addition of Lewisite Monitoring Capability to Minicams® (61)

D.R. Coleman, CMS Research Corporation

Detection of GF Using Ion Mobility Spectrometry (62)

D.B. Shoff and L.D. Hoffland, U.S. Army Chemical Research, Development and Engineering Center

Raman Spectroscopy of the Nicotinic Acetylcholine Receptor (63)
S.D. Christesen and J.J. Height, U.S. Army Chemical Research, Development and Engineering Center

Laser Desorption/Ionization of Biological Materials (64)
S.R. Long, C.C. Chou and R.M. Serino, U.S. Army Chemical Research, Development and Engineering Center

An Investigation of Curie-Point Py-MS of Nucleic Acids and Peptides (65)
A.S. Noguera and K.J. Voorhees, Colorado School of Mines

ENVIRONMENTAL STUDIES POSTER

Detection of Thiodiglycol and its Sulfoxide and Sulfone Analogues in Environmental Waters by High Performance Liquid Chromatography (115)
P.C. Bossle, M.W. Elzy and J.J. Martin, U.S. Army Chemical Research, Development and Engineering Center

MATERIALS POSTERS

Jet Engine Dissemination of Microencapsulated Aerosols (145)
M. Guelta and H. Carlton, U.S. Army Chemical Research, Development and Engineering Center

Properties of Vulcanized Natural Rubber and Trans-Polyisoprene Blends (146)
J.M. Sloan, U.S. Army Materials Technology Laboratory

Compositional Differences in Butyl Gum Rubber by Mass Spectrometry (147)
D.A. Bulpitt, U.S. Army Materials Technology Laboratory

Silicon Oxide Laminates: Flexible, Transparent Chemical Barriers (148)
M.D. Gilbert and E.E. Engwall, U.S. Army Materials Technology Laboratory

New Test Methods for NBC Survivability (149)
P.S. Grasso and P.L. Cannon, Jr., U.S. Army Chemical Research, Development and Engineering Center

Scanning Electron Microscopy of Carbon Fiber Bundles (150)
D.A. Paterno, U.S. Army Chemical Research, Development and Engineering Center.

NMR INVESTIGATIONS POSTERS

Metal-Ion Promoted Oxidation of DIMP (121)
D.R. Leslie, Materials Research Laboratory, Australia; *J.R. Ward*, U.S. Army Chemical Research, Development and Engineering Center

DMMP-TC Reaction Study (122)
L.J. Szafraniec, L.L. Szafraniec and V.B. May, U.S. Army Chemical Research, Development and Engineering Center

Applications of High-Resolution Solid-State NMR Spectroscopy to the Study of Sorption by Polymeric Materials (123)
P.J. Toscano, J. Waechter and E.J. Schermerhorn, State University of New York-Albany

Structure Determination of Compound 34 (124)

D.R. Leslie, Materials Research Laboratory, Australia; *L.L. Szafraniec, D.K. Rohrbaugh and L.J. Szafraniec*, U.S. Army Chemical Research, Development and Engineering Center

PROTECTION POSTERS

Decontamination Survivability of Selected Defense Equipment (18)

C.K. Ramachandran, U.S. Army Dugway Proving Ground

Barrier Properties of Matrices for Reactive Systems - A Reactivity Probe (19)

J. Halliday and J. Walker, U.S. Army Natick Research, Development and Engineering Center

Removal of Diethyl Sulfide from Breathing Air by the NRL-1000 Oxidation Catalyst (20)

V.A. Shamamian, K.W. Pierson and D.S.Y. Hsu, Naval Research Laboratory

A Comprehensive Analytical Scheme for the Catalytic Decomposition of CW-Agent (21)

R.J. Dihu, S. Mainer and K.S. Rajan, IIT Research Institute

Analytical Model of the Filtration Process by High Velocity Liquid Aerosols (22)

E. Rodriguez and T.E. Wenzel, David Taylor Research Center; *A. Gomezplata*, Engineering Computer Optecnomics, Inc.

Process Evaluation for the Development of a Reactive Carbon Adsorbent (23)

C.J. Karwacki, J. Rehrmann and G. Stickel, U.S. Army Chemical Research, Development and Engineering Center

SYNTHESIS & PROPERTIES POSTERS

Enolate Chemistry of the Nitrogen Protected 4-Piperidone System (32)

G.D. Clark, P.F. Hudrlik and A.M. Hudrlik, Howard University

Predicting Liquid Densities of Organic Compounds I: Halogenated and Oxygenated (33)

G. Wood and T. Weaver, Los Alamos National Laboratory

Relations Between Nucleophilicity and Acidity of Oximes (34)

F. Guir and F. Terrier, Centre d'Etudes du Bouchet, France

Some Physicochemical Characteristics of 1-Substituted-4-Phenyl-4-Piperidinols and their Esters (35)

W.R. Hydro and J.W. King, U.S. Army Chemical Research, Development and Engineering Center

Synthesis and Bioactivity of 2-(α -Hydroxy-p-Alkoxybenzyl) and 2-Alkoxyarylamino Analogs of Etonitazene (36)

J.W. King, U.S. Army Chemical Research, Development and Engineering Center; *J.P. Cleveland*, Eastman Chemical Company; *W.J. Lennox*, U.S. Army Medical Research Institute of Chemical Defense

Thermal Analysis of Colored Smoke Dyes (37)

A. Turetsky and A. Brozena, U.S. Army Chemical Research, Development and Engineering Center

TOXICOLOGY POSTERS

Inhibition of Sulfur Mustard-Increased Protease Activity of Niacinamide, N-Acetyl-L-Cysteine or Dexamethasone (72)

F.M. Cowan, C.A. Broomfield and W.J. Smith, U.S. Army Medical Research Institute of Chemical Defense

Dissociation of Opiate-Induced Sedation and Respiratory Depression in Ferrets by Opiate Antagonist Coadministration: Potential Pharmacological Mechanisms (73)

R. Mioduszewski and S. Reutter, U.S. Army Chemical Research, Development and Engineering Center

The Fate of Sulfur Mustard after Intravenous Intoxication of Rats (74)

A. Maisonneuve, I. Callebat, L. Debordes and C. Imbert, Centre d'Etudes du Bouchet, France

Increased Proteolytic Activity in Human Epithelial Cells Following Exposure to Sulfur Mustard (75)

W.J. Smith, F.M. Cowan and C.A. Broomfield, U.S. Army Medical Research Institute of Chemical Defense

Sulfur Mustard-Induced Alterations of DNA Structure and Kinetics in Proliferating Human Cells in Culture (76)

W.J. Smith, K.M. Sanders, J.E. Caulfield and C.L. Gross, U.S. Army Medical Research Institute of Chemical Defense

Enzymatic Cyanide Detoxification (77)

S.A. Katz and H. Salem, U.S. Army Chemical Research, Development and Engineering Center

Buffet Dinner

Aberdeen Area Officer's Club

Wednesday, 20 November 1991

6:00 - 7:00 Cocktails

7:00 - 8:30 Dinner

8:30 - 9:30 Guest Speaker

Menu

*Carved Roast Sirloin of Beef
Baked Chicken with Cornbread Dressing
Glazed Carrots
Green Beans
Mashed Potatoes
Dessert Table*

Cash Bar

\$15.00 per person, tax and gratuity included

Thursday, 21 November 1991

SESSION 4 - BIOTECHNOLOGY

Chairman: *James J. Valdes*, U.S. Army Chemical Research, Development and Engineering Center

Conference Center

Part I: Molecular Biology

Moderator: *Elias K. Michaelis*, The University of Kansas

- 0800 Olfaction, Olfactomedin and the Dynamic Range of Smell (78)
R. Anholt, Duke University Medical Center
- 0825 Olfactory Receptor Binding Protein (abstract not available)
D. Lancet, Weizmann Institute of Science, Israel
- 0850 Suppression Cloning of a Novel Calcium Channel Subunit cDNA (80)
C.B. Gundersen and J.A. Umbach, University of California, Los Angeles
- 0915 Advances in the Isolation, Reconstitution and Cloning of a Neuronal Receptor-Ion Channel Complex, the NMDA Receptor (81)
E.K. Michaelis, University of Kansas
- 0935 BREAK
- 0955 Comparison of Receptor-Based LAPS and Fiber-Optic Biosensors (82)
M. Eldefrawi, University of Maryland School of Medicine; *K. Rogers*, U.S. Army Chemical Research, Development and Engineering Center
- 1020 Using a Silicon Microphysiometer to Detect Agents that Alter Cellular Physiology (83)
J.C. Owicki, H.G. Wada and J.W. Parce, Molecular Devices Corporation
- 1045 Chemical Agent Biosensor Method with Electrochemical Transduction by Ion Channel Synthesis (84)
G.D. Case, S.T. Ohnishi, M. Koes and A.M. Soltis, Resource Technologies Group, Inc.; *M.M. Howton and D.S. Beattie*, West Virginia University; *S.N. Agathos*, Rutgers University; *L.J. Luskus*, Brooks Air Force Base

Thursday, 21 November 1991

SESSION 4A - ENVIRONMENTAL STUDIES (CONCURRENT)

Moderator: *Janis K.D. Seegar*, U.S. Army Chemical Research, Development and Engineering Center

Chapel Annex

- 0800 Integrating Liquid-Solid Extraction with Ion Mobility Spectrometry (IMS) for Monitoring Semi-Volatile Organic Compounds in Water (110)
G.A. Eiceman, New Mexico State University; *E.J. Poziomek*, University of Nevada
- 0820 Supercritical Fluid Extraction of Chemical Warfare Agent Simulants from Soil (111)
W.H. Griest, C.-H. Ho, R.S. Ramsey and W.M. Caldwell, Oak Ridge National Laboratory

- 0840 Novel Methods for Investigating Chemical Migration and Transformation in Soil (112)
R.T. Checkai, R.O. Nwanguma and R.S. Wentzel, U.S. Army Chemical Research, Development and Engineering Center; *M.A. Major*, U.S. Army Biomedical Research and Development Laboratory
- 0900 Dose/Response Relationships of HC (Hexachloroethane) Smoke: Foliar Injury of Trees (113)
M.C. Sadusky and M. Simini, Geo-Centers, Inc.; *J.M. Skelly*, Pennsylvania State University; *R.S. Wentzel*, U.S. Army Chemical Research, Development and Engineering Center
- 0920 Low Pressure Burner Apparatus for Incineration Studies (114)
A.W. Miziolek, R.C. Sausa, S.L. Howard, D.C. Dayton and S.A. Barts, U.S. Army Ballistic Research Laboratory
- 0940 BREAK

Thursday, 21 November 1991

SESSION 4B - NMR INVESTIGATIONS (CONCURRENT)

Moderator: *Linda L. Szafraniec*, U.S. Army Chemical Research, Development and Engineering Center

Chapel Annex

- 1000 Purity Determination of Chemical Agents Using Multinuclear NMR Spectroscopy (116)
W.T. Beaudry and L.L. Szafraniec, U.S. Army Chemical Research, Development and Engineering Center
- 1020 Position of Bond Cleavage in the Hydrolysis of Organophosphonate Esters Using ^{18}O NMR Analysis (117)
L.L. Szafraniec, L.J. Szafraniec and J.R. Ward, U.S. Army Chemical Research, Development and Engineering Center
- 1040 NMR Spectroscopy Determination of Relative Binding Constants for Arsenical-Antidote Adducts (118)
R.J. O'Connor, E.L. McGown and V.L. Boyd, Letterman Army Institute of Research; *K. Dill*, Clemson University; *S.F. Hallowell*, U.S. Army Chemical Research, Development and Engineering Center
- 1100 Use of ^{31}P Nuclear Magnetic Resonance (NMR) to Assess Blistering Agent Damage to Skin (119)
M.J. McCreery, D.J. Stralka and H. Aceto, Jr., U.S. Army Medical Research Institute of Chemical Defense
- 1120 Solid-State P-31 MAS NMR Study of G-Agent Simulants Adsorbed on Synthetic Resins (120)
W.T. Beaudry G.W. Wagner and J.R. Ward, U.S. Army Chemical Research, Development and Engineering Center

Thursday, 21 November 1991

SESSION 4C - FLUID DYNAMICS (CONCURRENT)

Part I: Liquid Filled Projectiles

Moderator: *Miles C. Miller*, U.S. Army Chemical Research, Development and Engineering Center

Conference Room #134, Building E3330

- 0800 Progress in the Moment Calculation for a Spinning and Nutating Cylinder with Silicone Fluid (125)
R. Li and Th. Herbert, The Ohio State University
- 0820 Effect of Low Viscosity Additives on the Moments Caused by Viscous Fluids in a Spinning and Coning Cylinder (126)
M. Selmi, University of Alberta, Canada; *Th. Herbert*, The Ohio State University
- 0840 Effect of Longitudinal Baffles on the Viscous Liquid-Fill Induced Destabilizing Moment (127)
M.C. Miller, U.S. Army Chemical Research, Development and Engineering Center
- 0900 Including Liquid Fill Effects in the Tricyclic Theory (128)
D. Weber, U.S. Army Chemical Research, Development and Engineering Center
- 0920 Instrumented Flight Tests and Data Reduction of Artillery Projectiles with Selected Liquid-Fills (129)
D. Hepner, U.S. Army Ballistic Research Laboratory; *D. Weber and J. Molnar*, U.S. Army Chemical Research, Development and Engineering Center
- 0940 BREAK

Part II: Rheology and Special Topics

Moderator: *Wendel J. Shuely*, U.S. Army Chemical Research, Development and Engineering Center

Conference Room #134, Building E3330

- 1000 Numerical Simulation of Fluid Dynamics and Payload Dissemination in a Dual-Chamber Grenade (130)
M. Nusca, U.S. Army Ballistic Research Laboratory
- 1020 Nonlinear Dynamics of Fluidized Suspensions and Interactive Aerodynamics (131)
D.D. Joseph, University of Minnesota
- 1040 A Comparison of Elongational Measurements Obtained with the Falling Cylinder and Impinging Jet Rheometer (132)
J. Matta, R. Tytus and D. Somerville, U.S. Army Chemical Research, Development and Engineering Center
- 1100 Formulation of Preferentially Soluble Polymer Solutions and Comparisons of Their First Normal Stress Difference and Extensional Viscosity (133)
B.S. Ince and W.J. Shuely, U.S. Army Chemical Research, Development and Engineering Center
- 1120 Magnet Enhanced Optical Falling Needle/Sphere Rheometer (134)
B. Chu and J. Wang, State University of New York at Stony Brook; *W.J. Shuely*, U.S. Army Chemical Research, Development and Engineering Center

Thursday, 21 November 1991

SESSION 5 - BIOTECHNOLOGY

Chairman: *James J. Valdes*, U.S. Army Chemical Research, Development and Engineering Center

Conference Center

Part II: Applications

Moderator: *James R. Wild*, Texas A&M University System

- 1300 Microbial Degradation of 3-Hydroxypiperidine and 3-Hydroxyquinuclidine (85)
J.J. DeFrank and C.N. Savage, U.S. Army Chemical Research, Development and Engineering Center
- 1325 Genetic Manipulation of Organophosphate Hydrolase Processing (86)
C.E. Miller, K. Dave and J.R. Wild, Texas A&M University System
- 1350 Catalytic Monoclonal Antibodies: Novel Biotechnology Poised for Application (87)
B.S. Green, The Hebrew University of Jerusalem, Israel
- 1415 Enzymatic Degradation of GF (88)
S. Harvey, U.S. Army Chemical Research, Development and Engineering Center
- 1435 BREAK
- 1455 Enzymes in Supercritical Fluids (89)
A. Russell, University of Pittsburgh
- 1520 Plant Cell Cultures for the Production of Bioactive Compounds (90)
C.L. Prince, Phytion Catalytic, Inc.
- 1545 The Role of the Pilot Plant in Bioprocess Development (91)
E.M. Sybert, University of Maryland

Thursday, 21 November 1991

SESSION 5A - MATERIALS (CONCURRENT)

Moderator: *Seok H. Hong*, U.S. Army Chemical Research, Development and Engineering Center

Chapel Annex

- 1330 Equilibrium Solubility and Diffusion Coefficient Measurements and Correlations with Predictive Properties (135)
B.S. Ince and W.J. Shuely, U.S. Army Chemical Research, Development and Engineering Center
- 1350 Simulation of Permeation from a Deposited Droplet (136)
J.H. Meldon and G. Severe, U.S. Army Materials Technology Laboratory
- 1410 Recent Developments in the Fundamentals of Gas Permeation in Rubbery Polymers (137)
C.R. Desper, U.S. Army Materials Technology Laboratory

- 1430 Control Material Formulation Development for MIL-STD-282 Static Diffusion Testing (138)
E.E. Engwall, U.S. Army Materials Technology Laboratory
- 1450 Novel Elastomeric Materials for Chemical Protective Clothing (139)
E. Wilusz, A. Galewski, J. Brennick, D. Gulliani, J. Marcotte and K.D. Hassler, U.S. Army Natick Research, Development and Engineering Center
- 1510 BREAK
- 1530 Emulsion Copolymerization of Methacrylates: A Scale-Up Study (140)
J.M. Park and J.W. Vanderhoff, Lehigh University; *S.H. Hong*, U.S. Army Chemical Research, Development and Engineering Center
- 1550 Chemical Agent Hardness of Transparent Polymers (141)
P.S. Grasso and L.M. Sturdivan, U.S. Army Chemical Research, Development and Engineering Center
- 1610 Solvent Effects on the Tensile Properties of Thermoplastic Composites (142)
Y.M. McHugh, W.J. Shuely and R.W. Brketch, U.S. Army Chemical Research, Development and Engineering Center
- 1630 A Preliminary Evaluation of Diamond-Like Carbon Coated Polycarbonate (143)
A.J. Hsieh, U.S. Army Materials Technology Laboratory
- 1650 Corrosion Behavior Study of Type II and Type III Anodized AL 5052-0 in Aqueous DS2 Solutions (144)
C.V. Zabielski and M. Levy, U.S. Army Materials Technology Laboratory

Friday, 22 November 1991

SESSION 6 - DECONTAMINATION

Moderator: *Joseph W. Hovanec*, U.S. Army Chemical Research, Development and Engineering Center

Conference Center

- 0800 Reaction of VX with Chloramine-B (151)
Y.-C. Yang, L.L. Szafraniec, W.T. Beaudry and J.R. Ward, U.S. Army Chemical Research, Development and Engineering Center
- 0820 Mechanisms of Dehalogenation of Aliphatic Halocarbons such as HD by $W_{10}O_{32}^{6-}$ (152)
C.L. Hill and D. Sattari, Emory University
- 0840 Complete Destruction of Agents in Microheterogeneous Solution and on Oxide Films (153)
M. Grätzel, Swiss Federal Institute of Technology
- 0900 Micellar Charge Effects on Sulfide Oxidation (154)
A. Blasko, C.A. Bunton, H. Foroudian, T. Taylor and S. Wright, University of California, Santa Barbara
- 0920 Activation of H_2O_2 Using Co-Catalysts in N-Methylpyrrolidinone Solvent (155)
R.S. Drago and D.E. Patton, University of Florida

- 0940 **BREAK**
- 1000 Mechanism of the Hydrolysis of Organophosphinates Catalyzed by Copper (II) N,N,N',N'-Tetramethylethylenediamine (CuTMED) (156)
M. Nakashima and D.M. Alabran, U.S. Army Natick Research, Development and Engineering Center
- 1020 Mechanistic Studies of the Reaction of Phenolates and Thiophenolates with 2-Chloroethyl Methyl Sulfide in Aprotic Solvents and Some Containing Water (157)
S.P. McManus, R.M. Karaman and J.M. Harris, University of Alabama in Huntsville
- 1040 Development of the Canadian Reactive Skin Decontaminant Lotion (158)
J.G. Purdon, Defence Research Establishment Suffield
- 1100 Exploration of Non-Enzymatic Broad Spectrum Catalysts for CW-Agent Decomposition (159)
K.S. Rajan and S. Mainer, IIT Research Institute; *J.E. Walker, D. Remy and J.W. Halliday*, U.S. Army Natick Research, Development and Engineering Center
- 1120 Luminescence Quenching and Electrochemical Studies in Microemulsions (160)
P.L. Cannon, Jr., S.D. Christesen, R.A. Mackay, N.M. Wong and F.R. Longo, U.S. Army Chemical Research, Development and Engineering Center; *S.M. Garlick*, Geo-Centers, Inc.; *A.C. Novelli*, Université Paul Sabatier, France
- 1140 The Hydrolytic Kinetics of Mustard Simulents in Polymer Solutions (161)
L.C. Cerny and E.L. Cerny, Utica College of Syracuse University

Friday, 22 November 1991

SESSION 6A - COMPUTATIONAL CHEMISTRY (CONCURRENT)

Moderator: *George R. Famini*, U.S. Army Chemical Research, Development and Engineering Center

Chapel Annex

- 0800 Conformational Analysis of Oligopeptides: Molecular Dynamics versus Monte Carlo Techniques (173)
D.C. Hack, U.S. Army Medical Research Institute of Infectious Diseases; *D.C. Feller*, Molecular Vaccines, Inc.
- 0820 PBI Hydration Study in the Development of Methodology for the Molecular Modeling of Mechanical Property Trends (174)
N. Iwamoto, Naval Weapons Center
- 0840 Structure Sedative Activity Relationships of Alpha2 Adrenergic Compounds (175)
W. Ashman, T. Nelson and B. Meehan, U.S. Army Chemical Research, Development and Engineering Center
- 0900 Some Interrelations of the Heats of Formation of Isosteric and Isoelectronic Oxygen and Fluorine Compounds (176)
C.A. Deakynne, Eastern Illinois University; *A.D. Fant, D.L. Kunkel and J.F. Liebman*, University of Maryland, Baltimore Campus

- 0920 **Ab Initio** Quantum Chemical Investigations of Solute/Solvent Polarity and Hydrogen-Bonding Parameters (177)
P. Politzer, J.S. Murray and T. Brinck, University of New Orleans
- 0940 **BREAK**
- 1000 Calculation of Electronic Spectra with the Valence Effective Hamiltonian Method (178)
L.A. Burke, Rutgers University
- 1020 Model of the Active Site Spectroscopy of the Rhodanese Enzyme (179)
M. Krauss, National Institute of Standards and Technology
- 1040 Computer Model for the Spectral Predictions of Nerve Agents (180)
H.F. Hamelka, University Pennsylvania; *J.O. Jensen*, U.S. Army Chemical Research, Development and Engineering Center
- 1100 Theoretical Prediction of Vibrational Circular Dichroism Spectra of Hexoses (181)
D. Zeroka, Lehigh University; *J.O. Jensen, A.H. Carrieri and J.L. Jensen*, U.S. Army Chemical Research, Development and Engineering Center
- 1120 Integration of the AVS Visualization Environment into Chemical Defense Research: Investigation of Alpha-2 Adrenergic Agonists (182)
J.M. Leonard, Stardent Computer Inc.; *W.P. Ashman*, U.S. Army Chemical Research, Development and Engineering Center

BLANK

1000

APPENDIX C
DELAYED PAPERS*

*The papers contained in this appendix were received too late to be included in their proper sections.

Blank

CHARACTERIZATION OF AN UNKNOWN POLYPEPTIDE FROM
NAJA NAJA atra

T. Krishnamurthy, J.G. Freedy and T.D. Cotten
U.S. Army Chemical Research, Development and Engineering Center,
Aberdeen Proving Ground, MD 21010-5423

Prof. K. Hayashi
Gifu Pharmaceutical University, Gifu, Japan

Molecular weight and partial sequences of a basic polypeptide isolated from *Naja Naja atra* (Chinese species) were determined by electrospray-MS and allied techniques.

INTRODUCTION

Most of the active snake venom components have been found to be polypeptides.¹ The cytotoxic and postsynaptic neurotoxic peptides contain 60-80 amino acids and the presynaptic ones are much longer.¹ Primary structures of most of these peptides were determined by automated Edman sequencing procedures. Recently, we have devised a scheme to determine the total amino acid sequences of a basic polypeptide isolated from a Chinese species of *Naja Naja atra*. This involves the application of electrospray ionization, tandem mass spectrometric techniques, automated amino acid analysis and Edman sequencing procedures. Molecular weight (7,596 Daltons) of the basic peptide and the number of cysteines (10) and disulfide bridges (5) present in the molecules were determined from the electrospray-MS spectra of the intact and ethylpyridyl derivative of the reduced peptide. Preliminary data indicates the proposed scheme could successfully be applied for obtaining the primary structure, total amino acid sequences, of the investigated basic peptide.

EXPERIMENTAL

Separation of the enzymatic degradation products and derivatives of the *Naja Naja atra* peptide were carried out using Applied Biosystems (ABI) 130A and 140A HPLC separation systems. Mass spectral investigations were carried out in Finnigan-MAT TSQ-70 tandem mass spectrometer fitted with electrospray ionization source manufactured by Analytica of Branford. Amino acid compositional analysis and n-terminus sequences were determined using ABI 430 automated amino acid analyzer and 477 automated peptide sequencer, respectively.

Fused silica capillary HPLC columns were purchased from LC Packings, San Francisco, CA. All solvents and reagents were HPLC

or analytical grade. Special reagents formulated by ABI were used during the amino acid analysis and automated Edman degradation procedures.

Basic Peptide Stock Solution: Accurately weighed out lyophilized purified peptide was dissolved in 1% aqueous acetic acid to make up solution (100 nmole/ μ l). The stock solution was further diluted with 1% aqueous acetic acid as needed. Stock solution was stored at -20°C until use.

Chromatographic Separations: Performed by reverse phase chromatography using ABI 130A and 140A HPLC separation systems. The Mixtures were loaded on a reverse phase narrowbore column (2.1 x 31mm, 7 μ). The components were eluted from the column by varying the solvent from 0% to 40% solvent B (0.085% TFA in acetonitrile) in solvent A (0.1% aqueous TFA) IN 40 minutes. The flow rate was maintained at 200 μ l/min and the collected fractions were lyophilized and stored at -20°C .

Degradation of Basic Peptide: The reduction, carboxymethylation, and derivatization (vinylpyridine) of the intact peptide and the enzymatic digestions of the peptide with trypsin, Asp-N, Glu-C, and chymotrypsin were carried out as per published procedure.²

Mass Spectral Analysis: Peptide solutions (~5 pmole/ μ l) were infused directly into the electrospray ionization source at a rate of 1 μ l/min and ionized (4 keV, N_2 as drying gas at 24 psi, and 250°C). The ions formed were detected by scanning the mass spectrometer from 350 to 2000 m/z in 5 secs.

Alternatively, solutions (1 μ l) containing mixtures were injected on a C_{18} fused silica capillary column (320 μ x 15 cm, 5 μ) column, fitted to ABI 140A syringe pumps. The components were eluted at a flow rate of 2.5 μ l/min., using the same solvent as above with a gradient 0-100% B in 40 minutes. The eluted compounds were introduced on-line to the electrospray ionization source and ionized (4 keV, N_2 as drying gas at 24 psi, and 250°C) using 2-methoxyethanol (2 μ l/min) and nitrogen (24 psi) as sheath flow and gas, respectively. The mass spectra were recorded by scanning from 350 to 2000 m/z in 5 sec.

Amino Acid Compositional Analysis: The fractions were subjected to on-line vapor phase hydrolysis (6N HCl, 160°C), derivatization (phenylisothiocyanate) and analysis (PTC- C_{18} , 2.1 x 31 mm, 7 μ) as per ABI protocol using the specially formulated solvents and reagents supplied by the company.

Automated Edman Sequence Analysis: The coupling with n-terminus residue (phenylisothiocyanate), cleavage (TFA) and rearrangement of the cleaved amino acid derivative (25% aqueous TFA, 60°C) were conducted using the ABI protocol for the automated Edman sequencer.

RESULTS AND DISCUSSION

Solution (5 pmole/ μ l) containing the purified basic peptide was subjected to electrospray ionization by direct infusion. The recorded mass spectrum (Figure 1) displayed the multiply charged ions with charges ranging from 4 to 8. The molecular weight (MW) calculated from the observed ions was 7595.9 \pm 0.5 Daltons.

FIGURE 1. ESI-MS SPECTRUM OF THE INTACT PEPTIDE

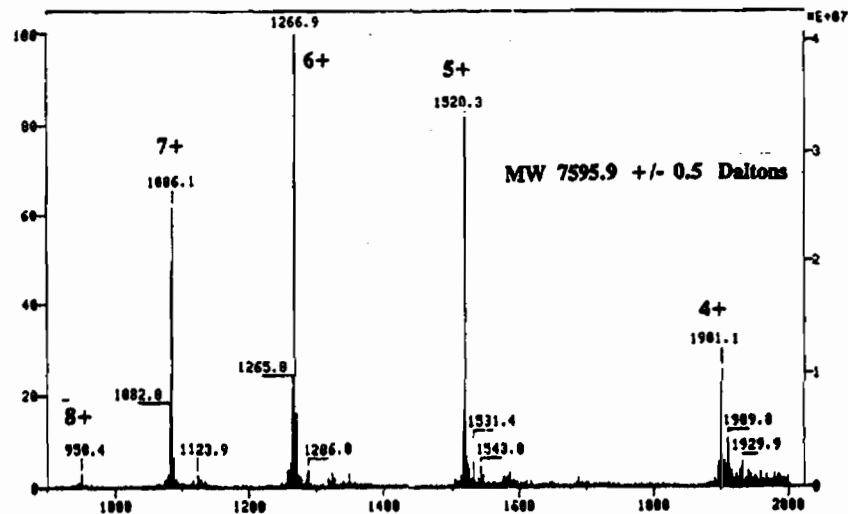


FIGURE 2. ESI-MS SPECTRUM OF ETHYLPYRIDYL DERIVATIVE

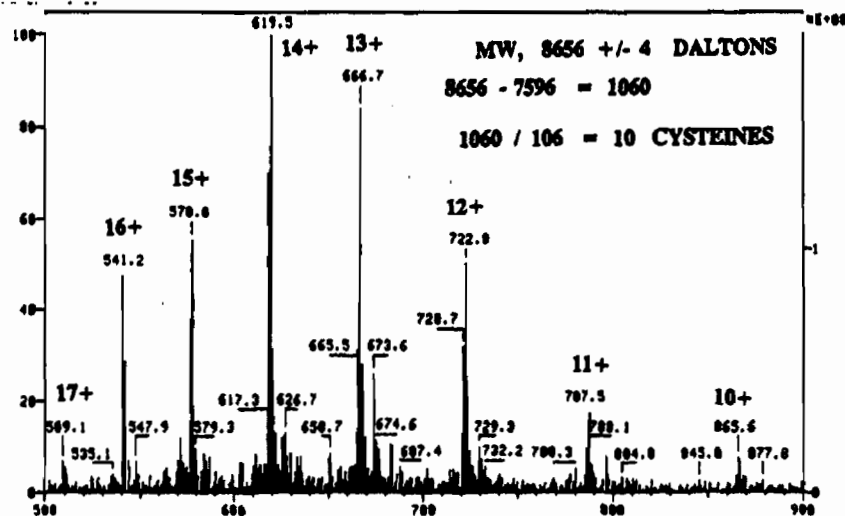


FIGURE 3. TOTAL ION CHROMATOGRAM OF TRYPTIC DIGEST

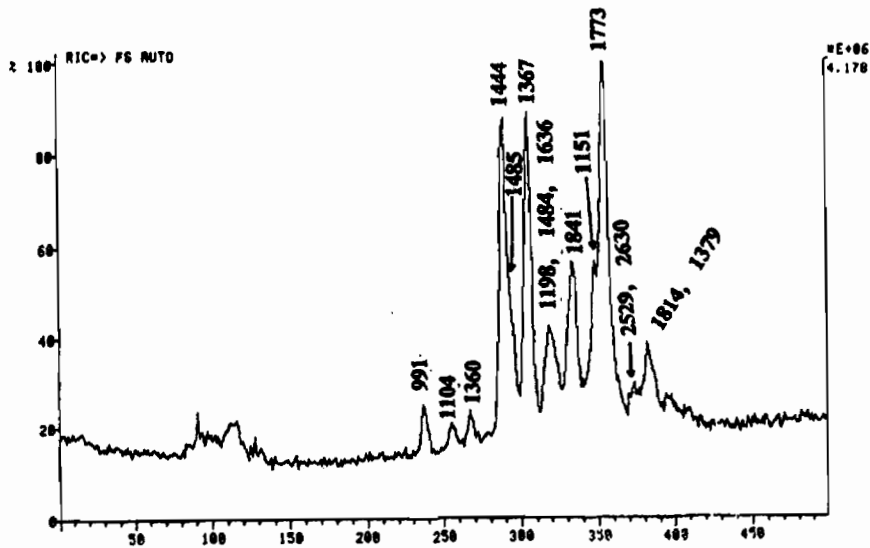
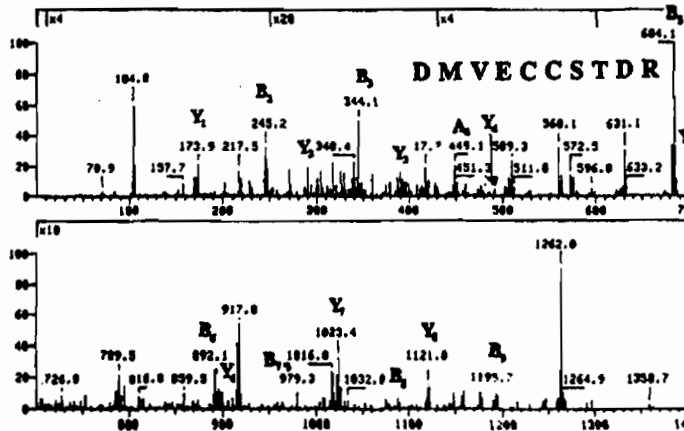


FIGURE 4. SEQUENCES OF A TRYPTIC FRAGMENT



CID SPECTRUM OF A TRYPTIC DIGEST FRAGMENT OF AN UNKNOWN PEPTIDE FROM *Naja Naja atra* VENOM. COLLISION GAS, ARGON; COLLISION ENERGY, 15 eV; COLLISION GAS PRESSURE, 2.8 mTorr.

Similarly, the MW of the ethylpyridyl derivative of the reduced peptide was determined to be 8656.0 +/- 4.0 Daltons (Figure 2). The difference between these two values accounted for the presence of 10 cysteines (increase in molecular weight per cysteine during the process is 106 Daltons) and 5 disulfide bridges. The calculated value for MW of the intact peptide from the measured amino acid analysis value was 9118 Daltons. The discrepancy between the two values is due to the limitation in the observed values for sulfur containing amino acids during the automated procedures. The automated Edman degradation results observed when 2 nmoles of the intact peptide was subjected

through the process is listed below.

LTCLNCPMFQKFGKIQGRNGEKICIKKLEQRRPFSLCRIRGKAAT

The intact peptide (2 nmole) was reduced and derivatized with 4-vinylpyridine. The product was purified over a reverse phase C₈ column and was subjected to tryptic digestion. The product was dissolved in 1% aqueous trifluoroacetic acid (10 μl) and injected (1 μl) into the C₈ microcapillary column. The eluent (1 μl) along with 2-methoxyethanol as the sheath fluid (2.5 μl) was subjected to electrospray ionization. The LC/MS data of the tryptic digest and the observed MW of the fragments generated are shown in Figure 3. One of the fragments (m/z 1360) on methylation produced the molecular ion at 1374 indicating the presence of one free carboxyl group in the molecule. The daughter spectra of the singly charged ions of the fragment (Figure 4) and its methyl ester (Figure 5) were used to deduce the sequences of the amino acids present in the fragment to be **DMVECCSTDR**. The amino acid sequences of few other tryptic fragments were determined by similar approach to be **GCAATCPETK**, **FQICR**, **ICFK**, and **WPFSLR**.

The ethylpyridyl derivative of the reduced basic peptide was also subjected to enzymatic degradation with Asp-N and Glu-C. Some of the fragments originating from the Asp-N were smaller (MW 1111, 1095, 999, 1138, 972, 1114), however few others (MW, 4147, 3163, 2696, 3414) exceeded the daughter spectral range. The ESI-MS spectra of one of such fragments is shown in figure 6. The larger fragments will be subjected to sub-digestion with trypsin to cleave into smaller fragments in order to determine their sequences from the corresponding MS/MS spectra. Similar results were observed during the digestion of the ethylpyridyl derivative with Glu-C. The sub-digestion of larger fragments and deduction of sequences of all fragments in order to determine the total sequences of the intact basic peptide isolated from Naja Naja atra venom is under way.

CONCLUSIONS

The proposed approach for determining the primary structure of the peptide under investigation, involving the combination of mass spectrometric technique with allied ones, seem to be adequate.

FIGURE 5. CID SPECTRUM OF ETHYL ESTER OF DMVECCSTR

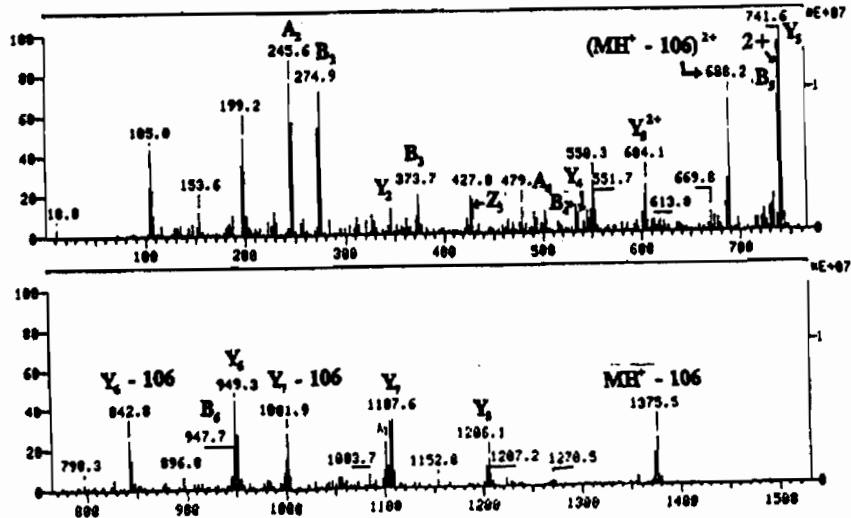
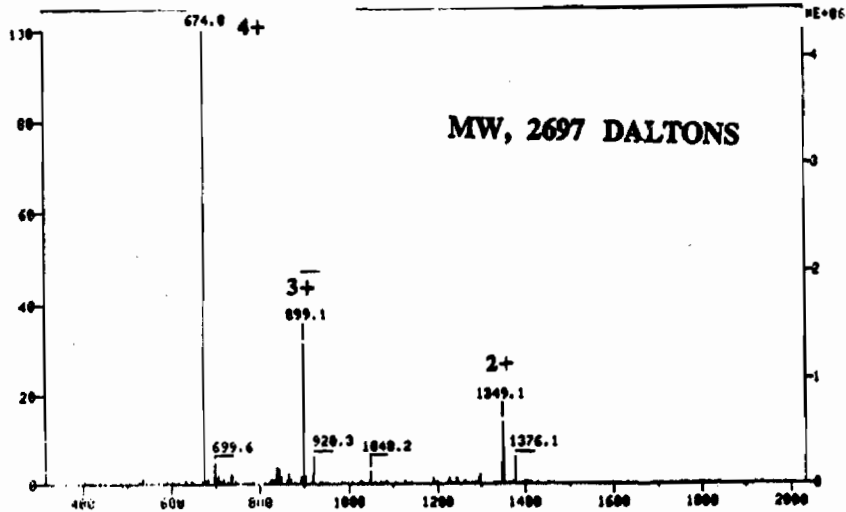


FIGURE 6. ESI-MS SPECTRUM OF AN ASP-N DIGEST FRAGMENT



REFERENCES

1. M.J. Dufton, R.C. Hider, "Conformational Properties of the Neurotoxins and Cytotoxins isolated from Elapid snake Venoms," *CRC Crit.Rev.Biochem.*, 14, 113-136 (1983)
2. D.F. Hunt, et al., "Protein and peptide Sequence Analysis by Tandem Mass Spectrometry in Combination with either Capillary Electrophoresis or Microcapillary HPLC," in "Advances in Life Sciences," H.Jornvall and J.O. Hoog, Ed., Birkhauser Verlag, Basel, Switzerland.

**A COMPREHENSIVE ANALYTICAL SCHEME
FOR THE CATALYTIC DECOMPOSITION OF CW-AGENT GD**

**Remon J. Dihu, Stephen Mainer, Krishna S. Rajan
IIT Research Institute, Chicago, Illinois**

ABSTRACT

Catalytic oxidation offers a viable alternative to the Whetlerite charcoal filter for collective protection from chemical warfare (CW) agents. It offers a long life potential and complete destruction of the agent rather than its temporary removal. In the development of catalytic oxidation processes, not only the agent, but also the decomposition products must be identified and quantitated. In connection with the operation of a catalytic oxidation system, the authors established a coordinated scheme of analytical procedures for the catalytic decomposition kinetics of agent GD (Soman). The scheme consists of analysis of GD levels in reactor inlet and outlet air streams, and analysis for acidic products, namely, fluoride and orthophosphate. Gas chromatography was used to analyze the reactor inlet stream, the MINICAMS[®] laboratory monitoring system for the outlet stream, the fluoride ion selective electrode method for F⁻ levels, and the ascorbic acid method for phosphorus levels.

INTRODUCTION

Absorption systems (e.g., Whetlerite and particulate filters) are used at present for chemical warfare (CW) protection. These systems have many limitations, including a short life potential, limited absorption capacity, and sensitivity to moisture and temperature. New generations of CW protection include the catalytic destruction of CW agents, which offers a long life potential and complete agent destruction rather than its temporary removal.

The analytical methods used for development of the absorption systems were limited to the agent under testing, in a pure form in an air stream. The catalytic oxidation process, however, requires analysis for the agent in the presence of impurities (by-products and acids). Moreover, potentially harmful acid by-products must be identified and quantitated prior to integration of the catalytic reactor into an environmental control system for collective protection. Prior to testing a 260-scfm (7400 slpm) monolithic Pt/TiO₂ oxidation catalyst system against nerve agent GD, various analytical methods were developed to identify and quantitate the agent and its acidic decomposition by-products. The development of these methods is the subject of this article.

BACKGROUND

Analytical schemes for catalytic systems that are designed for the removal of CW agents from air streams are different from those designed for charcoal filters. In addition to dealing with effluent concentrations of CW agents on the order of parts per billion (ppb) due to the potential high toxicity of the various agents, these analytical schemes have to be performed in the presence of acids and other decomposition by-products.

During the catalytic oxidation testing of a 260-scfm (7400 slpm) CW-contaminated air flow, various samples were analyzed for agent GD and for by-product acids containing fluoride ion and orthophosphate.

Analyses for GD were conducted in the reactor influent and effluent air streams and in the water condensate downstream of the reactor. Analyses for acids containing fluoride ion and phosphorus were conducted in the reactor effluent air stream and in the water condensate downstream of the reactor.

EXPERIMENTAL SETUP

Table 1 shows the equipment list for the test setup, which is shown schematically in Figure 1.

TABLE 1.

Test Setup Equipment List

Item Number	Description	Item Number	Description
1	Recuperator	14	Flow measuring section
2	Evaporator of refrigeration system	15	Reheater
3	Main heater	16	Solenoid
4	Refrigeration system	17	Filter
5	Air source	18	Steam injection system
6	Hot-air valve	19	Agent injection system
7	Hot-air bypass valve	20	Cold-air valve
8	Back pressure valve	21	Reactor test unit
9	Charcoal prefilter	22	Cold-air bypass valve
10	Valve controller	23	Check valve
11	Air source regulator	24	Mix tube
12	Check valve	25	Flow section
13	Filter		

PRECONDITIONING EQUIPMENT

During operation of the test system, ambient air is compressed, filtered, and dehumidified by the air source equipment (Item 5), then ducted into the test laboratory, where it is further conditioned. Air pressure is regulated by a regulator valve (Item 11). The air is divided into two streams: the first is heated by the test system recuperator (Item 1) and an electric heater (Item 3); the other bypasses the heating equipment.

The air stream is then recombined to provide the required temperature. At this point, steam and then a chemical agent (Items 18, 19) are injected into the air stream to provide the test unit with the proper humidity and agent concentration. The air is then directed through a static mixing section (Item 24) to ensure that the air stream is uniform in agent composition before it is introduced to the reactor test unit (Item 21).

CATALYST REACTOR TEST UNIT

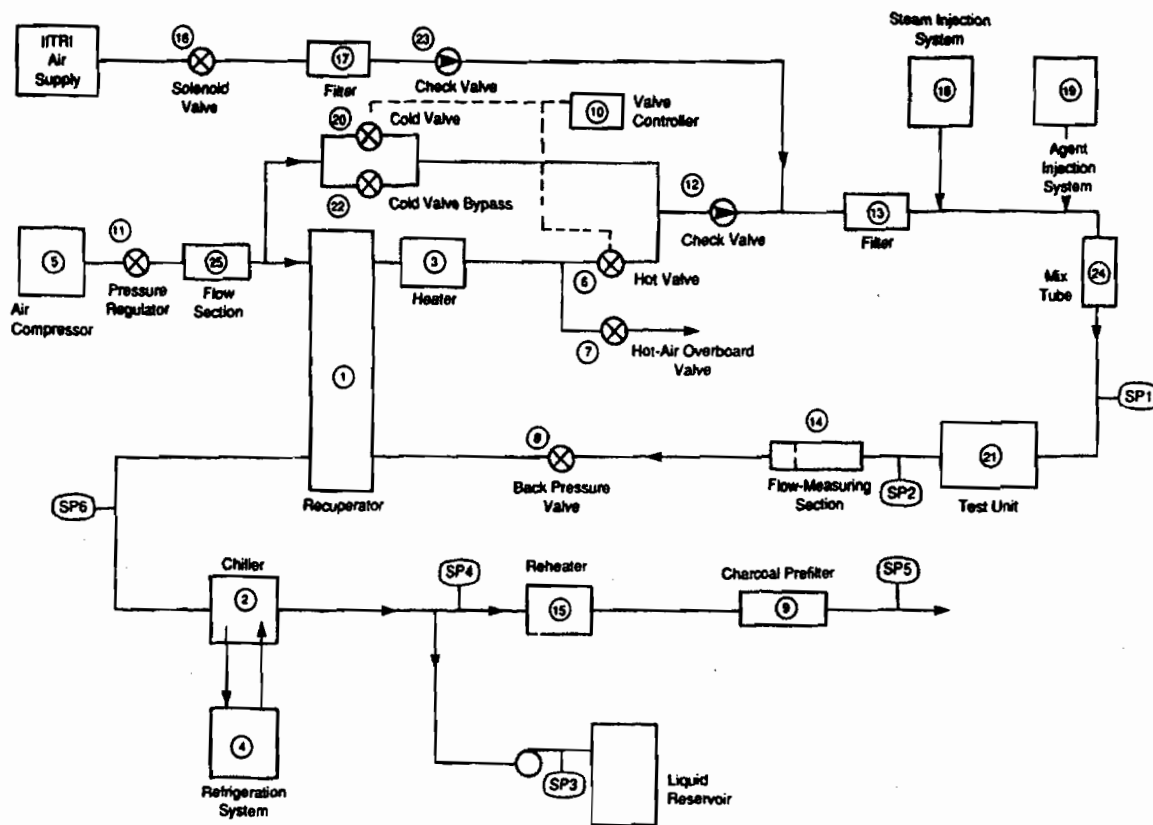
The catalyst reactor test unit consists of a recuperator, an electric heater, and a catalytic reactor. The air delivered to the catalyst test unit is preheated by the recuperator, then further heated by the electric heater to the catalyst operating temperature. The air then enters the reactor, where any chemical agent present is destroyed by catalytic reaction. The purified air then leaves the reactor and passes through the other side of the recuperator to preheat the incoming air.

POST-CONDITIONING EQUIPMENT

The process air must be post-conditioned before it is discharged into the atmosphere. The air pressure of the air leaving the reactor test unit is throttled by the back pressure valve (Item 8), and the air is

FIGURE 1.

Catalytic Oxidation Test Flow Diagram



cooled as it flows through the other side of the test system recuperator (Item 1). Final cooling is accomplished by the refrigeration system (Items 2 and 4). Condensed liquid is collected in the sump and pumped into reservoirs for decontamination. Minor heating of the air ensures its dryness before it enters the charcoal prefilters. The prefilters remove agent or simulant not destroyed in the reactor, and serve as a buffer to the surety laboratory filter bank. Finally, the air is directed to the facility hood filters for removal of any residual agent or simulant. Post-conditioning equipment is required for testing catalytic systems, but will not be required for a fielded device.

AGENT INJECTION SYSTEM

The agent injection system (Item 19) consists of an Isco LC 2600 syringe pump, a spray nozzle, and an air supply. The liquid agent delivered to the reactor test unit is aerosolized using a 30 ft³/min air supply through a nozzle. The aerosolized agent air is recombined into the air stream upstream of the static mixing section (Item 24).

ANALYTICAL PROCEDURES AND SAMPLE ANALYSIS

Test conditions and results are described in reference 1. During each test, samples were collected to measure the concentration of the following species in the reactor influent and effluent (refer to Figure 1 for sample port [SP] locations):

Agent GD

1. Vapor sample upstream of the reactor test unit (SP1)
2. Vapor sample downstream of the reactor test unit (SP2A)
3. Water condensate sample downstream of the chiller (SP3A)
4. Vapor sample downstream of the refrigeration system and chiller (SP4A)
5. Vapor sample downstream of the charcoal prefilter (SP5A)

By-product Hydrogen Fluoride

1. Vapor sample downstream of the reactor test unit (SP2B)
2. Vapor sample upstream of the refrigeration system (SP6B)
3. Water condensate sample downstream of the chiller (SP3B)
4. Vapor sample downstream of the refrigeration system and chiller (SP4B)

By-product H_3PO_4/P_2O_5

1. Vapor sample downstream of the reactor test unit (SP2C)
2. Vapor sample upstream of the refrigeration system (SP6C)
3. Water condensate sample downstream of the chiller (SP3C)
4. Vapor sample downstream of the refrigeration system and chiller (SP4C)

All SP1 samples were analyzed by gas chromatography (GC). The GC method was used because the GD concentrations in these samples were too high for MINICAMS®. All air samples designated A (SP2A, SP4A, and SP5A) were analyzed for the presence of agent GD using MINICAMS®. Water condensate samples designated A (SP3A) were analyzed for agent GD by either the GC method or the acetylcholinesterase method.² By-product samples designated B and C were analyzed for fluoride and phosphorus ion concentrations. The sampling frequency varied, but generally followed the schedule shown in Table 2. Sampling frequency was limited by test duration (generally 60-90 min of agent injection).

ANALYSIS FOR AGENT GD IN REACTOR INLET

All reactor inlet analytical studies for agent GD were performed on a Varian Model 3700 gas chromatograph equipped with a Varian dual-flame photometric detector. This unit is capable of operating in either the phosphorus or sulfur mode, and has a reported lower detection limit of $<10^{-12}$ g P/s (tributyl phosphate).

Reactor inlet analyses were performed as a check against the agent pump calibration. The reactor feed gas stream was sampled in two solvent bubblers connected in series, at the inlet sampling port, SP1 (Figure 1). Each bubbler was filled with 100 mL of scrubbing solution (pesticide-grade acetone).

When the analytical methods were developed for agent GD at the concentration ranges of interest, the use of a calibration curve in the range of 1-20 ppm GD proved desirable. Several standards in the range of 0.01 to 2 ppm were also prepared for a low-level calibration to determine if SP3 samples contained GD. The analysis was performed using a 0.5 μ L injection and external standard calibration methodology.

GD Analysis Instrument Parameters

Column: SPB 608 (Supelco); 15 m x 0.53 mm ID; 0.5 μ m wall-coated capillary

Chromatographic Conditions: Nitrogen carrier gas = 5.0 mL/min at 100°C; nitrogen make-up to FPD = 25.0 mL/min; temperature programming: start at 100°C, ramp at 20°C/min to T = 150°C, hold at 150°C for 4 min

Detector: Varian 3700 dual-flame FPD with electrometer; FPD filtered at 530 nm for phosphorus; electrometer set at 10^{-10} A/mV; internal time constant = 0.2 s; attenuation = as necessary; FPD detector temperature = 270°C; detector gas: air flow 1 = 80 mL/min, air flow 2 = 170 mL/min, H₂ flow = 140 mL/min
Injector: Injector temperature = 240°C; glass direct flash vaporization; injector liner used; residence time of syringe = 5 s
Retention Times: GD = 1.38 ± .02 min
Injection Volume: High concentration = 0.5 μL; low concentration = 0.9 μL
Minimum Detection Limit: 0.1 ng GD on column

ANALYSIS FOR AGENT GD IN REACTOR OUTLET

Analyses for agent GD concentrations in reactor outlet samples SP2, SP4, and SP5 were performed using MINICAMS®. The operation and sample collection methods of MINICAMS® are described below.

MINICAMS® Operation and Sample Collection

MINICAMS® is designed for the rapid determination of certain CW agents in air at their 8-h time-weighted average concentration (TWA). MINICAMS® operates by automatically collecting organic compounds in the air on a solid sorbent (HayeSep D preconcentrator tube). The organic compounds, including agent GD, are thermally desorbed onto a gas chromatography column, where they are separated. The CW agent is detected using a flame photometric detector. Instrument operation and data collection and processing are controlled by a personal computer.

MINICAMS® was connected to the reactor system by the stream selection switch. The reactor effluent stream was sampled at ports SP2A, SP4A, and SP5A. When a port was sampled, all of the other ports connected to the stream selection switch were shut off. The stream selection switch was operated manually to sample the appropriate port. MINICAMS® operations repeated automatically. Cycle times of 10 min were

TABLE 2.

Sampling Schedule and Method of Analysis

Sample Port ^a	Species	Method of Analysis	No. of Samples	Duration of Sample, min
SP1	GD	Gas Chromatography	3	10
SP2A	GD	MINICAMS®	4+ ^b	10
SP3A	GD	Gas Chromatography or Acetylcholinesterase Method	2-3	Varies ^c
SP4A	GD	MINICAMS®	0-1	10
SP5A	GD	MINICAMS®	0-1	10
SP2B	HF	Fluoride Ion Electrode	2	10
SP3B	HF	Fluoride Ion Electrode	2-3	Varies ^c
SP4B	HF	Fluoride Ion Electrode	2	10
SP6B	HF	Fluoride Ion Electrode	2	10
SP2C	H ₃ PO ₄ /P ₂ O ₅	Ascorbic Acid Method	2	10
SP3C	H ₃ PO ₄ /P ₂ O ₅	Ascorbic Acid Method	2-3	Varies ^c
SP4C	H ₃ PO ₄ /P ₂ O ₅	Ascorbic Acid Method	2	10
SP6C	H ₃ PO ₄ /P ₂ O ₅	Ascorbic Acid Method	2	10

^aSamples designated B and C were collected in two bubblers as one sample. The sample volume was divided to accommodate all analyses. Samples SP3A, B, and C were all taken as one sample, however.

^bThe number of samples taken was limited by agent GD total injection time, duration of sampling, and frequency of sampling SP4A and SP5A.

^cDuration of sampling the water condensate (SP3) depended on the presence of water in the reservoir (sump).

used. During the first 2 min of a new cycle, the sorbent was desorbed and the CW agent concentration was determined for the preceding cycle. During the remainder of the cycle, air was pumped through the sorbent by the MINICAMS® pump at a rate of about 1 L/min.

MINICAMS® Operating Parameters and Calibration

The standard MINICAMS® operating parameters for GD analysis were modified to allow the separation of GD from an unknown closely eluting compound. Also, the analysis variations were checked in the presence of acids HF, H₃PO₄, and P₂O₅ in the sample.

The 8-h TWA for GD is 0.03 ng/L air, or 0.144 ng in a 4.8-L sample. In the setup used to monitor the catalytic reactor system, the typical sampling rate was about 0.6 L/min for a total sample volume of 4.8 during the 8-min sample time of a 10-min cycle. A GD standard containing 0.072 ng/μL GD in hexane was prepared and used to calibrate MINICAMS®. Several injections of 2 μL (1 TWA), 5 μL (2.5 TWA), and 10 μL (5 TWA) were made into the inlet valve. MINICAMS® was then calibrated by selecting four of the peak height values so that a linear calibration was obtained. The calibration was checked (between two runs in the same day) by making several 10 μL injections of the 0.072 ng/μL standard and comparing that average to the average value for a 10 μL injection before the test. The preconcentrator tube was changed at the beginning of each test day, and between two tests in one day if the response had changed by 15 percent or more. A calibration was performed each time the preconcentrator tube was changed. A 95 percent confidence level was calculated for the pretest or background GD level. A value lower than the 95 percent level was considered 0 TWA of GD.

The calibration procedure calculates the amount (ng) of agent detected. This value is then divided by the air sample volume obtained from the mass flowmeter to yield the agent concentration.

BY-PRODUCT ANALYSIS

Only the acidic by-products HF and H₃PO₄ were determined in the reactor effluent air stream. Samples were collected from ports SP2, SP4, and SP6. Acids in the condensate were determined at sample port SP3.

The reactor effluent gas streams were sampled with two bubblers connected in series at the outlet of sampling ports SP2, SP4, and SP6. The bubblers were filled with 100 mL of 1.0 M NaOH. The filled bubblers were placed in an icewater bath, and the gas stream was sampled at one to two liters per minute for at least 10 minutes. The condensate samples taken at SP3 were presumed to contain GD, and therefore were stored in plastic bottles in the XDS refrigerator. An aliquot of the SP3 condensate was mixed with NaOH to make a sample solution containing 1 M NaOH. The SP3 mixtures were allowed to stand for 24 h before they were analyzed in the same manner as the samples collected in 1 M NaOH.

HF (or F) Analysis

The fluoride ion electrode was used to measure F⁻ ion in the range of 0.02 to 20 mg F/L. The method used for the analysis was a modification of the method given in *Standard Methods for the Examination of Water and Wastewater*. The major modifications were the neutralization of the 1 M NaOH with HCl and the use of a commercially available ionic strength adjustment buffer. Several blank solutions (1 M NaOH with no added F⁻) were analyzed. The value for the blanks was used to determine a 95 percent confidence limit using a t-test. Values of F⁻ below this limit were reported as zero.

H₃PO₄ (or P) Analysis

The ascorbic acid method of analysis was used for P (as H₃PO₄ or P₂O₅) analysis. The method was a modification of the one given in *Standard Methods for the Examination of Water and Wastewater*. A

95 percent confidence limit was determined by analyzing several blank (1.0 M NaOH with no added PO_4^{3-}) solutions. A one-fail t-test was used to determine the 95 percent confidence limit of the blank solutions. Values below this limit were reported as zero.

GD PRESENCE IN CONDENSATE ANALYSIS

The condensate collected at SP3 may contain GD as well as fluoride or phosphate. The samples were collected in plastic bottles and stored in the XDS refrigerator. Within 24 hours, the samples were analyzed for GD using the acetylcholinesterase method. Since this method is not specific for GD, the presence of other acetylcholinesterase inhibitors (e.g., fluoride ions) could interfere with the GD determination. Large concentrations of HF (or F^-) could inhibit acetylcholinesterase and be reported as GD. Thus, the GD concentration reported for SP3 was the maximum amount of GD that could be present. The reported concentration represents the sum of the inhibition caused by GD, F^- , and any other inhibitor present in the condensate.

The method used for GD air monitoring uses acetylcholine inhibition to determine the GD concentration. Since the method is not specific for GD, other acetylcholinesterase inhibitors may interfere with the GD determination. However, since other agents were not used in the laboratory while the GD was being used, this was not likely.

CONCLUSIONS

A full-scale catalytic oxidation process was designed and successfully tested for the purification of a 260 scfm (7400 slpm) CW-contaminated air stream. The analytical schemes developed under this study offer a detailed approach toward defining whether a catalytic post-filter is required to provide collective protection against chemical threats. The full-scale tests showed that:

- Agent GD concentration in the effluent air stream for all conditions tested was below the 0.1 TWA level ($0.00003 \text{ mg GD/m}^3$), thereby achieving agent reduction ratios of 200,000,000 in a residence time of less than 0.2 s.
- Acid by-product HF concentration was below the short-term (15-min) allowable exposure limit of 2.5 mg/m^3 at the condenser outlet. Most of the acid HF, however, was removed downstream of the reactor.
- Acid by-product H_3PO_4 (samples analyzed for phosphorus ion) was removed in the reactor, but any remaining H_3PO_4 was removed downstream of the reactor.

ACKNOWLEDGMENTS AND DISCLAIMER

This work was supported by Air Force Contract No. F33615-86-R-3409. Ms. Mayra Martinez was the Contracting Officer's Representative. The catalytic reactor system was designed and fabricated by Allied Signal AiResearch, Los Angeles Division. The live agent tests were conducted at IIT Research Institute. The views expressed in this article are those of the authors and do not reflect the official policy or position of the Department of Defense or the U.S. Government.

REFERENCES

1. K. J. Clarke, R. Tom, and G. Lester. Catalytic Oxidation of GD over a Monolithic PT/TiO_2 Oxidation Catalyst. Presented at the Scientific Conference on Chemical Defense Research, U.S. Army Research, Development and Engineering Center, 19-22 November 1991.
2. G. L. Ellman, K. D. Lowtney, V. Anders, Jr., and R. M. Featherstone. *Biochem. Pharmacol.* 7:88-95 (1960)

Blank

CHARACTERIZATION OF DISULFIDE LINKAGES IN A CARDIOTOXIN BY ELECTROSPRAY IONIZATION

T. Krishnamurthy*, A.J. Kubis, J.G. Freedy, T.D. Biggs

U.S. Army Chemical Research, Development, and Engineering Center, Aberdeen Proving Ground, MD 21010-5423, USA

C.R. Hauer

University of Virginia, Charlottesville, VA 22901

K. Hayashi

Gifu Pharmaceutical University, Gifu 502, Japan

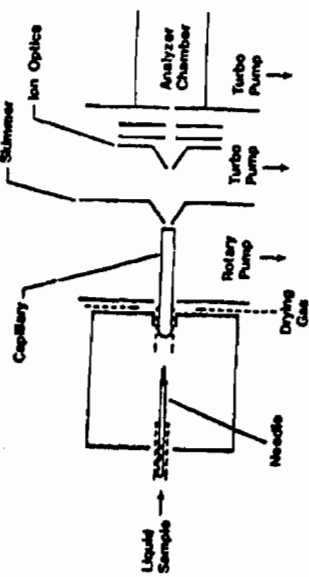
The disulfide linkages in a cytotoxic peptide were identified using a few nanomoles of the intact peptide and techniques such as enzymatic cleavages, electrospray ionization, and mass spectrometry. The results are comparable with x-ray crystallographic data.

INTRODUCTION

Recently introduced electrospray technique (Figure 1), involving the new approach in sample introduction and ionization, overcomes most of the difficulties experienced so far in the detection and characterization of polar higher molecular weight molecules.¹ The ionization technique involves the introduction of the aqueous solution containing methanol and sample through a capillary needle and applying the electric potential across the needle. The charged droplets thus formed, containing the ionized molecules with multiple charges surrounded by solvent molecules, undergo desolvation while moving through a glass capillary. The solvent molecules are removed by multistage pumping and the separated multiply charged ions are focused through a set of lenses and detected by mass spectrometric technique.¹⁻²

The number of ions with various charge distributions formed during the ionization process depends on the number of basic sites present in the molecule. As a result, a series of ions with charges +1 to +n (in the positive mode) are formed while ionizing a molecule with n basic sites. The m/z of compounds with molecular weights exceeding several thousand Daltons are thus reduced, which enables the accurate measurement of the m/z of the corresponding multiply charged ions, and hence, the molecular weight of the compound.¹ The technique could be applied for the measurement of molecular weights of molecules ranging from 200 to at least 100,000 Daltons, with an sensitivity exceeding by an order of magnitude that during the FAB or liquid-SIMS ionization.²

Figure 1. ELECTROSPRAY IONIZATION SOURCE.



ENZYMATIC FRAGMENTS

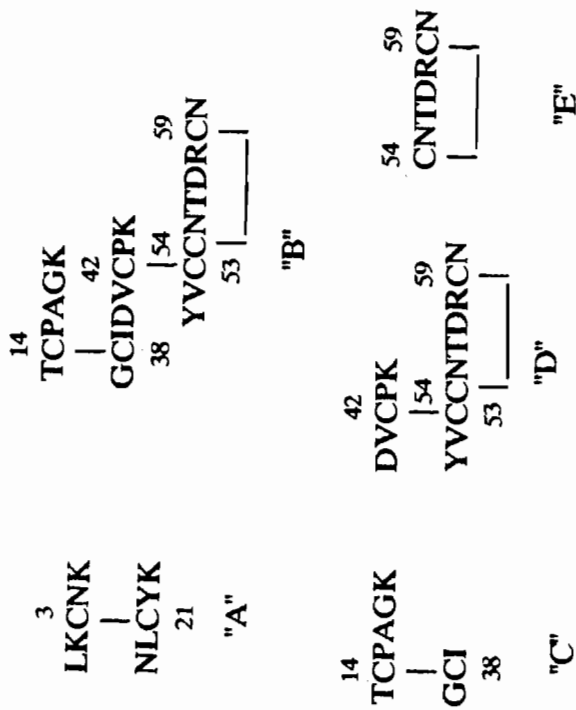
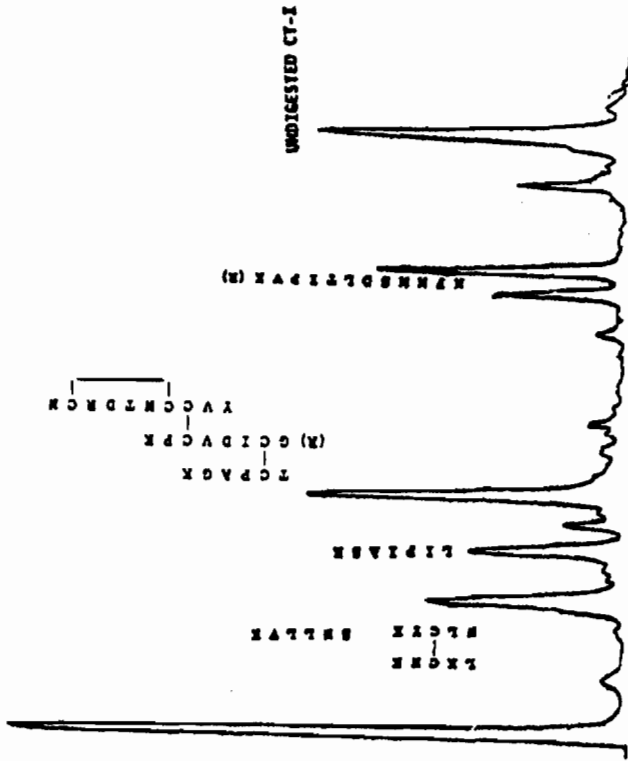


Figure 2. LC CHROMATOGRAM OF TRYPTIC DIGEST OF CARDIOTOXIN.
(RP-300, 0-40% solvent B in 40 minutes, A=0.1% aqueous TFA, B=0.085% TFA in Acetonitrile.)



We have also applied this electrospray ionization technology in combination with enzymatic cleavage (trypsin, Asp-N endoproteinase) and microbore HPLC technique to characterize the four disulfide bridges between cysteines present in a 60 residue basic polypeptide cardiotoxin.³ Such information could be obtained thus far only by complex techniques such as x-ray crystallography and 3d-nmr spectroscopy, both approaches requiring several micromoles of pure intact compounds.

EXPERIMENTAL

The entire investigation was conducted using a Finnigan-MAT TSQ-70 tandem mass spectrometer fitted with an electrospray ionization source manufactured by Analytica of Branford. Purification of standard materials and enzymatic and chemical degradation products was carried out on an Applied Biosystems 130-A microbore HPLC system.

All peptide and protein standards and proteolytic enzymes were purchased from Sigma Chemicals, St. Louis, MO, and Boehringer Mannheim, Indianapolis, IN. Cardiotoxin (CT-1) was isolated from *Naja Naja atra* by Prof. Kyoza Hayashi, Gifu Pharmaceutical University, Gifu, Japan.

Stock solutions of standards and samples (100-500 pmole/ul) were made up by dissolving the accurately weighed amount in 1-2% aqueous acetic acid. Any required dilution was carried out using the same solvent and treated with equal volume of methanol. The analyte concentration was adjusted to be 5-20 picomole/ul in the solution used during the analysis.

Electrospray-MS Analysis: The solution containing the analyte in the appropriate concentration was infused into the electrospray ionization source at a rate of 1 ul/min from a 100 ul syringe. Liquid nitrogen was used as the drying gas maintaining the temperature of the heater at 180°C. A potential of 2800 volts was applied through the needle inducing the ionization. The multiply charged ions were detected by maintaining the multiplier voltage at 1400-1800 volts.

Tryptic Digestion of Intact Cardiotoxin I: The polypeptide (1 nmol) was dissolved in solution (pH 8.6, 100 ul) containing 5M urea and 200mM tris and further diluted with water (100 ul). The solvent was made fresh and cyanate free. The peptide solution was treated with trypsin (0.7 ug), maintaining the enzyme/protein ratio to be 1/10. The resultant solution was incubated overnight at 37°C. The reaction mixture was frozen at -50°C to halt the proteolysis and lyophilized. The lyophilized mixture was dissolved in either aqueous 0.1% trifluoroacetic acid or 2% acetic acid solution and subjected to HPLC separation prior to MS analysis.

Cleavage of Tripeptide with Asp-N Endoproteinase: The tripeptide (1-2 nM) residue was treated with 6M urea (25 ul), 200mM tris buffer (pH, 8.0; 20 ul), water (155 ul) and 100mM Magnesium Chloride (3ul) and incubated with Asp-N endoproteinase (1 part per 100 parts of protein w/w) at 37°C overnight. The reaction mixture was freeze dried and redissolved in 0.1% aqueous TFA and chromatographed over an RP300 microbore column prior to MS analysis.

Figure 3. DIPEPTIDE FROM TRYPTIC DIGEST OF CARDIOTOXIN.

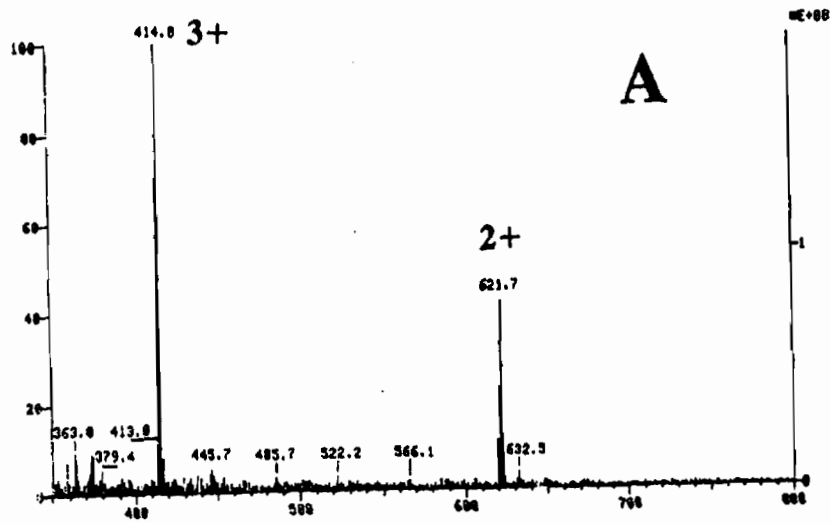
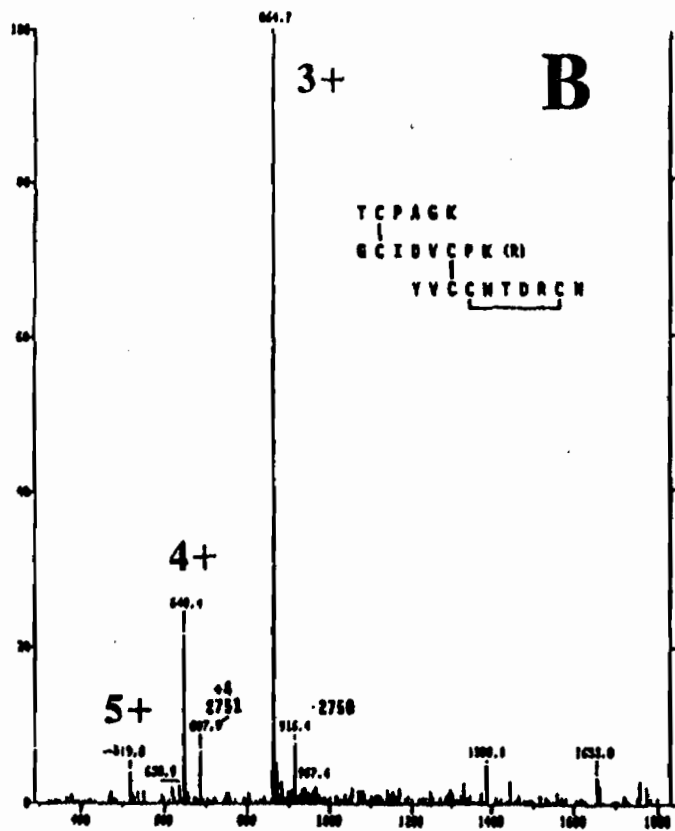


Figure 4. TRIPEPTIDE FROM TRYPTIC DIGESTION OF CARDIOTOXIN.



RESULTS AND DISCUSSION

The primary structure determined earlier by microsequencing method³ is illustrated below:

```
          10          20          30
L K C N K L I P I A S K T C P A G K N L C Y K M F M M S D L
          40          50          60
T I P V K R G C I D V C P K S N L L V K Y V C C N T D R C N
```

The complexity imposed by steric limitations in the proteolysis of the intact cardiotoxin with trypsin was overcome by using a denaturant such as 2M urea. The denaturant also reduced the activity of trypsin hence 1:10 ratio of trypsin to cardiotoxin was required to cleave the intact polypeptide even with limited efficiency. Due to these limitations, the degree of proteolysis was observed to be ranging from 10-50%. The product was lyophilized, dissolved in 0.1% aqueous trifluoroacetic acid and chromatographed over a RP300 reverse phase microbore HPLC column (Figure 2). The separated fractions were lyophilized and redissolved in 1:1 ratio of 1% aqueous acetic acid and methanol. The solutions were infused into the electrospray ionization source and their corresponding mass spectra were recorded.

All fragments formed during the tryptic digestion of cardiotoxin were identified, as shown in Figure 2. One of the fragments (Figure 3, 1,241 Daltons) could only have been formed by the combination of two portions, LKCNK and NLCYK, of the intact molecule. This established one of the four disulfide bridges to be between cysteine-3 and cysteine-21 ("A").

A fragment with m/z 2592 (Figure 4) was also observed, which later identified to be a tripeptide with 6 cysteines linked by three disulfide bridges. It produced three peptides on reduction with dithiothreitol which were identified from their corresponding ESI mass spectra to be GCIDVCPK (834 Daltons), YVCCNTDRCN (1190 Daltons), and TCPAGK (576 Daltons). The structure of the tripeptide was assigned to be "B".

On digestion with Asp-N endoproteinase of the tripeptide two products (Figure 5 & 6) were isolated. They were identified as "C" (864 Daltons) and "D" (1,745 Daltons) based on their measured molecular weights. The detection of the former residue established the second disulfide linkage to be present between Cys-14 and Cys-38.

The positions of the other two disulfide linkages cannot be established by enzymatic cleavages of either "A" or "C" due to the presence of two adjacent peptide linked cysteines (Cys-53 and Cys-54). Hence, the tripeptide was subjected to automated Edman sequencing process.⁴ The amino acids cleaved during the first cycle were identified to be T, G, and Y. During the next two cycles, the amino acids cleaved were identified to be V (cycle 2) followed by P and I (cycle 3). The cysteines are not identified during the process. The remnant after the third Edman cycle was desorbed from the PVDF membrane (Pro-blott) using 70% aqueous isopropanol (50 ul). The desorbed product was lyophilized and subjected to ESI-mass spectral analysis. The observed peaks (Figure 7) at m/z 412 and 823 in Figure 7 corresponded to the peptide "E", establishing the third disulfide bridge to be between Cys-54 and Cys-59 and the fourth by default to be between Cys-42 and Cys-53.

Figure 5. ASP-N PRODUCT OF TRIPEPTIDE.

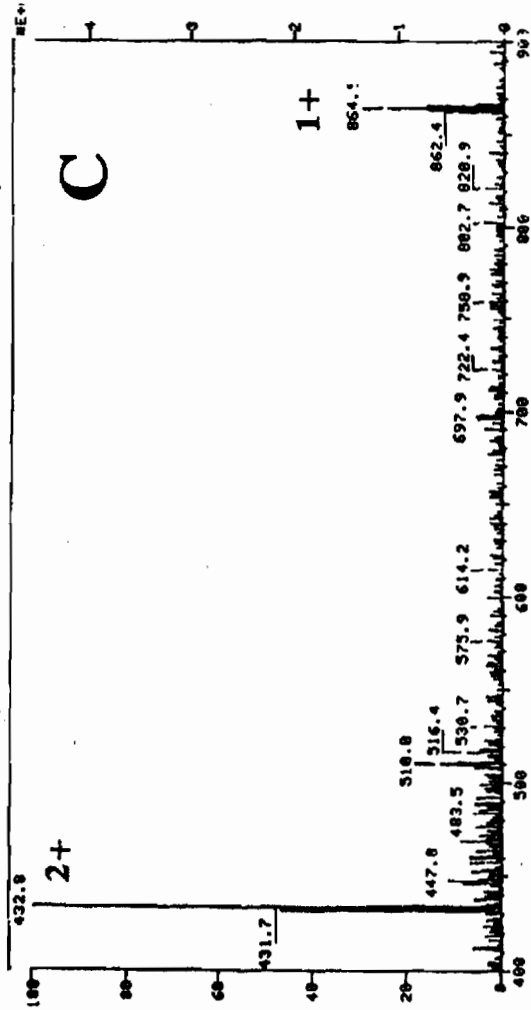


Figure 6. ASP-N PRODUCT OF TRIPEPTIDE.

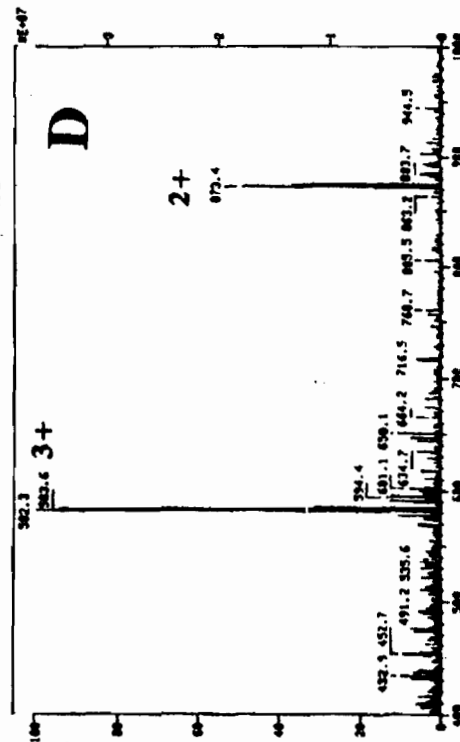
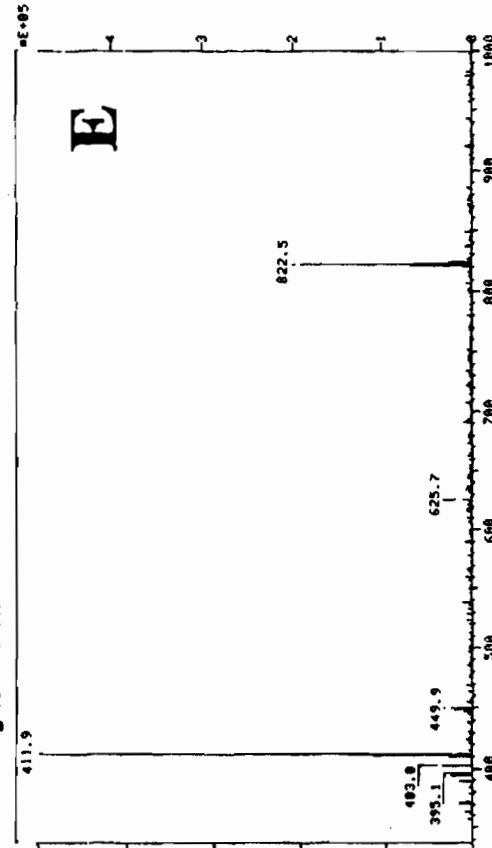


Figure 7. EDMAN DEGRADATION PRODUCT OF TRIPEPTIDE.



CHARACTERIZATION OF CONOTOXINS

T. Krishnamurthy, J.G. Freedy, A.J. Kubis, T.D. Biggs, and J.H. Brzezinski
U.S. Army Chemical Research, Development, and Engineering Center, Aberdeen Proving Ground, MD, 21010, U.S.A.

Peptides from *Conus betulinus*, found in the Bay of Bengal, crude venom were separated and purified. The amino acid compositional analysis, molecular weights, n-terminus sequences of some of the peptide components are reported.

INTRODUCTION

All cone snail species are predators and utilize the venom to capture their prey.¹ The venom contains, totaling well over 20, a variety of toxic peptides affecting ion channels and receptors in the neuromuscular system. The conus peptides are 10-30 amino acids length and rich in disulfide bonds.¹ The peptides targeting the acetylcholine receptor are made up of only 13-15 amino acids compared to 40-100 amino acid length peptides with similar activity produced by spiders, scorpion and elapidae snakes.¹ Despite their extreme toxicity, these peptides have been applied for the characterization and isolation of receptor proteins and specific blockage of ion channels.¹

Recently, we have initiated the characterization of venom from fish and snail hunting cone snails found in the Bay of Bengal area. Our strategy for characterizing peptides found in *Conus betulinus* venom involved the application of electrospray ionization, mass spectrometry and tandem mass spectrometry, amino acid analysis and automated Edman sequencing procedures. The crude venom was subjected to rigorous clean-up and separation over size exclusion and reverse phase HPLC columns prior to any investigations. The peptides, isolated from *Conus betulinus*, thus far characterized indicated them to be similar in structure to other conotoxins.¹

EXPERIMENTAL

Separation and purification of the components were carried out using ISCO LC-2600, Applied Biosystems (ABI) 130A and 140A, and Beckman 112 HPLC systems. Mass spectra were recorded using Finnigan-MAT TSQ-70 tandem mass spectrometer fitted with electrospray ionization source manufactured by Analytica of Branford. The amino acid compositional analysis and the sequencing data were obtained using Applied Biosystems 420A amino acid analyzer and 477A peptide sequencer, respectively.

Fused silica C-18 column was purchased from LC Packings, San Francisco, CA. All reagents and solvents used were HPLC or analytical grade. Special reagents supplied by

FIGURE 1
 Size exclusion Chromatography of Crude *Conus betulinus*
 Venom- ISCO LC-2600 HPLC System; G200SW Column; Isocratic
 Elution (0.1% Aqueous TFA, 1 ml/min.)

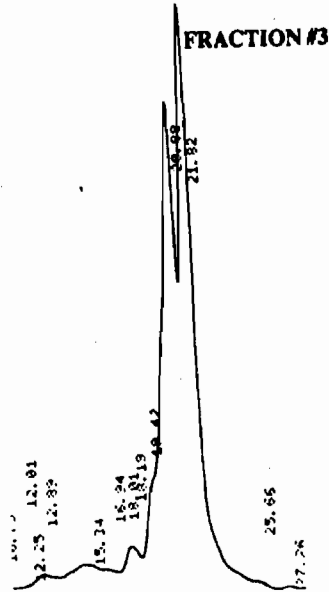
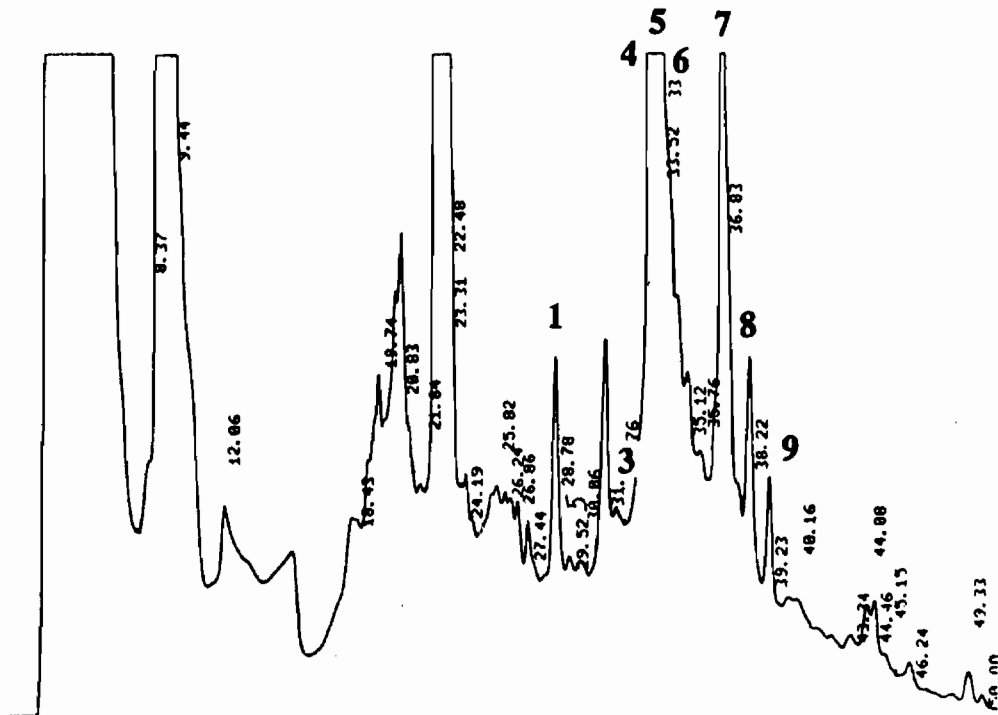


FIGURE 2
 Separation of *Conus betulinus* Venom Components- C₁₈ Column
 (2.1 x 30 mm, 7u); 0-40% Solvent B (0.085% TFA in Acetonitrile) in
 Solvent A (0.1% Aqueous TFA) in 40 minutes.



ABI were utilized to obtain compositional analysis and sequencing information. The polytetrafluoroethylene (PTFE) syringe filters were purchased from Baxter Scientific Products, Columbia, MD.

Conus betulinus Stock Solution: The lyophilized crude venom (35 mg) was treated with 0.2% aqueous trifluoroacetic acid (TFA, 2 ml) in aliquots. The mixture was vortexed vigorously after each addition of the solvent. The solution was filtered through a 0.45 μ PTFE (Gelman) syringe filter to remove any insoluble particles present. The remnant in the filter was washed with additional (3x50 μ l) 0.2% aqueous TFA. The combined filtrate was transferred in 100 μ l aliquots to 1.5 ml polypropylene vials and stored at -20°C until use.

Chromatographic Separation of Conus betulinus Venom: The preliminary separation, based on the previously reported molecular weights of the conus peptides¹, were performed using ISCO LC-2600 HPLC system (70psi) and a G200SW HPLC column. The crude solution (100 μ l) was injected into the column and eluted isocratically (0.1% TFA, 1ml/min). The effluent was monitored at 254nm (0.5 AUFS) and fractions were collected for each peak. The collected fractions were lyophilized and stored at -20°C until further use.

The further separation was performed by reverse phase chromatography using ABI 130A HPLC system. Each of the above fractions were redissolved in 0.2% aqueous TFA and loaded into a OD300 (2.1 x 30 mm, 7 μ) column. The components were eluted from the column by varying the solvent from 0% to 40% solvent B (0.085% TFA in acetonitrile) in solvent A (0.1% aqueous TFA) in 40 minutes. The flow rate was maintained at 200 μ l/min throughout the process. Collected fractions were lyophilized and stored at -20°C.

Mass Spectral Analysis of Conus betulinus Components: Solution (1 μ l) containing chromatographically purified component(s) was injected onto a fused silica C-18 column (320 μ x 15cm, 5 μ) column fitted in an ABI 140A HPLC syringe pump. The component was eluted at a flow rate of 2.5 μ l/min using the same solvent system mentioned above. The eluted compound was introduced on-line into the electrospray ionization source and ionized (4keV, N₂ as drying gas at 24 psi, and 250°C) using 2-methoxyethanol (2 μ l/min) and nitrogen (24 psi) as sheath flow and gas, respectively. The mass spectra were recorded by scanning from 350 to 2000 m/z in 5 sec.

Amino Acid Compositional Analysis: The fractions were subjected to on-line vapor phase hydrolysis (6N HCl, 160°C), derivatization (phenylisothiocyanate), and analysis (C-18, 2.1 x 30mm, 7 μ , same solvent system as above) as per Applied Biosystem protocol using the specially formulated solvents and reagents supplied by the company.

Automated Edman Sequence Analysis: The coupling with n-terminus residue (phenylisothiocyanate), cleavage (TFA), and rearrangement of the cleaved amino acid derivative (25% aqueous TFA, 60°C) were conducted using the ABI protocol for the automated Edman sequencer.

RESULTS AND DISCUSSION

The filtered solution of the crude venom was subjected to size exclusion chromatography (SEC) over a G2000SW column (Figure 1). Fraction 3 was further separated over a

TABLE 1

AMINO ACID	CONUS FRACTIONS								
	1	2	3	4	5	6	7	8	9
Asp		1	1	3	2	3	2		1
Glu	8		1	1	2	2	2	1	
Ser			1	3	2	2			
Gly	1		1	4	3	3	4	2	2
His				1	1	1			
Arg									
Thr		1	1			1			1
Ala			1	3	2	2	2		
Pro							5	4	6
Tyr				2	1	1			
Val						1	1		
Met									
Cys				3	2	3			
Ile	9			1	1	1		1	1
Leu		1	1			1	1		1
Phe									
Lys					1				

TABLE 2

FRACTION #	MW*	SEQUENCE INFO [†]
2	1064.7	
4	3996.6	GSXGG?XIQDSHHG?SXAXXDAYSYA.....
5	1186.6 1418.4	
6	1642.6	NTLXPLIPG

* From electrospray mass spectral data
[†] ?, hydroxyproline?; X, cysteine

TABLE 3

PEAK NUMBER*	PARTIAL SEQUENCES [†]
1	G-X-G-G-V-X-A-Y-G-S-E-X-HYPRO-S-S-X-N-T-G-Y-S-X-Q-Q-X
2	G-X-G-G-V-X-A-Y-G-S-E-X-HYPRO-S-S-X-N-T
3	G-S-X-G-G-HYPRO-X-I-Q-D-S-H-H-G-HYPRO-S-X-A-X-HYPRO-D-D-A-Y-S-Y-A
4	S-R-L-D-G-T-Y-X-X-N-R-F-Q-X-X-X

* Refer to Figure 5.
[†] HYPRO, hydroxyproline; X, cysteine

reverse phase C-18 column (Figure 2). The collected fractions were lyophilized and redissolved in 0.2% TFA.

Each of the fractions were loaded on a clean glass disc provided by ABI. The disc was dried and subjected through automated procedure for hydrolysis, derivatization and on-line HPLC analysis. The eluted derivatives of the amino acids, released during the hydrolysis of the individual peptides, were analyzed quantitatively by previously established values for the amino acid standards (Pierce H). The compositional values established thus far are listed in Table 1. These values may not be absolute due to the destruction (tryptophan), oxidation (methionine, cysteine), and hydrolysis of the amide side chain to the carboxylic group (asparagine, glutamine) during the acid hydrolysis of the peptide. The data was hence evaluated critically due to these limitations. However, it would be extremely valuable for the selection of potential enzymes for cleavage of the peptides into smaller fragments of adequate size for determining the total sequences of the amino acids in the intact peptide.

The separated components were also subjected to electrospray ionization in order to measure their corresponding molecular weights. The component(s) were loaded on a microcapillary C-18 column, to ensure optimum separation, and introduced into the electrospray source. The molecular ions formed with single or multiple charges were detected. In most cases the doubly charged molecular ions were more pronounced than the corresponding singly charged ion. The number of ions formed with multiple charges is based on the number of basic amino acids present in the peptide. The observed m/z values times the number of charges on the ion will provide the accurate molecular weight of the peptide (Figure 3,4). However, at times the number of charges on the ions observed in the mass spectrum cannot be evaluated, either due to presence of more than one component or when the compounds with higher molecular weights form too many ions with multiple charges. Under such conditions, the charges of the individual ions and the molecular weights are calculated by the procedure established by Smith, et al.² The molecular weights thus determined are listed in Table 2.

The n-terminus sequences of some of the fractions were determined by loading purified individual peptide on a porous glass fiber filter treated with Biobrene plus (ABI trademark). The Edman degradation processes were conducted as per the manufacturer's protocol. The sequence of the amino acids were determined from the n-terminus side of the peptide. The observed n-terminus sequence information are also listed in Table 2. Similarly partial sequences of some of the components present in the SEC fraction 2 (Figure 5), determined by automated Edman Degradation methods, are listed in Table 3.

Further investigation for improving the techniques and characterization of all of the peptides found in the *Conus betulinus* venom is under way.

CONCLUSIONS

Our proposed strategy, combining powerful and complimentary techniques such as HPLC, compositional analysis, automated Edman degradation procedure for sequencing n-terminus residues, electrospray ionization, and mass (and tandem mass) spectrometry,

FIGURE 3
Conus betulinus Fraction #2

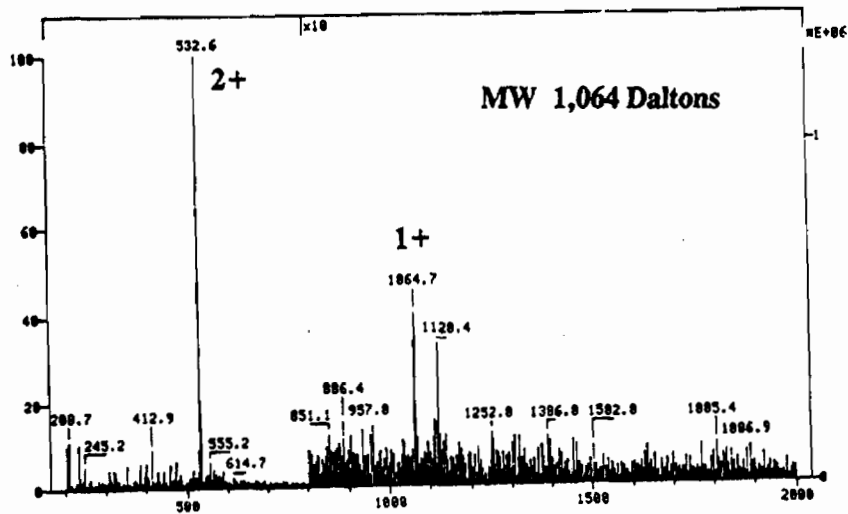
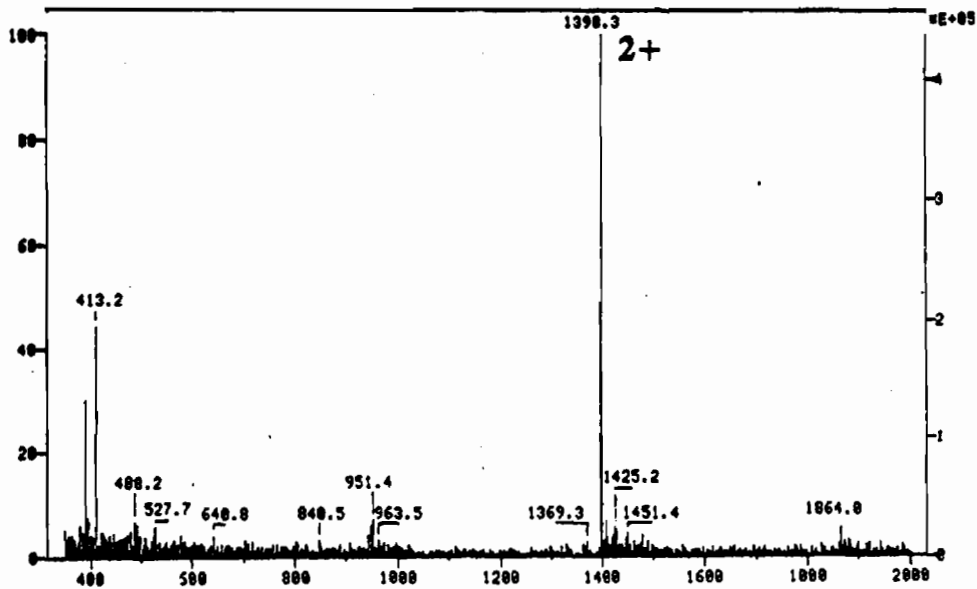


FIGURE 4
Conus betulinus Fraction #4

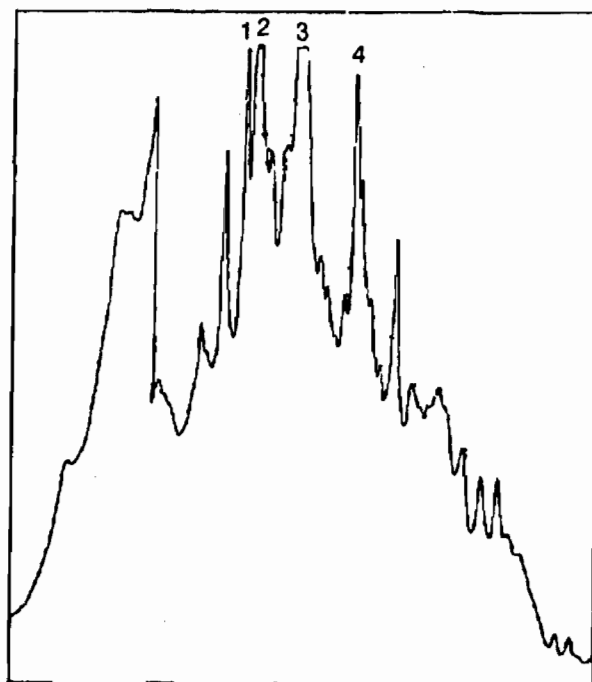


seems to be extremely effective in characterizing the complex mixture of peptides found in the *Conus betulinus* venom.

REFERENCES

1. B.M. Olivera, et al, *Science*, **249**, 257-263 (1990).
2. C.G. Edmonds and R.D. Smith in "Mass Spectrometry," *Methods in Enzymology*, Vol 193, ed J.A. McCloskey, pp. 412-434, (1990).

FIGURE 5
C₁₈ Chromatogram of SEC Peak 1, *Conus betulinus*



U.S. GOVERNMENT PRINTING OFFICE 1993:343:285, 80013